MEDICAL
RADIOLOGY

Diagnostic
Imaging

A. L. Baert
M. Knauth
K. Sartor

Pediatric Chest Imaging

Chest Imaging in Infants and Children

2nd Revised Edition

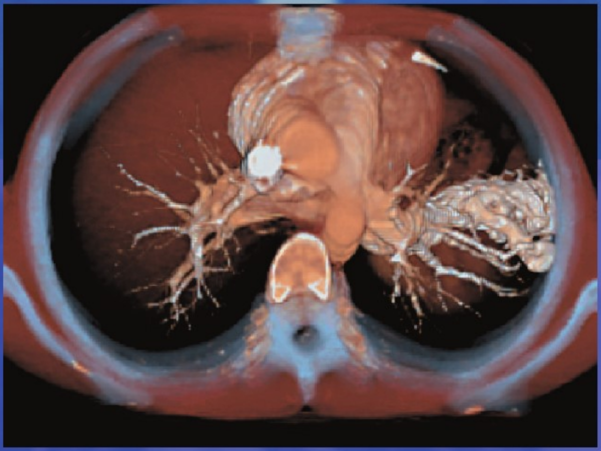

J. Lucaya
J. L. Strife
Editors

Springer

MEDICAL RADIOLOGY

Diagnostic Imaging

Editors:
A. L. Baert, Leuven
M. Knauth, Göttingen
K. Sartor, Heidelberg

J. Lucaya · J. L. Strife (Eds.)

Pediatric Chest Imaging

Chest Imaging in Infants and Children

2nd Revised Edition

With Contributions by

C. Aso · J. Bar-Ziv · A. S. Brody · A. Castellote · T. Chung · E. J. Crotty · P. A. Daltro
L. F. Donnelly · H. D. Le Pointe · G. F. Eich · G. Enriquez · D. P. Frush · P. García-Peña
M. J. Gelfand · D. L. Gilday · S. C. Kaste · C. J. Kellenberger · B. Z. Koplewitz
R. Krishnamurthy · L. Lucaya · J. M. Mata · K. McHugh · E. Nunez-Santos
C. M. Owens · L. Sena · X. Serres · J. L. Strife · H. Werner · U. V. Willi

Foreword by

A. L. Baert

With 445 Figures in 925 Separate Illustrations, 54 in Color and 19 Tables

Springer

Javier Lucaya, MD
Emeritus, Department of Pediatric Radiology
and Institute of Diagnostic Imaging
Vall d'Hebron Hospitals
Ps. Vall d'Hebron 119–129
08035 Barcelona
Spain
and
Director, Department of Radiology
Hospital Quirón, Plaça Alfonso Comin 5–7
08023 Barcelona, Spain

Janet L. Strife, MD, FACR
Professor of Radiology and Pediatrics
University of Cincinnati College of Medicine
Department of Radiology
Cincinnati Children's Hospital Medical Center
3333 Burnet Avenue
Cincinnati, OH 45229–3039
USA

Medical Radiology · Diagnostic Imaging and Radiation Oncology
Series Editors:
A. L. Baert · L. W. Brady · H.-P. Heilmann · M. Knauth · M. Molls · C. Nieder · K. Sartor

Continuation of Handbuch der medizinischen Radiologie
Encyclopedia of Medical Radiology

Library of Congress Control Number: 2007922037

ISBN 978-3-540-32675-5 Springer Berlin Heidelberg New York

This work is subject to copyright. All rights are reserved, whether the whole or part of the material is concerned, specifically the rights of translation, reprinting, reuse of illustrations, recitations, broadcasting, reproduction on microfilm or in any other way, and storage in data banks. Duplication of this publication or parts thereof is permitted only under the provisions of the German Copyright Law of September 9, 1965, in its current version, and permission for use must always be obtained from Springer-Verlag. Violations are liable for prosecution under the German Copyright Law.

Springer is part of Springer Science+Business Media

http//www.springer.com
© Springer-Verlag Berlin Heidelberg 2008
Printed in Germany

The use of general descriptive names, trademarks, etc. in this publication does not imply, even in the absence of a specific statement, that such names are exempt from the relevant protective laws and regulations and therefore free for general use.

Product liability: The publishers cannot guarantee the accuracy of any information about dosage and application contained in this book. In every case the user must check such information by consulting the relevant literature.

Medical Editor: Dr. Ute Heilmann, Heidelberg
Desk Editor: Ursula N. Davis, Heidelberg
Production Editor: Kurt Teichmann, Mauer
Cover-Design and Typesetting: Verlagsservice Teichmann, Mauer

Printed on acid-free paper – 21/3180xq – 5 4 3 2 1 0

Foreword

This second, completely revised and updated edition provides a comprehensive overview of modern imaging of the pediatric chest.

As in the first highly successful edition, the main emphasis is put on the actual role of cross-sectional imaging methods in conjunction with standard chest radiography. This volume superbly covers our current knowledge and new insights into the indispensable role that radiological imaging plays in the appropriate management of infants and children with acute or chronic chest diseases.

The editors, Dr. J. Lucaya and Dr. J.L. Strife, have been very successful in engaging several international experts in the field, all with outstanding qualifications, to contribute to individual chapters and I would like to thank and congratulate them for the expeditious and excellent coordination of the editorial preparation of this second edition.

I am confident that this outstanding textbook will again stimulate great interest among both general and specialised pediatric radiologists, as well as among neonatologists, pediatricians and pediatric surgeons. It will certainly enjoy the same success with our readers as its first edition.

Albert L. Baert
Series editor

Preface

It has been 5 years since the first edition of Pediatric Chest Imaging and there continue to be advancements in imaging technology which contribute to improved patient care and to our understanding of chest diseases. The pediatric chest is still the most commonly ordered imaging study in the world and pediatricians, neonatologists, radiologists and pediatric radiologists will appreciate the information on new technology, as well as that on advancements in knowledge concerning diseases. All chapters have been updated and new chapters on important topics such as neonatal chest, cardiac CT and fetal MR have been added.

The book was dedicated to Dr. Frederic Silverman and Dr. Benjamin Felson, who were instrumental in our early training in radiology. This past year, Dr. Frederic Silverman, one of the giants in pediatric radiology, died. He was one of the early radiologists to recognize the skeletal manifestations of child abuse. He was an advocate for children and tried to stress the importance of clinical information as it pertained to appropriate imaging of the pediatric patient. We have great respect for his opinions and for his legacy. In this new edition, we have tried to re-enforce one of the priorities of the first edition, which is to recognize the importance of imaging children with as little radiation and aggression as possible. We were saddened by the untimely death of one of our authors, Jack Haller, M.D., who was an enthusiastic teacher, writer and scholar.

As the editors are preparing for retirement, we thought it was appropriate to dedicate the book to all of our trainees and colleagues, many of whom have become leaders in pediatric imaging. These individuals are the future of our subspecialty and through their dedication, expertise, knowledge and stewardship, we know that the subspecialty will be in good hands. We are grateful to the authors, many of whom are our friends, colleagues and former trainees. A special thanks is extended to Kathy Umberg and Judy Racadio, M.D., who helped coordinate the project and facilitated communication with the European office. We are particularly grateful to Ms. Ursula Davis and Mr. Kurt Teichmann at Springer-Verlag for their editorial assistance in providing expertise and knowledge.

We hope their second edition of Pediatric Chest Imaging will be helpful to all those physicians caring for children and that the updated information will ultimately improve outcomes in both common and rare diseases of the pediatric heart and lungs.

Barcelona — Javier Lucaya
Cincinnati — Janet L. Strife

Contents

1 **Chest Ultrasound (US)**
Goya Enriquez, Celesino Aso, and Xavier Serres 1

2 **The Contribution of Nuclear Medicine to Pulmonary Imaging**
Michael J. Gelfand and David L. Gilday 37

3 **Helical Multidetector Chest CT**
Pilar García-Peña and Catherine M. Owens 47

4 **High-Resolution CT of the Lung in Children**

Part I: Technique, Indications, Anatomy and Features of Lung Disease
Javier Lucaya 78

Part II: Clinical Applications
Hubert Ducou Le Pointe 100

5 **Pulmonary Malformations Beyond the Neonatal Period**
Josep M. Mata and Amparo Castellote 123

6 **CT of Acute Pulmonary Disease: Infection, Infarction, and Trauma**
Lane F. Donnelly 147

7 **Pediatric Tuberculosis**
Pedro A. Daltro and Eloá Nunez-Santos 165

8 **How to Perform and Interpret MR Sleep Studies for Obstructive Sleep Apnea in Children**
Lane F. Donnelly 183

9 **Foreign Body Aspiration: Imaging Aspects**
Benjamin Z. Koplewitz and Jacob Bar-Ziv 195

10 **Imaging Evaluation of the Thymus and Thymic Disorders in Children**
Donald P. Frush 215

11 **Lymphoma – Controversies in Imaging the Chest**
Sue C. Kaste 241

12 **Chest Tumours Other than Lymphoma**
Kieran McHugh 263

13 **Thoracic Manifestations of Systemic Diseases**
Alan S. Brody 289

14 **Radiology of the Chest Wall**
Georg F. Eich, Christian J. Kellenberger, and Ulrich V. Willi 313

15 **Pediatric Cardiac MRI**
Rajesh Krishnamurthy and Taylor Chung. 337

16 **Pediatric Cardiac CT**
Laureen Sena, Rajesh Krishnamurthy, and Taylor Chung 361

17 **Fetal MRI of the Chest**
Pedro A. Daltro and Heron Werner 397

18 **Neonatal Chest Imaging**
Janet L. Strife and Eric J. Crotty 417

Subject Index 441

List of Contributors. 449

Chest Ultrasound (US)

1

Goya Enriquez, Celestino Aso, and Xavier Serres

CONTENTS

1.1 **Introduction** *1*

1.2 **Lung Parenchyma** *2*
1.2.1 Examination Technique *2*
1.2.2 Normal US Appearance and Artifacts *2*
1.2.3 Indications for Lung US *2*
1.2.4 Pulmonary Lesions *3*
1.2.4.1 Congenital Malformations of the Lung *3*
1.2.4.2 Lung Consolidation *8*
1.2.4.3 Lung Tumors *14*

1.3 **Pleura** *14*
1.3.1 Examination Technique *14*
1.3.2 Normal Sonographic Appearance and Artifacts *14*
1.3.3 Indications for Pleural US *15*
1.3.4 Pleural Abnormalities *16*
1.3.4.1 Pneumothorax *16*
1.3.4.2 Pleural Effusions *16*
1.3.4.3 Pleural Tumors *19*

1.4 **Mediastinum** *20*
1.4.1 Examination Technique *20*
1.4.2 Normal US Appearance, Artifacts and Pitfalls *21*
1.4.3 Indications for Mediastinal US *26*
1.4.4 Mediastinal Abnormalities *26*
1.4.4.1 Anterior Mediastinum *26*
1.4.4.2 Middle Mediastinum *31*
1.4.4.3 Posterior Mediastinum *32*

1.5 **Diaphragmatic Lesions** *32*

1.6 **Conclusion** *33*

References *33*

1.1 Introduction

Ultrasound (US) was initially applied mainly to detect pleural fluid; however, the applications of US for the chest have been widely extended over time (Yang et al. 1992a; Pan-Chyr et al. 1992; Civardi et al. 1993; Ben-Ami et al. 1993; Gehmacher et al. 1995; Seibert et al. 1998; Kim et al. 2000; Wernecke et al. 2000; Durand et al. 2001; Williams et al. 2003; Coley et al. 2005). Although air in healthy lungs and calcium in bony structures hinder transmission of the US beam, chest lesions involving the lung, mediastinum and pleura can be studied through anatomical "acoustic windows"(supraclavicular, suprasternal, parasternal and intercostal spaces), and by the transdiaphragmatic (subxiphoid and subcostal) approach. Furthermore, the lack of costal cartilage ossification and low bone mineral content in infants facilitates transosseous (trans-sternal and transcostal) scanning.

Technological advances in the geometry of the transducers have facilitated access to the chest through these acoustic windows. Color and power Doppler abilities permit study of vascular structures without the use of intravenous contrast material. Improvements in the resolution of the equipment provide images of excellent quality, which facilitates recognition of parenchymal, pleural and extra-pleural lesions (Weinberg et al. 1986; Muller 1993; Wernecke 2000; Gorguner et al. 2003; Zhu et al. 2005; De Pascale et al. 2006).

The technique has several advantages that are particularly beneficial in children: unlike CT, US does not use ionizing radiation or require administration of contrast material to identify vascular structures, most patients do not require sedation and examination can be performed at bedside. Fur-

---

G. Enriquez, MD
C. Aso, MD
Department of Pediatric Radiology, Vall d'Hebron Hospitals, ps. Vall d'Hebron 119–129, 08035 Barcelona, Spain
X. Serres, MD
Department of Radiology, Vall d'Hebron Hospitals, ps. Vall d'Hebron 119–129, 08035 Barcelona, Spain

thermore, sonography is the only technique that permits visualization of the lesions in real time and in different planes.

We have divided this chapter into lung parenchyma, pleura, mediastinum and diaphragm.

1.2
Lung Parenchyma

1.2.1
Examination Technique

Ultrasound examination of the lung parenchyma should be performed following careful evaluation of chest radiographs. According to the location of the lesion, the patient is placed in the supine, prone or lateral decubitus position, and the appropriate transducer and acoustic window are selected. Longitudinal, transverse or oblique views can be obtained as required. The transdiaphragmatic approach using the liver and spleen as acoustic windows is recommended to study lesions located at the base of the lung. The supraclavicular, parasternal and paravertebral approaches are indicated for evaluating apical and paramediastinal lesions. The remaining lung parenchyma should be approached intercostally.

The type of transducer used depends on the capabilities of the instrument and the operator's preferences; however, we can offer some general guidelines. We recommend sector or convex transducers for the transdiaphragmatic approach. When the patient is studied through the parasternal and intercostal windows, linear or convex transducers provide better identification of the pleuro-pulmonary interface. Sector transducers are not recommended with these two approaches since they produce reverberation artifacts in the near field that preclude identification of anatomical structures. When using the supraclavicular window, sector or small linear probes are highly appropriate. Transducer frequency varies with patient age and depth of the lesion. High-frequency transducers (5–10 MHz) are best for imaging neonates and infants and for very superficial lesions.

Color and power Doppler are very useful for complementing conventional studies in certain situations, e.g. when identifying vascular supply in pulmonary sequestration, assessing vascularity of lung consolidation and studying flow patterns within lung masses.

Sedation is seldom required for US exams performed in neonates and small children. In this regard it helps to warm the gel and to avoid examining hungry infants. It may be a good idea to show the children toys or movies to hold their attention during the study.

1.2.2
Normal US Appearance and Artifacts

The normal aerated lung produces echogenic images with characteristic posterior comet-tail reverberations behind the visceral pleura. These echogenic structures are induced by the air flowing in the alveoli and their intensity depends on their distance from the probe. When using a subcostal approach the comet-tail reverberations related to the aerated lung bases are observed adjacent to the diaphragm (Fig. 1.1a,b). During respiration the normal lung exhibits in real time a characteristic to-and-fro movement against the visceral pleura, known as the "gliding sign" (Ben-Ami et al. 1993; Seibert et al. 1998).

The main artifacts produced on US study of the aerated lung parenchyma are the so-called mirror image artifacts, caused by sound wave reflection when the ultrasound beam strikes the lung surface. Depending on the angle at which the US beam is directed during transdiaphragmatic scanning of the lung base, a dual image of the liver or spleen can be displayed above the diaphragm, simulating parenchymal consolidation. This artifact, known as pseudo-consolidation (Ben-Ami et al. 1993), is indicative of normal air-filled lung. Mirroring of the image can also occur when using color Doppler, resulting in duplication of vascular structures (Fig. 1.2).

1.2.3
Indications for Lung US

US of the lung parenchyma is indicated for the initial evaluation and follow-up of pulmonary congenital malformations discovered by prenatal ultrasound and to study pulmonary consolidations and masses. It can also be used to guide biopsies of superficially located lung tumors.

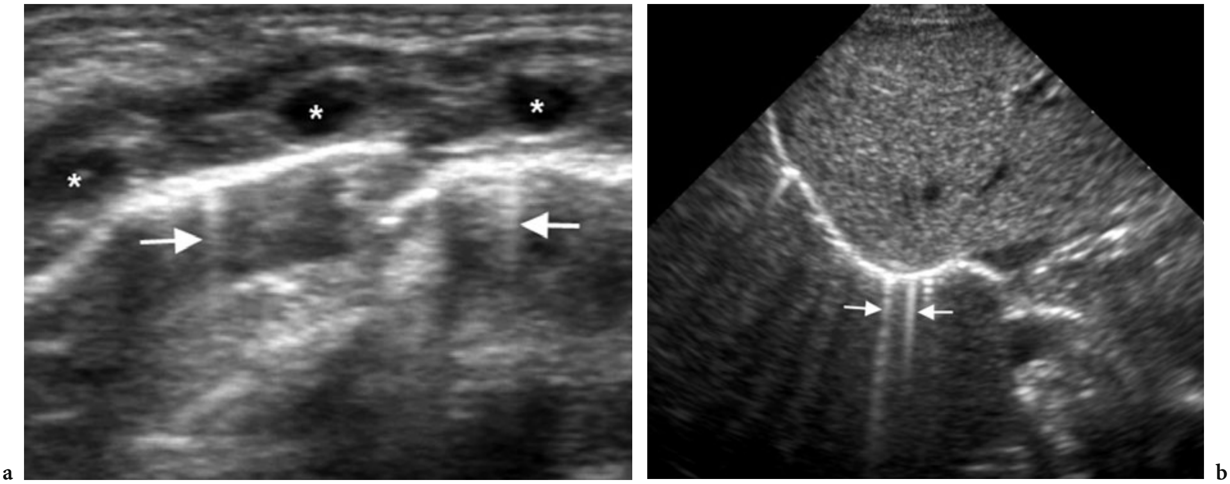

Fig. 1.1a,b. Normal lung in a 3-month-old boy. **a** Parasternal longitudinal US scan shows comet tail artifacts (*arrows*) evoked by alveolar air flow. Non-ossified costal cartilage (*) allows visualization of the lung and pleura (upper echogenic line). **b** Transdiaphragmatic transverse view of the right lower lobe. Comet tail reverberations are seen adjacent to the diaphragm (*arrows*)

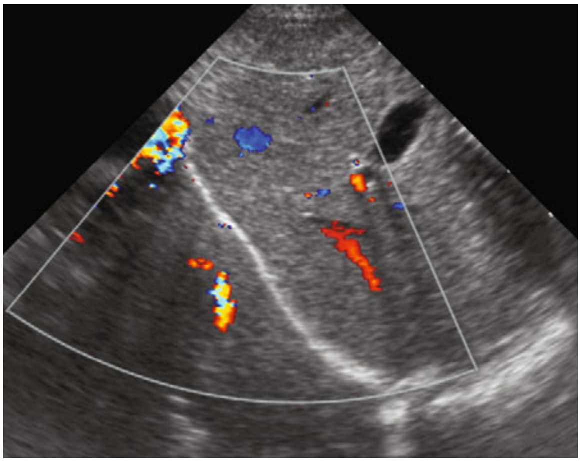

Fig. 1.2. Mirror image artifact. Transdiaphragmatic longitudinal US scan in a 2-month-old boy shows "duplication" of the liver and its Doppler signals, projecting over the right lung base

1.2.4
Pulmonary Lesions

1.2.4.1
Congenital Malformations of the Lung

In countries where obstetric sonography is routinely performed, the detection rate of congenital lung malformations has risen considerably. In recent years, over 500 cases of antenatally diagnosed cystic lung malformations have been reported (Davenport et al. 2004). The fetal lung can be easily identified on prenatal US studies using a transverse four-chamber view of the fetal chest, a routine component of obstetric ultrasound protocols. It is seen as a solid structure of medium-level echogenicity that varies slightly throughout gestation. This US appearance is produced by the combination of the lung water content and parenchymal network of bronchial, vascular and mesenchymal elements. Furthermore, lung vascularization can be readily assessed by color or power Doppler (Fig. 1.3a,b).

Fetal lung anomalies present as an area of abnormal echogenicity exerting a mass effect on adjacent structures. The mass is hyperechoic with respect to the normal lung parenchyma and either homogeneous or with coexisting cysts. The size of the lesion may be overestimated since the compressed non-affected lung and bronchi can acquire echogenicity similar to that of the lesion and be considered a part of the mass. US is a sensitive technique for detecting congenital lung malformations, but is less reliable for establishing a specific diagnosis, since a similar echo pattern can be seen in many of them.

A presumptive diagnosis of pulmonary sequestrations is based on their posteroinferior location, triangular shape, homogeneous hyperechogenicity, demonstration of arterial feeders and coexistence of ipsilateral hydrothorax (6%–9% of sequestrations). Cysts within the lesion point to congenital cystic adenomatoid malformation.

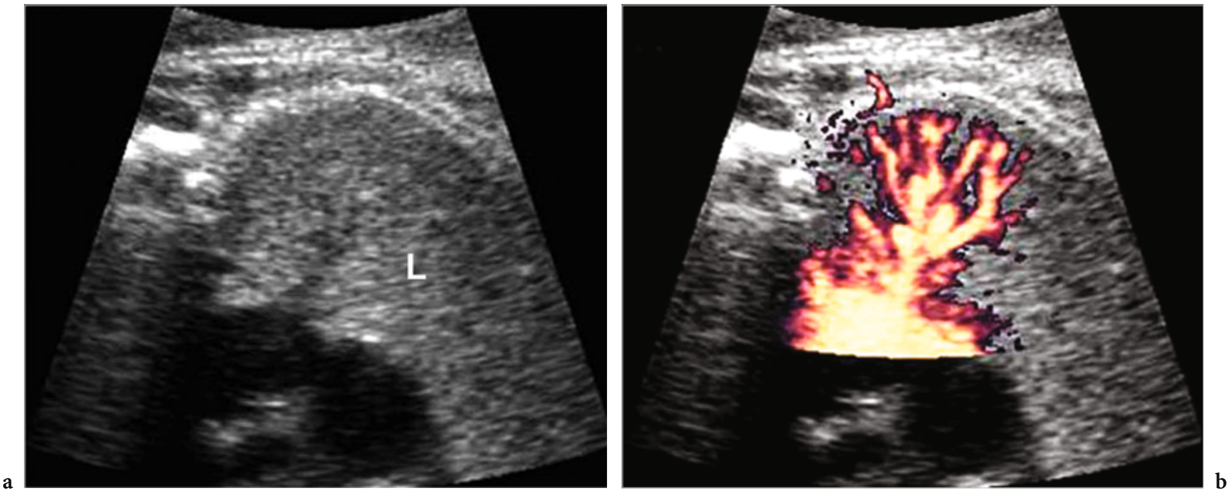

Fig. 1.3a,b. US scan of normal fetal lung at 23 weeks'gestational age. **a** Four-chamber view shows the lung as a solid medium-level echogenic structure (*L*). **b** Pulmonary vessels and their ramifications are very well seen on Power Doppler. Courtesy of Dr. Edgar Hernández, Ph. D. Clinic Hospital Barcelona

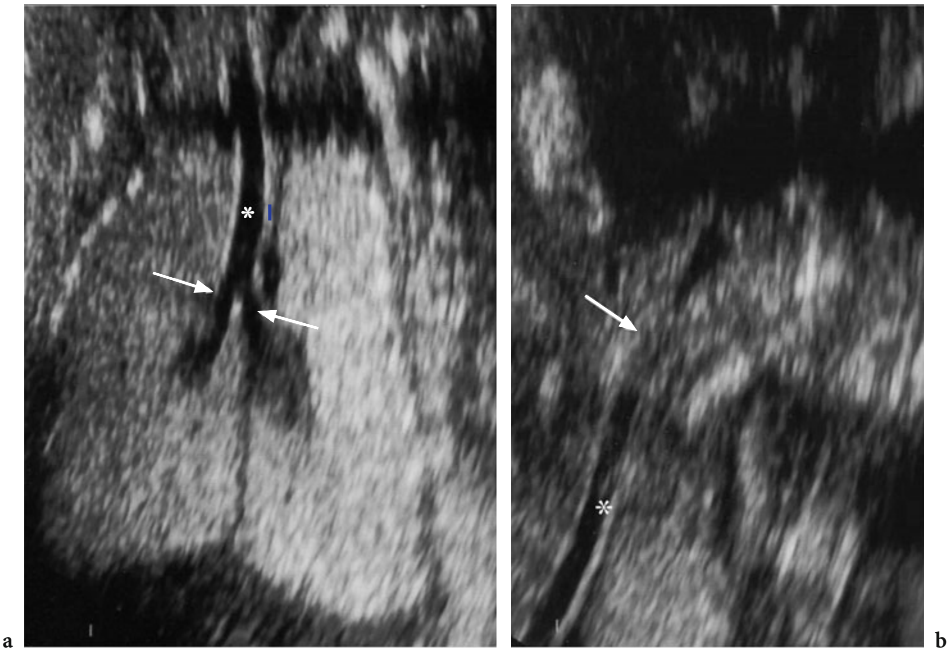

Fig. 1.4a,b. Laryngeal atresia in a 21-week gestational age fetus. **a** Coronal view of the fetal chest shows bilateral pulmonary overdistention with inversion of the diaphragms and increased echogenicity. Secretion- filled trachea (*) and main bronchi (*arrows*) can be seen. **b** Longitudinal view of the upper airway showing an echogenic area (*arrow*) corresponding to intrinsic laryngeal atresia (CHAOS syndrome). Courtesy of Dr. Elena Carreras, Ph. D. Autonomus University of Barcelona.

Several classifications and terminologies are in use to describe bronchopulmonary foregut malformations, which classically include congenital cystic adenomatoid malformation (CCAM), pulmonary sequestration (PS), bronchogenic cyst, bronchial atresia and congenital lobar emphysema. Additional anomalies such as pulmonary agenesis, tracheal bronchus, esophageal and tracheal atresia, and tracheoesophageal fistula are now recognized as part of the spectrum (Newman 2006). According to some authors (Langston 2003), these dysplastic pulmonary changes develop secondary to an intrauterine airway obstruction. The type of malformation that occurs depends on the level and timing of the obstruction, with the vascular abnormality being an associated feature.

A diagnosis of laryngeal or tracheal obstruction, either intrinsic or extrinsic, should be considered when a generalized increase in the size and echogenicity of both lungs is observed (Shum et al. 2007). In this condition, which is also known as CHAOS syndrome (congenital high airway obstruction), the pulmonary overdistention is due to an accumulation of bronchial secretions (Fig. 1.4a,b). Observation of these features in fetal ultrasound led to the development of fetoscopic endoluminal tracheal occlusion to reduce the degree of pulmonary hypoplasia in fetuses with congenital diaphragmatic hernia. Following evaluation of the degree of pulmonary hypoplasia by the lung-to-head ratio, laparoscopic insertion of an intratracheal plug (vascular catheter inflated with 5 cc of isotonic solution) is performed, usually at 26 weeks of gestation. The plug should be removed at 34 weeks and gestation should end at 37 weeks, either spontaneously or by caesarean section. In fetuses with a lung-to-head ratio between 0.6 and 1.0, the survival rate is substantially improved by fetoscopic tracheal occlusion, compared with those managed expectantly (Jani et al. 2006) (Fig. 1.5a–e).

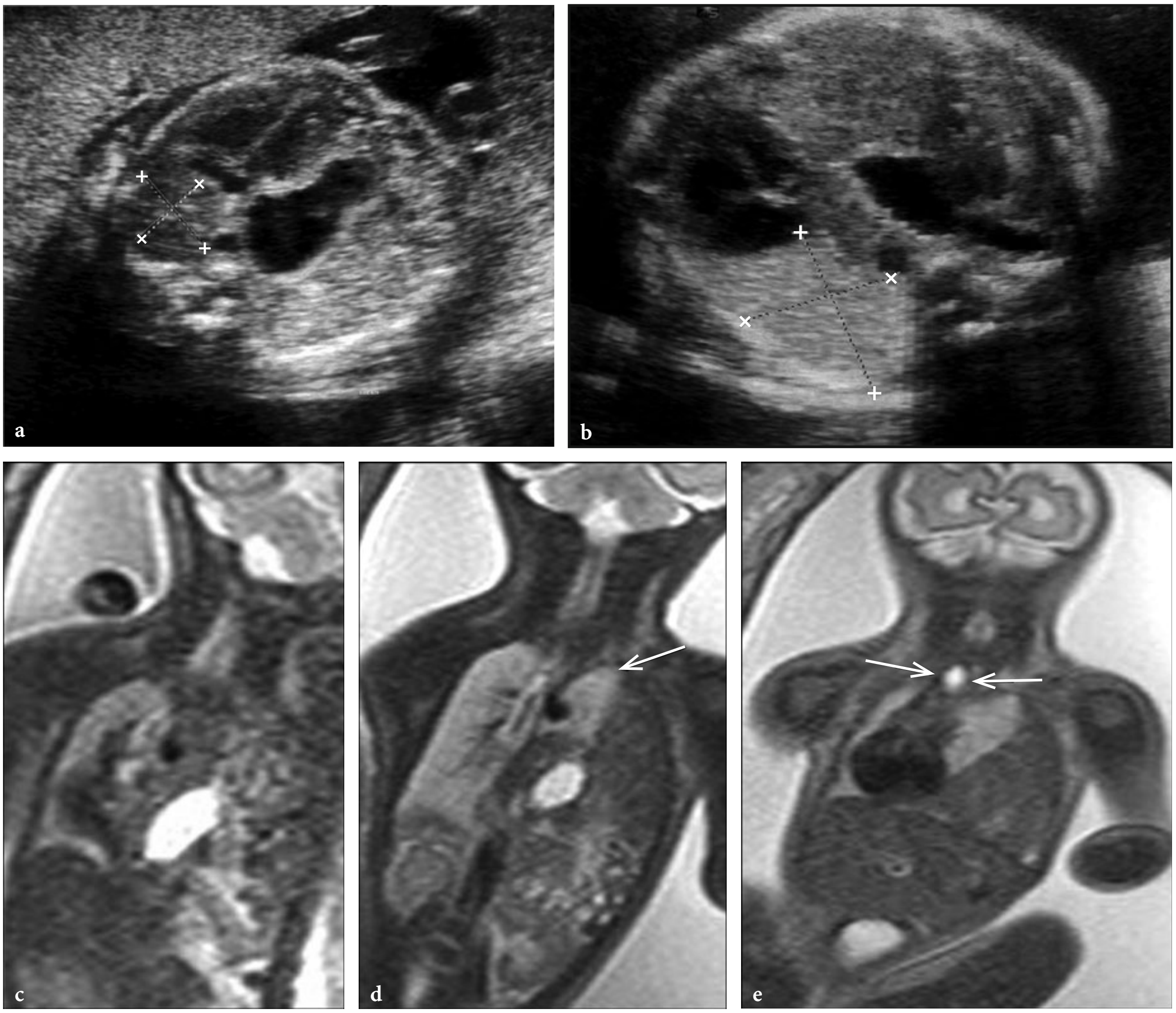

Fig. 1.5a–e. Congenital left diaphragmatic hernia treated prenatally. **a** Four-chamber US view prior to laparoscopic placement of a tracheal plug shows the small size of the contralateral fetal lung (*crosses*). **b** US performed 3 weeks later shows increased size and echogenicity of the lung (*crosses*). **c** Fetal MRI performed at diagnosis shows the left hemithorax filled with abdominal content. Hyperintense image corresponding to the stomach. **d** Remarkable increase in size of the right lung and upper part of the left lung (*arrow*) (previously not seen) is observed after insertion of a tracheal plug. **e** The plug (*arrows*) is seen on MRI as a hyperintese structure

1.2.4.1.1
Cystic Adenomatoid Malformation of the Lung

Cystic adenomatoid malformation of the lung accounts for 75%–85% of all fetal lung masses detected by US. Sonographic findings vary depending on the type of malformation (May et al. 1993). Stocker et al. (1977) initially classified CCAM into three histologic types. Type 1 is the most common form and appears as single or multiple large cysts, often affecting the entire pulmonary lobe. In type 2, the mass has an echogenic appearance with numerous small cysts. Type 3 malformations appear as homogeneous echogenic masses without cysts. More recently, Stocker (1994) proposed classifying CCAM into five types according to the site of origin. Sonographic differentiation between CCAM and pulmonary sequestration may not always be possible. A systemic vessel arising from the aorta has also been described in patients with adenomatoid malformation of the lung (Winters et al. 1997). Furthermore, hybrid lesions, consisting of CCAM associated with pulmonary sequestration in the same malformation, are frequent, reaching around 50% of the cases in some series (Conran and Stoker 1999). The abnormal lung communicates with the tracheobronchial tree and the cysts fill with air at birth during respiration, making them more difficult to recognize individually by US. The air-filled cluster of cysts is seen as an area of increased echogenicity with a banded appearance. This US finding, which is known as the “aurora sign”, has also been reported in several acquired interstitial lung diseases (Kohzaki et al. 2003) (Fig. 1.6a,b). CT and MRI are, therefore, more suitable for postnatal study of the internal components of this malformation.

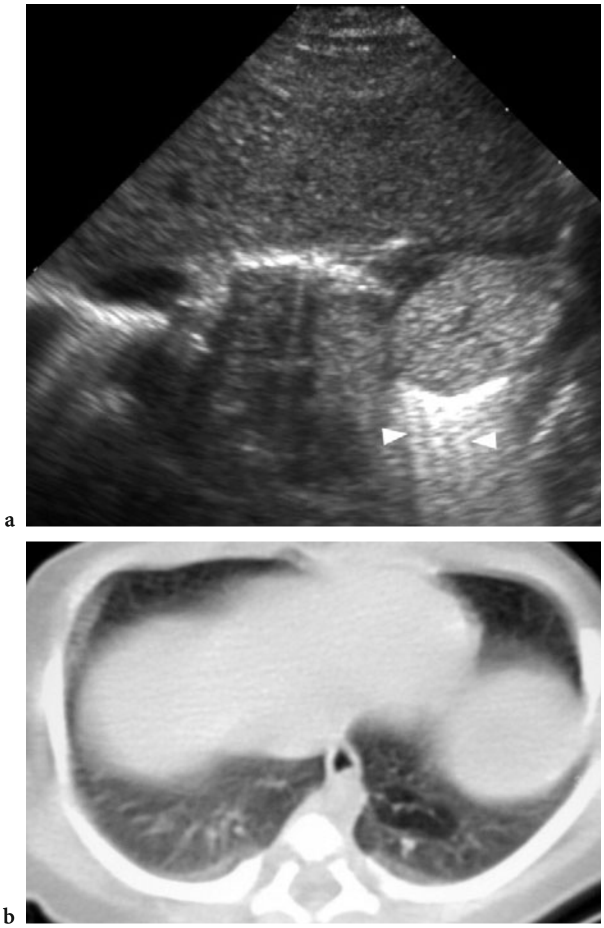

Fig. 1.6a,b. Postnatal US and CT of prenatally diagnosed cystic adenomatoid malformation. **a** Transverse US scan through a subxifoid approach shows multiple echogenic lines (*arrowheads*) in the left inferior lobe with a typical appearance of the “Aurora Sign”. These lines are more echogenic than the so called „comet tails“. **b** CT shows an area of hyperlucency in the left lung base

1.2.4.1.2
Sequestration

Pulmonary sequestration is a congenital malformation composed of pulmonary tissue, which lacks normal connection to the tracheobronchial tree and the pulmonary arteries. The tissue is usually supplied by a systemic artery that arises from the thoracic or abdominal aorta. Two types are classically recognized: intralobar and extralobar. Intralobar sequestration has been said to occur in older infants and some authors have considered it an acquired lesion (Frazier et al. 1997). Extralobar sequestration has its own pleural covering and venous drainage is into the systemic circulation (azygos-hemiazygos system, portal vein or inferior vena cava) and has been considered a congenital condition (May et al. 1993; Ko et al. 2000). Currently, this categorical classification is not universally accepted since mixed systemic and pulmonary venous drainage has been observed in several cases of extralobar sequestration (Pumberger et al. 2003). Moreover, the intralobar type is also found in neonates and is now considered a congenital rather than an acquired lesion (Newman 2006).

At US study, sequestration is seen as a homogeneous or heterogeneous echogenic mass in the lower pulmonary lobes, juxtadiaphragmatic region, or suprarenal region. Collateral air drift can produce small hyperechogenic images within the mass. We recommend a subxiphoid approach to study the mass, search for an anomalous feeding vessel arising from the aorta, and investigate the systemic or pulmonary venous drainage (Fig. 1.7a,b). The azygos may be enlarged in cases of systemic drainage to the azygos-hemiazygos system (Ko et al. 2000). Pulmonary venous drainage is better delineated by CT or MRI than by US (Fig. 1.8a,b).

Solid pulmonary sequestration should be differentiated from congenital neuroblastoma (Manson and Daneman 2001). The presence of calcifications (common in neuroblastoma and exceedingly rare in neonatal sequestration) as well as the obstetric history (sequestration occurs early in gestation and neuroblastoma in the third trimester) are the main distinguishing factors.

1.2.4.1.3
Bronchogenic Cyst

Bronchogenic cysts, are usually located in the subcarinal region and occasionally within the pulmo-

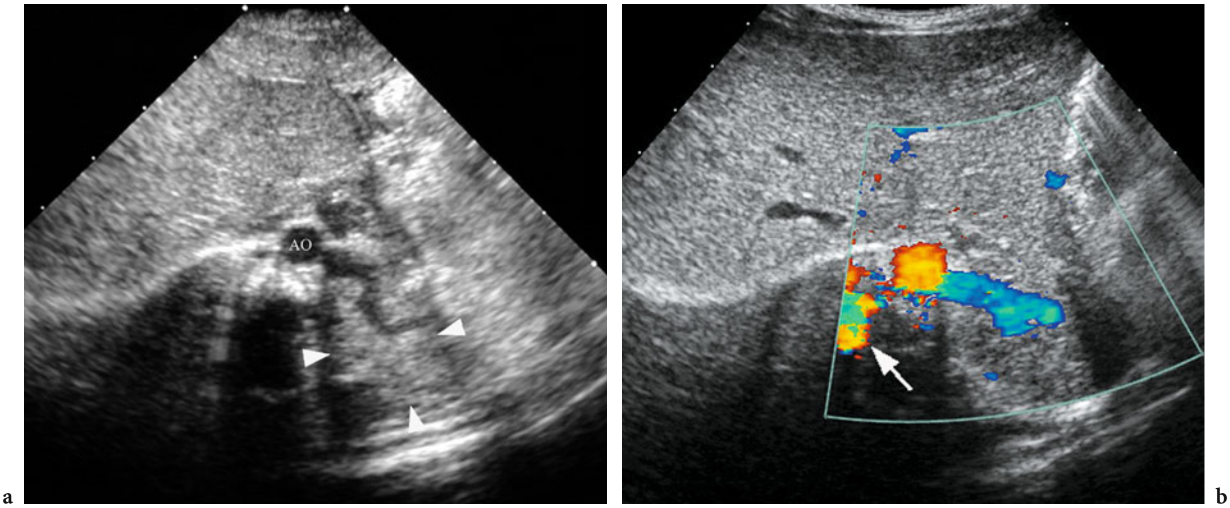

Fig. 1.7a,b. Extralobar solid sequestration in a 2-month-old boy. **a** In this subxiphoid transverse scan, an echogenic mass (*arrowheads*) can be seen behind the left lobe of the liver. A tortuous vessel, likely to be a persistent primitive post-brachial artery, is seen arising from the aorta (AO). **b** Color Doppler shows the abnormal vessel originating at the aorta and supplying the mass. Venous drainage is inferred to be through the enlarged azygos (*arrow*)

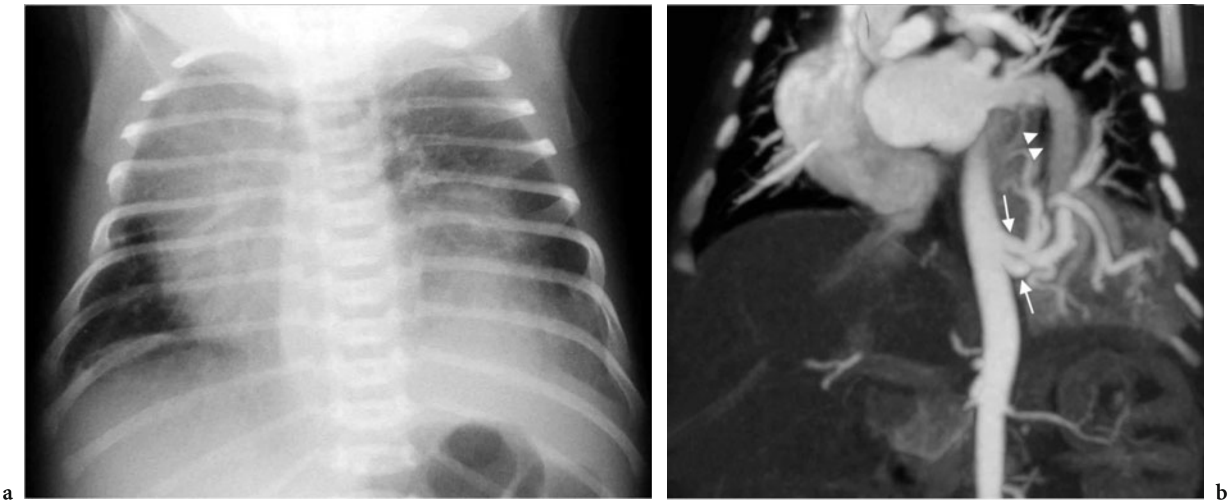

Fig. 1.8a,b. Intralobar sequestration in a newborn boy. **a** Chest X-ray shows opacification of the left lung base. **b** CT angiography demonstrates several systemic vessels arising from the aorta supplying the sequestration (*arrows*). A large vein is seen draining into the left atrium (*arrowheads*)

nary parenchyma. Depending on their content, intrapulmonary cysts are seen as unilocular anechoic or weakly echogenic lesions. US is particularly helpful in cases where CT is inconclusive about the solid or cystic nature of the lesion (see Chap. 5, Fig. 5.6c).

1.2.4.1.4
Management of Congenital Malformations of the Lung

Postnatal management of antenatally-diagnosed lung malformations is highly controversial since partial or complete involution of the mass may occur during the third trimester of gestation and most newborns with prenatally recognized malformations are asymptomatic (Aziz et al. 2004; Laberge et al. 2004). There is a trend in the literature towards conservative management of this group of lesions, particularly in cases of solid pulmonary sequestration, because the malformation can regress spontaneously (Fig. 1.9a,b). Nonetheless, routine resection of all CCAM is still proposed by some authors (Papagiannopoulus et al. 2001; Hasiotou et al. 2004) based on the risk of infection and potential malignant transformation to rhabdomyosarcoma or pulmonary blastoma. Prospective studies with sufficient follow-up are needed to quantify the advantages and drawbacks of conservative versus surgical management to provide a solid basis for treatment guidelines.

1.2.4.2
Lung Consolidation

Lung consolidation is the term applied to a lung parenchyma pattern in which there is a decrease in or absence of pulmonary air, as occurs in pneumonic consolidation and atelectasis. Pneumonic consolidation refers to filling of the normal air spaces with fluid and inflammatory cells, thereby converting the highly reflective lung into a solid structure through which sound is easily transmitted. The air-filled bronchi in the consolidated lung are seen as echogenic branching linear structures converging towards the lung root. This feature is known as sonographic air bronchogram (Weinberg et al. 1986; Acunas et al. 1986; Yang et al. 1992; Seibert et al. 1998; Kim et al. 2000) and is equivalent to the air bronchogram observed on chest X-rays (Fig. 1.10a,b). The loss of lung volume in atelectasis produces a characteristic crowding of the air-filled bronchi and pulmonary vessels (Fig. 1.11a,b) (Weinberg et al. 1986). In our experience, sonobronchograms are often visualized in patients in whom air bronchograms were not seen on X-rays, a fact that makes US a useful technique for clarifying misleading plain film findings (Fig. 1.12a,b).

In patients with asthma, cystic fibrosis or severe inflammatory processes, the bronchi contain mucus or secretions. In these cases, US demonstrates an-

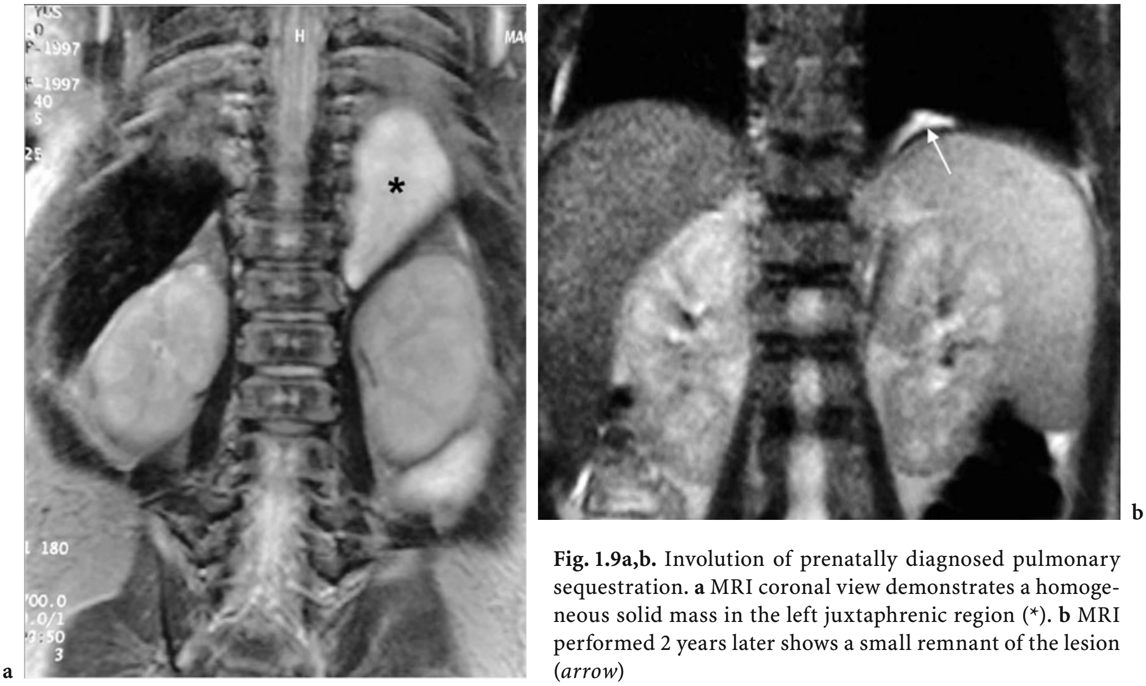

Fig. 1.9a,b. Involution of prenatally diagnosed pulmonary sequestration. **a** MRI coronal view demonstrates a homogeneous solid mass in the left juxtaphrenic region (*). **b** MRI performed 2 years later shows a small remnant of the lesion (*arrow*)

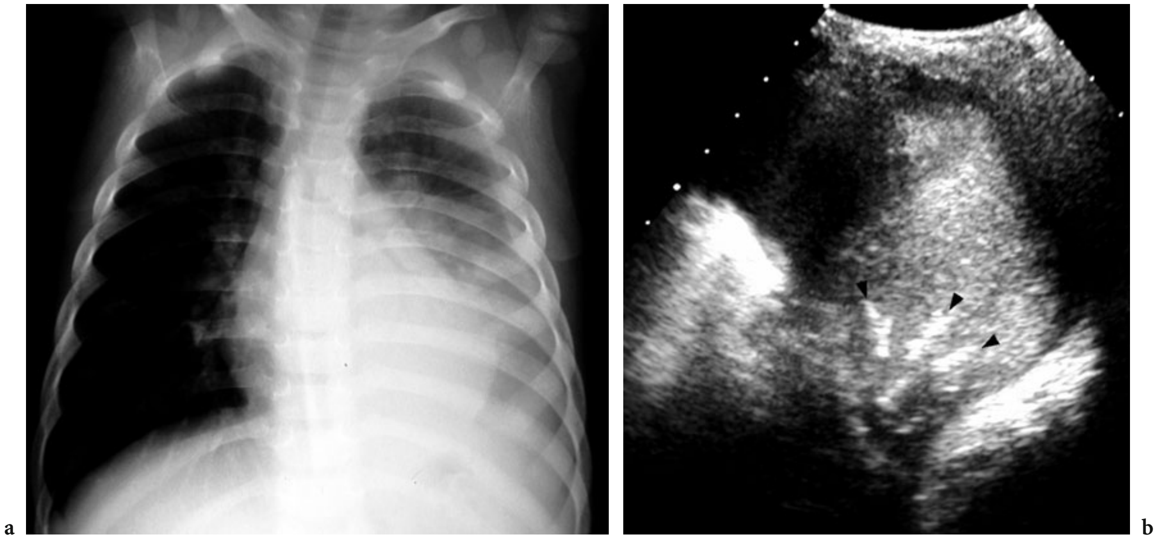

Fig. 1.10a,b. A 6-year-old girl with left-sided pneumonia and pleural effusion. **a** Increased opacity of the left lung base associated with pleural fluid is visible on the chest radiograph. **b** Intercostal axial US scan with the patient in a right decubitus position shows multiple bright, linear, branching structures (*arrowheads*), corresponding to air sonobronchograms

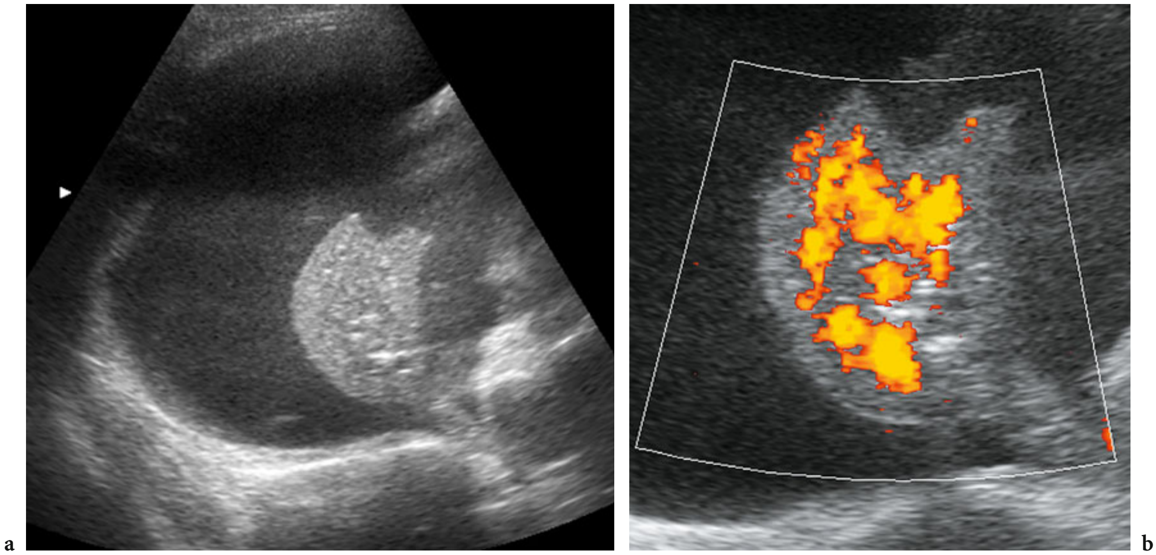

Fig. 1.11a,b. A 10-year-old boy with pleural effusion and secondary atelectasis of the ipsilateral lung. **a** Transverse US scan of the right hemithorax shows profuse pleural fluid and atelectatic lung. **b** Crowded pulmonary vessels, characteristic of pulmonary collapse, are demonstrated by power Doppler. This US finding explains why atelectasis is seen as a hyperintense lesion on CT

echoic tubular branching structures known as sonographic fluid bronchogram. (Yang et al. 1992b; Kim et al. 2000). The fluid-filled bronchi have imperceptible walls and may contain air bubbles. On conventional US these features differentiate fluid bronchograms from pulmonary vessels (Fig. 1.13). Definitive differentiation is made by color Doppler. The vessels seen within the consolidation on color or power Doppler can be identified as normal pulmonary arteries by their characteristic polyphasic (mainly quadriphasic) pattern depicted with spectral Doppler (Fig. 1.14).

The presence of sonographic air bronchograms, fluid bronchograms, as well as recognition of pulmonary vessels within the lesion are the characteristic features of lung consolidation and are never seen in

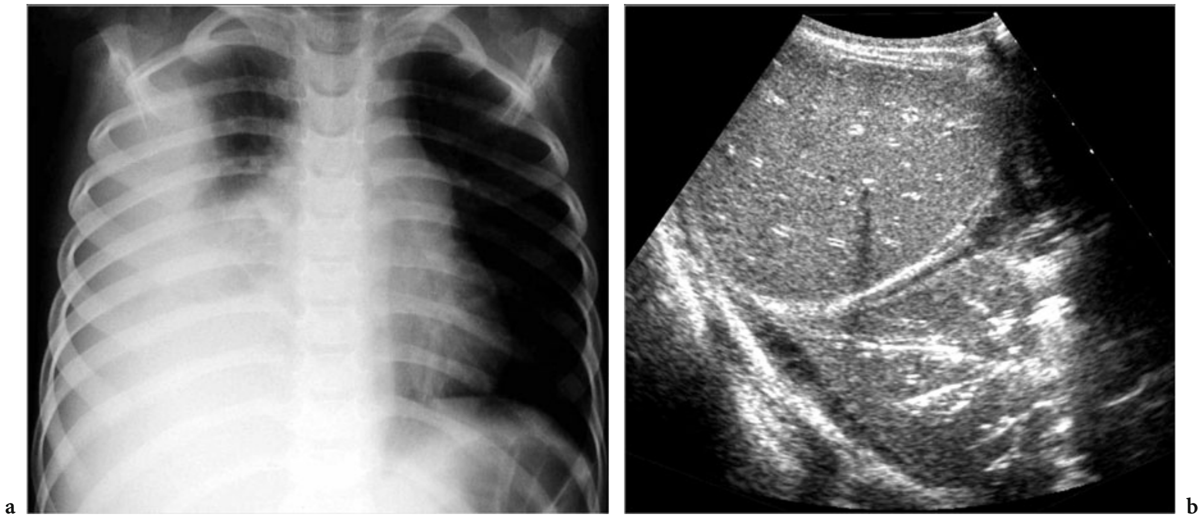

Fig. 1.12a,b. Numerous sonobronchograms not visualized on the chest plain film. **a** Chest radiograph of a 4-year-old boy shows almost complete opacification of the right hemithorax. No airbronchograms are identified, hence differentiation between consolidation and pleural fluid is not possible. **b** Subcostal US view shows that the opacification corresponds to a pulmonary consolidation with a huge sonobronchograms

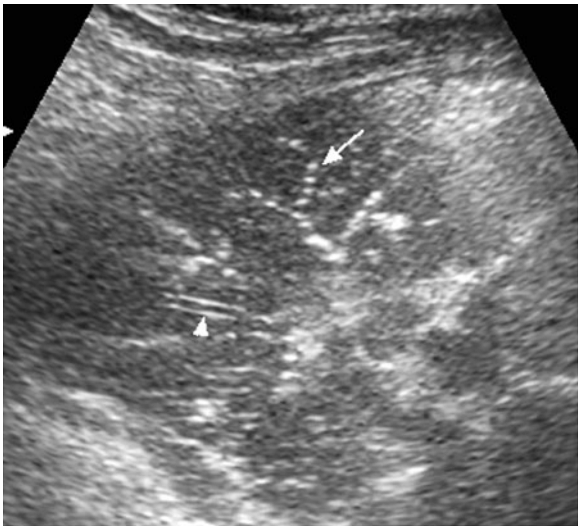

Fig. 1.13. Sonographic fluid bronchogram in a 6-year-old boy with asthma. Transverse intercostal scan shows bright dots that moved in real time over a hypoechoic background (*arrows*). The well-defined walls of the pulmonary vessel are clearly seen (*arrowhead*) while the bronchus wall is imperceptible

pleural effusion or tumors. Hence, these findings are essential for differentiating among these entities and should be actively investigated (Fig. 1.15 a–c). In peripheral lung consolidation, visualization of pulmonary vessels may be the only sonographic clue to establish the diagnosis.

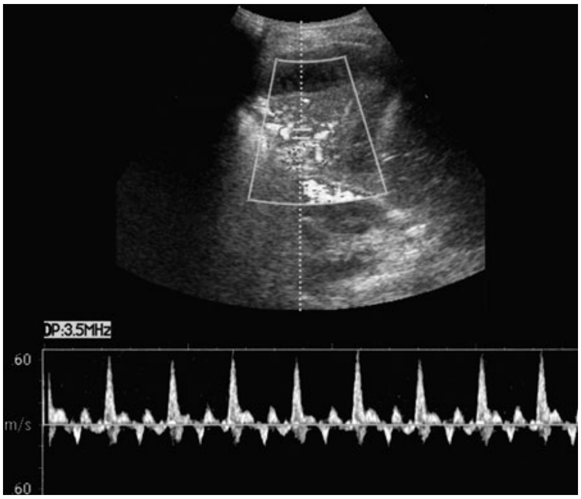

Fig 1.14. Characteristic spectral Doppler in pulmonary consolidation. Color Doppler US in a patient with pulmonary consolidation shows the characteristic quadriphasic pattern of the pulmonary arteries

In a prospective US study including color and power Doppler in 19 patients with lobar pneumonia, we were able to classify lung consolidation into 3 groups according to sonographic findings and degree of vascularization:

- Well-vascularized pneumonia. In these cases the consolidation presented a homogeneous appearance (similar to the echogenicity of the liver

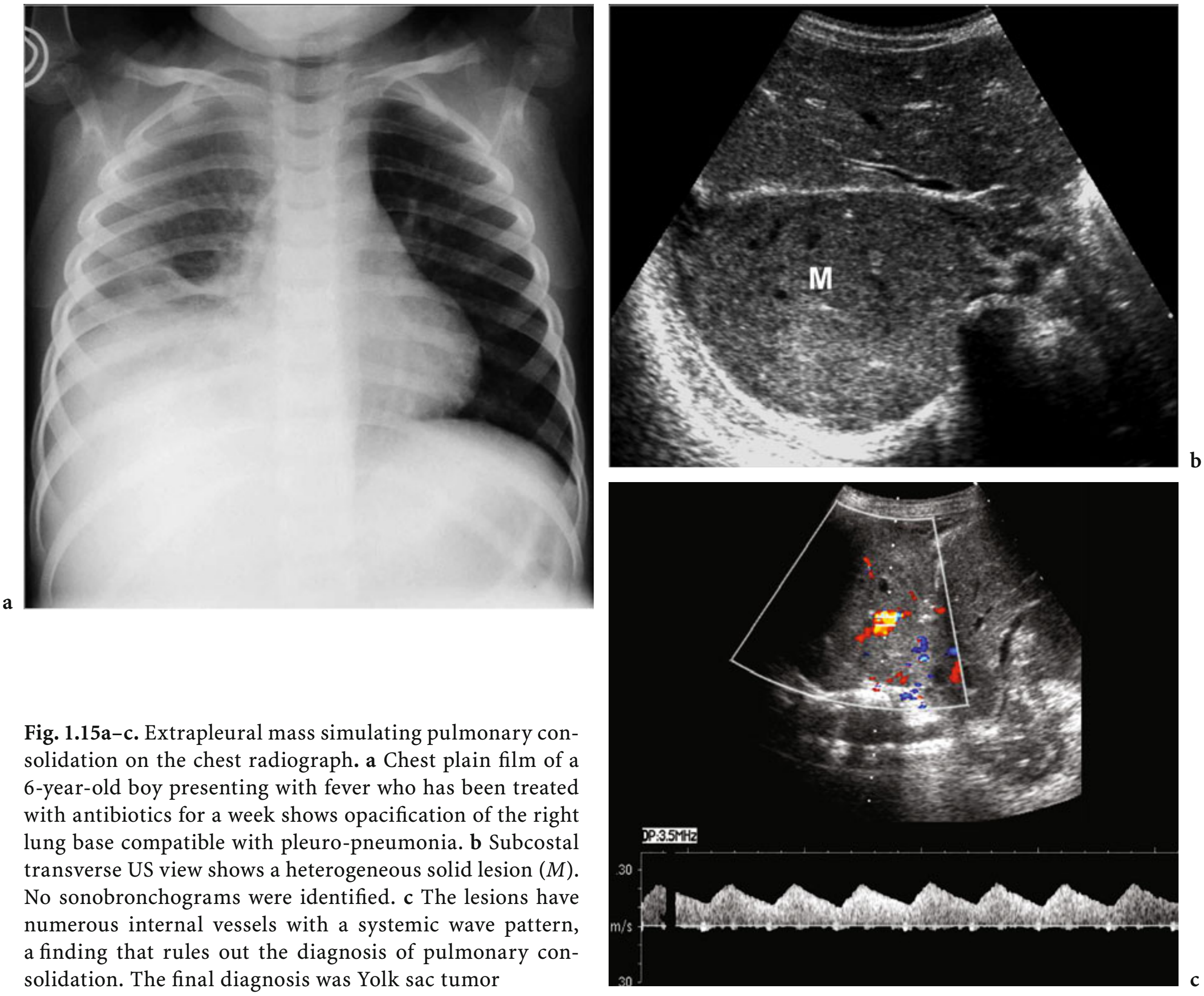

Fig. 1.15a–c. Extrapleural mass simulating pulmonary consolidation on the chest radiograph. **a** Chest plain film of a 6-year-old boy presenting with fever who has been treated with antibiotics for a week shows opacification of the right lung base compatible with pleuro-pneumonia. **b** Subcostal transverse US view shows a heterogeneous solid lesion (*M*). No sonobronchograms were identified. **c** The lesions have numerous internal vessels with a systemic wave pattern, a finding that rules out the diagnosis of pulmonary consolidation. The final diagnosis was Yolk sac tumor

parenchyma) with multiple vascular structures (Fig. 1.16a–c).

- Poorly vascularized pneumonia without necrotic areas. In contrast to the first type, the number of vessels in the consolidated lung was scant, but the lesion remained homogeneous (Fig. 1.17a–c).
- Poorly-vascularized pneumonia with necrotic areas. Consolidation was usually heterogeneous with cavitation seen as hypoechoic areas, sometimes containing internal echogenic debris (Fig. 1.18a,b). Absence of vascularization can be localized or involve the whole area of consolidation. (Fig. 1.19a–c).

This last type, known as necrotizing pneumonia, results from necrosis of the lung parenchyma due to occlusion of alveolar capillaries following severe lung infection. *Streptococcus Pneumoniae* is one of the most common microorganisms causing this complication in children (Kerem et al. 1994; Hedlund et al. 1999). In adults, the outcome of necrotizing pneumonia is generally poor and early surgical excision of the gangrenous lung is indicated. However, children can recover completely with medical treatment, although their clinical evolution is long and may require extended hospitalization (Ben-Ami et al. 1993). Thus, in our experience, US provides diagnostic and prognostic information which may influence therapy in children with lobar pneumonia.

Contrast-enhanced chest CT in children with lobar pneumonia can provide information similar to that obtained with chest US (Donnelly and Klosterman 1997).

Chest X-ray should be the initial imaging procedure used in cases of suspected pneumonia. According to our experience, we recommend complementary chest US studies in patients with pneumonia and associated pleural fluid, in those with lobar pneu-

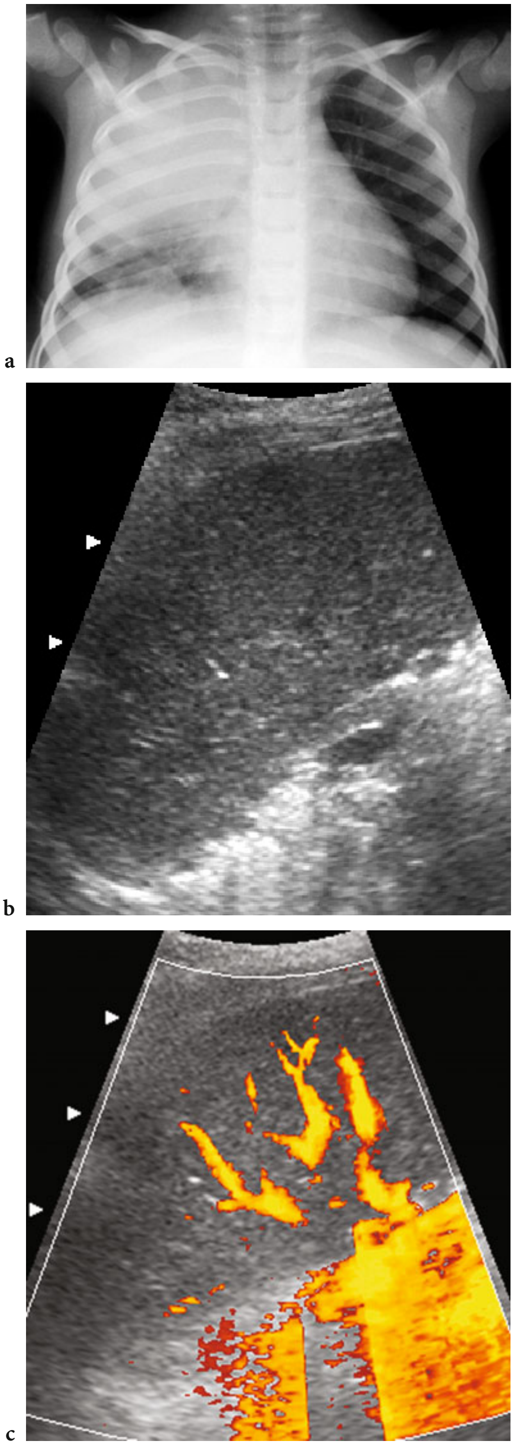

Fig. 1.16a–c. An 8-year-old boy with well-vascularized lobar pneumonia. **a** Chest radiograph shows opacification of the right upper lobe. **b** The consolidated lung has a homogeneous echogenicity (similar to that of the liver) in this intercostal oblique US scan obtained with the patient in a prone position. **c** Numerous pulmonary vessels are seen on power Doppler

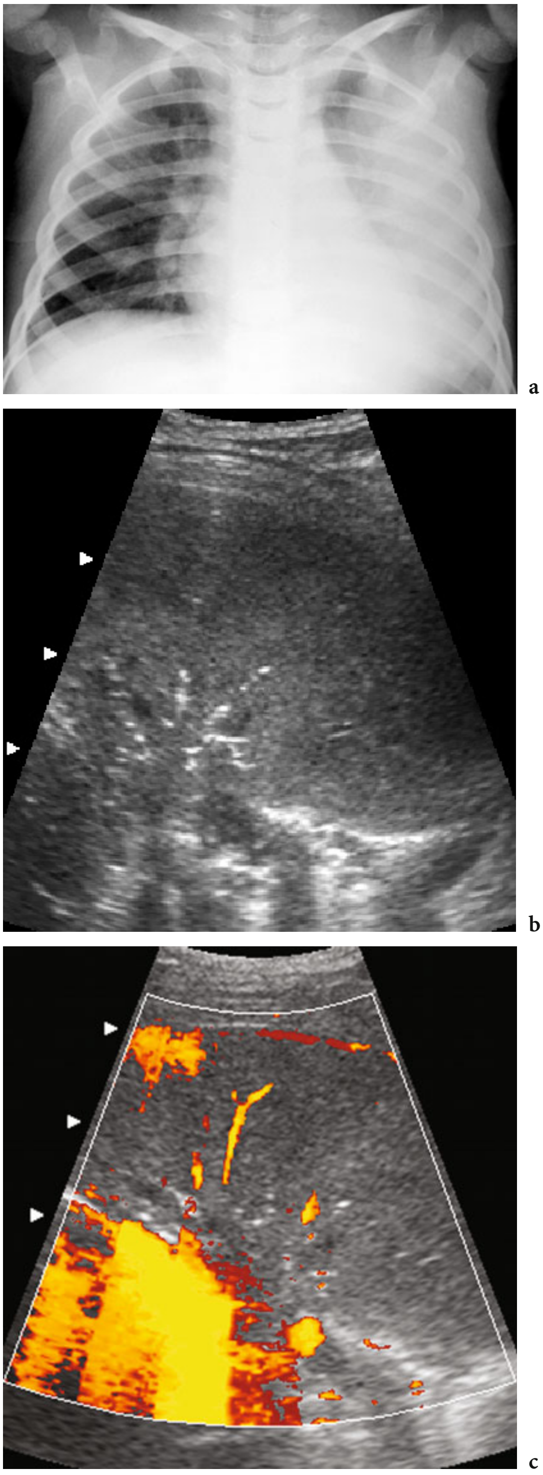

Fig. 1.17a–c. A 6-year-old girl with poorly-vascularized pneumonia. **a** The chest radiograph discloses evidence of left lung opacification. **b** Intercostal oblique US scan with the patient in a prone position shows homogeneous appearance of the affected lung base with central air sonobronchograms. **c** Very few vessels are seen within the consolidation

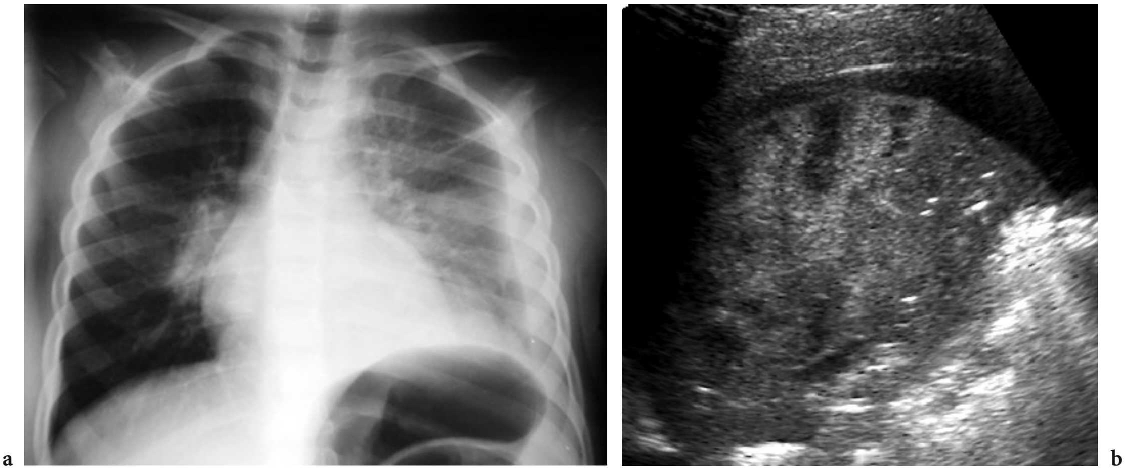

Fig. 1.18a,b. Pneumonia with peripheral necrotic areas in a 7-year-old boy. **a** Increased opacity in the left lower lobe and pleural effusion is visualized in the radiograph. **b** US scan discloses very heterogeneous appearance of the left lung base with peripheral hypoechoic areas representing necrosis. The sonolucent band corresponds to pleural fluid. HRCT (not shown) confirmed the diagnosis of necrotizing pneumonia

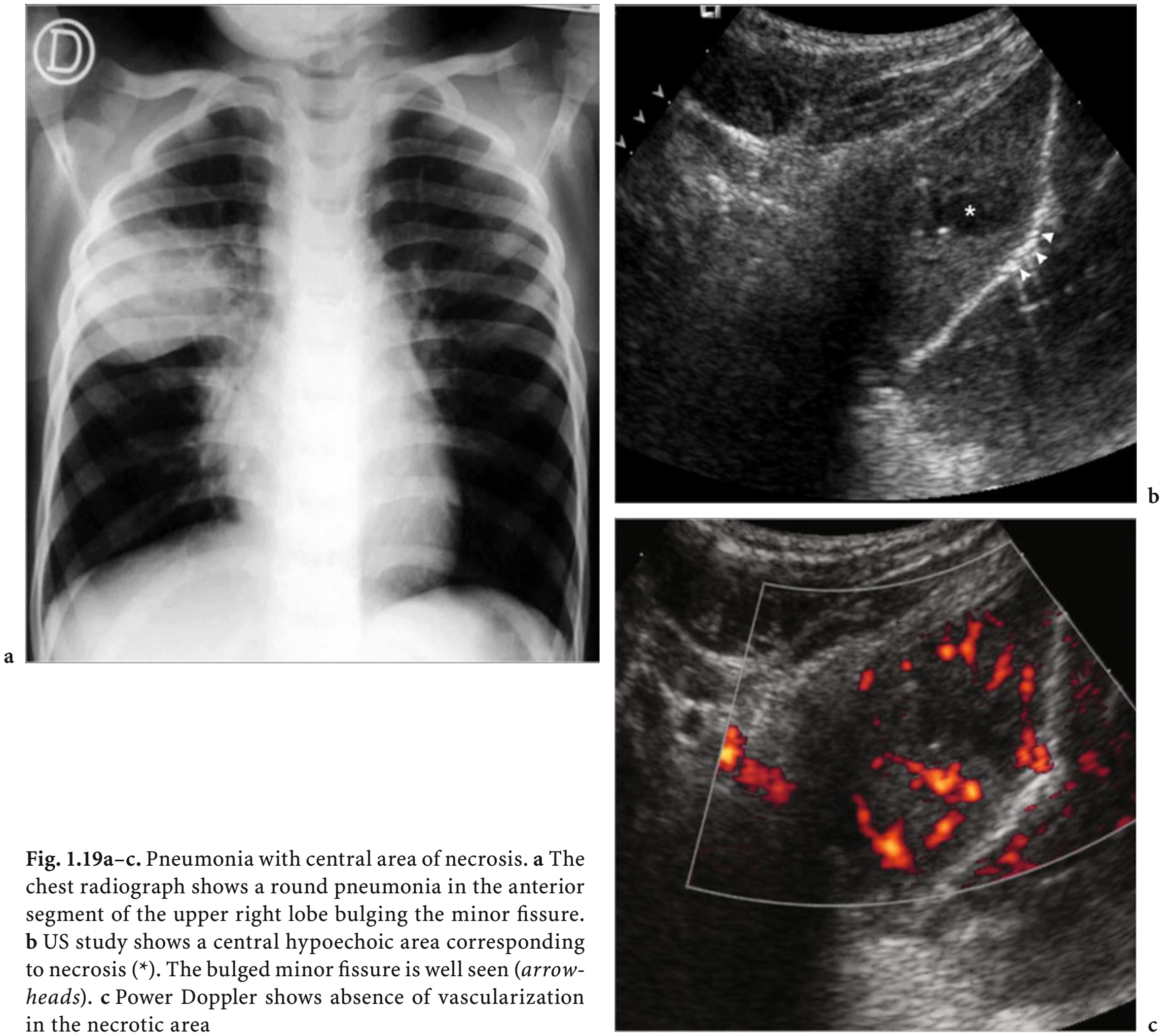

Fig. 1.19a–c. Pneumonia with central area of necrosis. **a** The chest radiograph shows a round pneumonia in the anterior segment of the upper right lobe bulging the minor fissure. **b** US study shows a central hypoechoic area corresponding to necrosis (*). The bulged minor fissure is well seen (*arrowheads*). **c** Power Doppler shows absence of vascularization in the necrotic area

monia and severe clinical symptoms and in patients who do not respond well to antibiotic therapy.

When studying consolidation, the radiologist should be aware of the inability of US to determine the extent of a deep lesion. Acoustic reverberation artifacts, caused by areas of aerated lung interposed between the transducer and the area of interest, can hinder visualization of the entire lesion.

1.2.4.3
Lung Tumors

Primary lung tumors, including blastoma, mucoepidermoid carcinoma, hemangiopericytoma and rhabdomyosarcoma, are rare in children. The most common of these is pulmonary blastoma. It usually has a complex echogenic appearance and is located in the periphery of the lung. Due to the peripheral location of this lesion, sonography can be used to guide percutaneous biopsy of the mass.

1.3
Pleura

1.3.1
Examination Technique

The pleura is located very superficially and is therefore easily evaluated by sonography. Most of the pleural surface can be imaged through intercostal and subcostal approaches. However the mediastinal and the apical pleurae require scanning through the parasternal or supraclavicular approaches, respectively (Ben-Ami et al. 1993; Wernecke 2000).

Excellent visualization of the pleura-lung interface is obtained with high frequency (8–10 MHz) convex or linear transducers applied at the intercostal, parasternal and supraclavicular spaces. Sector or convex transducers are recommended when using the subcostal approach. While performing the study, certain ultrasound features that are of great diagnostic value should be carefully observed. In real-time sonography, the visceral pleura moves with the respiratory excursions and recognition of this movement provides clues to the diagnosis of several pathologies, such as pneumothorax and pleural infiltration by pulmonary or extrapleural tumors. The absence of visceral pleura movement is a useful finding for sonographic diagnosis of pneumothorax. Similarly, observation of a fixed pulmonary tumor during respiration indicates that the pleura is infiltrated (Wernecke 2000).

1.3.2
Normal Sonographic Appearance and Artifacts

The pleura is composed of two membranes, the visceral and parietal pleurae. They are separated by a potential space, which can be inferred as a thin hypoechoic band during the respiratory excursions of the visceral pleura in real-time. On the intercostal longitudinal scan, the pleura is visualized as an intensely echogenic linear structure that acquires a curving configuration at the transverse view (Fig. 1.20). On subcostal studies the diaphragm, seen as a bright, curving, echogenic line, cannot be differentiated from the parietal pleura covering its thoracic side.

Mirror artifacts are often seen when studying the pleura. These consist in a "duplication" of structures external to the pleura projected over the lung and are caused by total reflection of the sound waves at the pleural surface when the US beam strikes it at

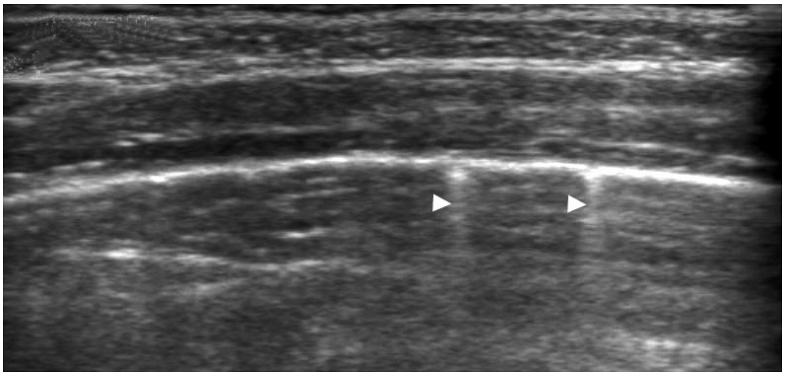

Fig. 1.20. Intercostal transverse view of the normal pleura. The curving pleura-lung interface is well visualized. The small echogenic dots superimposed on the linear interface (*arrowheads*) represent air in the alveoli as they glide against the pleura with respiratory motion

certain angles (Figs. 1.2 and 1.51). As a consequence, intercostal muscles of the chest wall can be projected over the lung, simulating pulmonary pathology. This physical phenomenon can also produce a double image of the diaphragm. The two sonographic diaphragms (the anatomic diaphragm and the duplicated image) are separated by a hypolucent band, probably corresponding to the liver, which can be misinterpreted as pleural effusion.

1.3.3
Indications for Pleural US

The main indication of pleural US is to confirm suspected pleural effusion on AP chest plain films. Ultrasound is a more sensitive for this purpose (Eibenberger et al. 1991) and we believe it should replace the routine practice of lateral decubitus plain film confirmation.

Another major indication is to study patients presenting with an opaque hemithorax on chest films which, in most cases, is caused by massive pleural effusion, but can also be due to other entities, such as pulmonary masses or consolidation. US can differentiate between these processes (Fig. 1.21a–c).

US can also be used to provide imaging guidance for pleural drainage procedures, particularly when the pleural fluid is loculated. With US one can determine the depth of the collection and decide on the safest manner and approach to drain it (Shankar et al. 2000). Pneumothorax, the most common complication of pleural taps, is exceedingly rare when the procedure is performed under US control (Raptopoulos et al. 1991). In patients with malignant intrathoracic or extrathoracic tumors, pleural

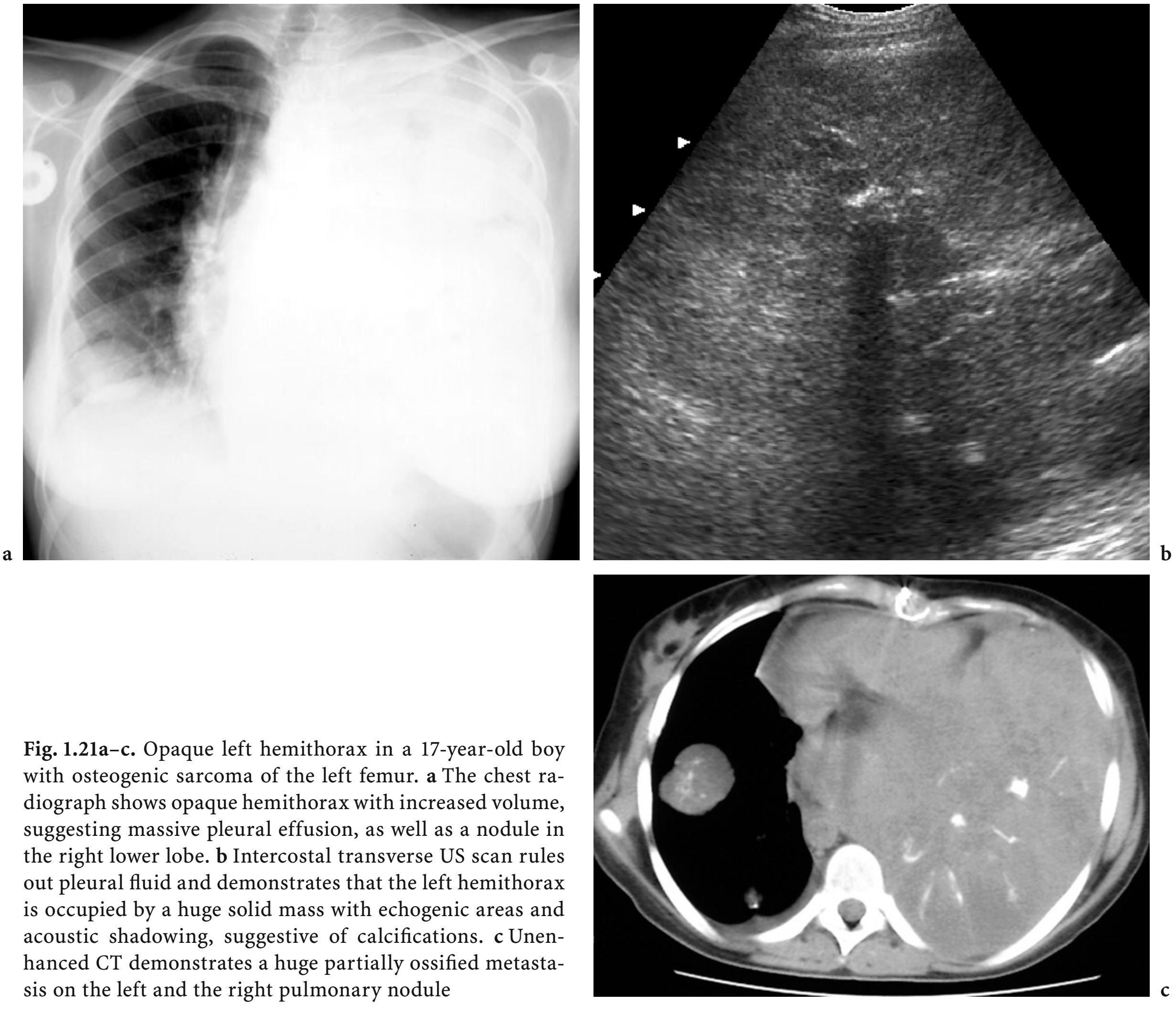

Fig. 1.21a–c. Opaque left hemithorax in a 17-year-old boy with osteogenic sarcoma of the left femur. **a** The chest radiograph shows opaque hemithorax with increased volume, suggesting massive pleural effusion, as well as a nodule in the right lower lobe. **b** Intercostal transverse US scan rules out pleural fluid and demonstrates that the left hemithorax is occupied by a huge solid mass with echogenic areas and acoustic shadowing, suggestive of calcifications. **c** Unenhanced CT demonstrates a huge partially ossified metastasis on the left and the right pulmonary nodule

implants may “hide” behind pleural fluid collections and go unnoticed on chest X-rays. In these patients, sonography can be useful to indicate the origin of the pleural collection and to guide pleural biopsy (Sheth et al. 2000).

1.3.4
Pleural Abnormalities

1.3.4.1
Pneumothorax

Small pockets of air in the pleural space appear as bright, echogenic lines or points. In contrast to what is seen in the normal aerated lung, the image of air in the pleural space does not show comet tail artifacts, always evoked by air-flow in the alveoli (Fig. 1.22). A large pneumothorax can impede visualization of visceral pleura movement, an important indirect sign of air in the pleural space. The presence of air and fluid in the pleural space (hydropneumothorax) results in an air-fluid level on US that can produce a particular movement in real time known as the “curtain sign” (Ben-Ami et al. 1993).

Chest X-ray remains the method of choice for the diagnosis of pneumothorax but several projections may be required to reveal its presence. In severely ill or traumatized patients who cannot be easily moved, pneumothorax can be confirmed or ruled out with use of US without changing the patient’s position.

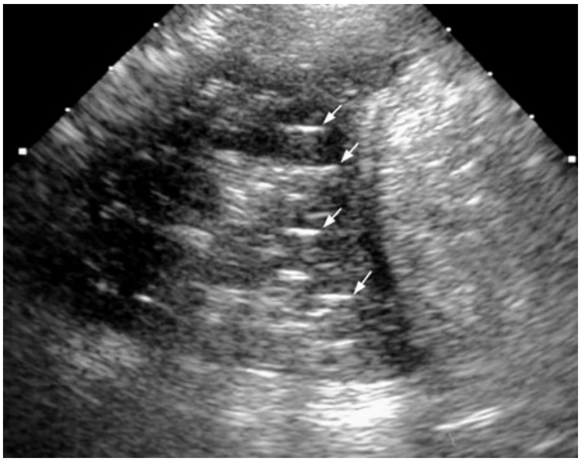

Fig. 1.22. Longitudinal transdiaphragmatic US scan of the lung base in a 7-year-old girl. Air bubbles within the pleural effusion are seen as linear echogenic images without comet tail artifacts (*arrows*)

1.3.4.2
Pleural Effusions

On US imaging through an intercostal approach, pleural fluid is identified as a band-like collection separating the parietal and visceral pleura surfaces. When scanning through the abdomen, the collection is seen just above the diaphragm, blurring the costophrenic angle (Fig. 1.23a,b).

There are several sonographic signs typical of pleural fluid that help to distinguish it from ascites. The three most important are: (1) presence of septa within the collection that move with respiration,

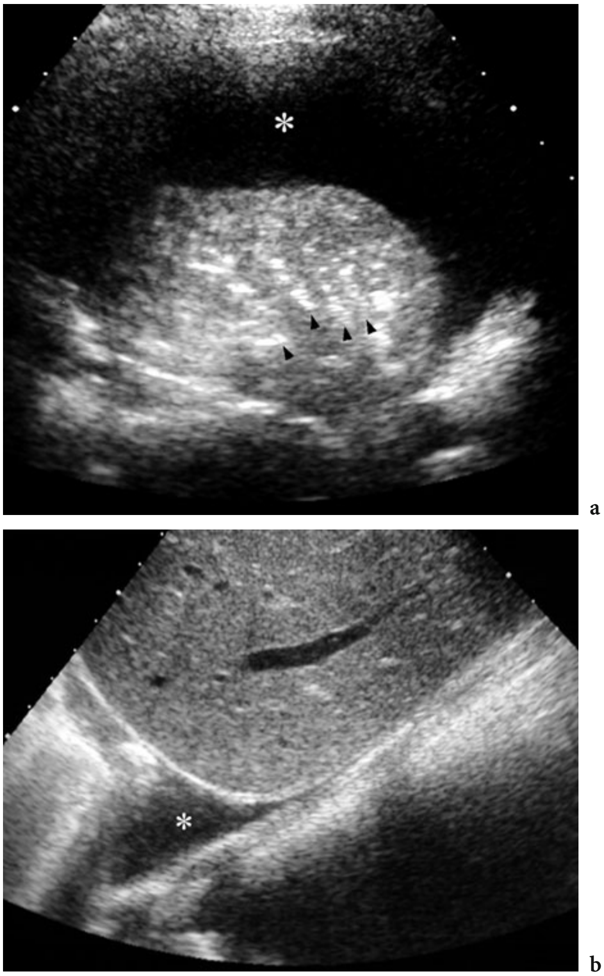

Fig. 1.23a,b. Sonographic appearance of pleural effusion. **a** The pleural fluid (*) is seen as an anechoic band between the parietal and visceral pleurae in this intercostal, transverse US scan. Note air-bronchograms (*arrowheads*) in the consolidated lung. **b** Longitudinal sector scan through the liver shows the pleural fluid (*) blurring the costophrenic angle

(2) the crus sign, (3) the bare area sign (Seibert et al. 1998). The crus sign, pathognomonic of pleural collection, results from displacement of the diaphragmatic crus away from the spine due to interposition of fluid between this structure and the vertebral column (Fig. 1.24). The posterior part of the right lobe of the liver is known as the "bare area" because it is directly attached to the diaphragm without the covering layer of peritoneum. Peritoneal fluid cannot extend behind the right lobe at this point; thus, all fluid collections visualized behind the bare area are necessarily located in the pleural space.

The main role of sonography in the study of pleural effusion is to characterize the simple or complicated nature of the fluid (Yang et al. 1992a). Pleural effusion presenting an anechoic appearance on US study is considered to be simple. Complicated effusions are those that present one or more of the following features: weakly echogenic debris with a swirling movement on real time (Fig. 1.25), mobile fibrin strands, septations (Fig. 1.26), or a honeycomb appearance (Fig. 1.27). Recognition of the septated nature of the pleural collection, information that influences patient management, is not usually provided by chest CT scans (Fig. 1.28a,b).

The sonographic appearance of pleural effusion can be related to the classical division of pleural fluid into exudate or transudate according to its protein content, pleural/serum LDH ratio and other biochemical parameters. On sonography, both transudates and exudates can be anechoic; however, collections presenting some of the complicated features mentioned above are always exudates.

Most exudative pleural effusions in pediatric patients are of infectious origin (Alkrinawi and

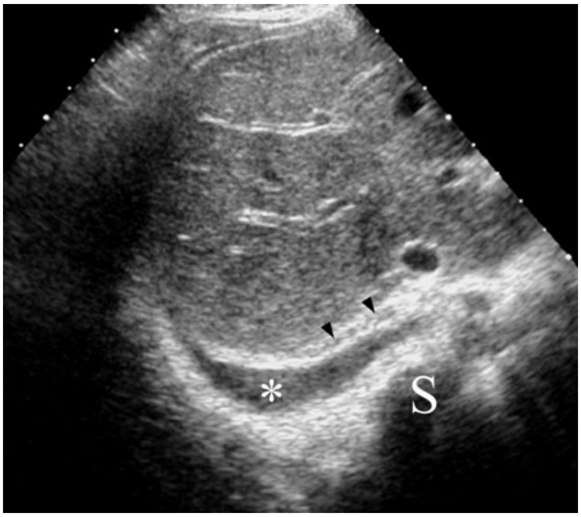

Fig. 1.24. Sector transverse US scan through the liver shows useful sonographic findings that differentiate pleural effusion from ascites. Pleural effusion (*) displaces the right diaphragmatic crus (*arrowheads*) away from the spine (*S*) and extends behind the right posterior portion of the liver (bare area)

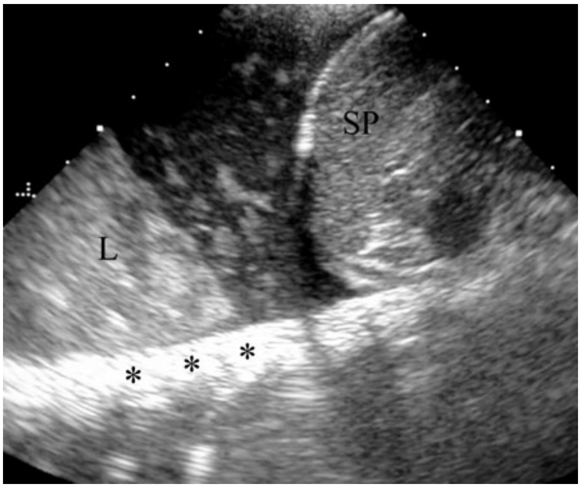

Fig. 1.25. Pleural effusion with floating debris. Longitudinal transdiaphragmatic US demonstrates pleural effusion containing echogenic particles (evidencing its exudative nature) located between the spleen (*SP*) and the consolidated left lower lobe (*L*). The high echogenicity of the ribs (*) results from good transmission of the sound beam through the consolidated lung and pleural fluid

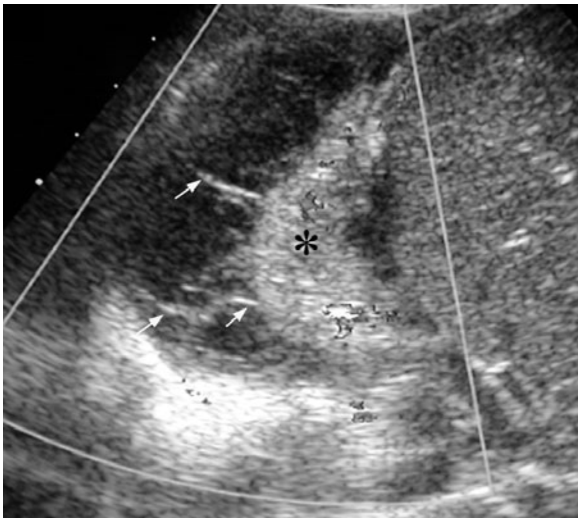

Fig. 1.26. Right sector intercostal longitudinal view demonstrates a collapsed right lower lobe (*) surrounded by pleural effusion with multiple fibrin bands (*arrows*)

Chernick 1996). These collections are known as parapneumonic effusions, a term that is often used interchangeably with empyema. The diagnosis of empyema is established when pleural fluid is grossly purulent, organisms are identified on Gram stain or culture, pleural fluid has a white blood cell count greater than 5×10^9 cells per liter, pH is below 7.0 or glucose level is less than 40 mg/dL.

There is still a great deal of controversy around the clinical management of parapneumonic effusions and empyema. (Givan and Eigen 1998; Ramnath et al. 1998; Maskell et al. 2005; Barnes et al. 2005; Jaffé and Balfour-Lynn 2005). Two main treatment approaches are used: nonoperative, in which patients are treated with antibiotics alone or combined with thoracocentesis or tube thoracostomy; and operative, consisting of pleural debridement or decortication. The goal of both these methods of treatment is to evacuate infected debris and re-expand the lung, and to reduce hospital stay and morbidity.

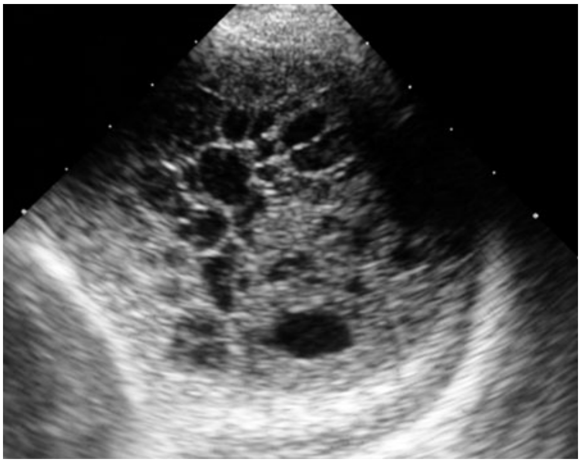

Fig. 1.27. Left transverse, intercostal scan in an 8-year-old boy with streptococcal pneumonia. The pleural space is filled with profuse septations with a honeycomb appearance. This type of collection is not amenable to thoracentesis

Patients who present pleural fluid with few echoes due to debris (low-grade pleural effusion) can be treated with antibiotics alone or antibiotics plus external tube drainage. It has been reported that there is no difference in length of hospitalization between patients treated with either of these options (Ramnath et al. 1998). In patients presenting loculations and septations on US studies, most authors advocate the use of IV antibiotics, together with intrapleural fibrinolytics, mainly urokinase, administered through a thoracostomy tube (Park et al. 1996; Bouros et al. 1997). When these measures fail, decortication or video thoracostomy may shorten the usually lengthy hospital stay. In patients with a severe honeycomb pattern on the initial US scan, early surgical treatment should be considered.

Management of these patients according to the US appearance of pleural collections seems clear-cut; however in our experience small exudates can rapidly (within 24 h) increase in volume and change their sonographic appearance, despite antibiotic therapy. Thus, close sonographic surveillance of children with pleuro-pneumonia is recommended.

It is clear that sonography has important implications in the management of pleural effusion be-

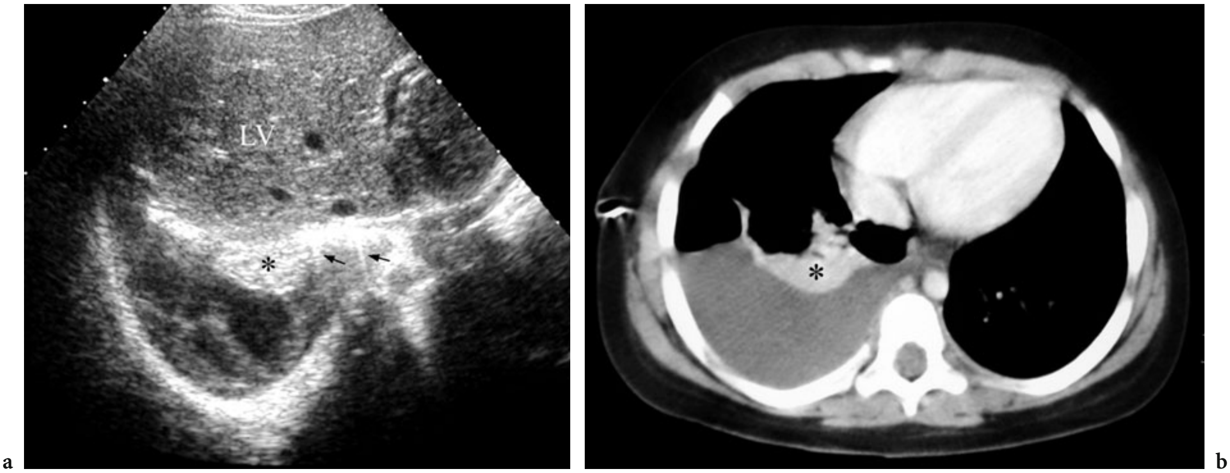

Fig. 1.28a,b. Transverse US scan (a) through the liver (LV) and enhanced CT scan (b) of a 5-year-old girl with pleural pneumonia. The compressed, atelectatic lung (*) is clearly seen in both studies, but the septated nature of the pleural collection is only evident on the US scan. Note comet tail artifacts in the normal aerated lung adjacent to the collapse (*arrows*)

cause of its ability to characterize the internal composition of pleural fluid and monitor the course of the underlying process. Moreover, it is a valuable tool for localizing loculations for thoracocentesis or thoracostomy tube placement (Fig. 1.29a,b). The incidence of pneumothorax is considerably reduced when pleural taps are sonographically guided, particularly in the case of small or loculated collections (Raptopoulos et al. 1991; Shankar et al. 2000).

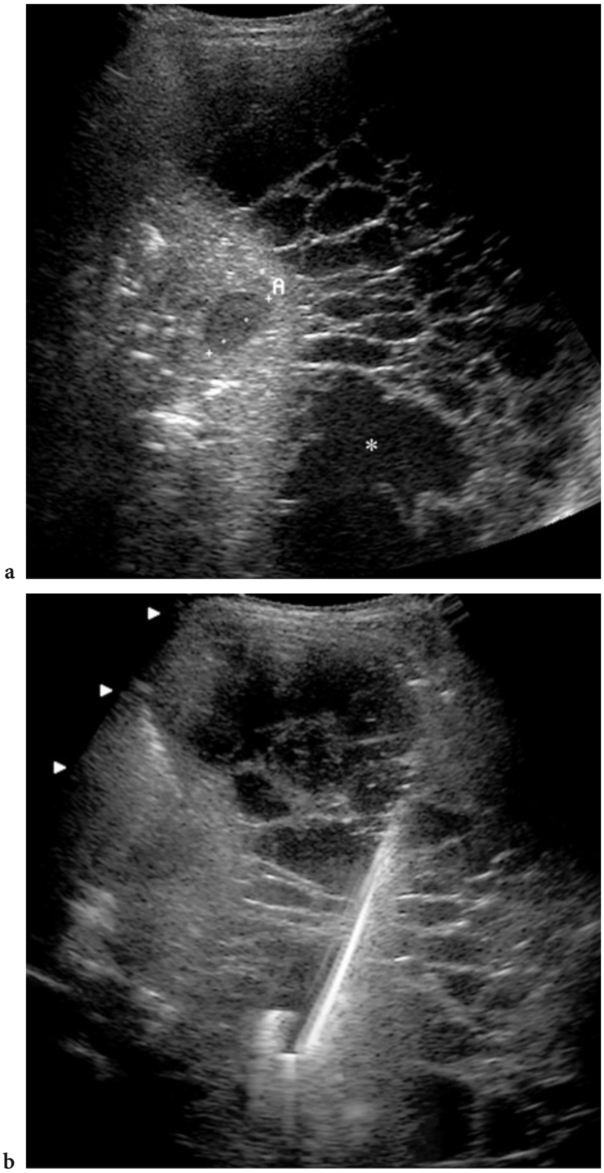

Fig. 1.29a,b. Pleural effusion with multiple septations in a 12-year-old boy with cavitary pneumonia. **a** Caliper measures area of necrosis in the affected lung. The large loculus (*) is selected for urokinase instillation by means of an ultrasound-guided pigtail catheter (**b**)

1.3.4.3
Pleural Tumors

Primary tumors originating in the pleura, such as mesothelioma, are very rare in children, and tumoral involvement of this structure is most often due to metastasis. Metastatic disease to the pleura often causes large pleural effusions that are probably due to impaired lymphatic drainage. This secondary pleural fluid, which can be profuse in some patients, may mask the tumoral mass on chest X-rays and in these cases ultrasound is particularly helpful (Fig. 1.30a,b). Metastatic involvement of the

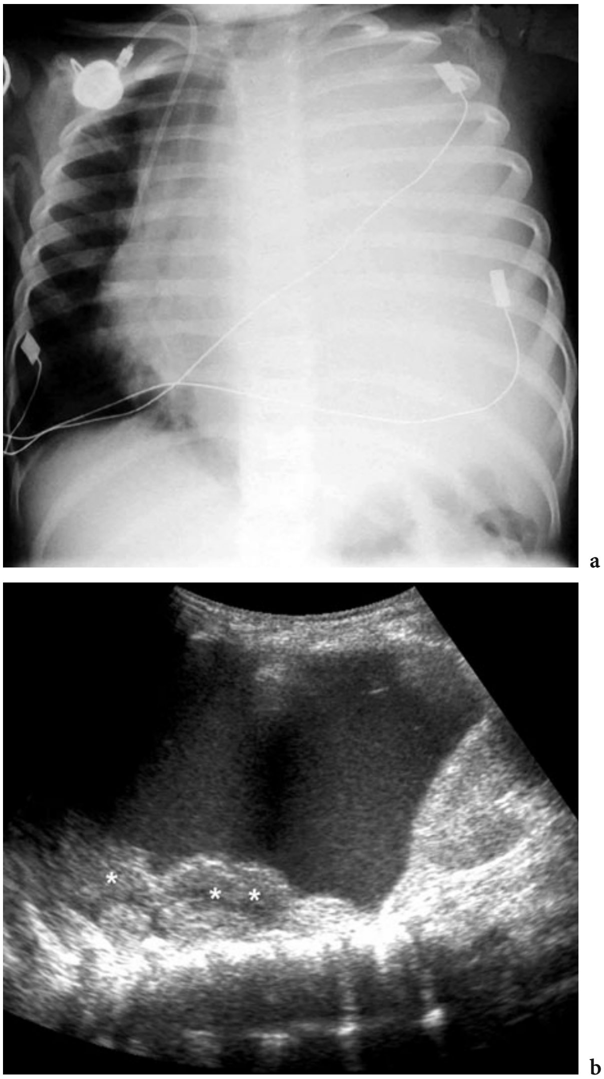

Fig. 1.30a,b. Massive pleural effusion in a patient with lymphoma. **a** Chest radiograph shows opaque left hemithorax with mediastinal displacement to the right. **b** Several pleural-based lymphomatous nodules (*) are identified through the pleural fluid on US examination

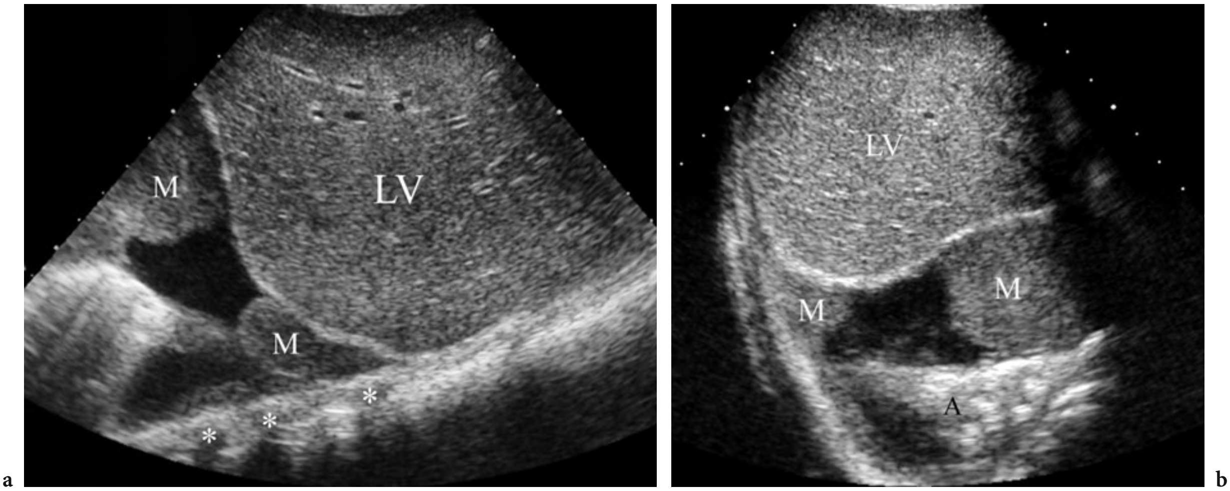

Fig. 1.31a,b. Pleural metastasis in a 5-year-old boy with rhabdomyosarcoma of the biliary tract. **a** Longitudinal view through the liver (LV) shows several echogenic nodules (*M*) associated with pleural effusion. The chest wall is delineated by echogenic ribs (*). **b** Transverse view additionally demonstrates a crowded bronchogram that differentiates the atelectatic lung (*A*) from the metastatic masses (*M*)

pleura can be caused by various intrathoracic or extrathoracic tumors, such as Wilms' tumor, lymphoma, neuroblastoma and rhabdomyosarcoma. These are generally seen as well-delineated, solid echogenic masses (Fig. 1.31a,b).

1.4
Mediastinum

1.4.1
Examination Technique

To study the mediastinum in the pediatric population, we recommend small sector or convex multifrequency probes. High-frequency linear transducers are particularly useful in newborns or for studying lesions located superficially. It is advisable to adjust the depth to the region of interest, decrease the number of foci, and reduce the lateral field of vision in order to increase the frame rate. We recommend including a large vessel or cardiac chamber in the field of study to establish anatomic relationships and to analyze the echogenicity of the lesion to determine if it is cystic or solid.

We divide the mediastinum into anterior, middle and posterior compartments. The anterior mediastinum or prevascular region is found in front of the superior vena cava, aorta and pulmonary artery, and behind the sternum. The middle mediastinum can be further divided into four anatomic regions: paratracheal, supra-aortic, aortopulmonary and subcarinal (Fig. 1.32). The paratracheal region refers to the right paratracheal area. The supra-aortic refers to the upper portion of the left paratracheal region, above the aortic arch. The aortopulmonary region includes the area below the aortic arch and above the right pulmonary artery and the left bronchus. The subcarinal region is located behind the bifurcation of the pulmonary artery, above the left atrium in front of the esophagus and below the carina. The posterior mediastinum comprises the pre- and paravertebral spaces.

The anterior and middle mediastinum can be well accessed with the following approaches: suprasternal, supraclavicular, parasternal, subxiphoid, and subcostal; the most important of these are the suprasternal and the left parasternal. When using the suprasternal approach, the patient should be in a supine decubitus position with a cushion under the back and the neck slightly extended. The transducer is placed above the sternal manubrium and tilted caudally. To obtain an oblique sagittal view, the probe is displaced laterally to encounter the space between the trachea and sternocleidomastoid muscle. For the parasternal approaches, a right or left lateral decubitus position (the examined side down) is recommended to displace the mediastinum downwards and increase the acoustic window (Fig. 1.33a,b).

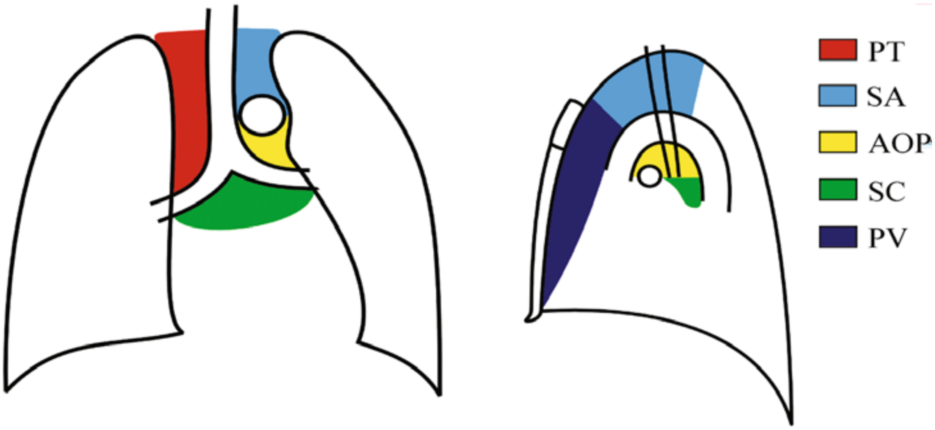

Fig. 1.32. Diagrams showing US division of the anterior and middle radiologic mediastinal regions: *PV*, prevascular; *PT*, paratracheal; *SA*, supraaortic; *AOP*, aortopulmonary; *SC*, subcarinal

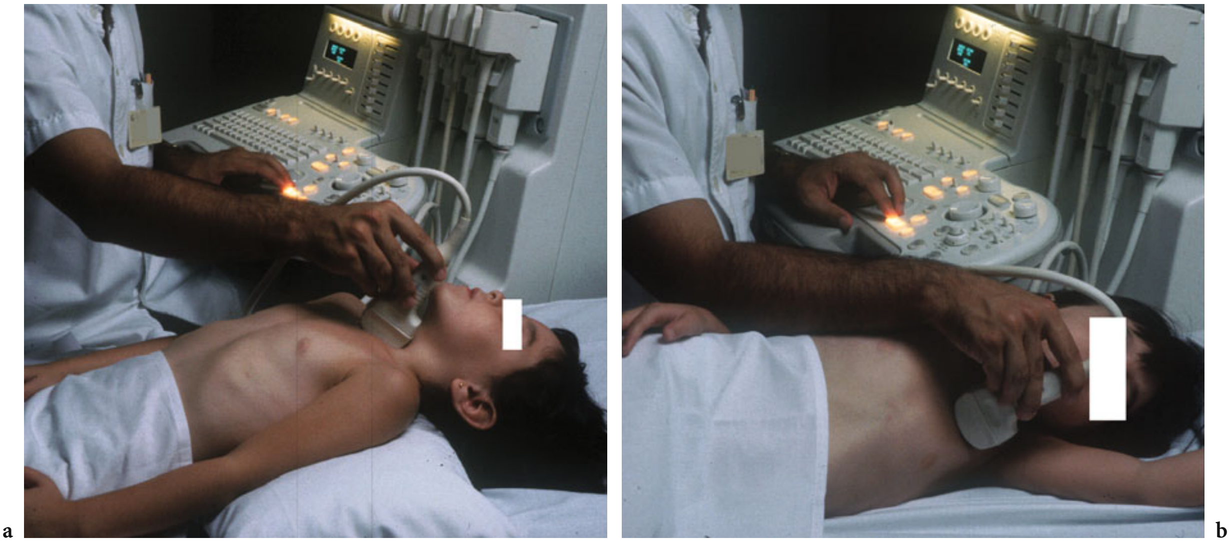

Fig. 1.33a,b. Patient positioning for US access to the mediastinum using the suprasternal (**a**) and left parasternal (**b**) approaches

The supraclavicular approach is useful for increasing the field of view of the paratracheal regions. The subxiphoid and subcostal approaches are used to visualize the cardiophrenic and retrocrural regions, which will be discussed in another section of this chapter. If the sternum is not completely ossified, the trans-sternal approach can be used to study the prevascular and subcarinal regions. The latter region can also be visualized in young children using the thymus as acoustic window. In older children the subcarinal area can be accessed through the cardiac chambers, placing the transducer at the fifth intercostal space, in an oblique position. The posterior mediastinum is accessed through a paravertebral approach.

1.4.2
Normal US Appearance, Artifacts and Pitfalls

Sonographic study of the mediastinum requires a meticulous technique and extensive knowledge of the mediastinal anatomy. We recommend the use of five standard sonographic slices (three obtained with the suprasternal approach and two with the left parasternal) to visualize the complete anterior and middle regions of the mediastinum. We stress that these standard US slices differ from those obtained with CT. The majority are obtained in oblique, coronal or sagittal planes and therefore, the same slice may show structures corresponding to more than one anatomic region.

Oblique coronal view through the suprasternal approach is shown in Figure 1.34. This section is used to visualize the paratracheal region, located between the right upper pulmonary lobe and the trachea. It is also useful for studying the aortopulmonary region, which is seen in this view as an echogenic triangular image. The probe is placed almost perpendicular to, and slightly compressing, the right sternocleidomastoid muscle. The anatomic reference for this region is the innominate artery and the scan should include the pleural surface of the right upper lobe, the trachea and the upper margin of the left bronchus. The paratracheal region is a virtual space and is considered normal when the pleural surface of the upper lobe abuts the trachea. Pathology in this region is recognized by a separation of these two structures (Fig. 1.34a–c).

Coronal view through the suprasternal approach is shown in Figure 1.35. This scan is not used to study a specific mediastinal region, but is very useful for visualizing the vessels, particularly the superior vena cava. The view should include the right pulmonary artery and its bifurcation, located within the mediastinum (Fig. 1.35a,b). It is particularly helpful to confirm or rule out superior vena cava thrombosis in patients with a central venous catheter.

Oblique parasagittal view through the suprasternal approach is shown in Figure 1.36. This view is used to visualize the aortopulmonary region, which has a characteristic ultrasound appearance and should be identified in all patients submitted to mediastinal exams. The probe is placed above the sternal manubrium between the trachea and left sternocleidomastoid muscle. Due to the presence of mediastinal fat at this level, the aortopulmonary region is seen as a highly echogenic, half-moon-shaped image. The anatomic reference for this region is the aortic arch and the section should also include the origins of the left carotid and subclavian arteries (Fig. 1.36a–c).

Axial view through the left parasternal approach is shown in Figure 1.37. This section is used to study

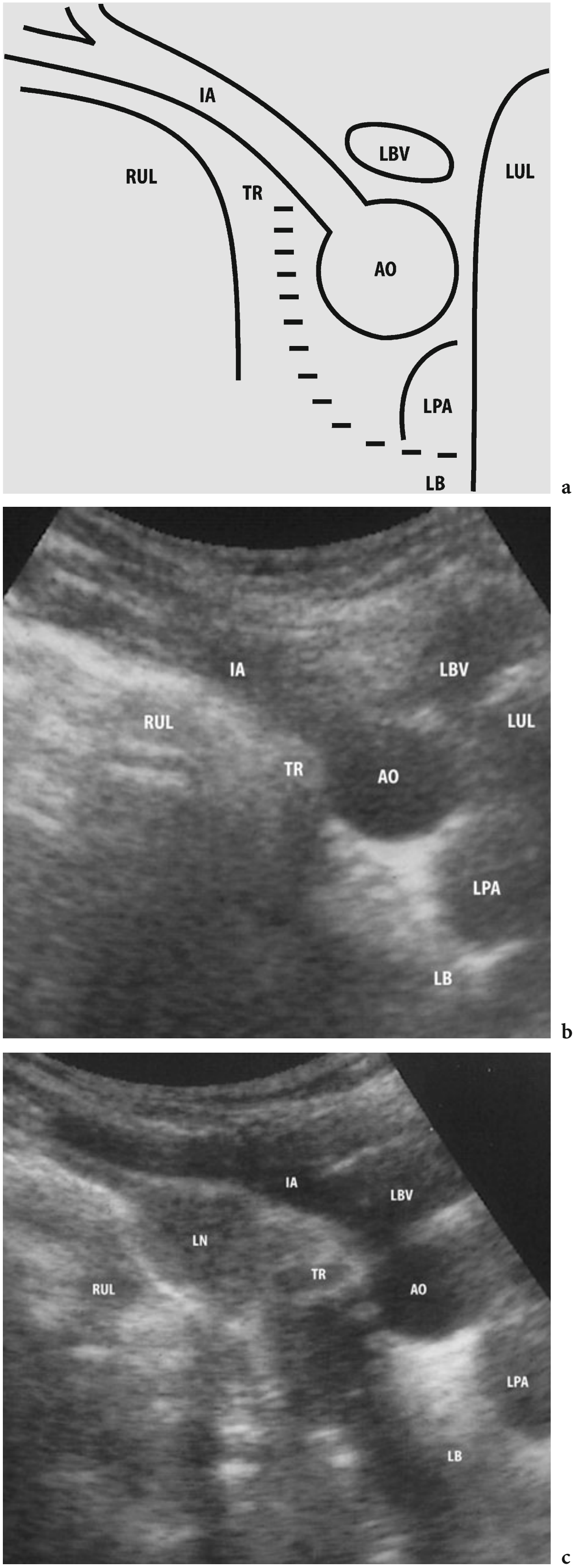

Fig. 1.34a–c. Suprasternal, oblique coronal section. **a** Diagram. **b** Normal US scan. Note echogenic line of the pleura-lung interface where the right upper lobe abuts the trachea. **c** In a patient with lymphadenopathy, the echogenic line is bowed and displaced by the mass (*IA*, innominate artery; *LBV*, left brachiocephalic vein; *AO*, aorta; *TR*, trachea; *LB*, left bronchus; *RUL*, right upper lobe; *LUL*, left upper lobe; *LPA*, left pulmonary artery; *LN*, lymph node)

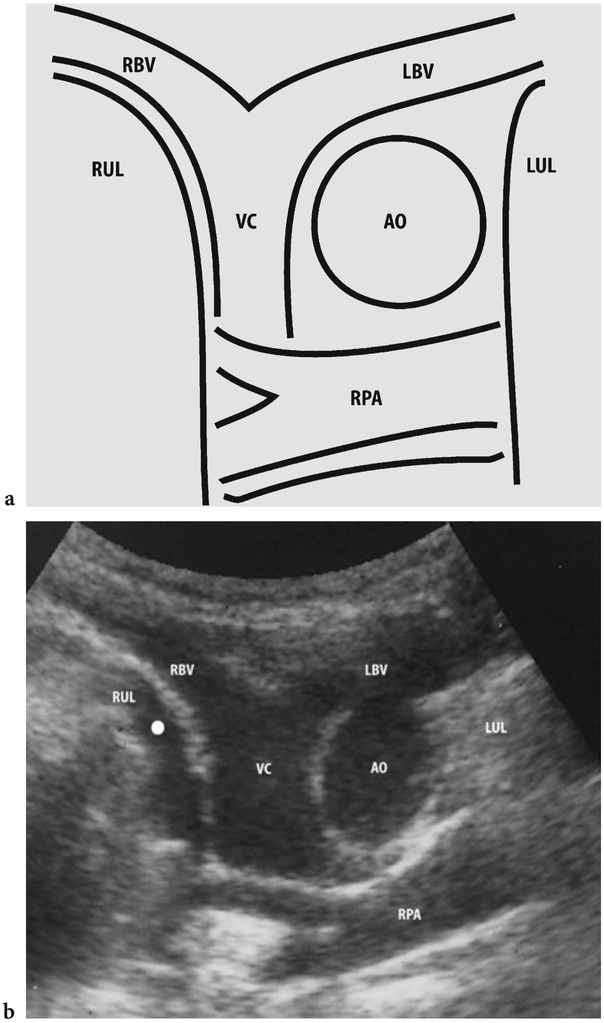
a
RBV
LBV
RUL
LUL
VC
AO
RPA
b
RBV
LBV
RUL
LUL
VC
AO
RPA

Fig. 1.35a,b. Suprasternal coronal section. **a** Diagram. **b** Normal US scan. (*RBV*, right brachiocephalic vein; *LBV*, left brachiocephalic vein; *AO*, aorta; *RUL*, right upper lobe; *LUL*, left upper lobe; *RPA*, right pulmonary artery; *VC*, vena cava). The *dot* indicates a mirror artifact of the vessels adjacent to the pleura, mimicking pleural effusion

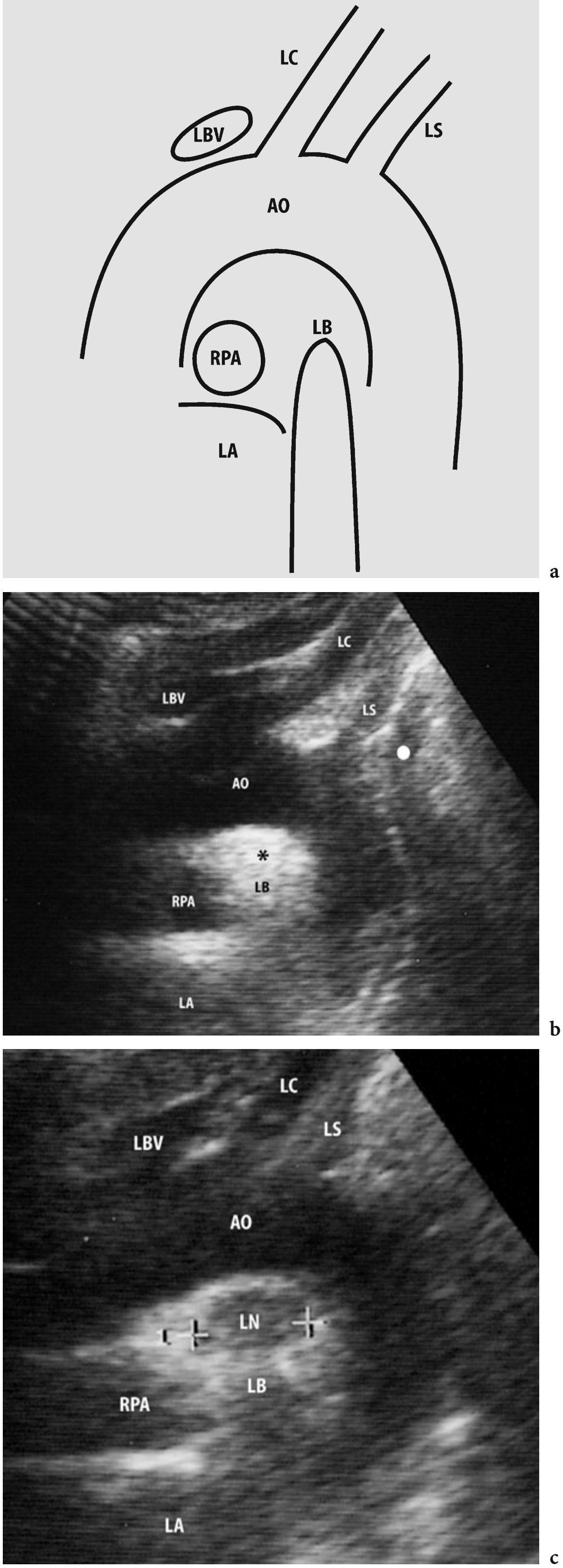
a
LC
LBV
LS
AO
LB
RPA
LA
b
LC
LBV
LS
AO
*
LB
RPA
LA
c
LC
LBV
LS
AO
LN
LB
RPA
LA

Fig. 1.36a–c. Suprasternal oblique parasagittal section. **a** Diagram. **b** Normal US scan. Note the normal hyperechoic appearance of the aortopulmonary region (*). **c** US scan in a patient with lymphadenopathy in this region. (*LBV*, left brachiocephalic vein; *AO*, aorta; *RPA*, right pulmonary artery; *LC*, left carotid artery; *LS*, left subclavian artery; *LA*, left atrium; *LB*, left bronchus; *LN*, lymph node. The *dot* indicates a mirror artifact of the vessel

the subcarinal and prevascular regions and is similar to the CT slices obtained for this area. The transducer is placed at the second intercostal space. The anatomic reference for this view is the pulmonary artery bifurcation (Fig. 1.37 a–c).

Parasagittal view through the left parasternal approach is shown in Figure 1.38. Also used to study the subcarinal and prevascular regions, the references for this section are the ascending aorta, the trachea and the esophagus (Fig. 1.38a–c). It is important to identify the esophagus by making the patient swallow saliva or water. For the two parasternal approaches, the patients should be placed in a left decubitus position to increase the size of the anatomic acoustic window.

A number of artifacts are generated during mediastinal sonography. The most common are “mirror artifacts” consisting in duplicated images of vessels or normal and abnormal structures adjacent to the mediastinal pleura. Vascular “duplication” in this location can simulate a pleural fluid collection (Fig. 1.35b). The tracheal and bronchial cartilage can interrupt the air-column and produce multiple parallel echogenic images with a step-ladder appearance that we refer to as “stair artifact” (Fig. 1.39).

Some normal anatomic structures, such as the pericardial recesses and the esophagus can have a misleading sonographic appearance and simulate pathology. For example, the superior pericardial recess can mimic adenopathy in the aortopulmonary region (Fig. 1.40). The location, triangular shape, changes in size with the heartbeat, and anechoic appearance are the clues that differentiate the pericardial recess from lymph nodes.

The normal esophagus may simulate a subcarinal solid mass, but can be properly identified by asking the patient to swallow saliva or fluid during the examination. The saliva is seen as an echogenic image passing through the apparently solid structure, thereby ruling out a mediastinal mass (Fig. 1.41a,b). In patients with gastro-esophageal reflux, the passage of gastric content to the esophagus can be visualized in real-time.

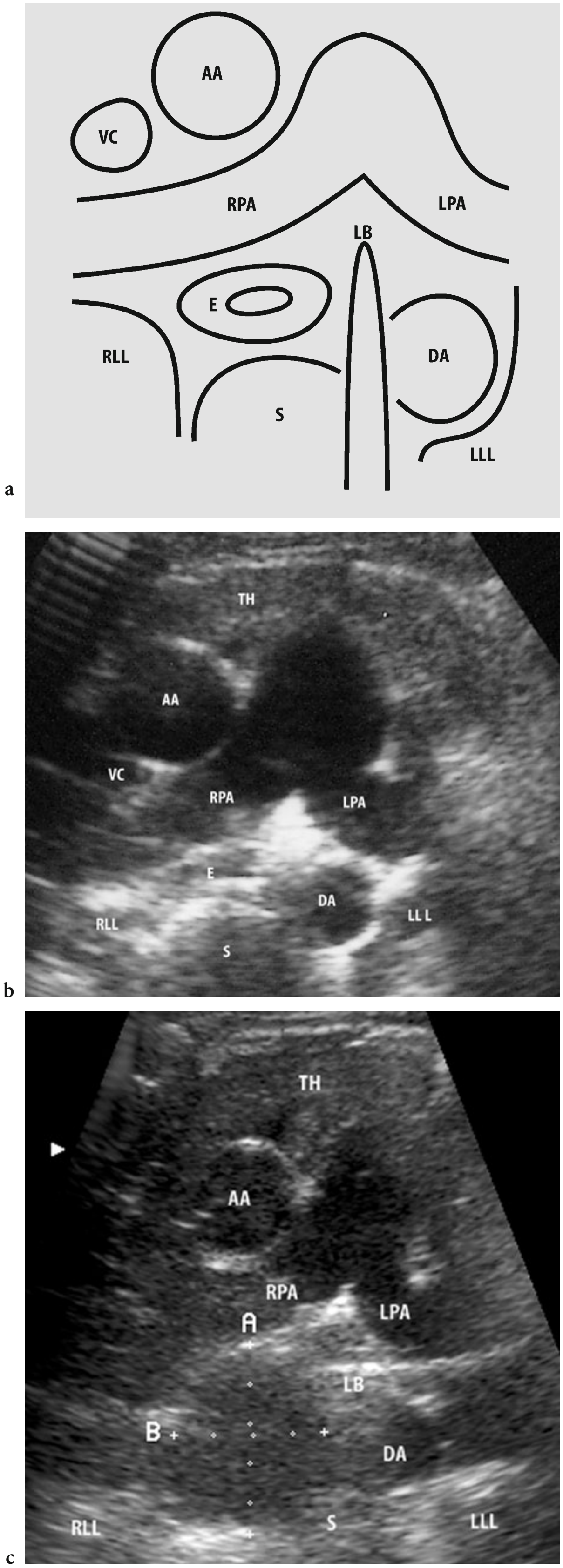

Fig. 1.37a–c. Left parasternal axial section. **a** Diagram. **b** Normal US scan. **c** US scan in a patient with lymphadenopathy (*AB*, calipers) in the subcarinal space. (*TH*, thymus; *AA*, ascending aorta; *DA*, descending aorta; *E*, esophagus; *RPA*, right pulmonary artery; *LPA*, left pulmonary artery; *VC*, vena cava; *LB*, left bronchus; *RLL*, right lower lobe; *LLL*, left lower lobe; *S*, spine)

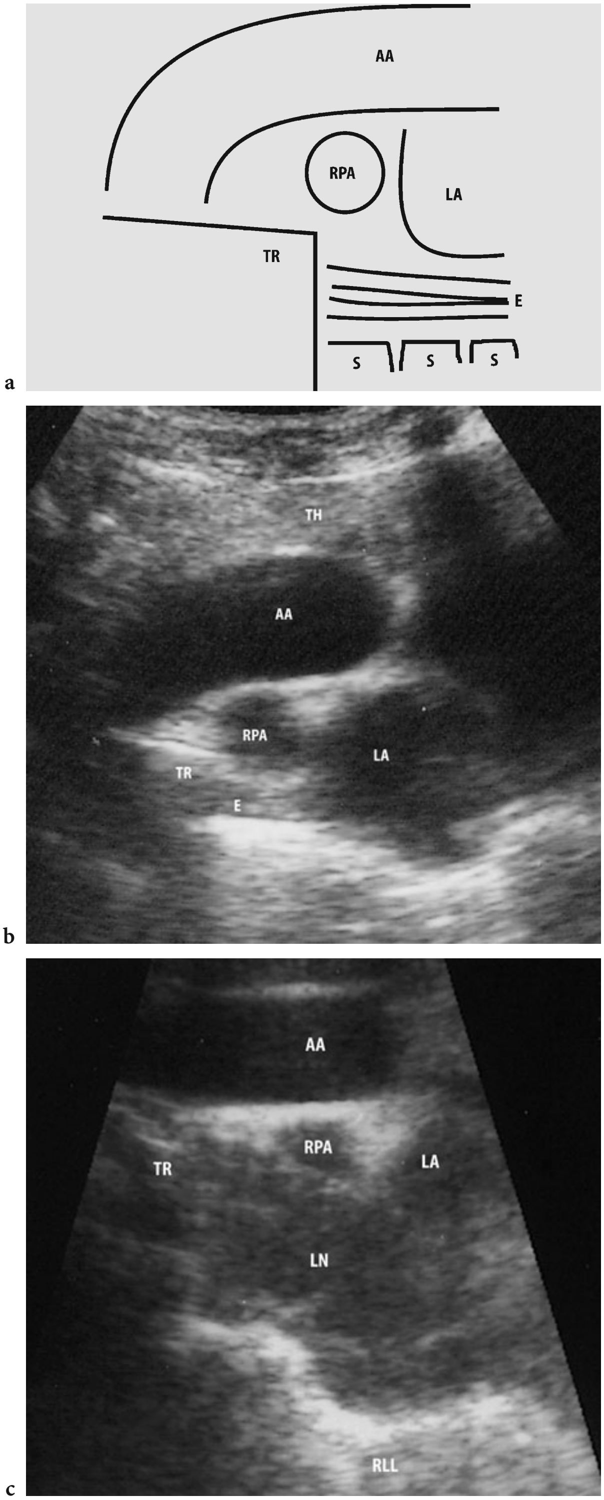

Fig. 1.38a–c. Left parasternal parasagittal section. **a** Diagram. **b** Normal US scan. **c** US scan in a patient with lymphadenopathy in the subcarinal space compressing the right pulmonary artery (*AA*, ascending aorta; *RPA*, right pulmonary artery; LA, left atrium; *S*, spine; *TR*, trachea; *TH*, thymus; *E*, esophagus; *LN*, lymph node)

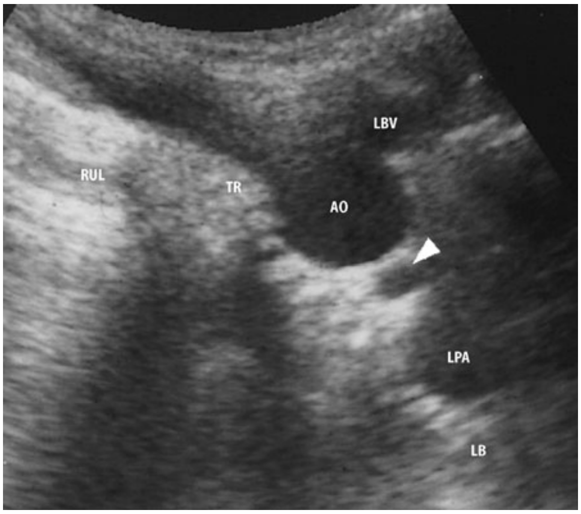

Fig. 1.39. Suprasternal oblique coronal view shows a stair-step artifact caused by tracheal (*TR*) and left bronchial (*LB*) cartilage. *Arrowhead* shows superior sinus of the pericardium (*RUL*, right upper lobe; *LBV*, left brachiocephalic vein; *LPA*, left pulmonary artery)

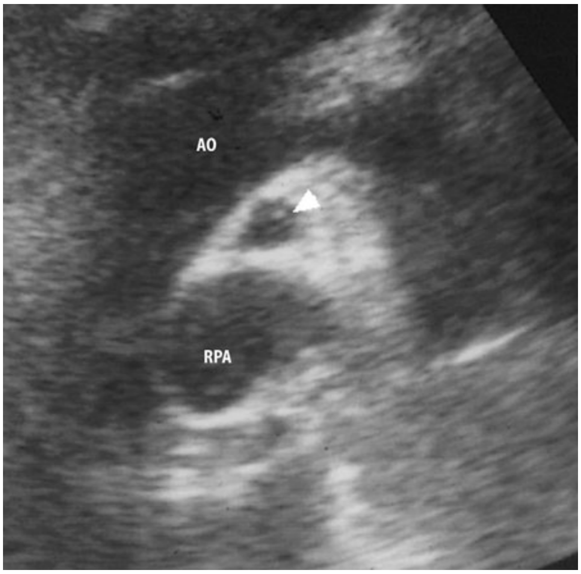

Fig. 1.40. Suprasternal oblique parasagittal section shows the superior pericardial recess (*arrowhead*) simulating adenopathy in the aortopulmonary region. Its typical triangular shape and anechoic echotexture permit proper identification. Compare with Fig. 1.25c (*AO*, aorta; *RPA*, right pulmonary artery; *LA*, left atrium)

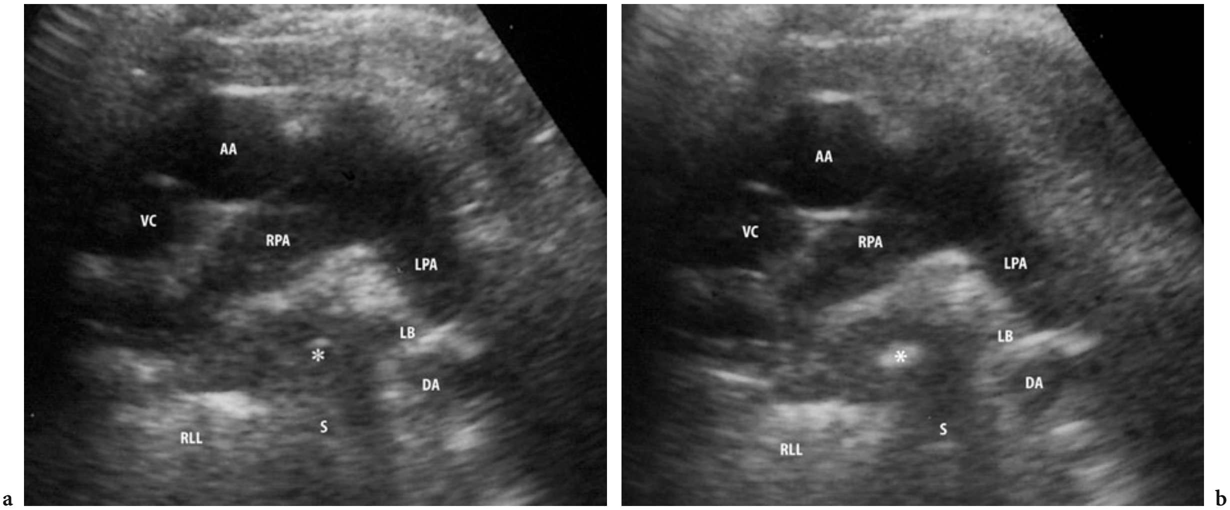

Fig. 1.41. **a** Esophagus (*) simulates a mass in the subcarinal region in this axial view through the left parasternal approach. **b** After the patient swallows, an echogenic image (*) corresponding to saliva identifies the esophagus. (*AA*, ascending aorta; *DA*, descending aorta; *RPA*, right pulmonary artery; *LPA*, left pulmonary artery; *LB*, left bronchus; *RLL*, right lower lobe; *S*, spine; *VC*, vena cava)

1.4.3
Indications for Mediastinal US

Scanning of children with mediastinal widening, evaluation of vascular anomalies and the search for lymph nodes are the main indications for mediastinal US in children. It can also be used to evaluate oesophageal atresia and tracheo-oesophageal fistula (Gassner et al. 2005), to assess possible complications in patients with indwelling catheters (Maruyama et al. 2006) and to perform mediastinal biopsies (Annessi et al. 2003; Gorguner et al. 2003).

1.4.4
Mediastinal Abnormalities

For illustrative purposes, we have organized mediastinal pathologies according to the region (anterior, middle and posterior) where they most frequently occur.

1.4.4.1
Anterior Mediastinum

Anterior mediastinum pathology in children is commonly related to the thymus; thus, knowledge of the normal US appearance of this organ is essential to recognize lesions in this compartment. On chest X-rays the thymus is identified by characteristic radiological signs, such as the “sail” and “thymic wave” signs. However, it often has a misleading appearance on plain films and simulates a mediastinal mass. In this situation US can clarify the doubtful findings and avoid the practice of more invasive explorations.

On US, the normal thymus has a bilobulated appearance and a homogeneous echotexture with some echogenic strands (Kim et al. 2000). It is hypoechoic relative to the thyroid gland and has a smooth, well-defined margin due to its fibrous capsule. It is a soft organ that does not compress neighboring vascular structures, a characteristic that can help the radiologist to differentiate it from mediastinal masses (Fig. 1.42). The normal thymus can vary considerably in position, extension, size and configuration. In small children the organ can extend from the cervical region to the diaphragm (Swischuk and John 1996; Fitoz et al. 2001). During respiration and particularly when the child is crying, the thymus can displace to above the sternal manubrium and simulate a cervical mass (Figs. 1.43 and 1.44a,b).

One important characteristic of the thymus is its tendency to vary in size in response to acute stress. Rapid and severe involution of the gland, a process mediated by endogenous corticosteroid production, occurs in numerous clinical situations (e.g. burns, chemotherapy, severe disease). Weeks to months after cessation of the stress, the thymus can regenerate

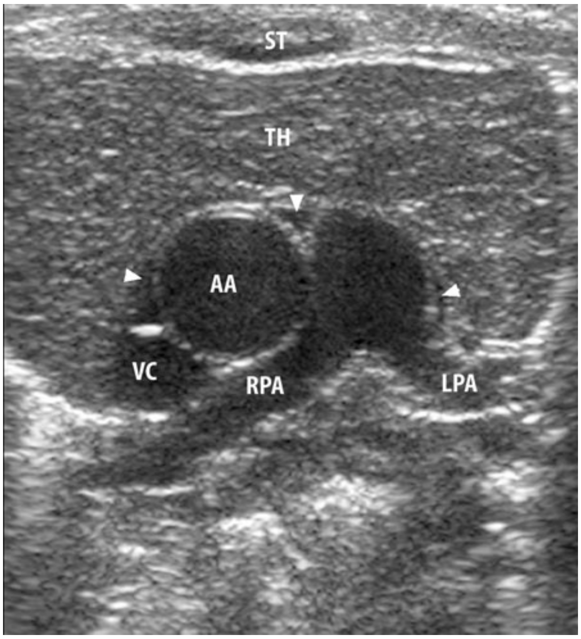

Fig. 1.42. Transverse view of normal thymus (*TH*) in a 4-year-old boy. Vascular structures are not compressed by the gland , which has a rounded configuration (*AA*, ascending aorta; *VC*, vena cava; RPA, right pulmonary artery; *LPA*, left pulmonary artery; *ST*, sternum; arrowheads, superior pericardial recesses)

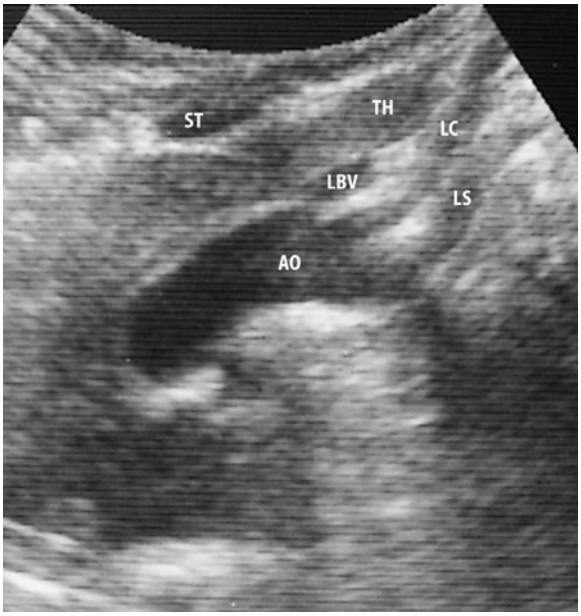

Fig. 1.43. Oblique suprasternal sagittal view in a 2-month-old boy evidences cervical extension of the thymus (*TH*), which is seen anterior to left carotid (*LC*) and left subclavian (*LS*) arteries (*AO*, aorta; *ST*, sternum; *LBV*, left brachiocephalic vein)

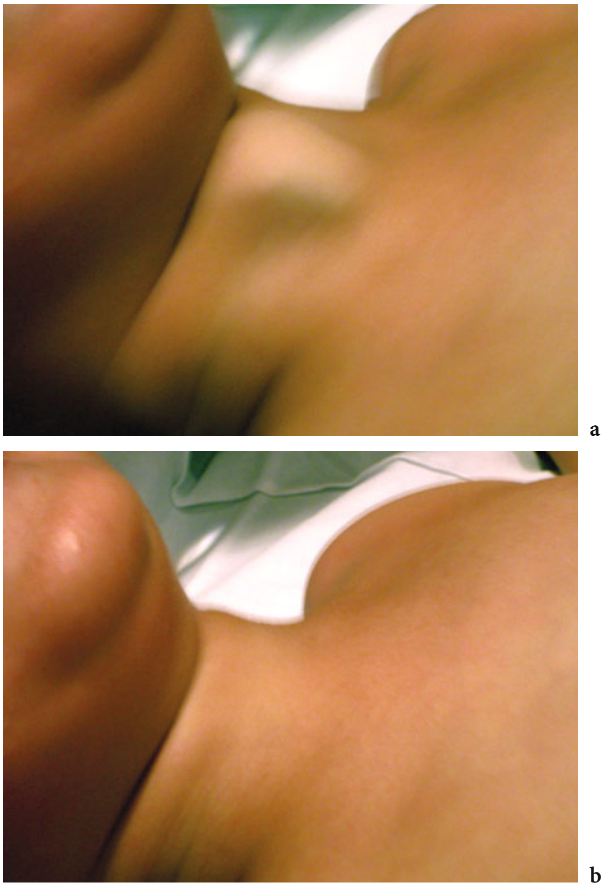

Fig. 1.44a,b Clinical photos of a 2-month-old-boy with a cervical mass corresponding to thymus extending above the esternal manubrium. **a** Clinical photo during which the boy is crying. **b** Clinical photo with the boy at rest

and even enlarge by "rebound growth" (Fig. 1.45a,b). This enlargement of the thymus affects both the cortex and medulla and must be differentiated from thymic growth associated with autoimmune diseases. Thymic growth in these cases is known as lymphoid follicular hyperplasia and affects only the medulla. It is a frequent finding in children with HIV infection.

Thymic aplasia and hypoplasia are two congenital anomalies generally associated with immunologic deficiency syndromes, such as DiGeorge's syndrome, Nezelof's disease, and ataxia telangiectasia. Other congenital alterations of the thymus include position anomalies, which are classified as ectopic or aberrant (Koumanidou et al. 1998). Ectopic thymus refers to thymic tissue located in any position except the normal pathway of embryologic descent of the gland (Fitoz et al. 2001). It is occasionally a

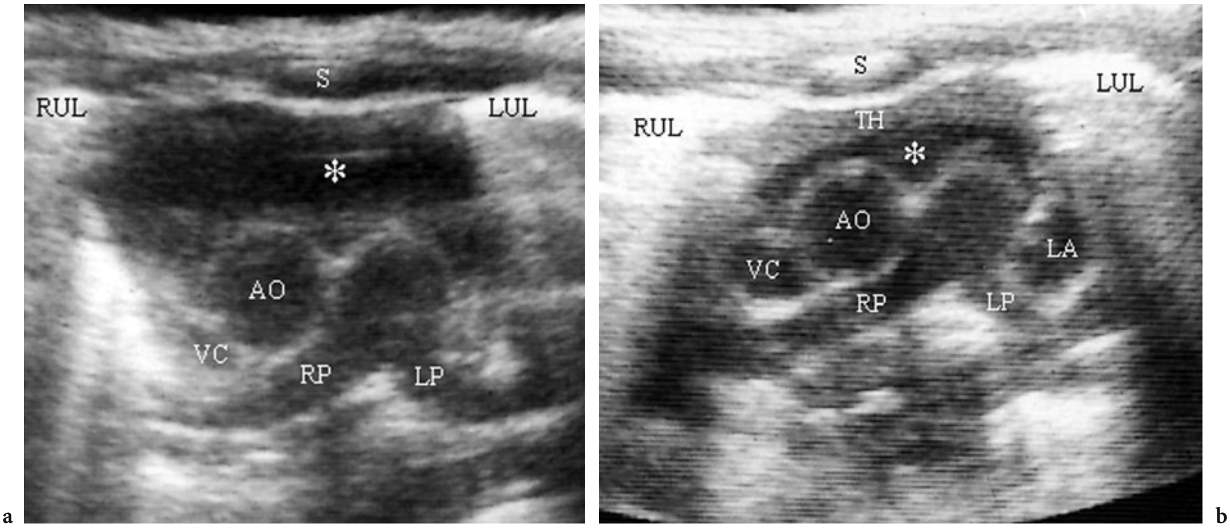

Fig. 1.45a,b. Premature newborn boy with severe respiratory distress. **a** On suprasternal axial US, the thymus is not visualized and the anterior space is filled with pericardial fluid (thymic involution). **b** After 12 days the boy had improved clinically and the thymus is clearly seen on US (thymic rebound) (*TH*, thymus; *AO*, ascending aorta; *RP*, right pulmonary artery; *LA*, left atrium; *VC*, vena cava; asterisk, pericardial fluid; *LUL*, left upper lobe; *RUL*, right upper lobe; *S*, sternum; *LP*, left pulmonary artery)

life-threatening condition due to airway compression. US can detect this anomaly, but is not helpful in patients with ectopic tissue located behind the trachea or in the posterior mediastinum. Aberrant thymus refers to thymic tissue located anywhere along the normal pathway of embryologic descent of the gland. This condition is predominantly asymptomatic and presents as a cervical or suprasternal mass, which can be easily characterized by US. Aberrant thymus should be suspected when the mass presents the same echogenicity as normal thymus (Fig. 1.46a–c).

With the use of sonography, thymic cysts are now increasingly detected. They are seen as well-defined uni- or multilocular anechoic lesions, which can have peripheral calcifications (Rudick and Wood 1980). Multilocular thymic cysts are seen in approximately 1% of pediatric patients with HIV infection (Avila et al. 1996) and, since this entity does not require specific treatment, US is recommended for serial follow-up (Fig. 1.47a,b).

Primary tumors of the thymus (thymolipoma and thymoma) are exceedingly rare in children. Most thymic tumors in the pediatric age group are secondary to lymphoma or leukemia. The affected gland enlarges and appears as a hypoechoic, hyperechogenic or heterogeneous, fixed mass compressing the adjacent anatomic structures (Lemaitre et al. 1987; Hamrick-Turner et al. 1994; Kim et al. 2000; De Pascale et al. 2006). All thymic masses that are heterogeneous on US should be further examined by CT or MRI.

Germ cell tumors include a wide spectrum of histological types (teratoma, seminoma, endodermal sinus tumor, choriocarcinoma and embryonal carcinoma) and 94% are located in the anterior mediastinum. The most common germ cell tumor is mature teratoma. On US the tumor may be mostly cystic or have a complex appearance with echogenic fat, soft tissue components and calcifications. In contrast to normal thymus, these tumors often compress the neighboring anatomic structures (Fig. 1.48a,b). CT and MRI are superior to US for delineating the extension of the tumor and for detecting spread to the pericardium or pleura in cases of tumor rupture, a common occurrence in mediastinal teratoma (Sasaka et al. 1998). Lipomas and lymphangiomas are benign tumors that often extend from the cervical area to the anterior mediastinum through the thoracic inlet. Although they can be detected with US), MRI better delineates the entire tumor, including the cervical extension (Castellote et al. 1999; Ching et al. 2002) (Fig. 1.49a–c).

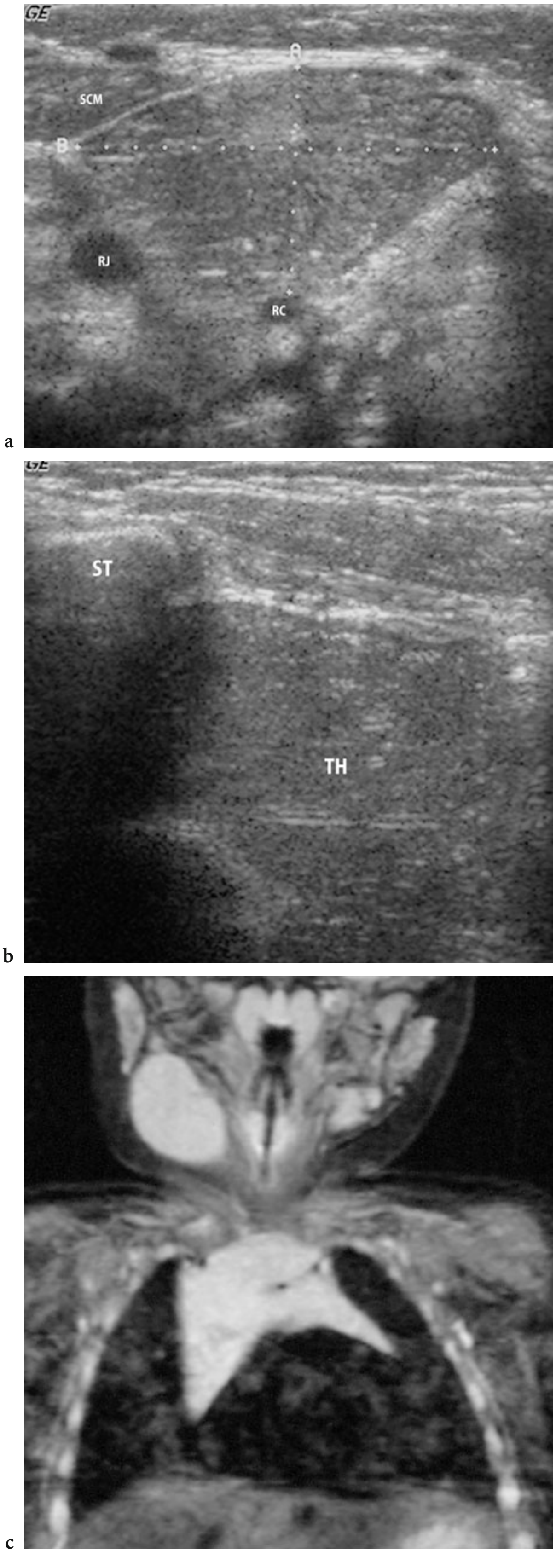

Fig. 1.46a–c. Aberrant thymus in a 1-month-old boy with right cervical mass. **a** US axial view shows the mass (between calipers *AB*) located front of the right jugular vein (*RJ*) and right carotid artery (*RC*) and medial to the right sternocleidomastoid muscle (*SCM*). **b** The mass presents the same echogenicity as the normal retrosternal thymus (*TH*) (*ST*, sternum). **c** On coronal FAT SAT MRI, T2- weighted image the cervical mass presents a signal intensity identical to normal thymus

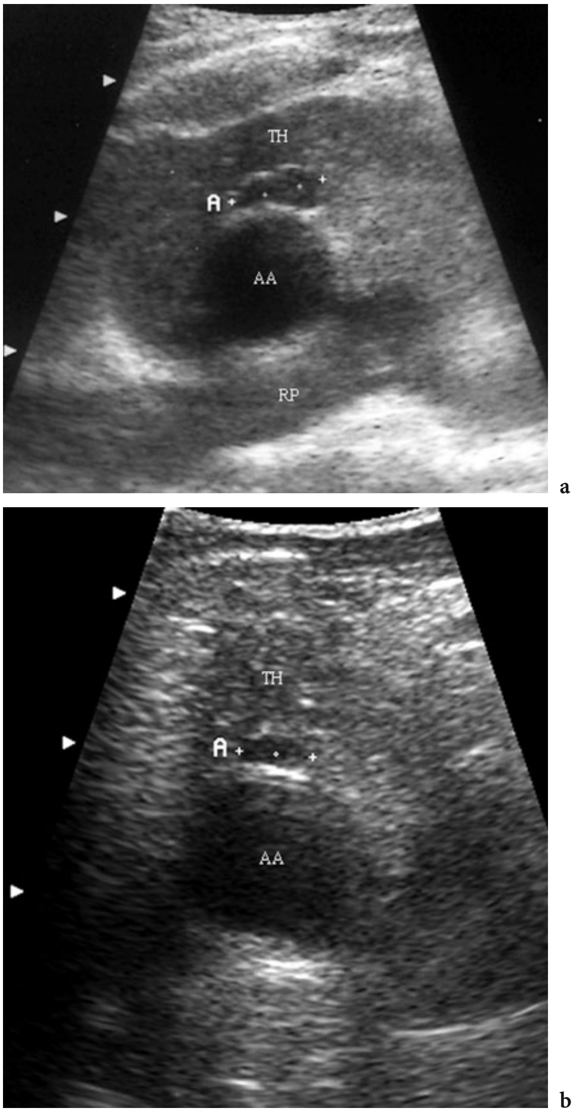

Fig. 1.47a,b. Thymic cyst in a 1-year-old immunodeficient patient. **a** Left parasternal US view shows a simple thymic cyst (calipers). **b** After 3 years the cyst has considerably decreased in size (*TH*, thymus; *AA*, ascending aorta; *RP*, right pulmonary artery)

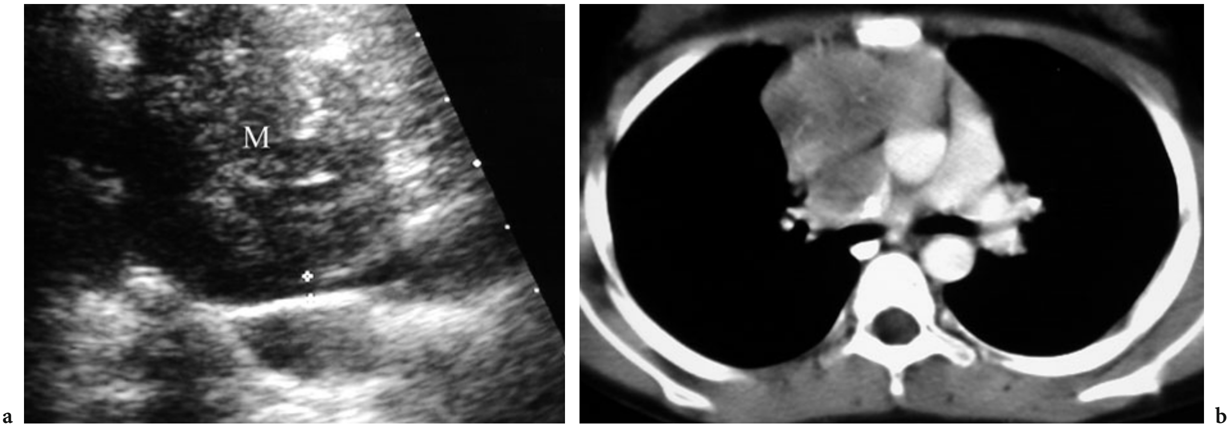

Fig. 1.48a,b. Germ cell tumor of the anterior mediastinum in a 4-year-old girl. **a** Transverse US scan obtained with a parasternal approach shows a mass (*M*) with heterogeneous echotexture compressing the superior vena cava (between calipers). **b** Enhanced CT scan reveals the same findings as US. Note compression of the superior vena cava

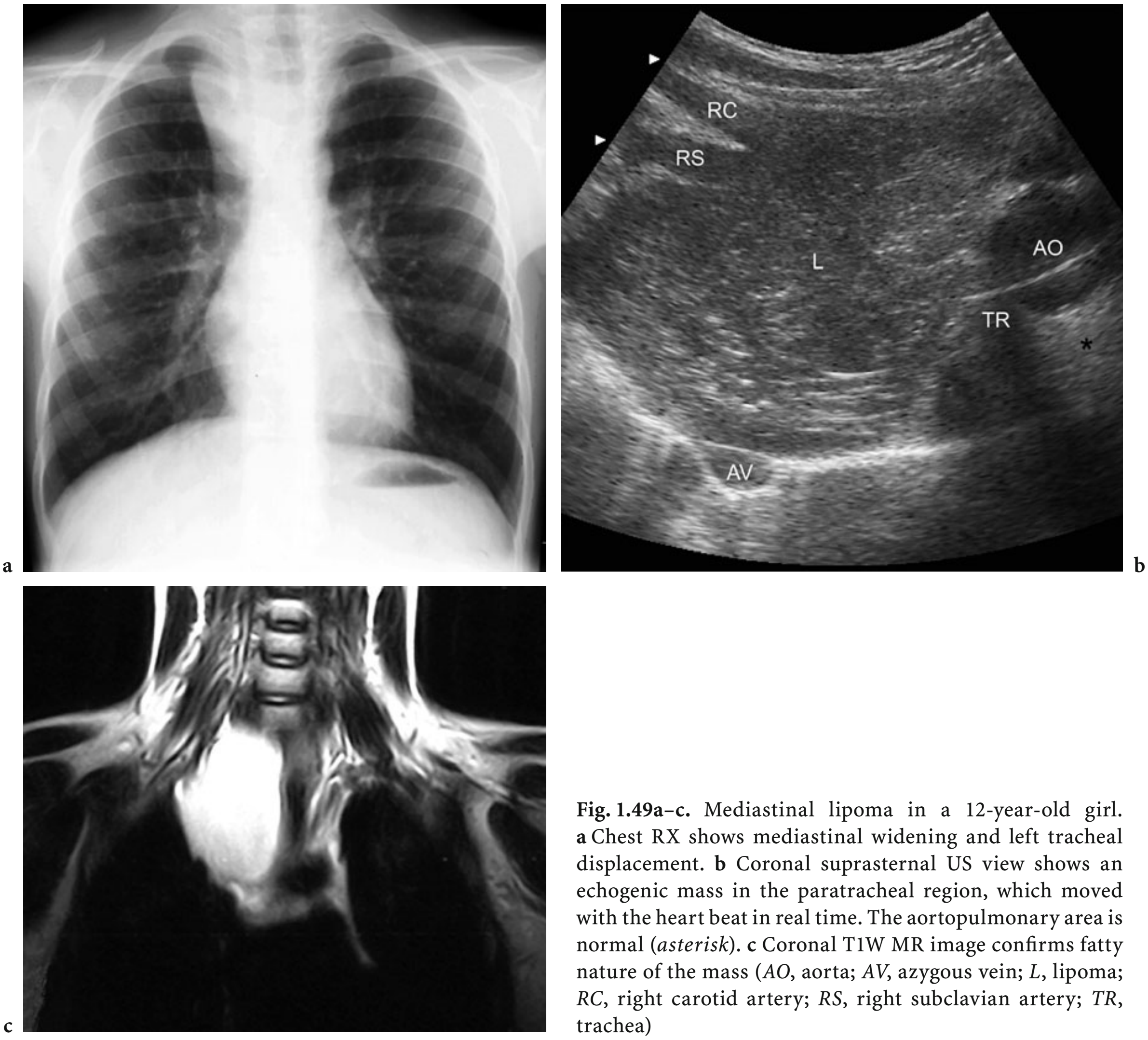

Fig. 1.49a–c. Mediastinal lipoma in a 12-year-old girl. **a** Chest RX shows mediastinal widening and left tracheal displacement. **b** Coronal suprasternal US view shows an echogenic mass in the paratracheal region, which moved with the heart beat in real time. The aortopulmonary area is normal (*asterisk*). **c** Coronal T1W MR image confirms fatty nature of the mass (*AO*, aorta; *AV*, azygous vein; *L*, lipoma; *RC*, right carotid artery; *RS*, right subclavian artery; *TR*, trachea)

1.4.4.2
Middle Mediastinum

The lesions usually found in the middle mediastinum are congenital malformations (including vascular anomalies) and lymphadenopathy. The most common congenital malformations are bronchogenic cysts, esophageal duplication cysts and neuroenteric cysts. Bronchogenic cysts, generally located in the subcarinal region, are usually seen as solitary thin-walled anechoic masses with a serous content that can vary in shape during respiration. In some cases fatty material or mucus within the cysts causes internal echoes that simulate a solid mass. Swirling of internal debris seen on real-time examination, the rounded shape, and well-defined wall are the clues that differentiate bronchogenic cyst from a solid mass. Patients are usually asymptomatic, but internal bleeding or infection can produce a sudden increase in size and associated symptoms of airway compression (Davis and Umlas 1992).

Most esophageal duplication cysts are found along the lower third of the esophagus. Neuroenteric cysts are the least common type of congenital cysts and are due to incomplete separation of the notochord from the foregut. Although they may be found in the middle mediastinum, they are more common in the posterior mediastinum (paravertebral region) and are often associated with congenital defects of the spine. Due to the different growth patterns of the spine and the thoracic cage, the level of the cyst may not coincide with that of the associated spinal defect. The sonographic features of both esophageal and neuroenteric cysts are identical to those of bronchogenic cysts.

Vascular malformations, including double aortic arch, aberrant left pulmonary artery and anomalous venous return, can also be detected by US. However, multidetector CT (MDCT) and MRI are the techniques of choice for the study of these malformations.

Lymphadenopathy, secondary to infectious, neoplastic, immunologic, toxic or metabolic processes, is the most common mass found in the middle mediastinum. At US lymphadenopathy is seen as scattered or clustered nodules with varying degrees of echogenicity. These clusters are more easily identified by US than CT, where they can simulate a simple solid mass. The right paratracheal region, pulmonary hilum and subcarinal space are the most common sites of pathologic lymph nodes (Fig. 1.50). Most mediastinal lymphadenopathies are of infectious origin. We have observed them in 83% of children with pneumonia of undetermined cause, 94% of children with tuberculosis disease (positive PPD, clinical symptoms and abnormalities on chest X-ray) and 50% of children infected by tuberculosis (positive PPD, no respiratory symptoms and normal chest X-ray). In our experience, US is more sensitive than chest X-ray for the detection of mediastinal lymphadenopathy in children with tuberculosis and is also useful for follow-up (Bosch-Marcet et al. 2004, 2007). The US appearance of tuberculous nodes can change following treatment and present a hypoechoic center and echogenic halo, probably due to internal caseous material (Fig. 1.51a–c). Mediastinal lymphadenopathy can also be found in patients with immunologic processes, such as Kawasaki disease (Bosch et al. 1998), Castelman disease and autoimmune thyroiditis.

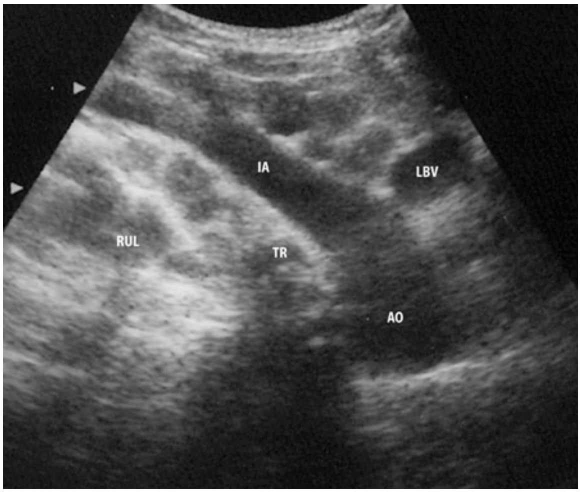

Fig. 1.50. Mediastinal lymphadenopathy in a 6-year-old boy with lymphoma. Oblique coronal view through the suprasternal space shows multiple, enlarged, hypoechoic lymph nodes at both sides of the innominate artery (*IA*) (*AO*, aorta; *LBV*, left brachiocephalic vein; *RUL*, right upper lobe; *TR*, trachea)

Leukemia and lymphoma are the most frequent neoplastic processes in children that result in lymphadenopathy, which when massive, can extend to the anterior mediastinum. In an attempt to distinguish benign or reactive from malignant adenopathy, color and power Doppler has been recently applied to study the perfusion patterns within the nodes (Tschammler et al. 1998; Steinkamp et al. 2002). Although good results have been obtained in individual cases, more experience with this method is required to obtain conclusive data as to its value for this purpose.

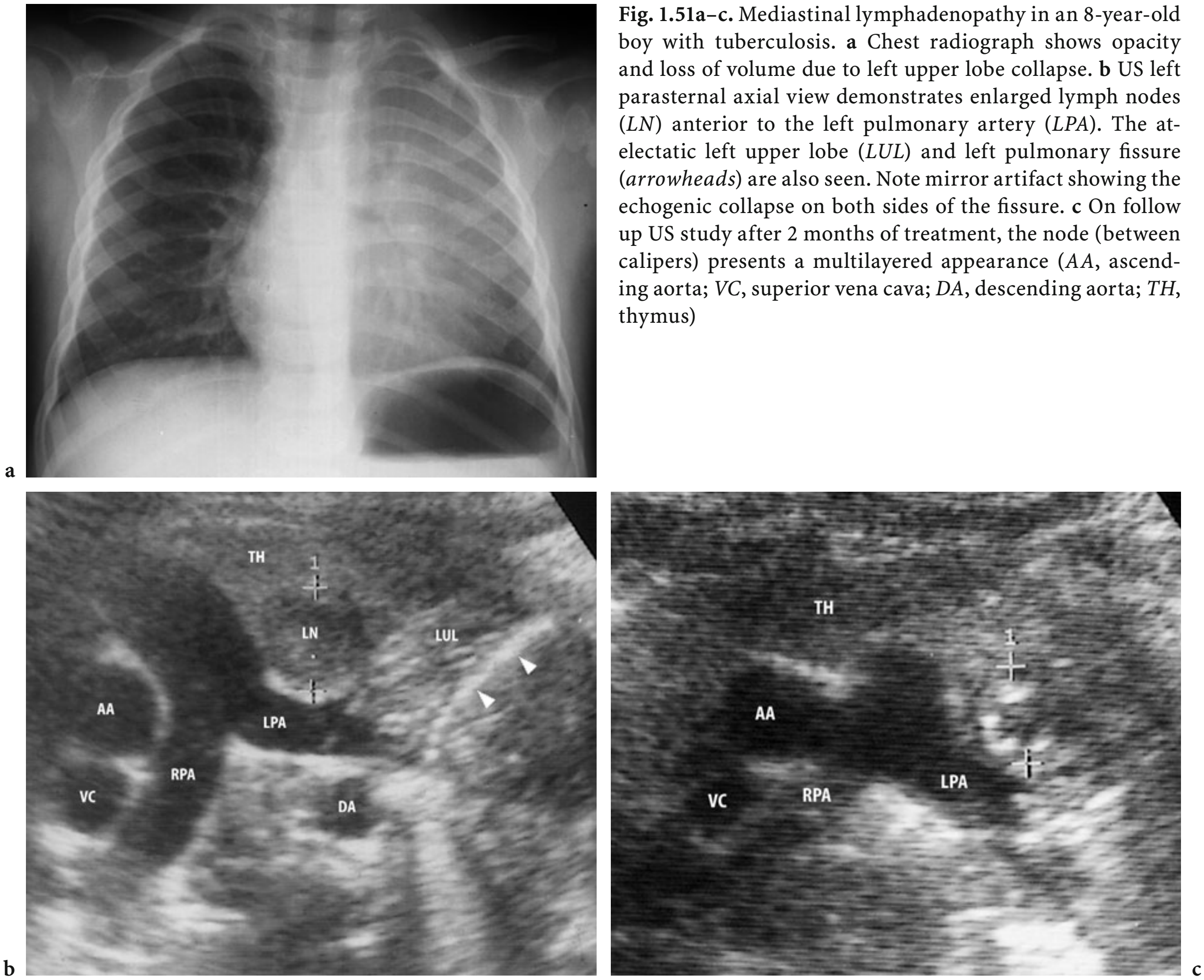

Fig. 1.51a–c. Mediastinal lymphadenopathy in an 8-year-old boy with tuberculosis. **a** Chest radiograph shows opacity and loss of volume due to left upper lobe collapse. **b** US left parasternal axial view demonstrates enlarged lymph nodes (*LN*) anterior to the left pulmonary artery (*LPA*). The atelectatic left upper lobe (*LUL*) and left pulmonary fissure (*arrowheads*) are also seen. Note mirror artifact showing the echogenic collapse on both sides of the fissure. **c** On follow up US study after 2 months of treatment, the node (between calipers) presents a multilayered appearance (*AA*, ascending aorta; *VC*, superior vena cava; *DA*, descending aorta; *TH*, thymus)

1.4.4.3
Posterior Mediastinum

Among the three mediastinal regions, the posterior mediastinum is the least suitable for study by ultrasound. The majority of lesions located in this region are neurogenic tumors, which frequently extend to the spinal canal, a region that is better studied by MRI or CT. However, lesions located in the lower part of the posterior mediastinum (juxtaphrenic or paravertebral masses) can be studied with ultrasound using a subxiphoid or transdiaphragmatic approach. These approaches may be particularly helpful for examining children with paravertebral soft tissue widening (Donnelly et al. 2000) in order to differentiate normal patients from those with tumor, atelectasis in the area of the pulmonary ligament or azygos continuation of the inferior vena cava. In neurogenic tumors, US demonstrates a solid mass with frequent granular or fleck-like calcifications. In atelectasis one will encounter typical signs described for lung consolidation. The vascular nature of the lesion is readily assessed by color Doppler without administration of intravenous contrast material.

1.5
Diaphragmatic Lesions

A common US study requested in clinical practice is assessment of diaphragmatic motility, which before the development of US, was performed with fluoroscopy. Diaphragmatic paralysis is not uncommon after cardiac surgery or liver transplantation, and US evaluation of this condition can be performed at bedside in the intensive care unit. Since the paralysis is usually unilateral, the movement of the affected diaphragm can be compared to the normal contralateral one by real-time observation in the coronal plane. Use of M-mode allows spectral representation of the impaired and normal diaphragmatic movement (Epelman et al. 2005).

Congenital and traumatic diaphragmatic hernias can present a misleading aspect on plain chest X-ray and simulate pulmonary consolidation when located on the right side, with the liver being the main component of the hernia. In traumatic liver herniation, the echogenicity of the intrathoracic liver may be different from that of the intra-abdominal liver. This finding represents the sonographic manifestation of the so-called “collar sign” (Aoki et al. 1998) (Fig. 1.52a,b).

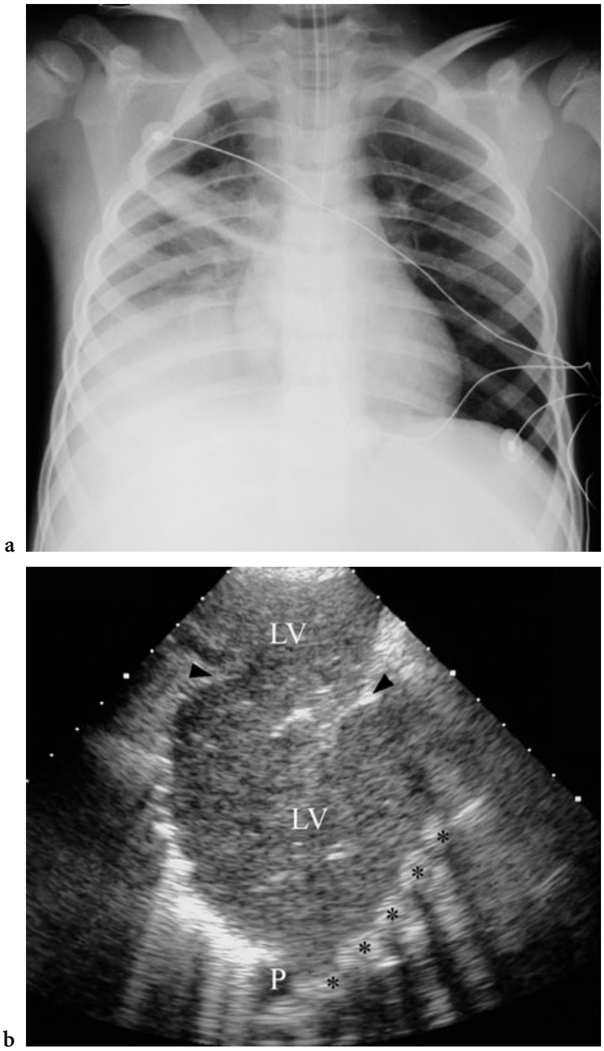

Fig. 1.52a,b. Diaphragmatic hernia in a 5-year-old girl with a motor vehicle injury. **a** Chest Radiograph shows opacification of the right lung base and linear atelectasis in the right upper lobe. **b** Longitudinal view of the right hemithorax reveals that the opacity corresponds to herniation of the liver (*LV*) through a diaphragmatic rupture (*arrowhead*) (*P*, pleural effusion). The chest wall is delineated by the ribs (*)

1.6
Conclusion

Sonography is a useful technique for evaluating pediatric chest diseases related to the lung, pleura and mediastinum. It is especially helpful for rapid assessment of patients with complete opacification of a hemithorax on chest X-ray. Due to its Doppler capabilities, the technique permits noninvasive identification of vascular structures in many congenital and acquired lesions. US is superior to CT for characterizing pleural fluid collections as simple or complicated, thus providing important information for establishing proper treatment. It is the method of choice for screening patients with mediastinal widening, thereby avoiding more invasive study of a normal thymus. Sonography can characterize the solid vs cystic nature of a mediastinal mass in doubtful cases and detect the presence of lymphadenopathy in the paratracheal, aortopulmonary and subcarinal regions.

References

Acunas B, Celik L, Acunas A (1986) Chest sonography. Acta Radiol 30:273–275

Alkrinawi S, Chernick V (1996) Pleural fluid in hospitalized pediatric patients. Clin Pediatr 35:5–9

Annessi V, Paci M, De Franco S et al. (2003) Diagnosis of anterior mediastinal masses with ultrasonically guided core needle biopsy. Chir Ital 55(3):379-84

Aoki AA, Mock CK, Talner LB (1998) Traumatic rupture of the right hemidiaphragm in an automobile accident victim. AJR Am J Roentgenol 171:386

Avila NA, Mueller BU, Carrasquillo JA et al. (1996) Multilocular thymic cysts: imaging features in children with human immunodeficiency virus infection. Radiology 201:130–134

Aziz D, Langer JC, Tuuha SE et al. (2004) Perinatally diagnosed asymptomatic congenital cystic adenomatoid malformation: to resect or not? J Pediatr Surg 39:329–334

Barnes NP, Hull J, Thomson AH (2005) Medical management of parapnuemonic pleural disease. Pediatr Pulmonol 39:127–134

Ben-Ami TE, O'Donovan JC, Yousefzadeh DK (1993) Sonography of the chest in children. Radiol Clin North Am 31:517–531

Bosch J, Serres X, Peñas M et al. (1998) Mediastinal lymphadenopathy: a variant of incomplete Kawasaki disease. Acta Paediatr 87(11):1200–1202

Bosch-Marcet J, Serres-Creixams X, Zuasnabar-Cotro A et al. (2004) Comparison of ultrasound with plain radiography and CT for the detection of mediastinal lymphadenopathy in children with tuberculosis. Pediatr Radiol 4(11):895-900

Bosch-Marcet J, Serres-Créixams X, Borrás-Pérez et al. (2007) Value of sonography for follow-up of mediastinal lymphadenopathy in children with tuberculosis. J Clin Ultrasound 35(3):118-24

Bouros D, Schiza S, Patsourakis G et al. (1997) Intrapleural streptokinase versus urokinase in the treatment of complicated parapneumonic effusions. A prospective, double-blind study. Am J Respir Crit Care Med 155:291–295

Castellote A, Vazquez E, Vera J et al. (1999) Cervicothoracic lesions in infants and children. Radiographics 19:583–600

Ching AS, Lee SF, Chan YL (2002) Diagnosing paediatric mediastinal lipoblastoma using ultrasound-guided percutaneous needle biopsy:review and report. Clin Imaging 26:23–26

Civardi G, Fornari F, Cavanna L et al. (1993) Vascular signals from pleura-based lung lesions studied with pulsed Doppler ultrasonography. J Clin Ultrasound 21:617–622

Coley BD. (2005) Pediatric chest ultrasound. Radiol Clin North Am 43(2):405-18

Conran RM, Stocker JT (1999) Extralobar sequestration with frequently associated congenital cystic malformation, type 2: report of 50 cases. Pediatr Dev Pathol 2:454–463

Davenport M, Warne SA, Cacciaguerra S et al. (2004) Current outcome of antenatally diagnosed lung disease. J Pediatr Surg 39:549–556

Davis SD, Umlas SL (1992) Radiology of congenital abnormalities of the chest. Curr Opin Radiol 4:25–35

De Pascale A, Giorcelli R, Garofalo G et al. (2006) Follow-up of mediastinal lymphoma: role of ultrasonography. Radiol Med 111:759–772

Donnelly LF, Klosterman LA (1997) Pneumonia in children; decreased parenchymal contrast enhancement – CT sign of intense illness and impeding cavitary necrosis. Radiology 205:817–820

Donnelly LF, Frush DP, Zheng J-Y et al. (2000) Differentiating normal from abnormal inferior thoracic paravertebral soft tissues on chest radiography in children. AJR Am J Roentgenol 175:477–483

Durand C, Garel C, Nugues F, Baudain P. (2001) Sonography of thoracic diseases in children. J Radiol 82(6 Pt 2):729-37

Eibenberger K, Dode W, Metz V et al. (1991) Value of supine thoracic radiography in the diagnosis and quantification of pleural effusions: comparison with sonography. Rofo Fortschr Geb Rontgenstr Neuen Bildgeb Verfahr 155:323–326

Epelman M, Navarro OM, Daneman A et al. (2005) M-mode sonography of diaphragmatic motion: description of technique and experience in 278 pediatric patients. Pediatr Radiol 35:661–667

Fitoz S, Atasoy C, Turkoz E et al. (2001) Sonographic findings in ectopic cervical thymus in an infant. J Clin Ultrasound 29(9):523-6

Frazier AA, Rosado de Christenson ML, Stocker JT et al. (1997) Intralobar sequestration: radiologic-pathologic correlation. Radiographics 17:725–745

Gassner I, Geley TE. (2005) Sonographic evaluation of oesophageal atresia and tracheo-oesophageal fistula. Pediatr Radiol 35(2):159-64

Gehmacher O, Mathis G, Kopf A et al. (1995) Ultrasound imaging of pneumonia. Ultrasound Med Biol 21:1119–1122

Givan DC, Eigen H (1998) Common pleural effusions in children. Clin Chest Med 19:363–371

Gorguner M, Misirlioglu F, Polat P et al. (2003) Color Doppler sonographically guided transthoracic needle aspiration of lung and mediastinal masses. J Ultrasound Med 22(7):703-8

Hamrick-Turner JE, Saif MF, Powers CI et al. (1994) Imaging of childhood non-Hodgkin lymphoma: assessment by histologic subtype. Radiographics 14:11–28

Hasiotou M, Polyviou P, Strantzia CM et al. (2004) Pleuropulmonary blastoma in the area of a previously diagnosed congenital lung cyst: report of two cases. Acta Radiol 45:289–292

Hedlund GL, Navoy JF, Galliani CA et al. (1999) Aggressive manifestations of inflammatory pulmonary pseudotumor in children. Pediatr Radiol 29:112–116

Jaffé A, Balfour-Lynn IM (2005) Management of empyema in children. Pediatr Pulmonol 40:148–156

Jani JC, Nicolaides KH, Gratacós E et al. (2006) Fetal lung-head ratio in the prediction of survival in severe left-sided diaphragmatic hernia treated by fetal endoscopic tracheal occlusion.Am J Obstet Gynecol 195:1646–1650

Kerem E, Bar Ziv Y, Rudenski B et al. (1994) Bacteremic necrotizing pneumococcal pneumonia in children. Am J Respir Crit Care Med 149:242–244

Kim OH, Kim WS, Kim MJ et al. (2000) US in the diagnosis of pediatric chest diseases. Radiographics 20:653–671

Ko SF, Ng SH, Lee TY et al. (2000) Noninvasive imaging of bronchopulmonary sequestration. AJR Am J Roentgenol 175:1005–1018

Kohzaki S, Tsurusaki K, Uetani M, Nakanishi K, Hayashi K (2003) The aurora sign: an ultrasonographic sign suggesting parenchymal lung disease. Br J Radiol 76(907):437–443

Koumanidou CH, Vakaki M, Theophanooulou M et al. (1998) Aberrant thymus in infants: sonographic evaluation. Pediatr Radiol 28:987–989

Laberge CJM, Bratu I, Frageole H (2004) The management of asymptomatic congenital lung malformations. Paediatr Resp Rev 5:305–312

Langston C (2003) New concepts in the phatology of congenital lung malformations. Semin Pediatr Surge 12:17–37

Lemaitre L, Leclerc F, Marconi V et al. (1987) Ultrasonographic findings in thymic lymphoma in children. Eur J Radiol 7:125–129

Manson DE, Daneman A (2001) Pitfalls in the sonographic diagnosis of yuxtadiaphragmatic pulmonary sequestrations. Pediatr Radiol 31:260–264

Maruyama K, Koizumi T. Hydromediastinum associated with a peripherally inserted central venous catheter in a newborn infant. J Clin Ultrasound 34(4):195-8

Maskell NA, Davies CW, Nunn AJ et al. (2005) Controlled trial of intrapleural streptokinase for pleural infection. N Engl J Med 352:865–874

May DA, Barth RA, Yeager S et al. (1993) Perinatal and postnatal chest sonography. Radiol Clin North Am 31:499–516

Muller LM (1993) Imaging the pleura. Radiology 186:297–309

Newman B (2006) Congenital bronchopulmonary foregut malformations: concepts and controversies. Pediatr Radiol 36:773–791

Pan-Chyr Y, Dun-Bing CH, Chong-Jen Y et al. (1992) Ultrasound-guided core biopsy of thoracic tumors. Am Rev Respir Dis 146:763–767

Papagiannopoulus KA, Sheppard M, Bush AP et al. (2001) Pleuropulmonary blastoma: is prophylactic resection of congenital lung cysts effective. Ann Thorac Surg 72:604–605

Park CS, Chung WM, Lim MK et al. (1996) Transcatheter instillation of urokinase into loculated pleural effusion. Analysis of treatment effect. AJR Am J Roentgenol 167:649–652

Pumberger W, Hormann M, Deutigner J et al. (2003) Longitudinal observation of antenatally detected congenital lung malformations (CLM): natural history, clinical outcome and long-term follow-up. Eur J Cardiothorax Surg 24:703–711

Ramnath RR, Heller RM, Ben-Ami T et al. (1998) Implications of early sonographic evaluation of parapneumonic effusions in children with pneumonia. Pediatrics 101(1):68–71

Raptopoulos V, Davis LM, Lee G et al. (1991) Factors affecting the development of pneumothorax associated with thoracentesis. AJR Am J Roentgenol 156:917–920

Rudick MG, Wood BP (1980) The use of ultrasound in the diagnosis of a large thymic cyst. Pediatr Radiol 10:113–115

Sasaka K, Kurihara Y, Nakajima Y et al. (1998) Spontaneous rupture: a ‚complication of benign mature teratomas of the medistinum. AJR Am J Roentgenol 170:323–328

Seibert JJ, Glasier CH, Leithiser RE (1998) The pediatric chest. In: Shankar S, Gulati M, Kang M et al. (2000) Image-guided percutaneous drainage of thoracic empyema. Eur Radiol 10(3):495–499

Shankar S, Gulati M, Kang M et al. (2000) Image-guided percutaneous drainage of thoracic empyema. Eur Radiol 10(3):495-499

Sheth S, Hamper UM, Stanley DB et al. (2000) US guidance for thoracic biopsy: a valuable alternative to CT. Radiology 210:721–726

Shum DJ, Clifton MS, Coakley FV et al. (2007) Prenatal tracheal obstruction due to double aortic arch: a potential mimic of congenital high airway obstruction syndrome. AJR Am J Roentgenol 188:256

Steinkamp HJ, Wissgott C, Rademaker et al. (2002) Current status of power Doppler and color Doppler sonography in the differential diagnosis of lymph node lesions. Eur Radiol 12:1785–1793

Stocker JT (1994) Congenital and developmental diseases. In: Dail DH, Hammmar SP (eds) Pulmonary pathology, 2nd edn. Springer, Berlin Heidelberg New York, pp 155–190

Stocker JT, Madewell JE, Drake RM (1977) Congenital cystic adenomatoid malformation of the lung. Classification and morphological spectrum. Hum Pathol 8:155–171

Swischuk LE, John S (1996) Normal thymus extending between the right brachiocephalic vein and the innominate artery. AJR Am J Roentgenol 166:1462–1464

Tschammler A, Ott G, Schang T et al. (1998) Lymphadenopathy: differentiation of benign from malignant disease. Color Doppler US assessment of intranodal angioarchitecture. Radiology 208:117–123

Weinberg B, Diakoumakis EE, Kass EG et al. (1986) The air bronchogram. AJR Am J Roentgenol 147:593–595

Wernecke K (2000) Ultrasound study of the pleura. Eur Radiol 10:1515–1523

Williams HJ, Alton HM. Imaging of paediatric mediastinal abnormalities. Paediatr Respir Rev 4(1):55-66

Winters WD, Effmann EL, Nghiem HV et al. (1997) Disappearing fetal lung masses: importance of postnatal imaging studies. Pediatr Radiol 27:535–539

Yang PC, Lutz KT, Chang DB et al. (1992a) Value of sonography in determining the nature of pleural effusion: analysis of 320 cases. AJR Am J Roentgenol 159:29–33

Yang PC, Lutz KT, Chang DB et al. (1992b) Ultrasonographic evaluation of pulmonary consolidation. Am Rev Resp Dis 146:757–762

Zhu SY, Liu RC, Chen LH, Luo F, Yang H, Feng X, Liao XH. Sonographic demonstration of the normal thoracic esophagus. J Clin Ultrasound 33(1):29-33

The Contribution of Nuclear Medicine to Pulmonary Imaging

Michael J. Gelfand and David L. Gilday

CONTENTS

2.1 **Introduction** *37*

2.2 **Technique – Planar Scintigraphy and SPECT** *37*
2.2.1 Aerosol Ventilation Imaging *37*
2.2.2 Ventilation Imaging with Noble (Inert) Gases *38*
2.2.3 Qualitative Perfusion Scintigraphy *38*
2.2.4 Quantitative Perfusion Lung Scintigraphy *38*
2.2.5 Salivagram *38*

2.3 **Clinical Interpretation – Planar Imaging and SPECT** *39*

2.4 **Technique – PET and PET/CT Imaging** *42*

2.5 **Clinical Interpretation – PET and PET/CT Imaging** *44*

References *45*

2.1
Introduction

One of the oldest nuclear medicine tests is perfusion lung scintigraphy, which was introduced to diagnose pulmonary embolism. Until recently, pulmonary embolism was considered rare in pediatrics. Another important indication for lung scintigraphy is to evaluate pulmonary perfusion in children with either congenital or acquired pulmonary artery stenosis. Quantifying the distribution of ^{99m}Tc MAA is especially useful in following up the results of stenting or dilatation of a pulmonary artery, and to evaluate pulmonary perfusion after unifocalization procedures. Similarly pulmonary artery branch narrowing can be followed-up with this technique. It has the advantage of being simple and easy to perform even with the most uncooperative young child or infant. Using ventilation techniques, bronchial obstructive diseases can be evaluated, although computed tomography (CT) has largely supplanted this technique.

Investigation of respiratory problems using nuclear medicine techniques involves assessing the perfusion (Q) and ventilation (V) of the lungs. Ventilation and perfusion studies (V/Q) are used together to better detect and evaluate lung abnormalities. Multiple views are obtained as part of both the ventilation and perfusion portion of the study. The ventilation study can be done with either a noble (inert) gas such as ^{81m}krypton or ^{133}xenon, or with ^{99m}Tc diethylenetriamine pentaacetic acid (DTPA) aerosol.

Recently positron emission tomography (PET) using [^{18}F]2-fluoro-2-deoxyglucose (FDG) has become available for tumor imaging; this has been the most important use of FDG PET to date.

2.2
Technique – Planar Scintigraphy and SPECT

2.2.1
Aerosol Ventilation Imaging

Aerosol imaging is the technique most commonly used for imaging of pulmonary ventilation. It also

---

M. J. Gelfand, MD, ABNM
Professor of Radiology and Pediatrics, University of Cincinnati, College of Medicine, Department of Radiology, Cincinnati Children`s Hospital Medical Center, 3333 Burnet Ave., Cincinnati, OH, 45229-3039, USA
D. L. Gilday, MD, B.Eng (EE), FRCPC, ABNM
Professor Emeritus, Medical Imaging, Toronto Nuclear Medical Services, Suite 210, 123 Edward Street, Toronto, ON, M5G 1E2, Canada

the easiest and cheapest, and is widely available. The equipment needed to perform an aerosol study consists of a commercial nebulizer, which produces droplets that will be deposited on the surface of the bronchioles. This results in a very accurate picture of the pattern of ventilation. These droplets are produced from a liquid containing ^{99m}Tc DTPA that is placed in the nebulizer. An aerosol ventilation study can be performed if the child is able maintain a tight seal around the mouthpiece that is connected to the nebulizer. Studies in patients who are unable to co-operate and in patients on a ventilator present significant technical challenges. Up to eight images are obtained in anterior, posterior, left lateral, right lateral, 45° left anterior oblique (LAO), left posterior oblique (LPO), right anterior oblique (RAO), and right posterior oblique (RPO) projections.

2.2.2
Ventilation Imaging with Noble (Inert) Gases

The commonly used radioactive noble gases are ^{133}xenon and ^{81m}krypton (a generator-produced radiotracer). The gas is inhaled using a plastic breathing bag equipped with a one-way valve connected to a mouthpiece and another one-way valve connected to a waste collection bag. The imaging study is obtained as follows: the patient breathes in from the bag containing the radioactive noble gas and then exhales into the collection bag. The one-way valves permit breathing in only from the breathing bag and the exhaled air can only go to the collection bag. After equilibrium is attained, the child breathes in room air until all the radioactive gas is washed out.

If ^{133}xenon is used, only the wash in phase, the equilibrium phase, and the washout phase can be imaged. With ^{133}xenon, only a single projection is acquired. If ^{81m}krypton is available, then additional views in each of the eight standard lung views may be obtained, but only the wash in phase is evaluated.

2.2.3
Qualitative Perfusion Scintigraphy

A chest X-ray done within the previous 24 h should be available for review. The radiopharmaceutical, ^{99m}Tc MAA, is injected with the patient supine. Immediately following injection, eight images are obtained in the anterior, posterior, left lateral, right lateral, 45° LAO, LPO, RAO, and RPO projections. There should be a symmetrical appearance of both perfusion and ventilation in both lungs (Fig. 2.1). In selected cases, single photon tomography (SPECT) can provide additional diagnostic information (Touya et al. 1986).

2.2.4
Quantitative Perfusion Lung Scintigraphy

This procedure is carried out on patients with pulmonary artery stenosis to assess perfusion to each lung (Glass et al. 1991). Follow-up studies are also performed after surgery or balloon dilatation to assess perfusion. A quantitative perfusion study may also be useful after unifocalization or Fontan procedures.

The radiopharmaceutical is injected into the patient using the technique previously described. The amount of ^{99m}Tc MAA is reduced for this technique, and in infants and patients with right to left shunts, the number of particles injected should be significantly reduced (Gelfand 1978). Immediately following injection, anterior and posterior projections are acquired. The relative perfusion to each lung is calculated using comparable regions of interest on both the anterior and posterior images, using a geometric mean of the values determined from the two images. Additional oblique and lateral images are acquired as needed.

2.2.5
Salivagram

Initial nuclear medicine attempts to detect aspiration were accomplished by imaging the chest after a radiotracer labeled drink (usually milk or formula) (McVeagh et al. 1987). Although this did detect some cases of aspiration secondary to reflux, it was unable to do so if reflux was not present. The salivagram was introduced as a means of detecting aspiration secondary to disordered pharyngeal motility (Heyman 1989; Heyman and Respondek 1989).

The patient is placed in a supine position on the imaging table, beneath which the camera is positioned. The infant or child must be well restrained to minimize motion during the study acquisition. A small dosage of ^{99m}Tc sulfur colloid is placed under the patient's tongue or in each buccal pouch and allowed to mix with the saliva. Sequential im-

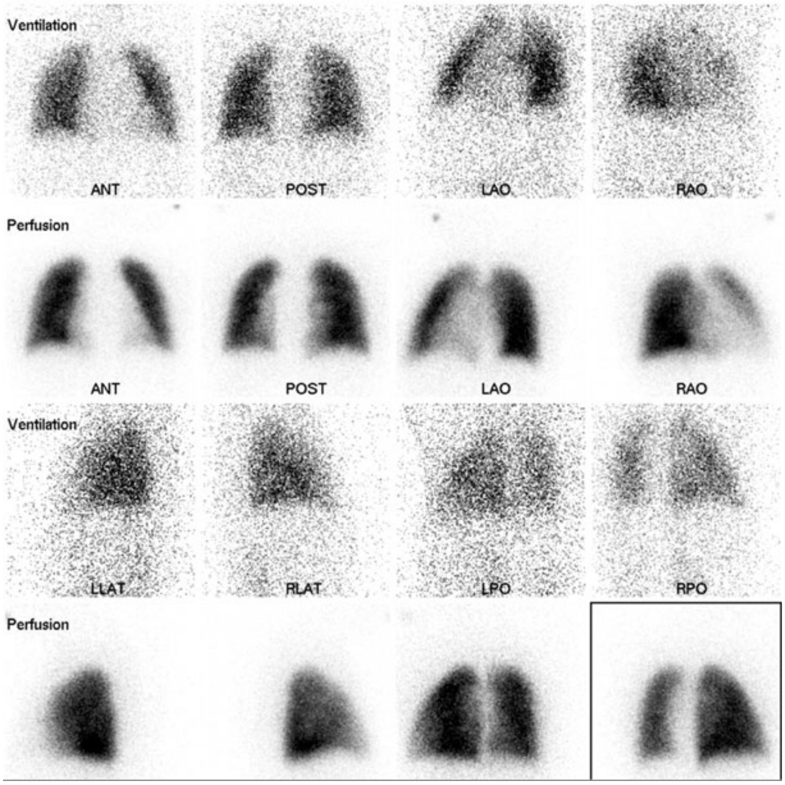

Fig. 2.1. Normal ventilation and perfusion scan. There is a very close match in the distribution of the tracer between the ventilation and the perfusion images. *ANT*, anterior; *POST*, posterior; *LAO*, left anterior oblique; *RAO*, right anterior oblique; *LLAT*, left lateral; *RLAT*, right lateral; *LPO*, left posterior oblique; *RPO*, right posterior oblique

ages are acquired until the activity clears from the mouth. The imaging sequence may be repeated to optimize the chance of detecting aspiration. If activity is seen anywhere in the chest area, the patient's clothing is removed and repeat images acquired to ensure that there is no external contamination. If activity is still seen, a lateral image of the appropriate side is acquired.

2.3
Clinical Interpretation – Planar Imaging and SPECT

Ventilation perfusion scintigraphy continues to be useful in the evaluation of children for the presence pulmonary emboli. CT angiography (CTA) has supplanted V/Q scintigraphy for this purpose in many institutions, in both adults and children. In the last few years, however, evidence has emerged that adult patients, who have a normal chest X-ray and no history of chronic lung disease, have a low incidence of indeterminate V/Q studies, only slightly higher than the incidence of indeterminate CTA studies (Daftary et al. 2005; Forbes et al. 2001; Jones and Wittram 2005; Jones 2005; Eyer et al. 2005). Recently, this has been demonstrated to be true in pediatric patients as well (Gelfand et al. 2006). V/Q imaging has a lower effective radiation dose than CTA and a much lower dose to the female breast (Studler et al. 2005; Parker et al. 2005; Stabin and Gelfand 1998). For this reason, in most cases it is preferred as the first test in children and adolescents, as long as there is no prior history of lung disease and the chest X-ray is normal or nearly normal.

Although not nearly as common in children as in adults, pulmonary embolism is increasing in incidence. This is in part due to better recognition that pulmonary embolism occurs in childhood, but, even more importantly, it is due to increased use of medical therapies that can cause pulmonary embolism, including the increased use of central venous access catheters. The main indication for V/Q imaging is to determine whether pulmonary embolism is present. The diagnosis is usually made according to modified PIOPED criteria. However, the criteria were established for adults and do not apply in their entirety to the pediatric population (Freitas et al. 1995; Stein et al. 1996a,b). Typically, there are two or more large subsegmental defects, often involving both lungs, with normal ventilation of these segments. The lower lobes tend to be involved more frequently due to the greater perfusion (Fig. 2.2).

Lung scintigraphy can also be used to map those portions of the lung that function well. V/Q imaging may be used for this purpose, and when ventilation imaging cannot be performed, perfusion imaging alone may be adequate. With rare exceptions, in patients who do not have a history of pulmonary em-

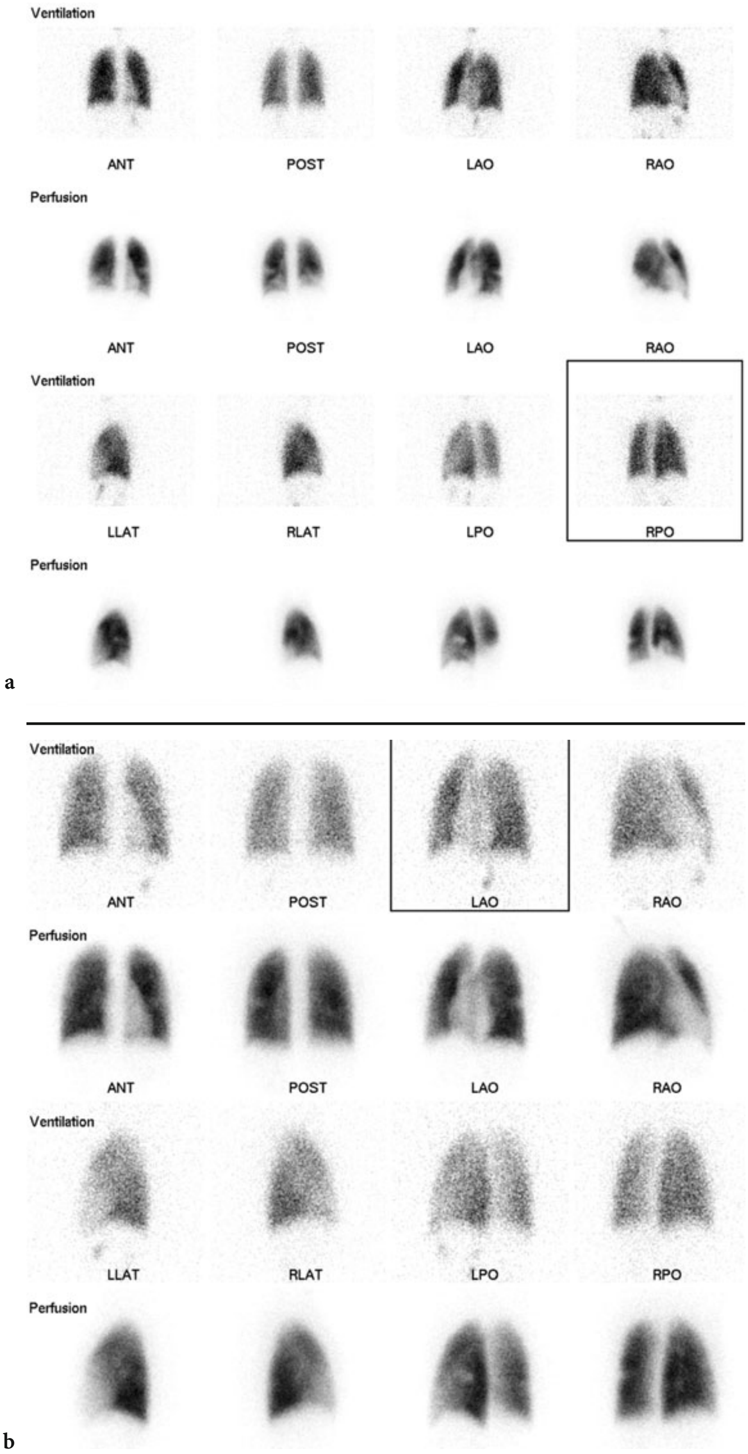
Ventilation
ANT
POST
LAO
RAO
Perfusion
ANT
POST
LAO
RAO
Ventilation
LLAT
RLAT
LPO
RPO
Perfusion
a
Ventilation
ANT
POST
LAO
RAO
Perfusion
ANT
POST
LAO
RAO
Ventilation
LLAT
RLAT
LPO
RPO
Perfusion
b

Fig. 2.2a,b. Pulmonary embolism. **a** In the initial study, there are perfusion defects present in both lower lobes that are not present in the ventilation images. **b** In the follow up study, the perfusion defects have dramatically decreased in size. *ANT*, anterior; *POST*, posterior; *LAO*, left anterior oblique; *RAO*, right anterior oblique; *LLAT*, left lateral; *RLAT*, right lateral; *LPO*, left posterior oblique; *RPO*, right posterior oblique boli, who are not wheezing and who are relatively free of secretions in their bronchi, ventilation and perfusion imaging are nearly identical (Hayward et al. 2007). SPECT perfusion imaging can be used to demonstrate functioning lung tissue in a tomographic format, and may demonstrate significantly more extensive perfusion abnormalities than are appreciated on planar perfusion scintigraphy, as has been shown in cystic fibrosis patients (Donnelly et al. 1997).

Quantitative perfusion imaging alone can be used to evaluate the relative perfusion to each lung or lobe due to pulmonary artery stenosis (Fig. 2.3) (Glass et al. 1991). The technique is especially valuable in following up the effects of intervention for the correction of pulmonary arterial narrowing. In some children's hospitals, this is the most common indication for nuclear medicine imaging in pediatric lung disease. It should be remembered that only pulmonary arterial perfusion is evaluated after intravenous injection with ^{99m}Tc MAA. In children with a history of cyanotic heart disease, non-segmental perfusion defects may also be due to predominant bronchial arterial perfusion in a volume of lung with a ^{99m}Tc MAA perfusion abnormality.

In same way that perfusion abnormalities can be evaluated in patients with pulmonary stenosis, patients with lung disease may be evaluated with ventilation perfusion or perfusion imaging to determine regional lung function after lung injury. This approach has been used in patients with bronchopulmonary dysplasia and cystic fibrosis (Soler et al. 1997; De Cesare et al. 1982). Perfusion and ventilation to each lung can also be evaluated in patients with severe scoliosis, pectus excavatum and after repair of congenital diaphragmatic hernia (Blickman et al. 1985; Jeandot et al. 1989; Hayward et al. 2007). Congenital diaphragmatic hernia is one of the few conditions in which a patient may have a ventilation perfusion mismatch in the absence of pulmonary arterial or airway obstruction.

The diagnosis of aspiration in infants is difficult. Gastroesophageal (GE) reflux imaging and pH studies are done to determine whether GE reflux is present. The "milk scan" was invented to try to document aspiration after reflux (McVeagh et al. 1987). A limitation of this study is that the only aspiration detectable is that secondary to GE reflux. The salivagram is a simple study that was devised to see if saliva was being aspirated in children with pharyngeal dysfunction (Heyman 1989; Heyman and Respondek 1989). It has proved to be a very sensitive and specific study (Fig. 2.4).

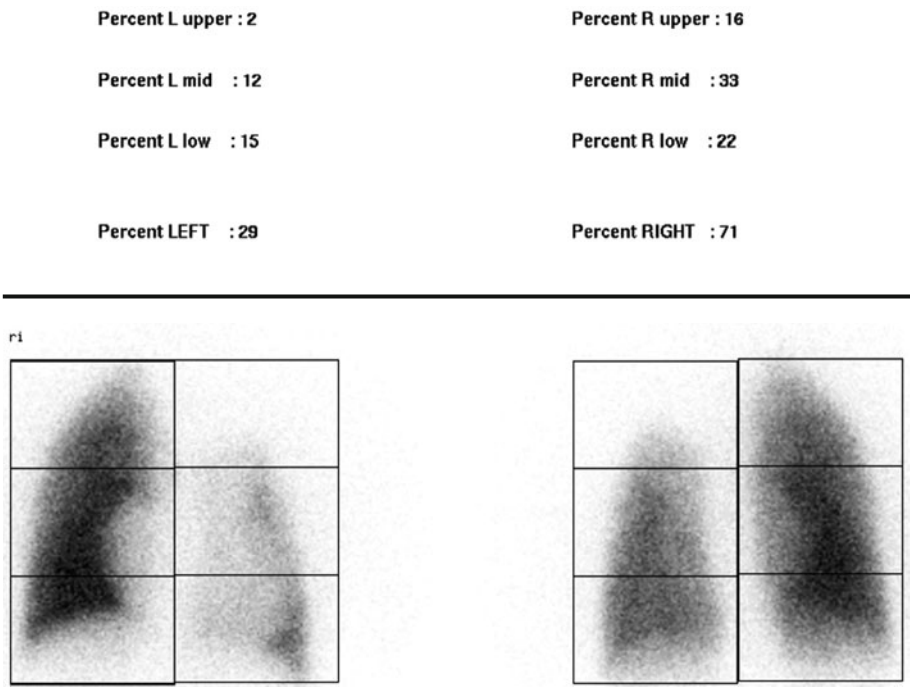
Percent L upper : 2
Percent L mid : 12
Percent L low : 15
Percent LEFT : 29
Percent R upper : 16
Percent R mid : 33
Percent R low : 22
Percent RIGHT : 71

Fig. 2.3. Quantitative lung perfusion. Each lung is quantitated in both the anterior and posterior images

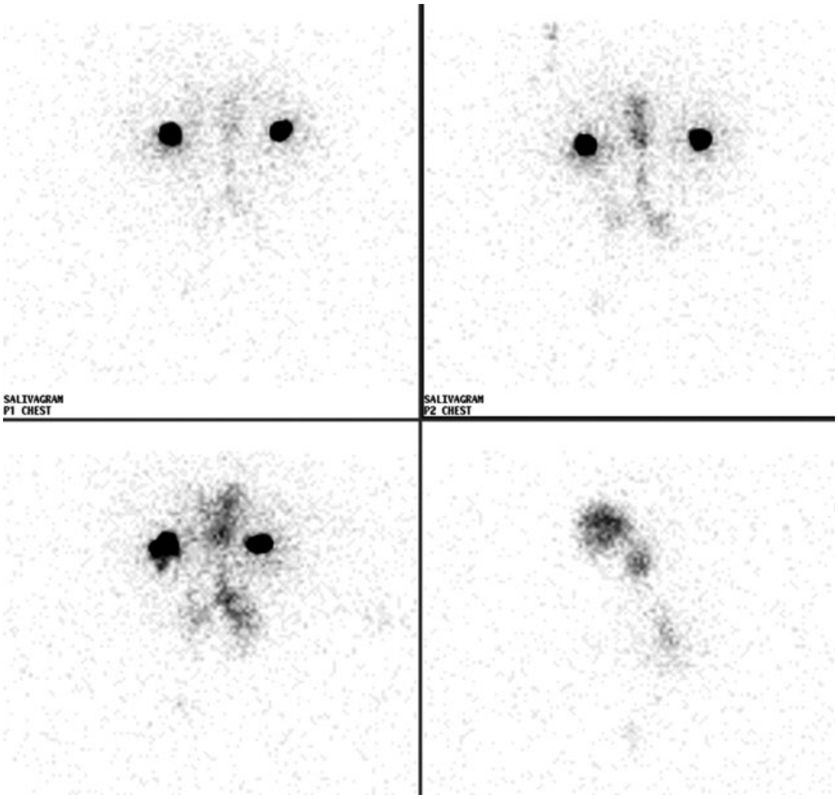

Fig. 2.4. Tracheal and bronchial aspiration. After swallowing of the radioactive saliva, some tracer entered the trachea and then entered the bronchi

2.4
Technique – PET and PET/CT Imaging

PET imaging is performed at a minimum of 40 min and preferably at 60 min after intravenous injection of FDG. The patient should be kept quiet at rest between FDG injection and beginning of the imaging study in order to prevent uptake in skeletal muscles that have been actively used during the FDG absorption period. All PET studies should be attenuation corrected to avoid artifactual low grade uptake in the lungs and near the skin surface; this is accomplished in older PET only studies by measuring attenuation of the 511 keV photons using an isotopic source, and in PET/CT scanners by using the absorption data generated by the CT scan. The CT portion of the PET/CT study also provides accurate localization information, as long as the patient does not move between the CT and PET acquisitions. Depending on the CT acquisition parameters, the effective dose to the patient from the CT portion of a PET/CT study may be significantly less than, equal to or greater than the effective dose from the PET portion of the study.

The techniques used for PET and PET/CT imaging of the chest are usually identical to those used for PET imaging of the rest of the body. In most cases, the PET examination of the chest is part of a study that may extend from the base of the brain either to the thighs or ankles. Key technical factors in PET imaging of the chest are mostly related to the CT portion of the PET/CT examination.

CT chest imaging parameters are lower than those used for the abdomen and pelvis. If the PET examination is limited to the chest, the CT exposure parameters should be appropriate for chest imaging, and lower than those used for imaging of abdomen and pelvis (with a saving in effective dose attributable to the CT portion of the study).

The optimum position of the diaphragm for detection of pulmonary nodules on CT is during full inspiration. The PET portion of the study must be performed during tidal respiration because of the much longer duration of the PET imaging phase of the study. The best anatomic match of diaphragmatic position during a PET/CT study occurs when the CT is performed during end tidal respiration or quiet tidal respiration (Goerres et al. 2003). Pulmonary nodules are best detected when the CT is acquired at full inspiration, but there will be a significant anatomic mismatch with PET images acquired during tidal respiration (Allen-Auerbach et al. 2006; Sharp et al. 2007). It may be impossible to acquire both an optimal diagnostic CT study and an accurately co-registered PET examination at the same time. At the diaphragm, co-registration errors may be as great as 3 cm.

Brown adipose tissue is present in children and adolescents. Low level stimulation by a cold environment will activate sympathetically mediated non-shivering thermogenesis in brown adipose tissue, and activated brown adipose tissue utilizes not only fatty acids, but also large amounts of glucose. The cold exposure may be as subtle as a mild chill from hospital air conditioning. Avid glucose uptake in brown adipose tissue may be seen in 15%–30% of children and adolescents undergoing PET imaging. Brown adipose tissue in the neck, supraclavicular regions, axillae and mediastinum is found immediately adjacent to many lymph node groups (Gelfand et al. 2005). Uptake in brown adipose tissue is sometimes present adjacent to costovertebral junc-

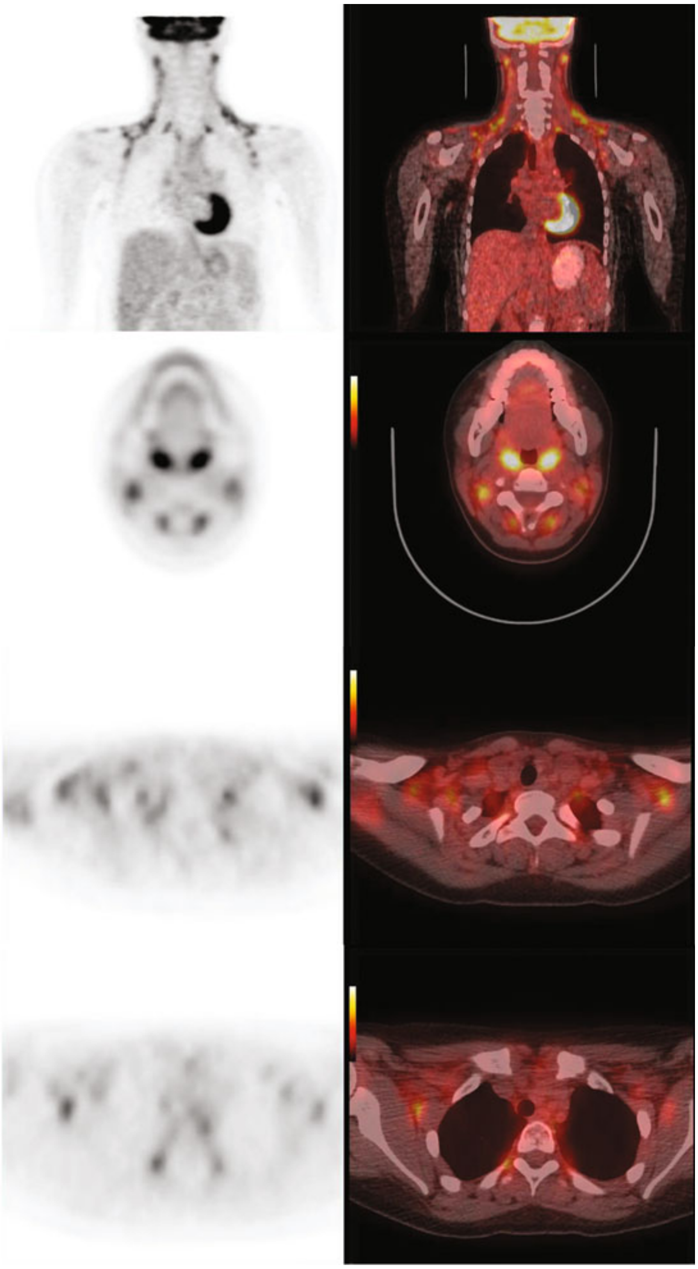

Fig. 2.5. Uptake in brown adipose tissue. PET/CT demonstrates brown adipose tissue uptake on [^{18}F]2-fluoro-2-deoxyglucose (FDG) images on coronal views and at three levels on axial views. PET images are *on the left* and co-registered fused PET/CT images are *on the right*

tions and may also rarely be seen in the upper abdomen near the kidneys. Although PET/CT should permit localization of FDG uptake to fat, this is not always possible because of small amounts of patient movement. In addition, the added sensitivity of FDG PET in identifying tumor in some smaller than 1 cm lymph nodes is compromised when there are multiple foci of brown adipose tissue uptake in the same lymph node groups (Fig. 2.5).

FDG uptake in brown adipose tissue can be prevented by physical and pharmacological means in most patients. Warming the patient for 30–60 min prior to FDG injection has been used in some institutions (Garcia et al. 2004, 2006). A variety of medications may be used to prevent transmission of cold impulses through the hypothalamus. In children and adolescents, fentanyl and diazepam have been used, with an apparent reduction in incidence of brown adipose tissue uptake of FDG that is severe enough to create problems in scan interpretation (Barrington and Maisey 1996; Tatsumi et al. 2004; Gelfand et al. 2005). Because of the high incidence of significant uptake of FDG in brown adipose tissue on PET scans in children and adolescents, an attempt should be made to suppress brown fat uptake in most children who undergo PET and PET/CT imaging.

2.5
Clinical Interpretation – PET and PET/CT Imaging

Positron emission tomography (PET) with FDG now plays a major role in the evaluation and follow up of lymphoma. Use of FDG PET in lymphoma is described in Chapter 11.

FDG PET imaging is useful in other chest neoplasia. FDG PET may be used for initial evaluation and follow up of patients with chest wall tumors such as Ewing sarcoma, primitive neuroectodermal tumor (PNET) and rhabdomyosarcoma (Fig. 2.6). Patients can be evaluated at diagnosis to determine if metastases are present and confirm that the tumor is FDG avid. They can be followed with FDG PET imaging to detect metastatic involvement, evaluate response to chemotherapy and radiation and monitor for recurrence. Detection of FDG uptake in small lung metastases is inconsistent; therefore, diagnostic quality CT imaging is recommended instead for the detection of lung metastases.

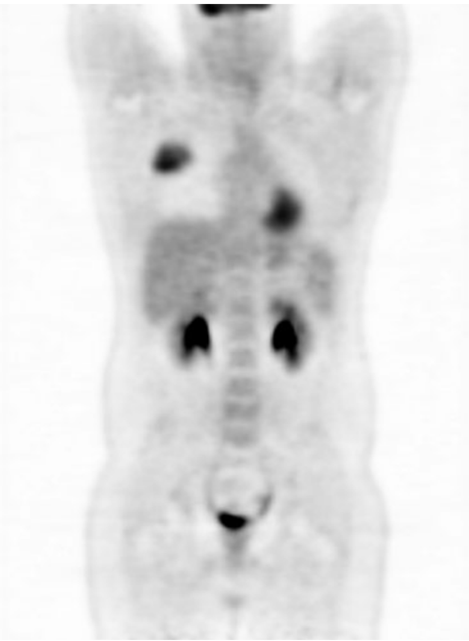

Fig. 2.6. Primitive neuroectodermal tumor (PNET) of the right chest wall. FDG PET images demonstrate intense tumor uptake

FDG uptake is not only seen in neoplasia. FDG is also taken up by cold-stimulated brown adipose tissue, by normal structures such as the thymus gland and by inflammatory processes (Hany et al. 2002).

Uptake of FDG in inflammatory process is another example of the non-specificity of FDG uptake. However, FDG uptake in the lung, unrelated to tumor, usually does not pose a diagnostic problem. Rather lung uptake of FDG may be used to diagnostic advantage. FDG uptake often represents an inflammatory process when seen in a region of parenchymal CT radiodensity.

Increased FDG localization has been noted in a wide variety of pulmonary inflammatory processes, including sarcoidosis and many forms of pneumonitis (Bleeker-Rovers et al. 2004, 2005; Mackie and Pohlen 2005; Mascarenhas et al. 2006). FDG uptake in lung has been also used to map lung inflammation in children with cystic fibrosis, and foci of lung infection in chronic granulomatous disease (Fig. 2.7) (Ozashin et al. 1998; Gungor et al. 1998; Chen et al. 2001).

Uptake in inflammatory lymph nodes, however, may sometimes cause confusion, particularly low level uptake in axillary and cervical nodes. FDG uptake may also be seen in cutaneous and soft tissue inflammatory processes. Uptake in recent surgical

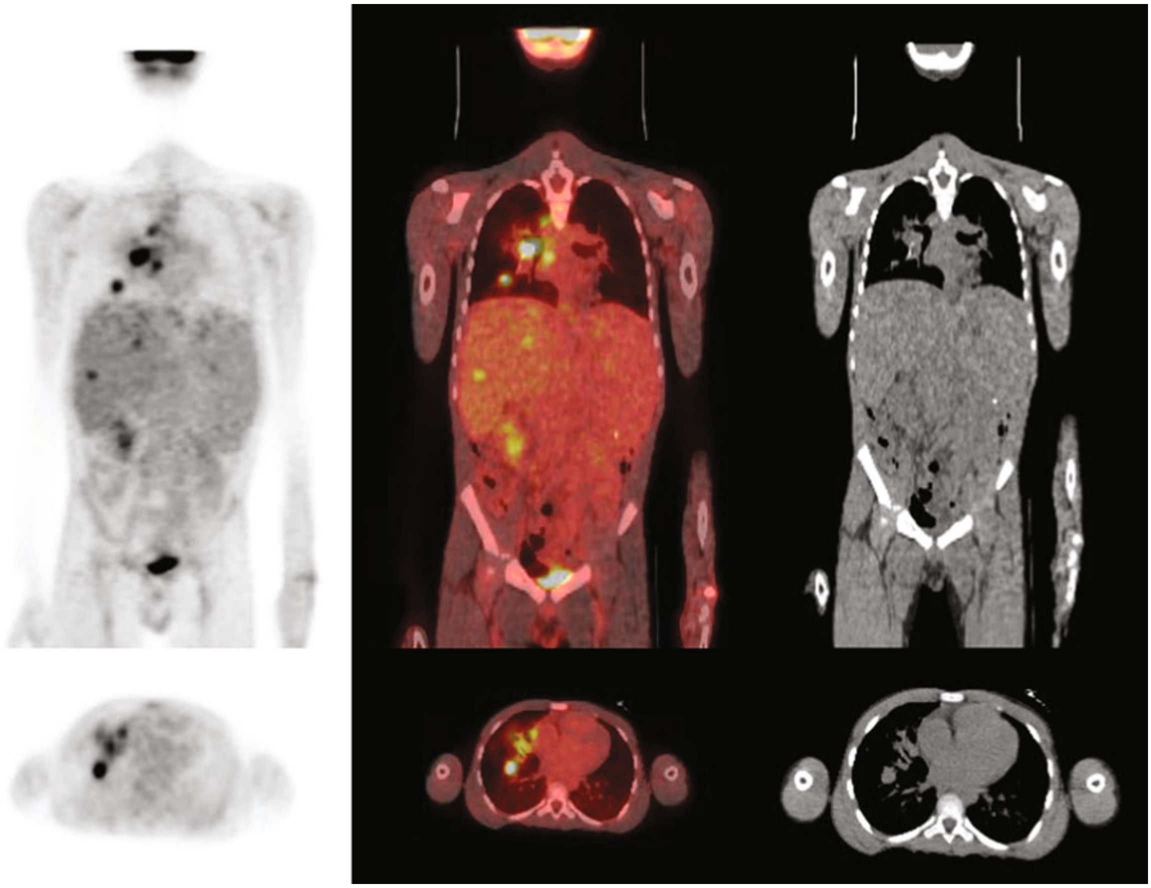

Fig. 2.7. Chronic granulomatous disease. Coronal (*top row*) and axial (*bottom row*) FDG PET images demonstrate uptake in lesions in the mediastinum, right hilum, lung and liver. PET images are in the *left column*, co-registered fused PET/CT images are in the *middle column* and CT images are in the *right column*

incisions is approached with an appropriate history, physical examination and/or reference to CT images.

References

Allen-Auerbach M, Yeom K, Park J et al. (2006) Standard PET/CT of the chest during shallow breathing is inadequate for comprehensive staging of lung cancer. J Nucl Med 47(2):298–301

Bleeker-Rovers CP, de Kleijn EM, Corstens FH et al. (2004) Clinical value of FDG PET in patients with fever of unknown origin and patients suspected of focal infection or inflammation. Eur J Nucl Med Mol Imaging 31(1):29–37

Bleeker-Rovers CP, Vos FJ, Wanten GJA et al. (2005) 18F-FDG PET in detecting metastatic infectious disease. J Nucl Med 46(12):2014–2019

Blickman JG, Rosen PR, Welch KJ et al. (1985) Pectus excavatum in children: pulmonary scintigraphy before and after corrective surgery. Radiology 156(3):781–782

Chen DL, Ferkol TW, Mintun MA et al. (2001) Quantifying pulmonary inflammation in cystic fibrosis with positron emission tomography. Am J Respir Crit Care Med 173(12):1363–1369

Daftary A, Gregory M, Daftary A et al. (2005) Chest radiograph as a triage tool in the imaging-based diagnosis of pulmonary embolism. AJR Am J Roentgenol 185:132–134

Donnelly LF, Gelfand MJ, Brody AS et al. (1997) Comparison between morphologic changes seen on high-resolution CT and regional pulmonary perfusion seen on SPECT in patients with cystic fibrosis. Pediatr Radiol 27(12):920–925

Eyer BA, Goodman LR, Washington L (2005) Clinicians' response to radiologists' reports of isolated subsegmental pulmonary embolism or inconclusive interpretation of pulmonary embolism using MDCT. Radiology 184:623–628

Forbes KP, Reid JH, Murchison JT (2001) Do preliminary chest X-ray findings define the optimum role of pulmonary scintigraphy in suspected pulmonary embolism? Clin Radiol 56:397–400

Freitas JE, Sarosi MG, Nagle CC et al. (1995) Modified PIOPED criteria used in clinical practice. J Nucl Med 36(9):1573–1578

Garcia CA, Van Nostrand D, Majd M et al. (2004) Benzodiazepine-resistant "brown fat" pattern in positron emission tomography: two case reports of resolution with temperature control. Mol Imaging Biol 6(6):368–372

Garcia CA, Van Nostrand D, Atkins F et al. (2006) Reduction of brown fat 2-deoxy-2-[F-18]fluoro-D-glucose uptake by controlling environmental temperature prior to positron emission tomography scan. Mol Imaging Biol 8(1):24–29

Gelfand MJ (1978) Shunts of the heart and great vessels. In: Proceedings of the 19th Annual Meeting and Continuing Education Lectures of the Southeastern Chapter, Society of Nuclear Medicine. Atlanta, Georgia. Southeastern Chapter, Society of Nuclear Medicine 9.1–9.23

Gelfand MJ, O'Hara SM, Curtwright LA et al. (2005) Premedication to block [(18)F]FDG uptake in the brown adipose tissue of pediatric and adolescent patients. Pediatr Radiol 35(10):984–990

Glass T, Heyman S, Seliem M et al. (1991) Use of Tc-99 m MAA in determining the etiology of increasing cyanosis following SVC-PA anastomosis for the hypoplastic left heart syndrome. Clin Nucl Med 16(6):410–412

Goerres GW, Burger C, Schwitter MR et al. (2003) PET/CT of the abdomen: optimizing the patient breathing pattern. Eur Radiol 13(4):734–739

Gungor T, Engel-Bicik I, Eich G et al. (2001) Diagnostic and therapeutic impact of whole body positron emission tomography using fluorine-18-fluoro-2-deoxy-D-glucose in children with chronic granulomatous disease. Arch Dis Child 85(4):341–345

Hany TF, Gharehpapagh E, Kamel EM et al. (2002) Brown adipose tissue: a factor to consider in symmetrical tracer uptake in the neck and upper chest region. Eur J Nucl Med Mol Imaging. 29(10):1393–1398

Hayward MJ, Kharasch V, Sheils C et al. (2007) Predicting inadequate long-term lung development in children with congenital diaphragmatic hernia: an analysis of longitudinal changes in ventilation and perfusion. J Pediatr Surg 42(1):112–116

Heyman S (1989) The radionuclide salivagram for detecting the pulmonary aspiration of saliva in an infant. Pediatr Radiol 19(3):208–209

Heyman S, Respondek M (1989) Detection of pulmonary aspiration in children by radionuclide "salivagram". J Nucl Med 30(5):697–699

Jeandot R, Lambert B, Brendel AJ et al. (1989) Lung ventilation and perfusion scintigraphy in the follow up of repaired congenital diaphragmatic hernia. Eur J Nucl Med 15(9):591–596

Jones SE, Wittram C (2005) The indeterminate CT pulmonary angiogram: imaging characteristics and patient clinical outcome. Radiology 237:329–337

Mackie GC, Pohlen JM (2005) Mediastinal histoplasmosis: F-18 FDG PET and CT findings simulating malignant disease. Clin Nucl Med 30(9):633–635

Mascarenhas NB, Lam D, Lynch GR et al. (2006) PET imaging of cerebral and pulmonary Nocardia infection. Clin Nucl Med 31(3):131–133

McVeagh P, Howman-Giles R, Kemp A et al. (1987) Pulmonary aspiration studied by radionuclide milk scanning and barium swallow roentgenography." Am J Dis Child 141(8):917–921

Ozsahin H, von Planta M, Muller I et al. (1998) Successful treatment of invasive aspergillosis in chronic granulomatous disease by bone marrow transplantation, granulocyte colony-stimulating factor-mobilized granulocytes, and liposomal amphotericin-B. Blood 92(8):2719–2724

Parker MS, Hui FK, Camacho MA et al. (2005) Female breast radiation exposure during CT pulmonary angiography. AJR Am J Roentgenol 185:1228–1233

Sharp SE, Helton KJ, Gelfand MJ et al. (2007) Detection of pulmonary nodules on localization CT scans acquired during PET/CT imaging (abstract). Pediatr Radiol (in press)

Soler C, Figueras J, Roca I et al. (1997) Pulmonary perfusion scintigraphy in the evaluation of the severity of bronchopulmonary dysplasia. Pediatr Radiol 27(1):32–35

Stabin MG, Gelfand MJ (1998) Dosimetry of pediatric nuclear medicine procedures. Q J Nucl Med 12:93–112

Stein PD, Henry JW, Gottschalk A et al. (1996a) Small perfusion defects in suspected pulmonary embolism. J Nucl Med 37(8):1313–1316

Stein PD, Relyea B, Gottschalk A et al. (1996b) Evaluation of individual criteria for low probability interpretation of ventilation-perfusion lung scans. J Nucl Med 37(4):577–581

Studler U, Gluecker T, Bongartz et al. (2005) Image quality from high-resolution CT of the lung: comparison of axial scans and of sections reconstructed from volumetric data acquired using MDCT. AJR Am J Roentgenol 185:602–607

Tatsumi M, Engles JM, Ishimori T et al. (2004) (18)F-FDG uptake in brown fat can be reduced pharmacologically. J Nucl Med 45(7):1189–1193

Touya JJ, Corbus HF, Savala KM et al. (1986) Single photon emission computed tomography in the diagnosis of pulmonary thromboembolism. Semin Nucl Med 16(4):306–336

Helical Multidetector Chest CT

3

Pilar García-Peña and Catherine M. Owens

CONTENTS

3.1 **Introduction** *47*

3.2 **Technical Considerations** *48*
3.2.1 Helical Technique *48*
3.2.1.1 Limitations and Disadvantages of Helical CT Technique *51*
3.2.1.2 Pitfalls of Helical CT Technique *52*
3.2.2 Personnel and Environment Requirements *52*
3.2.3 Previous Exam Evaluation *52*
3.2.4 Preparation of the Patient: Fasting Requirements *52*
3.2.5 Immobilization and Other Practical Tips *52*
3.2.6 Breath-Holding Information *53*
3.2.7 Sedation *53*
3.2.8 Intravenous Contrast Material Administration *53*
3.2.9 Technical Parameters and Protocols *54*
3.2.10 Image Postprocessing *57*

3.3 **Helical Chest Main Applications** *65*
3.3.1 Evaluation of Pulmonary Nodules and Chest Masses *65*
3.3.2 Evaluation of Vascular Anatomy: CT Angiography *69*
3.3.3 Evaluation of Central Airways *71*
3.3.4 Evaluation of Difficult Areas: Cervicothoracic Junction, Peridiaphragmatic Area and Chest Wall *71*
3.3.5 Evaluation of Critically Ill Patients *72*
3.3.6 Evaluation of Inconclusive Images on Chest Radiography *72*

3.4 **Conclusions** *73*

References *73*

3.1
Introduction

Computed tomography (CT) in children poses unique problems that are not encountered in adults. The relative lack of visceral fat combined with patient motion results in degradation of image quality making the recognition of normal anatomical structures and some pathologies more difficult to visualise. The recent major advances in technology in conjunction with meticulous attention paid to CT techniques and better training of radiologists have all combined together to improve the sensitivity and specificity of paediatric CT imaging and have resulted in more precise diagnostic possibilities. The introduction of helical CT and more specifically multidetector CT (MDCT), have further increased the utility and extended the indications for CT in the evaluation of paediatric patients. Indeed in 1998 CT examinations accounted for only 4% of diagnostic radiology examinations performed in the United Kingdom, but contributed 40% of the collective population dose from medical radiation (Shrimpton and Edyream 1998). In our own practices, there has been a greater than 60% increase in requests for paediatric CT between 1998 and 2006, and much of this relates to cardiothoracic and neurovascular work.

Many of the significant changes in current diagnostic practice are solely related to the introduction of helical CT technology and MDCT, which have enabled the study of airway and vascular structures, the development of CT angiography and virtual endoscopy, and improvements in the quality of multiplanar reconstructions.

Helical CT technology has several potential benefits for paediatric patients. The use of IV contrast agents can be optimized, sedation rates reduced, and radiation exposure to the patient can be decreased by using extended pitch and by eliminat-

---

P. García-Peña, MD
Department of Paediatric Radiology, Vall d'Hebron Hospitals, ps. Vall d'Hebron 119–129, 08035 Barcelona, Spain
C. M. Owens, BSc, MRCP, FRCR
Department of Paediatric Radiology, Great Ormond Street Hospital for Children, NHS Trust, Great Ormond Street, London WC1N 3JH, UK

ing the need to re-scan non diagnostic data. MDCT radiation doses can be significantly reduced using custom designed in house modification of manufacturers' protocols balancing adequate signal to noise ratios with diagnostic image quality.

MDCT also improves the overall image quality of two- and three-dimensional (2- and 3D) reconstructions, an important factor when analyzing specific diseases in children.

3.2
Technical Considerations

3.2.1
Helical Technique

In contrast to conventional CT, which is based on the collection of data from sequential scans, helical CT data is obtained continuously during table motion and results in a volumetric acquisition of scan data. If direct reconstruction were performed on this data the resulting images would be of poor quality, being compromised by motion artefacts. Thus, to compensate for the problems induced by table motion, the image data is interpolated prior to reconstruction (Brink et al. 1995; Napel 1995; Siegel and Luker 1995; Siegel 2003).

When compared to conventional section-by-section CT, helical CT has a number of advantages in the examination of paediatric patients.

By using the reconstruction capabilities of helical CT we can obtain overlapping slices, a fact that improves lesion depiction without increasing radiation exposure. Post processing of overlapping slices provides high-quality 2- and 3D images, extending the diagnostic applications. Fortunately in children, due to the possibility of very thin acquisition with some MDCT equipment, it is usually unnecessary to use overlapping slices to obtain a better quality of image for reconstruction.

As a result of isotropic data set acquisition image reconstruction can be performed along any slice using z-axis interval scanning.

Due to the relatively short scanning time more precise delivery of contrast medium and enhanced studies can be performed during peak vascular enhancement. This also allows a reduction of at least 25% in the volume of contrast agent needed (Costello et al. 1992a). As the speed of scanning a particular anatomic area is determined by the collimation thickness and the pitch (defined as the ratio of the table speed, expressed in millimetres per second to collimation thickness, expressed in millimetres multiplied by the time to acquire 360° of data), shorter scan times may help eliminate or decrease motion artefacts (Rubin et al. 1998). Some MDCT equipment, instead of using the pitch concept, use the table feed concept expressed in millimetres (millimetres that table moves after each acquisition). High-speed acquisition allows high-quality 2- and 3D image reconstruction and decreases the need for sedation, (a very important consideration in paediatric patients).

Radiation dose can be reduced in helical scanning without compromising diagnostic image quality (Takahashi et al. 1998). This is more pertinent as children are relatively more radiosensitive than adults and have a longer life span in which to manifest radiation-related disease – great care must be taken with the use of radiation.

There is essentially no difference in radiation dose in conventional CT (18.3 ± 1.5 mGy) vs 1.0:1 pitch helical CT scanning (17.2 ± 2.1 mGy), obtained using a comparable technique [100 mA, 120 kV(p) 10 mm thickness and 10 mm intervals]. However, dose can be reduced in helical scanning by lowering milliamperes (as in conventional CT) or by increasing pitch (Rogalla et al. 1999). In our institution we performed a study in 2 groups of 50 patients maintaining constant parameters of milliamperes, kilovolt (peak) and thickness while varying the pitch. The dose for helical CT performed with 100 mA, 120 kV(p), 10 mm collimation and pitch of 1.0:1 was 18.9 ± 2.2 mGy, while for a pitch of 1.5:1 it was 12.2 ± 1.0 mGy (Garcia-Peña and Lucaya 1999).

Radiation dose is a contentious issue in paediatrics as it is well established that the lifetime cancer mortality risks attributable to CT examinations are considerably higher than for adults (Callahan 1998).

As proposed by the ALARA principle "as low as reasonably achievable", the selection of appropriate scanning parameters focuses on the optimization of the image quality whilst delivering the lowest possible radiation dose and shifting the risk-benefit balance towards benefit (Shrimpton and Edytream 1998; Callahan 1998; Patterson et al. 2001; Oddone et al. 2005).

Technical parameters that need to be selected for any scan include: thickness of collimation, tube current – milliamperage and kilovoltage. The thickness of collimation is the minimum section thickness that can be acquired once the scan is finished and in a 16-row MDCT scanner is usually 1.5 mm. Thinner collimation (0.75 mm) increases the radiation dose by approximately 15%–20% with our in house reduced protocol and is applied only in selected cases of vascular abnormalities, visualization of small structures and in cardiac CTs (Tables 3.1a and 3.2). The axial images are reconstructed at 3 mm or 5 mm thickness and archived to PACS system within our hospital. Symetric 64-row MDCT equipments allow only thin collimation (0.625 mm) (Table 3.1b).

In recent years we have made efforts to standardize low-dose protocols for the children scanned in our institution, and the currently applied parameters are summarized in the Tables 3.1a,b and 3.3–3.5. Methods adopted to minimize radiation dose in MDCT include:

1. Applying a dose modulation function, where the system samples the patient thickness and adjusts (e.g. reduces) the exposure accordingly when the tube is in the AP/PA position, as patients are narrower in AP than side-to-side orientation (approximately 10%–30% reduction in radiation dose).
2. Reduction of the kilo-voltage to 100 kVp when imaging the thorax. Further reduction to 80 kVp is possible for CTA, but as resolution of the lung parenchyma is not ideal this is applied only if lung pathology is unlikely.
3. Selecting tube collimation of 1.5 mm. The 0.75-mm collimation improves spatial resolution but as already mentioned increases the radiation dose and is therefore reserved for CTA or where thin slice reconstruction is indicated for high resolution lung parenchymal detail in addition to volumetric data with mediastinal details. Symetric 64-row MDCT allow only 0.625-mm collimation.
4. Appropriate mAs selection dependent on the patient's weight or cross sectional diameter using the dose modulation function with its significant dynamic real time reduction in dose according to patient thickness.

Unlike the helical single-row scanner, an increase or decrease in table feed on the MDCT scanner only affects the overall scanning time. An increase in table speed results in concomitant increase in mA and this has no effect on the dose delivered. The tube current is automatically compensated to ensure that the preset effective and total mAs is delivered, i.e. a fast table movement results in an automatic increase in the mA keeping the mAs constant.

Table 3.1a. Protocol: chest survey. Imaging protocol of the paediatric chest with 16-row MDCT scanner

	"Routine scan"	"Combi scan" / CTA
Indication	Strictures Tumours masses and metastases Tracheomalacia In focal disease the study should include only the area of interest	Cardiovascular anomalies Small tracheobronchial stenoses Peripheral airways disease
Anatomic area	Thoracic inlet to diaphragm/area of interest	
Tube Collimation **Slice width – reconstructed**	1.5 mm 3–5 mm 2 mm (2D-3D)	0.75 mm 3–5 mm 1 mm (2D-3D)
Table feed	24 mm/rotation	12 mm/rotation
Exposure factors	100 KVp 20–75 effective mAs (dependent on patient weight) 0.75 second scan time	100 KVp 20–75 effective mAs (dependent on patient weight) 0.75 second scan time
Respiration	Suspended inspiration; single breath hold where possible otherwise quiet breathing 3–5 expiratory scans for tracheomalacia/small airways disease	
Contrast material	As required No IV contrast is used in pulmonary metastasis studies	Yes Trigger for PAs/aorta
Algorithm	Soft tissue (B30f) High resolution for lung parenchyma (B60f)	Soft tissue (B30f) High resolution for lung parenchyma (B60f)

Table 3.1b. Protocol: chest survey. Imaging protocol of the paediatric chest with 64-row MDCT scanner

	"Routine scan" / CTA/airways
Indication	Strictures Tumours masses and metastases Tracheomalacia Cardiovascular anomalies Small tracheobronchial stenoses Peripheral airways disease In focal disease the study should include only the area of interest
Anatomic area	Thoracic inlet to diaphragm/area of interest
Tube collimation **Slice width – reconstructed**	0.625 mm 3–5 mm 1 mm (2D-3D)
Table feed	40 mm/rotation
Exposure factors	80–120 KVp 20–75 effective mAs (dependent on patient weight) 0.50 second scan time
Respiration	Suspended inspiration; single breath hold where possible otherwise quiet breathing 3–5 expiratory scans for tracheomalacia/small airways disease
Contrast material	As required Trigger for PAs/aorta No IV contrast is used in pulmonary metastasis studies
Algorithm	Soft tissue: standard Lung parenchyma: high resolution

Table 3.2. Dose comparison for different scanning protocols in a phantom study in our institution

	Effective dose in mSv									
	Volume (1.5 mm)		Combi (0.75 mm)		HRCT		CTA		CXR In house protocols	
	M	F	M	F	M	F	M	F	AP	LAT
< 15 kg	0.77	0.90	0.9	1.05	0.36	0.42	1.30	1.51	0.00487	0.00799
15–24 kg	0.93	1.09	1.13	1.31	0.36	0.42	1.62	1.89	0.00874	0.01086
25–4 kg	1.34	1.56	1.58	1.84	0.54	0.63	2.24	2.62	0.01163	0.00968
35–44 kg	2.11	2.46	2.48	2.89	1.00	1.17	2.57	3.0	0.01769	0.01452

Anatomical coverage for imaging of the paediatric thorax extends from the thoracic inlet to the diaphragm. Greater degree of coverage may be warranted in certain clinical cases, such as an extralobar pulmonary sequestration which may be present in the upper abdominal cavity.

In order to increase spatial resolution, the field of view (FOV) should closely approximate the cross-sectional area of the body part being studied. A large FOV would result in waste of matrix space and partial volume averaging would generate poor quality images (Callahan 1998).

Helical equipment is remarkably silent as compared to conventional scanners. For this reason, paediatric patients are not usually frightened and remain calm and still. This in itself reduces the need for sedation and improves image quality.

The quality of multiplanar reformatted images, MPR (coronal, sagittal and curved) and 3D images is significantly improved with MDCT, which decreases motion-related artefacts and provides a smoothing effect of overlapped image reconstruction or due to the thin collimation of the new equipment, reducing stair-step artefacts. Such 3D images can be opti-

Table 3.3. Protocol: volumetric CT chest scanning parameters according to child's weight (routine and Combi scan protocol performed with16MDCT)

	< 15 kg		15–24 kg		25–34 kg		35–44 kg		45–55 kg	
	Volume 1.5 mm	Combi 0.75 mm	Volume	Combi	Volume	Combi	Volume	Combi	Volume	Combi
kVp	100	100	100	100	100	100	100	100	100	100
eff. mAs	20	20	25	25	35	35	55	55	75	75
Collimation mm	1.5	0.75	1.5	0.75	1.5	0.75	1.5	0.75	1.5	0.75
Scan slice width mm	5	5	5	5	5	5	5	5	8	8
Table feed mm	24	12	24	12	24	12	24	12	24	12
Scan time s	0.5	0.5	0.5	0.5	0.5	0.5	0.5	0.5	0.5	0.5
'Calculated Effective Dose (mSv) – CT EXPO'	0.9	1.0	1.13	1.31	1.58	1.75	2.48	2.75	3.38	3.75

Table 3.4. Protocol: HRCT chest scanning parameters according to child´s weight

	< 15 kg	< 30 kg	> 30 kg
kVp	100	100	100
eff. mAs	20	30	55
Collimation mm	1	1	1
Scan slice width mm	1	1	1
Table feed mm	10	10	10
Scan time s	0.36	0.75	0.75
'Calculated Effective Dose (mSv) – CT EXPO'	0.21	0.32	0.59

Table 3.5. Protocol: CT angiography scanning parameters according to weight

	< 15 kg	15–24 kg	24–34 kg	35–44 kg	45–55 kg
kVp	100	100	100	100	100
eff. mAs	20	25	35	40	50
Collimation mm	0.75	0.75	0.75	0.75	0.75
Scan slice width mm	1	1	1	1	1
Table feed mm	9	9	9	9	9
Scan time s	0.75	0.75	0.75	0.75	0.75
'Calculated Effective Dose (mSv) – CT EXPO'	1.5	1.9	2.6	3.0	3.5

mally rotated to display specific normal and abnormal structures allowing analysis of selected parts.

3.2.1.1
Limitations and Disadvantages of Helical CT Technique

Helical CT technology does have some technical limitations and disadvantages. These include: a) heat build-up in the X-ray tube, which limits the milliamperes that can be generated; b) postprocessing delays related to reconstruction of the images after the data have been acquired; and c) z-axis blurring (blurring along the longitudinal table axis) with increased pitch because of the faster table speeds. These disadvantages are overcome by using the new generation of MD scanners. Compared with single-row helical CT, 4-16-40-64 multidetector–row helical CT provides a twofold, threefold or greater improvement in volume coverage speed with better resulting diagnostic image quality (Hu et al. 2000).

3.2.1.2
Pitfalls of Helical CT Technique

A common technical artefact associated with helical data acquisition is the stair-step artefact (Wang and Vannier 1994). These occur along high-contrast interfaces that are oriented obliquely to the direction of patient travel. Stair-casing causes the edges of longitudinally oriented structures to appear as steps rather than as straight lines (Fig. 3.1.b). The thinner slice acquisition with MD scanners minimises this technical artefact and image reconstructions are now very smooth and of very high-quality).

Another potential pitfall with MDCT is related to commencing scanning before optimal organ or vessel enhancement by the contrast agent occurs in homogeneous fashion (Silverman et al. 1995). These flow artefacts, caused by the mixing of contrast material and non-opacified blood are much more frequent in abdominal studies than in chest CT, in part because the circulation of blood is faster in the chest compared with abdominal blood circulation.

3.2.2
Personnel and Environment Requirements

The optimal team for performing paediatric MDCT includes a paediatric radiologist, a technician and a nurse trained in paediatric care. It is important to ensure an optimal environment for paediatric patients in the scanning area and every effort should be made to create a warm welcoming atmosphere that minimises patient and parental anxiety. Soft lighting, toys, a quiet room decorated with children in mind and the presence of a relative can help to comfort and console a child.

It is essential to have immediate access to a resuscitation cart with appropriate drugs and equipment for paediatric patients of all ages.

3.2.3
Previous Exam Evaluation

It is mandatory to check the patient's clinical records and all available previous imaging studies before performing a helical CT scan. This helps to decide if the indication is correct and allows the exam to be tailored to the specific requirements of the patient. It is particularly important with regard to the need for sedation and IV contrast administration. Careful planning can prevent difficulties during the study and minimize the potential for unanswered questions afterwards. The radiologist/radiographer should explain all aspects of the procedure and the objectives of the study to the parents before obtaining parental consent.

3.2.4
Preparation of the Patient: Fasting Requirements

The patients, parents and nursing staff should be informed of fasting requirements before the day of the procedure. Sometimes, no preparation is required (e.g. when studying pulmonary metastasis). When children need sedation or IV contrast material is to be given during the examination, we use the following fasting regimes before the procedure: In newborns, fasting is decided upon consultation with the neonatologist; infants are kept NPO for 3 h, children for 4 h and adolescents for 6 h.

3.2.5
Immobilization and Other Practical Tips

Sandbags, adhesive bandages, or blankets wrapped around the patient can all be used to immobilize the patient. It is advisable to wrap a lead apron around the child in the regions adjacent to those to be scanned. This protects them from scattered radiation and, at the same time, can help to immobilize the patient. Overlying radio protective bismuth latex can be placed on breasts and thyroid gland to minimize local radiation absorption to these radiosensitive tissues. These devices may increase the incident mA when automated dose control is used as the X-ray tube recognises increased attenuation around the patient and thereby automatically increases the incident mA/dose so this can have mixed effects.

Toys hanging from the gantry and films or image projection on the gantry can be used to attract the attention of the child and help to keep them quiet. A system for maintaining body temperature such as warming lamps or heating blankets should be used in infants.

3.2.6
Breath-Holding Information

Children under 6 years of age who cannot follow breath-holding commands are examined under normal quiet breathing. In this age group attempts at breath-holding usually result in exams severely compromised by artefacts. Older children are carefully instructed in breath-holding before the study.

3.2.7
Sedation

Helical CT has reduced the need for sedation (White 1995; Kaste et al. 1997). Since the introduction of silent helical CT and high speed MDCT in our institutions, our overall rate of sedation is only 1% of patients for MDCT vs 18% for our previous conventional CT studies. In patients under the age of 6 years, 50% required sedation with conventional CT and only 8% with helical CT and 2% with MDCT. Among the patients in this age group who needed IV contrast, 77% had to be sedated with conventional CT, only 18% with single slice helical CT and 3% with MDCT. Finally, among those who did not need IV contrast material, 24% required sedation with conventional CT, only 2% with helical CT and 1% with MDCT. We believe that the relative silence of the helical equipment and the high speed of acquisition have determined this reduced need for sedation. It has been widely reported that with multidetector CT the rate of sedation can be reduced (Pappas et al. 2000).

The need for sedation is decided upon depending on the behaviour of the child once inside the gantry. In our experience infants less than 3 months of age can often be successfully imaged after normal feeding and swaddling. Sleep deprivation the night before the examination has no proven benefit in either decreasing the dose of sedative drugs or the number of sedation procedures and can be disruptive for patients. Before performing an examination with the use of sedation, the radiologist must decide whether its benefits outweigh the associated risks and verify that fasting requirements have been observed. In our institution informed consent for sedation is covered by the standard consent for admission and CT scan examination.

In children under 18 months of age we usually administer oral chloral hydrate at a dose of 50–100 mg/kg (to a maximum dose of 2000 mg) 20 min prior to starting the examination. When using this regimen and if IV contrast injection is contemplated, the intravenous line is placed in the preparation room before the patient is brought to the CT unit.

In Spain, patients of 18 months of age and older are given intravenous sodium pentobarbital, 6 mg/kg to a maximum dose of 200 mg, diluted in 10 cc saline. The syringe containing the sedation must be appropriately labelled with the drug name. A dose of 2–3 mg/kg should be given initially as slow bolus over 1–2 min. In most children, this dose is adequate and they will fall asleep within the next 4–5 min. If not, an additional dose of 2–3 mg/kg may be given. If the patient still remains awake an additional dose of 2 mg/kg can be given some 30 min later. However, this is rarely necessary. Occasionally, in some patients over 6 months of age who need IV contrast, sodium pentobarbital in the above-mentioned doses is used. Paediatric sedation techniques have been extensively described in the literature (Cook et al. 1992; Frush et al. 1996; Egelhoff et al. 1997).

In the UK (GOSH) the following CT protocol for sedation is undertaken:

1. Less than 45 weeks gestation – nil, feed and wrap/swaddle only
2. Older than 45 weeks but less than 5 kg – Chloral Hydrate 50 mg/kg PO
3. 5–12 kg – Chloral Hydrate 50–75 mg/kg PO (max dose 1 g)
4. >12 kg – Alimemazine 2 mg/kg PO (max dose 60 mg) + Morphine 200 μg/kg IM (max dose 6 mg)

Intravenous "top ups"

If the sedation (1–4) is not effective, supplementary sedation may be given only by a doctor who is skilled in paediatric resuscitation. Dose: Diazemuls 0.2–0.3 mg/kg in increments of 0.1 mg/kg MAX dose 0.3 mg/kg or 10 mg. NB sedation will sometimes fail and these doses must not be exceeded. If sedation fails, an anaesthesia service must be booked for another day.

Every child undergoing sedation in the CT suites should receive oxygen and be monitored during and after the examination (see Chap. 4).

3.2.8
Intravenous Contrast Material Administration

Intravenous administration of a bolus of contrast material for helical CT studies in children can be more complicated than in adults because of the greater variations in vessel and patient size in the paediatric population. Dosage is based on the patient's body weight. Contrast material is administered by hand or power injector, depending on these variations (Frush et al. 1997; Kaste and Young 1996). To avoid the artefact caused by contrast in the axillary vein just after the injection, the syringe is placed vertically downwards and filled with saline solution and contrast. Since saline is less dense than contrast material, it will remain in the syringe until the end of the injection and then flush the vein of contrast. This will help to obtain better images (Hopper et al. 2000). Newer power injectors have double system of syringes, one syringe for contrast material and a second syringe for saline solution. Usually, the double power injector is programmed to inject the contrast material first followed by 5–10 cc of saline solution. It is necessary to check the venous line is functioning prior to contrast media injection to prevent extravasation occurring.

If contrast material is to be given, an intravenous catheter or a butterfly needle should be placed before the child arrives in the CT suite. This will avoid the distress associated with venupuncture performed immediately before scanning begins and help to reduce the need for sedation. Local topical analgesics, such as lidocaine cream, can be applied to the intended venupuncture site to minimize the pain from cannula placement. Usually, we use catheters 20–26 Gauge, permitting injection rates of 4.0–1.0 ml/s. Butterfly needles 19–25 Gauge, which give injection rates of 4.0–0.5 ml/s can also be used. (Table 3.6a,b). One should always use the largest cannula suitable for each patient, though rates as low as 0.5–1.0 ml/s in children can still result in excellent enhanced studies. If the patient already has a central intravenous line in situ, it should be used to gain venous access, using aseptic technique.

Non-ionic, low- (240 mg of iodine per milliliter) or high- (300 mg of iodine per milliliter) osmolar contrast media can be used for CT examinations in children (Stokberger et al. 1998). In our practice, we use 240 mg/ml in infants and 300 mg/ml in older children.

The usual dose of contrast media is 1–3 ml/kg, to a maximum dose of 100 ml. In newborns the dose used is 2–3 ml/kg, in infants 2 ml/kg, in children 1.5 ml/kg, and in adolescents 1 ml/kg.

In our experience, helical CT has allowed a 20% reduction in the volume of intravenous contrast medium given when compared to conventional CT. Similar findings have been described in the literature (Costello et al. 1992a). Optimal contrast enhancement during helical scanning depends on careful selection of the appropriate time of scanning, as well as on choosing the precise amount of contrast material and the optimal injection rate. The rate of injection depends on the needle or catheter size (Table 3.6a,b). The timing of the onset of scanning is a crucial factor in successful imaging, but is also one of the trickiest aspects of performing paediatric helical CT.

Table 3.6a. Protocol: suggested delay times from the injection of contrast medium

	Manual injection	Pressure injector
Scan initiation time delay	Immediately from termination of injection	15–25 s from start of injection (depending on patients's weight)
Flow rate		2 ml/s
Age range	All age groups	All age groups

Table 3.6b. Protocol: rate of contrast media injection depending on catheter or needle gauge

Catheter		Needle	
Gauge	Flow rate	Gauge	Flow rate
26 G	1.0 ml/s	25 G	0.5 ml/s
24 G	2.0 ml/s	23 G	0.5–0.8 ml/s
22 G	3.0 ml/s	21 G	0.8–2.0 ml/s
20 G	4.0 ml/s	19 G	2.0–4.0 ml/s

3.2.9
Technical Parameters and Protocols

Helical CT has virtually replaced conventional CT for examinations in which the entire chest is to be evaluated. However, low-dose high-resolution CT remains the technique of choice for the evaluation of the pulmonary parenchyma since it allows scanning at spaced intervals, significantly reducing radiation to the patient while providing excellent definition (Ambrosino et al. 1994; Lucaya et al. 2000b).

Several techniques are used for data acquisition in helical studies of the chest: standard helical CT, high-resolution helical CT, dynamic helical CT and low-dose helical CT.

Standard helical CT scanning usually suffices for most helical CT examinations of the chest. When a large area of the chest is to be scanned, such as in a screening examination of the lungs or mediastinum, we use the routine chest survey protocol (see above), with a section thickness depending on the age of the child. When finer detail and higher-resolution images are required over a smaller area of interest, such as in tracheobronchial stenosis, dehiscences, endobronchial lesions, central airway disease and vascular anomalies, we recommend the airway disease or CT-angiography protocols (see abvove), using a thinner section to achieve better image quality. Multiplanar and 3D reconstructions can be useful in the evaluation of airway abnormalities, certain vascular lesions and cervicothoracic or diaphragmatic and peridiaphragmatic lesions. Three-dimensional images can be rotated to display optimally pathologic entities and selected parts of the reconstruction can be analyzed separately.

Helical high-resolution CT scanning of the lung is performed with thin sections (0.5–1 mm) using a high-resolution reconstruction algorithm. This technique is similar to high-resolution CT scanning, but involves continuous data acquisition (Engeler et al.1994). Lowering the milliamperage setting reduces radiation dose, but the continuous data acquisition of helical CT still delivers more radiation than the low-dose high-resolution CT technique (see Tables 3.3 and 3.4), in which acquisition is performed with thin collimation and wide sampling intervals. In our institutions we prefer low-dose high-resolution CT for the evaluation of pulmonary parenchymal detail when diffuse airway or interstitial disease is suspected.

Dynamic helical CT has enabled scanning at maximum inspiration and rescanning at maximum expiration. This method has been used to evaluate lung attenuation in patients with air trapping and emphysema. However, it requires cooperative breath-holding by the patient. Software programs (available on some helical scanners) have enabled dynamic CT densitometry of the lungs (Johnson et al. 1998b). Dynamic helical CT can also be used to demonstrate respiratory changes in the cross-sectional area of the central airway, e.g. in patients with tracheobronchomalacia. In our practice, we do not use this technique to evaluate air trapping and emphysema. We prefer limited (three) expiratory scans with a low-dose high-resolution technique (Lucaya et al. 2000a).

Low-dose helical CT scanning can be used in many situations. The X-ray tube current should be as low as possible, without compromising image quality (Takahashi et al. 1998; Rogalla et al. 1999). With helical CT technique, a further reduction in radiation dose can be achieved by increasing table speed if automated dose modulation is not available or enabled. Use of a targeted approach to image localized processes can also reduce the radiation dose administered. We use low-dose helical CT when examining children under the age of 6 years, which in this age group provides diagnostic-quality exams. We also apply this technique for the non-contrast scan in children having both non-contrast and contrast-enhanced exams, and for delayed scans.

The performance of high-quality helical CT requires proper selection of technical parameters, including collimation (section thickness), field of view (FOV), table speed (or pitch), reconstruction intervals, reconstruction algorithms, scan time duration, exposure factors (kilovoltage and milliamperage) and scan initiation (Brink 1995; Frush and Donnelly 1998). These parameters should be based on the patient's size and the body part to be examined. However, reduction in some of these parameters can lead to problems. Noise increases with decreasing collimation. Scan coverage decreases with reductions in collimation and table speed. Radiation dose increases with reductions in table speed and with reduction in collimation. Decreasing the reconstruction intervals increases processing time. So, the final choice of parameters always involves a balance among these options to achieve diagnostic image resolution and low dose to the patient. As a general rule, thin collimation should be reserved for instances when intricate detail of small structures are required.

MDCT scanners have sub-second gantry rotation times. So, reducing rotation time from 1 s to 0.5 s, we will halve the radiation dose and the scan time if the mA is fixed.

The kVp has not routinely been adjusted in the past for body CT exams in children. Reducing the kVp can reduce the radiation dose substantially. In our experience, when the voltage is dropped from 120 down to 90, the radiation dose is decreased by 40%. The effect on image quality is important, as both image noise and tissue contrast are affected. The kVp can be reduced (80,100), related to the child's size or when scanning body regions with high inherent contrast such as the chest, airways, and in skeletal studies and CT angiography.

Table speed (pitch), traditionally affected image quality and radiation dose, i.e. as with the older generation of scanners, the greater the pitch, the lower the radiation dose. Studies using single slice scanners show that radiation dose can be reduced by one-third by increasing the pitch from 1.0 to 1.5 (García-Peña and Lucaya 1999) Pitch of 1.5 was often used in paediatric radiology, as any greater pitch can lead to a reduction in image quality.

This does not apply when the Automated dose Control/Modulation (ADC/ADM) functions are available or used on more recent scan models. When dose modulation is operated the scanner will automatically override an increase in pitch by increasing the mA in order to keep the mAs constant.

Also the more modern MDCT scanners have sub-mm collimation. Thinner slice widths improve spatial resolution but increase the noise. Increasing the mA (with an increase in dose) or increasing the thickness of the reconstructed slice width (will not affect the dose) can solve the problem of noise. The radiation dose can be minimized when we avoid the narrowest collimation and only use it for specific exams as CT angiography and high resolution lung parenchymal detail in very small children. The radiation dose will be reduced, as it takes less time to cover the same scan length, compared to thinner collimation.

The number of detector rows also can affect dose radiation. MDCT scanners have an inherent dose problem in relation to the X-ray beam, which extends beyond the confines of the detector rows (overscanning). This effect decreases with more detector rows. In modern scanners, the X-ray beam is filtered, contouring its shape very closely to remove photons that otherwise will be absorbed by the patient, thus decreasing the radiation dose to the patient.

Post-processing techniques using noise reduction filters can allow the use of low mAs (less dose) and thus improve the quality of the images for diagnostic purposes (Kalra et al. 2003).

Another method for radiation dose optimisation is to use the modulation tube current system that is available in most of the new multidetector-row equipment (Greess et al. 2004). The tube current is modified to follow the anatomy of the patient, maintaining the same noise level within the images. Two methods are available, modulation in the x- and y-axes (angular modulation) and z-axis modulation. Angular modulation adjusts the tube current while the X-ray tube passes around the patient´s body, and can reduce the radiation dose by up to 30% (Greess et al. 2002, 2004). Dose reduction in CT examinations of children by an attenuation-based on-line modulation of tube current (CARE dose) is also possible (Gress et al. 2002). The z-axis current modulation needs the selection of an acceptable noise level and a maximum and minimum tube current, which are chosen before the examination. Thence, the scanner can adjust the tube current within the selected range and maintain the noise level, using data from the scout or during gantry rotation. The reduction in tube current can be around 40% using this technique (Kalra et al. 2004).

Nowadays, most of the MDCT scanner manufacturers make an effort to help with radiation dose control. They have made changes in their equipment to give information on dose and how to use modulation dose systems to maintain image quality, and to produce age or size adjusted protocols, which are very useful as a guide for paediatric dose reduction.

Within the radiology community, there has been an increasing emphasis on trying to reduce radiation dose in children, and to attempt to optimise the balance between image noise and dose. Ongoing investigations allow us to post-process the original examination by adding a controlled and variable amount of noise, in order to mimic the appearance, which would have been obtained by using a lower mAs (Frush et al. 2002). Such technology will be very helpful in modifying and improving paediatric protocols in future.

The image reconstruction interval is usually set at an interval equal to the collimation. If multiplanar or 3D reconstructions are required, reconstruction with 50% overlap can be performed for better definition. Moreover, overlapping images increase lesion depiction, which is useful in the evaluation of pulmonary nodules.

The most frequent reconstruction algorithm used is the low-spatial frequency (standard) algorithm. The pulmonary parenchyma can also be analyzed with a high-spatial frequency algorithm (bone algorithm).

Scan duration should be tailored as much as possible to the breath-holding ability of the child.

The scan delay time varies with the region of interest and the clinical indication of the study (see Table 3.6a.) The scan delay time for CT angiography is more complex and will be the arterial time, obtained by monitoring the contrast enhancement in the descending aorta. This is done by acquiring very low mA scans at the same level (one scan every 3 s over 15 s) and determining the time of peak contrast. Alternatively, an automated bolus-tracking technique can be used to monitor contrast enhancement and initiate scanning. Scanning begins once an arbitrary threshold level of contrast enhancement is reached (150 CT units in the thoracic aorta). Specific recommendations for the selection of parameters are given in the examination protocols presented above.

3.2.10
Image Postprocessing

Post processing of the volumetric data is usually performed with four reconstruction displays: multiplanar reformations or reconstructions (MPRs), 3D shaded-surface-displays(SSDs), multi-projective volume reconstructions (MPVRs) and 3D volume renderings (VRs).

In fact, the axial images include all the information about the anatomy that is provided with 2D and 3D reformats.

However, post-processing gives added value to imaging since the axial scan that need to be studied are usually numerous. Also oblique structures as well as interfaces and surfaces parallel to the axial plane are poorly demonstrated and same times occult.

Multiplanar reformations (MPRs) provide additional diagnostic information in different planes and are as accurate as the axial scans due to the nature of the isovolumetric acquisition of the data .MPRs are 1-voxel-thick, 2D tomographic sections that can be displayed in coronal, sagittal, or parasagittal planes or in a single tomographic “curved” plane, along the axis of a structure of interest, e.g. a bronchus or a feeding vessel (Siegel 2003; Salvolini et al. 2000). They are real-time, easy-to-reconstruct images, producible as soon as the axial sections are completed. They generally improve our perception of images and give information that although contained in transverse images, is less effectively displayed (Fig. 3.1a). Their diagnostic value is substantial in demonstrating and documenting the presence of small focal lesions, defining the vertical extent of a bronchial stenosis, which may go undiagnosed from the axial source CT images, and are invaluable prior to surgical remodeling of vascular rings and the tracheobronchial tree. However, to avoid misinterpretations due to partial volume effect, e.g. overestimation of the degree of a stenosis, overlapping and thinner cuts should be applied when processing the raw data. Likewise, when processing curved MPRs, the trace should be centered within the lumen of interest to avoid anatomic distortion.

Three-dimensional (3D) imaging is a diagnostic tool necessary only in certain cases as it usually requires more time and post-processing skills to provide information already included and demonstrated in the axial images and the MPRs. There is no doubt however that the 3D reformatted images may further increase the diagnostic confidence which eventually affects patient management, particularly pertinent in pre-surgical assessment. Communication with the referring clinicians is simplified as they portray spatial relationships of important anatomic structures.

Shaded-surface-display 3D techniques (SSDs) are applied in the imaging of the central airways, vessels and bone strucutres and they are usually more visually impressive than clinically useful.

SSD generates images with depth and 3D information. Using binary classification, voxels with attenuation values above a preset threshold are set to white and voxels with lower attenuation values are set to black (Brink 1995). This method first computes a mathematical model of a surface that connects neighbouring pixels with CT intensities above a preset threshold. Depth or 3D perception is created by shading techniques using an imaginary light source that can be arbitrarily positioned. Such data can be then rotated, allowing the image to be viewed from any perspective (Fig. 3.11c).

Their generation from original data is time-consuming and they carry the risk of loss of density information due to problems with thresholding. The threshold must be carefully chosen and should be based on the intensity of the contrast material in the area of interest. The choice of threshold will strongly affect the evaluation of some lesions, such as the degree of stenosis. Choosing too low a threshold may increase noise and also allow the higher density soft tissue to obscure the target vasculature. Choosing a too-high threshold may result in small vessels disappearing and/or stenoses being falsely implied.

Another problem encountered with SSD is that the reduction of CT volume data to a single surface removes the inherent CT quantitative density values, losing gray scale levels. With this threshold technique one cannot differentiate between solid organ intraparenchymal vasculature and enhancing parenchyma, or between high attenuation structures in vessel walls and intraluminal contrast enhancement.

Multiplanar volume reconstructions (MPVRs) are “selective” 3D images that resemble the 2D MPRs

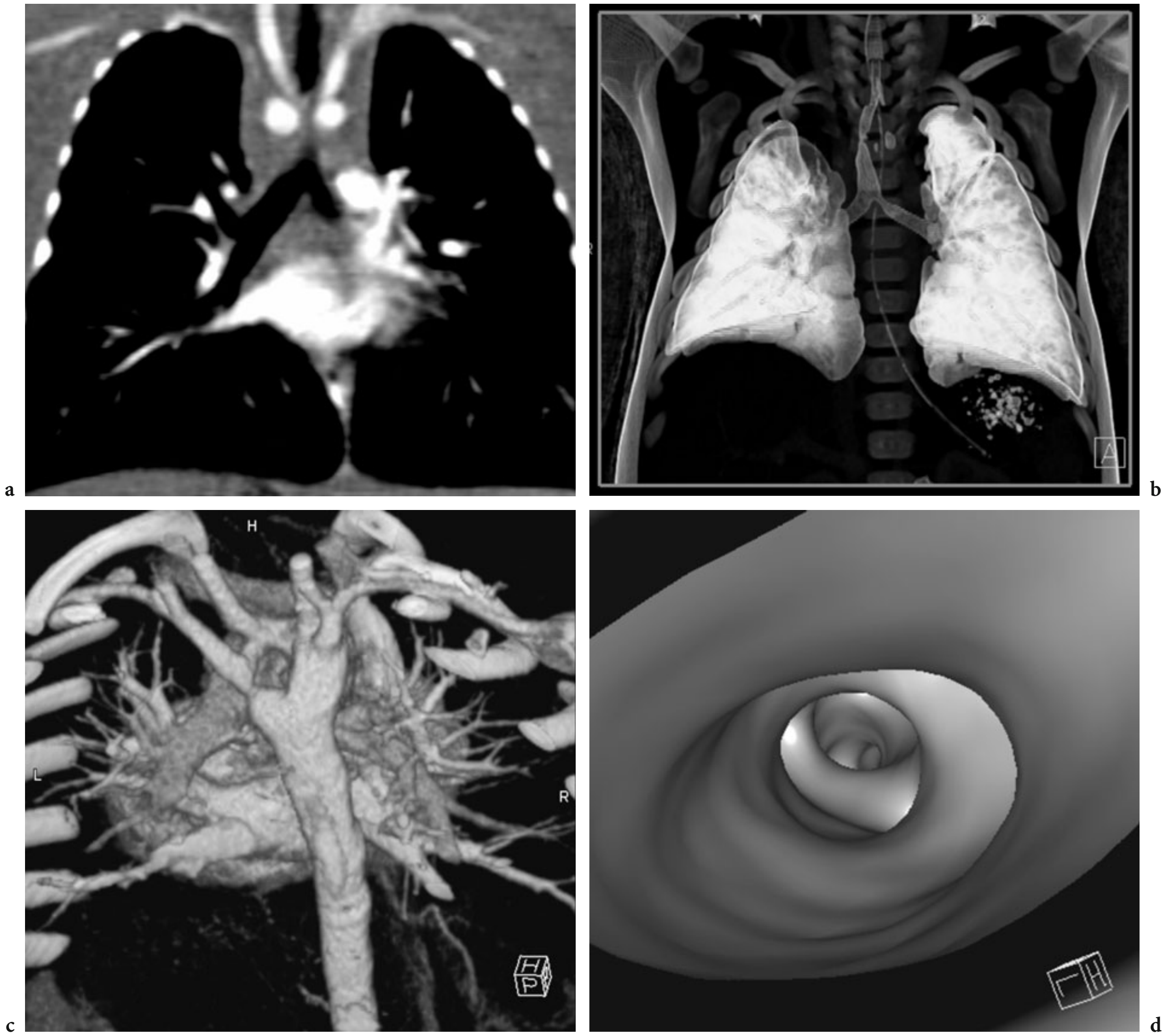

Fig. 3.1a–d. Post-processing techniques. **a** Multi-planar reformats (MPR). MPR initially in coronal and sagittal planes should be the initial post-processing technique: with pixel isotropy, no information is lost, and the reformatted plane often gives a better depiction of the anatomical relationships. The coronal image shows a double aortic arch and its effect on the airway. **b** Multiplanar volume reconstructions (MPVRs). MPVRs combine volume rendered images with multi-planar imaging to produce 3D 'slabs' of the area of interest. By applying a minimal intensity projection technique a view of the airways can be produced such as this example of a congenital tracheal and left main bronchial stenosis in a 3-year-old boy with bronchiolitis. This technique is sometimes referred to as a "virtual bronchogram". Historic stair-step artefact in traditional single slice volume-rendered image (bronchographic anteroposterior view). The artefact occurs along the left bronchus, which is oriented obliquely to the direction of patient travel during data acquisition. **c** Three-dimensional (3D) volume rendering (VR) is an excellent technique for giving an overview of complex vascular anatomy. This example is a posterior view of the great vessels with the spine and posterior ribs 'cut-away', showing a double aortic arch with a dominant right arch. **d** Virtual bronchoscopy is a supplementary volume rendering technique that produces images simulating the view from fibreoptic bronchoscopy. The point of view is placed in the airway. This example demonstrates complete tracheal rings in congenital tracheal stenosis: note the abnormally rounded shape to the airway, which is normally ovoid

and depict peripheral airways better than individual sections. With this technique, a combination of the spatial resolution of thin sections with the anatomical display of thicker slices is achieved and all the information acquired in the raw data set is used. The routine CT images are combined in multiples to create an image thicker in voxels, the volume "slab", which constitutes an interactive sum of axial, coronal and sagittal reconstructed sections (Siegel 2003; Salvolini et al. 2000). By using different algorithms and setting thresholds, maximum or minimum intensity voxels can be highlighted within the slab. For the evaluation of the airways, minimum intensity projections within the slab are usually applied. Slabs are useful in detecting and localizing micronodular or microtubular patterns and in analyzing mild forms of uneven attenuation of the lungs (Remy-Jardin et al. 1993). However, they are time-consuming and should be reserved for cases of complex morphology, to give the clinicians a comprehensive multilevel roadmap 3D image.

MIP images are generated by mapping the maximum attenuation value along each ray to produce a gray-scale image. Thus, bone and calcified structures are bright and are distinguishable from both iodinated contrast material and soft tissue. In a vascular examination, it will be necessary to postprocess the image to avoid bone images (Brink 1995).

MIP images are useful for displaying vascular structures and for CT angiography. They reliably display vessel calibre, metallic stents, and wall calcifications, but provide poor separation of overlapping vessels because 3D relationships are lost (Fig. 3.11b). The display of MIP images in a cine loop to simulate a rotating viewing direction improves the lack of 3D depth. This allows visualization of 3D relationships and may provide clues to the nature of eccentric stenoses and the crossing or looping of vessels.

MinIP images map the minimal attenuation value to a gray-scale image. MinIP images are valuable in examinations of the central airways (Fig. 3.2c).

(STS-MIP) and/or STS-minIP is a cross-sectional imaging post-processing technique that computes overlapping MIPs of limited depth. The sections are typically thin 2–3 mm sections rendered into approximately 20–30 mm slabs (Napel and Jeffrey 1993). STS-MIP can improve the visualization of vessels over greater portions of their lengths. Vascular anatomy is frequently difficult to comprehend from standard cross-sectional images. Blood vessels that are perpendicular or oblique to the section will appear as small circles or ellipses and may mimic the appearance of a pulmonary nodule. With STS-MIP, one can integrate the path of vessels and their connections with other structures into the larger picture of vascular anatomy.

STS-minIP enables airway anatomy to be visualized. It is also useful for displaying the whole volume of parenchymal cysts bullae or overinflation (Fig. 3.2).

Three-dimensional (3D) volume renderings (VRs) represent the main technique for 3D reformatting of the airways and the vascular structures of the mediastinum. The VR technique is particularly useful for displaying structures that course parallel or oblique to the transverse plane and those that develop or extend into multiple planes (Siegel 2003; Salvolini et al. 2000) (Figs. 3.3, 3.5 and 3.6). Thus the added value in cardiothoracic imaging to depict complex anatomy of the heart, great vessels and lungs in 3D has revolutionised cardiothoracic imaging (Figs. 3.1, 3.4, 3.5 and 3.6).

However, preliminary editing is still necessary and can be time consuming, altering work patterns in CT. In VR, different anatomical tissues are represented by proportional values that are assigned to every voxel and depend on the range of tissue attenuation values in the original data set. Voxels are selected by the probability of belonging to the object of interest; thus they are displayed in different colours or several shades of grey, different transparency or opacity. Transition from the reconstructed surface to the surrounding media is gradual and the depiction of interfaces, like the inner tracheal lining, is supposed to approach the true appearances.

VR from extraluminal visualization of the tracheobronchial tree creates images similar to conventional bronchograms and is applicable in clinical practice without the concomitant administration of a contrast agent. Other clinical applications include cardiovascular imaging and chest wall disease (Johnson et al. 1998a) (Figs. 3.1b, 3.5d and 3.9c).

Albeit this 3D segmentation technique is better and more complicated than the others previously mentioned, some information is lost during processing so that the axial images are still indispensable for the radiologist to assess extra-luminal disease and identify artefacts. Three-dimensional VR reconstructed images are attractive and appealing to the clinicians as they may better illustrate short focal areas of narrowing, the craniocaudal length of a tracheobronchial stenosis, and complex congenital cardiovascular and tracheobronchial anomalies.

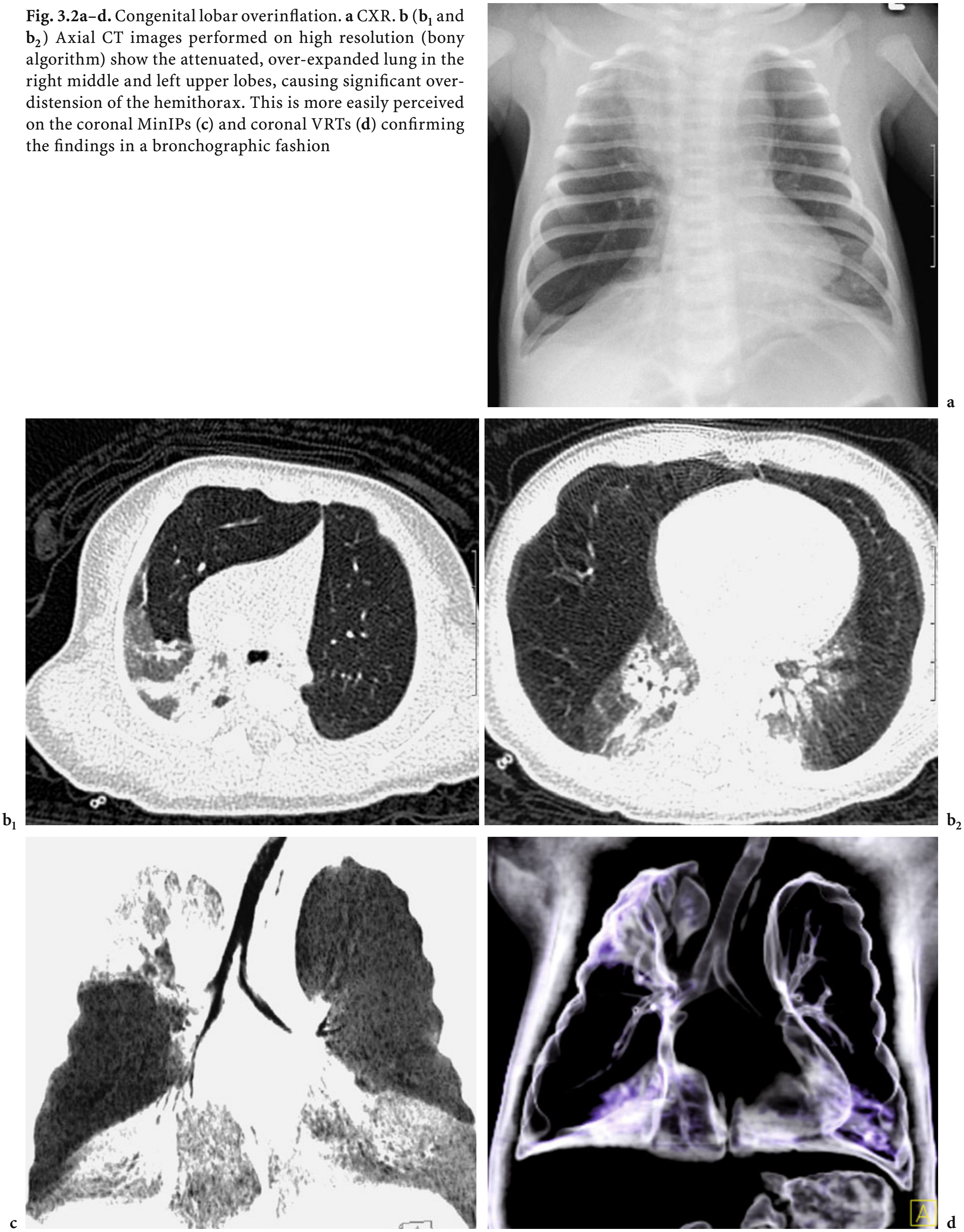

Fig. 3.2a–d. Congenital lobar overinflation. **a** CXR. **b** (**b**$_1$ and **b**$_2$) Axial CT images performed on high resolution (bony algorithm) show the attenuated, over-expanded lung in the right middle and left upper lobes, causing significant overdistension of the hemithorax. This is more easily perceived on the coronal MinIPs (**c**) and coronal VRTs (**d**) confirming the findings in a bronchographic fashion

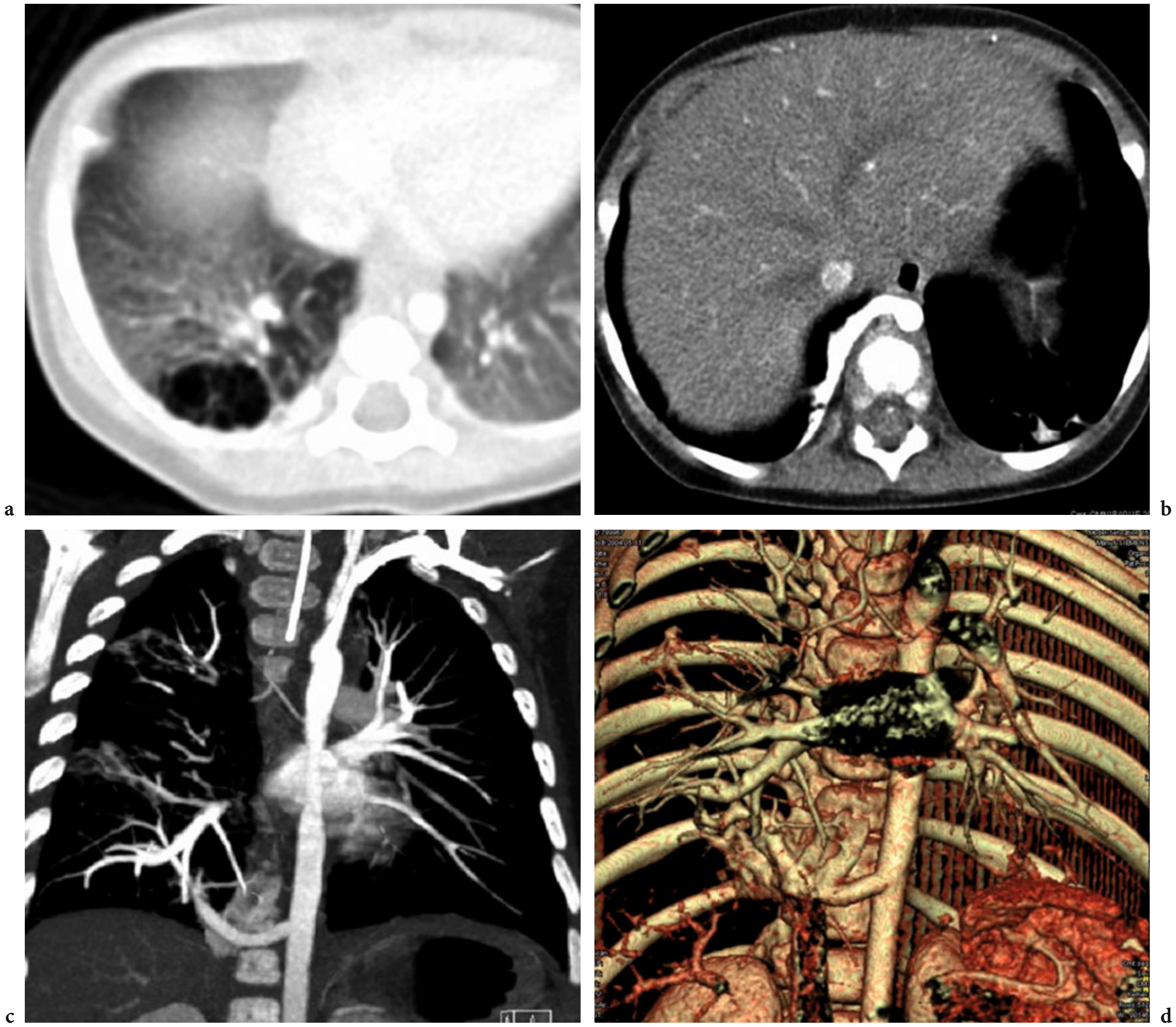

Fig. 3.3a–d. Combi scan in an 11-month-old child with a hybrid lesion in the right lower lobe. **a** Axial CT on lung window settings shows the multicystic nature of the lesion. **b** Axial soft tissue slice shows large arterial feeder to the lesion form the aorta. **c** Coronal oblique MIP, shows the course of the systemic arterial feeder to the lesion. This is more easily visualized and appreciated better with this oblique orientation along the axis of the vessel. **d** Three-dimensional (3D) VRT This image additionally demonstrates the pulmonary venous drainage [into inferior pulmonary vein] of the lesion, i.e. intra-lobar sequestration

The inner surface of air-containing tracheobronchial tree can be displayed with *Virtual Bronchoscopy (VB)* (Figs. 3.1d, 3.4c and 3.10c) which is performed with either polygonal SSD or direct VR. VB is a non-invasive and accurate technique that can provide "bronchoscopic" views of the central and the peripheral airways.

This technique, as the fiberoptic bronchoscopy, is considered supplementary to CT and referral to the axial sections is again valuable to recognize artefacts and to gain perception of the orientation within the virtual airways. VB uses perspective surface rendering, which takes advantage of the natural contrast between the airway and the surrounding tissues (Heyer et al. 2004). The point for viewing is located intraluminally so that external structures do not overlap and editing takes shorter time periods. Sub-millimeter (0.625 mm, 0.75 mm) slice thickness allows deeper penetration and visualization of the bronchial surface down to the bronchial diameters of below 5 mm; it is associated however with inevitable increase in radiation dose (Khan et

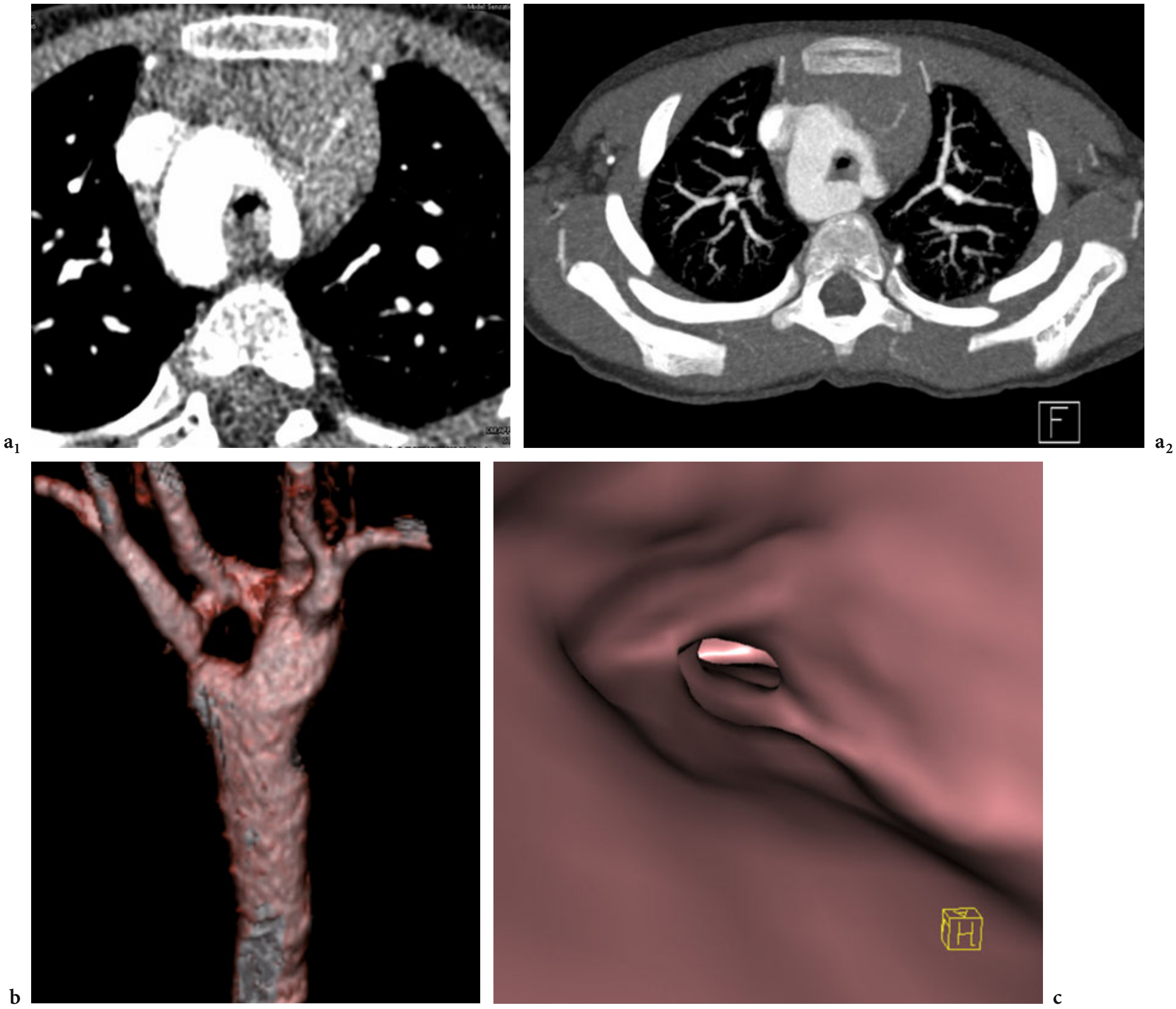

Fig. 3.4a–c. Double aortic arch in a 1-month-old boy with important respiratory distress. This illustrates the more common right dominant double aortic arch on CTA: the right arch is larger than the left which is stenotic at the origin of the left subclavian artery. Note the marked narrowing of the airway at this level. **a** Thin axial image (**a$_1$**) and axial maximal intensity projection (MIP) (**a$_2$**). **b** Posterior volume rendered tomogram (VRT) image of the aorta showing the double aortic arch encasing the trachea. **c** Virtual bronchoscopic image shows concentric tracheal narrowing related to complete encirclement of the trachea by the double arch

Fig. 3.5a–e. Pulmonary artery sling. **a** CXR shows widening of the carinal angle due to associated long segment tracheal stenosis and left lung atelectasis. **b** Axial image CTA demonstrates the left pulmonary artery arising from the right pulmonary artery, running between the oesophagus and trachea, which is narrowed. The tracheal narrowing is in fact due predominantly to intrinsic long segment (complete cartilaginous ring) tracheal stenosis. **c** Axial images showing various post processing algorithms on which the data can be viewed at B30f for soft tissue (**c$_1$**) and lung parenchyma (**c$_2$**), and at B60f for high resolution lung parenchymal detail (**c$_3$**). **d** VR image 'virtual bronchogram' shows long segment tracheal narrowing and stenosis alongside. **e** The conventional invasive tracheobronchogram

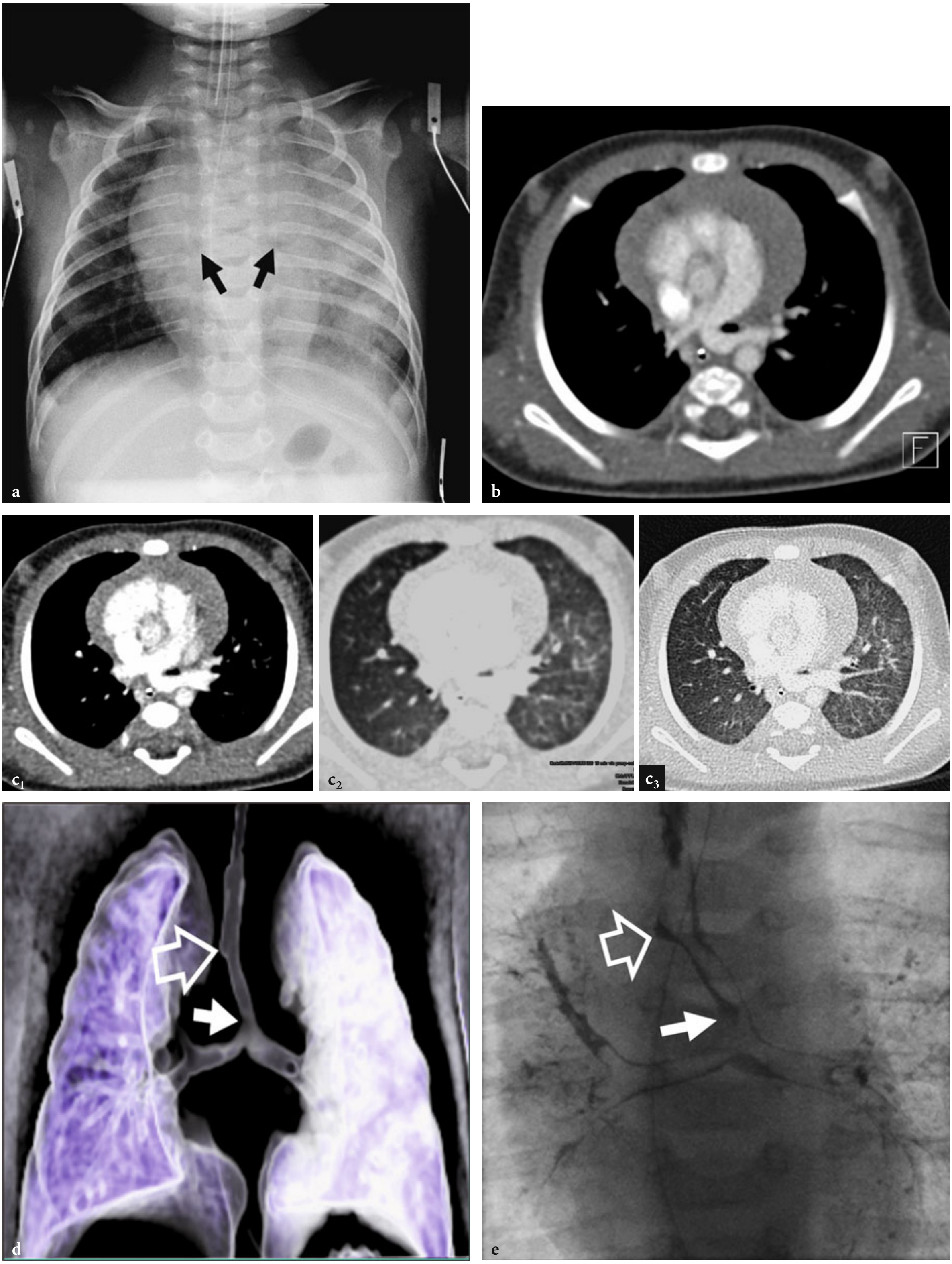
a
b
F
c_1
c_2
c_3
d
e

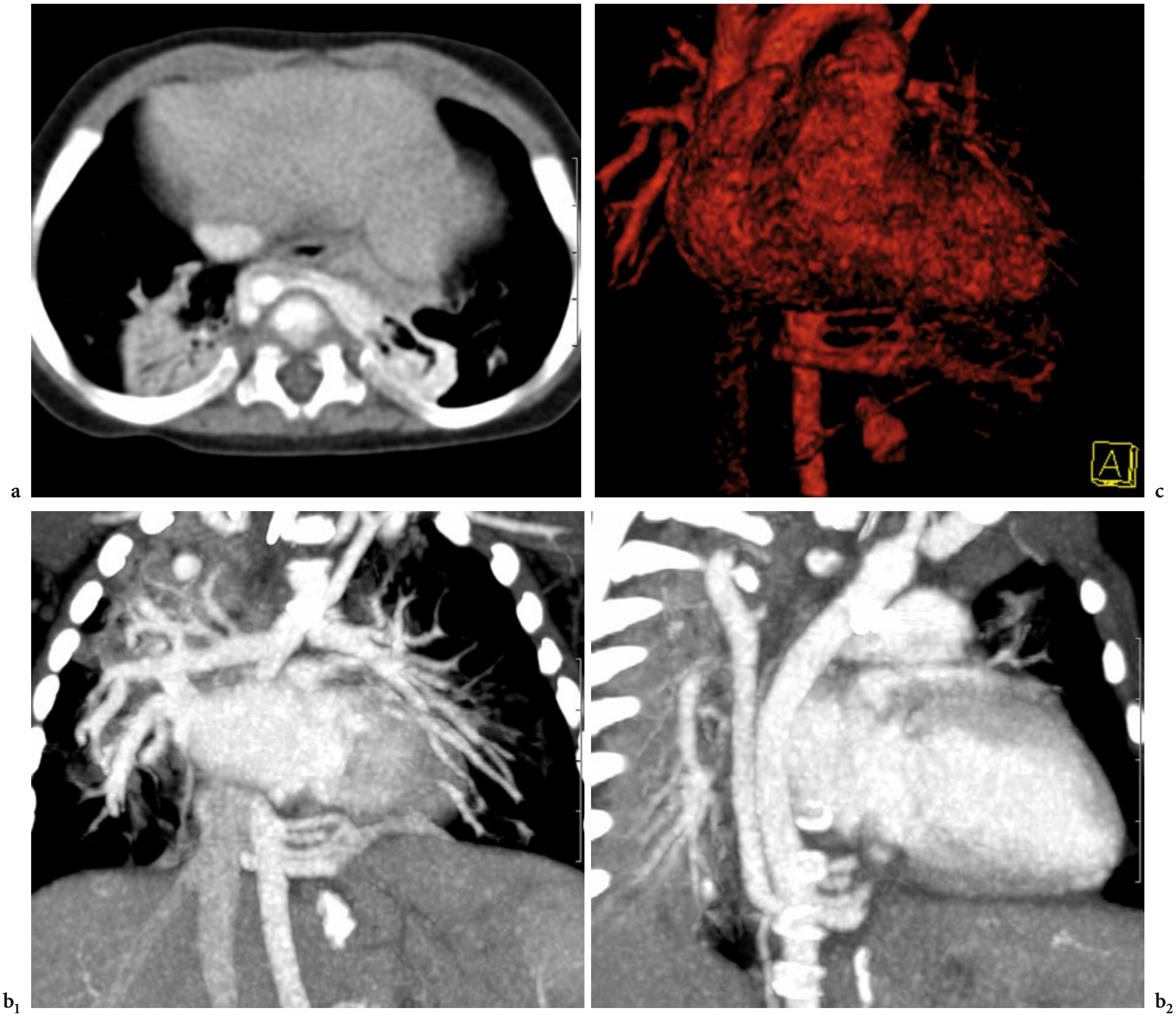

Fig. 3.6a–c. Left lower lobe extralobar sequestration in a 10-month old with multiple congenital abnormalities. **a** Axial CT maximum-intensity projection images shows a large artery arising from the aorta, supplying a L lower lobe pulmonary mass. **b** Anteroposterior (**b$_1$**) and sagittal oblique (**b$_2$**) maximum intensity projection images show three systemic vessels arising from the aorta to feed the pulmonary sequestration, which drains into the azygous (systemic venous) system. **c** Posteroanterior VRT image. The 3D depth perception created by the VRT technique improves recognition of the spatial relationships of the three vessels arising from the aorta. A single horizontal vein is shown draining into the enlarged azygous vein

al. 2004; Venkatraman et al. 2006; Heyer et al. 2004).

Again, VB often does not add anything new to the established diagnosis. However, the pulmonologists may prefer and relate to these images in conjunction with the axial or the reformatted ones (Bal et al. 2004). In practice, VB is of limited value, reserved for cases where bronchoscopy is not applicable (children at risk of undergoing traditional bronchoscopy) or precise navigation is not possible to guide airway interventional procedures and in emergencies such as infant airway (tracheal) stenosis which can not be evaluated otherwise (Khan et al. 2004). The produced images resemble the true bronchoscopic images and can additionally "advance" distally to an airway obstruction, where the real endoscope cannot penetrate (Salvolini et al. 2000; Hoppe et al. 2004). However, when compared to fiberoptic bronchoscopy, VB precludes any therapeutic manoeuvring, it is incapable of detecting endoluminal lesions smaller than 2–3 mm, and provides limited information about mucosal details (morphology, vascularity and colour) making differentiation between pathologic processes and retained secretions difficult (Heyer et al. 2004). There is consensus that measurements should be better performed in 2D sections as they may be otherwise inaccurate. The technique is additionally affected by the partial volume effect, which may lead to misinterpretation of severe stenoses as occlusions, and the threshold level is therefore of importance for displaying accurate simulations (Hoppe et al. 2004).

Dynamic and functional inspiratory and expiratory scanning with single breath-hold MDCT helps identification of strictures, areas of air-trapping and tracheobronchomalacia, but is rarely applied in paediatric practice because of the associated radiation burden (Johnson et al. 1998b; Siegel 2003).

Peripheral airways: modern volumetric techniques have partially overcome the difficulty of demonstrating 3D images of the peripheral airways. Data are acquired and reconstructed at a later time, allowing for thin-slice high-resolution images at any level, so that a whole affected bronchiectatic segment can be displayed on a single MPR/VR oblique section with images that resemble conventional bronchography and may influence the approach for tissue sampling (Salvolini et al. 2000; Remy-Jardin et al. 1998; Bonnel et al. 2004; Pifferi et al. 2004). If there is suspicion of small airways disease, some additional expiratory cuts may be useful. Whatever the application we perform, all the techniques are considered as an adjunct to "conventional" HRCT evaluation of the peripheral airways which allows accurate and precise assessment of diffuse lung disease at very low doses equivalent to approximately 10 chest radiographs (Salvolini et al. 2000; Owens 2004; Garcia-Peña 2004).

3.3
Helical Chest Main Applications

The introduction of helical technology has extended the clinical indications of chest CT.

The most important diagnostic indications in children include evaluation of pulmonary nodules and thoracic masses, lesions located in difficult areas (e.g. cervico-thoracic, diaphragmatic, peri-diaphragmatic or chest wall regions) and in the central airways, definition of vascular anatomy and study of critically ill patients (Valencia et al. 2006; Bal et al. 2004). In our institution, the most common indications for chest studies are the detection and characterization of pulmonary nodules and definition of mediastinal masses in children with known or suspected malignancies, investigation of infection in the immunocompetent and immunocompromised child (Figs. 3.7–3.10), congenital malformations, combined airway and vascular studies (Figs. 3.1–3.6) and diagnosis and follow up of bronchiectasis and diffuse lung disease.

3.3.1
Evaluation of Pulmonary Nodules and Chest Masses

Several studies have demonstrated that at least 10% more pulmonary nodules can be identified with helical than with conventional CT (Costello et al. 1991; Remy-Jardin et al. 1993). The ability to obtain overlapping reconstructions at thinner sections with the consequent contiguous volume data acquired, increases the certainty that scans are obtained through the centre of any lesion. These images depict the lesion without any volume averaging effect. In the setting of suspected metastatic disease using a single breath-hold technique, helical CT eliminates respiratory misregistration in patients caused by variations in the depth of respiration. This improves its ability to detect small nodules.

In children unable to breath-hold who must be scanned during quiet respiration, helical CT has evidenced no significant loss of accuracy in the detection of pulmonary metastases (Coakley et al. 1997a). The problem of variable respiratory excursion is further minimized by volume acquisition and the possibility of overlapping image reconstruction (Buckley et al. 1995; Coakley et al. 1997b).

The volumetric data created during helical CT and the coronal and sagittal images reconstructed from them are useful for delineating the anatomy of vascular lesions that appear similar to nodules. It can also clarify the spatial relationships of a nodule to the pleura or diaphragm (Brink et al. 1994a), a task that is especially difficult with conventional section-by-section CT because of the large excursion of the diaphragm between breaths.

Low-dose helical CT of the chest is highly sensitive for detecting pulmonary nodules, and could be an ideal alternative to conventional-dose heli-

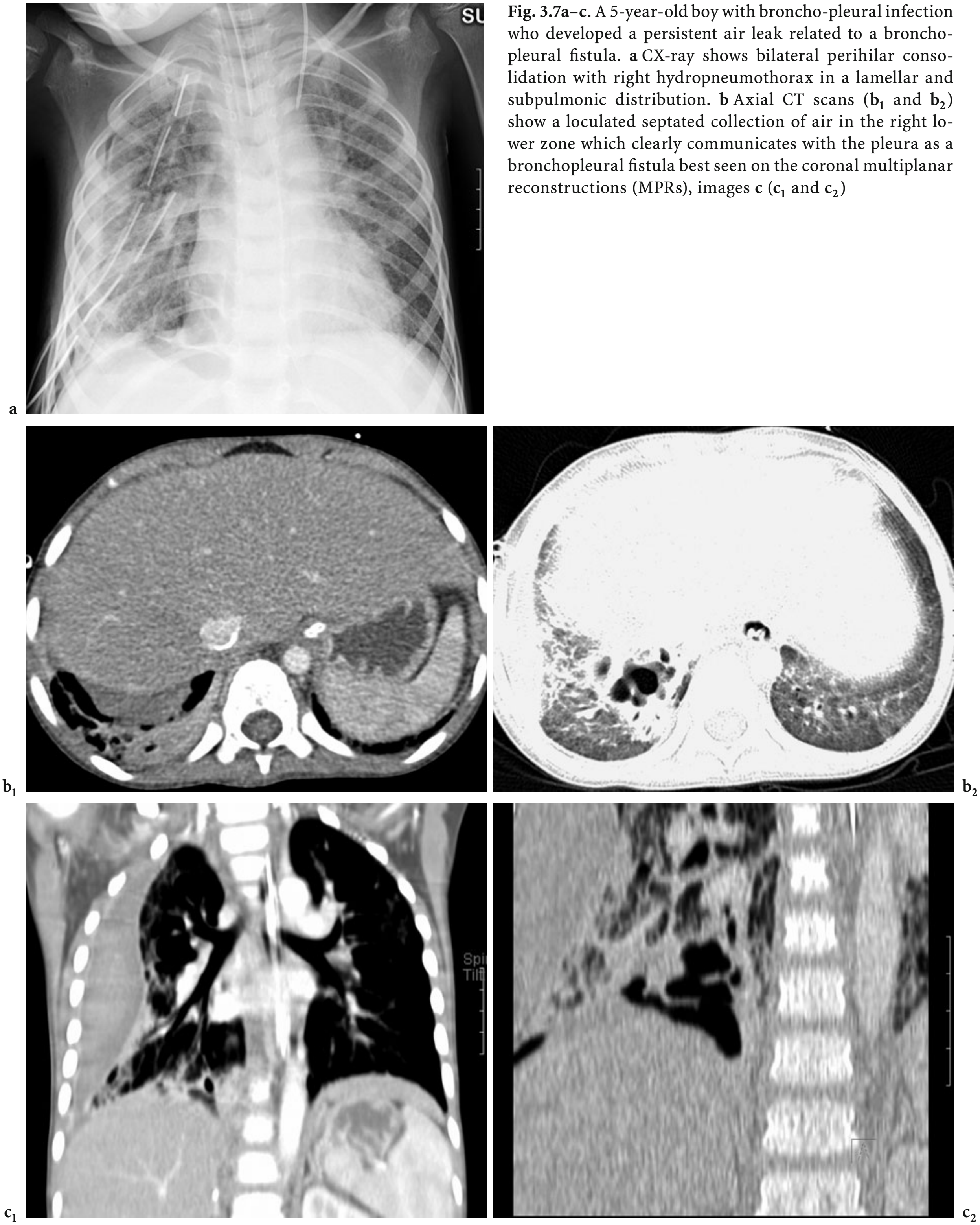

Fig. 3.7a–c. A 5-year-old boy with broncho-pleural infection who developed a persistent air leak related to a bronchopleural fistula. **a** CX-ray shows bilateral perihilar consolidation with right hydropneumothorax in a lamellar and subpulmonic distribution. **b** Axial CT scans (**b_1** and **b_2**) show a loculated septated collection of air in the right lower zone which clearly communicates with the pleura as a bronchopleural fistula best seen on the coronal multiplanar reconstructions (MPRs), images **c** (**c_1** and **c_2**)

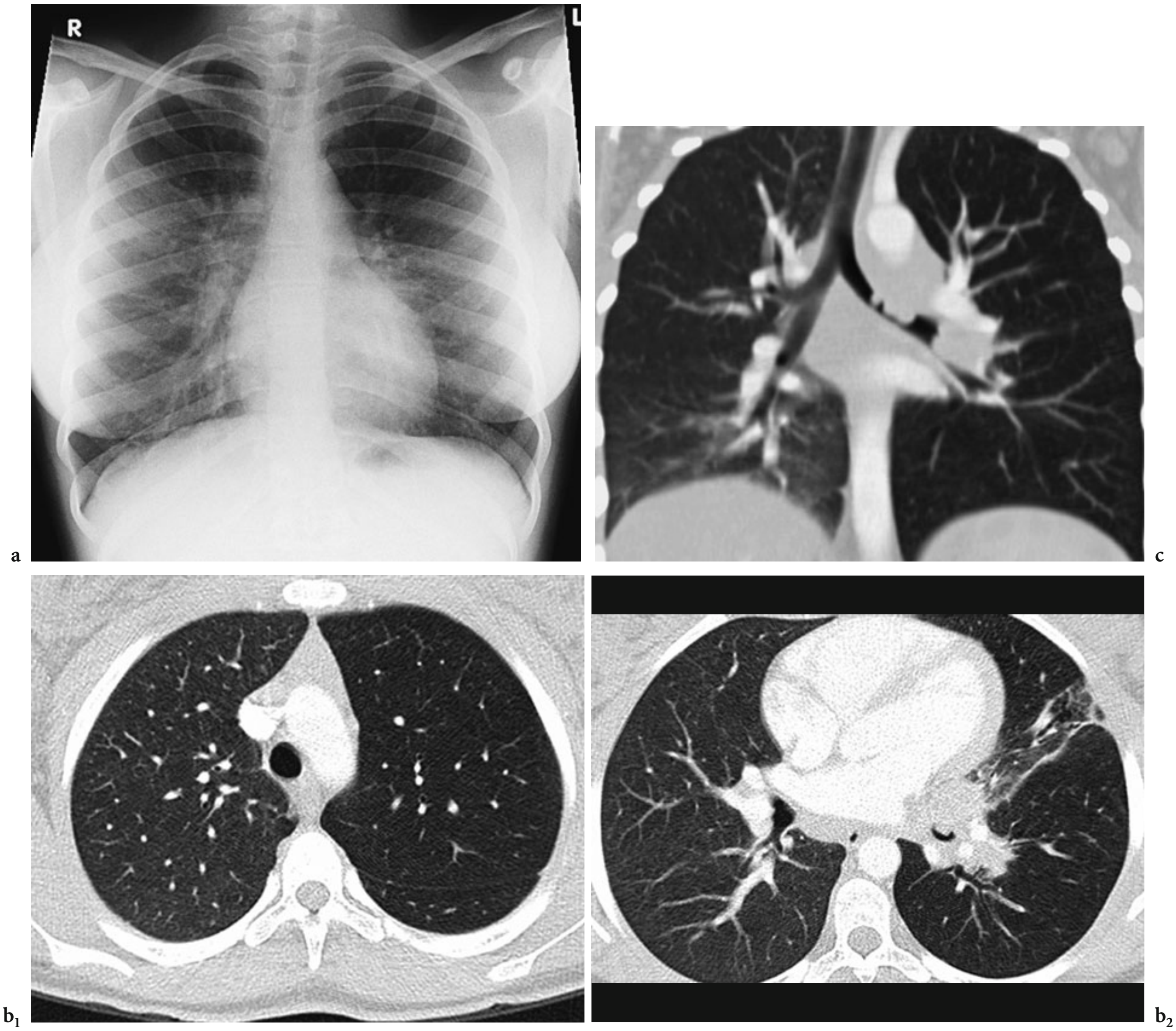

Fig. 3.8a–c. Intrabronchial aspergillus infection with persistent overinflation of the left lung related to delayed diagnosis of bronchopulmonary aspergillosis secondary to chronic granulomatous disease (CGD). **a** CXR relatively unremarkable. **b** Axial CT images (**b**$_1$ and **b**$_2$). The left main bronchus shows an endoluminal polypoid mass with distal overinflation of the left lung due to ball valve effect. **c** Coronal multiplanar reformation (MPR) image through the left main bronchus show overinflation of the left lung compared to the right and the soft tissue images show endoluminal bronchial wall thickening causing ball valve effect in the left lung

cal CT for screening purposes (Gartenschläger et al. 1998). Recommendations for the selection of parameters are given in the 'routine chest protocol' (Table 3.1a,b). It is not usually necessary to use intravenous contrast agents in the evaluation of pulmonary nodules.

To evaluate solitary pulmonary masses and mediastinal lesions, another indication of helical CT, we recommend the 'routine chest protocol' with IV contrast material (Table 3.1a,b). The rapid scanning speed facilitates scanning during the time of peak contrast enhancement, permitting optimal definition of anatomic features. This is particularly important in children, who have little mediastinal fat and hence lack intrinsic contrast differences.

Scanning during peak contrast levels optimizes the evaluation of mediastinal and hilar lymph nodes and masses. Mediastinal vascular structures and masses are easily differentiated. Helical CT is the procedure of choice for evaluating anterior or middle mediastinal masses. Posterior mediastinal masses can also be studied by helical CT, but MRI is

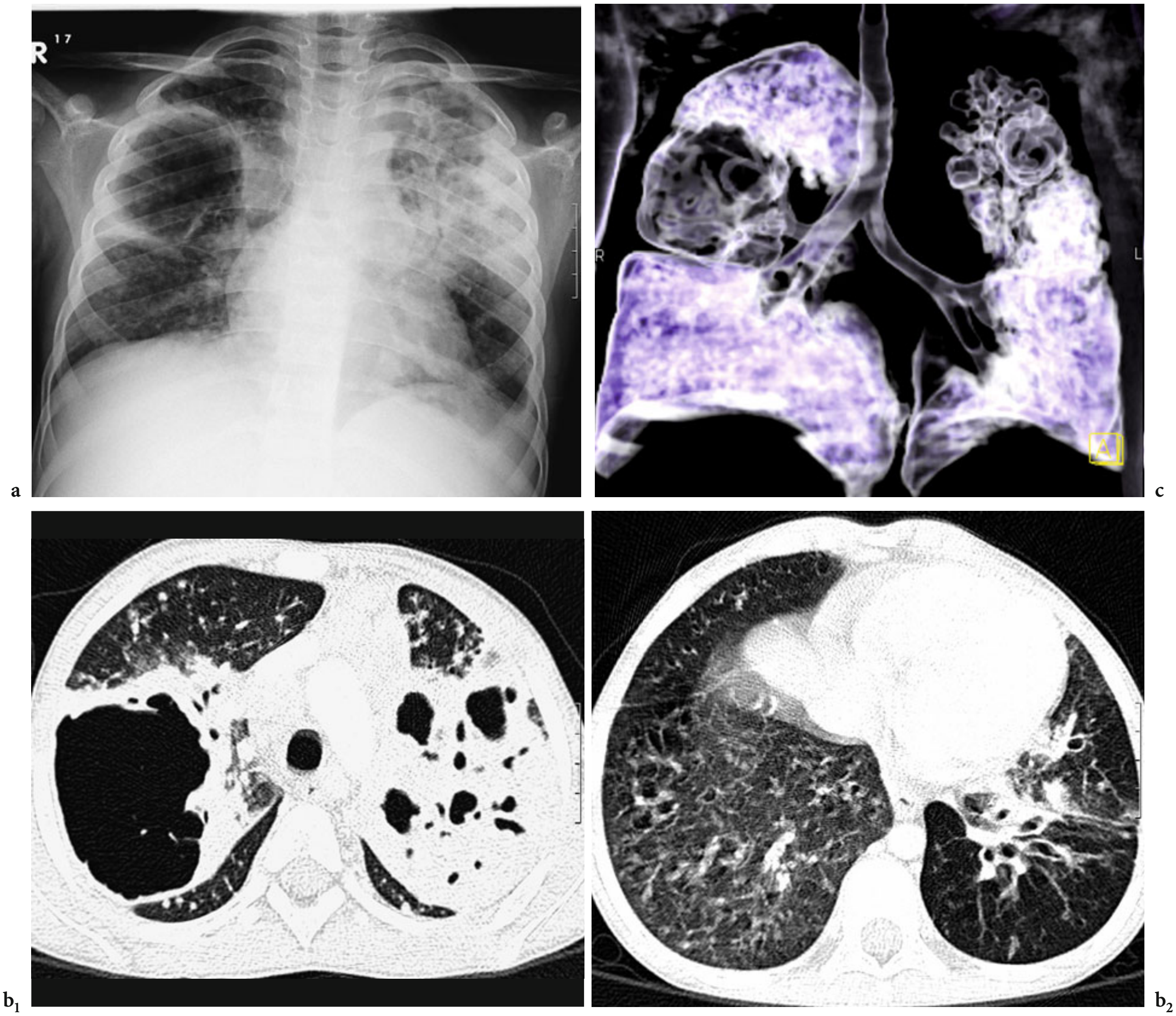

Fig. 3.9a–c. Child with both endobronchial and haematogenous (miliary) tuberculosis with centrilobular miliary nodules and cavitating lesions in the left and right upper lobes shown on CXR, axial CT and coronal VRTs. The axial images show bronchiectasis in the L lower lobe. **a** CXR. **b** Axial CT image (**b_1** and **b_2**). **c** Coronal VRTs images

the procedure of choice in these cases. Special attention should be given to intraspinal extension.

An important indication for helical CT is tumour staging and the follow-up evaluation of treatment. Compared with conventional CT, helical CT can facilitate identification of infiltration, vascular encasement, airway displacement and enlarged hilar lymph nodes. Multiplanar reconstructions can be very useful for identifying infiltration, encasement or compression of vital structures, and intraspinal extension. The resulting information can facilitate surgical planning or radiation therapy. Another advantage is that chest and abdominal studies can be performed in a single session with a single dose of IV contrast material. This is especially important in the evaluation of patients with lymphoma.

Other abnormalities that can benefit from helical CT studies at peak contrast enhancement include congenital large vessel abnormalities (Figs. 3.4 and 3.5), congenital chest masses (pulmonary sequestration, cystic adenomatoid malformation) (Figs. 3.2, 3.3 and 3.6), pulmonary and pleural infections (Figs. 3.7–3.10), chest trauma, the definition of surgical shunts and postoperative vascular anatomy, vascular masses (angiomas), and central pulmonary thromboemboli (Remy-Jardin et al. 1992).

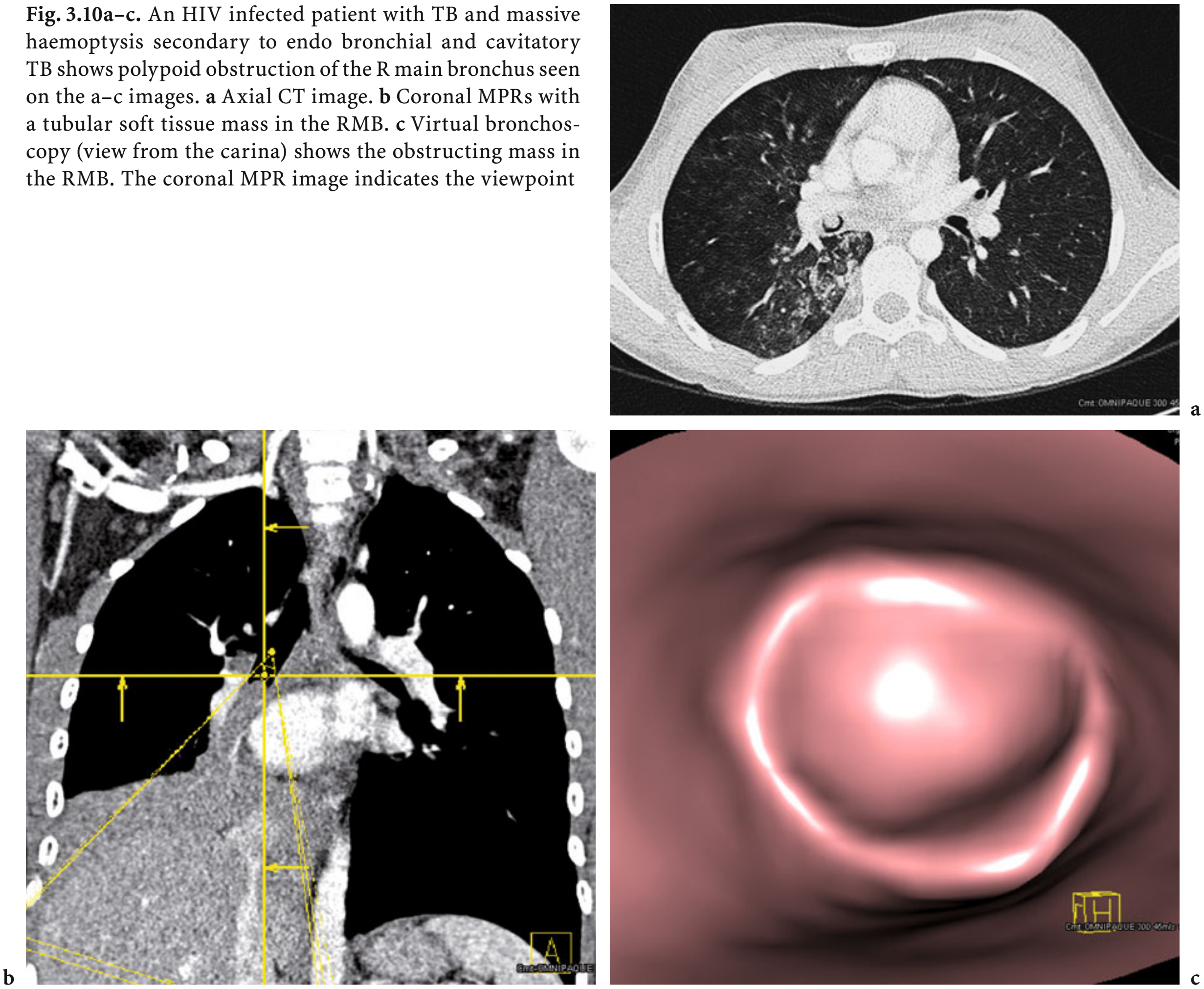

Fig. 3.10a–c. An HIV infected patient with TB and massive haemoptysis secondary to endo bronchial and cavitatory TB shows polypoid obstruction of the R main bronchus seen on the a–c images. **a** Axial CT image. **b** Coronal MPRs with a tubular soft tissue mass in the RMB. **c** Virtual bronchoscopy (view from the carina) shows the obstructing mass in the RMB. The coronal MPR image indicates the viewpoint

3.3.2 Evaluation of Vascular Anatomy: CT Angiography

CT angiography is a relatively new, exciting and possibly one of the most important applications of helical CT (Choo et al. 2006). CT angiography can depict congenital and acquired vascular abnormalities of the chest in children because of its high-quality vascular imaging. Standardized CT angiography and arterial timing test (or bolus-tracking technique) protocols are recommended in such cases (see above). Optimal contrast enhancement is best achieved using a power injector, which should be used whenever possible. With CT angiography one can analyze vascular abnormalities of the pulmonary arteries and veins, aortic arch and great vessels (double_aortic arch, pulmonary sling, etc.) (Katz et al. 1995; Ghersin et al. 2005) (Figs. 3.1, 3.4 and 3.5), as well as congenital lung malformations (pulmonary sequestration, cystic adenomatoid malformation) (Figs. 3.3, 3.6 and 3.11) in which depiction of the systemic (aortic feeding) vessel is important for the definitive diagnosis (Turner et al. 2005).

The improved contrast enhancement and the use of multiplanar and 3D reconstructions afforded by helical CT are useful for characterizing normal and abnormal vascular anatomy. MRI is usually the technique of choice for evaluating congenital large vessel anomalies and other vascular anomalies, but helical CT can be an alternative in patients whose clinical condition requires a quick exam and where a lengthy MRI study would not be advisable. CT is also invaluable as a one-stop shop when combining vascular and airway abnormalities. Children benefit

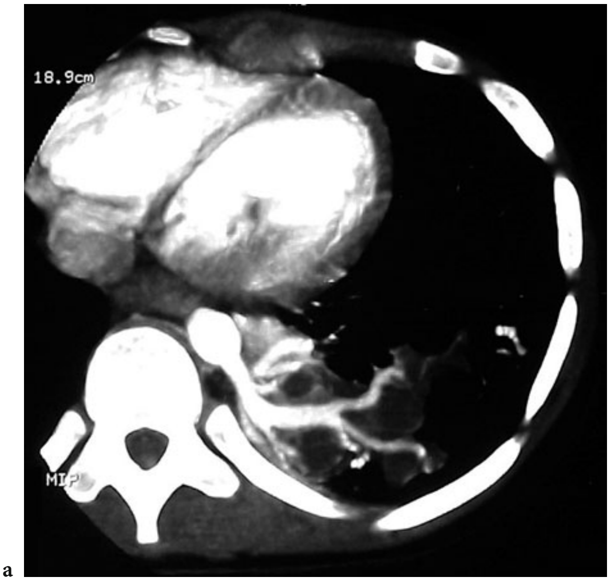

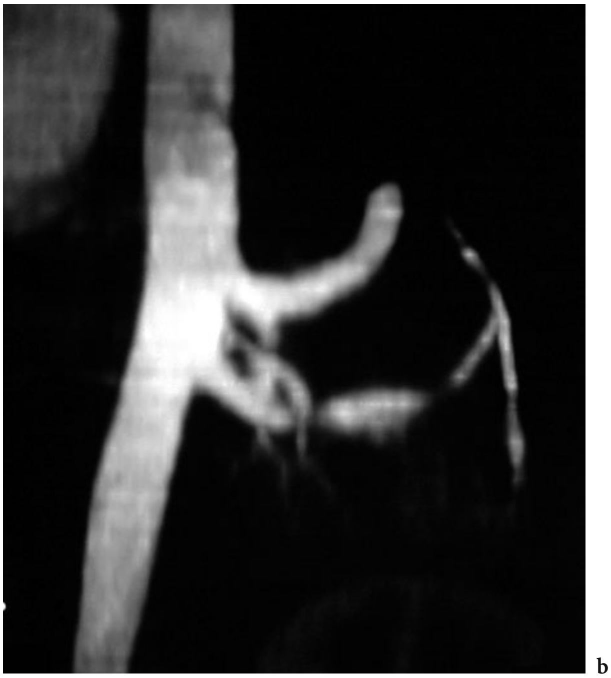

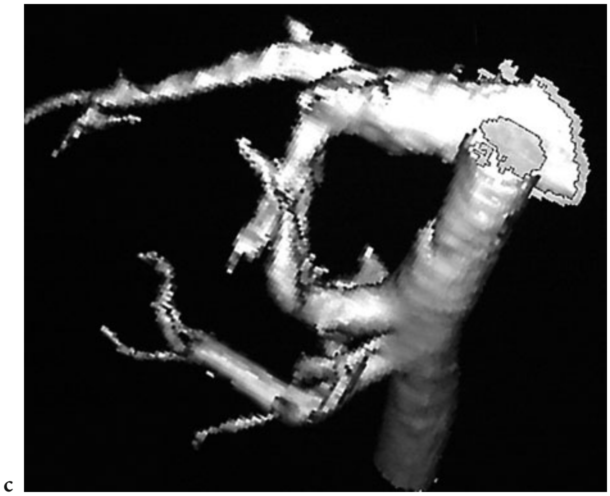

Fig. 3.11a–c. CT angiography of a pulmonary sequestration in a 6-year-old boy who was asymtomatic, but had a persistent dense image in the left pulmonary base. **a** Axial CT image. A large vessel is seen arising from the aorta, with multiple branches supplying a pulmonary mass. **b** Anterioposterior maximum intensity projection image. Three systemic vessels coming from the aorta are seen to feed the pulmonary sequestration. **c** Posteroanterior shaded surface display (SSD) image. The 3D depth perception created by SSD technique improves recognition of spatial relationships of the three vessels arising from the aorta. Two veins are also shown in the upper area of the image. With a cine-loop rotating image, the origin and the course of vessels can be better depicted

from the high-speed scan acquisition and the low sedation rates.

There are several postprocessing techniques available to analyze the vascular anatomy. Curved multiplanar reconstructions are useful for displaying serpentine vascular structures, such as a systemic vessel in pulmonary sequestration, but they are highly operator-dependent and time-consuming. STS-MIP requires less computer time and can be used as an alternative to curved MPR to improve the depiction of vessels (Fig. 3.6b).

MIP, SSD and VR images, the most frequently used to provide information on vascular anatomy, are comparable or indeed superior to conventional angiograms. Since these three-dimensional images can be rotated in a movie-loop, they enable the visualization of lesions from innumerable viewing angles. This can facilitate the analysis of underlying pathologies and improve the display of the vessel origin on superimposed images (Figs. 3.1c, 3.3c,d, 3.4b and 3.6b,c). Relationships with other important structures (the airways) can also be appreciated.

CT angiography can replace conventional angiography in selected applications. Helical CT angiocardiography with 3D reconstructions is superior to echocardiography for the noninvasive assessment of pulmonary artery anatomy and is equal to angiography in patients with complex congenital heart disease (Vestra et al. 1999). As compared to conventional arteriography, CT angiography has the advantages of lower patient morbidity, and reductions in cost and time.

3.3.3
Evaluation of Central Airways

Helical CT of the central airways is performed with thin collimation during one breath-hold or during quiet respiration (Table 3.1a,b). As a result of the thin section volumetric scanning, more detailed anatomy can be obtained without partial volume effects. A comparison of standard CT at 8 mm contiguous increment and helical CT with thin collimation and reconstruction at 50% overlap showed that helical CT was the superior imaging technique (Shafer et al. 1991).

Helical CT demonstrates 95% of the normal segmental bronchial anatomy. The inferior and superior lingular segmental bronchi, which are often difficult to visualize on conventional CT scans, can be demonstrated in 85% of patients on helical scans (Costello et al. 1992b). MPR, MIP, SSD and VR images beautifully depict the central airways and are of great clinical value in their assessment (Kauczor et al. 1996; Ferreti et al. 1996; Nicotra et al. 1997; Venkatraman et al. 2006).

Helical CT of the airways is mainly indicated in the study of congenital and acquired abnormalities of the tracheobronchial tree, postpneumectomy complications, complications after lung transplantation and endobronchial lesions (Figs. 3.8–3.10).

Intensive care and postoperative patients are good candidates for assessment by helical CT. Following pneumonectomy, a dehiscence or a bronchopleural fistula can occur at the anastomotic region. Bronchopleural fistula (Fig. 3.7) is best shown on coronal reformats. Helical CT may demonstrate a bronchopulmonary fistula when conventional axial imaging may be confusing. Two- and three-dimensional images are better than axial images to identify stenotic lesions, especially stenoses in obliquely oriented bronchi. Multiplanar reconstructions along the axis of the bronchus are also useful.

Endobronchial lesions and intrabronchial metallic stent location are best shown on multiplanar reconstructions along the axis of the bronchus. (Figs. 3.8c and 3.10b). Endobronchial lesions (endobronchial tumors, long-standing foreign bodies) can also be shown with virtual endoscopy images (Fig. 3.10c).

Intrabronchial foreign bodies can be difficult to diagnose. There is often no history of foreign body aspiration. These patients are usually sent for thoracic CT examination due to foreign body complications. CT scanning can help in detecting the intrabronchial lesion in these cases.

Helical CT can be very useful in evaluating the tracheobronchial tree when using bronchographic images depicted by the VR technique. Tracheobronchography is quite invasive and can carry a significant risk in paediatric patients. This risk is greatest in conditions that compromise the tracheal lumen. Moreover, airway lesions may not be isolated anomalies. It is important to emphasize the possibility offered by helical CT of simultaneously providing bronchographic images as well as angiographic reconstructions. This combination of data allows the evaluation of complex malformations in a single examination and can avoid unnecessary invasive diagnostic procedures (Figs. 3.1, 3.4 and 3.5).

Virtual bronchoscopy can be useful for presurgical assessment of strictures which preclude direct passage of a conventional bronchoscope, and also for evaluation of endoluminal lesions (Honnef et al. 2006) (Fig. 3.10c).

3.3.4
Evaluation of Difficult Areas: Cervicothoracic Junction, Peridiaphragmatic Area and Chest Wall

Helical CT is useful for imaging lesions in areas that are difficult to evaluate on axial images and are better assessed on 2- or 3D reformatted images. Multiplanar reconstructions, generated from helical CT data, are particularly helpful in lesions located in cervicothoracic and apical areas (Harty and Kramer 1998), peridiaphragmatic and diaphragmatic areas (Israel et al. 1996; Brink et al. 1994a) and the chest wall (Fig. 3.12). The reformatted images better depict the extension of lesions and their relationship to adjacent anatomic structures.

Although uncommon in children, tumours of the chest wall are frequently malignant and may aggressively invade the pleural space, lung, spinal canal or mediastinum. The preoperative imaging evaluation should focus on assessment of the size and extent of the primary tumour and any possible bony invasion or involvement of the chest wall musculature. Both CT and MRI can identify bone and soft-tissue involvement by chest wall tumours (Donnelly et al. 1997). CT is more sensitive in detecting cortical bone disruptions and calcifications, but MRI is better at depicting soft-tissue and marrow involve-

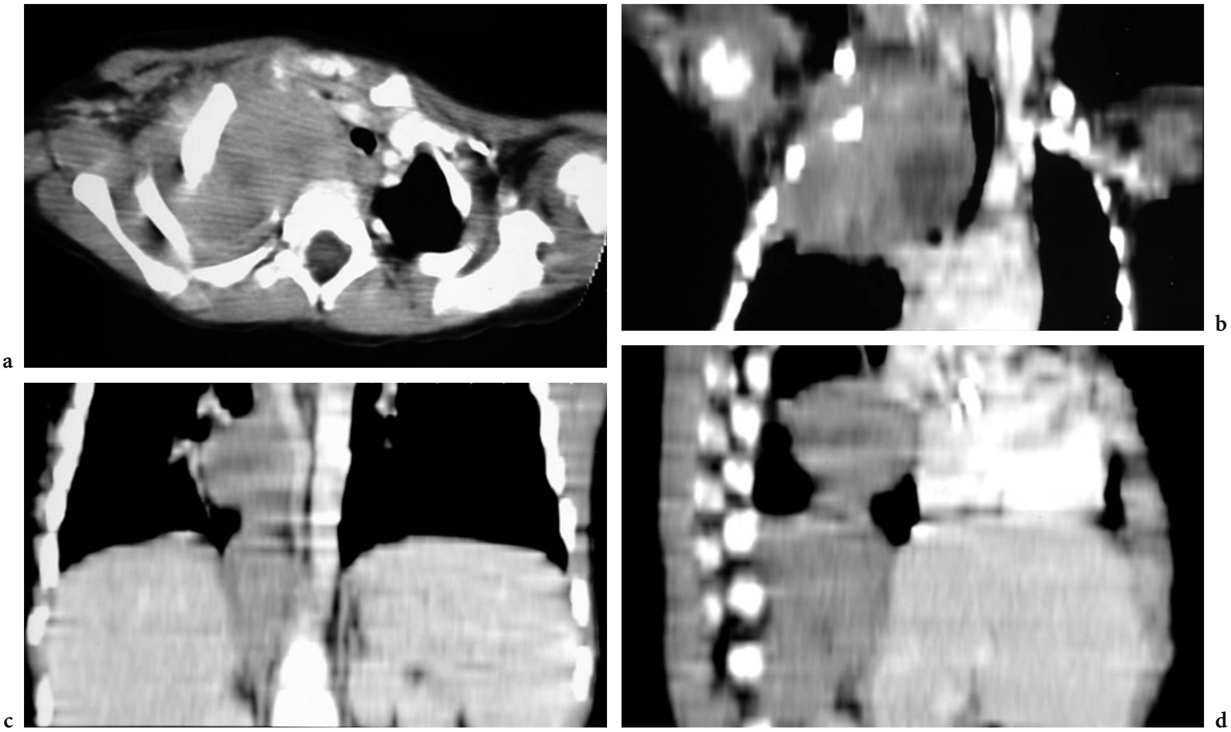

Fig. 3.12a–d. Cervicothoracic tumor (PENET) in a 3-year-old boy with a cervical mass and weight loss. **a** Axial CT image. A heterogeneous mass located in the thoracic apex is seen to displace the trachea. **b** Coronal multiplanar reformation(MPR) image. The extension of the apical mass into the neck and the lateral wall is better shown. **c** Coronal MPR image from the same patient 1 year after the diagnosis demonstrates mediastinal metastasis progressing to the abdomen. MPR images better show the anatomical relationship between the abdominal mass and the diaphragm. The hourglass-shaped mass displaces the diaphragm laterally. **d** Saggital MPR image. The mass extends to the abdomen and displaces the diaphragm anteriorly

ment. Three-dimensional reconstructions also play a role in the depiction of bony structures of the chest wall and the spine. SSD images can be useful in depicting the chest wall deformity in pectus excavatum but VR images are now more often used for this purpose.

3.3.5
Evaluation of Critically Ill Patients

One of the greatest advantages of helical CT is its speed; examinations are shorter and the need for sedation is greatly reduced. This means that some patient groups (e.g. very ill patients and trauma cases), not previously considered to be good candidates, can now benefit from CT studies. In these patients the speed of helical CT allows an enormous amount of information to be obtained in a very short time, and enables both the chest and abdomen to be examined with only one data acquisition and a single dose of intravenous contrast material Helical CT studies in these cases should be done under the supervision of the intensive care physician, who also oversees the transport of the child to the CT facilities. The images can be reconstructed and reformatted retrospectively after the patient has been returned to the intensive care unit (Veys and Owens 2002) (Fig. 3.8).

3.3.6
Evaluation of Inconclusive Images on Chest Radiography

Helical CT and its technical capabilities of multiplanar and 3D imaging are often useful for defining an inconclusive image seen on chest X-rays and for establishing its exact anatomical location (Figs. 3.8–3.10 and 3.13).

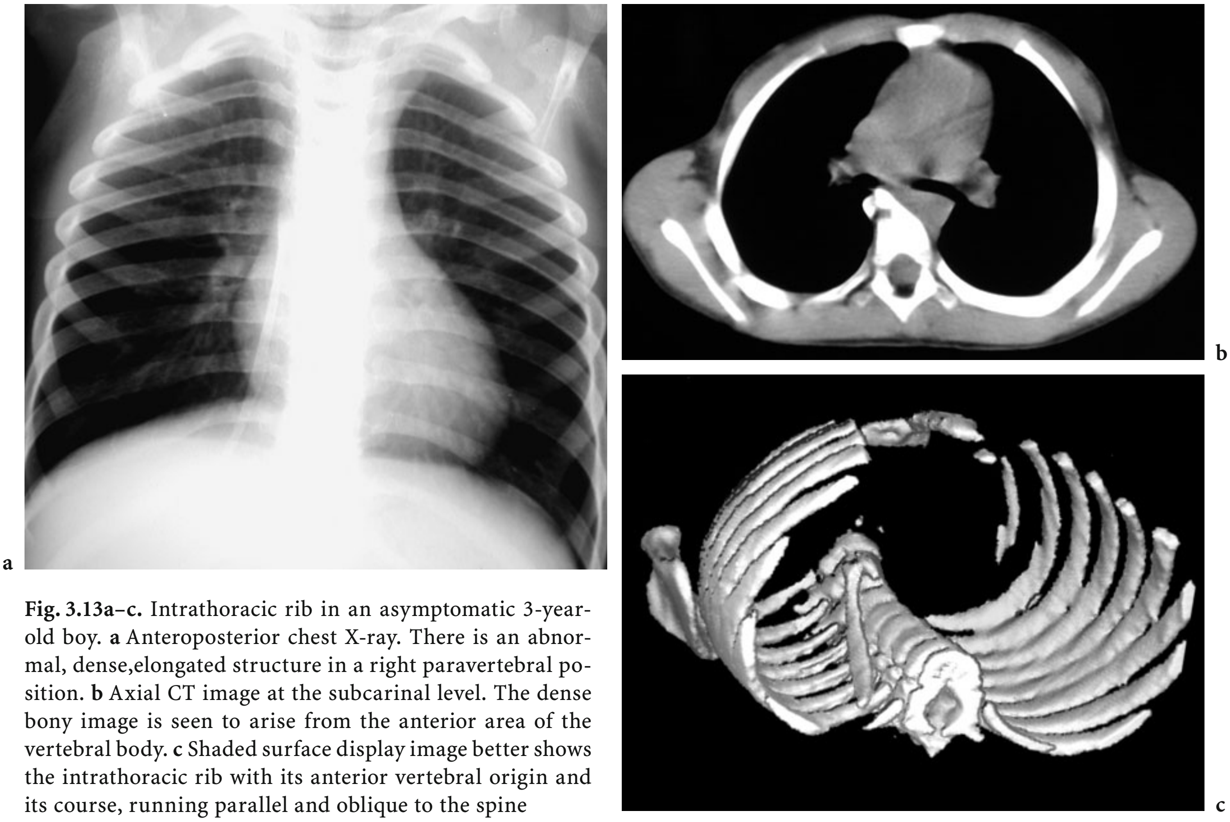

Fig. 3.13a–c. Intrathoracic rib in an asymptomatic 3-year-old boy. **a** Anteroposterior chest X-ray. There is an abnormal, dense,elongated structure in a right paravertebral position. **b** Axial CT image at the subcarinal level. The dense bony image is seen to arise from the anterior area of the vertebral body. **c** Shaded surface display image better shows the intrathoracic rib with its anterior vertebral origin and its course, running parallel and oblique to the spine

3.4
Conclusions

Helical CT technology has many potential clinical benefits when used in paediatric patients. These include speed, improved image quality and reductions in the volume of contrast material required, in the use of sedation, and in radiation exposure (using extended pitch when indicated and remembering the limitations with automated dose). Two- or three-dimensional reformatted images that are of great value in clinical diagnosis can be generated with the available post-processing methods. The technical aspects of this technique, the clinical indications and the suggested protocols to be used have been set out in this chapter.

References

Ambrosino MM, Genieser NB, Roche KJ et al. (1994) Feasibility of high-resolution low-dose chest CT in evaluating the paediatric chest. Pediatr Radiol 24:6–10

Bal CS, Kumar A, Chandra P et al. (2004) Is chest X-ray or high-resolution computed tomography scan of the chest sufficient investigation to detect pulmonary metastasis in pediatric differentiated thyroid cancer? Thyroid 14:217–225

Bonnel AS, Song SM, Kesavarju K et al. (2004) Quantitative air-trapping analysis in children with mild cystic fibrosis lung disease. Pediatr Pulmonol 38:396–405

Brink JA (1995) Technical aspects of helical (spiral) CT. Radiol Clin North Am 33:825–841

Brink JA, Heiken JP, Semenkovich J et al. (1994a) Abnormalities of the diaphragm and adjacent structures: findings on multiplanar spiral CT scan. AJR Am J Roentgenol 163:307–310

Brink JA, Heiken JP, Wang G et al. (1994b) Helical CT: principles and technical considerations. Radiographics 14:887–893

Buckley JA, Scott WWJ, Siegelman SS et al. (1995) Pulmonary nodules: effect of increased data sampling on detection with spiral CT and confidence in diagnosis. Radiology 196:395–400

Callahan CW (1998) Primary tracheomalacia and gastroesophageal reflux in infants with cough. Clin Pediatr (Phila) 37:725–731

Choo KS, Lee HD, Ban JE et al. (2006) Evaluation of obstructive airway lesions in complex congenital heart disease using composite volume-rendered images from multislice CT. Pediatr Radiol 36:219–223

Coakley FV, Cohen MD, Waters DJ et al. (1997a) The detection of pulmonary metastases with pathologic correlation in canine model: effect of breathing on the accuracy of helical CT. AJR Am J Roentgenol 169:1615–1618

Coakley FV, Cohen MD, Waters DJ et al. (1997b) Detection of pulmonary metastases with pathologic correlation: effects of breathing on accuracy of spiral CT. Pediatr Radiol 27:576–579

Cook BA, Bass JW, Nomizu S, Alexander ME (1992) Sedation of children for technical procedures: current standards of practice. Clin Pediatr 31:137–142

Costello P, Anderson W, Blume D (1991) Pulmonary nodule: evaluation with spiral volumetric CT. Radiology 179:875–876

Costello P, Dupuy DE, Ecker CP et al. (1992a) Spiral CT of the thorax with reduced volume of contrast material: a comparative study. Radiology 183:663–666

Costello P, Kruskal J, Dupuy D et al. (1992b) Evaluation of tracheobronchial tree with spiral CT. Radiology 185:355

Donnelly LF, Taylor CNR, Emery KH et al. (1997) Asymptomatic, palpable, anterior chest wall lesions in children: is cross-sectional imaging necessary? Radiology 202:829–831

Egelhoff JC, Ball WS Jr, Kock BL et al. (1997) Safety and efficacy of sedation in children using a structured sedation program. AJR Am J Roentgenol 168:1259–1262

Engeler CE, Tashjian JH, Engeler CM (1994) Volumetric high-resolution CT in the diagnosis of interstitial lung disease and bronchiectasis: diagnostic accuracy and radiation dose. AJR Am J Roentgenol 163:31–35

Ferreti GR, Vining DJ, Knoplioch J et al. (1996) Tracheobronchial tree: three-dimensional spiral CT with bronchoscopic perspective. J Comput Assist Tomogr 20:777–781

Frush DP, Donnelly LP (1998) Helical CT in children: technical considerations and body applications. Radiology 209:37–48

Frush DP, Bisett GS III, Hall SC (1996) Paediatric sedation in radiology: the practice of safe sleep. AJR Am J Roentgenol 167:1381–1387

Frush DP, Siegel MJ, Bisset GS III (1997) Challenges of paediatric spiral CT. Radiographics 17:939–959

Frush DP, Slack CC, Hollingswarth CL et al. (2002) Computed-simulated radiation dose reduction for abdominal multidetector CT of paediatric patients. AJR Am J Roentgenol 179:1107–1113

Garcia-Peña P (2004) High-resolution CT in children, technique and indications. Eur Radiol 14:13–30

Garcia-Peña P, Lucaya J (1999) Chest CT-scan in children: main applications and advantages. Pediatr Pneumonol 18:56–59

Gartenschläger M, Schweden F, Gast K et al. (1998) Pulmonary nodules: detection with low-dose vs conventional-dose spiral CT. Eur Radiol 8:609–614

Ghersin E, Khoury A, Litmanovich D et al. (2005) Comprehensive multidetector computed tomography assessment of severe cardiac contusion in a pediatric patient: correlation with echocardiography. J Comput Assist Tomogr 29:739–741

Greess H, Nómayr A, Wolf H et al. (2002) Dose reduction in CT examination of children by an attenuation-based online modulation of tube current (CARE dose). Eur Radiol 12:1571–1576

Greess H, Lutze J, Nömayr A et al. (2004) Dose reduction in subsecond multislice spiral CT examination in children by online tube current modulation. Eur Radiol 14:995–999

Harty MP, Kramer SS (1998) Recent advances in paediatric pulmonary imaging. Curr Opin Pediatr 10:227–235

Heyer CM, Kagel T, Lemburg SP et al. (2004) Evaluation of tracheobronchial anomalies in children using low-dose multidetector CT: report of a 13-year-old boy with a tracheal bronchus and recurrent pulmonary infections. Pediatr Pulmonol 38:168–173

Honnef D, Wildberger JE, Das M et al. (2006) Value of virtual tracheobronchoscopy and bronchography from 16-slice multidetector-row spiral computed tomography for assessment of suspected tracheobronchial stenosis in children. Eur Radiol 16:1684–1691

Hoppe H, Dinkel HP, Walder B et al. (2004) Grading airway stenosis down to the segmental level using virtual bronchoscopy. Chest 125:704–711

Hopper KD, Singapuri K, Finkel A (2000) Body CT and oncologic imaging. Radiology 215:27–40

Hu H, He HD, Foley WD et al. (2000) Four multidetector-row helical CT: image quality and volume coverage speed. Radiology 215:55–62

Israel RS, Mayberry JC, Primack SL (1996) Diaphragmatic rupture. Use of helical CT scanning with multiplanar reformations. AJR Am J Roentgenol 167:1201–1203

Johnson PT, Fishman EK, Duckwall JR et al. (1998a) Interactive three-dimensional volume rendering of spiral CT data: current applications in the thorax. Radiographics 18:165–187

Johnson JL, Kramer SS, Mahboubi S (1998b) Air trapping in children: evaluation with dynamic lung densitometry with spiral CT. Radiology 206:95–101

Kalra MK, Wittram C, Maher MM (2003) Can noise reduction filters improve low-radiation-dose chest CT images? Pilot study. Radiology 228:257–264

Kalra MK, Maher MM, Toth TL et al. (2004) Comparison of Z-axis automatic tube current modulation technique with fixed tube current CT scanning of abdomen and pelvis. Radiology 232:347–353

Kaste SC, Young CW (1996) Safe use of power injectors with central patient motion and peripheral venous access devices for paediatric CT. Pediatr Radiol 26:449–501

Kaste SC, Young CW, Holmes TP et al. (1997) Effect of helical CT on the frequency of sedation in paediatric patients. AJR Am J Roentgenol 168:1001–1003

Katz M, Konen E, Rozenman J, Szeinberg A et al. (1995) Spiral CT and 3D image reconstruction of vascular rings and associated tracheobronchial anomalies. J Comput Assist Tomogr 19:564–568

Kauczor HU, Wolcke B, Fisher B et al. (1996) Three-dimensional helical CT of the tracheobronchial tree: evaluation of imaging protocols and assessment of suspected stenosis with bronchoscopic correlation. AJR Am J Roentgenol 167:419–424

Khan MF, Herzog C, Ackermann H et al. (2004) Virtual endoscopy of the tracheo-bronchial system: sub-millimeter collimation with the 16-row multidetector scanner. Eur Radiol 14:1400–1405

Lucaya J, Garcia-Peña P, Herrera L et al. (2000a) Expiratory chest CT in children. AJR Am J Roentgenol 174:1–7

Lucaya J, Piqueras J, Garcia-Peña P et al. (2000b) Low-dose high-resolution CT of the chest in children and young adults: dose, cooperation, artifacts incidence, and image quality. AJR Am J Roentgenol 175:985–992

Napel SA (1995) Basic principles of spiral CT. In: Fishman EK, Jeffrey RB Jr (eds) Spiral CT: principles, techniques, and clinical application. Raven, New York, pp 1–9

Napel SA, Jeffrey RB Jr (1993) STS-MIP: a new reconstruction technique for CT of the chest. J Comput Assist Tomogr 17:832–838

Nicotra JJ, Mahboubi S, Kramer SS (1997) Three-dimensional imaging of the paediatric airway. Int J Pediatr Otorhinolaryngol 41:299–305

Oddone M, Granata C, Vercellino N et al. (2005) Multi-modality evaluation of the abnormalities of the aortic arches in children: techniques and imaging spectrum with emphasis on MRI. Pediatr Radio 35:947–960

Owens C (2004) Radiology of diffuse interstitial pulmonary disease in children. Eur Radiol 14:L2–12

Pappas JN, Donnelly LF, Frush DP (2000) Reduced frequency of sedation of young children with multisection helical CT. Radiology 215:897–899

Paterson A, Frush DP, Donnelly LF (2001) Helical CT of the body: are settings adjusted for paediatric patients? AJR Am J Roentgenol 176:1–6

Pifferi M, Caramella D, Bulleri A et al. (2004) Pediatric bronchiectasis: correlation of HRCT, ventilation and perfusion scintigraphy, and pulmonary function testing. Pediatr Pulmonol 38:298–303

Remy-Jardin M, Remy J, Wattinne L et al. (1992) Central pulmonary thromboembolism: diagnosis with spiral volumetric CT with the single-breath-hold tecnique comparison with pulmonary angiography. Radiology 185:381–387

Remy-Jardin M, Remi J, Giraud F et al. (1993) Pulmonary nodules detection with thick-section spiral CT versus conventional CT. Radiology 187:513–520

Remy-Jardin M, Remy J, Artaud D et al. (1998) Volume rendering of the tracheobronchial tree: clinical evaluation of bronchographic images. Radiology 208:761–770

Rogalla P, Stöver B, Scheer I et al. (1999) Low-dose spiral CT: applicability to paediatric chest imaging. Pediatr Radiol 28:565–569

Rubin GD, Leung AN, Robertson VJ et al. (1998) Thoracic spiral CT: influence of subsecond gantry rotation on image quality. Radiology 208:771–776

Salvolini L, Bichi S E, Costarelli L et al. (2000) Clinical applications of 2D and 3D CT imaging of the airways – a review. Eur J Radiol 34:9–25

Schafer CM, Prokop M, Dohring W et al. (1991) Spiral CT of the tracheobronchial system: optimized technique and clinical applications. Radiology 181:274

Shrimpton PC, Edyream S (1998) CT scanner dosimetry. Br J Radiol 71:1–3

Siegel MJ (2003) Multiplanar and three-dimensional multidetector row CT of thoracic vessels and airways in the paediatric population. Radiology 229:641–650

Siegel MJ, Luker GD (1995) Paediatric applications of helical (spiral) CT. Radiol Clin North Am 33:997–1022

Silverman PM, Cooper CI, Welman DI et al. (1995) Helical CT: practical considerations and potential pitfalls. Radiographics 15:25–36

Stokberger SM Jr, Hicklin JA, Liang Y et al. (1998) Spiral CT with ionic and non-ionic contrast material: evaluation of patient motion and scan quality. Radiology 208:631–636

Takahashi M, Maguire WM, Ashtari M et al. (1998) Low-dose spiral computer tomography of the thorax. Invest Radiol 33:68–73

Turner A, Gavel G, Coutts J (2005) Vascular rings – presentation, investigation and outcome. Eur J Pediatr 164:266–270

Valencia R, Denecke T, Lehmkuhl L et al. (2006) Value of axial and coronal maximum intensity projection (MIP) images in the detection of pulmonary nodules by multislice spiral CT: comparison with axial 1-mm and 5-mm slices. Eur Radiol 16:325–332

Venkatraman R, Raman R, Raman B et al. (2006) Fully automated system for three-dimensional bronchial morphology analysis using volumetric multidetector computed tomography of the chest. J Digit Imaging 19:132–139

Vestra SJ, Hill JA, Alejos JC et al. (1999) Three-dimensional helical CT of pulmonary arteries in infants and children with congenital heart disease. AJR Am J Roentgenol 173:109–115

Veys P, Owens C (2002) Respiratory infections following haemopoietic stem cell transplantation in children. Br Med Bull 61:151–74

Wang G, Vannier MW (1994) Stair-step artifacts in three-dimensional helical CT: an experimental study. Radiology 191:79–83

White KS (1995) Reduced need for sedation in patients undergoing helical CT of the chest and abdomen. Pediatr Radiol 25:344–346

High-Resolution CT of the Lung in Children

4

JAVIER LUCAYA and HUBERT DUCOU LE POINTE

CONTENTS

Part I Technique, Indications, Anatomy and Features of Lung Disease 78
JAVIER LUCAYA

4.1 Introduction 78

4.2 Technique 78

4.3 Sedation 80

4.4 Special Techniques 82
4.4.1 "Focused" Chest CT 82
4.4.2 "Limited Slice" Chest CT 82
4.4.3 Expiratory Slices. Lateral Decubitus and Prone Views 83

4.5 Normal Lung Anatomy 85

4.6 HRCT Features of Lung Disease 88
4.6.1 Ground-Glass Opacity 88
4.6.2 Consolidation 90
4.6.3 Pulmonary Nodule 90
4.6.4 Bronchiolar Disease and Tree-in-Bud 91
4.6.5 Air-Trapping 92
4.6.6 Septal Thickening 93
4.6.7 Parenchymal Bands 94
4.6.8 Honeycombing 95
4.6.9 Mosaic Perfusion 95
4.6.10 Architectural Distortion 96
4.6.11 Air-Filled Cystic Lung Lesions: Bullae, Pneumoceles and Cysts 97
4.6.12 Reversed Ventilatory Pattern 98
4.6.13 Emphysema 98
4.6.14 Halo Sign 98
4.6.15 Signet-Ring Sign 99
4.6.16 Crazy Paving Pattern 99

Part II Clinical Applications 100
HUBERT DUCOU LE POINTE

4.7 Airway 100
4.7.1 Bronchiectasis 100
4.7.1.1 Cystic Fibrosis 102
4.7.1.2 Immotile Cilia 102
4.7.2 Asthma. Allergic Bronchopulmonary Aspergillosis 103
4.7.3 Constrictive Bronchiolitis 103
4.7.4 Bronchiolitis Obliterans Organizing Pneumonia 104

4.8 HRCT Findings in Specific Diseases 105
4.8.1 Chronic Diffuse Infiltrative Lung Disease 105
4.8.1.1 Langerhans' Cell Histiocytosis 105
4.8.1.2 Extrinsic Allergic Alveolitis 106
4.8.1.3 Sarcoidosis 107
4.8.1.4 Pulmonary Alveolar Proteinosis 108
4.8.1.5 Pulmonary Fibrosis and Chronic Interstitial Pneumonias 108
4.8.1.6 Lymphocytic Interstitial Pneumonia (LIP) 109
4.8.1.7 Pulmonary Lymphangitic Carcinomatosis 110
4.8.1.8 Collagen-Vascular Disease and Pulmonary Vasculitis 110
4.8.1.9 Pulmonary Lymphangiectasia 111
4.8.1.10 Lymphangiomatosis and Gorham's Disease 112
4.8.1.11 Pulmonary Hemorrhage 112
4.8.1.12 Pulmonary Alveolar Microlithiasis 112
4.8.1.13 Pulmonary Gaucher's Disease 113
4.8.1.14 Bronchopulmonary Dysplasia 114
4.8.2 Air-Space Diseases 114
4.8.2.1 Invasive Pulmonary Aspergillosis 114
4.8.2.2 Pneumocystic Carinii Pneumonia (PCP) 114

4.9 Conclusion 115

References Part I 115

References Part II 117

J. LUCAYA, MD
Emeritus, Department of Pediatric Radiology and Institute of Diagnostic Imaging, Vall d'Hebron Hospitals, Ps. Vall d'Hebron 119–129, 08035 Barcelona, Spain
Director, Department of Radiology. Hospital Quirón. Plaça Alfonso Comín 5–7, 08023. Barcelona. Spain
H. DUCOU LE POINTE, MD
Service de Radiologie Pédiatrique, Hôpital d'Enfants Armand-Trousseau, 26 avenue du Docteur-Arnold-Netter, 75012 Paris, France

Part I
Technique, Indications, Anatomy and Features of Lung Disease

Javier Lucaya

4.1
Introduction

High-resolution computed tomography (HRCT) of the chest is a technique able to image the lung with excellent spatial resolution, offering precise anatomic detail (Garcia Peña and Lucaya 2004). HRCT can demonstrate the morphologic characteristics of both the normal and abnormal lung parenchyma and its interstitium (Webb et al. 1996). In this regard, it provides more information than chest radiographs and conventional chest CT. In addition, an HRCT study delivers significantly less radiation to the patient than conventional or helical CT. In our experience the average dose for HRCT of the chest is between 10% and 20%, depending on patient age, of the dose used for a helical exam. This explains the increasing demand for this technique in the evaluation of most pediatric lung disorders.

With the introduction of the multiple detector CT scanners, it has become possible to obtain high-resolution CT scans of the lung with helical technique; however, we do not use it routinely since it delivers significantly more radiation to the patient than classical HRCT with 1-mm slices at either 10-mm or 20-mm intervals.

4.2
Technique

To optimize spatial resolution it is necessary to use thin sections. In keeping with most authors, we use 1.0-mm collimation, but good images can be obtained with 3-mm collimation. It has been shown that there is no diagnostic difference with use of 1.5- or 3-mm-thick sections (Murata et al. 1988). However, since radiation dose with 1.0-mm sections at 10-mm intervals is lower than with 3-mm scans at the same intervals (Rothenberg and Pentlow 1992), we recommend using the thinner sections. As a general rule we use 10-mm intervals and in premature infants we sometimes use 5-mm intervals.

Use of a high-spatial frequency algorithm (bone algorithm) is critical when performing HRCT of the lungs. The bone algorithm reduces image smoothing and increases spatial resolution, making the structures appear sharper (Mayo et al. 1987). In contrast to what occurs with the lungs, the quality of mediastinal images is poor with all HRCT techniques. This is because low-contrast structures, such as the mediastinum, are affected more by noise than high-contrast structures, such as the lung. The quality of mediastinal imaging improves somewhat with use of the low-spatial frequency (standard) algorithm; thus, we always use this filter to reconstruct mediastinal images.

Scanning should be performed with the smallest field of view (FOV) able to encompass the patient. Decreasing the FOV effectively reduces pixel size and improves spatial resolution (Mayo et al. 1987; Murata et al. 1989). The combination of a 512 × 512 matrix and a 40-cm FOV results in a pixel size of 0.78 mm. With targeted image reconstruction using a FOV of 25 cm, pixel size decreases to 0.49 mm and spatial resolution correspondingly increases. With an 18-cm FOV, pixel size is further reduced to 0.35 mm. We recommend the use of a 15–18-cm FOV for neonates and small infants, 25-cm for larger infants and 35–45-cm for older children and adolescents. Generally, the smallest structures visible on HRCT range from 0.3–0.5 mm in thickness. Thinner structures, measuring 0.1–0.2 mm are occasionally seen (Webb et al. 1996).

In addition to increasing image sharpness, HRCT techniques increase image noise. Much of this noise is quantum-related and can be reduced by increasing the kilovolt peak or milliamperes used However, when scanning children we should try to use the minimal radiation dose able to produce a diagnostic-quality exam. Owing to the reduced X-ray beam attenuation secondary to lower body mass, lower-weight patients can greatly benefit from radiation dose reductions (Sigal-Cinqualbre et al. 2004). A 4-cm reduction in body diameter causes the X-ray attenuation to decrease by 50% (Suess and Cheng 2002). In our experience using 90 kV and 40 mAs, the effective dose for 15 1-mm-thick slices varies from 0.10 mSv to 0.38 mSv depending on the weight of the patient. Using 120 kV and 25 mAs, the dose increases around 35%, yet the diagnostic quality of the exam does not change significantly, particularly in patients weighing under 30 kg. At present, we recommend using 90 kV and 25 mAs for neonates. Beyond the neonatal period, we recommend 90 kV and 40 mAs for patients weighing 30 kg or less. For heavier patients, we will use 120 kV and 25 mAs (Table 4.1).

Combining HRCT scans at 20-mm intervals with low-dose scans (90 kV and 40 mAs) would result in an average skin dose comparable to that associated with chest radiography (Mayo et al. 1993). Moreover, with properly performed HRCT, one can manage to study the lung with even less radiation to the female breast than with conventional radiography.

When examining children, the potential side effects of radiation exposure should always be kept in mind. With use of data obtained in A-bomb survivors it has been predicted that delivery of 1 Rad (0.01 Gy) of radiation to a woman's breast before the age of 35 fractionally increases her risk of breast cancer by 13.6% over the expected spontaneous rate for the general population (Land et al. 1993). This is one of the main reasons why we strongly support the use of low-dose techniques for children. When examining children with HRCT, we try to either skip the area around the nipple or protect the breasts with thin layers of radiation-absorbent material such as bismuth-coated latex shields (Fig. 4.1). These measures provide girls with some breast radiation protection without affecting the diagnostic quality of the images (Hopper et al. 1998). A study using an in-plane bismuth breast shield (1.7 g of bismuth per square centimeter) for multidetector CT of the chest and abdomen in 50 female pediatric patients revealed a 29% reduction in radiation dose to the breasts (Fricke et al. 2003).

In children under 8 years of age the mean attenuation value of normal lung ranges from –500 HU to –700 HU and in those 8 years or older it is about -800 HU, which is similar to the attenuation value in healthy adults (–700 HU to –800 HU). It should be emphasized that there are no "correct" or ideal window settings for demonstrating lung anatomy, to be used when photographing an HRCT study. Often the precise window width and levels chosen are a matter of personal preference. However, it is important that at least one lung window setting be used consistently in all patients. If this is not done, it is difficult to develop an understanding of what appearances are normal and abnormal, to compare cases and to compare sequential examinations in the same patient. Level and width settings of approximately –700/1000 HU are appropriate for routine lung windows. Window level/width settings of 50/350 are best for evaluating the mediastinum and hila (Webb et al. 1996). The recommended scanning parameters for HRCT of the chest in children are shown in Table 4.1.

Since the diagnostic sensitivity and specificity of HRCT of the lung are superior to those of conventional chest X-rays, the indications for HRCT in children will undoubtedly increase. We are convinced that in the future the study of several lung diseases in children will be routinely performed with HRCT. Therefore, we should ensure that the examination is the least aggressive possible. For this purpose, scans should be tailored to the specific clinical problem, the number of sections and exposure parameters should be decreased as much as possible, low-dose

Table 4.1. Recommended scanning parameters for HRCT of the chest in children

Slice thickness	1 mm
Interval	10 mm (in premature infants we may use use 5 mm)
KVp	90–120
mA	20–40
Seconds	0.6–1.0 s
FOV	15–40
Filter	High-spatial-frequency algorithm (bone). Use standard for mediastinum

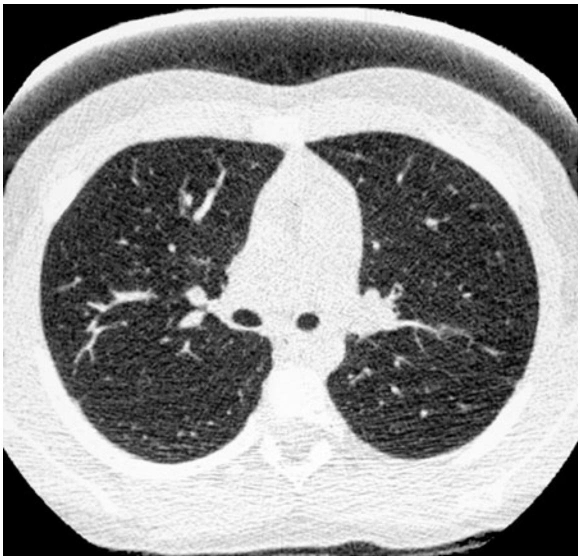

Fig. 4.1. A 10-year-old girl. HRCT of the lungs performed using a 1 mm-thick bismuth-coated latex shield over both nipples. Notice there are no significant artefacts

Table 4.2. HRCT: Indications

Screening of patients with repeated respiratory infections
Bronchiectasis
Cystic fibrosis
Bronchopulmonary dysplasia
Severe asthma
Bronchiolitis obliterans
Diffuse pulmonary disease
Control of some malformations

techniques should be used routinely and scout views spared. Table 4.2 shows the main indications of HRCT in children.

To tailor the examination to diagnostic needs, the radiologist should know the patient's clinical features and previous imaging findings. Furthermore, to obtain the greatest diagnostic information that HRCT can provide, the radiologist should directly supervise the study and decide whether additional or special slices (prone, lateral decubitus, expiratory, etc.) are required. This approach avoids unnecessary examinations and virtually eliminates incomplete studies.

Needless to say, the routine use of low-dose techniques is mandatory to minimize the potential side effects of ionizing radiation exposure. This is extremely important for extending the indications of HRCT in children so they can benefit from the excellent diagnostic information it provides.

4.3
Sedation

Another important measure aimed at reducing the aggressiveness of HRCT is to avoid anesthesia and use sedation as little as possible. In our practice we have never used general anesthesia for HRCT in children and we have reduced the use of sedation in children under 6 years old to a mere 1.5%. Since we could not know in advance which patients would require sedation and aspiration is a major clinical concern in sedated children, we used to keep all our patients NPO (nothing by mouth) for 4 h before the exam in children under 1 year old and for 6 h in those 1 year or older. Considering the extremely low incidence of sedation currently required for HRCT, we have recently changed this policy. Nowadays. none of our patients are kept NPO and those who, once in the gantry, behave poorly and require sedation, are rescheduled. Since well-fed infants behave better than hungry ones, this policy will undoubtedly further reduce the 1.5% of patients needing sedation.

We resort to all sorts of tricks to keep the non-sedated patients still. We make sure they are warm and allow the parents to hold their hands and talk to them. To attract a fidgety child's attention, we project and move a spot of light, such as that produced by a flashlight, on the gantry. They usually become captivated at once, stop moving and crying and try to follow the light with their eyes. At that moment we take a section. If they start crying again we repeat the "diversion maneuvers" until the examination is complete. We can also project known TV cartoons onto the gantry (Fig. 4.2) or play music through the gantry speakers. It is also helpful to offer them a bottle with glucose water.

When all our maneuvers fail, we reschedule the study, keep the patient NPO for 4–6 h and administer sedation before the exam. We use chloral hydrate p.o. at a dose of 50–75 mg/kg, with a maximum dosage of 2000 mg. Children are given an initial dose of 50 mg/kg and are kept in the sedation area. If after 20–30 min the patient has not fallen asleep, a second dose of chloral hydrate, usually half the initial dose (25 mg/kg) is given. Exceptionally, we may go up to a total dose of 100 mg/kg. The onset of action is usually within 25–30 min and the duration of sedation is 30–40 min. Chloral hydrate has a bitter taste that children dislike. Attempts to conceal it with sweeteners like cherry syrup are not very helpful. Although the taste improves somewhat, it still remains unpleasant. Furthermore, the total volume of fluid to

Tinky Winky
Dipsy
Laa-laa
Po

Fig. 4.2. Teletubbies projected onto the gantry

be administered increases and dose control becomes difficult. Consequently, we always use undiluted chloral hydrate administered directly by syringe or with a nipple connected to a syringe. With time and patience most children swallow it well. Although we use chloral hydrate mainly in children under 2 years of age, it can also be used in older patients.

Chloral hydrate is a successful sedative in 95–99% of children (Karian et al. 1999; Pereira et al. 1993) and has a very low rate of side effects. Transient respiratory depression (oxygen desaturation 10% below baseline for a patient for more than 15 s, despite repositioning of the head and neck to clear the airway) is the most common during or after sedation, yet it occurs in less than 1% of patients. Delayed complications such as vomiting, irritability and mild respiratory difficulty are also rare (Egelhoff et al. 1997). Some authors prefer to use oral Nembutal rather than chloral hydrate to sedate their patients (Chung et al. 2000; Rooks et al. 2003). Their results are quite similar to those we have had with chloral hydrate and therefore we have not changed our sedation policy. Use of multidrug sedation regimens should be avoided (Sanborn et al. 2005).

All sedated patients are given oxygen by mask or nasal prong to increase pulmonary oxygen reserves and permit prolonged apnea or airway obstruction without hypoxia. Oxygen should be administered to all patients receiving sedative medications with the possible exception of neonates at risk for retinopathy of prematurity, in which case a neonatologist should be consulted. There are no rules about the amount of supplemental oxygen that a patient requires; rather, administration of any amount improves the margin of safety. Thus, there is no legitimate reason to not administer oxygen routinely when patients are sedated (Fisher 1990). Continuous monitoring of the vital signs (at least every 5 min) must be performed and recorded during each use of sedation.

The physiologic measurements we monitor include oxygenation (with pulse oximetry), heart rate, respiratory rate and temperature. The alarm on the pulse oximeter is usually set at 90% oxygen saturation, but any decrease below 95% is immediately investigated. The majority of apparent desaturations are due to patient motion and loss of sensor contact. A small number of patients, however, demonstrate significant decreases in pO_2. Most of these are transient and are quickly corrected by repositioning the head and extending the neck. Occasionally, a patient requires suctioning of the oral cavity. A suction device and size-appropriate recovery equipment must be on hand during each sedation procedure. Children who have medical conditions that compromise the airway require special attention with respect to cardiopulmonary monitoring and airway management. These children may not be appropriate candidates for sedation by personnel who do not routinely deal with pediatric airway management and cardiopulmonary resuscitation. Children who fall into this monitoring category include those with anatomic airway anomalies (craniofacial defects), those with airway diseases such as obstructive adenotonsillar hyperplasia, acute respiratory infection, and uncontrolled asthma, and those with significant cardiopulmonary, neurologic and hepatorenal disorders. Life-threatening airway obstruction or respiratory depression with hypoxia can occur in these children (Vade et al. 1995).

Once the examination is over, all sedated patients are discharged home or transported to the inpatient wards when they meet the postanesthesia care unit discharge criteria recommended by the American Academy of Pediatrics (American Academy of Pediatrics Committee on Drugs 1992):

1. Cardiovascular function and airway patency are satisfactory and stable.
2. The patient is easily arousable, and protective reflexes are intact.
3. The patient can talk (if age-appropriate).
4. The patient can sit unaided (if age-appropriate).
5. The state of hydration is adequate.
6. For a very young or handicapped child, incapable of the expected responses, the presedation level of responsiveness or a level as close as possible to the normal level for that child should be achieved.

Parents are instructed not to feed the children until their level of consciousness and motor function have returned to presedation ranges. When examining critically ill patients, we require the assistance of a pediatrician from the intensive care unit. After the examination is completed, these patients are returned to their wards immediately under the supervision of the specialist. Other sedation regimes (see chapter on Helical CT) are practically never required for HRCT. There have been several reports in the literature on the use of oral pentobarbital sodium, claiming that its acceptance is better than that of chloral hydrate (Chung et al. 2000). However, we have not use it.

Certain patients are difficult to sedate, such as children with mental retardation, patients receiving chemotherapy or antiseizure medication and those habituated to sedation (Hubbard et al. 1992).

4.4
Special Techniques

4.4.1
"Focused" Chest CT

In patients with known "localized" lung disorders we recommend a "focused" technique, performing 1-mm slices at 10-mm intervals through the abnormal area of the lung. The rest of the lung is not scanned. We believe that study of the entire lung should not be performed in patients being controlled for known localized disease whose clinical symptoms and/or chest radiographs do not suggest progression to other lobes. The "focused" scan is used in the follow-up of bronchiectasis, right middle lobe syndrome, cystic emphysema (Fig. 4.3), cavitated pneumonia and some pulmonary malformations not considered tributary of surgical treatment. In many of these cases, three or four low-dose HRCT slices will provide more information with less radiation dose to the female breast than PA and lateral chest radiographs. As always with HRCT, we try to skip the scout view to save on radiation exposure, though occasionally, and particularly when we want to reduce the exam to a mere two or three slices, we may use it. We center the exam with the light collimator. When we want to explore the right middle lobe, lingula and both lower lobes, we start the study midway between the sternal manubrium and the xifoid. When examining the upper lobes, we start the study at the level of the clavicles and stop at the inferior border of the abnormal lobe.

4.4.2
"Limited Slice" Chest CT

The "limited slice" technique, consisting of 1-mm slices at 20-mm intervals, is a type of "sampling" technique that can be used for studying generalized lung disorders. Radiation dose is halved with this technique, making it particularly useful for follow-up of patients with chronic lung disorders who require repeated examinations. The main indication for limited slice is in the control of patients with cystic fibrosis, bronchopulmonary dysplasia (Fig. 4.4), histiocytosis X, alveolar proteinosis, and interstitial pneumonias.

In our experience use of both the "focused" and the "limited-slice" techniques has increased steadily over the last few years, particularly when examining female patients with chronic lung disorders. In addition to providing reliable diagnostic information, these techniques permit a reduction in radiation exposure to the breasts. If radiographs are still required in this group of patients, we obtain the AP or PA views only. The lateral projection is not routinely performed.

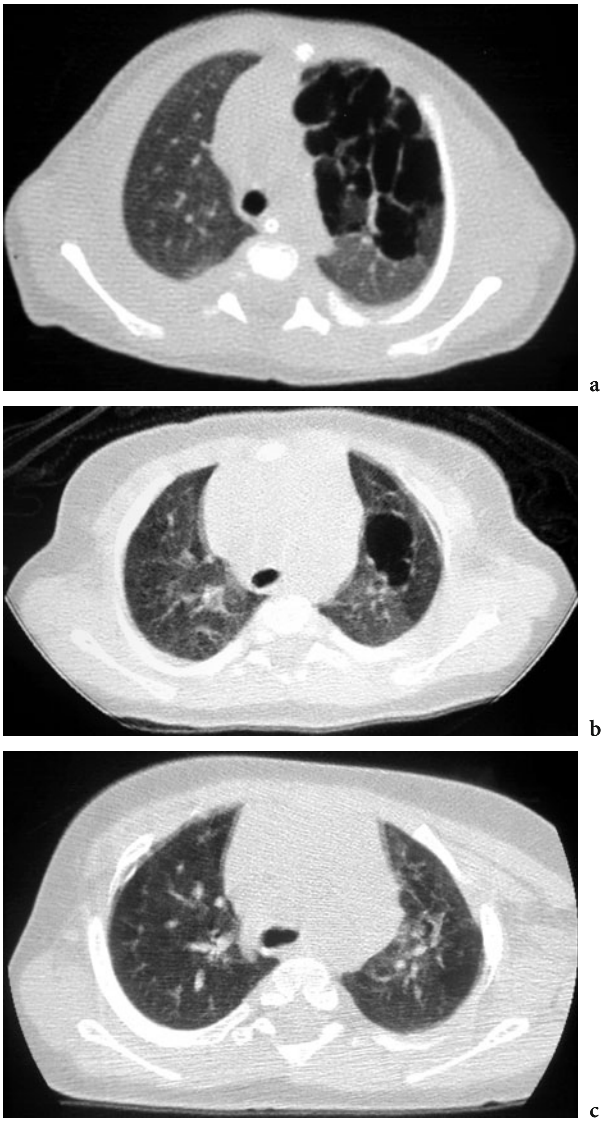

Fig. 4.3a–c. A 2-week-old premature baby with RDS treated with mechanical ventilation. Developed localized pulmonary emphysema in left upper lobe (**a**) Three months later (**b**) the lesions have decreased in size. At the age of 10 months (**c**) the CT is normal

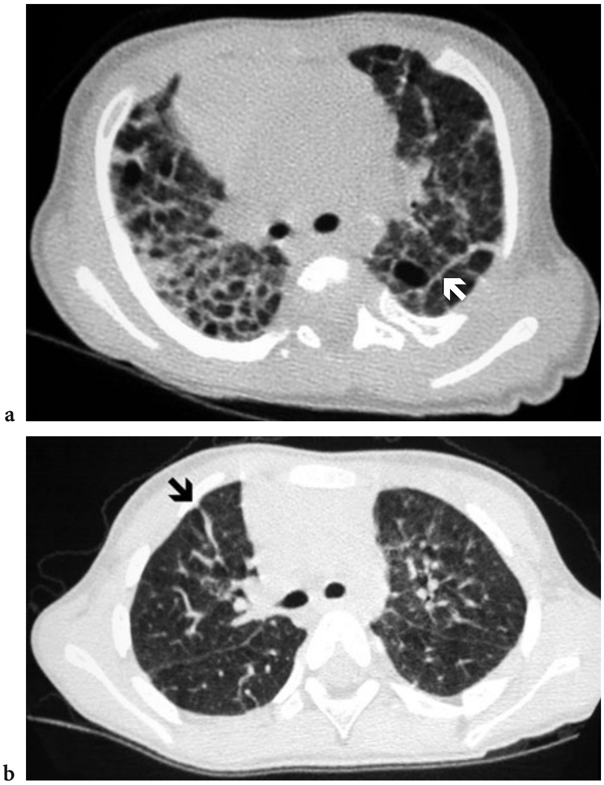

Fig. 4.4a,b. Bronchopulmonary dysplasia at the age of 2 months (**a**) shows marked septal thickening, parenchymal bands (*arrow*) and multiple hyperlucent areas. Repeated HRCT at the age of 2 years (**b**) shows a mosaic pattern and some residual parenchymal bands (*arrow*)

4.4.3
Expiratory Slices. Lateral Decubitus and Prone Views

Expiratory slices are extremely helpful when examining patients suspected of having airway abnormalities or patients with a history of repeated pulmonary infections who are found to have a normal or questionably normal inspiratory CT exam (Lucaya et al. 1999) (Fig. 4.5). They are also useful when the inspiratory sections demonstrate a mosaic pattern, characterized by visible differences in lung attenuation. Since children do not usually suffer pulmonary thromboembolic disorders, a mosaic pattern is almost always due to small airway disease with obstruction.

When the examined child presents clinical or radiological features commonly associated with small airway disease, we routinely complete the HRCT examination with three additional expiratory slices at three equally-spaced levels, one in the upper, one in the middle and one in the lower lobes. We use the table level information provided by the inspiratory exam to center these slices. Whereas the "level" of the upper lobes does not change significantly on expiration, the middle lobe, lingula and particularly the lower lobes will "move upwards" significantly, from 2 to 5 cm, depending on the size of the patient. To obtain good expiratory scans it is mandatory to spend some time teaching the child how to exhale well.

A useful method for obtaining expiratory scans in uncooperative children is to use the lateral decubitus technique (Capitanio and Kirkpatrick 1972; Lucaya et al. 1999; Choi et al. 2002). The patients are scanned in both lateral decubitus positions. With the child on his side, the dependent hemithorax is splinted and movement of the thoracic cage is restricted on that side. When movement of the hemithorax is limited, the lung on the dependent side tends to be underaerated. Con-

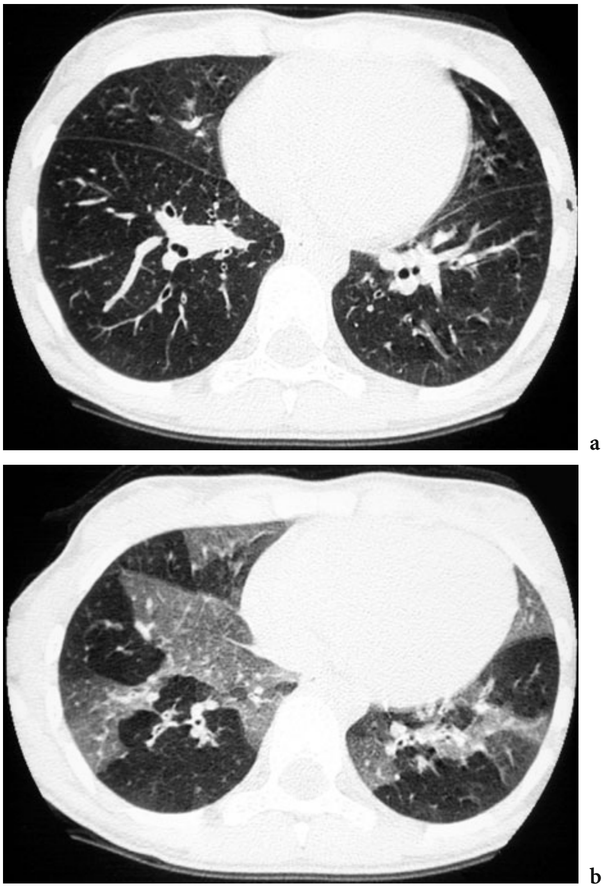

Fig. 4.5a,b. A 9-year-old boy with severe asthma. Inspiratory scan (**a**) shows questionable mosaic pattern, which is evident on the expiratory scan (**b**)

versely, the hemithorax facing upwards is not restricted and the lung is well aerated. If air trapping is present, either diffusely or patchy, the affected lung, lobe or segment will remain hyperlucent when that side of the thorax is in the dependent position (Fig. 4.6). Occasionally, in non-co-operative patients with normal chest X-rays and known diseases such as cystic fibrosis or severe asthma, in whom the initial HRCT abnormality is usually the presence of a mosaic perfusion pattern secondary to air-trapping, we will limit their initial HRCT exam to three scans in each lateral decubitus position (Fig.4.7).

This simple technique can also be used when trying to obtain good inspiratory examinations in non-co-operative patients. As mentioned, the lung facing upwards is usually well aerated. Awareness of this fact is particularly helpful when examining non-co-operative patients whose supine scans show a ground glass pattern consistent either with lung disease or with normal lung on expiration. When the lungs are normal, the ground glass pattern will no longer persist in the lung facing upwards (Fig. 4.8). This same principle of gravity-dependent aeration is the rationale for using prone views to obtain good inspiratory scans of the lower lobes (Fig. 4.18c,d).

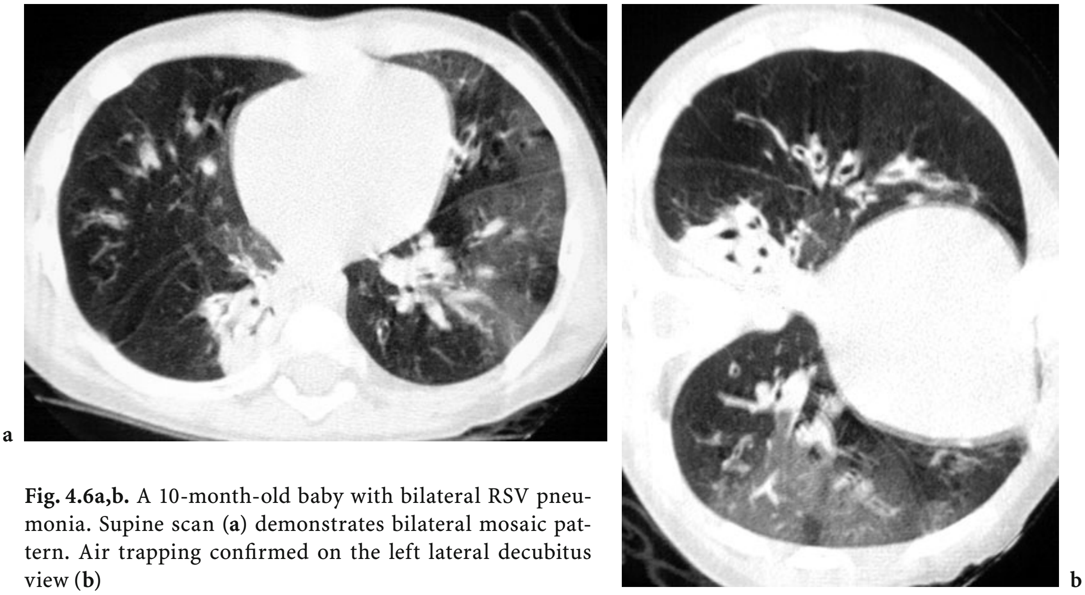

Fig. 4.6a,b. A 10-month-old baby with bilateral RSV pneumonia. Supine scan (**a**) demonstrates bilateral mosaic pattern. Air trapping confirmed on the left lateral decubitus view (**b**)

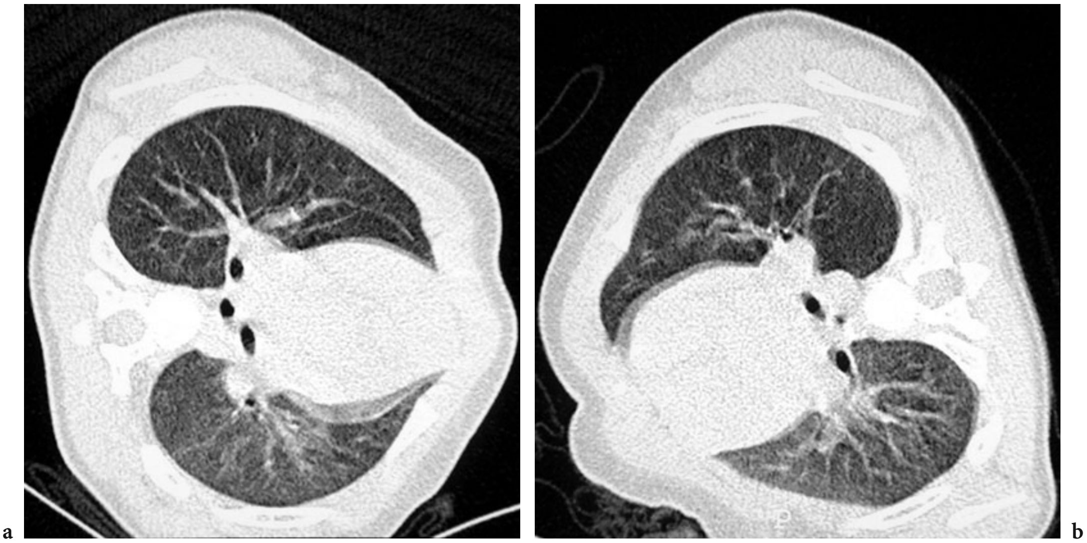

Fig. 4.7a,b. A 12-month-old boy with known cystic fibrosis. Initial CT scan in both lateral decubiti shows no abnormality

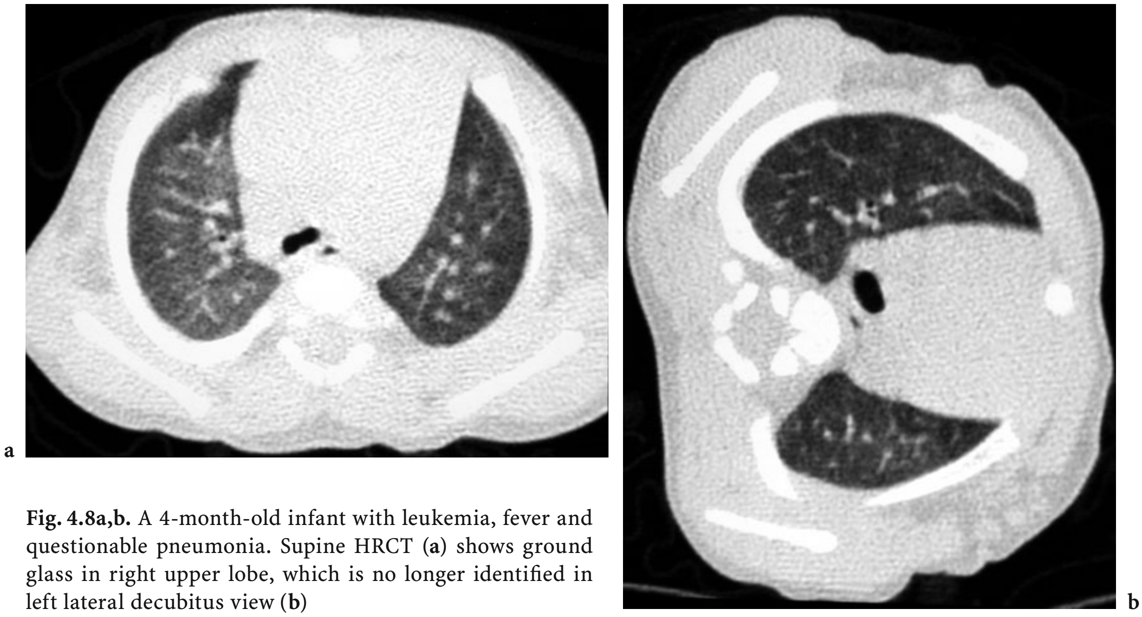

Fig. 4.8a,b. A 4-month-old infant with leukemia, fever and questionable pneumonia. Supine HRCT (**a**) shows ground glass in right upper lobe, which is no longer identified in left lateral decubitus view (**b**)

4.5
Normal Lung Anatomy

The lung is supported by a network of connective tissue fibers known as the lung interstitium (Fig. 4.9). For the purpose of interpreting HRCT images and identifying abnormal findings, the interstitium can be thought of as having several components. The peribronchovascular interstitium is a system of fibers that invests the large bronchi and pulmonary arteries in the parahilar regions and forms a continuum with the centrilobular interstitium, surrounding the small centrilobular bronchi, arteries and some lymphatic vessels. The subpleural interstitium is located beneath the visceral pleura and envelops the lung in a fibrous sac from which connective tissue septa (interlobular septa) invaginate into the lung parenchyma. The pulmonary veins and lymphatic vessels travel in the interlobular septa. The last component is the intralobular interstitium, a network of thin fibers in the walls of the alveoli bridging the gap between the centrilobular interstitium and the interlobular septa or subpleural interstitium (Weibel 1979).

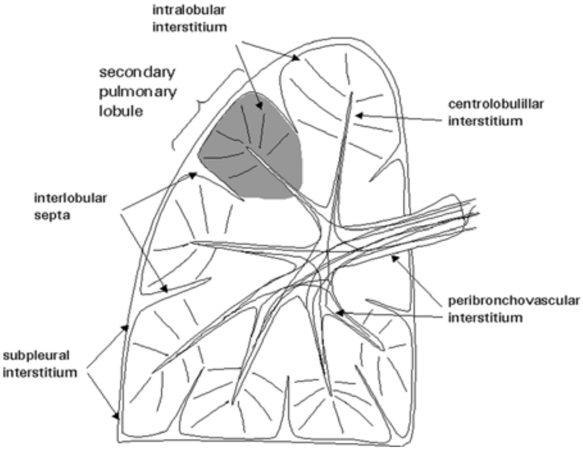
intralobular interstitium
secondary pulmonary lobule
centrolobulillar interstitium
interlobular septa
peribronchovascular interstitium
subpleural interstitium

Fig. 4.9. Components of the lung interstitium and secondary pulmonary lobule. [Modified and reprinted with permission from Webb et al. 1996]

The secondary pulmonary lobule is the smallest lung unit delineated by the connective tissue septa and the smallest functional unit that can be discretely visualized by HRCT (Fig. 4.10). With a diameter of 1–2.5 mm, it can have a polyhedric or prismatic shape, but more frequently resembles a truncated pyramid. Each secondary lobule has a central supporting tissue (centrilobular interstitium) containing a small bronchiole, pulmonary artery and lymphatic vessel (bronchovascular bundle) and is marginated by interlobular septa that contain pulmonary veins and lymphatic branches. The substance of the secondary lobule, surrounding the lobular core and contained within the interlobular septa, consists of a variable number of lung acini (ranging from 3 to 24) and the associated capillary bed, supplied by small airways and branches of the pulmonary arteries and veins. (Giovagnorio and Cavallo 1995). Secondary lobules are difficult to visualize in HRCT scans of children except in patients with abnormal septal thickening (Figs. 4.11, 4.12, 4.27, 4.28, 4.44, and 4.45).

The terminal bronchiole and the artery supplying the lobule are located in its center and give off smaller branches at intervals along their courses. On HRCT scans the vessels can be seen as linear, branching or dot-like structures near the center of the secondary pulmonary lobule and extending to within 5–10 mm of the pleural surface; the smallest arteries resolved are as small as 0.2 mm. Normal intralobular bronchioles cannot be identified because their walls are less than 0.15 mm thick. In one in vitro study, only bronchioles having a diameter of 2 mm or more were visible using HRCT (Murata et al. 1986). This explains why normal bronchi within 2 cm of the pleural surface are not visible (Fig. 4.13) (Teel et al. 1996). Bronchiolar abnormalities can be detected only when there is thickening of the bronchiolar wall, peribronchial inflammation, fibrosis or bronchiolectasis, with or without filling of the dilated bronchiole with secretions.

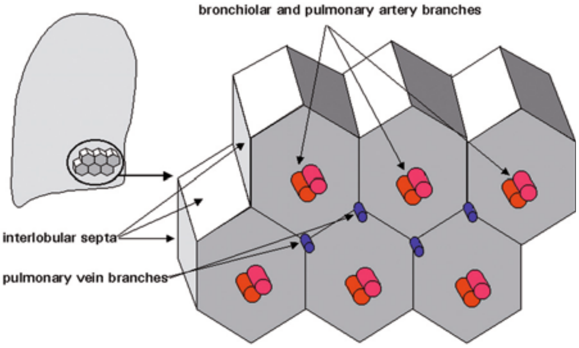

Fig. 4.10. The secondary pulmonary lobule, as defined by Miller. [Modified and reprinted with permission from Webb et al. 1996]

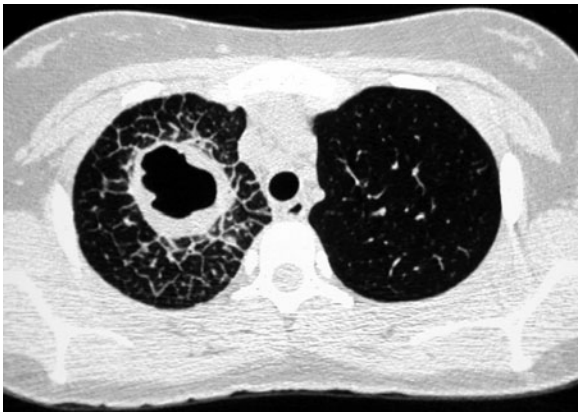

Fig. 4.11. A 15-year-old girl with fever and cough of 10 days' duration, treated with oral antibiotics. HRCT demonstrates a cavity with a thick, irregular wall in the right upper lobe. There is marked interlobular septal thickening around the lesion. Cultures were negative. The patient responded to intravenous antibiotic therapy

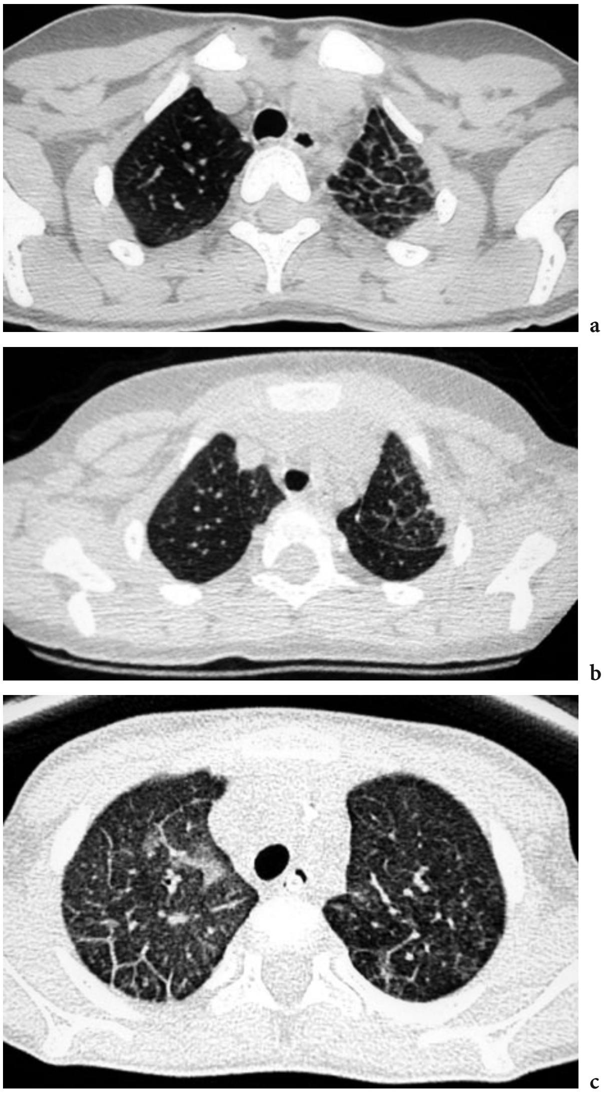

Fig. 4.12a–c. Septal thickening delineating the secondary pulmonary lobule in a 2-year-old patient with congenital atresia of the pulmonary veins (**a**). A 3-year-old boy with stenosis of the left upper pulmonary vein secondary to radiofrequency catheter ablation of the pulmonary veins for paroxysmal tachycardia (**b**) and a 5-year-old girl with pulmonary hypertension secondary to veno-occlusive disease (**c**)

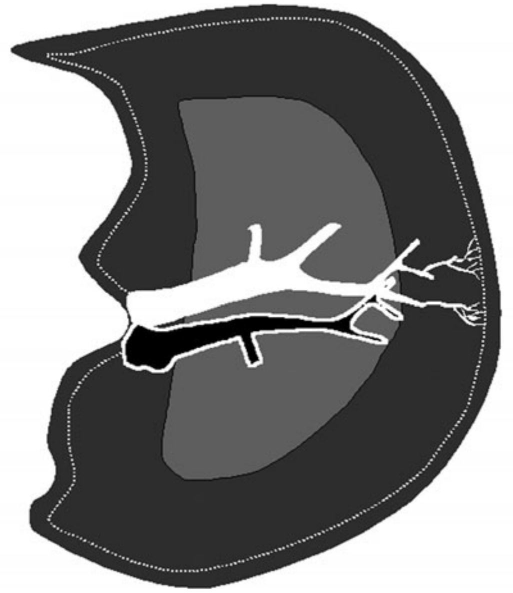

Fig. 4.13. Extent of visualization of airways (*black*) and vessels (*white*) at HRCT. [Modified and reprinted with permission from Teel et al. 1996]

The attenuation of the normal air-containing lung varies with the phase of respiration and with the region of the lung being examined. With the child in a supine position, attenuation is usually higher posteriorly (lower lobes) than anteriorly (right middle lobe and lingula). This is due to physiologic hyperemia and the tendency of the dependent lobes to be incompletely expanded. This gravity-dependent density is accentuated at partial expiration, is reversible with full inspiration or with the patient in a prone position, and is most frequently observed in scans of children not following breath-holding commands whose studies are practically never performed on full inspiration. The opposite situation, i.e. anterior lobes denser than the dependent lobes, is always abnormal and indicates disease in the anterior lobes or air trapping in the dependent lobes (Fig. 4.14).

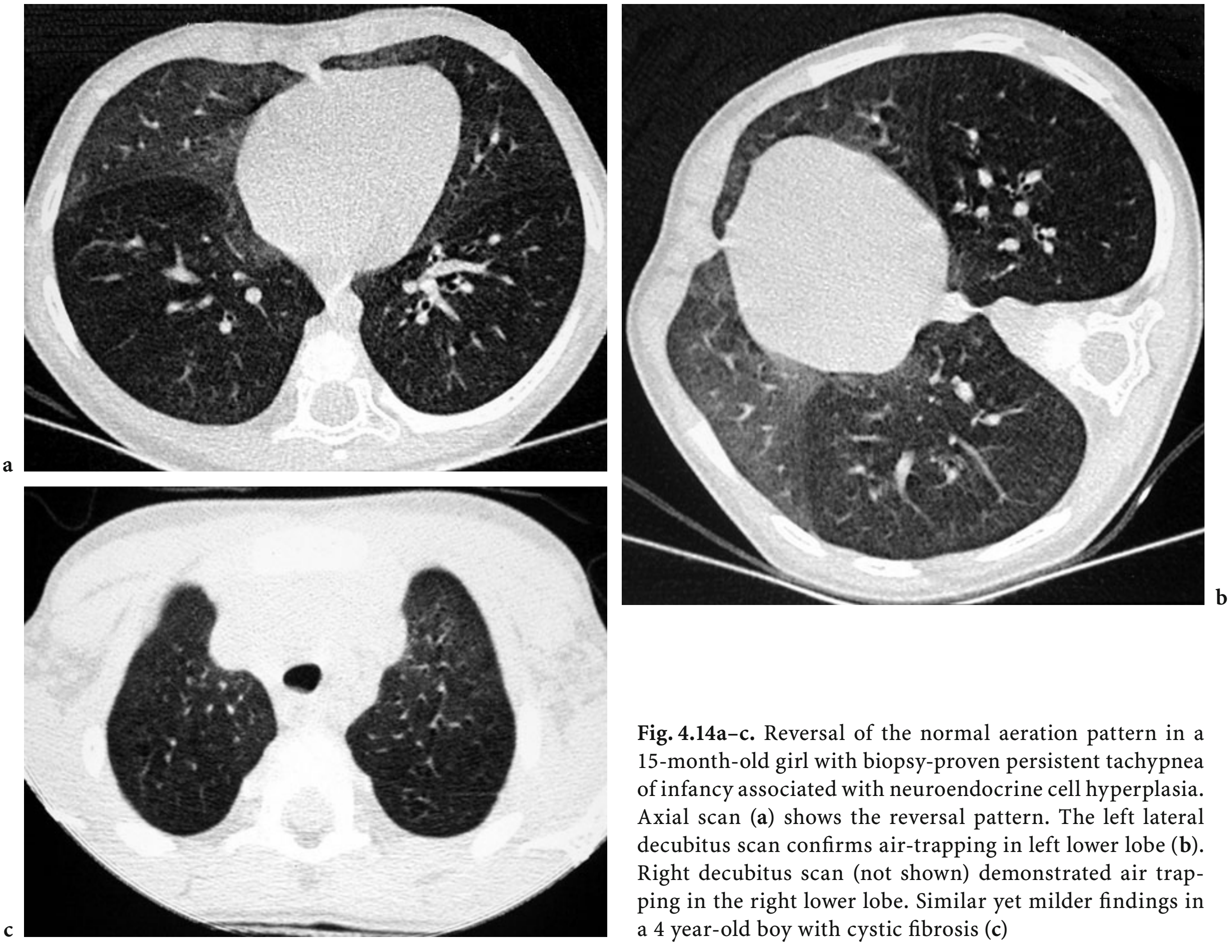

Fig. 4.14a–c. Reversal of the normal aeration pattern in a 15-month-old girl with biopsy-proven persistent tachypnea of infancy associated with neuroendocrine cell hyperplasia. Axial scan (**a**) shows the reversal pattern. The left lateral decubitus scan confirms air-trapping in left lower lobe (**b**). Right decubitus scan (not shown) demonstrated air trapping in the right lower lobe. Similar yet milder findings in a 4 year-old boy with cystic fibrosis (**c**)

4.6
HRCT Features of Lung Disease

The most common HRCT features of lung disease in children are grouped in Figure 4.15.

4.6.1
Ground-Glass Opacity

Ground-glass opacity (GGO) refers to hazy increased attenuation of the lung with preservation of the bronchial and vascular margins, caused by partial filling of the air spaces, interstitial thickening, partial collapse of alveoli, normal expiration, or increased capillary blood volume. It is sometimes associated with air bronchograms and can be patchy, resulting in a mosaic pattern of lung attenuation (Austin et al. 1996; Collins and Stern 1997).

Lung attenuation normally increases with expiration. This increased attenuation can mask underlying GGO from infiltrative lung disease or create an appearance of diffuse lung disease if the expiratory nature of the examination is not recognized. The tracheal configuration changes from round on inspiration to flat or crescent-shaped on expiration and can be used to determine at what phase of respiration the HRCT scan was performed (Collins and Stern 1997).

Recognition of GGO is based on subjective assessment of the lung attenuation. When uniform GGO is observed in scans of children not following breath-holding commands, it probably corresponds to normal lung on expiration. Lateral decubitus views can help in this regard (Figs. 4.6, 4.8, and 4.14a,b). When the GGO is patchy, it can cause a mosaic pattern of lung attenuation, which in children is usually due to small airway disease, with the GGO corresponding to areas of normal lung on expiration (Fig. 4.5b). Again, lateral decubitus views will help to establish whether the mosaic pattern corresponds to patchy ground-glass secondary to lung disease or to patchy air-trapping. Assessment of true GGO in the scans of children following breath-holding commands is significantly easier. Its presence in these patients, whose scans are usually obtained in full inspiration, is always abnormal and is due to air-space or interstitial disease or both. The differential diagnosis of pathological GGO in the pediatric age group is extensive, with infectious pneumonia of any etiology being its most common cause (Fig. 4.16). GGO can

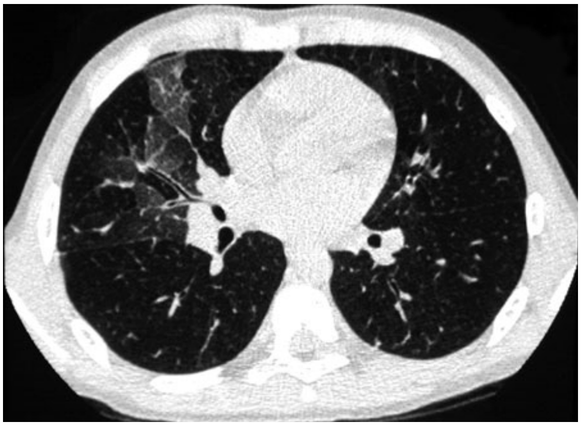

Fig. 4.16. Ground glass pattern due to infectious right middle lobe pneumonia in a 9-year-old girl

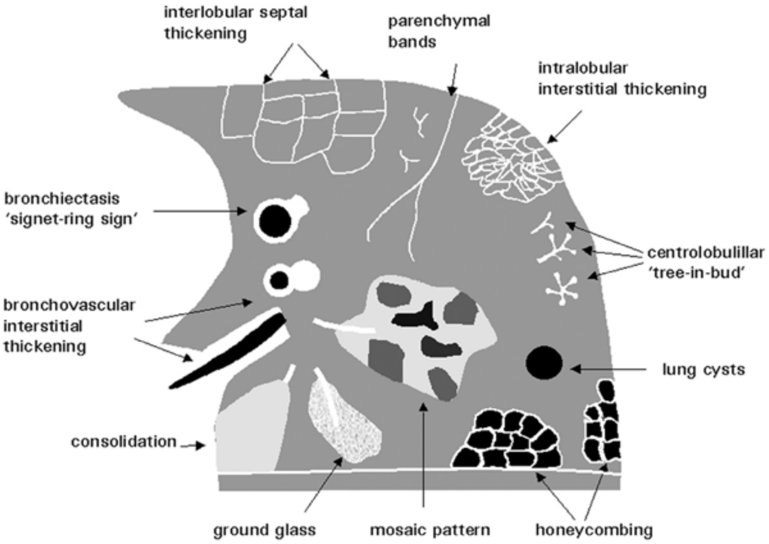
interlobular septal thickening
parenchymal bands
intralobular interstitial thickening
bronchiectasis 'signet-ring sign'
centrolobulillar 'tree-in-bud'
bronchovascular interstitial thickening
lung cysts
consolidation
ground glass
mosaic pattern
honeycombing

Fig. 4.15. HRCT features of lung disease. [Modified and reprinted with permission from Webb et al. 1996]

also be seen in pulmonary edema, hemorrhage, leukemic infiltration of the lung, lung contusion, acute lung transplant rejection, adult respiratory distress syndrome, collagen disease (Fig. 4.17), extrinsic allergic alveolitis, drug toxicity, interstitial pneumonia (Fig. 4.18) (Katzenstein et al. 1995; Newman et al. 2001; Canakis et al. 2002) sarcoidosis, alveolar proteinosis (Fig. 4.44), bronchiolitis obliterans organizing pneumonia, idiopathic pulmonary fibrosis and following bronchoalveolar lavage.

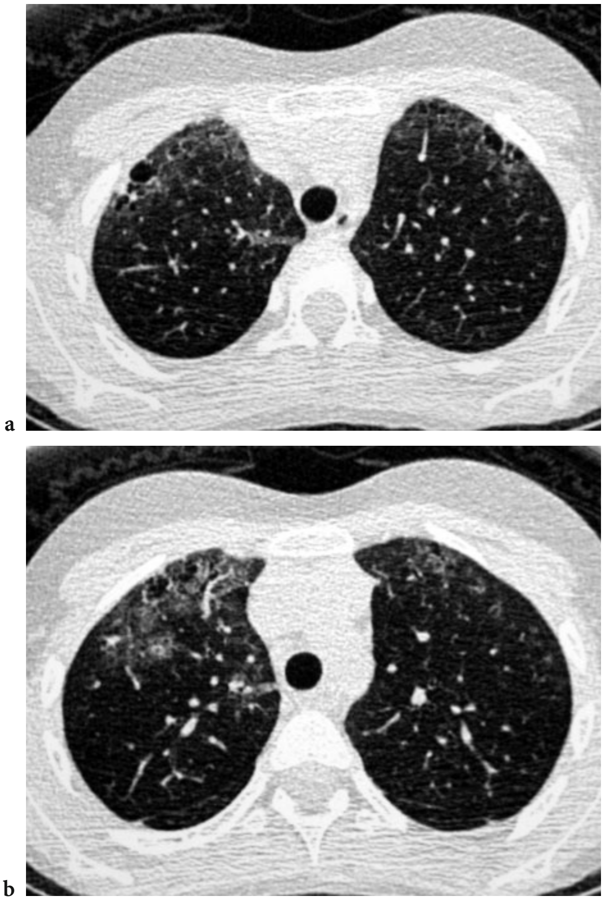

Fig. 4.17a,b. A 10-year-old girl with scleroderma. HRCT shows areas of ground glass and honeycombing

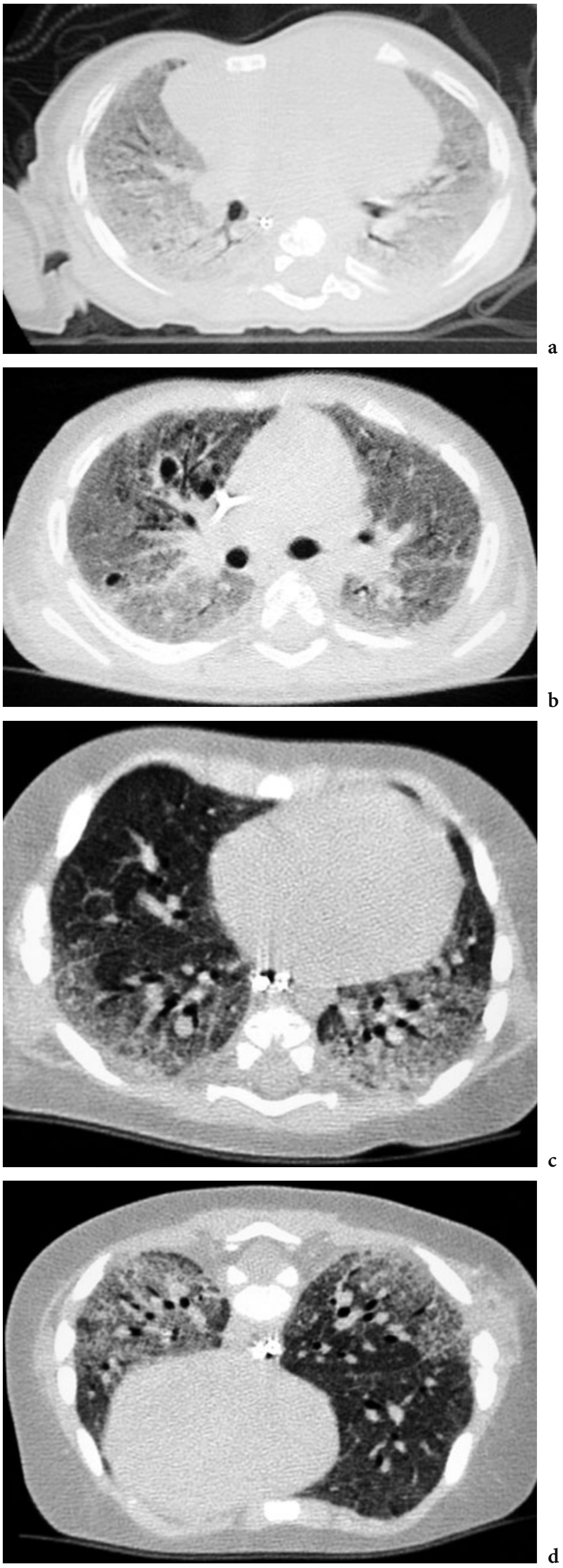

Fig. 4.18a–d. A 6-month-old boy with chronic pneumonitis of infancy. HRCT shows generalized ground glass (**a**). Repeated CT scan after the patient had been on mechanical ventilation shows the appearance of multiple pulmonary cysts due to interstitial emphysema (**b**). Chronic pneumonitis of infancy in a 4-month-old boy. Supine scan shows ground glass in both lower lobes (**c**).This finding remained unchanged in the prone scans (**d**)

4.6.2
Consolidation

A homogeneous increase in pulmonary parenchymal attenuation that obscures the margins of vessels and airway walls is referred to as consolidation. Air bronchograms may be present. By definition, diseases that produce consolidation are characterized by a replacement of alveolar air by fluid, cells, tissue or other material. The differential diagnosis of consolidation overlaps that of GGO and, in fact, it is common to find a mixture of both findings. Pneumonia of any etiology, pulmonary edema or hemorrhage and lung contusion are the most common causes of lung consolidation in children.

4.6.3
Pulmonary Nodule

Pulmonary nodules are focal, rounded opacities of varying size, which can be well- or ill-defined. They have been described as either air space or interstitial nodules, but it is more practical to classify them according to their size and distribution. Small nodules (< 5 mm) can be centrilobular or distributed at random (Fig. 4.19). Centrilobular nodules are located in the region of the bronchioarteriolar core of secondary pulmonary lobules. On HRCT they are adjacent to, surround, or obscure the centrilobular arteries, and are centered or clustered 5–10 mm from the periphery of the lobe, pleural surface or interlobar septa. Most centrilobular nodules in children are secondary to bronchiolar disease that also involves the peribronchiolar interstitium. They are common in cystic fibrosis (Fig. 4.20), bronchiectasis, , infectious bronchitis and bronchogenic spread of tuberculosis. They may also be present in immotile cilia syndrome (Fig. 4.21), hypersensitivity pneumonia, asthma (especially when there is superim-

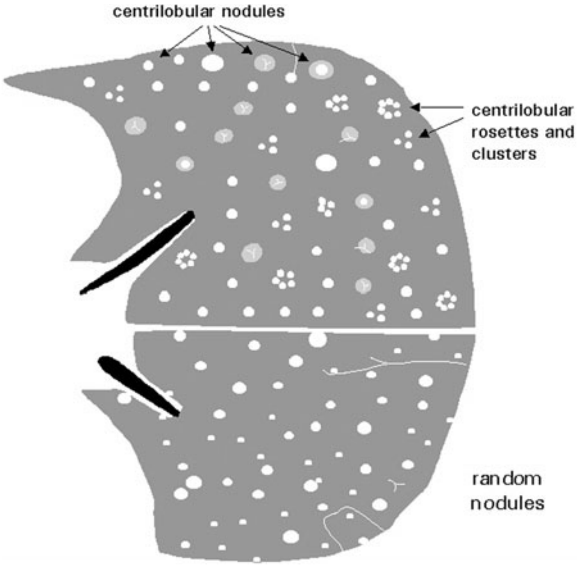

Fig. 4.19. Appearance of centrilobular and randomly distributed nodules. [Modified and reprinted with permission from Webb et al. 1996]

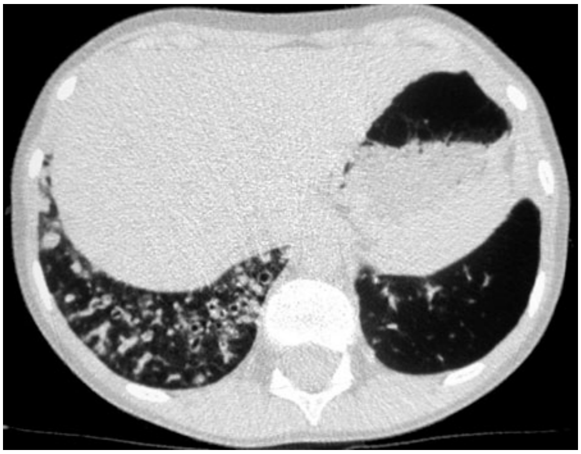

Fig. 4.20. Centrilobular nodules and tree-in-bud in a 13-year-old girl with cystic fibrosis

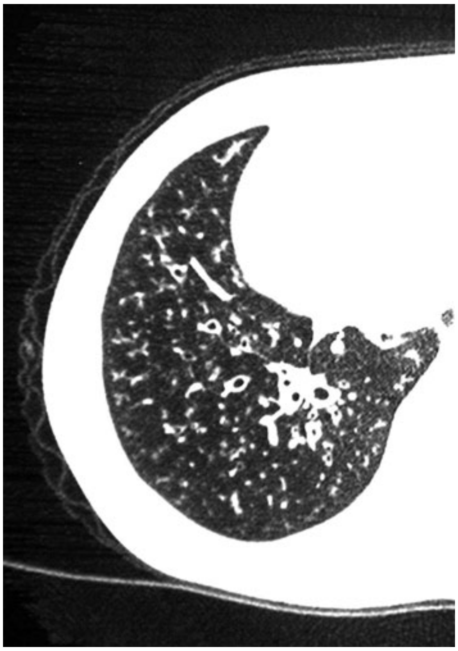

Fig. 4.21. A 14-year-old girl with immotile cilia syndrome. HRCT shows centrilobular nodules, bronchiectasis and peribronchial thickening

posed infection), histiocytosis, lymphocytic interstitial pneumonitis (LIP) in immunocompromised patients, congenital pulmonary lymphangiectasia, bronchiolitis obliterans, Wegener's granulomatosis (Levine et al. 2007) and pulmonary hemosiderosis (Gruden et al. 1994).

Small nodules that appear randomly distributed in relation to secondary lobule structures are often seen in patients with miliary tuberculosis, (Choi et al. 1999) fungal infections, hematogenous metastasis (Fig. 4.22) and histiocytosis X (Moon et al. 1996). Contrary to what occurs with centrilobular nodules, these can be seen in close proximity to the interlobular septa and the pleural surfaces.

The differential diagnosis of multiple, larger (> 5 mm) nodules includes metastatic disease, tuberculosis, histoplasmosis, mycotic infections, lymphoproliferative disorders, pulmonary spread of laryngeal papillomatosis, septic emboli, vasculitis, histiocytosis, bleomycin lung (Rimmet et al. 1985), lipid granulomas in patients with total parenteral nutrition (Landry and Melhem 1989), cholesterol granulomas in rheumatoid arthritis (Schultz et al. 2001) (Fig. 4.23), Wegener's granulomatosis (Levine et al. 2007) and bronchiolitis obliterans with organizing pneumonia (Fig. 4.24).

4.6.4
Bronchiolar Disease and Tree-in-Bud

The direct CT findings of bronchiolar disease include bronchiolar wall thickening, bronchiolar dilatation, and luminal impaction. Assessment of bronchial wall thickening on HRCT is quite subjective. Moreover, the apparent thickening of the bronchial wall represents not only the wall itself, but also the surrounding peribronchovascular interstitium. Peribronchovascular interstitial thickening, also known as peribronchial cuffing, can result in apparent bronchial wall thickening on HRCT. Bronchial wall/peribronchial thickening should be suspected when the bronchial "walls" are clearly seen in the distal third of the lung or when the walls of the more proximal aspects represent more than one third of the bronchial diameter (Ambrosino et al. 1994).

Small airways that are dilated and/or filled with mucus, pus or inflammatory material appear in some patients as small, well-defined, centrilobular, nodular, linear or branching structures of soft tissue opacity. The "tree-in-bud" pattern represents severe bronchiolar impaction with "clubbing" of distal

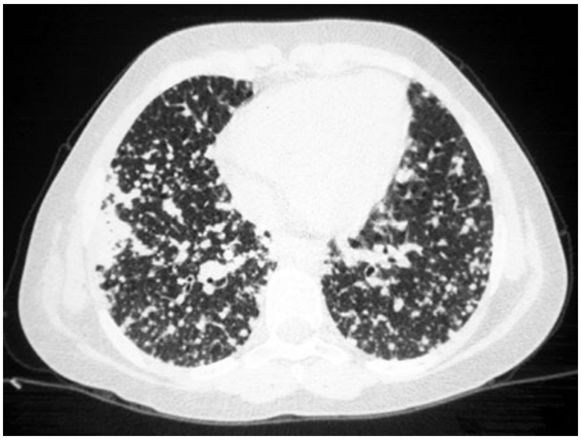

Fig. 4.22. Lung metastasis from thyroid carcinoma in a 6-year-old girl. Pulmonary nodules are distributed at random

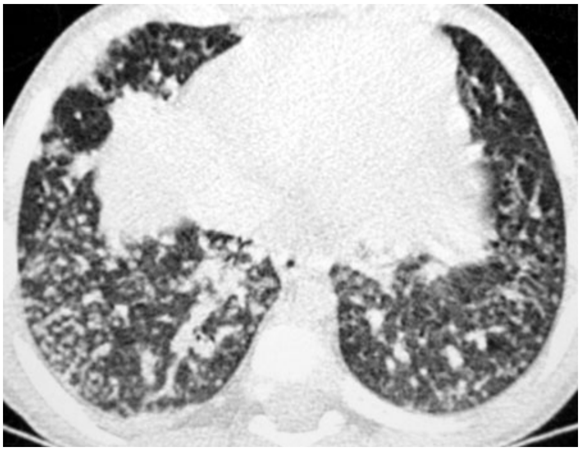

Fig. 4.23. Biopsy-proven cholesterol granulomas in a 3-year-old boy with rheumatoid arthritis. HRCT shows multiple centrilobular nodules

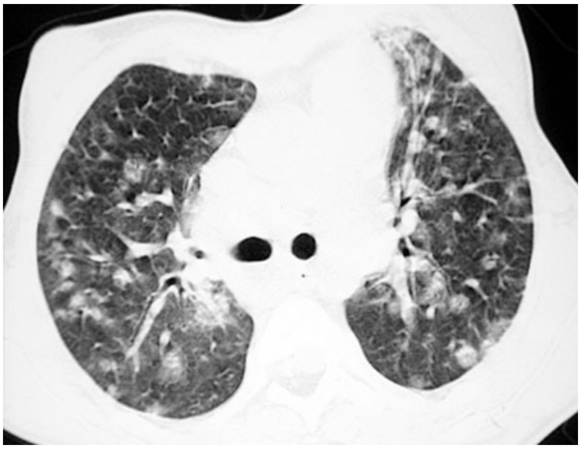

Fig. 4.24. Biopsy-proven BOOP in a 15-year-old girl with hypogammaglobulinemia and respiratory difficulty. HRCT shows multiple nodules and some areas of ground glass. Lesions disappeared with steroid therapy

bronchioles. Seen in profile, the pattern resembles the “finger-in-glove” appearance of impacted bronchi. In cross section, tree-in-bud patterns may resemble childhood toy jacks. The tree-in-bud pattern is most commonly seen in infectious bronchiolitis of any etiology, endobronchial spread of tuberculosis, cystic fibrosis (Fig. 4.20), allergic bronchopulmonary aspergillosis and immotile cilia syndrome (Rossi et al. 2005). Occasionally, it will be seen in bronchiolitis obliterans (Aquino et al. 1996).

4.6.5
Air-Trapping

The retention of excess air in all or part of the lung (especially during expiration), as a result of complete or partial airway obstruction or local abnormalities in pulmonary compliance, is known as air-trapping. Partial airway obstruction is particularly frequent in children. Recognition of a mosaic perfusion pattern on the inspiratory scans can suggest its presence. However, the expiratory scans often demonstrate marked air-trapping while the inspiratory scans show normal findings or only subtle abnormalities, such as decreased vascularity of the affected segment or lobe (Arakawa and Webb 1998). In our experience, the diagnostic yield of inspiratory scans is lower than that of expiratory scans in children with peripheral airway disease. The latter should always be included when performing HRCT of the lungs in cooperative children with clinical features suggesting airway disease (Fig. 4.5).

Air trapping is particularly common in bronchiolitis obliterans, cystic fibrosis, bronchiectasis (Fig. 4.26) and asthma (Fig. 4.5), in which it can disappear following bronchodilator therapy (Fig. 4.25). It has also been reported in children with follicular hyperplasia of a bronchus (Oh et al. 1999) and in persistent tachypnea of infancy associated with neuoroendocrine cell hyperplasia. Since bronchiolitis obliterans distal to bronchiectasis is a universal finding (Shepard 1995), air trapping is always found in the segments or lobes harboring bronchiectasis. This is a feature of significant diagnostic value, particularly when examining children whose studies show “questionable” bronchiectasis. In such cases the presence of associated air-trapping favors the diagnosis (Hansell et al. 1994). It also helps in the follow-up evaluation of children with known cylindrical bronchiectasis that have been treated and maintained infection-free. Occasionally the bronchiectasis becomes difficult to identify, yet the air trapping persists (Fig. 4.26).

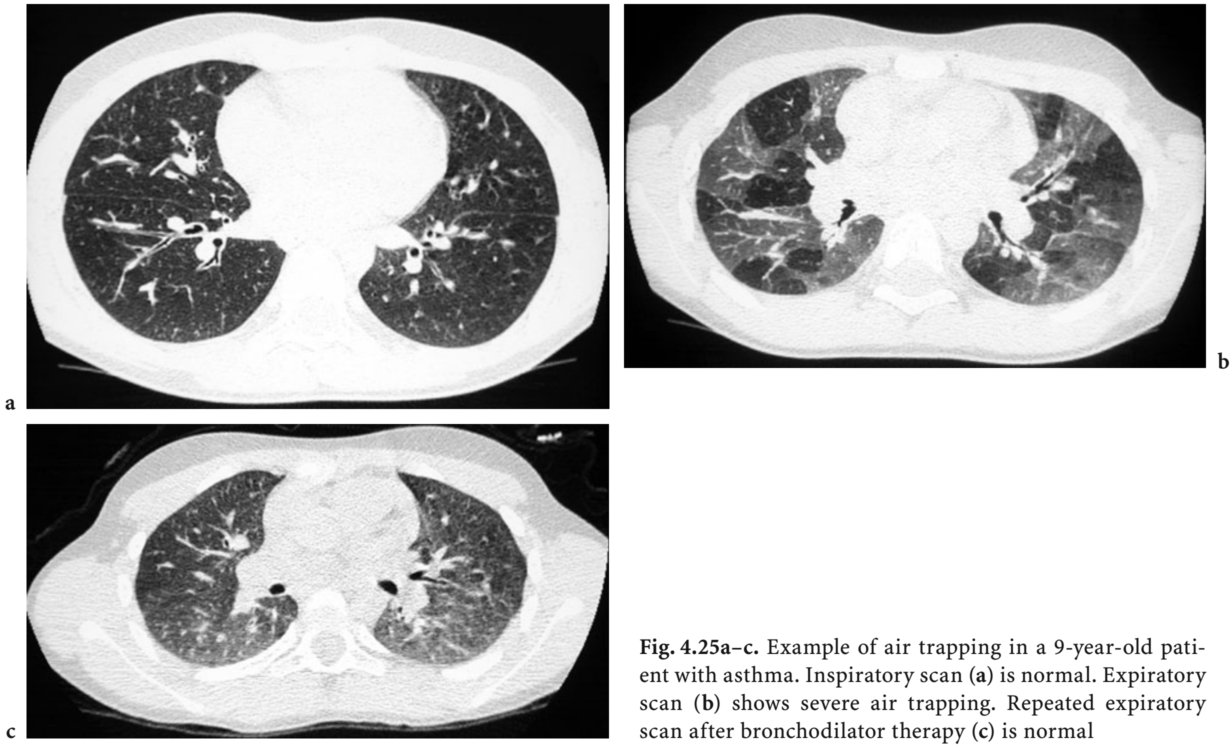

Fig. 4.25a–c. Example of air trapping in a 9-year-old patient with asthma. Inspiratory scan (**a**) is normal. Expiratory scan (**b**) shows severe air trapping. Repeated expiratory scan after bronchodilator therapy (**c**) is normal

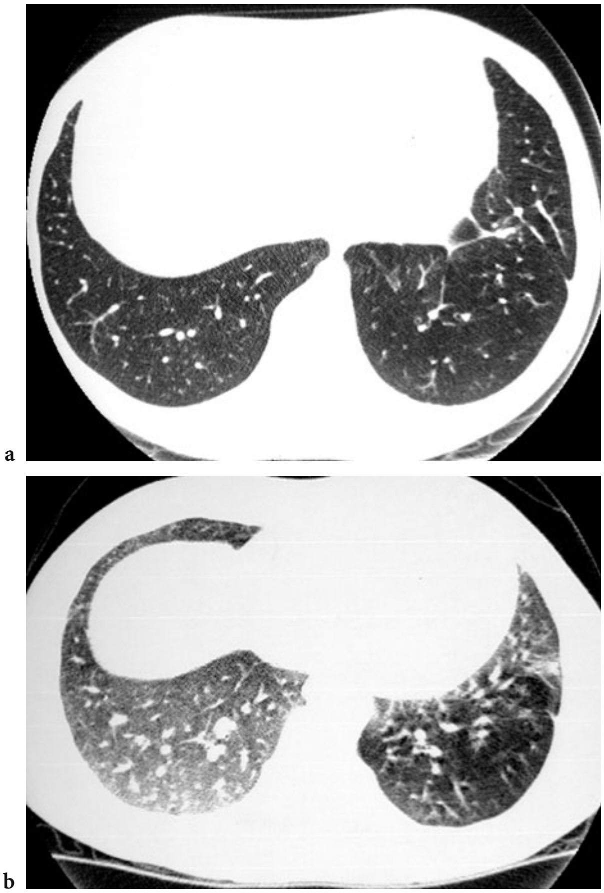

Fig. 4.26a,b. A 14-year-old girl with long-standing left lower lobe bronchiectasis treated with physiotherapy and antibiotics. Follow-up inspiratory HRCT (**a**) shows some architectural distortion and hypovascularity in the left lower lobe. Bronchiectases are no longer seen. Marked air trapping is evident on the expiratory scan (**b**)

4.6.6
Septal Thickening

Interlobular septal thickening, also known as septal lines, is defined as abnormal widening of an interlobular septum or septa. On HRCT it presents as short (1–2 cm in length), fine linear opacities perpendicular to and abutting the pleural surface (Fig. 4.27), or as a fine, polygonal pattern of lines in the more central lung (Figs. 4.11, 4.12, and 4.28). Interlobular septal thickening is usually due to interstitial edema of any cause (Fig. 4.12), but it is also seen in neoplasms, infectious processes (Fig. 4.11), pulmonary fibrosis, bronchopulmonary dysplasia (Fig. 4.27), pulmonary lymphangiectasia, Niemann-Pick disease (Fig. 4.28) (Feretti et al. 1996), Gaucher's disease collagen vascular disorders, tuberous sclerosis, alveolar proteinosis (Fig. 4.45), sarcoidosis and pulmonary venous obstruction (Fink et al. 2003; Newman 2006) (Fig. 4.12). Septal thickening is usually smooth. It can be irregular in cases of fibrosis and irregular or nodular in sarcoidosis or lymphangitic spread of tumor (Fig. 4.29) (Lynch et al. 1999; Moon et al. 1996).

Intralobular lines, rarely observed in children, correspond to thickening of the intralobular interstitium. When numerous, they may appear as a fine reticular pattern.

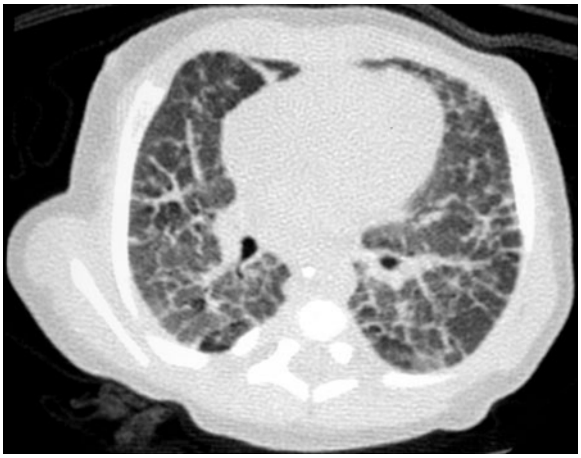

Fig. 4.27. Septal lines in a 2-month-old infant with bronchopulmonary dysplasia

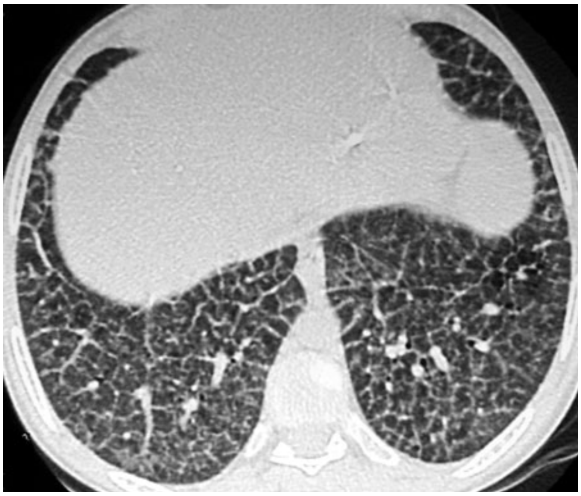

Fig. 4.28. A 16-year-old boy with Niemann-Pick disease and respiratory insufficiency. HRCT shows thickening of the interlobular septa. Areas of ground glass were seen in other slices (not shown). Interstitial thickening is due to infiltration of lymphatics and interlobular septa with lipid-laden macrophages. (Courtesy of Dr. Ucar, Argentina)

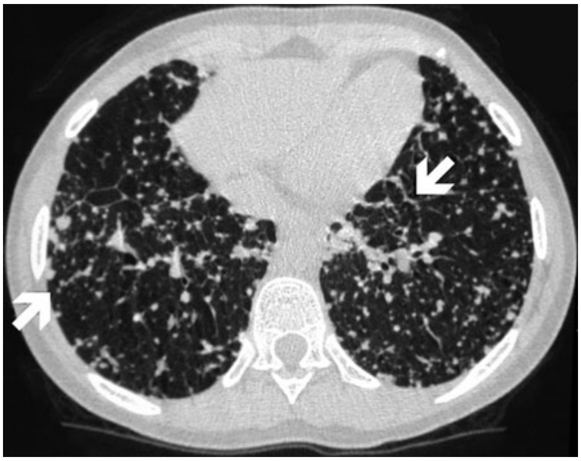

Fig. 4.29. A 14-year-old girl with thyroid carcinoma. HRCT demonstrates irregular nodular thickening of interlobular septa (*arrows*) corresponding to lymphangitic spread. Small nodules randomly distributed through both lungs, characteristic of hematogenous metastasis, are also seen

4.6.7
Parenchymal Bands

Visualized as elongated opacities, parenchymal bands are usually 2–5 cm in length and often represent several contiguous thickened septa. They can also correspond to areas of peribronchovascular fibrosis, coarse scars or atelectasis associated with lung or pleural fibrosis. Parenchymal bands can extend to the pleura, which may be thickened and retracted at the site of contact. The pleural retractions are visualized as pleural-based triangular opacities. These features are commonly seen in children with long-standing bronchopulmonary dysplasia. Most parenchymal bands in bronchopulmonary dysplasia are in the upper lobes (Figs. 4.4b, 4.30) (Aquino et al. 1999; Oppenheim et al. 1994). Pleural-based triangular opacities, have been observed in the HRCTs of toddlers as the only residual anomaly of previous bronchopulmonary dysplasia (Fig. 4.31). Similar findings have been reported in adolescents born prematurely even without having suffered bronchopulmonary dysplasia (Aukland et al. 2006). We have also seen linear opacities in patients with interstitial pneumonia (Figs. 4.32 and 4.33).

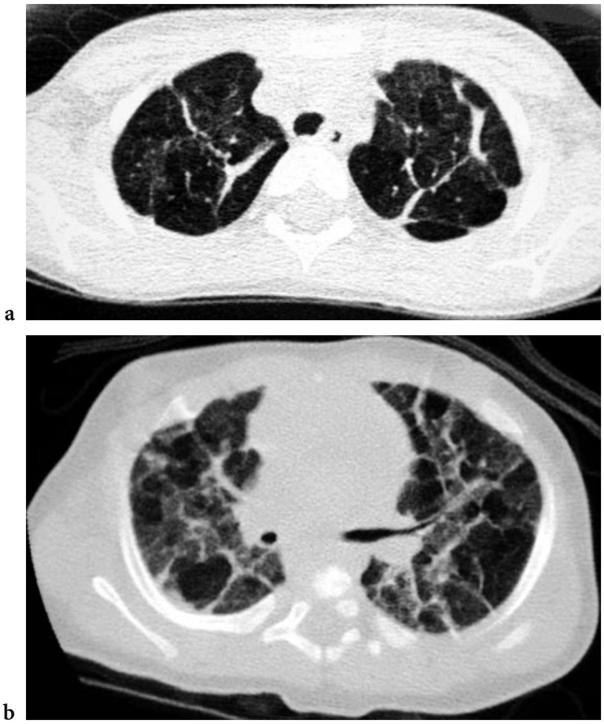

Fig. 4.30a,b. Parenchymal bands in a 4-year-old boy with bronchopulmonary dysplasia (**a**). Typical features of bronchopulmonary dysplasia were present on the initial CT scan performed at the age of 3 months (**b**)

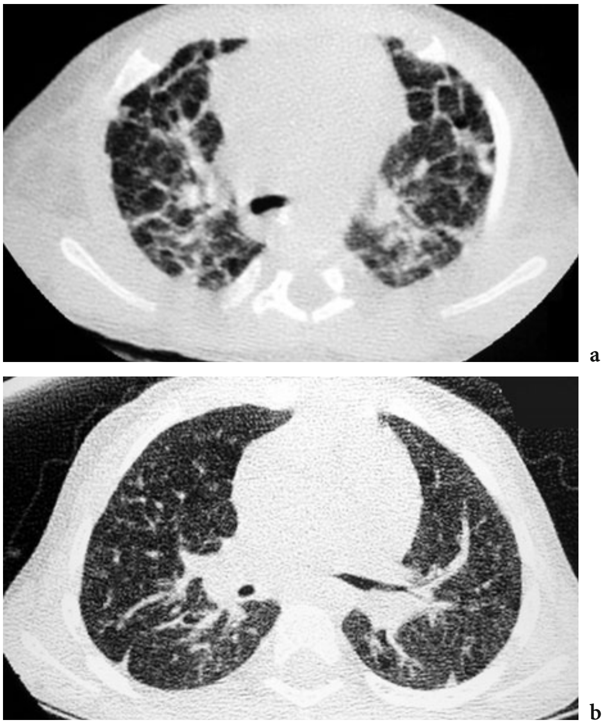

Fig. 4.31a,b. Typical features of bronchopulmonary dysplasia on the HRCT performed at the age of 3 months. Repeated HRCT at the age of 2.5 years disclosed the presence of a few peripherial wedge-shaped densities as the only anomaly

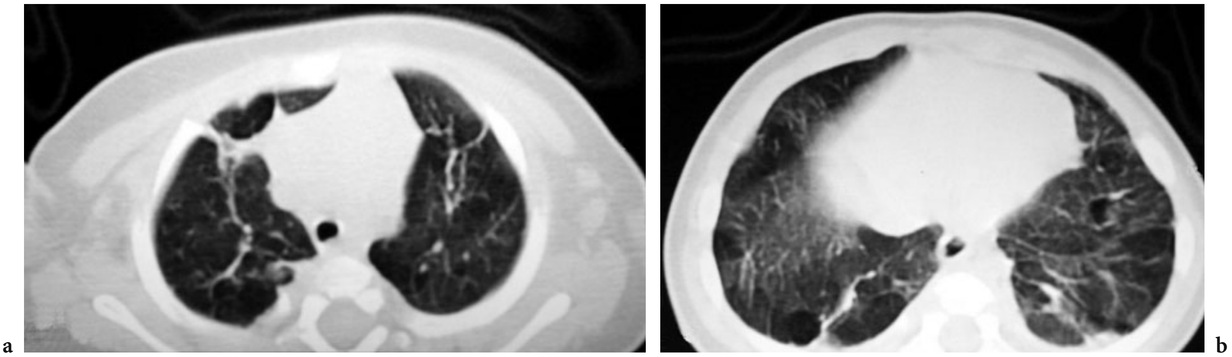

Fig. 4.32a,b. A 6-month-old boy with biopsy-proven pulmonary interstitial glycogenosis. HRCT demonstrates a mosaic perfusion pattern and multiple and bilateral linear densities

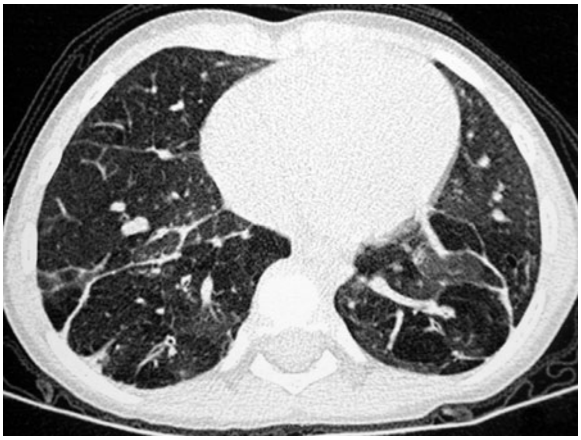

Fig. 4.33. A 5-year-old with biopsy-proven non-specific interstitial pneumonia (cellular type). HRCT shows a mosaic perfusion pattern and multiple bilateral linear densities

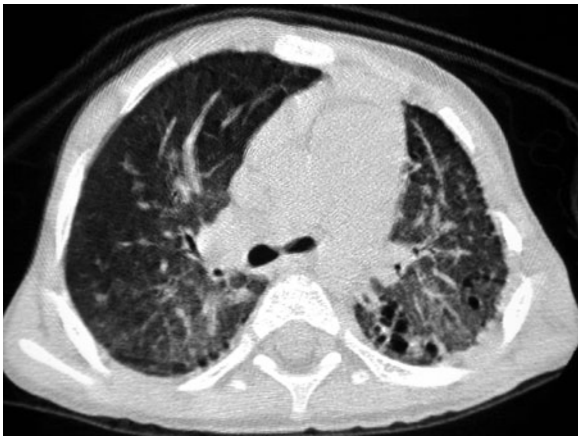

Fig. 4.34. Honeycombing secondary to pulmonary fibrosis in a 3-year-old girl with congenital pulmonary vein atresia

4.6.8
Honeycombing

A sign of destroyed, fibrotic and cystic lung, honeycombing represents complete loss of acinar and bronchiolar architecture at the end stage of fibrosing lung disease. On HRCT of the lung it presents as clustered cystic air spaces with clearly definable walls, measuring 1–3 mm in thickness and predominantly found in peripheral and subpleural lung regions, often in several contiguous layers. True honeycomb cysts do not change in size during exhalation (Johkoh et al. 1999a). Honeycombing is not a common finding in children, but it can be seen in chronic interstitial lung disorders, such as non-specific interstitial pneumonitis, desquamative interstitial pneumonitis (Copley et al. 2000), scleroderma (Fig. 4.17) (Seely et al. 1998), lupus and end-stage pulmonary fibrosis (Fig. 4.34).

4.6.9
Mosaic Perfusion

A patchwork of varied attenuation, mosaic perfusion has been interpreted as secondary to regional differences in perfusion. The HRCT mosaic pattern of lung attenuation is a non-specific finding that can reflect the presence of airway abnormalities, ground-glass interstitial or air-space infiltrates or vascular disease (Stern et al. 1995). In small airway disease and pulmonary vascular disease, the pulmonary vessels within the lucent regions of the lung are small relative to the vessels in the more opaque lung. In primary vascular diseases, such as thromboembolism or pulmonary hypertension, which are exceedingly rare in children, the reduced vascularity in the lucent lesions results from the primary vascular disease. In contrast, when mosaic perfusion is due to small airway disease, the commonest cause of this pattern in children, the reduced vascularity in the lucent areas results from abnormal ventilation, air-trapping and secondary hypoxic vasoconstriction. Recognition of a mosaic perfusion pattern secondary to airway disease is enhanced with the use of expiratory slices. Asthma (Figs. 4.5 and 4.25), bronchiolitis obliterans (Fig. 4.35), cystic fibrosis and bronchopulmonary dysplasia are the most common causes of a mosaic perfusion pattern in the pediatric age group.

The third cause of HRCT mosaic patterns of lung attenuation is infiltrative lung disease, producing areas of ground-glass attenuation in a lobular or multilobular distribution. The areas of ground-glass can be due to interstitial or air-space infiltrates, or both. In these cases the vessel caliber and number are similar in both the normal lower attenuation regions and the abnormal higher attenuation regions of the lung. Furthermore, there is no air-trapping on expiration.

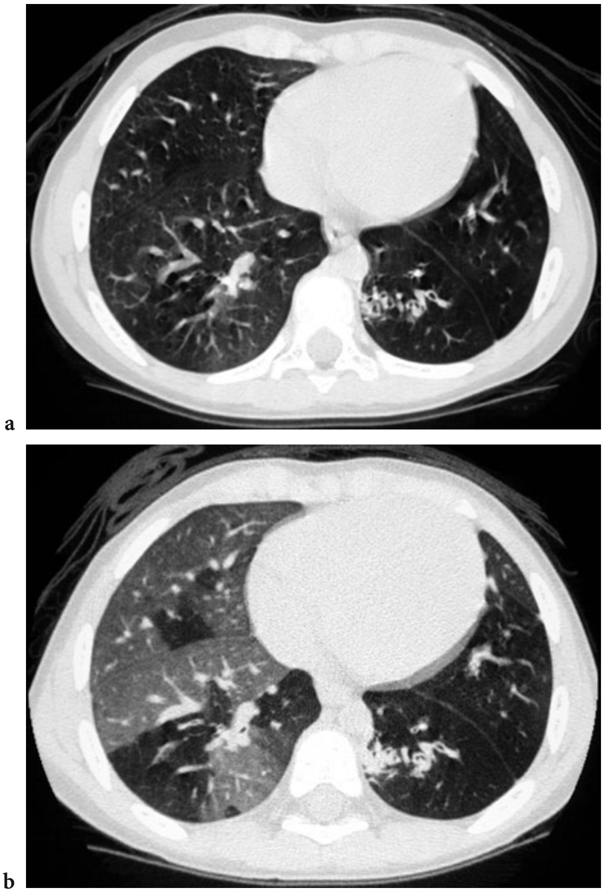

Fig. 4.35a,b. Inspiratory (**a**) and expiratory (**b**) HRCT scans in a 6-year-old boy with postinfectious bronchiolitis obliterans (Swyer-James syndrome). There is left lower lobe bronchiectasis and a bilateral mosaic perfusion pattern with air trapping

4.6.10 Architectural Distortion

A manifestation of lung disease in which bronchi, pulmonary vessels, fissures and/or septa are abnormally displaced. Usually there are fewer vessels and their branching pattern is anomalous. This finding can be observed in pulmonary hypoplasia (Fig. 4.36), but it is most common in lung diseases associated with small airway obstruction (Fig. 4.26). In the latter, architectural distortion may be the only ab-

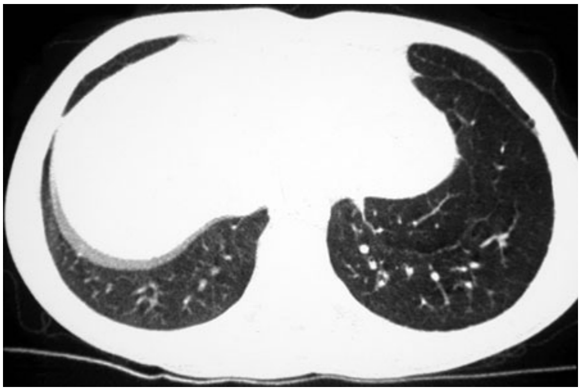

Fig. 4.36. Example of architectural distortion of the left lower lobe in a 5-year-old boy with unilateral pulmonary hypoplasia secondary to congenital left-sided diaphragmatic hernia operated in the neonatal period

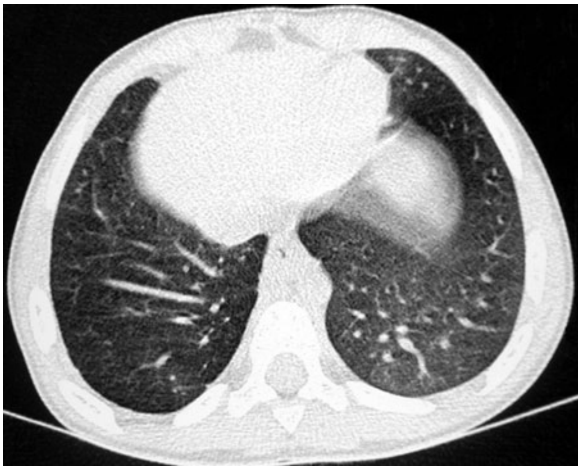

Fig. 4.37. A 4-year-old boy with history of cystic adenomatoid malformation of the right lower lobe. HRCT performed following right lower lobe lobectomy shows an unusual distribution of the pulmonary vessels in the right lung

normality seen in the inspiratory slices; expiratory scans will demonstrate air- trapping (Fig. 4.26).

In our experience previous lobectomy may cause an evident abnormal vascular branching pattern in the remaining lobes (Fig. 4.37).

4.6.11
Air-Filled Cystic Lung Lesions: Bullae, Pneumoceles and Cysts

Air-filled cystic lung lesions correspond to intrapulmonary air collections surrounded by a visible wall of varying thickness. In our experience, it is extremely difficult, if not impossible, to differentiate between air-filled cysts, bullae, pneumatoceles and even some cases of cystic bronchiectasis or localized emphysema on imaging findings alone. Clinical features and evolution are essential to establish the diagnosis.

The differential diagnosis of air-filled cystic lung lesions in children includes congenital cyst, inflammatory pneumatoceles secondary to hydrocarbon ingestion (Fig. 4.38) or infectious pneumonia (Fig. 4.39), interstitial emphysema due to barotrauma (Fig. 4.3), Langerhans´ cell histiocyto-

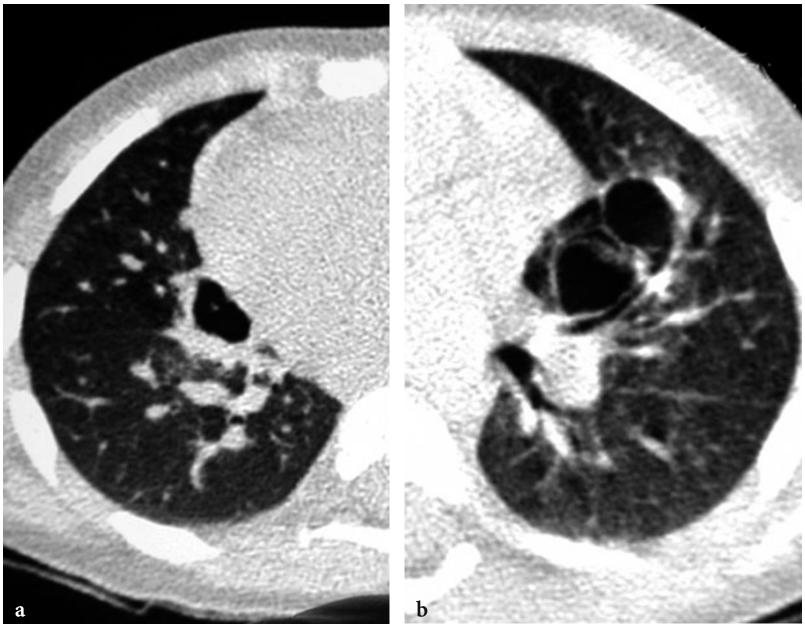

Fig. 4.38a,b. Bilateral pulmonary pneumatoceles, which appeared 6 days after hydrocarbon ingestion in an 18-month-old girl

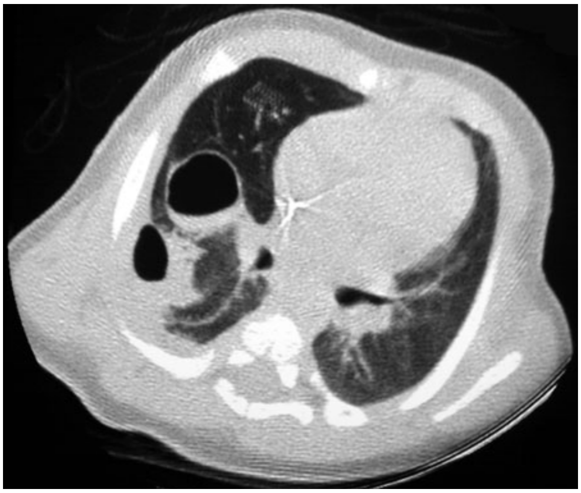

Fig. 4.39. Infectious pneumatocele in a 3-month-old infant

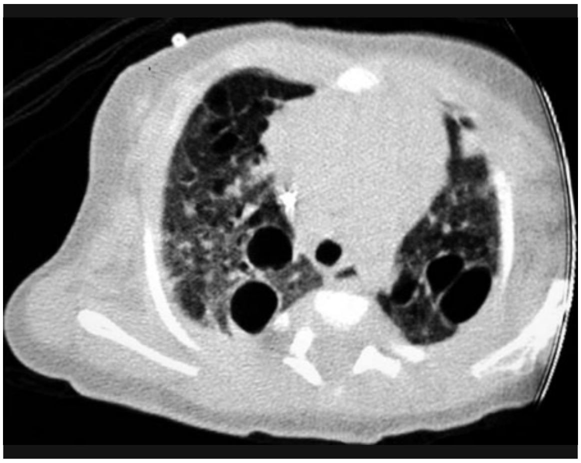

Fig. 4.40. Cystic pulmonary lesions in a 3-month-old infant with histiocytosis X

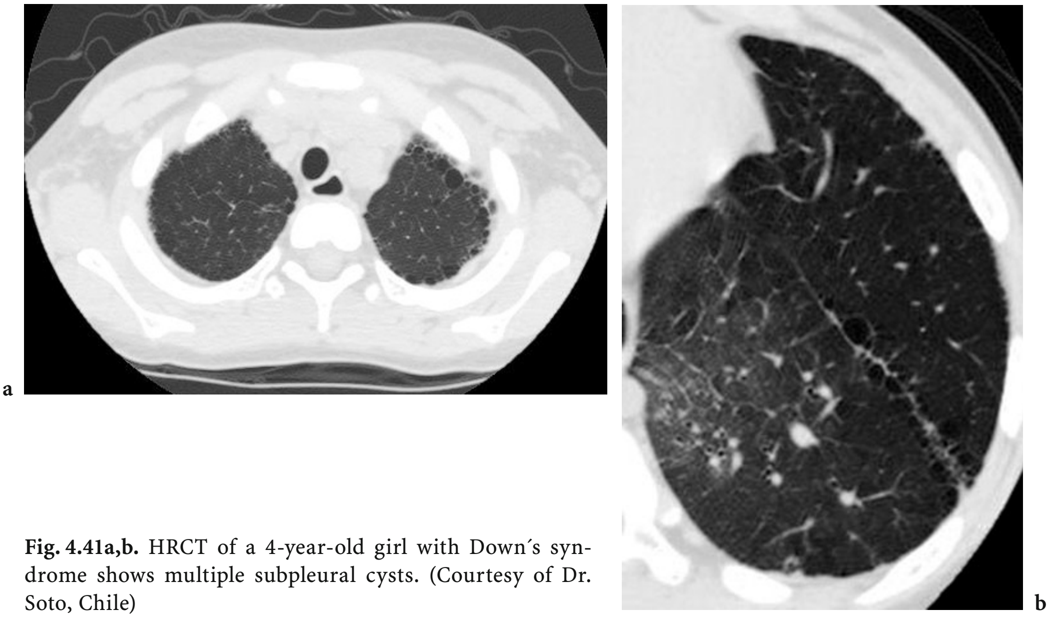

Fig. 4.41a,b. HRCT of a 4-year-old girl with Down´s syndrome shows multiple subpleural cysts. (Courtesy of Dr. Soto, Chile)

sis (Fig. 4.40), tuberous sclerosis, papillomatosis, septic pulmonary emboli, Wegener´s granulomatosis, Ehler-Danlos, Marfan or Williams-Campbell syndromes (Hartman et al. 1994) and trisomy 21 (Fig. 4.41) (Tyrrell et al.1999).

4.6.12
Reversed Ventilatory Pattern

Increased subpleural attenuation occurs in a region of the dependent lung and disappears when the lung is nondependent. Dependent increased attenuation is a normal finding. It can be particularly evident in patients who have been examined using deep sedation or general anesthesia. The opposite, i.e. the posterior lung being more hyperlucent than the anterior on the CT scan of a none-co-operative patient examined in the supine position is always abnormal and indicative of airway disease (Fig. 4.14). This has been described in cases of follicular bronchitis (Oh et al. 1999) and in persistent tachypnea of infancy associated with neuroendocrine cell hyperplasia (Brody 2005; Brody and Crotty 2006; Deterding et al. 2005). We have also seen it in patients with cystic fibrosis (Fig. 4.14) or bronchiolitis obliterans.

4.6.13
Emphysema

Emphysema is characterized by permanent, abnormal enlargement of the air spaces distal to the terminal bronchioles, accompanied by destruction of their walls. It is visible on HRCT as a focal region or regions of low attenuation, usually without visible walls, resulting from actual or perceived enlarged air spaces and destroyed alveolar walls (Austin et al. 1996). It can be associated with air-trapping. Emphysema is classified morphologically relative to the pulmonary lobule as centrilobular, panlobular or paraseptal.

4.6.14
Halo Sign

The halo sign is a ground-glass opacity surrounding the circumference of a nodule or mass. It can be seen in patients with invasive pulmonary aspergillosis (Fig. 4.42), tuberculosis, lymphoproliferative disorders, bacterial and viral infections (Escuissato et al. 2005), Wegener’s, pulmonary hemorrhage, metastatic osteosarcoma (Tomiyama et al. 1994; Kim et al. 1999; Pinto 2004) and pulmonary visceral larva migrans (Sakai 2006).

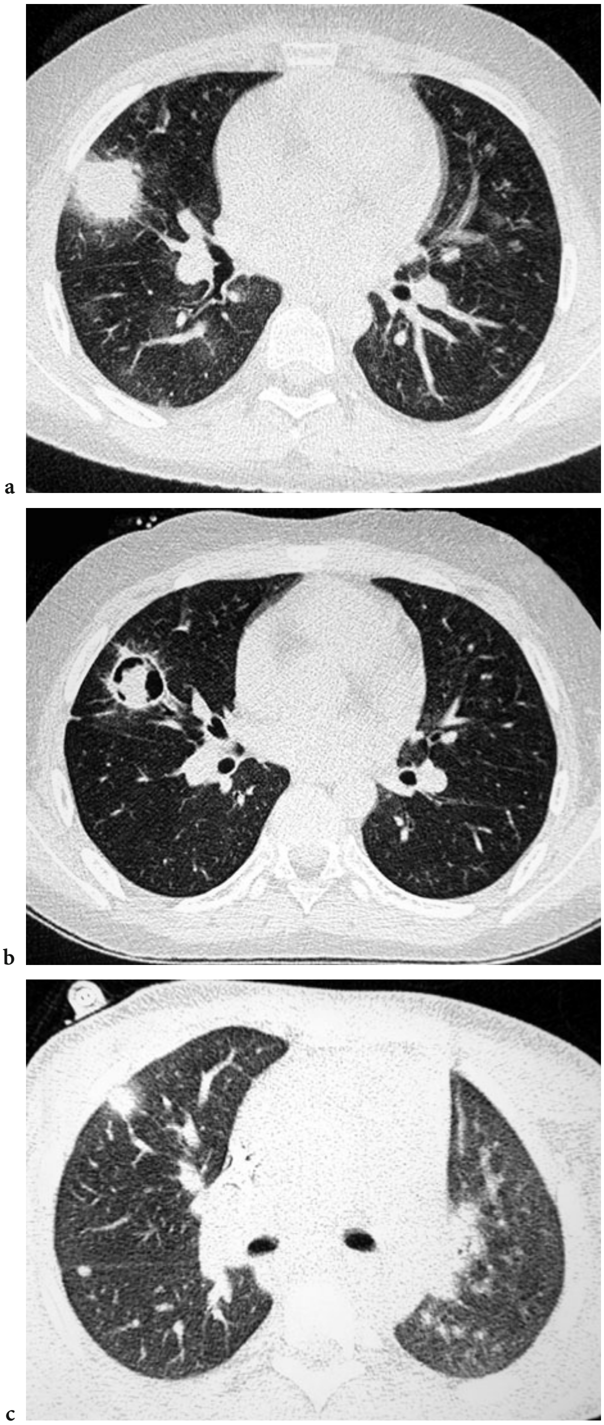

Fig. 4.42a–c. A 14-year-old girl with leukemia and pulmonary aspergillosis. Initial CT shows a nodule surrounded by a halo of ground glass (**a**). Follow-up CT performed 5 weeks later shows cavitation of the nodule (**b**)

4.6.15
Signet-Ring Sign

A ring of opacity (usually representing a dilated, thick-walled bronchus) associated with a smaller, round, soft-tissue opacity (the adjacent pulmonary artery) is known as the signet-ring sign. In children this finding indicates bronchiectasis (Fig. 4.43) (Ouellete 1999).

4.6.16
Crazy Paving Pattern

Crazy paving pattern is a combination of areas of ground glass attenuation and smoothly thickened interlobular septa, within the areas of air space disease (Fig. 4.44). This finding has been considered to be strongly suggestive of alveolar proteinosis. However, it can occur in other diseases such as lipoid pneumonia (Fig. 4.45), adult respiratory distress syndrome, acute interstitial pneumonia drug-induced pneumonitis , bacterial pneumonia, radiation pneumonitis and pulmonary hemorrhage (Franquet et al. 1998; Johkoh et al. 1999b; Lee et al. 2005; Lee 2007).

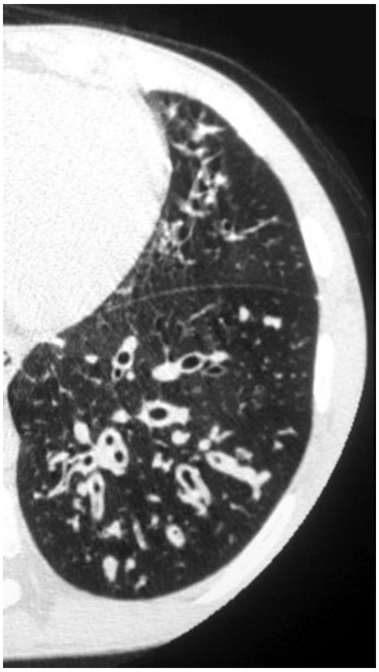

Fig. 4.43. Signet ring sign in an 8-year-old patient with cystic fibrosis and left lower lobe bronchiectasis

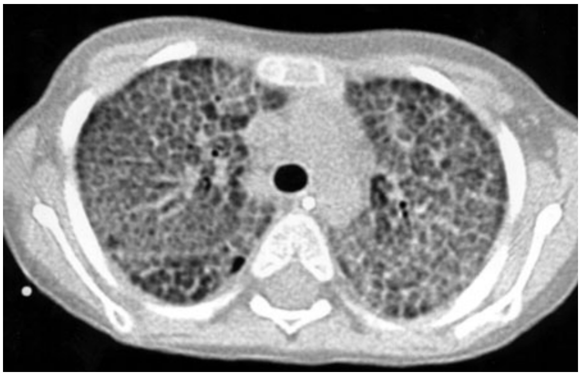

Fig. 4.44. A 3-year-old girl with alveolar proteinosis. HRCT shows thickened interlobular septa in background of ground-glass opacification (crazy-paving pattern). [Reprinted with permission, from Copley et al. 2000]

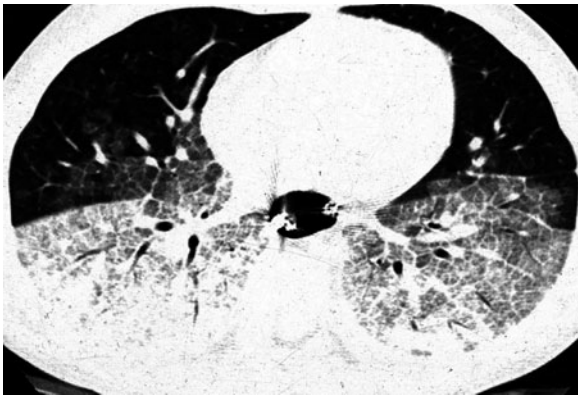

Fig. 4.45. A 6-year-old girl with a bilateral crazy-paving pattern involving both lower lobes, secondary to squalene aspiration pneumonia.(Courtesy of Drs. Lee and Kim, Korea)

Part II
Clinical Applications

Hubert Ducou Le Pointe

HRCT has proven to be of great value for the diagnosis and management of patients with lung disease, particularly when the chest X-ray is normal. Volumetric HRCT is possible with the introduction of multidetector computed tomography (MDCT) and could allow better diagnosis. In this chapter we discuss airway disease, chronic diffuse infiltrative lung disease and air-space disease.

4.7
Airway

HRCT is the imaging technique of choice for the evaluation of most lesions of the bronchial tree: bronchiectasis, constrictive bronchiolitis, bronchiolitis obliterans organizing pneumonia (BOOP), and asthma.

4.7.1
Bronchiectasis

Bronchiectasis is defined pathologically as the irreversible dilatation of the bronchial tree. In children, a radiological diagnosis should be considered with caution. Reversible bronchial dilatation or improvement in appearance with medical treatment has been reported (Gaillard et al. 2003). Numerous disorders are associated with bronchiectasis (postinfective bronchial damage, bronchial obstruction, immune deficiency, mucociliary clearance defect, fibrosis …).

HRCT has proven to be a reliable, noninvasive technique for assessing the presence, severity and extension of bronchiectasis and has largely eliminated the need for bronchography in children (Herman et al. 1993; Rossi and Owens 2005). High-resolution MDCT using 1-mm contiguous slices improves the presence, extent and severity of bronchiectasis compared with conventional bronchectasis (Dodd et al. 2006). Despite this fact some authors do not recommend this technique in children due to a considerably higher radiation dose delivered. In non-cystic fibrosis bronchiectasis, a stronger correlation between the extent and severity of bronchiectasis explored by HRCT and pulmonary function test was observed, than when they are explored by chest X-ray (Edwards et al. 2003).

The HRCT criteria for diagnosing bronchiectasis have been well described (Hansell 1998): internal diameter of the bronchus larger than the diameter of the adjacent pulmonary artery branch, absence of normal tapering of bronchi, bronchial wall thickening, and visualization of a bronchus in the lung periphery. This last criterion is not clearly defined in the literature. Several authors (Grenier et al. 1986; Webb 1994; McGuinness and Naidich 1995) consider all bronchi visible within 2–3 cm from the pleural surface to be abnormal. Kim et al. (1997) defined the visualization of bronchi within 1 cm of costal or paravertebral pleura or visualization of bronchi abutting the mediastinal pleura as abnormal. These differences in criteria could be related to improvements in CT technology. We consider abnormal the visualization of bronchi in the peripheral 1 cm of the lung.

Bronchiectasis has been classified into three types – cylindrical, varicose and cystic -based on the morphology of the abnormal bronchi. Cylindrical bronchiectasis is diagnosed when there is a lack of bronchial tapering and bronchial walls are smooth or slightly irregular (Fig. 4.46). Varicose bronchiectasis is easily recognized when bronchi are parallel to the scan plane, as the dilated bronchi have a beaded appearance (Fig. 4.47). Cystic bronchiectasis has a cystic or saccular appearance (Fig. 4.48). Air-fluid levels caused by retained secretions are sometimes seen in the dilated bronchi. Cystic and varicose bronchiectasis imply more bronchial destruction than cylindrical bronchiectasis.

Retained bronchial secretions, atelectasis, and/or mosaic perfusion, can also be seen in HRCT scans of patients with bronchiectasis. When the bronchus is perpendicular to the scan plane, retained bronchial secretions in the central lung appear as nodular or oval shaped opacities. When the bronchus is parallel to the scan plane, they are recognized as lobulated linear or branching structures. In the peripheral bronchi, retained mucus is visualized as centrilobular nodules or tree-in-bud appearance (Grenier et al. 1990). Mosaic perfusion, secondary to air-trapping and reflecting the presence of small airway disease distal to the bronchiectasis, is extremely common.

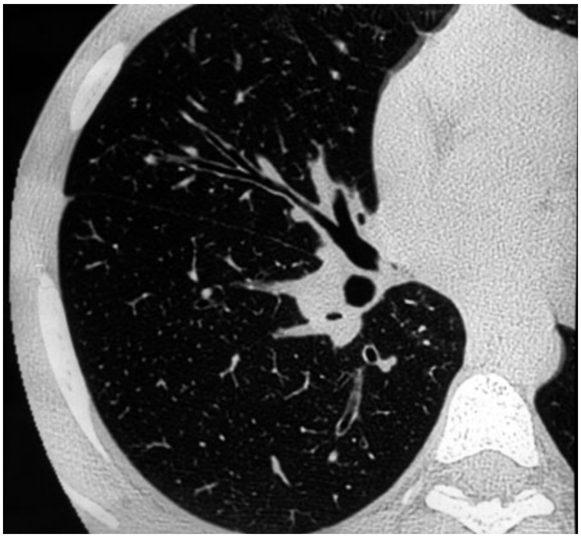

Fig. 4.46. A 14-year-old boy with cylindrical bronchiectasis in the middle lobe. Bronchi are dilated and slightly irregular

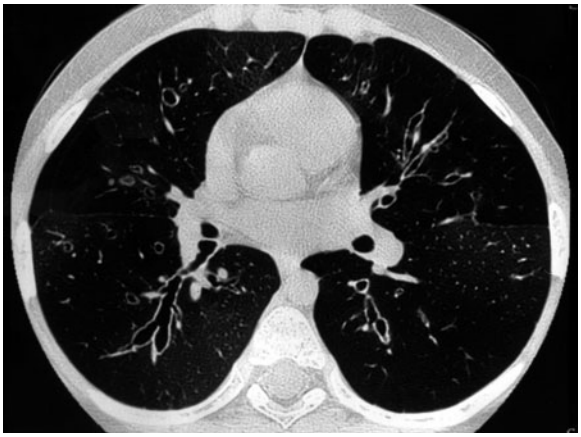

Fig. 4.47. An 11-year-old boy with varicose bronchiectasis. In the right lower lobe. Bronchi have an irregular and beaded appearance

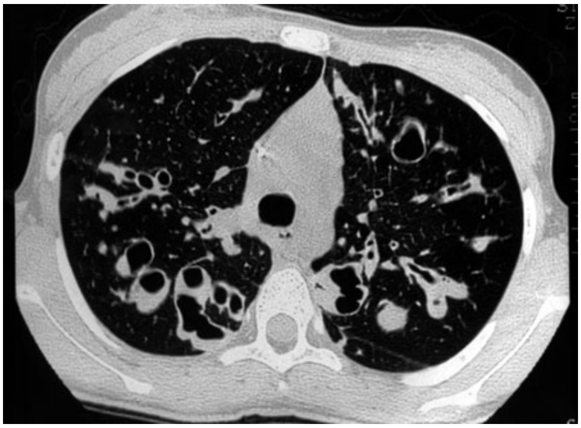

Fig. 4.48. A 14-year-old girl with cystic bronchiectasis. Saccular bronchiectasis with retained secretions are seen in both upper lobes

The pattern and distribution of abnormalities revealed by HRCT in patients with bronchiectasis are influenced by the underlying cause, and distinctive HRCT appearances have been well-described in a few conditions: cystic fibrosis, immotile cilia, allergic asthma, bronchopulmonary aspergillosis, tuberculosis and hypogammaglobulinemia (Cartier et al. 1999).

Bilateral, predominantly upper lobe bronchiectasis is seen most commonly in patients with cystic fibrosis and allergic bronchopulmonary aspergillosis, unilateral upper lobe predominance in patients with tuberculosis, and lower lobe predominance as a sequela of childhood pulmonary infections.

4.7.1.1
Cystic Fibrosis

Cystic fibrosis is the most common cause of pulmonary insufficiency in childhood (Ruzal-Shapiro 1998). HRCT and high-resolution MDCT technique have been used for the evaluation of cystic fibrosis lung disease. HRCT technique allows lower dose CT scanning and may be useful for qualitative evaluation. HRCT images at interval greater than 10 mm underestimate the severity of the disease (de Jong 2005). High-resolution MDCT is recommended for longitudinal evaluation and for quantitative evaluation (Brody et al. 2005). This opinion is not accepted by all authors. They still prefer to reduce the dose using pre-selected CT cuts (Jiménez et al. 2006). Bronchiectasis in cystic fibrosis is usually widespread, with upper lobe involvement being almost universal and both central and peripheral bronchiectasis being present in approximately two-thirds of patients. Although cystic and varicose types are not uncommon, cylindrical bronchiectasis usually predominates, particularly in young children. Peribronchial thickening, mucoid impaction and a mosaic perfusion pattern secondary to air-trapping are very common in cystic fibrosis (Fig. 4.49). Mosaic perfusion may be the initial (and only) HRCT abnormality early in the course of the disease. Mucoid impaction can present as large nodules in the central lung or as centrilobular or tree-in-bud pattern in the lung periphery. Mucus plugging may lead to lobar and segmental atelectasis. Partial or total resolution of mucus plugging is a finding that can reflect therapeutic efficacy and is useful for monitoring.

Several authors have devised scoring systems based on chest X-ray findings to assess the severity of the disease (Nathanson et al. 1991; Sockrider et al. 1994; Cleveland et al. 1998). The Brasfield method is one of the most commonly used (Brasfield et al. 1980). New scoring systems based on HRCT have been proposed (Shah et al. 1997; Brody et al. 1999; Helbich et al. 1999). The most popular is the Bhalla method (Bhalla et al. 1991), which attempts to provide an objective assessment of the severity and extension of lung disease. Dissociation between CT score and lung function was reported (de Jong et al. 2004; Brody et al. 2004). HRCT is a more sensitive technique than pulmonary function tests to detect structural changes and disease progression. However, the clinical relevance of HRCT scoring systems has not yet been demonstrated (Brody et al. 2005).

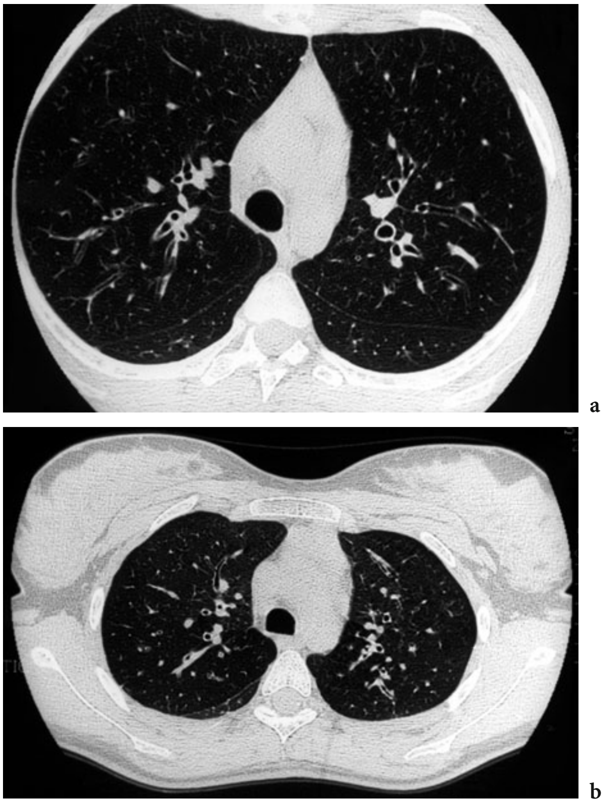

Fig. 4.49a,b. A 15-year-old girl with cystic fibrosis. HRCT detects cylindrical bronchiectasis with bronchial wall thickening (**a**). Expiratory air-trapping reflects the presence of small airways disease (**b**)

4.7.1.2
Immotile Cilia

Immotile cilia or primary ciliary dyskinesia (PCD) is a term including diseases that occur as a direct result of congenital defects in the airway cilia (Meeks and Bush 2000). The main features of PCD are recurrent sinopulmonary infections, situs inversus and subfertility. The association between chronic respiratory disease and PCD is well recognized. Kartagener's syndrome, characterized by situs inversus totalis, bronchiectasis and paranasal sinusitis accounts for 50% of all patients with PCD (Hiddema and Engelshove 1999). The radiological and clinical features of PCD are similar to those of cystic fibrosis but are less severe and progressive. Hyperinflation and bronchial thickening are the most common abnormalities. Bronchiectasis (particularly in the right middle lobe), mucus plugging (Fig. 4.50), atelectasis and consolidation are also frequent (Nadel et al. 1985; Fauré et al. 1986; Reyes de la Rocha et al. 1987).

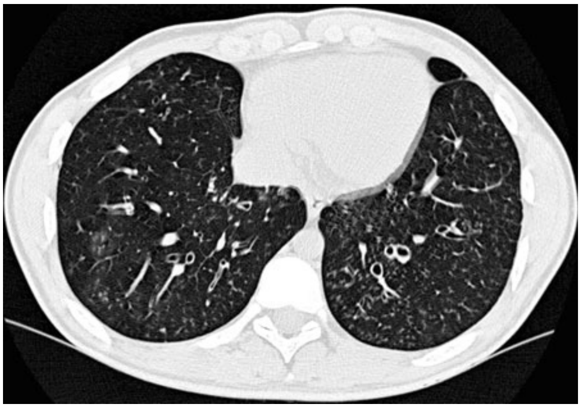

Fig. 4.50. A 15-year-old girl with primary ciliar dyskinesia. Cylindrical bronchiectasis with mucus plugging (tree-in-bud pattern) is seen in both lower lobes

4.7.2
Asthma. Allergic Bronchopulmonary Aspergillosis

Asthma is a disorder of the tracheobronchial tree characterized by inflammation, reversible airway obstruction and tracheobronchial mucosal hyperreactivity to numerous stimuli. Asthma often coexists with other allergic disorders (e.g. allergic rhinitis and atopic dermatitis). Radiography is indicated to exclude other causes of wheezing and to detect complications. Air-trapping due to small airway disease is the most common HRCT feature in children with asthma and can disappear after therapy with bronchodilators (Lucaya et al. 2000) (Fig. 4.25a–c). The sensitivity of HRCT for asthma is likely superior to pulmonary function test; patchy subsegmental involvement can be detected by HRCT even when pulmonary function tests are normal (Sharma et al. 2002). Atelectasis, particularly in the right middle lobe, is also common (Altamirano et al. 1991; Carlsen and Smevik 1999)

Other reported HRCT features include bronchial wall thickening, bronchiectasis and mucoid impaction (McLean et al. 1998; Paganin et al. 1992; Grenier et al. 1996). The pathogenesis of bronchial wall thickening in asthmatic patients is not clear. Lynch (1998) has suggested that it is due to inflammation, muscle hypertrophy and peribronchial fibrosis. The prevalence of bronchiectasis seems to be associated with disease severity (Paganin et al. 1992; Grenier et al. 1996). In contrast with adults with severe asthma, pediatric patients did not have CT evidence bronchiectasis, mucoid impaction, emphysema; but bronchial wall thickening seems to be a criterion of asthma severity in children (Marchac et al. 2002).

Central bronchiectasis associated with asthma is considered to be highly suggestive of allergic bronchopulmonary aspergillosis (ABPA) (Shah et al. 1992; Silva et al. 2004). ABPA is an immunological disorder characterized by immediate hypersensitivity due to endobronchial growth of *Aspergillus fumigatus*. In patients with IgE-mediated asthma, *A. fumigatus* may trigger an asthmatic reaction. The diagnosis of ABPA is based on a clinical history of asthma, skin test reactivity, elevated IgE and measurement of serum precipitins. The presence of randomly distributed, predominantly central, moderate to severe bronchiectasis affecting three or more lobes, bronchial wall thickening and centrilobular nodules in an asthmatic patient is highly indicative of ABPA (Ward et al. 1999; Mitchell et al. 2000).

4.7.3
Constrictive Bronchiolitis

Constrictive bronchiolitis (bronchiolitis obliterans) is a rare disease characterized by thickening of the bronchiole walls due to submucosal collagenization, with few changes in the distal parenchyma (Colby 1998). Progressive bronchiole narrowing is associated with distortion of the lumen, mucostasis and chronic inflammation. Bronchiolectasis and bronchiolar smooth-muscle hypertrophy may also be seen.

Constrictive bronchiolitis can be idiopathic or secondary to various insults, such as viral, bacterial or mycoplasma infections, bone marrow or lung transplantation, collagen vascular diseases or toxic fume inhalation (Chang et al. 1998; Lau et al. 1998;

Sargent et al. 1995; Siegel 1999). It has also been reported to occur in association with Stevens-Johnson syndrome (Kim and Lee 1996). Chest X-rays are usually normal, although hyperaeration and vascular attenuation are sometimes seen. HRCT demonstrates a mosaic perfusion pattern due to oligemia and air-trapping, which is better detected on expiratory scans. Central or peripheral bronchiectasis, bronchial thickening and mucus plugging of the centrilobular bronchioles may also be noted.

Swyer-James or Macleod's syndrome is a variant of postinfectious constrictive bronchiolitis (Marti-Bonmati et al. 1989), and is characterized by unilateral small or normal-sized hyperlucent lung with air-trapping (Stern and Samples 1992; Moore et al. 1992). It is usually the result of a viral or mycoplasma respiratory infection in early childhood. HRCT reveals unilateral hyperlucency and decreased pulmonary vascularity in all patients. Other common findings are a mosaic perfusion pattern and bronchiectasis, each of which are seen in approximately 70% of patients. Expiratory HRCT scans show air-trapping in the hyperlucent lung in all cases. Contralateral lung involvement, characterized by patchy areas of air-trapping, is present in half the patients (Fig. 4.35a,b). Bronchiectasis can be cylindrical or varicose and may be associated with collapse. Children without bronchiectasis or with cylindrical bronchiectasis had a lower incidence of pneumonia episodes than those with varicose bronchiectasis (Lucaya et al. 1998). Several authors reported that the disease might occur in various forms including partial involvement of one lung or bilateral disease (Lucaya et al. 1998; Arslan et al. 2001).

Constrictive bronchiolitis may occur after heart-lung transplantation (50% of patients) or bone-marrow transplantation (10% of patients). It is thought to be the consequence of repeated episodes of rejection. Clinically, the patients may present with cough and dyspnea. The triad of mosaic perfusion pattern, bronchial dilatation and bronchial wall thickening after lung transplantation is indicative of constrictive bronchiolitis (Fig. 4.51). A mosaic perfusion pattern without the associated bronchial changes has been observed in a large percentage of transplant patients with normal pulmonary function tests (Lau et al. 1998). In lung transplant recipients, the extent of air trapping (in excess of 32% of the parenchyma) seems to be very suggestive of constrictive bronchiolitis (Bankier et al. 2001).

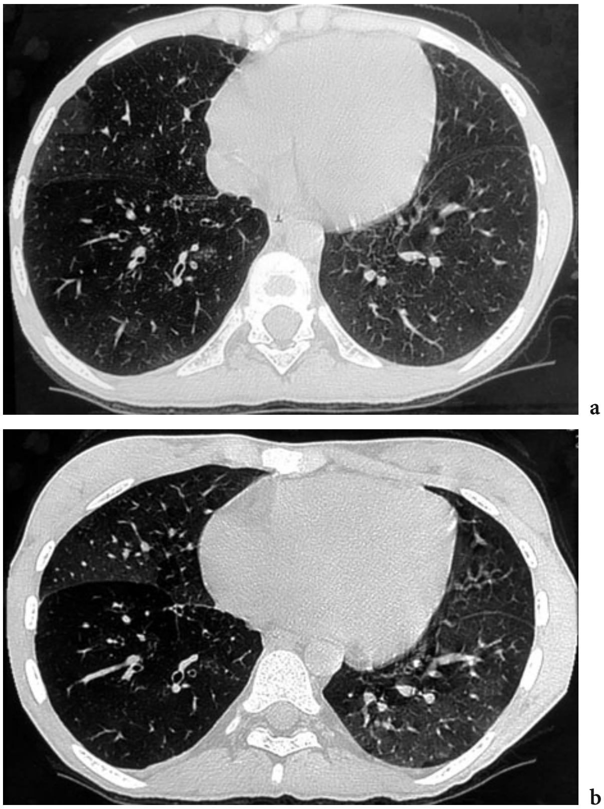

Fig. 4.51a,b. A 17-year-old girl with constrictive bronchiolitis after heart-lung transplantation. Bronchial dilatation in the right lower lobe with bronchial wall thickening are seen on inspiratory HRCT (**a**). Mosaic perfusion is better seen on expiratory HRCT (**b**)

4.7.4
Bronchiolitis Obliterans Organizing Pneumonia

Bronchiolitis obliterans organizing pneumonia (BOOP) is characterized pathologically by the presence of granulation tissue within the lumen of bronchioles and alveolar ducts and associated patchy areas of organizing pneumonia. BOOP rarely occurs in children. It may be idiopathic but is more commonly seen in children after chemotherapy. It can also occur after bone marrow transplantation or as a response to toxic inhalents, drugs, or viral, mycoplasmal or bacterial infection (Inoue et al. 1996; Mathew et al. 1994; Kleinau et al. 1997). The main symptoms are cough, dyspnea, fever and weight loss. Physical examination is unremarkable except for crackles on auscultation of the lungs. Pulmonary function tests show a restrictive ventilatory defect with impaired gas transfer.

The HRCT findings in BOOP most commonly consist of patchy consolidation or ground glass opacities, often with a subpleural and/or peribronchial distribution (Müller et al. 1990; Flowers et al. 1992; Akira et al. 1998) (Fig. 4.24). Peripheral nodular opacities, irregular linear opacities, bronchial wall thickening and dilatation, and small pleural effusions may also be present (Webb et al. 1996; Lee et al. 1994a). Although nonspecific, the HRCT findings can suggest the diagnosis and help to select the site for biopsy.

In adults, a new classification and terminology is now preferred. The preferred term is organizing pneumonia. Organizing pneumonia is defined pathologically by the presence in the distal airspaces of buds of granulation tissue progressing from fibrin exudates to loose collagen containing fibroblast. The lesions occur predominantly within alveolar spaces but are associated with buds of granulation tissue occupying the bronchiolar lumen (Cordier 2000). The organizing pneumonia, in adult population, is often secondary to a known cause (rheumatoid arthritis, viral pneumonia, dug reactions). The term cryptogenic organizing pneumonia is used when histologic features are demonstrated and the cause is idiopathic (Wittram et al. 2003; Ujita et al. 2004). This new terminology is not widely used in the pediatric literature.

4.8
HRCT Findings in Specific Diseases

4.8.1
Chronic Diffuse Infiltrative Lung Disease

A specific diagnosis of chronic diffuse infiltrative lung disease (CDILD) is essential to prescribe treatment. The diagnosis is based on clinical information, pulmonary function tests, bronchoalveolar lavage and chest imaging. Studies in adults have demonstrated the superiority of HRCT over radiography for obtaining the correct diagnosis of CDILD because many of these patients have distinguishing features (characteristic appearances and distributions) when evaluated with this technique (Grenier et al. 1994; Lee et al. 1994b; Bonelli et al. 1998; Swensen et al. 1997). According to recent publications the same results were obtained in children (Lynch et al. 1999; Copley et al. 2000; Koh and Hansell 2000). In some cases, lung biopsy can be avoided. HRCT can also be useful to determine the optimal site for biopsy and to assess the extent of the disease. Because CDILD is uncommon in children, the applications of HRCT are less developed. Our experience suggests that HRCT contributes to the diagnosis and monitoring of pediatric CDILD.

4.8.1.1
Langerhans' Cell Histiocytosis

Infiltration and accumulation of monocytes and large histiocytes in various tissues and organs characterize the histological appearance of Langerhans' Cell Histiocytosis (LCH). Pulmonary involvement is present in 23%–50% of the children with the multisystemic form (Smets et al. 1997; Odame et al. 2006). Localized LCH is the mildest and most common form (70% of all cases) and involves either bone or lung. The lung is the second most common site of LCH (Sminiotopoulos et al. 1999). HRCT detects peribronchial or peribronchiolar granulomas, usually 1–10 mm in diameter; larger nodules are less common. These nodules can disappear or cavitate (Brauner et al. 1989b) and become thick-walled cysts that can progress to thin-walled cysts (Brauner et al. 1997) (Fig. 4.52).

Thick or thin walled pulmonary cysts are the main feature of LCH. They may be round or irregularly shaped, probably due to the fusion of several cysts (Fig. 4.53). LCH lesions are mostly found in the upper and middle lung zones. The costophrenic angles are generally spared (Moore et al. 1989). Rupture of subpleural cysts may cause pneumothorax (Fig. 4.54). Pneumothorax occurs in up to 25% of patients over the course of their disease (Abbott et al. 2004). In children, LCH lesions may remain stable over long periods or progress rapidly, leading to destruction of the pulmonary parenchyma within a few weeks or months after diagnosis (Seely et al. 1997). In our experience, patients with a poor lung involvement are asymptomatic.

Thymic involvement associated with parenchymal lesions has been also reported (Donnelly 2000). In the multisystemic form of LCH pulmonary involvement does not mean that the disease is more severe or suggests a poorer prognosis (Smets et al. 1997; Braier et al. 2004), yet it may influence the choice of treatment.

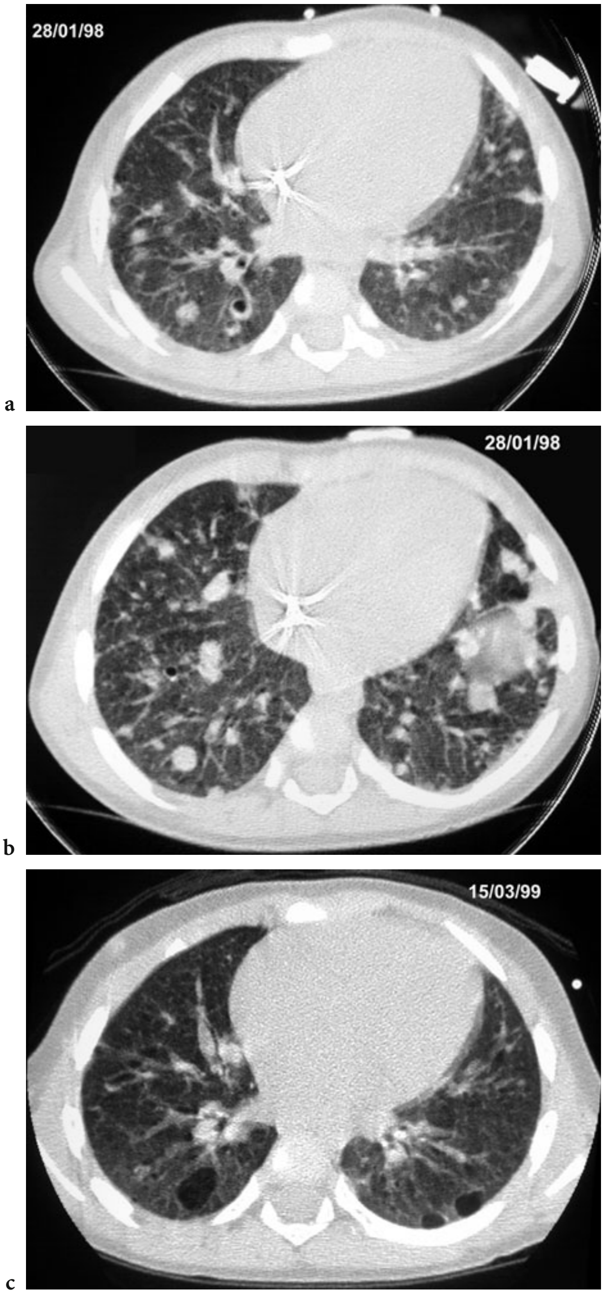

Fig. 4.52a–c. A 14-month-old girl with Langerhans‘ cell histiocytosis. Initial HRCT (**a**,**b**) shows nodules and small cystic lesions. Follow-up HRCT (**c**) at the age of 30 months shows larger cystic lesions

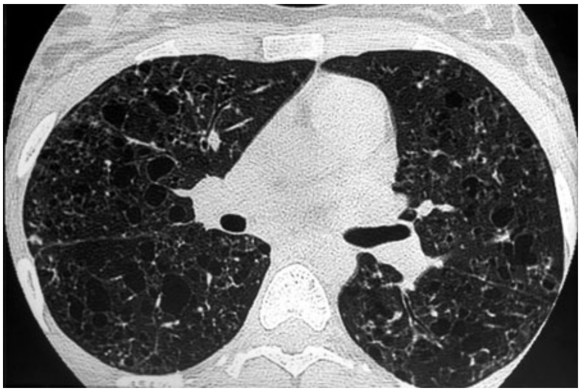

Fig. 4.53. A 16-year-old girl with Langerhans‘ cell histiocytosis. HRCT shows thick- and thin-walled cysts; a few micronodules are also seen

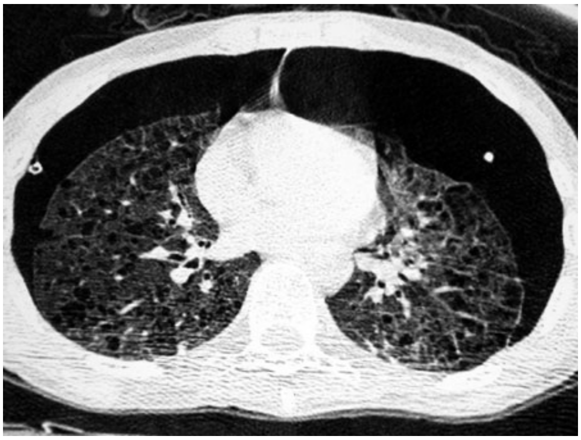

Fig. 4.54. A 15-year-old boy with Langerhans‘ cell histiocytosis, with multiple skin lesions, diabetes insipida and recurrent bilateral pneumothoraces. Chest CT shows multiple pulmonary cystic lesions, some located subpleurally, and bilateral pneumothorax

4.8.1.2
Extrinsic Allergic Alveolitis

Extrinsic allergic alveolitis (EAA) is caused by the repeated inhalation of particulate organic antigens. Farmer‘s lung is the best-known EAA syndrome and is a rare entity in young children (Stauffer et al. 2006). The development of EEA requires massive acute or prolonged low-grade exposure. Many inhaled responsible antigens have been described, including animal and plant proteins and fungal microorganisms (thermophilic actinomycetes). Extrinsic allergic alveolitis is divided into acute, subacute and chronic forms (Vincent et al. 1992). The diagnosis of EAA in its earliest stages is controversial and remains primarily clinical. Symptoms occur 4–8 h after exposure, and include shortness of breath, dry cough, malaise and fever. Subacute and chronic forms have an insidious onset with progressive shortness of breath and cough.

HRCT abnormalities are very suggestive of the disease and depend on the stage of the disease. HRCT could be useful to evaluate the inflammatory activity of the disease (Sterclova et al. 2006). HRCT could allow the diagnosis in asymptomatic family members of an index case (Ceviz et al. 2006). HRCT is rarely performed in the early stage. In the acute and subacute stages EAA presents as airway disease characterized by small poorly defined centrilobular nodules (<5 mm in diameter) and areas of ground glass (Hansell and Moskovic 1991) (Fig. 4.55). Ground-glass opacities are slightly more marked in the middle and lower lung zones. Areas of decreased attenuation and air-trapping, consistent with small airway disease, are also common findings (Small et al. 1996).

Chronic EAA is characterized by fibrosis that seems to spare the lung bases.

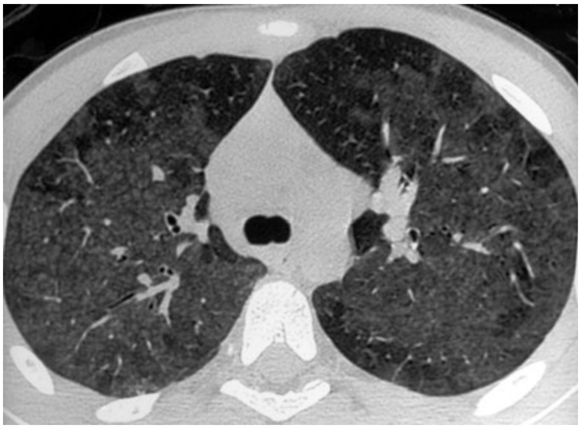

Fig. 4.55. A 12-year-old boy with extrinsic allergic alveolitis. HRCT shows small, ill-defined rounded opacities with patchy ground-glass opacities

4.8.1.3
Sarcoidosis

Sarcoidosis is a chronic granulomatous disorder of unknown etiology. It is uncommon in children and occurs most often in young adults (Pattishall and Kendig 1996). The majority of pediatric patients are 9–18 years of age (Grossman et al. 1985). Prognosis in is more severe in younger children and in case of multi-organ involvement (Fauroux and Clément 2005) Respiratory symptoms include cough, dyspnea and, sometimes, chest pain. Mediastinal and/or bilateral hilar adenopathy, often isolated, is the most common intrathoracic finding in sarcoidosis. The characteristic HRCT finding consists in small 2–10-mm nodules with irregular margins distributed along the lymphatics in the bronchovascular sheath and in the interlobar septa and pleura. This distribution can produce a beaded appearance of the bronchovascular bundles and interlobular septa and fissural nodularity (Brauner et al. 1989a; Dawson and Müller 1990; Traill et al. 1997) (Fig. 4.56).

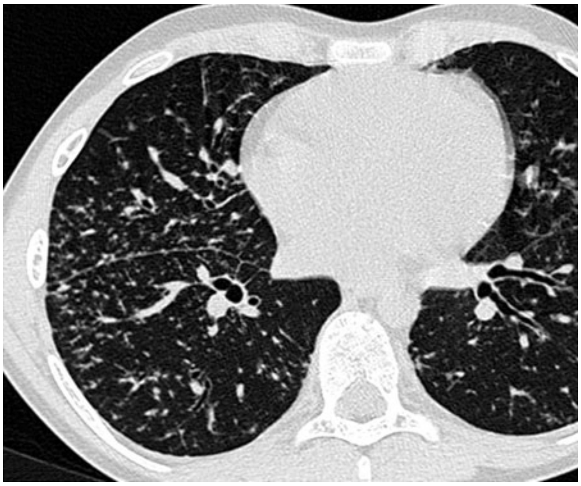

Fig. 4.56. An 11-year-old boy with sarcoidosis. HRCT detects small nodules in a perilymphatic distribution (note the beaded appearance of the bronchovascular bundles and subpleural nodularity)

Confluence of granulomas may result in large opacities with poorly defined contours, or areas of frank consolidation. Air-bronchograms may be seen within these opacities. Large nodules can cavitate, but this is uncommon. Patchy areas of ground-glass opacity may also be present and may be due to the presence of numerous sarcoid granulomas below the resolution of HRCT (Nishimura et al. 1995). Ground-glass opacities, architectural distortion, displacement of interlobar fissures, traction bronchiectasis, cystic air spaces and honeycombing are signs of advanced disease with fibrosis (Abehsera et al. 2000). Posterior displacement of the main or upper lobe bronchus is a classical finding, which indicates loss of volume in the posterior segment of the upper lobes.

HRCT could assess the severity of the disease. The appearance and the extent of the disease on HRCT (thickening of the bronchovascular bundle, intra-parenchymal nodules, septa and non-septal lines and focal pleural thickening are associated with parameters of respiratory functional impairment (Drent et al. 2003).

4.8.1.4
Pulmonary Alveolar Proteinosis

Pulmonary Alveolar Proteinosis (PAP) is a rare intrinsic lung disease characterized by alveolar filling with amorphous lipoproteinaceous material (Schumacher et al. 1989). The cause of alveolar proteinosis is unclear. One possible cause may be dysfunction of intralveolar macrophages, another cause relates to an abnormal surfactant C protein function which predisposes certain patients to diffuse lung disease (Nowers et al. 2002). Plain films show alveolar infiltrates, a reticulonodular pattern or both. Pleural effusion and adenopathy are absent (McCook et al. 1981). HRCT shows areas of consolidation or ground glass, often with a geographic distribution, and/or widespread miliary nodules (Godwin et al. 1988; Murch and Carr 1989; Albafouille et al. 1999) (Fig. 4.57). Smooth thickening of the interlobular septa within the areas of air space disease resulting in a crazy paving appearance (Fig. 4.44) is suggestive of, but not specific to, alveolar proteinosis (Franquet et al. 1999; Coullier et al. 1999; Johkoh et al. 1999b; Rossi et al. 2003).

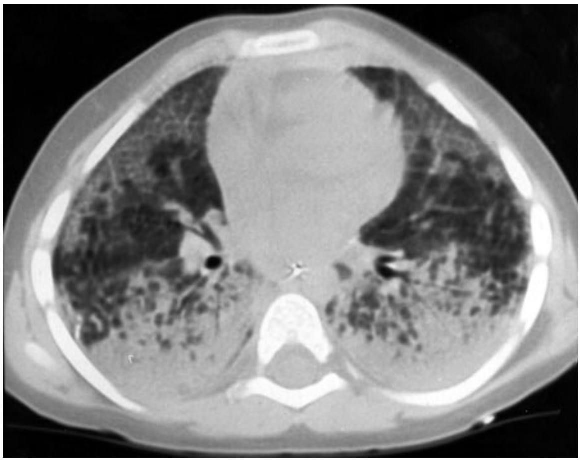

Fig. 4.57. A 3-year-old boy with biopsy-proven pulmonary alveolar proteinosis. Despite the 5-mm slice thickness alveolar consolidation and alveolar infiltrates are clearly visualized

4.8.1.5
Pulmonary Fibrosis and Chronic Interstitial Pneumonias

Pulmonary fibrosis is a chronic inflammatory interstitial lung disorder, characterized by an initial accumulation of inflammatory and immunoregulatory cells in the pulmonary interstitium and the alveolar space. Inflammation leads to modification of the alveolar structures with progression to interstitial fibrosis and thickening of alveolar walls. In children, pulmonary fibrosis is the result of a heterogeneous group of disorders that share common histological features (Osika et al. 1997). The known causes include infectious disorders, reactions to environmental exposures, drugs, collagen-vascular disorders or gastroesophageal reflux with chronic aspiration. For idiopathic pulmonary fibrosis (IPF), classification by histological features into usual interstitial pneumonitis (UIP) and desquamative interstitial pneumonitis (DIP) has been proposed. The distinction between these two forms of fibrosing alveolitis is now questioned (UIP and DIP can be seen simultaneously). These entities may represent different stages of a lung injury (Webb et al. 1996) with associated thickening of alveolar walls and many mononuclear cells in the alveolar space.

Because of the rarity of these entities in children, most HRCT findings have been reported in adults. On HRCT, the main sign in DIP is the presence of bilateral and symmetric areas of ground-glass opacity (the predominant lesion in DIP is alveolar spaces filled with macrophages) (Hartman et al. 1993). The ground-glass areas of attenuation are seen mainly in lower lung zones. Other findings in DIP are those of UIP: reticular opacities, which correspond to areas of irregular fibrosis, honeycombing and traction bronchiectasis (Nishimura et al. 1992). Less common HRCT findings include discrete nodules and interlobular septal thickening. Mild enlargement of mediastinal lymph nodes is commonly seen, whereas large lymph nodes are uncommon.

The main HRCT findings of IPF in children are areas of ground-glass attenuation involving mostly the subpleural regions Seely et al. (1997). Large subpleural air cysts in the upper lobes adjacent to areas of ground-glass opacities seem to be unique to childhood IPF. These cysts are interpreted as paraseptal or irregular emphysema (Fig. 4.58). Intralobular lines, irregular interlobular septal thickening and honeycombing seem to be less common findings and, thus, less contributive to diagnosis.

Recently, two new forms of idiopathic interstitial pneumonia have been described: acute interstitial pneumonia (AIP) (Katzenstein et al. 1986) and nonspecific interstitial pneumonia and fibrosis (NIPF) (Katzenstein and Fiorelli 1994).

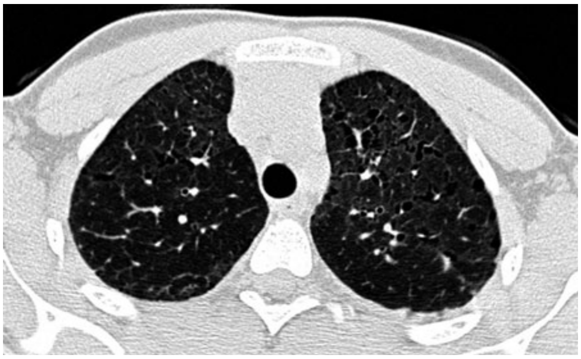

Fig. 4.58. A 13-year-old boy with biopsy-proven idiopathic pulmonary fibrosis. HRCT shows ground-glass attenuation, intralobular lines and air cysts and involving mostly the subpleural regions

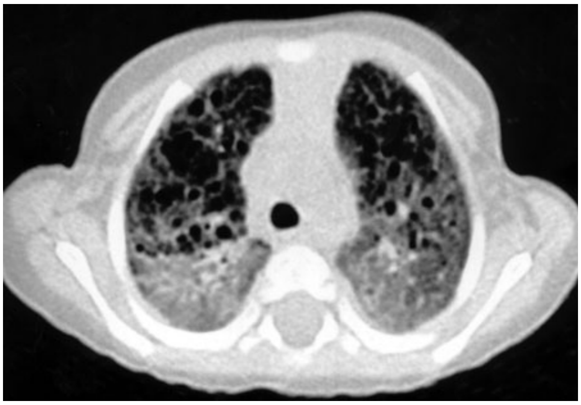

Fig. 4.59. A 10-month-old female infant with biopsy-proven non-specific interstitial pneumonitis. HRCT shows ground glass and honeycombing. [Reprinted with permission from Copley et al. 2000]

AIP is a fulminant disease of unknown etiology that is histologically characterized as diffuse alveolar damage. The latter manifests as injury to the alveolar lining and endothelial cells, pulmonary edema, hyaline membrane formation and, later, proliferative changes involving alveolar and bronchiolar lining cells, and interstitial cells. The histologic appearance of AIP can be separated into acute exudative, subacute proliferative and chronic fibrotic phases. The radiological finding on chest radiographs is progressive parenchymal consolidation. HRCT images include diffuse air-space consolidation and patchy or diffuse ground-glass opacities, traction bronchiectasis and, occasionally, focal honeycombing (Primack et al. 1993; Ichikado et al. 1997). These findings are usually bilateral, symmetrical, and basilar in distribution. Ground-glass opacities are seen in all three histological phases and reflect different histological findings. During the acute exudative phase, they reflect the presence of alveolar septal edema and hyaline membranes along the alveolar walls. During the subacute proliferative phase, ground-glass opacities are due to intraalveolar and interstitial organization. During the fibrotic phase, ground-glass attenuation results from alveolar septal fibrosis. Bronchiectasis within areas of ground-glass attenuation may correspond to fibrosis and its severity (Johkoh et al. 1999a, c).

NIPF describes the group of interstitial pneumonias that cannot be classified as UIP, DIP, AIP or BOOP. NIPF is essentially a diagnosis of exclusion. It is characterized by varying degrees of interstitial inflammation and fibrosis that persist (Müller and Colby 1997). Copley et al. (2000) reported six cases of NIPF in children. In three of them, HRCT showed a predominantly upper-zone honeycomb pattern with parenchymal distortion superimposed on a background of widespread ground-glass opacification (Fig. 4.59). For the other three patients with NIPF, one had widespread ground-glass opacification, honeycombing with mid- and lower-zone predominance, and traction bronchiectasis; another had widespread ground-glass opacification; and the last one had widespread ground-glass opacification with peripheral consolidation. None of the patients had interlobular septal thickening.

Genetic studies will perhaps help us to better understand these entities in children. Recently, mutations in the gene encoding surfactant protein C associated with familial interstitial lung disease have been identified in familial cases (Nogee et al. 2001). Few authors report familial cases of NIPF and UIP with mutation in surfactant protein C (Thomas et al. 2002; Chibbar et al. 2004).

4.8.1.6
Lymphocytic Interstitial Pneumonia (LIP)

LIP is a benign lymphoproliferative disorder described by Liebow and Carrington (1973) and characterized by pulmonary infiltration of lymphocytes and plasma cells. LIP occurs in patients who have systemic disorders, such as Sjögren's syndrome, multicentric Castleman's disease or acquired immunodeficiency syndrome (AIDS). In children, LIP has been reported to be frequently associated with AIDS. In a series of 77 human immunodeficiency virus positive (HIV+) children evaluated by Amorosa et

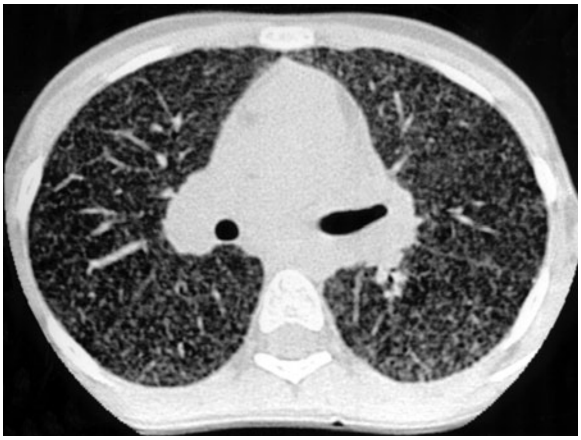

Fig. 4.60. A 13-year-old girl with biopsy-proven lymphocytic interstitial pneumonia. The patient was immunocompromised because of postviral neutropenia. HRCT shows profuse nodules with random distribution. [Reprinted with permission from Copley et al. 2000]

al. (1992), 32 were diagnosed as having LIP. The appearance of LIP on chest radiography is nonspecific and includes a fine reticular pattern and nodular opacities or a diffuse confluent pattern. HRCT findings include extensive bilateral ground-glass attenuation, focal air-space consolidation, ill-defined, micronodules with a perilymphatic distribution, and thin-walled cystic lesions (Carignan et al. 1995; McGuinness and Naidich 1995; Becciolini et al. 2001) (Fig. 4.60). Associated bronchiectasis and hilar or mediastinal lymphadenopathy may be present (Johkoh et al. 1999b). No pleural effusion is seen in LIP.

4.8.1.7
Pulmonary Lymphangitic Carcinomatosis

Pulmonary lymphangitic carcinomatosis (PLC) refers to tumor growth in the lymphatics of the lung. The histological findings are characterized by thickening of the interlobular septa and the peribronchovascular interstitium. In most cases, the primary tumor disseminates hematogenously to the lungs and secondarily penetrates vessel walls and invades the surrounding interstitium and lymphatics. In children PLC is uncommon but can occur in lymphoma, thyroid carcinoma, sarcoma and neuroblastoma (Kuhn 1993). In our experience, PLC was most common in lymphoma.

Chest X-ray findings are normal or show nonspecific findings in many patients with PLC (Munk et al. 1988). HRCT findings (Johkoh et al. 1992) correlate well with the two types of lymphatic drainage systems described by pathologists. Axial drainage is seen on HRCT as smooth or nodular peribronchovascular interstitial thickening in the parahilar lung and enhanced visibility of the branching arteries in the pulmonary lobule. Peripheral drainage (interlobular and subpleural) is seen as interlobular septal thickening or as thickening of fissures, which may be smooth or nodular. HRCT abnormalities can be focal, unilateral or diffuse (Fig. 4.29, 4.61). Despite axial and peripheral interstitial abnormalities, lung architecture remains normal, a finding that is useful to differentiate between PLC and sarcoidosis.

4.8.1.8
Collagen-Vascular Disease and Pulmonary Vasculitis

Pulmonary vasculitis can be due to primary systemic vasculitides, such as Wegener‘s granulomatosis, Churg-Strauss angiitis or microscopic polyangitis. In addition, pulmonary vasculitis may accompany systemic connective tissue disease, including systemic lupus erythematosus, dermatomyositis or systemic sclerosis. Connolly et al. (1996) identified a pattern on HRCT of perivascular, centrilobular, ill-defined densities in eight children with vasculitis. In the appropriate clinical setting this pattern indicates pulmonary involvement and may obviate the need for lung biopsy.

Collagen-vascular disease, especially progressive systemic sclerosis (PSS), is commonly associated with pulmonary fibrosis in children. Seely et al. (1998) described a series of 11 patients with PSS who had interstitial lung disease. HRCT revealed abnormality in 91% of the patients. The main features were ground-glass opacities, subpleural micronodules, non-septal linear opacities, honeycombing and subpleural cysts. HRCT was able to demonstrate interstitial lung disease in 53% of patients with lupus erythematosus (Fenlon et al. 1996) (Fig. 4.62). Juvenile rheumatoid arthritis, on the other hand, seldom leads to pulmonary fibrosis in children (Seely et al. 1998). The HRCT pattern of fibrosis associated with collagen-vascular disease is similar to that of idiopathic pulmonary fibrosis and consists predominantly of areas of ground-glass involving mostly the subpleural lung regions, large and thin-walled cysts or bullae in the affected upper-lung zones, and smooth or irregular intralobular septal thickening.

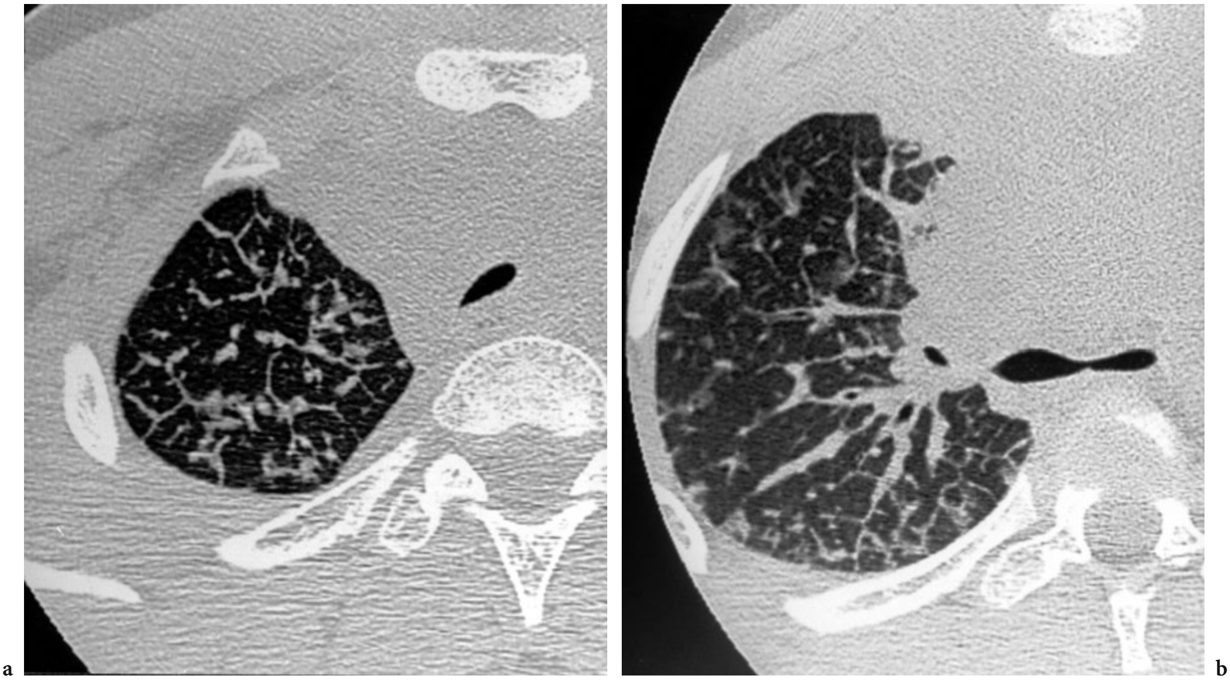

Fig. 4.61a,b. A 14-year-old boy with Hodgkin's disease. HRCT shows thickening of the interlobular septa (**a**), smooth peribronchovascular interstitial thickening (**b**), and ground-glass attenuation

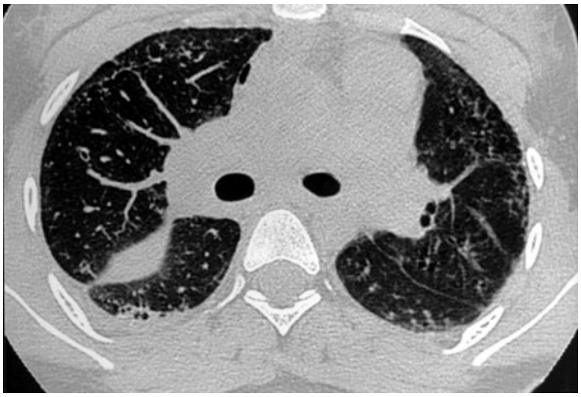

Fig. 4.62. A 16-year-old girl with systemic lupus erythematous. HRCT shows honeycombing, predominantly in the periphery, and pleural effusion. Note the right pneumomediastinum

4.8.1.9
Pulmonary Lymphangiectasia

According to Noonan et al. (1970), pulmonary lymphangiectasia can be divided into three groups. In the first, pulmonary lymphangiectasia is part of a generalized disease, the major clinical manifestations being related to the intestinal involvement. The pulmonary involvement is less severe and is associated with a much better prognosis than for the following two groups. In the second group with associated heart disease, dilatation of the lung lymphatics occurs secondary to obstruction of pulmonary venous flow. The third group, termed congenital pulmonary lymphangiectasia (CPL), includes patients with a primary developmental defect of lung lymphatics, which are dilated. Histological examination is characterized by subpleural, interlobar, perivascular and peribronchial lymphatic dilatation. Radiological findings include bilateral pulmonary hyperinflation and a reticulonodular pattern throughout the lung fields. Occasional small cystic areas, representing aerated distal bronchial and alveolar ducts, may also be present. Pleural effusion and pneumothorax may be associated. Unilateral or lobar involvement has been reported (Verlaat et al. 1994; Li et al. 1985; Rettwitz-Volk et al. 1999).

Prolonged survival of patients with CPL is rare. The chest radiograph and HRCT findings in survivors have recently been reviewed by Chung et al. (1999). Chest radiograph findings include increased interstitial markings, hyperinflation that generally increases with age, pleural effusion and pectus excavatum. The presence of patchy subpleural or perihilar ground glass opacities that are fixed in location and tend to decrease with time was the most characteristic HRCT feature. Hyperinflation and interstitial thickening were often seen.

4.8.1.10
Lymphangiomatosis and Gorham's Disease

Lymphangiomatosis, a malformation of the lymphatic system, is a very rare entity that occurs mainly in children and adolescents. It is believed to be caused by either a developmental defect or obstruction of the lymphatic channels. The main abnormalities seen on HRCT are thickening of the interlobular septa and vascular bundles, and areas of ground glass opacification (Swensen et al. 1995). Bilateral pleural effusions or smooth thickening of the pleura and increased attenuation of the mediastinal fat are also seen in most patients (Mitchell et al. 1993; Dutheil-Doco et al. 1997). Chest involvement in Gorham's or "vanishing bone" disease, in which there is replacement of a single or several contiguous bones by lymphangiomatous tissue, may present with severe and progressive osteolysis associated with septal thickening (Fig. 4.63) and chylothorax (Konez et al. 2000).

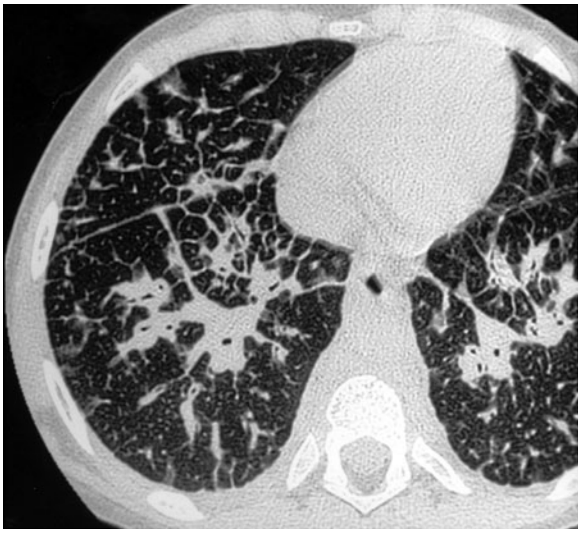

Fig. 4.63. A 6-year-old girl with Gorham's disease. Note the prominent diffuse smooth septal thickening, bronchovascular bundles and ground-glass attenuation

4.8.1.11
Pulmonary Hemorrhage

Pulmonary hemorrhage is frequently found in children with idiopathic hemosiderosis (Kiper et al. 1999; Koh and Hansell 2000) and may also be seen in systemic lupus erythematosus, Wegener's granulomatosis and Goodpasture's syndrome (Ramirez et al. 1984; von Vigier et al. 2000). Pulmonary hemorrhage appears on HRCT as patchy, frequently bilateral areas of ground-glass attenuation or consolidation (Fig. 4.64). Idiopathic hemosiderosis is characterized by recurrent pulmonary hemorrhages. The etiology remains unknown and prognosis is poor since pulmonary fibrosis develops rapidly (Primack et al. 1995) (Fig. 4.65).

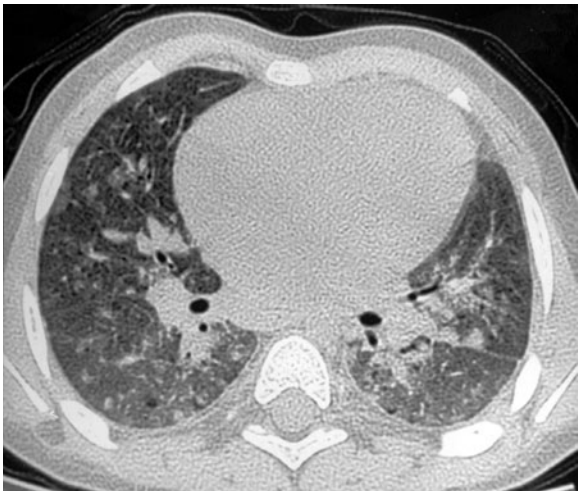

Fig. 4.64. A 3-year-old girl with hemosiderosis. HRCT shows ground-glass attenuation due to pulmonary hemorrhage

4.8.1.12
Pulmonary Alveolar Microlithiasis

Pulmonary alveolar microlithiasis (PAM) is characterized by calcium deposits within the alveoli of both lungs with a predominantly symmetrical middle- and lower-lung zone distribution. The etiology is unknown, but evidence supporting an autosomal recessively inherited defect is accumulating (Wallis et al. 1996). HRCT findings are ground-glass opacities and tiny calcifications along the bronchovascular bundles, pleura and interlobular septa (Cluzel et al. 1991). Parenchymal calcifications are described as nodular in adults and as micronodular in children. Parenchymal and subpleural cysts have also

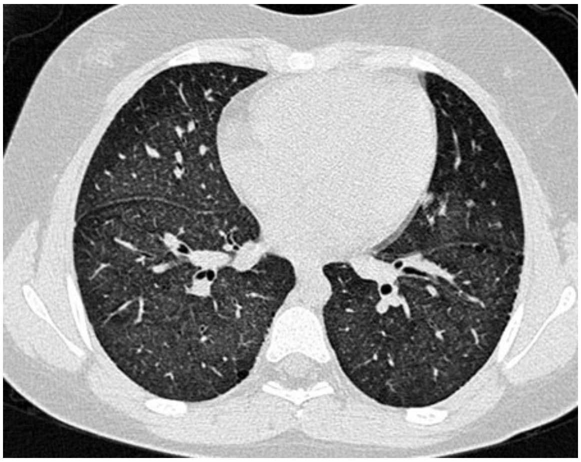

Fig. 4.65. An 11 year-old-girl with hemosiderosis. HRCT shows ground glass attenuation and air cysts, involving subpleural regions

been reported as signs of fibrosis in PAM. However, in the two pediatric cases studied by Helbich et al. (1997), no intraparenchymal cysts were seen. In PAM a proportional relationship between profusion of micronodules and parenchymal alterations is found and a correlation between the parenchymal alterations and the degree of pulmonary function loss (Deniz et al. 2005).

4.8.1.13
Pulmonary Gaucher's Disease

Gaucher's disease is a genetic disorder characterized by beta-glucocerebrosidase deficiency with secondary accumulation of glucocerebrosides in the reticuloendothelial system. The liver, spleen, bone marrow, brain and lungs may be involved. Three clinical forms have been described. In the adult form (type I), the central nervous system is intact and pulmonary involvement is rare. The infantile form (type II) is characterized by early CNS involvement and death within two years. The juvenile form (type III) is a subacute variant of the disease that comprises cases with combined involvement of the CNS and other organs. Pulmonary involvement is not unusual in the infantile form but is particularly rare in the adult form. However, HRCT pulmonary findings have only been reported in the adult type (Tunaci et al. 1995; Aydin et al. 1997; Yassa and Wilcox 1998). These include interlobular and intralobular septal thickening, ground-glass opacities, and small nodules within the secondary lobules. Thickening of the septa reflects infiltration of the pulmonary interstitium by Gaucher cells (Fig. 4.66). Ground-glass opacities may indicate interstitial or intra-alveolar involvement and micronodules are probably due to accumulation of Gaucher cells within airspaces. Similar HRCT features have been reported in patients with Niemann-Pick disease (Fig. 4.67) (Feretti et al. 1996).

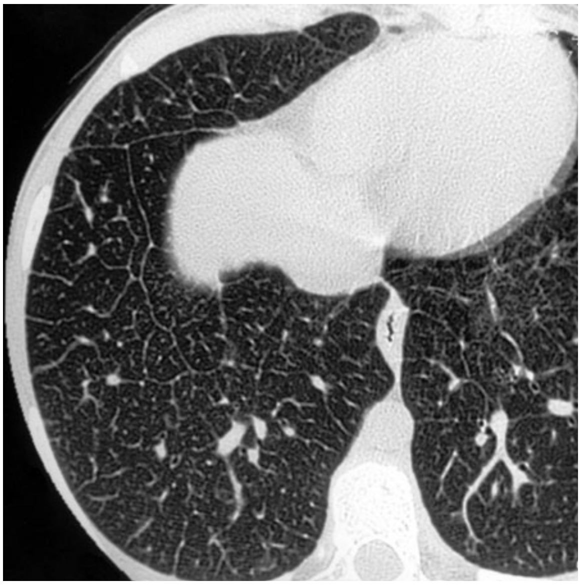

Fig. 4.66. A 13-year-old girl with Gaucher's disease. Interlobular septal and intralobular interstitial thickening are seen on HRCT

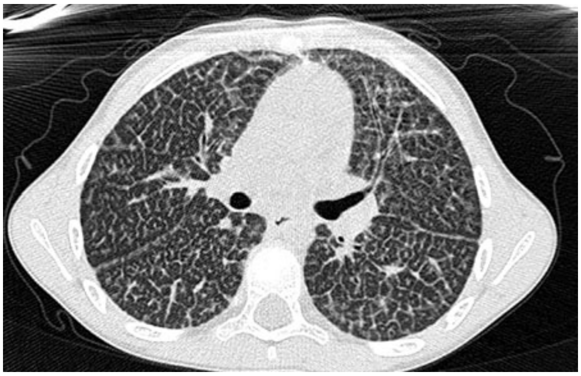

Fig. 4.67. A 7-year-old-boy with Niemann-Pick. HRCT shows a crazy paving pattern (ground glass attenuation with superimposed interlobular septal thickening)

4.8.1.14
Bronchopulmonary Dysplasia

Bronchopulmonary dysplasia (BPD) occurs in premature infants and as the chronic sequela of lung disease (mostly surfactant deficiency) and its treatment. In the early phase HRCT shows thickening of the peribronchial and interlobular interstitium, subpleural parenchymal bands and hyperexpanded cyst-like areas, corresponding to hyperaerated lung and atelectatsis, that give the lung a "cobblestone" appearance (Fig. 4.4). In most survivors of BPD respiratory symptoms and radiologic abnormalities show a slow but continuous improvement. After the age of 2 years HRCT scans in children who have had BPD will be abnormal and characterized by the presence of a mosaic attenuation pattern due to air-trapping, parenchymal bands, thickened interlobular septa, peripheral wedge-shaped subpleural opacities, and architectural distortion (Fig. 4.4, 4.30) (Oppenheim et al. 1994; Aquino et al. 1999). In the experience of Aquino, the correlation between these findings and physiologic evidence of air-trapping and obstructive lung disease was statistically significant. The HRCT features of BPD in older children may resemble those seen in constrictive bronchiolitis. Whereas parenchymal bands and architectural distortion are more common in BPD, bronchiectasis is significantly more frequent in constrictive bronchiolitis.

4.8.2
Air-Space Diseases

4.8.2.1
Invasive Pulmonary Aspergillosis

Invasive pulmonary aspergillosis is a common complication in immunocompromised patients (acute leukemia with neutropenia, organ transplantation, use of immunosuppressive drugs, …) (Bomelburg et al. 1992; Taccone et al. 1993). The invasive form is characterized by occlusion of large or medium caliber arteries by plugs of hyphae. Lesions caused by Aspergillus microorganisms are endobronchial at the beginning followed by transbronchial vascular invasion.

Radiographic findings are initially nonspecific: patchy nodular opacities or lobar-type air-space disease. The two most common HRCT findings of invasive pulmonary aspergillosis are segmental consolidation with surrounding ground-glass attenuation and nodules surrounded by a halo corresponding to pulmonary hemorrhage (Logan et al. 1994; Thompson et al. 1995). These two signs are not specific and have been reported in other entities, such as mucormycosis, lymphoma, organizing pneumonia and pulmonary hemorrhage (Won et al. 1998).

Cavitation occurs in half of the cases as a consequence of pulmonary infarction and increased granulocytic response associated with bone-marrow recovery. The cavitation process is characterized on HRCT by the air-crescent sign (Fig. 4.68), which represents air between retracted infarcted lung and the adjacent parenchyma. In the appropriate clinical setting though this sign is suggestive, but not diagnostic, of the disease. It may be seen in other diseases, such as tuberculosis, actinomycosis, bacterial abscess or septic emboli.

4.8.2.2
Pneumocystic Carinii Pneumonia (PCP)

PCP is the most common pulmonary opportunistic infection in immunosuppressed children, occurring in up to 90% of HIV+ patients during the course of their illness (Sivit et al. 1995).

Radiographically, PCP presents as diffuse bilateral, progressively coalescing pulmonary infiltrates. In about 10%–20% of microbiologically documented cases, the chest radiograph remains normal.

HRCT is considered to be more sensitive than chest radiography for the detection of early parenchymal disease. HRCT findings include patchy air-

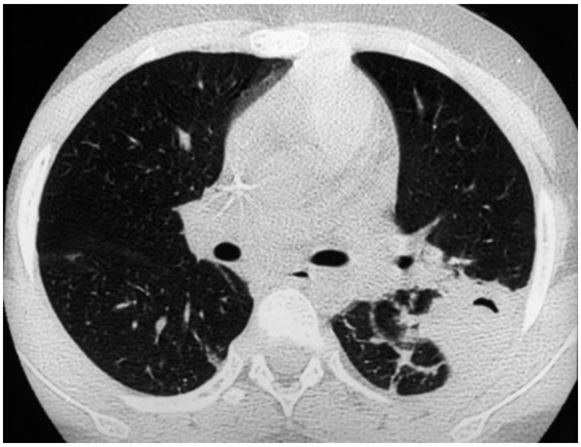

Fig. 4.68. A 7-year-old girl with acute leukemia and invasive pulmonary aspergillosis. HRCT shows pulmonary consolidation with an air crescent sign

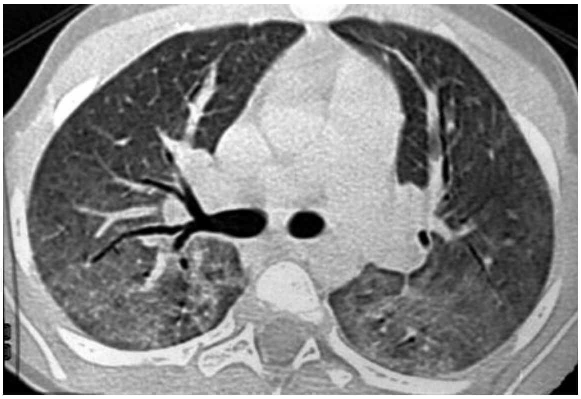

Fig. 4.69. A 6-year-old HIV+ girl with *Pneumocystis carinii* pneumonia. Diffuse homogeneous ground-glass opacities are seen on the HRCT scan

space disease with a geometric or mosaic pattern and diffuse homogeneous ground-glass opacities (Fig. 4.69). Interlobular septal thickening and reticular densities have also been reported. Cysts are frequently observed and are highly suggestive of the diagnosis. Lymphoadenopathy, pleural effusion and pulmonary nodules are uncommon.

HRCT is now a well established technique for evaluating pediatric airway diseases. HRCT findings have also been described in most chronic diffuse infiltrative lung disease despite the fact that diffuse lung disease is relatively uncommon in children and that the range of disease is more heterogenous than in adults. Concerning pulmonary fibrosis and chronic interstitial pneumonias more definitive categorization of the histopathology is needed to increase diagnostic accuracy of HRCT.

4.9
Conclusion

High resolution CT of the lung is an excellent technique for the study of lung disorders in the pediatric age group. With very few exceptions, it can be performed without the need for patient preparation or sedation and using very low radiation dose to the patient. Careful technique is extremely important. In some cases, particularly in the study of chronic pediatric lung disorders, HRCT provides more information than conventional chest films with comparable radiation exposure; thus it could be an alternative for routine use in these patients. HRCT has replaced bronchography as the gold-standard for diagnosing bronchiectasis in children. We have described the normal anatomy of the lung and the HRCT features of pediatric lung disorders. Most HRCT features are non-specific, but when related to the clinical findings, they can suggest the proper diagnosis and obviate biopsy.

References Part I

Abe K, Kamata N, Okazaki E et al. (2002) Chronic pneumonitis of infancy. Eur Radiol 12:S155–S157

Ambrosino NM, Genieser NB, Roche KJ et al. (1994) Feasibility of high-resolution, low-dose chest CT in evaluation of the pediatric chest. Pediatr Radiol 24:6–10

American Academy of Pediatrics Committee on Drugs (1992) Pediatrics 89:1110–1115

Aquino SL, Gamsu G, Webb WR et al. (1996) Tree-in-bud pattern: frequency and significance on thin section CT. J Comput Assist Tomogr 20:594–599

Aquino SL, Schechter MS, Chiles C et al. (1999) High-resolution inspiratory and expiratory CT in older children and adults with bronchopulmonary dysplasia. AJR Am J Roentgenol 173:963–967

Arakawa H, Webb WR (1998) Air-trapping on expiratory high-resolution CT scans in the absence of inspiratory scan abnormalities. AJR Am J Roentgenol 170:1349–1353

Aukland SM, Halvorsen T, Fosse KR et al. (2006) High-resolution CT of the chest in children and young adults who were born prematurely: findings in a population-based study. AJR Am J Roentgenol 187:1012–1018

Austin JHM, Müller NL, Friedman PJ et al. (1996) Glossary of terms for CT of the lungs: recommendations of the nomenclature committee of the Fleischner Society. Radiology 200:327–331

Brody AS (2005) Imaging considerations: Interstitial lung disease in children. Radiol Clin N Am 43:391–403

Brody AS, Crotty EJ (2006) Neuroendrocrine cell hyperplasia of infancy (NEHI) Pediatr Radiol 36:1328

Canakis AM, Cutz E, Manson D et al. (2002) Pulmonary interstitial glycogenosis. A new variant of neonatal interstitial lung disease. Am J Respir Crit Care Med 165:1557–1565

Capitanio MA, Kirkpatrick JA (1972) Lateral decubitus film: an aid in determining air-trapping in children. Radiology 103:460–462

Choi D, Lee KS, Suh GY et al. (1999) Pulmonary tuberculosis presenting as acute respiratory failure: radiologic findings. J Comput Assist Tomogr 23:107–113

Choi SJ, Choi BK, Kim HJ et al. (2002) Lateral decubitus HRCT: a simple technique to replace expiratory CT in children with air trapping. Pediar Radiol 32:179–182

Chung T, Hoffer FA, Connor L et al. (2000) The use of oral pentobarbital sodium (Nembutal) versus oral chloral hydrate in infants undergoing CT and MRI imaging - a pilot study. Pediatr Radiol 30:332–335

Copley SJ, Coren M, Nicholson AG et al. (2000) Diagnostic accuracy of thin-section CT and chest radiography of pediatric interstitial lung disease. AJR Am J Roentgenol 174:549–554

Cronin P, Sneider MB, Kazerooni EA et al. (2004) MDCT of the left atrium and pulmonary veins in planning radiofrequency ablation for atrial fibrillation: a how-to guide. AJR Am J Roentgenol 183:767–778

Deterding RR, Pye C, Fan LL et al. (2005) Persistent tachipnea of infancy is associated with neuroendocrine cell hyperplasia. Pediat Pulmonol 40:157–165

Egelhoff JC, Ball WS Jr, Koch BL et al. (1997) Safety and efficacy of sedation in children using a structured sedation program. AJR Am J Roentgenol 168:1259–1262

Escuissato DL, Gasparetto EL, Marchiore E et al. (2005) Pulmonary infections after bone marrow transplantation: high-resolution CT findings in 111 patients. AJR Am J Roentgenol 185:608–615

Feretti GR, Lantuejoul S, Brambilla E et al. (1996) Pulmonary involvement in Niemann-Pick disease subtype B: CT findings. J Comput Assist Tomogr 20:990–992

Fink C, Schmaelh A, Bock M, Tuengerthal S, Delorme S (2003) Pulmonary vein stenosis after radiofrequency ablation for atrial fibrillation. Image findings with multiphasic pulmonary magnetic resonance angiography. Circulation. 107:e129–e130

Fisher DM (1990) Sedation of pediatric patients: an anesthesiologist's perspective. Radiology 175:613–615

Franquet T, Gimenez A, Bordes R et al. (1998) The crazy paving pattern in exogenous lipoid pneumonia. CT-Pathologic correlation. AJR Am J Roentgenol 170:315–317

Fricke BL, Donelly LF, Frush DP et al. (2003) In-plane bismuth breaset shields for pediatric CT: effects on radiaction dose and image quality using experimental and clinical data. AJR Am J Roentgenol 180:407–411

Funama Y, Hawai K, Nakayama Y et al. (2005) Radiation dose reduction with without degradation of low-contrast detectability at abdominal multisection CT with low-tube voltage technique: phantom study. Radiol 237:905–910

Garcia-Pena P, Lucaya J (2004) HRCT in children: techique and indications. Eur Radiol 14:L13–L30

Giovagnorio F, Cavallo V (1995) HRCT evaluation of secondary lobules and acini of the lung. J Thorac Imaging 10:129–133

Gruden JF, Webb WR, Warnock M et al. (1994) Centrilobular opacities in the lung on high-resolution CT: diagnostic considerations and pathologic correlation. AJR Am J Roentgenol 162:569–574

Hansell DM, Wells AU, Rubens MB et al. (1994) Bronchiectasis: functional significance of areas of decreased attenuation at expiratory CT. Radiology 193:369–374

Hartman TE, Primack SL, Lee KS et al. (1994) CT of bronchial and bronchiolar diseases. Radiographics 14:991–1003

Hopper KD, King SH, Lobell ME et al. (1998) The breast: in-plane X-ray protection during diagnostic thoracic CT-shielding with bismuth radioprotective garments. Radiology 205:853–858

Hubbard AM, Markowitz RI, Kimmel B et al. (1992) Sedation for pediatric patients undergoing CT and MRI. J Comput Assist Tomogr 16:3–6

Johkoh T, Müller NL, Ichikado K et al. (1999a) Respiratory change in size of honeycombing: Inspiratory and expiratory spiral volumetric CT analysis of 97 cases. J Comput Assist Tomogr 23:174–180

Johkoh T, Müller NL, Pickford HA et al. (1999b) Lymphocytic interstitial pneumonia: thin-section CT findings in 22 patients. Radiology 212:567–572

Karian VE, Burrows PE, Zurakowski D et al. (1999) Sedation for pediatric radiological procedures: analysis of potential causes of sedation failure and paradoxical reactions. Pediatr Radiol 29:869–873

Katzenstein AL, Fiorelli RF (1994) Nonspecific interstitial pneumonia/fibrosis. Histologic features and clinical significance. Am J Surg Pathol 18:136–147

Katzenstein AL, Myers JL, Mazur MT (1986) Acute interstitial pneumonia. A clinicopathologic, ultrastructural, and cell kinetic study. Am J Surg Pathol 10:256–267

Katzenstein AL, Gordon LP, Oliphant M et al. (1995) Chronic pneumonitis of infancy: a unique form of interstitial lung disease occurring in early childhood. Am J Surg Pathol 19:439–447

Koh DM, Hansell DM (2000) Computed tomography of diffuse interstitial lung disease in children. Clin Radiol 55:659–667

Land CE, Tokunaga M, Tokuaka AS et al. (1993) Early-onset breast cancer in A-bomb survivors. Lancet 342:237

Landry BA, Melhem RE (1989) Pulmonary nodules secondary to total parenteral alimentation. Pediatr Radiol 19:456–457

Lee KH, Kim WS, Cheon JE et al. (2005) Squalene aspiration pneumonia in children:radiographic and CT findings as the first clue to diagnosis. Pediatr Radiol 35:619–623

Lee C. H, (2007) The Crazy-paving Sign. Radiology 243: 905–906

Levine D, Akikusa J, Manson D et al. (2007) Chest CT findings in pediatric Wegener's granulomatosis. Pediatr Radiol 37:57–62

Lucaya J, Garcia-Peña P, Herrera L et al. (1999) Expiratory chest CT in children. AJR Am J Roentgenol 174:235–241

Lucaya J, Piqueras J, Garcia-Peña P et al. (2000) Low-dose high-resolution CT of the chest in children and young adults: dose, cooperation, artifact incidence, and image quality. AJR Am J Roentgenol 175:985–992

Lynch DA, Hay T, Newell JD Jr et al. (1999) Pediatric diffuse lung disease. AJR Am J Roentgenol 173:713–718

Mayo JR, Webb WR, Gould R et al. (1987) High resolution CT of the lungs: an optimal approach. Radiology 163:507–510

Mayo JR, Jackson SA, Müller NL (1993) High-resolution CT of the chest: radiation dose. AJR Am J Roentgenol 160:479–481

Moon WK, Kim WS, Kim IO et al. (1996) Diffuse pulmonary disease in children. High-resolution CT findings. AJR Am J Roentgenol 167:1405–1408

Murata K, Itoh H, Todo G et al. (1986) Centrilobular lesions of the lung: demonstration by high-resolution CT and pathologic correlation. Radiology 161:641–645

Murata K, Khan A, Rojas KA et al. (1988) Optimization of computed tomography technique to demonstrate the fine structure of the lung. Invest Radiol 23:170–175

Murata K, Khan A, Herman PG (1989) Pulmonary parenchymal diseases: evaluation with high-resolution CT. Radiology 170:629–635

Newman B, Kuhn JP, Kramer SS et al. (2001). Congenital surfactant protein B deficiency. Emphasis on imaging. Pediatr Radiol 31:327–331

Oh YW, Effmann EL, Redding GJ et al. (1999) Follicular hyperplasia of bronchus-associated lymphoid tissue causing severe air-trapping. AJR Am J Roentgenol 172:745–747

Oppenheim C, Mamou-Mani T, Sayegh N et al. (1994) Bronchopulmonary dysplasia: value of CT in identifying pulmonary sequelae. AJR Am J Roentgenol 163:169–172

Osika E, Muller MH, Boccon-Gibod L (1997) Idiopathic pulmonary fibrosis in infants. Pediatr Pulmonol 23:49–547
Ouellete H (1999) The signet ring sign. Radiology 212:67–68
Pereira JK, Burrows PE, Rickards HM et al. (1993) Comparison of sedation regimens for pediatric outpatient CT. Pediatr Radiol 23:341–344
Pinto PS (2004) The halo sign. Radiology 230:109–110
Rimmer MJ, Dixon AK, Flower DR et al. (1985) Bleomycin lung: computed tomographic observations. Br J Radiol 58:1041–1045
Rooks VJ, Chung T, Connor N et al. (2003) Comparison of oral pentopharbital sodium (neumbutal) and oral chroral hydrate for sedtion of infants during radiologic imaging. Preliminary results. AJR Am J Roentgenol 180:1125–1128
Rossi SE, Franquet T, Volpacchio M et al. (2005) Tree-in-bud pattern and think-section CT of the lungs: radiologic-pathologic overview. Radiografics 25:789–901
Rothenberg LN, Pentlow KS (1992) Radiation dose in CT. Radiographics 12:1225–1243
Saki S, Shida Y, Takahashi N et al. (2006) Pulmonary lesions associated with visceral larva migrans due to ascaris suum or toxocara canis: imaging of six cases. AJR Am J Roentgenol 186:1697–1702
Sanborn PA, Michna E, Zurazowski D et al. (2005) Adverse cardiovascular and respiratory events during sedation of pediatric patients for imaging examinations. Radiology 237:288–294
Schultz R, Mattila J, Gappa M et al. (2001) Development of progressive pulmonary interstitial and intra-alveolar cholesterol granulomas associated with therapy-resintent chronic systemic juvenile arthritis. Pediat Pulmonol 32:397–402
Scott A, Schroeder MD, Shannon DC et al. (1992) Cellular interstitial pneumonitis in infants. Chest 101:1065–1069
Seely JM, Effmann EL, Müller NL (1997) High-resolution CT of pediatric lung disease: imaging findings. AJR Am J Roentgenol 168:1269–1275
Seely JM, Jones LT, Wallace C (1998) Systemic sclerosis: using high-resolution CT to detect lung disease in children. AJR Am J Roentgenol 170:691–697
Sigal-Cinqualbre AB, Hennequin R, Abada HT et al. (2004) Low-kilovoltage multi-detector row chest CT in adults: feasibility and effect on image quality and iodine dose. Radiology 231:169–174
Stern EJ, Müller NL, Swensen SJ et al. (1995) CT mosaic pattern of lung attenuation: etiologies and terminology. J T Thorac Imaging 10:294–297
Suess C, Cheng X (2002) Dose optimization in pediatric CT: current tecnologie and future innovations. Pediatr Radiol 32:729–734
Teel GS, Engeler CE, Tashijian JH et al. (1996) Imaging of small airway disease. Radiographics 16:27–41
Tyrrell VJ, Asher MI, Chan Y (1999) Subpleural lung systs in Down's syndrome. Pediat Pulmonol 28:145–148
Vade A, Sukhani R, Dolenga M et al. (1995) Chloral hydrate sedation of children undergoing CT and MR imaging: safety as judged by American Academy of Pediatrics guidelines. AJR Am J Roentgenol 165:905–909
Webb WR, Müller NL, Naidich DP (1996) High-resolution CT of the lung, 2nd edn. Lippincott-Raven Publishers, Philadelphia New York
Weibel ER (1979) Looking into the lung: what can it tell us? AJR Am J Roentgenol 133:1021–1031
Won HJ, Lee KS, Cheon JE et al. (1998) Invasive pulmonary aspergillosis: prediction at think-section CT in patients with neutropenia. A prospective study. Radiol 208:777–782
Zwirewich CV, Mayo JR, Müller NL (1991) Low-dose high-resolution CT of lung parenchyma. Radiology 180:413–417

References Part II

Abbott GF, Rosado-de-Christenson ML, Franks TJ et al. (2004) Pulmonary Langerhans cell histriocytosis. Radiographics 24:821–841
Abehsera M, Valeyre D, Grenier P et al. (2000) Sarcoidosis with pulmonary fibrosis: CT patterns and correlation with pulmonary function. AJR Am J Roentgenol 174:1751–1757
Akira M, Yamamoto S, Sakatani M (1998) Bronchiolitis obliterans organizing pneumonia manifesting as multiple large nodules or masses. AJR Am J Roentgenol 170:291–295
Albafouille V, Sayegh N, De Coudenhove S et al. (1999) CT scan patterns of pulmonary alveolar proteinosis in children. Pediatr Radiol 29:147–152
Altamirano HG, McGeady SJ, Mansmann HC (1991) Right middle lobe syndrome in asthmatic children. Pediatr Asthma Allergy Immunol 5:33–37
Amorosa JK, Miller RW, Laraya-Cuasay L et al. (1992) Bronchiectasis in children with lymphocytic interstitial pneumonia and acquired immune deficiency syndrome. Pediatr Radiol 22:603–607
Aquino SL, Schechter MS, Chiles C et al. (1999) High-resolution inspiratory and expiratory CT in older children and adults with bronchopulmonary dysplasia. AJR Am J Roentgenol 173:963–967
Arslan N, Ilgan S, Ozkan M et al. (2001) Utility of ventilation and perfusion scan in the diagnosis of young military recruits with an incidental findings of hyperlucent lung. Nucl Med Commun 22:525–530
Aydin K, Karabulut N, Demirkazik F et al. (1997) Pulmonary involvement in adult Gaucher's disease: high-resolution CT appearance. Br J Radiol 70:93–95
Bankier AA, Van Muylen A, Knoop C et al. (2001) Bronchiolitis obliterans syndrome in heart-lung transplant recipients: diagnosis with expiratory CT. Radiology 218:533–539
Becciolini V, Gudinchet F, Cheseaux JJ et al. (2001) Lymphocytic interstitial pneumonia in children with AIDS: high-resolution CT findings. Eur Radiol 11:1015–1020
Bhalla M, Turcios N, Aponte V et al. (1991) Cystic fibrosis: scoring system with thin-section CT. Radiology 179:783–788
Bomelburg T, Roos N, von Lengerke HJ et al. (1992) Invasive aspergillosis complicating induction chemotherapy of childhood leukaemia. Eur J Pediatr 151:485–487
Bonelli FS, Hartman TE, Swensen SJ et al. (1998) Accuracy of high-resolution CT in diagnosing lung diseases. AJR Am J Roentgenol 170:1507–1512

Braier J, Latella A, Balancini B et al. (2004) Outcome in children with pulmonary Langerhans cell histiocytosis. Pediatr Blood Cancer 43:765–769

Brasfield D, Hicks G, Soong SJ et al. (1980) Evaluation of scoring system of the chest radiograph in cystic fibrosis: a collaborative study. AJR Am J Roentgenol 134:1195–1198

Brauner MW, Grenier P, Mompoint D et al. (1989a) Pulmonary sarcoidosis: evaluation with high-resolution CT. Radiology 172:467–471

Brauner MW, Grenier P, Mouelhi MM et al. (1989b) Pulmonary histiocytosis X: evaluation with high-resolution CT. Radiology 172:255–258

Brauner MW, Grenier P, Tijani K et al. (1997) Pulmonary Langerhans cell histiocytosis: evolution of lesions on CT scans. Radiology 204:497–502

Brody AS, Molina PL, Klein JS et al. (1999) High-resolution computed tomography of the chest in children with cystic fibrosis: support for use as an outcome surrogate. Pediatr Radiol 29:731–735

Brody AS, Klein JS, Molina PL et al. (2004) High-resolution computed tomography in young patients with cystic fibrosis: distribution of abnormalities and correlation with pulmonary function test. J Pediatr 145:32–38

Brody AS, Tiddens HA, Castile RG et al. (2005) Computed tomography in the evaluation of cystic fibrosis lung disease. Am J Respir Crit Care Med 172:1246–1252

Carignan S, Staples CA, Müller NL (1995) Intrathoracic lymphoproliferative disorders in the immunocompromised patient: CT findings. Radiology 197:53–58

Cartier Y, Kavanagh PV, Johkoh T et al. (1999) Bronchiectasis: accuracy of high-resolution CT in the differentiation of specific diseases. AJR Am J Roentgenol 173:47–52

Ceviz N, Kaynar H, Olgun H et al. (2006) Pigeon breeder's lung in childhood: is family screening necessary? Pediatr Pulmonol 41:279–282

Chang AB, Masel JP, Masters B (1998) Post-infectious bronchiolitis obliterans: clinical, radiological and pulmonary function sequelae. Pediatr Radiol 28:25–29

Chibbar R, Shih F, Baga M et al. (2004) Non specific interstitial pneumonia and usual interstitial pneumonia with mutation in surfactant protein C in familial pulmonary fibrosis. Mod Pathol 17:973–980

Chung CJ, Fordham LA, Barker P et al. (1999) Children with congenital pulmonary lymphangiectasia: after infancy. AJR Am J Roentgenol 173:1583–1588

Cleveland RH, Staub Neish A, Zurakowski D et al. (1998) Cystic fibrosis: a system for assessing and predicting progression. AJR Am J Roentgenol 170:1067–1072

Cluzel P, Grenier P, Bernadac P et al. (1991) Pulmonary alveolar microlithiasis: CT findings. J Comput Assist Tomogr 15:938–942

Colby TV (1998) Bronchiolitis. Pathologic considerations. Am J Clin Pathol 109:101–109

Connolly B, Manson D, Eberhard A et al. (1996) CT appearance of pulmonary vasculitis in children. AJR Am J Roentgenol 167:901–904

Copley SJ, Coren M, Nicholson AG et al. (2000) Diagnostic accuracy of thin-section CT and chest radiography of pediatric interstitial lung disease. AJR Am J Roentgenol 174:549–554

Cordier JF (2000) Organising pneumonia. Thorax 55:318–328

Coulier B, Mailleux P, Mairesse M et al. (1999) Pulmonary alveolar proteinosis, high-resolution CT findings and evolution in 5 patients. JBR-BTR 82:277–281

Dawson WB, Müller NL (1990) High-resolution computed tomography in pulmonary sarcoidosis. Semin Ultrasound, CT and MR 11:423–429

Deniz O, Ors F, Tozkoparan E et al. (2005) High-resolution computed tomographic features of pulmonary alveolar microlithiasis. Eur J Radiol 55:452–460

Dodd JD, Souza CA, Muller NL (2006) Conventional high-resolution CT versus helical high-resolution MDCT in the detection of bronchiectasis. AJR Am J Roentgenol 187:414–420

Donnelly LF (2000) Langerhan's cell histiocytosis showing low-attenuation mediastinal mass and cystic lung disease. AJR Am J Roentgenol 174:877–878

Drent M, De Vries J, Lenters M et al. (2003) Sarcoidosis: assessment of disease severity using HRCT. Eur Radiol 13:2462–2471

Dutheil-Doco A, Ducou le Pointe H, Larroquet M et al. (1997) Maladie de Gorham à manifestation pleuro-pulmonaire prédominante. J Radiol 78:665–667

Edwards EA, Metcalfe R, Milne DG (2003) Retrospective review of children presenting with non cystic fibrosis bronchiectasis: HRCT features and clinical relationships. Pediatr Pulmonol 36:87–93

Fauré C, Verderi D, Schmit P et al. (1986) The chest film in immotile cilia syndrome in children. Ann Radiol 29:301–311

Fauroux B, Clément A (2005) Paediatric sarcoidosis. Paediatr Respir Rev 6:128–133

Fenlon HM, Doran M, Sant SM et al. (1996) High-resolution chest CT in systemic lupus erythematosus. AJR Am J Roentgenol 166:301–307

Feretti GR, Lantuejoul S, Brambilla E et al. (1996) Pulmonary involvement in Niemann-Pick disease subtype B: CT findings. J Comput Assist Tomogr 20:990–992

Flowers JR, Clunie G, Burke M et al. (1992) Bronchiolitis obliterans organizing pneumonia: the clinical and radiological features of seven cases and a review of the literature. Clin Radiol 45:371–377

Gaillard EA, Carty H, Heaf D et al. (2003) Reversible bronchial dilatation in children: comparison of serial high-resolution computer tomography scans of the lungs. Eur J Radiol 47:215–220

Godwin JD, Müller NL, Takasugi JE (1988) Pulmonary alveolar proteinosis: CT findings. Radiology 169:609–613

Grenier P, Maurice F, Musset D et al. (1986) Bronchiectasis: assessment by thin-section CT. Radiology 161:95–99

Grenier P, Lenoir S, Brauner M (1990) Computed tomographic assessment of bronchiectasis. Semin Ultrasound, CT and MR 11:430–441

Grenier P, Chevret S, Beigelman C et al. (1994) Chronic diffuse infiltrative lung disease: determination of the diagnostic value of clinical data, chest radiography, and CT with Bayesian analysis. Radiology 191:383–390

Grenier P, Mourey-Gerosa I, Benali K et al. (1996) Abnormalities of the lung and lung parenchyma in asthmatics: CT observations in 50 patients and inter- and intraobsever variability. Eur Radiol 6:199–206

Grossman H, Merten DF, Spock A et al. (1985) Radiographic features of sarcoidosis in pediatric patients. Semin Roentgenol, 20:393–399

Hansell DM (1998) Bronchiectasis. Radiol Clin N Am 36:107–128

Hansell DM, Moskovic E (1991) High-resolution computed tomography in extrinsic allergic alveolitis. Clin Radiol 43:8–12

Hartman TE, Primack SL, Swenson SJ et al. (1993) Desquamative interstitial pneumonia: thin-section CT findings in 22 patients. Radiology 187:787–790

Helbich TH, Wojnarovsky C, Wunderbaldinger P et al. (1997) Pulmonary alveolar microlithiasis in children: radiographic and high-resolution CT findings.AJR Am J Roentgenol 168:63–65

Helbich TH, Heinz-Peer G, Fleischmann D et al. (1999) Evolution of CT findings in patients with cystic fibrosis. AJR Am J Roentgenol 173:81–88

Herman M, Michalkova K, Kopriva F (1993) High-resolution CT in the assessment of bronchiectasis in children. Pediatr Radiol 23:376–379

Hiddema A, Engelshove HA (1999) Kartagener's syndrome. JBR-BTR 82:112

Honda O, Johkoh T, Ichikado K et al. (1999) Differential diagnosis of lymphocytic interstitial pneumonia and malignant lymphoma on high-resolution CT. AJR Am J Roentgenol 173:71–74

Ichikado K, Johkoh T, Ikezoe J et al. (1997) Acute interstitial pneumonia: high-resolution CT findings correlated with pathology. AJR Am J Roentgenol 168:333–338

Inoue T, Toyoichiro K, Kikui M (1996) Idiopathic bronchiolitis obliterans organizing pneumonia (idiopathic BOOP) in childhood. Pediatr Pulmonol 22:67–72

Jimenez S, Jimenez JR, Crespo M et al. (2006) Computed tomography in children with cystic fibrosis: a new way to reduce radiation dose. Arch Dis Child 91:388–390

Johkoh T, Ikezoe J, Tomiyama N et al. (1992) CT findings in lymphangitic carcinomatosis of the lung: correlation with histologic findings and pulmonary function tests. AJR Am J Roentgenol 158:1217–1222

Johkoh T, Müller NL, Cartier Y et al. (1999a) Idiopathic interstitial pneumonias: diagnostic accuracy of thin-section CT in 129 patients. Radiology 211:555–560

Johkoh T, Müller NL, Pickford HA et al. (1999b) Lymphocytic interstitial pneumonia: thin-section CT findings in 22 patients. Radiology 212:567–572

Johkoh T, Müller NL, Taniguchi H et al. (1999c) Acute interstitial pneumonia: thin section CT findings in 36 patients. Radiology 211:859–863

Jong de PA, Ottink MD, Robben SG et al. (2004) Pulmonary disease assessment in cystic fibrosis: comparison if CT scoring systems and value of bronchial and arterial dimension measurements. Radiology 231:434–439

Jong de PA, Nakano Y, Lequin MH et al. (2006) Dose reduction for CT in children with cystic fibrosis: is feasible to reduce the number of images per scan. Pediatr Radiol 36:50–53

Katzeinstein AL, Fiorelli RF (1994) Nonspecific interstitial pneumonia/fibrosis. Histologic features and clinical significance. Am J Surg Pathol 18:136–147

Katzenstein AL, Myers JL, Mazur MT (1986) Acute interstitial pneumonia. A clinicopathologic, ultrastructural, and cell kinetic study. Am J Surg Pathol 10:256–267

Kim MJ, Lee KY (1996) Bronchiolitis obliterans in children with Stevens-Johnson syndrome: follow-up with high-resolution CT. Pediatr Radiol 26:22–25

Kim JS, Müller NL, Park CS et al. (1997) Cylindrical bronchiectasis: diagnostic findings on thin-section CT. AJR Am J Roentgenol 168:751–754

Kiper N, Gocmen A, Ozcelik U et al. (1999) Long-term clinical course of patients with idiopathic pulmonary hemosiderosis (1979–1994): prolonged survival with low-dose corticosteroid therapy. Pediatr Pulmonol 27:180–184

Kleinau I, Perez-Canto A, Schmid HJ et al. (1997) Bronchiolitis obliterans organizing pneumonia and chronic graft-versus-host disease in a child after allogeneic bone marrow transplantation. Bone Marrow Transplant 19:841–844

Koh DM, Hansell DM (2000) Computed tomography of diffuse interstitial lung disease in children. Clin Radiol 55:659–667

Konez O, Vyas PK, Goyal M (2000) Disseminated lymphangiomatosis presenting with massive chylothorax. Pediatr Radiol 30:35–37

Kuhn JP (1993) High-resolution computed tomography of pediatric pulmonary parenchymal disorders. Radiol Clin North Am 31:533–551

Lau DM, Siegel MJ, Hildebolt CF et al. (1998) Bronchiolitis obliterans syndrome: thin-section CT diagnosis of obstructive changes in infants and young children after lung transplantation. Radiology 208:783–788

Lee KS, Kullnig P, Hartman TE et al. (1994a) Cryptogenic organizing pneumonia: CT findings in 43 patients. AJR Am J Roentgenol 162:543–546

Lee KS, Primack SL, Staples CA et al. (1994b) Chronic infiltrative lung disease: comparison of diagnostic accuracies of radiography and low- and conventional-dose thin-section CT. Radiology 191:669–673

Li YW, Snow J, Smith W et al. (1985) Localized pulmonary lymphangiectasia. AJR Am J Roentgenol 145:269–270

Liebow AA (1968) New concepts and entities in pulmonary disease. Monogr Pathol 8:332–365

Liebow AA, Carrington CB (1973) Diffuse pulmonary lymphoreticular infiltrations associated with dysproteinemia. Med Clin North Am 57:809–843

Logan PM, Primack SL, Miller RR et al. (1994) Invasive aspergillosis of the airways: radiographic, CT and pathologic findings. Radiology 193:383–388

Lucaya J, Gartner S, Garcia-Pena P et al. (1998) Spectrum of manifestations of Swyer-James-MacLeod syndrome. J Comput Assist Tomogr 22:592–597

Lucaya J, Garcio-Pena P, Herrera L et al. (2000) Expiratory chest CT in children. Am J Roentgenol AJR 174:235–241

Lynch DA (1998) Imaging of asthma and allergic bronchopulmonary mycosis. Radiol Clin North Am 36:129–142

Lynch DA, Hay T, Newell JD Jr et al. (1999) Pediatric diffuse lung disease: diagnosis and classification using high-resolution CT. AJR Am J Roentgenol 173:713–718

Marchac V, Emond S, Mamou-Mani T et al. (2002) Thoracic CT in pediatric patients with difficult-to-treat asthma. AJR Am J Roentgenol 179:1245–1252

Marti-Bonmati L, Ruiz Perales F, Catala F et al. (1989) CT findings in Swyer-James syndrome. Radiology 172:477–480

Mathew P, Bozeman P, Krance RA et al. (1994) Bronchiolitis obliterans organizing pneumonia (BOOP) in children after allogeneic bone marrow transplantation. Bone Marrow Transplant 13:221–223

McCook TA, Kirks DR, Merten DF et al. (1981) Pulmonary alveolar proteinosis in children. AJR Am J Roentgenol 137:1023–1027

McGuinness G, Naidich DP (1995) Bronchiectasis: CT/clinical correlations. Semin Ultrasound, CT and MR 16:395–419

Mclean AN, Sproule MW, Cowan MD et al. (1998) High-resolution computed tomography in asthma. Thorax 53:308–314

Meeks M, Bush A (2000) Primary ciliary dyskinesia (PCD). Pediatr Pulmonol 29:307–316

Mitchell CS, Parisi MT, Osborn RE (1993) Gorham's disease involving the thoracic skeleton. Pediatr Radiol 23:543–544

Mitchell TA, Hamilos DL, Lynch DA et al. (2000) Distribution and severity of bronchiectasis in allergic bronchopulmonary aspergillosis (ABPA) J Asthma 37:65–72

Moore AD, Godwin JD, Müller NL et al. (1989) Pulmonary histiocytosis X: comparison of radiographic and CT findings. Radiology 172:249–254

Moore AD, Godwin JD, Dietrich PA (1992) Swyer-James syndrome: CT findings in eight patients. AJR Am J Roentgenol 158:1211–1215

Müller NL, Colby TV (1997) Idiopathic interstitial pneumonias: high-resolution CT and histologic findings. RadioGraphics 17:1016–1022

Müller NL, Staples CA, Miller RR (1990) Bronchiolitis obliterans organizing pneumonia: CT features in 14 patients. AJR Am J Roentgenol 154:983–987

Munk PL, Müller NL, Miller RR et al. (1988) Pulmonary lymphangitic carcinomatosis: CT and pathologic findings. Radiology 166:705–709

Murch CR, Carr DH (1989) Computed tomography appearances of pulmonary alveolar proteinosis. Clin Radiol 40:240–243

Nadel HR, Stringer DA, Levison H et al. (1985) The immotile cilia syndrome: radiological manifestations. Radiology 154:651–655

Nathanson I, Conboy K, Murphy S et al. (1991) Ultrafast computerized tomography of the chest in cystic fibrosis: a new scoring system. Pediatr Pulmonol 11:81–86

Nishimura K, Kitaichi M, Izumi T et al. (1992) Usual interstitial pneumonia: histologic correlation with high-resolution CT. Radiology 182:337–342

Nishimura K, Itoh H, Kitaichi M et al. (1995) CT and pathological correlation of pulmonary sarcoidosis. Semin Ultrasound, CT and MR 16:361–370

Nogee LM, Dunbar AE, Wert SE et al. (2001) A mutation in the surfactant protein C gene associated with familial interstitial lung disease. N Engl J Med 344:573–579

Noonan JA, Walters LR, Reeves JT (1970) Pulmonary lymphangiectasis. Am R Dis Child 120:314–319

Nowers K, Rasband JD, Berges G et al. (2002) Semin Ultrasound, CT and MR 23:302–323

Odame I, Li P, Lau L et al. (2006) Pulmonary Langerhans cell histiocytosis: a variable disease in childhood. Pediatr Blood Cancer 47:889–893

Oppenheim C, Mamou-Mani T, Sayegh N et al. (1994) Bronchopulmonary dysplasia: value of CT in identifying pulmonary sequelae. AJR Am J Roentgenol 163:169–172

Osika E, Muller MH, Boccon-Gibod L (1997) Idiopathic pulmonary fibrosis in infants. Pediatr Pulmonol 23:49–54

Paganin F, Trussard V, Seneterre E et al. (1992) Chest radiography and high-resolution computed tomography of the lungs in asthma. Am Rev Respir Dis 146:1084–1087

Pattishall EN, Kendig EL (1996) Sarcoidosis in children. Pediatr Pulmonol 22:195–203

Primack SL, Hartman TE, Ikezoe J et al. (1993) Acute interstitial pneumonia: radiographic and CT findings in nine patients. Radiology 188:817–820

Primack SL, Miller RR, Müller NL (1995) Diffuse pulmonary hemorrhage: clinical, pathologic, and imaging features. AJR Am J Roentgenol 164:295–300

Ramirez RE, Glasier C, Kirks D et al. (1984) Pulmonary hemorrhage associated with systemic lupus erythematosus in children. Radiology 152:409–412

Rettwitz-Volk W, Schlober R, Ahrens P et al. (1999) Congenital unilobar pulmonary lymphangiectasis. Pediatr Pulmonol 27:290–292

Reyes de la Rocha S, Pysher TJ, Leonard JC (1987) Dyskinetic cilia syndrome: clinical, radiographic and scintigraphic findings. Pediatr Radiol 17:97–103

Rossi SE, Erasmus JJ, Volpacchio M et al. (2003) RadioGraphics 23:1509–1519

Rossi UG, Owens CM (2005) The radiology of chronic lung disease in children. Arch Dis Child 90:601–607

Ruzal-Shapiro C (1998) Cystic fibrosis. An overview. Radiol Clin North Am 36:143–161

Sargent MA, Cairns RA, Murdoch MJ et al. (1995) Obstructive lung disease in children after allogeneic bone marrow transplantation: evaluation with high-resolution CT. AJR Am J Roentgenol 164:693–696

Schumacher RE, Marrogi AJ, Heidelberger KP (1989) Pulmonary alveolar proteinosis in a newborn. Pediatr Pulmonol 7:178–182

Seely JM, Effmann EL, Müller NL (1997) High-resolution CT of pediatric lung disease: imaging findings. AJR Am J Roentgenol 168:1269–1275

Seely JM, Jones LT, Wallace C (1998) Systemic sclerosis: using high-resolution CT to detect lung disease in children. AJR Am J Roentgenol 170:691–697

Shah A, Pant CS, Bhagat R et al. (1992) CT in childhood allergic bronchopulmonary aspergillosis. Pediatr Radiol 22:227–228

Shah RM, Sexauer W, Ostrum BJ et al. (1997) High-resolution CT in the acute exacerbation of cystic fibrosis: evaluation of acute findings, reversibility of those findings, and clinical correlation. AJR Am J Roentgenol 168:375–380

Sharma V, Shaaban AM, Berges G et al. (2002) The radiological spectrum of small-airway diseases. Semin Ultrasound, CT and MR 23:339–351

Siegel MJ (1999) Pediatric body CT. Lippincott, Williams and Wilkens, Philadelphia, p. 126

Silva CI, Colby T, Muller NL (2004) Asthma and associated conditions: high resolution CT and pathologic findings. AJR Am J Roentgenol 183:817–824

Sivit CJ, Miller CR, Rakusan TA et al. (1995) Spectrum of chest radiographic abnormalities in children with AIDS and Pneumocystis carinii pneumonia. Pediatr Radiol 25:389–392

Small JH, Flower CD, Traill ZC et al. (1996) Air-trapping in extrinsic allergic alveolitis on computed tomography. Clin Radiol 51:684–688

Smets A, Mortelé K, De Praeter G et al. (1997) Pulmonary and mediastinal lesions in children with Langerhans cell histiocytosis. Pediatr Radiol 27:873–876

Sminiotopoulos JG, Lonergan GJ, Abbott RM et al. (1999) Image interpretation session: 1998. RadioGraphics 19:205–233

Sockrider MM, Swank PR, Seilheimer DK et al. (1994) Measuring clinical status in cystic fibrosis: internal validity and reliability of the modified NIH score. Pediatr Pulmonol 17:86–96

Stauffer Ettlin M, Pache JC, Renevey F et al. (2006) Bird breeder's disease: a rare diagnosis in young children. Eur J Pediatr 165:55–61

Sterclova M, Vasakova M, Dutka J et al. (2006) Extrinsic allergic alveolitis: comparative study of the bronchoalveolar lavage profiles and radiological presentation. Postgrad Med J 82:598–601

Stern EJ, Samples TL (1992) Dynamic ultrafast high-resolution CT findings in a case of Swyer-James syndrome. Pediatr Radiol 22:350–352

Swensen SJ, Hartman TE, Mayo JR et al. (1995) Diffuse pulmonary lymphangiectasis: CT findings. J Comput Assist Tomogr 19:348–352

Swensen SJ, Aughenbaugh GL, Myers JL (1997) Diffuse lung disease: diagnostic accuracy of CT in patients undergoing surgical biopsy of the lung. Radiology 205:229–234

Taccone A, Occhi M, Garaventa A et al. (1993) CT of invasive pulmonary aspergillosis in children with cancer. Pediatr Radiol 23:177–180

Thomas AQ, Lane K, Philipps J et al. (2002) Heterozygosity for a surfactant protein C gene mutation associated with usual interstitial pneumonitis and cellular nonspecific interstitial pneumonitis in one kindred. Am J Respir Crit Care Med 165:1322–1328

Thompson BH, Stanford W, Galvin JR et al. (1995) Varied radiologic appearances of pulmonary aspergillosis. RadioGraphics 15:1273–1284

Traill ZC, Maskell GF, Gleeson FV (1997) High-resolution CT findings of pulmonary sarcoidosis. AJR Am J Roentgenol 168:1557–1560

Tunaci A, Berkmen YM, Gokmen E (1995) Pulmonary Gaucher's disease: high-resolution computed tomographic features. Pediatr Radiol 25:237–238

Ujita M, Renzoni EA, Veeraraghavan S et al. (2004) Organizing pneumonia: perilobular pattern at thin-section CT. Radiology 232:757–761

Verlaat CW, Peters HM, Semmekrot BA et al. (1994) Congenital pulmonary lymphangiectasis presenting as a unilateral hyperlucent lung. Eur J Pediatr 153:202–205

Vincent JM, Armstrong P, Wilson AG (1992) Extrinsic allergic alveolitis and eosinophilic pneumonia. Imaging 4:5–13

von Vigier RO, Trummler SA, Laux-End R et al. (2000) Pulmonary renal syndrome in childhood: a report of twenty-one cases and a review of the literature. Pediatr Pulmonol 29:382–388

Wallis C, Whitehead B, Malone M et al. (1996) Pulmonary alveolar microlithiasis in childhood: diagnosis by transbronchial biopsy. Pediatr Pulmonol 21:62–64

Ward S, Heyneman L, Lee MJ et al. (1999) Accuracy of CT in the diagnosis of allergic bronchopulmonary aspergillosis in asthmatic patients. AJR Am J Roentgenol 173: 937–942

Webb WR (1994) High-resolution computed tomography of obstructive lung disease. Radiol Clin North Am 32:745–757

Webb WR, Müller NL, Naidich DP (1996) High-resolution CT of the lung, 2nd edn. Lippincott-Raven, Philadelphia New York

Wittram C, Mark EJ, McLoud TG (2003) CT-Histologic correlation of the ATS/ERS 2002 classification of idiopathic interstitial pneumonias. RadioGraphics 23:1057–1071

Won HJ, Lee KS, Cheon JE et al. (1998) Invasive pulmonary aspergillosis: prediction at thin-section CT in patients with neutropenia – a prospective study. Radiology 208:777–782

Yassa NA, Wilcox AG (1998) High-resolution CT pulmonary findings in adults with Gaucher's disease. Clin Imaging 22:339–342

5

Pulmonary Malformations Beyond the Neonatal Period

Josep M. Mata and Amparo Castellote

CONTENTS

5.1 **Introduction** *123*

5.2 **Focal Malformations** *123*
5.2.1 Congenital Lobar Overinflation: Lobar Emphysema and Bronchial Atresia *124*
5.2.1.1 Congenital Lobar Emphysema *124*
5.2.1.2 Bronchial Atresia *124*
5.2.2 Single Congenital Thoracic Cyst *126*
5.2.3 Congenital Cystic Adenomatoid Malformation – Pulmonary Sequestration Complex *129*
5.2.3.1 Congenital Cystic Adenomatoid Malformation *129*
5.2.3.2 Pulmonary Sequestration *131*
5.2.4 Isolated Systemic Supply to Normal Lung *135*

5.3 **Dysmorphic Lung** *135*
5.3.1 Lung Agenesis – Hypoplasia Complex *136*
5.3.2 Lobar Agenesis – Aplasia Complex *138*
5.3.2.1 Hypogenetic Lung Syndrome *138*
5.3.2.2 Lobar Agenesis – Aplasia with Anomalous Unilateral Single Pulmonary Vein *138*
5.3.2.3 Lobar Agenesis – Aplasia with Levo-atriocardinal Vein *141*
5.3.2.4 Congenital Venolobar Syndrome *141*
5.3.2.5 Horseshoe Lung *142*
5.3.2.6 Accessory Diaphragm *143*

References *144*

5.1
Introduction

Congenital lung malformations include a heterogeneous group of anomalies affecting the lung parenchyma, the arterial supply to the lung and its venous drainage (Heitzman 1984). From the morphological-radiological viewpoint, these malformations can be divided into two groups: focal malformations (congenital lobar overinflation, single congenital thoracic cyst, congenital adenomatoid malformation, pulmonary sequestration and isolated systemic supply to normal lung) and dysmorphic lung (lung agenesis-hypoplasia complex and lobar agenesis-aplasia complex).

5.2
Focal Malformations

Focal congenital malformations usually involve only a part of the lung. They are a heterogeneous group, whose boundaries are not well defined and whose radiologic and pathologic manifestations vary and can be difficult to classify, especially if infection is present. They may cause symptoms in early life or be discovered incidentally.

Focal congenital malformations can be separated according to their radiologic and pathologic manifestations, with the understanding that significant degrees of overlap may occur. They can be considered a spectrum: at one extreme we find isolated bronchopulmonary anomaly (congenital lobar overinflation: lobar emphysema and bronchial atresia, single congenital thoracic cyst, congenital adenomatoid malformation); next, associated systemic vascularization in the diseased lung (pulmonary sequestration); and at the other extreme isolated

---

J. M. Mata, MD
UDIAT, Servei de Diagnòstic per la Imatge, Corporació Parc Taulí, Parc Taulí s/n, 08208 Sabadell, Spain
A. Castellote, MD
Servei de Radiologia Pediàtrica, Hospital Vall d'Hebron, Ps. Vall d'Hebron 119–129, 08035 Barcelona, Spain

systemic arterial anomalies (isolated systemic supply to normal lung).

Although these developmental lesions are usually isolated, there are too many cases of concurrent association of two or more of these anomalies to be chance alone. The theory of a variable level, completeness and timing of the obstruction with secondary pulmonary dysplastic changes may help in understanding these overlapping malformations (Langston 2003; Newman 2006).

The prenatal ultrasound (US) and magnetic resonance (MR) examination of the fetus has facilitated recognition and has added new information of many intrathoracic malformations. Nowadays, in countries where fetal US is routinely used, most congenital malformations are discovered antenatally, and confirmed in the neonatal period.

5.2.1
Congenital Lobar Overinflation: Lobar Emphysema and Bronchial Atresia

5.2.1.1
Congenital Lobar Emphysema

Congenital lobar emphysema (CLE) is characterized by progressive hyperexpansion of a lobe, usually the left upper or the right middle lobe. Its basic pathologic abnormality is overdistension of otherwise normal alveoli without destruction of alveolar walls. Proposed etiologies include focally deficient bronchial wall cartilage, deficient connective tissue stroma resulting in abnormal support of alveolar walls, and intrinsic or extrinsic obstruction of an affected bronchus. These abnormalities are believed to result in a check-valve mechanism, with progressive hyperinflation of the affected lobe after birth. Infrequently, lobar emphysema can be acquired. It can be caused by extrinsic compression from a vascular anomaly such as an enlarged pulmonary artery or vein (Figs. 5.1 and 5.2), a patent ductus arteriosus or a mediastinal mass (Winters and Effmann 2001). Clinically, most infants with CLE present within the first 6 months of life, with symptoms and signs of respiratory distress. Radiographs obtained beyond the neonatal period always demonstrate hyperlucency and overexpansion of the affected lobe and variable degrees of atelectasis of the ipsilateral lobe or lobes with associated mediastinal shift. CT is useful to exclude other causes of lobar emphysema, such as vascular anomalies or a mediastinal mass. CT findings of CLE are an expanded hemithorax, an overinflated low-attenuation lobe with stretching and attenuation of the pulmonary vessels, and atelectasis of the adjacent lobes. The paucity of vascular shadows within the overexpanded lung is, in itself, diagnostic of obstructive emphysema. Expiratory slices will confirm severe air-trapping in the affected lobe. Follow-up scans of patients who have minimal or no symptoms and, therefore, are treated conservatively, usually demonstrate either no changes or a progressive reduction in the degree of overexpansion of the affected lobe. However, significant air-trapping on expiration persists. Bilateral or multifocal involvement is rare (Hugosson et al. 1995).

5.2.1.2
Bronchial Atresia

Bronchial atresia is an anomaly characterized by obliteration of the proximal lumen of a segmental bronchus, with preservation of the distal structures. Its pathogenesis is unknown, although it may be due to a vascular insult. Air enters the affected segment via collateral channels, producing overinflation and air-trapping. The mucus secretions generated in the bronchi accumulate at the point of obstruction, originating mucus impaction (Lemire et al. 1970; Felson 1979). The mucocele can be linear, branched, ovoid or spherical. Bronchial atresia almost always affects just one segment, and rarely affects a lobar bronchus. Involvement of multiple segments has been reported in a few cases (Ward and Morcos 1999). Bronchial atresia is characteristically located in the left upper lobe (apico-posterior segment), but can involve any lobe (Remy-Jardin et al. 1989; Medelli et al. 1979) and can be associated with other congenital anomalies. It is usually asymptomatic and is an incidental finding on radiological study. Infection of the unconnected lung is rare.

The chest plain film usually demonstrates pulmonary insufflation with trapped air during expiration, accompanied by a tubular, branched or spherical image in a central position, which corresponds to the mucocele (Jederlinic et al. 1986). CT shows the segmental overinflation and mucous impaction with great precision. When bronchial atresia does not involve the left upper lobe or when it does not present characteristic radiological findings in the plain film, CT is diagnostic, demonstrating the combination of emphysema and bronchial impaction that is the hallmark of this condition (Pugatch and Gale 1983; Finck and Milne 1988) (Fig. 5.3). In some

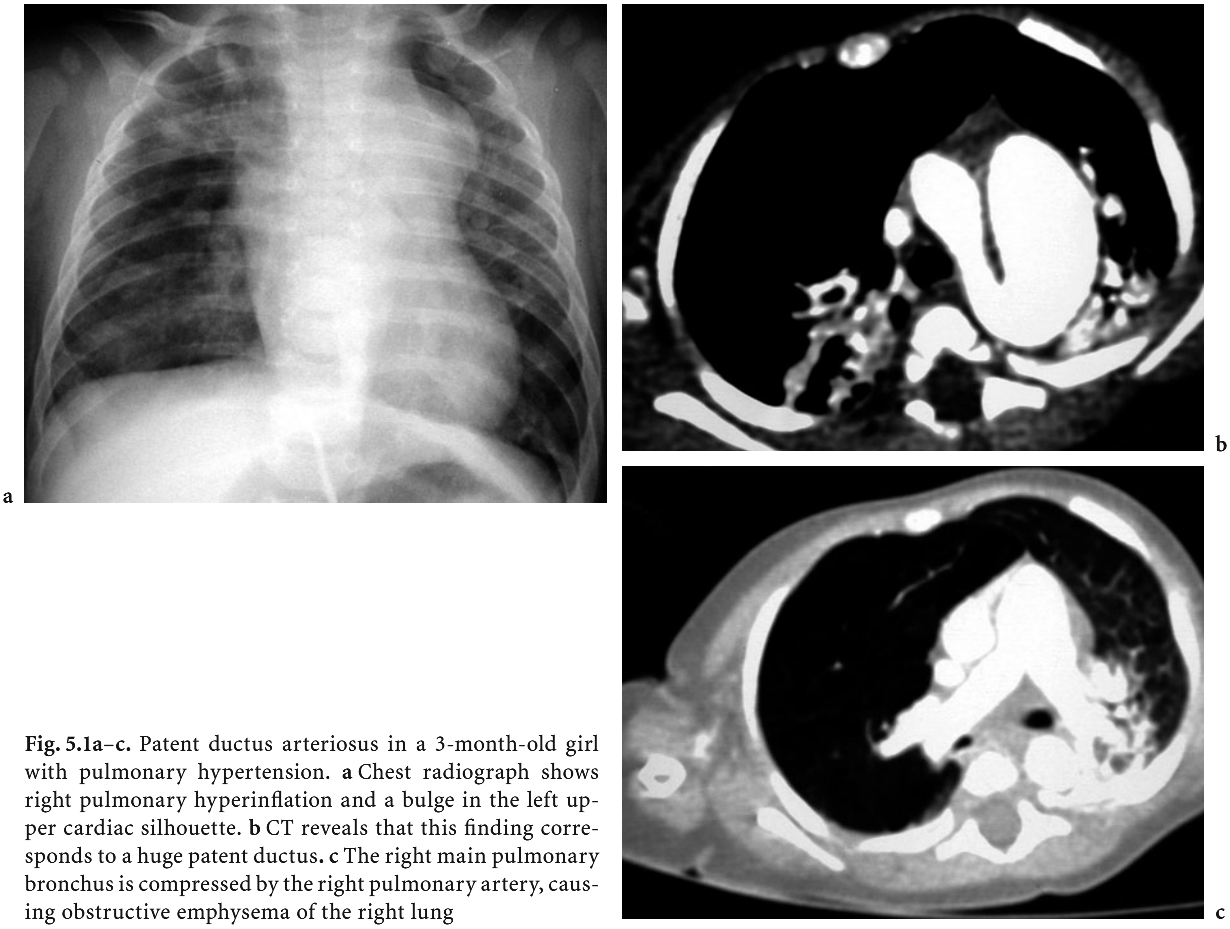

Fig. 5.1a–c. Patent ductus arteriosus in a 3-month-old girl with pulmonary hypertension. **a** Chest radiograph shows right pulmonary hyperinflation and a bulge in the left upper cardiac silhouette. **b** CT reveals that this finding corresponds to a huge patent ductus. **c** The right main pulmonary bronchus is compressed by the right pulmonary artery, causing obstructive emphysema of the right lung

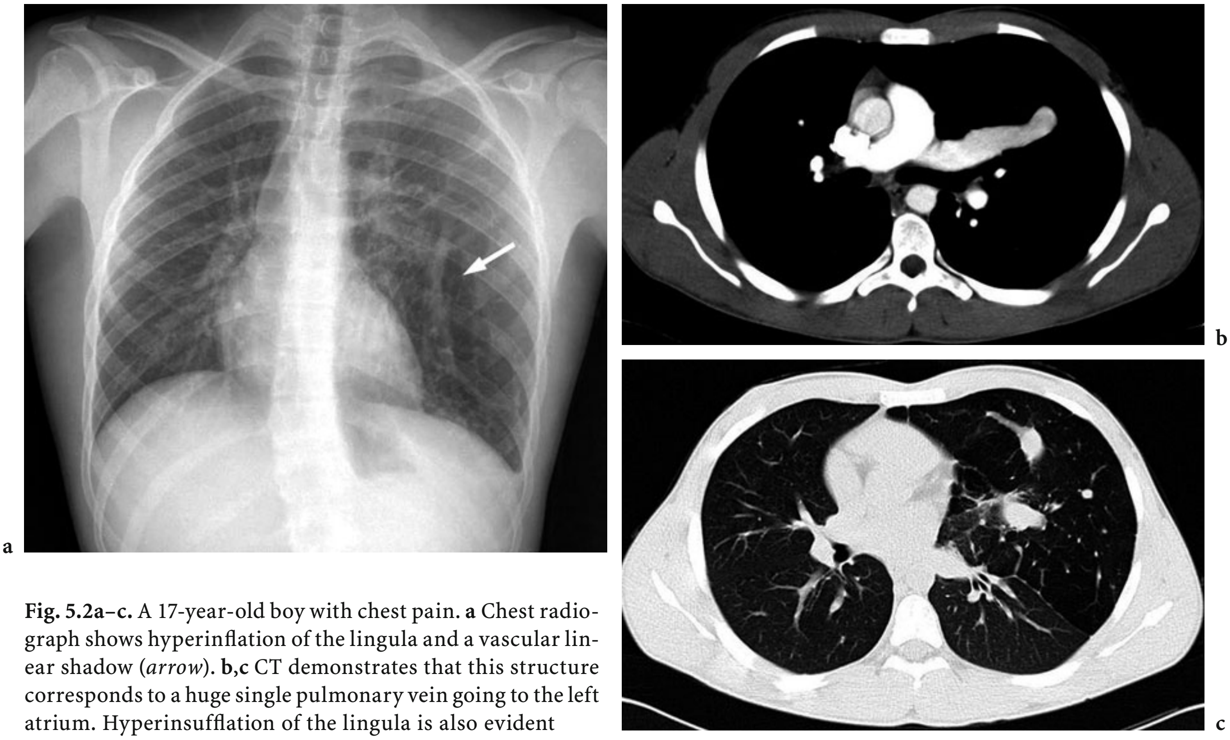

Fig. 5.2a–c. A 17-year-old boy with chest pain. **a** Chest radiograph shows hyperinflation of the lingula and a vascular linear shadow (*arrow*). **b,c** CT demonstrates that this structure corresponds to a huge single pulmonary vein going to the left atrium. Hyperinsufflation of the lingula is also evident

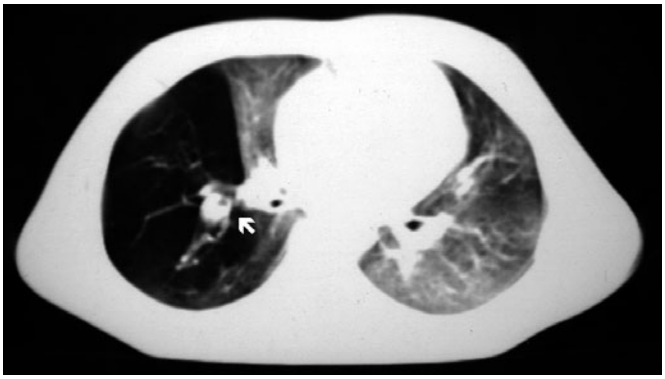

Fig. 5.3. Bronchial atresia in a 7-year-old girl. Expiratory CT scan imaged with lung window shows the bronchocele (*arrow*) and hyperinflation of the right upper lobe

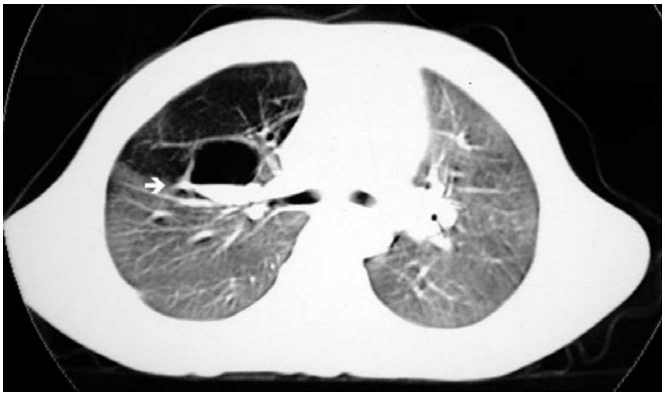

Fig. 5.4. Bronchial atresia in a 4-year-old boy. CT scan imaged with lung window shows a cystic lesion containing gas and fluid at the right hilum (*arrow*) corresponding to the dilated right upper lobe bronchus and hyperinflated right upper lobe

cases, a cystic lesion containing gas and fluid corresponding to a severely dilated bronchus just distal to segmental bronchial atresia can also be seen (Griscom 1993) (Fig. 5.4).

When the mucocele cannot be identified, radiological diagnosis of bronchial atresia vs congenital lobar emphysema may be impossible. In both these entities symptoms may be absent and radiological features may progressively improve. Nonetheless, the degree of mediastinal shift and collapse of the ipsilateral lobes is much more significant in most cases of lobar emphysema than in bronchial atresia (Castellote et al. 2005).

5.2.2
Single Congenital Thoracic Cyst

We include under the term single congenital thoracic cyst (SCTC) all congenital cysts located in the mediastinum (bronchogenic cysts, duplication cysts and pleuropericardial cysts) and lung parenchyma. Treatment of SCTC depends on the symptoms. The best approach in asymptomatic patients with mediastinal cysts is periodic control, avoiding surgery. For practical purposes of clinical management, all cysts located within the lung parenchyma can be considered bronchogenic cysts requiring surgery. The definitive diagnosis of SCTC should be established on the basis of the study of the cyst wall. When there is associated inflammation and in some cases of mediastinal cysts, diagnosis can be difficult.

The most frequent location of bronchogenic cyst varies according to the published series (DuMontier et al. 1985; Baker 1989; Patcher and Lattes 1963; Rogers and Osmer 1964). In the most recent series including 68 bronchogenic cysts (McAdams et al. 2000), 58 (85%) were mediastinal and seven (10%) were intrapulmonary, demonstrating a clear predominance of mediastinal cysts. Mediastinal cysts are most often found in a subcarinal location, whereas intrapulmonary bronchogenic cysts are most frequently located in the lower lobes. Bronchogenic cysts can be found in the diaphragm, below the diaphragm (Braffman et al. 1988) and even in the liver (Kimura et al. 1990) or neck and can be associated with pericardial agenesis (Kwak et al. 1971). They are usually solitary and spherical in shape with thin walls of bronchial epithelium, and have a viscous gelatinous, mucoid, hemorrhagic or watery, translucent fluid content. They occasionally contain calcium, have calcified walls, or are completely calcified and they can be air-filled when they communicate with the bronchial tree (Rogers and Osmer 1964; Reed and Sobonya 1975). Bronchogenic cysts are sometimes found in association with other congenital pulmonary malformations such as sequestration, lobar emphysema and bronchial atresia (Kuhn and Kuhn 1992; Grewal and Yip 1994).

In infants mediastinal SCTC tend to compress or distort the esophagus, the trachea and bronchi, resulting in clinical respiratory compromise, but the condition can be asymptomatic and be discovered fortuitously. Compression of a main bronchus may result in obstructive pulmonary hyperinflation of the ipsilateral lung (Fig. 5.5). These cysts can also compress the pulmonary artery or superior vena cava (Bankoff et al. 1985). Mediastinal and intrapulmonary SCTC can disappear spontaneously (Martin et al. 1988), change form due to decreases in their internal pressure, or diminish in size, making themselves invisible to the chest plain film (Fig. 5.6).

The basic radiological study used to detect SCTC is the chest plain film. In the majority of cases, this technique detects the lesion and some of the complications (e.g. compression on neighboring structures). Ultrasound and CT allow a better evaluation of SCTC and its anatomic relationship with adjacent structures. Currently CT is the examination of choice for assessing SCTC (Fitch et al. 1986). CT reveals a round or ovoid mass with water or soft-tissue attenuation. Almost 50% of SCTC appear iso- or even hyperdense at CT due to intracystic hemorrhage, protein content, or milk of calcium. In these latter cases, MRI can contribute confirmatory information. On MRI, SCTC are homogeneously and markedly hyperintense on T2-weighted images. The intracystic signal intensity on T1-weighted images is more variable, and, depending upon the cyst content, low, intermediate, and high signal intensity cases have been reported (Naidich et al. 1998; Nakata et al. 1993). Relatively high signal intensity on T1 is due to a high protein content and or the presence of methemoglobin. Fluid–fluid levels have also been reported (Lyon and McAdams 1993). When air–fluid levels are seen within the cyst, it is usually infected, although we have seen cysts with air–fluid levels in asymptomatic patients (Fig. 5.7). Minimal wall enhancement is expected with gadolinium enhancement.

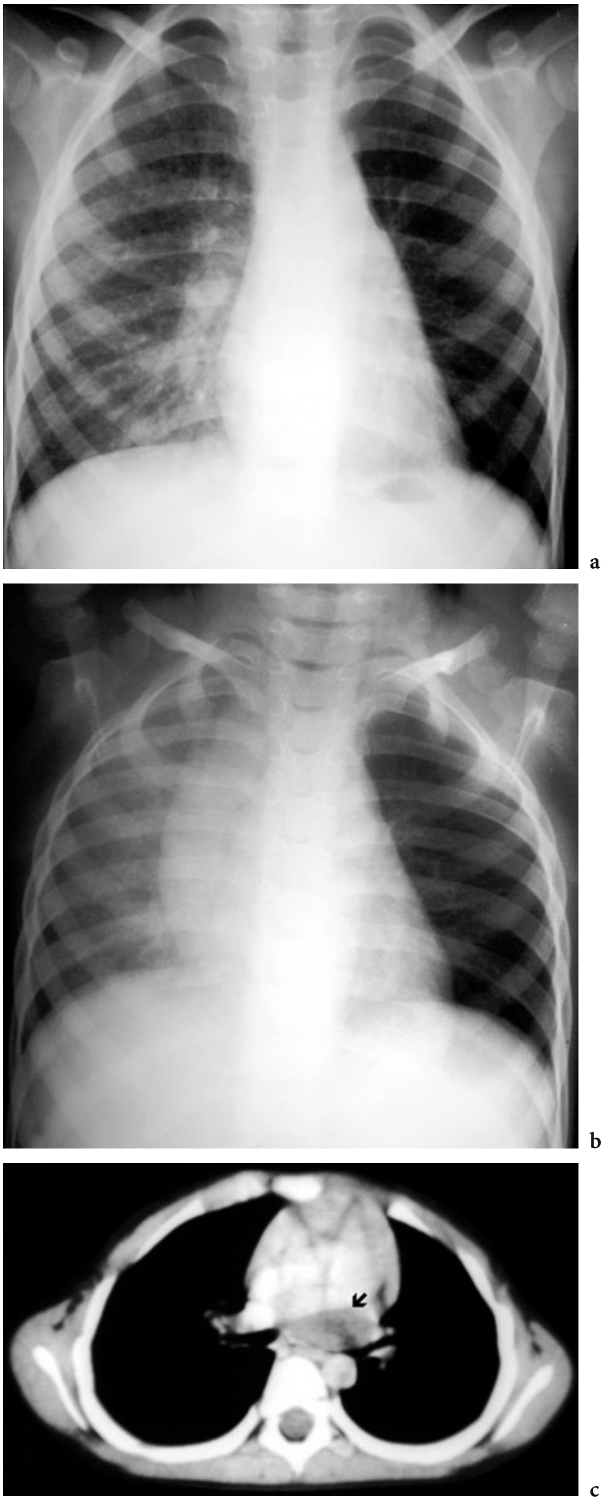

Fig. 5.5a–c. Bronchogenic cyst in a 3-year-old boy. **a** Inspiratory chest radiograph shows hyperlucency and decreased vascular perfusion in the left lung. **b** Expiratory chest radiograph demonstrates air-trapping in the left lung. **c** A subcarinal cyst compressing the left main bronchus is seen in the CT scan (*arrow*)

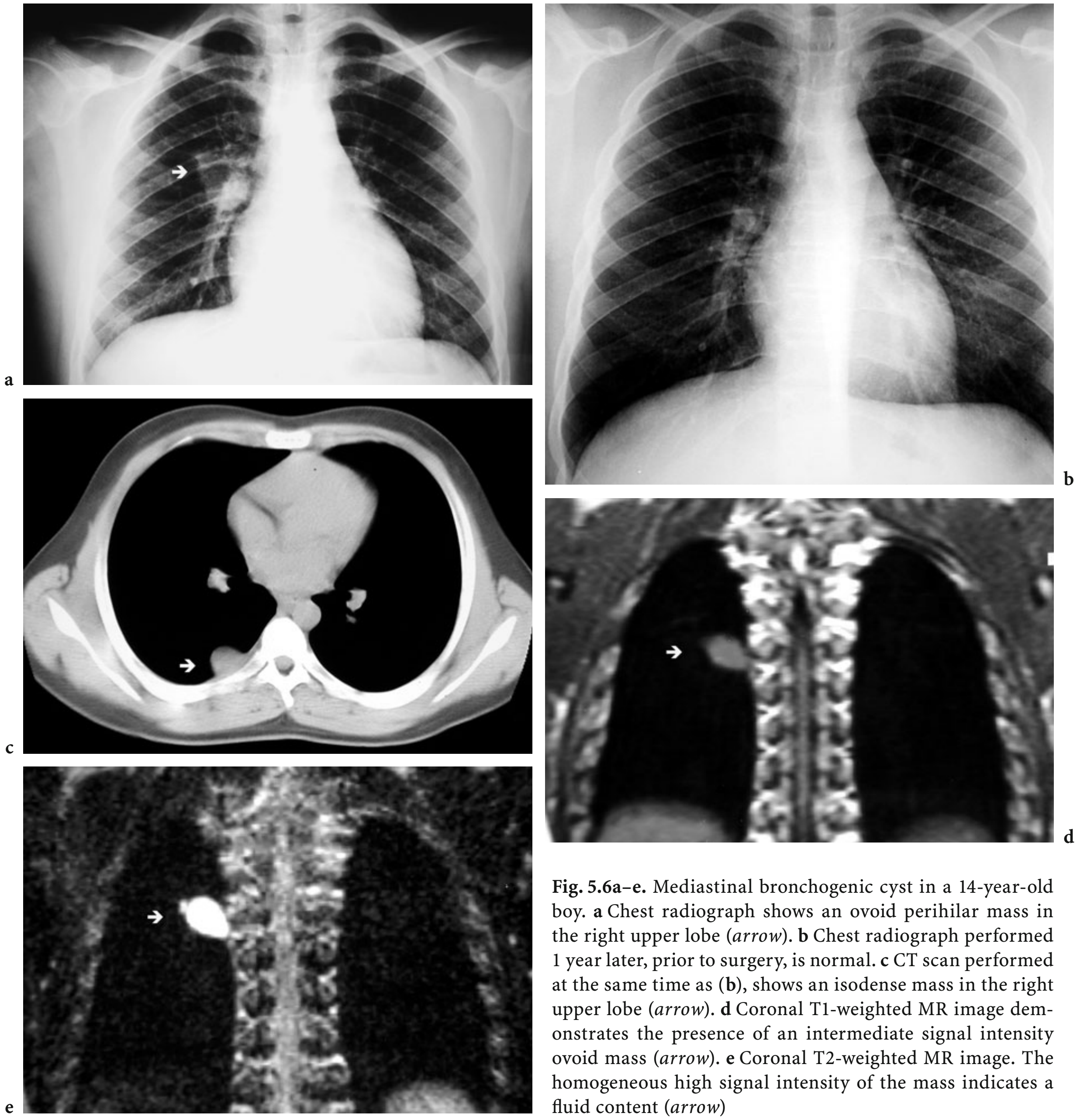

Fig. 5.6a–e. Mediastinal bronchogenic cyst in a 14-year-old boy. **a** Chest radiograph shows an ovoid perihilar mass in the right upper lobe (*arrow*). **b** Chest radiograph performed 1 year later, prior to surgery, is normal. **c** CT scan performed at the same time as (**b**), shows an isodense mass in the right upper lobe (*arrow*). **d** Coronal T1-weighted MR image demonstrates the presence of an intermediate signal intensity ovoid mass (*arrow*). **e** Coronal T2-weighted MR image. The homogeneous high signal intensity of the mass indicates a fluid content (*arrow*)

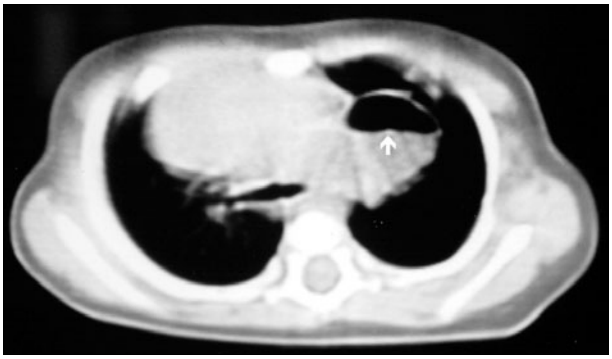

Fig. 5.7. Bronchogenic cyst in an asymptomatic 6-month-old boy. CT scan shows an air–fluid level within the cyst (*arrow*)

5.2.3
Congenital Cystic Adenomatoid Malformation – Pulmonary Sequestration Complex

5.2.3.1
Congenital Cystic Adenomatoid Malformation

Congenital cystic adenomatoid malformation (CCAM) consists of an intrapulmonary mass of disorganized pulmonary tissue that may or may not be accompanied by macroscopic cysts and has been alternatively referred to as congenital pulmonary airway malformation (CPAM) (Stocker 2002). When present, the cysts communicate with the airways and their vascular supply comes from pulmonary circulation. However, there are numerous examples of CCAM fed by systemic blood vessels and in these cases it is extremely difficult to differentiate CCAM from pulmonary sequestration, as they correspond to overlapping malformations (Winters et al. 1997). From the radiological viewpoint the differentiation between CCAM with systemic supply and pulmonary sequestration is impossible. These malformations correspond to the same clinical and radiological entity, although they have a different anatomo-pathological expression.

Ch'in and Tang (1949) first applied the name "congenital cystic adenomatoid malformation" to a congenital cystic pulmonary anomaly. The essential discovery is an adenomatoid proliferation of the terminal bronchioles that produces cysts of varying sizes coated with bronchial epithelium. There is considerable controversy over the classification and nomenclature of this condition. Congenital pulmonary airway malformation has recently been recommended as the preferred term to congenital cystic adenomatoid malformation because not all the lesions are cystic and only type III is adenomatoid. Stocker et al. (1977) divided CAM into three groups, depending on whether the cysts were larger than 2 cm (type I), smaller than 2 cm (type II), or the malformation was solid without cysts (type III). An expanded classification (types 0–4) has been proposed, representing malformations of the larger through the smaller airways. In an attempt to maintain a similar ordering of the three types published in 1977, types I, II and III become types 1, 2, and 3, and the added "distal acinar" lesion is type 4, which presents features of a large cyst generally located at the periphery of the lung. Type 0 is characterized by the fact that it affects all lobes of the lung and is incompatible with life (Table 5.1). A number of reports have suggested a relationship between CCAM and pleuropulmonary blastoma (PPB), but this remains uncertain. Based on his experience, Stocker feels that they are separate lesions, whereas other authors (MacSweeney et al. 2003) consider that the lesions from both conditions show overlapping features on histology.

CCAM can be associated with other congenital malformations, such as pulmonary sequestration,

Table 5.1. The extended classification of congenital cystic adenomatoid malformation

Type	Incidence	Gross appearance	Microscopy	Other features
0	1–3%	Solid; both lungs are small and firm	Bronchial-type airways that have cartilage, smooth muscle, and glands are separated by abundant mesenchymal tissue	Incompatibility with life
1	60–70%	Large cysts (up to 10 cm)	The cysts are lined by pseudostratified ciliated cells that are often interspersed with rows of mucous cells	May be late; best overall prognosis; less than 1% carcinomatous change
2	10–15%	Sponge-like composed of multiples cysts (up to 2 cm) and solid pale tumor-like tissue	The cysts resemble dilated bronchioles separated by normal alveoli; striated muscle in 5%	Neonates; cardiac and renal anomalies; poor prognosis
3	5%	Solid	Scattered bronchiolar/alveolar duct-like structures are lined with low cuboidal epithelium and surrounded by alveoli lined with cuboidal epithelium	Neonates, almost exclusively in males; poor prognosis
4	15%	Large cysts (up to 10 cm) generally at the periphery of the lung	The cysts are lined by a flattened epithelium resting on loose mesenchymal tissue	Neonates and infants; good prognosis; overlap with PPB

Adapted from MacSweeney et al. (2003) Am J Surg Pathol, Vol. 27, No. 8

tracheal bronchus, tracheal atresia, tracheal diverticulum (Restrepo et al. 2004), or bronchogenic cyst. CAAM can also be associated with congenital bronchial atresia in the same lobe (Cachia and Sobonya 1981), can affect more than one lobe, or be bilateral. In our experience, this condition occurs more frequently in the lower lobes. CCAM can cause severe respiratory distress in the neonatal period. Beyond this time it is usually discovered when it becomes infected or as an incidental radiological finding (Pulpeiro et al. 1987).

The malformation can escape detection on plain films. Nevertheless, CCAM is now diagnosed with increasing frequency on antenatal US examinations, where it is seen as an echogenic mass, which may or may not contain cysts. Antenatal MR imaging can help to assess associated pulmonary hypoplasia and predict the prognosis. The lesions can disappear completely, remain unchanged, or increase in size and be associated with the development of polyhydramnios or nonimmune hydrops fetalis (Fig. 5.8) (Paterson 2005).

The appearance of CCAM on radiographs and CT depends on the relative presence of cystic and solid components and whether there is superimposed infection. On plain films, type I presents as one or more dominant cysts with adjacent smaller cysts and solid tissue elements. Type II displays smaller, more evenly sized and spaced cysts. Type III, which is very rare, appears as a solid mass. Large masses produce significant mediastinal displacement. Air-fluid levels are often seen, mainly, but not always, associated with infection. On chest CT, CCAM is seen as multiple thin- or thick-walled, air- or fluid-filled cysts of variable size, expanding the affected lung. CCAM may mimic cystic pleuropulmonary blastoma. PPB is probably the same tumor that several authors have reported as mesenchymal sarcoma or rhabdomyosarcoma arising in congenital lung cysts (Ueda et al. 1977). It has also been stated that pleuropulmonary blastoma can arise from preexisting cystic lung disease, but is reasonable to assume that the cystic changes are a component of the pleuropulmonary blastoma, itself (Murphy et al. 1992). As the initial manifestation, pneumothorax is more frequently seen in pleuropulmonary blastoma than in adenomatoid congenital malformation (Fig. 5.9) (Senac et al. 1991). However, pneumothorax can be found associated with both entities and the available information does not support the use of this finding as a differentiating diagnostic criteria (Lejeune et al. 1999).

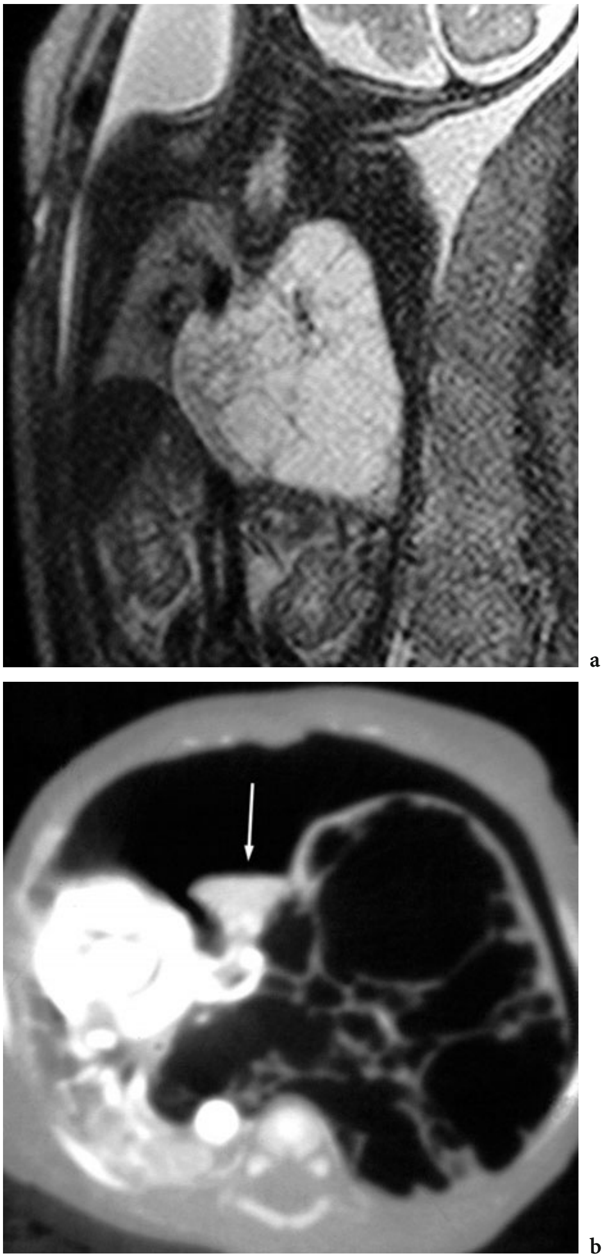

Fig. 5.8a,b. CCAM type 1. **a** Coronal MR Haste image in a 27-week-old fetus shows a large, high signal intensity, slightly heterogeneous mass with multiple septa arising from the left lung and crossing the midline. **b** CT when the patient was 5 days old shows an anterior pneumothorax and multiple cysts occupying the left hemithorax, crossing the midline, and displacing the heart and the aorta to the right. A small collapsed superior lobe is seen (*arrow*)

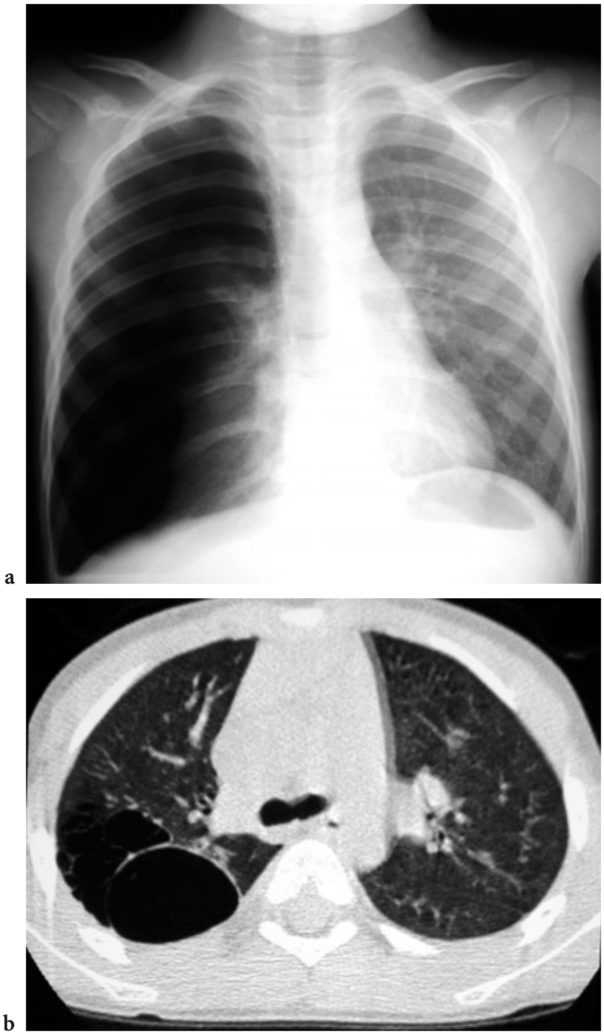

Fig. 5.9a,b. Congenital cystic adenomatoid malformation type I in a 6-year-old girl with chest pain and dyspnea. **a** Chest radiograph shows right-sided pneumothorax. A chest tube was inserted and the lung was re-expanded. **b** Chest CT performed 1 week later reveals multiple cysts at the right upper lobe

Cases of CCAM/pulmonary sequestration that dramatically decreased in size or disappear completely during pregnancy and infancy have been reported (Fig. 5.10). However, the clinical management of an asymptomatic child with a congenital mass of the lung remains controversial. Some authors advocate close clinical observation and radiological surveillance (MacGillivray et al. 1993), whereas others, considering the possibility that cystic pulmonary lesions may harbor or develop pleuropulmonary blastoma, favor elective surgical resection (Samuel and Burge 1999).

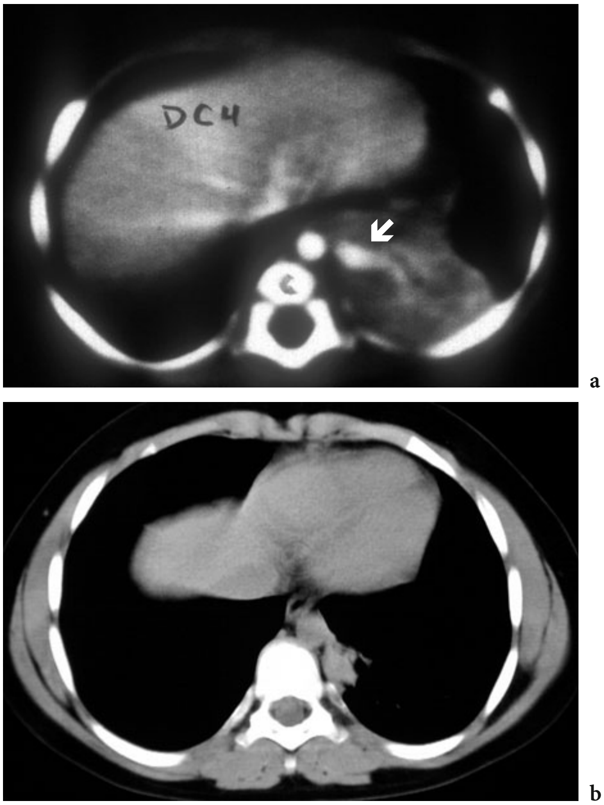

Fig. 5.10a,b. Spontaneous involution of a pulmonary sequestration. **a** Contrast-enhanced chest CT at the age of 3 months shows a soft tissue density mass with a large feeding vessel originating from the aorta (*arrow*). **b** Significant shrinkage of the mass is seen in the scan at the age of 10 years

5.2.3.2
Pulmonary Sequestration

Pulmonary sequestration consists of a mass of pulmonary tissue disconnected from the bronchial tree that receives its blood supply from the systemic circulation (Heitzman 1984). Pulmonary sequestration is divided into two groups: intralobar sequestration, in which the tissue is surrounded by normal lung and found in the interior of the visceral pleura, and extralobar sequestration, in which the tissue is disconnected from the bronchial tree and has its own pleural coating. Pryce (1946) identified intralobar sequestration as a clinical-pathological entity. He was the first to apply the term "sequestration" and further classified the lesion as intralobar or extralobar on the basis of the morphologic patterns of the malformation. There are also mixed cases with characteristics of both intralobar and extralobar sequestration.

Pulmonary sequestration is an uncommon anomaly; the intralobar form is more frequent than the extralobar. Intralobar sequestration constitutes 75% of all pulmonary sequestrations and is located en the left lower lobe in 60% of the cases. Only 2% occur in the upper lobes and 0.25% in the middle lobe. The affected lung can maintain the normal lung architecture, behave like a mass, or present internal cysts. Vascularization in the majority of cases is through the thoracic aorta (Savic et al. 1979), or less commonly, through systemic vessels originating from the abdominal aorta or one of its branches (Pedersen et al. 1988). The systemic supply can be formed by multiple, small-caliber blood vessels or by a single vessel, which are histologically similar to the pulmonary artery. This favors the early appearance of atherosclerosis (Ikezoe et al. 1990). Intralobar sequestration does not receive blood from the pulmonary arteries and it drains through pulmonary veins. Since Pryce's description of pulmonary sequestration, there has been considerable controversy about its origin. Some authors contend that intralobar sequestration is, in fact, acquired (Gebauer and Mason 1959; Holder and Langston 1986), resulting from endobronchial obstruction leading to chronic pulmonary infection and hypertrophy of the systemic arteries in and around the area of the pulmonary ligament. This explains why, in the past, when infections were poorly controlled, intralobar sequestration was overdiagnosed. However, congenital intralobar sequestration does occur, since this anomaly has been recognized on prenatal US and has been detected in newborns (West et al. 1989; Laurin and Hägertrand 1999).(Fig. 5.11).

Intralobar sequestration is usually discovered because the patient has developed a pulmonary infection, although some patients are asymptomatic when the lesion is found. In a small number of cases intralobar sequestration debuts as a pulmonary hemorrhage (Fig. 5.12), pleural effusion (Kim et al. 1997; Lucaya et al. 1984), or pleural bleeding secondary to infarction of the sequestrated lung (Zumbro et al. 1974). On plain films, intralobar sequestration appears as a homogenous opacity mostly in the lower lobes. This opacity can simulate a mass with a well-defined border, or show internal air–fluid levels and a poorly defined border. In rare cases calcifications are present within the sequestration or in the systemic blood vessel. An unusual presentation of intralobar sequestration is localized emphysema without an associated opacity or mass (Ko et al. 2000).

Extralobar sequestration is usually located between the lower lobe and the diaphragm, more frequently at the left thoracic base, in 77% of cases (Savic et al. 1979). To a much lesser degree it has also been found in the mediastinum, pericardium (Stocker and Kagan-Hallet 1979), diaphragm or retroperitoneum (Baker et al. 1982). Vascular supply occurs through a systemic artery and venous drainage through the azygos or portal sys-

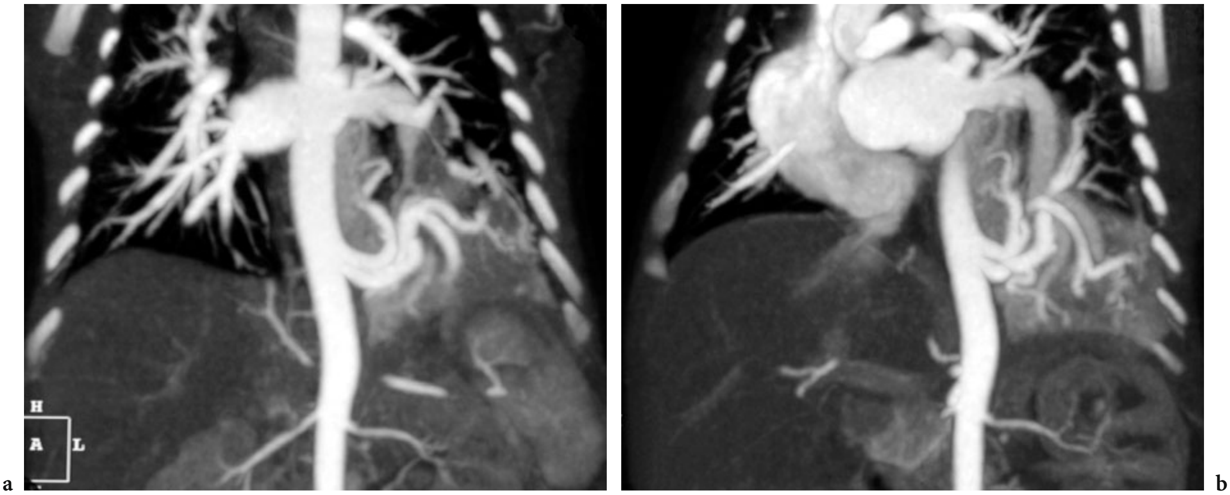

Fig. 5.11a,b. Intralobar pulmonary sequestration in a 10-day-old boy with an echogenic mass in the left lower lobe seen on prenatal US. **a** Coronal CT MIP reconstructed image shows two anomalous arteries arising from the thoracic aorta. **b** Drainage is through the lower left pulmonary vein

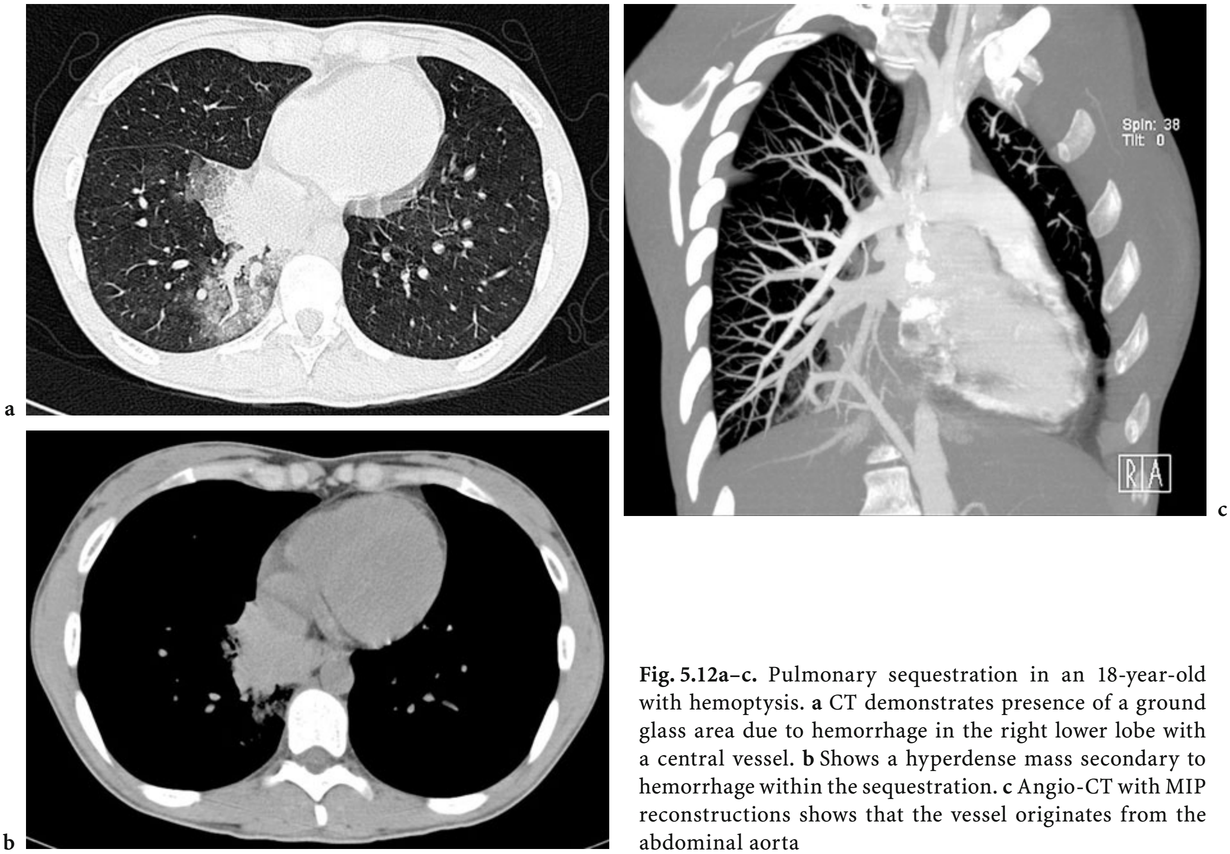

Fig. 5.12a–c. Pulmonary sequestration in an 18-year-old with hemoptysis. **a** CT demonstrates presence of a ground glass area due to hemorrhage in the right lower lobe with a central vessel. **b** Shows a hyperdense mass secondary to hemorrhage within the sequestration. **c** Angio-CT with MIP reconstructions shows that the vessel originates from the abdominal aorta

tem (Rees 1981), although nearly 25% are completely or partially drained by pulmonary veins. Extralobar sequestration is associated with other congenital malformations in 65% of cases, such as diaphragmatic hernia, bronchogenic cyst, bronchial atresia, scimitar syndrome, pericardial defect and, as previously stated, CAAM (Savic et al. 1979), and these are much more frequent than those associated with the intralobar form. Both types of sequestration occasionally connect with the digestive tract (bronchopulmonary foregut malformation) (Hruban et al. 1989). The presence of air bronchograms within a mass thought to be ELS should suggest the diagnosis of bronchopulmonary foregut malformation. Communications between the tracheobronchial tree and the GI tract should be examined by upper GI series or CT. Extralobar sequestration is usually detected fortuitously and can also be associated with pleural effusion. It may be seen as a homogeneous mass or a small bump on the posterior hemidiaphragm that may be subtle and occasionally inapparent on the chest radiograph.

Ultrasound, CT and MRI are useful in the study of sequestrations, since they enable characterization of the lesion and identification of the anomalous arterial blood supply (Fig. 5.13). CT not only recapitulates the radiographic findings but also shows the complexity of the sequestration. Intralobar sequestration typically manifests as a homogeneous or inhomogeneous solid mass, with or without definable cystic changes. It can also appear as an aggregate of multiple small cystic lesions with air or fluid content (Fig. 5.14), a well-defined cystic mass, or a large cavitary lesion with air–fluid level. The lesion may enhance with contrast material (Frazier et al. 1997; Rosado-de-Christenson et al. 1993). An appearance simulating emphysema, possibly resulting from collateral ventilation and air-trapping, can sometimes be seen in sequestration. Expiratory CT scans are helpful for delineating the extent of the malformation (Fig. 5.15) (Stern et al. 2000; Lucaya et al. 2000). Extralobar sequestration is seen on chest CT as a homogeneous, well-delimited mass, sometimes with internal cystic areas (Rosado-de-Christenson et al. 1993).

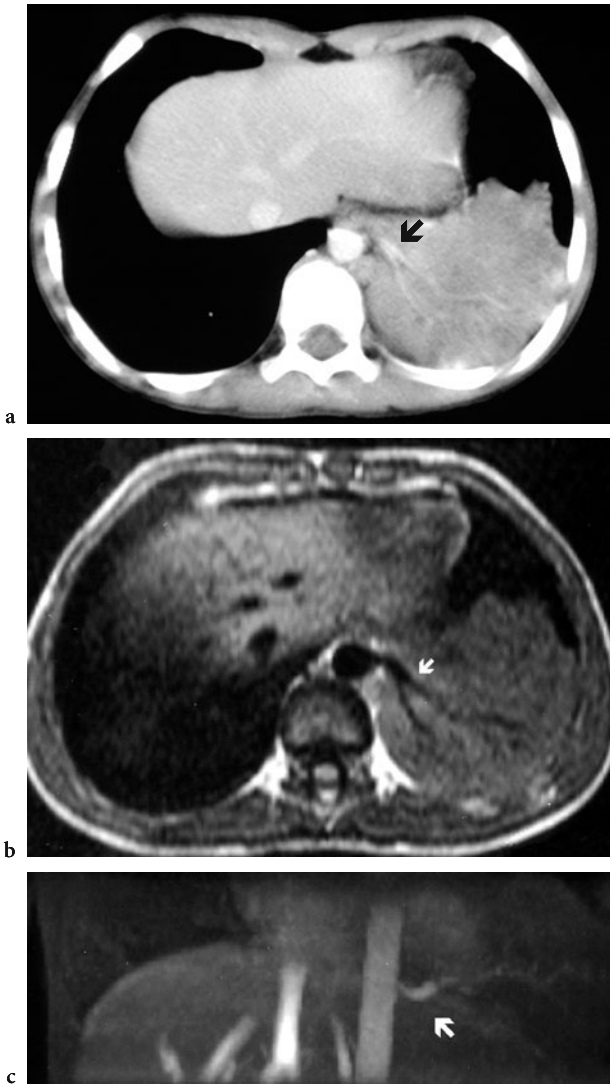

Fig. 5.13a–c. Intralobar pulmonary sequestration of the left lower lobe in a 2-year-old boy. **a** Contrast-enhanced chest CT shows the sequestration and a systemic branching vessel originating from the aorta (*arrow*). **b** Axial SE T1-weighted and **c** coronal 2D TOF MIP reconstruction images demonstrate a branching feeding vessel originating from the descending aorta and supplying the pulmonary sequestration (*arrows*)

MR imaging is well suited for the diagnosis of bronchopulmonary sequestration (Naidich et al. 1988) This anomaly is seen as a well-defined, irregular or branch-like mass. MR can also reveal the presence of cystic areas, as well as the variable solid, fluid, hemorrhagic and mucus-containing components. However, MR imaging cannot delineate focal thin-walled cysts or the emphysematous changes of sequestration as clearly as CT. The size, origin and

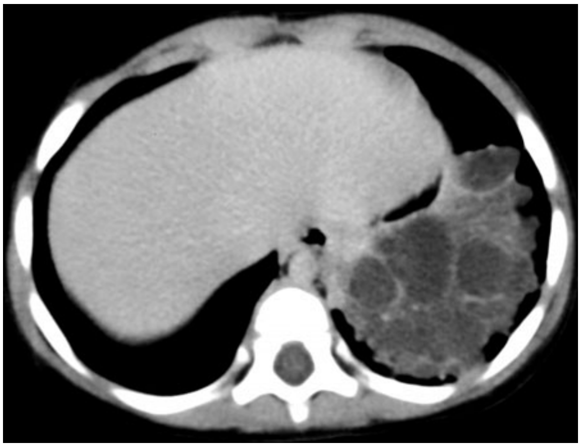

Fig. 5.14. Intralobar pulmonary sequestration in a 2-year-old boy. CT scan shows a mass with multiple fluid-filled cysts in the left lower lobe

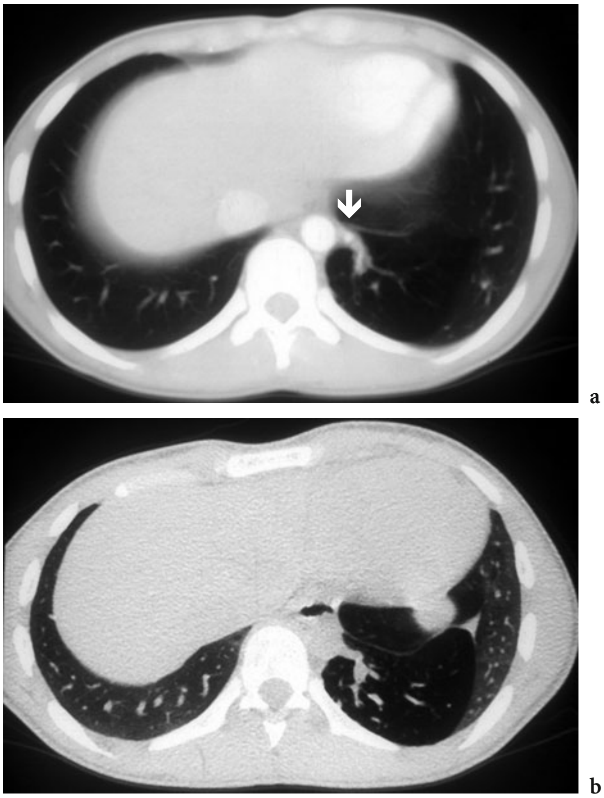

Fig. 5.15a,b. Intralobar pulmonary sequestration in left lower lobe in a 15-year-old boy. **a** Enhanced CT scan shows hyperlucency in left lower lobe. A systemic vessel (*arrow*) originating from the aorta and feeding the sequestration is well defined. **b** In an expiratory high-resolution CT scan at same level as (**a**), air-trapping can be seen within the sequestered lung. (Reprinted with permission)

course of the aberrant systemic artery and the venous drainage can be demonstrated by MR imaging. Two-dimensional time-of-flight MR angiography can reveal the aberrant artery, but this method is limited by low spatial resolution and turbulent flow. According to some reports and in our experience, breath-hold (if possible) or non breath-hold three-dimensional contrast-enhanced MR angiography offer excellent display of the aberrant vessel without flow artifacts (Ko et al. 2000).

Helical CT provides better evaluation of lung parenchyma. With low-dose three-dimensional rendering, multidetector row CT can identify the arterial and venous angioarchitecture of the sequestration (Lee et al. 2004); thus, we consider it to be the technique of choice to study children with bronchopulmonary sequestration. To our knowledge there are no studies that objectively compare the various imaging techniques for depicting and defining pulmonary sequestration (Frush and Donelly 1997). Nowadays, there is no place for conventional angiography in the diagnosis of pulmonary sequestration. Vascular studies should be limited to cases in which embolization of the feeding vessels is contemplated.

Bronchopulmonary sequestration can decrease and even spontaneously disappear; therefore some authors recommend nonsurgical management in asymptomatic patients (see Fig. 5.10) (Garcia-Peña et al. 1998).

5.2.4
Isolated Systemic Supply to Normal Lung

Isolated systemic supply to normal lung is a variant of pulmonary sequestration. This malformation corresponds to type I of Pryce's classification (Pryce et al. 1947). The artery is typically large and supplies the normal lung connected to the bronchial tree; the lung bases are affected more often (Mäkinen et al. 1981). Patients are usually asymptomatic, although there may be a continuous murmur on the thoracic wall or heart failure secondary to left-to-left shunt. Associated hemoptysis occurs occasionally.

Chest radiographs show increased opacity due to the systemic artery. Sometimes well-defined tubular or rounded images produced by the anomalous vessels can be recognized (Fig. 5.16). The pulmonary parenchyma does not present any other changes, unless there is associated hemorrhage. Definitive diagnosis can be established with CT identification of a systemic artery originating in the thoracic or abdominal aorta and absence of pathology of the underlying lung (Mata et al. 1991).

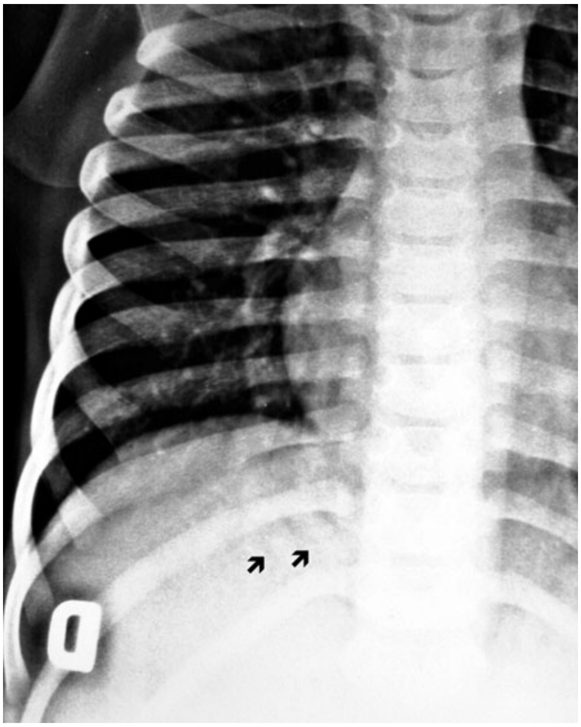

Fig. 5.16. Isolated systemic supply to normal lung in a 14-year-old boy. Chest radiograph shows tubular images produced by anomalous vessels in the right lower lobe in an otherwise normal lung (*arrows*). Angiography (not shown) demonstrated two systemic arteries arising from the aorta. (Reprinted with permission)

5.3
Dysmorphic Lung

Dysmorphic lung (DL) is characterized by arrested development of either a whole lung (lung agenesis–hypoplasia complex) or a lobe (lobar agenesis–aplasia complex). Absence of a lobe may be associated with other abnormalities, some of them common and others highly unusual. Dysmorphic lung can be recognized on chest radiographs when we are aware of its existence and it is sometimes possible to reach a diagnosis based solely on plain film evidence. In doubtful cases it is advisable to use CT (Mata et al. 1990; Woodring et al. 1994), or MRI (Baxter et al. 1990) to confirm the diagnosis.

5.3.1
Lung Agenesis – Hypoplasia Complex

Arrested development of a whole lung (lung agenesis–hypoplasia complex) is uncommon and occurs equally often in either hemithorax. Although the terms agenesis (absence of bronchus and lung), aplasia (absence of lung with bronchus present), and hypoplasia (bronchus and rudimentary lung present) describe different anomalies (Boyden 1955), we group all three under the term "agenesis–hypoplasia complex" because all have a similar radiologic appearance on the chest radiograph. In pediatric patients the prognosis for right-sided agenesis is worse than for left-sided lesions, due to a greater shift of the heart and mediastinum, resulting in a greater distortion of the airway and great vessels. Respiratory distress and recurrent infections are common in children with right-lung agenesis. Airway compression by vascular structures, such as the aortic arch, pulmonary artery and patent ductus arteriosus, as well as intrinsic tracheobronchial anomalies and tracheobronchomalacia have been described in patients with right-lung agenesis (Newman and Gondor 1997) (Fig. 5.17). A similar appearance has been reported in patients with the so-called right post-pneumectomy syndrome.

Lung agenesis–hypoplasia complex can be associated with malformations in other systems, including the skeletal, digestive, cardiac and urinary systems, and even in the contralateral lung (Brünner and Nissen 1963). The incidence of lung agenesis–hypoplasia with malformations in the skeleton or other organs is very high in some series (Osborne et al. 1989). A common origin, such as insult to the neural crest in the embryo has been postulated to explain these phenomena, giving rise to the VACTERL syndrome of anomalies (Knowles et al. 1988).

Characteristically, lung agenesis–hypoplasia complex appears on the posteroanterior view as a diffuse opacity of one hemithorax with mediastinal shift, reminiscent of the appearance of whole lung atelectasis. Occasionally it presents an atypical appearance that is more difficult to recognize on plain film. The small hemithorax, aerated lung and apparent pleural thickening, simulate chronic pleural disease (Calenoff and Friederici 1964). This appearance results from the marked herniation of the contralateral lung. Typical and atypical cases show the same radiological appearance on the lateral chest view: retrosternal hyperclarity with the heart and large mediastinal vessels displaced backwards (Mata and Cáceres 1996).

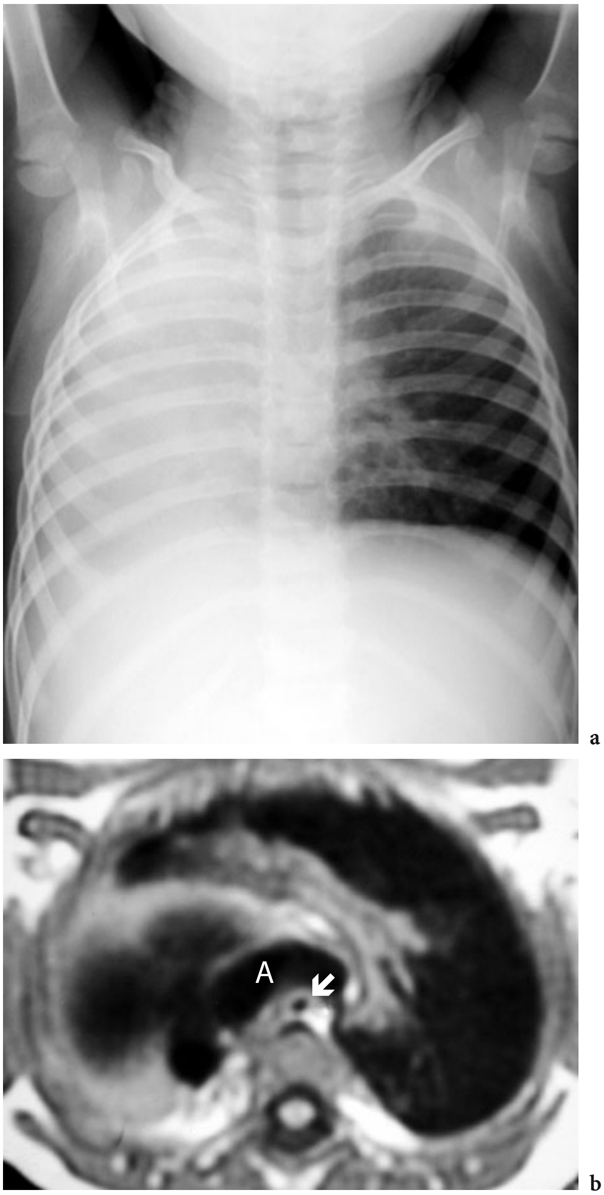

Fig. 5.17a,b. Right lung aplasia in a 2-year-old boy with respiratory symptoms. **a** Chest radiograph shows opaque right hemithorax with cardiomediastinal displacement and left lung hyperinflation. **b** Axial MR image at the level of the aortic arch demonstrates severe narrowing and posterior displacement of the distal trachea (*arrow*) by the crossing arch (*A*)

CT demonstrates the reasons for the two distinct radiological presentations. Pulmonary herniation takes place behind the sternum in both groups and accounts for the retrosternal hyperclarity. Mediastinal rotation explains the posterior displacement of the heart and mediastinum. If the herniation of the contralateral lung is not severe, the plain film shows the typical appearance of a small opaque hemithorax. In atypical cases, the extensive herniation of the contralateral lung crosses the midline to penetrate deep into the malformed hemithorax, giving the appearance of aerated lung on plain films. The pseudothickening of the pleura is produced by accumulation of subpleural fatty tissue, filling the space left by the absent or underdeveloped lung (Mata et al. 1990). Lung agenesis, aplasia and hypoplasia can be differentiated with use of CT, although the distinction is of little clinical significance. CT reveals the presence or absence of bronchi and pulmonary tissue, and allows measurement of the ipsilateral pulmonary artery (Mata and Cáceres 1996). Although lung agenesis–hypoplasia complex is said to go together with a small ipsilateral pulmonary artery, on CT or MRI studies a small number of patients show a near normal-sized pulmonary artery with substantial blood flow.

Absence (atresia or interruption) of the main right or left pulmonary artery (APA) is an isolated vascular malformation that goes together with small homolateral lung, but should not be considered a part of lung agenesis–hypoplasia complex. It usually occurs in association with cardiac anomalies; isolated APA is rare (Kleinman 1979). During childhood APA produces substantial bronchial and transpleural (intercostal arteries) collateral circulation. The enlarged bronchial and intercostal arteries that feed the lung sometimes produce hemoptysis. At radiologic study, APA is seen as a small lung with mediastinal shift and no identifiable pulmonary artery. Collateral systemic supply produces peripheral linear opacities and pleural thickening. CT and MRI show absence of the pulmonary artery and can identify the enlarged systemic arteries (Fig. 5.18).

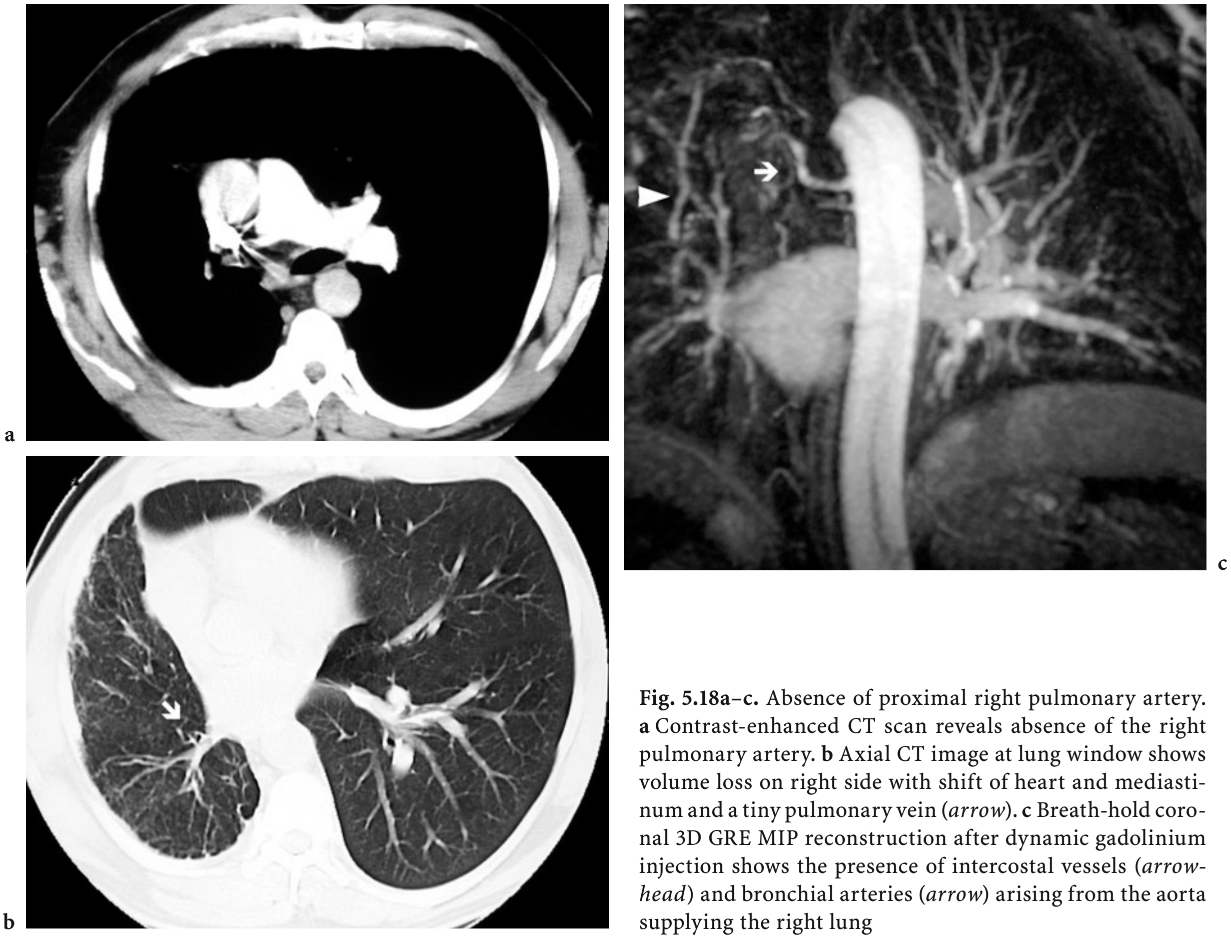

Fig. 5.18a–c. Absence of proximal right pulmonary artery. **a** Contrast-enhanced CT scan reveals absence of the right pulmonary artery. **b** Axial CT image at lung window shows volume loss on right side with shift of heart and mediastinum and a tiny pulmonary vein (*arrow*). **c** Breath-hold coronal 3D GRE MIP reconstruction after dynamic gadolinium injection shows the presence of intercostal vessels (*arrowhead*) and bronchial arteries (*arrow*) arising from the aorta supplying the right lung

5.3.2
Lobar Agenesis – Aplasia Complex

Lobar agenesis–aplasia complex is a group of pulmonary malformations affecting, almost exclusively, the right hemithorax. All of these malformations present pulmonary anomalies in the form of one or more absent or underdeveloped pulmonary lobe. Depending upon the associated venous malformation, we can look at this group as a continuum. At one extreme, the pulmonary malformation is isolated and the veins are normal (hypogenetic lung syndrome). The second step in the continuum includes the anomalous unilateral single pulmonary vein, which drains all the lung parenchyma into the left atrium (Hasuo et al. 1981). Next in line is the levo-atriocardinal vein; in this malformation there is an anomalous vein that drains the entire lung and connects the left atrium with a systemic vein (Edwards and DuShane 1950). Last in the continuum is an anomalous vein draining into the systemic venous system (venolobar syndrome). Accessory diaphragm (part of the right lung trapped by a membranomuscular duplication of the diaphragm) (Nazarian et al. 1971) and horseshoe lung (tissue from the malformed lung crossing the mediastinum to meet or fuse with the left lower lobe) (Dische et al. 1974) can accompany any of these malformations (Fig. 5.19). Systemic supply from the thoracic aorta is almost always present, although it is hardly ever seen on plain film or CT scans (Fig. 5.20). Sometimes the systemic artery is thick, mimicking a scimitar vein (Partridge et al. 1988).

5.3.2.1
Hypogenetic Lung Syndrome

In hypogenetic lung syndrome there is agenesis or aplasia of one or two pulmonary lobes. Patients are usually asymptomatic. This entity almost always occurs in the right hemithorax; left hemithorax involvement is exceptional.

The chest radiograph shows a small right hemithorax with mediastinal shift to the right and haziness of the right cardiac border. In some cases, the right hilum is hidden by mediastinal rotation and cannot be seen, and in others the shape of the hilum is reminiscent of the left hilum. In most cases, lateral chest films show a retrosternal band caused by the interface between the shifted mediastinum and the anterior border of the underdeveloped lung (Ang and Proto 1984).

CT provides a wealth of information (Godwin and Tarver 1986; Mata and Cáceres 1996) by demonstrating the size of the pulmonary artery, the branching of the bronchi, and accompanying anomalies of the diaphragm (diaphragmatic hernias). If underdevelopment is very pronounced, one can observe extrapleural fat deposits along the thoracic wall simulating pleural thickening similar to, though not as striking as, those seen in the lung agenesis-hypoplasia complex (Mata et al. 1990). The right upper lobe is the most often affected. This gives a bronchial pattern of the right lung similar to that observed in the left lung in normal conditions (hypoarterial bronchus) (Fig. 5.21). CT demonstrates the pulmonary veins draining into their normal location, ruling out venous anomalies.

5.3.2.2
Lobar Agenesis – Aplasia with Anomalous Unilateral Single Pulmonary Vein

The second step in the continuum is a symptom-free malformation, first described by Benfield et al. in 1971. It has received several names since its description: pulmonary varix, meandering right pulmonary vein or scimitar sign with normal pulmonary venous drainage. In our experience, in most cases this malformation consists of a hypogenetic lung with a single anomalous vein draining the entire lung parenchyma into the left atrium. The vein follows an unusual pathway before it meets the left atrium.

In the chest radiograph anomalous unilateral single pulmonary vein usually has the same appearance as hypogenetic lung syndrome, plus a tubular and serpiginous shadow due to the anomalous vein. In rare cases the anomalous vein mimics a scimitar vein (Herer et al. 1988). CT and MRI provide the right diagnosis, showing a serpiginous shadow running through the lung and ending in the left atrium (Mata and Cáceres 1996) (Fig. 5.22). In some cases of anomalous unilateral single pulmonary vein, the vein drains into an extracardiac chamber located behind the left atrium (cor triatriatum).

Exceptionally we can see atypical cases with anomalous pulmonary veins affecting both lungs. This has been described as idiopathic prominence of pulmonary veins or “meandering pulmonary veins” (Kriss et al. 1995; Mata et al. 2000). The veins of both lungs follow an unusual pathway and drain into the left atrium (see Chap. 3, Fig. 3.5). Meandering pulmonary veins are occasionally associated with hypogenetic lung.

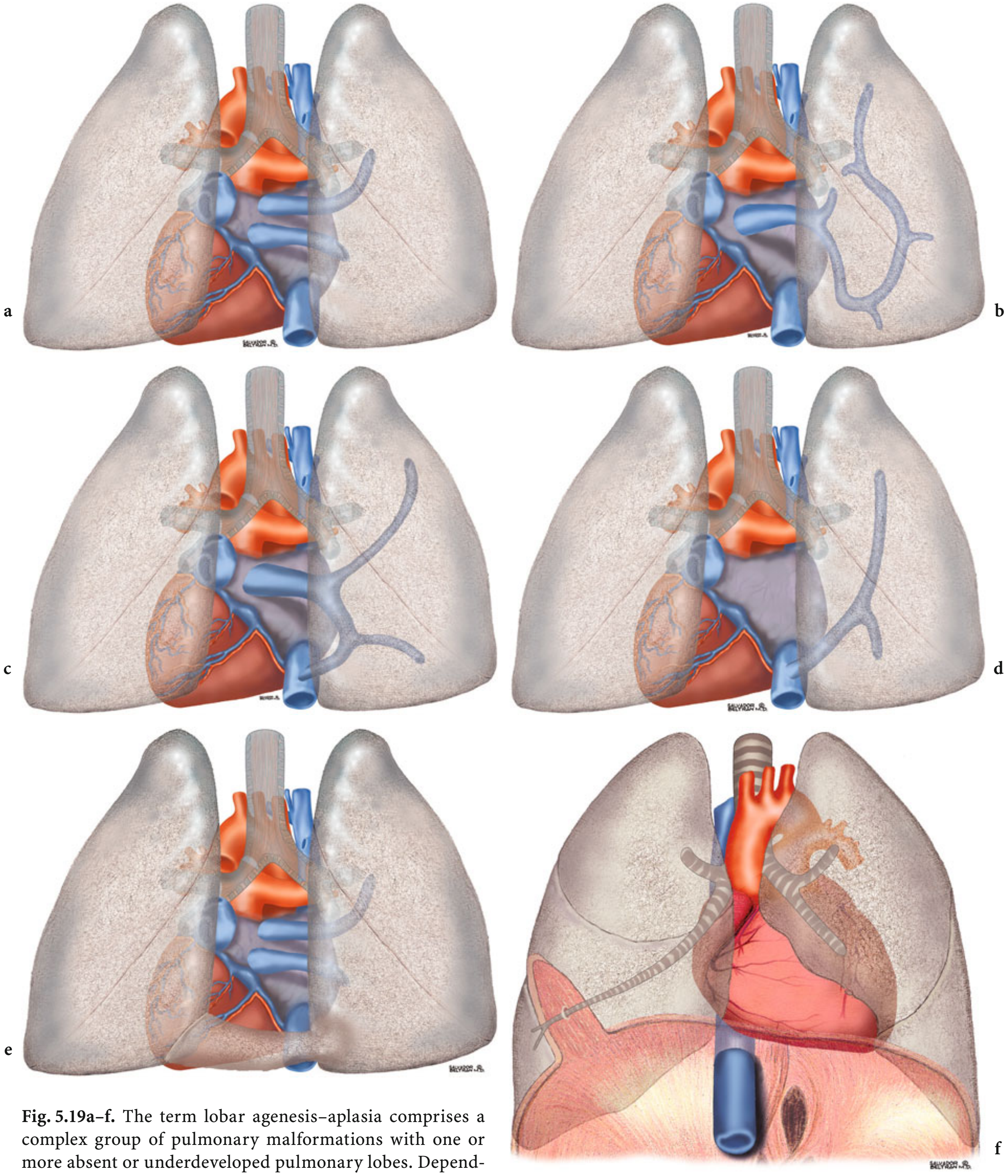

Fig. 5.19a–f. The term lobar agenesis–aplasia comprises a complex group of pulmonary malformations with one or more absent or underdeveloped pulmonary lobes. Depending on the associated venous malformation, this group can be viewed as a continuum. At one extreme, the pulmonary malformation is isolated, and the veins are normal and drain into the left atrium (**a**). The second step of the continuum includes the anomalous unilateral single pulmonary vein, which drains the entire lung parenchyma into the left atrium (**b**). Next in line is the levo-atriocardinal vein, in which there is an anomalous vein that drains the entire lung and connects the left atrium with a systemic vein (inferior vena cava in the drawing) (**c**). Last in the continuum is an anomalous vein draining into the systemic venous system (venolobar syndrome) (**d**). Horseshoe lung (tissue from the malformed lung crossing the mediastinum to meet or fuse with the left lower lobe) (**e**) and accessory diaphragm (part of the right lung trapped by a membranomuscular duplication of the diaphragm) (**f**) can accompany any of these malformations

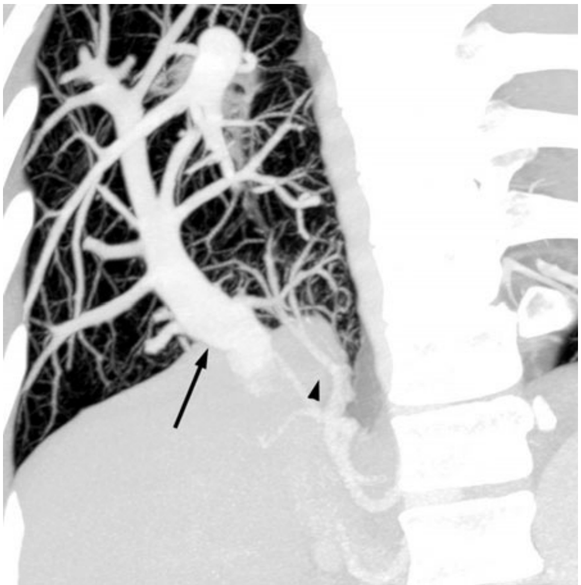

Fig. 5.20. Multiplanar reformatted image. Congenital venolobar syndrome. The scimitar vein (*arrow*) is evident, as well as the systemic supply, which comes from the abdominal aorta and goes to the right pulmonary base (*arrowhead*)

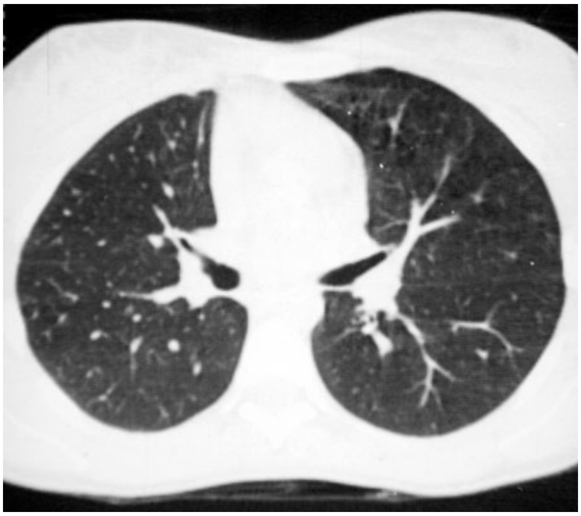

Fig. 5.21. Hypogenetic lung syndrome. CT scan shows left bronchial pattern in both lungs. The right lung is smaller than the left lung. (Reprinted with permission)

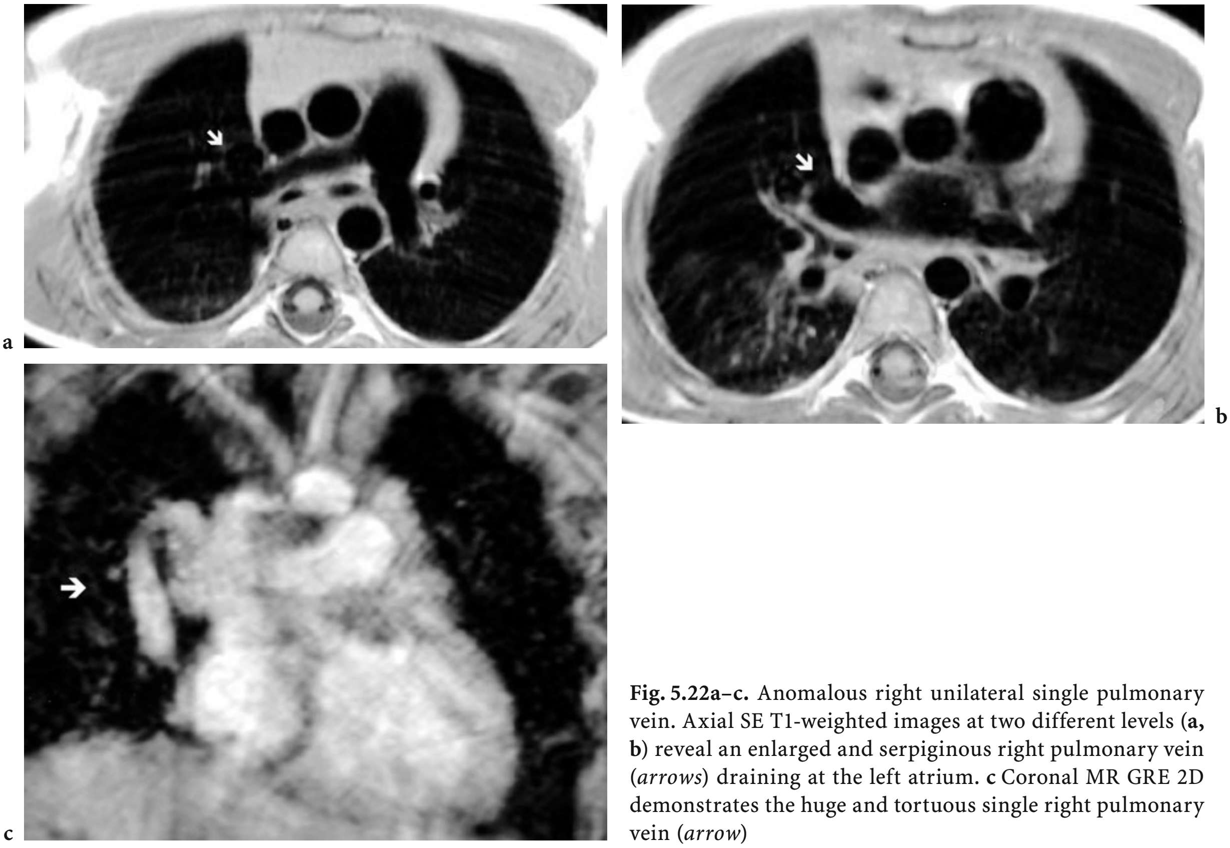

Fig. 5.22a–c. Anomalous right unilateral single pulmonary vein. Axial SE T1-weighted images at two different levels (**a**, **b**) reveal an enlarged and serpiginous right pulmonary vein (*arrows*) draining at the left atrium. **c** Coronal MR GRE 2D demonstrates the huge and tortuous single right pulmonary vein (*arrow*)

5.3.2.3
Lobar Agenesis – Aplasia with Levo-atriocardinal Vein

Levo-atriocardinal vein is defined as an anomalous vein that connects the left atrium and one vein of the systemic venous system. The systemic venous system derives from the embryological system known as cardinal veins. The malformation consists of a hypogenetic lung with the anomalous vein connecting the left atrium and one of the main systemic veins. Levo-atriocardinal vein would be the mid-point in the continuum between anomalous unilateral single pulmonary vein and venolobar syndrome. It is a very uncommon malformation.

On chest radiography the levo-atriocardinal vein looks very similar to the anomalous unilateral single pulmonary vein. CT demonstrates the usual findings of hypogenetic lung syndrome and the vein joining the left atrium and a systemic vein (Fig. 5.23). The anomalous vein drains all the pulmonary veins, and MRI shows the pathway of the vein as well as the points where it meets with the systemic vein and the left atrium (Fig. 5.24) (Mata et al. 2000). MRI can demonstrate that there is no gradient between the left atrium and the systemic vein.

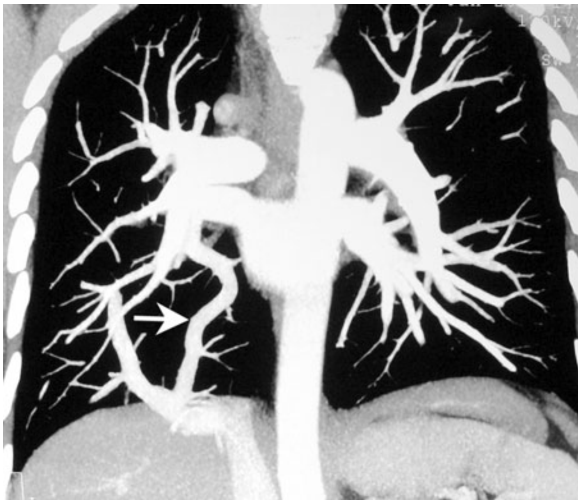

Fig. 5.23. Multiplanar reformatted image showing a levoatriocardinal vein (*arrow*) connecting an anomalous vein draining into the inferior cava vein and a pulmonary vein draining into the left atrium (Courtesy of Dr. José Cáceres, Barcelona)

5.3.2.4
Congenital Venolobar Syndrome

In congenital venolobar syndrome (CVS), also known as scimitar syndrome, partial anomalous venous return (PAVR) is associated with hypogenetic lung syndrome. This malformation is one of the extremes of the dysmorphic lung continuum. Most patients are asymptomatic. The left–right shunt produced by the anomalous drainage is usually small and has

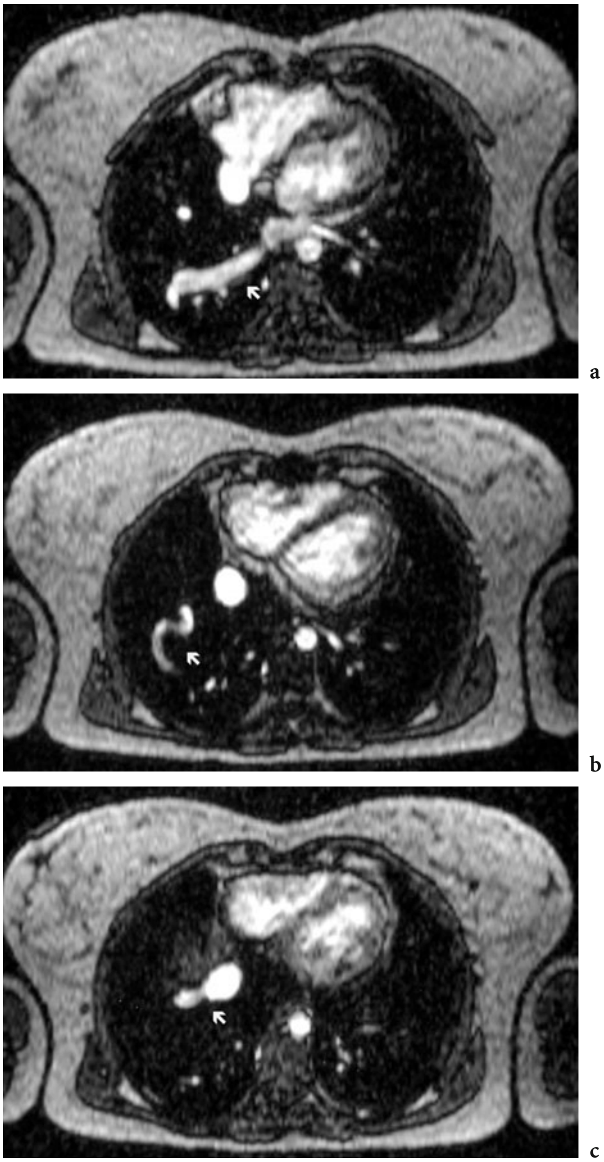

Fig. 5.24a–c. Levoatriocardinal vein in the right lung. Axial MR GRE 2D images at three different levels (**a–c**) show the tortuous vein that goes from the left atrium to the inferior vena cava (*arrows*)

no clinical repercussions, though on rare occasions it can lead to pulmonary hypertension (Haworth et al. 1983). Associated cardiac malformations may cause symptoms in pediatric patients (Canter et al. 1986). CVS occurs almost exclusively in the right hemithorax.

Plain film findings are similar to those of hypogenetic lung. The differential finding is the anomalous vein. The vessel is seen as a widening tubular shadow that extends toward the base of the lung, originating the term scimitar syndrome. The anomalous vein usually drains into the inferior vena cava or the right atrium. The fact there may be more than one vein or that a single vein may be hidden behind the displaced heart, accounts for the fact that the PAVR is not seen on plain film in half of the cases.

CT allows visualization of the anomalous vein and where it drains (Mata et al. 1990; Woodring et al. 1994) (Fig. 5.25), and the absence of inferior pulmonary vein. PAVR is associated with an accessory pulmonary fissure that is visible on CT study (Godwin and Tarver 1986). The anomalous vein can be seen with MRI (Baxter et al. 1990), and in some cases the entire course of the vessel can be followed in a single plane. In our experience, MRI is less useful than CT for this malformation, as it cannot show the bronchial anomaly.

5.3.2.5
Horseshoe Lung

Horseshoe lung is associated with hypogenetic lung syndrome and occurs when a small quantity of right pulmonary tissue arising from the lower lobe crosses the midline and joins the left lower lung. The right and left lower lobes may fuse, or be separated by a fissure. The isthmus of pulmonary tissue crosses

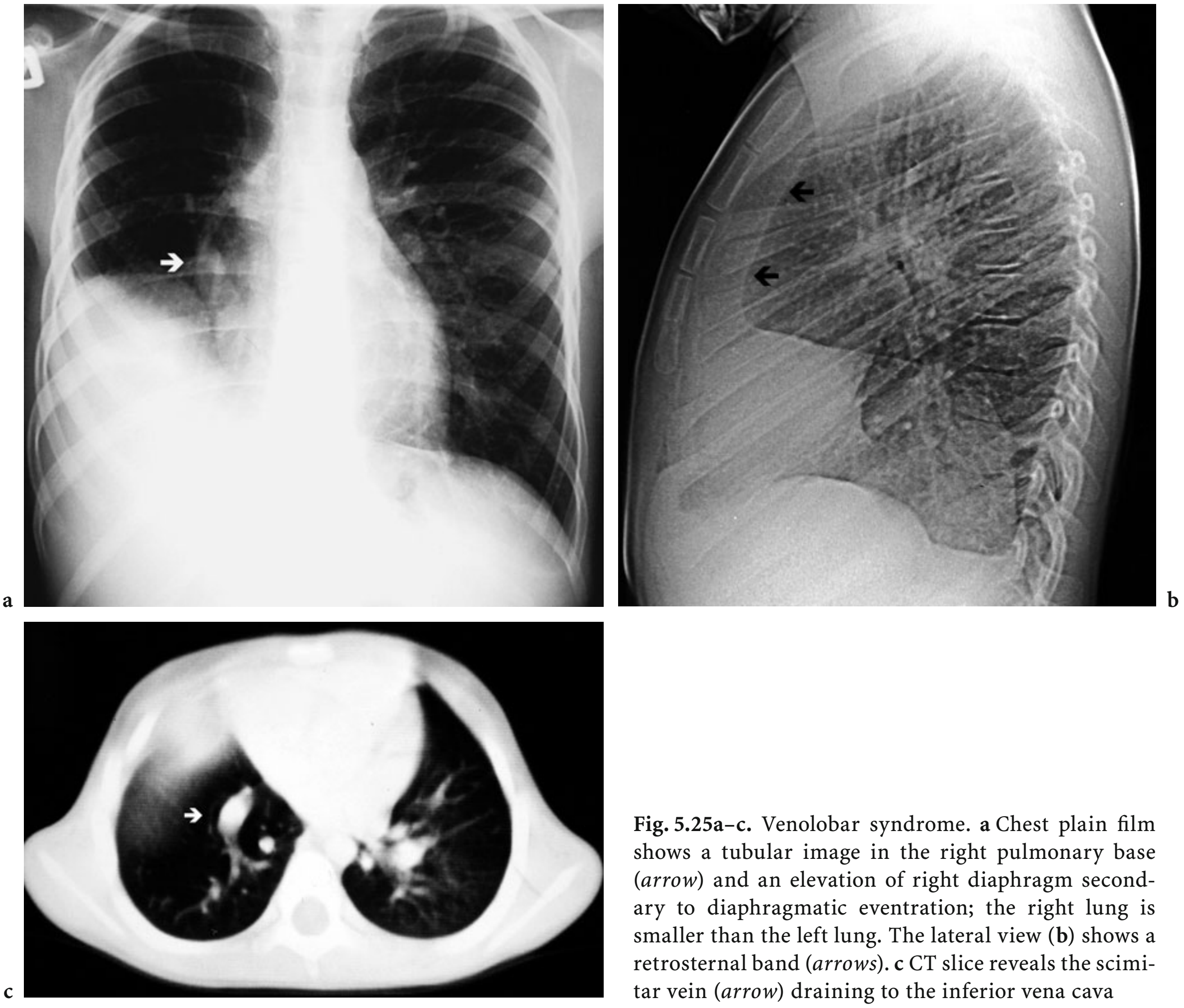

Fig. 5.25a–c. Venolobar syndrome. **a** Chest plain film shows a tubular image in the right pulmonary base (*arrow*) and an elevation of right diaphragm secondary to diaphragmatic eventration; the right lung is smaller than the left lung. The lateral view (**b**) shows a retrosternal band (*arrows*). **c** CT slice reveals the scimitar vein (*arrow*) draining to the inferior vena cava

the mediastinum behind the pericardium, in front of the aorta and the esophagus and it is supplied by the right lower lobe vessels and bronchus (Frank et al. 1986; Freedom et al. 1986).

The chest radiograph shows hypogenetic lung syndrome or congenital venolobar syndrome together with an anomalous fissure in the base of the left lung. This finding suggests the correct diagnosis on the PA chest film (Frank et al. 1986). Sometimes the anomalous fissure can be seen as a thick opacity due to internal fat. CT shows the typical findings of hypogenetic lung, with or without abnormal veins, plus two additional findings: mediastinal discontinuity behind the heart, with the vessels of the right lower lobe crossing the midline and, when present, an anomalous fissure located at the base of the left lung (Fig. 5.26) (Beitzke et al. 1982).

5.3.2.6
Accessory Diaphragm

Accessory diaphragm, also known as diaphragmatic duplication, is a rare congenital anomaly associated with the lobar agenesis–aplasia complex. It does not occur as an isolated malformation. Accessory diaphragm was first described by Drake et al. in 1950. These authors postulated that the anomaly is produced in the initial stages of embryonic development when the septum transversum, which gives rise to the diaphragm, is in a very high position. If for some reason the descent of the septum transversum is arrested, part of the primitive lung can be trapped by it. The septum transversum would remain anchored to the posterior wall, creating an additional diaphragmatic leaf.

Accessory diaphragm is a thin fibromuscular membrane fused anteriorly with the diaphragm and coursing posterosuperiorly to join the posterior chest wall. It produces two compartments in the right hemithorax, trapping part of the lung parenchyma (Wille et al. 1975). The vessels and bronchi that supply the trapped lung pass through a central hole in the accessory diaphragm.

The accessory diaphragm can have two different appearances in the chest radiograph. When the central hiatus is very narrow, the trapped lung is not aerated and appears as a mass. When the trapped lung is aerated, the accessory diaphragm appears in plain film as a thin oblique line in either the posteroanterior or lateral chest view. In some patients a haziness is visible where the duplicated diaphragm joins the normal one.

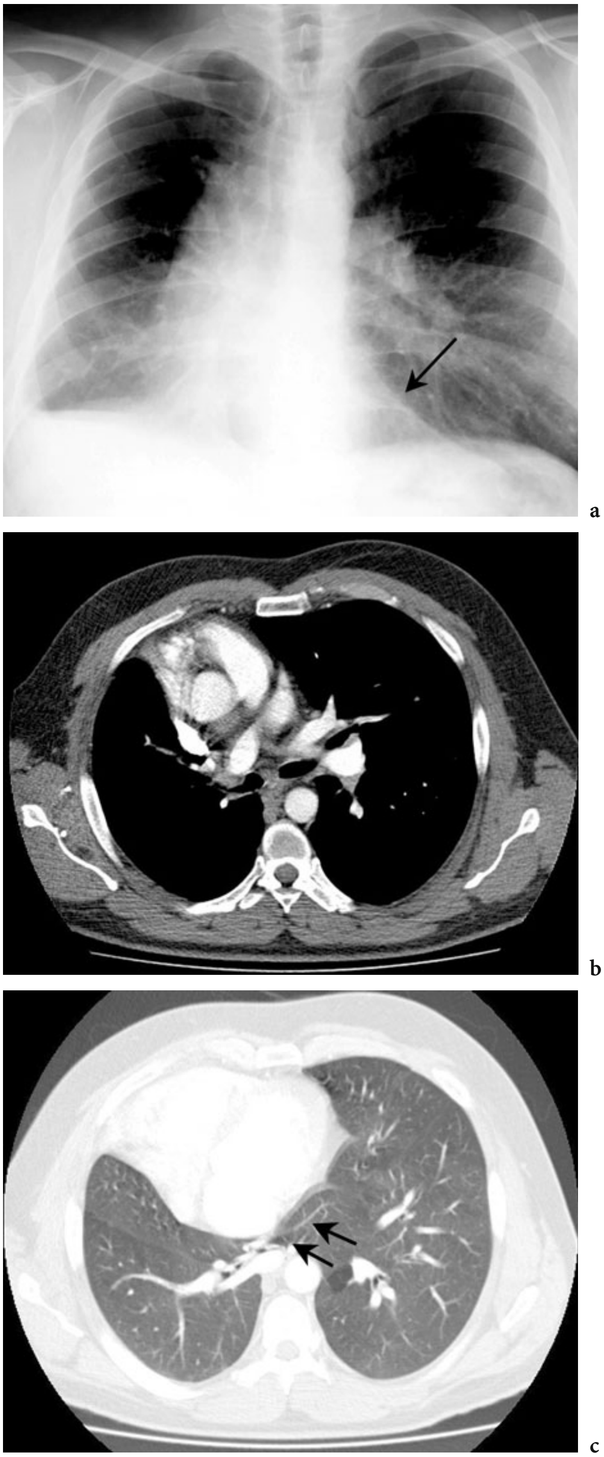

Fig. 5.26a–c. Horseshoe lung. **a** Plain film shows a small right hemithorax and a linear image in the left pulmonary base (*arrows*). **b** CT demonstrates anomalous pattern of the right bronchial tree and mediastinal shift. **c** depicts mediastinal discontinuity behind the heart and right lower lobe arteries, and bronchus (*arrows*) crossing the midline and running to the left pulmonary base

When the lung is aerated, CT scans show the accessory diaphragm as a fissure-like line with a hole in the center (Woodring et al. 1994; Hidalgo et al. 2006) (Fig. 5.27). Depending upon the size of the central hole, the CT appearance varies. When the hole is large, it may be difficult to identify the accessory diaphragm. When the hole is small, the trapped lung may be opaque or hyperlucent, due to air-trapping. Vessels and bronchi are crowded together when they go through the central hiatus.

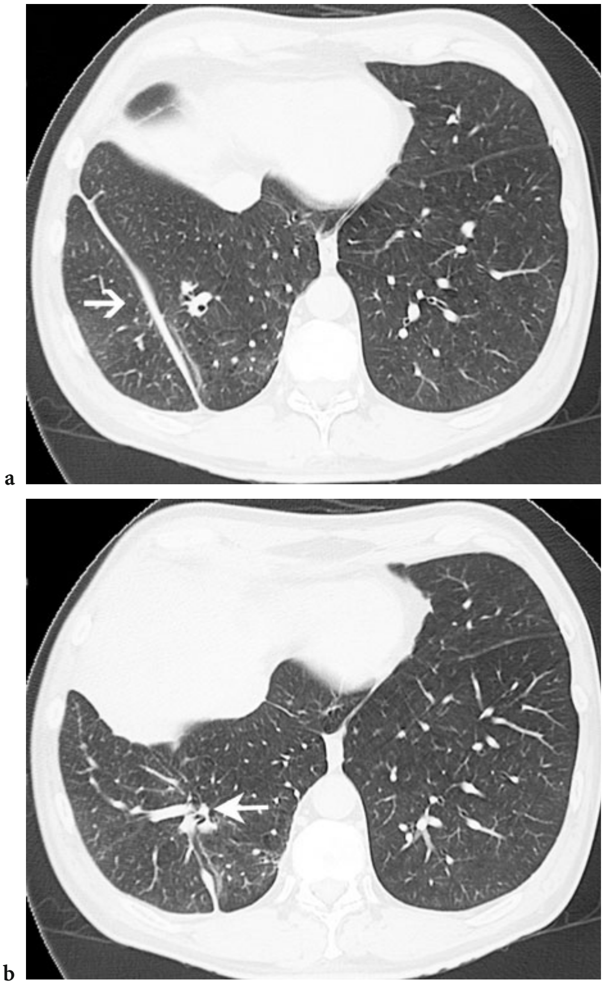

Fig. 5.27a,b. Accessory diaphragm. **a** The accessory diaphragm can be seen by CT as a line, simulating a fissure (*arrow*). **b** The vessels and bronchus are crowded together as they go through the central hole (*arrow*)

References

Ang JGP, Proto A (1984) CT demonstration of congenital pulmonary venolobar syndrome. J Comput Assist Tomogr 8:753–757

Baker EL, Gore RM, Moss AA (1982) Retroperitoneal pulmonary sequestration: computed tomographic findings. AJR Am J Roentgenol 138:956–957

Baker EM (1989) Intrathoracic duplication cysts: a review of 17 patients. J Med Imag 3:127–134

Bankoff MS, Daly BDT, Johnson HA, Carter BL (1985) Bronchogenic cyst causing superior vena cava obstruction: CT appearance. J Comput Assist Tomogr 9:951–952

Baxter R, McFadden PM, Gradman M, Wright A (1990) Scimitar syndrome: cine magnetic resonance imaging demonstration of anomalous pulmonary venous drainage. Ann Thorac Surg 50:121–123

Beitzke VA, Gypser G, Sager WD (1982) Scimitarsyndrom mit Hufeisenlunge. ROFO 136:265–269

Benfield JR, Gots RE, Mills D (1971) Anomalous single left pulmonary vein mimicking a parenchymal nodule. Chest 59:101–102

Boyden EA (1955) Developmental anomalies of the lung. Am J Surg 89:79–89

Braffman B, Keller R, Stein Gendal E, Finkel SI (1988) Subdiaphragmatic bronchogenic cyst with gastric communication. Gastrointest Radiol 13:309–311

Brünner S, Nissen E (1963) Agenesis of the lung. Am Rev Respir Dis 78:103–106

Cachia R, Sobonya RE (1981) Congenital cystic adenomatoid malformation of the lung with bronchial atresia. Hum Pathol 12:947–950

Calenoff L, Friederici HH (1964) Unilateral pulmonary hypoplasia in an adult. AJR Am J Roentgenol 91:265–272

Canter CE, Martin TC, Spray TL, Weldon CS, Strauss AW (1986) Scimitar syndrome in childhood. Am J Cardiol 58:652–654

Castellote A, Enriquez G, Lucaya J (2005) Congenital malformations of the chest beyond the neonatal period. In: Carty H, Brunelle F, Stringer DA, Kao S (eds) Imaging children. Elsevier

Ch'in KY, Tang My (1949) Congenital adenomatoid malformation of one lobe of the lung with general anasarca. Arch Pathol 48:221–229

Dische MR, Teixeira ML, Winchester PA, Engle MA (1974) Horseshoe lung associated with a variant of the "scimitar" syndrome. Br Heart J 36:617–620

Drake EH, Portland ME, Lynch JP (1950) Bronchiectasis associated with anomaly of the right pulmonary vein and right diaphragm. J Thorac Surg 19:433

DuMontier C, Graviss ER, Silberstein MJ, McAlister WH (1985) Bronchogenic cysts in children. Clin Radiol 36:431–436

Edwards JE, DuShane JW (1950) Thoracic venous anomalies. Arch Pathol 49:517

Felson B (1979) Mucoid impaction (inspissated secretions) in segmental bronchial obstruction. Radiology 133:9–16

Finck S, Milne ENC (1988) A case report of segmental atresia: radiologic evaluation including computed tomography and magnetic resonance imaging. J Thorac Imag 3:53–57

Fitch SJ, Tonkin ILD, Tonkin AK (1986) Imaging of foregut duplication cysts. Radiographics 6:189–201

Frank JL, Poole CA, Rosas G (1986) Horseshoe lung: clinical, pathologic, and radiologic features and a new plain film finding. AJR Am J Roentgenol 146:217–226

Frazier AA, Rosado-de-Christenson M, Stocker JT, Templeton PA (1997) Intralobar sequestration: radiologic-pathologic correlation. Radiographics 17:725–745

Freedom RM, Burrows PE, Moes CAF (1986) “Horseshoe” lung: report of five new cases. AJR Am J Roentgenol 146:211–215

Frush DP, Donelly LF (1997) Pulmonary sequestration spectrum: a new spin with helical CT. AJR Am J Roentgenol 169:679–682

Garcia-Peña P, Lucaya J, Hendry GMA et al. (1998) Spontaneous involution of pulmonary sequestration in children: a report of two cases and review of the literature. Pediatr Radiol 28:266–270

Gebauer PW, Mason CB (1959) Intralobar pulmonary sequestration associated with anomalous pulmonary vessels: a nonentity. Dis Chest 35:282–287

Godwin JD, Tarver RD (1986) Scimitar syndrome: four new cases examined with CT. Radiology 159:15–20

Grewal RG, Yip CK (1994) Intralobar pulmonary sequestration and mediastinal bronchogenic cyst. Thorax 49:615–616

Griscom NT (1993) Diseases of the trachea, bronchi, and smaller airways. Radiol Clin North Am 31:605–615

Hasuo K, Numaguchi Y, Kishikawa T, Ikeda J, Matsuura K (1981) Anomalous unilateral single pulmonary vein mimicking pulmonary varices. Chest 79:602–604

Haworth SG, Sauer U, Bühlmeyer K (1983) Pulmonary hypertension in scimitar syndrome in infancy. Br Heart J 50:182–189

Heitzman ER (1984) The lung: radiologic-pathologic correlations. Mosby, St Louis

Herer B, Jaubert F, Delaisements C, Huchon G, Chretien J (1988) Scimitar sign with normal pulmonary venous drainage and anomalous inferior vena cava. Thorax 43:651–652

Hidalgo A, Franquet T, Gimenez A (2006) 16-MDCT and MR angiography of accessory diaphragm. AJR Am J Roentgenol 187:149–152

Holder PD, Langston C (1986) Intralobar pulmonary sequestration (a nonentity?). Pediatr Pulmonol 2:147–153

Hruban RH, Shumway SJ, Orel SB, Dumler JS, Baker RR, Hutchins M (1989) Congenital pulmonary foregut malformations. Intralobar and extralobar pulmonary sequestration communicating with the foregut. Am J Clin Pathol 91:403–408

Hugosson C, Rabeeah A, Al-Rawaf A et al. (1995) Congenital bilobar emphysema. Pediatr Radiol 25:649–651

Ikezoe J, Murayama S, Godwin JD, Done SL, Verschakelenm JA (1990) Bronchopulmonary sequestration: CT assessment. Radiology 176:375–379

Jederlinic PJ, Sicilian LS, Baigelman W, Gaensler EA (1986) Congenital bronchial atresia. Medicine 65:73–83

Kim WS, Lee KS, Kim IO et al. (1997) Congenital cystic adenomatoid malformation of the lung. CT-pathologic correlation. AJR Am J Roentgenol 168:47–53

Kimura A, Makuuchi M, Takayasu K, Sakamoto M, Hiroshashi S (1990) Ciliated hepatic foregut cyst with solid tumor appearance on CT. J Comput Assist Tomogr 14:1016–1018

Kleinman PK (1979) Pleural telangiectasia and absence of a pulmonary artery. Radiology 132:281–284

Knowles S, Thomas RM, Lindenbaum RH, Keeling JW, Winter RM (1988) Pulmonary agenesis as part of the VACTERL sequence. Arch Dis Child 63:723–726

Ko SF, Ng SH, Lee TZ et al. (2000) Noninvasive imaging of bronchopulmonary sequestration. AJR Am J Roentgenol 175:1005–1012

Kriss VM, Woodring JH, Cottrill CM (1995) “Meandering” pulmonary veins: report of a case in an asymptomatic 12-year-old girl. J Thorac Imaging 10:142–145

Kuhn C, Kuhn JP (1992) Coexistence of bronchial atresia and bronchogenic cyst: diagnostic criteria and embryologic considerations. Pediatr Radiol 22:568–570

Kwak GL, Stork WI, Greenberg SD (1971) Partial defect of the pericardium associated with a bronchogenic cyst. Radiology 101:287–288

Langston C (2003) New concepts in the pathology of congenital lung malformations. Semin Pediatr Surg 12:17–37

Laurin S, Hägertrand I (1999) Intralobar bronchopulmonary sequestration in the newborn – a congenital malformation. Pediatr Radiol 29:174–178

Lee EY, Siegel MJ, Sierra LM et al. (2004) Evaluation of angioarchitecture of pulmonary sequestration in pediatric patients using 3D MDCT angiography. AJR Am J Roentgenol 183:183–188

Lejeune C, Deschildre A, Thumerelle C et al. (1999) Pneumothorax revealing cystic adenomatoid malformation of the lung in a 13 year old boy. Arch Pediatr 6:863–866

Lemire P, Trepanier A, Hebert G (1970) Bronchocele and blocked bronchiectasis. AJR Am J Roentgenol 110:687–693

Lucaya J, García-Conesa JA, Bernadó L (1984) Pulmonary sequestration associated with unilateral pulmonary hypoplasia and massive pleural effusion. Pediatr Radiol 14:228–229

Lucaya J, García-Peña P, Herrera L et al. (2000) Expiratory chest CT in children. AJR Am J Roentgenol 174:235–241

Lyon RD, McAdams HP (1993) Mediastinal bronchogenic cyst demonstration of a fluid-fluid level at MR imaging. Radiology 186:427–428

MacGillivray TE, Harrison MR, Goldstein RB, Adzik SA (1993) Disappearing fetal lung lesions. J Pediatr Surg 28:1321–1325

MacSweeney F, Papagiannopoulos K, Goldstraw P (2003) An assessment of the expanded classification of congenital cystic adenomatoid malformations and their relationship to malignant transformation. Am J Surg Pathol 27:1139–1146

Mäkinen EO, Merikanto J, Rikalinen H, Satokari K (1981) Intralobar pulmonary sequestration occurring without alteration of pulmonary parenchyma. Pediatr Radiol 10:237–240

Martin KW, Siegel MJ, Chesna E (1988) Spontaneous resolution of mediastinal cysts. AJR Am J Roentgenol 150:1131–1132

Mata JM, Cáceres J (1996) The dysmorphic lung: imaging findings. Eur Radiol 6:403–414

Mata JM, Cáceres J, Lucaya J, García-Conesa JA (1990) CT of congenital malformations of the lung. Radiographics 10:651–674

Mata JM, Cáceres J, Lucaya X (1991) CT diagnosis of isolated systemic supply to the lung: a congenital broncho-pulmonary vascular malformation. Eur J Radiol 13:138–142

Mata JM, Cáceres J, Castañer E, Gallardo X, Andreu J (2000) The dysmorphic lung: imaging findings. Postgrad Radiol 20:3–15

McAdams HP, Kirejczyk WM, Rosado-de-Christenson ML, Matsumoto S (2000) Bronchogenic cyst: imaging features with clinical and histopathologic correlation. Radiology 217:441–446

Medelli J, Lattaignant JC, Bertoux JP, Goudot B, Remond A (1979) L'atrésie bronchique segmentarie. Poumon 35:53–58

Murphy JJ, Blair GK, Fraser GC et al. (1992) Rabdomyosarcoma arising within congenital pulmonary cysts: report of three cases. J Pediatr Surg 27:1364–1367

Naidich DP, Rumancick WM, Ettenger NA et al. (1988) Congenital anomalies of the lung in adults: MR diagnosis. AJR Am J Roentgenol 151:13–19

Nakata H, Egashira K, Warnanake H (1993) MRI of bronchogenic cysts. J Comput Assist Tomogr 17:267–270

Nazarian M, Currarino G, Webb WR, Willis K, Kiphart RJ, Wilson HE (1971) Accessory diaphragm: report of a case with complete physiological evaluation and surgical correction. J Thorac Cardiovasc Surg 61:293

Newman B (2006) Congenital bronchopulmonary foregut malformations: concepts and controversies. Pediatr Radiol 36:773–791

Newman B, Gondor M (1997) MR evaluation of right pulmonary agenesis and vascular airway compression in pediatric patients. AJR Am J Roentgenol 168:55–58

Osborne J, Masel J, McCredie J (1989) A spectrum of skeletal anomalies associated with pulmonary agenesis: possible neural crest injuries. Pediatr Radiol 19:425–432

Partridge JB, Osborne JM, Slaughter RE (1988) Scimitar etcetera: the dysmorphic lung. Clin Radiol 39:11–19

Patcher MR, Lattes R (1963) Mediastinal cysts: a clinicopathologic study of twenty cases. Dis Chest 44:416–422

Paterson A (2005) Imaging evaluation of congenital lung abnormalities in infants and children. Radiol Clin North Am 43:303–323

Pedersen ML, LeQuire MH, Spies JB, Ladd WA (1988) Computed tomography of intralobar bronchopulmonary sequestration supplied from the renal artery. J Comput Assist Tomogr 12:874–875

Pryce DM (1946) Lower accessory pulmonary artery with intralobar sequestration of lung, report of seven cases. J Pathol Bacteriol 58:457–467

Pryce DM, Holmes Sellors T, Blair LG (1947) Intralobar sequestration of lung associated with an abnormal pulmonary artery. Br J Surg 35:18–29

Pugatch RD, Gale ME (1983) Obscure pulmonary masses: bronchial impaction revealed by CT. AJR Am J Roentgenol 141:909–914

Pulpeiro JR, López I, Sotelo T, Ruiz JC, García-Hidalgo E (1987) Congenital cystic adenomatoid malformation of the lung in a young adult. Br J Radiol 60:1128–1130

Reed JC, Sobonya RE (1975) RCP from the AFIP. Radiology 117:315–319

Rees S (1981) Arterial connections of the lung. Clin Radiol 32:1–15

Remy-Jardin M, Remy J, Ribet M, Gosselin B (1989) Bronchial atresia: diagnostic criteria and embryologic considerations. Diagn Interv Radiol 1:45–51

Restrepo S, Villamil MA, Rojas JC (2004) Association of two respiratory congenital anomalies: tracheal diverticulum and cystic adenomatoid malformation of the lung. Pediatr Radiol 34:263–266

Rogers LE, Osmer JC (1964) Bronchogenic cyst. A review of 46 cases. AJR Am J Roentgenol 91:273–283

Rosado-de-Christenson M, Stocker JT (1991) Adenomatoid malformation. Radiographics 11:865–886

Rosado-de-Christenson M, Frazier AA, Stocker JT, Templenton PA (1993) Extralobar sequestration: radiologic-pathologic correlation. Radiographics 13:425–441

Samuel M, Burge DM (1999) Management of antenatally diagnosed pulmonary sequestrations associated with congenital cystic adenomatoid malformation. Thorax 54:701–706

Savic B, Birtel FJ, Tholen W, Funke HD, Knoche R (1979) Lung sequestration: report of seven cases and review of 540 published cases. Thorax 34:96–101

Senac MO, Wood BP, Isaacs H, Weller M (1991) Pulmonary blastoma: a rare childohood malignancy. Radiology 179:743–746

Stern EJ, Webb WR, Warnock ML et al. (2000) Bronchopulmonary sequestration: dynamic, ultrafast, high-resolution CT evidence of air trapping. AJR Am J Roentgenol 74:235–241

Stocker JT (2002) Histopathology 41(suppl):424–431

Stocker JT, Kagan-Hallet K (1979) Extralobar pulmonary sequestration. Analysis of 15 cases. Am J Clin Pathol 72:917–925

Stocker JT, Madewell JE, Drake RM (1977) Congenital cystic adenomatoid malformation of the lung. Hum Pathol 8:155–171

Ueda K, Gruppo R, Unger F, Martin L, Bove K (1977) Rhabdomyosarcoma of the lung arising in congenital cystic adenomatoid malformation. Cancer 40:383–388

Ward S, Morcos SK (1999) Congenital bronchial atresia. Presentation of three cases and a pictorial review. Clin Radiol 54:144–148

West MS, Donaldson JS, Shkolnik A (1989) Pulmonary sequestration. Diagnosis by ultrasound. J Ultrasound Med 8:125–129

Wille L, Holthusem W, Willich E (1975) Accessory diaphragm: report of 6 cases and a review of the literature. Pediatr Radiol 4:14–20

Winters WD, Effmann EL (2001) Congenital masses of the lung: prenatal and postnatal imaging evaluation. J Thorac Imaging 16:196–206

Winters WD, Effmann EL, Nghiem HV et al. (1997) Disappearing fetal lung masses: importance of postnatal imaging studies. Pediatr Radiol 27:535–539

Woodring JH, Howard TA, Kanga JF (1994) Congenital pulmonary venolobar syndrome revisited. Radiographics 14:349

Zumbro GL, Green DC, Brott W, Tresaure RL (1974) Pulmonary sequestration with spontaneous intrapleural hemorrhage. J Thorac Cardiovasc Surg 68:673–674

CT of Acute Pulmonary Disease: Infection, Infarction, and Trauma

Lane F. Donnelly

CONTENTS

6.1 **Introduction** *147*
6.2 **CT in the Evaluation of Immunocompetent Children with Pneumonia** *147*
6.2.1 Complications of Pneumonia *148*
6.2.1.1 Primary Evaluation of Parapneumonic Effusions *148*
6.2.1.2 Evaluation of Persistent or Progressive Symptoms *151*
6.2.1.3 Lung Parenchymal Complications *152*
6.2.1.4 Pleural Complications *155*
6.2.1.5 Purulent Pericarditis *156*
6.2.2 Chronic Complications of Pneumonia *156*
6.3 **CT in the Evaluation of Immunocompromised Children with Suspected Pneumonia** *156*
6.4 **CT in the Evaluation of Pulmonary Trauma** *158*
6.5 **Pulmonary Embolism and Infarction** *161*
6.6 **Conclusion** *162*
References *162*

6.1
Introduction

Chest radiography is the primary means of imaging acute lung disease. Chest radiography is inexpensive, easy to obtain, rapidly processed, low in radiation dose, and available on a ubiquitous basis. However, there are a number of scenarios in which CT is playing an increasing role in evaluating acute lung disease. Because CT of the lung can be performed with tube currents as low as 40 mAs, high quality images can be obtained while minimizing radiation dose. Acute pulmonary processes can be related to infection, trauma, or infarction. Helical CT is playing an increasing role in the evaluation for pulmonary embolism and lung infarction in adults. This article will review the roles of and findings seen with CT imaging of pulmonary infection, suspected embolism, and trauma.

6.2
CT in the Evaluation of Immunocompetent Children with Pneumonia

Respiratory tract infection is the most common cause of illness in children and continues to be a significant cause of morbidity and mortality (Donnelly 1999; Condon 1991). The roles of imaging in the evaluation of immunocompetent children with community acquired pneumonia are multiple: confirmation or exclusion of pneumonia, characterization and prediction of infectious agent, exclusion of other cause of symptoms, evaluation when there is failure to resolve, and evaluation of related complications (Donnelly 1999). CT is also used in the follow up for chronic complications of pneumonia, such as bronchiectasis. Radiography of the chest remains the primary imaging modality in the majority of these scenarios and CT plays a secondary role in most of these respects.

Concerning confirmation or exclusion of pneumonia, CT usually plays no role in making the diagnosis of pneumonia and consequently deciding on treatment and patient disposition. This is accomplished with chest radiography (Grossman and Caplan 1988; Leventhal 1982; Alario et al. 1987; Peter 1988; Zukin et al. 1986). Concerning characterization and prediction of infectious agents, the

---

L. F. Donnelly, MD
Professor, Radiologist-in-Chief, Department of Radiology, Children's Hospital Medical Center MLC 5031, 3333 Burnet Avenue, Cincinnati, OH 45229-3039, USA

previously described patterns of radiographic and CT findings which suggest a specific infectious agent are rarely of clinical relevance in the previously healthy child who is imaged for suspected pneumonia. The more general issue in the evaluation of the child with suspected pneumonia is whether the infectious agent is likely bacteria or viral. The differentiation between viral and bacterial pneumonia is accomplished through a combination of clinical examination and radiography of the chest (Donnelly 1999; Turner et al. 1987; Swischuk and Hayden 1986; Bettenay et al. 1988; Osborne 1978; Wildin et al. 1988; Conte et al. 1970). CT plays no role.

CT can sometimes play a role in the child who has pneumonia that is recurrent or fails to resolve. Unlike in adults, in whom post obstructive pneumonia secondary to bronchogenic carcinoma is a concern, follow-up radiography to ensure resolution of radiographic findings is not routinely necessary in an otherwise healthy child who has had pneumonia. There is a tendency to obtain follow-up radiographs both too early and too often (Hedlund et al. 1997). Follow-up radiographs should be reserved for those children who have persistent or recurrent symptoms and those who have an underlying condition such as immunodeficiency. The radiographic findings of pneumonia can persist for two to four weeks, even when the patient is clinically recovering appropriately. When follow-up radiographs are indicated, ideally they should not be obtained until at least two to three weeks have passed (Hedlund et al. 1997). Causes of failure of suspected pneumonia to resolve include infected developmental lesions, bronchial obstruction, gastroesophageal reflux and aspiration, and underlying systemic disorders. Developmental lung masses that may become infected and present as recurrent or persistent pneumonia include sequestration, bronchogenic cyst, and cystic adenomatoid malformation. CT may be helpful in confirming and characterizing the presence of these developmental masses. In cases of sequestration, CT is capable of identifying the characteristic systemic arterial supply (Frush and Donnelly 1997) and may demonstrate cystic structures in cases of bronchogenic cyst and cystic adenomatoid malformation.

6.2.1
Complications of Pneumonia

The potential uses of CT in the evaluation of complications related to pneumonia can be divided into two clinical scenarios: primary evaluation of parapneumonic effusions and evaluation of the child who has persistent or progressive symptoms despite medical or surgical therapy.

6.2.1.1
Primary Evaluation of Parapneumonic Effusions

Bacterial pneumonia is often complicated by parapneumonic effusions in children. There are multiple therapeutic options available in the management of parapneumonic effusions including antibiotic therapy alone, repeated thoracentesis, chest tube placement, urokinase therapy, and thoracoscopy with surgical debridement (Donnelly and Klosterman 1997a; Light 1985, 1995; Bouros et al. 1994; Rosen et al. 1993; Moulton et al. 1995; Kern and Rogers 1993; Silen and Weber 1995; Strovroff et al. 1995). There are great differences in opinions regarding the timing and aggressiveness of the management of parapneumonic effusions. Many investigators advocate antibiotics, drainage tube placement, and thrombolytic therapy (Donnelly and Klosterman 1997a; Light 1985, 1995; Bouros et al. 1994; Rosen et al. 1993; Moulton et al. 1995). Other investigators advocate early intervention with thoracoscopy and debridement (Kern and Rogers 1993; Silen and Weber 1995; Strovroff et al. 1995). Traditionally, the aggressiveness of therapy has been based on categorizing parapneumonic effusions as empyema or transudative effusion (Donnelly and Klosterman 1997a; Light 1985, 1995; Bouros et al. 1994; Rosen et al. 1993; Moulton et al. 1995; Kern and Rogers 1993; Silen and Weber 1995; Strovroff et al. 1995). This differentiation has been based on aspiration and analysis of pleural fluid (Light 1985). Traditional wisdom has advocated that parapneumonic effusions that meet the criteria for empyema are unlikely to resolve with antibiotic therapy alone and will often progress to a fibrinopurulent organized stage if left undrained (Light 1985). Multiple attempts have been made to use imaging criteria to differentiate empyema from transudative effusion, so that every child with a parapneumonic effusion does not have to undergo diagnostic thoracentesis.

CT was previously advocated in the differentiation between empyema and transudative parapneumonic effusion (Waite et al. 1993; Muller 1993; Stark et al. 1983; Baber et al. 1980). Initially, the CT findings of empyema were described in the context of differentiating empyema from peripheral pulmonary abscess (Stark et al. 1983; Baber et al. 1980). Later, CT findings of enhancement and thickening of the parietal and visceral pleura, thickening of the extrapleural subcostal tissues, and increased attenuation of the extrapleural subcostal fat (Fig. 6.1) were described as highly accurate in differentiating empyema from transudate (Muller 1993; Stark et al. 1983) and were advocated as useful in making therapeutic decisions concerning parapneumonic effusions. Enhancement of the parietal pleura was advocated as the most sensitive finding of empyema and thickening of and increase from fat to soft tissue attenuation of the extrapleural space the most specific findings (Waite et al. 1993; Muller 1993). However, later studies have shown these findings to be inaccurate in determining which parapneumonic effusions meet the laboratory criteria for empyema in children (Donnelly and Klosterman 1997a). No individual CT findings (pleural enhancement, pleural thickening, extrapleural subcostal tissue abnormality, or adjacent chest wall edema) nor a score based on a combination of CT findings accurately separated empyema from effusion (Donnelly and Klosterman 1997a). These authors concluded that CT characteristic of parapneumonic effusions do not allow radiologists to accurately predict empy-

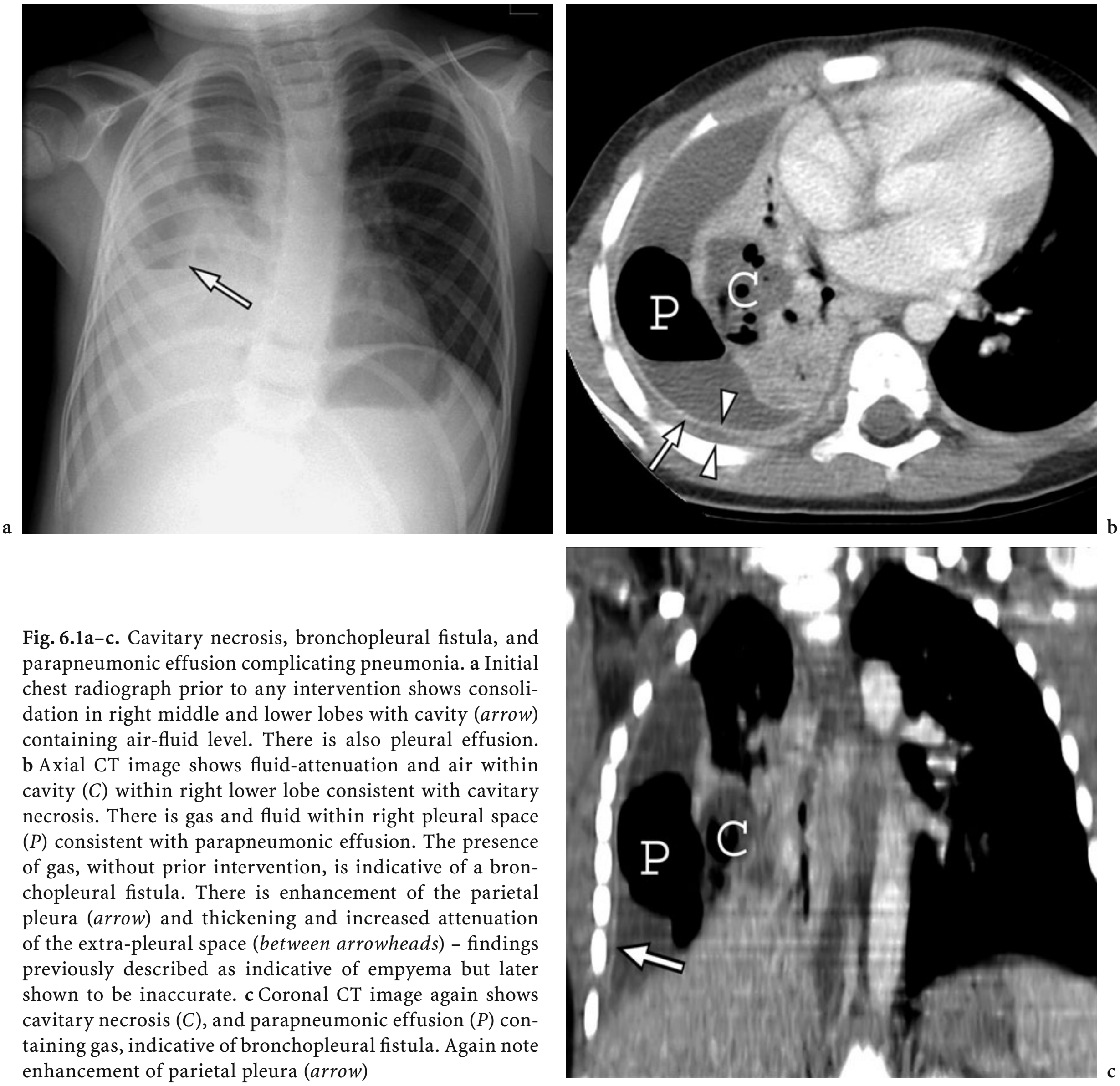

Fig. 6.1a–c. Cavitary necrosis, bronchopleural fistula, and parapneumonic effusion complicating pneumonia. **a** Initial chest radiograph prior to any intervention shows consolidation in right middle and lower lobes with cavity (*arrow*) containing air-fluid level. There is also pleural effusion. **b** Axial CT image shows fluid-attenuation and air within cavity (*C*) within right lower lobe consistent with cavitary necrosis. There is gas and fluid within right pleural space (*P*) consistent with parapneumonic effusion. The presence of gas, without prior intervention, is indicative of a bronchopleural fistula. There is enhancement of the parietal pleura (*arrow*) and thickening and increased attenuation of the extra-pleural space (*between arrowheads*) – findings previously described as indicative of empyema but later shown to be inaccurate. **c** Coronal CT image again shows cavitary necrosis (*C*), and parapneumonic effusion (*P*) containing gas, indicative of bronchopleural fistula. Again note enhancement of parietal pleura (*arrow*)

ema and that the presence or absence of such CT findings should not influence therapeutic decisions concerning the management of parapneumonic effusions (Donnelly and Klosterman 1997a). In fact, it is common when encountering cases in which a child has been evaluated with both CT and ultrasound, that the CT will show no evidence of loculations and the ultrasound will show multiple septations and loculations (Figs. 6.2 and 6.3).

Another method of imaging advocated in the evaluation of parapneumonic effusions is radiography obtained with the patient in decubitus positioning. If there is a significant change in the position and appearance of the pleural fluid on the decubitus images as compared to the upright radiograph, the fluid is considered free flowing and "non-loculated". If there is no change in position of the pleural fluid, the fluid is considered loculated. In my experience, these decubitus radiographs are more confusing than helpful and we do not advocate the use of decubitus radiographs to evaluate pleural effusions at our institution.

Ultrasound has also been advocated as an aid in making therapeutic decisions for parapneumonic effusions (Ramnath et al. 1998). In one study, parapneumonic effusions were categorized as low-grade

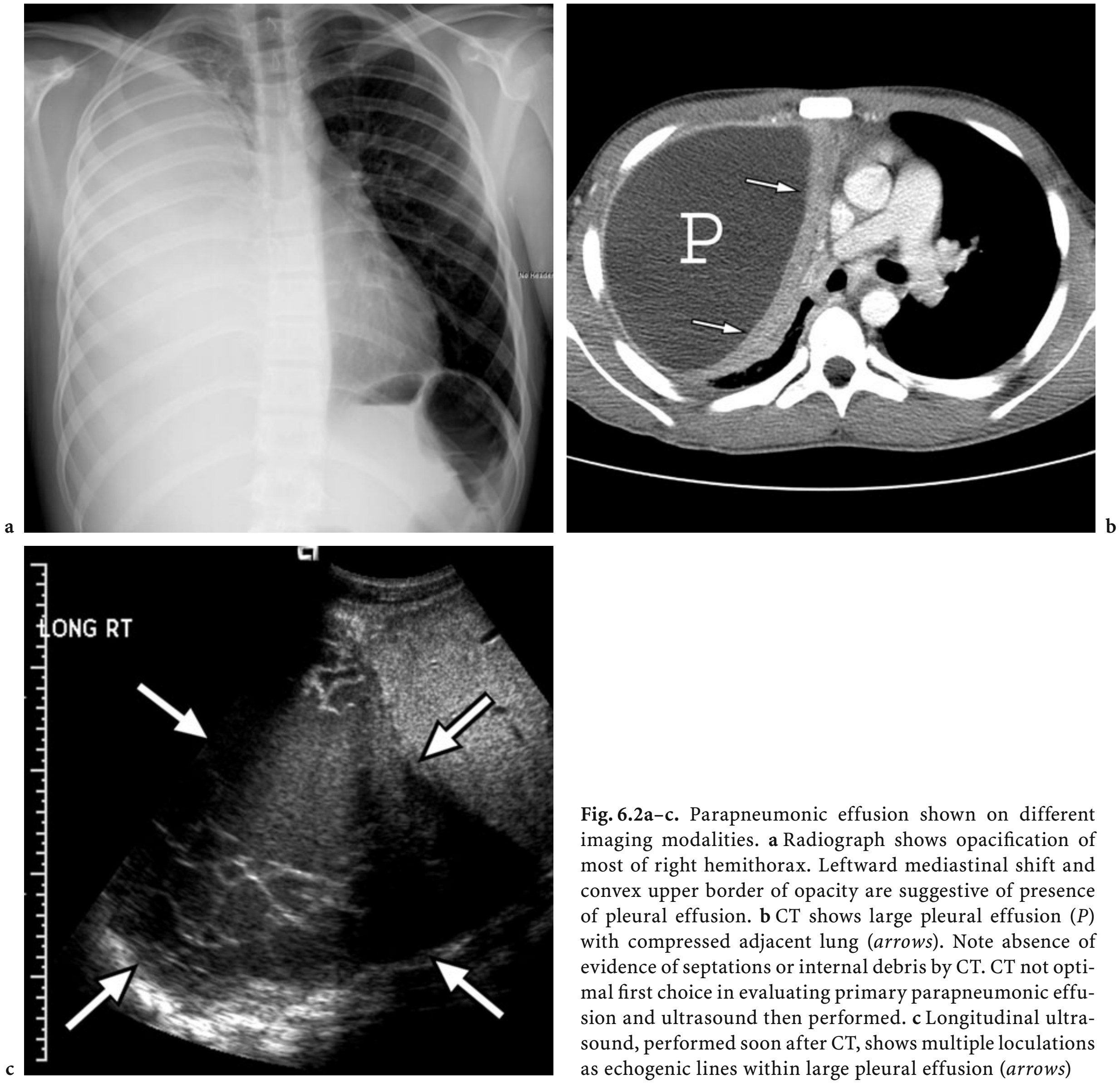

Fig. 6.2a–c. Parapneumonic effusion shown on different imaging modalities. **a** Radiograph shows opacification of most of right hemithorax. Leftward mediastinal shift and convex upper border of opacity are suggestive of presence of pleural effusion. **b** CT shows large pleural effusion (*P*) with compressed adjacent lung (*arrows*). Note absence of evidence of septations or internal debris by CT. CT not optimal first choice in evaluating primary parapneumonic effusion and ultrasound then performed. **c** Longitudinal ultrasound, performed soon after CT, shows multiple loculations as echogenic lines within large pleural effusion (*arrows*)

(anaechoic fluid without internal heterogeneous echogenic structures) or high-grade (fibrinopurulent organization demonstrated by the presence of fronds, septations, or loculations) (Figs. 6.2–6.4). In children whose effusions were high-grade, hospital stay was reduced by nearly 50% when operative intervention was performed (Ramnath et al. 1998). The length of hospital stay in children with low-grade effusions was not affected by operative intervention (Ramnath et al. 1998). Therefore, sonography may play a more useful role than CT in the early evaluation of parapneumonic effusions. We currently advocate ultrasound, rather than CT or decubitus radiographs, in the primary evaluation of parapneumonic effusions.

6.2.1.2
Evaluation of Persistent or Progressive Symptoms

Underlying suppurative complications are often present when children exhibit persistent or progressive symptoms (fever, respiratory distress, sepsis) despite appropriate medical management of pneumonia (Donnelly and Klosterman 1997b, 1998b). Potential suppurative complications include parapneumonic effusions, such as empyema, other inad-

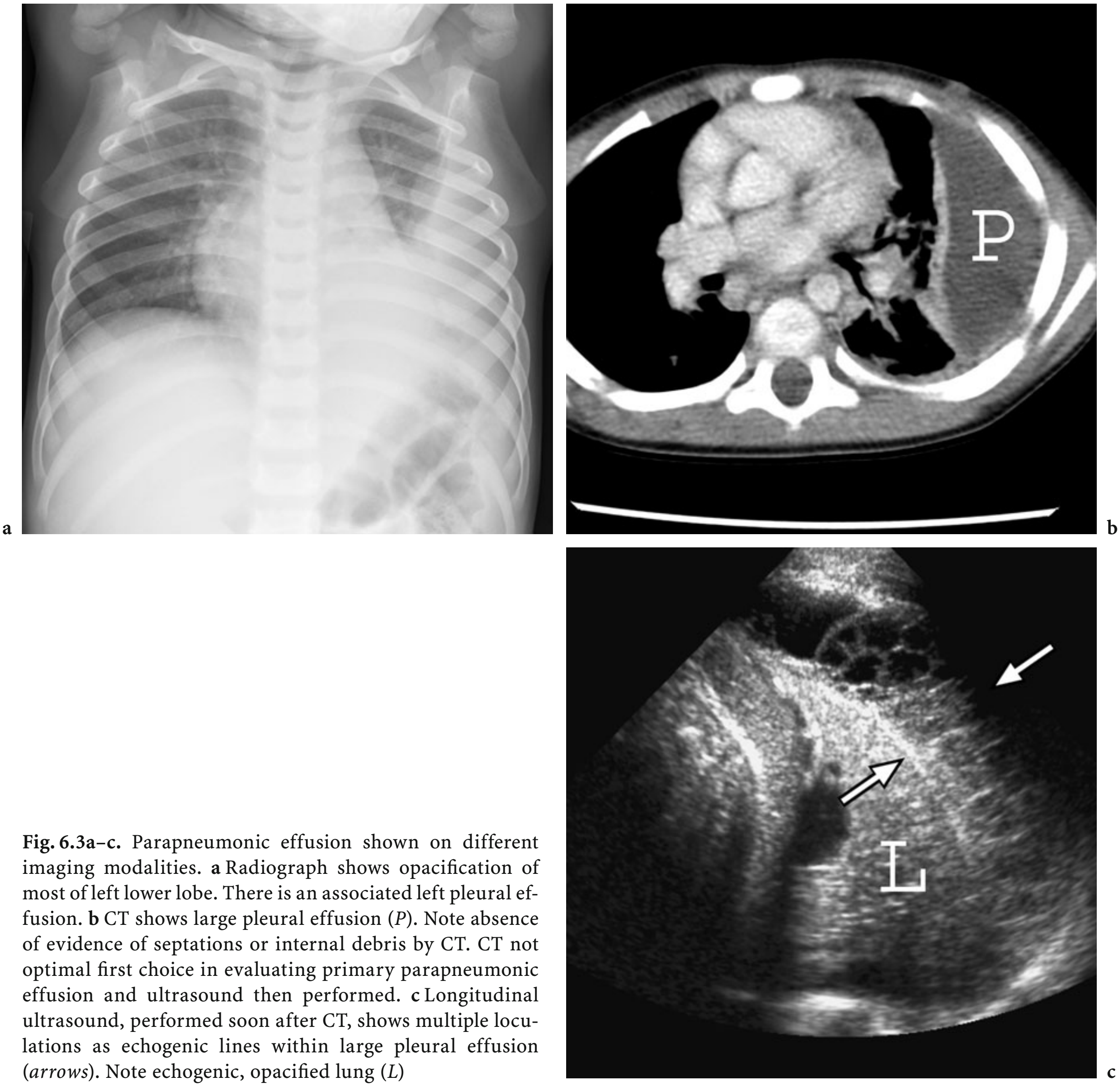

Fig. 6.3a–c. Parapneumonic effusion shown on different imaging modalities. **a** Radiograph shows opacification of most of left lower lobe. There is an associated left pleural effusion. **b** CT shows large pleural effusion (*P*). Note absence of evidence of septations or internal debris by CT. CT not optimal first choice in evaluating primary parapneumonic effusion and ultrasound then performed. **c** Longitudinal ultrasound, performed soon after CT, shows multiple loculations as echogenic lines within large pleural effusion (*arrows*). Note echogenic, opacified lung (*L*)

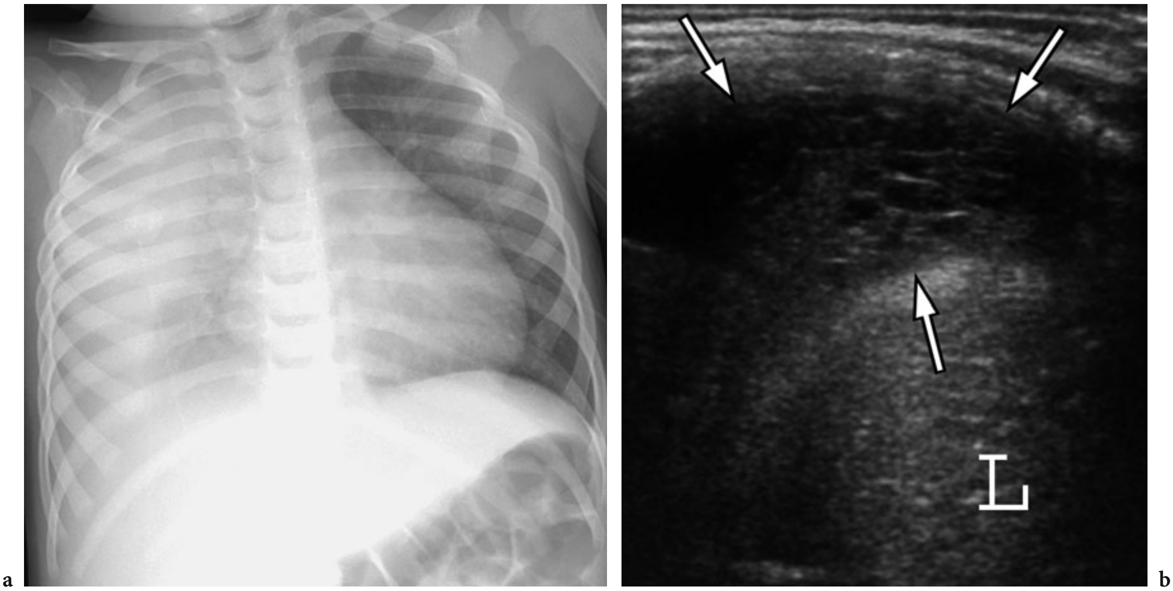

Fig. 6.4a,b. Parapneumonic effusion shown on different imaging modalities. **a** Radiograph shows right pleural effusion. **b** Ultrasound shows multiple loculations as echogenic lines within large pleural effusion (*arrows*). Note echogenic, opacified lung (*L*)

equately drained effusions, or malpositioned chest tubes; parenchymal complications, such as cavitary necrosis or lung abscess; and purulent pericarditis (Donnelly 1999; Donnelly and Klosterman 1998a,b; Donnelly and Klosterman 1997b). Although chest radiography is the primary imaging modality to detect such complications, a significant percentage of these complications will not be demonstrated by radiography (Donnelly 1999; Donnelly and Klosterman 1997b, 1998a,b). In the setting of a child with a noncontributory radiograph who has not responded appropriately to therapy, contrast-enhanced CT has been shown to be useful in detecting clinically significant suppurative complications (Donnelly and Klosterman 1998b). This is one of the few areas where lung is being evaluated that contrast enhancement is helpful. CT has been shown to be accurate for the identification of lung abscess, the differentiation of lung abscess form empyema, the detection of parapneumonic effusions, the identification of bronchopleural fistulas, and the identification of malpositioned chest tubes or failure of lung re-expansion after chest-tube placement, both of which help to indicate when chest-tube drainage therapy will be unsuccessful (Donnelly 1999; Waite et al. 1993; Muller 1993; Donnelly and Klosterman 1997b, 1998a,b; Naidich et al. 1991; Stern et al. 1996; Pugatch and Sprin 1985; Himelman and Callen 1986; Stark et al. 1983). CT can help differentiate whether the reason for persistent illness is pleural or parenchymal, directing therapy in the appropriate direction (Donnelly 1998b).

6.2.1.3
Lung Parenchymal Complications

On contrast-enhanced CT, non-compromised lung parenchyma consolidated with pneumonia typically diffusely enhances (Donnelly and Klosterman 1997b). This enhancement is not surprising given the degree of inflammation associated with pneumonia. Areas of atelectasis also enhance. Large areas of decreased or absent enhancement are indicative of underlying parenchymal ischemia or impending infarction (Donnelly and Klosterman 1997b). In one study, the presence of decreased enhancement was associated with a significantly increased rate of admission to the intensive care unit, increased length of hospital stay, and increased incidence of development of cavitary necrosis (Donnelly and Klosterman 1997b). Therefore, the detection of the presence of decreased lung enhancement in this setting yields important prognostic information.

Suppurative lung parenchymal complications represent a spectrum of abnormalities and include cavitary necrosis (Figs. 6.1, 6.5, and 6.6), lung abscess, pneumatocele, bronchopleural fistula, and

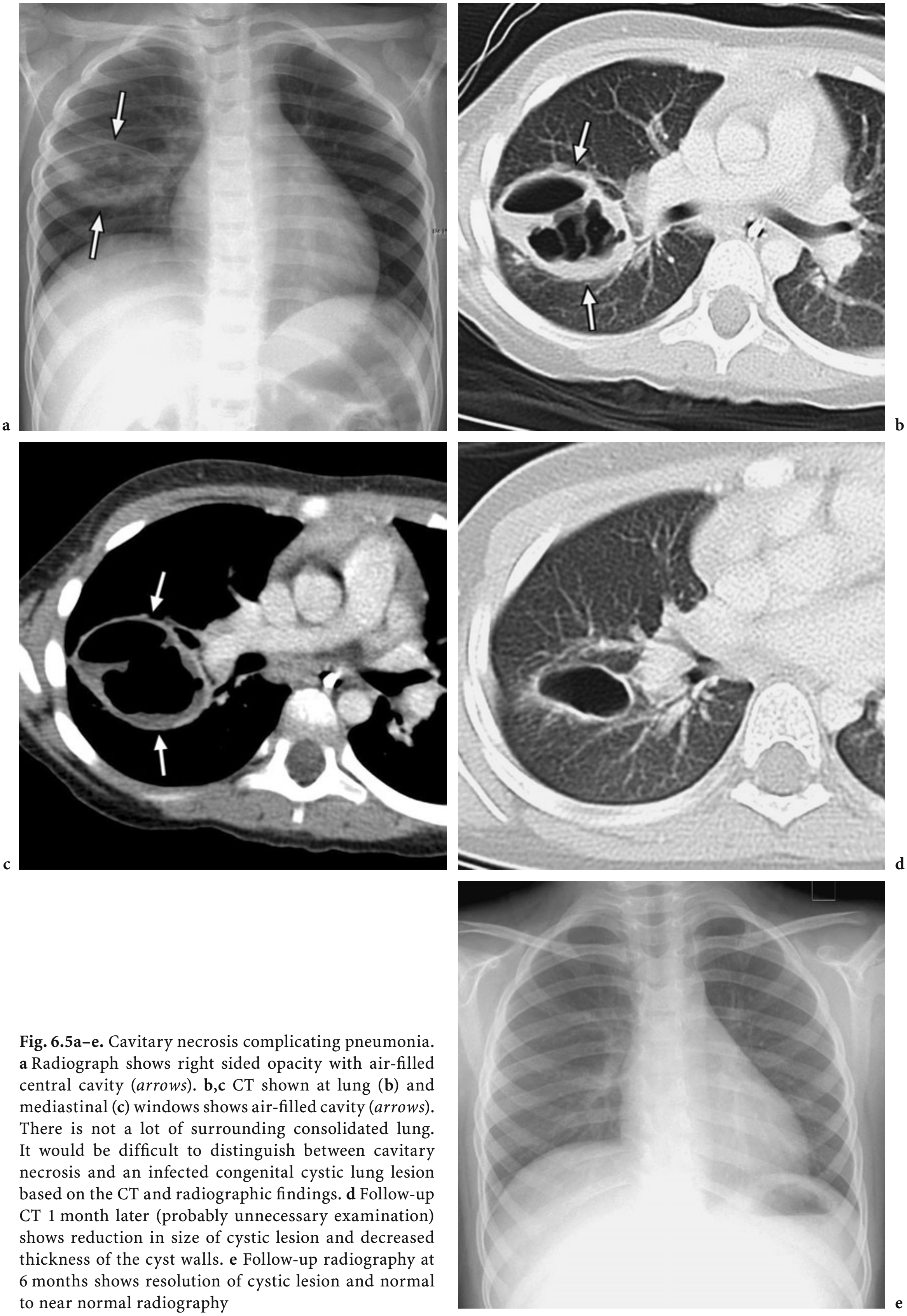

Fig. 6.5a–e. Cavitary necrosis complicating pneumonia. **a** Radiograph shows right sided opacity with air-filled central cavity (*arrows*). **b**,**c** CT shown at lung (**b**) and mediastinal (**c**) windows shows air-filled cavity (*arrows*). There is not a lot of surrounding consolidated lung. It would be difficult to distinguish between cavitary necrosis and an infected congenital cystic lung lesion based on the CT and radiographic findings. **d** Follow-up CT 1 month later (probably unnecessary examination) shows reduction in size of cystic lesion and decreased thickness of the cyst walls. **e** Follow-up radiography at 6 months shows resolution of cystic lesion and normal to near normal radiography

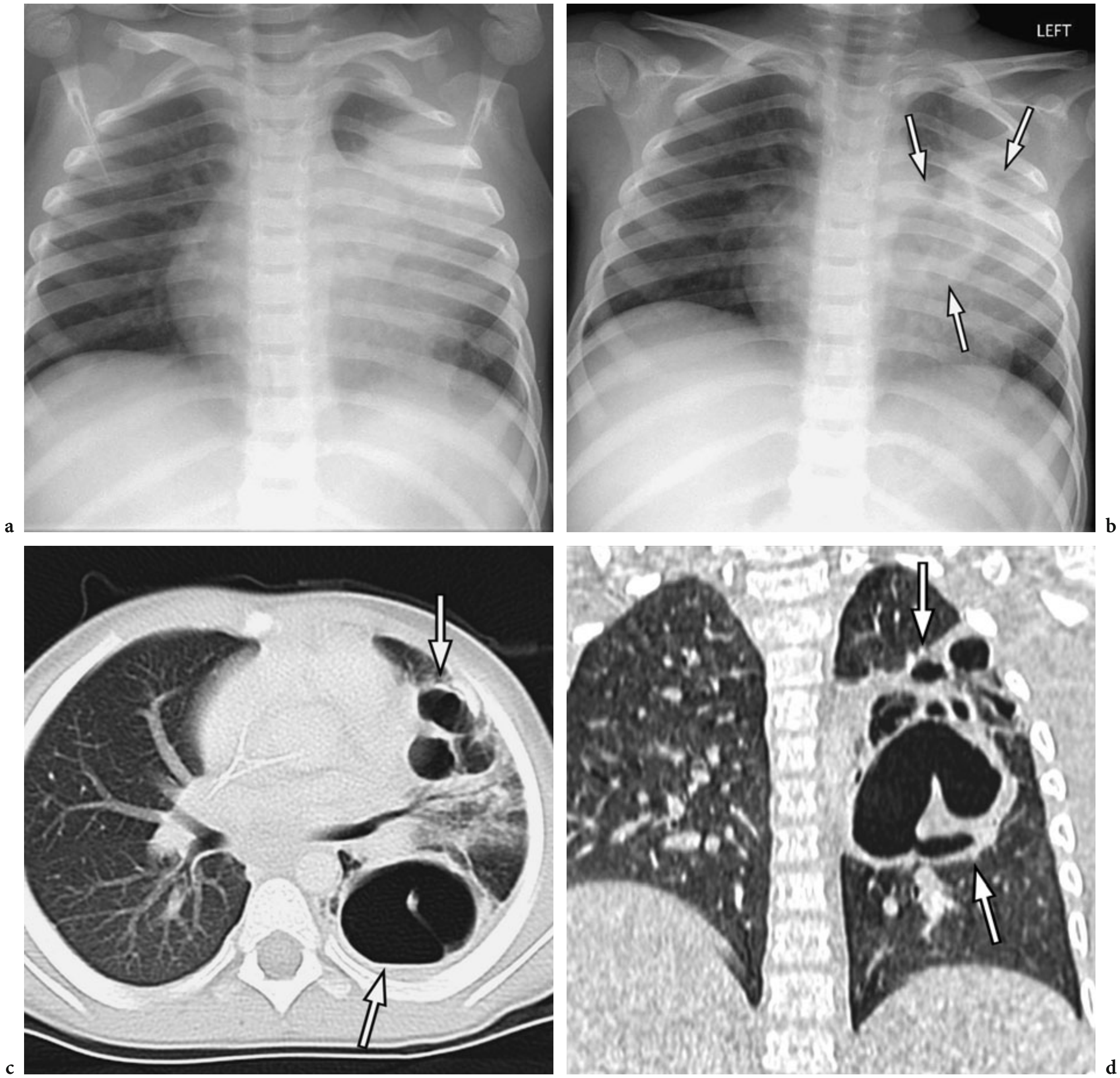

Fig. 6.6a–d. Cavitary necrosis complicating pneumonia. **a** Initial chest radiograph shows consolidated left upper lobe. **b** Radiograph 4 days later shows development of multiple cystic lucencies (*arrows*). **c,d** CT shown in axial (**c**) and coronal (**d**) planes shows multiple thin-walled cysts (*arrows*). CT appearance is very similar to congenital cystic adenomatoid malformation on this study alone. Temporal development of cysts within pre-existing consolidated pneumonia is key to diagnosis of cavitary necrosis

pulmonary gangrene (Donnelly and Klosterman 1997b). The name given to the suppurative process depends on several factors including the severity and distribution of the process, condition of the adjacent lung parenchyma, and temporal relationship with disease resolution (Donnelly and Klosterman 1997b).

Cavitary necrosis represents a dominant area of necrosis of a consolidated lobe associated with a variable number of thin walled cysts (Donnelly and Klosterman 1997b, 1998a,b; Naidich et al. 1991). The mechanism of necrosis complicating pneumonia is related to thrombotic occlusion of alveolar capillaries associated with adjacent inflammation, resulting in ischemia and eventually necrosis of the lung parenchyma. Initially on CT, decreased enhancement may be the only finding. The characteristic CT findings of cavitary necrosis include loss of normal lung architecture, decreased parenchymal enhancement, loss of the lung-pleural margin, and multiple thin-walled cavities containing air or fluid and lacking an enhancing border (Donnelly and Klosterman 1998a) (Figs. 6.1, 6.5, and 6.6). Historically, cavitary necrosis has been described as uncommon and usually associated with staphylococcal pneumonias (Donnelly and Klosterman 1998a; Kerem et al. 1994; Torres et al. 1984; Isaacs 1986; Yangco and Derensinski 1980; Danner et al. 1968; Gutman et al. 1973; Knight et al. 1975; O'Reilly et al. 1978). However, more recently, cavitary necrosis has become a more common complication of pneumonia and is most commonly encountered in children with *Streptococcus pneumoniae* infection (Donnelly and Klosterman 1998a; Kerem et al. 1994; Torres et al. 1984; Isaacs 1986; Yangco and Derensinski 1980). Chest radiography is less sensitive than CT in detecting cavitary necrosis (Donnelly and Klosterman 1998a). Only 41% of cases of cavitary necrosis identified on CT are seen on chest radiography and of those cases identified on chest radiography, over 90% are visualized later on chest radiography than CT (Silen and Weber 1995). When lung first becomes necrotic, the necrotic tissue liquefies and forms fluid-filled cavities (Donnelly and Klosterman 1998a). When portions of this necrotic fluid are expectorated via bronchial communications, the cavities may fill with air. Fluid-filled cavities are isodense to adjacent opacified lung on chest radiography. This sequence of progression from fluid-filled to air-filled cavities contributes to the earlier detection and increased sensitivity of CT compared with radiography (Donnelly and Klosterman 1998a). Most children with cavitary necrosis are severely ill (Donnelly and Klosterman 1997b, 1998a). Such prognostic information helps in patient management decisions concerning intensity of management and, by outlining the patients expected course of illness, decreases unnecessary diagnostic tests and helps in counseling the patient's family. However, unlike in adults in whom the mortality rate of cavitary necrosis is high and early surgical removal of the affected lung has been advocated (Danner et al. 1968; Gutman et al. 1973), the long term outcome of children with cavitary necrosis is favorable with medical management alone (Donnelly and Klosterman 1998a). In children, the presence of cavitary necrosis should not be considered an indication for surgical lung resection unless the patient's condition continues to worsen with medical management. Amazingly, in children with cavitary necrosis, follow-up radiographs obtained at greater than 40 days after the acute illness are most often normal, lacking any evidence of chronic scarring, persistent cavity formation, or other sequelae (Donnelly and Klosterman 1998a) (Figs. 6.5 and 6.6). Therefore, in these patients, resolution should be the expected course and, like in children with non-complicated pneumonia, long-term follow-up radiographs are not considered routinely necessary (Donnelly and Klosterman 1998a).

Lung abscess represents a dominant focus of suppuration surrounded by well-formed fibrous wall (Donnelly and Klosterman 1997b; Naidich et al. 1991). On contrast enhanced CT, lung abscesses appear as fluid- or air-filled cavities with definable, enhancing walls (Donnelly 1999; Donnelly and Klosterman 1997b, 1998a,b; Naidich et al. 1991). Typically there is no evidence of necrosis in the surrounding lung. Pneumatocele is a term given to thin walled cysts seen at imaging and may represent a later or less severe stage of resolving or healing necrosis (Donnelly 1999; Donnelly and Klosterman 1997b). On CT, a thin walled cyst containing air with or without fluid is identified. The wall does not enhance. The surrounding lung may be opacified but does not demonstrate findings of necrosis. Bronchopleural fistula is identified on CT when a direct communication is visualized between the airspaces of the lung and the pleural space.

It may sometimes be difficult on a single imaging study to differentiate a suppurative lung parenchymal complication from an underlying cystic congenital lung lesion that has become secondarily infected. Infected congenital cystic adenomatoid malformations (CCAM) may appear very similar to cavitary necrosis. Obviously, historic imaging studies showing a lack of a cystic lesion exclude underlying CCAM. Resolution of the cystic lesion on follow up studies ensures that the lesion is no longer clinically relevant and makes cavitary necrosis much more likely (Figs. 6.5 and 6.6). However, some CCAM have been reported to scar down and resolve after becoming infected.

6.2.1.4
Pleural Complications

The cause of persistent sepsis in a child being treated for pneumonia may also be related to a pleural complication. This is most often the unrecognized cause of sepsis when previous intervention has been performed to treat a parapneumonic effusion. CT yields helpful information regarding the management of parapneumonic effusions such as depicting a loculated pleural collection not in communication with an indwelling chest tube, poor chest tube placement, or failure of lung re-expansion (Muller 1993; Stark et al. 1983; Baber et al. 1980; Ramnath et al. 1998; Donnelly and Klosterman 1997b, 1998a,b; Naidich et al. 1991; Stern et al. 1996; Pugatch and Sprin 1985; Himelman and Callen 1986; Kerem et al. 1994; Torres et al. 1984; Isaacs 1986; Yangco and Derensinski 1980; Danner et al. 1968; Gutman et al. 1973; Knight et al. 1975; O'Reilly et al. 1978). All of these findings suggest a need for a change in drainage strategy. Drainage catheters may need to be repositioned or replaced with larger bore catheters and thoracoscopic debridement may need to be considered. Finally, on chest radiography, it is often difficult to determine how much of an opacity seen is due to pleural effusion and how much is due to consolidated lung, when both are present. Accurate determination of the amount of pleural fluid provided by CT also affects therapeutic decisions regarding drainage (Donnelly and Klosterman 1998b).

6.2.1.5
Purulent Pericarditis

Although rare, purulent pericarditis is fatal if not rapidly diagnosed and treated. Prior to the advent of antibiotics, purulent pericarditis was a common complication of childhood pneumonia and the one of the most frequent causes of death (Donnelly et al. 1999). Although the classic presentation of purulent pericardiditis is septicemia and enlarging cardiopericadial silhouette on chest radiograph, cardiac enlargement is often not present in children. In fact, children can progress to cardiac tamponade prior to enlargement of the pericardial silhouette being present on chest radiography (Donnelly et al. 1999). With the increasing number of antimicrobial resistant bacteria, the incidence of purulent pericarditis may be rising. In one study of children who underwent CT to evaluate for complications of pneumonia, pericardial fluid was present in 23% (Wagner et al. 1988). Two cases had large effusions and clinically unrecognized cardiac tamponade (Donnelly et al. 1999). Therefore, it is important to evaluate for pericardial effusion in children being imaged for complications of pneumonia.

6.2.2
Chronic Complications of Pneumonia

There are a number of potential complications from pneumonia that can cause chronic respiratory difficulties. These include parenchymal scarring, fibrothorax, bronchiectasis, and Swyer-James syndrome. Swyer-James syndrome is defined as the presence of a unilateral hyperlucent lung in association with decreased pulmonary vasculature. The lucent lung is typically enlarged and demonstrates air-trapping on fluoroscopy or expiratory CT. It is thought to represent a obliterative bronchiolitis that occurs secondary to viral infection, often with adenovirus.

Bronchiectasis is probably the most common chronic complication of childhood pneumonia. It is defined as dilatation of the bronchi. On high resolution CT, the bronchus is considered dilated if it is larger than the associated companion pulmonary artery. Reversible bronchiectasis can occur during acute pneumonia (see chapters on HRCT). Chronic bronchiectasis most commonly occurs secondary to adenovirus or bacterial infection.

6.3
CT in the Evaluation of Immunocompromised Children with Suspected Pneumonia

The number of immunocompromised children continues to increase. Children can be immunocompromised for a variety of reasons including cancer therapy, bone marrow transplantation, solid organ transplantation, primary immunodeficiency, and AIDS. At most tertiary children's medical centers, the number of CT examinations of the chest performed in immunocompromised children far out number those performed in immunocompetent children. It is also important for those working in imaging departments at community hospitals to have an understanding of those processes as many of these patients receive much of their primary care in their home towns.

Acute pulmonary processes are a common cause of morbidity and mortality in immunocompromised children (Worthy et al. 1997; Mori et al. 1991; McAdams et al. 1995; Marks et al. 1996; Winer-Muram et al. 1994; Brown et al. 1994).

Because of the fragile condition of these patients, prompt diagnosis and treatment of pulmonary infections is imperative. When a pulmonary process is suspected on the basis of imaging, invasive diagnostic procedures such as bronchoscopy may be performed or new therapies may be empirically started. In regards to confirmation or exclusion of pneumonia, as in immunocompetent patients, chest radiography is the primary imaging modality. However, because of the poor condition of many of these patients and risk associated with exposure to multiple persons, radiographic evaluation of these patients is often performed with portable technique. These patients are also often not able to take deep breaths rendering low lung volume radiographic examinations. The negative predictive value of such radiographs is low in comparison to frontal and lateral radiographs obtained at full inspiration. Because of these factors as well as the greater risk of progressive illness if infection is not promptly diagnosed, CT plays a greater role in the detection and exclusion of pulmonary infection. The detection of pulmonary abnormalities with CT is excellent (Mori et al. 1991). In an immunocompromised child with clinical findings that could be attributed to pneumonia and a noncontributory radiograph, we do not hesitate to perform CT. The amount of disease that is often present on CT but not detected on chest radiograph is continuously surprising. When detected, CT localizes high yield areas for diagnostic procedures such as bronchoscopy or needle aspiration.

In immunocompetent children, the primary characterization of pulmonary infections is determining whether the infectious agent is bacterial or viral. In immunocompromised hosts, the issue is more complex. The array of agents that can cause aggressive infections is great and includes fungal infections such as *Aspergillus* and Candida, viral infections such as cytomegalovirus infection, and *Pneumocystis carinii* (Mori et al. 1991; McAdams et al. 1995; Marks et al. 1996; Winer-Muram et al. 1994; Brown et al. 1994). In addition, there are a variety of noninfectious pulmonary processes that can present with acute or subacute clinical findings mimicking pulmonary infection (Mori et al. 1991). These include alveolar hemorrhage, pulmonary edema, drug reaction, idiopathic pneumonia, lymphoid interstitial pneumonitis (Fig. 6.7), bronchiolitis obliterans, bronchiolitis obliterans with organizing pneumonia, and chronic graft-vs-host disease (Mori et al. 1991; McAdams et al. 1995; Marks et al. 1996; Winer-Muram et al. 1994; Brown et al. 1994).

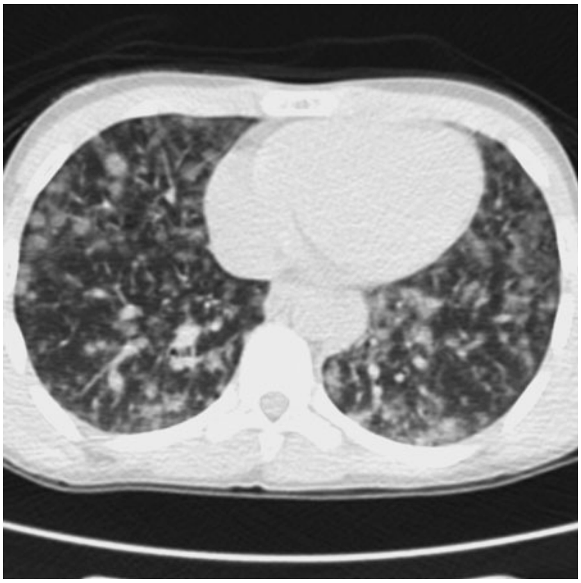

Fig. 6.7. Lymphoid interstitial pneumonia in child with congenital immunodeficiency. CT shows multiple poorly defined pulmonary nodules bilaterally

The CT findings of many of these entities are nonspecific, with overlap of the findings seen between different etiologies. However, the combination of certain CT findings, in conjunction with clinical findings, can be very suggestive of a specific diagnosis. The clinical issue that we most often encounter is whether there are CT findings which suggest the possibility of fungal infection. The hallmark CT finding which is associated with possible fungal infection is the presence of nodules (Mori et al. 1991; McAdams et al. 1995) (Figs. 6.8 and 6.9). These nodules are often clustered and can demonstrate any of the following associated findings: poorly defined margins, cavitation, or a surrounding halo of ground glass opacity (Mori et al. 1991; McAdams et al. 1995; Marks et al. 1996; Winer-Muram et al. 1994; Brown et al. 1994). Pathologically, the central nodular density on CT represents the actual fungal infection and the surrounding halo represents hemorrhagic infarction caused by thrombosis secondary to vascular invasion by the fungus (Mori et al. 1991). These findings are, however, nonspecific and can be seen with nonfungal infections such as cytomegalovirus infection (see Fig. 6.12) (Mori et al. 1991; Kang et al. 1996).

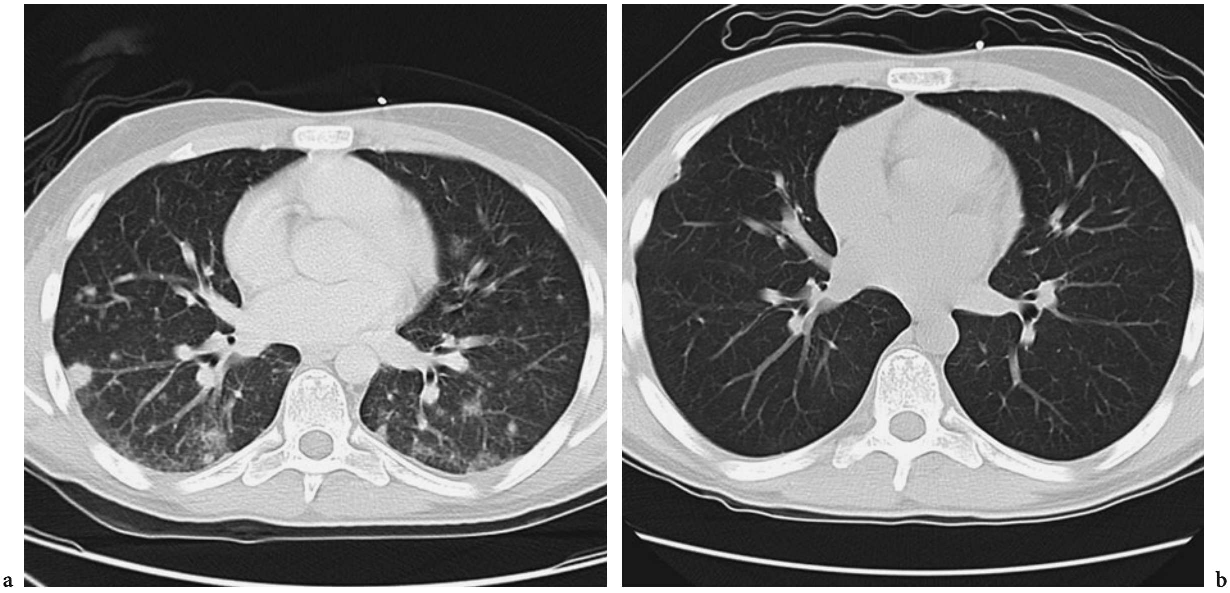

Fig. 6.8a,b. Fungal infection in a 17-year-old bone marrow transplant recipient. **a** CT shows multiple poorly defined pulmonary nodules. The nodules are clustered. **b** Baseline CT prior to infection shows clear lungs for comparison

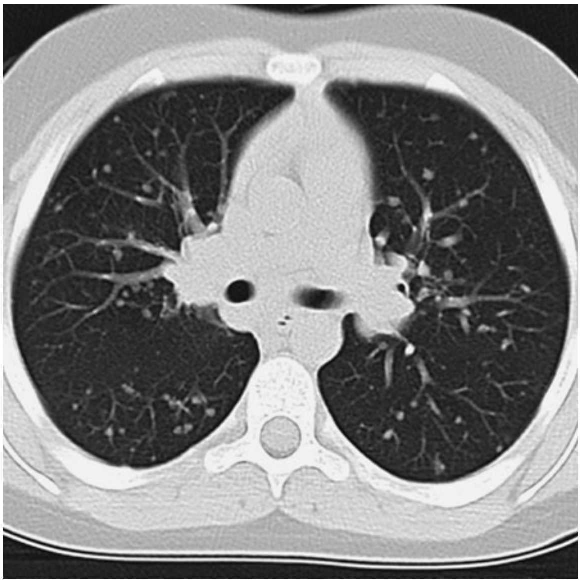

Fig. 6.9. Systemic histoplasmosis infection in immunocompromised 15-year-old. CT shows multiple pulmonary nodules bilaterally

6.4
CT in the Evaluation of Pulmonary Trauma

There are a number of causes of lung consolidation in children who have underwent traumatic injury. These include contusion, laceration, aspiration, atelectasis, and pre-existing lung opacification such as from pneumonia (Sivit et al. 1989a; Eichelberger et al. 1988; Donnelly and Klosterman 1997c). CT is uncommonly performed for the primary purpose of evaluating for pulmonary trauma. However, the inferior lung is often visualized when CT is performed to evaluate for traumatic injury to the contents of the abdomen and pelvis and CT of the chest is sometimes performed to evaluate for suspected thoracic aortic injuries. When CT is being performed to evaluate for traumatic injury to either the abdominal contents or mediastinum, it is important to evaluate the lung for lung contusion or other trauma related lung opacity.

Lung contusion is defined as hemorrhage and edema formation in the alveoli and interstitium secondary to blunt chest trauma, without accompanying parenchymal laceration (Sivit et al. 1989a; Eichelberger et al. 1988; Donnelly and Klosterman 1997c; Manson et al. 1993; Wagner et al. 1988; Williams and Stembridge 1964; Shackford 1987; Kirsh et al. 1972). The presence of lung contusion has been reported to be associated with an adverse effect on patient outcome (Sivit et al. 1989a; Eichelberger et al. 1988). In one study, mortality was 1.3% for pediatric trauma victims without lung contusions and 10.8% for those with contusions (Sivit et al. 1989a). Therefore, accurate identification of lung contusion and differentiation from other causes of lung opacification is helpful when planning management of pediatric trauma patients. Also, the incidence of lower thoracic trauma is not uncommon in child abuse (Sivit et al. 1989b). Accurate identification of lung opacification as contusion when child abuse is suspected may facilitate evidence in criminal proceedings and help in decisions regarding the removal of a child from a high risk environment.

On CT, lung contusions are characteristically nonsegemental in distribution, not following segmental or lobar anatomic boundaries (Sivit et al. 1989a; Donnelly and Klosterman 1997c). Contusions are usually located posteriorly (85%), have crescentic (50%) or amorphous (45%) shape, and are mixed confluent and nodular quality (70%) (Donnelly and Klosterman 1997c) (Fig. 6.10). The lung contusions of children may also demonstrate a 1–2 mm region of uniformly nonopacified subpleural lung, separating the area of lung consolidation from the adjacent chest wall (Donnelly and Klosterman 1997c). This finding is referred to as subpleural sparing and is seen with many lung contusions and is not seen with other causes of airspace opacification and is therefore helpful in identifying contusions (McAdams et al. 1995). The larger the lung contusion, the less likely subpleural sparing is to be present (Donnelly and Klosterman 1997c).

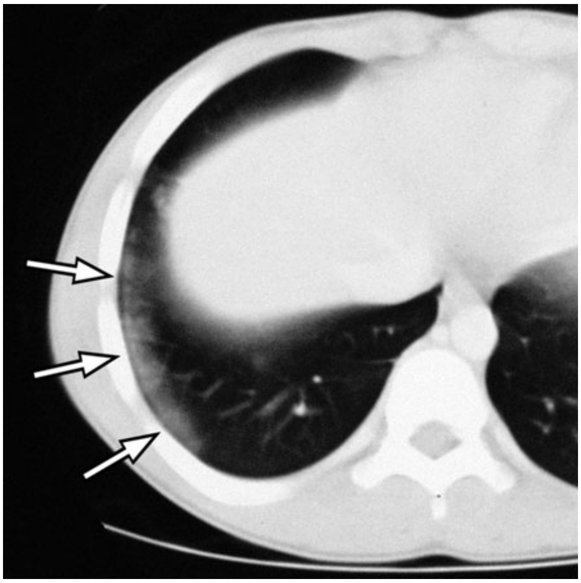

Fig. 6.10. Lung contusion. CT shows crescentic, peripheral density (*arrows*). There is subpleural sparing

The CT appearance of lung contusion in children is related to both the plasticity of the anterior thorax seen in children and the rapid deceleration mechanism encountered in most motor vehicle accidents. In high speed collisions, rib fractures occur much more commonly in adults than in children (Manson et al. 1993; Wagner et al. 1988; Williams and Stembridge 1964; Shackford 1987; Kirsh et al. 1972; Sivit et al. 1989b; Eichelberger and Randolph 1981). The decreased incidence in children is related to increased pliability of the anterior chest wall. This pliability of the anterior chest wall in combination with the contra-coup forces of rapid deceleration injury most likely compresses the relatively fixed posterior lung against the immediately adjacent, less compliant posterior ribs and vertebral column (Manson et al. 1993; Williams and Stembridge 1964). The distribution of the disruptive forces along the least mobile regions of lung explains both the posterior location and crescentic shape of most contusions (Donnelly and Klosterman 1997c). The diffuse distribution of force associated with blunt trauma also explains the nonsegmental distribution of pulmonary contusions (Manson et al. 1993).

The exact mechanism explaining the association of subpleural sparing and pulmonary contusion is speculative. Lung contusions are the result of alveolar capillary damage with extravazation of edema and hemorrhage into alveoli and interstitial spaces (Williams and Stembridge 1964). Anatomically, terminal arterial branches terminate prior to the subpleural region of lung. The resultant sparse vascularity of this region may protect the subpleural lung from hemorrhage. Also, when contra-coup forces compress the posterior lung against the chest wall and result in contusion, the subpleural lung may be compressed against the chest wall during the time of injury, "squeezing" the extravasated blood and edema into the more central lung and resulting in a spared zone of aerated subpleural lung (Donnelly and Klosterman 1997c). Larger lung contusions are less likely to demonstrate both the characteristic crescentic shape and subpleural sparing than were smaller contusions. This may be related to the tendency of larger areas of hemorrhage to extend into the subpleural space and more central lung, related to persistent bleeding after the moment of trauma (Donnelly and Klosterman 1997c).

Chest radiography is a relatively insensitive diagnostic test for detecting lung contusions (Sivit et al. 1989a; Eichelberger et al. 1988; Donnelly and Klosterman 1997c; Manson et al. 1993; Wagner et al. 1988). In one study, 69% of lung contusions were either underestimated (24%) or not identified (45%) by plain radiographs (Donnelly and Klosterman 1997c).

Pulmonary laceration differs from contusion in that with laceration there is a frank tear within the lung parenchyma. The characteristic CT finding of pulmonary laceration is the presence of an air or fluid filled cavity (Sivit et al. 1989a; Eichelberger et al. 1988; Donnelly and Klosterman 1997c; Manson et al. 1993; Wagner et al. 1988; Tocino and Miller 1987) (Fig. 6.11). The CT findings of atelectasis include triangular shape, segmental distribution, and obvious signs of volume loss (Sivit et al. 1989a, b).

Traumatic rupture of the bronchi or trachea is rare and only has been sparsely reported in children (Mahboubi and O'Hara 1981). The diagnosis is usually questioned in the setting of a pneumothorax that does not resolve with tube placement or an area of persistent collapsed lung (Mahboubi and O'Hara 1981; Wan et al. 1997; Weir et al. 1988; Harvey-Smith et al. 1980). The diagnosis is usually confirmed with bronchoscopy or primarily investigated surgically. Because of the low incidence of this traumatic entity and primary evaluation with bronchoscopy, the role of CT is not well defined. CT can demonstrate findings of bronchial rupture. Findings

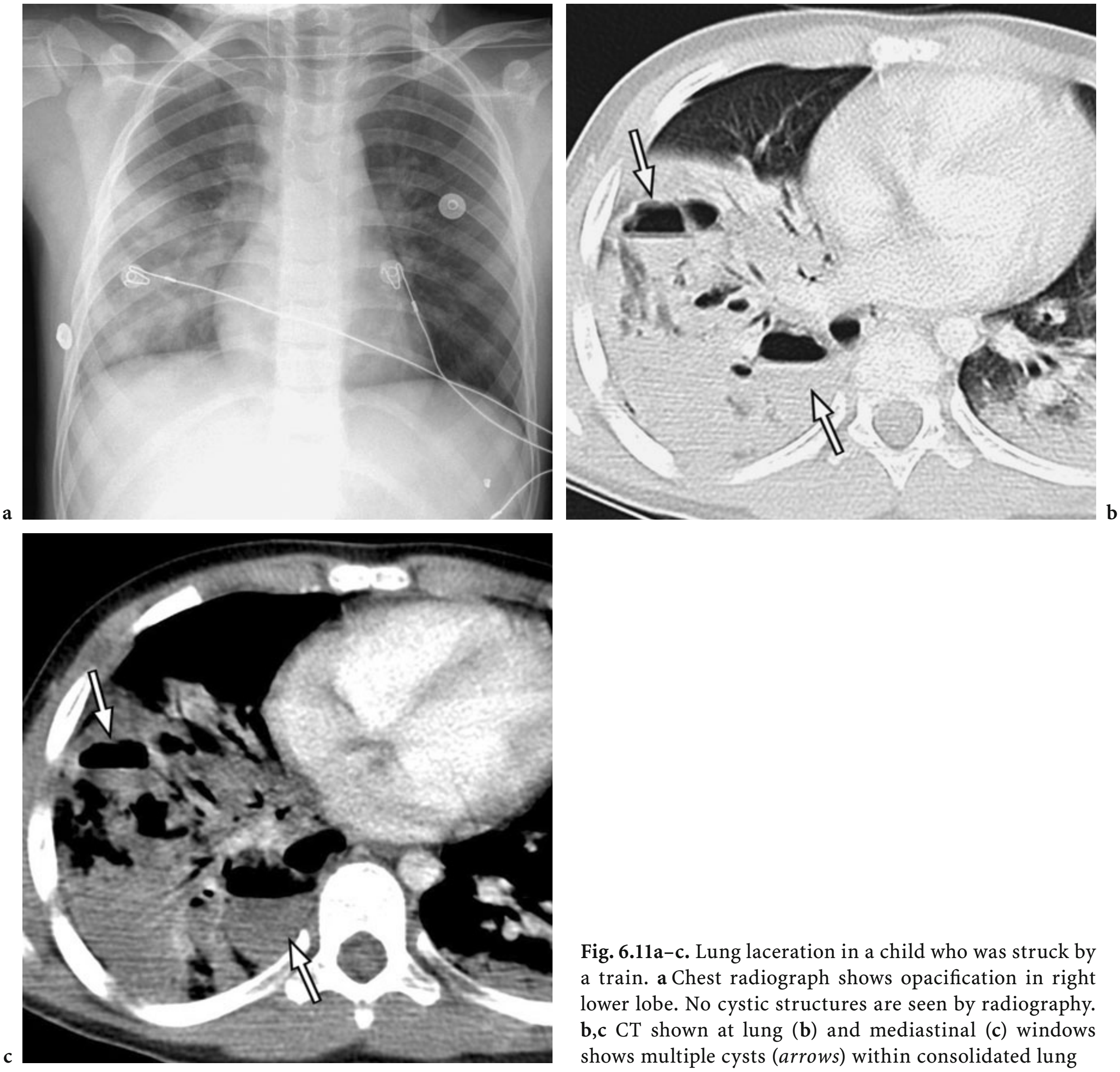

Fig. 6.11a–c. Lung laceration in a child who was struck by a train. **a** Chest radiograph shows opacification in right lower lobe. No cystic structures are seen by radiography. **b,c** CT shown at lung (**b**) and mediastinal (**c**) windows shows multiple cysts (*arrows*) within consolidated lung

include a discontinuous bronchus in conjunction with pneumothorax or pneumomediastinum (Wan et al. 1997; Weir et al. 1988). 3D helical CT may be helpful in showing such a discontinuous bronchus.

6.5
Pulmonary Embolism and Infarction

Pulmonary embolism and infarction is thought of as primarily an adult disease. However, with the increasing complexity and acuity of the medical conditions of hospitalized children, pulmonary embolism is being seen with increased frequency at pediatric institutions. Pulmonary embolism can be seen in children with predisposition to clotting, obesity, complex surgery, oral contraceptive use, sickle cell anemia, nephritic syndrome, smoking, systemic lupus erythematosus, and other conditions.

Multidetector CT and CT angiography (Garg 2005; Schoepf and Costello 2004; Yankelevitz et al. 2000) are playing an increasing role in the evaluation for potential pediatric embolism. Technically, the method of acquiring CT angiography for pulmonary embolism in children is similar to adults, with radiation adjustments such as weight based adjustment of tube current for smaller children.

Imaging findings of pulmonary embolism and infarction are also similar in children as in adults. Findings include identification of non-enhancing clot within the enhancing branches of the pulmonary arteries (Figs. 6.12 and 6.13), peripheral

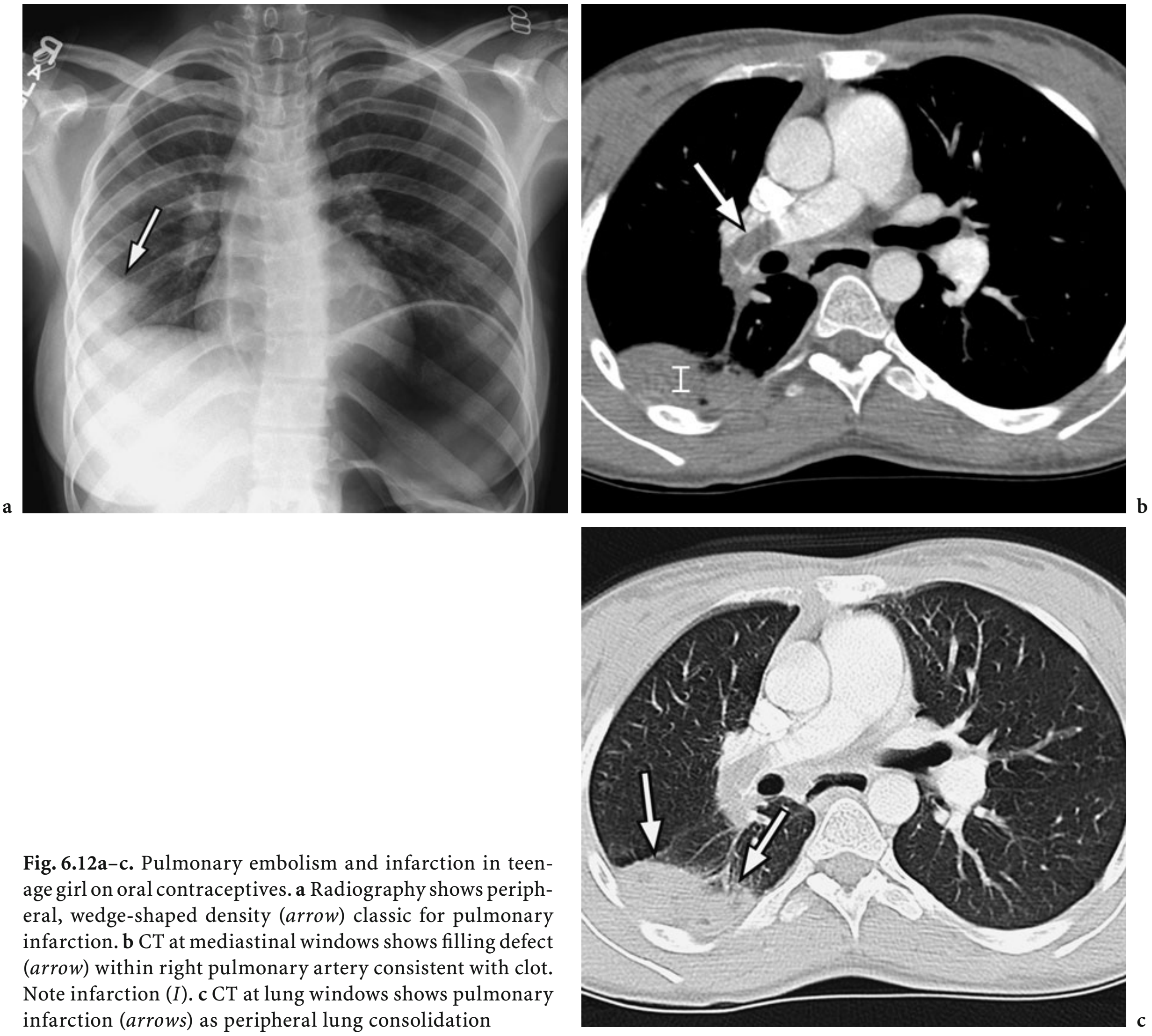

Fig. 6.12a–c. Pulmonary embolism and infarction in teenage girl on oral contraceptives. **a** Radiography shows peripheral, wedge-shaped density (*arrow*) classic for pulmonary infarction. **b** CT at mediastinal windows shows filling defect (*arrow*) within right pulmonary artery consistent with clot. Note infarction (*I*). **c** CT at lung windows shows pulmonary infarction (*arrows*) as peripheral lung consolidation

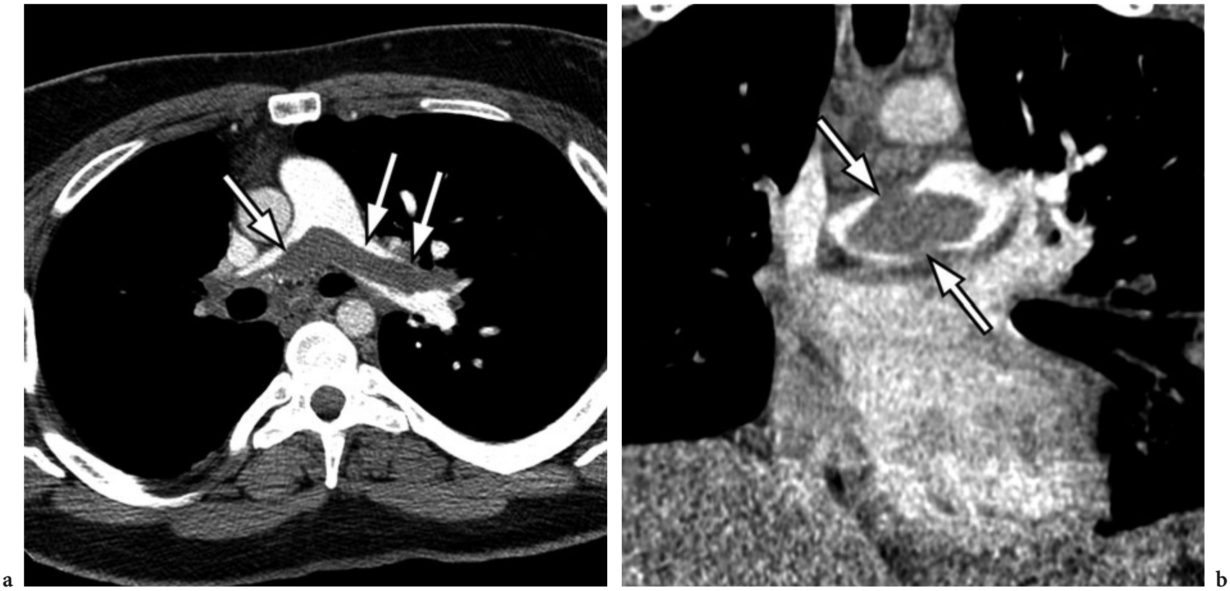

Fig. 6.13a,b. Pulmonary embolism in teenage boy with clotting disorder. CT shown in axial (**a**) and coronal (**b**) planes shows large saddle pulmonary embolism (*arrows*)

wedge shaped lung consolidation from infarction (Fig. 6.12), and associated pleural effusion. Small branch subsegmental emboli may be missed with CT angiography. However, in most cases of emboli, the findings are multiple and not a diagnostic challenge. Sensitivity has been reported as high as 100% and negative predictive value for a significant health complication as high as 99% in the presence of a negative CT angiogram (Garg 2005; Schoepf and Costello 2004; Yankelevitz et al. 2000). As high as 2%–4% of CT angiography exams can be non-diagnostic because of motion artifact. This number may even be higher in children. Emboli are considered acute when the filling defect is identified centrally within the vascular lumen and considered chronic when the defect is eccentric and contiguous with the vessel's periphery (Garg 2005; Schoepf and Costello 2004; Yankelevitz et al. 2000).

6.6
Conclusion

Chest radiography is the primary means of imaging acute lung disease. However, there are a number of scenarios in which CT is playing an increasing role in evaluating acute lung disease. The information yielded by CT can be very helpful in evaluating infection, infarction, and trauma when CT is utilized for appropriate indications.

References

Alario AJ, McCarthy PL, Markowitz R, Kornguth P, Rosenfield N, Leventhal JM (1987) Usefulness of chest radiographs in children with acute lower respiratory tract disease. J Pediatr 111:187–193

Baber CD, Hedlund LW, Oddson TA, Putman CE (1980) Differentiating empyemas and peripheral pulmonary abscess. The value of computed tomography. Radiology 135:755–758

Bettenay FAL, de Campo JF, McCrossin DB (1988) Differentiating bacterial from viral pneumonias in children. Pediatr Radiol 18:453–454

Bouros D, Schiza S, Panagou P, Drositis J, Siafakas N (1994) Role of streptokinase in the treatment of acute loculated parapneumonic pleural effusions and empyema. Thorax 49:852–855

Brown MJ, Miller RR, Muller NL (1994) Acute lung disease in the immunocompromised host: CT and pathologic examination findings. Radiology 190:247–254

Condon VR (1991) Pneumonia in children. J Thorac Imaging 6:31–44

Conte P, Heitzman ER, Markarian B (1970) Viral pneumonia. Radiology 95:267–272

Danner PK, McFarland DR, Felson B (1968) Massive pulmonary gangrene. AJR Am J Roentgenol 103:548–554

Donnelly LF (1999) Maximizing the usefulness of imaging in children with community-acquired pneumonia. AJR Am J Roentgenol 172:505–512

Donnelly LF, Klosterman LA (1997a) CT appearance of parapneumonic effusions in children: findings are not specific for empyema. AJR Am J Roentgenol ;169:179–182

Donnelly LF, Klosterman LA (1997b) Pneumonia in children: decreased parenchymal contrast enhancement – CT sign of intense illness and impending cavitary necrosis. Radiology 205:817–820

Donnelly LF, Klosterman LA (1997c) Subpleural sparing: a CT finding of lung contusion in children. Radiololgy 204:385–387

Donnelly LF, Klosterman LA (1998a) Cavitary necrosis complicating pneumonia in children: sequential findings on chest radiography. AJR Am J Roentgenol 171:253–256

Donnelly LF, Klosterman LA (1998b) The yield of CT of children who have complicated pneumonia and noncontributory chest radiography. AJR Am J Roentgenol 170:1627–1631

Donnelly LF, Kimball TR, Barr LL (1999) Purulent pericarditis presenting as acute abdomen in children: abdominal imaging findings. Clin Radiol 54:691–693

Eichelberger MR, Randolph JG (1981) Thoracic trauma in children. Surg Clin North Am 61:1181

Eichelberger MR, Mangubat EA, Sacco WJ, Bowman LM, Lowenstein AD (1988) Outcome analysis of blunt injury in children. J Trauma 28:1109–1115

Frush DP, Donnelly LF (1997) Pulmonary sequestration spectrum: a new spin with helical CT. AJR Am J Roentgenol 169:679–682

Garg K (2005) Acute pulmonary embolism (helical CT). In: eMedicine for WebMD. http://www.emedicine.com/radio/topic582/htm. Updated 6/9/05. Cited 1/3/07

Grossman LK, Caplan SE (1988) Clinical, laboratory, and radiographic information in the diagnosis of pneumonia in children. Ann Emerg Med 17:43–46

Gutman E, Pongdee O, Park YS (1973) Massive pulmonary gangrene. Radiology 107:293–294

Harvey-Smith W, Bush W, Northrop C (1980) Traumatic bronchial rupture. AJR Am J Roentgenol 134:1189–1193

Hedlund GL, Griscom NT, Cleveland RH, Kirks DR (1997) Respiratory system. In: Kirks DR (ed) Practical pediatric imaging, 3rd edn. Little, Brown, and Company, Boston, pp 619–821

Himelman RB, Callen PW (1986) The prognostic valve of loculations in parapneumonic pleural effusion. Chest 90:852–856

Isaacs RD (1986) Necrotizing pneumonia in bacteremic pneumococcal infection. Br J Dis Chest 80:295–296

Kang EY, Patz EF, Muller NL (1996) Cytomegalovirus pneumonia in transplant patients: CT findings. J Comput Assist Tomogr 20:295–299

Kerem E, Bar BZ, Rudenski A, Katz S, Kleid D, Branski D (1994) Bacteremia necrotizing pneumococcal pneumonia in children. Am J Respir Crit Care Med 149:242–244

Kern JA, Rogers BM (1993) Thoracoscopy in the management of empyema in children. J Pediatr Surg 23:1128–1132

Kirsh MM, Pellegrini RV, Sloan HE (1972) Treatment of blunt chest trauma. Surg Ann 4:51–90

Knight L, Fraser RG, Robson HG (1975) Massive pulmonary gangrene: a severe complication of Klebsiella pneumonia. Can Med Assoc J 112:196–198

Leventhal JM (1982) Clinical predictors of pneumonia as a guide to ordering chest roentgenograms. Clin Pediatr 21:730–734

Light RW (1985) Parapneumonic effusions and empyema. Clin Chest Med 6:55–62

Light RW (1995) A new classification of parapneumoic effusions and empyema. Chest 108:229–301

Mahboubi S, O'Hara AE (1981) Bronchial rupture in children following blunt chest trauma. Report of five cases with emphasis on radiologic findings. Pediatr Radiol 10:133–138

Manson D, Babyn PS, Palder S, Bergman K (1993) CT of blunt chest trauma in children. Pediat Radiol 23:1–5

Marks MJ, Haney PJ, McDermott MP, White CS, Vennos AD (1996) Thoracic diseases in children with AIDS. RadioGraphics 1349–1362

McAdams HP, Rosado-de-Christenson ML, Templeton PA, Lesar M, Moran CA (1995) RadioGraphics 15:271–286

Mori M, Galvin JR, Barloon TJ, Gingrich RD, Stanford W (1991) Fungal pulmonary infections after bone marrow transplantation: evaluation with radiography and CT. Radiology 178:721–726

Moulton JS, Benkert RE, Weisiger KH, Chambers JA (1995) Treatment of complicated pleural fluid collections with image-guided drainage and intracavitary urokinase. Chest 108:1252–1259

Muller NL (1993) Imaging of the pleura. Radiology 186:297–309

Naidich DP, Zerhouni EA, Siegelman SS (1991) Computed tomography and magnetic resonance of the thorax, 2nd edn. Raven, New York, pp 423–426

O'Reilly GV, Dee PM, Otteni GV (1978) Gangrene of the lung: successful medical management of three patients. Radiology 126:575–579

Osborne D (1978) Radiologic appearance of viral disease of the lower respiratory tract in infants and children. AJR Am J Roentgenol 130:29–33

Peter G (1988) The child with pneumonia: diagnostic and therapeutic considerations. Pediatr Infect Dis J 7:453–456

Pugatch RD, Sprin PW (1985) Radiology of the pleura. Clin Chest Med 6:17–32

Ramnath RR, Heller RM, Ben-Ami T, Miller MA et al. (1998) Implications of early sonographic evaluation of parapneumonic effusions in children with pneumonia. Pediatrics 101:68–71

Rosen H, Nadkarni V, Theroux M, Padman R, Klein J (1993) Intrapleural streptokinase as adjunctive treatment for persistent empyema in pediatric patients. Chest 103:1190–1193

Schoepf UJ, Costello P (2004) CT angiography for diagnosis of pulmonary embolism: state of the art. Radiology 230:329–337

Shackford SR (1987) Blunt chest trauma: the intensivist's perspective. J Intensive Care Med 1:125–136

Silen ML, Weber TR (1995) Thoraccoscopic debridement of loculated empyema thoracis in children. Ann Thorac Surg 59:1166–1168

Sivit CJ, Taylor GA, Eichelberger MR (1989a) Chest injury in children with blunt abdominal trauma: evaluation with CT. Radiology 171:815–818

Sivit CJ, Taylor GA, Eichelberger MR (1989b) Visceral injury in battered children: a changing perspective. Radiology 173:659–661

Stark DD, Federle MP, Goodman PC, Podrasky AE, Webb WR (1983) Differentiating Lund abscess and empyema: radiography and computed tomography. AJR Am J Roentgenol 141:163–167

Stern EJ, Sun H, Haramati LB (1996) Peripheral bronchopleural fistulas: CT imaging features AJR Am J Roentgenol 167:117–120

Strovroff M, Teaque G, Heiss KF, Parker P, Ricketts RR (1995) Thoracoscopy in the management of pediatric empyema. J Pediatr Surg 30:1211–1215

Swischuk LE, Hayden CK Jr (1986) Viral vs. bacterial pulmonary infections in children (is roentgenographic differentiation possible?) Pediatr Radiol 16:278–284

Tocino I, Miller MH (1987) Computed tomography in blunt chest trauma. J Thorac Imaging 2:45–59

Torres A, Agusti GA, Rodriques-Roisin R, Etopa R, Agusti-Vidal A (1984) Cavitation in bacteremic pneumococcal pneumonia. Am Rev Respir Dis 130:533–534

Turner RB, Lande AE, Chase P et al. (1987) Pneumonia in pediatric outpatients: cause and clinical manifestations. J Pediatr 111:194–200

Wagner RB, Crawford WO Jr, Schimpf PP (1988) Classification of parenchymal injuries of the lung. Radiology 167:77–82

Waite RJ, Carbonneau RJ, Balikian JP, Umali CB, Pezzella AT, Nash J (1990) Parietal pleural changes in empyema: appearance at CT. Radiology 175:145–150

Wan YL, Tsai KT, Yeow KM, Tan CF, Wong HF (1997) CT findings of bronchial transection. Am J Emerg Med 15:176–177

Weir IH, Muller NL, Connell DG (1988) CT diagnosis of bronchial rupture. J Comput Assist Tomogr 12:1035–1036

Wildin SR, Chonmaitree T, Swischuk KE (1988) Roentgenographic features of common pediatric viral respiratory tract infections. Am J Dis Child 142:43–46

Williams JR, Stembridge VA (1964) Pulmonary contusion secondary to nonpenetrating chest trauma. AJR Am J Roentgenol 91:284–290

Winer-Muram HT, Rubin SA, Fletcher BD, Kauffman WM, Jennings SG, Arheart KL, Bozeman PM (1994) Childhood leukemia: diagnostic accuracy of bedside chest radiography for severe pulmonary complications. Radiology 193:127–133

Worthy SA, Flint JD, Muller NL (1997) Pulmonary complications after bone marrow transplantation: high-resolution CT and pathologic findings. RadioGraphics 17:1359–1357

Yangco B, Derensinski S (1980) Necrotizing or cavitary pneumonia due to Streptococcus pneumonia: report of four cases and review of the literature. Medicine 59:449–457

Yankelevitz DF, Gamsu G, Shah A et al. (2000) Optimization of combined CT pulmonary angiography with lower extremity CT venography. AJR Am J Roentgenol 174: 67–69

Zukin DD, Hoffman JR, Cleveland RH, Kushner DC, Herman TE (1986) Correlation of pulmonary signs and symptoms with chest radiographs in the pediatric age group. Ann Emerg Med 15:792–796

Pediatric Tuberculosis

7

Pedro A. Daltro and Eloá Nunez-Santos

CONTENTS

7.1 **Introduction and Historical Aspects** *165*

7.2 **Epidemiology** *166*

7.3 **Pathogenesis** *167*
7.3.1 Infection *167*
7.3.2 Disease *167*

7.4 **Clinical Aspects** *168*

7.5 **Imaging: Technique and Features** *169*
7.5.1 Chest X-Ray *169*
7.5.2 Computed Tomography (CT) *170*
7.5.3 Magnetic Resonance Imaging (MRI) *170*
7.5.4 Ultrasound (US) *170*
7.5.5 Infection – The Primary Complex *170*
7.5.6 Primary Pulmonary Tuberculosis *170*
7.5.7 Progressive Primary Pulmonary Tuberculosis *172*
7.5.8 Chronic and Postprimary Pulmonary Tuberculosis *175*
7.5.9 Acute Disseminated Disease *175*
7.5.10 Congenital Tuberculosis *177*
7.5.11 Pleural and Pericardial Effusions *178*
7.5.12 Unusual Presentations and Complications *179*

7.6 **Conclusions** *180*

References *180*

7.1
Introduction and Historical Aspects

Tuberculosis (TB) is a transmittable chronic bacterial disease caused by infection with the *Mycobacterium tuberculosis* complex. Pathologically it is characterized by the formation of granulomas. Clinical signs and symptoms depend upon the location of the lesions. TB can affect every organ in the body, but pulmonary infection is by far the most common.

Tuberculosis has been known to affect man as far back as historical data can record. Skeletal remains of prehistoric humans dating back to 8000 BC and Egyptian mummies dating from between 2500 and 1000 BC have revealed clear evidence of the disease in the spine (Cremin and Jamieson 1995). The best-documented confirmation of TB infection has come from DNA studies of an 8-year-old male Inca mummy who lived in around 700 AD. Radiographic study of his lumbar spine showed evidence of Pott's disease and smears of the lesion revealed acid-fast bacilli, most likely *Mycobacterium bovis* (Dutt and Stead 1999).

Jean Antoine Villemin (1827–1892) was the first to prove the infectious nature of tuberculosis by passing it from humans to cattle, and from cattle to rabbits. The actual agent of TB, the tubercle bacillus, was identified by Robert Koch, in Germany, in 1882. The vaccination against tuberculosis [bacille Calmette-Guérin (BCG)] was developed in the early part of the twentieth century by the French researchers Calmette and Guérin. Effective therapy against tuberculosis became available in 1943 with Waksman's discovery of streptomycin, the first antituberculosis drug.

P. A. Daltro, MD
Instituto Fernandes Figueira – Fiocruz and Clinica de Diagnóstico por Imagem – Barrashopping – Av. das Américas 4666, Sala 325-Barra da Tijuca, Rio de Janeiro, RJ 22649-900, Brazil
E. Nunez-Santos, MD
Instituto Fernandes Figueira – Fiocruz, Rua Almirante Guillobel, 93/402 Lagoa, Rio de Janeiro, RJ 22471-150, Brazil

7.2
Epidemiology

Mycobacterium tuberculosis is the most devastating bacterial pathogen of all time. Approximately one-third of the world's population is infected with this bacteria and therefore at risk of developing the disease (Cremin and Jamieson 1995). In 1993, more than a century after the TB causal agent discovery, followed by decades of research on and implementation of appropriate chemical therapy, the World Health Organization (WHO) declared tuberculosis a global emergency. This was the first time in the history of the organization that such a document was issued. The worldwide incidence of all forms of TB reached 140 per 100,000 population in 2004 and was growing at about 0.6% annually (WHO/HTM/TB/2006.361 *GUIDELINES FOR THE PROGRAMMATIC MANAGEMENT of drug-resistant tuberculosis*). Without treatment, tuberculosis is often fatal. It is estimated that 50%–60% of the untreated patients are likely to die within 5 years after diagnosis (Maher and Raviglione 1999).

Tuberculosis has always been a public health problem in developing countries, especially among young people. Each year, about 9 million people develop TB, of whom about 2 million die. Of the 9 million annual TB cases, about 1 million (11%) occur in children under 15 years of age. Of these childhood cases, 75% occur annually in 22 high-burden countries (HBC) (WHO/FCH/CAH/2006).

There are many reasons for the alarming worldwide resurgence of tuberculosis. Poverty and poor living conditions (resulting in malnutrition and crowding), associated with lack of appropriate antituberculosis drugs and sometimes governmental lack of interest in the control of tuberculosis are the most important causes in many developing countries.

In developed countries, tuberculosis has also proven burdensome. The disease has been mainly reported in HIV-positive patients, intravenous drug users, groups of people living in enclosed, crowded settings (prisons, shelters and nursing homes) and, last but not least, in outer unsanitary city areas, as well as among immigrants or refugees from countries where tuberculosis is endemic (Cremin and Jamieson 1995).

The worldwide distribution of registered tuberculosis cases mapped by WHO (from the Global Tuberculosis Programme: Global Tuberculosis Control revised in March 2006) is as follows: 33% in the South-East Asian region, 22% in the Western Pacific Region, 29% in the African Region, 5% in the European Region, 7% in the Eastern Mediterranean Region and 4% in the American Region (WHO Tuberculosis Fact sheet N°104 – Global and regional incidence. March 2006, Retrieved on 6 October 2006).

The most recent factor allowing for the increase of tuberculosis is the HIV pandemic, affecting both developed and developing countries. In African countries and South-East Asia, the association between tuberculosis and HIV has progressively increased.

Multidrug-resistant tuberculosis is a new face of the disease. Drug resistance results from inappropriate drug treatment or patient non-adherence to treatment and has a potentially dramatic impact on the epidemiology and control of tuberculosis worldwide (WHO/IUATLD Global Project on Anti-Tuberculosis Drug Resistance Surveillance 1997–2000). Drug-resistant strains of TB have emerged and are spreading; in 2000–2004; 20% of cases were resistant to standard treatments, and 2% were also resistant to second-line drugs.(Centers for Disease Control – CDC. Emergence of *Mycobacterium tuberculosis* with Extensive Resistance to Second-Line Drugs – Worldwide, 2000–2004).

In 1997, in response to the growing concern about global tuberculosis control, the WHO adopted a new strategy, DOTS (Directly Observed Treatment Short Course), based on five pillars:

- Governmental political support
- Microscopic detection of the cases by sputum-smear examination
- Short and supervised therapy
- Regular supply of antituberculosis drugs
- A standardized recording and reporting system for program supervision and evaluation

The aims of this program are to prevent the emergence of resistant strains of *M. tuberculosis* and to detain their spread but although the cohort of patients treated under DOTS has grown from 240,000 in 1994 to 1.7 million in 2003, treatment success has edged closer to the 85% target, falling just short of it in 2003 (82%) (WHO/HTM/TB/361).

The global average has been held below the target mainly by the African and European regions, where high proportions of patients fail treatment or die, or are lost from DOTS cohorts. HIV/AIDS and MDR-TB are major obstacles to TB control.

Treatment of drug-resistant TB is still inadequate in many countries. In some, laboratory diagnosis is of poor quality; others lack national policies on MDR-TB management; first- and second-line drugs of uncertain quality are widely available; and large numbers of MDR-TB patients are subject, outside National Tuberculosis Programmes (NTPs), to inappropriate diagnostic and treatment procedures. The high proportions of re-treatment cases reported by some NTPs also indicate that drug-resistant TB could be common in some populations where no surveys have yet been done (WHO/HTM/TB/2006.361–371).

Since tuberculosis is a global emergency, the disease will only be defeated by a global alliance, bringing together public health agencies, the pharmaceutical industry and the academia. Effective control programs must foster private–public partnership in order to succeed.

7.3
Pathogenesis

7.3.1
Infection

Humans are the only species in which *M. tuberculosis* is a self-perpetuating pathogen. The only epidemiologically important mode of transmission is air borne with infection occurring through inhalation of viable bacilli in an enclosed space. Pediatric tuberculosis infection almost invariably occurs by contact with an adult or adolescent with cavitary pulmonary tuberculosis, most often at home, but also at school or in the day care center. In outside air the bacilli are rapidly killed by ultraviolet light and viable bacilli are so widely dispersed that inhalation of even a single bacillus is extremely improbable.

Tuberculosis spreads more easily among family members or among people who share the same facilities. However, contact alone is not bound to develop the disease. Immunologic and genetic factors affect the child's response to the initial infection (Starke 1999). Children under 5 years of age, and especially those under 2, are less resistant to the organism and, therefore, disseminated forms of the disease are more common in this age group. There is less risk of progressive primary disease in later childhood, between 6 and 12 years of age.

Child-to-child transmission is virtually unknown, mainly because children do not show the tussive force of an adult and have only sparse secretions. However, they play a peculiar role in the transmission of tuberculosis because they may harbor a partially healed infection that lies dormant, only to be reactivated as infectious pulmonary TB many years later (Starke 1999). Thus, children constitute a long-lasting reservoir of tuberculosis in the population from which future generations will be infected (Cremin and Jamieson 1995).

In more than 95% of cases, the entrance door of tuberculous infection is the lung, by inhalation of bacilli. Infection through the oro-pharynx, throat, eye or skin rarely occurs. The exposed child inhales aerosolized particles containing 1–3 bacilli. These bacillary particles can be moved up the bronchial tree by cilia and might eventually be swallowed, causing no infection. They can also reach the alveoli, where they will be ingested by the alveolar macrophages. The bacilli can be killed or inhibited by these cells. If the bacilli are quite virulent, they grow and multiply inside the alveolar macrophage until it bursts, releasing a greater number of pathogens. These bacilli will be then ingested by other alveolar and blood macrophages (i.e. monocytes), forming the *tubercle*, which consists of an aggregation of macrophages, epithelioid cells and lymphocytes. Central necrosis inside the tubercle is formed by destruction of macrophages. This immune response is mainly tissue-damaging delayed-type hypersensitivity, and at this time, usually 3–8 weeks after infection, the tuberculin skin test will usually be positive. Eventually, sclerosis and calcification of the lesion may develop (Dannenberg 1999).

In the next stage, cell-mediated immunity is very important. If only poor cell-mediated immunity develops, bacilli escape from the edge of the caseous necrosis, multiply again and spread from the tubercle to nearby mediastinal lymph nodes. These three items together – the alveolar site of infection, the infected lymph nodes and associated lymphangitis – form the "primary (Ranke's) complex".

7.3.2
Disease

From the infected lymph nodes, bacilli can travel via the lymphatics or bloodstream to many parts of the body, such as the liver, spleen, kidneys, bone metaphysis, brain and other organs, or return to the lungs causing secondary lung lesions. Infants and young children have poor cell-mediated immunity. So, when infected, they show a higher incidence of tuberculosis than adults or older children. Lesions in the lymph nodes and extrapulmonary sites are common. Sometimes a pulmonary lesion spreads locally causing pneumonitis and pleural disease. Occasionally the caseous center of the granuloma progresses to liquefaction and is expelled through a bronchus, leaving a cavity and leading to bronchogenic spread, following the pattern of adult pulmonary tuberculosis (Fig. 7.1).

In children, the disease usually develops soon after the primary infection (primary tuberculosis) but the bacilli can also lie dormant in tissue macrophages for many years, only to develop the disease some decades later (secondary tuberculosis). Complete eradication of the bacillus by the immune system never occurs, and it is still very difficult even with the use of effective antituberculosis therapy (Ehlers 1999). Calcified lesions are sterile in 85% and fibrotic lesions in 86%. In contrast, solid caseous lesions are sterile in only 50% (Moulding 1999).

It is important always to bear in mind that tuberculosis-infected children, left untreated, will house the bacilli for longer periods of time than adults and can become a source of tuberculosis in future years (Inselman 1996).

7.4
Clinical Aspects

Most cases of infection with *M. Tuberculosis* do not result in disease, but the risk of developing disease is higher for children than for adults. Children under 6 years of age have the highest case rates and the most serious disease (Costello and Rook 1995).

The risk of a child acquiring tuberculous infection is environmental, depending on whether the child has had contact with an adult or adolescent

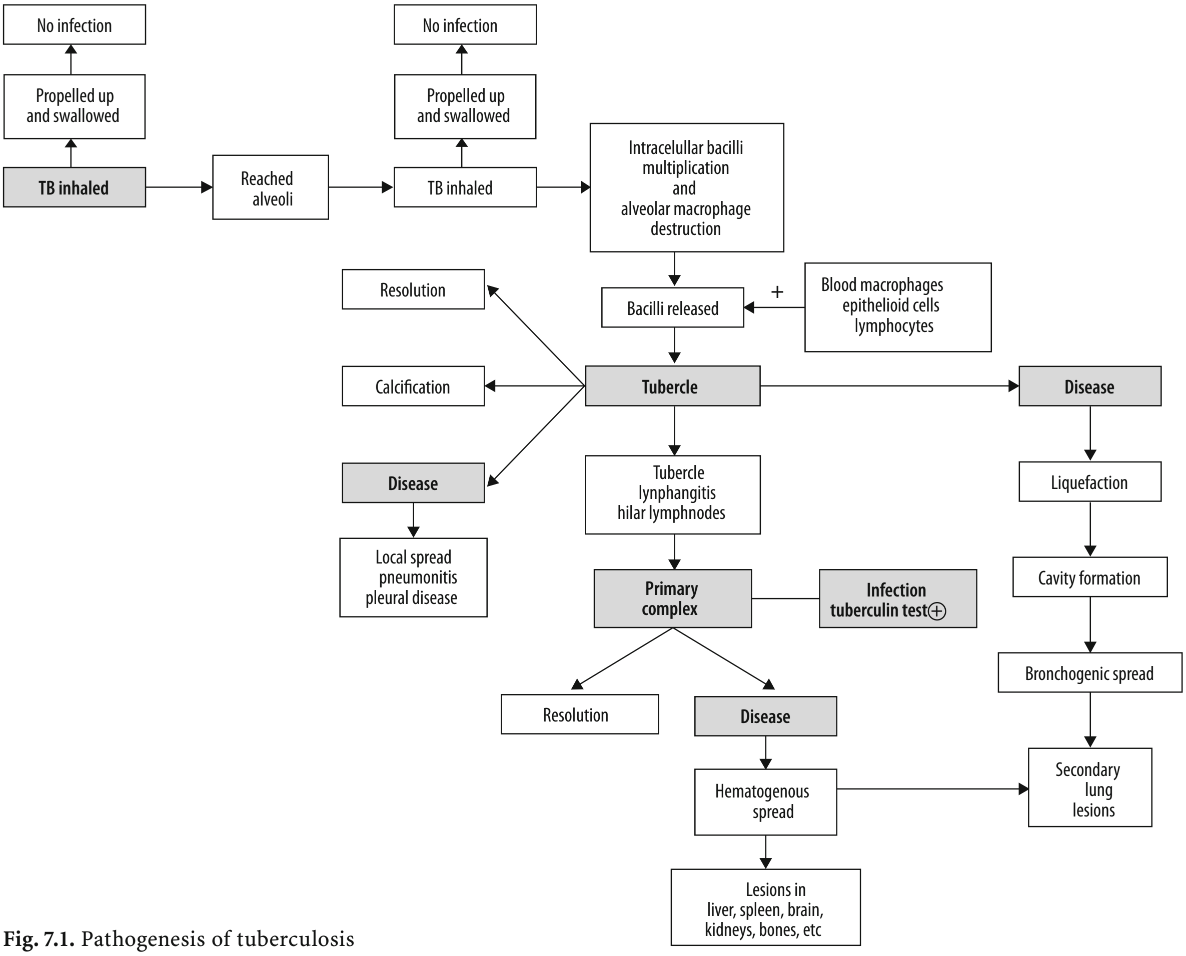
No infection
Propelled up and swallowed
TB inhaled
Reached alveoli
No infection
Propelled up and swallowed
TB inhaled
Intracelullar bacilli multiplication and alveolar macrophage destruction
Bacilli released
+
Blood macrophages epithelioid cells lymphocytes
Resolution
Calcification
Tubercle
Disease
Disease
Local spread pneumonitis pleural disease
Tubercle lynphangitis hilar lymphnodes
Liquefaction
Cavity formation
Primary complex
Infection tuberculin test⊕
Bronchogenic spread
Resolution
Disease
Hematogenous spread
Secondary lung lesions
Lesions in liver, spleen, brain, kidneys, bones, etc

Fig. 7.1. Pathogenesis of tuberculosis

with pulmonary TB. Not all infected children have the same risk of developing the disease; the patient's immunocompetence, age, and certain genetic factors all play a part. The virulence of the bacillus is also important (Starke 1999).

The high-risk categories for exposed children to develop tuberculous disease are infants and children under 4 years of age who have had close contact with a person with smear-positive TB, children with HIV disease or some other immunodeficiency, and those receiving high-dose corticosteroids.

Most infants and children who become infected with *M. tuberculosis* are completely asymptomatic and will never develop disease. Those who do, demonstrate few symptoms or signs of pulmonary disease at the outset. Fewer than half develop non-specific symptoms such as fever, anorexia and weight loss. Most develop cough and many wheeze. If untreated, symptoms and signs of pulmonary bronchopneumonia and extrapulmonary disease may become apparent. Tuberculous infection is defined by a reactive tuberculin skin test. During the period of infection (3–8 weeks), usually the child has no symptoms and the chest radiograph is normal.

For the absolute diagnosis of TB the demonstration on culture of *M. tuberculosis* in secretions or tissue of the patient is required. A positive tuberculin skin test demonstrates that the individual has been infected with *M. tuberculosis* but it cannot tell whether the bacilli are living in a quiescent latent state or actively replicating and causing disease. When the pathology is virtually confined to the lungs, as is usually the case in adults with pulmonary TB, it is relatively easy to confirm the diagnosis by sputum culture. When the principle focus of infection is the intrathoracic lymph nodes, as often is the situation in infants and young children, the organisms are inaccessible and it becomes difficult to prove that the patient has TB. Furthermore, children produce little sputum, which, in addition, contains few microorganisms, and they generally swallow it. Because of these factors and the difficulties associated with obtaining adequate samples of swallowed sputum from the stomach, the diagnosis of TB is confirmed bacteriologically in considerably less than half (range 10%–75%) of infants and young children who are treated for TB (Klein and Iseman 1999). Thus, the triad of a positive tuberculin skin test, abnormal chest radiographs and a history of exposure to an adult with TB remains the most effective method for diagnosing TB in children.

Primary TB has been used to describe pediatric pulmonary disease that arises as a complication of the tuberculous infection. In children, disease frequently complicates the initial infection immediately, making the distinction between the two stages impossible. Miliary and meningeal TB can develop any time, but they are more likely to occur during the initial 3 months following the primary infection. Endobronchial TB can also develop at this time. Tuberculosis of the pleura and peritoneum characteristically occurs 3–7 months after demonstration of a positive skin test (Inselman 1996) (Table 7.1).

Imaging methods such as chest X-ray, chest US and chest CT are extremely important tools for the diagnosis of pediatric pulmonary TB. In some instances, particularly in difficult cases, they offer the only way to reach a correct diagnosis and a thorough evaluation of the extent of the disease.

Table 7.1. Clinical types of pulmonary tuberculosis in children (adapted from Inselman 1996)

Clinical types
Infection
● Positive tuberculin skin test reaction without clinical, radiographic or laboratory evidence of disease
Pulmonary disease
● Primary pulmonary tuberculosis (hilar adenopathy with or without primary parenchymal disease)
● Progressive pulmonary tuberculosis (pneumonia, endobronchial disease)
● Chronic pulmonary tuberculosis (cavitary, fibrosis, tuberculoma)
● Acute disseminated disease
● Tuberculous pleural and pericardial effusion
● Unusual presentations

7.5
Imaging: Technique and Features

7.5.1
Chest X-Ray

Chest radiography (AP-PA and lateral X-rays) remains the first and most widely used imaging technique for the evaluation of pulmonary TB in children. It is usually very effective for detecting parenchymal lesions and lymphadenopathy in most of the cases.

7.5.2
Computed Tomography (CT)

CT is the examination of choice in unusual, complicated or disseminated presentations of the disease. It may also be helpful for the evaluation of asymptomatic infants and toddlers with positive skin test, normal or equivocal chest X-rays and recent exposure to TB. In such cases, we recommend CT if the information it can provide cannot be obtained with mediastinal US and may influence treatment. In small children with miliary TB, head CT should always be performed as well. Recognition of brain lesions, which commonly occur in these patients, can influence therapy.

The advantages of CT over conventional radiographs in defining the extent of the disease and its possible complications (bronchial, pleural, pericardiac and chest wall involvement) have been well documented in the literature (WS Kim et al. 1997). Since the search for lymph nodes is crucial in the study of chest TB in children, we recommend studying these patients with contrast-enhanced scans using the helical technique with the parameters described in the chapter on helical CT (Chap. 3). Unenhanced scans are not routinely obtained. Multiplanar and 3D reconstructions are also helpful in some cases, particularly in the evaluation of tracheobronchial disease. Occasionally we will take unenhanced or delayed scans of suspicious areas to acquire additional information, such as, the presence of calcifications or low-attenuation areas.

7.5.3
Magnetic Resonance Imaging (MRI)

MRI is an excellent method for detecting mediastinal lymph node involvement and has the advantage of multiplanar imaging capacity. However, high cost, need for sedation in most cases and poor visualization of the lung parenchyma limits its use.

7.5.4
Ultrasound (US)

US is an easy-to-use, inexpensive, non-aggressive technique that is useful for identifying mediastinal lymph nodes (Bosch et al. 2004) and differentiating them from a large normal thymus in patients who present mediastinal widening. It is also helpful for detecting pleural and pericardial effusion (see Chap. 1).

7.5.5
Infection – The Primary Complex

The primary (Ranke's) complex consists of the primary parenchymal lesion, draining lymphatic vessels and regional lymph nodes. It can develop in any part of the lung, although the middle lobe has a lower frequency of occurrence (Inselman 1996). At the onset of hypersensitivity to tuberculin, most often 4–8 weeks after mycobacterial inoculation, the primary complex may become visible on the chest X-ray or CT (Fig. 7.2).

Of infected children, 95% will not develop disease. In these cases the primary complex becomes fibrotic, calcifies or resolves completely and the chest radiograph appears normal or demonstrates calcifications (Fig. 7.3). Viable mycobacteria can persist for decades even within calcified lesions.

7.5.6
Primary Pulmonary Tuberculosis

The hallmark and most constant feature of pulmonary TB in infancy and childhood is mediastinal and/or hilar lymphadenopathy, and most radiologists would be reluctant to consider the diagnosis of TB in its absence. Whenever this feature is observed in the chest radiograph, particularly in infants, tuberculin skin testing should be considered. The right side is more commonly affected than the left because of the usual pattern of lymphatic circulation within the lungs. A left-sided parenchymal focus often leads to bilateral hilar adenopathy, whereas a right-sided focus is usually associated only with right-sided lymphadenitis (Starke 1999).

Lymphadenopathy is not always easy to detect on conventional radiographs. Computed tomography has a higher sensitivity. On chest plain films lymphadenopathy usually presents as asymmetrically distributed paratracheal, hilar and/or sub-carinal lobulated nodes with sharp or ill-defined borders. The enlarged lymph nodes can compress and stretch the bronchi (Fig. 7.4), or compress and displace the trachea. Sub- carinal lymph node involvement can cause splaying of the mainstem bronchi. Shift of the mediastinum may not occur because of the fixed nature of these lymph nodes (Inselman 1996).

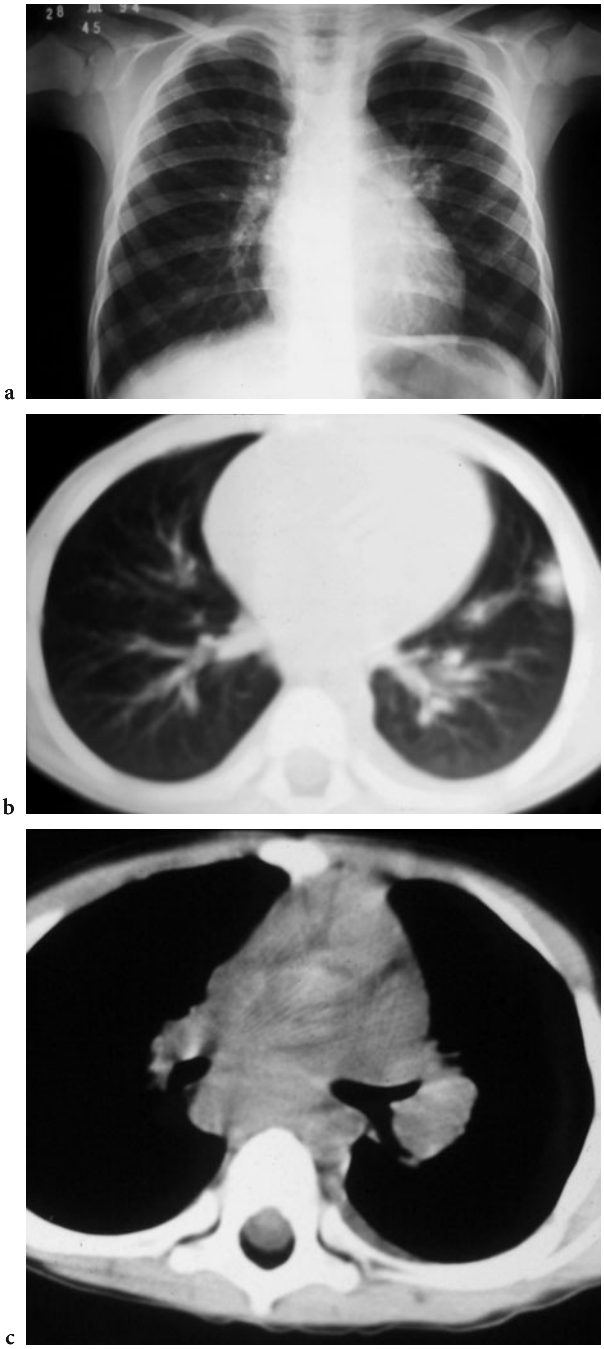

Fig. 7.2. **a** Chest X-ray of an 8-year-old boy shows slight enlargement of the left hilum. **b** Unenhanced CT of the same patient demonstrates peripheral pulmonary focus in the left lower lobe and lymphangitis. **c** Mediastinal window shows left hilar adenopathy

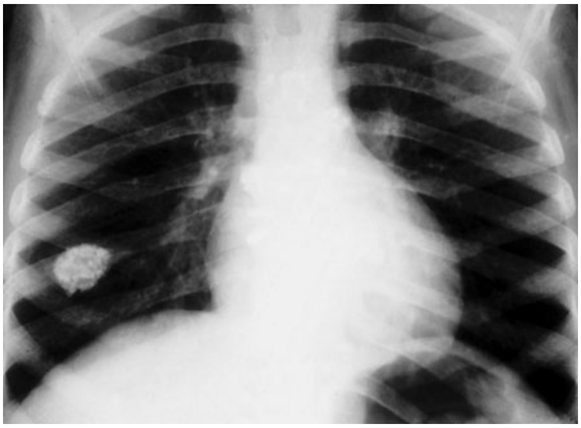

Fig. 7.3. Primary complex with calcified pulmonary focus in a 6-year-old child

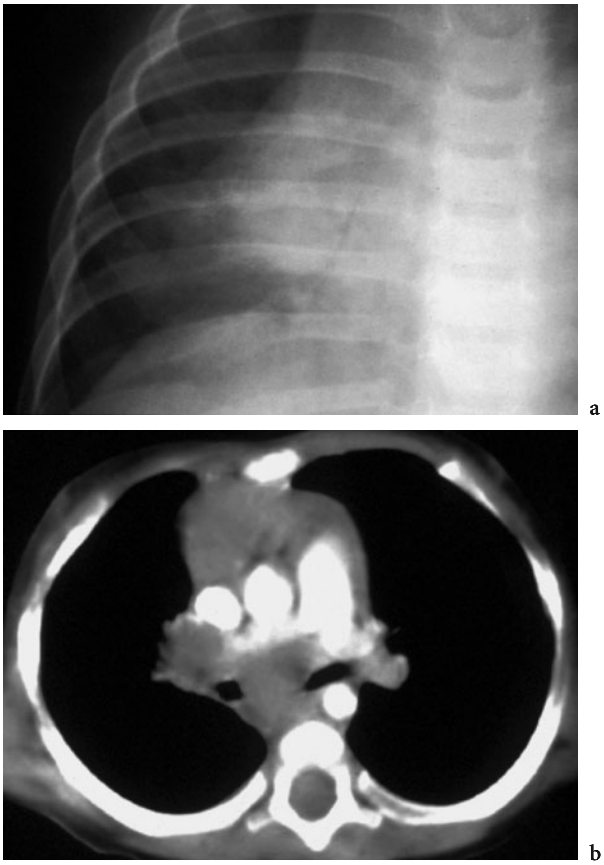

Fig. 7.4. **a** An 11-month-old boy. Chest X-ray shows a "stretched bronchus" sign. **b** CT demonstrates that it corresponds to the intermediate bronchus encased by two large lymph nodes

On CT, the enlarged nodes can be partially or completely calcified or appear as soft tissue density masses. In our experience heavily calcified nodes indicate long-standing infection. Following contrast administration, nodes that are not completely calcified will enhance homogeneously or present ring-like enhancement with low-attenuation centers due to internal caseous material (Figs. 7.5 and 7.10c). Delayed images can be extremely helpful for differentiating paratracheal lymph nodes from normal retrocaval thymus.

Enlarged and edematous hilar, paratracheal and sub-carinal lymph nodes may encroach upon the regional bronchus. This compression can cause bronchial stenosis and lead to hyperinflation in the distal lung secondary to air-trapping, (Fig. 7.6) or completely occlude an airway and produce lung collapse.

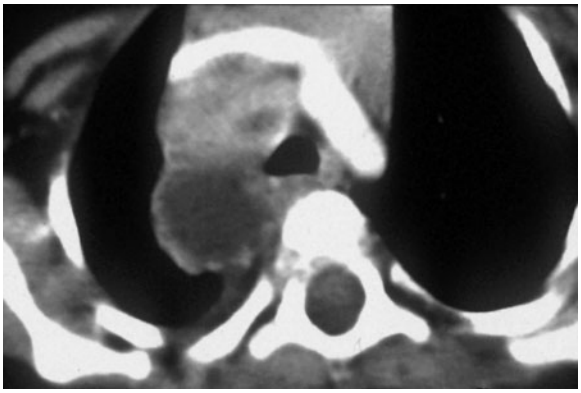

Fig. 7.5. A 12-month-old boy with TB. Contrast enhanced CT shows enhancement of the anterior node while the posterior remains centrally hypodense

7.5.7
Progressive Primary Pulmonary Tuberculosis

Inflamed nodes sometimes erode a bronchial wall and discharge caseous material into the bronchus (Fig. 7.7), leading to bronchogenic spread. On HRCT this will manifest as poorly defined nodules or rosettes of nodules, 2–10 mm in diameter that can be identified as centrilobular or branching centrilobular opacities mimicking the “tree in bud” image. Coalescence of the centrilobular opacities results in focal areas of bronchopneumonia (Webb et al. 1996). Extensive bronchogenic spread can cause other patterns, such as pulmonary consolidation, or multiple nodules throughout the lungs (Fig. 7.8). Occasionally, the primary parenchymal lesion continues to enlarge, resulting in focal pneumonitis or lobar pneumonia with thickening of the overlying pleura without distinct hilar lymphadenopathy (Fig. 7.9).

When tuberculosis is progressively destructive, liquefaction of lung parenchyma leads to formation of a primary tuberculous cavity (Fig. 7.10). Hematogenous spread can also develop, though it is less frequent (Inselman 1996).

Another rare complication is the appearance of bullous or cystic lesions in the lung. These have been reported to occur during treatment (Matsaniotis et al. 1967), but we have observed them before therapy was initiated (Fig. 7.11). Occasionally peripheral bullous lesions will lead to pneumothorax.

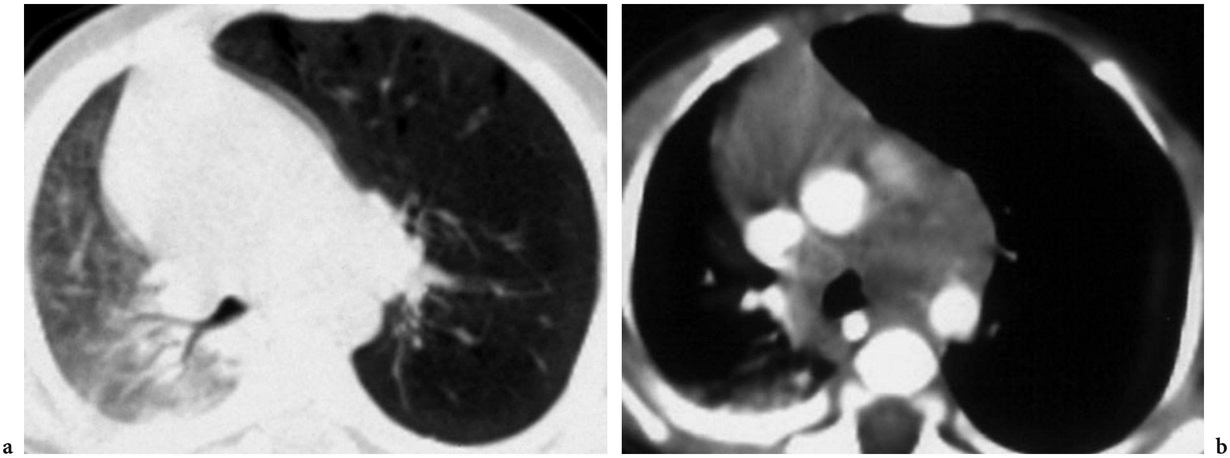

Fig. 7.6a,b. CT of a 4-month-old boy with obstructive emphysema of the left lung caused by hilar adenopathy

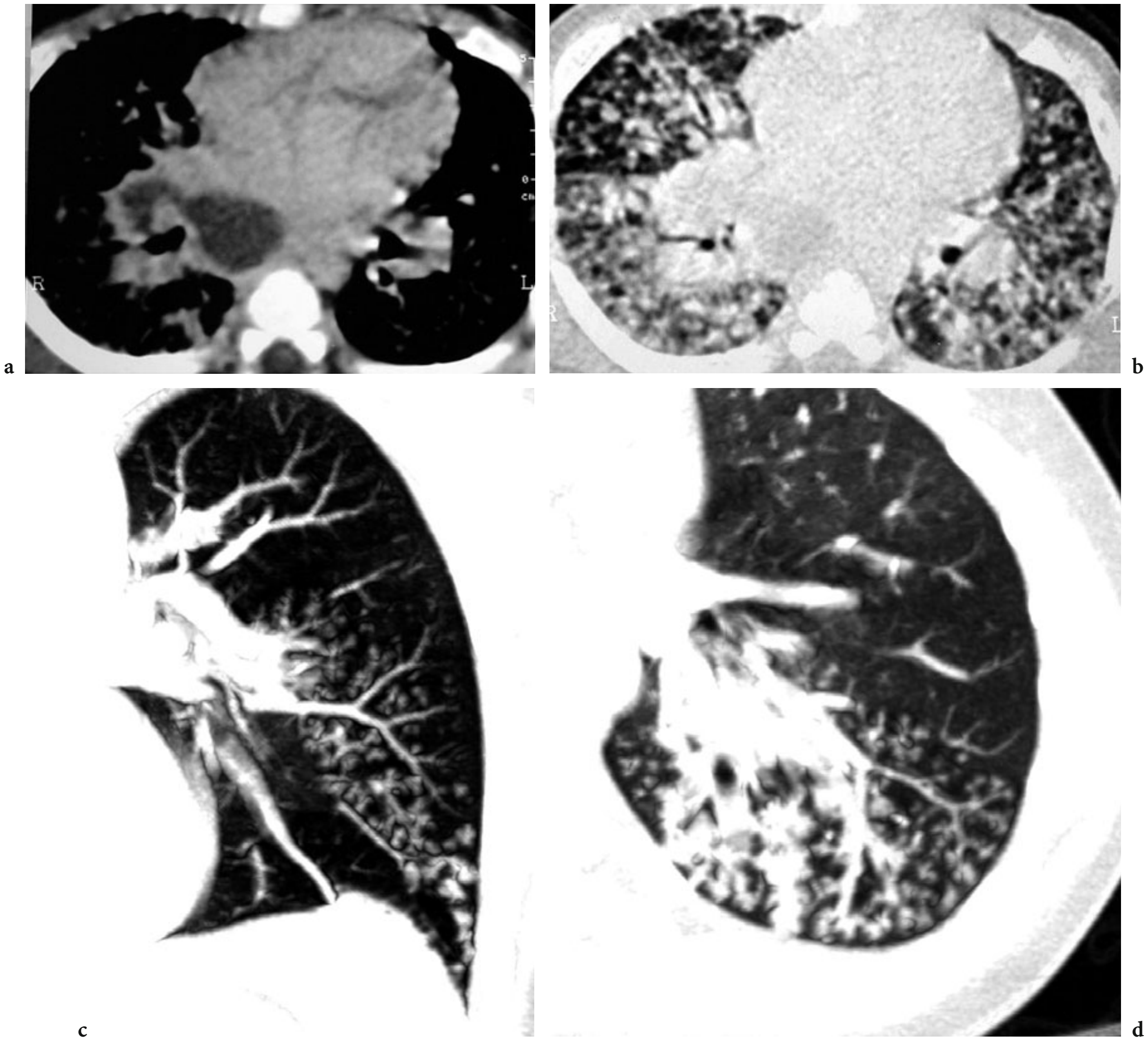

Fig. 7.7a–d. Unenhanced CT (mediastinal window) (**a**) in a 6-month-old boy shows right hilar lymph node with hypodense center (caseum) with fistulous tract to the right main bronchus, causing bronchogenic spread with multiple pulmonary nodules of different sizes (**b**). CT of a 7-years-old boy, MIP reconstructed images reveals bronchogenic spread with tree-in-bud pattern (**c**). Note the secondary pulmonary lobule and centrilobular opacities (**d**)

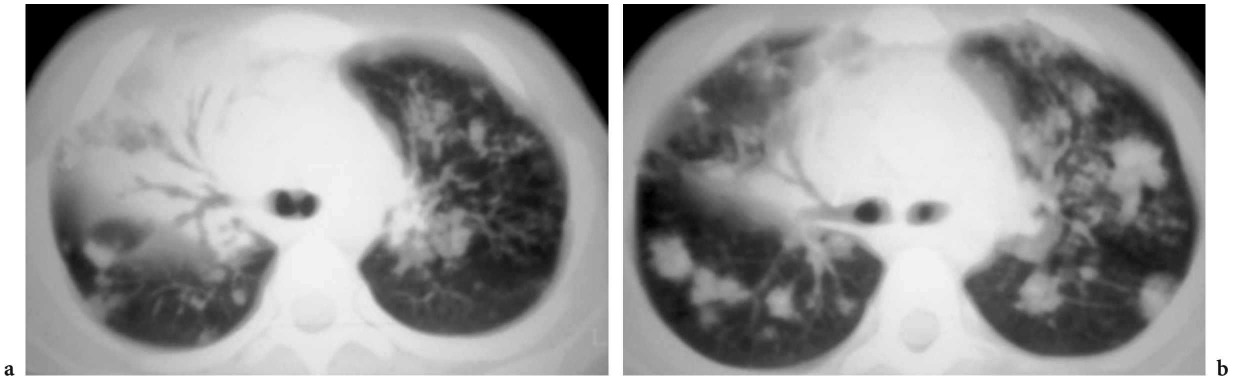

Fig. 7.8a,b. CT of a 10-year-old girl shows alveolar consolidation of the right upper lobe and bilateral confluent, nodular opacities

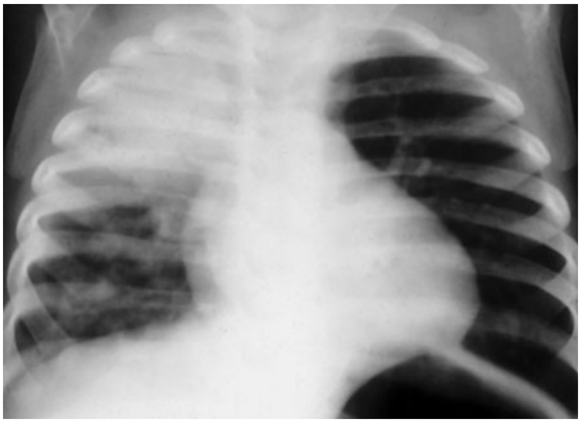

Fig. 7.9. Chest X-ray of a 3-year-old boy shows extensive consolidation of the right upper lobe, without evident lymphadenopathy

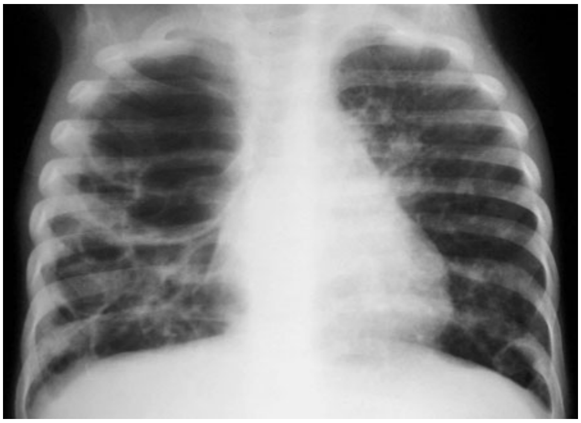

Fig. 7.11. Chest X-ray in a 6-year-old boy with multiple bullous tuberculous lesions in both lungs that appeared prior to receiving antituberculosis therapy

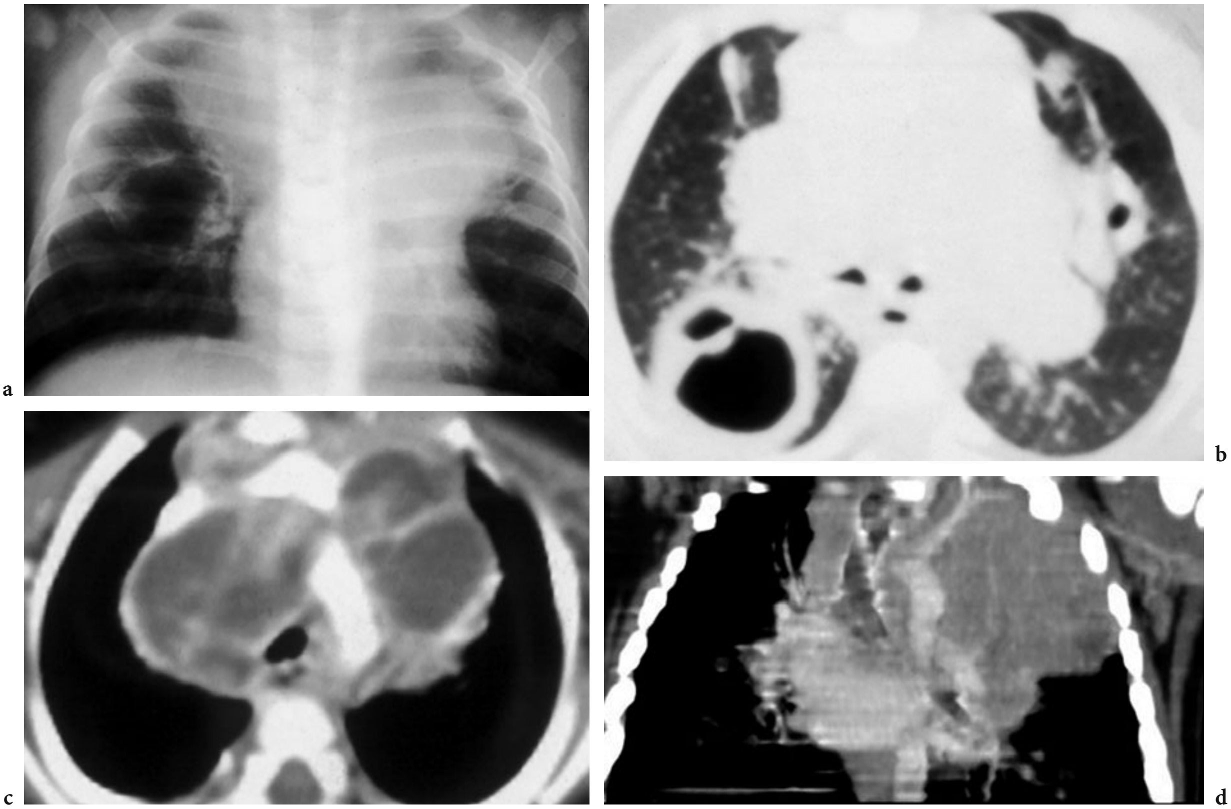

Fig. 7.10a–d. Chest X-ray in a 2-month-old boy with a huge mediastinal and hilar lymphadenopathy with a cavitary lesion in the right lung (**a**). HRCT better demonstrates the cavity in the right lung (**b**). Enhanced CT shows widened superior mediastinum due to large, rim-enhancing TB lymph nodes (**c**). Enhanced CT. Coronal reconstruction – 5 month old girl with large left adenopathy simulating a mediastinal mass (**d**)

7.5.8
Chronic and Postprimary Pulmonary Tuberculosis

It is very common for tuberculous lymph nodes to affect the adjacent airways by compression from without or by infiltration of the wall and eventual erosion into the lumen. Epituberculosis is one of the terms applied to the radiographic consequences of this event. Airway involvement can cause bronchial stenosis, bronchiectasis or collapse, which may be segmental, lobar or involve the entire lung. Helical CT with multiplanar and 3D reconstructions are particularly helpful for examining the airways (Figs. 7.12 and 7.13).

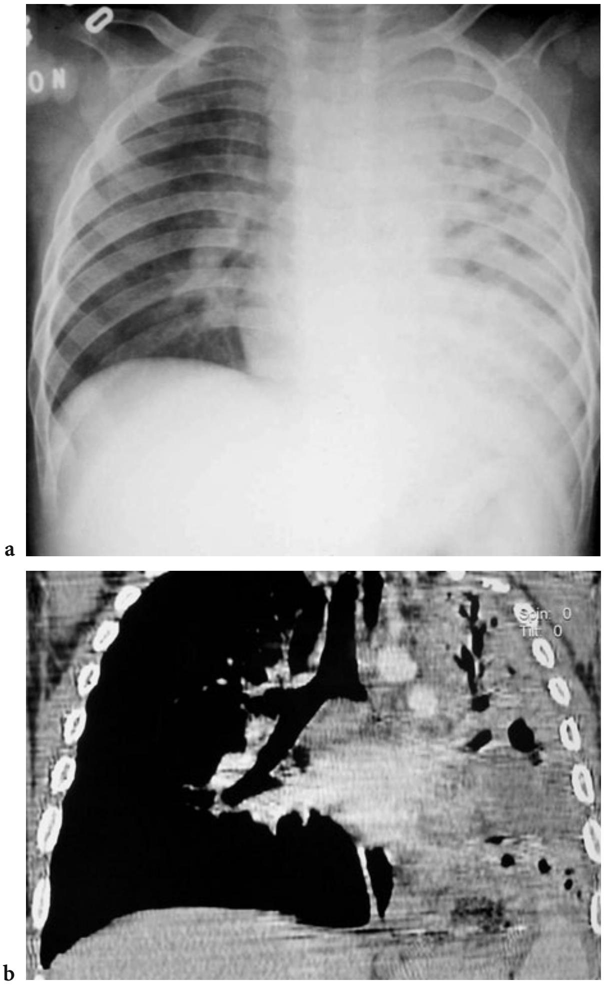

Fig. 7.12. a Chest X-ray of a 1-year-old boy with consolidation and loss of volume of the left lung. **b** CT coronal reconstruction shows obstruction of the left main bronchus causing the lung opacity. Moderate bronchial dilatation can also be observed

Tuberculosis disease that occurs more than 1 year after the primary infection is thought to be secondary to endogenous regrowth of persistent bacilli from the primary infection and subclinical dissemination. Exogenous reinfection is very rare.

Postprimary tuberculosis occurs in patients previously sensitized to *Mycobacterium tuberculosis*. Reactivation of dormant bacilli occurs during periods of immunosuppression, malnutrition and debilitation. Postprimary tuberculosis in the pediatric age group mainly occurs in adolescents and most commonly involves the apical and posterior segments of the upper lung lobes, and the superior segments of the lower lobes. The lesions are often smaller in adolescents than adults and lordotic views or even CT may be necessary to demonstrate small lesions (Starke 1999). The CT findings of active post-primary tuberculosis include centrilobular nodules, tree-in-bud, lobular consolidation, cavitation and bronchial wall thickening (Fig. 7.14).

Dissemination during postprimary tuberculosis is rare among immunocompetent adolescents, but is very common in HIV-infected or immunocompromised adolescents.

7.5.9
Acute Disseminated Disease

Miliary spread complicating the primary infection occurs most often in infants and small children, usually no later than 3–6 months after the infection. The organs most commonly seeded are the lungs, liver, spleen, meninges, peritoneum, lymph nodes, pleura and bones. Pulmonary dissemination leads to the formation of pulmonary nodular interstitial granulomas, usually 1–2 mm in size, widely disseminated throughout the lungs.

On chest radiographs, the lungs usually show a miliary pattern. Brain involvement is common in miliary TB (Schuit 1979). Therefore, head CT should be performed in all children with miliary tuberculosis even if they do not show neurological symptoms (Fig. 7.15).

On CT, miliary tuberculosis appears as numerous small, well-defined nodules of up to several millimeters in diameter uniformly distributed through the lungs. A random distribution of nodules with respect to the lobule is observed (Webb et al. 1996) (Fig. 7.16). In addition, CT can reveal hilar or mediastinal lymph nodes (Fig. 7.17) and occasionally

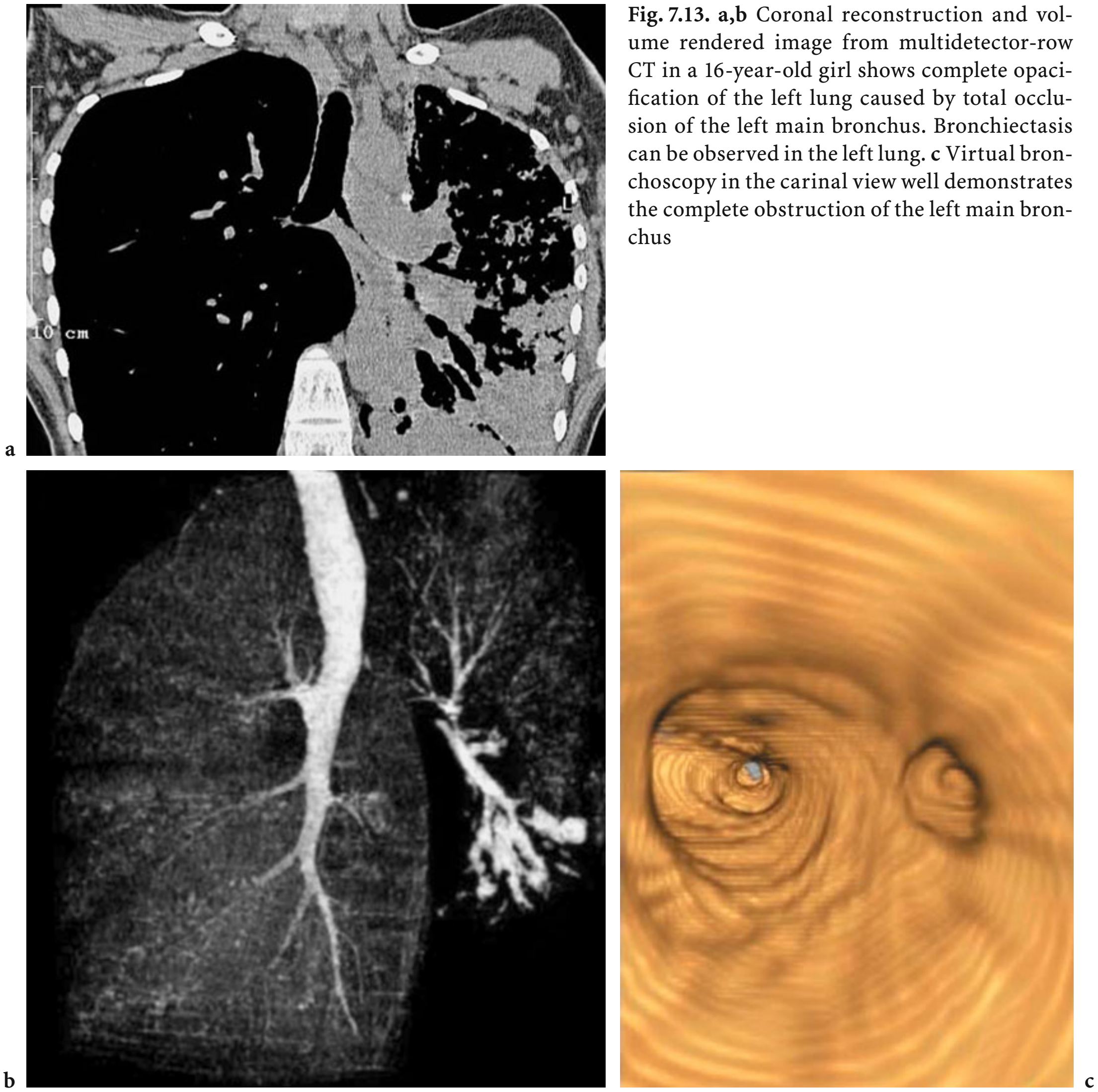

Fig. 7.13. a,b Coronal reconstruction and volume rendered image from multidetector-row CT in a 16-year-old girl shows complete opacification of the left lung caused by total occlusion of the left main bronchus. Bronchiectasis can be observed in the left lung. **c** Virtual bronchoscopy in the carinal view well demonstrates the complete obstruction of the left main bronchus

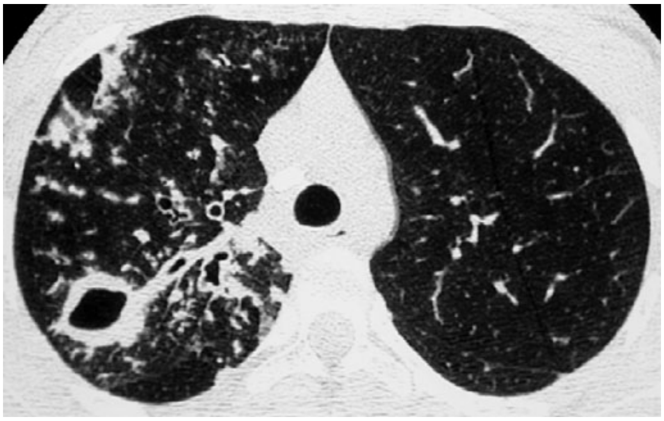

Fig. 7.14. A 10-year-old girl with secondary apical tuberculosis. CT demonstrates nodules (some with a hazy halo), ground-glass opacities and a cavity

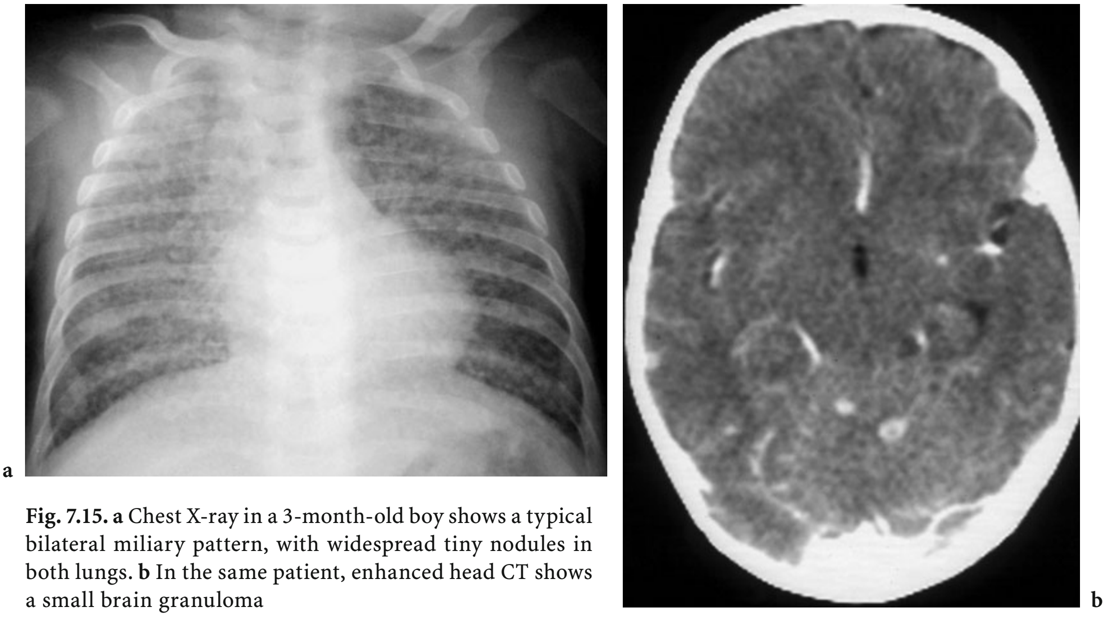

Fig. 7.15. a Chest X-ray in a 3-month-old boy shows a typical bilateral miliary pattern, with widespread tiny nodules in both lungs. **b** In the same patient, enhanced head CT shows a small brain granuloma

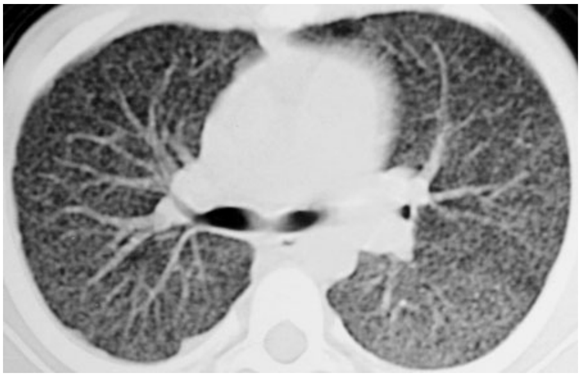

Fig. 7.16. HRCT of an 8-year-old boy shows a typical miliary pattern with tiny, widespread, randomly distributed nodules in both lungs

small pleural effusions (Oh et al. 1994). Exceptionally, pulmonary involvement by the miliary nodules will be asymmetrical (Fig. 7.17).

7.5.10
Congenital Tuberculosis

Congenital tuberculosis (CTb) could be defined as an infection due to the *Mycobacterium tuberculosis* transmitted from the mother to the fetus during the intra-uterus period (Stallworth et al. 1980). It is extremely rare, even in countries with high preva-

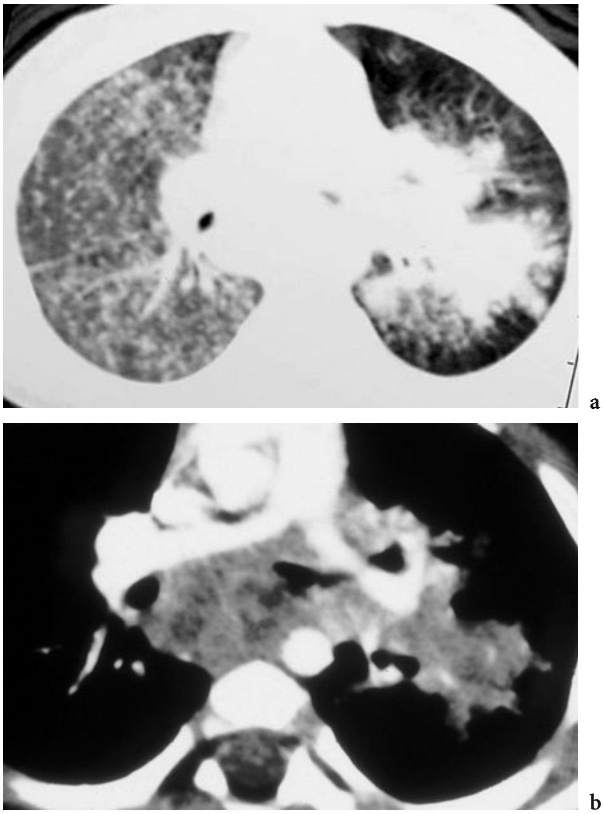

Fig. 7.17a,b. Chest CT of a 1-year-old boy with miliary spread mostly in the right lung. This asymmetrical involvement was due to obstructive emphysema with decreased perfusion of the left lung secondary to marked compression of the left bronchus by huge subcarinal and left hilar lymph nodes

lence of tuberculosis, with less than 300 reported cases (Asensi et al. 1990).

Transmission could occur transplacental, with the primary complex developing in the liver, with involvement of periportal lymph nodes and further dissemination to numerous organs. The hypoxic intra-uterus medium avoids the mycobacterium growing, with the lungs being latent until the delivery. As a result, children being infected during the pregnancy can be asymptomatic until 2–4 weeks after the delivery. Another way of transmission is the genital tract of the mother. During the delivery, mycobacterium can be swallowed, resulting in primary complex on the lungs, or the amniotic fluid ingestion could result in gastrointestinal primary complex (Machin et al. 1992)

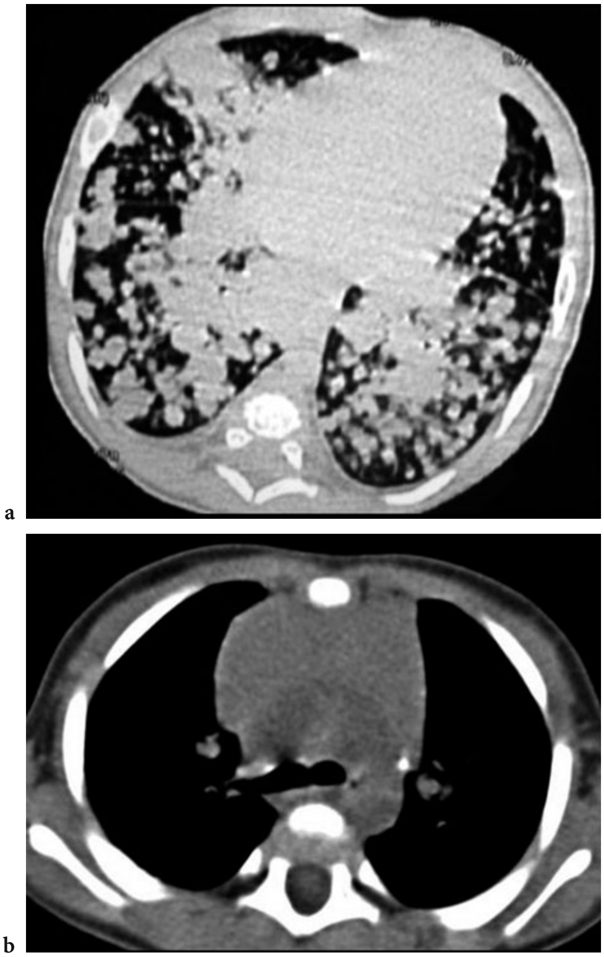

Fig. 7.18.a,b Unenhanced CT of a 2-month-old boy with broncogenic spread causing huge parenchymal opacities (**a**). Same patient, 3 months later, shows left hilar nodal calcification (**b**)

Early diagnosis requires high suspicious level (Myers et al. 1981; Souza et al. 2006). All the newborns with pneumonia unresponsive to the treatment, mostly those with mothers with history of tuberculosis and from endemic areas, should be considered at risk for CTb (Resinger et al. 1974). The maternal endometrial biopsy could improve the diagnostic accuracy of CTb. (Nemir and O’Hare 1985; Ravij et al. 2005).

The symptoms can be demonstrated at birth, but commonly occur during the 2nd and 4th weeks of life. The chest radiographs can be normal during the early infection. However, the lesions are usually progressive and present a miliary pattern. Parenchymal opacities and mediastinal lymph nodes enlargement may also be seen (Ray et al. 2002) (Fig. 7.18).

The diagnostic criteria for CTb were first proposed by Beitzke in 1935, and further modified by Cantwell and colleagues. They defined the diagnosis of CTb in the patients with at least one of the following: lesions during the first week of life, hepatic primary complex or hepatic granulomas (Fig. 7.18), confirmation of tuberculosis infection on the placenta or genital tract of the mother, and exclusion of post-natal transmission through investigation of contacts, including hospital staff (Cantwell et al. 1994).

The specific treatment for CTb should be immediately initiated in suspicious cases due to the risk of disease progression and death (Mazade et al. 2001; Souza et al. 2006; Welsoly et al. 2004).

7.5.11
Pleural and Pericardial Effusions

Tuberculous pleural effusion results from rupture of a subpleural lesion into the pleural space, spread from caseous lymph nodes or an adjacent spinal lesion (Hulnick et al. 1983). Tuberculous pleural effusion is infrequent in children under 6 years of age and rare in those under 2. The fluid is usually unilateral to the primary parenchymal lesion, but may occur in both pleural spaces with bilateral primary complexes and with miliary dissemination (Fig. 7.19) (Inselman 1996). However, in our experience pleural effusion is exceedingly rare in miliary tuberculosis. Even without treatment, the fluid usually resorbs without sequelae, but empyema can ensue.

Pericarditis and pericardial effusion are complications resulting from secondary extension of in-

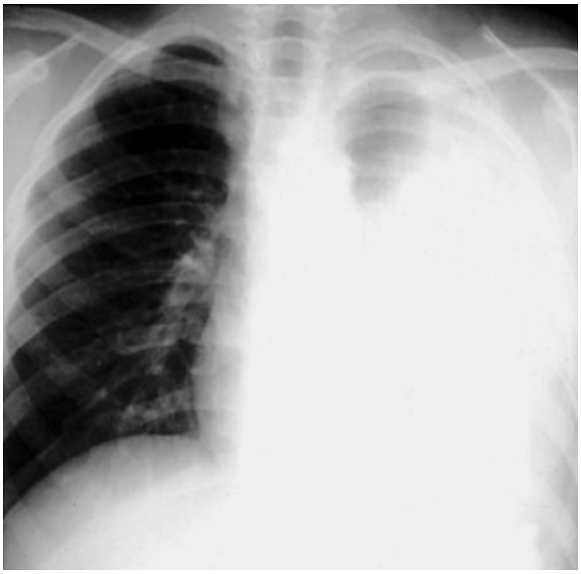

Fig. 7.19. A 14-year-old girl. Chest X-ray depicts unilateral pleural effusion. Pleural fluid culture yielded *M. tuberculosis*

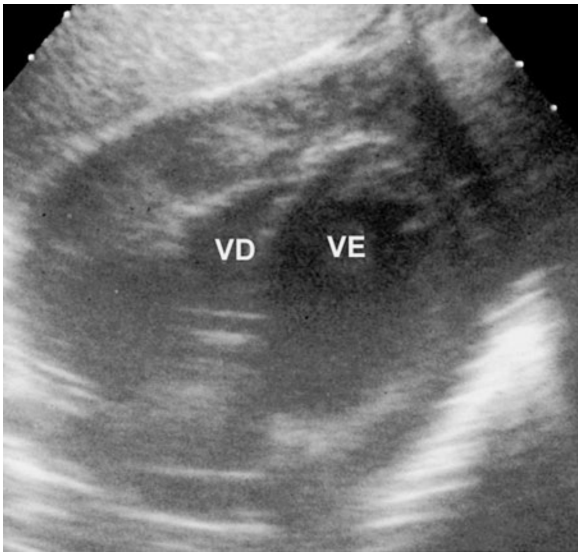

Fig. 7.20. Ultrasound of an 8-year-old boy shows pericardial effusion. *VD*, right ventricle; *VE*, left ventricle

fected peribronchial nodes to the pericardium. Ultrasound and CT are very useful in the diagnosis of pericardial tuberculous lesions (Fig. 7.20).

7.5.12
Unusual Presentations and Complications

Pneumothorax, hemothorax, and bronchopleural or bronchoesophageal fistulas are unusual complications of pulmonary tuberculosis. Aortic rupture, which can result from spread of lymph nodes into the vessel, is even rarer (Inselman 1996).

Tuberculosis infection of the endothoracic fascia is highly uncommon. It is a peripleuritis caused by peripleural Inflammation of the endothoracic fascia (Broglia et al. 2006).

The peripleura is a mass of lax cell tissue that supports the parietal pleura in areas corresponding to the chest wall, thorax vertex, and mediastinal-suprahilar region.

CT scan can show round images on the front, lateral, and back regions of the thorax, projecting toward the parietal pleura in the corresponding peripleura region (Fig. 7.21).

Rasmussen aneurysm is an exceedingly unusual complication of tuberculosis in children. It corresponds to a pseudoaneurysm caused by erosion of a peripheral pulmonary artery branch by an adjacent tuberculous cavity lesion. It is almost exclusively seen in advanced pulmonary cavitary forms of tuberculosis in adults and can occur despite adequate treatment. The typical Rasmussen aneurysm is a peripheral, solitary lesion in the upper lobes, but uncommon presentations can also be seen (Fig. 7.22).

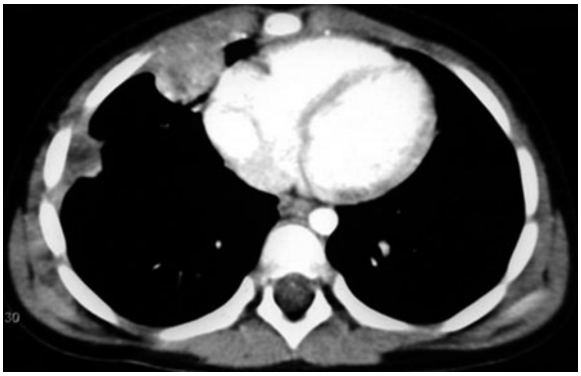

Fig. 7.21. Enhanced CT of a child showing frontal and lateral round images on the right chest wall, projecting toward the parietal pleura

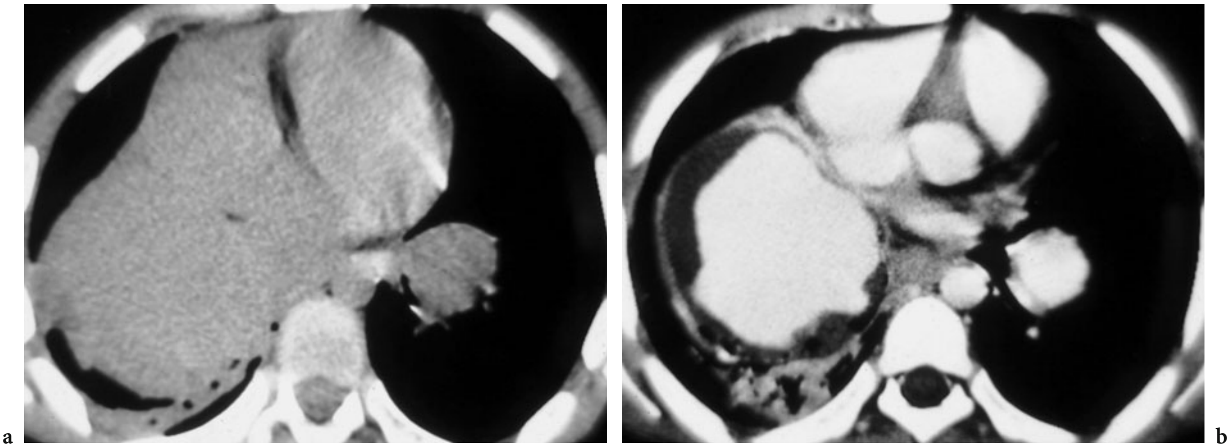

Fig. 7.22. a Unenhanced CT performed in an 11-year-old girl demonstrates extensive opacity in the right hemithorax and a small nodular lesion on the left. **b** Following contrast enhancement, opacification of a huge right pulmonary artery with parietal thrombosis can be seen. There is a smaller aneurysmal dilatation of the left pulmonary artery. The patient died 15 days later due to severe hemoptysis (Courtesy of Dr. Alexandre Kalil; Hospital São Rafael, Salvador, Brazil)

7.6
Conclusions

Diagnosis of pulmonary tuberculosis presents a continuing challenge to pediatricians and radiologists. Careful clinical history, tuberculin skin testing, and chest radiography remain the basic elements for establishing diagnosis. Chest US, MRI and particularly chest CT can provide information not available with conventional imaging, and thereby clarify diagnosis and influence therapy.

Acknowledgements. The authors thank Dr. Laurinda Higa and Dr. Selma Sias for their contribution to the clinical aspects of TB.

References

Asensi F, Otero MC, Perez-Tamarit D et al. (1990) Congenital tuberculosis, still a problem. Pediatr Infect Dis J 9:223–224

Bosch J, Serres X, Zuasnabar A et al. (2004) Comparison of ultrasound with plain radiography and CT for the detection of mediastinal lymphadenopathy in children with tuberculosis. Pediatr Radiol 34:895–900

Broglia B, Bisero E, Sclavo L, Andreozzi P (2006) Tuberculosis of the endothoracic fascia. Pediatr Pulmonol 41:441–444

Cantwell MF, Shehab ZM, Costello AM et al. (1994) Brief report: congenital tuberculosis. N Engl J Med 330:1051–1054

Costello AM, Rook G (1995) Tuberculosis in children. Curr Opin Pediatr 7:6–12

Cremin BJ, Jamieson DH (1995) Imaging of pulmonary tuberculosis. In: Cremin BJ, Jamieson DH (eds) Childhood tuberculosis: modern imaging and clinical concepts. Springer, Berlin Heidelberg New York, pp 19–50

Dannenberg AM Jr (1999) Pathophysiology: basis aspects. In: Schlossberg D (ed) Tuberculosis and nontuberculous mycobacterial infections, 4th edn. Saunders, Philadelphia, pp 17–47

Dutt AK, Stead WW (1999) Epidemiology and host factors. In: Schlossberg D (ed) Tuberculosis and nontuberculous mycobacterial infections, 4th edn. Saunders, Philadelphia, pp 3–16

Ehlers S (1999) Immunity to tuberculosis: a delicate balance between protection and pathology. FEMS Immun Med Microbiol 23:149–158

Hulnick DH, Naidich DP, McCauley DI (1983) Pleural tuberculosis evaluated by computed tomography. Radiology 149:759–765

Inselman LS (1996) Tuberculosis in children: an update. Pediatr Pulmonol 21:101–120

Kim WS, Moon WK, Kim IO et al. (1997) Pulmonary tuberculosis in children: evaluation with CT. AJR 168:1005–1009

Klein M, Iseman MD (1999) Mycobacterial infections. In: Taussig LM, Landau LI (eds) Pediatric respiratory medicine. Mosby, St Louis, pp 702–732

Machin GA, Honoré LH, Fanning EA, Molesky M (1992) Perinatally acquired neonatal tuberculosis: report of two cases. Pediatr Pathol 12:707–716

Maher D, Raviglione MC (1999) The global epidemic of tuberculosis: a World Health Organization Perspective. In: Schlossberg D (ed) Tuberculosis and nontuberculous mycobacterial infections, 4th edn. Saunders, Philadelphia, pp 104–115

Matsaniotis N, Kattamis C, Economou-Mavrou C et al. (1967) Bullous emphysema in childhood tuberculosis. J Pediatr 71:703–707

Mazade MA, Evans EM, Starke JR et al. (2001) Congenital tuberculosis presenting as sepsis syndrome: case and review of the literature. Pediatr Infect Dis J 20:439–442

Moulding T (1999) Pathogenesis, pathophysiology, and immunology: clinical orientations. In: Schlossberg D (ed) Tuberculosis and nontuberculous mycobacterial infections, 4th edn. Saunders, Philadelphia, pp 48–56

Myers JP, Perlstein PH, Light IJ, Towbin RB, Dincsoy HP, Dincsoy MY (1981) Tuberculosis in pregnancy with fatal congenital infection. Pediatrics 67:89–94

Nemir RL, O'Hare D (1985) Congenital tuberculosis. Review and diagnostic guidelines. Am J Dis Child 139:139–287

Oh YW, Kim YH, Lee NJ et al. (1994) High-resolution CT appearance of miliary tuberculosis. J Comput Assist Tomogr 18:862–866

Ravij K, Nomeeta G, Arvind S et al. (2005) Congenital tuberculosis. Indian J Pediatr 72:631–633

Ray M, Dixit A, Vaipei K et al. (2002) Congenital tuberculosis. Indian Pediatr 39:1167–1168

Resinger KS, Evans P, Yost G, Rogers KD (1974) Congenital tuberculosis: report of a case. Pediatrics 54:74–76

Schuit KE (1979) Miliary tuberculosis in children. Clinical and laboratory manifestations in 19 patients. Am J Dis Child 133:583–585

Souza ELS, Moreira LMO, Silva MF (2006) Perinatal tuberculosis: a diagnostic challenge. BJID 10:228–229

Stallworth JR, Brasfield DM, Tiller RE (1980) Congenital miliary tuberculosis proved by open lung biopsy specimen and successfully treated. Am J Dis Child 134:320–321

Starke JR (1999) Tuberculosis in infants and children. In: Schlossberg D (ed) Tuberculosis and nontuberculous mycobacterial infections, 4th edn. Saunders, Philadelphia, pp 303–324

Webb R, Muller N, Naidich D (1996) High resolution CT of the lung, 2nd edn. Lippincott-Raven, Philadelphia

Welsoly DL, Khan AM, Elidemir O et al. (2004) Congenital tuberculosis requiring extracorporeal membrane oxygenation. Pediatric Pulmonology 37:470–473

How to Perform and Interpret MR Sleep Studies for Obstructive Sleep Apnea in Children

8

Lane F. Donnelly

CONTENTS

8.1 **Background** *183*
8.2 **Clinical Indications** *184*
8.3 **Technique** *184*
8.3.1 Sedation *184*
8.3.2 MR Imaging Technique *185*
8.3.3 Special Technical Considerations *185*
8.3.4 Interpretation *186*
8.4 **Common Diagnoses** *187*
8.4.1 Enlarged Adenoid Tonsils *187*
8.4.2 Enlarged Palatine Tonsils *188*
8.4.3 Enlarged Lingual Tonsils *188*
8.4.4 Other Anatomic Causes of Obstruction *189*
8.4.4.1 Abnormality of the Soft Palate *189*
8.4.4.2 Tongue *190*
8.5 **Dynamic Motion Abnormalities** *190*
8.5.1 Glossoptosis *190*
8.5.2 Hypopharyngeal Collapse *192*
8.6 **Summary** *192*
References *192*

8.1 Background

It is estimated that up to 3% of all children are affected by obstructive sleep apnea (Donnelly 2005; Guilleminault et al. 1982; Ali et al. 1993, 1994; Owen et al. 1996; Rosen 1999; Owens et al. 1998). This common disorder is increasingly being associated with substantial morbidity. Obstructive sleep apnea has been shown to cause excessive daytime sleepiness, hyperactivity, attention deficit disorder, poor hearing, failure to thrive, and physical debilitation (Donnelly 2005; Guilleminault et al. 1982; Ali et al. 1993, 1994; Owen et al. 1996; Rosen 1999; Owens et al. 1998). Many of these morbidities such as hyperactivity and attention deficit disorder may greatly improve or resolve altogether with appropriate management of obstructive sleep apnea. In fact, many patients who are labeled with attention deficit disorder actually have underlying obstructive sleep apnea.

The majority of children with obstructive sleep apnea are actually otherwise healthy children with enlarged palatine and adenoid tonsils being the anatomic abnormality leading to obstructive sleep apnea (Donnelly 2005; Guilleminault et al. 1982; Ali et al. 1993, 1994; Owen et al. 1996; Rosen 1999; Owens et al. 1998). In these children, the role of imaging in their management is relatively limited. On physical examination, the palatine tonsils can be easily visualized. Many otolaryngologists and other physicians caring for these children will order lateral radiographs of the supraglottic airway in order to evaluate for the size of the adenoid tonsils. Typically no other imaging is needed in such children. There is a subgroup of such patients with obstructive sleep apnea who have more complex problems. This subgroup includes children with syndromes that predispose them to obstruction at multiple levels, such as Down syndrome or other syndromes associated with craniofacial abnormalities like micrognathia, and children who have undergone prior surgery directed at the elimination of obstructive sleep apnea but still have persistent obstructive sleep apnea despite that surgery (Donnelly 2005). In such patients, dynamic imaging such as MR sleep studies have been shown to affect management decisions in over 50% of cases (Donnelly 2005; Gibson et al.

L. F. Donnelly, MD
Radiologist-in-Chief, Department of Radiology, Cincinnati Children's Hospital Medical Center MLC 5031, Professor of Radiology and Pediatrics, University of Cincinnati, College of Medicine, 3333 Burnet Avenue, Cincinnati, OH 45229-3039, USA

1996; Shott and Donnelly 2004). Such studies can be used to direct conservative or surgical management of the patients (Donnelly 2005; Gibson et al. 1996; Shott and Donnelly 2004; Donnelly 2004). Some of these patients will have multiple causes of persistent obstructive sleep apnea and multiple surgeries can be performed under one general anesthesia. Studies have shown that the success rates in dealing with obstructive sleep apnea are increased when such data is utilized in management decisions (Gibson et al. 1996; Shott and Donnelly 2004).

There is a long history of utilization of dynamic imaging studies for the evaluation of obstructive sleep apnea in such children at Cincinnati Children's Hospital Medical Center (Donnelly 2005; Gibson et al. 1996; Shott and Donnelly 2004; Fricke et al. 2006; Kalra et al. 2006; Abbott et al. 2006; Donnelly et al. 2000a,b, 2001a,b, 2002a,b, 2003, 2004; Abbott et al. 2003). In the 1980s and 1990s fluoroscopic sleep studies were utilized to evaluate such children. These efforts were primarily pioneered by Janet L. Strife MD. In such cases, the child was sedated and imaged with lateral fluoroscopy in an interventional radiology suite during times of oxygen desaturation. Both dynamic and anatomic issues related to the airway could then be evaluated. In 1999, gradient echo techniques were utilized in MRI to create cine images to evaluate the airway. At first, this was used as a research tool to identify how much motion should be considered normal, studying patients sedated for neurologic MRI studies unrelated to the airway. It became apparent that the tool could be utilized on a clinical basis and a protocol for MR sleep studies was created and began to be used clinically in 2001. By 2003, the examination was considered a routine schedulable exam on the clinical service. Currently, we do more than 200 of these such studies per year.

The purpose of this chapter will be to review issues related to the technique and interpretation of MR sleep studies.

8.2
Clinical Indications

MR sleep studies are performed for a very small fraction of the total number of children with obstructive sleep apnea. Again, most children with obstructive sleep apnea are otherwise normal healthy children with enlarged adenoid and palatine tonsils. MR sleep studies do not play a role in such children. However, there is a group of children with more complex problems related to predisposition to obstruction at multiple sites, craniofacial abnormalities, other syndromes, decreased muscular tone, or prior surgery with recurring and persistent obstructive sleep apnea (Donnelly 2005). It is this group of patients who most benefit from the information obtained at MR sleep studies.

At our institution, the following indications are utilized for MR sleep studies:

- A persistent obstructive sleep apnea despite previous surgery (most commonly previous tonsillectomy and adenoidectomy)
- Predisposition to multi-level obstruction (most commonly in patients with Down syndrome)
- Evaluation of patients prior to complex airway surgery
- Obstructive sleep apnea in severe obesity
- Children with difficulty in tracheotomy decannulation and symptoms of obstructive sleep apnea

All patients being considered for evaluation with MR sleep studies are required to have documentation of obstructive sleep apnea based on the results of overnight polysomnography.

8.3
Technique

8.3.1
Sedation

Since symptoms of obstructive sleep apnea in children only occur during sleep, children must either be asleep or sedated for MR sleep study evaluation. Due to the impracticality of having children be able to fall asleep during the assigned slot of a busy MRI schedule as well as the fact that the gradient echo image sequences create a great deal of noise and typically awake a sleeping child, we have found that scanning children during natural sleep is impractical. We perform our MR sleep studies under sedation. There is some argument that the degree of decreased muscular tone associated with natural sleep and with sedation are not exactly the same. However, it is our belief that they are similar enough such that the motion and anatomic abnormalities depicted under sedation are predictive of the similar occurrences when the patient is under natural sleep. We have been making surgical decisions based on this information for multiple decades with success.

The sedation program for MR sleep studies has been in a state of evolution over the past several decades. Initially, sedation was managed by the radiologist and the most common drug of choice was nembutal (Donnelly et al. 2001b). Currently, all MR sleep studies at our institution are performed under sedation administered by anesthesiology (Donnelly 2005), and propofol is the most common anesthetic agent utilized. When starting an MR sleep program, one of the cultural hurdles that needs to be overcome is the concept of sedating a child without a protected airway when the child has an underlying problem with that airway. Although the safety of such practice has been questioned, there are several articles that demonstrate outstanding safety records when the studies are performed to protocol and in the hands of experienced sedation facilities (Donnelly et al. 2001b).

8.3.2
MR Imaging Technique

We perform our MR sleep studies on one of a number of 1.5 Tesla MR units. The patient is positioned such that the supraglottic airway is focused on. The field of view should include from the level of the superior aspect of the nasopharynx to at least the level of the mid trachea. In smaller patients, often the entire airway to the level of the carina can be visualized. Once the patient is under sedation and asleep, they are placed either in a head-and-neck vascular coil or head coil depending on the MR imaging system. The patient is optimally placed with the cervical spine in neutral position.

Imaging sequences include stand T1-weighted images, T2-weighted images, and a gradient echo sequence utilized to create cine images (Donnelly 2005). The T1-weighted images are utilized primarily to demonstrate anatomic detail. The T2-weighted images are ideal for demonstrating the tonsils as high signal in contrast to a low signal background. The gradient echo cine images are utilized to demonstrate the motion of the airway during sleep. The most ideal planes of imaging are the sagittal and transverse planes.

Specifically, our imaging procedure includes:

- Sagittal and transverse T1-weighted spin-echo sequences
- Transverse and sagittal T2-weighted fast-spin-echo inversion recovery (FSEIR) images
- Gradient echo cine images in the sagittal midline and in the transverse plane at the level of the mid portion of the tongue from the superior to inferior aspect (between the inferior aspect of the soft palate and the superior tip of the epiglottis)

The fast gradient echo sequence utilized to create the cine images includes the following parameters: 82,000/3600, 80° flip angle, 12 mm slice thickness. Approximately 128 consecutive images are obtained in the same anatomic location during an imaging time of approximately 2 min. Therefore, each image correlates with approximately 1 s. The images are then displaced in cine format and create a real-time “movie” of airway motion.

8.3.3
Special Technical Considerations

Dental braces are made of variable substances and the degree of MR artifact caused by dental braces has wide variability (Donnelly 2005). With some dental braces, the artifact can obscure the region of interest within the oropharynx, nasopharynx, and hypopharynx. The presence of dental braces should be identified and evaluated before the patient is sedated for the procedure. If the child is of age and mentation to be able to cooperate with imaging without sedation, before sedation is induced, we will typically place that patient in the scanner and perform a test imaging sequence to evaluate the extent of MR artifact (Donnelly 2005). If the artifact is minimal, we will then sedate the patient and proceed with the MR examination. If the artifact from dental braces obscures the region of interest, the referring physician and family have the option of having the dental braces removed and the study being rescheduled for a time to be performed without the dental braces in place.

Another specific circumstance to beware of is the case in which the patient has obstructive sleep apnea that is so severe that anesthesiology has difficulty achieving a state in which the patient is both adequately asleep and is able to maintain adequate oxygenation without the presence of an artificial airway. This occurs in the minority of patients. We have adopted the following strategy in such patients:

a nasal trumpet is placed such that it bypasses obstruction at the level of the nasopharynx and hypopharynx (Donnelly 2005). Since the causes of obstructive sleep apnea in these patients are typically at that level, the nasal trumpet will almost always stabilize the patient. We then perform the static T1 and T2-weighted imaging with the nasal trumpet in place. After completion of these sequences, the nasal trumpet is removed, if possible, and then the cine images are obtained in the sagittal and axial plane as quickly as possible without the nasal trumpet in place. In the overwhelming majority of cases, by this time during the sedation process, the patient will tolerate a period of time long enough to be able achieve both these two cine imaging sequences.

There are several other technical issues of which to be aware. In patients with severe obstructive sleep apnea, the head and mandible tend to bob up and down during sleep. Therefore, in cases with severe obstructive sleep apnea, there is more motion artifact than is typically encountered in patients without obstructive sleep apnea (Donnelly 2005). Despite this additional artifact, the pertinent information can almost always be obtained.

Another technical issue which often arises particularly when institutions are initiating an MR sleep sequence are questions related to the anatomic positioning of the imaging sequences. Since the FSEIR images are obtained to evaluate the tonsillar tissue, it is important for these imaging sequences to cover the area of the adenoid, palatine, and lingual tonsils but not lower than the level of the inferior aspect of the lingual tonsils. Therefore, these images should be obtained from the superior aspect of the nasopharynx to the inferior aspect of the base of the tongue. The T1-weighted axial images are obtained to evaluate anatomy. Therefore, these should be obtained from the level of the superior aspect of the nasopharynx to the most inferior aspect possible given coil limitations. There is also a tendency to place the level of the transverse cine image either too low or too high. Again, this should be placed at the mid-level of the tongue inferior to the inferior tip of the soft palate and superior to the superior aspect of the epiglottis (Donnelly 2005).

8.3.4
Interpretation

One aspect that is paramount to appropriate interpretation of these studies is utilizing definitions and terms for anatomy which optimizes communication between the radiologist and referring physicians. As with all complex anatomic regions, there are various grouping of anatomic definitions and terms. Although which system of naming is chosen is not written in stone, an understanding of what exactly the terminology refers to is important for communication. The definitions which we use differ somewhat anatomically from those often shown in traditional anatomy textbooks (Donnelly 2005). The terms lend themselves to distinguishing anatomic areas where causes of obstructive sleep apnea commonly occur. The nasopharynx is defined as the portion of the airway bordered by the soft palate anteriorly, the nasal trumpets anteriorly and superiorly, and adenoids posteriorly and superiorly (Donnelly 2005). The inferior border is at the level of the inferior tip of the uvula. The oral cavity is defined as the aerated space between the hard palate superiorly, the tongue inferiorly, and the soft palate posteriorly (Donnelly 2005). In normal sleeping children, the oral cavity is collapsed and the mouth is closed. The aerated space bordered by the posterior aspect of the tongue anteriorly, the posterior pharyngeal wall posteriorly, and the inferior aspect of the soft palate anteriorly is referred to as either the hypopharynx or the retroglossal pharynx (Donnelly 2005). Note that in traditional anatomic descriptions this area is often referred to as the oropharynx. In the healthy sleeping child, the naso- and hypopharynx are always patent and demonstrate very minimal motion of the airway walls (less than 2 mm) (Donnelly 2003; Donnelly et al. 2002b). When interpreting the MR sleep studies, the cine images are utilized to evaluate for abnormal patterns of motion of the walls of the airway or, in other words, abnormal patterns of collapse of the airway. In the normal healthy sleeping child, the caliber of the airway in the nasopharynx and hypopharynx changes only minimally with respiration. These changes should be less than several millimeters with respiration. Any motion greater than 5 mm should certainly be considered abnormal (Donnelly 2003; Donnelly et al. 2002b). Intermittent collapse of the nasopharynx or hypopharynx is not encountered in normal patients and indicates pathologic obstructive sleep apnea. The T1-weighted images are utilized to evaluate the anatomy of the structures surrounding the airway for pathologic enlargement. The FSEIR images are particularly well suited to demonstrate enlargement of the tonsillar tissue as the tonsils appear as high signal intensity compared with the low signal intensity background tissues.

8.4
Common Diagnoses

8.4.1
Enlarged Adenoid Tonsils

One of the more common causes of obstructive sleep apnea in children is enlargement of the adenoid tonsils. The adenoid tonsils are typically absent at birth and then rapidly proliferate during infancy (Vogler et al. 2000; Jaw et al. 1999). They reach their maximum size sometime between 2 and 10 years of age and then during the second decade of life begin to progressively decrease in size (Vogler et al. 2000; Jaw et al. 1999). The adenoid tonsils are measured in the midline sagittal plane. The maximal diameter is measured at the level of the maximal convexity in the plane perpendicular to the anterior clival surface (Donnelly 2005; Vogler et al. 2000; Jaw et al. 1999). There is much debate about what number is the upper limit of normal size for the adenoid tonsils. This is depicted in the literature anywhere between 7 and 15 mm (Vogler et al. 2000; Jaw et al. 1999). Certainly, there are children with adenoid tonsils larger than 12 mm that do not demonstrate symptoms of obstructive sleep apnea. If you pay attention to the region of the adenoid tonsils on cervical spine films obtained for trauma, the variability of the adenoid tonsils is great. On MR sleep studies, we consider adenoids to be abnormally enlarged when they are greater than 12 mm in size and associated with intermittent collapse of the posterior nasal pharynx on cine MR images (Fig. 8.1). Most children with obstructive sleep apnea who reach the level of having an MR sleep study have already had their adenoid tonsils removed. Recurrence and enlargement of the adenoid tonsils is a very common cause of recurrent or persistent obstructive sleep apnea despite previous tonsillectomy and adenoidectomy (Donnelly 2005; Shott and Donnelly 2004; Donnelly et al. 2004). This is in part related to the fact that the adenoid tonsils are not a well encapsulated area of tonsillar tissue and there is often tonsillar tissue left in the lateral aspects of the posterior nasal pharynx after adenoidectomy. This tissue often grows back and can cause recurrent symptoms. Related to this, the residual amount of tissue in cases of previous adenoidectomy tends to appear with a wedge-like central defect on transverse images (Donnelly 2005) (Fig. 8.2). The tonsillar tissue begins to grow from the lateral recesses and then encroach upon the nasopharynx centrally.

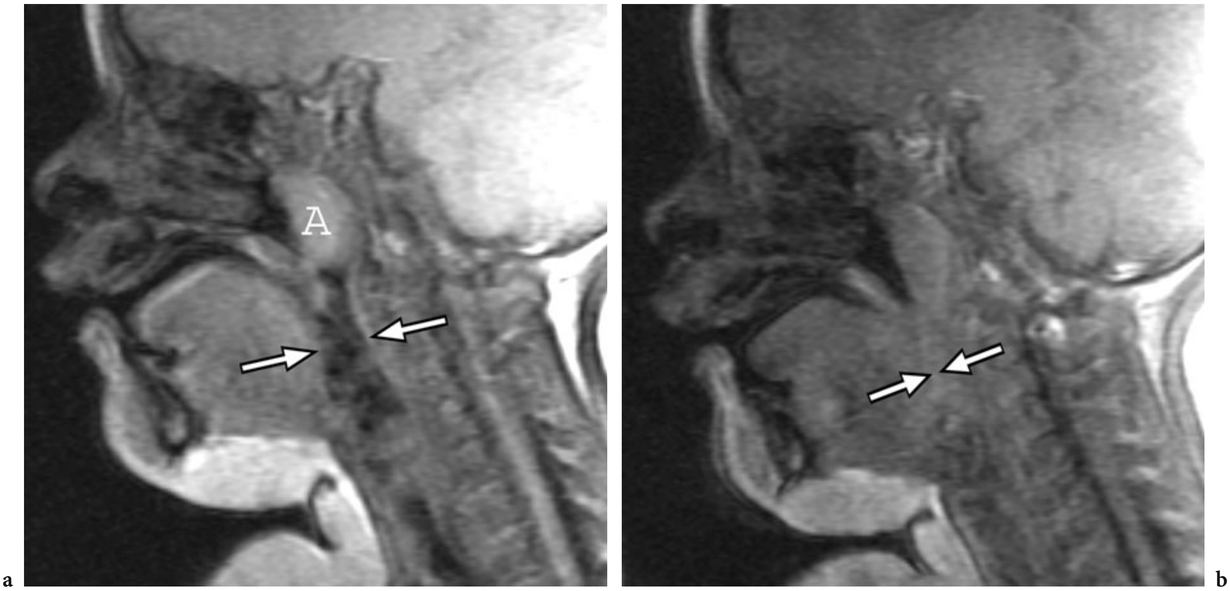

Fig. 8.1a,b. Recurrent and enlarged adenoid tonsils with associated hypopharyngeal collapse. **a** Sagittal cine image at time airway is open shows open retroglossal airway (*arrows*). Note enlarged adenoid tonsils (*A*). **b** Sagittal cine image at time airway is closed shows complete collapse of retroglossal airway (*arrows*)

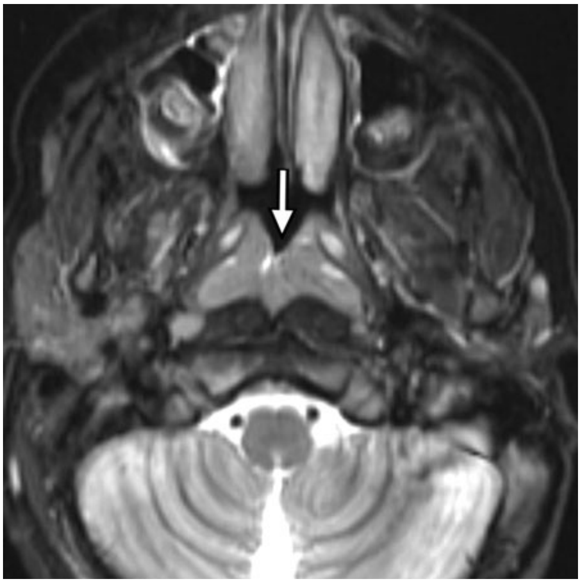

Fig. 8.2. Recurrent and enlarged adenoid tonsils shown on axial FSEIR MR image. Note wedge-shaped central defect (*arrow*) in adenoid tonsil, typical of postoperative appearance

8.4.2
Enlarged Palatine Tonsils

While enlargement of the palatine tonsils is a common anatomic cause of obstructive sleep apnea in the general pediatric population, large palatine tonsils are rarely seen on MR sleep studies. This is because again most patients that reach the point of having an MR sleep study have already had tonsillectomy. Unlike the adenoid tonsils which commonly recur, recurrence and enlargement of the palatine tonsils post tonsillectomy is almost unheard of (Donnelly 2005). I have never seen such a case. The palatine tonsils are well encapsulated and typically removed in their entirety during surgery. When palatine tonsils are encountered at MRI, they appear as round, well-defined masses of high signal intensity on T2-weighted images and are positioned with the palatine fossa (Fig. 8.3). There are no well established criteria for the size at which the palatine should be considered enlarged at imaging. However, if the palatine tonsils are seen as prominent structures and are associated with inferior and central motion on cine images leading to intermittent obstruction of the hypopharynx, they should be considered abnormally enlarged (Donnelly 2005).

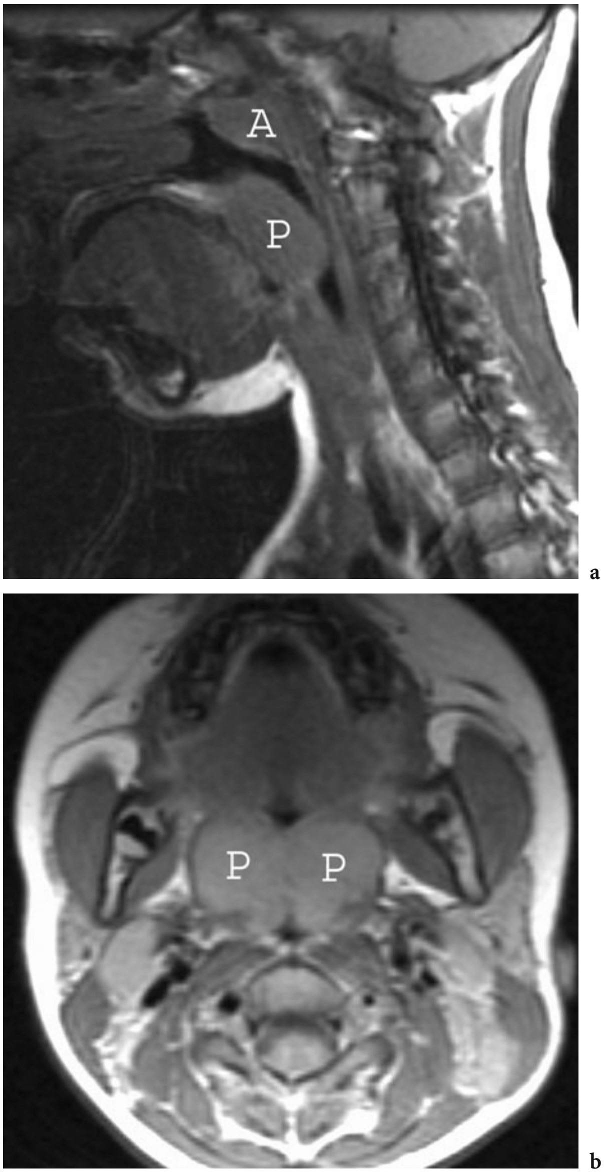

Fig. 8.3a,b. Massively enlarged "kissing" bilateral palatine tonsils. **a** Sagittal T1-weighted image shows markedly enlarged palatine tonsils (*P*) and enlarged adenoid tonsils (*A*). **b** Axial proton-density image shows bilateral markedly enlarged palatine tonsils (*P*) touching in the midline and obstructing airway – so called "kissing" tonsils

8.4.3
Enlarged Lingual Tonsils

Enlargement of the lingual tonsils was previously thought to be a rare cause of obstructive sleep apnea and only had been reported in a handful of cases. In our experience, enlargement of the lingual tonsils is a much more common cause of recurrent obstructive sleep apnea than was previously recognized (Donnelly 2005; Donnelly et al. 2004; Fricke et al. 2006). Particularly in patients with Down syndrome or underlying obesity who have had previous tonsillectomy and adenoidectomy, enlargement of the lingual tonsils is not an uncommon cause of obstructive sleep apnea (Shott and Donnelly 2004; Donnelly et al. 2004). In a series of patients with Down syndrome and previous tonsillectomy and adenoidectomy, enlargement of the lingual tonsils was the cause of recurrent obstructive sleep apnea in 17% of such cases (Donnelly 2004). On imaging, normal lingual tonsils are often not even visible in children but when visualized appear as bilateral small crescentic areas of high signal intensity on T2-weighted images adjacent to the posterior or inferior lateral aspects of the tongue (Fricke et al. 2006). Abnormally enlarged lingual tonsils appear as large masses arising posteriorly at the level of the base of the tongue with high signal in FSEIR images (Donnelly 2005; Shott and Donnelly 2004; Donnelly et al. 2004; Fricke et al. 2006) (Fig. 8.4). Often the two lingual tonsils will grow together and appear like a dumbbell-shaped mass filling and obstructing the level of the hypopharynx. Lingual tonsils may also grow superiorly into the region of the palatine tonsillar fossa. Care must be taken in patients status post tonsillectomy not to mistake lingual tonsils grown up into this region as palatine tonsils. It is important to identify lingual tonsils as a cause of persistent obstructive sleep apnea as this is a very surgically treatable condition (Donnelly 2005; Shott and Donnelly 2004; Donnelly et al. 2004). Also it is worth noting that although it would seem that identification of the lingual tonsils at the posterior aspect of the tongue as being enlarged on physical examination would be easy, this is not the case. Special maneuvers must be performed in order to visualize the lingual tonsils on physical examination. This is one of the reasons why this cause of obstructive sleep apnea has previously gone underrecognized.

8.4.4
Other Anatomic Causes of Obstruction

8.4.4.1
Abnormality of the Soft Palate

An abnormally elongated or thickened soft palate has been reported as a contributing factor in the development of obstructive sleep apnea (Donnelly 2005). Uvulopalatopharyngoplasty or surgical reduction of the size of the soft palate has been shown

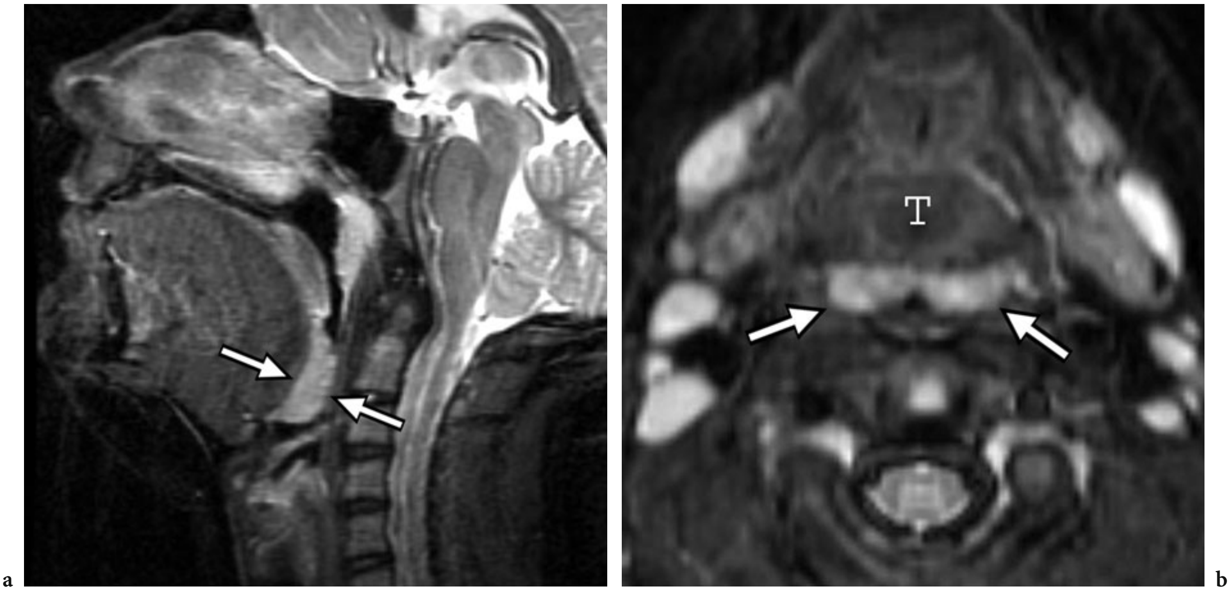

Fig. 8.4a,b. Enlarged lingual tonsils. **a** Sagittal FSEIR image shows enlarged lingual tonsils (*arrows*) completely obstructing the retroglossal pharynx. **b** Axial FSEIR shows enlarged bilateral lingual tonsils (*arrows*) as dumbbell-shaped area of high signal intensity posterior to tongue (*T*)

to be one way to improve the symptoms of patients with obstructive sleep apnea in a prominent soft palate. There are no well established guidelines regarding imaging criteria for when a soft palate should be considered abnormally prominent. Criteria that we have found helpful include the soft palate draping over and abutting the tongue and the inferior aspect of the soft palate extending inferiorly below the mid portion of the tongue (Fig. 8.5). When these anatomic findings are associated with intermittent collapse of the nasopharynx on cine images, we consider the soft palate abnormally prominent (Donnelly 2005).

Another imaging finding related to the soft palate is the presence of abnormal increased T2-weighted signal throughout the soft palate (Donnelly 2005) (Fig. 8.5). This finding is thought to be the correlation of the "woody" or edematous soft palate seen often in patients with obstructive sleep apnea on physical examination. The imaging findings are thought to correlate with the edema related to recurrent microtrauma from snoring. Normal soft palates have low signal intensity similar to that of the tongue musculature (Donnelly 2005). We speculate that with increased trauma and edema, the signal intensity of the soft palate becomes abnormally increased. The presence of an edematous soft palate at imaging is an indication of severe obstructive sleep apnea. In addition, an enlarging more edematous soft palate may also play a role in further exacerbating sleep apnea by becoming a space occupying process.

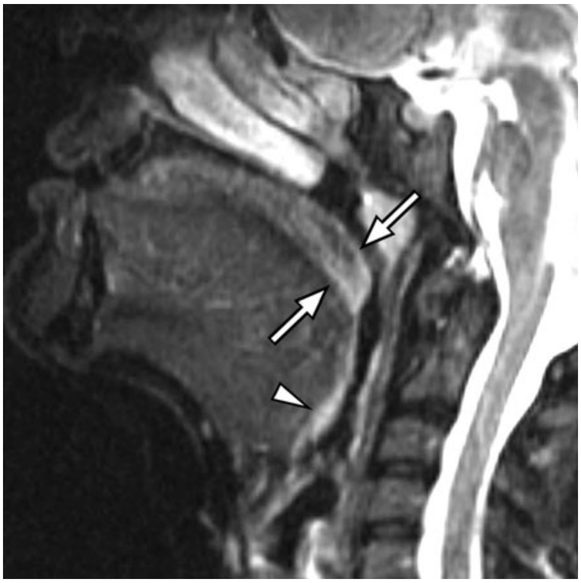

Fig. 8.5. Prominence and increased signal intensity of soft palate. Soft palate (*arrows*) is of increased signal intensity as compared to tongue musculature. Note crescentic high signal of non-enlarged palatine tonsil

8.4.4.2
Tongue

Abnormal enlargement of the tongue, or macroglossia, can be seen as a cause of obstructive sleep apnea (Donnelly 2005; Donnelly et al. 2000a,b). An enlarged tongue may encroach upon the posterior hypopharynx to the degree that it compromises respiratory flow. This is most commonly seen in patients with Down syndrome who have an enlarged tongue relative to the size of their oral cavity (Fig. 8.6). There is no quantitative imaging criteria for macroglossia. The imaging diagnosis is usually made subjectively at imaging. In addition to macroglossia, other abnormalities of the tongue often seen in Down syndrome include fatty infiltration, which appears as high signal intensity within the substance of the tongue on T1-weighted images (Donnelly et al. 2004). Patients with Down syndrome often also lack a normal median sulcus, instead demonstrating a bulbous appearing rounded posterior aspect of the tongue on axial images (Donnelly et al. 2004).

8.5
Dynamic Motion Abnormalities

8.5.1
Glossoptosis

Glossoptosis is defined as posterior motion of the tongue during sleep (Shott and Donnelly 2004; Donnelly et al. 2000a,b, 2004). The posterior aspect of the tongue moves posteriorly, such that it intermittently abuts the posterior wall of the hypopharynx leading to obstruction of the airway at this level (Fig. 8.7). This phenomenon occurs in patients with macroglossia, macrognathia, or decreased muscular tone. As Down syndrome patients have all three of these conditions, they are particularly predisposed to glossoptosis. On cine MR images, the tongue is seen moving intermittently posteriorly, obstructing the hypopharynx (Donnelly 2005). The tongue may also displace the soft palate posteriorly in addition causing intermittent obstruction of the nasopharynx.

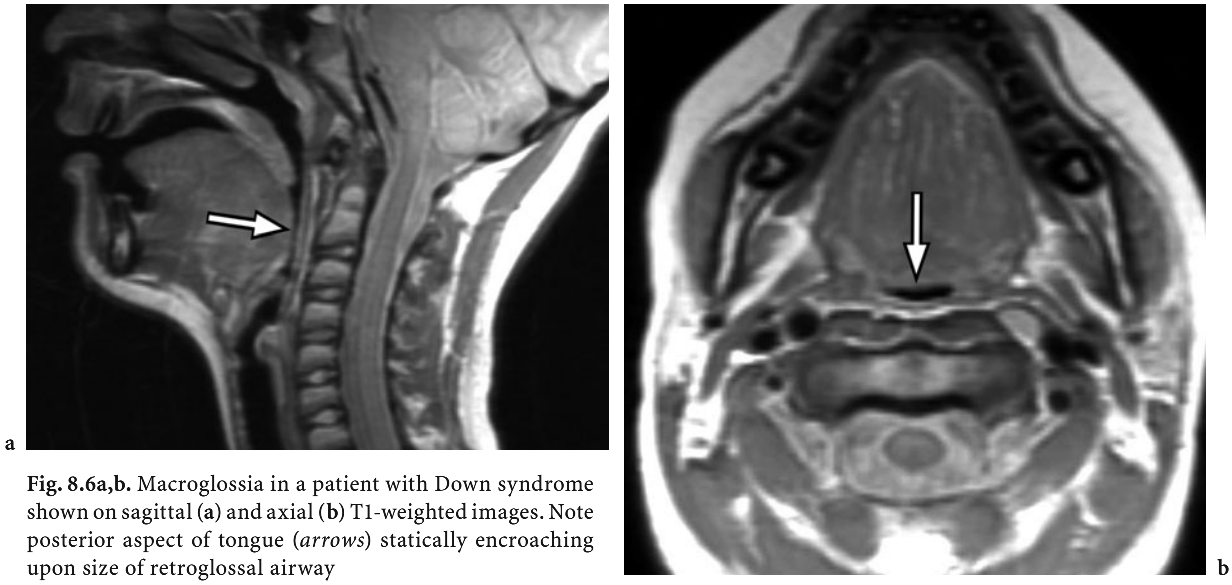

Fig. 8.6a,b. Macroglossia in a patient with Down syndrome shown on sagittal (**a**) and axial (**b**) T1-weighted images. Note posterior aspect of tongue (*arrows*) statically encroaching upon size of retroglossal airway

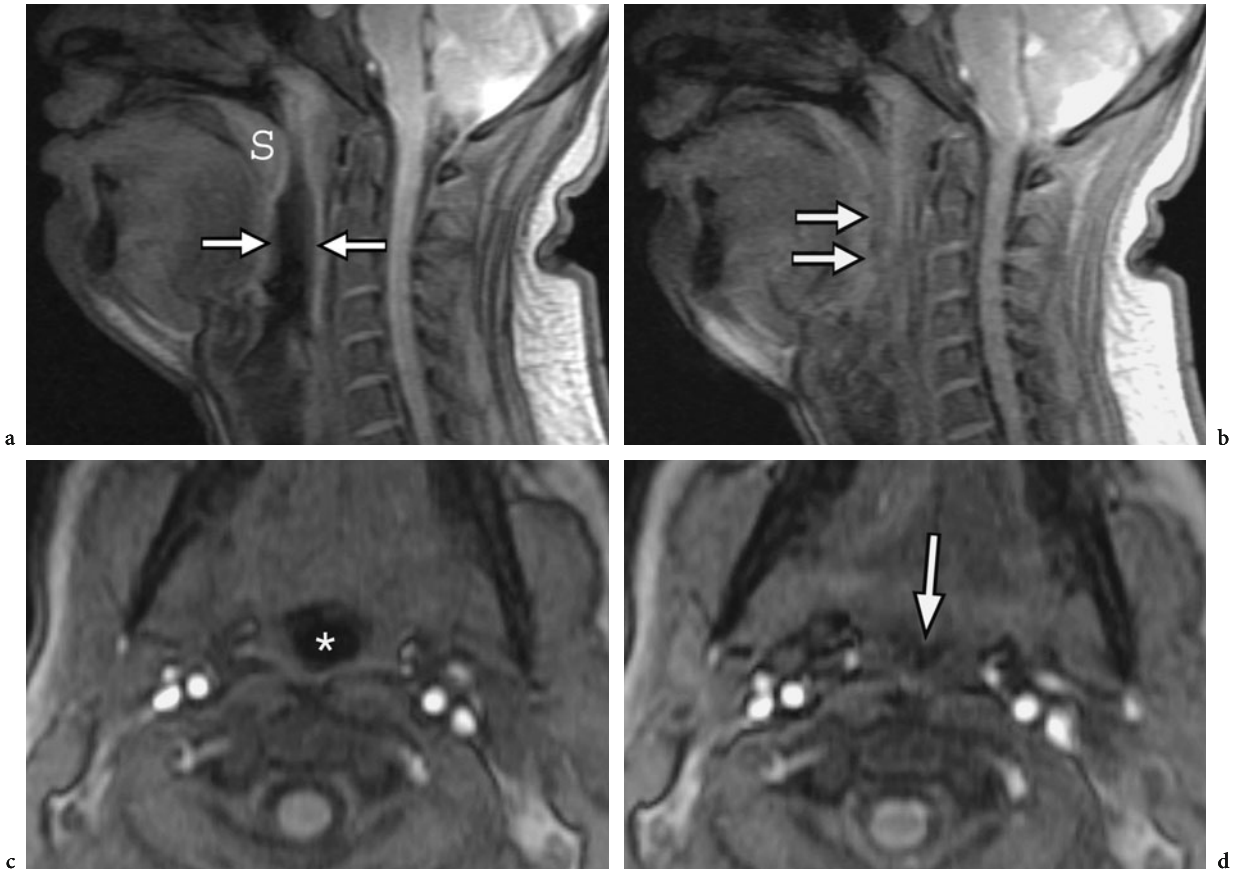

Fig. 8.7a–d. Glossoptosis. **a** Sagittal cine image at time when airway is patent. Note aerated retroglossal airway (*arrows*). Also note prominent soft palate (*S*). **b** Sagittal cine image at time when airway is obstructed. Note tongue has moved posteriorly (*arrows*) such that the posterior aspect of tongue abuts both soft palate and posterior pharyngeal wall leading to airway obstruction. **c** Axial cine image at time when airway is patent. Note aerated retroglossal airway (*). **d** Axial cine image at time when airway is obstructed. Note tongue has moved posteriorly (*arrow*) such that the posterior aspect of tongue abuts posterior pharyngeal wall leading to airway obstruction

8.5.2
Hypopharyngeal Collapse

Hypopharyngeal collapse can occur as a primary phenomenon related to decreased muscular tone (increased elasticity of the hypopharyngeal walls) or as a secondary problem related to obstruction in a more superior part of the airway, resulting in increased negative pressure and hypopharyngeal collapse (Donnelly 2005). This most commonly is seen in obstruction of the nasopharynx related to enlarged adenoid tonsils with secondary collapse of the hypopharynx (Fig. 8.8). On cine images, there is intermittent cylindrical narrowing of the hypopharynx (Donnelly 2005). In other words, all of the walls including the posterior, anterior, and left and right lateral walls of the hypopharynx move in a cylindrical fashion and meet centrally and obstruct the hypopharynx. This is in contrast to the isolated posterior motion of the posterior aspect of the tongue seen in glossoptosis. The differentiation between glossoptosis and hypopharyngeal collapse can be most easily characterized on the axial cine images at the level of the mid portion of the tongue (Donnelly 2005). It is important to different true glossoptosis from hypopharyngeal collapse because the surgical techniques and options for therapy are very different for the two conditions.

8.6
Summary

MR sleep studies have been shown to be a means of obtaining useful information in the management of children with complicated obstructive sleep apnea. Information regarding anatomic and dynamic causes of obstructive sleep apnea can be obtained. Such information has been shown to be helpful in making decisions about both conservative and surgical management of these patients. This is particularly true in patients who have more than one anatomic or dynamic problem contributing to obstructive sleep apnea, as multiple surgical procedures can be planned for a single anesthesia.

References

Abbott MB, Dardzinski BJ, Donnelly LF (2003) Using volume segmentation of cine MR data to evaluate dynamic motion of the airway in pediatric patients. AJR Am J Roentgenol 181:857–859

Abbott MB, Donnelly LF, Dardzinski BJ, Poe SA, Chini BA, Amin RS (2004) Obstructive sleep apnea: MR imaging volume segmentation analysis. Radiology 232:889–895

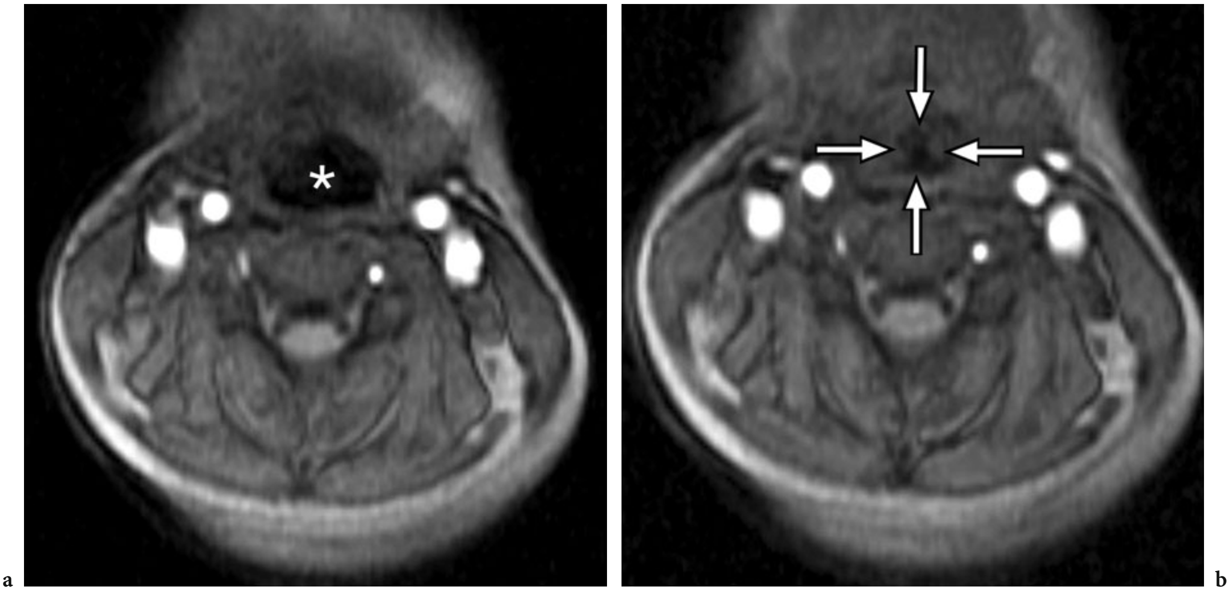

Fig. 8.8a,b. Hypopharyngeal collapse. **a** Axial cine image at time airway is open shows open retroglossal airway (*arrows*). **b** Axial cine image at time airway is closed shows complete collapse of retroglossal airway (*arrows*). Note that lateral left and right, anterior, and posterior walls all move cylindrically to the center of airway, in contrast to tongue moving posteriorly as seen with glossoptosis

Ali NJ, Pitson DJ, Stradling JR (1993) Snoring, sleep disturbance, and behavior in 4–5 year olds. Arch Dis Child 68:360–366

Ali NJ, Pitson DJ, Stradling JR (1994) Natural history of snoring and related behavior problems between the ages of 4 and 7 years. Arch Dis Children 71:74–76

Donnelly LF (2005) How I do it. Obstructive sleep apnea in pediatric patients: evaluation with cine MR sleep studies. Radiology 236:768–778

Donnelly LF, Jones BV, Strife JL (2000a) Imaging of pediatric tongue abnormalities. AJR Am J Roentgenol 175:489–493

Donnelly LF, Strife JL, Myer CM (2000b) Glossoptosis (posterior displacement of the tongue) during sleep: a frequent cause of sleep apnea in pediatric patients referred for dynamic sleep fluoroscopy. AJR Am J Roentgenol 175:1557–1559

Donnelly LF, Strife JL, Myer CM (2001a) Dynamic sleep fluoroscopy in children with obstructive sleep apnea. Appl Radiol 30:30–34

Donnelly LF, Strife JL, Myer CM III (2001b) Is sedation safe during dynamic sleep fluoroscopy of children with obstructive sleep apnea? AJR Am J Roentgenol 177:1031–1034

Donnelly LF, Casper KA, Chen B (2002a) Correlation on cine MR imaging of size of adenoid and palatine tonsils with degree of upper airway motion in asymptomatic sedated children. AJR Am J Roentgenol 179:503–508

Donnelly LF, Casper KA, Chen B, Koch BL (2002b) Defining normal upper airway motion in asymptomatic children during sleep by means of cine MR techniques. Radiology 223:176–180

Donnelly LF, Surdulescu V, Chini BA, Casper KA, Poe SA, Amin RS (2003) Upper airway motion depicted at cine MR imaging performed during sleep: comparison between young patients with and those without obstructive sleep apnea. Radiology 227:239–245

Donnelly LF, Shott SR, LaRose CR, Chini BA, Amin RS (2004) Causes of persistent obstructive sleep apnea despite previous tonsillectomy and adenoidectomy in children with trisomy 21 as depicted on MR cine studies. AJR Am J Roentgenol 183:175–181

Fricke BL, Donnelly LF, Shott SR, Kalra M, Poe SA, Chini BA, Amin RS (2006) Comparison of lingual tonsil size as depicted on MR imaging between children with obstructive sleep apnea despite previous tonsillectomy and adenoidectomy and normal controls. Pediatr Radiol 36:518–523

Gibson SE, Myer CM III, Strife JL, O'Connor DM (1996) Sleep fluoroscopy for localization of upper airway obstruction in children. Ann Otol Rhinol Laryngol 105:678–683

Guilleminault C, Winkle R, Korobkin R et al. (1982) Children and nocturnal snoring: evaluation of the effects on sleep related respiratory resistive load and daytime functioning. Eur J Pediatr 139:165–171

Jaw TS, Sheu RS, Liu GC, Lin WC (1999) Development of adenoids: a study by measurement with MR images. Kaohsiung J Med Sci 15:12–18

Kalra M, Donnelly LF, McConnell K, O' Brien KJ, Sandhu J, Johnson J, Amin RS (2006) Determination of respiratory phase during acquisition of airway cine MR images. Pediatr Radiol 36:965–969

Owen GO, Canter RJ, Robinson A (1996) Snoring, apnea, and ENT symptoms in the paediatric community. Clin Otolaryngol 21:130–134

Owens J, Opipari L, Nobile C, Spirito A (1998) Sleep and daytime behavior in children with obstructive sleep apnea and behavioral sleep disorders. Pediatrics 102:1178–1184

Rosen CL (1999) Clinical features of obstructive sleep apnea hypoventilation syndrome in otherwise healthy children. Pediatr Pulmonol 27:403–409

Shott SR, Donnelly LF (2004) Cine magnetic resonance imaging: evaluation of persistent airway obstruction after tonsil and adenoidectomy in children with Down syndrome. Laryngoscope 114:1724–1729

Vogler RC, Ii FJ, Pilgrim TK (2000) Age-specific size of the normal adenoid pad on magnetic resonance imaging. Clin Otolaryngol 24:392–395

Foreign Body Aspiration: Imaging Aspects

9

Benjamin Z. Koplewitz and Jacob Bar-Ziv

CONTENTS

9.1 **Introduction** *195*
9.2 **Etiology/Types of Foreign Bodies** *196*
9.3 **Mechanisms of Airway Obstruction** *198*
9.4 **Clinical Findings and Differential Diagnosis** *199*
9.5 **Imaging Techniques** *201*
9.6 **Imaging Findings** *206*
9.7 **Complications** *207*
9.8 **Conclusion** *209*
References *210*

9.1
Introduction

Aspiration of foreign bodies into the respiratory tract can occur at any age, but is most common in young children and in the elderly population. Foreign body aspiration is the most frequent pediatric domestic accident, and has serious and sometimes fatal sequelae (Black et al. 1994; Fitzpatrick and Guarisco 1998; Bhana et al. 2000; Ciftci et al. 2003). Most cases occur under the age of 4 years (Mantel and Butenandt 1986; Esclamado and Richardson 1987; Piepsz 1988; Schmidt et al. 2000; Oguz et al. 2000; Lima and Fischer 2002). When the history of a foreign body aspiration is definite, bronchoscopy is the modality of choice for both diagnosis and management. Until recently, rigid or flexible bronchoscopy was used for diagnosis, while removal of foreign bodies was carried out by rigid bronchoscopy only (Friedman 2000; Lima and Fischer 2002; Ayed et al. 2003; Ciftci et al. 2003). With the advance of technology, removal of foreign bodies can now be done by flexible bronchoscopy, which is a shorter and safer procedure (Swanson and Edell 2001). The complication rate of bronchoscopy varies between 1% and 8% (Black et al. 1984; Steen and Zimmermann 1990; Zerella et al. 1998; Zaytoun et al. 2000; Ayed et al. 2003; Ciftci et al. 2003), and the mortality rate is as low as 0.25%–1% (Mu et al. 1990; Steen and Zimmermann 1990; Hoeve and Rombout 1992; Ciftci et al. 2003).

In many cases, however, the aspiration event is not witnessed, and the classical triad of choking, cough and wheeze is missing. Diagnosis is then delayed or overlooked, and many children present with unresolved pneumonia, atelectasis or other complications. The role of the radiologist in cases of foreign body aspiration is not only to confirm a clinically suspected diagnosis, but also to suggest the diagnosis in patients with non-specific clinical symptoms and radiologic features that could be related to long-standing foreign bodies. Often the radiologist is the first to raise the possibility of foreign body aspiration.

This chapter discusses imaging techniques and findings related to the various types and mechanisms of obstruction and to the complications of foreign body aspiration.

B. Z. Koplewitz, BSc, MD
Lecturer, Department of Medical Imaging, Hadassah-Hebrew University Medical Center, P.O. Box 12000, 91120 Jerusalem, Israel
J. Bar-Ziv, MD
Professor in Radiology, Department of Medical Imaging, Hadassah-Hebrew University Medical Centre, P.O. Box 12000, 91120 Jerusalem, Israel

9.2
Etiology/Types of Foreign Bodies

Most cases of foreign body aspiration occur between the age of 6 months and 3 years, with the highest incidence during the 2nd year of life (Mantel and Butenandt 1986; Piepsz 1988; Fitzpatrick and Guarisco 1998; Lima and Fischer 2002). Infants and toddlers in this age group are already ambulatory and can therefore "disappear" from parent or guardian supervision for varying periods of time. They tend to act as "vacuum cleaners", and examine new objects of any size or shape by inserting them into their mouth. The combination of natural curiosity, lack of posterior dentition, inadequate control of deglutition and a startle response facilitates entry of solids into the larynx (Witt 1985; Byard 1994). The size and variety of objects that can pass through the vocal cords are quite astonishing (Fig. 9.1).

Food particles and organic materials constitute the vast majority of aspirated objects (Blazer et al. 1980; Keith et al. 1980; Teixidor de Otto et al. 1980; Svensson 1985; Mantel and Butenandt 1986; Piepsz 1988; Mu et al. 1990; Linegar et al. 1992; Black et al. 1994; Baharloo et al. 1999; Metrangelo et al. 1999; Diaz et al. 2000; Siddiqui et al. 2000; Brkic et al. 2001; Lima and Fischer 2002; Ayed et al. 2003). The nature of the aspirated material varies according to geographic and sociologic circumstances. Peanuts are the most common aspirated particles in North America, Europe, India and South Africa (Teixidor de Otto et al. 1980; Mantel and Butenandt 1986; Mu et al. 1990; Linegar et al. 1992; Diaz et al. 2000; Shegal et al. 2002; Shivakumar et al. 2003), whereas sunflower and watermelon seeds are more common in the Middle East (Farkash et al. 1982; Elhassani 1988; Oguz et al. 2000; Pasaoglu et al. 1991). Due to their high protein concentration, most organic foreign bodies absorb water from bronchial secretions and tend to increase in size. Candies have been reported to have a similar effect due to their high sugar concentration (Mearns and England 1975). Oil, salt and vegetable proteins in cooked food irritate the mucosa, causing edema and formation of granulation tissue with resultant narrowing of the bronchial lumen. Hence, an organic foreign body can grow to be larger than the original diameter of the bronchus, and what was initially a partial obstruction can progress to become a complete obstruction (Fig. 9.2) (Aytac et al. 1977; Cataneo et al. 1997).

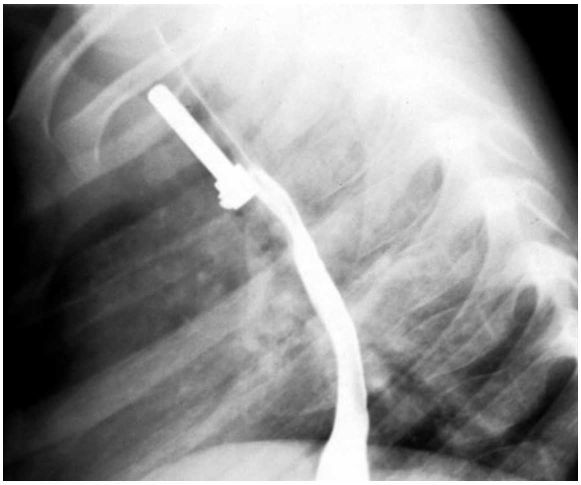

Fig. 9.1. Lateral view of a barium swallow shows a metallic bolt in the trachea of a 2-year-old boy

Grass inhalation is not uncommon and has some unique characteristics. The literature contains reports describing aspiration of several types of grass heads, all with the same structure of side spurs along the main stem. When inhaled stump-first, the spikes

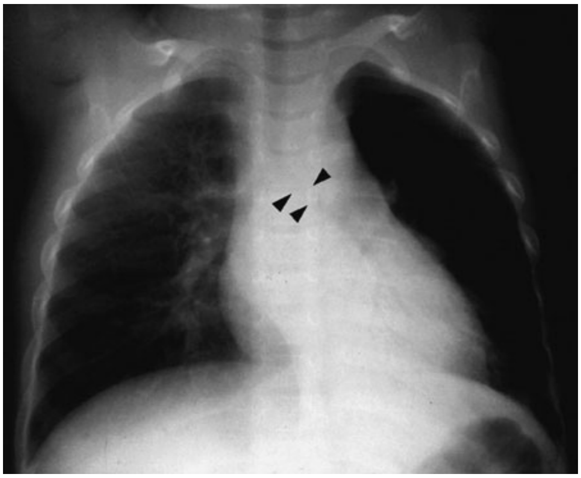

Fig. 9.2. A 3-year-old girl had cough and fever for 2 weeks. The history of an episode of choking on an almond was obtained from the mother following repeated questioning. Anteroposterior film using high kilovoltage copper filter technique demonstrates a segment in the left main bronchus deficient of air (*arrowheads*) and atelectasis of left lower lobe, with air-trapping in the left upper lobe. Notice air bronchogram in the atelectatic left lower lobe, in keeping with peripheral type of atelectasis. Bronchoscopy revealed a piece of almond in the proximal left main bronchus

carry the grass heads distally into the bronchial tree and lung parenchyma. Being resistant to organic decay, they can remain in the chest for a long time and can cause unusual infections, as well as other complications (Spencer et al. 1981; Maayan et al. 1993; Dindar et al. 1994; Basok et al. 1997; Newson et al. 1998).

Non-organic objects comprise 5%–9% of the foreign bodies aspirated by children (Farkash et al. 1982). Of these, coins are the most common (Reilly and Walter 1992), followed by plastic toy pieces and sharp objects such as pencils and pull-tabs from aluminum cans (Rogers and Igini 1975; Burrington 1976; Blazer et al. 1980; Strickland et al. 1987; Applegate et al. 2001). Inert foreign bodies have little effect on the bronchial mucosa and, unless they cause an obstruction by virtue of their size, can remain undiagnosed for long periods of time (Adegboye et al. 2003). Aspiration of pacifiers is not uncommon among toddlers (Jain et al. 1986; Barrett and Debelle 1995). Partially inflated balloons and Nylon bags are particularly hazardous (Anas and Perkin 1983; Abdel-Rahman 2000).

A tooth can be aspirated by a sleeping child at the age of permanent tooth eruption. This happened to a 10-year-old girl who had a loose deciduous tooth when she fell asleep at night. When she woke up the next morning the tooth had disappeared from her mouth. The episode was forgotten; 10 days later she developed symptoms of left lower lobe pneumonia, with no response to antibiotic therapy over several months. When she was admitted to the hospital, the missing tooth was evident in the left lower lobe bronchus on a chest radiograph, with atelectasis of most of the basal segments (Fig. 9.3). The tooth was removed by bronchoscopy; 2 months later residual bronchiectatic changes could still be seen in the left lower lobe.

Aspiration of tooth and dental fillings can also occur following minor trauma (Holan and Ram 2000), during anesthesia, dental treatment (Steelman et al. 1997), and intubation or resuscitation procedures, especially in victims of road traffic accidents.

Aspiration of gravel, dirt or sand can happen during a traffic accident or in a cave-in (Bergeson et al. 1978; Wales et al. 1983; Avital et al. 1989; Choy and Idowu 1996; Glinjongol et al. 2004). Airway obstruction has also been reported as a result of non-accidental trauma, when forcible introduction of a foreign body caused tracheal obstruction, with a resultant death reported in one case (Nolte 1993; Barrett and Debelle 1995). Aspiration of headscarf needles (Turban pins) has been reported in young girls and adolescents in Islamic populations (Ucan et al. 1996; Kaptanoglu et al. 1999; Murthy et al. 2001; Hamdan et al., personal communication).

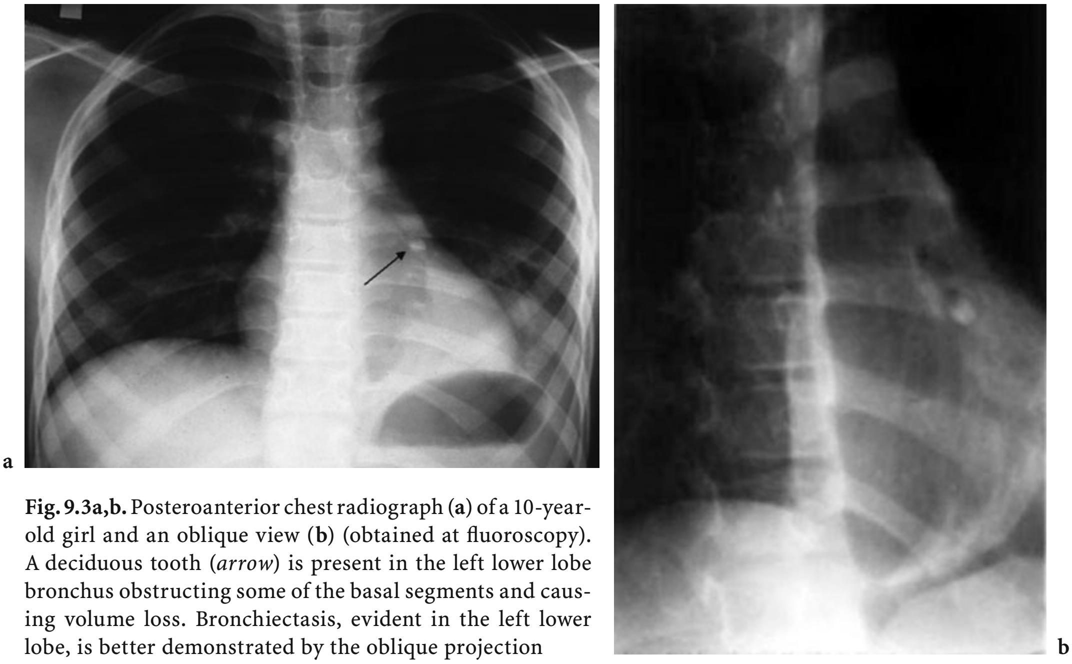

Fig. 9.3a,b. Posteroanterior chest radiograph (**a**) of a 10-year-old girl and an oblique view (**b**) (obtained at fluoroscopy). A deciduous tooth (*arrow*) is present in the left lower lobe bronchus obstructing some of the basal segments and causing volume loss. Bronchiectasis, evident in the left lower lobe, is better demonstrated by the oblique projection

9.3
Mechanisms of Airway Obstruction

A foreign body in the respiratory tract does not necessarily cause an obstruction, i.e. air can be inhaled and exhaled freely around the foreign body. This is known as a “two-way valve mechanism”, and occurs when the foreign body, which is usually located in the trachea, is small in relation to the airway. A foreign body can cause complete obstruction when air entry is blocked during inspiration and the air cannot be exhaled during expiration. This is called a “no-way valve mechanism”. A foreign body can allow air entry during inspiration but prevent the exit of air during expiration in a “one-way valve mechanism”. This mechanism is explained by the larger diameter of the airway during inspiration due to higher intra-thoracic negative pressure, and the smaller diameter during expiration.

Chest X-rays performed in cases of a non-obstructive tracheal or bronchial foreign body demonstrate uniform aeration bilaterally both in inspiration and expiration. In partial obstruction due to the one-way valve mechanism, the chest radiograph usually demonstrates air-trapping. Inspiratory films are often normal, and the air-trapping may become evident only in an expiratory study. In cases of complete airway obstruction (most commonly at the level of a bronchus), we often notice a combination of air-trapping in the non-dependent lobes with atelectasis of the dependent lobes. This is due to mucus plugging and the accumulation of secretions in the bronchial tree of the dependent segments (Figs. 9.2, 9.4, and 9.5).

The incidence of right and left bronchial foreign bodies is almost equal in infants and young children (Mu et al. 1990; Black et al. 1994; Burton et al. 1996; Cataneo et al. 1997; Senkaya et al. 1997; Metrangelo et al. 1999; Oguz et al. 2000; Van Looij et al. 2003; Ayed et al. 2003; Pinto et al. 2006), as opposed to predominance of the right bronchial tree in older children, adolescents and adults (Baharloo et al. 1999). The only slightly higher incidence of foreign bodies in the right bronchial tree in children is explained by the almost symmetrical tracheo-bron-

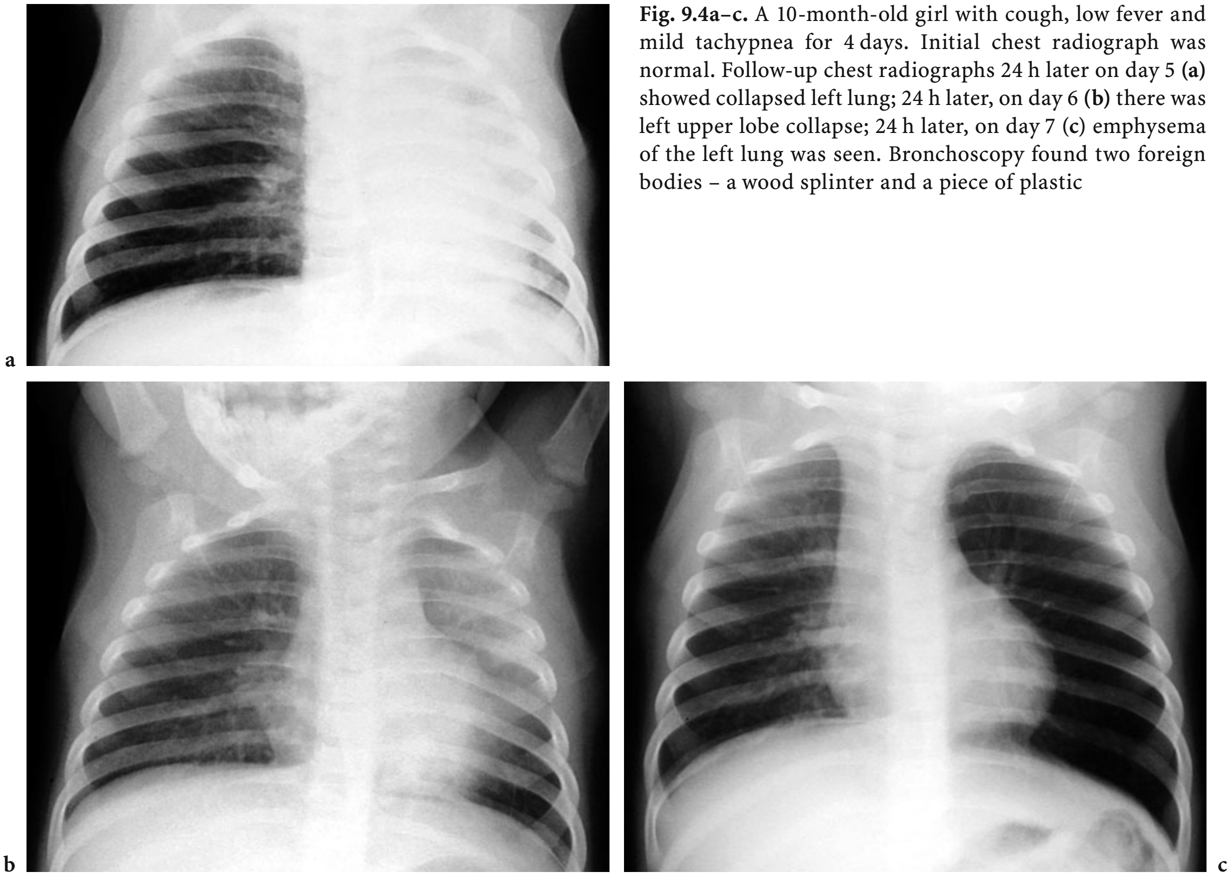

Fig. 9.4a–c. A 10-month-old girl with cough, low fever and mild tachypnea for 4 days. Initial chest radiograph was normal. Follow-up chest radiographs 24 h later on day 5 (**a**) showed collapsed left lung; 24 h later, on day 6 (**b**) there was left upper lobe collapse; 24 h later, on day 7 (**c**) emphysema of the left lung was seen. Bronchoscopy found two foreign bodies – a wood splinter and a piece of plastic

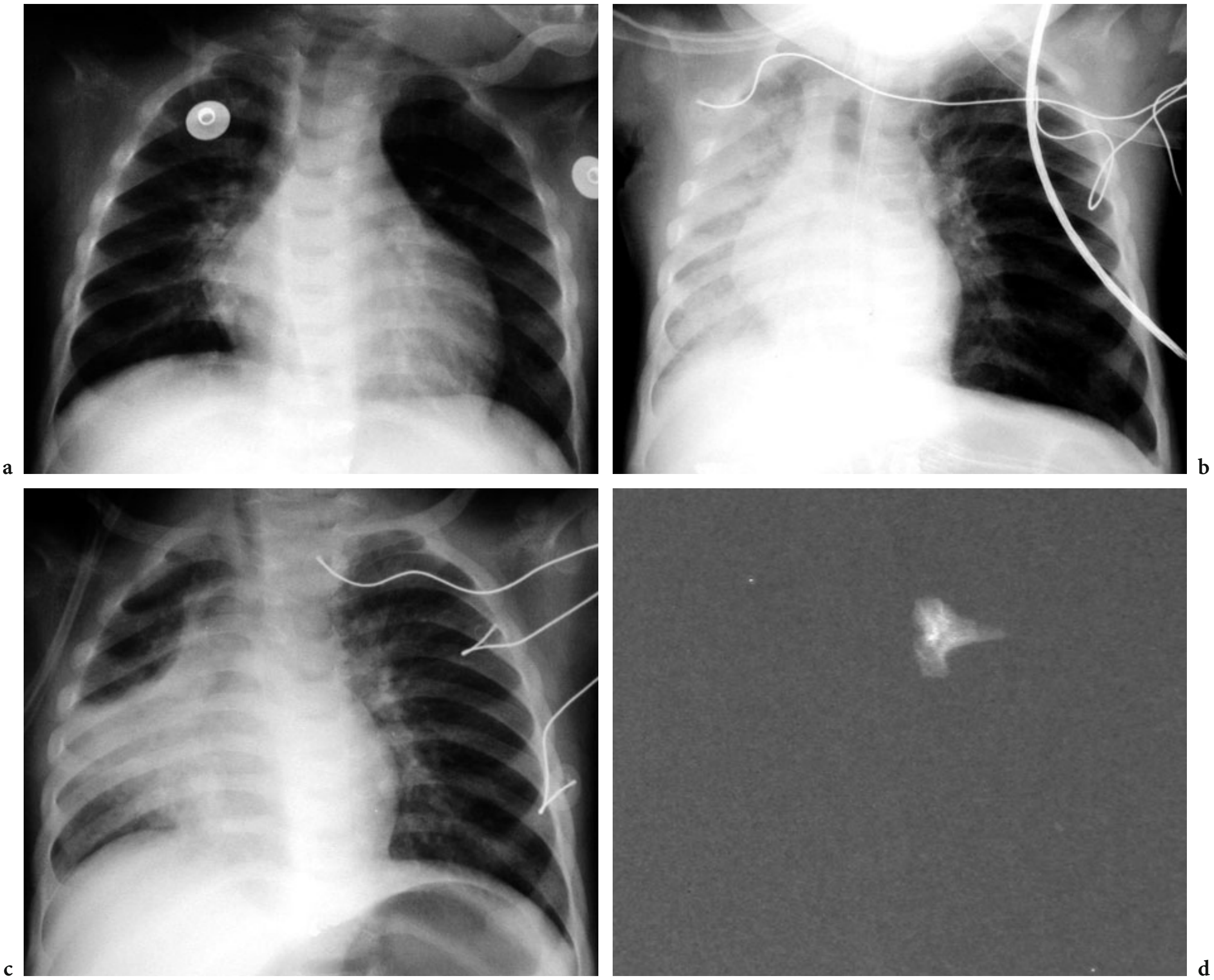

Fig. 9.5a–d. A 10-month-old boy with rickets aspirated a chicken bone. Initial chest radiograph **(a)** was normal (the chicken bone was missed). Follow-up chest radiographs 24 h **(b)** and 48 h **(c)** later showed progressive collapse of the right lung. A chicken bone **(d)** was removed from the right main bronchus on bronchoscopy

chial angle in this age group (Cleveland 1979). Migration of a small foreign body within the airways during different phases of the respiratory cycle, secondary to alterations of posture or following cough is rare, but does occur, and can change the clinical and imaging findings (Metrangelo et al. 1999). The authors witnessed a case in which a foreign body that was located in the right main bronchus migrated to the right upper lobe bronchus when the father of the child turned her upside down in an attempt to expel the foreign body from the airway. Since in those days only rigid bronchoscopy was available, the foreign body could not be endoscopically removed and the patient required thoracotomy and lobectomy.

9.4
Clinical Findings and Differential Diagnosis

The clinical manifestations of aspirated foreign bodies vary according to the location and degree of obstruction.

Laryngeal and subglottic foreign bodies make up about 5% of foreign bodies in the airways (Mantel and Butenandt 1986; Esclamado and Richardson 1987; Cohen et al. 1993; Black et al. 1994; Baharloo et al. 1999). When large enough, their presence in the major airway causes dyspnea, and when located adjacent to the vocal cords they may induce hoarseness, sudden loss of voice and inspiratory stridor (Blazer et al. 1980; Hanukoglu et al. 1986; Laks and Barzilay 1988). Cyanosis may occur secondary to laryngeal spasm (Halvorson et al. 1996; Baharloo et al. 1999; Ciftci et al. 2003). Similar symptoms can be induced by other processes such as a laryngeal web (Chen et al. 1998), viral or bacterial croup, epiglottitis, papilloma or hemangioma, angioneurotic edema, or hypocalcemic tetany (Grad and Taussig 1990). Laryngeal or tracheal hirudiniasis following leech infestation while drinking infected stream water can cause the same symptoms due to mechanical obstruction. In addition, the combination of the grasp of the mucosa by the leech cutting plates and secretion of an anticoagulant causes hemorrhage that can result in prolonged hemoptysis and anemia (Yousser et al. 2002).

Tracheal foreign bodies constitute 4%–13% of foreign bodies in the airways (Mu et al. 1990; Black et al. 1994; Burton et al. 1996; Metrangelo et al. 1999). In one series, they represented 23% of the cases with early diagnosis and 7% of the cases with late diagnosis (Oguz et al. 2000). In most patients there is a history of choking and dyspnea, yet they tend to be diagnosed later than bronchial foreign bodies, probably because they cause less severe respiratory symptoms (Esclamado and Richardson 1987). Inspiratory stridor and wheeze can also be caused by tracheomalacia or external compression on the trachea by a vascular structure (vascular ring, sling, etc.), bronchogenic cyst, enlarged lymph nodes (secondary to viral or bacterial infection or due to tuberculosis), mediastinal tumors (e.g., lymphoma), or an esophageal foreign body (Fig. 9.6).

Bronchial foreign bodies – the majority of aspirated foreign bodies (67%–80%) are found in the main bronchi (Blazer et al. 1980; Mantel and Butenandt 1986). A history of sudden choking is the most important clue for diagnosis (Farkash et al. 1982; Esclamado and Richardson 1987; Silva et al. 1998; Zerella et al. 1998; Metrangelo et al. 1999; Oguz et al. 2000; Ciftci et al. 2003). Such a history, however, was documented in only about one third of the cases in one series (Oguz et al. 2000). The classical triad of a choking episode, cough and wheeze was found in over 90% of the patients in another series (Blazer et al. 1980). Hemoptysis can be a presenting symptom (even in cases of a blunt foreign body) (Scully et al. 1983; Maayan et al. 1993; Fabian and Smitheringale 1996; Cataneo et al. 1997; Abellan Martinez et al. 2000; Zuniga et

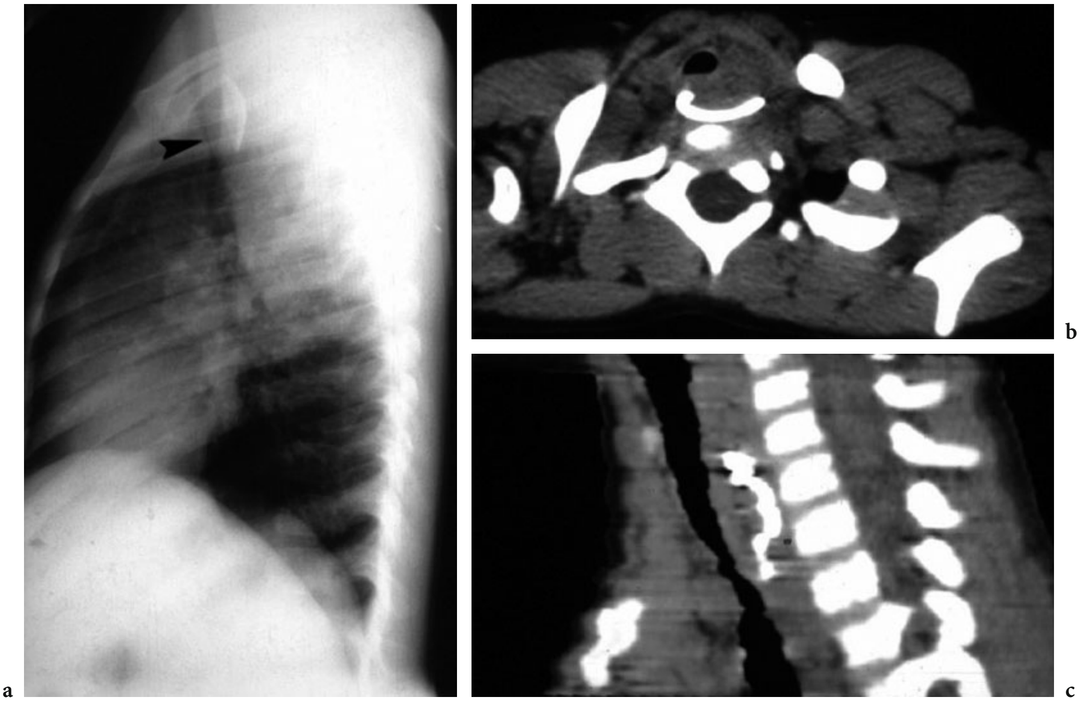

Fig. 9.6a–c. A 4-year-old child with stridor. Lateral chest radiograph (**a**), axial chest CT (**b**) and sagittal reconstructions (**c**) demonstrate a clam shell in the esophagus causing severe tracheal narrowing

al. 2000; Yousser et al. 2002). Physical examination will reveal unequal chest expansion during inspiration, as well as decreased breath sounds over the obstructed lung (Laks and Barzilay 1988; Oguz et al. 2000). Occasionally, a slapping sound of a loose foreign body can be heard (Felman 1982).

In cases of delayed diagnosis, pneumonia is a common presentation. The presence of an aspirated foreign body should be suspected in any patient with unexplained chronic pulmonary symptoms. Foreign body aspiration, however, is by no means the most common cause of recurrent pneumonia. Recurrent pneumonia can also result from impaired clearance of secretions from the tracheo-bronchial tree as in asthma, ciliary dysmotility, cystic fibrosis, infected bronchiectasis or secondary to an immune deficiency. Tumors of the tracheo-bronchial tree are uncommon in children, but, when present, may cause a varying degree of airway obstruction.

Esophageal foreign bodies can mimic foreign bodies in any location of the airway due to external compression of the larynx, trachea or bronchi (Fig. 9.6). Such compression may cause laryngeal or tracheal spasm, resulting in respiratory distress, stridor or wheeze (Smith et al. 1974). A tracheo-esophageal fistula may develop as a result of a decubitus ulcer caused by an esophageal foreign body of long-standing duration (Szold et al. 1991).

Nasal foreign bodies, when present for a long time, usually cause swelling of the nostrils or nasal discharge that may be foul smelling. They can ulcerate and damage the nasal septum or dislodge into the nasopharynx and be aspirated into the tracheobronchial tree (Cohen et al. 1993; Fini-Storchi and Ninu 1996).

9.5
Imaging Techniques

Chest Radiograph – the plain chest X-ray remains the initial study in the evaluation of a suspected aspirated foreign body. Abnormal findings are found in 50%–65% of chest X-rays in children with proven foreign bodies (Laks and Barzilay 1988; Mu et al. 1990; Black et al. 1994; Oguz et al. 2000). These rates increase when using inspiratory–expiratory techniques (Black et al. 1984, 1994; Losek 1990). Opaque foreign bodies are easily identified, but most are radiolucent (see Figs. 9.1 and 9.2).

In cases of a non-opaque foreign body, *inspiratory and expiratory films* can provide important information. Comparison of the two hemithoraces is mandatory. The inspiratory film is often normal or near normal, while the expiratory film shows obvious air-trapping. The obstructed lung is of larger volume and more radiolucent. The decrease in ventilation of the obstructed lobe causes an increase in pCO_2. The higher pCO_2 leads to arterial vasoconstriction and therefore to reduced pulmonary perfusion. Thus, the vessels in the obstructed region become narrow and sparse. This finding, characteristic of obstructive emphysema, can be seen on both plain films and CT. There is usually a mediastinal shift to the opposite side in expiration, as well as a lower ipsilateral hemidiaphragm (Fig. 9.7).

In young children, whose cooperation is not always optimal, two lateral decubitus films, one on each side, can replace the inspiratory–expiratory films (Capitanio and Kirkpatrick 1972). An unobstructed dependent lung shows smaller volume and crowded vessels as a result of gravitational forces on the abdominal and mediastinal organs. In cases of partial obstruction, the dependent lung does not deflate as expected. The relative hyperinflation of the dependent lung thus indicates the presence of partial bronchial obstruction.

Alternatively, expiratory films can be obtained in non-cooperative patients by applying manual pressure on the upper abdomen using a lead glove during the examination (Wesenberg and Blumhagen 1979). In infants this can also be done by inflating a blood-pressure cuff, wrapped around the abdomen. Careful monitoring must be performed to ascertain that at no time the pressure in the cuff exceeds the child's systolic blood pressure. Oblique projections enable better visualization of the trachea and main bronchi, and may demonstrate an otherwise "hidden" foreign body or discontinuation of the air column, depicted as an "absent segment" of the airway (Figs. 9.2, 9.3, and 9.8).

The high kilovoltage (kV) copper filter technique increases the visibility of the major airways and of non-opaque foreign bodies (Figs. 9.8 and 9.9). This technique combines the use of high kV with filters that absorb most of the low energy photons. As a result, the contrast between soft tissue and bone is reduced and the contrast between air and all other tissues is increased. Thus, the airway and its contents are sharply delineated over the background

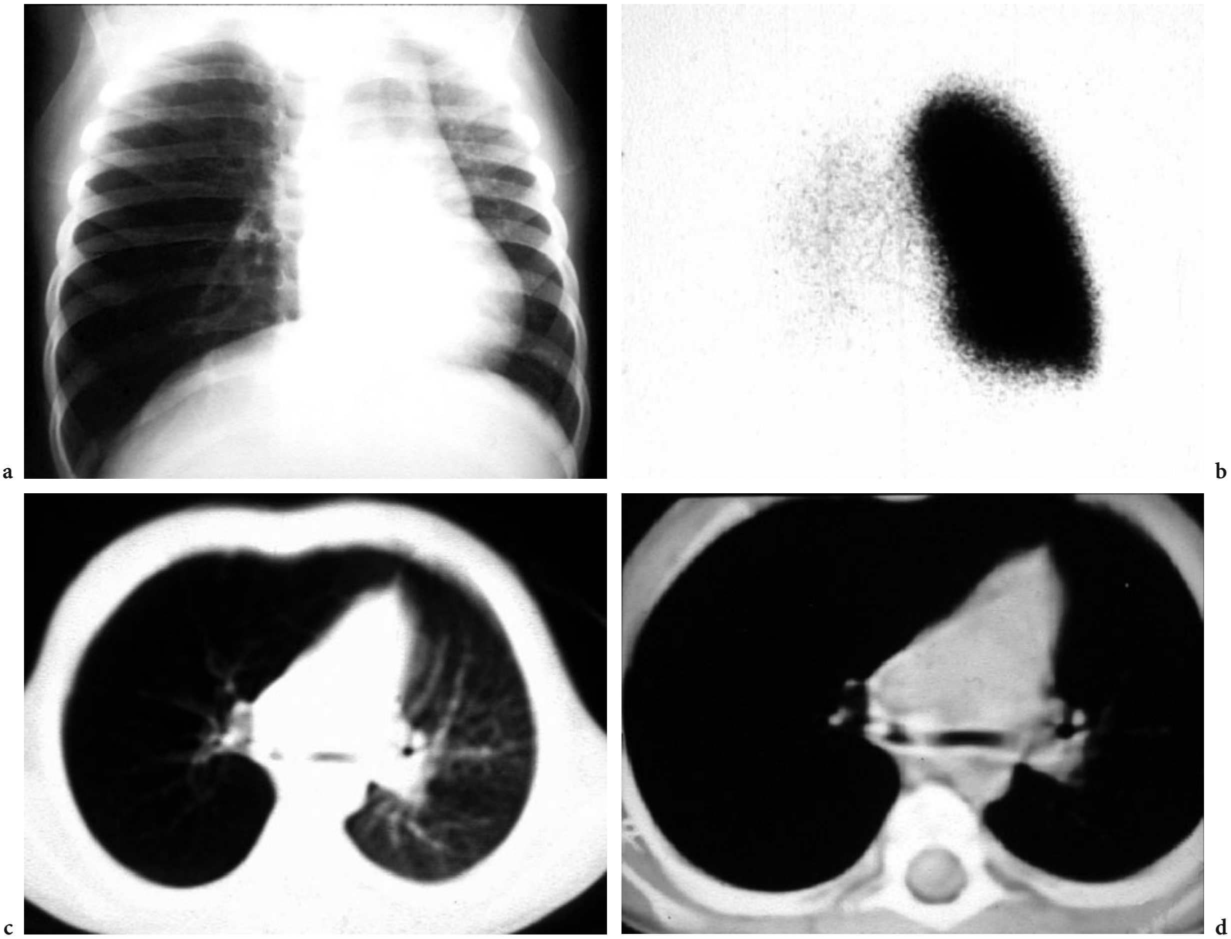

Fig. 9.7a–d. A 20-month-old boy had a choking episode. Initial chest radiograph (**a**) demonstrated obstructive emphysema of the right lung; bronchoscopy failed to reveal a foreign body. Lung scan (**b**) showed lack of perfusion to the right lung. Chest CT demonstrated obstructive emphysema of the right lung with contralateral mediastinal shift (**c**), as well as a foreign body in the right main bronchus (**d**). Repeat bronchoscopy identified a lentil

of the other tissues. Various filters have been used; however, the combination of 0.4 mm of tin, 0.5 mm of copper and 0.75 mm of aluminum is probably the most useful. The use of this technique enables improved visualization of the major airways with reduced radiation dose (Joseph et al. 1976).

The sensitivity, specificity and accuracy of chest radiographs for the detection and diagnosis of aspirated foreign bodies have been shown to be low when compared to bronchoscopy or to clinical signs in several retrospective studies (Svedstrom et al. 1989; Hoeve and Rombout 1992; Barrios Fontoba et al. 1997; Silva et al. 1998; Zerella et al. 1998; Shegal et al. 2002; Ayed et al. 2003; Pinto et al. 2006). In one series, up to 50% of chest X-rays obtained in children with proven foreign bodies were found to be normal when filmed in the early period (within 3 days) following aspiration; however, expiratory radiographs were not routinely obtained in this study (Zerella et al. 1998). Expiratory films have a high diagnostic value, but without clinical suspicion of foreign body aspiration, they will not be routinely performed. Therefore, it is mandatory that the clinician provide this sort of information to the radiologist in charge of the exam. Chest X-rays may also be normal in cases of bilateral bronchial foreign bodies (Wiseman 1984; Musemeche and Kosloske 1986; Laks and Barzilay 1988).

Fluoroscopy used to be helpful in the investigation of foreign body aspiration. The proponents of this modality advocate its use because it is widely available, easy to use, and rapidly diagnostic in up to 90% of cases of a bronchial foreign body (Blazer et al.

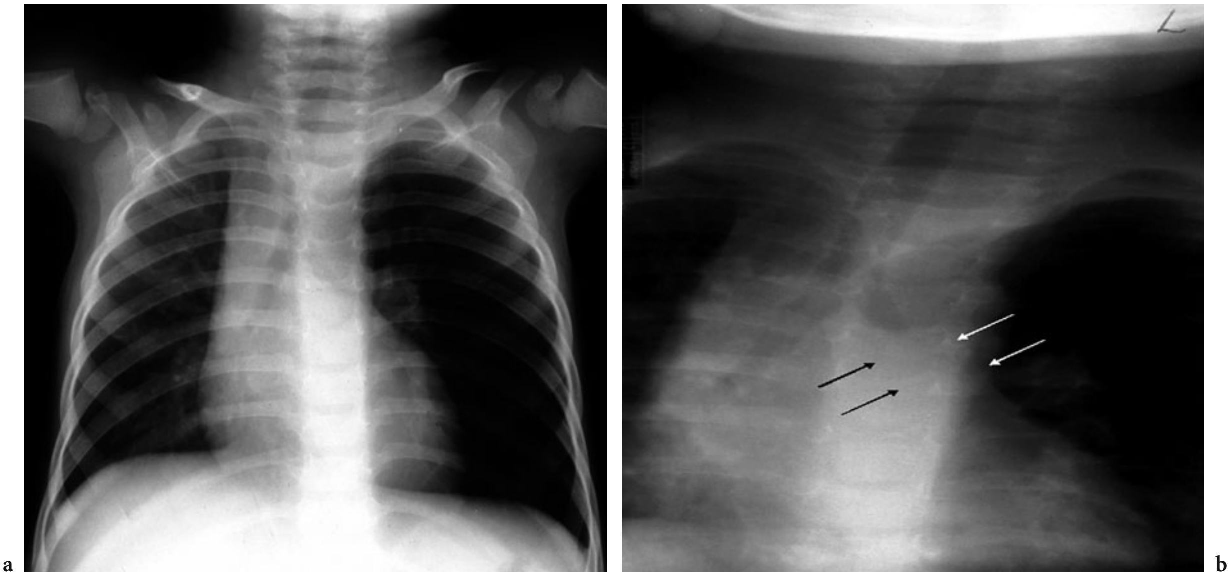

Fig. 9.8a,b. Anteroposterior chest radiograph (**a**) and a high kilovoltage (kV) copper filter technique film (**b**) of the major airways of a 2-year-old girl. The chest radiograph demonstrates air-trapping in the left lung while the high kV copper filter technique demonstrates an "absent segment" (*arrows*) in the left main bronchus

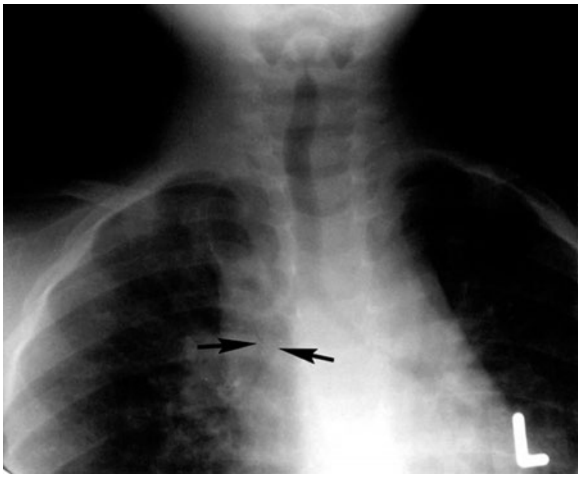

Fig. 9.9. High kilovoltage copper filter technique of the tracheobronchial tree of a 15-month-old girl. A non-opaque foreign body (*arrows*) surrounded by air is seen at the carina and in the right main bronchus . The inspiration and expiration films did not reveal air-trapping or any other pulmonary pathology

1980; Zerella et al. 1998). In our practice, fluoroscopy is seldom used. Nevertheless, the radiologist can optimally visualize the airways and detect obstruction or the presence of an opaque foreign body with fluoroscopy (see Fig. 9.2b), especially if a copper filter is used adjacent to the X-ray tube or close to the patient (Berdon, personal communication). Mediastinal shift towards the obstructed side during inspiration and towards the contralateral side during expiration is easily recognized (Theander 1970; Laks and Barzilay 1988; Mu et al. 1990). Unequal descent or ascent of the hemidiaphragms on inspiration and expiration can be seen in crying babies and in older children when requested to sniff rapidly. Diminished excursions of the diaphragmatic leaflets are invariably seen on the affected side, either with hyperinflation (in partial obstruction) or with volume loss (in complete obstruction) (Theander 1970). Use of any technique for assisted expiration, as described earlier, can facilitate demonstration of air-trapping. Digital subtraction fluoroscopy has been described as a sensitive method for the demonstration of tarcheal and bronchial narrowing secondary to the presence of a radiolucent aspirated foreign body (Ikeda et al. 2001).

Computed tomography (CT), due to its high contrast resolution, enables demonstration of foreign bodies that are frequently not visible on the chest X-ray. CT is usually utilized as a part of work-up for unclear cases of persistent, non-resolving respiratory symptoms, for which foreign body aspiration can be one of the reasons. When initial imaging studies or bronchoscopy are negative, CT may reveal the presence and location of a previously undiagnosed foreign body (Berger et al. 1980; Bertolani et al. 1999). CT is a very sensitive modality for demonstrating small dense objects, such as thin fish or chicken bones, that may not be detected on plain films (Braverman et al. 1993; Mignon et al. 1997).

CT is also an efficient tool for the demonstration of small plastic toy particles such as LEGO pieces (Appplegate et al. 2001) or rubber products. The presence and location of an intraluminal lesion can easily be detected and multiple intra-bronchial findings can at times be identified (Figs. 9.11 and 9.12), as well as the "interrupted bronchus" sign. Intravenous contrast administration can enhance discrimination between an intraluminal foreign body and other endobronchial, bronchial wall or extrinsic findings, such as a hemangioma or lymph nodes. By varying window width and level, one can see not only the foreign body, but also the reaction of the tissue around and distal to it. One can also assess the presence and extent of complications such as air-trapping, atelectasis, pneumonia, empyema, bronchiectasis or chest wall involvement (Figs. 9.7, 9.10–9.12) (Haliloglu et al. 2003; Kosucu et al. 2004; Adaleti et al. 2007). Air-trapping is well demonstrated by decubitus scans (Fig. 9.13) (Garcia-Pena and Lucaya 1999; Lucaya et al. 2000; Choi et al. 2002). Scanning in the semi-coronal plane can provide accurate localization of the obstructing foreign body (Figs. 9.11 and 9.12) (Bar-Ziv and Solomon 1990). However, with current helical, multi-detector scanners using volumetric acquisition of data, a high pitch and a short scanning time, accurate multi-planar reconstructions can be obtained, thereby replacing the semi-coronal scans.

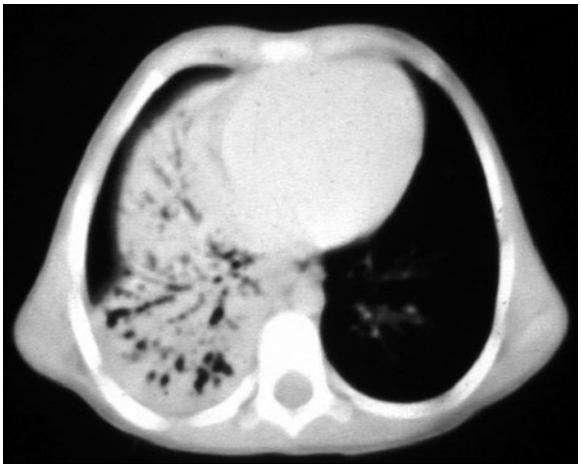

Fig. 9.10. Axial CT of the lower chest in a case of chronic foreign body aspiration into the right intermediate bronchus, causing collapse and bronchiectasis in the right middle lobe and right lower lobe

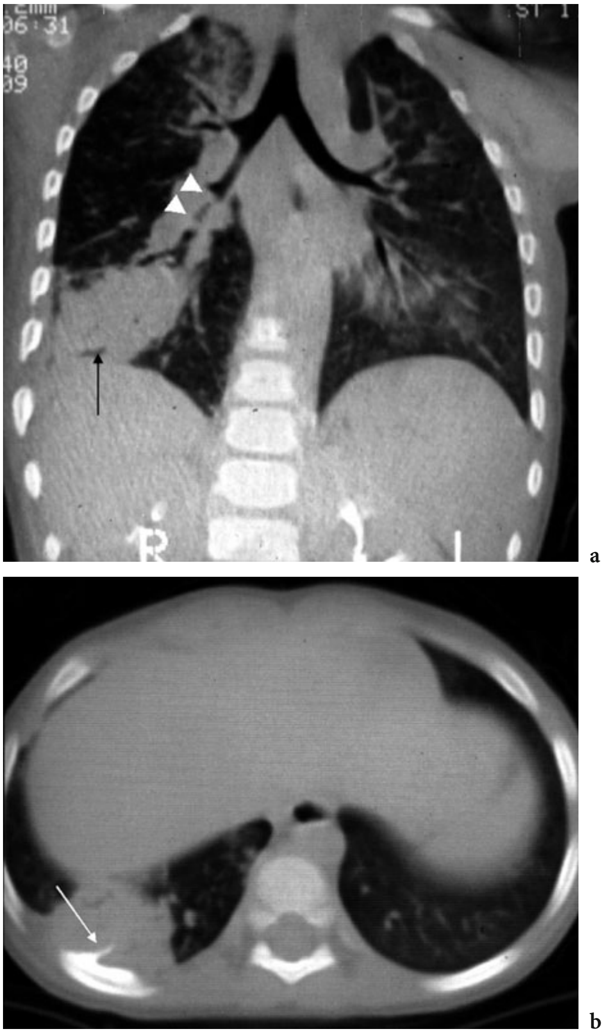

Fig. 9.11a,b. A 3-year-old boy aspirated a branch of Timothy grass. Semi-coronal (**a**) and axial (**b**) chest CT demonstrate narrowing and irregularity of the bronchus intermedius (*arrowheads*), distal atelectasis and abscess formation (*arrow*). Also note sclerosis of the adjacent rib representing osteomyelitis (*white arrow* in **b**)

We routinely use a helical technique with 3-mm collimation, 3-mm reconstructions for adolescents and children, with the smallest possible field of view. For infants and toddlers we may use 2-mm collimation with 1-mm reconstructions. Tube current can be reduced to as low as 25 mA–60 mA for such studies, and kV can be reduced to as low as 80–90, depending on child age and weight. Multiplanar reconstructions are helpful in detecting airway foreign bodies (Kosucu et al. 2004; Kocaoglu et al. 2006; Adaleti et al. 2007). Virtual bronchoscopy can further contribute to the diagnosis and location of a presumed

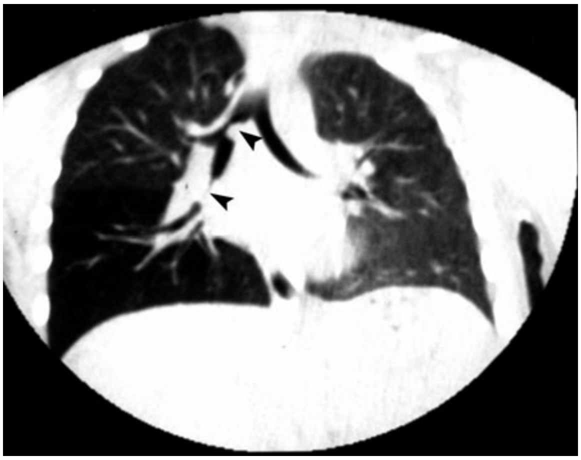

Fig. 9.12. A semi-coronal chest CT (lung settings) of a 2-year-old boy, obtained in expiration. Soft tissue density is demonstrated in the bronchus intermedius causing a partial obstruction (*arrow*). This is the equivalent of the "absent segment" sign that results from the presence of an obstructing foreign body and inflammatory changes in the adjacent bronchial wall. Note also the obvious air-trapping in the right lower lobe as compared to the normal-sized right upper lobe and left lung. Another partially obstructing foreign body is seen adjacent to the medial wall of the right main bronchus (*arrowhead*)

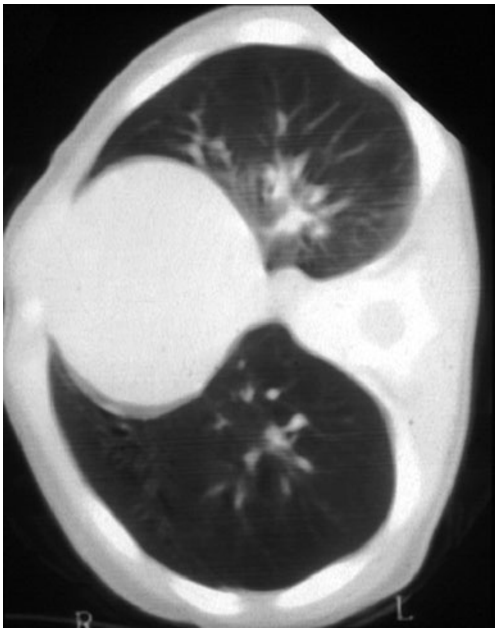

Fig. 9.13. Right lateral decubitus chest CT demonstrates air-trapping in the right (dependent) lung, following aspiration of a piece of an eraser

aspirated foreign body when a chest radiograph is not informative (Konen et al. 1998; Haliloglu et al. 2003; Kosucu et al. 2004; Kocaoglu et al. 2006; Adaleti et al. 2007). Virtual bronchoscopy has the advantage of demonstrating smaller airways then possible to view with conventional bronchoscopy, as well as the airways beyond an obstructed bronchus (Haliloglu et al. 2003; Kosucu et al. 2004; Adaleti et al. 2007). However, reconstructions are time consuming and have not been shown to contribute additional information over multi-planar reconstructions (Kosucu et al. 2004; Kocaoglu et al. 2006). The major disadvantage of CT examinations is the inherent radiation exposure of the young patient, despite improved technology and increasing awareness of both manufacturers and radiologist to minimize radiation dose. Therefore, it is imperative to weight the potential benefit of the additional data yielded as a result of each study against the potential risk, especially in cases when conventional bronchoscopy, that might be both diagnostic and therapeutic, is to be carried out as well (McHugh 2005).

Nuclear medicine is not recommended for the diagnosis of a bronchial foreign body. When used, however, the lung scan can be helpful in defining regional decrease in ventilation and perfusion (see Fig. 9.7b), as well as air-trapping, and can thus guide endoscopy to the area of suspected obstruction (Holland and Trumbull 1979; Lull et al. 1980).

Magnetic resonance imaging (MRI) studies are also rarely used for investigating suspected foreign body aspiration, especially because at present the use of sedation is mandatory. Nevertheless, several reports have described the utility of MRI in the management of foreign body aspiration. Due to the multiplanar nature of this modality, MRI can accurately locate the foreign body prior to bronchoscopy, and can also reveal foreign bodies in multiple sites during the same study (Imaizumi et al. 1994; Morijiri et al. 1994). The high fat content of aspirated peanuts, as well as the high water content of most organic foreign bodies enable clear delineation of their size and site (O'Uchi et al. 1992; Tashita et al. 1998). Ultrasound can be of value in defining the presence, nature and extent of complications of foreign bodies, such as consolidation with an air bronchogram, pleural effusion or empyema, loculated pockets of fluid, chest wall abscess or rib osteomyelitis (Seibert et al. 1986; Giudicelli et al. 1996). Ultrasound can presumably demonstrate the foreign body within the collapsed lung; however the authors do not have experience in this.

9.6
Imaging Findings

Imaging findings in cases of foreign body aspiration are determined by the presence and the degree of airway obstruction, the site of the foreign body, its type and the time that has elapsed between aspiration and the performance of imaging studies.

A foreign body can be present in the airway without causing obstruction. This situation almost always involves an oblong foreign body in the trachea, small enough to have been aspirated yet not large enough to block the (relatively) larger airway. In such a case the chest X-ray and fluoroscopy will usually be negative, although pneumonia might be present (Esclamado and Richardson 1987; Mu et al. 1990; Cataneo et al. 1997). A high kV soft tissue technique with a copper filter may reveal the foreign body (see Figs. 9.8 and 9.9). CT (Gupta and Berry 1991; Malis and Hayes 1995; Bertolani et al. 1999) and MR imaging (O'Uchi et al. 1992; Imaizumi et al. 1994; Morijiri et al. 1994; Tashita et al. 1998) can demonstrate the presence and often the nature of such a foreign body when the initial imaging is negative.

Obstruction of the airway can vary in severity and occur at different levels of the tracheo-bronchial tree. Laryngeal or sub-glottic foreign bodies tend to be thinner and are often arranged in an anteroposterior direction in the region of the vocal cords, as opposed to esophageal foreign bodies, which lie in a transverse direction. If the foreign body is a thin, rounded object (e.g., a coin or an egg shell), it will be seen as a thin line on the anteroposterior chest X-ray when located between the vocal cords, and as a rounded shadow when located in the esophagus. Tracheal foreign bodies usually cause no obstruction or incomplete obstruction. The imaging findings, when present, are often bilateral: either bilateral volume loss or bilateral hyperinflation. In the latter case, the diaphragms are flattened and in a low position. When small enough, the foreign body may move in the tracheobronchial tree during the different phases of the respiratory cycle or as a result of coughing, with consequent changes in the clinical and imaging findings (Metrangelo et al. 1999).

About three-quarters of airway foreign bodies are found in the main bronchi (Blazer et al. 1980; Mantel and Butenandt 1986), where they cause partial or complete obstruction. Plain films and fluoroscopy seldom demonstrate a nonopaque foreign body. An oblique projection obtained with these modalities, placing the upper airway over the mediastinal soft tissues, creates better contrast and enhances demonstration of the foreign body (see Fig. 9.3). This technique may also indirectly reveal the presence of a foreign body by virtue of focal absence of the air column in the obstructed bronchus, the so-called "absent segment" or the "interrupted bronchus" sign (Figs. 9.2 and 9.8) (Grunebaum et al. 1979; Lim-Dunham and Yousefzadeh 1999). Partial obstruction results in localized air-trapping distal to the site of the foreign body, with resultant widening of the intercostal spaces, and flattening of the ribs and diaphragms, and blunting of the costophrenic angles (Laks and Barzilay 1988; Mu et al. 1990; Black et al. 1994; Ernst and Mahmud 1994; Oguz et al. 2000). Pulmonary hyperexpansion with sparse vascularity or displacement of the mediastinum to the contralateral side on expiration indicates the presence of obstructive emphysema (Figs. 9.2a, 9.7–9.10) (Mu et al. 1990). Complete obstruction also causes segmental or lobar atelectasis (see Figs. 9.2–9.5), or even total collapse of the ipsilateral lung (Figs. 9.4 and 9.5). The collapsed area may initially be homogeneously opaque, due to the absence of air in the alveoli and bronchi. Collateral diffusion of air to the bronchioles distal to the obstructing foreign body may result in a faint air bronchogram. In cases with lobar atelectasis, compensatory emphysema of the ipsilateral respected lobes and of the contralateral lung is often present (Theander 1970). In contrast to obstructive emphysema, pulmonary vessels are prominent in compensatory emphysema.

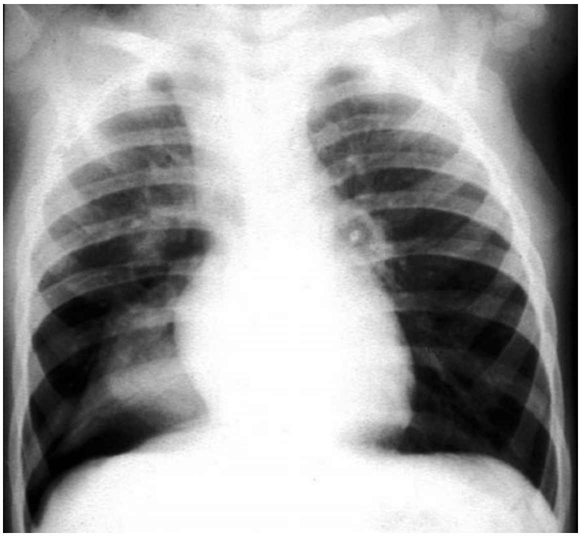

Fig. 9.14. Collapsed right lower lobe with localized pneumothorax due to acute foreign body aspiration

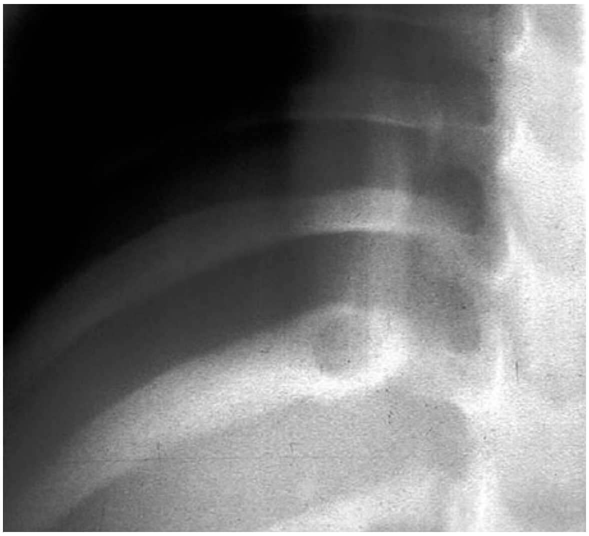

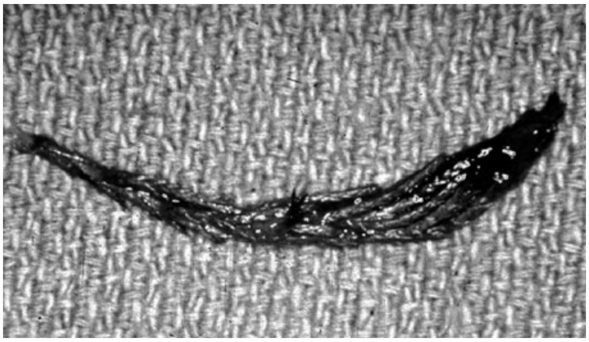

Fig. 9.15a,b. A 2-year-old girl had repeated episodes of right lower lobe pneumonia for several months following an episode of choking around Christmas. Chest radiograph **(a)** showed an osteolytic lesion with thickening and sclerosis in a rib at the right lower chest. At surgery, a pine tree needle **(b)** was found in the rib, with osteomyelitis

The presence of lobar collapse with localized pneumothorax should suggest the diagnosis of acute bronchial obstruction of any etiology (Berdon et al. 1984; Nimkin et al. 1995) (Fig. 9.14). The combination of increased pressure and the presence of a sharp object in the bronchi can result in a bronchopleural fistula. This complication, as well as pneumonia secondary to focal obstruction, may give rise to pleural effusion or empyema (Dogan et al. 1999). Pleural effusion as the only imaging sign of foreign body aspiration has also been reported (Auerback 1990). In prolonged cases, localized or multi-focal bronchiectasis may develop and be evident on the plain radiograph (Fig. 9.2) or on CT (Fig. 9.10); these are best evaluated by high-resolution CT with thin section collimation (Kuhn 1993). Subacute or chronic infection and inflammatory response may form a parenchymal abscess adjacent or distal to the foreign body, or a chest wall abscess and rib osteomyelitis (Figs. 9.11 and 9.15).

9.7
Complications

Complications of foreign body aspiration can be immediate or long term. A foreign body can cause *fatal asphyxia and death* when there is complete obstruction of the major airways (Buntain et al. 1979; Black et al. 1984, 1994; Byard 1994; Bhana et al. 2000; Ciftci et al. 2003). This occurrence is rare, although it was described in 7.5% of foreign body aspiration cases in one report (Menendez et al. 1991). This high incidence has not been observed in the author's experience and is not corroborated in other reports.

Complete obstruction can also occur during bronchoscopy for extraction of a foreign body, as happened to a 2.5-year-old girl who aspirated a broken piece of a metal zipper. During rigid bronchoscopy the foreign body got stuck between the vocal cords and the child could neither be ventilated nor intubated. Bradycardia and decrease in oxygen saturation necessitated resuscitation and emergency tracheostomy was performed. The foreign body was pushed down to the right bronchus. Following completion of tracheostomy the foreign body was pulled up to the level of the cords by flexible bronchoscopy and dislodged using surgical forceps.

Asphyxia and hypoxemia can result in hypoxic-ischemic encephalopathy, convulsions, severe neurologic deterioration over varying period of time and death within several days or following several months or years (Northcote 1983).

Atelectasis is reported by some as the most common complication of foreign body aspiration (Mu et al. 1990; Cataneo et al. 1997; Oguz et al. 2000), and is seen in half of the patients who are diagnosed 24 h or more after the suspected aspiration event (Wiseman 1984). Though atelectasis usually develops gradually, collapse of the entire lung may occur within 1 h. When this happens on the right side, kinking of the superior vena cava may cause a sudden decrease of venous return to the heart and lead to loss of consciousness. Elevation of jugular venous pressure should alert the examining physician to the possibility of such a complication.

Pneumonia appears in 20%–50% of patients with an aspirated foreign body diagnosed 3 days or later consequent to the aspiration event (Cataneo et al. 1997; Oguz et al. 2000; Diaz et al. 2000). The pneumonia in these cases is usually located in the lower lobes, does not resolve following antibiotic therapy and is frequently associated with a pleural effusion. Pneumonia may at times be due to uncommon pathogens (Cavens et al. 1973; Baethge et al. 1990). Dirt or shallow water aspiration can lead to diffuse pneumonitis (Mangge et al. 1993).

Air leak – a sudden increase in alveolar pressure due to proximal obstruction – can cause an air leak into the interstitial space, leading to interstitial emphysema, pneumomediastinum (Hanukoglu et al. 1980; Burton et al. 1989; Ramadan et al. 1992; Bratton and O'Rourke 1993; Oliveira et al. 2002; Ciftci et al. 2003), pneumothorax (see Fig. 9.14) (Berdon et al. 1984; Nimkin et al. 1995; Esclamado and Richardson 1987; Ramadan et al. 1992; Cataneo et al. 1997; Newson et al. 1998; Carron and Derkay 2000; Ciftci et al. 2003) or pneumopericardium (Tjhen et al. 1978; Bro and Thamsen 1989). The abrupt onset of an air leak in a child under 2 years of age, without a history of chest trauma or asthma, should raise the suspicion of an aspirated foreign body (Cataneo et al. 1997).

Long term complications – the incidence and severity of long-term complications are directly related to the length of time that has passed between the actual event of aspiration and establishment of the diagnosis (Auerback 1990; Mu et al. 1990; Linegar et al. 1992; Schmidt and Manegold 2000; Karakoc et al. 2002). Positive radiological findings are more common in cases diagnosed 24 h later consequent to the suspected aspiration (Esclamado and Richardson 1987; Mu et al. 1990); the longer the delay in diagnosis, the higher the rate of complications (Levy et al. 1983; Mu et al. 1990; Karakoc et al. 2002). In most cases of delayed diagnosis the original episode passed unnoticed and the parents or physician do not relate recent, recurrent signs and symptoms as being linked to such an episode or to each other (Mantel and Butenandt 1986). In such cases the presentation can be that of recurrent events of hyper-reactive airway disease, with incomplete response to treatment, or of recurrent pneumonia, with or without pleural effusion or empyema (Auerback 1990; Burton et al. 1989; Dogan et al. 1999; Hanukoglu et al. 1980).

Chronic bronchitis and bronchiectasis (see Figs. 9.2 and 9.10) secondary to long-standing foreign body aspiration constitute approximately 5% of chronic suppurative lung disease. The presence of a bronchial foreign body of long duration causes atelectasis that can become infected and lead to the development of bronchiectasis. This can become so severe that bronchoscopic extraction of the foreign body might not be possible, and surgical treatment may eventually be required (Spencer et al. 1981; Gatch et al. 1987; Maayan et al. 1993; Nikolaizik and Warmer 1994; Cataneo et al. 1997; Scully et al. 1998; Karakoc et al. 2002; Adegboye et al. 2003).

Grass heads of different types have been reported to cause a unique sequence of complications. If they have spikes that are soft and close together, as is the case of Timothy grass, they will soften with moisture following aspiration and will not penetrate into the lung periphery. The grass head may lodge in the bronchial tree and occlude it causing obstructive emphysema, collapse, pneumonia and lung abscess. If the spikes are stiff and do not become soft when moistened, or when inhaled stump-first, respiratory actions and cough can cause them to advance. Being carried by the spikes distally into the bronchial tree, they can penetrate the lung tissue and ultimately even extrude spontaneously through the chest wall (Hillman et al. 1980). During this process they can cause lung abscess (see Fig. 9.11), broncho-cutaneous fistula (Cavens et al. 1973; Baethge et al. 1990; Maayan et al. 1993; Dindar et al. 1994), rib osteomyelitis (Figs. 9.11, 9.15), chest wall abscess or pneumocutaneous fistula (Cheng et al. 1991). Among several of our patients who suffered such a complication, one was a 3-year-old boy who had aspirated a branch of Timothy grass. Subsequently, the child developed cough and fever. A chest radiograph obtained several weeks later showed consolidation and volume loss in the right lower lobe. A semi-coronal chest CT study revealed irregularity and narrowing of the right lower lobe bronchus, partial consolidation and atelectasis of the right lower lobe with abscess formation. Thickening, sclerosis and irregularity of the inner border of the adjacent rib were also noted (see Fig. 9.11). Pathology of the resected right lower lobe revealed the presence of

Timothy grass within the bronchus of the lateral basal segment with bronchiectasis and abscess formation.

Brain abscesses have been reported in association with foreign body aspiration, presumably due to faulty pulmonary capillary filter mechanisms (Spencer et al. 1981; Sane et al. 1999; Fuentes et al. 2001).

Prolonged presence of a tracheal or an esophageal foreign body can result in a decubitus ulcer that can progress to a tracheo-esophageal fistula (Fig. 9.16) with possible mediastinitis, which might require surgery (Szold et al. 1991).

Pulmonary edema may occur subsequent to relief of an upper airway obstruction, regardless of the etiology (Fig. 9.17). The pathophysiology of the pulmonary edema in these cases is not fully understood. It is thought that pulmonary congestion develops during obstruction as a result of raised pleural negative pressure, which increases venous return to the heart, in the presence of decreased left ventricular function. The hypoxia causes pulmonary hypertension and increased capillary permeability. This combination leads to greater pulmonary vascular volume, which may be radiographically difficult to detect because of associated air-trapping. Once the obstruction is relieved and lung aeration returns to normal, the pulmonary edema becomes apparent (Sofer et al. 1984a, b, 1985).

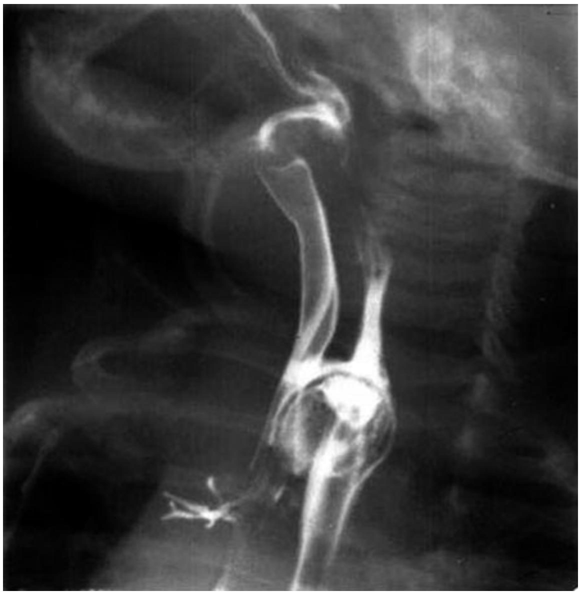

Fig. 9.16. A 6-week-old baby girl had suffered from respiratory symptoms since the age of 2 weeks. Tube esophagogram demonstrated a filling defect in the upper esophagus and a tracheo-esophageal fistula. A pistachio nutshell was surgically removed and the fistula excised

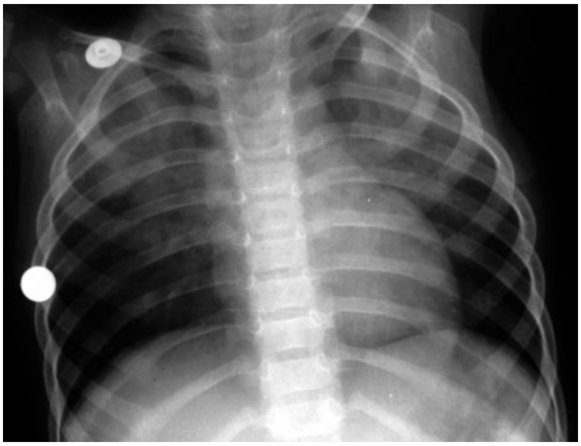

Fig. 9.17. Anteroposterior chest radiograph demonstrating ill-defined increased opacity of the upper zones bilaterally as a result of pulmonary edema following relief of obstruction after extraction of a foreign body

9.8
Conclusion

A wide variety of opaque or non-opaque foreign bodies can be aspirated by infants and young children. The history of choking is the most reliable clue for the diagnosis of foreign body aspiration, but many patients reach medical attention because of various non-specific clinical symptoms. The role of the radiologist in these cases is crucial. Knowledge of the imaging features of a foreign body in the respiratory tract is essential for diagnosis. Many clinical and imaging findings are the result of a one-way obstruction mechanism, most commonly affecting one of the main bronchi. A normal inspiratory chest radiograph does not rule out an endotracheobronchial foreign body. Hence, expiratory films are extremely important to demonstrate air-trapping. Alternatively, lateral decubitus or assisted expiration films can be used. The high kV copper filter technique is valuable for demonstrating the foreign body, and for indirectly showing an area of deficient aeration in the tracheo-bronchial tree, the “absent segment” sign.

Fluoroscopy can be very useful, but unfortunately the art of fluoroscopy is now almost lost. CT has become more valuable by virtue of its wide availability and high resolution. CT can establish the diagnosis of a foreign body, indicate its exact location and often show its composition, as well as any associated complications. Other imaging modalities can be used, though their role is not as well established. Nuclear scans are of some value only in cases of obstructive endobronchial foreign body. MRI has great potential and may be used extensively in the future. Currently, however, it is not widely available and usually requires sedation of the child. US is being used to demonstrate complications such as pleural effusion or chest wall abscesses.

An understanding of the mechanisms of obstruction and their resultant clinical and imaging manifestations, especially when foreign body aspiration is highly suspected, can lead to earlier diagnosis and lower the complication rate.

Acknowledgements. The authors thank Prof. C. Springer and Prof. B.S. Slasky for reviewing the manuscript; Prof. P. Mogle for his comments and for the contribution of the case described in Figure 9.16; Prof. J. Lucaya for the cases presented in Figures 9.4–9.7, 9.13, 9.14; Prof. J. Strife for the case described in Figure 9.15; and Mr. E. Koplewitz and Mrs. B. Koplewitz for their editorial comments and their continuous support.

References

Abdel-Rahman HA (2000) Fatal suffocation by rubber balloons in children: mechanism and prevention. Forensic Sci Int 108:97–105

Abellan Martinea MC, Mendez Martinez P, Sanchez Gasscon F et al. (2000) Repeated hemoptysis for foreign body bronchial aspiration. An Med Interna 17:652–654

Adaletli I, Kurugoglu S, Ulus S et al. (2007) Utilization of low-dose multidetector CT and virtual bronchoscopy in children with suspected foreign body aspiration. Pediatr Radiol 37:33–40

Adegboye VO, Osinowo O, Adebo OA (2003) Bronchiectasis consequent upon prolonged foreign body retention. Cent Afr J Med 49:53–58

Anas NG, Perkin RM (1983) Aspiration of a balloon by a 3-month-old infant. JAMA 250:385–386

Applegate KE, Dardinger JT, Lieber ML et al. (2001) Spiral CT scanning technique in the detection of aspiration of LEGO foreign bodies. Pediatr Radiol **31**:836–840

Auerback ML (1990) Pleural effusion due to unsuspected aspiration of vegetable matter in a three-year-old boy. N Engl J Med 322:1238

Avital A, Springer C, Mogle P et al. (1989) Successful treatment after 'drowning' in sand. Arch Dis Child 64:615–616

Ayed AK, Jafar AM, Owayed A (2003) Foreign body aspiration in children: diagnosis and treatment. Pediatr Surg Int 19:485–488

Aytac A, Yurdakul Y, Ikizler C et al. (1977) Inhalation of foreign bodies in children. Report of 500 cases. J Thorac Cardiovasc Surg 74:145–151

Baethge BA, Eggerstedt JM, Olash FA Jr (1990) Group F streptococcal empyema from aspiration of a grass inflorescence. Ann Thorac Surg 49:319–320

Baharloo F, Veyckemans F, Francis C et al. (1999) Tracheobronchial foreign bodies: presentation and management in children and adults. Chest 115:1357–1362

Bar-Ziv J, Solomon A (1990) Direct coronal CT scanning of tracheo-bronchial, pulmonary and thoraco-abdominal lesions in children. Pediatr Radiol 20:245–248

Barrett TG, Debelle GD (1995) Near-fatal aspiration of a child's dummy: design fault or deliberate injury? J Accid Emerg Med 12:154–155

Barrios Fontoba JE, Gutierrez C, Lluna J (1977) Bronchial foreign body: should bronchoscopy be performed in all patients with a choking crisis? Pediatr Surg Int 12:118–120

Basok O, Yaldiz S, Kilincer L (1997) Bronchiectasis resulting from aspirated grass inflorescences. Scand Cardiovasc J 31:157–159

Berdon WE, Dee GJ, Abramson SJ et al. (1984) Localized pneumothorax adjacent to a collapsed lobe: a sign of bronchial obstruction. Radiology 150:691–694

Berger PE, Kuhn JP, Kuhn LR (1980) Computed tomography and the occult trecheobronchial foreign body. Radiology 134:133–135

Bergeson PS, Hinchcliffe HW, Crawford RF, Sorenson MJ, Trump DS (1978) Asphyxia secondary to massive dirt aspiration. J Pediatr 92:506–507

Bertolani MF, Marotti F, Bergamini BM et al. (1999) Extraction of a rubber bullet from a bronchus after 1 year: complete resolution of chronic pulmonary damage. Chest 115:1210–1213

Bhana BD, Guanselvam JG, Dada MA (2000) Mechanical airway obstruction caused by accidental aspiration of part of a ballpoint pen. Am J Forensic Med Pathol 21:362–365

Black RE, Choi KJ, Syme WC et al. (1984) Bronchoscopic removal of aspirated foreign bodies in children. Am J Surg 148:778–781

Black RE, Johnson DG, Matlak MEB (1994) Bronchoscopic removal of aspirated foreign bodies in children. J Pediatr Surg 29:682–684

Blazer S, Naveh Y, Friedman A (1980) Foreign body in the airway. A review of 200 cases. Am J Dis Child 134:68–71

Bratton SL, O'Rourke PP (1993) Spontaneous pneumomediastinum. J Emerg Med 11:525–529

Braverman I, Gomori JM, Polv O et al. (1993) The role of CT imaging in the evaluation of cervical esophageal foreign bodies. J Otolaryngol 22:311–314

Brkic F, Delibegovic-Dedic S, Hajdarovic D (2001) Bronchoscopic removal of foreign bodies from children in Bosnia and Herzegovina: experience with 230 patients Int J Pediatr Otorhinolaryngol 60:193–196

Bro H, Thamsen H (1989) Pneumopericardium after aspiration of a pea into the respiratory tract. Ugeskr Laeger 151:2733

Buntain WL, Benton JW, Gutierrez JF (1979) Christmas bow tragedies. South Med J 72:1471–1472

Burrington DJ (1976) Aluminum "pop tops". A hazard to child health. JAMA 235:2614–2617

Burton EM, Riggs W Jr, Kaufman RA et al. (1989) Pneumomediastinum caused by foreign body aspiration in children. Pediatr Radiol 20:45–47

Burton EM, Brick WG, Hall JD et al. (1996) Tracheobronchial foreign body aspiration in children. South Med J 89:195–198

Byard RW (1994) Unexpected death due to acute airway obstruction in daycare centers. Pediatrics 94:113–114

Capitanio MA, Kirkpatrick JA (1972) The lateral decubitus film: an aid in determining air-trapping in children. Radiology 103:460–462

Carron JD, Derkay CS (2000) Potpourri aspiration presenting as tension pneumothorax. Am J Otolaryngol 21:349–351

Cataneo AJ, Reibscheid SM, Ruiz Junior RL et al. (1997) Foreign body in the tracheobronchial tree. Clin Pediatr (Phila) 36:701–706

Cavens TR, McGee MD, Miller RR et al. (1973) Pneumocutaneous fistula secondary to aspiration of grass. J Pediatr 82:737–738

Chen YT, Singh R, Brett RH (1998) Diagnostic red herring in an infant with stridor. Singapore Med J 39:471–472

Cheng T, Herman G, Coulter K (1991) A tale of two diseases: pneumonia and chest wall abscess. Pediatr Infect Dis J 10:414–418

Choi SJ, Choi BK, Kim HJ et al. (2002) Lateral decubitus HRCT: a simple technique to replace expiratory CT in children with air trapping. Pediatr Radiol 32:171–182

Choy IO, Idowu O (1996) Sand aspiration: a case report. J Pediatr Surg 31:1448–1450

Ciftci AO, Bingol-Kologlu M, Senocak ME et al. (2003) Bronchoscopy for evaluation of foreign body aspiration in children. J Pediatr Surg 38:1170–1176

Cleveland RH (1979) Symmetry of bronchial angles in children. Radiology 133:89–93

Cohen HA, Goldberg E, Horev Z (1993) Removal of nasal foreign bodies in children (letter). Clin Pediatr (Phila) 32:192

Diaz GA, Valledor L, Seda F (2000) Foreign bodies from the upper-aerodigestive tract of children in Puerto Rico. Bol Asoc Med P R 92:124–129

Dindar H, Konkan R, Cakmak M et al. (1994) A bronchopleurocutaneous fistula caused by an unusual foreign body aspiration simulating acute abdomen. Eur J Pediatr 153:136–137

Dogan K, Kaptanoglu M, Onen A et al. (1999) Unusual sites of uncommon endobronchial foreign bodies. Reports of four cases. Scand Cardiovasc J 33:309–311

Elhassani NB (1988) Tracheobronchial foreign bodies in the Middle East. A Baghdad study. J Thorac Cardiovasc Surg 96:621–625

Ernst KD, Mahmud F (1994) Reversible cystic dilatation of distal airways due to foreign body. South Med J 87:404–406

Esclamado RM, Richardson MA (1987) Laryngotracheal foreign bodies in children: a comparison with bronchial foreign bodies. Am J Dis Child 141:259–262

Fabian MC, Smitheringale A (1996) Hemoptysis in children: the hospital for sick children experience. J Otolaryngol 25:44–45

Farkash J, Liberman A, Bar-Ziv J et al. (1982) Respiratory tract foreign bodies in children. Harefuah 10:383–387

Felman AH (1982) The pediatric chest. Thomas, Springfield, Ill, pp 411–423

Fini-Storchi I, Ninu MB (1996) Atypical intranasal foreign body. Ear Nose Throat J 75:796–799

Fitzpatrick PC, Guarisco JL (1998) Pediatric airway foreign bodies. J LA State Med Soc 150:138–141

Friedman E (2000) Tracheobronchial foreign bodies. Otolaryngol Clin North Am 33:179–185

Fuentes S, Bouillot P, Regis J et al. (2001) Management of brain stem abscess. Br J Neurosurg 15:57–62

Garcia-Pena P, Lucaya J (1999) Chest CT in children: main applications and advantages. Pediatr Pulmonol S18:56–59

Gatch G, Myre L, Black RE (1987) Foreign body aspiration in children. Causes, diagnosis, and prevention. AORN J 46:850–861

Giudicelli J, Chapelon C, Louis D et al. (1996) Intrabronchial inhaled seed migration. Value of ultrasonography in the diagnosis of pleural-cutaneous fistula. Rev Mal Respir 13:428–429

Glinjongol C, Kiatchaipipat S, Thepcharoenniran S (2004) Severe sand aspiration: a case report with complete recovery. J Med Assoc Thai 87:825–828

Grad R, Taussig LM (1990) Acute infections producing uper airway obstruction. In: Chenick V, Kendig EL (eds) Disorders of the respiratory tract in children, Saunders, Philadelphia, pp 336–348

Grunebaum M, Adler S, Varsano I (1979) The paradoxial movement of the mediastinum. A diagnostic sign of foreign-body aspiration during childhood. Pediatr Radiol 8:213–218

Gupta AK, Berry M (1991) Detection of a radiolucent bronchial foreign body by computed tomography. Pediatr Radiol 21:307–308

Haliloglu M, Ciftci AO, Oto A (2003) CT virtual bronchoscopy in the evaluation of children with suspected foreign body aspiration. Eur J Radiol 48:188–192

Halvorson DJ, Merritt RM, Mann C et al. (1996) Management of subglottic foreign bodies. Ann Otol Rhinol Laryngol 105:141–144

Hanukoglu A, Fried D, Hadas E (1980) Pneumomediastinum and subcutaneous emphysema following foreign body aspiration. Harefuah 98:262–264

Hanukoglu A, Fried D, Segal S (1986) Loss of voice as sole symptom of subglottic foreign-body aspiration. Am J Dis Child 140:973

Hillman BC, Kurtzweg FT, McCook WW et al. (1980) Foreign body aspiration of grass inflorescences as a cause of hemoptysis. Chest 78:306–309

Hoeve LJ, Rombout J (1992) Pediatric laryngobronchoscopy. 1332 procedures stored in a data base. Int J Pediatr Otorhinolaryngol 24:73–82

Holan G, Ram D (2000) Aspiration of an avulsed primary incisor. Int J Paediatr Dent 10:150–152

Holland NJ, Trumbull HR (1979) Chronic foreign body aspiration diagnosed by lung scan. Clin Pediatr (Phila) 18:497–500

Ikeda M, Himi K, Yamauchi Y et al. (2001) Use of digital subtraction fluoroscopy to diagnose radiolucent aspirated foreign bodies in infants and children. Int J Pediatr Otorhinolaryngol 61:233–242

Imaizumi H, Kaneko M, Nara S et al. (1994) Definitive diagnosis and location of peanuts in the airways using magnetic resonance imaging techniques. Ann Emerg Med 23:1379–1382

Jain L, Sivieri E, Bhutani VK (1986) Aspiration of pacifiers. Pediatrics 78:955–956

Joseph PM, Berdon WE, Baker DH et al. (1976) Upper airway obstruction in infants and small children: improved radiographic diagnosis by combining filtration, high kilovoltage and magnification. Radiology 121:143–148

Kaptanoglu M, Dogan K, Onen A et al. (1999) Turban pin aspiration; a potential risk for young Islamic girls. Int J Pediatr Otorhinolaryngol 48:131–135

Karakoc F, Karadag B, Akbenlioglu C et al. (2002) Foreign body aspiration: what is the outcome? Pediatr Pulmonol 34:30–36

Keith FM, Charrette EJ, Lynn RB et al. (1980) Inhalation of foreign bodies by children: a continuing challege in management. Can Med Assoc J 122:55–57

Kocaoglu M, Bulakbasi N, Soylu K et al. (2006) Thin-section axial multidetector computed tomography and multiplanar reformatted imaging of children with suspected foreign-body aspiration: is virtual bronchoscopy overemphasized? Acta Radiol 47:746–751

Konen E, Katz M, Rozenman J et al. (1998) Virtual bronchoscopy in children: early clinical experience. Am J Roentgenol 171:1699–1702

Kosucu P, Ahmetoglu A, Koramaz I et al. (2004) Low-dose MDCT and virtual bronchoscopy in pediatric patients with foreign body aspiration. AJR Am J Roentgenol 183:1771–1777

Kuhn JP (1993) High-resolution computed tomography of pediatric pulmonary parenchymal disorders. Radiol Clin North Am 31:533–551

Laks Y, Barzilay Z (1988) Foreign body aspiration in childhood. Pediatr Emerg Care 4:102–106

Levy M, Glick B, Springer C et al. (1983) Bronchoscopy and bronchography in children. Experience with 110 investigations. Am J Dis Child 137:14–16

Lim-Dunham JE, Yousefzadeh DK (1999) The interrupted bronchus:a fluoroscopic sign of bronchial foreign body in infants and children. AJR Am J Roentgenol 173:969–972

Lima JA, Fischer GB (2002) Foreign body aspiration in children. Paediatr Respir Rev 3:303–307

Linegar AG, von Oppell UO, Hegemann S et al. (1992) Tracheobronchial foreign bodies. Experience at Red Cross Children's Hospital 1985–1990. S Afr Med J 82:84–87

Losek JD (1990) Diagnostic difficulties of foreign body aspiration in children. Am J Emerg Med 8:348–350

Lucaya J, Garcia-Pena P, Herrera L et al. (2000) Expiratory chest CT in children. AJR Am J Roentgenol 174:235–241

Lull RJ, Anderson JH, Telepak RJ et al. (1980) Radionuclide imaging in the assessment of lung injury. Semin Nucl Med 10:302–310

Maayan C, Avital A, Elpeleg ON et al. (1993) Complications following oat head aspiration. Pediatr Pulmonol 15:52–54

Malis DJ, Hayes DK (1995) Retained bronchial foreign bodies: is there a role for high-resolution computed tomography scan? Otolaryngol Head Neck Surg 112:341–346

Mangge H, Plecko B, Grubbauer HM et al. (1993) Late-onset miliary pneumonitis after near drowning. Pediatr Pulmonol 15:122–124

Mantel K, Butenandt I (1986) Tracheobronchial foreign body aspiration in childhood. A report on 224 cases. Eur J Pediatr 145:211–216

McHugh K (2005) CT dose reduction in pediatric patients. AJR 184:1706-1707

Mearns AJ, England JM (1975) Dissolving foreign bodies in the trachea and bronchus. Thorax 30:461–463

Menendez AA, Gotay Cruz F, Seda FJ et al. (1991) Foreign body aspiration: experience at the University Pediatric Hospital. P R Health Sci J 10:127–133

Metrangelo S, Monetti C, Meneghini L et al. (1999) Eight years' experience with foreign-body aspiration in children: what is really important for a timely diagnosis? J Pediatr Surg 34:1229–1231

Mignon F, Mesurolle B, Chambellan A et al. (1997) Foreign body granuloma mimicking bronchial tumor. Aspects in X-ray computed tomography with views by virtual endoscopy. J Radiol 78:1181–1184

Morijiri M, Seto H, Kageyama M et al. (1994) Assessment of peanut aspiration by MRI and lung perfusion scintigram. J Comput Assist Tomogr 18:836–838

Mu LC, Sun DQ, He P (1990) Radiological diagnosis of aspirated foreign bodies in children: review of 343 cases. J Laryngol Otol 104:778–782

Murthy PNS, Ingle VS, Edicula G et al. (2001) Sharp foreign bodies in the tracheobronchial tree. Am J Otolaryngol 22:154–156

Musemeche CA, Kosloske AM (1986) Normal radiographic findings after foreign body aspiration. When the history counts. Clin Pediatr (Phil) 25:624–625

Newson TP, Parshuram CS, Berkowitz RG et al. (1998) Tension pneumothorax secondary to grass head aspiration. Pediatr Emerg Care 14:287–289

Nikolaizik WH, Warmer JO (1994) Aetiology of chronic suppurative lung disease. Arch Dis Child 70:141–142

Nimkin K, Kleinman PK, Zwerdling RG et al. (1995) Localized pneumothorax with lobar collapse and diffuse obstructive airway disease. Pediatr Radiol 25:449–451

Nolte KB (1993) Esophageal foreign bodies as child abuse. Potential fatal mechanisms. Am J Forensic Med Pathol 14:323–326

Northcote RJ (1983) Pulmonary aspiration presenting with generalised convulsions. Scott Med J 28:368–370

Oguz F, Citak A, Unuvar E et al. (2000) Airway foreign bodies in childhood. Int J Pediatr Otorhinolaryngol 52:11–16

Oliveira CF, Almeida JF, Troster EJ et al. (2002) Complications of tracheobronchial foreign body aspiration in children: report of 5 cases and review of the literature. Rev Hosp Clin Fac Med Sao Paulo 57:108–111

O'Uchi T, Tokumaru A, Mikami I et al. (1992) Value of MR imaging in detecting a peanut causing bronchial obstruction. AJR Am J Roentgenol 159:481–482

Pasaoglu I, Dogan R, Demircin M et al. (1991) Bronchoscopic removal of foreign bodies in children: retrospective analysis of 822 cases. Thorac Cardiovasc Surg 39:95–98

Piepsz A (1988) Late sequelae of foreign body inhalation. A multicentric scintigraphic study. Eur J Nucl Med 13:578–581

Pinto A, Scaglione M, Pinto F et al. (2006) Tracheobronchial aspiration of foreign bodies: current indications for emergency plain chest radiography. Pediatr Radiol 111:497–506

Ramadan HH, Bu-Saba N, Baraka A et al. (1992) Management of an unusual presentation of foreign body aspiration. J Laryngol Otol 106:751–752

Reilly JS, Walter MA (1992) Consumer product aspiration and ingestion in children: analysis of emergency room reports to the National Electronic Injury Surveillance System. Ann Otol Rhinol Laryngol 101:739–741

Rogers LF, Igini JP (1975) Beverage can pull-tabs. Inadvertent ingestion or aspiration. JAMA 233:345–348

Sane SM, Faerber EN, Belani KK (1999) Respiratory foreign bodies and *Eikenella corrodens* brain abscess in two children. Pediatr Radiol 29:327–330

Schmidt H, Manegold BC (2000) Foreign body aspiration in children. Surg Endosc 14:644–648

Scully RE, Mark EJ, McNeely BU (1983) Case records of the Massachusetts General Hospital: case 48–1983. N Engl J Med 309:1374–1381

Scully RE, Mark EJ, McNeely BU (1998) Case records of the Massachusetts General Hospital: case 31–1998. N Engl J Med 339:1144–1151

Seibert RW, Seibert JJ, Williamson SL (1986) The opaque chest: when to suspect a bronchial foreign body. Pediatr Radiol 16:193–196

Senkaya I, Sagdic K, Gebitekin C et al. (1997) Management of foreign body aspiration in infancy and childhood. A life-threatening problem. Turk J Pediatr 39:353–362

Shegal A, Singh V, Chandra J et al. (2002) Foreign body aspiration. Indian Pediatr 39:1006–1010

Shivakumar AM, Naik AS, Prashanth KB et al. (2003) Tracheobronchial foreign bodies. Indian J Pediatr 70:793–797

Siddiqui MA, Banjar AH, Al-Najjar SM et al. (2000) Frequency of tracheobronchila foreign bodies in children and adolescents. Saudi Med J 21:368–371

Silva AB, Muntz HR, Clary R (1998) Utility of conventional radiography in the diagnosis and management of pediatric airway foreign bodies. Ann Otol Rhinol Laryngol 107(10/1):834–838

Smith PC, Swischuk LE, Fagan CJ (1974) An elusive and often unsuspected cause of stridor or pneumonia (the esophageal foreign body). Am J Roentgenol Radium Ther Nucl Med 122:80–89

Sofer S, Bar-Ziv J, Scharf SM (1984a) Pulmonary edema following relief of upper airway obstruction. Chest 86:401–403

Sofer S, Baer R, Gussarsky Y et al. (1984b) Pulmonary edema secondary to chronic upper airway obstruction. Hemodynamic study in a child. Intensive Care Med 10:317–319

Sofer S, Bar-Ziv J, Mogle P (1985) Pulmonary oedema following choking: report of two cases. Eur J Pediatr 143:295–296

Spencer MJ, Millet VE, Dudley JP et al. (1981) Grassheads in the tracheobronchial tree: two different outcomes. Ann Otol Rhinol Laryngol 90:406–408

Steelman R, Millman E, Steiner M et al. (1997) Aspiration of a primary tooth in a patient with a tracheostomy. Spec Care Dentist 17:97–99

Steen KH, Zimmermann T (1990) Tracheobronchial aspiration of foreign bodies in children: a study of 94 cases. Laryngoscope 100:525–530

Strickland AL, Elhassani SB, Stowe DG (1987) Aspiration of metallic foil by children: report of two cases. J S C Med Assoc 83:49–51

Svedstrom E, Puhakka H, Kero P (1989) How accurate is chest radiography in the diagnosis of tracheobronchial foreign bodies in children? Pediatr Radiol 19:520–522

Svensson G (1985) Foreign bodies in the tracheobronchial tree. Special references to experience in 97 children. Int J Pediatr Otorhinolaryngol 8:243–251

Swanson KL, Edell ES (2001) Tracheobronchial foreign bodies. Chest Surg Clin N Am 11:861–872

Szold A, Udassin R, Seror D et al. (1991) Acquired tracheoesophageal fistula in infancy and childhood. J Pediatr Surg 26:672–675

Tashita H, Inoue R, Goto E et al. (1998) Magnetic resonance imaging for early detection of bronchial foreign bodies. Eur J Pediatr 157:442

Teixidor de Otto J, Negro F, Gutierrez C (1980) Removal of foreign bodies from the upper airways and the bronchial tree of small children. Z Kinderchir Grenzgeb 30:137–140

Theander G (1970) Motility of diaphragm in children with bronchial foreign bodies. Acta Radiol (Diagn) 10:113–129

Tjhen KY, Schmaltz AA, Ibrahim Z et al. (1978) Pneumopericardium as a complication of foreign body aspiration. Pediatr Radiol 7:121–123

Ucan ES, Tahaoglu K, Mogolkoc N et al. (1996) Turban pin aspiration syndrome: a new form of foreign body aspiration. Respir Med 90:427–428

Van Looij MA, Rood PP, Hoeve LJ et al. (2003) Aspirated foreign bodies in children: why are they more commonly found on the left? Clin Otolaryngol Allied Sci 28:364–367

Wales J, Jackimczyk K, Rosen P (1983) Aspiration following a cave-in. Ann Emerg Med 12:99–101

Wesenberg RL, Blumhagen JD (1979) Assisted expiratory chest radiography: an effective technique for the diagnosis of foreign-body aspiration. Radiology 130:538–539

Wiseman NE (1984) The diagnosis of foreign body aspiration in childhood. J Pediatr Surg 19:531–535

Witt WJ (1985) The role of rigid endoscopy in foreign body management. Ear Nose Throat J 64:70–74

Yousser M, Rostum M, Dubaybo BA (2002) Laryngeal hirudiniasis: an unusual cause of airway obstruction and hemoptysis. Pediatr Pulmonol 33:224–226

Zaytoun GM, Rouadi PW, Baki DH (2000) Endoscopic management of foreign bodies in the tracheobronchial tree: predictive factors for complications. Otolaryngol Head Neck Surg 123:311–316

Zerella JT, Dimler M, McGill LC et al. (1998) Foreign body aspiration in children: value of radiography and complications of bronchoscopy. J Pediatr Surg 33:1651–1654

Zuniga S, De Manana M, Monge M et al. (2000) Vegetal foreign body in the airway: an unusual cause of hemoptysis in childhood. Rev Med Chil 128:323–329 (Spanish)

Imaging Evaluation of the Thymus and Thymic Disorders in Children

10

Donald P. Frush

CONTENTS

10.1 **Introduction** *215*

10.2 **Thymic Imaging: Historical Perspective** *216*

10.3 **Thymic Development** *218*

10.4 **Thymic Structure and Function** *218*

10.5 **Imaging Appearance of the Normal Thymus Gland** *222*

10.6 **Thymic Disorders: Pattern-Oriented Classification** *228*

10.6.1 Abnormalities in Thymic Size, Shape, or Location *228*

10.6.2 Focal Thymic Disorders *230*

10.6.3 Diffuse or Multifocal Thymic Disorders *233*

10.6.4 Specific Thymic Imaging Features: Calcification, Fat, Cysts *237*

10.7 **Conclusion** *239*

References *239*

10.1 Introduction

An understanding of the embryology and normal development, anatomy and histology, and the various pediatric disorders that can involve the thymus is important for radiologists for a number of reasons. First, familiarity with the spectrum of appearances, including size and location, of the normal thymus in infants and children, minimizes the potential for diagnostic errors. In addition, both the gross and microscopic constitution of the thymus gland contribute to the imaging appearance of the normal thymus. Each of the noninvasive imaging modalities including radiography, sonography, computed tomography (CT), magnetic resonance imaging (MRI), and nuclear scintigraphy (including PET-CT) can provide unique and often complementary information in the evaluation of thymic disorders in children. By understanding the benefits and limitations of each of these modalities with respect to these thymic disorders, the radiologist is better able to design and implement an effective and expeditious imaging algorithm.

To this end, this chapter is divided into the following sections: historical perspective; thymic embryology, normal anatomy and function; imaging modalities and normal imaging appearances; and a pattern-oriented approach to imaging in pediatric thymic disorders. This pattern-oriented approach has been selected as it provides a familiar and practical method for the radiologist in the recognition and classification of thymic disease and is based on imaging features including thymic masses (Table 10.1), diffuse thymic infiltration, and thymic calcification or fat (Table 10.2).

D. P. Frush, MD
Professor of Radiology, Chief, Division of Pediatric Radiology, Duke University Medical Center, 1905 McGovern-Davison Children's Health Center, Erwin Road, Box 3808, Durham, NC 27710, USA

Table 10.1. Pediatric thymic masses

Non-neoplastic masses

- Thymic cyst
- Vascular malformation
- Castleman's disease
- Hematoma
- Abscess

Neoplastic masses

- Epithelial tumors
  - Thymoma (invasive, noninvasive)
  - Thymic carcinoma
- Lymphoid tumors
  - Hodgkin lymphoma
  - Non-Hodgkin lymphoma
    - Lymphoblastic
    - Large cell
- Germ cell tumors
- Stromal tumors
  - Thymolipoma
- Neuroendocrine tumors
  - Carcinoid
- Hemangioma
- Metastasis
  - Neuroblastoma

Table 10.2. Specific thymic imaging features

Thymic cysts and cystic conditions

- True thymic cysts (unilocular, multilocular)
- Germ cell tumors
- Langerhans cell histiocytosis
- Lymphatic malformation (e.g. cystic hygroma)
- Lymphoma
- Treated lymphoma
- Thymic dysplasia of HIV infection
- Thymoma
- Thymic carcinoma

Thymic calcification

- Germ cell tumor
- Langerhans cell histiocytosis
- Lymphoma
- Thymic cysts

Fat containing thymic masses

- Thymolipoma
- Germ cell tumor (usually mature teratoma)
- Vascular malformations

10.2
Thymic Imaging: Historical Perspective

The history of the thymus gland is long, and is punctuated by a great deal of misunderstanding. This colorful history has been reviewed in greater detail (Jacobs et al. 1999). However, a brief summary of this historical perspective on the thymus gland is worthwhile, with particular emphasis on the relationship of the thymus to the origin and development of the subspecialty of pediatric radiology.

The name *thymus* is Latin and derived from the Greek *thymos* meaning "warty excrescence", a descriptor similar to the appearance of another namesake, the thyme plant. One of the earliest descriptions of the thymus dates back to circa 200 AD where the function of the thymus was said to be purification of the nervous system. It is interesting that the thymus gland was called, at that time, the "organ of mystery", a name which continues to have some truth even to this day. The first scientific treatise on the thymus was published in 1777. In 1832, Sir Astley Cooper published *The Anatomy of the Thymus Gland* in which he noted tremendous variability in size and appearance of the normal gland (Cooper 1832) (Fig. 10.1). While he offered no better explanation, Cooper did not believe the tenant of the time that the thymus gland simply occupied a space in the anterior mediastinum.

In the latter half of the nineteenth century, the thymus gland was implicated in two factitious conditions: thymic asthma and status thymicolymphaticus. Thymic asthma (also known as Kopp's asthma) was a disorder in which the "enlarged" thymus could cause sudden death, typically in infants. It is not hard to realize that those infants with sudden death (better known today as sudden infant death syndrome–SIDS) likely had normal sized thymic glands, while those succumbing to more chronic illnesses would have had thymic atrophy.

In 1889, a constitutional disorder known as status thymicolymphaticus was proposed as another disorder of the thymus responsible for sudden death (Paltauf 1889). This disorder was often implicated in the death of children during anesthesia. In fact, thymectomy was frequently advocated in children prior to anesthesia. About that time, the discovery

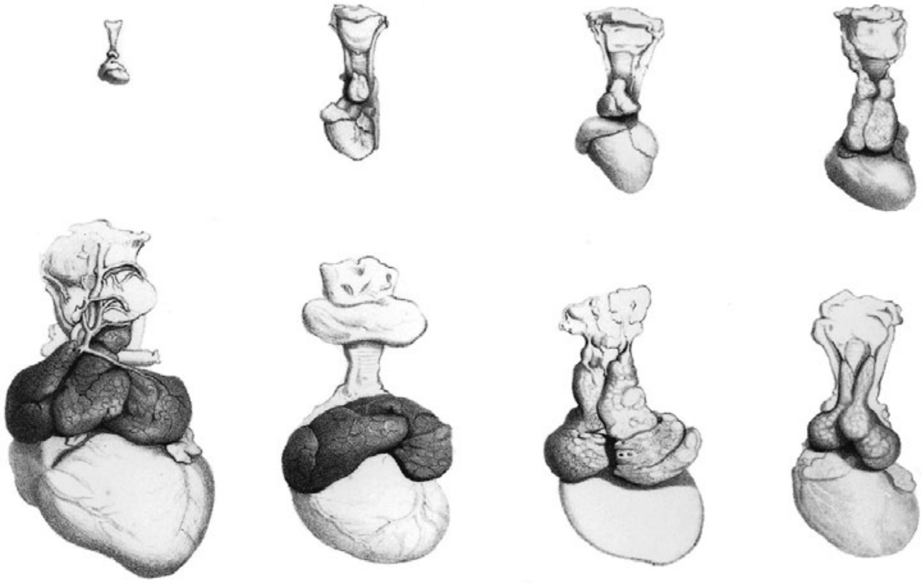

Fig. 10.1. Plate illustrating early work on the stages of thymic development. Each illustration, moving in a clockwise direction, represents the fetal thymus at monthly stages of development from 2 months (*left upper illustration*), to 9 months (*left lower illustration*). Cooper (1832) recognized the large normal thymic size

of X-rays provided an important diagnostic opportunity to help clarify the appearance of the thymus gland in children. However, this discovery also provided an unfortunate therapeutic option for both thymicolymphaticus and thymic asthma (Pohle 1950) (Figs. 10.2 and 10.3).

In 1907, the first treatment of thymic enlargement associated with substantial respiratory distress was reported, and reviewed by Oestreich (1995). This treatment provided a total dose of 75–200 rad (0.75–2.0 Gy) to the affected infant. Despite the connection between radiation-induced cancer and radiation over the next 2–3 decades, thymic irradiation was still a requested therapy even until the 1960s (Jacobs et al. 1999).

Dr. John Caffey, a pioneer in pediatric radiology, was instrumental in preventing further misunderstanding over the thymus gland, and the potential for misdiagnosis and ill-founded treatment. His description of the tremendous variability of the normal pediatric thymus gland is found in the earliest edition of his textbook (Caffey 1945). In addition, he felt that “destroying the thymus myth” (thymic asthma and status thymicolymphaticus) was one of his most important contributions to medicine (Jacobs et al. 1999).

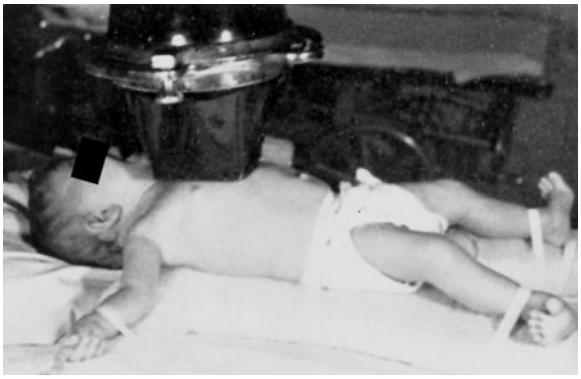
[redacted]

Fig. 10.2. The technique of thymic irradiation for status thymicolymphaticus or thymic asthma. (Reprinted with permission, Pohle 1950)

Despite the tremendous advances in understanding the appearance and nature of the thymus gland, there are still many mysteries left to be solved from an imaging standpoint. Work is still needed to clarify contemporary issues with the thymus gland. These include whether there is recurrent or residual thymic involvement by lymphoma, determining the functional activity of the normal thymic gland with positron emission tomography (PET), and characterizing the imaging manifestations of the thymus following immune constitution, such as thymic transplant for DiGeorge syndrome or bone marrow transplant for severe combined immune deficiency.

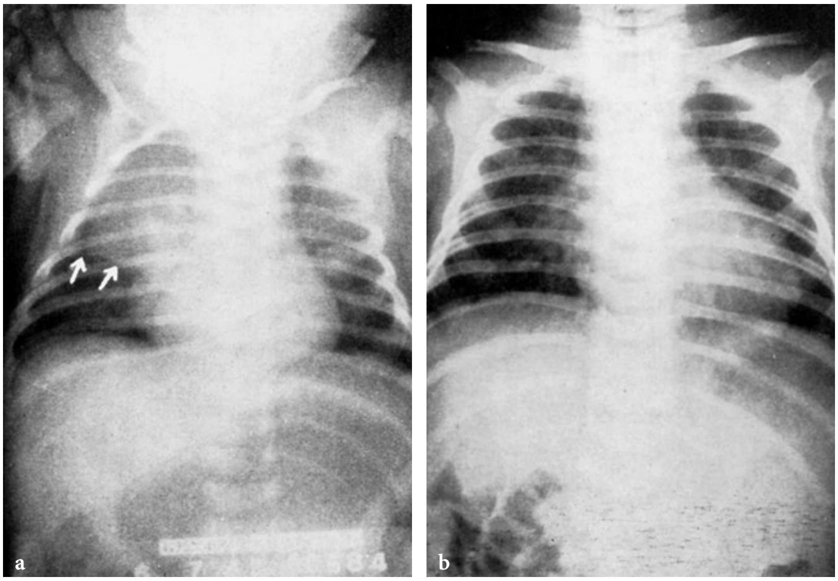

Fig. 10.3a,b. Effect of thymic irradiation on thymic size in an 8-week-old infant with "symptoms of thymic enlargement". **a** The opacity in the right upper lung was thought to be due to "atelectasis" secondary to thymic enlargement (*arrows*). **b** Following irradiation, frontal radiograph shows resolution of the opacity which likely represented normal thymic tissue. In the original text, it was noted that the child was "... now enjoying perfect health". (Reprinted with permission, Pohle 1950)

10.3
Thymic Development

A basic knowledge of the embryology and anatomy of the thymus is critical in understanding the variations in thymic anatomy and location. The thymus originates from the third pharyngeal pouch (Nishino et al. 2006; Priola et al. 2006); a smaller contribution by the fourth pouch can also occur (Kornstein 1995; Slovis et al. 1992). During fetal development, the thymus elongates with the development of the thymopharyngeal duct. This elongation begins in the neck, and the gland descends behind the thyroid and the sternocleidomastoid muscles. The two lobes fuse at the level of the transverse aorta (Slovis et al. 1992) beginning at about 8 weeks of gestational age. While the superior origin of the thymus gland usually atrophies, gross or microscopic rests of thymic tissue can persist from the origin of the gland, along the course of the thymopharyngeal duct. Thymopharyngeal duct remnants are the basis for thymic cysts.

Aberrant and ectopic locations of thymic tissue can be found with or without a coexistent normally located mediastinal thymus. While technically, aberrancy denotes tissue *along* the normal embryologic course, and ectopia denotes tissue *outside* this course, the terms are often used interchangeably. These aberrant or ectopic locations include the neck, and the thorax including retrocaval and posterior mediastinal locations simulating mediastinal or apical masses (Bach et al. 1991; Baysal et al. 1999; Kornstein 1995; Slovis et al. 1992; Swischuk and John 1996, Nishino et al. 2006).

Ectopic or aberrant thymic tissue does not usually cause symptoms. Reviews have noted that two-thirds of cases are seen in children under 10 years of age (Cure et al. 1995; Kacker et al. 1999; Marra et al. 1995). In one review of imaging literature, 13 cases of posterior mediastinal thymus were identified (Slovis et al. 1992). In the five cases in which thymic ectopia was isolated, the gland was always located on the right. Most cervical ectopic or aberrant thymic tissue is lateral in location. In the mediastinum, retrocaval extension of the thymic gland has been noted in up to 10% of children (Kuhn et al. 1993) (Fig. 10.4).

Both CT and MRI are well suited to the evaluation of abnormalities in thymic location. The thymic tissue, which can be cystic or solid, is well circumscribed. When cystic, the mass can be multilocular with septations (Cure et al. 1995).

10.4
Thymic Structure and Function

The normal thymus descends into the anterior mediastinum. The typical thymus gland is located just at or below the level of the left brachiocephalic vein,

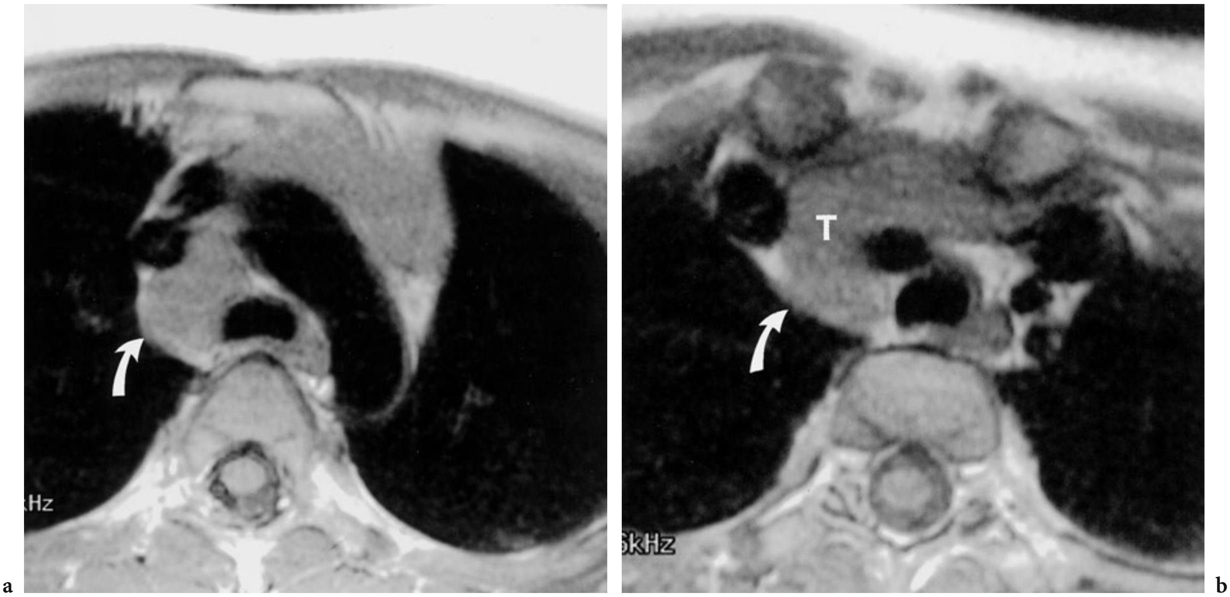

Fig. 10.4a,b. An 11-year-old male with retrocaval extension of normal thymus. **a** Axial T1-weighted (TR/TE 689/17; cardiac gated) magnetic resonance (MR) image at the level of the transverse thoracic aorta shows extension of the thymus (*curved arrow*) behind the superior vena cava. **b** MR image obtained at the level of the clavicular heads from the same sequence as in **a** shows the connection of the posteriorly extending thymus (*curved arrow*) to the thymus gland (*T*) in the typical anterior location. The MRI examination was obtained to evaluate for a mediastinal mass seen on echocardiography. The mass was the posterior extension of the thymus

and is bordered anteriorly by the sternum and more lateral anterior chest wall, posteriorly by the aortic arch and branch vessels, and inferiorly by either the pulmonary outflow tract, the anterior heart, or the anteromedial hemidiaphragms (depending on the level of inferior extent). In infancy and young childhood, the thymus takes on a quadrilateral configuration, with a triangular appearance in older children and adolescents. This configuration is best depicted with coronal imaging (Figs. 10.5 and 10.6).

The arterial supply for and venous drainage of the thymus are variable. In general, the thymic arteries originate from the internal thoracic artery, or superior and inferior thyroidal arteries. The arteries penetrate the gland laterally and superiorly; posterior penetration is less common (Kornstein 1995). In this latter case, the origin of the vessels can be from the common carotid or brachiocephalic arteries. Accessory thymic arteries can also occur. In addition, there may be asymmetry in vascular supply between the two lobes of the thymus in a child. Venous drainage is into the left brachiocephalic, internal thoracic, and inferior thyroidal veins. The thymic veins leave the gland through the medial aspect of both lobes. Occasionally, venous drainage can be into the superior vena cava or right brachiocephalic vein. While the vascular anatomy in the thymus gland has not received attention in imaging literature, these vessels can be identified, particularly with the cross-sectional imaging modalities. With the faster imaging times of multidetector array CT (MDCT), especially with CT angiographic technique, vascular opacification is improved and thymic vessels can be distinguished (Fig. 10.7). Using gradient recall sequences or MR angiography, vascular structures are also more readily identified than with spin echo sequences and can be distinguished from other similar appearing structures such as fibrous septa (Fig. 10.5).

Thymic size is highly variable even among children of the same size or age. Thymic size is either discussed in terms of weight (grams) or dimension (centimeters); the latter description is typical for imaging literature. The normal variations and abnormalities in thymus size will be discussed below.

Grossly, the appearance of the thymus is tan-yellow in color in children, being somewhat pinker in infancy. Because of fat, the adult gland becomes more yellow. Histologically, the thymus contains a collection of cells which are integral in the development of cellular immunity. It is these same cell types which

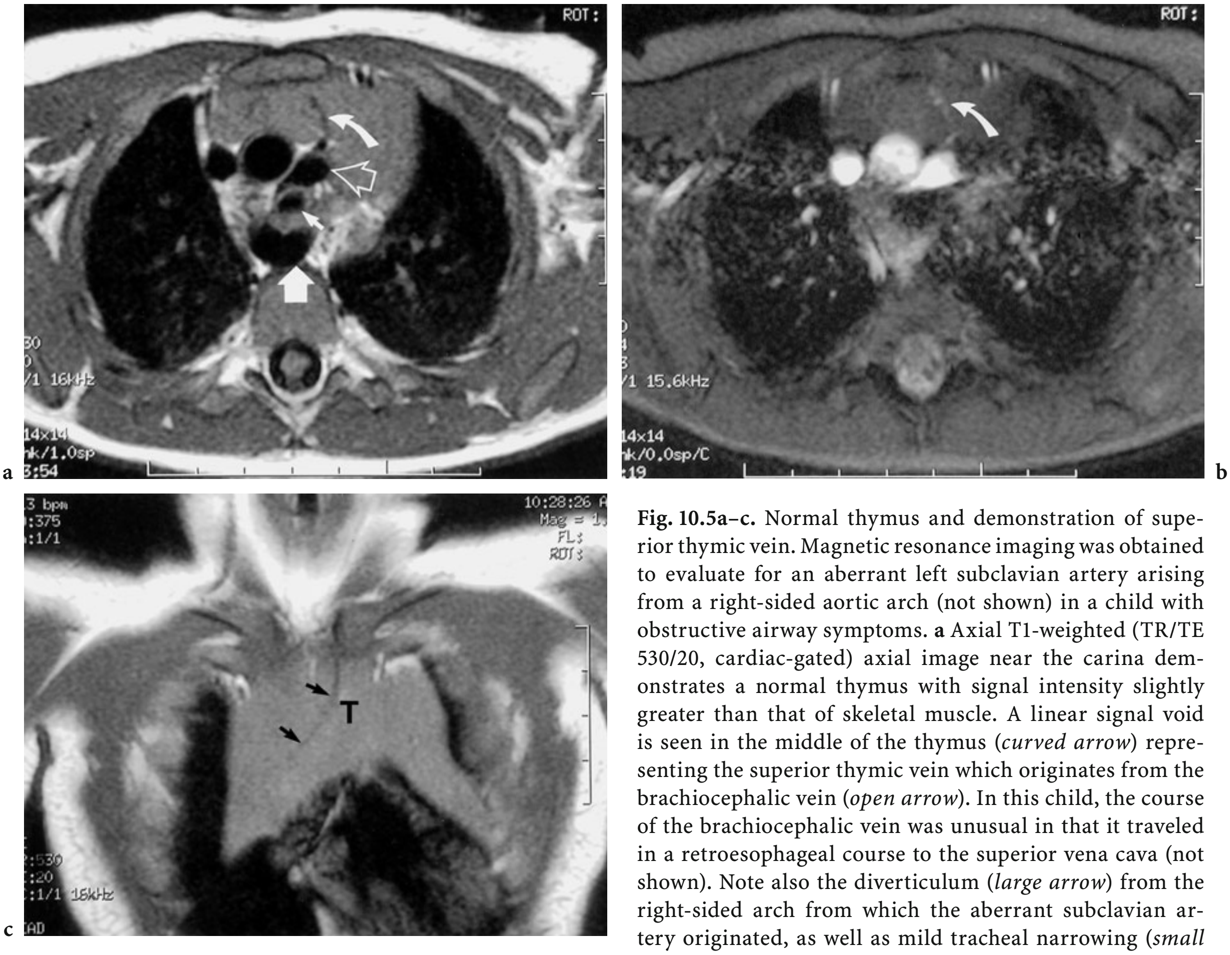

Fig. 10.5a–c. Normal thymus and demonstration of superior thymic vein. Magnetic resonance imaging was obtained to evaluate for an aberrant left subclavian artery arising from a right-sided aortic arch (not shown) in a child with obstructive airway symptoms. **a** Axial T1-weighted (TR/TE 530/20, cardiac-gated) axial image near the carina demonstrates a normal thymus with signal intensity slightly greater than that of skeletal muscle. A linear signal void is seen in the middle of the thymus (*curved arrow*) representing the superior thymic vein which originates from the brachiocephalic vein (*open arrow*). In this child, the course of the brachiocephalic vein was unusual in that it traveled in a retroesophageal course to the superior vena cava (not shown). Note also the diverticulum (*large arrow*) from the right-sided arch from which the aberrant subclavian artery originated, as well as mild tracheal narrowing (*small arrow*). **b** Gradient recall sequence (TR/TE 34/13; 33° flip angle) axial image identical to the level in **a** demonstrates high signal intensity representing flowing blood in the superior thymic vein (*curved arrow*). **c** Coronal T1-weighted (TR/TE 530/20, cardiac-gated) image of the anterior chest shows the quadrilateral configuration and the homogenous signal intensity of the thymus (*T*). The superior thymic vein (*small arrows*) that originates from the brachiocephalic vein is also evident

contribute to the variety of thymic masses, including epithelial, stromal, and lymphoid tumors. The thymic gland contains cortical and medullary regions. The cortex is composed primarily of lymphocytes (or thymocytes). Epithelial cells are found in both locations. Those located in the medulla, which contain keratin and mucin, are slightly different than those in the cortex. The medullary epithelial cells are known more familiarly as Hassall's corpuscles. The thymic gland also contains lymphocytes in various stages of maturation, macrophages and other mononuclear cells, and several other rarer cellular elements. One of these rarer types is the myxoid cell, which has a potential role in myasthenia gravis (Nishino et al. 2006).

Thymic involution begins to occur in puberty. This process involves replacement of the septa with fat and enlargement of the perivascular spaces (Kornstein 1995; Haynes and Hale 1999) (Fig. 10.8). In addition, there is an overall decrease in cellular density as well as cystic degeneration of existing cell populations. These age-related changes result in the fatty replaced thymus characteristic of adults. Notably, the overall gland *size*, given fatty replacement, changes little if at all (Haynes and Hale 1999). Age-related changes in thymic CT density have also been reported in children (Sklair-Levy et al. 2000). Based on the imaging features, these investigators concluded that this cellular involution and fatty replacement is at least in part responsible

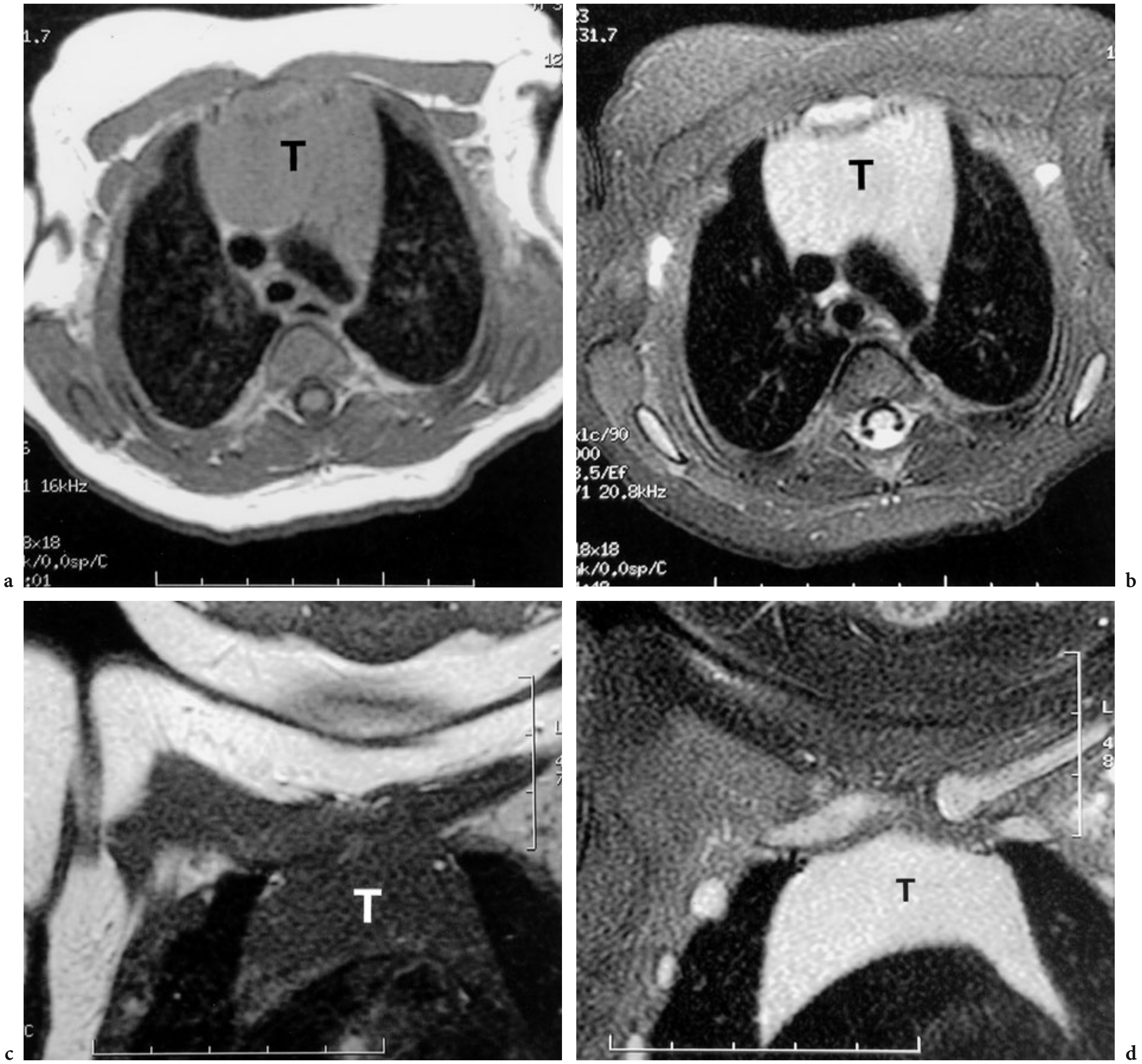

Fig. 10.6a–d. Magnetic resonance imaging (MRI) features of a normal thymus (*T*) in a 4-month-old male evaluated for Erb's palsy. **a** Axial T1-weighted (TR/TE 416/14) MR image at the level of the transverse thoracic aorta shows the homogeneous signal intensity which is isointense to skeletal muscle. **b** T2-weighted (TR/TE 4000/68; fast spin echo, fat saturated) MR image at the same level as in **a** demonstrates the homogeneous high signal intensity of the thymus. **c,d** Coronal T1-weighted (TR/TE 516/8) (**c**), and T2-weighted (TR/ 4000/65; fast spin echo, fat saturated) (**d**) MR images through the anterior mediastinum demonstrate the homogeneous signal intensity and quadrilateral configuration of the normal infant thymus

for the decrease in CT density seen with advancing age in children.

The thymus gland is an integral component in the development and maintenance of immunocompetency. The primary function of the gland is differentiation and maturation of T (thymic)-cells (this continues throughout life) which are key regulators in cellular immunity and normal B-cell (humoral) immunity (Hasselbalch et al. 1997). In disorders in which the thymus gland fails to develop normally (i.e., severe combined immunodeficiency or DiGeorge syndrome), the deficiency in thymic size seen by imaging can aid in the diagnosis of these disorders (Yin et al. 2000). For a recent in depth review of the histologic and molecular assessment of the thymus, the reader is referred elsewhere (Hale 2004).

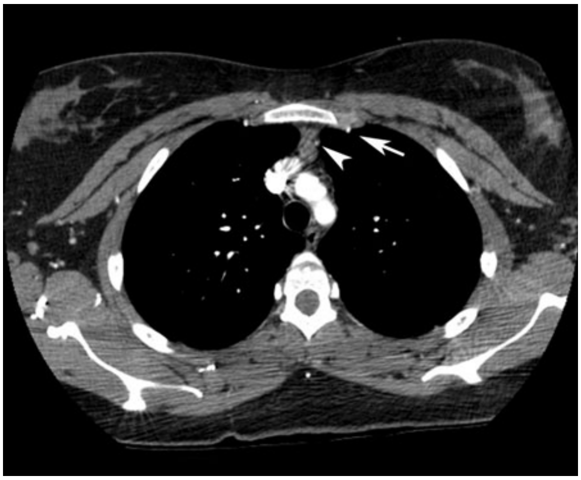

Fig. 10.7. A 17-year-old female with suspected pulmonary embolism (examination was normal). Axial image from MDCT angiogram demonstrates a thymic artery (*arrowhead*) which had originated from the left internal mammary artery (*arrow*)

10.5
Imaging Appearance of the Normal Thymus Gland

The normal thymus gland can have a variety of appearances (e.g., size, location, homogeneity) for an individual imaging modality. The modalities that are useful for thymic imaging consist of radiography, sonography, CT, MRI, and nuclear medicine. While we still have yet to fully understand the variety of morphologic and functional imaging appearances of the thymus gland in children, a great deal of valuable information has been obtained in the last 2–3 decades with the advent of several new imaging modalities. For this reason, the contribution of these relatively more recent modalities will be emphasized. As a basis for this more contemporary imaging approach, a brief discussion of the more traditional radiographic features (i.e., thymic size)

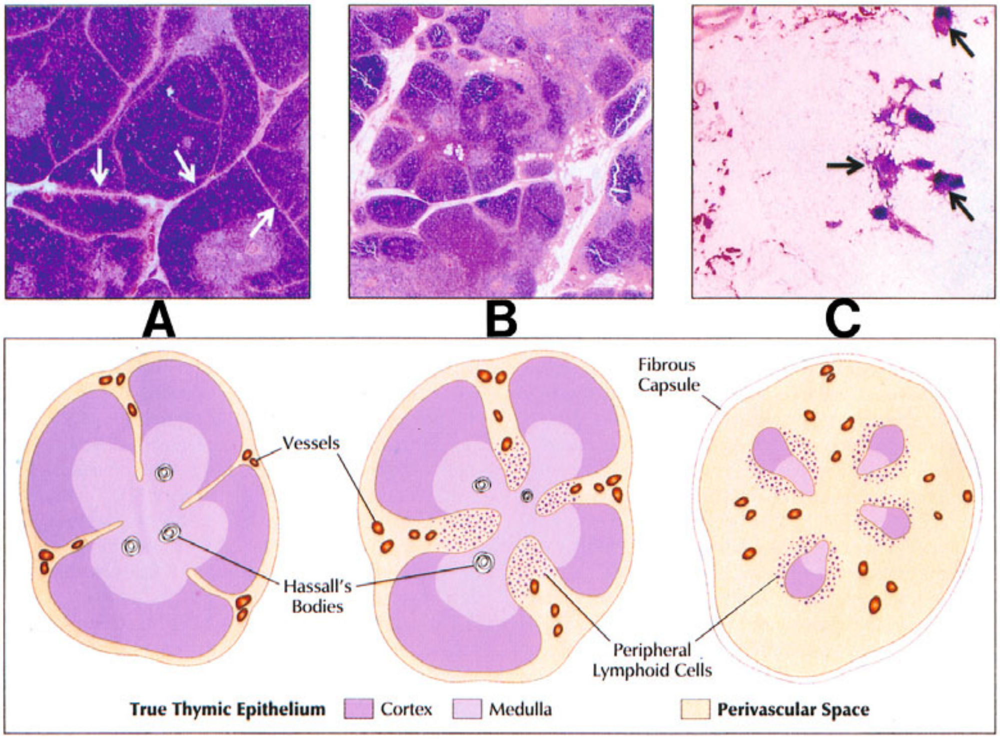

Fig. 10.8. Histologic and schematic representation of thymic structure at different ages. At 6 days of life (*A*), epithelial cells predominate. The perivascular compartment (*white arrows*) is small. At 15 years of age (*B*), the size of the perivascular space is increasing. At 65 years of age (*C*), the perivascular space contains fatty tissue, and surrounds small islands of true thymus (*white arrows*) (original histological preparations courtesy of Laura Hale, MD, Duke Medical Center; complete figure reprinted with permission, Haynes and Hale 1999)

will be provided, since this also applies to the more contemporary modalities.

The thymus can vary greatly in size during infancy and childhood. In infancy, the thymus makes up the greatest proportion of overall bodyweight compared to any other time in life. This relationship changes over time. The consensus has been that thymic size (in terms of weight) increases until puberty at which time the gland achieves its greatest gram weight. After this time, involution occurs. However, there is some disagreement about this; a recent review of this issue presented investigations that argued that thymic size actually varies little throughout childhood, ranging from 5 to 50 g from infancy to puberty (Kornstein 1995).

Radiographically, the variations in thymus gland size can virtually always be recognized based on location in the anterior mediastinum, homogeneous density, undulation of the lateral margins due to the effect of subjacent ribs on the pliable gland, and lack of mass effect on adjacent structures (Fig. 10.9). Most of these features, especially the homogeneity of the gland, transcend imaging modalities and provide a set of criteria which are important in determining whether the thymus is abnormal for other modalities as well.

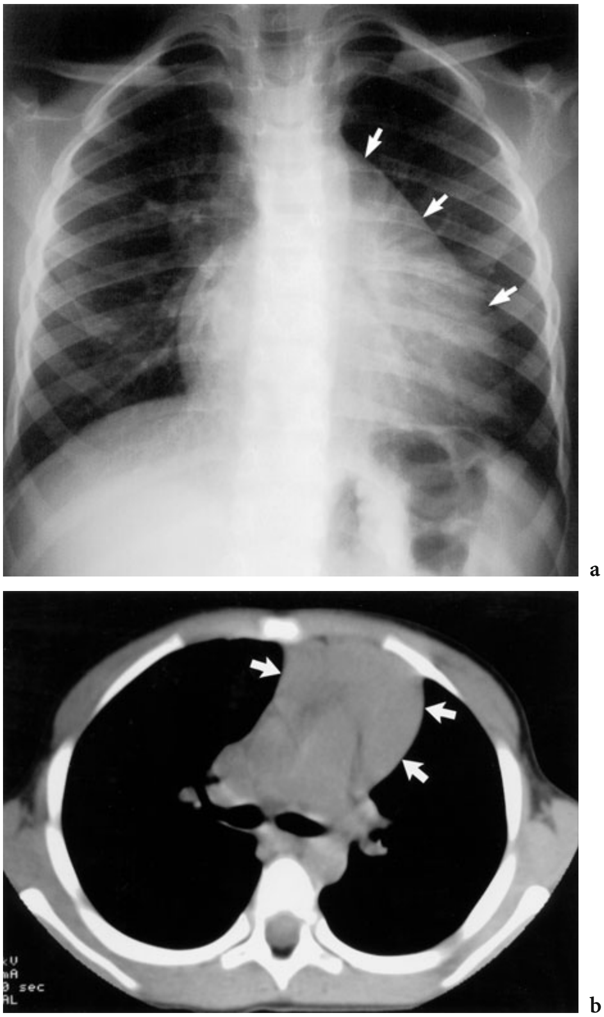

Fig. 10.9a,b. Normal thymic prominence in a 3-year-old boy referred for evaluation of a possible anterior mediastinal mass. **a** Posteroanterior chest radiograph demonstrates convex opacity that does not silhouette the main pulmonary artery (*arrows*). There is no displacement of the trachea or other mediastinal structures. **b** Axial non-contrast-enhanced CT image at the level of the main pulmonary artery demonstrates a normal thymus which is characterized by homogeneous soft tissue (isodense to skeletal muscle) in the anterior mediastinum with no displacement of intrathoracic structures

Sonographically, the thymus has an echotexture similar to the liver (Ben-Ami et al. 1993; Hasselbalch et al. 1997; Kim et al. 2000), but less than muscle (Ben-Ami et al. 1993), with punctate echoes and occasional echogenic lines (Fig. 10.10). Thymic size as determined using a thymic index (transverse and sagittal dimensions) has been reported to be variable in infants, but does correlate with birth weight (Hasselbalch et al. 1997; Iscan et al. 2000). Real time evaluation demonstrates the malleable appearance of the thymus during the respiratory cycle, which can help in separating normal thymic tissue from a large anterior mediastinal mass (Fig. 10.11). The gland is easily identified in infants under about 1 year of age due to incomplete ossification of the sternum and manubrium (Kim et al. 2000). Routine thymic sonography includes transverse, and sagittal midline and parasternal images (Coley 2005).

Sonography can be useful in thymic imaging given the lack of ionizing radiation, low cost, relative availability, and portability. One notable indication is for determining if an anterior mediastinal mass is normal thymus (Kim et al. 2000; Coley 2005). In the setting of a mass, the presence of various features including cysts, areas of calcification, or heterogeneous architecture, can suggest thymic pathology (Kim et al. 2000; Ben-Ami et al. 1993). Sonography should also be considered for biopsies or aspirations of thymic masses (Fig. 10.12). Recognition of variations in thymic position (e.g., retrocaval extension) during sonographic evaluation may also prevent additional and unnecessary imaging evaluation (Koumanidou et al. 1998; Linde et al. 1991; Wong et al. 2005) (see Fig. 10.4).

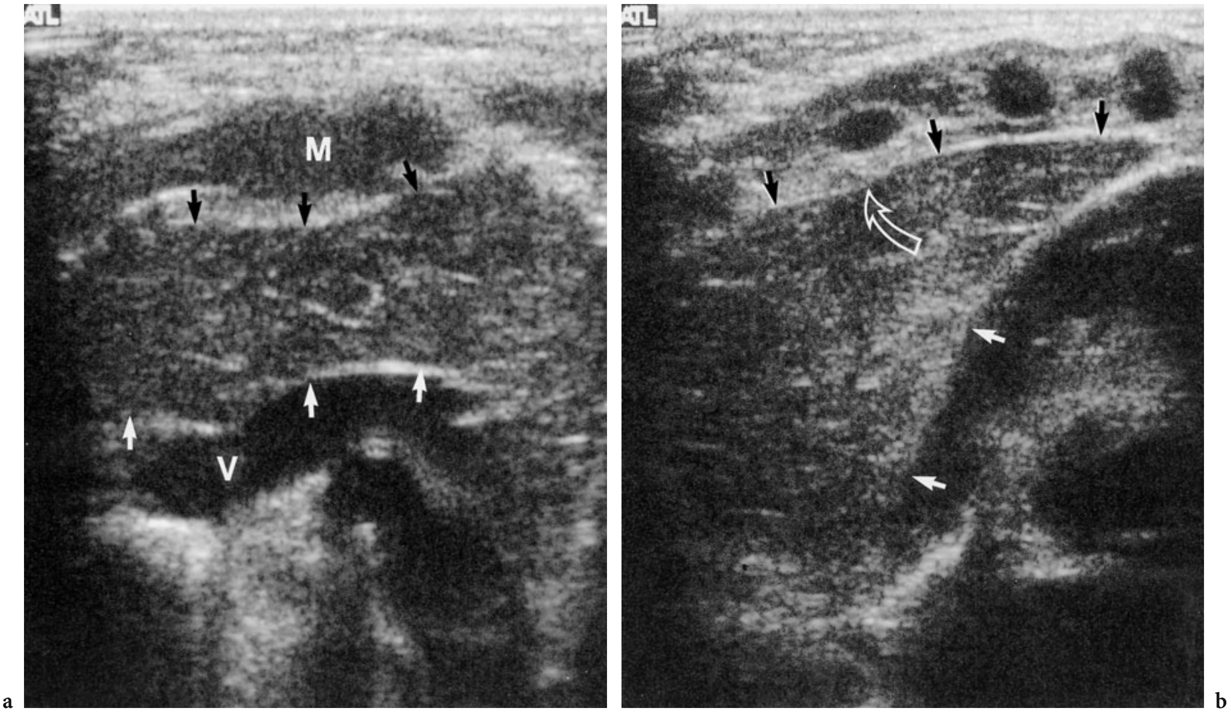
ATL
M
V
ATL
a
b

Fig. 10.10a,b. Normal thymic sonography in a 3-month-old male. **a** Transverse sonogram at the level of the brachiocephalic vein (*V*) shows hypoechoic thymic tissue (*arrows*) with punctate and linear echoes. Note how the manubrium (*M*) is not completely ossified. **b** Parasternal sagittal view of the thymus (*arrows*) shows the anterior undulation of the gland (*curved arrow*) due to the rib; this feature of the thymus gland is well recognized with radiography

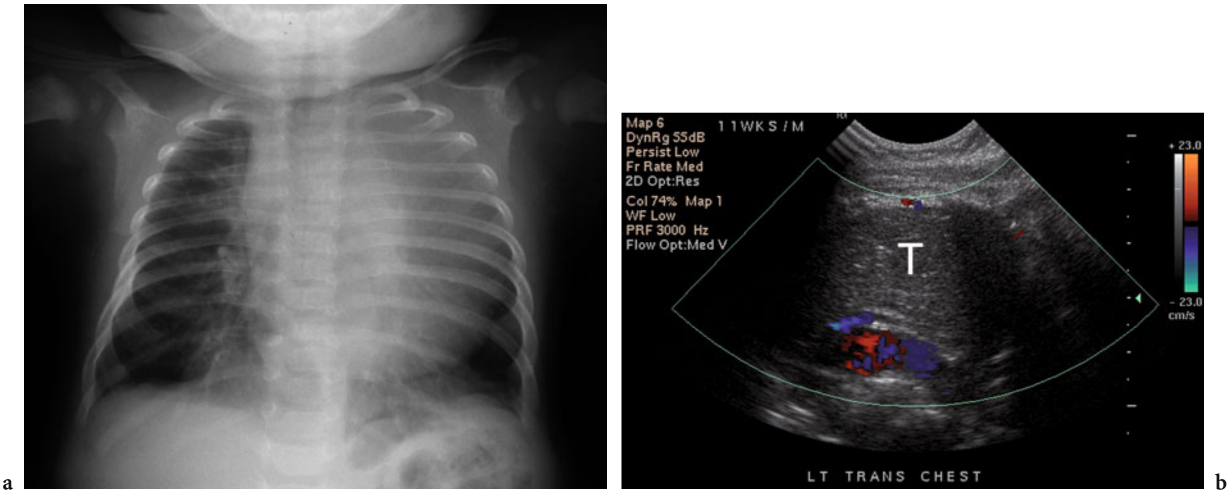
Map 6
DynRg 55dB
Persist Low
Fr Rate Med
2D Opt:Res
Col 74% Map 1
WF Low
PRF 3000 Hz
Flow Opt:Med V
11WKS/M
T
+ 23.0
- 23.0
cm/s
LT TRANS CHEST
a
b

Fig. 10.11a,b. Infant with cough and normal thymus. **a** Frontal chest radiograph demonstrates abnormal configuration to the upper mediastinum with hyperinflation. While it was felt that this was most likely airtrapping from airways disease and a normal thymus, this was confirmed by sonography. **b** Transverse sonogram at the level of the brachiocephalic vein (demonstrated with color Doppler) demonstrates normal prominent thymus (*T*)

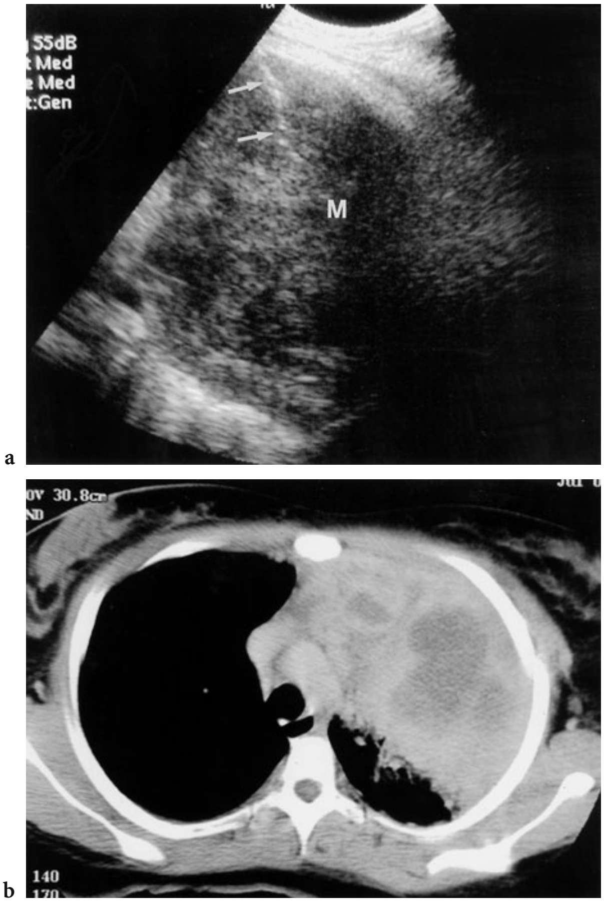

Fig. 10.12a,b. An 18-year-old female with Hodgkin lymphoma involving the anterior mediastinum and thymus gland. **a** Initial attempt at sonographically-guided percutaneous biopsy was unsuccessful given the high degree of fibrosis and necrotic tissue which was eventually determined after sternotomy and biopsy. Note that the needle track (*arrows*) is well seen in the mass (*M*). **b** Axial IV contrast-enhanced computed tomography examination at the level of the transverse arch reveals a heterogeneous mass in the anterior mediastinum. Low attenuation regions represent areas of necrosis

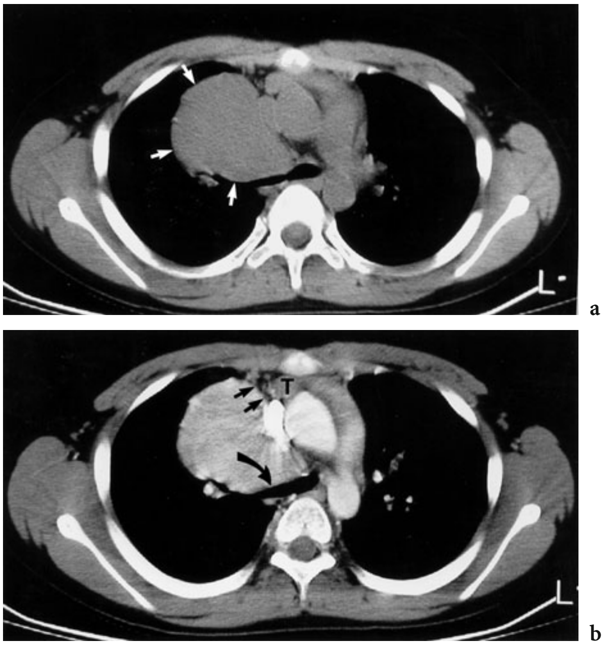

Fig. 10.13a,b. Distinguishing thymic from extrathymic disease: Castleman's disease of the anterior mediastinum in an 11-year-old boy. **a** Non-contrast-enhanced, axial computed tomography image just below the level of the transverse aorta arch demonstrates a mass in the anterior mediastinum (*arrows*). **b** Following administration of IV contrast material, there is greater enhancement than adjacent thymus. Note fat plane (*arrows*) separating nodal mass and thymus (*arrows*). The right main bronchus is also mildly narrowed (*curved arrow*)

CT is an excellent modality for thymic evaluation. While ionizing radiation, the use of intravenous contrast material, and relatively greater cost are disadvantages compared with sonography, low dose scanning can minimize radiation risk. In addition, IV contrast reactions are actually quite rare in children (Cohen and Smith 1994). CT provides excellent information on the thymus itself and the effect of thymic disorders on adjacent structures. CT helps to determine whether a mass or other opacity is thymic in origin (Figs. 10.13 and 10.14), and can be used as a problem solving tool in cases of uncertain radiographic findings (Figs. 10.15 and 10.16). Abnormalities such as calcification, fat, cysts, and soft tissue heterogeneity are well depicted (Fig. 10.17). In addition, the lung, airways and other adjacent structures are best evaluated by CT compared with sonography, MRI, or nuclear medicine.

The CT appearance of the normal thymus has been previously well described (St Amour et al. 1987). The thymus gland has homogenous soft tissue attenuation (see Fig. 10.9) with little variation in size in children aged 0–5 years (1.6 + 4.5 cm) to teenagers aged 16–19 years of age (1.8 + 4.2 cm) (St Amour et al. 1987). The left lobe is often slightly more prominent than the right lobe. The lateral edges of both the lobes are straight or slightly convex (infants and young children), or slightly concave (older children). Age-related changes in thymic density have been reported in children (Sklair-Levy et al. 2000). Thymic density was

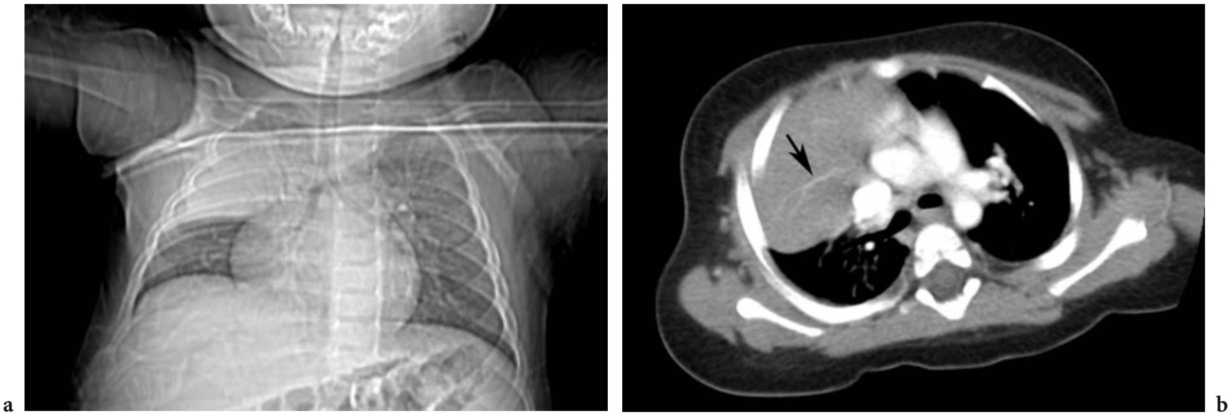

Fig. 10.14a,b. Normal thymus mimicking pneumonia. 6-month-old male treated for recurrent right upper lobe pneumonia. **a** Frontal view of CT topogram (scout) shows right upper level opacity. **b** With IV contrast enhanced CT examination, axial image of the upper chest demonstrates that this opacity is a prominent thymus. Note the ability to see thymic veins (*arrows*)

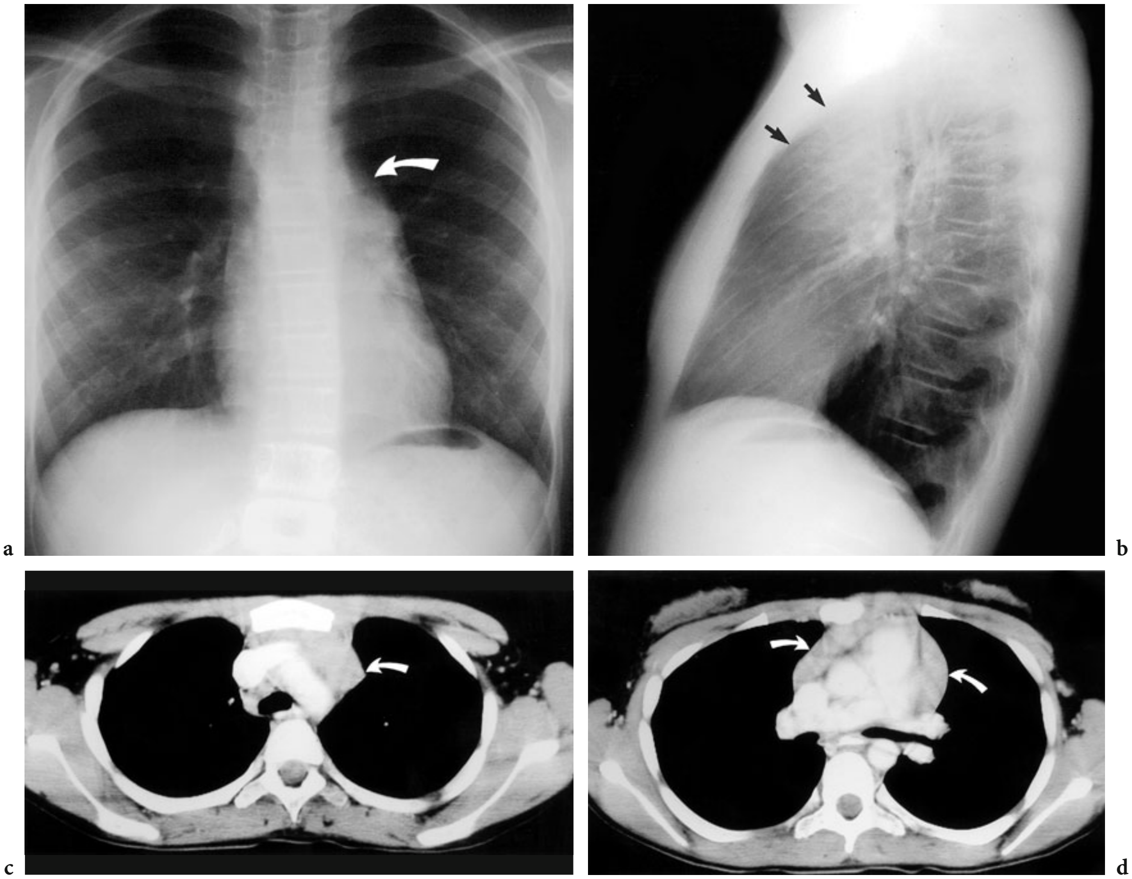

Fig. 10.15a–d. Unusual prominence of the thymus in a 12-year-old female who presented with substernal chest pain. **a** Posteroanterior view demonstrates soft tissue in the projection of the main pulmonary artery (*curved arrow*). **b** On the lateral radiograph there is increased opacity in the retrosternal region (*arrows*). **c,d** Axial IV contrast-enhanced chest computed tomography image at the level of the aortic arch (**c**) and at the pulmonary artery bifurcation (**d**) show a homogeneous convex opacity (*curved arrows*) in both regions. While the enhancement was homogenous and normal thymus was a consideration, it was elected to perform a thymic biopsy because of chest pain rather than perform follow-up imaging. The biopsy confirmed normal thymic tissue

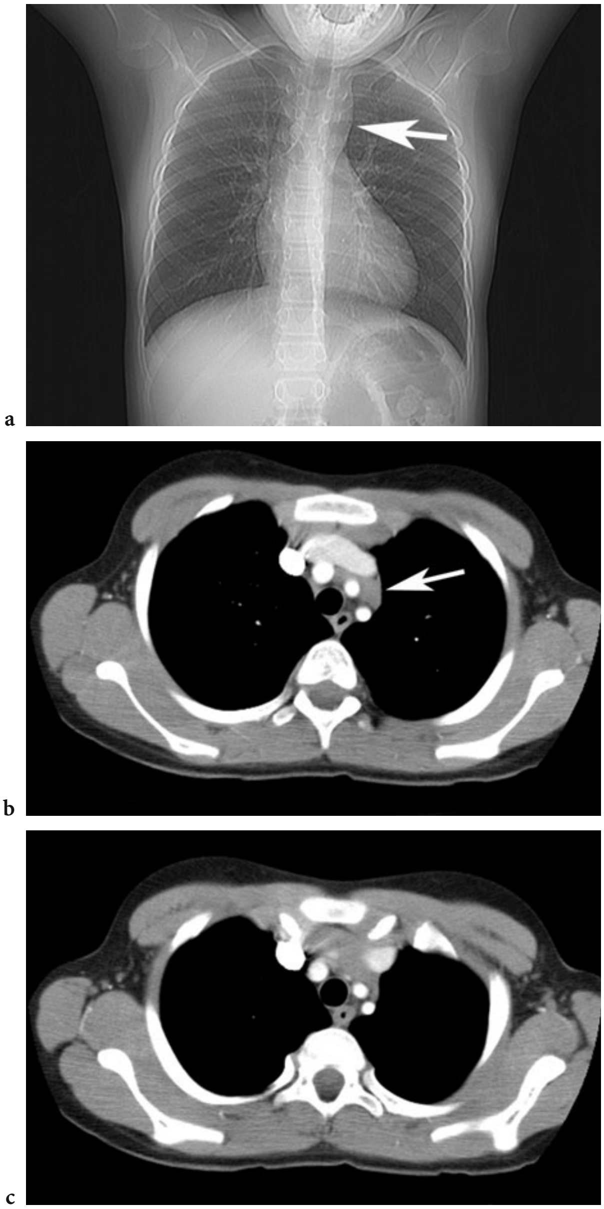

Fig. 10.16a–c. 12-year-old male with possible mediastinal mass, which turned out to be a normal thymus gland. **a** CT topogram (scout) demonstrates unusual contour of left paramediastinal region initially seen on chest radiography. **b** Axial contrast-enhanced image at the level of brachiocephalic vein demonstrates soft tissue attenuation (*arrows*) posterior to the brachiocephalic vein. **c** On a more superior image, this clearly connects with the thymus

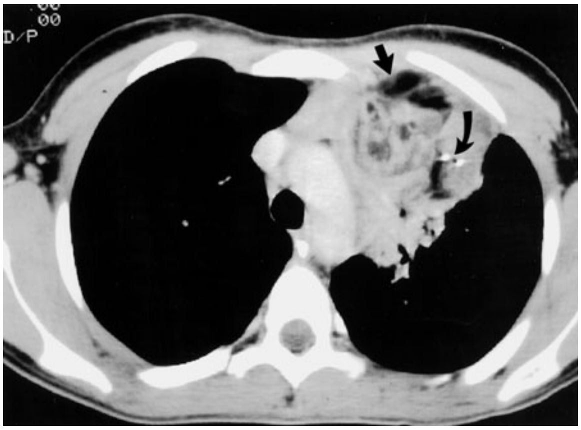

Fig. 10.17. A 12-year-old-female with a mature teratoma of the anterior mediastinum, involving the thymus. Axial IV contrast-enhanced computed tomography examination at the level of the transverse aorta shows a mixed attenuation mass of the left lobe of the thymus, involving the prevesicular region. Note soft tissue components, fat (*arrow*), and punctate calcification (*curved arrow*)

greatest during infancy with a mean attenuation of 80.8 HU with a gradual decrease in attenuation to 56 HU in teenage years probably due to fatty infiltration beginning in childhood (Sklair-Levy et al. 2000). Enhancement of the gland is homogenous, although the degree of enhancement in children has not been systematically addressed. With the advent of more rapid imaging provided by MDCT, thymic vessels have been more evident.

Routine chest CT techniques which have been previously described (Zeman et al. 1998; Frush 2006) are usually adequate for dedicated thymic imaging. As with any CT, scan parameters should be adjusted to the indication (Fig. 10.18). For example, if depiction of calcification is important, then low dose (e.g. 10–20 mAs; 80–100 kVp) images can be obtained to minimize additional radiation exposure prior to administration of contrast.

As with CT, the MRI appearance of the normal thymus has been well described (Boothroyd et al. 1992; Siegel et al. 1989; Molina et al. 1990). The multiplanar imaging sequences of MRI demonstrate the quadrilateral shape of the gland in the coronal plane in children under about 5 years of age (Siegel et al. 1989) (see Figs. 10.5 and 10.6), or the triangular shape in older children. MRI measurements of thymic dimensions support the contention that thymic size actually varies little during childhood. In one report, dimensions of the lobes were not significantly different from infancy

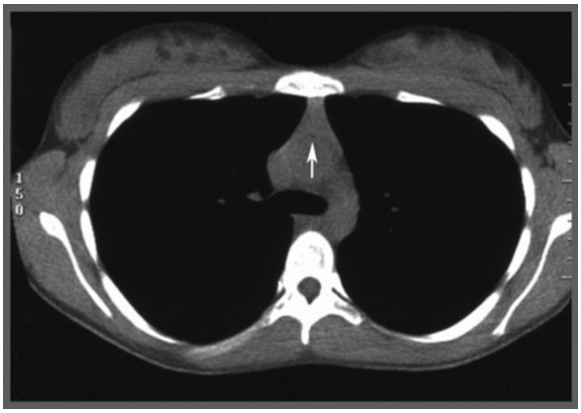

Fig. 10.18. Normal very low dose (8 mAs) chest CT examination in a teenage girl with myasthenia gravis performed to rule out thymoma. A soft tissue algorithm at the level of the aortic arch demonstrates normal triangular thymic configuration with clear delineation of this normal thymus from the subjacent aorta by a fat plane (*arrow*). No mass was present

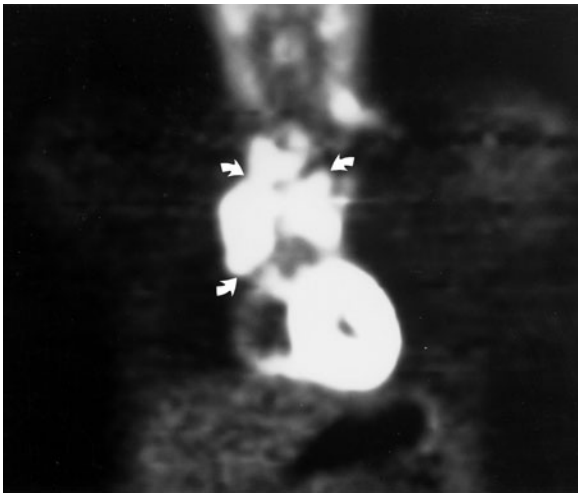

Fig. 10.19. A 15-year old male with Hodgkin lymphoma. Coronal ^{18}F-fluorodeoxyglucose positron emission tomogram (PET) shows marked increase in tracer activity in the anterior mediastinum (*small curved arrows*) as well as the left neck

(3.0 cm width, 1.6 cm thickness) to 15–18 years of age (2.8 cm width, 1.5 cm thickness) (Siegel et al. 1989). With T1-weighting, the signal intensity is homogeneous and equal to, or slightly greater than, skeletal muscle. With T2-weighting, the signal intensity of the gland increases and is similar to fat; fat saturation does not decrease the high signal intensity of the thymus (see Figs. 10.5 and 10.6). As with CT, normal thymic arteries and veins can be depicted with the use of relatively high-resolution sequences and dedicated coils. Recently, chemical shift imaging has been used to assess normal fatty replacement and this technology may be useful in differentiating normal thymus from infiltrative disorders (Nishino et al 2006; Takahashi et al. 2003).

The MRI technique for thymic evaluation is similar to techniques used with chest and mediastinal imaging (Boothroyd et al. 1992). Coil selection should be appropriate for age. A quadrature knee coil can be used for small infants. A head coil is appropriate for infants or small children. There are several torso coils designed for pediatric patients that provide excellent images; for isolated thymic imaging surface coils may be employed. Typical thymic evaluation consists of T1- and T2-weighted axial, and either coronal or sagittal (or both) sequences. Cardiac gating is usually not necessary.

Nuclear scintigraphy is generally used as an imaging modality in staging and follow-up of lymphoma. There is only a limited role for focused evaluation of the thymus (Larar et al. 1993). Gallium, thallium, and ^{18}F-fluorodeoxyglucose positron emission tomography (PET) have been useful in the evaluation of the anterior mediastinum. Unfortunately, gallium and thallium uptake in rebound hyperplasia limits the usefulness of these agents in the setting of thymic lymphoma (Larar et al. 1993; Roebuck et al. 1998). Increasing use of functional thymic imaging with fluorodeoxyglucose PET has provided helpful information in terms of lymphoma staging (O'Hara et al. 1999) (Fig. 10.19). However, PET remains problematic since physiologic rebound activity can be similar to that in lymphoma (Nishino et al. 2006).

10.6
Thymic Disorders: Pattern-Oriented Classification

10.6.1
Abnormalities in Thymic Size, Shape, or Location

The terms used to describe a small thymus include involution, hypoplasia, aplasia, and atrophy. Involution is the previously discussed normal process of age-related decrease in gland size. Thymic atrophy implies a previously normal thymus which has decreased in size most often due to some substantial systemic stress such as sepsis, major operative procedure, or agents such as steroids or a variety of chemotherapeutic agents. In these settings, thymic atrophy is easily recognized and transient and the thymus returns to normal size with resolution of the insult.

Thymic hypoplasia and aplasia are other descriptors of a small (or absent) thymus, and are associated with T-cell related immune function. These terms are most commonly used with DiGeorge syndrome. Approximately 90% of cases of DiGeorge syndrome have 22q11 deletion syndrome. This chromosomal deletion syndrome is also seen with truncus arteriosus and velocardial facial syndrome. DiGeorge syndrome is due to abnormal development of the third and fourth pharyngeal pouch. Because of this, the syndrome is characterized by variable T-cell deficiency and hypocalcemic seizures from parathyroid impairment. Great vessel and septal abnormalities and facial dysmorphology are also typical of DiGeorge syndrome. Thymic hypoplasia and aplasia are used interchangeably with partial (approximately 80% of cases) and complete DiGeorge syndrome, respectively. With partial DiGeorge syndrome, children can have a relatively intact immune system. This is in contradistinction to complete DiGeorge syndrome (thymic aplasia) in which the immune dysfunction is severe, similar in type and degree to severe combined immunodeficiency (Yin et al. 2000). CT and MRI are of little use in thymic evaluation of immune disorders involving the thymus; however, in the setting of DiGeorge syndrome, these modalities can be useful in defining cardiovascular abnormalities when echocardiography may be inconclusive. Thymic epithelial transplants or bone marrow transplant are only recommended in cases of complete DiGeorge syndrome (Markert et al. 1999).

The thymus can also be absent or dysplastic in other immunodeficiencies with T-cell abnormalities such as ataxia-telangiectasia, or severe combined immune deficiency (SCID) syndrome (Buckley et al. 1997; Yin et al. 2000). Perhaps the most familiar of these is SCID syndrome, which is characterized by a complete absence of normal thymic tissue in all cases (Yin et al. 2000) (Fig. 10.20). This lack of thymus can be an important observation in an infant in the first few months of life presenting with recurrent or severe infections; in this setting, the radiologist may be the first to suggest the diagnosis of an immunodeficiency (Yin et al. 2000).

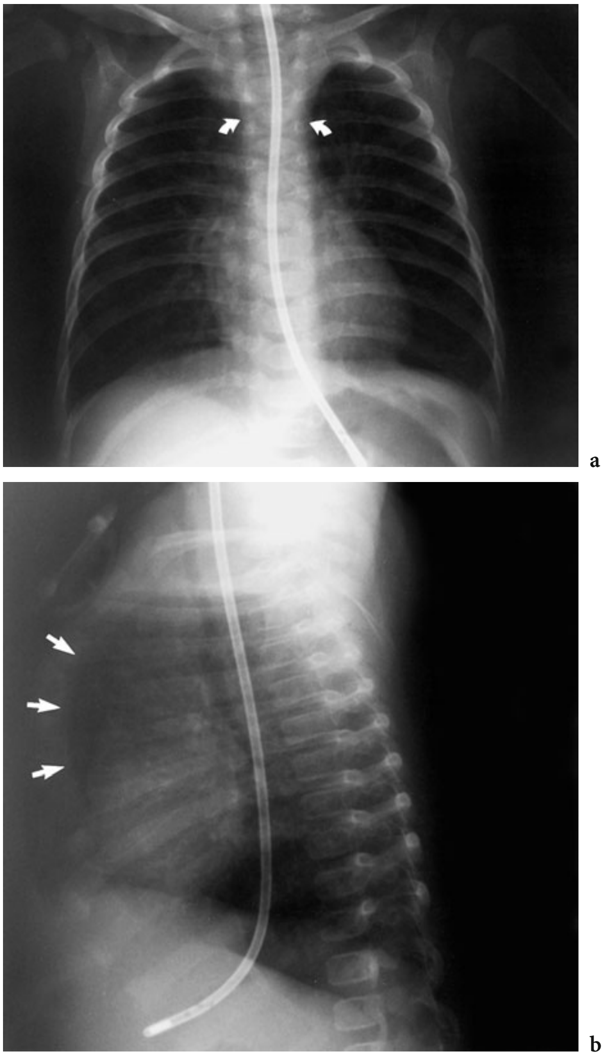

Fig. 10.20a,b. A 6-month-old female infant with severe combined immune deficiency syndrome. **a** Posteroanterior chest radiograph demonstrates absence of thymus (*curved arrows*). **b** On the lateral radiograph, there is increased lucency in the retrosternal region due to absent thymus. Hyperinflation is also present secondary to reactive airways disease due to past history of viral pneumonitis

The thymus may be apparently absent due to an ectopic location. Most ectopic thymus glands have been reported to reside in the neck (90%), are lateral, and cystic in nature (Kacker et al. 1999). The imaging appearance depends on whether the ectopic tissue is solid or cystic. Solid ectopic glands have features of normal thymic tissue. The differential for the solid gland includes other masses in the neck such as lymphadenopathy or lymphadenitis, vascular malformations, hemangiomas, abnormal thyroid tissue, and sarcomas. Cystic considerations include cystic adenopathy or adenitis, branchial cleft cysts, vascular malformations (i.e., lymphatic malformation or "cystic hygroma"), thyroglossal duct cysts, hematoma, lymphocele (e.g. post operative) and dermoids or epidermoids.

One area of continued contention reminiscent of the historical association of the thymus with significant airway distress is that of the cervical thymus and its relationship to airway compression. While it has been noted that cervical herniation of the thymus is associated with innominate artery compression of the trachea due to crowding (Mandell et al. 1994), similar anatomic relationships have been noted in children with no symptoms, or in children in whom the extent of tracheal narrowing is greater than that associated with a cervical thymus. In these children, investigators argue that the respiratory symptoms are due to an intrinsic problem with the trachea (Mahboubi et al. 1996).

Diffuse, homogeneous enlargement of the thymus gland is called hyperplasia (Linegar et al. 1993). The gland is considered hyperplastic if it is greater than about 50 g in weight. The hyperplastic thymus maintains the normal architecture and cellular components. Hyperplasia can be due to a provocation (e.g. systemic stress) with rebound (also known as lymphoid hyperplasia), or it can be associated with syndromes ("true" hyperplasia) such as Beckwith Widemann or T-cell dysfunction (Woysodt et al. 1999), or endocrine or other disorders (usually only in adults) such as Grave's disease or myasthenia gravis (Nishino et al. 2006). Finally, hyperplasia can be idiopathic, including the rare entity of giant thymic hyperplasia. Because of the association in adults with endocrine disorders, endocrine dysregulation is implicated as a possible mechanism; however, the etiology is unknown (Woysodt et al. 1999). The most familiar condition in pediatric radiology is the lymphoid hyperplasia found following treatment for cancer. This is usually well recognized.

Massive thymic hyperplasia is an extreme of hyperplasia where there is no known provocation, and weights of up to 1260 g, with diameters of 17 cm, have been reported (Linegar et al. 1993; Woysodt et al. 1999). Just over 70% of cases occur in children under 10 years of age, and virtually all cases are diagnosed during childhood, or before the third decade (Dimitriou et al. 2000; Linegar et al. 1993). Other than a massive enlargement, the imaging appearance is that of a normal thymus gland.

10.6.2
Focal Thymic Disorders

Overall, under 5% of all mediastinal masses arise from the thymus (Rubb et al. 2000). A variety of disorders can manifest with focal thymic disease in children (Table 10.1). While focal thymic disorders include non-neoplastic conditions such as abscesses and hemorrhage, these conditions, with the exception of thymic cysts, are sufficiently rare and clinically evident that the following discussion will focus on thymic neoplasms.

Thymic cysts are true epithelial lined fluid containing masses. Of all mediastinal cysts in children, anywhere from 3%–10% are of thymic origin (Davis et al. 1987; Takeda et al. 2003). Thymic cysts represent less than 1% of all mediastinal masses in children. Most thymic cysts are found in individuals of 20–50 years of age and are discovered incidentally. Ectopic locations of thymic cysts have already been discussed. Those arising from the normally located thymus can vary in size from 1 to 18 cm (Suster and Rosai 1991). The radiographic appearance is indistinguishable from a mediastinal mass or cardiac disease, including a pericardial effusion. Most cysts have fluid characteristics on CT (Figs. 10.21 and 10.22) or MRI, but the appearance of the fluid may be heterogeneous if there is associated hemorrhage (Suster and Rosai 1991).

Tumors of thymus, excluding lymphoma, are rare causes of mediastinal masses in children (Dehner et al. 1977). Thymic masses comprise 1%–3% of mediastinal masses in children (Yaris et al. 2006;

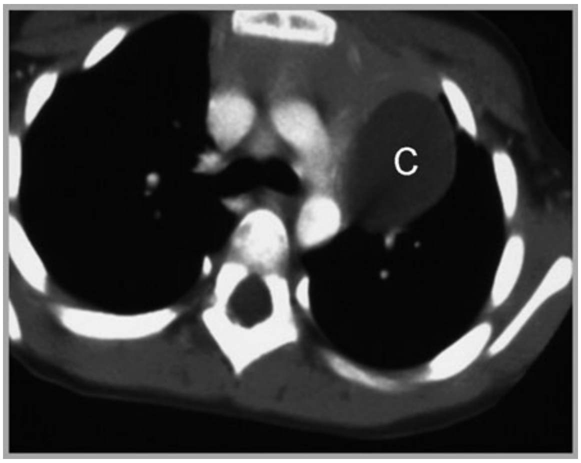

Fig. 10.21. Thymic cyst. Axial, IV contrast enhanced image just below the level of the aortic arch demonstrates a well defined, fluid attenuation thymic cyst (*C*)

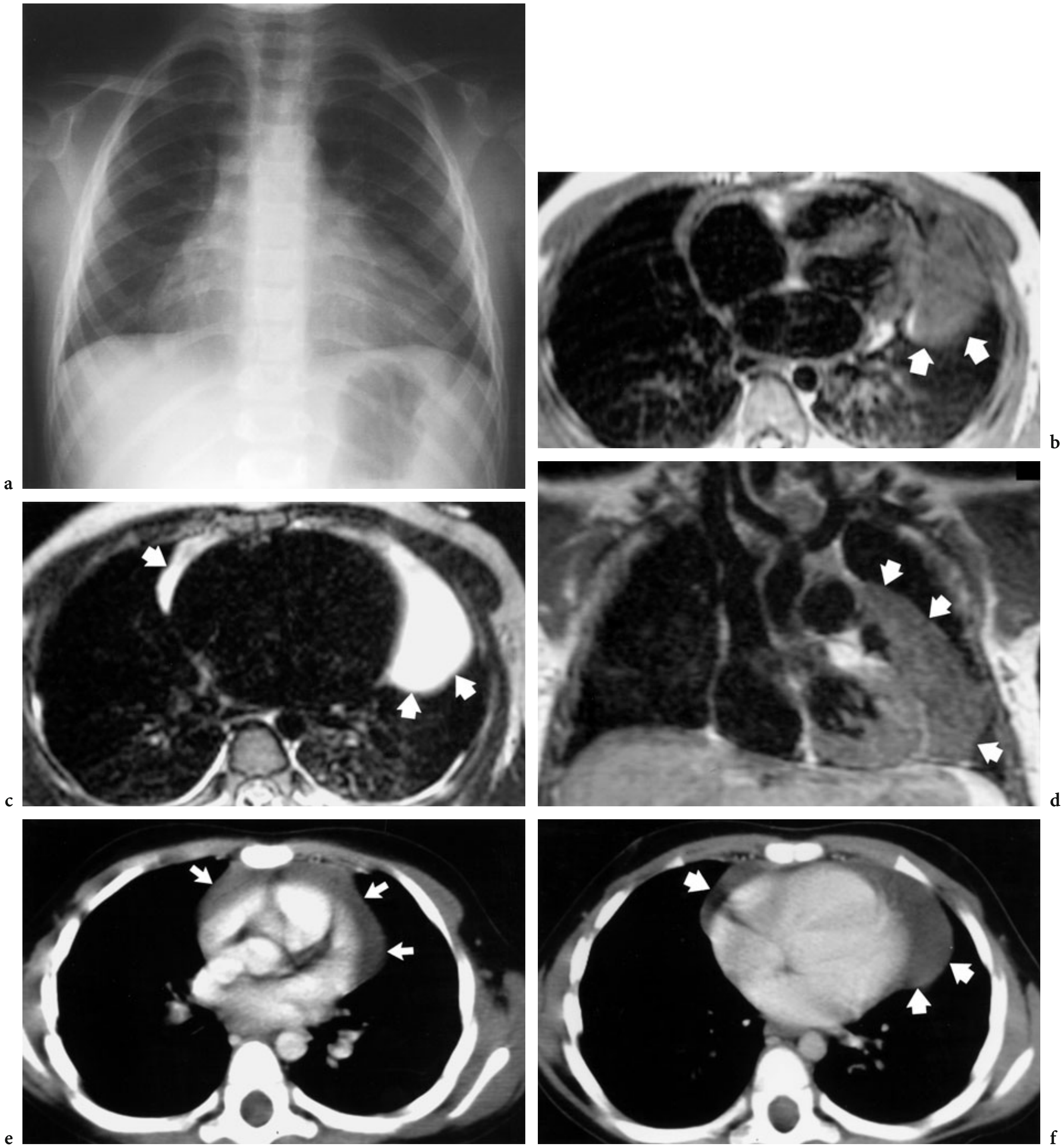

Fig. 10.22a–f. Thymic cyst in a 2-year-old-male. **a** Posteroanterior chest radiograph shows apparent cardiomegaly. **b,c** Axial T1-weighted (TR/TE 540/20, cardiac gated) (**b**) and T2-weighted (TR/TE 5,000/144 fast spin echo) (**c**) magnetic resonance (MR) images obtained near the cardiac apex show a well-defined mass with T1-weighted signal intensity similar to skeletal muscle and T2-weighted signal intensity greater than fat. The mass is adjacent to both the left and right cardiac margin. **d** Coronal T1-weighted (TR/TE 555/20; cardiac gated) MR image at the level of the superior vena cava demonstrates the superior and inferior extent of the abnormality. Because there was concern about slightly heterogeneous signal intensity of this mass on MR imaging at some levels (not shown), a CT examination was performed. **e,f** Axial IV contrast-enhanced CT examination at the level of the main pulmonary artery (**e**) and more inferiorly (**f**) demonstrate a homogenous fluid-attenuation mass which was confirmed at thoracotomy to be a thymic cyst (*arrows*). This was resected without complication. The heterogeneous signal intensity was due to hemorrhage within the cyst

Rothstein et al. 2005). Benign pediatric neoplasms include thymolipoma (Rubb et al. 2000) and thymoma, and very rarely, hemangioma (Niedzwiedki and Wood 1990). Malignant tumors can be divided into primary and secondary tumors. Primary thymic malignancies include invasive thymoma, thymic carcinoma, and lymphoid tumors (Rosai 1999). While germ cell tumors, lymphoma and neuroendicrine tumors can arise form the thymus, thymoma, thymolipoma, and thymic carcinoma are the only thymic neoplasms that originate from thymic precursors (Priola et al. 2006). Thymic metastatic disease is rare in children; in a pediatric oncology textbook, the only primary tumor reference with thymic metastases was neuroblastoma (Cohen 1992).

Thymic neoplasms can also be classified based on the cell type of origin. The most common are epithelial tumors (i.e., thymoma) and germ cell tumors; stromal tumors (i.e., thymolipoma) are rarer. The World Health Classification (WHO) for thymic epithelial tumors is as follows (from Nishino et al. 2006):

Type:	
A	Medullary
AB	Mixed
B1	Lymphocyte rich, predominantly cortical
B2	Cortical
B3	Epithelial (well-differentiated thymic carcinoma)
C	Thymic carcinoma

A thymolipoma is a tumor arising from thymic stroma. Most thymolipomas occur in children and young adults aged between 10 and 30 years. About one-third occur in individuals under 20 years of age, and half of these in the first decade (Gregory et al. 1997; Moran et al. 1995). The tumor has been reported in children as young as 2 years of age (Moran et al. 1995). Thymolipoma accounts for 2%–10% of all thymic masses (Nishino et al. 2006; Priola 2006; Gregory et al. 1997; Matsudaira et al. 1994). Thymolipomas are asymptomatic in over 50% of cases (Gregory et al. 1997; Moran et al. 1995).

The appearance of a thymolipoma is fairly unique. This benign hamartoma is encapsulated with variable contributions of fat and thymic tissue. The location is anteromedial in 80% of cases. Because of the contribution of fat, either CT or MRI is an excellent imaging option (Moran et al. 1995) (Fig. 10.23). The cross sectional imaging appearance is one of whorls of fatty tissue or soft tissue nodules interspersed in fat. These features are seen as low attenuation on CT and as high T1 and T2 signal intensity with MRI (Matsudaira et al. 1994; Molina et al. 1990; Moran et al. 1995). Calcification and cystic spaces are not imaging features. Size can range up to 36 cm (Moran et al. 1995). When this neoplasm also contains collagen, the mass is called a thymofibrolipoma (Moran et al. 1994). Other than a teratoma, or a fat-containing vascular malformation, fatty masses of the thymus (e.g., lipoma) are extremely rare (Cicciarelli et al. 1964).

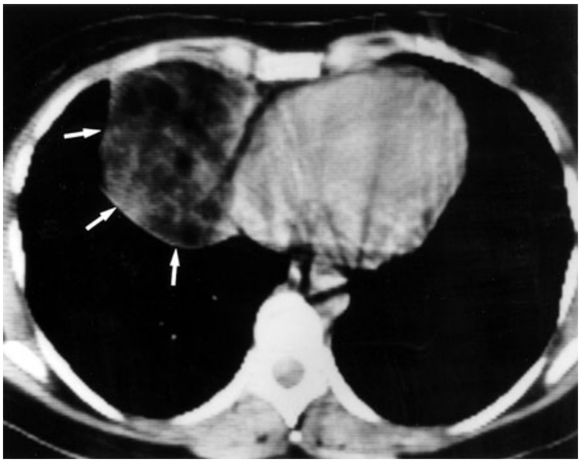

Fig. 10.23. Axial computed tomography (CT) scan shows a thymolipoma (*arrows*) with heterogeneous but predominately low (fatty) attenuation adjacent to the right atrium. (Original CT image courtesy of Daniel Melkus, MD, Herrin, Illinois; figure reprinted with permission, American College of Radiology

Thymomas are either benign or invasive epithelial tumors of the thymus. The mean age for thymoma is 40–50 years (Gripp et al. 1998). In total, 13% of thymomas occur between the ages of 10 and 29 years (Gripp et al. 1998), and approximately 2% occur in the first decade. The tumor has been reported in infancy (Dehner et al. 1977), however. Unlike in adults where there is a strong association with myasthenia gravis (30%–55%) (Gawrychowski et al. 2000; Gripp et al. 1998), thymomas in children are most often an isolated occurrence. There is an association in children with red cell aplasia and hypogammaglobulinemia (Kornstein 1995). Recently, Nishino et al. (2006) summarized disorders associated with thymoma. In addition to myasthenia gravis, other disorders include Lamber-Eaton syndrome, hemolytic anemia, acute leukemia, lymphoma, pancytopenia, inflammatory bowel disease, Addison disease, Cushing syndrome, hyperthyroidism, Grave's disease, systemic lupus erythematosus, polymyositis, and myocarditis.

Histologically, thymomas are encapsulated and are characterized by epithelial proliferation. Cysts may be present histologically in up to 20% of tumors. The determination of invasion can be difficult and is based on evidence of either microscopic or gross evidence of capsular disruption, or distant metastases (Kornstein 1995).

The appearance of a thymoma on CT or MRI is often non-specific. The tumor presents as a focal mass, which may be lobulated (St Amour et al. 1987; Nishino et al. 2006). Heterogeneous signal intensity with MRI has been noted, in addition to central hemorrhage (Siegel et al. 1989). CT is useful for determining extent, the effect on subjacent structures, and metastatic disease. Recently, CT features of thymic epithelial tumors at all ages were summarized. Those features which were associated with high-risk thymomas and carcinomas were lobulated contour, and mediastinal and/or great vessel invasion. Those CT features associated with recurrence and metastases were lobulated or irregular contour, oval shape, mediastinal fat or great vessel invasion, and pleural seeding (Nishino et al. 2006). The potential for FDG PET in discriminating carcinoma from other neoplasms (based on higher standard uptake values) has also been reviewed (Nishino et al. 2006).

Thymic carcinoma is also rare in children. Most tumors occur from between the ages of 40 and 60 years (Yaris et al. 2006), but have been noted in children as young as 4 years of age in a recent review (Kornstein 1995). Thymic carcinoma is histologically distinct from invasive thymoma. There is no capsule and the tumor consists of areas of necrosis and hemorrhage, rare cystic change, and malignant cytology including high nuclear-to-cytoplasmic ratio and mitotic figures, among others (Kornstein 1995). Because of these histologic features, attenuation or signal intensity is heterogeneous but non-specific (Fig. 10.24). Other thymic malignancies include thymic sarcoma (Iyer et al. 1998) and carcinoid (Lastoria et al. 1998). These are very rare in children.

Germ cell tumors of the thymus in children include teratomas (mature and immature), germinoma, embryonal carcinoma, yolk sac tumor, choriocarcinoma, and mixed types (Rosai 1999). Teratoma is the most common type, accounting for 80% of all primary mediastinal germ cell tumors (Rodgers and McGahren 1996). With the exception of a teratoma, where the presence of calcification (20%–43%) (Kornstein 1995), fat, cystic and soft tissue is characteristic (see Fig. 10.17), the features of germ cell tumors of the thymus are not specific (Iyer et al. 1998) (Fig. 10.25). Elevations of serum tumor markers of beta-human chorionic gonadotrophin (B-HCG) or alpha-fetoprotein (AFP) are useful in identifying and following malignant germ cell tumors. Again, it is often impossible to discriminate primary thymic sites of origin from invasion from extra thymic sites of origin. This distinction is not important clinically.

10.6.3
Diffuse or Multifocal Thymic Disorders

Diffuse involvement of the thymus can be found with lymphoma, Langerhans cell histiocytosis (eosinophilic granuloma), HIV associated cystic dysplasia (rarely seen now that anti-retroviral therapy is used), or involvement by large tumors of the thymus discussed above in Section 10.6.2.

Lymphoid processes of the thymus which present with multifocal or diffuse involvement include Hodgkin disease (usually nodular sclerosis is the most common histology), non-Hodgkin lymphomas (i.e., lymphoblastic and large cell lymphoma) and Castleman's disease. The presence of adenopathy is very helpful in distinguishing lymphoma of the thymus from other masses (Siegel et al. 1989; Spiers et al. 1997). For example, adenopathy was present in all children presenting with Hodgkin lymphoma of the thymus in one report (Spiers et al. 1997).

With lymphoma, the age of the child and presence of other regions of adenopathy can be helpful in prioritizing the histology (Cohen 1992). If the lymphoma is confined to thymus (or anterior mediastinum) in an older child or adolescent, a Hodgkin lymphoma is likely. Hodgkin disease is rare under 10 years of age; conversely, non-Hodgkin lymphoma can occur at any age. Large cell lymphoma occurs in older children.

The determination of whether or not residual thymic abnormalities represent residual disease is still problematic. In general, relapse is most often encountered in enlarged glands with heterogeneous signal intensity on MRI or attenuation with CT. On MRI, relapse is more likely if there are regions of T2-signal intensity greater than fat. T1-weighted signal intensity is not helpful; however, the presence of low heterogeneous signal intensity on T2-weighted se-

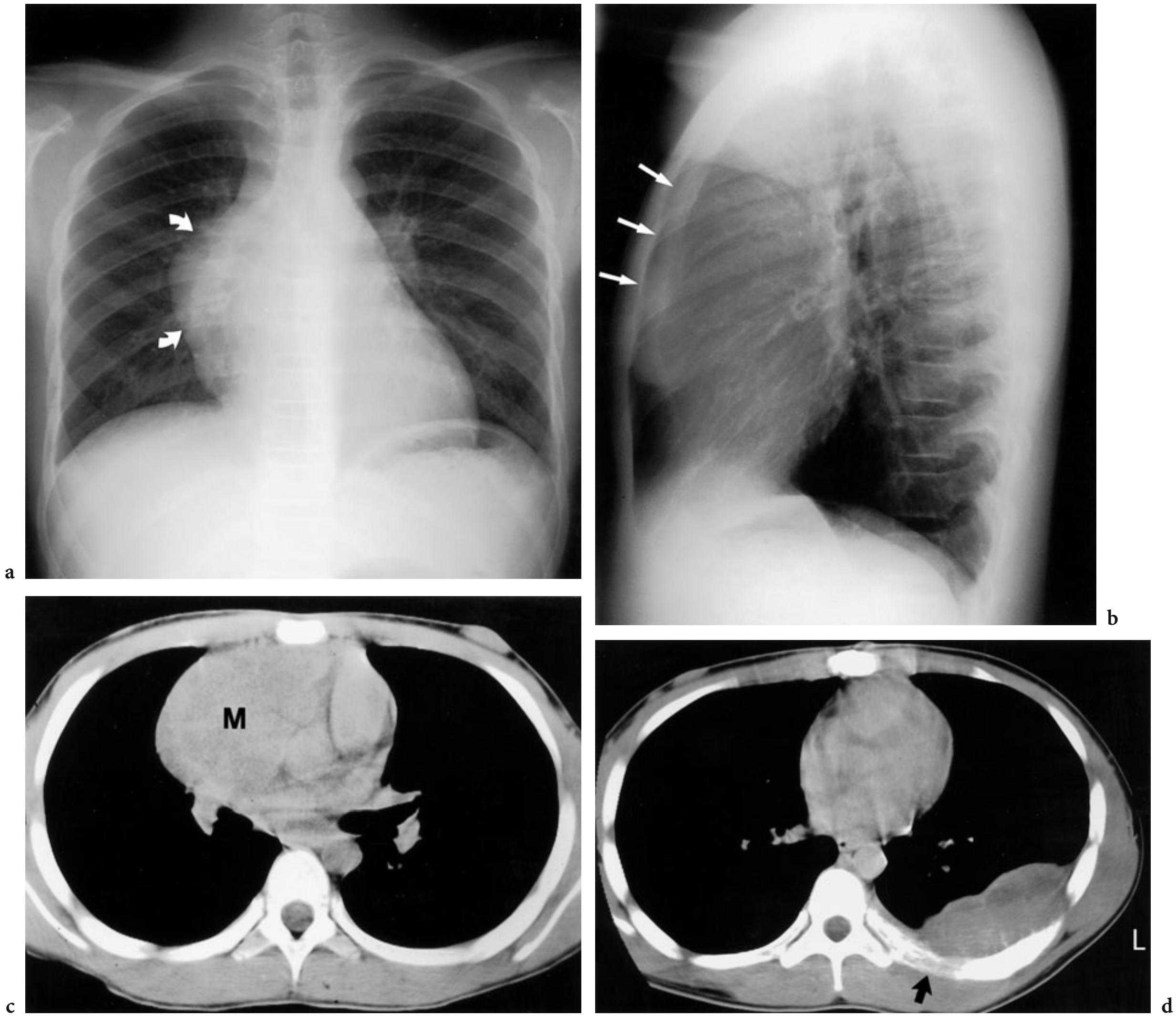

Fig. 10.24a–d. Thymic carcinoma in a teenage boy. **a** At 13 years of age, he presented with chest pain and an anterior mediastinal mass (*small curved arrows*) evident predominately to the right on the posteroanterior chest radiograph. **b** On the lateral radiograph, there is dense opacification of the retrosternal region (*arrows*). **c** Axial non-contrast computed tomography (CT) performed at that time demonstrated a mass (*M*) with subtle heterogeneity in the anterior mediastinum. This was indistinguishable from normal thymic tissue. Surgical findings and histology indicated that this was a thymoma. However, 18 months later he presented with pleural chest pain and a chest wall mass evident on a contrast-enhanced CT examination. **d** Note destruction of the adjacent rib (*arrow*). CT guided biopsy demonstrated that this was a carcinoma and the primary site was felt to be the previous thymic tumor

quences is reported to be seen only without relapse (Spiers et al. 1997).

CT is recommended for initial evaluation of lymphoma. The appearance can be homogeneous or heterogeneous, due to areas of necrosis or fibrosis (Fig. 10.12). It is important, as with any anterior mediastinal mass, to assess airway patency with radiography or CT. The MRI appearance of the thymus in lymphoma is variable. The gland can be diffusely enlarged, have asymmetric (lobar) enlargement, a lobular contour, or have normal architecture (Figs. 10.26 and 10.27). Areas of fibrosis are seen as relatively decreased T2-weighted signal intensity. Areas of hemorrhage and necrosis are seen as increased T2 signal intensity, greater than fat (Siegel et al. 1989).

T-cell lymphoblastic leukemia can also present as diffuse thymic disease (Fig. 10.28) with het-

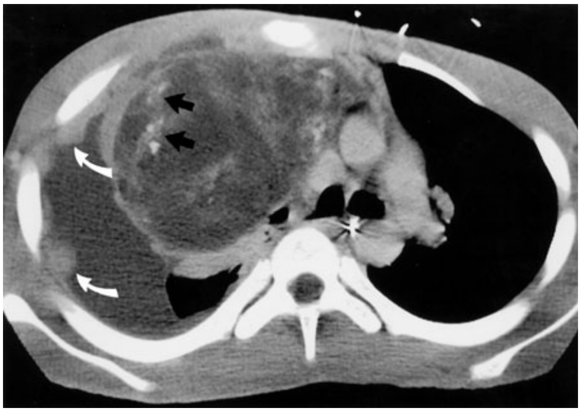

Fig. 10.25. A 14-year-old-male with a mixed germ cell tumor (seminoma and choriocarcinoma) involving the thymus. Image at the level of the carina from an axial IV contrast-enhanced computed tomography examination shows a heterogeneous, predominately low attenuation mass with areas of calcification (*arrows*). Note also malignant pleural effusion and pleural metastases (*curved arrows*)

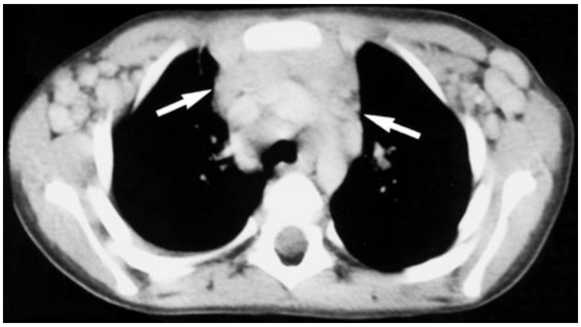

Fig. 10.26. A 3-year-old boy with T-cell non-Hodgkin lymphoma. Axial image from an IV contrast-enhanced computed tomography examination of the upper chest demonstrates anterior mediastinal adenopathy with lobular configuration of the thymus (*arrows*). Note also bilateral axillary adenopathy

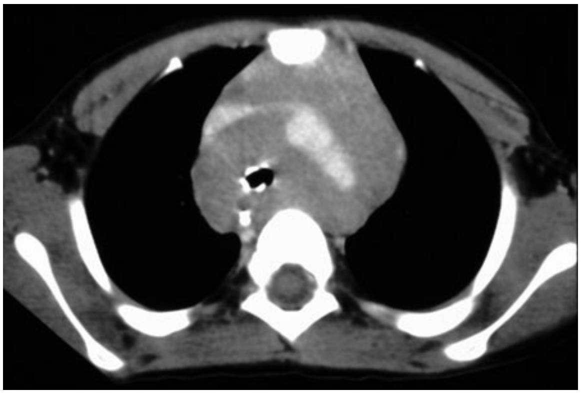

Fig. 10.27. Hodgkin lymphoma is shown encasing the brachiocephalic vein as well as the trachea. The patient is intubated. Note homogeneous soft tissue attenuation of the adenopathy and thymic involvement

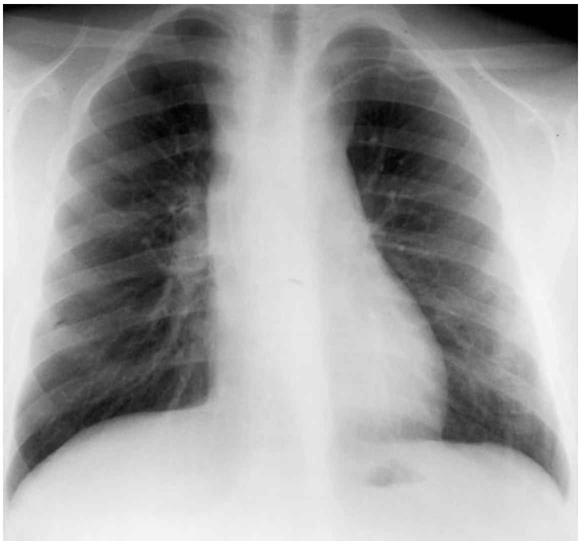

Fig. 10.28. A 15-year-old male with T-cell acute lymphoblastic leukemia. Posteroanterior chest radiograph shows anterior mediastinal widening which was due to thymic infiltration

erogeneous high signal on T2-weighted sequences (Molina et al. 1990). However, imaging of the thymus is not a routine evaluation for leukemia in children.

Langerhans cell histiocytosis (LCH) is a solitary or multiorgan disorder characterized by infiltration of histiocytes of the Langerhans cell type. Older nomenclatures for this disorder included eosinophilic granuloma. The incidence of thymic disease in LCH is unknown, but thymic involvement in up to 70% of children with multisystem disease has been reported (Heller et al. 1999; Junewick and Fitzgerald 1999). In one small series of five children with thymic disease, cystic changes were evident in four, calcification in one, and thymic enlargement in all (Junewick and Fitzgerald 1999). Diffuse heterogeneity with predominantly low attenuation with CT in systemic LCH with thymic involvement has also been reported (Donnelly and Frush 2000) (Fig. 10.29).

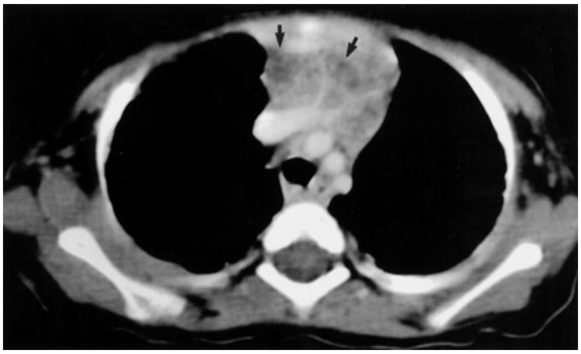

Fig. 10.29. A 20-month-old girl with thymic involvement by Langerhans cell histiocytosis. Axial IV contrast-enhanced computed tomography of the upper chest shows diffuse, heterogeneous, predominately low attenuation of the thymus gland (*arrows*)

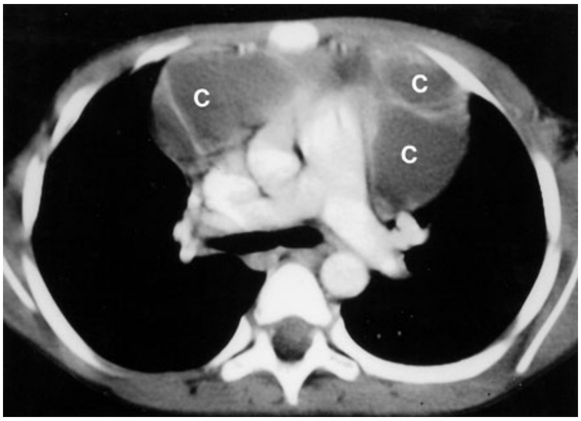

Fig. 10.30. HIV-associated cystic thymic dysplasia in an 8-year-old male. Axial IV contrast-enhanced computed tomography scan at the level of the pulmonary artery bifurcation shows variable-sized cystic spaces (*C*), with thin intervening septations, which replace the normal thymus gland

Diffuse thymic disease can also be found in children with HIV infection. In a small series of two children, the thymus was globally involved with cysts ranging in size from between 1 and 6 cm (Leonidas et al. 1996) (Fig. 10.30). While some solid elements were evident, the abnormality was predominately cystic. Cystic thymic involvement, similar in appearance to that of the parotid glands with HIV, is felt to be associated with an accelerated lymphoid response with a relatively milder disease course (Leonidas et al. 1996).

Other diffuse or multifocal processes of the thymus include vascular malformations (Fig. 10.31).

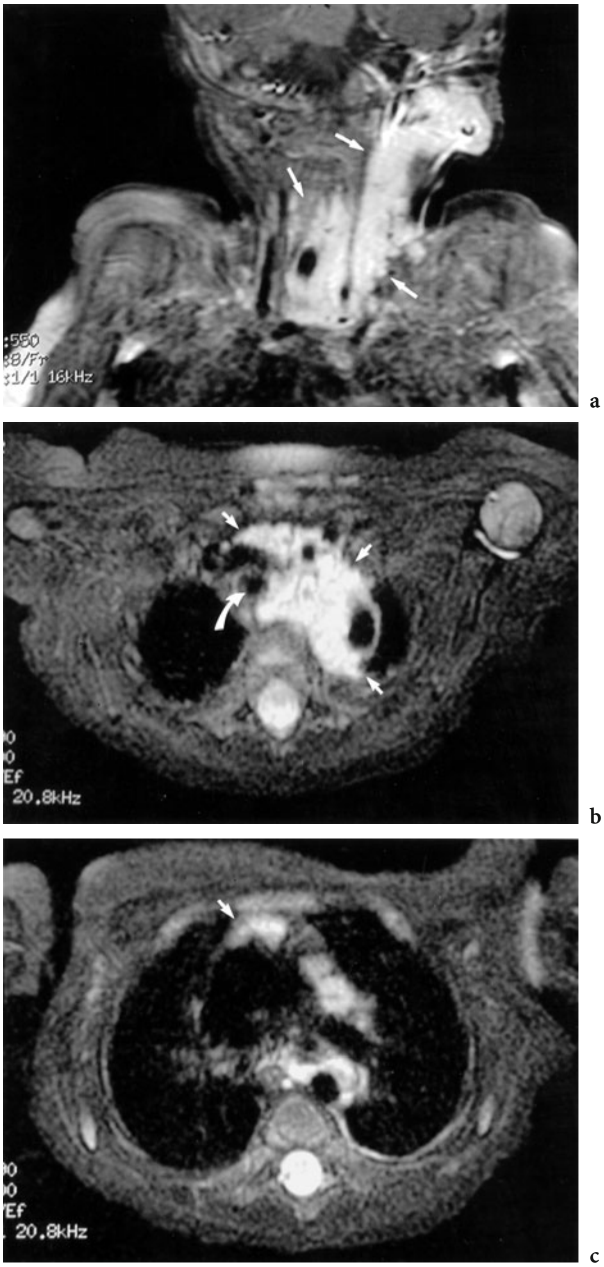

Fig. 10.31a–c. Thymic involvement by an extensive vascular malformation in a 3-month-old infant girl. **a** Coronal T1-weighted (TR/TE 550/8), contrast-enhanced magnetic resonance (MR) image shows the extensive involvement of the densely enhancing malformation (*arrows*) involving the left neck and mediastinum. **b** T2-weighted images (TR/TE 4000/96 fast spin echo; fat saturated) at the level of the brachiocephalic vein shows the infiltrating nature of the mass (*arrows*) and displacement of the trachea (*curved arrow*). **c** Axial MR image from the same sequence obtained at the level of the main pulmonary arteries demonstrates thymic involvement by the vascular malformation (*arrow*)

10.6.4

Specific Thymic Imaging Features: Calcification, Fat, Cysts

The identification of several imaging characteristics including thymic calcification, fat, or cysts (Figs. 10.32–10.34) (Table 10.2) is also useful in distinguishing between various thymic disorders. Recognition of these features and familiarity with additional individual imaging appearances on CT, sonography, and MRI (such as with a hematoma (Fig. 10.35)) are useful in the classification of thymic disorders.

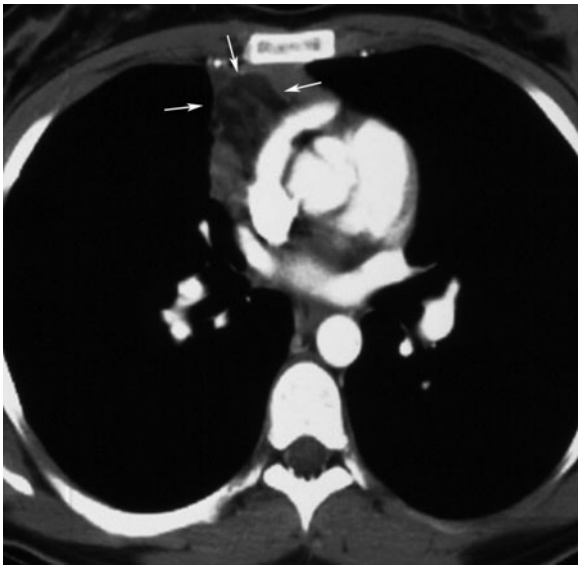

Fig. 10.32. Teenage female with abnormal right-sided paramediastinal configuration on chest radiograph. This was a venous malformation (biopsy confirmed). Image at the level of the left brachiocephalic vein following IV contrast administration demonstrates a fatty region involving the thymus (*arrows*). This was part of the venous malformation which included several punctate calcifications (not shown). This was proven following a biopsy

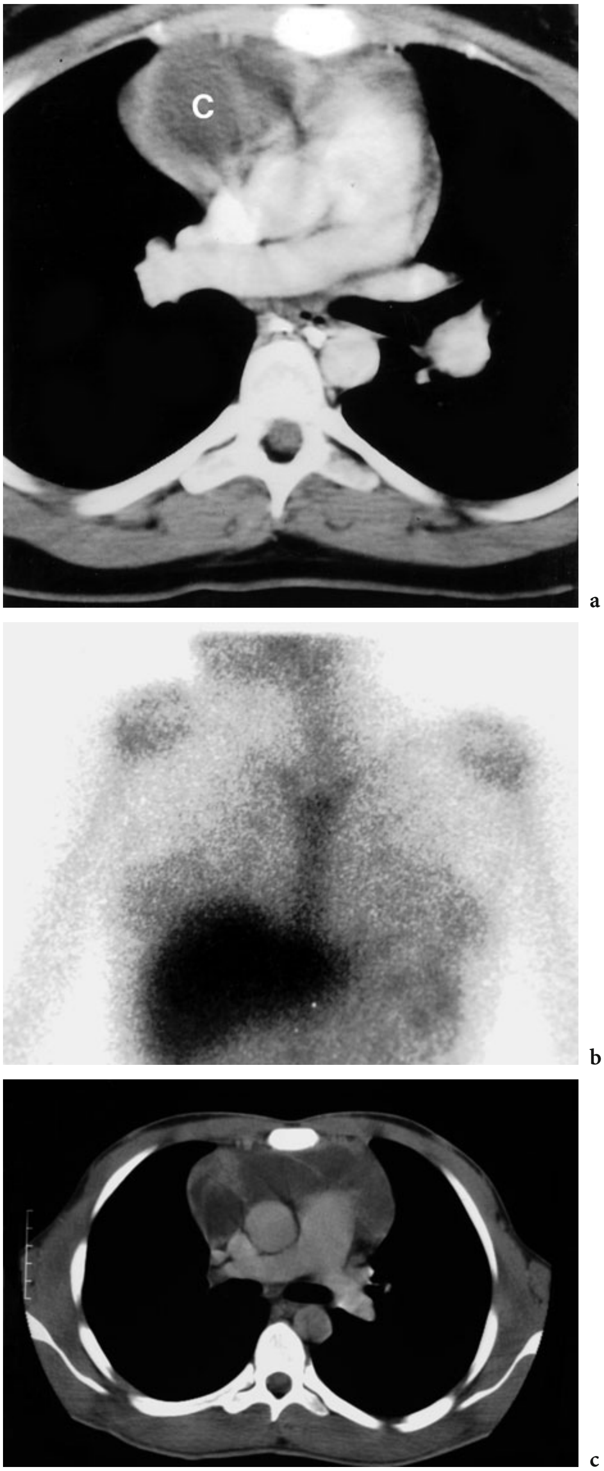

Fig. 10.33a–c Cystic lymphoma. **a** A thymic cyst (*C*) in an 18-year-old female in remission for Hodgkin lymphoma is shown on axial contrast-enhanced computed tomography examination at the level of the right pulmonary artery. High-density material in the region of the esophagus was due to previous lymphangiography. **b** At this time, a 67gallium-citrate study with images obtained at 72 h was negative for tracer activity in this region and the cyst gradually resolved during radiographic follow-up (not shown). **c** Lymphoma in a male. Axial IV contrast enhanced CT examination at the level of the pulmonary artery bifurcation demonstrates heterogeneous but predominantly low attenuation (cystic appearing) involvement of the thymus by lymphoma

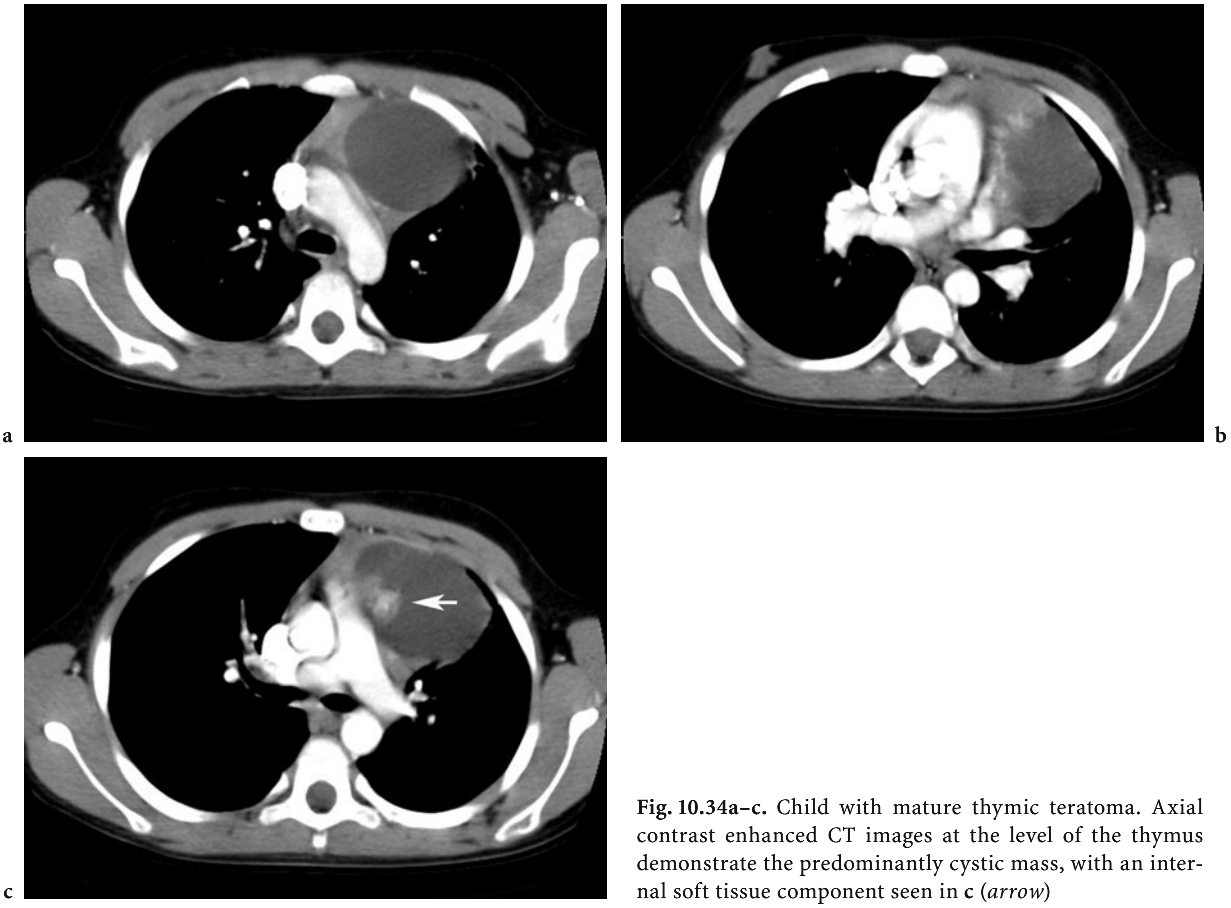

Fig. 10.34a–c. Child with mature thymic teratoma. Axial contrast enhanced CT images at the level of the thymus demonstrate the predominantly cystic mass, with an internal soft tissue component seen in **c** (*arrow*)

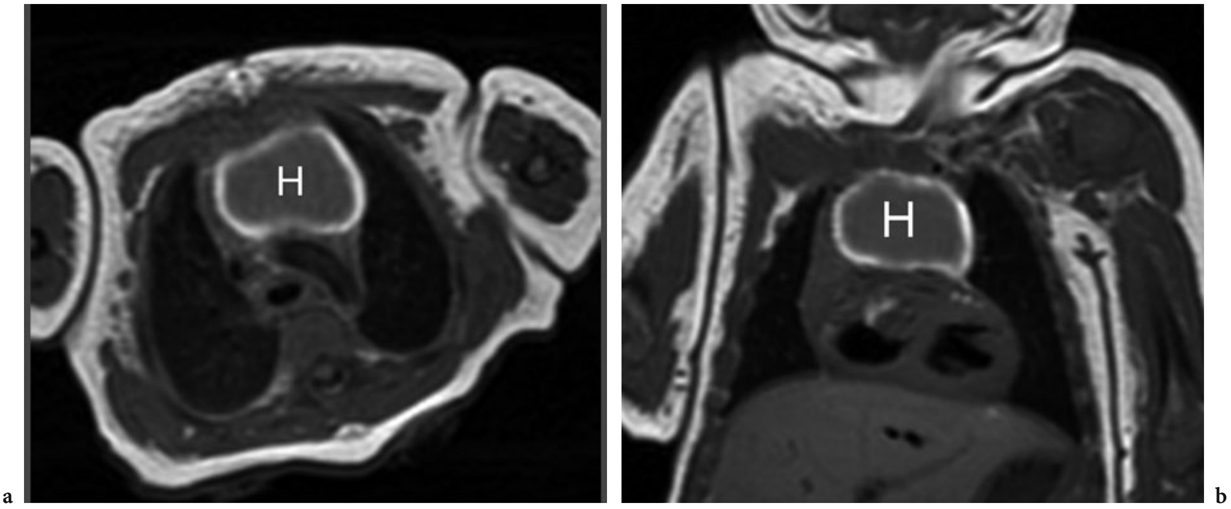

Fig. 10.35a,b. Post-operative hematoma in an infant following surgery for tetralogy of Fallot. Cardiac gated, T1-weighted axial images at the level of the aortic arch demonstrates an anterior mediastinal hematoma with signal intensity which is isointense to muscle centrally with a high signal intensity rim

10.7
Conclusion

Imaging evaluation of the pediatric thymus gland can be challenging given the normal variation, as well as the wide variety of disorders that can involve the gland. It is important to be familiar with the spectrum of normal imaging appearances to prevent misdiagnosis of thymic disease. When the thymus is truly abnormal, classifying the pattern of involvement, as well as identifying certain imaging features, is useful in establishing the diagnosis or at least limiting the diagnostic possibilities. Understanding the advantages and disadvantages of the imaging options, especially sonography, CT and MRI, provides the radiologist with an opportunity for focused and successful thymic imaging strategies.

References

Bach AM, Hilfer CL, Holgersen (1991) Left-sided posterior mediastinal thymus-MRI findings. Pediatr Radiol 21:440–441

Baysal T, Kutlu R, Kutlu O et al. (1999) Ectopic thymic tissue: a cause of emphysema in infants. Clin Imaging 23:19–21

Ben-Ami TE, O'Donovan JC, Yousefzadeh DK (1993) Sonography of the chest in children. Radiol Clin North Am 31:517–531

Boothroyd AE, Hall-Craggs MA, Dicks-Mireaux C et al. (1992) The magnetic resonance appearances of the normal thymus in children. Clin Radiol 45:378–381

Buckley RH, Schiff RI, Schiff SE et al. (1997) Human severe combined immunodeficiency: genetic, phenotypic, and functional diversity in one hundred eight infants. J Pediatr 130:378–387

Caffey J (1945) The mediastinum. In: Caffey J (ed) Pediatric X-ray diagnosis. Year Book, Chicago, pp 344–345

Cicciarelli FE, Soule EH, McGoon DW (1964) Lipoma and liposarcoma of the mediastinum: a report of 14 tumors including one lipoma of the thymus. J Thorac Cardiovasc Surg 47:411–429

Cohen MD (1992) Imaging of children with cancer, 1st edn. Mosby-Year Book, St Louis, pp 89–122, 136

Cohen MD, Smith JA (1994) Intravenous use of ionic and nonionic contrast agents in children. Radiology 191:793–794

Coley BD (2005) Pediatric chest ultrasound. Radiol Clin N Am 43:405-418

Cooper AP (1832) The anatomy of the thymus gland. Longmand, Rees, Orme, Green and Brown, London, pp 1–48

Cure JK, Tagge EP, Richardson MS et al. (1995) MR of cystic aberrant cervical thymus. AJNR 16:1124–1127

Davis RD, Oldham HN, Sabiston DC (1987) Primary cysts and neoplasms of the mediastinum: recent changes in clinical presentation, methods of diagnosis, management, and results. Ann Thorac Surg 44:229–237

Dehner LP, Martin SA, Sumner HW (1977) Thymus related tumors and tumor-like lesions in childhood with rapid clinical progression and death. Hum Pathol 8:53–66

Dimitriou G, Greenough A, Rafferty G et al. (2000) Respiratory distress in a neonate with an enlarged thymus. Eur J Pediatr 159:237–238

Donnelly LF, Frush DP (2000) Langerhans' cell histiocytosis showing low-attenuation mediastinal mass and cystic lung disease. AJR Am J Roentgenol 174:877–878

Frush DP (2006) Evidence-based principles and protocols for pediatric body multislice computed tomography. In: Knollman F, Coakley F (eds) Multislice CT: principles and protocols. Elsevier, Philadelphia, pp 179–201

Gawrychowski J, Rokicki M, Gabriel A et al. (2000) Thymoma – the usefulness of some prognostic factors for diagnosis and surgical treatment. Eur J Surg Oncol 26:203–208

Gregory AK, Connery CP, Resta-Flarer F et al. (1997) A case of massive thymolipoma. J Pediatr Surg 32:1780–1782

Gripp S, Hilgers K, Wurm R et al. (1998) Thymoma: prognostic factors and treatment outcomes. Cancer 83:1495–1503

Hale LP (2004) Histologic and molecular assessment of human thymus. Ann Diagn Pathol 8:50–60

Hasselbalch H, Jeppesen DL, Ersboll AK et al. (1997) Sonographic measurement of thymic size in healthy neonates. Relation to clinical variables. Acta Radiol 38:95–98

Haynes BF, Hale LP (1999) Thymic function, aging, and aids. Hospital Practice 34(3):59–87

Heller GD, Haller JO, Berdon WE, Sane S, Kleinman PK (1999) Punctate thymic calcification in infants with untreated Langerhans' cell histiocytosis: report of four new cases. Pediatr Radiol 29:813–815

Iscan A, Tarhan S, Guven H et al. (2000) Sonographic measurement of the thymus in newborns: close association between thymus size and birth weight. Eur J Pediatr 159:223–224

Iyer R, Jaffe N, Ayala AG et al. (1998) Thymic sarcoma in childhood. Br J Radiol 71:81–83

Jacobs MT, Frush DP, Donnelly LF (1999) The right place at the wrong time: historical perspective of the relation of the thymus gland and pediatric radiology. Radiology 210:11–16

Junewick JJ, Fitzgerald NE (1999) The thymus in Langerhans' cell histiocytosis. Pediatr Radiol 29:904–907

Kacker A, April M, Markentel CB et al. (1999) Ectopic thymus presenting as a solid submandibular neck mass in an infant: case report and review of literature. Int J Pediatr Otorhinolaryngol 20:241–245

Kim OH, Kim WS, Kim MJ et al. (2000) US in the diagnosis of pediatric chest diseases. Radiographics 20:653–671

Kornstein MJ (1995) Pathology of the thymus and mediastinum, 1st edn. Saunders, Philadelphia, pp 1–172

Koumanidou C, Vakaki M, Theophanopoulou M et al. (1998) Aberrant thymus in infants: sonographic evaluation. Pediatr Radiol 28:987–989

Kuhn JP, Slovis TL, Silverman FN et al. (1993) Part II: the neck and respiratory system. In: Silverman FN, Kuhn JP (eds) Caffey's pediatric X-ray diagnosis, 9th edn. Year Book Medical Publishers, Chicago, pp 637–695

Larar GN, O'Tuama LA, Treves ST (1993) Nuclear medicine in the pediatric chest. Radiol Clin North Am 31:481–498

Lastoria S, Vergara E, Palmieri G et al. (1998) In vivo detection of malignant thymic masses by indium-111-DTPA-D-Phe-octreotide scintigraphy. J Nucl Med 39:634–639

Leonidas JC, Berdon WE, Valderrama E et al. (1996) Human immunodeficiency virus infection and multilocular thymic cysts. Radiology 198:377–379

Linde LM, Marcus B, Padua E (1991) Normal thymus simulating pericardial disease: diagnostic value of magnetic resonance imaging. Pediatrics 88:328–331

Linegar AG, Odell JA, Fennell WMP et al. (1993) Massive thymic hyperplasia. Ann Thorac Surg 55:1197–1201

Mahboubi S, Harty MP, Hubbard AM et al. (1996) Innominate artery compression of the trachea in infants. Int J Pediatr Otorhinolaryngol 35:197–205

Mandell GA, McNicholas KW, Padman R et al. (1994) Innominate artery compression of the trachea: relationship to cervical herniation of the normal thymus. Radiology 190:131–135

Markert ML, Boeck A, Hale LP et al. (1999) Transplantation of thymus tissue in complete DiGeorge syndrome. N Engl J Med 341:1180–1189

Marra S, Hotaling AJ, Raslan W (1995) Cervical thymic cyst. Otolaryngol Head Neck Surg 112:338–340

Matsudaira N, Hirano H, Itou S et al. (1994) MR imaging of thymolipoma. Magn Reson Imaging 12:959–961

Molina PL, Siegel MJ, Glazer HS (1990) Thymic masses on MR imaging. AJR Am J Roentgenol 155:495–500

Moran CA, Zeren H, Koss MN (1994) Thymofibrolipoma: a histologic variant of thymolipoma. Arch Pathol Lab Med 118:281–282

Moran CA, Rosado-de-Christenson M, Suster S (1995) Thymolipoma: clinicopathologic review of 33 cases. Mod Pathol 8:741–744

Niedzwiecki G, Wood BP (1990) Radiological cases of the month. Thymic Hemangioma. Am J Dis Child 144:1149–1150

Nishino M, Ashiku SK, Kocher ON et al. (2006) The thymus: a comprehensive review. RadioGraphics 26:335–348

Oestreich AE (1995) William H Crane of Cincinnati and the first irradiation of the pediatric thymus. AJR Am J Roentgenol 165:1064–1065

O'Hara SM, Betts JB, Coleman RE (1996) F-18 FDG PET imaging of the thymus gland in pediatric patients: preliminary results (abstract). Radiology 201(P):376

O'Hara SM, Donnelly LF, Coleman RE (1999) Pediatric body applications of FDG PET. AJR Am J Roentgenol 172:1019–1024

Paltauf A (1889) Über die Beziehung der Thymus zum plötzlichen Tod. Wien Klin Wochenschr 2:877–881

Pohle EA (1950) The thymus. In: Pohle EA (ed) Clinical radiation therapy. Lea and Febiger, Philadelphia, pp 676–684

Priola AM, Priola SM, Cardinale L, Cataldi A, Fava C (2006) The anterior mediastinum: diseases. Radiol Med 111:312–342

Rodgers BM, McGahren ED (1996) Mediastinum and pleura. In: Oldham KT, Colombani PM, Foglia RP (eds) Surgery of infants and children. Lippincott-Raven, Philadelphia, p 928

Roebuck DJ, Nicholls WD, Bernard EJ et al. (1998) Misleading leads thallium-201 uptake in rebound thymic hyperplasia. Med Pediatr Oncol 30:297–300

Rosai J (1999) Histological typing of tumours of the thymus, 2nd edn. Springer, Berlin Heidelberg New York, pp 9–23

Rothstein DH, Voss SD, Isakoff M, Puder M (2005) Thymoma in a child: case report and review of the literature. Pediatr Surg Int 21:548–551

Rubb ME, Keilani R, Howatson AG et al. (2000) Benign symptomatic thymic tumors. J Pediatr Surg 35(9):1362–1364

Siegel MJ, Glazer HS, Wiener JI et al. (1989) Normal and abnormal thymus in childhood: MR imaging. Radiology 172:367–371

Sklair-Levy M, Agid R, Sella T et al. (2000) Age-related changes in CT attenuation of the thymus in children. Pediatr Radiol 30:566–569

Slovis TL, Meza M, Kuhn JP (1992) Aberrant thymus-MR assessment. Pediatr Radiol 22:490–492

Spiers ASD, Husband JES, MacVicar AD (1997) Treated thymic lymphoma: comparison of MR imaging with CT. Radiology 203:369–376

St Amour TE, Siegel MJ, Glazer HS et al. (1987) CT appearances of the normal and abnormal thymus in childhood. J Comput Assist Tomogr 11:645–650

Suster S, Rosai J (1991) Multilocular thymic cyst: an acquired reactive process. Am J Surg Pathol 15:388–398

Swischuk LE, John SD (1996) Case report – normal thymus extending between the right brachiocephalic vein and the innominate artery. AJR Am J Roentgenol 166:1462–1464

Takahashi K, Inaoka T, Murakami N et al. (2003) Characterization of the normal and hyperplastic thymus on chemical-shift MR imaging. AJR Am J Roentgenol 180:1265–1269

Takeda S, Miyoshi S, Minami M et al. (2003) Clinical spectrum of mediastinal cysts. Chest 124:125–132

Wong KT, Lee DL, Chan MS et al. (2005) Unusual anterior neck mass visible only during valsalva's maneuver in a child. AJR Am J Roentgenol 185:1355–1357

Woysodt A, Verhaart S, Kiss A (1999) Case report – massive true thymic hyperplasia. Eur J Pediatr Surg 9:331–333

Yaris N, Nas Y, Cobanoglu U, Yavuz M (2006) Thymic carcinoma in children. Pediatr Blood Cancer 47:224–227

Yin E, Frush DP, Donnelly LF, Buckley RH (2000) Primary immunodeficiency disorders in children: clinical features and imaging findings. AJR Am J Roentgenol (in press)

Zeman RK, Baron RL, Jeffrey RB Jr et al. (1998) Helical body CT: evolution of scanning protocols. AJR Am J Roentgenol 170:1427–1438

Lymphoma – Controversies in Imaging the Chest

11

Sue C. Kaste

CONTENTS

11.1 **Introduction** *241*

11.2 **Imaging Techniques for Differentiating Normal from Abnormal Thymic Tissue** *241*
11.2.1 Radiographs of the Chest *242*
11.2.2 Computed Tomographic Imaging of the Chest *242*
11.2.3 Ultrasonography of the Chest *243*
11.2.4 Magnetic Resonance Imaging of the Chest *243*
11.2.5 Nuclear Imaging *246*
11.2.5.1 ^{67}Gallium Scintigraphy *246*
11.2.5.2 ^{201}Thallium Scintigraphy *247*
11.2.5.3 FDG-PET Imaging *247*

11.3 **Lung Lesions: Differentiation Between Metastatic Sites and Benign Processes** *248*
11.3.1 Patterns of Pulmonary Lymphoma *248*
11.3.2 Imaging Characteristics of Pulmonary Nodules *251*
11.3.2.1 CT *251*
11.3.2.2 Nuclear Imaging *251*

11.4 **Detecting Recurrent Disease in Residual Mediastinal Mass** *253*
11.4.1 Radiography of the Chest *253*
11.4.2 CT Imaging of the Chest *253*
11.4.3 MR Imaging *257*
11.4.4 Nuclear Imaging *258*
11.4.4.1 ^{67}Gallium *258*
11.4.4.2 ^{201}Thallium *258*
11.4.4.3 ^{18}F-FDG-PET Imaging *259*

11.5 **Summary** *259*

References *260*

11.1
Introduction

In the United States each year, approximately three cases of pediatric Hodgkin's disease and four cases of pediatric non-Hodgkin's lymphoma occur per 100,000 members of the population (Leventhal and Donaldson 1993). In such cases, diagnostic imaging is an integral part of staging and monitoring disease progression. However, staging and assessing disease activity in the chest is particularly difficult in pediatric patients because of the presence of the thymus, the lack of mediastinal fat, and the small size of anatomic structures. Thymic rebound or regrowth further complicates disease assessment. This chapter addresses staging complications caused by thymic tissue, the distinction between lymphoma-related pulmonary nodules and those related to other processes, and methods of differentiating between recurrent active disease and residual quiescent disease. The strengths and weaknesses of available imaging techniques are incorporated into each section.

11.2
Imaging Techniques for Differentiating Normal from Abnormal Thymic Tissue

Abnormal thymic tissue varies in size, contour, imaging characteristics, and may even obscure a mediastinal mass (Boothroyd et al. 1992; Liang and Huang 1997). Thymic tissue may develop in unusual locations; when such unusual findings are accompanied by symptoms, clinical and imaging problems may arise (Heiberg et al. 1982; Lemaitre et al. 1987; Rollins and Currarino 1988; Thomas and Gupta 1988). In imaging studies, even normal

---

S. C. Kaste, DO
Member, Department of Radiological Sciences, Division of Diagnostic Imaging, St. Jude Children's Research Hospital, 332 N. Lauderdale St., Memphis, TN 38105, USA

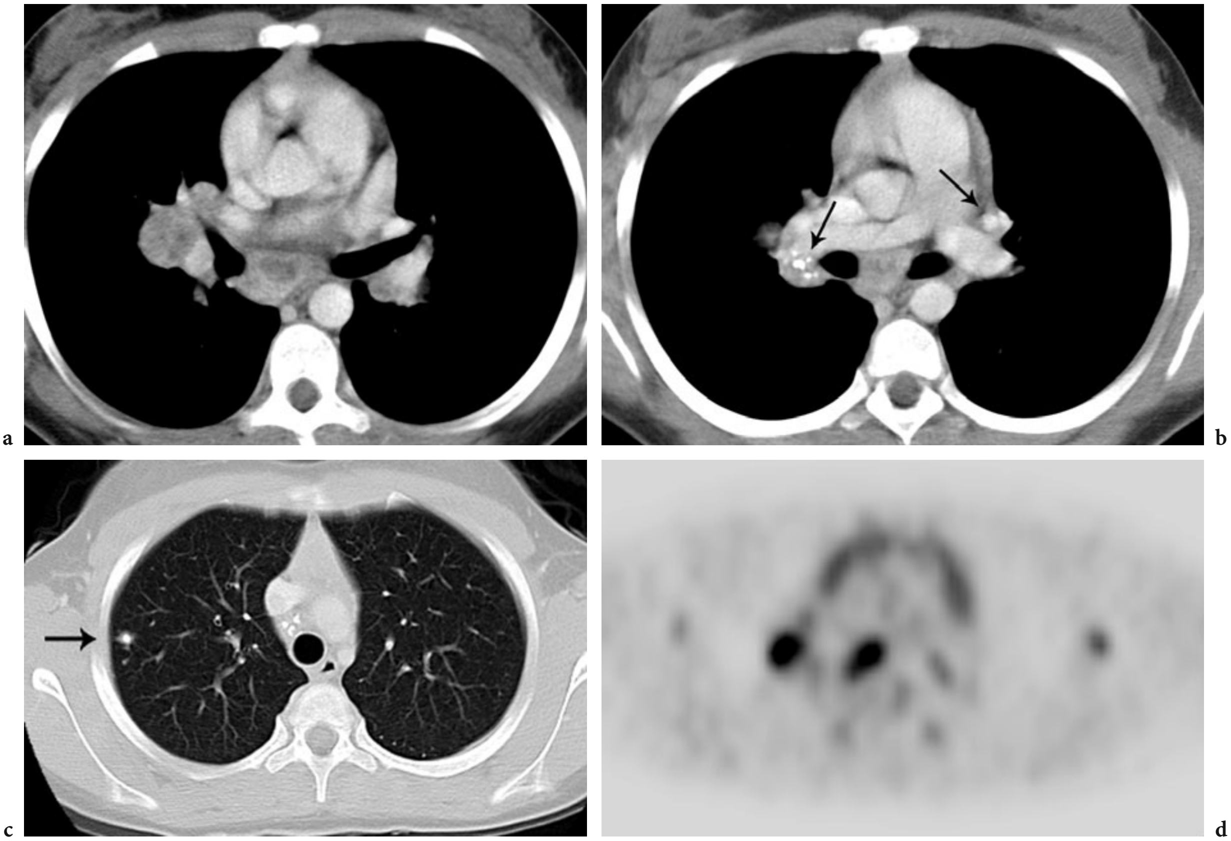

Fig. 11.1a–d. Asymptomatic 11 year-old girl, with positive PPD and increasing mediastinal mass while on anti-tuberculosis therapy underwent evaluation for possible lymphoma and histoplasmosis. Pathologic diagnosis was benign lymph node with fibrosis and non-caseating granulomatous inflammation. **a,b** Axial contrast-enhanced computed tomography of the chest show partially calcified bilateral hilar adenopathy (**a**) (*arrows*), bilateral noncalcified adenopathy and subcarinal mass (**b**). **c** A centrally calcified right upper lobe nodule is also present (*arrow*). **d** ^{18}F-FDG PET image demonstrates metabolic activity in sites of abnormal adenopathy

thymic tissue can mimic a mediastinal mass, and this fact can lead to a false-positive diagnosis (Adam and Ignotus 1993; Choyke et al. 1987; Han et al. 1989; Lemaitre et al. 1987; Liang and Huang 1997) (Fig. 11.1). In contrast, the thymus may be the only site of involvement by Hodgkin's disease in children (Luker and Siegel 1993). Thus, familiarity with the imaging characteristics of normal thymic tissue can facilitate staging and the differentiation of normal thymic tissue from diseased tissue (Cohen et al. 1980).

11.2.1
Radiographs of the Chest

Plain radiography is the least sensitive method of detecting normal thymic tissue. Characteristically, on plain radiographs the thymus appears as an anterior mediastinal mass that may be indented in relationship to anterior ribs. Although normal thymic tissue is usually low in density and appears relatively lucent, concurrent mediastinal disease may still be present (Cohen et al. 1980).

11.2.2
Computed Tomographic Imaging of the Chest

Because computed tomography (CT) is highly sensitive in detecting mediastinal, pericardial, pulmonary, and pleural abnormalities, it is the primary imaging method used for complete and accurate staging and follow-up of childhood Hodgkin's disease and non-Hodgkin's lymphoma (Choyke et al. 1987; Hamrick-Turner et al. 1994).

On CT images, the normal thymus generally has smooth, wavy lateral margins. During the first decade of life, the thymus usually maintains mildly convex lateral borders and a homogeneous density (Francis et al. 1985), although straight or biconcave contours with intermediate soft tissue density may also be seen (Heiberg et al. 1982; Luker and Siegel 1993). However, in older children and adolescents, the biconcave configuration is typical (Heiberg et al. 1982). After puberty, the density of the thymus becomes inhomogeneous because of fatty infiltration, and the gland itself becomes triangular in configuration (Francis et al. 1985). Nodularity of the thymus is not a normal finding for patients of any age (Francis et al. 1985; Moore et al. 1983).

One factor that may aid in differentiating normal thymic tissue from diseased tissue is that on CT images the normal thymus appears to mold around the heart, great vessels, and anterior mediastinum without deforming them. In contrast, diseased thymic tissue lacks this characteristic; it appears more nodular and lobulated and may distort the shape of normal structures (Heiberg et al. 1982; Lemaitre et al. 1987).

11.2.3
Ultrasonography of the Chest

Because ultrasonography is noninvasive, it is an attractive method for evaluating the mediastinum in children. However, the results of sonographic imaging can be compromised by the presence of dense cartilage of the anterior ribs and by the calcified sternum. Ultrasonography allows good visualization of the thymus in children younger than 2 years when the parasternal, transsternal, or suprasternal approaches are used (Lemaitre et al. 1987; Liang and Huang 1997). On ultrasonographic images, the normal thymus has a sharply defined smooth margin with homogeneously low echogenicity that is similar to that of liver (Han et al. 1989; Lemaitre et al. 1987; Liang and Huang 1997; Siegel et al. 1989). This normal pattern of echogenicity does not vary with the age of the patient. On transverse images, the thymus has a bilobar or trapezoidal configuration, whereas on longitudinal images a lunate contour is typical (Lemaitre et al. 1987; Liang and Huang 1997). The thymus is wider and thicker in boys than in girls, and its width increases with increasing age (Liang and Huang 1997).

11.2.4
Magnetic Resonance Imaging of the Chest

Magnetic resonance (MR) imaging is useful for defining the mediastinal structures without the need for radiation or iodinated contrast agents (Figs. 11.2–11.4). MR imaging for staging and disease monitoring is particularly advantageous for patients with a genetic predisposition to sensitivity to ionizing radiation (ex. ataxia telangiectasias) (Fig. 11.2).

However, the use of sedation, which is often needed to complete the examination in children, is particularly problematic when a mediastinal mass is compressing the airway. Furthermore, detection of adenopathy by MR imaging can be compromised by the limits of spatial resolution (Daldrup et al. 1998).

Boothroyd et al. (1992) used images obtained at a field strength of 1.5 Tesla (T) to study the thymus in 31 children aged between 2 weeks and 12 years. They found that normal thymus had an angular shape with acute angles, particularly in the coronal plane (one thymus had a rounded margin); homogeneous signal intensity similar to that of liver and muscle on T1-weighted sequences; signal intensity greater than that of fat on T2-weighted spin echo and short t inversion recovery (STIR) sequences; and normally distended mediastinal veins (Abrahamsen et al. 1994; Boothroyd et al. 1992). Siegel et al. (1989) further defined age-related MR imaging characteristics of normal thymus. In children younger than 5 years, the thymus was quadrilateral in shape with biconvex lateral margins; in older children and adolescents, it had a characteristic triangular configuration with straight margins. Although normal thymic tissue can occur in unusual locations, its normality can often be documented noninvasively by the presence of a homogeneous signal with intensity between those of muscle and fat on T1-weighted images and moderate intensity on T2-weighted images (Rollins and Currarino 1988) (Fig. 11.5).

In contrast, abnormal thymus has the following MR imaging characteristics: focal signal changes; an enlarged rounded shape with obtuse angles; heterogeneous signal intensity; and distortion, encasement, and displacement of mediastinal veins. In children with a histologically proven diagnosis of lymphoma, the thymus is characterized by rounded or distorted contours, focal signal changes, and extrinsic compression of the superior vena cava (Boothroyd et al. 1992; Siegel et al. 1989). When the thymus is involved by lymphoma, leukemia, or

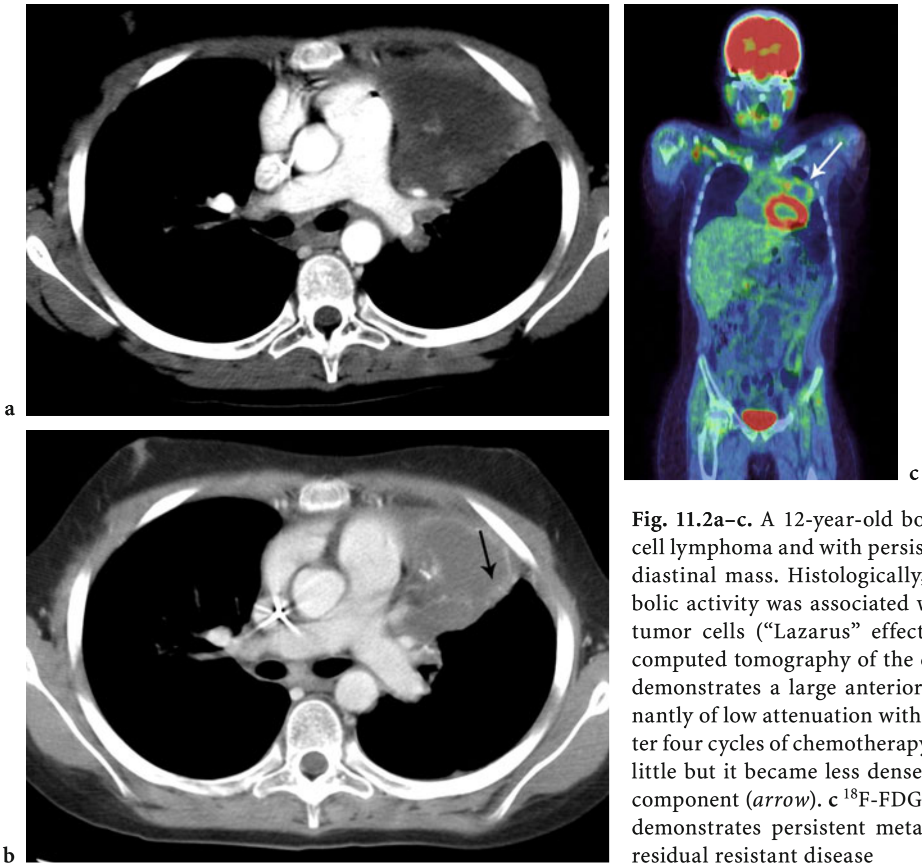

Fig. 11.2a–c. A 12-year-old boy receiving therapy for large cell lymphoma and with persistent metabolic activity in mediastinal mass. Histologically, the area of persistent metabolic activity was associated with newly necrotic and dead tumor cells (“Lazarus” effect). **a** Axial contrast-enhanced computed tomography of the chest at the time of diagnosis demonstrates a large anterior mediastinal mass, predominantly of low attenuation with scattered calcifications. **b** After four cycles of chemotherapy, the size of the mass changed little but it became less dense except for a peripheral solid component (*arrow*). **c** ^{18}F-FDG PET-CT 8 weeks into therapy demonstrates persistent metabolic activity of concern for residual resistant disease

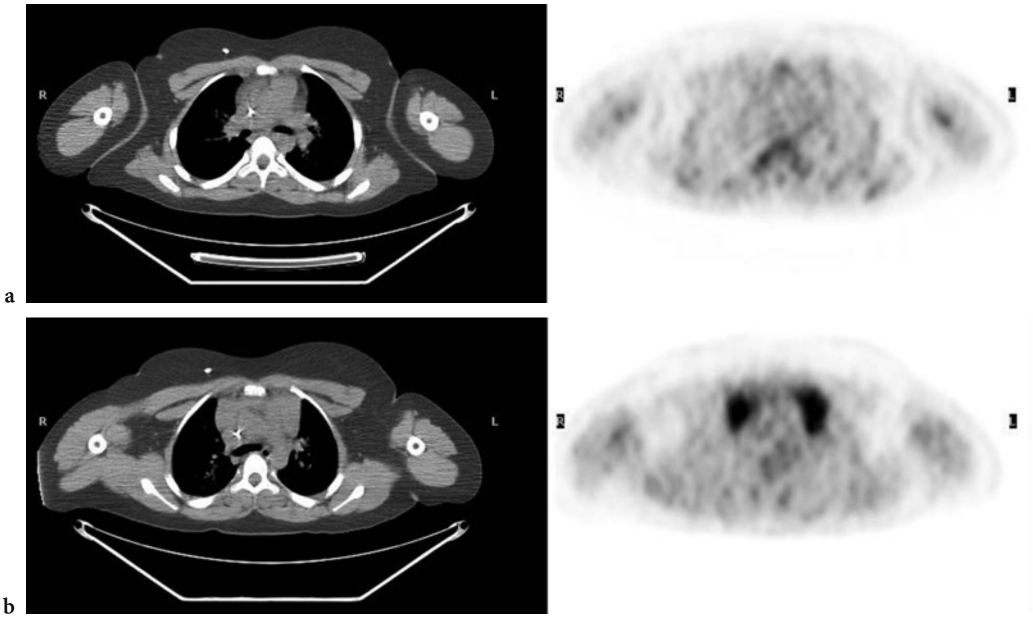

Fig. 11.3a,b. Altered metabolic activity and thymic rebound (hyperplasia) associated with therapy in this 14 year-old male. **a** Axial PET-CT image through the chest while on therapy demonstrates a normal thymic configuration without ^{18}F-FDG uptake. **b** Follow-up examination 6 months later (1 year from diagnosis) shows homogeneous metabolic activity in an enlarged thymus indicative of thymic hyperplasia

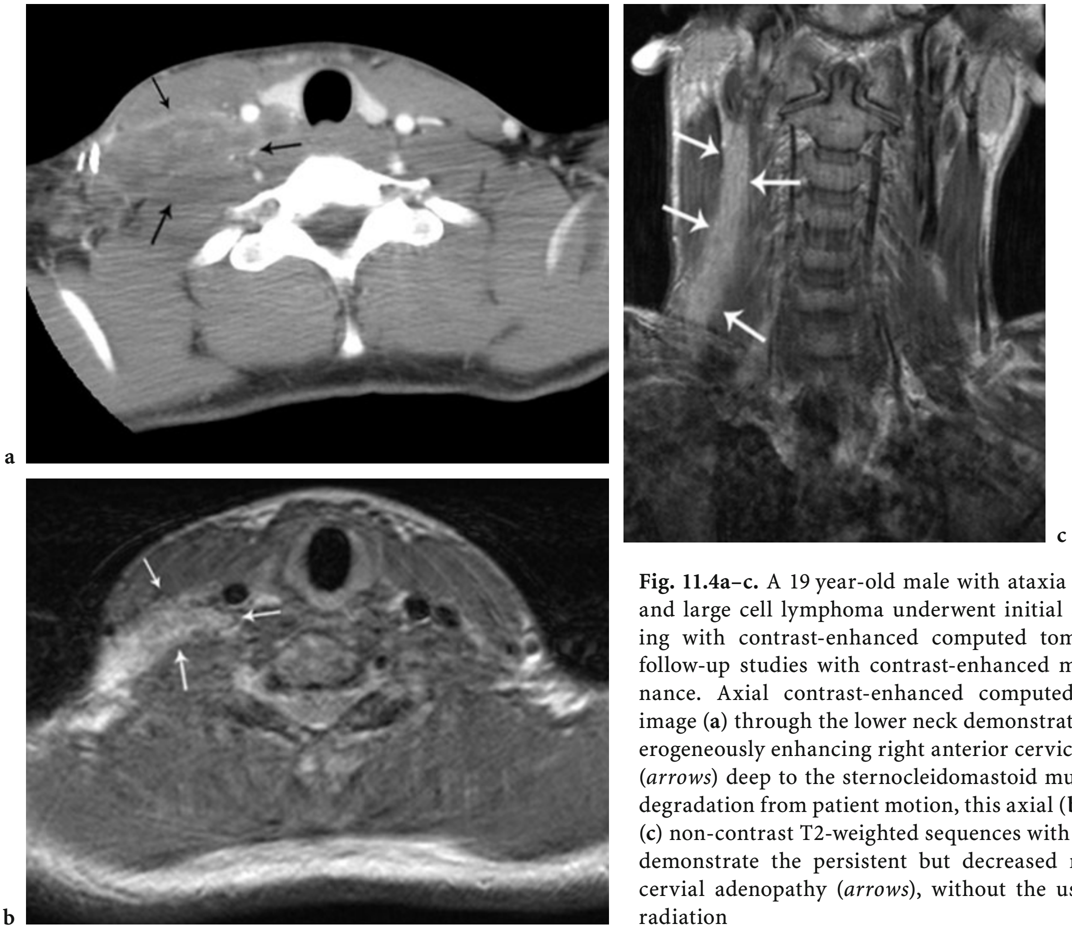

Fig. 11.4a–c. A 19 year-old male with ataxia telangiectasia and large cell lymphoma underwent initial staging imaging with contrast-enhanced computed tomography and follow-up studies with contrast-enhanced magnetic resonance. Axial contrast-enhanced computed tomography image (**a**) through the lower neck demonstrates a large heterogeneously enhancing right anterior cervical nodal mass (*arrows*) deep to the sternocleidomastoid muscles. Despite degradation from patient motion, this axial (**b**) and coronal (**c**) non-contrast T2-weighted sequences with fat saturation demonstrate the persistent but decreased right anterior cervial adenopathy (*arrows*), without the use of ionizing radiation

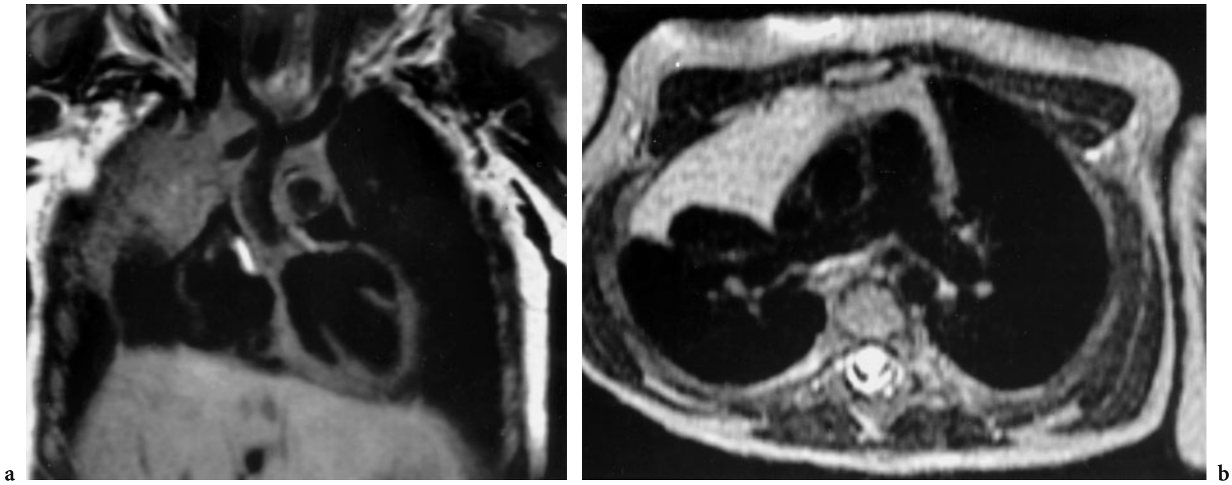

Fig. 11.5a,b. A 9-month-old girl undergoing evaluation for pulmonary hypoplasia. Coronal non-contrast T1-weighted (522/20) (**a**) and axial T2-weighted (2000/80) (**b**) magnetic resonance images of the chest show normal-appearing thymus gland occupying part of the right chests to compensate for right-sided pulmonary hypoplasia. Note homogeneous signal throughout the gland and distribution of the thymus molding around central structures. (Courtesy of Dr. Fred Hoffer)

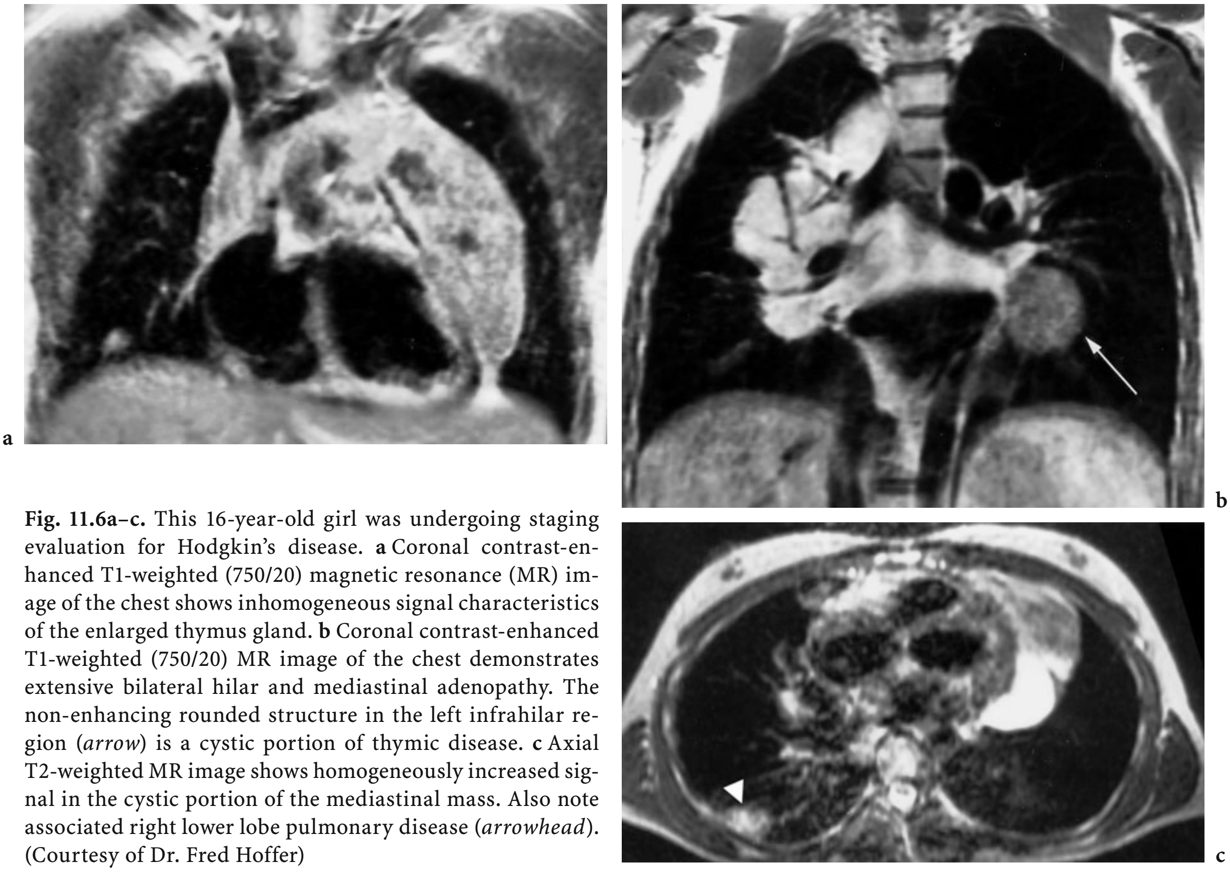

Fig. 11.6a–c. This 16-year-old girl was undergoing staging evaluation for Hodgkin's disease. **a** Coronal contrast-enhanced T1-weighted (750/20) magnetic resonance (MR) image of the chest shows inhomogeneous signal characteristics of the enlarged thymus gland. **b** Coronal contrast-enhanced T1-weighted (750/20) MR image of the chest demonstrates extensive bilateral hilar and mediastinal adenopathy. The non-enhancing rounded structure in the left infrahilar region (*arrow*) is a cystic portion of thymic disease. **c** Axial T2-weighted MR image shows homogeneously increased signal in the cystic portion of the mediastinal mass. Also note associated right lower lobe pulmonary disease (*arrowhead*). (Courtesy of Dr. Fred Hoffer)

hyperplasia, inhomogeneous signal characteristics result from cystic degeneration, septations, fibrosis, calcifications, or hemorrhage. When hilar or mediastinal adenopathy occurs with these heterogeneous signal characteristics, lymphomatous involvement of the thymus is even more strongly suggested (Siegel et al. 1989) (Fig. 11.6 and 11.7).

11.2.5
Nuclear Imaging

11.2.5.1
^{67}Gallium Scintigraphy

Although gallium nuclear scintigraphy is variably sensitive in detecting tumor, it has been the standard imaging modality for the staging of Hodgkin's disease and non-Hodgkin's lymphoma for several decades. In imaging non-Hodgkin's lymphoma, the sensitivity of this imaging method depends on the histologic subtype and grade of the disease (Hamrick-Turner et al. 1994). Gallium avidity in normal thymic tissue may complicate disease staging in children and adolescents. Hibi and colleagues found that gallium avidity occurred in 39% of cases of pediatric solid tumors and in 29% of thymus scans performed for cases of pediatric lymphoma. The incidence of gallium uptake by thymic tissue was greatest (90%) in children 1–2 years of age, regardless of tumor diagnoses, but including Hodgkin's disease and non-Hodgkin's lymphoma (Hibi et al. 1987). If gallium imaging is performed after therapy begins, false-negative findings may result. Furthermore, although ^{67}gallium scintigraphy is highly sensitive in detecting disease, its relative diagnostic accuracy is only 75%; when the findings are compared with those of other imaging modalities, false-positive findings occur in as many as 34% of cases (Cohen et al. 1986).

Single photon emission computed tomography (SPECT) can optimize the detection of avidity (Hamrick-Turner et al. 1994). This imaging method may be particularly helpful in conjunction with planar gallium imaging; because gallium is typically taken up by the normal skeleton, subtle areas of avidity may be obscured as the result of normal uptake of gallium by the bony thorax.

A study of 34 patients aged 8–49 years compared the sensitivity and specificity of ^{67}gallium scintigraphy and MR imaging in diagnosing Hodgkin's disease. The results showed that ^{67}gallium scintigraphy was less sensitive but more specific than MR imaging in detecting disease (gallium sensitivity and specificity, 85.7% and 100%, respectively; MR imaging sensitivity and specificity, 92.8% and 80.6%, respectively). Furthermore, the positive predictive value of ^{67}gallium imaging was 100%, whereas that of MR imaging was 68.4%. Thus, the accuracy of ^{67}gallium imaging was 95.5%, whereas that of MR imaging was 84.4% (Gasparini et al. 1993).

11.2.5.2
^{201}Thallium Scintigraphy

A study of thallium avidity in mediastinal Hodgkin's disease and non-Hodgkin's lymphoma attempted to solve the problem of differentiating gallium-avidity in normal thymus from thymic involvement by tumor. Fletcher et al. (1995) studied 33 pediatric patients with Hodgkin's disease and found that thallium scintigraphy is as accurate in predicting disease as either gallium scintigraphy or CT scanning. Thallium scintigraphy was 100% sensitive in detecting pediatric Hodgkin's disease; no false-positive findings occurred. However, Roebuck and colleagues reported a single case of false-positive avidity in a 7-year-old girl with rebound thymic hyperplasia (Roebuck et al. 1998).

Thallium scintigraphy may be preferable to gallium scintigraphy because thallium is not taken up by normal bones, delivers a relatively lower whole-body radiation dose than gallium (Tonami and Hisada 1977), and is not taken up by the normal mediastinum (Nadel 1993). In addition, thallium scintigraphy can be completed in one appointment, whereas gallium scintigraphy typically requires 2–3 days for completion (Fletcher et al. 1995). Thallium uptake may indicate tumor grade, because low-grade Hodgkin's disease is characterized by greater thallium uptake than intermediate or high-grade disease (Nadel 1993). Although thallium is not taken up by normal bones, its intensity may be attenuated by overlying soft tissues. Thus, SPECT imaging may be helpful in conjunction with planar thallium scintigraphy in detecting disease.

11.2.5.3
FDG-PET Imaging

Positron emission tomography (PET) with 18-fluorodeoxyglucose (FDG) provides characterization of functional metabolic tissue regardless of morphology (Zinzani et al. 1999). Though a very sensitive method of detecting metabolic activity, it is non-specific (Kaste et al. 2005). The role of FDG-PET in childhood lymphomas has not been fully defined. However, lymphomas demonstrate high FDG uptake that resolves after successful oncotherapy (Shulkin

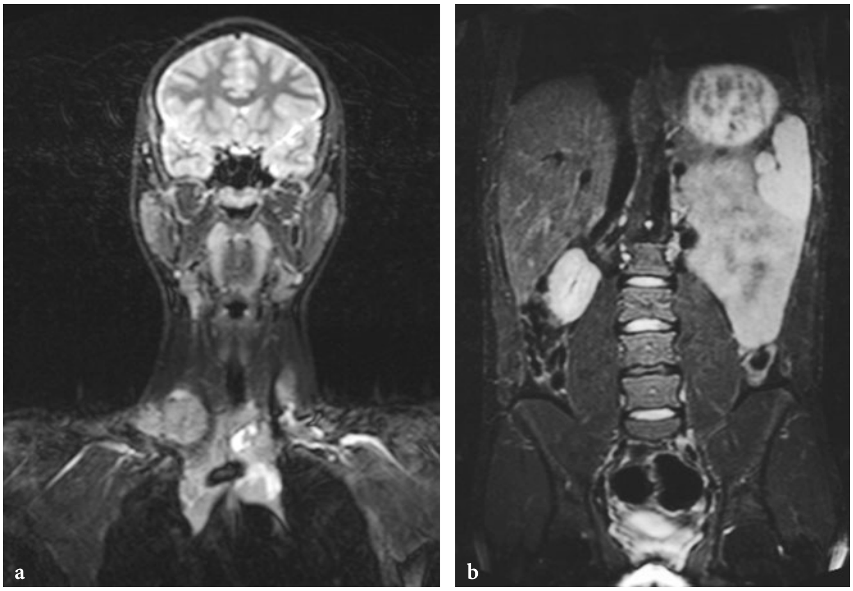

Fig. 11.7a,b. A 15 year-old male with strong history of adverse reaction to iodinated contrast material undergoing staging evaluation for Hodgkin's disease using whole body magnetic resonance imaging. Coronal short tau inversion recovery (STIR) images of the head, neck, chest (**a**) and, abdomen and pelvis (**b**) demonstrate bilateral cervical, right supraclavicular, paratracheal and anterior mediastinal adenopathy. Note heterogeneity of thymic signal indicative of disease involvement. No abnormal subdiaphragmatic adenopathy was demonstrated (**b**)

1997; Shulkin et al. 1995). Valk et al. (1996) found that in 25% of untreated and 100% of treated patients with recurrent disease, PET identified sites of disease and correctly staged disease at a more advanced stage than CT, gallium scintigraphy, or lymphangiography. These findings prompted alteration of planned therapy in 12% of untreated patients and in half of those with recurrent disease (Zinzani et al. 1999). In a study comparing conventional staging techniques with ^{18}F-FDG-PET and PET studies in 55 pediatric patients, Kabickova et al. (2006) found ^{18}F-FDG-PET correctly changed the stage in 15% of the cases. PET upstaged seven patients and downstaged two patients. The authors reported inaccurate staging by PET in 2 of 61 (3%) of imaged patients as PET failed to identify small lymphoma nodules that were detected by chest CT. Thus, PET is more accurate in diagnosing and staging recurrent Hodgkin's disease than are conventional imaging techniques (Zinzani et al. 1999).

11.3
Lung Lesions: Differentiation Between Metastatic Sites and Benign Processes

11.3.1
Patterns of Pulmonary Lymphoma

The presence of pulmonary metastatic disease is a characteristic of stage IV Hodgkin's disease; this finding considerably alters therapy and prognosis. Thus, differentiating between benign and metastatic disease is imperative for proper staging of the disease status, for counselling the patient and the family about prognosis, and for designing proper therapy.

Disease metastasizes to the lungs by hematogeneous dissemination, lymphangitic spread, direct invasion, or a combination of the three. In non-Hodgkin's lymphoma and Hodgkin's disease, the mechanism of spread is typically hematogeneous or lymphangitic. Most hematogeneously disseminated pulmonary metastasis occurs through the pulmonary circulation. However, it has been suggested that the disease may also be disseminated through bronchial arteries. Hematogeneous dissemination of tumor emboli may occur along lymphatic channels, or lymphatic involvement may develop by retrograde proliferation along the lymphatic channels from mediastinal or hilar lymph nodes. Lymphangitic spread is less commonly caused by direct extension (Snyder and Pugatch 1998).

In patients with Hodgkin's disease, the pulmonary parenchyma is rarely involved at the time of diagnosis unless mediastinal or hilar adenopathy is present (Au and Leung 1997). Rare cases of primary pulmonary Hodgkin's disease have been reported in adults without hilar or disseminated disease (Friedland et al. 1982; Nelson et al. 1983; Pik et al. 1986). The incidence of pulmonary involvement by Hodgkin's disease in all patients is 5%–10% at the time of diagnosis (Leone et al. 1990), increases to an overall incidence of 11%–40% (Friedland et al. 1982; Nelson et al. 1983; Pik et al. 1986; Shulkin 1997; Yousem et al. 1986), is nearly 50% just before death (Leone et al. 1990), and is more than 50% at the time of autopsy (Shahar et al. 1987; Yousem et al. 1986). In adults, pulmonary involvement is found in 50%–90% of cases of the nodular sclerosing subtype of Hodgkin's disease, but in only 5%–20% of cases of the other histologic subtypes (Friedland et al. 1982). Pulmonary involvement is twice as common in female patients; it is also more common among patients who are older at the time of diagnosis and those with B symptoms (Yousem et al. 1986), i.e., unexplained weight loss of at least 10% over the 6 months prior to diagnosis of Hodgkin's disease, unexplained fever for at least 3 consecutive days, and drenching night sweats (Leventhal and Donaldson 1993); these symptoms are usually associated with advanced-stage disease.

Pulmonary involvement by Hodgkin's disease or non-Hodgkin's lymphoma is most commonly characterized by single or multiple pulmonary nodules of various sizes (Au and Leung 1997; Leone et al. 1990) (Fig. 11.8). Whereas on CT images most pulmonary metastases originating from solid tumors are well-circumscribed solid nodules, pulmonary parenchymal tumors originating from the lymphomas may have somewhat irregular borders, may be cavitary, and may even mimic a pulmonary infiltrate (Shahar et al. 1987) (Figs. 11.9 and 11.10). In a study of 15 adults with primary pulmonary Hodgkin's disease, Yousem et al. (1986) and colleagues found that histologic examination of all solitary pulmonary nodules showed central necrosis surrounded by a cellular border of lymphocytes, plasma cells, eosinophils, and Reed-Sternberg cells. Alternatively, however, in the case of small bronchial obstructions, trapped air may lead to cavitation by a check-valve mechanism. The occurrence of cavitation after

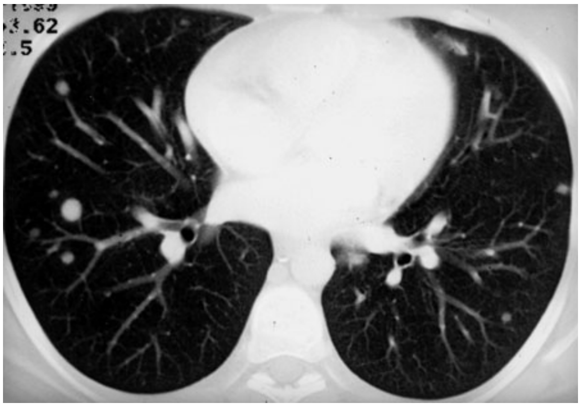

Fig. 11.8. This 19-year-old girl presented with multiple pulmonary nodules at the time of diagnosis of Hodgkin's disease as shown on this axial computed tomography image of through the chest, filmed with lung window

chemotherapy or radiation therapy is uncommon (Spiers et al. 1997).

Unlike Hodgkin's disease, non-Hodgkin's lymphoma is associated with pulmonary involvement at the time of diagnosis in fewer than 5% of cases; lung involvement may occur without concurrent mediastinal or hilar disease (Au and Leung 1997). Like pulmonary parenchymal Hodgkin's disease, pulmonary parenchymal non-Hodgkin's lymphoma is most commonly manifested by multiple pulmonary nodules, but cavitation of nodules is rare at the time of diagnosis (Au and Leung 1997).

Pulmonary Hodgkin's disease is characterized by three patterns on imaging studies. The first pattern is the presence of both pulmonary nodules and ipsilateral mediastinal adenopathy; when both factors are present, the probability that the nodules

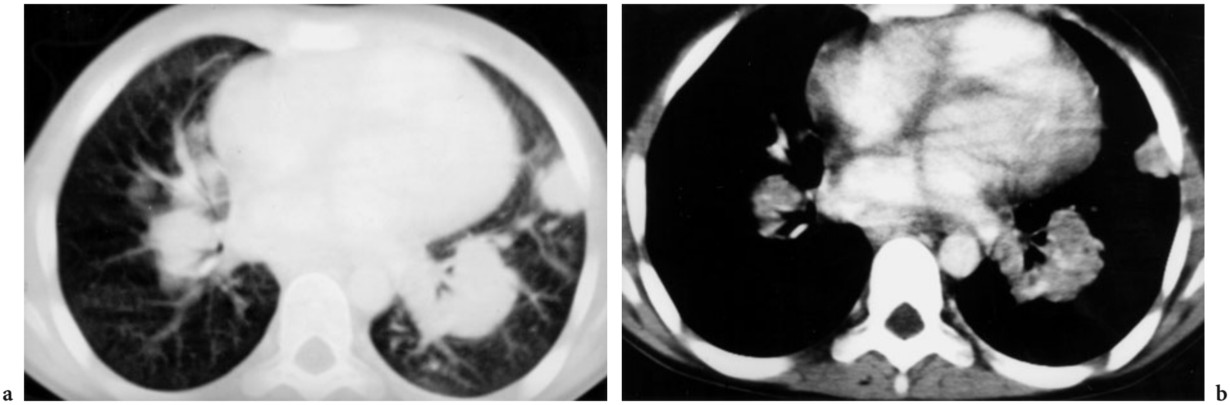

Fig. 11.9a,b. This 12-year-old boy was diagnosed with nodular sclerosing Hodgkin's disease. Axial contrast-enhanced chest computed tomography filmed with lung window (**a**) and mediastinal window (**b**), demonstrate multiple pulmonary masses in concert with extensive bilateral hilar and mediastinal adenopathy. Note confluence and irregular margins of the pulmonary masses

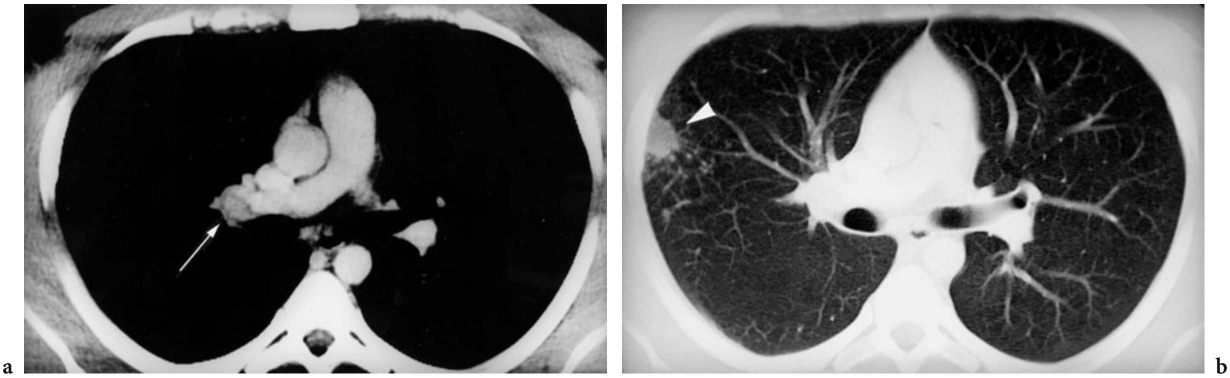

Fig. 11.10a,b. This 22-year-old man underwent routine off-therapy evaluation. Axial contrast-enhanced CT of the chest filmed with mediastinal (**a**) and lung windows (**b**), demonstrated right hilar adenopathy (*arrow*) and an irregular pleural-based pulmonary nodule (*arrowhead*). These findings were suspicious for pulmonary recurrence but serologic studies identified blastomycosis

are caused by metastatic lymphoma is increased (Au and Leung 1997). However, because histoplasmosis may also be characterized by pulmonary nodules with mediastinal adenopathy, making an accurate imaging diagnosis is more difficult when patients live in an area in which this inflammatory disease is endemic. Because pulmonary lymphoma does not typically form calcifications, the presence of central calcifications in lung nodules with or without mediastinal adenopathy suggests an inflammatory process such as histoplasmosis (Chai and Patz 1994; Gurney and Conces 1996). The presence of splenic calcifications, mediastinal calcifications, or both supports a granulomatous process (Fig. 11.11).

The second pattern characteristic of pulmonary Hodgkin's disease is the reticular interstitial pattern that results from venous or lymphatic obstruction caused by hilar or mediastinal adenopathy, or occurring intrinsically from interstitial tumor deposits (Au and Leung 1997) (Fig. 11.12). The third pattern characteristic of pulmonary Hodgkin's disease is lobar or segmental consolidation. This pattern also occurs in non-Hodgkin's lymphoma, and its appearance on radiographs may be confused with that of pneumonia (Au and Leung 1997). Primary extranodal pulmonary lymphoma with this pattern is thought to arise from bronchial lymphoid tissue and is usually a low-grade B-cell lymphoma (Au and Leung 1997).

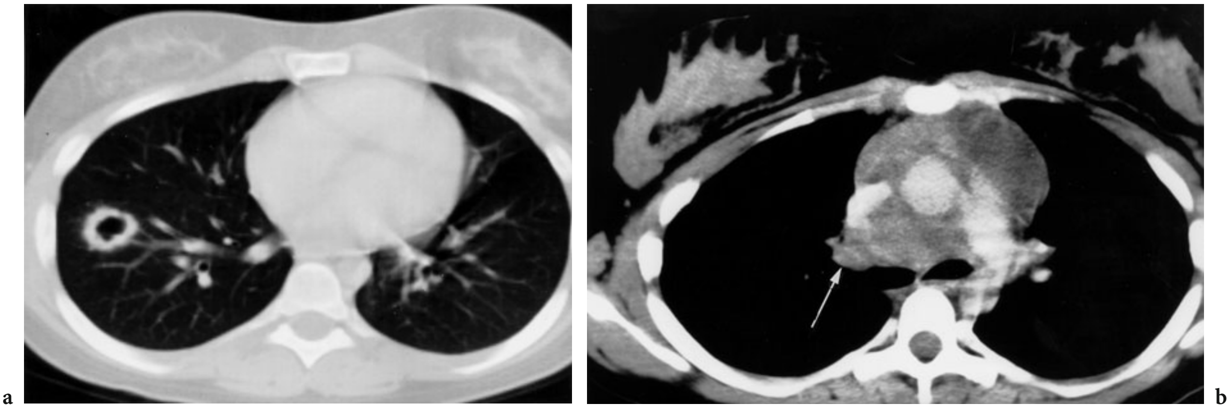

Fig. 11.11a,b. This 15-year-old girl was diagnosed with nodular sclerosing Hodgkin's disease. **a** Axial contrast-enhanced chest computed tomography filmed with lung window shows a cavitary right lower lobe pulmonary nodule with irregular margins. **b** Concurrent image filmed with mediastinal window shows extensive mediastinal and more subtle right hilar adenopathy (*arrow*)

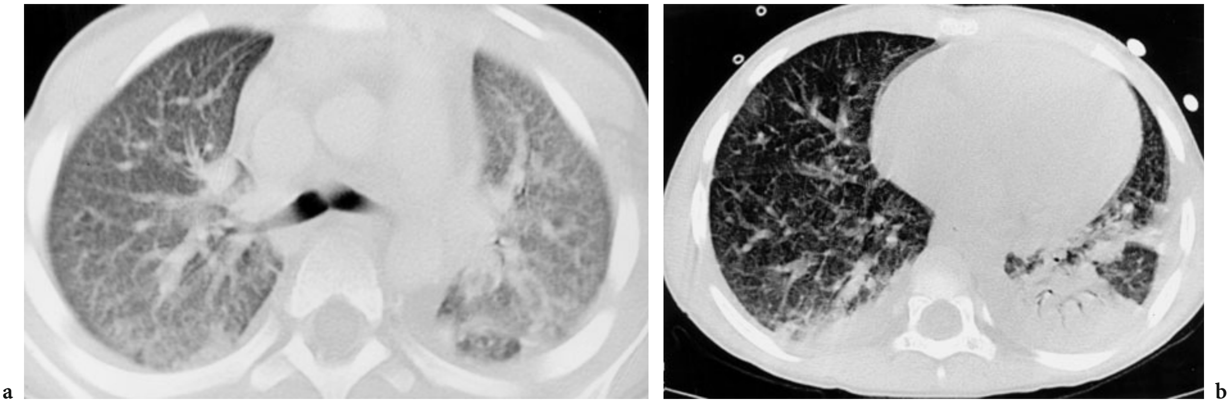

Fig. 11.12a,b. A 2-year-old boy presented in respiratory distress with anaplastic non-Hodgkin's lymphoma and biopsy proven pulmonary lymphoma. **a** Axial chest computed tomography, filmed with lung window, demonstrates diffuse bilateral interstitial pulmonary opacities associated with ground glass appearance of the lungs. **b** High resolution image of the chest, filmed with lung window, shows to better advantage the diffuse interstitial disease of pulmonary non-Hodgkin's lymphoma. Also note areas of consolidation with air bronchograms

Although imaging characteristics may suggest the correct diagnosis, a definitive diagnosis is possible only with biopsy. The results of percutaneous lung biopsy, which can be performed safely (Wittich et al. 1992), are as accurate as those obtained by thoracotomy (Diefenthal and Tashjian 1988; Ognibene et al. 1988). Alternatively, lung nodules may be adequately assessed by thoracoscopic biopsy with or without preoperative CT-directed localization.

11.3.2
Imaging Characteristics of Pulmonary Nodules

11.3.2.1
CT

The ability of CT to detect lung nodules has considerably improved tumor staging. Because CT can detect lung lesions as small as 2–3 mm in diameter, it is far more sensitive than chest radiography (Rosenfield et al. 1992). However, the radiographic appearance of pulmonary metastatic disease can mimic a wide spectrum of diseases including infectious and noninfectious diseases, intrapulmonary lymph nodes, drug reactions, and septic emboli (Snyder and Pugatch 1998). In pediatric patients with primary malignancies, a tiny nodule may result from either benign or malignant disease, whereas in adults as many as 60% of nodules detected by CT may be benign (Rosenfield et al. 1992). Similarly, pulmonary nodules that develop in children undergoing treatment for cancer may be caused by metastatic disease, by infection, or by inflammation (Hidalgo et al. 1983; Kaste 2000; Kaste et al. 1999; Rosenfield et al. 1992). In adults, solitary malignant nodules are more likely than benign nodules to be less densely calcified and to have irregular margins as seen on CT images (Siegelman et al. 1986). In other solid tumors, pulmonary nodules that enhance by at least 20 Housfield units are usually malignant (Swensen et al. 1992, 1995; Yamashita et al. 1995), but this finding has not been confirmed in the lymphomas. Rosenfield et al. (1992) have shown that these criteria used in adults are inadequate for differentiating benign from malignant lesions in children. Thus, development of more sensitive and more specific imaging methods for distinguishing benign from malignant pulmonary nodules in pediatric patients is warranted; radionuclide and immunoscintigraphic imaging may improve such characterization as discussed later in this chapter.

11.3.2.2
Nuclear Imaging

11.3.2.2.1
^{67}Gallium Imaging

Although gallium scintigraphy is a standard staging method for Hodgkin's disease and non-Hodgkin's lymphoma, it is nonspecific for malignancy (Kaste 2000; Posniak and Olson 1996). Lung nodules resulting from Hodgkin's disease and non-Hodgkin's lymphoma can be gallium-avid; however, inflammatory lesions such as infected pulmonary emboli from central venous access devices, or focal pneumonia reactive processes such as bronchiolitis obliterans-organizing pneumonia (BOOP), can also demonstrate gallium avidity (Kaste 2000; Posniak and Olson 1996). In the case of inflammatory lesions, the absence of gallium avidity may nearly exclude a diagnosis of active tumor.

11.3.2.2.2
^{201}Thallium

SPECT imaging with ^{201}thallium shows promise in detecting mediastinal and hilar lymph nodes and in differentiating benign from malignant lung lesions. Arbab et al. (1998) compared the results of thallium SPECT of lung nodules and hilar lymphadenopathy with those of helical CT. They determined that the sensitivity of CT imaging in detecting lymph nodes was 83%, its specificity was 60%, and its negative predictive value was 90%. In contrast, the sensitivity of ^{201}thallium SPECT was 50%, its specificity was 80%, and its positive predictive value was 80%. Furthermore, these authors determined that even lymph nodes larger than 1 cm on CT images could be considered benign if they were not thallium-avid (Arbab et al. 1998). However, Higashi et al. (2001) in a study comparing 66 pulmonary nodules in 63 patients, found ^{201}TI SPECT to show false positive results in 7 (53%) benign nodules.

11.3.2.2.3
^{18}F-FDG-PET Imaging

Recent experience indicates that ^{18}F-FDG-PET is a useful noninvasive method for estimating the risk that a pulmonary nodule is malignant (Gupta et al. 1992, 1996; Valk et al. 1996; Worsley et al. 1997). PET scanning detects increased glucose metabolism, thus exploiting the biochemical differences between benign and malignant cells. ^{18}F-FDG-PET has a sensitivity of 93%, a specificity of 88%, and a positive predictive value of 92% in differentiating malignant from benign solitary pulmonary nodules (Gupta et al. 1992, 1996). Negative results from a PET scan were associated with only a 4.7% likelihood of malignancy (Gupta et al. 1996). Although PET imaging shows promise in determining whether pulmonary nodules are malignant, its routine use is hampered by its cost and its limited availability (Arbab et al. 1998). However, in a study of cost-effectiveness of PET imaging, Valk et al. (1996) found that PET was more accurate than conventional imaging techniques in staging Hodgkin's disease and was more cost-effective than unnecessary surgical procedures in analyzing pulmonary nodules. In many medical centers, PET or PET-CT has replaced the use of ^{67}Gallium and ^{99m}Tc-MDP imaging.

The growing availability of integrated PET and CT as PET-CT has fostered the debate as to whether or not a diagnostic quality chest CT with suspended inspiration is warranted for evaluation of pulmonary nodules. Aquino et al. (2006) compared the accuracy of detecting small pulmonary nodules in 107 adults between attenuation correction chest CT and FDG-PET, and diagnostic chest CT. Detection of nodules in the right lung by PET-CT had a sensitivity of 37% and specificity of 79% compared with the diagnostic CT. In the left lung, the sensitivity and specificity of 41% and 96%, respectively. Thus, these authors consider a diagnostic chest CT to be essential for complete staging in patients with carcinoma; a similar study has yet to be published in patients with pediatric lymphomas.

The incorporation of PET/PET-CT imaging in current staging protocols improves the delineation of sites of disease involvement and hence prevents over- or under-treatment of a patient (Hudson et al. 2004; Krasin et al. 2004). PET/PET-CT has gradually replaced gallium imaging as the preferred functional imaging modality for staging of lymphomas (Hudson et al. 2004; Shulkin 1997; Jerusalem et al. 1999; Bar-Shalom et al. 2003) . Treatment outcomes in adults have been correlated with areas of abnormal 18F-FDG-determined metabolic activity (Hudson et al. 2004). PET/PET-CT has the advantages over gallium of the examination being completed in a single day and the ability to integrate functional and anatomic information, making it both accurate and cost-effective (Hudson et al. 2004).

As promising as PET/PET-CT appears to be, it is associated with unique challenges in pediatric lymphoma patients. Sedation is often needed to assure a quiet, nonmoving patient needed to optimize images. Metabolic activity in normal structures – such as metabolically active "brown fat", thymus, adenoids, and gonadal structures – may complicate image interpretation (Kaste et al. 2005; Hudson et al. 2004).

11.3.2.2.4
Somatostatin-Receptor Scintigraphy

Somatostatin receptors have been identified in both Hodgkin's disease and non-Hodgkin's lymphoma. However, few clinical trials have used somatostatin-receptor scintigraphy to identify disease (Bangerter et al. 1996; Bares et al. 1993; Krenning et al. 1993; Vanhagen et al. 1993). Bares et al. (1993) found that ^{111}In-labeled octreotide scintigraphy was useful in detecting supradiaphragmatic disease, but that infradiaphragmatic disease was largely obscured by the superimposition of the tracer on bowel, spleen, kidneys, and liver (Bangerter et al. 1996). However, using ^{111}In-labeled somatostatin analogs, Vanhagen et al. (1993) identified additional sites of disease in ten patients. Thus, with further clinical development, ^{111}In-labeled octreotide scintigraphy may aid in differentiating malignant from benign disease.

11.3.2.2.5
Immunoscintigraphy

As is true for somatostatin-receptor scintigraphy, clinical experience with immunoscintigraphy for Hodgkin's disease is limited. Immunoscintigraphic agents demonstrate affinity for the CD-30-associated antigen that is present in Hodgkin's disease and anaplastic large cell lymphoma (DaCosta et al. 1992; Falini et al. 1992; Schnell et al. 2005; Staak et al. 2003). Falini et al. (1992) used a ^{131}I-labeled Ber-H_2 (CD30) monoclonal antibody to study six patients with advanced Hodgkin's disease. Unlike immunohistological studies, this method only detected half of the tumor sites (Bangerter et al. 1996). DaCosta et al. (1992) found that ^{125}I-labeled HRS-3 Hodgkin-associated monoclonal antibody was highly specific in detecting disease in their study of 18 patients with Hodgkin's disease. Carde et al. (1990) had similar results using ^{123}I-labeled HRS-1 Hodgkin's associated monoclonal antibody. Development of other immunoscintigraphic agents (ex. ^{99m}Tc-labeled IMMU-LL2 and ^{131}I or - ^{904}-labeled anti-CD 20 antibiodies) may be useful in the future (Subbiah et al. 2003; Lamonica et al. 2002).

11.4
Detecting Recurrent Disease in Residual Mediastinal Mass

Disease response is typically associated with a decrease in the size of the primary mass and a decrease in adenopathy (Luker and Siegel 1993; Nyman et al. 1989; Rahmouni et al. 1993). In children, residual mediastinal abnormality is common, usually benign (Brisse et al. 1998; Luker and Siegel 1993; Peylan-Ramu et al. 1989; Thomas et al. 1988), and typically composed of necrosis, fibrosis, and inflammation (Durkin and Durant 1979). A residual mass may be present in as many as 88% of patients with Hodgkin's disease after the completion of therapy (Jochelson et al. 1985), and is most often associated with the nodular sclerosing subtype of Hodgkin's disease because of its large fibrotic component (Michel et al. 1995; Nyman et al. 1989). Residual mediastinal widening may also occur with non-Hodgkin's lymphoma, even though this disease less commonly involves the mediastinum (Smith et al. 1998). A decrease in the size of the mediastinal mass may continue for more than 8 months with therapy, and the size of the mass may not stabilize for as long as 20 months (Luker and Siegel 1993). Thus, the significance of residual mediastinal abnormality must be determined by correlating its presence with the clinical information obtained in each case (Fig. 11.13).

Residual mediastinal widening is managed in one of three ways: expectant watching, further evaluation by imaging or biopsy with action dictated by the results, or immediate therapeutic intervention for patients with high-risk disease (Djulbegovic et al. 1992). Notably, consideration of residual active disease or delineation of recurrent disease warrants therapeutic modifications or reinstitution of chemotherapy or additional radiation therapy (Fig. 11.14). In contrast, documentation of an inactive residual mediastinal mass obviates the need for more treatment (Fig. 11.15).

However, a recurrent mediastinal mass raises great concern about the tumor's response to therapy and about the possibility of unidentified recurrent disease (Figs. 11.16 and 11.17). Although the mediastinum is the most common site of relapse of Hodgkin's disease, thymic rebound can occur as soon as 1 week after completion of therapy in as many as 25% of pediatric patients and can complicate evaluation (Choyke et al. 1987; Fletcher et al. 1998; Michel et al. 1995; Peylan-Ramu et al. 1989). Thymic rebound is usually self-limiting and reversible, but increased ^{67}gallium avidity may persist in this tissue for 2–59 months (Harris et al. 1993; Peylan-Ramu et al. 1989). As with ^{67}gallium, a normal thymus may demonstrate metabolic activity when examined with ^{18}F-FDG. Heterogeneity of activity within the thymus, however, is strongly suggestions of recurrent disease (Fig. 11.6 and 11.7). Differentiating between thymic rebound and residual or recurrent disease may require further imaging studies when clinical findings are inconclusive.

11.4.1
Radiography of the Chest

As many as 88% of patients with mediastinal Hodgkin's disease have residual mediastinal abnormalities that are visible on chest radiographs and can persist for years after completion of therapy (Jochelson et al. 1985). Such changes include residual mediastinal widening, straightening of the aorticopulmonary window, and right paratracheal fullness. Patients with mediastinal disease that is larger than one-third the transthoracic ratio are more likely to have residual abnormalities; the treatment method – chemotherapy or radiation therapy – does not seem to affect the incidence of mediastinal abnormality (Jochelson et al. 1985). Furthermore, no difference was found in the incidence of relapse between patients with mild residual widening (< 6 cm) and those with larger widening (Jochelson et al. 1985).

11.4.2
CT Imaging of the Chest

Studies of patients with advanced Hodgkin's disease treated with chemotherapy, radiation therapy, or both found residual mediastinal abnormalities in 38%–64% (Orlandi et al. 1990; Radford et al. 1988). As was true for non-Hodgkin's lymphoma, the presence of mediastinal abnormality in association with Hodgkin's disease did not routinely predict relapse (Radford et al. 1988). However, in one series, the rate of isolated intrathoracic relapse was 11% for patients with no residual mass but 20.5% for those with residual widening (Orlandi et al. 1990).

Residual mediastinal soft tissue abnormalities are less common in patients with non-Hodgkin's lymphoma than in those with Hodgkin's disease.

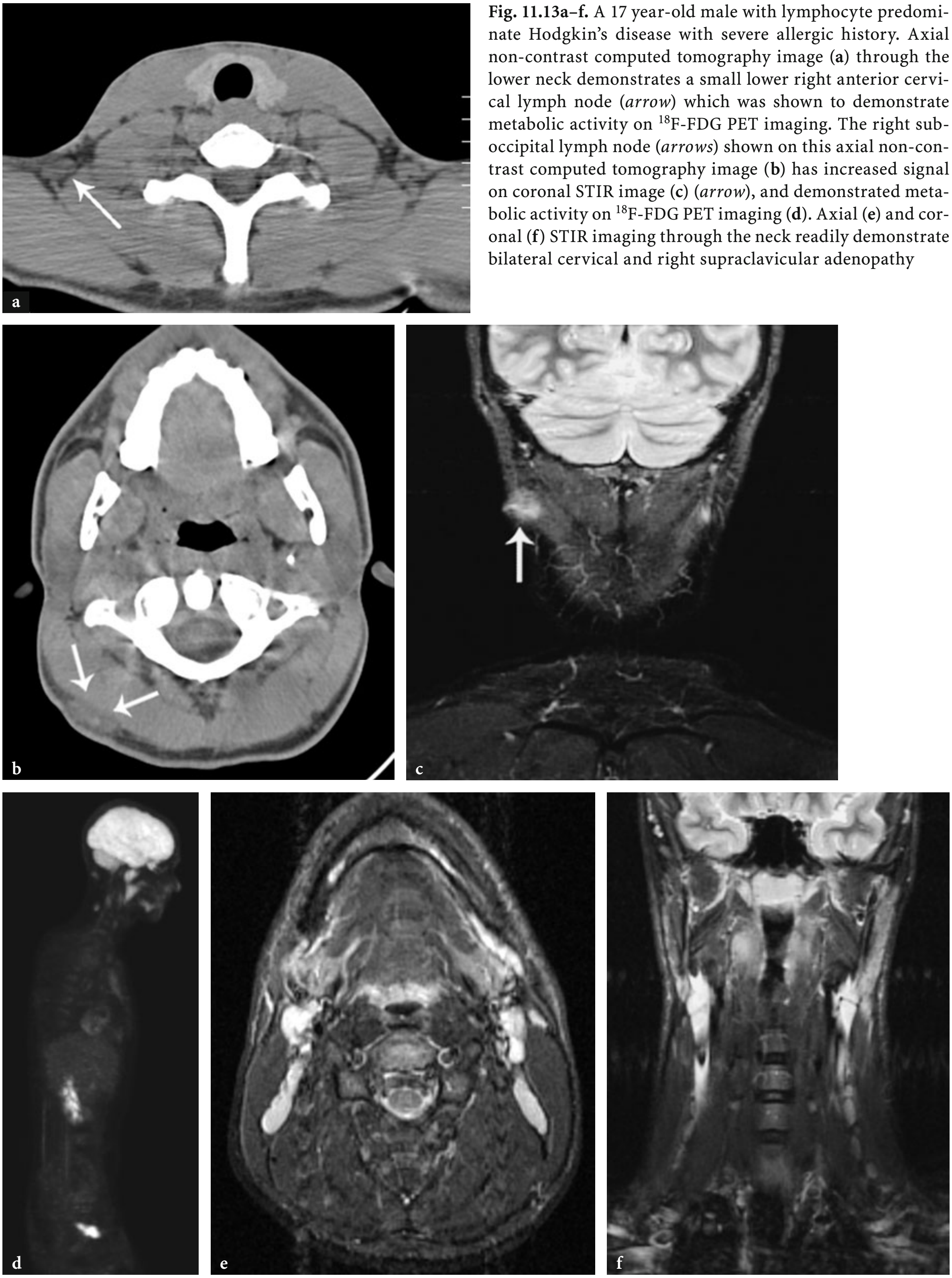

Fig. 11.13a–f. A 17 year-old male with lymphocyte predominate Hodgkin's disease with severe allergic history. Axial non-contrast computed tomography image (**a**) through the lower neck demonstrates a small lower right anterior cervical lymph node (*arrow*) which was shown to demonstrate metabolic activity on ^{18}F-FDG PET imaging. The right suboccipital lymph node (*arrows*) shown on this axial non-contrast computed tomography image (**b**) has increased signal on coronal STIR image (**c**) (*arrow*), and demonstrated metabolic activity on ^{18}F-FDG PET imaging (**d**). Axial (**e**) and coronal (**f**) STIR imaging through the neck readily demonstrate bilateral cervical and right supraclavicular adenopathy

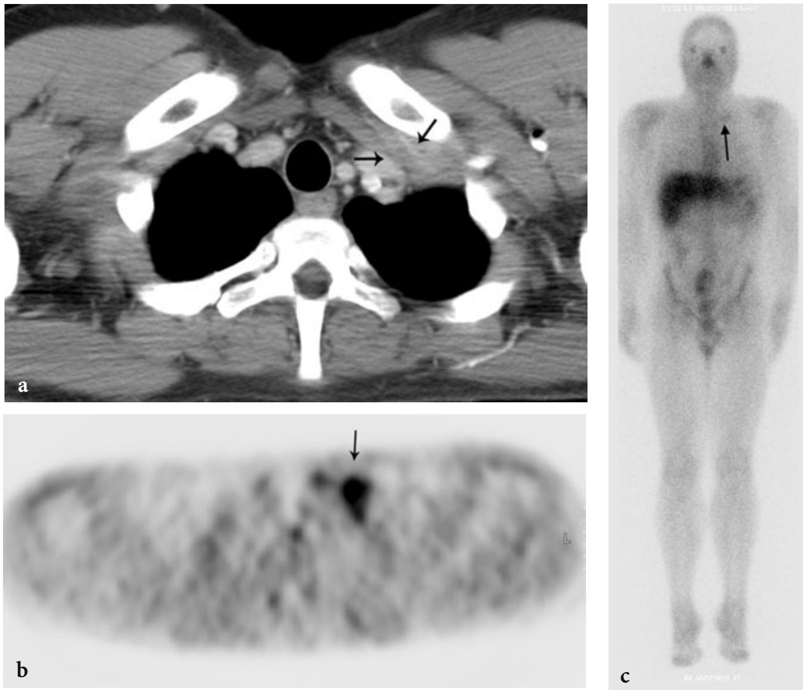

Fig. 11.14a–c. A 24 year-old male in second complete remission for relapsed Hodgkin's disease, who had completed salvage therapy 2 years earlier, underwent routine re-evaluation that demonstrated biopsy proven recurrent disease. **a,b** Axial contrast-enhanced computed tomography image (**a**) through the superior chest and corresponding axial ^{18}F-FDG PET (**b**) demonstrate asymmetric soft tissue in the left retroclavicular region (*arrow*) which is associated with abnormal metabolic activity (*arrow*). **c** Coronal wholebody ^{67}gallium scan shows mild activity in the left supraclavicular region (*arrow*) that corresponds to the findings shown in **a** and **b**

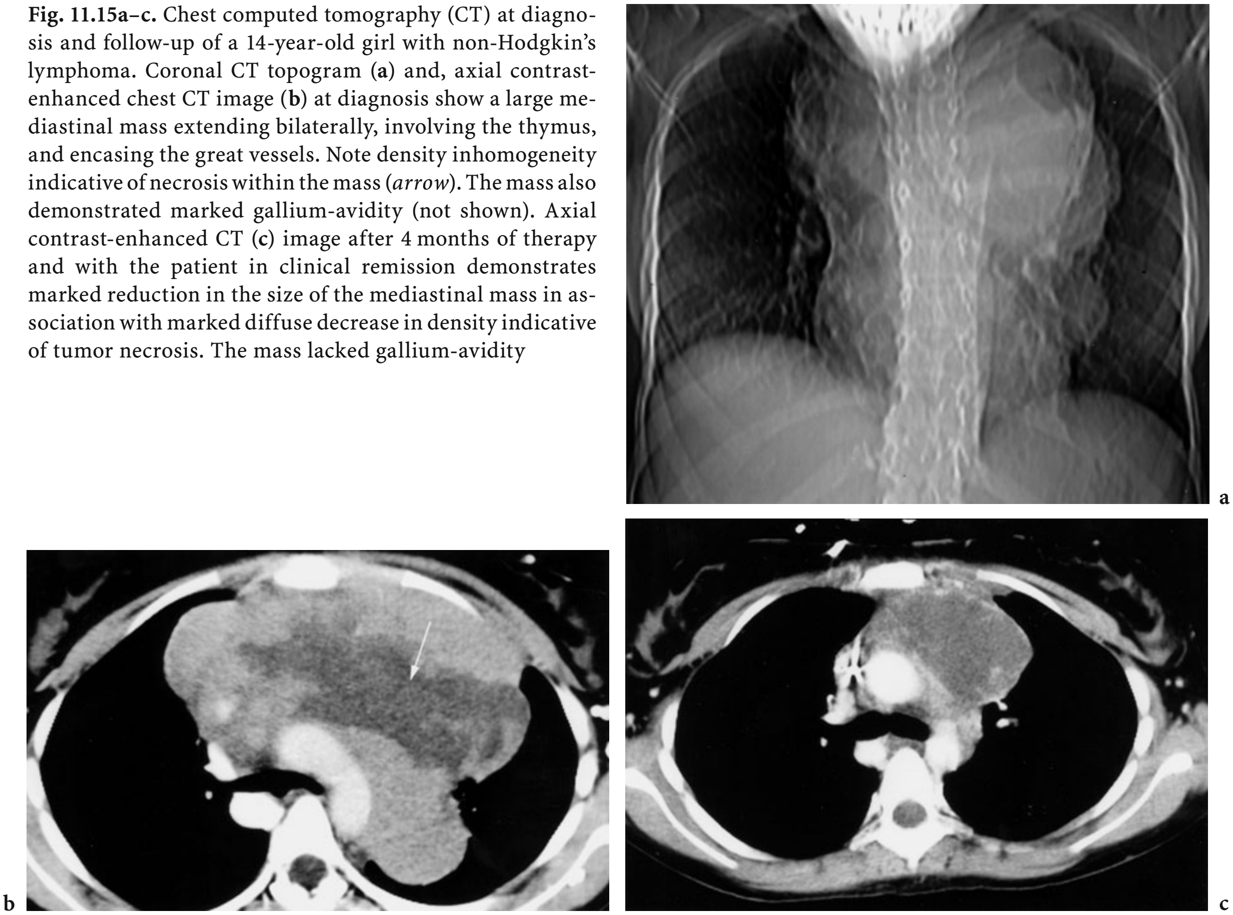

Fig. 11.15a–c. Chest computed tomography (CT) at diagnosis and follow-up of a 14-year-old girl with non-Hodgkin's lymphoma. Coronal CT topogram (**a**) and, axial contrast-enhanced chest CT image (**b**) at diagnosis show a large mediastinal mass extending bilaterally, involving the thymus, and encasing the great vessels. Note density inhomogeneity indicative of necrosis within the mass (*arrow*). The mass also demonstrated marked gallium-avidity (not shown). Axial contrast-enhanced CT (**c**) image after 4 months of therapy and with the patient in clinical remission demonstrates marked reduction in the size of the mediastinal mass in association with marked diffuse decrease in density indicative of tumor necrosis. The mass lacked gallium-avidity

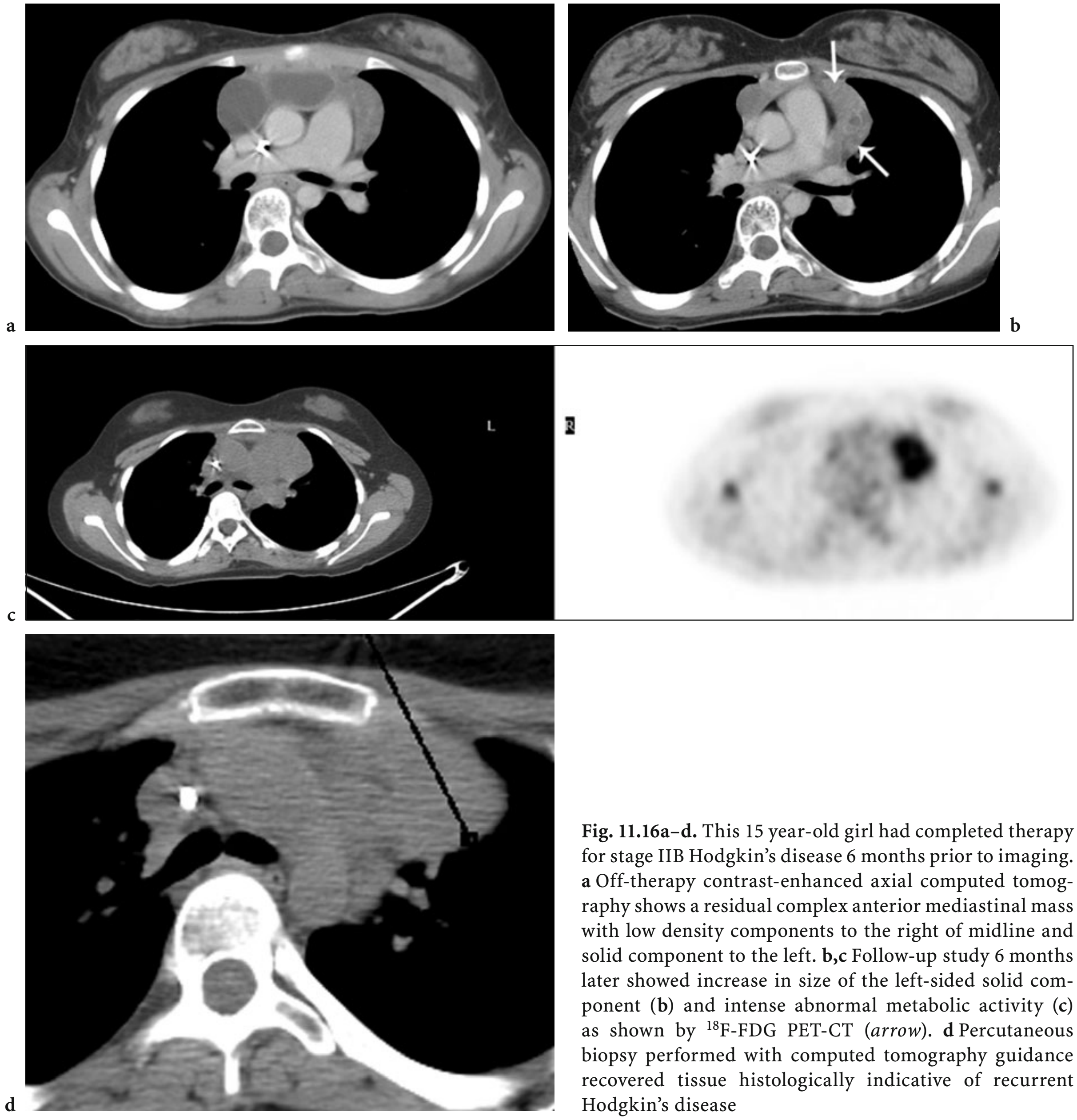

Fig. 11.16a–d. This 15 year-old girl had completed therapy for stage IIB Hodgkin's disease 6 months prior to imaging. **a** Off-therapy contrast-enhanced axial computed tomography shows a residual complex anterior mediastinal mass with low density components to the right of midline and solid component to the left. **b,c** Follow-up study 6 months later showed increase in size of the left-sided solid component (**b**) and intense abnormal metabolic activity (**c**) as shown by ^{18}F-FDG PET-CT (*arrow*). **d** Percutaneous biopsy performed with computed tomography guidance recovered tissue histologically indicative of recurrent Hodgkin's disease

In a large series of 252 adult and pediatric patients treated with chemotherapy for non-Hodgkin's lymphoma, Tredaniel and coworkers found an 8% incidence of residual mediastinal mass (defined as an abnormality larger than 2 cm in diameter) that initially responded to chemotherapy, remained stable in size for at least 3 months, and was associated with complete resolution of all clinical and biologic signs of active lymphoma. The predominant histological pattern of such masses was diffuse large cell non-Hodgkin's lymphoma. The investigators found no difference in estimates of disease-free survival or overall survival for those patients with residual mediastinal masses and for those with complete disease remission (Tredaniel et al. 1992). In contrast, a study of adults with mediastinal non-Hodgkin's lymphoma found that residual mediastinal disease at a volume of more than 100 ml predicted disease relapse (Smith et al. 1998).

CT is sensitive in detecting residual or recurrent mediastinal masses, but its specificity is limited, particularly in light of the intensive treatment that is

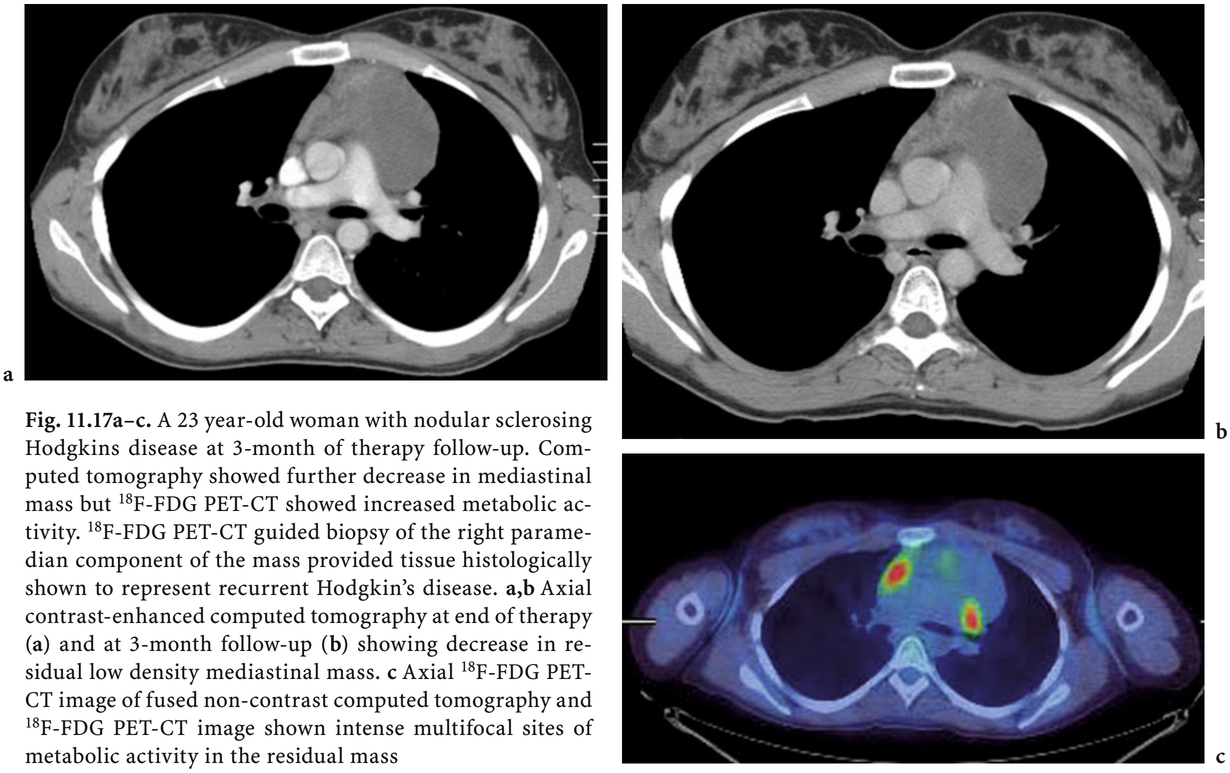

Fig. 11.17a–c. A 23 year-old woman with nodular sclerosing Hodgkins disease at 3-month of therapy follow-up. Computed tomography showed further decrease in mediastinal mass but ^{18}F-FDG PET-CT showed increased metabolic activity. ^{18}F-FDG PET-CT guided biopsy of the right paramedian component of the mass provided tissue histologically shown to represent recurrent Hodgkin's disease. **a,b** Axial contrast-enhanced computed tomography at end of therapy (**a**) and at 3-month follow-up (**b**) showing decrease in residual low density mediastinal mass. **c** Axial ^{18}F-FDG PET-CT image of fused non-contrast computed tomography and ^{18}F-FDG PET-CT image shown intense multifocal sites of metabolic activity in the residual mass

required for salvage therapy or bone marrow transplantation. Elkowitz et al. (1993) found that CT had a sensitivity of 100% in detecting residual mediastinal mass after therapy, a specificity of 27%, a positive predictive value of 17%, and a negative predictive value of 100%. CT cannot differentiate between fibrous tissue and viable neoplasm (Elkowitz et al. 1993; Lewis and Manoharan 1987; Tredaniel et al. 1992); however, cystic changes suggest that the mass is benign (Tredaniel et al. 1992).

Although recurrent mediastinal widening is cause for concern regarding disease relapse, thymic regrowth commonly mimics disease recurrence, but other factors may also cause mediastinal widening. Gallium-avid thymic hyperplasia has been reported in association with thyrotoxicosis after successful completion of therapy for Hodgkin's disease (Pendlebury et al. 1992). Thymic cysts typically appear on CT images as well-defined, low-density mediastinal masses and can occur during therapy for Hodgkin's disease, but are more common after completion of therapy (Borgna-Pignatti 1994; El-Sharkawi and Patel 1995; Lewis and Manoharan 1987; Murray and Parker 1984). They rarely occur after completion of therapy for non-Hodgkin's lymphoma and are probably degenerative in origin (Borgna-Pignatti et al. 1994; El-Sharkawi and Patel 1995; Lewis and Manoharan 1987; Murray and Parker 1984).

11.4.3
MR Imaging

The sensitivity of MR imaging in detecting mediastinal masses may complement CT findings (Tredaniel et al. 1992). However, motion significantly degrades mediastinal assessment. Thus, cardiac gating and sometimes respiratory gating are required for diagnostic MR imaging studies. Adenopathy and active tumor in a mediastinal mass are characterized by decreased signal on T1-weighted MR images and by increased signal on T2-weighted images. (Figs. 11.4, 11.7 and 11.13) Inactive tumor is characterized by decreased signal both on T1-weighted images and on T2-weighted sequences, and by a decrease in overall tumor volume (Michel et al. 1995; Nyman et al. 1989; Rahmouni et al. 1993). The most striking change in the appearance of mediastinal disease on MR images occurs during the early part of treatment (Nyman et al. 1989; Rahmouni et al. 1993).

Like CT, MR imaging has a sensitivity of 100% and a negative predictive value of 100% in detecting malignant mediastinal disease. However, the specificity of MR imaging (73%) and its positive predictive value (35%) are higher than those of CT. The improved specificity of MR imaging is largely due to detection of fibrotic changes in residual mediastinal mass as evidenced by decreased signal on T2-weighted images (Elkowitz et al. 1993). These signal changes may be due to tissue necrosis, active tumor, early fibrosis, or inflammation (Brisse et al. 1998; Elkowitz et al. 1993; Gasparini et al. 1993; Rahmouni et al. 1993). In the presence of clinical remission, inhomogeneous increase in signal within the mass may demonstrate fibrotic changes 3–5 months after documentation of remission. The persistent increase in signal on T2-weighted images may continue in some patients for more than 1 year even though clinical remission continues (Elkowitz et al. 1993).

In contrast, Spiers et al. (1997) found that signal changes detected by MR imaging in large-volume residual masses were associated with disease relapse; the authors advocated close follow-up or biopsy. The inflammatory changes caused by oncotherapy can cause the changes on MR images to be less specific in detecting residual disease (Rahmouni et al. 1993). Thus, the specificity of MR imaging is limited but exceeds that of CT. Signal changes indicative of fibrosis are useful for clinical decision making. However, when areas of increased signal on T2-weighted images persist in a residual mediastinal mass, MR imaging is no more specific than CT in identifying active disease (Elkowitz et al. 1993).

11.4.4
Nuclear Imaging

11.4.4.1
^{67}Gallium

Gallium scintigraphy has been used to assess tumor viability in the mediastinum. Absence of gallium avidity suggests a quiescent mass. In contrast, however, although the presence of gallium avidity strongly suggests active disease, false-positive results occur in as many as 43% of patients (Brisse et al. 1998).

Whole-body ^{67}gallium imaging is 95% sensitive in detecting lymphoma and 98% sensitive in detecting its recurrence (Front et al. 1993). One study found that ^{67}gallium scintigraphy could detect disease recurrence approximately 7 months prior to development of clinical symptoms or before CT detected an abnormality (Front et al. 1993). The whole-body imaging technique is particularly useful for patients with lymphoma as disease recurrence may develop at sites other than that of the original disease (Front et al. 1993).

False-positive results of gallium scintigraphy may suggest disease recurrence when in fact gallium avidity may be due to localization in normal thymic tissue (Brisse et al. 1998; Fletcher et al. 1998; Harris et al. 1993; Hibi et al. 1987). Thus, a patient may undergo therapy and suffer its toxic effects (including death) even though no active disease was present if determination of active disease rested with gallium avidity alone (Djulbegovic et al. 1992). Results of the study by Djulbegovic et al. (1992) of determining the probability of disease in residual mediastinal mass after completion of multiagent chemotherapy indicated that if the probability of disease relapse exceeds 3%, then gallium imaging is warranted before retreatment is initiated.

Gallium avidity in cases of thymic rebound tends to be more common in pediatric patients under the age of 15 years; it may or may not be associated with mediastinal widening (Peylan-Ramu et al. 1989). Clinical characteristics that can support a benign cause of ^{67}gallium avidity include the small noncleaved cell histologic subtype of non-Hodgkin's lymphoma, the absence of disease elsewhere, the absence of mediastinal disease at the time of diagnosis, and the lack of disease progression over the course of serial studies (Peylan-Ramu et al. 1989).

A comparison of the sensitivity of ^{67}gallium SPECT and MR imaging for patients with Hodgkin's disease found that MR imaging had 90% specificity for predicting relapse but only 45% sensitivity. The sensitivity of ^{67}gallium SPECT was similar to that of MR imaging, but its specificity was lower (33%) (Bangerter et al. 1996).

11.4.4.2
^{201}Thallium

^{201}Thallium imaging of the mediastinum has shown strong promise in differentiating benign from malignant mediastinal masses. As Fletcher et al. (1998) showed, ^{201}thallium is 100% sensitive in detecting active mediastinal disease at the time of diagnosis of Hodgkin's disease and is also useful for detecting relapse in treated patients. These investigators found that gallium scintigraphy has greater specificity (90% ± 5%) than thallium scintigraphy (85% ± 6%), but the specificity of thallium and gallium scintigraphy together (97% ± 2%) exceeds that of either modality independently (Fletcher et al. 1998). Thus, for pediatric patients less than 18 years of age, thallium scintigraphy coupled with gallium scintigraphy may be advantageous in differentiating benign thymic regrowth from recurrent disease (Fletcher et al. 1998; Harris et al. 1993). The absence of thallium uptake by residual or recurrent mediastinal mass suggests a quiescent process.

11.4.4.3
^{18}F-FDG-PET Imaging

^{18}F-FDG-PET imaging provides a metabolic road map of foci of increased glycolytic activity, which has been shown to be an indicator of increased metabolism in tumors. PET delineates active tumor mass rather than total tumor volume (Zinzani et al. 1999). Thus, it is useful for predicting malignant histology of hilar and mediastinal lymphadenopathy (Gupta et al. 1992, 1996), and can be particularly useful in differentiating active tumor from necrotic tumor when large masses remain after the completion of therapy (Fig. 11.18).

Zinzani et al. (1999) compared the findings of ^{18}F-FDG-PET and CT in 44 patients with Hodgkin's disease or non-Hodgkin's lymphoma and residual abdominal masses. They found that disease relapse occurred in 100% of patients with positive findings from both CT and ^{18}F-FDG-PET, but in only 4% of patients with positive CT findings but negative ^{18}F-FDG-PET findings. No relapses occurred in patients with negative findings on both studies. Thus, it may be beneficial to use ^{18}F-FDG-PET imaging to detect recurrent disease when CT scanning demonstrates residual mediastinal mass. (Fig. 11.17)

11.5
Summary

Pediatric Hodgkin's disease and non-Hodgkin's lymphoma present unique diagnostic challenges. Identifying active disease, differentiating quiescent residual mass from recurrent disease, and distinguishing findings related to lymphoma from those related to other causes are vital for proper disease staging and therapeutic planning. Contemporary imaging techniques do well at identifying anatomic abnormalities but are limited in determining disease activity. Established nuclear scintigraphic techniques, such as ^{18}F-FDG-PET, and evolving immunoscintigraphic techniques herald the evolution

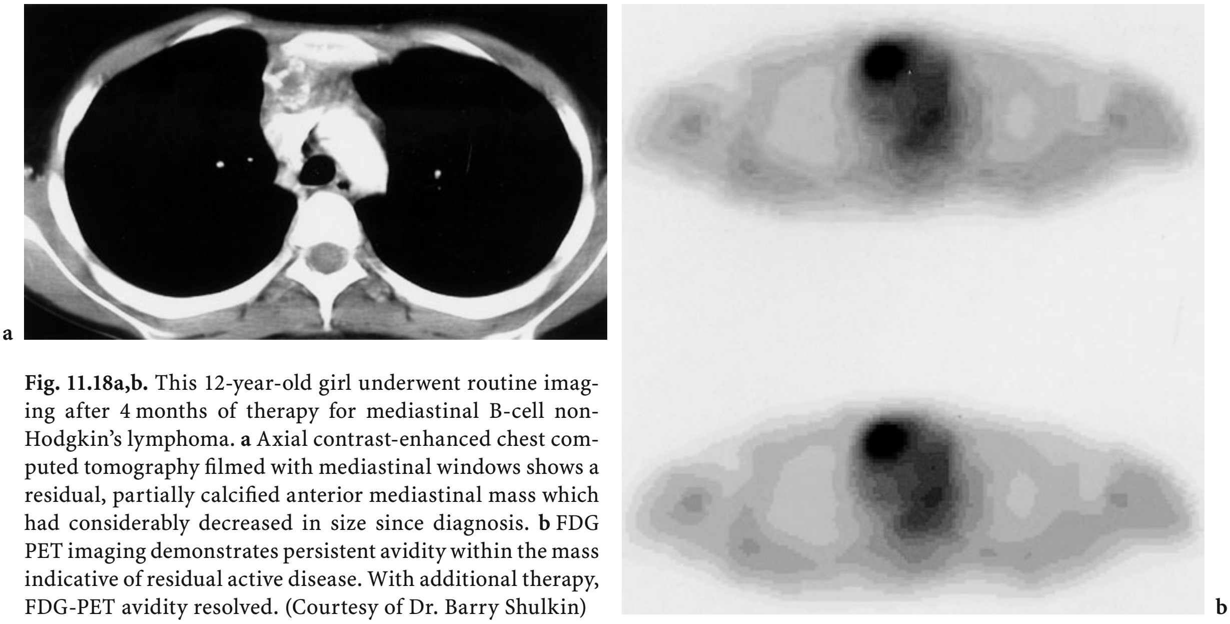

Fig. 11.18a,b. This 12-year-old girl underwent routine imaging after 4 months of therapy for mediastinal B-cell non-Hodgkin's lymphoma. **a** Axial contrast-enhanced chest computed tomography filmed with mediastinal windows shows a residual, partially calcified anterior mediastinal mass which had considerably decreased in size since diagnosis. **b** FDG PET imaging demonstrates persistent avidity within the mass indicative of residual active disease. With additional therapy, FDG-PET avidity resolved. (Courtesy of Dr. Barry Shulkin)

of functional and metabolic techniques with great promise in solving the problems discussed in this chapter.

Acknowledgements. The author thanks Sandra Gaither for manuscript preparation and Dr. Barry Shulkin for assistance in formatting PET-CT images.

References

Abrahamsen AF, Lien HH, Aas M et al. (1994) Magnetic resonance imaging and ^{67}gallium scan in mediastinal malignant lymphoma: a prospective pilot study. Ann Oncol 5:433–436

Adam EJ, Ignotus PI (1993) Sonography of the thymus in healthy children: frequency of visualization, size, and appearance. AJR Am J Roentgenol 161:153–155

Aquino SL, Kuester LB, Muse VV et al. (2006) Accuracy of transmission CT and FDG-PET in the detection of small pulmonary nodules with integrated PET/CT. Eur J Nucl Med Mol Imaging 33:692–696

Arbab AS, Koizumi K, Toyama K et al. (1998) Detection of lung lesions and lymph nodes with ^{201}T1 SPET. Nucl Med Commun 19:411–416

Au V, Leung AN (1997) Radiologic manifestations of lymphoma in the thorax. AJR Am J Roentgenol 168:93–98

Bangerter M, Griesshammer M, Binder T et al. (1996) New diagnostic imaging procedures in Hodgkin's disease. Ann Oncol 7 [Suppl 4]:55–59

Bares R, Galonska P, Dempke W et al. (1993) Somatostatin receptor scintigraphy in malignant lymphoma: first results and comparison with glucose metabolism measured by positron-emission tomography. Horm Metab Res Suppl 27:56–58

Bar-Shalom R, Yefremov N, Haim N et al. (2003) Camera-based FDG PET and 67 Ga SpECT in evaluation of lymphoma: comparative study. Radiology 227:353–360

Boothroyd AE, Hall-Craggs MA, Dicks-Mireaux C et al. (1992) The magnetic resonance appearances of the normal thymus in children. Clin Radiol 45:378–381

Borgna-Pignatti C, Andreis IB, Rugolotto S et al. (1994) Thymic cyst appearing after treatment of mediastinal non-Hodgkin lymphoma. Med Pediatr Oncol 22:70–72

Brisse H, Pacquement H, Burdairon E et al. (1998) Outcome of residual mediastinal masses of thoracic lymphomas in children: impact on management and radiological follow-up strategy. Pediatr Radiol 28:444–450

Carde P, DaCosta L, Manil L et al. (1990) Immunoscintigraphy of Hodgkin's Disease: in vivo use of radiolabelled monoclonal antibodies derived from Hodgkin cell lines. Eur J Cancer 26:474–479

Chai JL, Patz EF Jr (1994) CT of the lung: patterns of calcification and other high-attenuation abnormalities. AJR Am J Roentgenol 162:1063–1066

Choyke PL, Zeman RK, Gootenberg JE et al. (1987) Thymic atrophy and regrowth in response to chemotherapy: CT evaluation. AJR Am J Roentgenol 149:269–272

Cohen M, Hill CA, Cangir A et al. (1980) Thymic rebound after treatment of childhood tumors. AJR Am J Roentgenol 135:151–156

Cohen MD, Siddiqui A, Weetman R et al. (1986) Hodgkin disease and non-Hodgkin lymphomas in children: utilization of radiological modalities. Radiology 158:499–505

DaCosta L, Carde P, Lumbroso JD et al. (1992) Immunoscintigraphy in Hodgkin's disease and anaplastic large cell lymphomas: results in 18 patients using the iodine radiolabeled monoclonal antibody HRS-3. Ann Oncol Suppl 4:53–57

Daldrup HE, Link TM, Wörtler K et al. (1998) MR imaging of thoracic tumors in pediatric patients. AJR Am J Roentgenol 170:1639–1644

Diefenthal HC, Tashjian J (1988) The role of plain films, CT, tomography, ultrasound, and percutaneous needle aspiration in the diagnosis of inflammatory lung disease. Semin Respir Infect 3:83–105

Djulbegovic B, Hendler FJ, Hamm J et al. (1992) Residual mediastinal mass after treatment of Hodgin's disease: a decision analysis. Med Hypotheses 38:166–175

Durkin W, Durant J (1979) Benign mass lesions after therapy for Hodgkin's disease. Arch Intern Med 139:333–336

Elkowitz SS, Leonidas JC, Lopez M et al. (1993) Comparison of CT and MRI in the evaluation of therapeutic response in thoracic Hodgkin disease. Pediatr Radiol 23:301–304

El-Sharkawi AMM, Patel B (1995) Management of residual thymic cysts in patients treated for mediastinal Hodgkin's disease. Thorax 50:1118–1119

Falini B, Flenghi L, Fedeli L et al. (1992) In vivo targeting of Hodgkin and Reed-Sternberg cells of Hodgkin's disease with monoclonal antibody Ber-H2 (CD-30): immunohistological evidence. Br J Haematol 82:38–45

Fletcher BD, Kauffman WM, Kaste SC et al. (1995) Use of Tl-201 to detect untreated pediatric Hodgkin disease. Radiology 196:851–855

Fletcher BD, Xiong X, Kauffman WM et al. (1998) Hodgkin disease: use of Tl-201 to monitor mediastinal involvement after treatment. Radiology 209:471–475

Francis IR, Glazer GM, Bookstein FL et al. (1985) The thymus: re-examination of age-related changes in size and shape. AJR Am J Roentgenol 145:249–254

Friedland ML, Wittels EG, Deutsch A (1982) Hodgkin's disease with pulmonary cavitation. Postgrad Med J 58:794–796

Front D, Bar-Shalom R, Epelbaum R et al. (1993) Early detection of lymphoma recurrence with gallium-67 scintigraphy. J Nucl Med 34:2101–2104

Gasparini MD, Balzarini L, Castellani MR et al. (1993) Current role of gallium scan and magnetic resonance imaging in the management of mediastinal Hodgkin lymphoma. Cancer 72:577–582

Gupta NC, Frank AR, Dewan NA et al. (1992) Solitary pulmonary nodules: detection of malignancy with PET with 2-[F-18]-fluoro-2-deoxy-D-glucose. Radiology 184:441–444

Gupta NC, Maloof J, Gunel E (1996) Probability of malignancy in solitary pulmonary nodules using fluorine-18-FDG and PET. J Nucl Med 37:943–948

Gurney JW, Conces DJ (1996) Pulmonary histoplasmosis. Radiology 199:297–306

Hamrick-Turner JE, Saif MF, Powers CI et al. (1994) Imaging of childhood non-Hodgkin lymphoma: assessment by histologic subtype. Radiographics 14:11–28

Han BK, Babcock DS, Oestreich AE (1989) Normal thymus in infancy: sonographic characteristics. Radiology 170:471–474

Harris EW, Rakow JI, Weiner M et al. (1993) Thallium-201 scintigraphy for assessment of a gallium-67-avid mediastinal mass following therapy for Hodgkin's disease. J Nucl Med 34:1326–1330

Heiberg E, Wolverson MK, Sundaram M et al. (1982) Normal thymus: CT characteristics in subjects under age 20. AJR Am J Roentgenol 138:491–494

Hibi S, Todo S, Imashuku (1987) Thymic localization of gallium-67 in pediatric patients with lymphoid and nonlymphoid tumors. J Nucl Med 28:293–297

Hidalgo H, Korobkin M, Kinney TR et al. (1983) The problem of benign pulmonary nodules in children receiving cytotoxic chemotherapy. AJR Am J Roentgenol 140:21–24

Higashi K, Ueda Y, Sakuma T et al. (2001) Comparison of [18F]FDG PET and ^{201}TI SPECT in evaluation of pulmonary nodules. J Nucl Med 42:1489-1496

Hudson MM, Krasin MJ, Kaste SC (2004) PET imaging in pediatric Hodgkin's lymphoma. Pediatr Radiol 34:190–198

Jerusalem G, Begiun Y, Fassotte MF et al. (1999) Whole-body positron emission tomography using 18F-fluorode-oxyglucose for posttreatment evaluation in Hodgkin's disease and non-Hodgkin's lymphoma has higher diagnostic and prognostic value than classical computed tomography scan imaging. Blood 94:429–433

Jochelson M, Mauch P, Balikian J et al. (1985) The significance of the residual mediastinal mass in treated Hodgkin's Disease. J Clin Oncol 3:637–640

Kabickova E, Sumerauer D, Cumlivska E et al. (2006) Comparison of ^{18}F-FDG-PET and standard procedures for the pretreatment staging of children and adolescents with Hodgkin's disease. Eur J Nucl Med Mol Imaging 33:1025–1031

Kaste SC (2000) Infection imaging of children and adolescents undergoing cancer therapy: a review of modalities and an organ system approach. Semin Pediatr Infect Dis 11:122–141

Kaste SC, Pratt CB, Cain AM et al. (1999) Metastases detected at the time of diagnosis of primary pediatric extremity osteosarcoma at diagnosis: imaging features. Cancer 86:1602–1608

Kaste SC, Howard SC, McCarville EB et al. (2005) ^{18}F-FDG-avid sites mimicking active disease in pediatric Hodgkin's. Pediatr Radiol 35:141–154

Krasin MJ, Hudson MM, Kaste SC (2004) Positron emission tomography in pediatric radiation oncology: integration in the treatment-planning process. Pediatr Radiol 34:214–221

Krenning EP, Kwekkeboom DJ, Reubi JC et al. (1993) 111In-octreotide scintigraphy in oncology. Digestion 54[Suppl 1]:84–87

Lamonica D, Czuczman M, Nabi H et al. (2002) Radioimmunoscintigraphy (RIS) with bectumomab (Tc99m labeled IMMU-LL2, lymphoscan®) in the assessment of recurrent non-Hodgkin's lymphoma (NHL) 17:689–697

Lemaitre L, Marconi V, Avni F et al. (1987) The sonographic evaluation of normal thymus in infants and children. Eur J Radiol 7:130–136

Leone G, Castellana M, Rabitti C (1990) Escavative pulmonary Hodgkin's lymphoma: diagnosis by cutting needle biopsy. Eur J Haematol 44:139–141

Leventhal BG, Donaldson SS (1993) Hodgkin's disease. In: Pizzo PA, Poplack DG (eds) Principles and practice of pediatric oncology, 2nd edn. Lippincott, Philadelphia, pp 577–594

Lewis CR, Manoharan A (1987) Benign thymic cysts in Hodgkin's disease: report of a case and review of published cases. Thorax 42:633–634

Liang C-D, Huang S-C (1997) Sonographic study of the thymus in infants and children. J Formos Med Assoc 96:700–703

Luker GD, Siegel MJ (1993) Mediastinal Hodgkin disease in children: response to therapy. Radiology 189:737–740

Michel F, Gilbeau J-P, Six C et al. (1995) Progressive mediastinal widening after therapy for Hodgkin's disease. Acta Clin Belg 50:282–287

Moore AV, Korobkin M, Olanow W et al. (1983) Age-related changes in the thymus gland: CT-pathologic correlation. AJR Am J Roentgenol 141:241–246

Murray JA, Parker AC (1984) Mediastinal Hodgkin's disease and thymic cysts. Acta Haematol 71:282–284

Nadel HR (1993) Thallium-201 for oncologic imaging in children. Semin Nucl Med 23:243–254

Nelson S, Prince D, Terry P (1983) Primary Hodgkin's disease of the lung: case report. Thorax 38:310–311

Nyman RS, Rehn SM, Glimelius BLG et al. (1989) Residual mediastinal masses in Hodgkin disease: prediction of size with MR imaging. Radiology 170:435–440

Ognibene FP, Pass HI, Roth JA et al. (1988) Role of imaging and interventional techniques in the diagnosis of respiratory disease in the immunocompromised host. J Thorac Imaging 3:1–20

Orlandi E, Lazzarino M, Brusamolino E et al. (1990) Residual mediastinal widening following therapy in Hodgkin's disease. Hematol Oncol 8:125–131

Pendlebury SC, Boyages S, Koutts J et al. (1992) Thymic hyperplasia associated with Hodgkin disease and thyrotoxicosis. Cancer 70:1985–1987

Peylan-Ramu N, Haddy TB, Jones E et al. (1989) High frequency of benign mediastinal uptake of gallium-67 after completion of chemotherapy in children with high-grade non-Hodgkin's lymphoma. J Clin Oncol 7:1800–1806

Pik A, Cohen N, Weissgarten J et al. (1986) Primary pulmonary Hodgkin's disease with air bronchogram. Respiration 50:226–229

Posniak HV, Olson MC (1996) Correlative imaging of abdominal infection. In: Henkin RE, Boles MA, Dillehay GL et al. (eds) Nuclear medicine, vol II. Mosby, St Louis, pp 1662–1685

Radford J, Cowan R, Flanagan M et al. (1988) The significance of residual mediastinal abnormality on the chest radiograph following treatment for Hodgkin's disease. J Clin Oncol 6:940–946]

Rahmouni A, Tempany C, Jones R et al. (1993) Lymphoma: monitoring tumor size and signal intensity with MR imaging. Radiology 188:445–451

Roebuck DJ, Nicholls WD, Bernard EJ et al. (1998) Misleading leads. Thallium-201 uptake in rebound thymic hyperplasia. Med Pediatr Oncol 30:297–300

Rollins NK, Currarino G (1988) MR imaging of posterior mediastinal thymus. J Comput Assist Tomogr 12:518–520

Rosenfield NS, Keller MS, Markowitz RI (1992) CT differentiation of benign and malignant lung nodules in children. J Pediatr Surg 27:459–461

Schnell R, Dietlein M, Staak JO et al. (2005) Treatment of refractory Hodgkin's lymphoma patients with an iodine-131-labeled murine anti-CD30 monoclonal antibody. J Clin Oncol 23:4669–4678

Shahar J, Angelillo VA, Katz D et al. (1987) Recurrent cavitary nodules secondary to Hodgkin's disease. Chest 91:273–274

Shulkin BL (1997) PET applications in pediatrics. Q J Nucl Med 41:281–291

Shulkin BL, Mitchell DS, Ungar DR et al. (1995) Neoplasms in a pediatric population:2-[F-18]-fluoro-2-deoxy-D-glucose PET studies. Radiology 194:495–500

Siegel MJ, Glazer HS, Wiener JI et al. (1989) Normal and abnormal thymus in childhood: MR imaging. Radiology 172:367–371

Siegelman SS, Khouri NF, Leo FP et al. (1986) Solitary pulmonary nodules: CT assessment. Radiology 160:307–312

Smith D, Shaffer K, Kirn D et al. (1998) Mediastinal large cell lymphoma: prognostic significance of CT findings at presentation and after treatment. Oncology 55:284–288

Snyder BJ, Pugatch RD (1998) Imaging characteristics of metastatic disease to the chest. Chest Surg Clin North Am 8:29–48

Spiers ASD, Husband JES, MacVicar AD (1997) Treated thymic lymphoma: comparison of MR imaging with CT. Radiology 203:369–376

Staak JO, Dietlein M, Engert A et al. (2003) Hodgkin's lymphoma in nuclear medicine: diagnostic and therapeutic aspects. Nuklearmedizin 42:19–24

Subbiah K, Hamlin DK, Pagel JM et al. (2003) Comparison of immunoscintigraphy, efficacy, and toxicity of conventional and pretargeted radioimmunotherapy in CD20-expressing human lymphoma xenografts. J Nucl Med 44:437–445

Swensen SJ, Morin RL, Schueler BA et al. (1992) Solitary pulmonary nodule: CT evaluation of enhancement with iodinated contrast material – a preliminary report. Radiology 182:343–347

Swensen SJ, Brown LR, Colby TV et al. (1995) Pulmonary nodules: CT evaluation of enhancement with iodinated contrast material. Radiology 194:393–398

Thomas NB, Gupta SC (1988) Unilobar enlargement of normal thymus gland causing mass effect. Br J Radiol 61:244–246

Thomas F, Cosset JM, Cheret P et al. (1988) Thoracic CT-scanning follow-up of residual mediastinal masses after treatment of Hodgkin's disease. Radiother Oncol 11:119–122

Tonami N, Hisada K (1977) Clinical experience of tumor imaging with 201Tl-chloride. Clin Nucl Med 2:75–81

Tredaniel J, Brice P, Lepage E et al. (1992) The significance of a residual mediastinal mass following treatment for aggressive non-Hodgkin's lymphomas. Eur Respir J 5:170–173

Valk PE, Pounds TR, Tesar RD et al. (1996) Cost-effectiveness of PET imaging in clinical oncology. Nucl Med Biol 23:737–743

Vanhagen PM, Krenning EP, Reubi JC et al. (1993) Somatostatin analogue scintigraphy of malignant lymphomas. Br J Haematol 83:75–79

Wittich GR, Nowels KW, Korn RL et al. (1992) Coaxial transthoracic fine-needle biopsy in patients with a history of malignant lymphoma. Radiology 183:175–178

Worsley DF, Celler A, Adam MJ et al. (1997) Pulmonary nodules: Differential diagnosis using ^{18}F-fluorodeoxyglucose single-photon emission computed tomography. AJR Am J Roentgenol 168:771–774

Yamashita K, Matsunobe S, Tsuda T et al. (1995) Solitary pulmonary nodule: preliminary study of evaluation with incremental dynamic CT. Radiology 194:399–405

Yankelevitz DF, Henschke CI (1997) Does 2-year stability imply that pulmonary nodules are benign? AJR Am J Roentgenol 168:325–328

Yousem SA, Weiss LM, Colby TV (1986) Primary pulmonary Hodgkin's disease. A clinicopathologic study of 15 cases. Cancer 57:1217–1224

Zinzani PL, Magagnoli M, Chierichetti F et al. (1999) The role of positron emission tomography (PET) in the management of lymphoma patients. Ann Oncol 10:1181–1184

Chest Tumours Other than Lymphoma

Kieran McHugh

CONTENTS

12.1 **Introduction** *263*

12.2 **Clinical Features** *263*

12.3 **Imaging** *264*

12.4 **Pulmonary Tumours** *265*
12.4.1 Previous Cystic Lung Lesion *266*
12.4.2 Benign Tumours *266*
12.4.2.1 Inflammatory Myofibroblastic Tumour *266*
12.4.2.2 Hamartoma *268*
12.4.2.3 Leiomyoma *269*
12.4.2.4 Laryngotracheal Papilloma *270*
12.4.3 Malignant Tumours *271*
12.4.3.1 Bronchial Adenoma *271*
12.4.3.2 Pleuropulmonary Blastoma *273*
12.4.3.3 Bronchogenic Carcinoma *275*
12.4.3.4 Pulmonary Nodules and Metastases *275*

12.5 **Mediastinal Tumours** *278*
12.5.1 Germ Cell Tumours *278*
12.5.2 Thymoma *279*
12.5.3 Neuroblastoma *280*
12.5.4 Lymphatic Malformations *281*

12.6 **Chest Wall Tumours** *282*
12.6.1 Benign *282*
12.6.2 Malignant *282*
12.6.2.1 Ewing’s Sarcoma/Primitive Neuroectodermal Tumour *282*
12.6.2.2 Rhabdomyosarcoma and Other Sarcomas *283*
12.6.2.3 Mesothelioma *284*

12.7 **Tumours of the Diaphragm** *284*

12.8 **Conclusions** *285*

References *285*

12.1
Introduction

Thoracic tumours are generally arbitrarily classified, despite some inevitable overlap, as originating in three major compartments within the chest, namely the lung parenchyma, the mediastinum, and the chest wall. In the interests of simplicity and convention, that anatomical approach will be used in this chapter with an additional brief reference to diaphragmatic tumours. As most of the mediastinal tumours mentioned, other than the lymphatic malformations, have varying degrees of malignancy depending on the exact histological sub-type, that section has not been divided into benign and malignant categories. Benign chest wall tumours are described in Chapter 14 and will not be mentioned here. The imaging at diagnosis for all lesions has been emphasised throughout. The subsequent follow-up radiology of benign conditions is governed by the clinical course, and that of malignant masses is largely determined thereafter by imaging protocols devised by the various international paediatric oncology co-operative groups and should take place in specialist paediatric centres. PET/CT may be occasionally useful in the diagnostic work-up of some of the tumours mentioned in this chapter – the emerging role of PET/CT will be dealt with in more detail elsewhere in Chapter 2.

12.2
Clinical Features

Numerically, most tumours occurring in the thorax in childhood, particularly those encountered in paediatric oncology centers, are pulmonary metastases. These will usually be found during staging

---

K. McHugh, FRCR, FRCPI, DCH
Department of Radiology, Great Ormond Street Hospital for Children NHS Trust, Great Ormond Street, London WC1N 3JH, UK

of a known or new malignancy and the dominant clinical findings will be those of the primary lesion. Primary thoracic neoplasia is uncommon in childhood and seldom an early diagnostic consideration, but a wide variety of tumours within the chest do occur and ideally should be recognised and imaged appropriately. It is noteworthy that there is essentially no major difference between the sexes in the incidence of the primary chest tumours described here. Tumours occur in essence with relatively equal frequency in either lung.

Primary chest neoplasms largely manifest due to pressure effects secondary to local compression of adjacent organs, systemic symptoms when there is disseminated malignancy or as an incidental finding. Paraneoplastic syndromes are exceedingly rare. With airway obstruction or respiratory symptoms that do not respond to the usual medical treatment, computed tomography (CT) in particular can be very useful in excluding other pathology or documenting an unsuspected lesion. Whilst the presenting symptomatology can vary enormously even within the same histological group, some generalisations with regard to the presentation of chest masses can be made.

In both benign and malignant lung tumours the most frequent presenting complaints are fever, cough and pneumonitis (Hancock et al. 1993; Hartman and Shochat 1983). Haemoptysis and respiratory distress are more common with malignant pulmonary lesions. In one large review series, 27.9% of benign tumours were asymptomatic as compared to 6.3% of malignant lung tumours (Hancock et al. 1993). A child who is truly asymptomatic is twice as likely to harbour a benign pulmonary tumour, and this likelihood is even greater in children over 4 years of age. Endobronchial masses typically result in lung collapse, persistent hyperinflation or wheezing which again fails to respond to conventional treatment and may be complicated by bronchiectasis. The endobronchial location of many such lesions is often only apparent after bronchoscopy. Occasionally CT may reveal an abnormality prior to bronchoscopy being performed or, albeit less likely, when bronchoscopy is negative or not considered feasible.

Some chest wall tumours come to attention because of a superficial chest mass. Thoracic neuroblastoma and more especially the benign ganglioneuroma are often found incidentally on chest X-rays (CXRs) performed for other reasons. The majority of chest wall and mediastinal tumours generally present, however, with non-specific respiratory symptoms such as airway obstruction, cough or fever due to a complicating pneumonia. In contrast to many tumours of pulmonary origin, the likely nature of the illness becomes apparent after a chest radiograph has been performed – if the film is interpreted correctly. The lung opacity is generally not typical for pneumonia with often clearly defined margins suggesting a pleural or chest wall component. Mediastinal shift or adenopathy may be seen and rib changes, in particular, should be sought as this latter finding virtually always indicates an extrapleural malignancy. In fact, the majority of mediastinal and chest wall tumours seen in children are malignant.

12.3
Imaging

Radiological studies should always begin with a frontal chest radiograph. When an unusual opacity is evident, a lateral film can be particularly helpful in assessing the trachea for compression and/or displacement, and in accurately defining the location of the abnormality, which aids greatly in differential diagnosis. For pulmonary lesions the next imaging study should be CT, as this remains the best modality to evaluate the lung parenchyma. A few limited low dose non-enhanced sections may be performed to assess for calcification but in general that is seldom necessary as calcification is usually easily discernible on post-contrast studies also. It is crucial that intravenous contrast is given to best delineate tumour extent and the relationship of a mass to the adjacent airway, major blood vessels or chest wall. A solely non-enhanced study of the thorax in this context is often a waste of time and radiation, and such CT studies invariably need to be repeated. When bronchoscopy suggests an endobronchial lesion CT may be used to confirm these findings and assess the extrabronchial spread of disease. Reconstructions in the coronal or sagittal plane, now so readily achieved with multidetector CT (MDCT) scanners, may delineate the mass to better effect. In addition virtual bronchoscopy (VB) with MDCT can allow better definition of the endobronchial anatomy when an endobronchial lesion is present. The added value of VB in this setting is unknown, however. VB can increase total examination time and cost, and it may not provide additional information over MPR images (Kocaoglu et al. 2006). Despite meticulous technique in examining smaller endobronchial lesions associated with atelectasis, an atelectatic segment may nevertheless obscure tumour resulting in a false negative CT study. Alternatively, bronchiectasis with atelectasis may be the dominant clinical finding and so prompt a, simpler and lower dose, high-resolution chest CT (HRCT) study which, with 1–2-cm gaps between sections, could easily miss an underlying small endobronchial mass.

In the routine screening for pulmonary metastases, contiguous sections without intravenous contrast enhancement through the entire thorax are generally adequate in paediatric patients. When there is any suspicion of mediastinal adenopathy, it is mandatory that intravenous contrast is given as the lack of mediastinal fat in children, unlike in adult patients, makes evaluation of the mediastinum difficult. Many centres, including our own department, are increasingly tending to routinely administer intravenous contrast to evaluate the mediastinum more closely in all patients suspected of pulmonary metastatic disease, to improve detection of mediastinal lymphadenopathy. The lung parenchyma because of its high inherent contrast can also be adequately examined for pulmonary nodules at relatively low tube current, e.g. 50 mA or less (Diederich et al. 1999). Of note, low dose techniques increase noise and render assessment of the mediastinum less reliable. Maximum intensity projection (MIP) techniques can have improved sensitivity particularly for small, high-density pulmonary nodules (Coakley et al. 1998). This tool uses ray projection techniques through a stack of preselected images with the highest density object encountered by the ray traversing the stack projected onto the final image (Gruden et al. 2002). Although depth information is absent on MIP images, MIP processing has several advantages in the detection of small nodules: vascular structures appear as tubular and branching structures rather than as discrete nodules; the MIP slab preserves the inherent resolution of the original images; MIP images can be constructed in any plane; and image numbers are markedly reduced in comparison to the axial image set from a routine MDCT study (Gruden et al. 2002). MIP images improve the likelihood of small nodule detection because of improved depiction of pulmonary vessels and enhanced anatomic orientation. MIP images should not however substitute for axial image review. Computer assisted detection (CAD) via computerised image analysis has been used in some adult studies. CAD allows more nodules to be detected, reduces the missed nodule rate, allows faster reading times and so improves efficiency. CAD is not in widespread use in pediatric imaging and in everyday practice contiguous sections are adequate for nodule detection. Alternatively, manipulating the CT images in a 3D format with particular reliance on coronal or sagittal reformatted images often helps decision making with small nodules.

CT after intravenous contrast administration can accurately define mediastinal and chest wall masses and is sensitive in the detection of adjacent bony destruction. CT will also be necessary to evaluate the pulmonary parenchyma in patients with malignant tumours. Magnetic resonance imaging (MRI), however, where available, has become the optimal technique for examining the chest wall and mediastinum, mainly as a result of faster scanning parameters, improved gating techniques, and MR angiography, in addition to the usual advantages of better soft-tissue contrast, lack of radiation and multiplanar capability. Most tumours have intermediate T1 signal, are hyperintense to varying degrees on T2 and display variable contrast enhancement after gadolinium administration. Rather than actual signal characteristics, it is the pattern and site of tumour occurrence and the age of the patient that suggests the likely tumour in an individual case.

12.4
Pulmonary Tumours

Pulmonary masses are unusual in childhood. The absence of systemic upset or pyrexia excludes a round pneumonia or lung abscess as the likely cause, and so other diagnostic possibilities need to be considered. Low attenuating cystic appearances are common on CT with abscesses or bronchogenic cysts, for example, allowing correct diagnoses in most cases. Once the common causes of a pulmonary mass and a primary extra-thoracic malignancy with metastases have been excluded, primary tumours are the next major consideration in the differential diagnosis of pulmonary masses in childhood (Table 12.1) (Mas Estelles et al. 1995).

Table 12.1. Summary of primary pulmonary neoplasms in children. (Reprinted with permission, Hancock et al. 1993)

Tumour type	Number (%)
Benign ($n = 92$)	
Inflammatory	48 (52)
Hamartoma	22 (24)
Neurogenic tumour	9 (10)
Leiomyoma	6 (7)
Mucous gland adenoma	3 (3)
Malignant ($n = 291$)	
Bronchial ‘adenoma’	118 (40)
Bronchogenic carcinoma	49 (17)
Pulmonary blastoma	45 (16)
Fibrosarcoma	28 (10)
Rhabdomyosarcoma	17 (6)
Leiomyosarcoma	11 (4)
Sarcoma	6 (2)
Haemangiopericytoma	4 (1)

12.4.1
Previous Cystic Lung Lesion

The vast majority of lung neoplasms are thought to occur de novo without pre-existing lung pathology. The association between prior cystic lung lesions and subsequent pulmonary tumours has been controversial. Nevertheless, 4.3% of benign tumours and 8.6% of malignant tumours reported by Hancock et al. (1993) were associated with previously documented cystic malformations. Tagge et al. (1996) cite 16 reports noting a relationship in children between pulmonary cystic disease and pleuropulmonary blastoma and related tumours. Other tumours with known prior cysts have included hamartomas, bronchogenic carcinomas, rhabdomyosarcomas and other sarcomas. At least two reported cases of rhabdomyosarcoma have allegedly arisen in congenital cystic adenomatoid malformations. Some sarcomas, however, and probably the majority of such sarcomas previously reported in association with lung cysts are likely to have been unrecognised pleuropulmonary blastomas (Priest et al. 1997, 2006). So-called lung cysts have even included ‘pneumatoceles’ in some cases (Tagge et al. 1996).

The correct approach to asymptomatic lung cysts is therefore uncertain. Follow-up may need to be lifelong, e.g. two pulmonary adenocarcinomas developing in young adult non-smokers who had had large peripheral lung cysts of longstanding duration have been described (Tagge et al. 1996). It has even been suggested that an asymptomatic pulmonary cyst in a child should be resected unless radiographic evidence can show it to be acquired, as there is a widespread assumption that congenital lung lesions are more likely to undergo malignant change. There are a large number of cystic lung pathologies, e.g. congenital cystic adenomatoid malformation, bronchogenic cyst, sequestration, parenchymal cysts and pneumatoceles. There is an increasing tendency to manage at least some of these lesions conservatively, particularly if small, an asymptomatic antenatal pick-up or an incidental finding. When a solid component is detected in any of these abnormalities on CT, MRI or ultrasound, surgical resection should be strongly considered (Tagge et al. 1996). This topic is further alluded to in Section 12.4.3.2.

12.4.2
Benign Tumours

12.4.2.1
Inflammatory Myofibroblastic Tumour

Inflammatory myofibroblastic tumour has had a variety of other synonyms including plasma cell granuloma, fibroxanthoma and most notably inflammatory pseudotumour. It is an uncommon lesion characterised histologically by a localised proliferation of mononuclear inflammatory cells in the form of plasma cells, lymphocytes, eosinophils and mesenchymal cells comprising spindle cells and myofibroblasts (Brown and Shaw 1995). It occurs at all ages but most occur in individuals under 40 years of age. Inflammatory myofibroblastic tumour is the most common benign pulmonary tumour in childhood and accounts for approximately half of all benign lesions. The aetiology of inflammatory myofibroblastic tumour is likely multifactorial and seems to be an unregulated reparative response of injured tissue. The important function of the myofibroblast in tissue repair is also consistent with the hypothesis that an aberrant response to tissue injury is the pathogenesis of these lesions. Others speculate the lesion represents an immunologic response to an infectious agent. There is seldom however a history of trauma nor of preceding infection at the site of involvement by the inflammatory myofibroblastic tumour, although up to one-fifth of older patients give a history of recent lower respiratory tract infection. A variety of unusual micro-organisms have been implicated in individual case reports, including *Mycobacterium avium intra-cellulare*, *Corynebacterium equi*, *Coxiella burnetii*, and *Bacillus sphaericus* (Hedlund et al. 1999). More recently, viruses such as EBV and HHV-8 have also been implicated (Mergan et al. 2005). Despite these infectious associations, a neonatal myofibroblastic tumour has been reported (Castanon et al. 2005).

The condition has been increasingly recognised in children and the lung is the most common site in the body (Mas Estelles et al. 1995). A history of systemic upset with fever, malaise and weight loss is often present although up to 30% of children may be asymptomatic. An endobronchial lesion may manifest as an exacerbation of asthma and persistent hyperinflation (Jayne et al. 1997). Unusual for pulmonary masses, pain at the site of the lesion is not uncommon. An association with hypertrophic pulmonary osteoarthropathy has been reported and this association may be more frequent than is generally believed (Mas Estelles et al. 1995). Although bronchi and vessels may be trapped within the pulmonary masses and become narrowed distally or even obliterated, this seldom leads to radiologically obvious atelectasis. Focal collapse is evident in only 14% of paediatric patients (Verbeke et al. 1999). Pleural effusion is found in less than 5%.

Most patients present with a solitary sharply circumscribed peripheral mass in a lower lobe (Fig. 12.1).

The lesions are often around 3–4 cm in diameter with usually no invasion of adjacent structures. Masses that abut the pleura can be amenable to ultrasound evaluation and typically appear solid and homogeneous. CT, however, is the major modality used in the evaluation of these lesions in the chest. The masses are typically well circumscribed (Agrons et al. 1998). Three distinct CT appearances have been reported (Brown and Shaw 1995). The most common finding is of a large coin lesion that may contain areas of calcification (Fig. 12.1). In fact, calcification seems to be more a feature of inflammatory myofibroblastic tumours in young patients than in adults (Agrons et al. 1998). A small non-calcified endobronchial mass that can mimic an endobronchial adenoma is another manifestation in up to 20% of cases. The least common appearance is that of a large spiculated mass that may show features of necrosis or cavitation. Varied enhancement

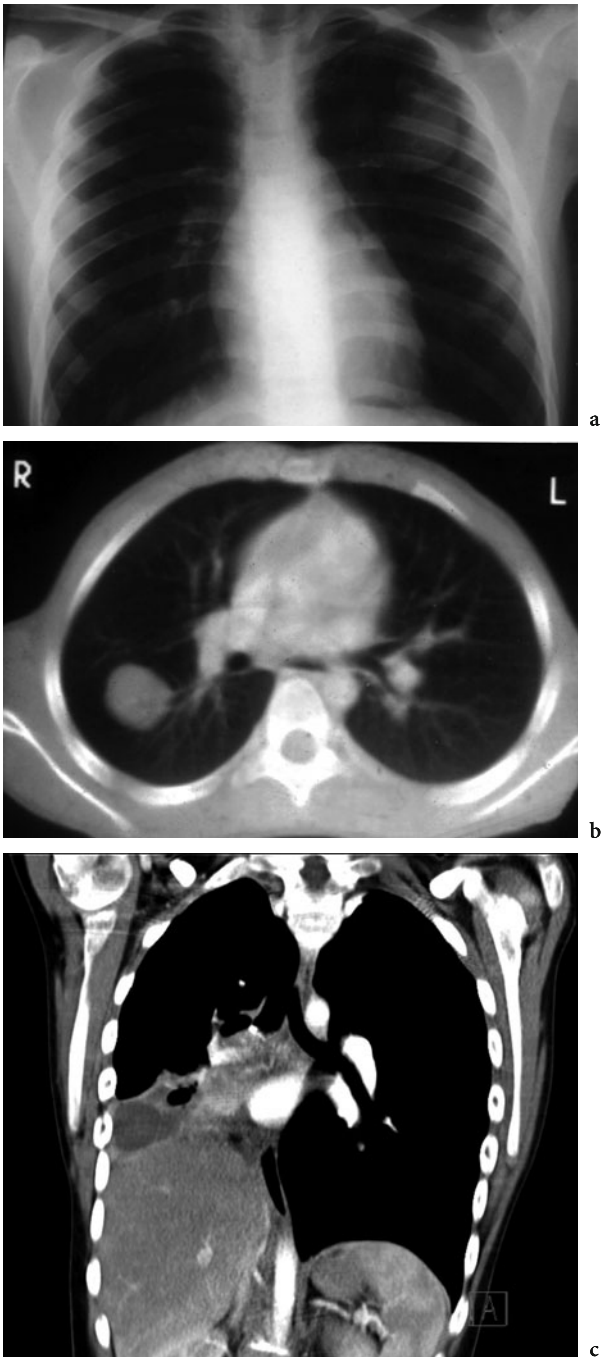

Fig. 12.1a–c. Inflammatory myofibroblastic tumour (IMT): varied appearances. **a** Chest radiograph revealing a rounded, well-circumscribed opacity in the left upper zone. Note absence of hilar adenopathy, pleural effusion and rib changes. **b** Axial CT showing a well-defined lesion in the right lower lobe. **c** Coronal contrast-enhanced CT image showing elevation of the right hemidiaphragm and liver due to a mass lesion occluding the bronchus intermedius. This proven IMT mass shows heterogenous attenuation with some calcification superiorly and it is invading the sub-carinal region of the mediastinum

is seen following intravenous contrast administration (Agrons et al. 1998). Hilar lymphadenopathy and pleural effusion are not commonly associated and their presence should cast doubt on this diagnosis (Mas Estelles et al. 1995). The CT features of inflammatory myofibroblastic tumours are notoriously non-specific, however. A few MRI studies have demonstrated signal characteristics of pulmonary masses that paralleled those of adjacent lung parenchyma, thus rendering the lesions difficult to visualise (Verbeke et al. 1999).

Atypical thoracic manifestations of inflammatory pseudotumours also occur. Lesions arising solely in the oesophagus have been described. More locally aggressive masses are occasionally seen and these are probably detected late in the natural history of the disorder. More extensive lesions may encase bronchi or other mediastinal structures, present as a mediastinal mass, or invade the chest wall, vertebrae or diaphragm (Hedlund et al. 1999; Verbeke et al. 1999). Invasive inflammatory myofibroblastic tumours appear to be more common in children than in adults. CT and MRI are both useful in characterising the extent of these aggressive lesions in relation to the tracheo-bronchial tree, oesophagus, vascular structures and chest wall. Angioinvasion including cardiac involvement may be better demonstrated with MRI or echocardiography (Hedlund et al. 1999). Barium studies are essential for characterising oesophageal involvement when suspected.

On presentation, these masses are often suspected to be primary thoracic malignancies and the diagnosis of inflammatory myofibroblastic tumour may not be entertained. In children without a known underlying malignancy a solitary peripheral pulmonary nodule or mass is more likely to represent an inflammatory myofibroblastic tumour than a neoplasm (Agrons et al. 1998). A calcified lesion may suggest a hamartoma but hamartomas are less common in the paediatric population.

The natural history of inflammatory myofibroblastic tumours is unpredictable. Stable residual disease is possible but so too is rampant spread of disease into adjacent organs. Although some cases have resolved without recourse to surgery, conservative pulmonary resection with removal of all gross evidence of disease is the mainstay of treatment and is curative for tumours confined to the lung. Locally aggressive lesions require more radical surgery including pneumonectomy rather than the more usual segmental or lobar resection. Tumour recurrence following incomplete resection or sclerosing mediastinitis may complicate the clinical course. The frequency of local recurrence of pulmonary inflammatory myofibroblastic tumours may be higher than previously suspected. 28% of recurrent inflammatory myofibroblastic tumours reported by Janik et al. (2003) were beyond the lung at the time of presentation. When these tumours have extended beyond the organ of origin at diagnosis, up to 35%–46% may relapse locally (Janik et al. 2003). Relapse or invasion of the mediastinum have occasionally been treated with immunosuppressive corticosteroid therapy and even multi-agent chemotherapy with good results (Verbeke et al. 1999; Janik et al. 2003).

12.4.2.2
Hamartoma

Hamartomas account for approximately 20% of benign tumours that occur in the lung parenchyma in childhood (Hancock et al. 1993). Hamartomas are generally regarded as developmental anomalies and are composed of tissues native to the lung but present in an abnormal configuration. Some consider congenital cystic adenomatoid malformation (CCAM) to be a hamartomatous lesion but this lesion is dealt with in more detail in Chapter 5. Briefly, the fundamental pathological feature of CCAM is a proliferation of bronchioles that form cysts instead of normal alveoli and so they are clearly different from classic lung hamartomas (Kim et al. 1997). Most patients with CCAMs present in the first 6 months of life with respiratory distress, older children tend to come to attention due to recurrent chest infections, and CCAMs are also being increasingly recognised antenatally. They usually manifest on plain radiographs and CT as multiple, thin-walled, air- or fluid-filled cysts expanding a lobe, in contrast to true hamartomas, which generally present as a solid mass lesion in older children.

Despite being regarded as possible developmental anomalies, the majority of pulmonary hamartomas are discovered in adults between the fourth and sixth decades. van den Bosch et al. (1987) cited 30 adults among their cohort of 154 patients with pulmonary hamartomas who had had preceding normal chest radiographs, thereby lending credence to the belief that hamartomas are actually acquired lesions. Pulmonary hamartomas are frequently asymptomatic and often incidental findings (Hartman and Shochat 1983). The characteristic radiological finding is a round opacity in the periphery of the chyma. Altogether, 10% of lesions show calcification, often with a curvilinear or speckled configuration, and sometimes this calcification has the classic 'popcorn' appearance. The frequency of calcification increases significantly with the size of the lesion. Occasionally a central fat density is seen on CT. Fat in such a nodule is proof of benignancy and is seen in up to 30% of hamartomas. A lipoid pneumonia may also of course have some fatty attenuation.

In contrast to adult patients, many of the reported cases of pulmonary hamartomas in younger children have fared poorly. Four lesions seen in the neonatal period were all fatal (Hartman and Shochat 1983). Only a minority of the reported paediatric cases have been asymptomatic. Other childhood pulmonary hamartomas have been reported as part of a triad of lesions in young girls that also included an extraadrenal paraganglioma and a gastric smooth muscle tumour (Hartman and Shochat 1983). Although pulmonary hamartomas manifest typically as isolated pulmonary nodules, in young children in particular these lesions may be quite large. Their true nature only becomes apparent at histological examination (Fig. 12.2).

Endobronchial hamartomas, which are particularly uncommon in childhood, present with respiratory symptoms or infections due to airway obstruction. A few sporadic reports of tracheal hamartomas exist. One tracheal hamartoma with a large extraluminal component was reported which manifested as a neck mass in a young girl (Gross et al. 1996). Surgery for all hamartomas is curative although the less common endobronchial hamartoma may require lobectomy or even pneumonectomy.

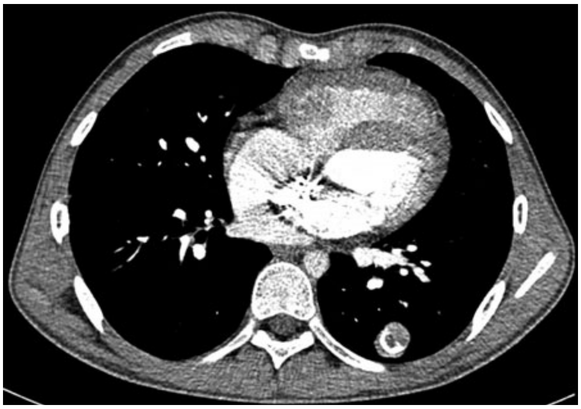

Fig. 12.2. Hamartoma. Axial contrast enhanced CT showing a small discrete lesion in the left lung with curvilinear calcification typical of a hamartoma

12.4.2.3
Leiomyoma

The majority of leiomyomas are found in the lung parenchyma; fewer than one-third of cases manifest as endobronchial lesions. Most leiomyomas are seen in adult patients, with only one in three cases presenting before 20 years of age (Karnak et al. 2000). Hartman and Shochat (1983) reported four leiomyomas in children between the ages of 5 and 11 years, which were all cured by surgery. They also cited two reports in the literature of neonates who died from respiratory distress secondary to large pulmonary leiomyomas. Although quite rare, leiomyoma is also the most common benign tumour of the oesophagus. The involved oesophagus demonstrates marked circumferential wall thickening and there is an association with Alport syndrome (Guest et al. 2000).

There is now a well documented association between the acquired immune deficiency syndrome (AIDS) and tumours of smooth muscle origin. Pulmonary leiomyomas have been seen in children with AIDS and it is likely that the incidence of these tumours will increase in paediatric practice (Chadwick et al. 1990). De Chadarevian et al. (1997) reported two further patients with AIDS who presented with recent onset of wheezing due to bronchopulmonary leiomyomas. This, they believed, underscored the clinical significance of this new symptom in young patients with AIDS, particularly when the wheezing is unilateral or does not respond to bronchodilators. Four centrally located leiomyomas were seen in one of their patients, and in their other patient a leiomyoma was evident on CT merely as severe narrowing of the left main bronchus with no direct evidence of a tumour mass. Similar tumours have been observed in patients with various immunocompromising conditions such as severe combined immunodeficiency, post bone marrow, renal or hepatic transplants. It is noteworthy that pulmonary leiomyomas in this setting may be multiple and asymptomatic. Epstein-Barr virus has been detected in virtually all AIDS-related soft tissue tumours and is assumed to play an active role in the development of these tumours (de Chadarevian et al. 1997). Prolonged survival in HIV positive paediatric patients may increase the risk of developing such tumours.

12.4.2.4
Laryngotracheal Papilloma

Laryngeal papilloma is the most common benign laryngeal epithelial tumour. It is caused by the human papillomavirus, mainly types 6 and 11. HPV-11 associated recurrent respiratory papillomatosis is likely more aggressive than HPV-6 associated disease (Soldatski et al. 2005). Papillomas spread inferiorly from the larynx by direct contiguous extension as far as the major bronchi but rarely beyond. Lower airway lesions may be seen in up to 8% of patients, with lung parenchymal nodules occurring in approximately 1%–2% of cases (Soldatski et al. 2005). The occurrence of lower airway and pulmonary lesions may be exacerbated by treatment to the primary laryngeal lesions, including tracheostomy for tracheal scarring stenosis and recurrent intubation. It is hypothesised that fragments are detached during endoscopy and are carried down the airways during inspiration. Those that lodge proximal to the respiratory bronchioles may be expelled by mucociliary clearance (Kramer et al. 1985). Those that travel more distally are not cleared and thus enlarge.

Airway papillomas may be localised or extensive. Conglomerate lesions typically manifest as endotracheal or endobronchial masses (Fig. 12.3).

Papillomas have a classic fimbriated or ‘salmon egg’ appearance on endoscopy. They are predominantly endoluminal with usually little submucosal infiltration although this does occur with more extensive papillomas. Pulmonary parenchymal lesions typically have a nodular appearance. Parenchymal lesions may be widely scattered remote from the major bronchi and a subpleural location is not uncommon. The nodules may be small or large, thin or thick-walled and may cavitate (Fig. 12.3). Air-fluid levels can be seen in larger pulmonary lesions, and these may occur without superadded infection. Some lesions occasionally resemble dilated bronchi or bronchiectasis but close inspection shows no direct communication to more central bronchi. An intraluminal airway mass with concomitant solitary or multiple pulmonary nodules or cavities, is very suggestive of laryngotracheal papillomatosis. There is usually a history of treated laryngeal papillomatosis. Asymptomatic lung nodules may be more frequent in this population than is generally believed but chest CT is not, of course, indicated in children who are symptom free. More significantly, severe lung damage may result from multiple destructive

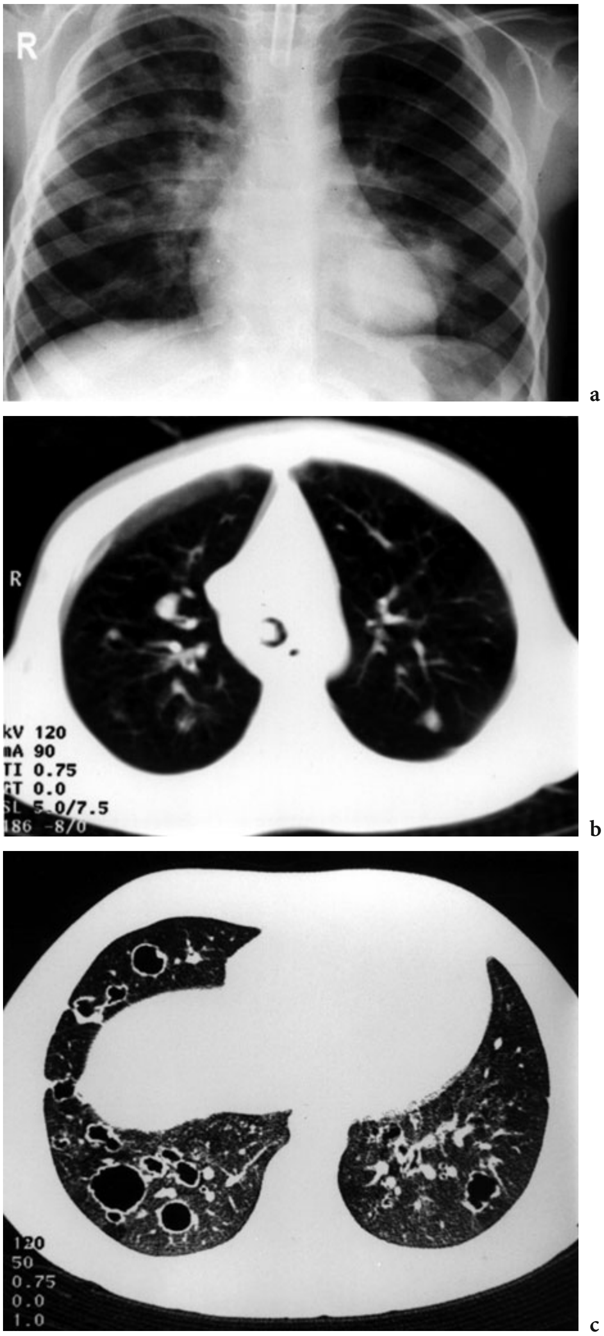

Fig. 12.3a–c. Laryngotracheal papillomatosis with lung involvement. **a** Frontal erect chest radiograph showing two cavitary lung nodules. The larger left-sided lesion has an air-fluid level but was not secondarily infected. Note the lower aspect of a tracheostomy tube. **b** Axial CT showing a relatively large endotracheal mass and parenchymal nodules in each lung. **c** Numerous cavitary nodules of varying size, many with irregular thick walls due to parenchymal spread of disease

parenchymal lesions such that symptoms of restrictive lung disease are seen in addition to upper airway obstruction. Malignant transformation of recurrent papillomatosis to squamous-cell carcinoma is a well recognised complication, again more likely with HPV-11 associated disease (Katz et al. 2005). A new soft tissue mass, often polypoid in shape, associated with a typical papillomatosis cavity should thus be viewed with suspicion.

12.4.3
Malignant Tumours

12.4.3.1
Bronchial Adenoma

The term 'adenoma' is a misnomer implying benign disease but is in common usage to categorise all neoplasms of the tracheobronchial glands. The tumours grouped under the label bronchial adenoma are low grade malignant lesions with the capacity for dissemination with the exception of the extremely rare true mucinous adenoma. The other tumours comprising this group include the bronchial carcinoid, mucoepidermoid carcinoma and adenoid cystic carcinoma (cylindroma). Most tumours occur in the main bronchi and are unusual in the trachea.

In reality, bronchial adenomas are difficult to suspect in everyday paediatric practice as commoner causes of persistent lung collapse such as an aspirated foreign body lead to a low threshold for bronchoscopy which often makes the diagnosis. Endobronchial lesions should be included in the differential diagnoses in such cases, however, and the airway should be scrutinised closely on radiographs and CT. An endobronchial mass is generally evident on CT when eventually performed, although it should be stressed fine sections are best to depict an endobronchial lesion when suspected. Thicker reconstructions may result in an indeterminate study – when there is doubt a repeat examination with intravenous contrast enhancement and fine collimation through the major airways should be performed. So-called three-dimensional (3D) CT virtual endoscopy may show endobronchial lesions elegantly, but bronchoscopic biopsy will ultimately be needed. Bronchography can demonstrate distinctive outward flaring of the bronchus proximal to an obstruction but is seldom now performed (Curtis et al. 1998). Previously, bronchography was important in considering the extent of surgical resection when bronchiectasis was present, but this role has now been replaced by CT.

Bronchial *carcinoid* tumours account for up to one half of all bronchial adenomas. Carcinoid tumours arise from the Kulchitsky cell of the respiratory epithelium, and their cell of origin is part of the amine precursor uptake and decarboxylase (APUD) system. The actual carcinoid syndrome is extremely rare in childhood, having been reported in a large review in only one child who had metastatic disease (Hancock et al. 1993). Cushing's syndrome from ectopic adrenocorticotrophic hormone secretion has also been described but is similarly uncommon (Wang et al. 1993). Children with bronchial carcinoids are much more likely than their adult counterparts to present with wheezing, haemoptysis or lobar collapse. In a series of 25 young patients with bronchial carcinoid tumours, none was asymptomatic (Wang et al. 1993). An asymptomatic young patient is probably more likely to have a peripheral pulmonary lesion since any resultant area of atelectasis could be clinically silent (Curtis et al. 1998). Endobronchial carcinoids (Fig. 12.4) have an intraluminal, mural and extrabronchial component.

They are vascular polypoid tumours and characteristically show prominent contrast enhance-

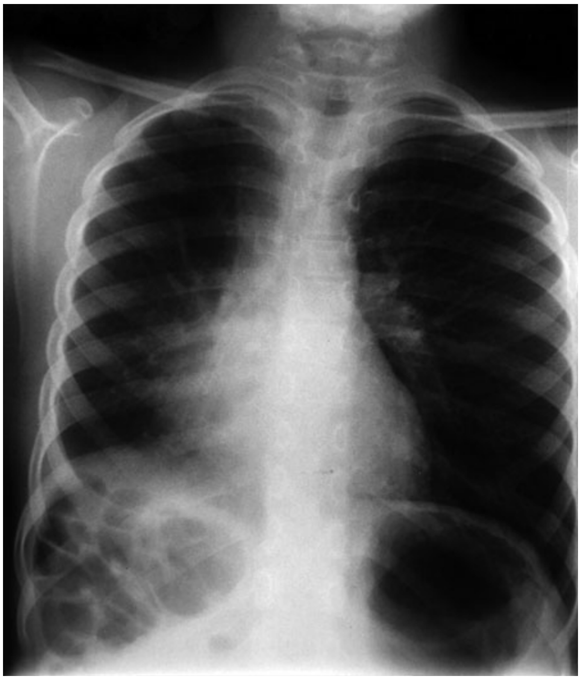

Fig. 12.4. Bronchial adenoma: carcinoid tumour. Persisting right middle and lower lobe collapse for over 6 months, proven at bronchoscopy to be due to an endobronchial carcinoid tumour in the bronchus intermedius

ment at CT. The majority of carcinoid tumours, despite generally occurring in the central airways, are not visible on chest radiography and their true extent may be difficult to determine on CT. Occasionally the mass external to the bronchus is larger than that in the lumen, and the extrabronchial component may consequently be visible as a hilar mass. The incidence of metastases with bronchial carcinoids, usually lymphatic metastases, has been reported in children to be between 5%–20% (Wang et al. 1993). Approximately one quarter of carcinoid tumours in adult patients are calcified, but the frequency of calcification appears to be much less in childhood.

Mucoepidermoid carcinoma accounts for up to one-third of bronchial adenomas. It is histologically similar to tumours described in the major salivary glands and is thought to originate from the minor salivary glands lining the tracheobronchial tree. As with other endobronchial lesions the history is usually that of respiratory infections or lobar collapse with or without air trapping. Calcification is seen in 50% of tumours. Contrast enhancement may be marked suggesting hypervascularity (Fig. 12.5).

Mucoepidermoid carcinoma can be classified as low or high grade, with childhood tumours usually having low grade malignant potential (Andronikou and Kader 2001). Childhood mucoepidermoid tumours generally arise in a mainstem bronchus or in the proximal portion of the lobar bronchi. Although endoscopy remains the diagnostic procedure of choice for endobronchial lesions, their iceberg-like appearance makes endoscopic resection inadvisable. Thoracotomy, with lymph node sampling, to ensure histologically negative margins is the recommended treatment (Morini et al. 2003). For tumours with low-grade malignant potential, without lymph node metastases, complete resection should result in a good outcome.

Adenoid cystic carcinoma or *cylindroma* is a malignant lesion, characterised by slow growth and a potential for submucosal spread. In upper airway lesions, pathological examination reveals invasion beyond the wall of the trachea in virtually all cases

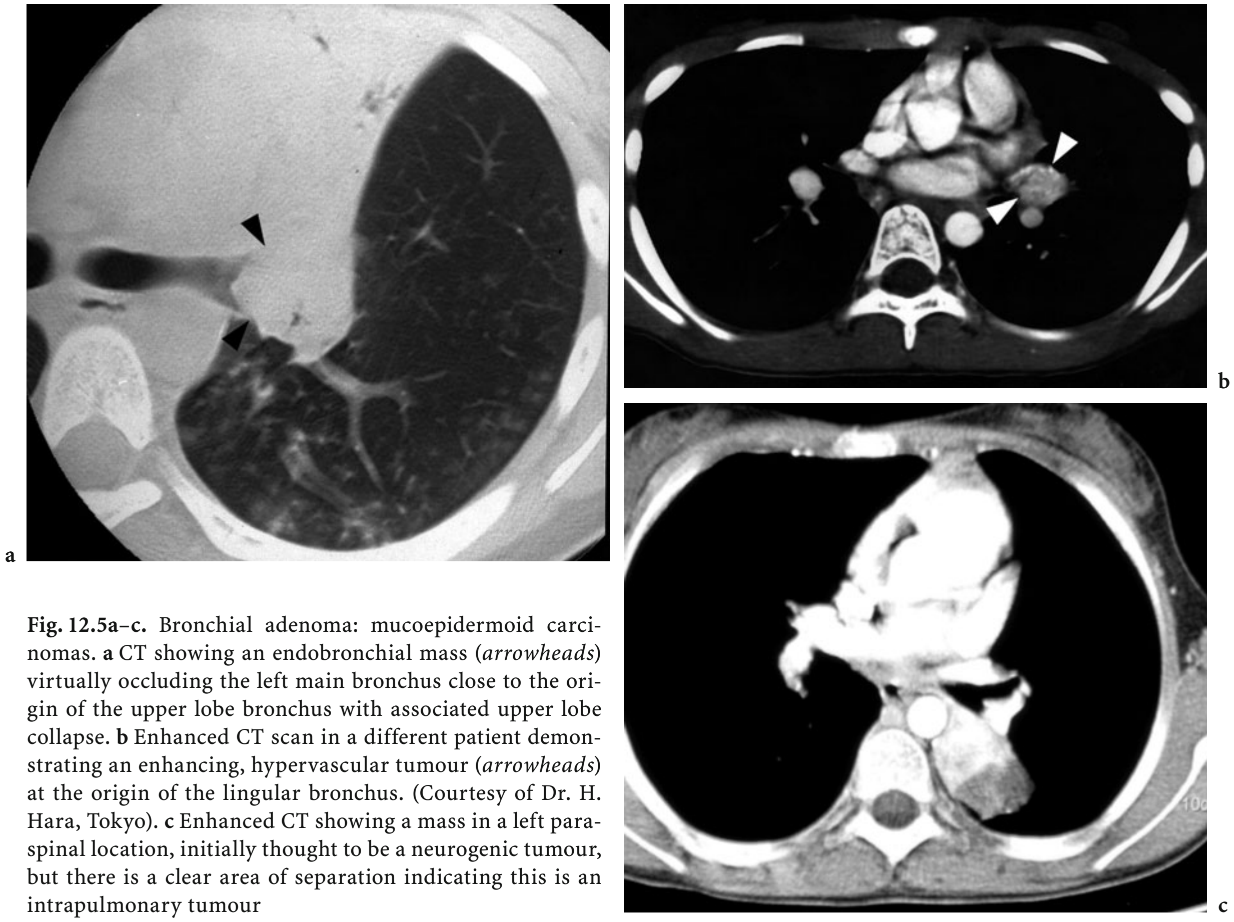

Fig. 12.5a–c. Bronchial adenoma: mucoepidermoid carcinomas. **a** CT showing an endobronchial mass (*arrowheads*) virtually occluding the left main bronchus close to the origin of the upper lobe bronchus with associated upper lobe collapse. **b** Enhanced CT scan in a different patient demonstrating an enhancing, hypervascular tumour (*arrowheads*) at the origin of the lingular bronchus. (Courtesy of Dr. H. Hara, Tokyo). **c** Enhanced CT showing a mass in a left paraspinal location, initially thought to be a neurogenic tumour, but there is a clear area of separation indicating this is an intrapulmonary tumour

(Maziak et al. 1996). Lung metastases may rarely be seen hence there is a need for both a detailed evaluation of the tumour mass in addition to a CT study of the entire pulmonary parenchyma.

Mucous gland adenoma is the sole truly benign bronchial adenoma. It originates from the submucosal glands of the trachea and larger bronchi, and is extremely rare. Seven reported paediatric cases were reviewed by Dickstein et al. (1993). A round opacity or merely lung hyperinflation or atelectasis may be evident on chest radiographs. Abundant mucous production may result in an apparent cystic mass on CT obscuring the endobronchial lesion.

12.4.3.2
Pleuropulmonary Blastoma

Pleuropulmonary blastoma is a rare lung tumour that occurs in children up to 12 years of age but the vast majority of pleuropulmonary blastomas are actually seen in children less than 5 years (Priest et al. 2006). It is now regarded as an entity distinct from true pulmonary blastoma, which is predominantly an adult tumour. Pleuropulmonary blastoma (PPB) has been mistaken for or classified as rhabdomyosarcoma arising in congenital cystic adenomatoid malformation (CCAM), pulmonary blastoma of childhood or other sarcomas (Priest et al. 2006). PPBs often show rhabdomyoblastic differentiation. PPBs are exclusively mesenchymal, there is an absence of epithelial carcinomatous elements with a variably mixed blastematous and sarcomatous appearance.

A recent hypothesis suggests pleuropulmonary blastoma may arise in a precursor lung developmental anomaly as in the relationship of nephrogenic rests and nephroblastomatosis to Wilms' tumour (Priest et al. 1997, 2006). Pleuropulmonary blastoma is regarded as a true dysembryonic neoplasm of thoracopulmonary mesenchyme in childhood. It is thus the pulmonary dysontogenetic analogue not only to Wilms' tumour but also to neuroblastoma in the adrenal gland and hepatoblastoma in the liver (Priest et al. 1997). PPBs are classified into types I to III (Dehner et al. 1995; Priest et al. 2006). Predominantly cystic (type I), cystic and solid (type II) and mainly solid (type III) sub-types are described with increasing histological evidence of malignancy. There appears to be a significant difference in the age at presentation. Type I lesions occur in infants, with types II and III being seen in slightly older children. In a review of 50 cases the median ages at diagnosis were 10 months for type I lesions, 34 months for type II, and 44 months of age in type III lesions (Priest et al. 2006).

There is a well documented association with prior cystic disease of the lung. In the Pleuropulmonary Blastoma Register cystic lung disease was present at diagnosis in almost 40% of patients (Romeo et al. 1999). As the radiological follow-up of some of these preceding lung abnormalities appears to have been brief, it is not clear how often these allegedly innocuous 'cysts' were actually an early manifestation of the tumour in a more benign and less complex form. Nevertheless, some pleuropulmonary blastomas do arise from pre-existing lung cysts, probably a PPB in a more benign form. The critical issue regarding cysts preceding the development of a PPB is whether they are benign malformations predisposing to cancer or early manifestations of the cancer itself. Priest et al. (2006) state that a type 4 CCAM shows significant overlap with type I PPB, and may be followed by a solid PPB. This raises the dilemma as to whether type 4 CCAM is really distinct from a type I PPB, and raises questions regarding a conservative approach to presumed CCAMs on CT. Such a phenomenon of progression of PPB through a distinctive sequence of pathologic changes, from a purely cystic stage (type I PPB) to a more aggressive cystic and solid (type II) or purely solid neoplasm (type III) is likely unique among the developmental neoplasms of childhood (Priest et al. 2006). In addition, 25% of cases occur in a constitutional and familial setting in which the patients themselves or other family members have other dysplastic or neoplastic conditions. For example, in the Pleuropulmonary Blastoma Register, children with contralateral CCAM and bilateral cystic lung changes have been seen and another child had a sibling with a CCAM (Priest et al. 1997). Multiple or bilateral lung cysts, renal cystic disease, or a family history of childhood neoplasia suggest a diagnosis of PPB in a child with lung cysts (Priest et al. 2006). A thorough family history is therefore essential. Synchronous and metachronous tumours have also been described. Early surgical intervention is indicated for any cystic pulmonary abnormality in children from these families.

Although lesions may be intrapulmonary adjacent to the mediastinum, most pleuropulmonary blastomas arise in a subpleural location with over half of cases occurring in the lower lobes (Fig. 12.6).

Type I lesions are confined to the lung parenchyma or visceral pleura. Involvement of the parietal pleura, mediastinum or diaphragm implies

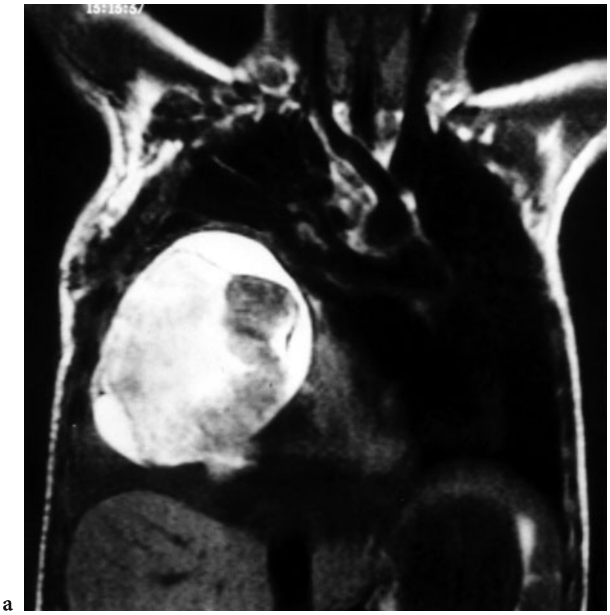

a

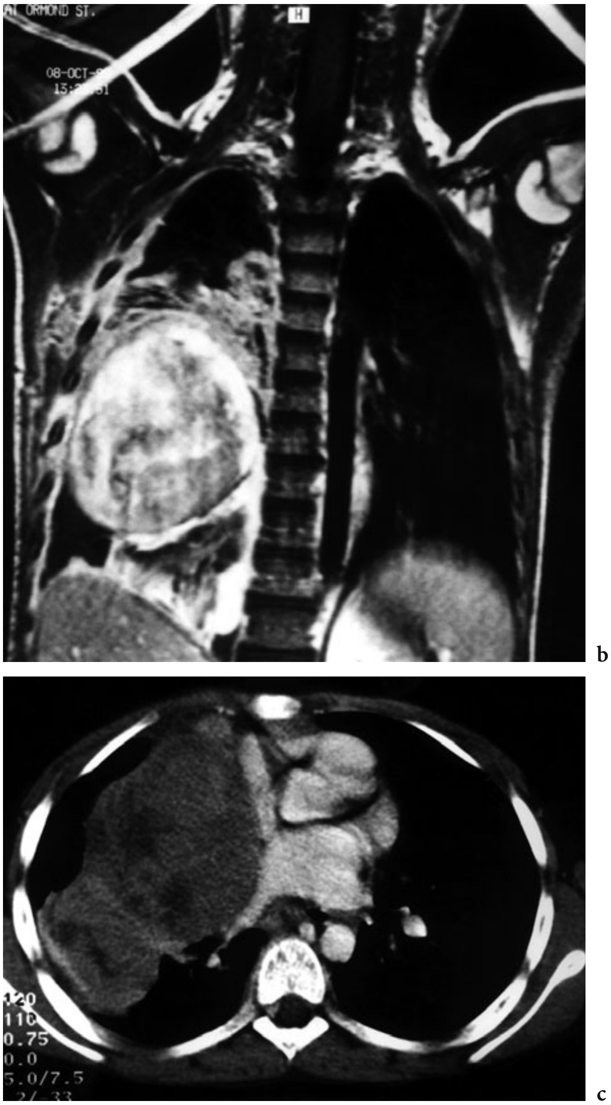

b

c

Fig. 12.6a–c. Pleuropulmonary blastomas. **a** Unenhanced coronal T1 W MRI showing a large hyperintense lesion in the region of the right middle lobe. This patient had had aspiration of haemorrhagic fluid on two occasions prior to this study and the hyperintense T1 appearance may be largely due to methaemoglobin. **b** Coronal T1 W MRI after gadolinium administration in the same patient showing diffuse pleural and lower lobe enhancement and upper lobe consolidation. Only haemorrhagic friable tissue was found at surgery and no discrete cyst could be identified. **c** Axial contrast-enhanced CT in another patient showing wide separation of the right pulmonary veins by a large heterogeneous intrapulmonary tumour. This 10-year-old boy had a right lung ‘cyst’ removed a few years previously and it is very unusual for a pleuropulmonary blastoma to occur at this age – the current lesion may well be a recurrence of the same tumour now in a more malignant form

invasive overgrowth of sarcomatous elements, justifying a type II or III PPB designation (Priest et al. 2006). Like all thoracic mass lesions the clinical symptomatology of pleuropulmonary blastomas is non-specific. Chest or abdominal pain, cough or pulmonary infections are the most frequent presenting complaints. A large pleural effusion may mimic an empyaema. Pneumothorax is an uncommon but well recognised presentation (Romeo et al. 1999). Pleuropulmonary blastomas manifest as mixed cystic and solid masses in the lung periphery often adjacent to the pleura in the lower zones. Large lesions occupying virtually the entire hemithorax with mediastinal displacement may occur (Senac et al. 1991). A pulmonary cyst or complex mass lesion of uncertain aetiology is the usual indication for surgery (Fig. 12.6). The solid components of the mass lesion are seen to enhance with intravenous contrast administration on CT and MRI. Some lesions are sharply demarcated from adjacent lung parenchyma while others may be more infiltrative. Confident designation as to the site of origin i.e. lung or pleura, is often difficult to determine with larger lesions. Cross-sectional imaging should include the mediastinum as hilar metastases can occur. As with all chest masses, precise diagnosis depends on histological evaluation which in most cases takes place after attempted or successful surgical resection. It is actually quite common that these tumours are so friable intra-operatively, and this has been our experience also, that empyaema is still suspected during surgery (Buyukavci et al. 2006). Thoracoscopic, open or percutaneous biopsy may be required for pre-operative diagnosis in more invasive, suspicious lesions as their peripheral location renders these tumours inaccessible to bronchoscopic biopsy.

Type I lesions, which are seldom suspected in advance of surgical removal and which comprise only 14% of all pleuropulmonary blastomas, have a better prognosis than the other sub-types. There is an advantage to adjuvant chemotherapy in addition to surgery for all three sub-types including type I PPB (Priest et al. 2006). Large lesions (> 5 cm) frequently recur or metastasise despite primary resection. Patients with pleural or mediastinal involvement fare significantly worse than those without such involvement. Actual metastatic disease is unusual at diagnosis but should be excluded. Metastases appear to occur exclusively in those with type II or III lesions. Pleuropulmonary blastomas have a particular tendency to metastasise to the central nervous system including the spinal cord – 44% of recurrences are in the CNS (Priest et al. 1997). All patients therefore merit craniospinal MRI for staging purposes and during follow-up. The second most common site for metastatic spread is the skeletal system. As there is little data on screening for skeletal metastases in children with pleuropulmonary blastoma, it seems advisable to perform Tc99m-MDP radionuclide bone scanning and possibly also radiographic skeletal surveys in all patients with types II and III tumours. The role of PET/CT is unknown in this context in this rare tumour. Responses to chemotherapy occur but the prognosis for other than type I lesions is not good. Overall survival has been reported as ranging from 80%–85% for type I to 45%–50% for type III (Priest et al. 2006). The prognosis for type II remains intermediate between types I and III.

12.4.3.3
Bronchogenic Carcinoma

Bronchogenic carcinoma is rare in childhood with approximately 60 cases reported in the world literature up to 2000 (Kim et al. 2000). Nevertheless, it accounts for 17% of malignant lung tumours in the paediatric age range. Undifferentiated tumours and adenocarcinomas account for 80% of lesions. There has been a notable scarcity of squamous cell tumours (12%) reported compared to an incidence in adults of 40%–50% (Hartman and Shochat 1983). Bronchogenic carcinoma in childhood is most common in adolescence. It is an aggressive malignancy with disseminated disease frequent at diagnosis and a mortality rate of around 90%. The common presenting complaints of cough, haemoptysis and weight loss are more likely to suggest pulmonary tuberculosis, particularly in endemic areas. As in adult patients, a central mass with endobronchial growth appears to be typical.

12.4.3.4
Pulmonary Nodules and Metastases

The ability to detect very small pulmonary nodules improves with each generation of CT scanner. This poses less of a dilemma in pediatric radiology than it probably does in adult practice. Nevertheless in some geographical areas where, for example, histoplasmosis is endemic it can be particularly difficult to distinguish innocent nodules from small volume metastatic disease in young patients. Multiple pulmonary nodules in a child with a known solid tumour, particularly when some lesions are over 1 cm in diameter, are invariably metastases (Fig. 12.7).

Diagnostic dilemmas arise when nodules are small (a few millimetres in diameter) and indistinct or only a solitary nodule is present. Co-existence of both benign and malignant nodules is also possible (McCarville et al. 2006). Clustering of multiple nodules in a single location in the lung tend to favour an infectious etiology, a diagnosis made easier if the child is systemically unwell. Spontaneously resolving small pulmonary nodules are recognised now in adults (Diederich et al. 2005). These nodules are of unknown causation but may be due to focal inflammatory lesions, mucoid impaction in small bronchi or intermittent enlargement of benign intrapulmonary lymph nodes (Diederich et al. 2005). This information on thoracic CT findings has come about as a result of mass screening of adults at risk of lung cancer, particularly life-long smokers, but routine CT screening of well children is not done nor is it ethically justifiable. Consequently it is not known if similar disappearing nodules occur in young patients.

The differential diagnosis of a few or even multiple pulmonary nodules includes tuberculosis or histoplasmosis, notably in areas with a high prevalence of these granulomatous diseases. Other diagnostic considerations include septic emboli, previous varicella infection, Wegener's granulomatosis, Langerhans cell histiocytosis, laryngeal papillomatosis and a variety of opportunistic infections in an immunodeficient child. In an oncology child on parenteral nutrition, complications such as lipid or septic

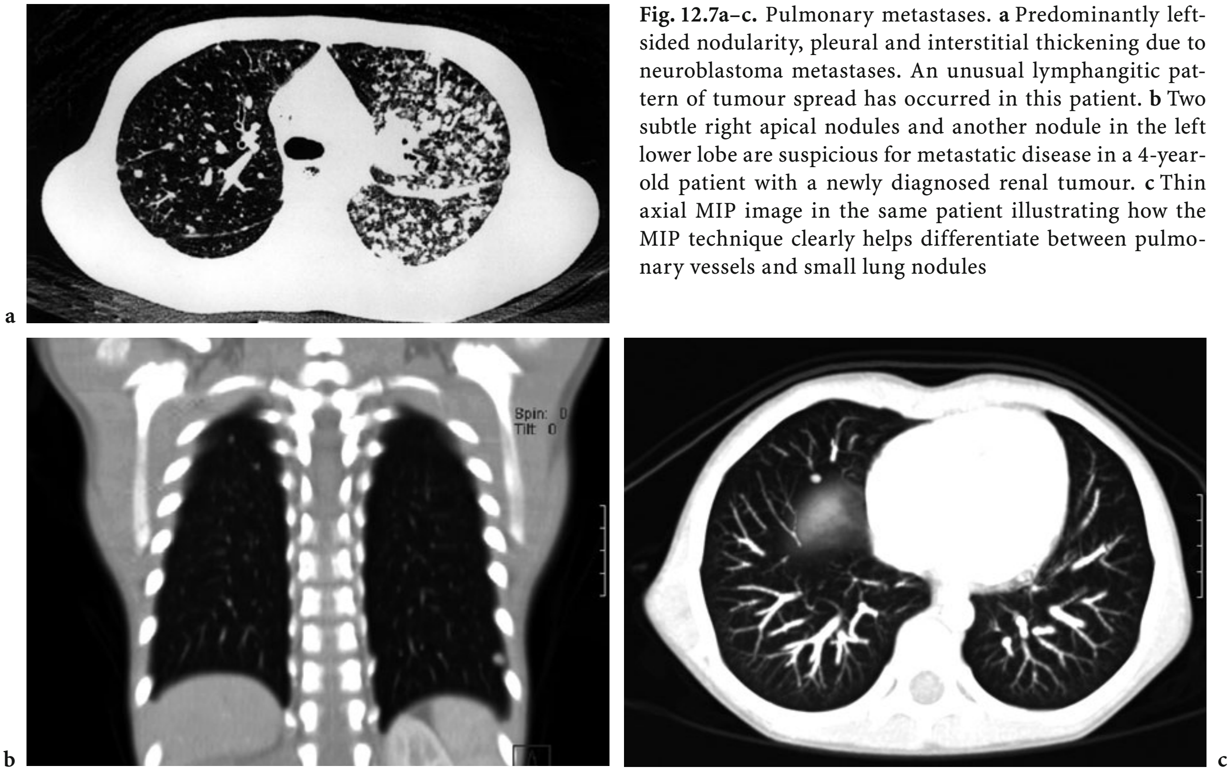

Fig. 12.7a–c. Pulmonary metastases. **a** Predominantly left-sided nodularity, pleural and interstitial thickening due to neuroblastoma metastases. An unusual lymphangitic pattern of tumour spread has occurred in this patient. **b** Two subtle right apical nodules and another nodule in the left lower lobe are suspicious for metastatic disease in a 4-year-old patient with a newly diagnosed renal tumour. **c** Thin axial MIP image in the same patient illustrating how the MIP technique clearly helps differentiate between pulmonary vessels and small lung nodules

emboli or infarction can be difficult to differentiate from metastases. Bleomycin or cyclophosphamide lung toxicity have been reported to produce fibrotic lung nodules which can also simulate metastases. Although all these possibilities should be borne in mind, the clinical picture at presentation of a solid tumour is usually more straightforward. Multiple lung nodules in a child with a newly diagnosed malignancy, who is neither pyrexial nor tachypnoeic, are usually indicative of metastatic disease.

Albeit seemingly often straightforward, McCarville et al. 2006 have shown how difficult it can be to distinguish benign from malignant pulmonary nodules on CT in young patients. Only the distinctness of nodule margins and the development of new nodules were significantly related to their radiologists' interpretations. Nodules with distinct margins in children may thus be more likely to be malignant than is the case in adults, in whom sharply defined nodules are more often benign (McCarville et al. 2006). Bilateral nodules, the development of new nodules, or progressive pleural thickening on follow-up studies increase the likelihood of malignancy. Nodule size, contrary to what is usually assumed, may not be a useful predictor of malignancy. In their study small nodules (< 5 mm) were as likely to be malignant as larger nodules (McCarville et al. 2006). In their cohort in whom the likelihood of malignancy was high, 44% underwent biopsy that revealed only benign nodules. Selection bias or geographical factors may have been confounding factors in their study and as the authors point out, better methods of assessing pulmonary nodules should be studied through more prospective clinical trials. The true frequency of malignant nodules detected by CT in children with cancer is thus unknown. A solitary lesion or a few small equivocal lesions require either biopsy, which is often impractical, or close surveillance to reveal their true nature. A conservative approach to these equivocal lesions is generally adopted in most centres. A lack of evidence also exists regarding the significance of mediastinal adenopathy in a child with a newly diagnosed malignancy. If the child has a normal lung parenchyma on CT or only equivocal lung nodule(s) with adenopathy, we have generally resorted to biopsy of the mediastinal lymph node usually to reveal previous infectious processes (unpublished data). In areas with a high prevalence of histoplasmosis or TB, co-incidental adenopathy is more likely.

Because of the difficulties in reliably identifying malignant pulmonary deposits when only one or two small lung lesions are discovered in a child with a solid tumour, some authors have reported resecting or biopsying lung nodules. In one group of 52 children with a variety of solid malignancies who underwent 74 thoracotomies, over 80% of small (10 mm or less) nodules were metastatic lesions (Crisp et al. 1996). In 18 Wilms' tumour patients with nodules visible on CT but not CXR, 15 positive biopsies for metastatic disease were found (Meisel et al. 1999). Connolly et al. (1999) reported a series of core needle biopsies of small pulmonary nodules in children under CT guidance using a co-axial system. The rationale behind a co-axial approach is that it allows multiple biopsies through a single pleural pass to be obtained which reduces the potential for haemo- or pneumothorax. In their study, biopsy of 18 nodules resulted in adequate cores of tissue for diagnosis in 15. Nine nodules were positive for malignancy, five were benign and there was one false-negative result in whom later thoracoscopic biopsy revealed malignancy. No clinically significant pneumothorax was encountered (Connolly et al. 1999). This type of interventional practice has not however gained widespread acceptance. Fine needle aspiration cytology is practised widely in adult patients with carcinoma and the yield is usually diagnostic. In children, however, sarcomas and lymphomas are relatively much more common. Differentiation from other cells can be extremely difficult on small cytological specimens and architectural information is lost such that aspiration cytology is generally regarded as unreliable for the diagnosis of childhood tumours.

Despite the above difficulties in CT interpretation, the lungs are known to be the predominant site of metastatic spread in the vast majority of solid extra-cranial malignancies. Disseminated neuroblastoma is an exception as it typically results in osseous secondaries and only rarely metastasises to the lung (Fig. 12.7). Pulmonary or pleural metastases in neuroblastoma are found in 1%–3% of cases but this figure may well be an underestimate as chest CT is not routinely performed in these patients at diagnosis (Cowie et al. 1997). The presence of lung metastases in children with neuroblastoma may be more important than is generally realised however, as their presence portends a poor outcome (Kammen et al. 2001). Common paediatric tumours which are associated with lung secondaries (with an approximate percentage incidence of pulmonary metastases at diagnosis) include Wilms' tumour (10%), rhabdomyosarcoma (15%), hepatoblastoma (10%), Ewing's (15%–20%) and osteosarcoma (15%–20%) (Paulussen et al. 1998; Kaste et al. 1999). All of these primary neoplasms, and also other less common malignancies, merit routine chest CT for staging purposes at diagnosis.

A successful response to chemotherapy should be accompanied by disappearance of pulmonary secondaries. Occasionally larger metastases may respond with some shrinkage but not total disappearance – residual fibrosis is then assumed but ultimately proof of benignancy rests on stable, unchanged appearances on follow-up, particularly off treatment in these so-called sterilised metastases. If the initial chest CT at diagnosis is negative for metastases, later follow-up is largely with chest radiography with CT reserved for suspected relapses or equivocal CXR findings. As up to 30%–40% of children with osteosarcoma eventually develop lung secondaries however, more routine screening with CT of patients with osteosarcoma is justified.

Small nodules, particularly if ossified, in a patient with osteosarcoma are almost always significant and should be regarded as malignant until proven otherwise. Osteosarcoma may also metastasise to the mediastinal lymph nodes and pleura, and even the heart, all of which can show ossified deposits. Innumerable tiny miliary metastases are a well-recognised manifestation of thyroid carcinoma. Cavitary metastases are unusual in childhood but are occasionally seen with sarcomatous tumours or rarely Wilms' tumour, or after chemotherapy or irradiation. There is some suggestion in adult patients that malignant lung nodules demonstrate contrast enhancement on CT and that absence of enhancement is predictive of benignancy, but no studies corroborating this have been performed in children.

Controversy used to exist regarding the significance of pulmonary nodules detectable only on CT in patients with Wilms' tumour. Co-operative paediatric oncology groups in North America and Europe all previously recommended that positive findings for pulmonary nodules on CT (presumed metastases) could be ignored if no lesions were visible on the postero-anterior and lateral chest radiograph. This is no longer the case within north American Children's Oncology Group (COG) studies, nor is it applied to the European-based SIOP studies. In future all Wilms' cases within COG trials will be subject to central review to determine metastatic disease. Wilms' studies by COG will instead exploit the initial response to therapy as the critical determinant for subsequent therapy, relying solely on CT (Grundy et al. 2005). For all patients with pulmonary lesions, a trial of chemotherapy will be given before pulmonary radiotherapy is used. The concept used here is that lesions which disappear because they represent co-incidental atelectasis or artifact or because they were truly responsive to chemotherapy will not require irradiation for successful outcome. Persistent lesions on CT after 6 weeks will require biopsy, reserving irradiation for those persistent nodules with proven relatively chemo-resistant disease (Grundy et al. 2005). Within SIOP Wilms' studies nodules greater than 1 cm in diameter on CT will be labelled as metastases (but it is not clear if these nodules should be measured on lung or mediastinal window settings - repeated measurements on the same lung window settings would, of course, seem sensible). It is noteworthy that these changes came about as there was confusion as to how to treat patients who were positive for nodules on CT but had normal CXRs. Different oncologists and different centres were staging these patients as either local abdominal disease (stages 1–3) or as metastatic disease (stage 4) which lead to many inconsistencies in staging within the same clinical trials.

Some paediatric abdominal tumours, most notably Wilms' tumour and adrenal carcinoma, have a propensity to invade the inferior vena cava (IVC) and occasionally result in tumour thrombus extending into the right atrium. This is regarded as local extension of tumour and not metastatic disease.

12.5
Mediastinal Tumours

12.5.1
Germ Cell Tumours

Primary germ cell tumours (GCT) account for up to 10% of all mediastinal masses in children and are second only to lymphoma as a cause of a thymic mass. They are most often located in the anterior mediastinum (Dulmet et al. 1993). Only 2%–3% of mediastinal GCTs occur in the posterior mediastinum. Intrapulmonary location is exceedingly rare but is described. There is an association between Kleinfelter's syndrome (XXY) and mediastinal germ cell tumours. In general, up to a half of all patients have no symptoms at the time of diagnosis (Sasaka et al. 1998). Conversely, large tumours causing tracheal compression or superior vena caval obstruction are also well recognised. Occasionally, ectopic production of sex hormones or insulin may lead to presentation with pseudoprecocious puberty or hypoglycaemia before the onset of respiratory symptoms. Germ cell tumours which include teratomas, teratocarcinomas, seminomas, dysgerminomas, embryonal cell carcinomas, endodermal sinus tumours and choriocarcinomas, usually present no earlier than the second decade of life. Overall, germ cell tumours are malignant in about 10% of cases. Malignant germ cell neoplasms are frequently associated with elevated serum levels of human chorionic gonadotropin or alpha-foetoprotein. Teratomas account for the vast majority of mediastinal germ cell lesions in children and they can have varied amounts of mature and immature somatic tissues. Teratomas are characteristically composed of well-differentiated ectodermal, mesodermal and endodermal derivatives. Mature teratomas are benign lesions. Immature teratomas are potentially malignant but in patients less than 15 years of age have biological and clinical behaviour similar to mature teratomas (Dulmet et al. 1993).

CT attenuation values and MR signal intensity for all these tumours are highly variable depending on the amount of fat, calcium or soft tissue in the mass (Fig. 12.8).

Most teratomas have well-defined margins, thick walls and some fatty tissue or calcification or both. Approximately 25% of teratomas contain calcification (Alper et al. 2005). Fatty tissue plus calcification in an anterior mediastinal mass almost invariably indicate a germ cell origin. Seminomas typically have more homogeneous, soft-tissue attenuation while the more malignant lesions frequently have large necrotic components but there is wide variation in the appearance of all these tumours.

Teratomas may rupture into adjacent structures such as the pleural space, pericardium, lung parenchyma or tracheobronchial tree. Up to one-third of mature benign mediastinal teratomas are reported to rupture, with malignant lesions having a significantly lesser tendency to leak their contents (Sasaka et al. 1998). Severe symptoms such as chest pain or haemoptysis are more commonly found in ruptured than in unruptured tumours (Choi et al. 1998). Proteolytic or digestive enzymes and sebaceous materials within these teratomas are thought to play a role in their tendency to rupture and cause adjacent non-infectious inflammation. High amylase levels have been found in pleural effusions and in the tumour contents (Sasaka et al. 1998). Ruptured

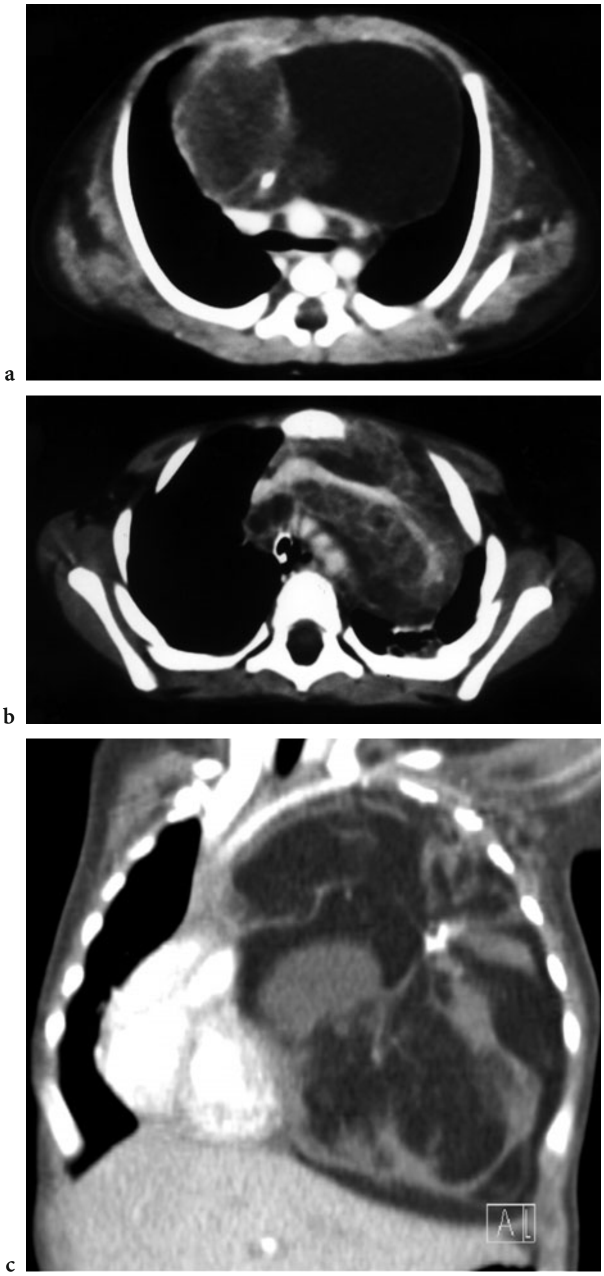

Fig. 12.8a–c. Germ cell tumours. **a** Contrast-enhanced CT, at the level of the carina, showing a typical anterior mediastinal teratoma with variable attenuation and one dense focus of calcification near the posteriorly displaced major vessels. **b** CT after intravenous contrast-enhancement in another child revealing a complex cystic and fatty immature teratoma causing compression of the left brachiocephalic vein. **c** Coronal contrast-enhanced CT showing a very large left teratoma displacing the mediastinum to the right. The mass contains solid and fatty tissues and calcification

tumours have a tendency to display more heterogeneity in their internal components than unruptured teratomas. Ancillary findings in ruptured tumours depend on the space into which the rupture occurs. Rupture into the lung or through the tracheobronchial tree may cause a chemical pneumonitis or fat-containing masses in the adjacent lung parenchyma. Haemoptysis with expectoration of hair or sebaceous material indicates a fistula between the tumour and the tracheobronchial tree and is said to be pathognomonic of a mature teratoma (Sasaka et al. 1998; Alper et al. 2005). Rupture into the pleura or pericardium results in pleural or pericardial effusions (Choi et al. 1998). Adjacent consolidation or atelectasis is suspicious for rupture but can also be seen with compressive atelectasis from any large mass. Rupture is important to recognise or suspect as inflammatory changes and adhesions secondary to extravasation of tumour contents may result in more hazardous and extensive surgery than had been anticipated.

12.5.2
Thymoma

Epithelial tumours of the thymus are classified as thymoma or thymic carcinoma, according to the absence or presence of clear-cut cytological atypia to the neoplastic epithelial cell component (Pescarmona et al. 1992). Histologically, the epithelial cell is the neoplastic component of thymoma, and lymphocytic cells are considered benign (Dhall et al. 2004). Thymomas are uncommon in children accounting for less than 1% of mediastinal tumours. Some patients are asymptomatic but in the majority of children the tumour has an aggressive course and often poor survival. Only approximately 30 thymomas occurring in children have been described in the literature (Rothstein et al. 2005). Thymoma in childhood usually occurs in isolation and is only rarely associated with myasthenia gravis. Red cell aplasia is another recognised associated paraneoplastic syndrome. True thymic carcinomas are very rare. The radiological findings of thymomas vary from a small focal heterogeneous mass adjoining either thymic lobe to a large lobulated tumour which replaces the whole thymus and distorts the mediastinal structures (Fig. 12.9).

Variable low attenuating lesions with moderate contrast enhancement are characteristic. Calcification is uncommon. Malignant lesions tend to be

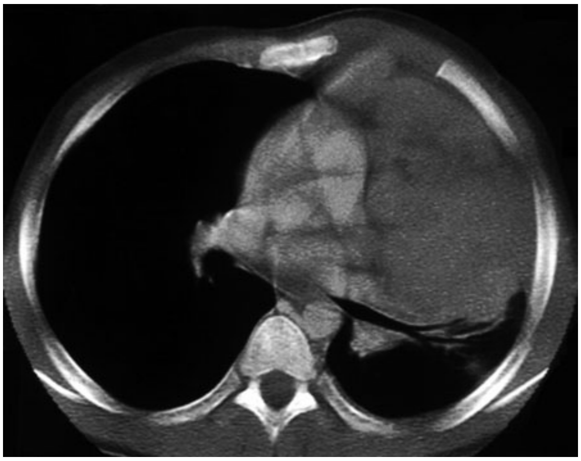

Fig. 12.9. Thymoma. Relatively homogeneous but non-enhancing left thymic mass proven to be a thymoma after resection and histological assessment

more invasive with pleural encasement or pulmonary metastases. As with many mediastinal masses, an associated pericardial effusion is often an indicator of an aggressive tumour with intrapericardial invasion. Irregular borders between the mass and adjacent lung also suggest an invasive lesion. Encapsulated thymomas have been treated successfully by surgery alone (Dhall et al. 2004). The other reported cases in the pediatric literature are too few to predict mortality accurately but the adult literature suggests poorer survival is related to incomplete resection, the pre-operative absence of myasthenia gravis and advanced pathologic grade (Rothstein et al. 2005).

12.5.3
Neuroblastoma

The majority of posterior mediastinal masses in children are neurogenic tumours arising from the paravertebral sympathetic chain. Although neurofibromas are seen in paediatric patients, most occur in children with neurofibromatosis. The major childhood neurogenic tumours are neuroblastoma, ganglioneuroblastoma and ganglioneuroma. Neuroblastoma and ganglioneuroblastoma occur in the first decade of life whereas the more benign ganglioneuroma, in which all cells are mature, is typically seen in older children and adolescents. Thoracic neuroblastoma accounts for 15% of all cases of neuroblastoma. There is typically less advanced malignancy than in primary abdominal neuroblastoma with an associated better outcome. In one series of 96 children with thoracic neuroblastoma, the median age at presentation was at 0.9 years, only 20% had metastatic disease, and actuarial survival was 88% at 4 years (Adams et al. 1993). Interestingly, in that study a posterior mediastinal mass was diagnosed incidentally on chest radiographs performed for non-tumour related symptoms in half the cases.

In most instances the chest film suggests the correct diagnosis, particularly when posterior rib erosion is seen indicating a posterior mediastinal mass (Fig. 12.10).

On CT most tumours are well-circumscribed, fusiform masses oriented vertically in a paraspinal location. Approximately 40% contain some calcification. Enlargement of intervertebral neural foramina and spread into the abdomen via the aortic or oesophageal hiatus or by direct invasion may also be evident (Fig. 12.10). Delineation of extent of disease is necessary for correct staging and is now most readily accomplished with MRI (Slovis et al. 1997; Siegel et al. 2002). Bone marrow involvement is also easily recognised on MRI (Siegel et al. 2002). There have been sporadic reports of using whole body MRI to screen for metastatic disease in young children with malignant disease. The evidence to date is however lacking as to whether this is superior to routine MRI plus scintigraphy in neuroblastoma. When MRI is not possible, then contrast-enhanced CT must be performed to best assess tumour margins and intraspinal extension. Coronal or sagittal reformats from MDCT sections provide excellent detail but at an increased radiation burden. As only 50% of children with intraspinal extension of tumour are symptomatic at the time of diagnosis, it is mandatory that intraspinal invasion is looked for in all patients, which also emphasises the need for MRI assessment of the spinal canal (Fig. 12.10). Although less common, it is also important that lymph node or chest wall involvement is recognised in order to help select the optimal therapeutic approach. Abdominal sonography, Tc99m-MDP bone and/or metaiodobenzylguanidine (MIBG) scintigraphy should also be routinely performed in all neuroblastoma patients to identify or exclude metastatic disease.

Ganglioneuroma in older children is indistinguishable radiologically from neuroblastoma – all patients need histological confirmation and staging to rule out metastatic disease. When histological assessment is unclear, biopsy not feasible or the diagnosis uncertain, MIBG scanning should be con-

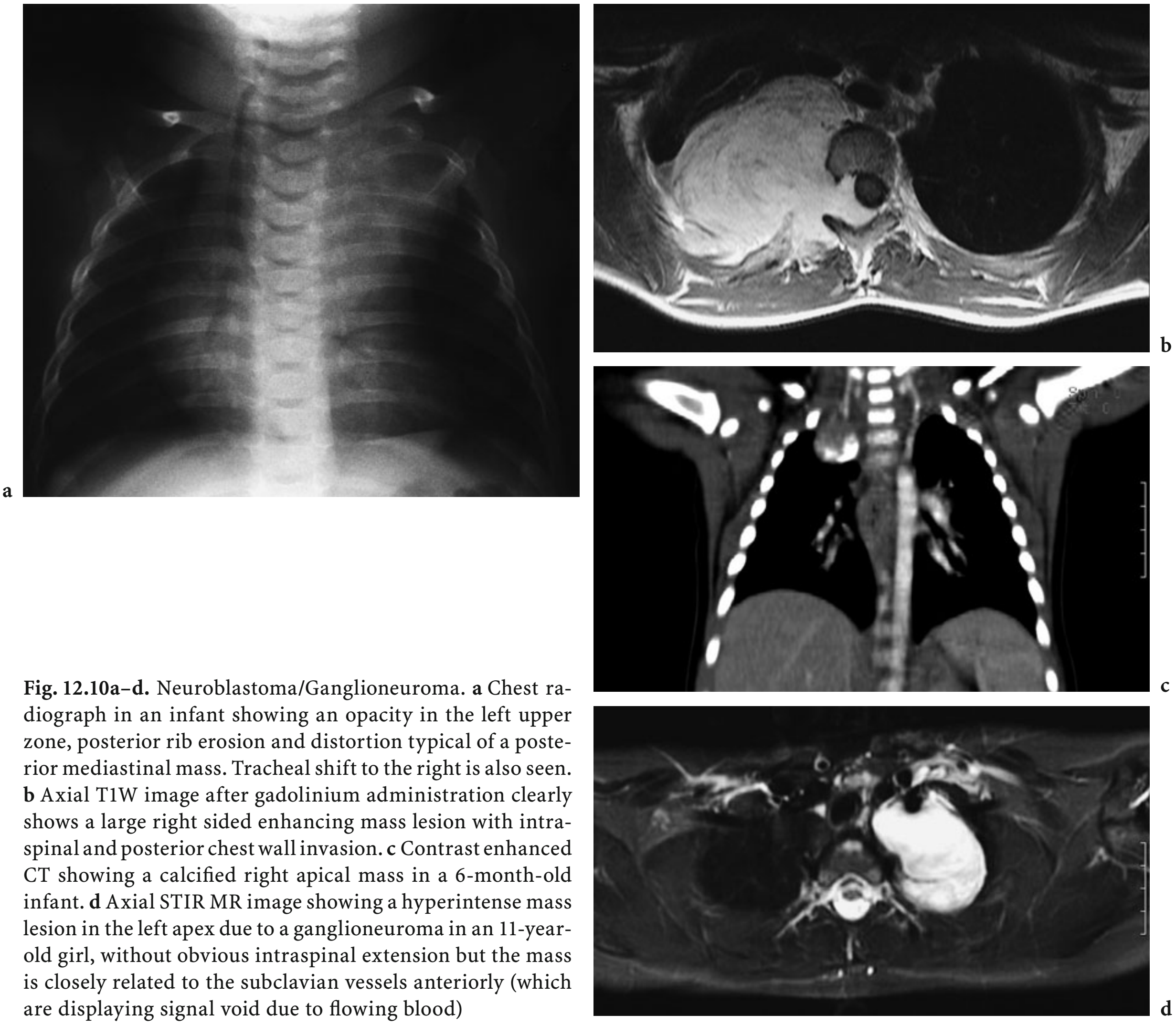

Fig. 12.10a–d. Neuroblastoma/Ganglioneuroma. **a** Chest radiograph in an infant showing an opacity in the left upper zone, posterior rib erosion and distortion typical of a posterior mediastinal mass. Tracheal shift to the right is also seen. **b** Axial T1W image after gadolinium administration clearly shows a large right sided enhancing mass lesion with intraspinal and posterior chest wall invasion. **c** Contrast enhanced CT showing a calcified right apical mass in a 6-month-old infant. **d** Axial STIR MR image showing a hyperintense mass lesion in the left apex due to a ganglioneuroma in an 11-year-old girl, without obvious intraspinal extension but the mass is closely related to the subclavian vessels anteriorly (which are displaying signal void due to flowing blood)

sidered. Positive uptake will be seen in over half of all cases, will confirm a neural crest tumour and simultaneously screens for metastases.

12.5.4
Lymphatic Malformations

Most lymphangiomas (cystic hygromas), now commonly referred to as lymphatic malformations, occur in the neck with up to 10% having an intrathoracic extension. These masses tend to be uniformly hyperintense on T2 W MRI with varied septations, and with some enhancement of these septa after gadolinium administration. Coronal and sagittal MRI clearly depict the degree of great vessel and airway displacement and mediastinal infiltration. Occasionally intraspinal extension is also seen. US can also be useful to confirm the cystic nature of a neck mass or an intrathoracic lesion that abuts the chest wall. CT will display a lymphangioma as a predominantly low attenuation mass but MRI is preferred for better overall assessment.

Lymphangiomatous malformations arising within the mediastinum and pulmonary parenchyma in children are being increasingly recognised (Wunderbaldinger et al. 2000; Aviv and McHugh 2000). Simultaneous chylous pleural effusion and pulmonary interstitial thickening have now been described in a number of these paediatric patients. Ectatic lymphatic channels that weep chyle into the pleural space, or diffuse involvement of the visceral and parietal pleura, with or without a mediastinal mass, are the likely causative processes.

Although lymphangiomas are benign lesions, those patients with generalised lymphangiomatosis and a chylothorax associated with osteolytic lesions have a poor prognosis. Intractable effusions and respiratory failure frequently supervene. There is likely a spectrum of angiomatous disease processes that includes lymphangiomatosis and vanishing bone disease and we have reported patients with proven lymphangiomatosis and non-contiguous bone resorption. Cross-sectional imaging has increased our awareness of the extent of soft tissue abnormality in the mediastinum and elsewhere in these patients (Fig. 12.11).

Concomitant cystic lesions in the spleen are commonly encountered in this unusual patient group.

Intrapulmonary lymphangiomas also occur. They are a rare form of localised lymphangectasia and are again part of the spectrum of lymphatic lung malformations. A pulmonary lymphangioma is typically seen in an older child or teenager. Imaging techniques show a large dense mass with varying cystic components which usually defies preoperative diagnosis (Drut and Mosca 1996).

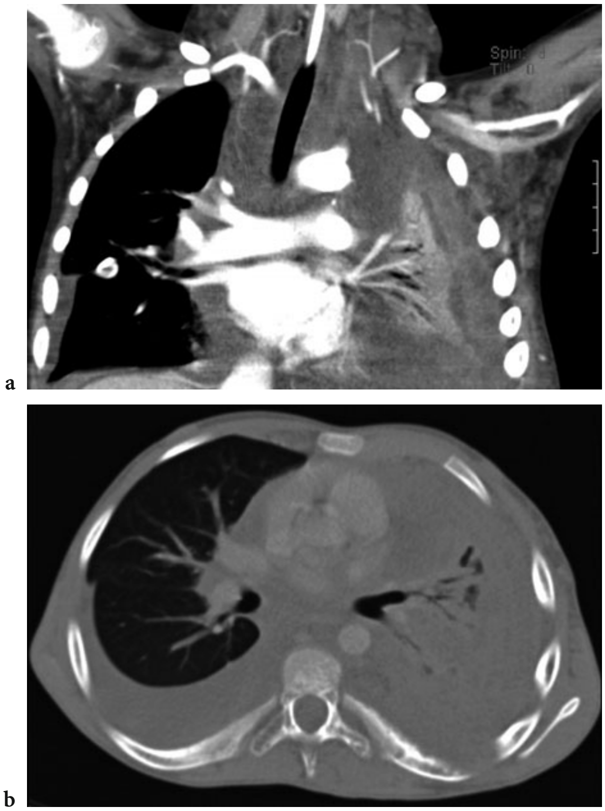

Fig. 12.11a,b. Lymphangiomatosis. **a** Coronal contrast-enhanced CT showing some enhancement in an otherwise consolidated and collapsed left lung. The left lung is surrounded by a large amount of low attenuating tissue (lymphangiomatous tissue) which extends into the left axilla and also into the right side of the mediastinum. **b** Axial bone windows in the same patient showing the collapsed left lung, right pleural effusion and ill-defined lucencies in a vertebra and posterior rib in keeping with lymphangiomatous infiltration

12.6
Chest Wall Tumours

12.6.1
Benign

Benign chest wall lesions are dealt with in Chapter 14.

12.6.2
Malignant

12.6.2.1
Ewing's Sarcoma/Primitive Neuroectodermal Tumour

Chest wall tumours constitute 1.8% of solid tumours in childhood (Soyer et al. 2006). Chest wall Ewing's sarcoma and primitive neuroectodermal tumours (PNET), also known as Askin tumours, albeit separate histological entities, are recognised as biologically related lesions (Sallustio et al. 1998). A classification that is gaining acceptance is to label all these tumours as 'malignant small round cell type'. From a radiological perspective they all generally manifest as peripheral chest wall masses, with or without associated rib destruction, and cannot be separated on imaging criteria alone.

Typically the chest radiograph will suggest the likely tumour based on the finding of a mass with intrathoracic growth, rib and chest wall involvement and concomitant pleural effusion (Fig. 12.12).

Rib destruction essentially excludes a benign process and should be actively sought on plain radiography and CT (actinomycosis and rib osteomyelitis are uncommon in childhood and generally present a different clinical picture). In a review of 29 PNETs from our institution, there were 11 chest PNETs in 4 of whom the whole hemithorax was occupied by tumour (Dick et al. 2001). The average diameter of the thoracic masses was 7 cm. A solid heteroge-

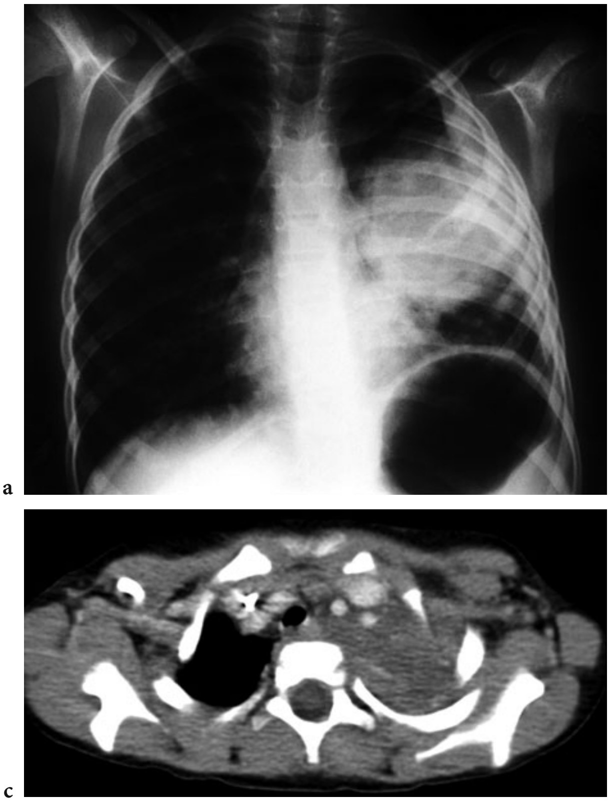

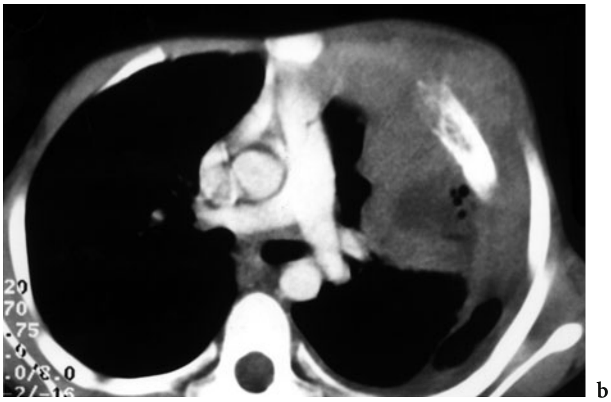

Fig. 12.12a–c. Ewing's sarcoma. **a** Chest X-ray displaying a rounded left mid-zone opacity with an elevated hemidiaphragm. Note lytic changes and expansion to the anterior third left rib in keeping with a malignant, aggressive lesion. **b** Axial enhanced CT in the same patient showing a thickened rib surrounded by a large chest wall mass. Gas bubbles are secondary to a percutaneous biopsy. A pleural effusion is noted and contralateral pulmonary metastases were evident on lung window settings. **c** Axial CT showing a left apical mass lesion in another patient. Ewings/PNETs are often located posteriorly in the chest and may mimic a neuroblastoma

neous mass is characteristic with the larger lesions having more low attenuating or necrotic centres on CT (Fig. 12.12). Regional lymphadenopathy may be seen including retrocrural adenopathy. Calcification within the tumour is uncommon and when present is relatively unremarkable. Ultrasound of these peripheral chest masses has on occasion proved superior to CT and MRI in excluding tumour infiltration of the lung or diaphragm. PNETs tend to displace adjacent structures such as the bronchi or major vessels rather than encase them (Dick et al. 2001). The tumours are characteristically hyperintense on T2-w MRI and of intermediate signal on T1-w sequences. Contrast enhancement is variable. MRI is probably superior in assessing tumour extent and local invasion but to some degree CT and MRI are complimentary studies, bearing in mind that CT is helpful in assessing adjacent rib changes and in evaluating the lung parenchyma for metastases. There are conflicting reports regarding the prognostic significance of local rib and chest wall invasion (Dick et al. 2001; Sallustio et al. 1998). All these patients also merit routine Tc99m-MDP bone scans for staging purposes. Patients with distant skeletal metastases at diagnosis have a poor outcome.

12.6.2.2
Rhabdomyosarcoma and Other Sarcomas

Rhabdomyosarcoma is the most common soft tissue sarcoma in childhood, accounting for up to 10% of solid paediatric malignancies (McHugh and Boothroyd 1999). Primary intrathoracic rhabdomyosarcoma is, however, rare in the paediatric age group as other primary sites are much more common. Rhabdomyosarcoma can arise from virtually any compartment in the chest including the lung and chest wall. The thorax is regarded as an unfavourable primary site for rhabdomyosarcoma with a tendency towards more alveolar (and less embryonal) histology, advanced disease at presentation and tumours occurring in older children. All these factors are known to be associated with a worse outcome in rhabdomyosarcoma patients. These tumours most commonly present as large or rapidly enlarging solid masses (Fig. 12.13), and a pleural effusion is not infrequent. Irregular contrast enhancement with variable areas of low attenuation are typical on CT examination. Calcification within the mass is not a feature but destruction of adjacent ribs is occasionally seen.

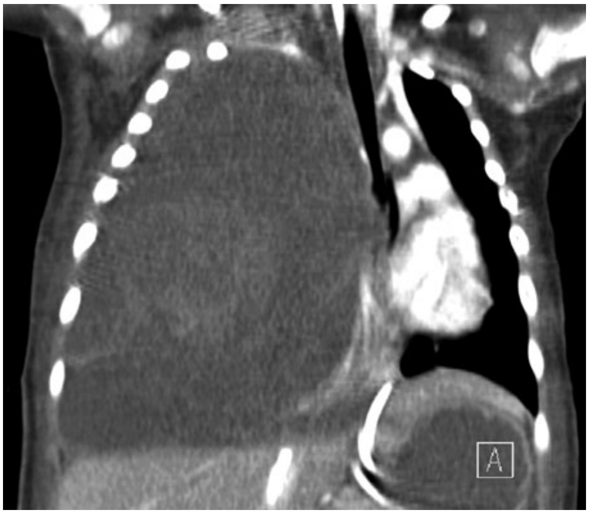

Fig. 12.13. Rhabdoid tumour. Contrast enhanced CT showing a large mass lesion occupying all the right chest and displacing the mediastinum to the left in a 1-year-old boy. The differential diagnosis for this mass would be wide and would include sarcomatous tumours

Fibrosarcoma, unspecified sarcoma, rhabdoid tumour and thoracic rhabdomyosarcomas are all indistinguishable radiologically, relying on histological examination for their differentiation. A leiomyosarcoma could also appear similar but increasingly now would typically be seen in a young HIV positive patient. The whole family of sarcoma tumours accounts for one fifth of all intrapulmonary malignancies in children. The majority of sarcomas are, however, chest wall masses.

12.6.2.3
Mesothelioma

Although there is some controversy regarding the nomenclature and origin, mesothelioma in childhood does occur (Fraire et al. 1988). Primary tumours may originate from the pleura, pericardium or peritoneum with two thirds of cases arising in the pleural space. Pleural mesothelioma usually presents as chest pain or as a symptomatic pleural effusion.

The radiological appearances can be similar to mesothelioma in adults (Goyal et al. 2000). Diffuse tumours are more common than localised lesions. Benign and malignant mesothelioma cannot be differentiated on histological or radiological grounds, although diffuse or invasive masses are more likely to be malignant and, of course, lesions that metastasise are by definition malignant. Some tumours in childhood may have an indolent course, and disease-free survival is possible. Fraire et al. (1988) were of the opinion that childhood mesothelioma is a sporadic, distinct entity separate from adult mesothelioma. There has been some speculation that either asbestos or isoniazid exposure or irradiation may predispose to these tumours in childhood, but the available evidence to date does not support a direct causal link.

12.7
Tumours of the Diaphragm

Primary tumours arising in the diaphragm are extremely rare in childhood. Tumours derived from muscle, blood vessels, fat or fibrous tissue are possible. Rhabdomyosarcoma is the most common malignant diaphragmatic tumour reported in children. Sixteen primary rhabdomyosarcomas of the diaphragm have been described in patients less than 18 years to date (Cada et al. 2006). Chest associated symptoms are more common than abdomen associated symptoms (Cada et al. 2006). A pronounced diaphragmatic ‘hump’ on a frontal chest radiograph is said to be the classic sign of a primary tumour arising from the diaphragm. Diaphragmatic masses, however, can mimic an elevated hemidiaphragm or eventration but ultrasound evaluation should easily demonstrate a mass lesion thus excluding those more common diagnoses. If there is no hepatic invasion the mass should be seen to move separately from the liver on sonography. Malignant tumours may present with a pleural effusion which may obscure an underlying mass lesion. In a case reported by Gupta et al. (1999) the tumour was clearly located cranial to the liver on axial CT and sharply demarcated from it indicating an extrahepatic origin. Coronal or sagittal MRI would be the optimal method for demonstrating a neoplasm arising from the diaphragm. MRI is generally more useful, however, in demonstrating the site of origin of a large mass abutting the hemidiaphragm, the relationship of the diaphragm to the mass including diaphragmatic integrity and in delineating the extent of such a mass lesion.

12.8
Conclusions

The above-mentioned thoracic tumours are all relatively uncommon in childhood. Nevertheless, when there is failure to respond to the usual medical treatment, and particularly when there is mediastinal displacement or a mass plus rib changes, the possibility of neoplasia increases significantly. Some other even rarer chest tumours (Fig. 12.14) inevitably also occur from time to time and often merit individual case reports but have not been detailed here. Vertebral neoplasms have not been discussed as these are generally categorised and dealt with in skeletal texts.

Cardiac tumours are noteworthy but are also extremely rare in paediatrics and fall predominantly within the practice of the paediatric cardiologist. Cardiac rhabdomyomas are the commonest of these neoplasms, usually occurring in children with tuberous sclerosis (TS) or a family history of TS (Liang et al. 2000). In symptomatic neonates cardiac rhabdomyomas are generally fatal. Patients with no major dysrhythmia or haemodynamic obstruction, however, have an excellent prognosis. Over half of all tumours completely or partially regress over time, and in children who can be managed conservatively other lesions tend to remain stable (Liang et al. 2000).

Although further improvements in MDCT and MRI will undoubtedly aid diagnosis in patients with thoracic tumours in the future, PET/CT holds great promise also in the evaluation of childhood malignancies not only for detection but also for staging and assessing response to therapy. PET/CT is dealt with elsewhere in the text but it is likely to be of use in some of the malignant conditions mentioned here, perhaps initially on an individual basis particularly when dilemmas regarding metastatic disease arise.

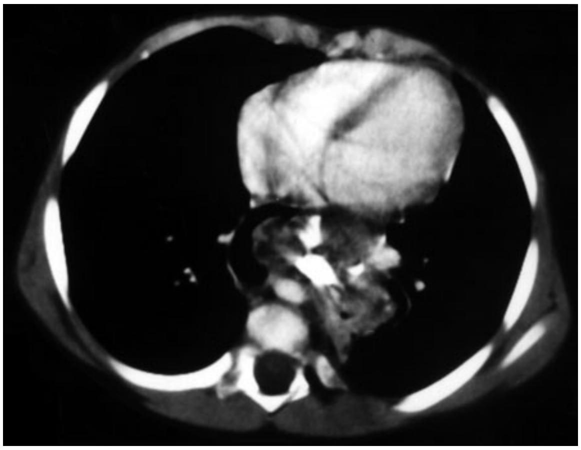

Fig. 12.14. Esophageal teratoma. Teratomas may rarely occur in the posterior mediastinum but seldom involve the esophagus to this degree. Contrast-enhanced CT here demonstrates a large, calcified mass anterior to the descending thoracic aorta within the lumen of a markedly distended esophagus

References

Adams GA, Shochat SJ, Smith EI et al. (1993) Thoracic neuroblastoma: a Pediatric Oncology Group study. J Pediatr Surg 28:372–377

Agrons GA, Rosado-de-Christenson ML, Kirejczyk WM et al. (1998) Pulmonary inflammatory pseudotumor: radiologic features. Radiology 206:511–518

Alper F, Kaynar H, Kantarci M et al. (2005) Trichoptysis caused by intrapulmonary teratoma: computed tomography and magnetic resonance imaging findings. Australas Radiol 49:53–56

Andronikou S, Kader E (2001) Bronchial mucoepidermoid tumour in a child with organomegaly due to secondary amyloidosis: case report and review of the literature. Pediatr Radiol 31:348–350

Aviv R, McHugh K (2000) Mechanisms of chylous effusions in lymphangiomatosis. AJR Am J Roentgenol 175:1191

Brown G, Shaw DG (1995) Inflammatory pseudotumours in children: CT and ultrasound appearances with histopathological correlation. Clin Radiol 50:782–786

Buyukavci M, Atlas S, Salman B, Eren S (2006) An aggressive childhood tumour mimicking pleural empyema: pleuropulmonary blastoma. J Pediatr Hematol Oncol 28(4):257–259

Cada M, Gerstle JT, Traubici J et al. (2006) Approach to diagnosis and treatment of pediatric primary tumors of the diaphragm. J Pediatr Surg 41:1722–1726

Castanon M, Saura L, Weller S et al. (2005) Myofibroblastic tumor causing severe neonatal distress. Successful surgical resection after embolisation. J Pediatr Surg 40: E9–E12

Chadwick EG, Connor EJ, Guerra Hanson C et al. (1990) Tumours of smooth muscle origin in HIV-infected children. JAMA 263:3182–3184

Choi S-J, Lee JS, Song KS, Lim T-H (1998) Mediastinal teratoma: CT differentiation of ruptured and unruptured tumors. AJR Am J Roentgenol 171:591–594

Coakley FV, Cohen MD, Johnson MS et al. (1998) Maximum intensity projection images in the detection of simulated pulmonary nodules by spiral CT. Br J Radiol 71:135–140

Connolly BL, Chait PG, Duncan DS, Taylor G (1999) CT-guided percutaneous needle biopsy of small lung nodules in children. Pediatr Radiol 29:342–346

Cowie F, Corbett R, Pinkerton CR (1997) Lung involvement in neuroblastoma: incidence and characteristics. Med Ped Oncol 28:429–432

Crisp AJ, Babyn PS, Weitzman S, Thorner P (1996) Significance of lung nodules at CT in children with solid malignant tumours. Presented at International Pediatric Radiology, Boston

Curtis JM, Lacey D, Smyth R, Carty H (1998) Endobronchial tumours in childhood. Eur J Radiol 29:11–20

de Chadarevian J-P, Wolk JH, Inniss S et al. (1997) A newly recognised cause of wheezing: AIDS-related bronchial leiomyomas. Pediatr Pulmonol 24:106–110

Dehner LP, Watterson J, Priest J (1995) Pleuropulmonary blastoma: a unique intrathoracic-pulmonary neoplasm of childhood. Perspect Pediatr Pathol 18:214–226

Dhall G, Ginsburg H, Bodenstein L et al. (2004) Thymoma in children: report of two cases and review of literature. J Pediatr Hematol Oncol 26(10):681–685

Dick EA, McHugh K, Kimber C, Michalski A (2001) Radiology of non-central nervous system primitive neuroectodermal tumours: diagnostic features and correlation with outcome. Clin Radiol 56:206–215

Dickstein PJ, Amaral SMM, Silva AMLF et al. (1993) Bronchial mucous gland adenoma presenting as a bronchogenic cyst. Pediatr Pulmonol 16:370–374

Diederich S, Lenzen H, Windmann R et al. (1999) Pulmonary nodules: experimental and clinical studies at low dose CT. Radiology 213:289–298

Diederich S, Hansen J, Wormanns D (2005) Resolving small pulmonary nodules: CT features. Eur Radiol 15:2064–2069

Drut R, Mosca HH (1996) Intrapulmonary cystic lymphangioma. Pediatr Pulmonol 22:204–206

Dulmet EM, Macchiarini P, Suc B, Verley JM (1993) Germ cell tumours of the mediastinum: a 30 year experience. Cancer 72:1894–1901

Fraire AE, Cooper S, Greenberg SD et al. (1988) Mesothelioma of childhood. Cancer 62:838–847

Goyal M, Swanson KF, Konez O et al. (2000) Malignant pleural mesothelioma in a 13 year old girl. Pediatr Radiol 30(11):776–778

Gross E, Chen MK, Hollabaugh RS, Joyner RE (1996) Tracheal hamartoma: report of a child with a neck mass. J Pediatr Surg 31:1584–1585

Gruden JF, Ouanounou S, Tigges S et al. (2002) Incremental benefit of maximum-intensity-projection images on observer detection of small pulmonary nodules revealed by multidetector CT. AJR Am J Roentgenol 179:149–157

Grundy P, Perlman E, Rosen NS et al. (2005) Current issues in Wilms tumor management. Curr Probl Cancer 29:223–260

Guest AR, Strouse PJ, Chung Hiew C, Arca M (2000) Progressive esophageal leiomyomatosis with respiratory compromise. Pediatr Radiol 30:247–250

Gupta AK, Mitra DK, Berry M (1999) Primary embyonal rhabdomyosarcoma of the diaphragm in a child: case report. Pediatr Radiol 29:823–825

Hancock BJ, Di Lorenzo M, Youssef S et al. (1993) Childhood primary pulmonary neoplasms. J Pediatr Surg 28:1133–1136

Hartman GE, Shochat SJ (1983) Primary pulmonary neoplasms of childhood: a review. Ann Thorac Surg 36:108–119

Hedlund GL, Navoy JF, Galliani CA, Johnson WH Jr (1999) Aggressive manifestations of inflammatory pseudotumor in children. Pediatr Radiol 29:112–116

Janik JS, Janik JP, Lovell MA et al. (2003) Recurrent inflammatory pseudotumors in children. J Pediatr Surg 38(10):1491–1495

Jayne D, Bridgewater B, Lawson RAM (1997) Endobronchial inflammatory pseudotumour exacerbating asthma. Postgrad Med J 73:98–99

Kammen BF, Matthay KK, Pacharn P et al. (2001) Pulmonary metastases at diagnosis of neuroblastoma in pediatric patients: CT findings and prognosis. AJR Am J Roentgenol 176(3):755–759

Karnak I, Akcoren Z, Senocak ME (2000) Endobronchial leiomyoma in children. Eur J Pediatr Surg 10:136–139

Kaste SC, Pratt CB, Cain AM et al. (1999) Metastases detected at the time of diagnosis of primary pediatric extremity osteosarcoma: imaging features. Cancer 86:1602–1608

Katz SL, Das P, Ngan B-Y et al. (2005) Remote intrapulmonary spread of recurrent respiratory papillomatosis with malignant transformation. Pediatr Pulmonol 39:185–188

Kim CK, Chung CY, Koh YY (2000) Primary small cell bronchogenic carcinoma in a 14 year old boy. Pediatr Pulmonol 29:317–320

Kim WS, Lee KS, Kim IO et al. (1997) Congenital cystic adenomatoid malformation of the lung: CT-pathologic correlation. AJR Am J Roentgenol 168:47–53

Kocaoglu M, Bulakbasi N, Soylu K et al. (2006) Thin section axial multidetector computed tomography and multiplanar reformatted imaging of children with suspected foreign body: is virtual bronchoscopy overemphasized? Acta Radiol 47(7):746–751

Kramer SS, Wehunt WD, Stocker JT, Kashima H (1985) Pulmonary manifestations of juvenile laryngotracheal papillomatosis. AJR Am J Roentgenol 144:687–694

Liang CD, Ko SF, Huang SC (2000) Echocardiographic evaluation of cardiac rhabdomyoma in infants and children. J Clin Ultrasound 28:381–386

Mas Estelles F, Andres V, Vallcanera A et al. (1995) Plasma cell granuloma of the lung in childhood: atypical radiologic findings and association with hypertrophic osteoarthropathy. Pediatr Radiol 25:369–372

Maziak DE, Todd TR, Keshavjee SH et al. (1996) Adenoid cystic carcinoma of the airway: thirty-two year experience. J Thorac Cardiovasc Surg 112:1522–1531

McCarville MB, Lederman HM, Santana VM et al. (2006) Distinguishing benign from malignant pulmonary nodules with helical chest CT in children with malignant solid tumors. Radiology 239:514–520

McHugh K, Boothroyd AE (1999) The role of radiology in childhood rhabdomyosarcoma. Clin Radiol 54:2–10

Meisel JA, Guthrie KA, Breslow NE et al. (1999) Significance and management of computed tomography detected pulmonary nodules: a report from the National Wilms' Tumor Study Group. Int J Radiation Oncol Biol Phys 44:579–585

Mergan F, Jaubert F, Sauvat F et al. (2005) Inflammatory myofibroblastic tumor in children: clinical review with anaplastic lymphoma kinase, Epstein-Barr virus and human herpes virus 8 detection analysis. J Pediatr Surg 40:1581–1586

Morini F, Quattrucci S, Cozzi DA et al. (2003) Bronchial adenoma: an unusual cause of recurrent pneumonia in childhood. Ann Thorac Surg 76:2085–2087

Paulussen M, Ahrens S, Craft AW et al. (1998) Ewing's tumour with primary lung metastases: survival analysis of 114 (European Intergroup) Cooperative Ewing's Sarcoma Studies patients. J Clin Oncol 16:3044–3052

Pescarmona E, Giardini R, Brisigotti M et al. (1992) Thymoma in childhood: a clinicopathological study of five patients. Histopathology 21:65–68

Priest JR, McDermott MB, Bhatia S et al. (1997) Pleuropulmonary blastoma: a clinicopathologic study of 50 cases. Cancer 80:147–161

Priest JR, Hill AD, Williams GM et al. (2006) Type I Pleuropulmonary blastoma: a report from the International Pleuropulmonary Blastoma Registry. J Clin Oncol 24(27):4492–4498

Romeo C, Impellizzeri P, Grosso M et al. (1999) Pleuropulmonary blastoma: long-term survival and literature review. Med Pediatr Oncol 33:372–376

Rothstein DH, Voss SD, Isakoff M, Puder M (2005) Thymoma in a child: case report and review of the literature. Pediatr Surg Int 21:548–551

Sallustio G, Pirronti T, Lasorella A et al. (1998) Diagnostic imaging of primitive neuroectodermal tumour of the chest wall (Askin tumour). Pediatr Radiol 28:697–702

Sasaka K, Kurihara Y, Nakajima Y et al. (1998) Spontaneous rupture: a complication of benign mature teratomas of the mediastinum. AJR Am J Roentgenol 170:323–328

Senac MO Jr, Wood BP, Isaacs H, Weller M (1991) Pulmonary blastoma: a rare childhood malignancy. Radiology 179:743–746

Siegel MJ, Ishwaran HI, Fletcher BD et al. (2002) Staging of neuroblastoma at imaging: report of the Radiology Diagnostic Oncology Group. Radiology 223:168–175

Slovis TL, Meza MP, Cushing B et al. (1997) Thoracic neuroblastoma: what is the best imaging modality for evaluating extent of disease? Pediatr Radiol 27:273–275

Soldatski I, Onufrieva E, Steklov A, Schepin NV (2005) Tracheal, bronchial and pulmonary papillomatosis in children. Laryngoscope 115(10):1848–1854

Soyer T, Karnak I, Ciftci AO et al. (2006) The results of surgical treatment of chest wall tumors in childhood. Pediatr Surg Int 22:135–139

Tagge EP, Mulvihill D, Chandler JC et al. (1996) Childhood pleuropulmonary blastoma: caution against nonoperative management of congenital lung cysts. J Pediatr Surg 31:187–190

van den Bosch JMM, Wagenaar SS, Corrin B et al. (1987) Mesenchymoma of the lung (so called hamartoma): a review of 154 parenchymal and endobronchial cases. Thorax 42:790–793

Verbeke JIM, Verbene AAPH, den Hollander JC, Robben SGF (1999) Inflammatory myofibroblastic tumour of the lung manifesting as progressive atelectasis. Pediatr Radiol 29:816–819

Wang LT, Wilkins EW Jr, Bode HH (1993) Bronchial carcinoid tumors in pediatric patients. Chest 103:1426–1428

Wunderbaldinger P, Paya P, Partik B et al. (2000) CT and MR imaging of generalised cystic lymphangiomatosis in pediatric patients. AJR Am J Roentgenol 174:827–832

Thoracic Manifestations of Systemic Diseases

Alan S. Brody

CONTENTS

13.1 **Introduction** *289*

13.2 **Examination Techniques** *290*
13.2.1 Plain Radiographs and Computed Radiography *290*
13.2.2 Computed Tomography *290*
13.2.3 Magnetic Resonance Imaging *291*
13.2.4 Nuclear Medicine *292*

13.3 **Connective Tissue Diseases** *293*

13.4 **Immune Deficiencies** *295*

13.5 **Immunodeficiency Syndromes** *296*
13.5.1 B Cell Disorders *296*
13.5.1.1 Selective IgA Deficiency *296*
13.5.1.2 X-Linked (Bruton) Agammaglobulinemia *296*
13.5.1.3 Common Variable Immunodeficiency *296*
13.5.2 T Cell Disorders *297*
13.5.2.1 Thymic Hypoplasia (DiGeorge's Syndrome) *297*
13.5.2.2 X-Linked Immunodeficiency with Hyper IgM *297*
13.5.3 B and T Cell Combined Disease *297*
13.5.3.1 Severe Combined Immunodeficiency *297*
13.5.3.2 Combined Immunodeficiency (Nezelof's Syndrome) *297*
13.5.3.3 Wiskott-Aldrich Syndrome *298*

13.6 **Chronic Granulomatous Disease** *298*
13.7 Sickle Cell Disease *299*

13.8 **Langerhan's Cell Histiocytosis** *300*

13.9 **Cystic Fibrosis** *301*
13.9.1 Genetics *302*
13.9.2 Diagnosing Cystic Fibrosis *302*
13.9.3 Pulmonary Pathophysiology of Cystic Fibrosis *303*
13.9.4 Lung Care in Cystic Fibrosis *303*
13.9.5 Imaging in Cystic Fibrosis *304*
13.9.5.1 Plain Radiographs *304*
13.9.5.2 Computed Tomography *304*
13.9.5.3 Nuclear Medicine *305*
13.9.5.4 Magnetic Resonance Imaging *305*

13.10 **Phacomatoses** *306*
13.10.1 Tuberous Sclerosis *306*
13.10.2 Neurofibromatosis *307*

13.11 **Lysosomal Storage Disorders** *307*

References *309*

13.1
Introduction

This chapter will concentrate on the evaluation of the thorax in children with systemic disorders. Following a discussion of examination techniques, specific systemic conditions that have known thoracic manifestations will be discussed. For each condition or group of conditions, the general features of the condition will be described, followed by a review of the imaging characteristics of thoracic manifestations. Imaging evaluation will emphasize advanced imaging techniques and recent developments. The reader is encouraged to review the overall description of the different conditions as well as the specific imaging information. Knowledge of the clinical and laboratory features of these diseases may allow the radiologist to be the first to suggest an underlying systemic disease in a child with a thoracic abnormality. Knowledge of the associated pulmonary abnormalities frequently narrows the differential of lung findings in these children.

In addition to specific associated thoracic abnormalities, many systemic diseases produce effects that can be reflected by thoracic findings on diagnostic imaging. Increased central venous pressure or decreased capillary oncotic pressure can result in pul-

---

A. S. Brody, MD
Professor of Radiology and Pediatrics, Dept. of Radiology, Children's Hospital Medical Center, 3333 Burnet Avenue, Cincinnati, OH 45229-3039, USA

monary edema. Abnormal host defenses frequently result in both an increased incidence of pulmonary infection and a change in the spectrum of infection. Abnormalities of muscle strength or the nervous system can result in aspiration with direct chemical insult to the lungs as well as an increase in infection. The likelihood of such effects should be borne in mind, as in the proper clinical situation these abnormalities may be more common than pathologies associated with a specific systemic disease.

13.2
Examination Techniques

13.2.1
Plain Radiographs and Computed Radiography

Plain radiographs remain the most common imaging study of the chest. Pediatric chest radiography requires expertise on the part of the radiology technologist in order to obtain correct patient position, lung volume, lack of motion, and correct technique. Interstitial lung disease is frequently very subtle in children. In addition, viral infections are very common, and produce findings of interstitial lung disease that are frequently indistinguishable from noninfectious causes.

Computed radiography has replaced film radiography at many sites. While the resolution of computed radiography is lower than that of film/screen radiography, computed radiography provides the ability to adjust the window and level of the study, as well as provides ready availability of the images to multiple health care providers. No studies have specifically compared the two systems in the evaluation of pediatric interstitial lung disease, but computed radiography has been found to provide the necessary diagnostic quality. Radiologists should remain aware that computed radiography and PACS incorporate factors including imaging plate characteristics, system resolution, and image compression that can all impact the ability to detect subtle lung disease (Kido et al. 1996). This may be particularly important when compression is used to archive images. It has been calculated that the use of computed radiography can decrease radiation exposure (Hufton et al. 1998). However, because overexposed studies can be adjusted to provide diagnostic images, it is possible to increase markedly the radiation dose to children when using computed radiography (Don 2004). Techniques should be monitored to insure that ALARA (As Low As Reasonably Achievable) standards are being used.

13.2.2
Computed Tomography

Computed tomography (CT) is the primary cross-sectional imaging modality for evaluating the thorax. All components of the thorax can be well evaluated with CT. There are specific areas that are better evaluated with magnetic resonance imaging (MRI), but MRI cannot currently fully evaluate the lung parenchyma and does not provide a complete means of evaluating the chest.

Numerous studies have demonstrated the superiority of CT over chest radiographs in detecting thoracic abnormalities (Kuhn 1993; Lynch et al. 1999; Nathanson et al. 1991). Due to the increased sensitivity and specificity of CT compared to chest radiographs, CTs may be ordered either to evaluate radiographic abnormalities better or to assess definitively the presence and extent of a suspected complication of systemic disease. CT scanning can show parenchymal abnormalities when chest radiographs are normal. With increasing therapeutic options in many systemic diseases, the additional information provided by CT scanning is of increasing value to clinicians. This has resulted in a marked increase in the number of chest CTs ordered. Examination technique must be carefully planned in order to minimize radiation exposure while maximizing image quality.

The use of multichannel CT scanners has dramatically decreased the time necessary to obtain a CT scan (Frush 2005). In addition, systems with 16 or more channels allow routine 5-mm sections to be reconstructed to the approximately 1-mm thickness used for high-resolution CT (HRCT). While there is an increase in image noise, these reconstructed images will frequently provide sufficient information so that a separate HRCT examination is not necessary. Recent CT scanner interfaces are optimized for rapid acquisition of contiguous slices. It is important to remember that directly acquired HRCT studies have better resolution and a radiation dose usually less than half the dose of a contiguous slice CT.

These new systems allow further reduction of radiation dose from the low dose protocols developed for single channel systems (Lucaya et al. 2000;

Rogalla et al. 1999). All guidelines adjust the CT technique for the size of the patient, with smaller patients requiring less radiation for the same image noise. Age, weight, height, and thoracic diameter can all be used to determine technique, with thoracic diameter being most directly related to image noise (Menke 2005; Vock 2005). In addition to adjusting tube current and time (mAs), recent recommendations also reduce peak kilovoltage (kVp) for smaller patients. Unlike mAs changes which affect noise but do not otherwise alter image appearance, lower kVp levels increase contrast and may thereby improve image quality, particularly for CT scans performed with intravenous contrast material (Siegel et al. 2004; Sigal-Cinqualbre et al. 2004). Beam hardening artifact has been reported to limit image quality at 80 kVp (Cody et al. 2004), so 100–120 kVp is recommended for all but very small children. Published guidelines for technique are available (Donnelly et al. 2001; Donnelly and Frush 2003; Kalra et al. 2004), but advances in CT scanner technology are sufficiently rapid that improved techniques are likely to continue to be developed.

Additional advances in CT scanning include the use of the noise index to automatically vary mA along the Z axis based on attenuation measured with the localization topogram. The mA increases in areas where more soft tissue causes greater attenuation of the X-ray beam, so mA increases at the level of the shoulders and diaphragm and decreases at the mid lung level. This technique can decrease radiation dose, but careful choice of the noise index, and often the use of a preset lower limit for mA, is necessary for adequate image quality.

Radiation to the breast is an area of concern that can be addressed with the use of breast shielding. Breast shields can reduce the dose to the breast by 30% without significantly increasing image noise (Fricke et al. 2003). The preservation of image quality with breast shielding takes advantage of the physics of imaging the chest with consistent mAs. Newer CT scanners that vary mAs as the X-ray tube moves around the patient may not show this benefit. In addition, when mA is varied in the Z axis based on the topogram, breast shields should be placed following the topogram view so that the CT scanner does not increase the dose through the level of the breast shields.

Motion blurring will markedly degrade CT images, particularly HRCT images. We have found, however, that HRCT may still provide more information than helical CT despite the presence of some motion blurring. It is very important to limit gross body movement, but images obtained during quiet respiration can often provide useful information. While many children can be studied without sedation, the ability to adequately sedate patients is an important component of the pediatric imaging department.

With faster CT scanners patient motion is markedly decreased. During quiet breathing, lung volumes are frequently low and inspiratory and expiratory images cannot be obtained. Three techniques have been suggested to control lung volumes and improve the quality of chest CT images. The simplest technique is decubitus imaging. In the decubitus position the volume of the superior lung is high and the volume of the inferior lung is low. This allows images similar to conventional inspiration and expiration images (Lucaya et al. 2000). The controlled ventilation technique, in which sedated young children are imaged during a respiratory pause induced by mask ventilation, can produce excellent quality inspiration and expiration images (Long and Castile 2001; Long et al. 1999). General anesthesia is the most invasive method, but it provides the most complete control of lung volume and motion. Special effort is necessary, using deep sigh breaths and imaging as quickly as possible, to avoid atelectasis.

HRCT is the method of choice for the evaluation of diffuse parenchymal disease. Evaluation of the mediastinum and chest wall should be performed with contiguous section helical CT. If both evaluations are needed, helical CT should be performed first. If a 16-channel or higher CT scanner is used, the data should be reconstructed to approximately 1 mm thickness. These images will be similar to directly obtained HRCT images. If these images are not of adequate quality, limited HRCT images can be performed subsequently, using the helical CT to suggest appropriate levels. The use of intravenous contrast will not degrade HRCT images. Limited image quality from the original data set is often due to low lung volumes or respiratory motion. In this case the lung volume control techniques described above should be considered prior to obtaining the HRCT images.

13.2.3
Magnetic Resonance Imaging

Rapid imaging techniques have improved the ability of magnetic resonance imaging (MRI) to visualize lung parenchyma (Bader et al. 2002). However, MRI remains limited in the lung by the relatively small number of protons in normal lung and the loss of signal caused by dephasing at air/soft tissue interfaces. An important advantage of MRI is the lack of radiation that allows dynamic imaging (Chu et al. 2006) and serial follow-up examinations (Hebestreit et al. 2004) to be performed without concern for the cumulative radiation dose.

Recent reports have shown that nodules as small as 2 mm can be detected with MRI (Luboldt et al. 2006), but parenchymal findings such as interstitial fibrosis, ground glass increased density, and air trapping cannot reliably be detected (Bader et al. 2002). While MRI does not provide a complete evaluation of the lung parenchyma, it has been used in specific clinical situations, such as the demonstration of pulmonary hemorrhage (Hsu et al. 1992). In a study of children with suspected pneumonia, MRI demonstrated all of the lesions seen on CXR and more accurately identified small infiltrates and pleural effusions (Rupprecht et al. 2002). In a study of immunocompromised patients, MRI was found to be superior to CT in demonstrating early necrotizing pneumonia (Leutner et al. 2000).

MRI has a greater scope of application in evaluating the chest wall, where it is the most sensitive means of evaluation and is better able to demonstrate soft tissue inflammation and bone marrow changes in the ribs than CT. When spinal abnormalities are suspected, MRI is the modality of choice.

Mediastinal vascular anatomy is well demonstrated by both CT and MRI. Mediastinal masses can also be evaluated with either modality. MRI is preferred in posterior mediastinal masses because it more accurately evaluates spinal involvement. In the anterior and middle mediastinum, both modalities are useful, with CT preferred to identify calcification, and MRI better able to discriminate mediastinal masses from normal mediastinal tissues. Cardiac and pericardial masses are best evaluated with MRI.

In addition to imaging considerations, differences in imaging time and environment may be factors in choosing between CT and MRI. MRI requires longer imaging time and frequently requires sedation. At most institutions availability is limited compared to CT. Support equipment may be more difficult to maintain in the MRI environment.

An additional MRI technique currently being investigated is the use of hyperpolarized helium (He MRI). Hyperpolarized helium has a very short T1 that produces a strong MRI signal on appropriate pulse sequences. The patient inhales this gas which fills the ventilated lung. Dynamic imaging can be performed to evaluate wash in and wash out of gas as well as overall ventilation (Donnelly et al. 1999). Ventilation changes in numerous pediatric diseases including asthma (de Lange et al. 2006) and cystic fibrosis (Mentore et al. 2005) have been evaluated with He MRI. Recent investigations have used sophisticated imaging techniques to evaluate the fine structure of the lung. Using diffusion-weighted imaging, changes in lung morphology (Shanbhag et al. 2006) and alveolar size (Altes et al. 2006) have been evaluated with He MRI. This is a potentially powerful technique that combines the resolution of MRI with the functional information usually provided by nuclear medicine lung scanning. The hyperpolarized helium must be generated using dedicated and expensive equipment, and has a short half-life. This may limit the general availability of this technique.

13.2.4
Nuclear Medicine

Nuclear medicine adds functional information to the morphological information provided by CT and MRI. Gallium imaging can be used to assess disease activity (Kapala et al. 1983). Single photon emission CT (SPECT) is becoming increasingly available and markedly improves the localization of abnormalities seen with nuclear medicine. Imaging time for nuclear medicine studies is longer than for CT and more often requires sedation. Pediatric expertise is important, particularly when studies require cooperation, for example when performing ventilation scans.

Positron emission tomography (PET), most commonly performed with 2-deoxy-2-[18F] fluoro-D-glucose (FDG) provides functional information on metabolic activity. Combined with CT scanning, PET/CT is now widely used as a method of identifying and following neoplasms. The ability to measure metabolic activity also allows PET and PET/CT to assess inflammation and other non-malignant disorders (Alavi et al. 2002). Investigators have used PET to quantify inflammation in patients with cystic fibrosis (Chen et al. 2006). PET/CT may be of value in assessing the activity of other disease processes in the lung.

13.3
Connective Tissue Diseases

The connective tissue diseases (CTDs) are a group of diseases characterized by immune system abnormalities and inflammation affecting different systems and tissues. Common CTDs in children include juvenile rheumatoid arthritis (JRA), dermatomyositis (DM) and systemic lupus erythematosus (SLE). Patients may present with features of multiple CTDs. This presentation has been called mixed connective tissue disease (MCTD) or overlap syndrome.

Lung involvement varies with the type of CTD. Clinically apparent pulmonary abnormalities are very rare in JRA, rare in DM, and more common in SLE (Cerveri et al. 1992). Overlap syndromes also more commonly show lung involvement (Fig. 13.1). In a study of pulmonary function in children with CTD, pulmonary function abnormalities were found in the majority of children with active disease, although none had abnormalities on chest radiographs (Cerveri et al. 1992).

Clinically evident pulmonary disease is rare in JRA, occurring in 4% in one study (Athreya et al. 1980). However, when pulmonary function tests were performed in 16 children with JRA, 10 had abnormalities (Wagener et al. 1981). Respiratory muscle weakness has been suggested as a factor in lung function abnormalities (Knook et al. 1999). Among imaging findings, pleural and pericardial effusions have been found to be the most common abnormalities, occurring in five of 191 children studied by Athreya et al. (1980) (Fig. 13.2). Lymphocytic interstitial pneumonitis (LIP) occurred in two children in this group. In two additional cases, LIP preceded other symptoms of JRA by as much as 2 years (Lovell et al. 1984; Uziel et al. 1998). These reports described nonspecific interstitial infiltrates on chest radiographs. No report of CT findings was given. The reported appearance of LIP on HRCT showed predominantly ground glass opacity with associated consolidation, nodules, and cysts (Lynch et al. 1999) (Fig. 13.3). In adults with rheumatoid arthritis 49% had HRCT abnormalities, with interstitial disease in 28% and bronchiectasis in 19% (Zrour et al. 2005).

Scleroderma is characterized by fibrotic infiltration of connective tissues. Involvement of the skin and the gastrointestinal tract, particularly the esophagus, is most common. The term systemic sclerosis is used to describe disseminated disease. Scleroderma presents most commonly in adult women, but 10% of patients present in the pediatric age. Both pulmonary function test abnormalities and parenchymal abnormalities are common in scleroderma. Pulmonary complications are the most common cause of death (Chen et al. 2006). In a study of 11 scleroderma patients aged 5–19 years old, 8 had interstitial lung disease on HRCT. A broad range of abnormalities was described. The most common were ground glass opacity in eight, subpleural nodules in seven, peripheral linear opacities in six, and honeycombing in five. Chest radiographs were positive in only two patients (Seely et al. 1997, 1998). In adults lung disease is usually basal with poorly defined densities initially appearing in the subpleural posterior lower lobes. Over time additional abnormalities develop as described above (Remy-Jardin et al. 1993). Mea-

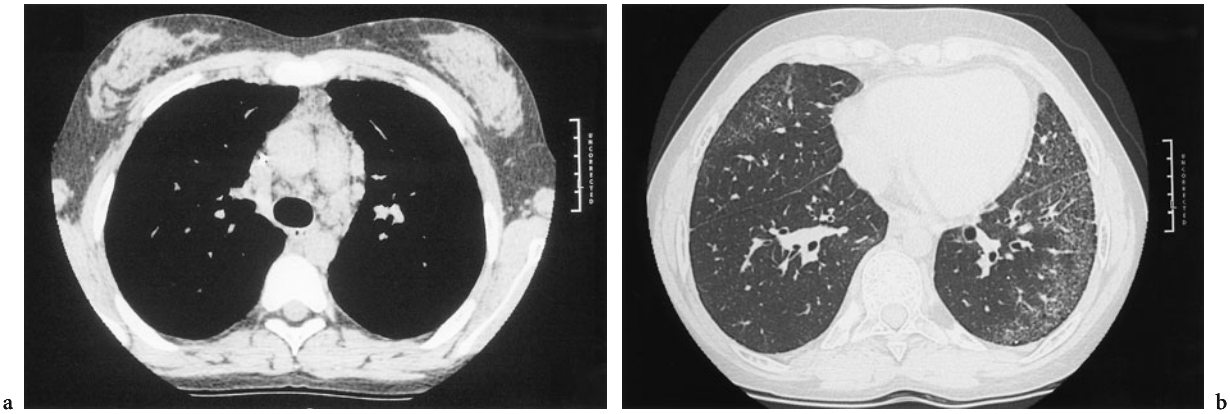

Fig. 13.1a,b. HRCT image through the lower lungs in a 13-year-old with mixed connective tissue disease. **a** Mediastinal windows show multiple small lymph nodes throughout the mediastinum. **b** Lung windows show peripheral small cystic spaces separated by well-seen fibrous walls. This honeycombing appearance suggests pulmonary fibrosis. These changes had been slowly progressing for several years, but the patient had only minimal pulmonary symptoms

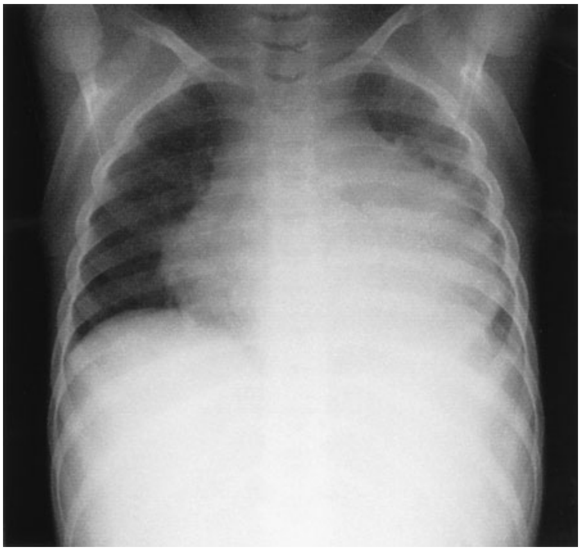

Fig. 13.2. Large pericardial effusion and small left pleural effusion in an 8-year-old boy with juvenile rheumatoid arthritis

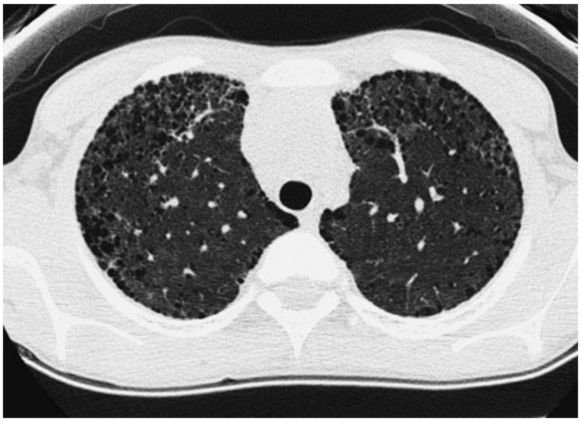

Fig. 13.3. HRCT demonstrates diffuse ground glass opacity and multiple peripheral cysts in this 9-year-old with juvenile rheumatoid arthritis. The pathologic diagnosis was follicular bronchiolitis. The imaging appearance is also consistent with lymphoid interstitial pneumonitis

suring serum levels of KL-6 has been suggested as a means of evaluating fibrotic interstitial lung disease in juvenile systemic sclerosis (Vesely et al. 2004).

Interstitial lung disease occurs in up to 50% of adults with DM. Abnormal PFTs are reported in more than more than half of patients with juvenile DM, but interstitial lung disease is rare (Takizawa et al. 1987). In one report of five cases, interstitial pneumonia was reported in three and bronchiolitis obliterans organizing pneumonia in two. All had abnormalities on physical examination or imaging studies at the time of presentation of their DM, although in two cases these were initially mild (Kobayashi et al. 2003).

SLE is a multisystem disease characterized by persistent B-cell activation that results in the overproduction of numerous autoantibodies and immune complexes. Both the activity of the antibodies and deposition of the immune complexes are associated with organ dysfunction (Lehman 1995). The prevalence of SLE in childhood is 5–10 per 100,000 children. Approximately one fifth to one-sixth of SLE patients present before the age of 16 years (Arkachaisri and Lehman 1999). Recent advances in genetics suggest that SLE results from a combination of genetic and environmental factors.

Lung disease is common in children with SLE, probably occurring in more than half of patients. The most common abnormality is restrictive lung disease detected on pulmonary function tests. Clinically apparent disease is less common, with estimates as low as 5%. The most common abnormality is pleural disease with resulting effusions. On imaging studies pleural effusions, alveolitis, pneumonia, obliterative bronchiolitis, vasculitis, pulmonary hemorrhage and pulmonary emboli are all increased in SLE (Babyn and Doria 2005). HRCT reliably identifies parenchymal lung disease more frequently than chest radiographs in adults with SLE (Bankier et al. 1995). Lupus pneumonitis is a rare condition that can be difficult to diagnose due to a nonspecific presentation of shortness of breath and a variable appearance of parenchymal opacity (Fig. 13.4).

Massive pulmonary hemorrhage is more common and of greater clinical concern. This condition is not seen in other CTDs. Patients present with parenchymal abnormalities and a decrease in hematocrit. Hemoptysis may not occur. This frequently fatal complication can be treated with steroids and cytotoxic agents, so identification is clinically important (Schwab et al. 1993). Alveolar opacities and a reticulonodular appearance can be seen on radiographs. The HRCT appearance also includes ground glass opacity. The appearance of pulmonary hemorrhage is not specific on plain radiographs or CT; lupus pneumonitis and infection can produce the same appearance. MRI has been reported as a means of specifically identifying hemorrhage by T2 shortening (Hsu et al. 1992).

"Shrinking lung syndrome" is a term used to describe a progressive decrease in lung volume seen in some patients with SLE. This is usually identified on chest radiographs as a progressive elevation of the diaphragm despite attempted full inspiration. The

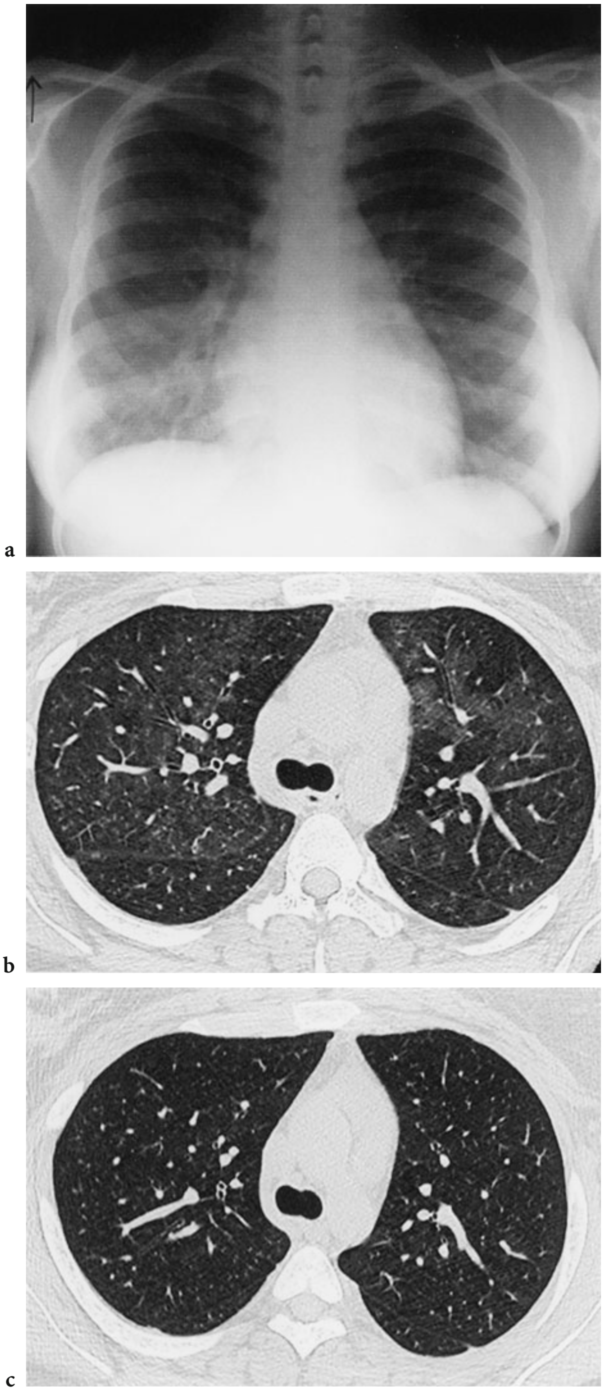

Fig. 13.4a–c. Lupus pneumonitis in a 17-year-old young woman with systemic lupus erythematosus who presented with shortness of breath. **a** Chest radiograph showed questionable basilar increased markings without other abnormality. **b** Initial HRCT demonstrates bilateral areas of ground glass attenuation throughout both lungs. No other abnormality was seen. **c** HRCT following steroid treatment shows resolution of the parenchymal abnormalities

etiology is unknown, but may relate to a combination of pleural restriction due to recurrent pleural inflammation, pulmonary restriction due to fibrosis, and muscle weakness of the diaphragm and chest wall. African American patients are most commonly affected. While most descriptions of shrinking lung syndrome are in adults, it has been reported in children (Ferguson and Weinberger 2006).

In addition to the pulmonary parenchymal abnormalities described above, pulmonary hypertension has been reported in JRA, scleroderma, and SLE.

13.4
Immune Deficiencies

Defenses against infection include physical barriers, B cells, T cells, natural killer cells, phagocytes, and compliment proteins. Defects in all of these occur, and result in increased infections. The lungs are directly exposed to infectious agents and are frequently the site of infection in children with abnormal infection fighting ability. Therefore, involvement of the lungs is seen to varying degrees in all immunodeficiencies.

The radiologist has several roles when evaluating the lungs of children who may have an immunodeficiency. These include suggesting the possibility of an immunodeficiency, identifying imaging characteristics consistent with a certain immunodeficiency, and evaluating infections as part of the acute care of these patients. The radiologist may be the first to suggest the possibility of an immunodeficiency, by noticing frequent infections such as recurrent pneumonia or by identifying unusual patterns of disease or slow resolution of infections. In suspected immunodeficiencies, imaging findings such as the presence of the thymus or lymphadenopathy may limit the differential diagnosis. The pathogens most likely to cause disease differ in different immunodeficiency syndromes, again narrowing the differential diagnosis.

Increased understanding of the molecular basis of the immune system as well as immunogenetics is allowing a far more detailed understanding of the immunodeficiency syndromes (Jones and Gaspar 2000). With this increased understanding has come increased complexity in evaluating and classifying these children. The radiologist is now more likely to be faced with new or extremely uncommon syndromes.

When interpreting imaging studies on these patients, it is frequently of benefit to ask the clinicians to relate the patient's disease to one or more of the well-described immunodeficiency syndromes included at the end of this section. This will allow the radiologist both to limit the differential diagnosis and to point out inconsistencies between the imaging appearance in a specific child and the expected appearance of the syndrome.

The primary role of thoracic imaging in children with immunodeficiencies is the evaluation of pulmonary infections. Plain radiographs remain the most frequently obtained imaging study. However, CT scanning is both more sensitive (Padley et al. 1995) and specific (Mathieson et al. 1989) than chest radiographs. HRCT has been reported to be useful clinically in children with antibody deficiency disorders to demonstrate the extent and severity of lung disease (Manson et al. 1997). Active mycobacterium infection will frequently show a "tree in bud" appearance of infectious material filling and dilating distal bronchioles. Invasive aspergillosis may show a "halo" appearance of ground glass opacity surrounding parenchymal nodules (Seely et al. 1997). Pneumocystis has a broad range of appearances. In a review of adult patients, a patchy distribution of ground glass opacity was most common, followed by cystic spaces and bullae (Kuhlman et al. 1990). Other features included adenopathy and pleural effusions. When a specific etiology is needed, CT can be used to guide bronchoscopy and fine needle biopsy in order to increase the yield of these more invasive procedures (Spencer et al. 1996).

CT scanning can be overused in children with immunodeficiencies. In one study of children with primary humoral immunodeficiency and chronic cough there was little progression over 3 years and the authors suggested that annual surveillance may be more than is necessary (Rusconi et al. 2003).

13.5
Immunodeficiency Syndromes

13.5.1
B Cell Disorders

B cells are named for their association with the bursa of Fabricius in chickens. In humans, B cells are associated with the bone marrow. The fetal liver may act as a bursal equivalent in humans. B cell disorders result from a decreased ability to form immunoglobulins and are the most frequent primary immunodeficiencies. IgA deficiency occurs in as many as 1 in 333 blood donors. Agammaglobulinemia occurs in approximately 1 in 50,000 live births.

13.5.1.1
Selective IgA Deficiency

IgA is the immunoglobulin secreted onto epithelial surfaces. It is present in smaller amounts in serum as well. IgA deficiency can be seen in people with no associated increase in infections. However, increased infections are frequently present and are usually limited to the respiratory, gastrointestinal, and genitourinary systems. In one study, the presence of IgA and IgG subclass antibody deficiencies was associated with greater pulmonary damage in children with recurrent respiratory infections (Ozkan et al. 2005).

13.5.1.2
X-Linked (Bruton) Agammaglobulinemia

Infants with X-linked agammaglobulinemia present clinically after maternally transmitted IgG antibodies decrease in the second half of the 1st year of life. Without IgG therapy, recurrent bacterial infections occur. Organisms include streptococci, pneumococci, *H. influenza*, and mycoplasma. Hepatitis and enterovirus infections are increased, while other viral infections are usually handled normally. *Pneumocystis carinii* and fungal infections are rare. The adenoids, tonsils, and lymph nodes are usually small. The lateral airway radiograph can be very helpful in suggesting this diagnosis when adenoid tissue is absent. Beware the patient who has had an adenoidectomy, of course.

13.5.1.3
Common Variable Immunodeficiency

Common variable immunodeficiency is usually less severe than agammaglobulinemia, but otherwise similar in clinical manifestations. The tonsils, adenoids, and lymph nodes are normal in size. Splenomegaly is seen in about 25% of cases, and lymphadenopathy is common.

13.5.2 T Cell Disorders

T lymphocytes are named for their association with the thymus. T cells function in the initial response to an antigen and in limiting the potentially harmful immune response. In addition to infection fighting, T cells are responsible for delayed hypersensitivity reactions and for graft rejection. Children with T cell disorders have more severe problems with infection than those with B cell disorders.

Children with T cell disorders are susceptible to infections with acid fast bacilli, fungi, viruses, and *Pneumocystis carinii* (Fig. 13.5).

13.5.2.1 Thymic Hypoplasia (DiGeorge's Syndrome)

The combination of thymic absence, hypocalcemia, and immune deficiency form DiGeorge's syndrome. The thymus and parathyroid glands are usually hypoplastic rather than absent. Presentation in the neonatal period is more often due to hypocalcemia induced seizures than to immunodeficiency. The later clinical course is similar to children with severe combined immunodeficiency (SCID).

13.5.2.2 X-Linked Immunodeficiency with Hyper IgM

These children are identified by an elevated IgM and decreased IgG and IgA in serum. While this would suggest a B cell defect, the B cells in these children can form normal immunoglobulins when they are tested with normal T cells. Immunohistochemical staining shows normal numbers of circulating B cells. Presentation is similar to agammaglobulinemia.

13.5.3 B and T Cell Combined Disease

13.5.3.1 Severe Combined Immunodeficiency

This is the most severe of the immunodeficiencies with absent T and B cell function. Most cases present between 2 and 6 months of age following loss of maternal antibodies (Manson et al. 2000). Without bone marrow transplantation, survival beyond the 2nd year of life is rare. A number of different genetic defects underlie SCID including autosomal recessive and X-linked forms. SCID is rare, occurring in less than 1:100,000 live births.

The role of radiology of the thorax in these children is in the evaluation of the recurrent infections that are the primary cause of mortality (Fig. 13.6). While these patients have a small thymus, imaging is not usually helpful in suggesting this diagnosis prior to the onset of infections.

13.5.3.2 Combined Immunodeficiency (Nezelof's Syndrome)

In these patients, antibody formation is decreased but not absent. Neutropenia is common, and immunoglobulins are usually increased. Chronic pulmonary infections, chronic diarrhea, and failure to

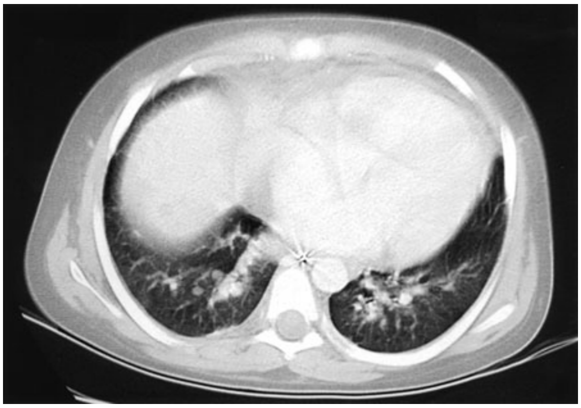

Fig. 13.5. A 9-year-old with T-cell deficiency. CT demonstrates multiple bilateral basilar nodules due to aspergillus infection

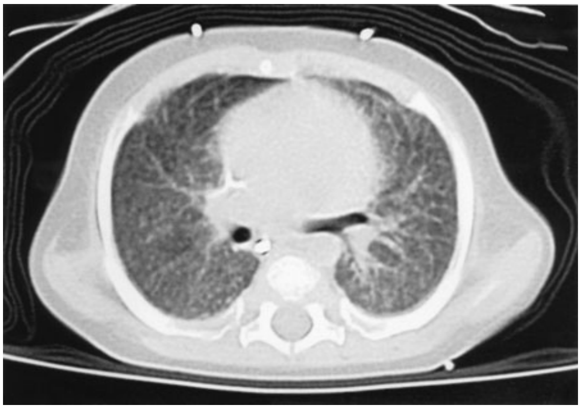

Fig. 13.6. An 8-month-old boy with severe combined immunodeficiency syndrome and cytomegalovirus pneumonia. HRCT shows diffuse ground glass attenuation with fine nodules throughout the lungs

thrive are common. This syndrome can be confused with pediatric AIDS.

13.5.3.3
Wiskott-Aldrich Syndrome

This syndrome consists of recurrent infections, eczema, and thrombocytopenia. Infections due to organisms with polysaccharide capsules including pneumococcus are common. Herpes virus infections and skin superinfections occur. *Pneumocystis carinii* and pneumococcus are common causes of pulmonary infection in these children.

13.6
Chronic Granulomatous Disease

Children with chronic granulomatous disease (CGD) have a phagocyte defect that interferes with microorganism killing. The phagocytes are otherwise normal, but after engulfing a microorganism, the superoxide burst necessary for killing does not occur. CGD occurs in both X-linked and autosomal forms.

Symptoms usually develop in the first 2 years of life. Presentation and ongoing complications are related to granuloma and abscess formation (Fig. 13.7). Suppurative lymphadenopathy is common, as are chronic skin infections. The liver is commonly enlarged. These manifestations are likely due to ongoing inflammatory response to viable microorganisms. Histopathologic studies have shown that the granulomas in these patients may contain relatively few organisms; the largest portion of the granulomas results from the exuberent inflammatory response (Moskaluk et al. 1994).

Staphylococcus aureus is the most commonly cultured organism in the granulomas, although enteric bacilli are also frequently isolated. Streptococcal disease is relatively rare in these patients (Johnston and McMurry 1967). Fungi and atypical mycobacteria are other causes of infection. Children with CGD are at high risk for invasive aspergillosis (Tabone 2003).

Pneumonias and abscesses are the most common thoracic manifestations, and the lungs are the most common site of infection (Moskaluk et al. 1994). Infections involving both the lungs and the chest wall may suggest the diagnosis (Fig. 13.7). The chronicity of lung lesions in this disease may lead to

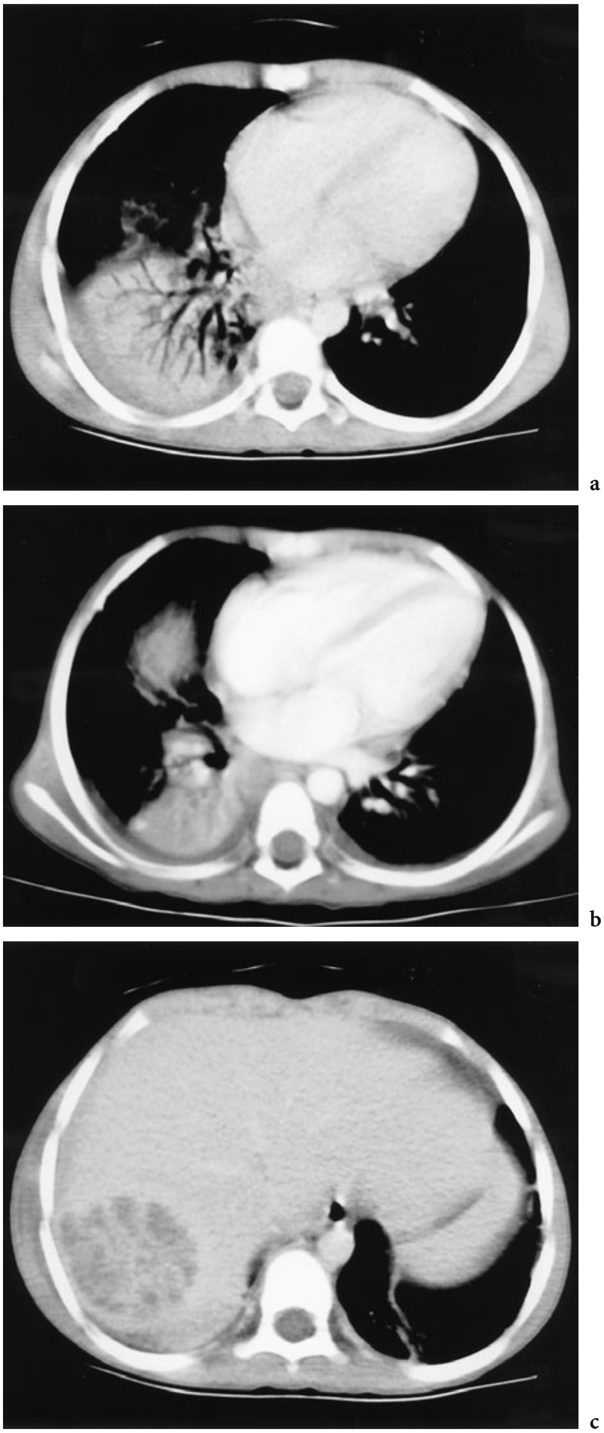

Fig. 13.7a–c. CT images performed on a boy with chronic granulomatous disease. At age 3 years, a CT scan (**a**) showed right middle lobe pneumonia with effusion and calcification. At age 5 years, CT again shows a right middle lobe pneumonia (**b**), along with a hepatic abscess (**c**). Drainage procedure demonstrated a *Staphylococcus aureus* infection extending through the diaphragm

development of a systemic blood supply to areas of pulmonary infection, also referred to as pseudosequestration (Matsuzono et al. 1995). PET scanning has been used to differentiate active from inactive lesions in children with CGD (Gungor et al. 2001).

13.7
Sickle Cell Disease

The sickle hemoglobinopathies all include the presence of hemoglobin S within red blood cells. A substitution of valine for glutamic acid in the hemoglobin beta chain changes the structure of hemoglobin, allowing the hemoglobin to crystallize under conditions of low oxygen state, dehydration, and acidosis. When the hemoglobin crystallizes, the red blood cell becomes less flexible and assumes the familiar sickle shape. These sickle cells have a decreased life span with a resulting hemolytic anemia. These nondeformable cells often obstruct small capillaries where slow flow promotes the conditions that encourage further sickling in a cascade effect.

Homozygous hemoglobin (Hgb) S produces the most severe disease. Different mutations are associated with different amounts of hemoglobin F, with higher levels of Hgb F being associated with decreased disease severity. Compound heterozygous conditions present a spectrum of disease severity depending on the non-S hemoglobin. The most common are hemoglobin S with hemoglobin C (Hgb S/C) and hemoglobin S with b hemoglobin thalassemia (Hgb S/B). Hemoglobin S with homozygous b thalassemia is similar to HgbSS, while S plus heterozygous b thalassemia and Hgb SC disease will often have preserved splenic function and less risk of occlusive crisis and infection. Heterozygous hemoglobin S and hemoglobin A is the asymptomatic carrier state.

Infants with sickle cell disease show no abnormalities; symptoms develop as fetal hemoglobin is replaced by defective adult type hemoglobin. Hand-foot syndrome, a painful swelling of the hands and feet, may be an early presentation, in which case soft tissue swelling and periosteal new bone formation are seen radiographically. Anemia and painful crises in other locations then develop. Decreased splenic function causes an increased susceptibility to infection. The most common organisms affecting the lung are pneumococcus and nontypable hemophilus species.

The two most common chest complications of sickle cell disease are pneumonia and the acute chest syndrome. Functional asplenia can occur as young as 6 months of age. Children are then particularly susceptible to infections caused by bacteria with polysaccharide capsules. Pneumococcal infections are the most common cause of death in young children with sickle cell disease.

The most common thoracic findings in children with sickle cell disease are mild cardiomegaly and increased lung markings. Biconcave vertebral bodies develop due to endplate microinfarcts resulting in softening of the bone that is then impressed by the nucleus pulposus of the intervertebral disk.

Lung function can be abnormal from an early age. Evidence of obstructive pulmonary disease has been shown on pulmonary function tests in infants and young children (Koumbourlis et al. 1997). The presence of myocardial perfusion abnormalities in children has also been reported (Acar et al. 2000).

The acute chest syndrome (ACS) is a major cause of morbidity and mortality in sickle cell disease. This is a largely descriptive term applied to the clinical situation in which the patient with sickle cell disease develops a new infiltrate on chest radiograph accompanied by chest pain, fever, and respiratory symptoms. ACS accounts for 30% of deaths in sickle cell patients under 10 years old (Martin and Buonomo 1997). In a prospective study of 538 patients admitted for ACS, overall mortality was 3% (Vichinsky et al. 2000). A specific cause can be identified in ACS in 40%–70% of cases. Etiologies include infection, fat embolism, and pulmonary infarction (Vichinsky et al. 2000). Rib infarctions have also been identified in ACS (Gelfand et al. 1993) (Fig. 13.8). Asthma has been associated with an increased risk of ACS (Boyd et al. 2006). Episodes of ACS have been reported to predispose children to increased airway resistance (Sylvester et al. 2006).

The infiltrates of ACS must occupy at least one complete bronchopulmonary segment without evidence of volume loss. The appearance of the individual infiltrates is not helpful in suggesting an etiology. Longitudinal evaluation may be of benefit; a lack of resolution of parenchymal infiltrates has been associated with the presence of an infectious etiology and longer clinical course (Martin and Buonomo 1997). The presence of infiltrates in four or more lobes on the admission chest radiograph has been associated with an incidence of complications nine times that of involvement in one lobe (Vichinsky et al. 2000). Increasing infiltrates over the first days of hospitalization are also associated with an increase in complications and prolonged hospitalization.

CT has also been studied in ACS. Using 3 mm thick sections, Bhalla et al. (1993) found evidence of de-

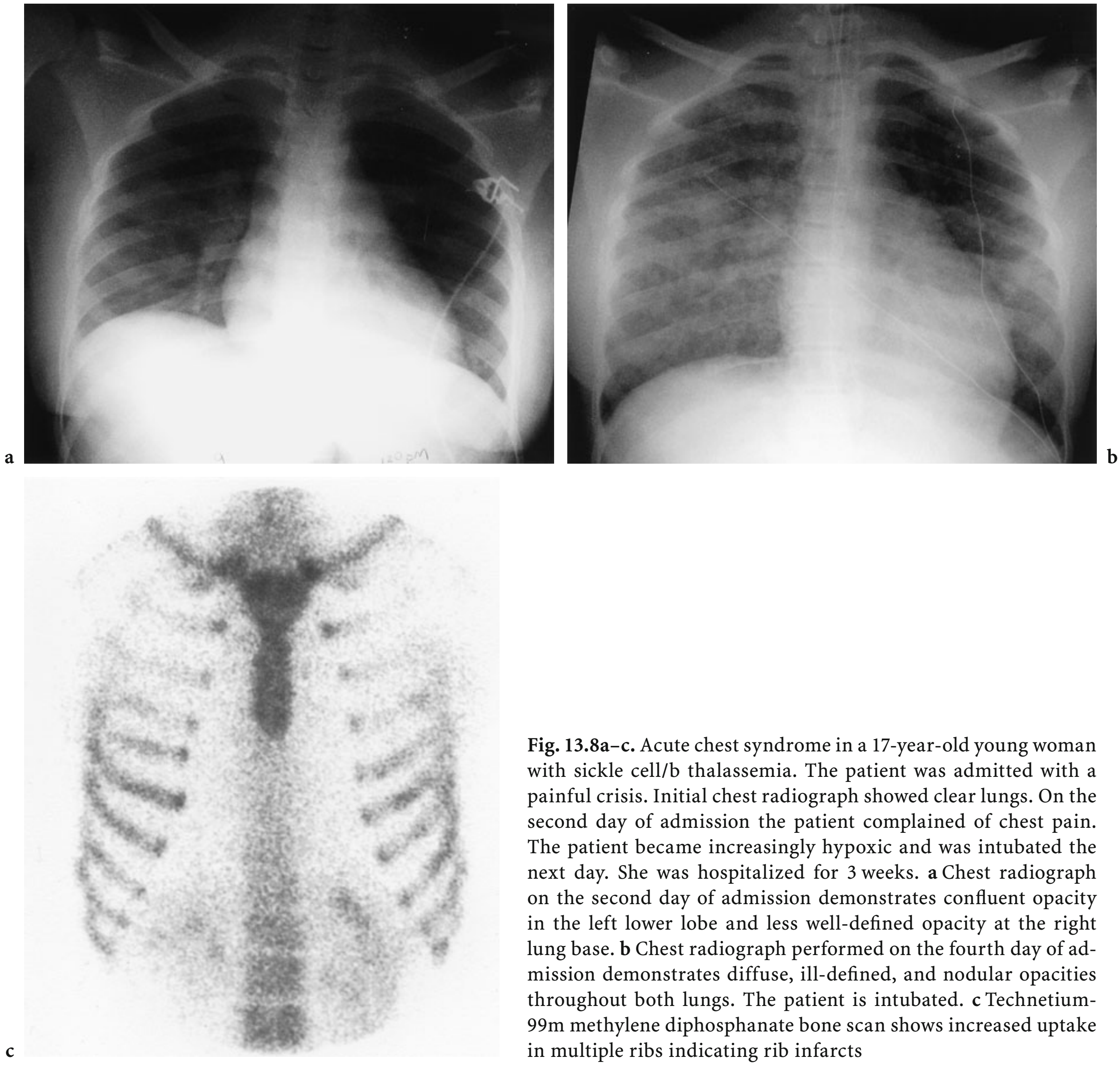

Fig. 13.8a–c. Acute chest syndrome in a 17-year-old young woman with sickle cell/b thalassemia. The patient was admitted with a painful crisis. Initial chest radiograph showed clear lungs. On the second day of admission the patient complained of chest pain. The patient became increasingly hypoxic and was intubated the next day. She was hospitalized for 3 weeks. **a** Chest radiograph on the second day of admission demonstrates confluent opacity in the left lower lobe and less well-defined opacity at the right lung base. **b** Chest radiograph performed on the fourth day of admission demonstrates diffuse, ill-defined, and nodular opacities throughout both lungs. The patient is intubated. **c** Technetium-99m methylene diphosphanate bone scan shows increased uptake in multiple ribs indicating rib infarcts

creased peripheral pulmonary vessels in children with ACS. This decrease was not seen in children without sickle cell disease whose CT scans were used as controls. These findings suggest that there is a component of microvascular occlusion in these children.

13.8
Langerhan's Cell Histiocytosis

Langerhan's cell histiocytosis (LCH) is characterized by tissue infiltration by cells of bone marrow origin with characteristic large histiocytes. These cells are monocytes that can be identified by the presence of Birbeck granules in the cytoplasm or immunohistochemically by CD-1 positivity.

Previous classification into eosinophilic granuloma, Letterer-Siwe disease, and Hand-Schüller-Christian disease are no longer used. The current classification divides these patients into those with single system involvement and those with multisystem involvement. The presence of multisystem involvement requires more intensive therapy than single system involvement. Pulmonary involvement can be seen either in isolated (or primary) pulmonary LCH or in multisystem disease. Isolated pulmonary LCH is more common in young adults but has been reported in children as young as 2 years (Al-Trabolsi et al. 2006).

In one study, the records of 220 children with LCH were reviewed. Thirty six had pulmonary involvement. Thirty four of those had multisystem LCH and two had primary pulmonary LCH. Diffuse interstitial involvement was found in all cases. The presence of pulmonary disease did not change 5 year survival probability (Braier et al. 2004).

In a review of 42 children with LCH, 8 had pulmonary abnormalities on chest radiographs. In this study, all those with pulmonary abnormalities had multisystem disease (Smets et al. 1997). Four had lung lesions at the time of diagnosis and six of the eight were symptomatic. One presented with bilateral pneumothoraces. All children showed interstitial changes, predominantly reticulonodular densities. Follow up CT scans were performed in four of the eight, and revealed nodules, a mediastinal mass, and lung cysts (Fig. 13.9). Two patients developed macronodules up to 4 cm in size associated with increasing disease in other systems. Other unusual findings include mediastinal lymphadenopathy (Shaker et al. 1995).

The most specific CT findings of LCH are pulmonary cysts (Fig. 13.10). Most reports describe small cysts with thin or imperceptible walls. During active stages of disease, cysts and nodules coexist and cavitating nodules may be seen. Lung involvement by laryngeal papillomatosis and cavitating lung metastases are other causes of this appearance. A highly suggestive feature of LCH cysts in adults is the irregular shapes formed by the cysts, likely due to the coalescence of smaller cysts.

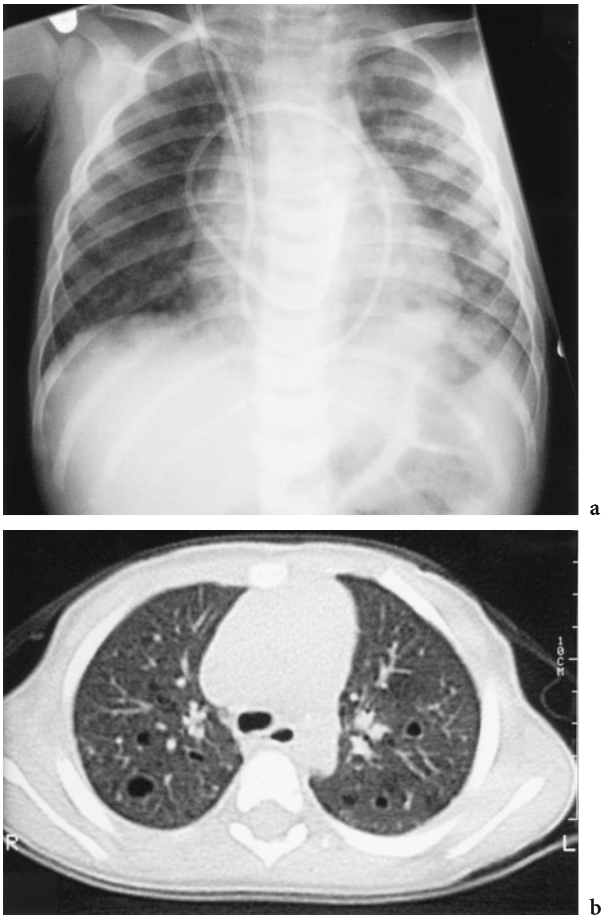

Fig. 13.10 a,b. A 1-year-old child who presented with fever and tachypnea. **a** Initial chest radiograph demonstrated bilateral nodular parenchymal opacities. These opacities resolved over several weeks. Biopsy of a bone lesion revealed Langerhan's cell histiocytosis. **b** HRCT performed 3 months later demonstrates multiple bilateral small cysts with thin walls

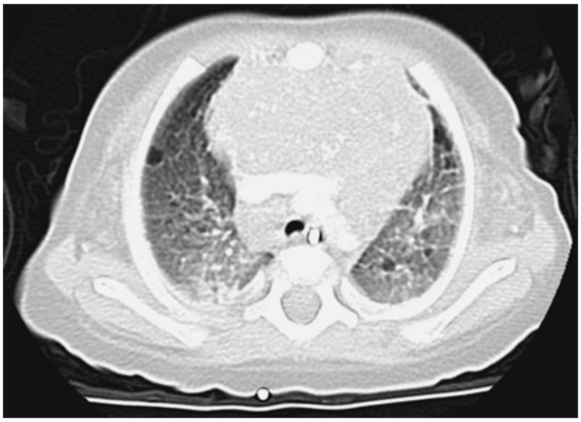

Fig. 13.9. CT scan of the chest in this 7-month-old with Langerhan's cell histiocytosis reveals a large mediastinal mass with multiple calcifications

13.9
Cystic Fibrosis

The lungs of an infant born with cystic fibrosis (CF) are histologically normal. Within a few months, the presence of airway inflammation and infection can be identified (Khan et al. 1995). Bronchiectasis and mucous plugging follow and become the distinctive features of CF lung disease. Born with normal lungs, 95% of people with CF will die of respiratory complications with a mean life expectancy in the mid-30s. The presence of normal lungs at birth presents the opportunity to eliminate these respiratory complications if an early cure can be found. Even without a cure as yet, the history of CF is one of dramatic advances. This progress is reflected in the fact that the best predictor of life expectancy in CF is the patient's year of birth.

Children with CF are a more heterogeneous group than originally described. Pulmonary disease and pancreatic disease are the primary abnormalities in CF, although in 15% of patients pancreatic function is adequate. The severity of lung disease in CF is also more variable than often appreciated. The range of disease in patients with homozygous delta 508 mutations ranges from the development of bronchiectasis in the first few years of life to a 20-year-old patient with normal pulmonary function tests and chest radiograph. Complete bilateral absence of the vas deferens (CBAVD) is the mildest form of the CF spectrum. At the present time, genotype predicts phenotype in pancreatic sufficiency, but not the severity or pattern of respiratory disease.

13.9.1
Genetics

CF is an autosomal recessive disease that affects approximately 1 in 4000 live births in the United States. CF occurs most commonly in Caucasians, in whom the incidence is 1 in 2500 live births, with progressively lower frequency in black, Hispanic, and Asian populations. The gene for CF is located on the long arm of chromosome 7. The CF gene encodes the CF transmembrane conductance regulator (CFTR). CFTR is a single chain protein that forms a membrane bound regulated chloride channel activated by cyclic adenosine monophosphate (cAMP). CFTR functions primarily at the apical cell membrane where it regulates fluid balance across the cell membrane with effects on both chloride and sodium. The most common mutation is a three base pair deletion that causes a deletion of phenylalanine at position 508 of the protein product. This delta 508 mutation is present in 90% of those with CF (Cystic Fibrosis Foundation 2000). Homozygous delta 508 is responsible for 70% of cases of CF (Cystic Fibrosis Foundation 2000). Nearly 1000 additional mutations of the CF gene have been identified.

13.9.2
Diagnosing Cystic Fibrosis

Of the children with CF, 70% present within the first year, 80% by 4 years, and 90% by the age of 12 years. The median age at diagnosis of patients with CF listed in the Cystic Fibrosis Patient Registry in 2004 was 6 months (Cystic Fibrosis Foundation 2004). In the first year, gastrointestinal findings are more common than respiratory disease. In North America, nearly all Caucasian infants with meconium ileus have CF. In a series of 1175 infants with CF, 13% presented with meconium ileus. In 1999, 19% of infants diagnosed with CF had meconium ileus (Cystic Fibrosis Foundation 2000). Gastrointestinal findings after the neonatal period and within the first year include malabsorption and failure to thrive. CF should be suspected in children with these symptoms without regard to the presence of pulmonary disease.

After the first year, respiratory complaints increase, becoming the most common reason to suspect CF. Cystic fibrosis care continues to improve patient outcome. In 1990 median forced expiratory volume at 1 s (FEV_1) at 13 years was 80% of predicted. In 2004 median FEV_1 was 90% of predicted at 13 years and did not decline to 80% until 17 years (Cystic Fibrosis Foundation 2004). Predicted median survival in 2004 was 35.1 years.

One of the earliest recognized characteristics of the child with CF was the salty taste of the child's skin. Abnormal sweat chloride was reported in 1953 (Di Sant'Agnese et al. 1953). Sweat chloride determination remains the most common diagnostic test for CF. This test requires careful technique and should only be performed at centers with expertise in sweat chloride determination. Values greater than 60 mEq/ml are generally regarded as positive, 40–60 mEq/ml indeterminate, and less than 40 mEq/ml negative. Other methods of making the diagnosis include genotyping and neonatal screening.

In 1999, 7% of children diagnosed with CF were identified by neonatal screening (Cystic Fibrosis Foundation 2000). Neonatal screening is performed by measuring the level of immunoreactive trypsinogen in a dried blood spot. Positive screening tests must be confirmed by further tests including meconium lactase, sweat chloride, or genotyping. A controlled trial of neonatal screening in Wisconsin has shown improved growth and nutritional status in children with CF identified by neonatal screening (Farrell et al. 2001). A study in Australia demonstrated improvement in both nutrition and pulmonary function (Waters et al. 1999) in children identified by neonatal screening.

A report by Massie et al. (2000) found that even in a screened population, cases of CF are still detected on clinical grounds. In this group, gastrointestinal symptoms remain more common at presentation than pulmonary symptoms. Of nine children diagnosed with CF after negative neonatal screening, eight presented with failure to thrive or steatorrhea, and one with respiratory symptoms.

13.9.3
Pulmonary Pathophysiology of Cystic Fibrosis

Abnormal CFTR causes a change in the composition of the fluid lining the airways, which results in numerous changes in the normal function of the airway epithelium. Mucous is abnormal with resulting plugging of airways and decreased mucociliary clearance. Abnormal mucous in CF likely results both from abnormal mucous production by the mucous glands, and the presence of cellular degradation products from white blood cells. Deoxyribonucleic acid is a major component of the degradation products, and is a major contributor to the increased viscosity and tendency of the mucous to form long strands. Both infection and inflammation result in increased proteolytic enzymes that damage the epithelium and the supporting structure of the airways.

Repeated infection and increased inflammatory response cause airway damage which makes the airways more susceptible to infection. Infection then increases in both frequency and severity, inciting greater inflammatory response. A snowball effect results in progressive respiratory compromise. The hallmarks of CF lung disease are bronchiectasis secondary to obstruction and airway damage and mucous plugging due to the tenacious mucous produced in CF.

13.9.4
Lung Care in Cystic Fibrosis

One of the most important factors improving longevity in CF patients in North America is the use of skilled care through a network of CF centers. Two important concepts of care are routine monitoring and early intervention. Pulmonary exacerbations are treated with aggressive pulmonary physiotherapy and parenteral antibiotics.

Regular pulmonary care in CF has traditionally been directed at the clearance of lower airway secretions and the treatment of infection. In the last decade, numerous new techniques have become available. In addition to manual external percussion, mechanical airway clearance techniques include airway oscillators and high frequency chest compression with an inflatable vest. The tenacity of secretions can be treated by the administration of recombinant human deoxyribonuclease which breaks up DNA strands, decreasing the stickiness of CF mucous (Fig. 13.11). Inhaled bronchodilators and hypertonic salines can also be administered.

In addition to oral antibiotics, inhaled antibiotics have been shown to improve pulmonary function in initial short term trials (Ramsey et al. 1999). Airway inflammation can also be directly treated. In a 4-year study, Konstan et al. (1995) showed that inhaled ibuprofen decreased the decline of pulmonary function in CF. This effect was most marked in children.

For many patients, the progression of lung disease results in respiratory insufficiency that persists

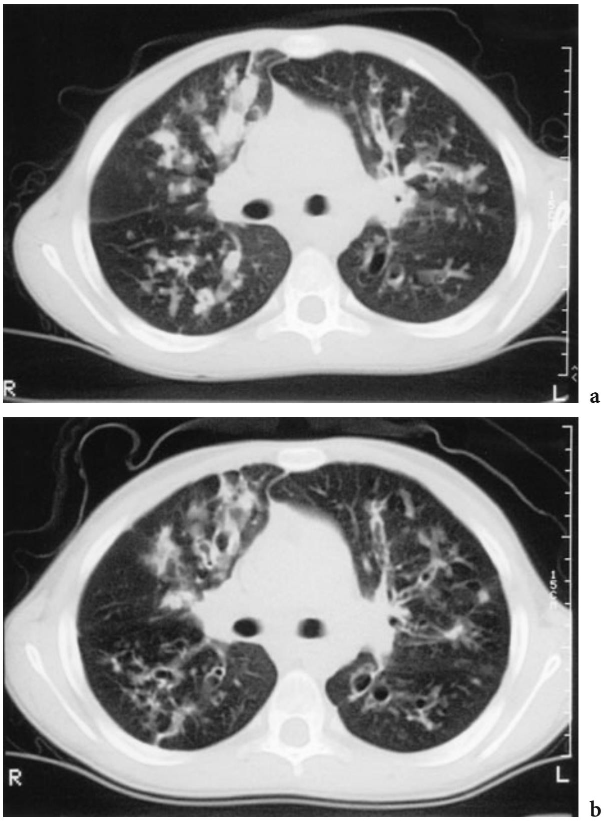

Fig. 13.11a,b. HRCT images in an 11-year-old boy with cystic fibrosis showing improvement in mucous plugging following treatment with human recombinant DNase. **a** Images obtained prior to beginning daily inhalation therapy with DNase show bronchiectasis, bronchial wall thickening, and multiple areas of mucoid impaction seen as large tubular structures. **b** Images obtained after several months of daily DNase therapy. Mucous has cleared from many of the ectatic bronchi

despite medical treatment. Lung transplantation is the treatment for end stage CF pulmonary disease. Both cadaveric transplantation and living donor lobe transplantation are used. In the 2004 CF registry, 160 bilateral lung transplant recipients and 17 lobar transplant recipients are listed.

13.9.5
Imaging in Cystic Fibrosis

The role of imaging in the care of children with CF is changing. Historically, care has been based on clinical evaluation, with plain radiographs used to confirm clinical impressions, and as an indicator of overall disease severity. Plain radiographs remain the most common imaging study performed in patients with CF. CF center directors report that CTs are frequently obtained, although little has been written on the use of CT in the care of patients with CF. Nuclear medicine studies of lung ventilation and perfusion and of aerosol deposition have been reported primarily as a research tool. PET scanning is currently under investigation as a means of evaluating the degree of inflammation in the CF lung. MRI has been suggested as a way to follow CF lung disease without the use of ionizing radiation.

13.9.5.1
Plain Radiographs

Radiographs in the first year are usually normal. Abnormal chest radiographs will show changes typical of airways disease, with the appearance being the same as seen with viral or atypical infections. Features more typical of CF including bronchiectasis and mucous plugging are not seen in the first several years.

Scoring systems for the evaluation of lung disease on chest radiographs include the Brasfiled (Brasfield et al. 1979), Chrispin-Norman (Chrispin and Norman 1974) and NIH (Sockrider et al. 1994) scores. One chest radiograph scoring system was specifically developed for use in young children with CF (Weatherly et al. 1993). Comparison between different scores shows similar results (Sawyer et al. 1994; Terheggen-Lagro et al. 2003). While these scores correlate with disease severity in older patients, they are insensitive when used in young children (Weatherly et al. 1993). Although early chest radiographs do not correlate well with clinical changes in young children with mild disease (Koscik et al. 2000), chest radiographs showed a higher correlation with pseudomonas acquisition than pulmonary function tests (Kosorok et al. 2001).

No pediatric study has been performed to evaluate the ability of plain radiographs to reflect changes due to short term treatment. In an adult study, Greene et al. (1994) found that chest radiographs obtained during an acute exacerbation could not be differentiated from radiographs obtained when the patients were clinically well.

Over the long term, however, serial chest radiographs have shown a slower progression of lung disease measured by Brasfield scores when children were treated with aerosolized tobramycin (Slattery et al. 2004). A database of chest radiograph scoring changes over time has been developed to provide comparison for groups undergoing new treatment (Cleveland et al. 1998).

13.9.5.2
Computed Tomography

Currently, HRCT is the most accurate means of evaluating the morphologic changes of CF lung disease. HRCT can detect and quantify the changes seen in children with CF including bronchiectasis, peribronchial thickening, mucous plugging, parenchymal air trapping, and lung destruction.

Jacobsen et al. (1986) compared chest radiographs and CT in 12 adult patients with CF. The authors found that CT was more sensitive for the detection of bronchiectasis, mucous plugging, and hilar adenopathy. Bhalla et al. (1991) described a scoring system for HRCT in CF. This scoring system evaluates the severity of bronchiectasis and peribronchial thickening, and the extent of bronchiectasis, mucous plugging, sacculations or abscesses, bullae, emphysema, and collapse or consolidation. The authors found again that CT was more accurate than chest radiographs in detecting abnormalities. The score correlated with the pulmonary function test ratio of forced expiratory volume in 1 min to forced vital capacity (FEV1/FVC). In the same year, Nathanson et al. (1991) published a scoring system for CF using electron beam CT in a pediatric population. This scoring system correlated well with pulmonary function tests and clinical scores. A scoring system devised by Maffessanti et al. (1996) has been adopted and used by several authors.

More recent efforts have examined the ability of HRCT to evaluate progression of disease and response to treatment. An adult study showed that the findings differed when HRCTs obtained during exacerbations were compared to those obtained when patients were at their baseline health. HRCT scores were higher during exacerbations. Air fluid levels in ectatic bronchi during exacerbations resolved on follow-up scans. Centrilobular nodules and mucous plugging improved in about one third of the cases (Shah et al. 1997).

In a pediatric study, the HRCT appearance was compared between admission and discharge for treatment of an acute pulmonary exacerbation (Brody et al. 1999). In this study, the HRCT appearance improved in 13 of 15 admissions. Peribronchial thickening, mucous plugging, and the overall appearance were all significantly improved on the discharge HRCT. A second study of 17 children also showed HRCT improvement following treatment for exacerbation (Robinson et al. 2001).

A study that included patients aged between 2 and 32 years evaluated the change in HRCT appearance over time. The authors found that HRCT scores increased significantly when the interval between studies was more than 18 months, with no significant change over shorter intervals (Helbich et al. 1999). In a study of children with a mean age of 11 years, de Jong et al. (2004) found that CT scans showed progressive disease over two years despite stable pulmonary function tests. CT scanning has been shown to be more sensitive than pulmonary function tests for the presence of lung disease. One study of children 6 to 10 years old found bronchiectasis in 30% of children with normal pulmonary function tests (Brody et al. 2004). Changes on CT scanning have also been shown to correlate with the number of pulmonary exacerbations, supporting the use of CT scanning as an outcome surrogate for CF lung disease (Brody et al. 2005).

The above information provides support for the continued development of HRCT as part of the clinical care of children with CF. At the time of writing, however, no studies have evaluated the impact of using HRCT as part of the care of these children. One report has pointed out that useful patient care information can be obtained with a combination of pulmonary function tests and chest radiographs, as well as with HRCT (Santamaria et al. 1998).

13.9.5.3
Nuclear Medicine

The functional information provided by nuclear medicine imaging has been used to evaluate pulmonary ventilation/perfusion relationships, aerosol deposition, and mucous clearance in patients with CF (Laube et al. 1992; Sirr et al. 1986). The findings of nuclear medicine pulmonary blood flow have been shown to correlate with HRCT images (Donnelly et al. 1997). The relative sensitivities of the two modalities have not been determined.

18-Fluorodeoxyglucose PET scanning has been used to quantify inflammation in the CF lung (Al-Trabolsi et al. 2006). This could provide a method to evaluate the effect of anti-inflammatory or antibiotic treatment on the lungs without the need for bronchoscopy.

13.9.5.4
Magnetic Resonance Imaging

Initial attempts to use MRI to evaluate CF lung disease were disappointing. The relatively small number of protons in aerated lung and magnetic susceptibility artifacts from the air/soft tissue interfaces resulted in very little MR signal. One early study demonstrated the ability of MRI to detect hilar adenopathy and bronchiectasis with mucous plugging (Fiel et al. 1987). Carr et al. (1995) compared conventional axial CT to MRI and found that the resolution of MRI did not allow adequate evaluation of the gross features of CF lung disease.

Advances in MRI technology have improved the ability of conventional proton MRI to demonstrate pulmonary parenchymal abnormalities. The resolution of MRI remains lower than that of CT, but MRI can now provide similar results in demonstrating bronchial wall thickening, mucous plugging, and infiltrates (Puderbach et al. 2006). Early findings of CF lung disease such as air trapping are not seen with MRI; however, once more advanced findings have developed, MRI may provide a cross-sectional modality that can follow disease progression without the use of ionizing radiation.

An additional MR technique is the use of hyperpolarized helium. This gas has a very strong MR signal. When inhaled, all ventilated portions of the lung show this high signal, and unperfused areas are seen as focal defects. The appearance is grossly similar to nuclear medicine ventilation scans, but with much higher resolution (Fig. 13.12). No ionizing radiation is used with this technique. Hyperpolarized helium has a short half-life, and the availability of the gas will likely limit the use of this technique.

A preliminary report using hyperpolarized helium and conventional proton MR in four patients with CF (Donnelly et al. 1999) found extensive ventilation defects that were frequently much more striking than the associated morphologic defects. This technique is well tolerated in children (van Beek et al. 2006). Further investigation has shown that ventilation defects are increased in patients with CF and normal pulmonary function tests compared to subjects without CF. The ventilation defects change with treatment and correlate with spirometry (Mentore et al. 2005).

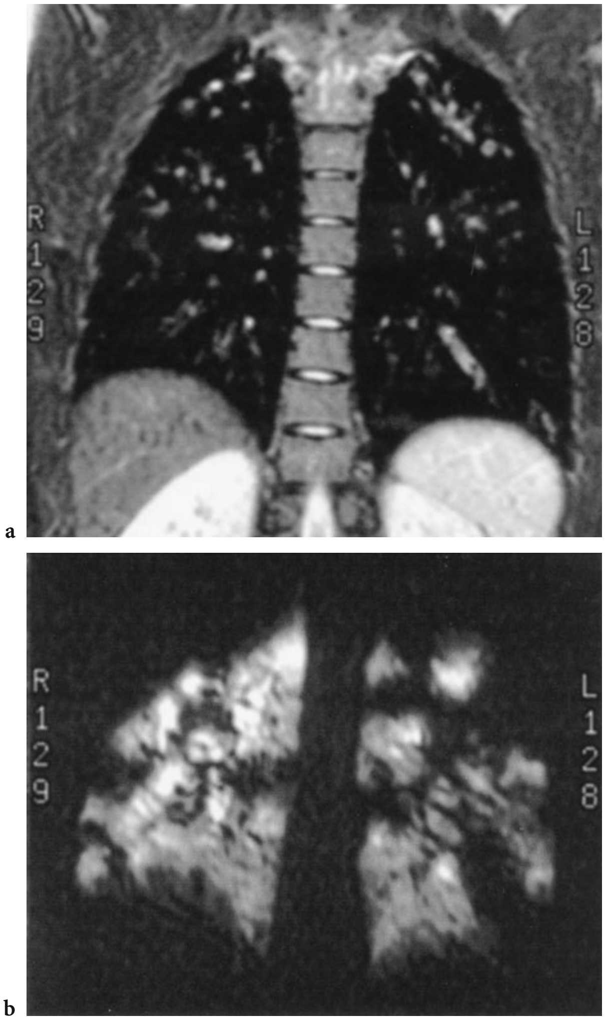

Fig. 13.12a,b. Coronal 10 mm thick MR images of the posterior lungs in a patient with cystic fibrosis. **a** Fast spin echo T2-weighted MR images demonstrate nodular and linear areas of increased signal greatest at the lung apices corresponding to mucous filled ectatic bronchi. **b** Hperpolarized helium MR images demonstrate multiple filling defects in the high signal due to the inhaled helium-3 indicating areas of absent or decreased ventilation. These defects are much greater than the airway abnormalities seen on the conventional MR image. (Images courtesy of Lane F. Donnelly, MD)

13.10
Phacomatoses

13.10.1
Tuberous Sclerosis

Tuberous sclerosis (TS) is one of a group of neurocutaneous syndromes that also includes neurofibromatosis and Sturge-Weber syndrome. TS is a genetic disease with autosomal dominant transmission and variable penetration. The incidence is approximately 1:30,000.

The classic clinical triad includes mental retardation, seizures, and adenoma sebaceum. TS, however, affects multiple organ systems. In addition to the central nervous system abnormalities, abnormal cellular proliferation results in angiomyolipomas of the kidneys, rhabdomyomas of the heart, and lymphangioleiomyomatosis (LAM) of the lungs. There is a characteristic rash which has been described as a butterfly rash over the cheeks with a narrower affected area on the nose.

LAM affects women of reproductive age, with most patients presenting in the third decade; however, children as young as 11 years old have been diagnosed with LAM. Clinical presentation is with dyspnea or spontaneous pneumothorax. LAM is not seen on chest radiographs until extensive fibrosis has developed late in the course of the disease. The early appearance of LAM is characterized by the presence of multiple small cysts with thin or imperceptible walls. These cysts are evenly distributed through the lungs. Unlike the cysts of LCH, cysts in LAM are round and do not usually coalesce. The presence of normal lung parenchyma between the cysts is useful in differentiating these cysts from other causes of destructive lung disease.

The commonly reported incidence of LAM in TS is less than 1%. In a prospective HRCT screening study of young women with TS, however, the incidence of lung cysts was 30% (McCormack et al. 2002). This higher incidence likely reflects a high incidence of mild findings that do not present clinically and are not apparent on chest radiographs (Fig. 13.13).

The incidence of cardiac rhabdomyomas in TS is 20%–30%. Half of all cardiac rhabdomyomas are found in patients with TS. This is the most common cardiac tumor of childhood (Becker 2000). Cardiac rhabdomyomas usually present in the first year. Obstruction of blood flow, reduced overall contractility, and interference with electrical conduction can all cause symptoms. Clinical presentations include prenatal demise and sudden death. The most common presentations are cardiac, including congestive heart failure and arrhythmias. Asymptomatic tumors have been found on screening echocardiography. Regression of these tumors has also been reported (Sallee et al. 1999). Cardiac rhabdomyomas are frequently multiple, and are usually located in the ventricles.

Rhabdomyomas are most often detected on echocardiography. MRI is usually performed to further evaluate these masses. The MRI appearance is variable with most lesions showing increased signal compared to the myocardium on short TR/short TE images (Lund et al. 1989). Rhabdomyomas may be isointense on multiple pulse sequences, as well as before and after contrast administration (Semelka et al. 1992). For this reason, small, intramural lesions may not be detected on MRI. Cardiac lipomas and fibromas are less common than rhabdomyomas, but can be seen in children with TS. The characteristic signal patterns of fat and fibrosis may suggest the presence of one of these lesions when assessing cardiac masses in TS.

13.10.2
Neurofibromatosis

Neurofibromatosis is the most common of the phacomatoses with a prevalence of 1 in 2–4000. Neurofibromatosis is transmitted as an autosomal dominant, but half of cases arise from a new mutation. Two distinct forms of neurofibromatosis are designated NF-1 and NF-2. NF-1 accounts for 90% of cases of neurofibromatosis and can present in many different ways including café-au-lait spots, axillary or inguinal freckling, Lisch nodules of the iris, neurofibromas, bone lesions, and optic gliomas. NF-2 is associated with bilateral acoustic neuromas.

Thoracic manifestations in children include neurofibromas, rib erosions, scoliosis, and spinal erosions (Fig. 13.14). Spinal erosions can occur secondary to dural ectasia, neurofibromas, or lateral meningoceles. Lateral meningoceles and neurofibromas can be differentiated on CT scanning by administering intravenous contrast, with neurofibromas showing enhancement (Rossi et al. 1999). On MRI, a characteristic target appearance can be seen on T2-weighted sequences with a low signal center and very high signal peripherally. Contrast-enhanced T1-weighted sequences can also be used to distinguish meningoceles from neurofibromas.

Pulmonary manifestations in adults include pulmonary fibrosis and bulla formation (Burkhalter et al. 1986; Webb and Goodman 1977). Neither of these findings has been reported in children. The presence of interstitial abnormalities in children has been mentioned anecdotally by several observers. It is possible that the adult disease begins in the first two decades, but does not become symptomatic or evident on chest radiographs until later. A recent review included only adults over 25 years old, and stated that pulmonary fibrosis in neurofibromatosis is not seen in children (Zamora et al. 2007).

13.11
Lysosomal Storage Disorders

Lysosomal storage disorders (LSDs) are genetic diseases characterized by the absence or dysfunction

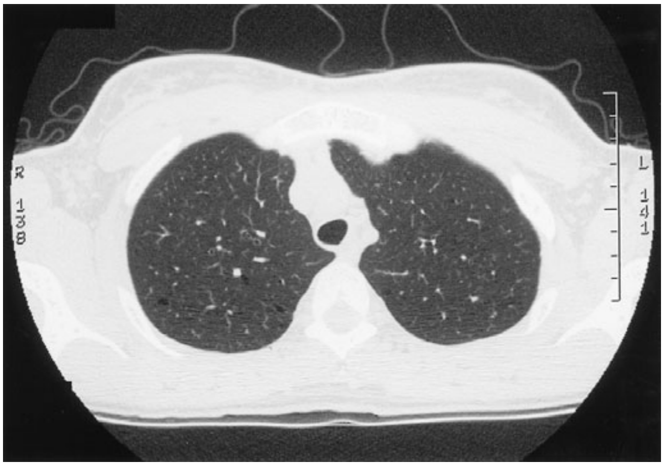

Fig. 13.13. HRCT image through the upper lungs in an asymptomatic young adult woman with tuberous sclerosis. Multiple cysts of less than 1 cm with imperceptible walls are seen in the right lung. These likely represent early changes of lymphangioleiomyomatosis

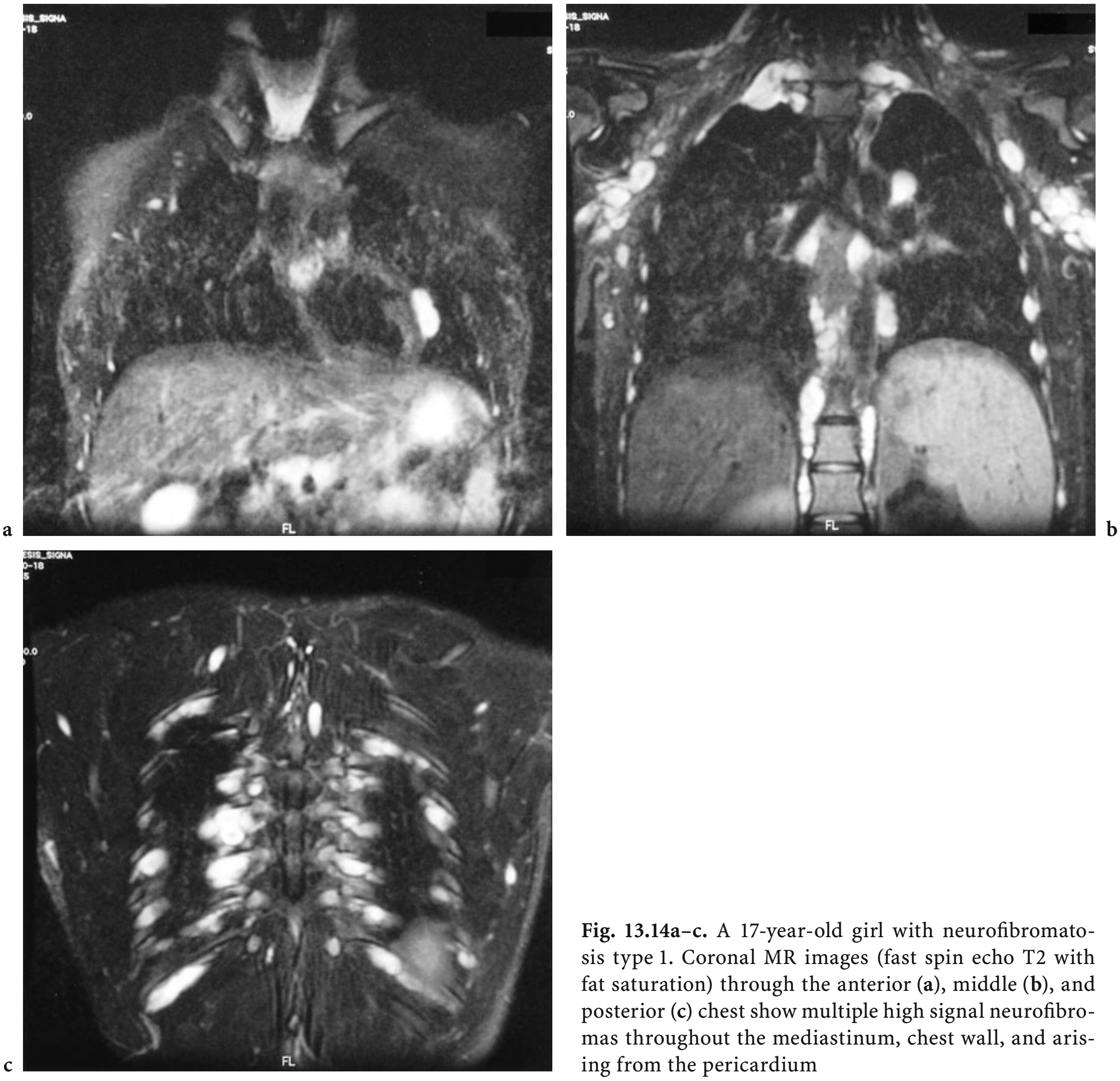

Fig. 13.14a–c. A 17-year-old girl with neurofibromatosis type 1. Coronal MR images (fast spin echo T2 with fat saturation) through the anterior (**a**), middle (**b**), and posterior (**c**) chest show multiple high signal neurofibromas throughout the mediastinum, chest wall, and arising from the pericardium

of any of the lysosomal enzymes. This results in accumulation of the substrate associated with the defective enzyme. These diseases have a broad phenotypic range depending on the rate, amount, and effect of substrate accumulation.

The most common of the LSDs is Gaucher disease (GD). GD is due to a defect in β-glucocerebrosidase. This results in accumulation of macrophages containing glucocerebroside (Gaucher cells) in the reticuloendothelial system. The most common symptoms and findings are caused by involvement of the liver, spleen, and bone marrow. Lung involvement is relatively rare, reported in 2% in one study (Goitein et al. 2001). Lung abnormalities may be caused by infiltration of Gaucher cells, liver disease, or aspiration secondary to neurological compromise (McHugh et al. 2004). Reticulonodular changes can be seen on chest radiographs; HRCT findings include nodules, ground glass opacities, and septal thickening (Tunaci et al. 1995). Enzyme therapy has not been found to improve the lung disease in these patients (Goitein et al. 2001).

In Niemann Pick disease sphingomyelinase is deficient and therefore sphyngomyelin accumulates. Pulmonary involvement is a major cause of morbidity and mortality in patients with Niemann Pick disease. Pulmonary involvement is greatest in Type B disease, which is characterized by chronic visceral involvement. HRCT findings of septal thickening and ground glass opacity have been reported (Nicholson et al. 2006; Rodrigues et al. 2004) (Fig. 13.15).

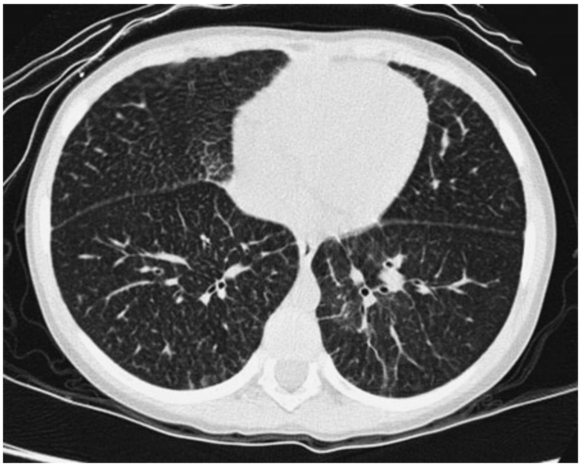

Fig. 13.15. Axial section through the mid lung level in a 5-year-old girl with Niemann Pick disease type B demonstrates diffuse septal thickening and reticulonodular opacities. An area of ground glass opacity is seen in the left perihilar area

The mucopolysaccharidoses (MPS) are characterized by accumulation of glycosaminoglycans that cause multisystem disease. The different diseases are now best described by the numerical type of MPS. Eponyms for these diseases include Hurler, Hunter, Sanfilippo and Morquio syndrome. Deposition of glycosaminoglycans in the lung can cause interstitial lung disease (Dinwiddie and Sonnappa 2005). In addition, deposition in the soft tissues can narrow the upper airway and hepatosplenomegaly can limit diaphragmatic motion. Enzyme replacement for MPS 1 (Hurler, Hurler-Scheie, and Scheie syndrome) has been shown to improve pulmonary function tests and exercise tolerance (Wraith et al. 2004).

References

Acar P, Sebahoun S, de Pontual L et al. (2000) Myocardial perfusion in children with sickle cell anaemia. Pediatr Radiol 30:352–354

Alavi A, Gupta N, Alberini JL et al. (2002) Positron emission tomography imaging in nonmalignant thoracic disorders. Semin Nucl Med 32:293–321

Altes TA, Mata J, de Lange EE et al. (2006) Assessment of lung development using hyperpolarized helium-3 diffusion MR imaging. J Magn Reson Imaging 24:1277–1283

Al-Trabolsi HA, Alshehri M, Al-Shomrani A et al. (2006) “Primary” pulmonary Langerhans cell histiocytosis in a two-year-old child: case report and literature review. J Pediatr Hematol Oncol 28:79–81

Arkachaisri T, Lehman TJ (1999) Systemic lupus erythematosus and related disorders of childhood. Curr Opin Rheumatol 11:384–392

Athreya BH, Doughty RA, Bookspan M et al. (1980) Pulmonary manifestations of juvenile rheumatoid arthritis. A report of eight cases and review. Clin Chest Med 1:361–374

Babyn P, Doria AS (2005) Radiologic investigation of rheumatic diseases. Pediatr Clin North Am 52:373–411, vi

Bader TR, Semelka RC, Pedro MS et al. (2002) Magnetic resonance imaging of pulmonary parenchymal disease using a modified breath-hold 3D gradient-echo technique: initial observations. J Magn Reson Imaging 15:31–38

Bankier AA, Kiener HP, Wiesmayr MN et al. (1995) Discrete lung involvement in systemic lupus erythematosus: CT assessment. Radiology 196:835–840

Becker AE (2000) Primary heart tumors in the pediatric age group: a review of salient pathologic features relevant for clinicians. Pediatr Cardiol 21:317–323

Bhalla M, Turcios N, Aponte V et al. (1991) Cystic fibrosis: scoring system with thin-section CT. Radiology 179:783–788

Bhalla M, Abboud MR, McLoud TC et al. (1993) Acute chest syndrome in sickle cell disease: CT evidence of microvascular occlusion. Radiology 187:45–49

Boyd JH, Macklin EA, Strunk RC et al. (2006) Asthma is associated with acute chest syndrome and pain in children with sickle cell anemia. Blood 108:2923–2927

Braier J, Latella A, Balancini B et al. (2004) Outcome in children with pulmonary Langerhans cell Histiocytosis. Pediatr Blood Cancer 43:765–769

Brasfield D, Hicks G, Soong S et al. (1979) The chest roentgenogram in cystic fibrosis: a new scoring system. Pediatrics 63:24–29

Brody AS, Molina PL, Klein JS et al. (1999) High-resolution computed tomography of the chest in children with cystic fibrosis: support for use as an outcome surrogate. Pediatr Radiol 29:731–735

Brody AS, Klein JS, Molina PL et al. (2004) High-resolution computed tomography in young patients with cystic fibrosis: distribution of abnormalities and correlation with pulmonary function tests. J Pediatr 145:32–38

Brody AS, Sucharew H, Campbell JD et al. (2005) Computed tomography correlates with pulmonary exacerbations in children with cystic fibrosis. Am J Respir Crit Care Med 172:1128–1132

Burkhalter JL, Morano JU, McCay MB (1986) Diffuse interstitial lung disease in neurofibromatosis. South Med J 79:944–946

Carr DH, Oades P, Trotman-Dickenson B et al. (1995) Magnetic resonance scanning in cystic fibrosis: comparison with computed tomography. Clin Radiol 50:84–89

Cerveri I, Bruschi C, Ravelli A et al. (1992) Pulmonary function in childhood connective tissue diseases. Eur Respir J 5:733–738

Chatkin JM, Bastos JC, Stein RT et al. (1993) Sole pulmonary involvement by Langerhans’ cell histiocytosis in a child. Eur Respir J 6:1226–1228

Chen DL, Ferkol TW, Mintun MA et al. (2006) Quantifying pulmonary inflammation in cystic fibrosis with positron emission tomography. Am J Respir Crit Care Med 173:1363–1369

Chrispin AR, Norman AP (1974) The systematic evaluation of the chest radiograph in cystic fibrosis. Pediatr Radiol 2:101–105

Chu WC, Li AM, Ng BK et al. (2006) Dynamic magnetic resonance imaging in assessing lung volumes, chest wall, and diaphragm motions in adolescent idiopathic scoliosis versus normal controls. Spine 31:2243–2249

Cleveland RH, Neish AS, Zurakowski D et al. (1998) Cystic fibrosis: a system for assessing and predicting progression. AJR Am J Roentgenol 170:1067–1072

Cody DD, Moxley DM, Krugh KT et al. (2004) Strategies for formulating appropriate MDCT techniques when imaging the chest, abdomen, and pelvis in pediatric patients. AJR Am J Roentgenol 182:849–859

Cystic Fibrosis Foundation (2000) Annual data report. Cystic Fibrosis Foundation patient registry. Cystic Fibrosis Foundation, pp 1–22

Cystic Fibrosis Foundation (2004) Annual data report. Cystic Fibrosis Foundation patient registry. Cystic Fibrosis Foundation, pp 1–12

de Jong PA, Nakano Y, Lequin MH et al. (2004) Progressive damage on high resolution computed tomography despite stable lung function in cystic fibrosis. Eur Respir J 23:93–97

de Lange EE, Altes TA, Patrie JT et al. (2006) Evaluation of asthma with hyperpolarized helium-3 MRI: correlation with clinical severity and spirometry. Chest 130:1055–1062

Di Sant'Agnese PA, Darling RC, Perera GA et al. (1953) Sweat electrolyte disturbances associated with childhood pancreatic disease. Am J Med 15:777–784

Dinwiddie R, Sonnappa S (2005) Systemic diseases and the lung. Paediatr Respir Rev 6:181–189

Don S (2004) Radiosensitivity of children: potential for overexposure in CR and DR and magnitude of doses in ordinary radiographic examinations. Pediatr Radiol 34 Suppl 3:S167–172; discussion S234–241

Donnelly LF, Frush DP (2003) Pediatric multidetector body CT. Radiol Clin North Am 41:637–655

Donnelly LF, Gelfand MJ, Brody AS et al. (1997) Comparison between morphologic changes seen on high-resolution CT and regional pulmonary perfusion seen on SPECT in patients with cystic fibrosis. Pediatr Radiol 27:920–925

Donnelly LF, MacFall JR, McAdams HP et al. (1999) Cystic fibrosis: combined hyperpolarized 3He-enhanced and conventional proton MR imaging in the lung – preliminary observations. Radiology 212:885–889

Donnelly LF, Emery KH, Brody AS et al. (2001) Minimizing radiation dose for pediatric body applications of single-detector helical CT: strategies at a large Children's Hospital. AJR Am J Roentgenol 176:303–306

Farrell PM, Kosorok MR, Rock MJ et al. (2001) Early diagnosis of cystic fibrosis through neonatal screening prevents severe malnutrition and improves long-term growth. Wisconsin Cystic Fibrosis Neonatal Screening Study Group. Pediatrics 107:1–13

Ferguson PJ, Weinberger M (2006) Shrinking lung syndrome in a 14-year-old boy with systemic lupus erythematosus. Pediatr Pulmonol 41:194–197

Fiel SB, Friedman AC, Caroline DF et al. (1987) Magnetic resonance imaging in young adults with cystic fibrosis. Chest 91:181–184

Fricke BL, Donnelly LF, Frush DP et al. (2003) In-plane bismuth breast shields for pediatric CT: effects on radiation dose and image quality using experimental and clinical data. AJR Am J Roentgenol 180:407–411

Frush DP (2005) Technique of pediatric thoracic CT angiography. Radiol Clin North Am 43:419–433

Gelfand MJ, Daya SA, Rucknagel DL et al. (1993) Simultaneous occurrence of rib infarction and pulmonary infiltrates in sickle cell disease patients with acute chest syndrome. J Nucl Med 34:614–618

Goitein O, Elstein D, Abrahamov A et al. (2001) Lung involvement and enzyme replacement therapy in Gaucher's disease. Qjm 94:407–415

Greene KE, Takasugi JE, Godwin JD et al. (1994) Radiographic changes in acute exacerbations of cystic fibrosis in adults: a pilot study. AJR Am J Roentgenol 163:557–562

Gungor T, Engel-Bicik I, Eich G et al. (2001) Diagnostic and therapeutic impact of whole body positron emission tomography using fluorine-18-fluoro-2-deoxy-d-glucose in children with chronic granulomatous disease. Arch Dis Child 85:341–345

Hebestreit A, Schultz G, Trusen A et al. (2004) Follow-up of acute pulmonary complications in cystic fibrosis by magnetic resonance imaging: a pilot study. Acta Paediatr 93:414–416

Helbich TH, Heinz-Peer G, Fleischmann D et al. (1999) Evolution of CT findings in patients with cystic fibrosis. AJR Am J Roentgenol 173:81–88

Hsu BY, Edwards DK III, Trambert MA (1992) Pulmonary hemorrhage complicating systemic lupus erythematosus: role of MR imaging in diagnosis. AJR Am J Roentgenol 158:519–520

Hufton AP, Doyle SM, Carty HM (1998) Digital radiography in paediatrics: radiation dose considerations and magnitude of possible dose reduction. Br J Radiol 71:186–199

Jacobsen LE, Houston CS, Habbick BF et al. (1986) Cystic fibrosis: a comparison of computed tomography and plain chest radiographs. Can Assoc Radiol J 37:17–21

Johnston R, McMurry J (1967) Choronic familial granulomatosis. Report of five vases and review of the literature. Am J Dis Child 114:370–378

Jones AM, Gaspar HB (2000) Immunogenetics: changing the face of immunodeficiency. J Clin Pathol 53:60–65

Kalra MK, Maher MM, Toth TL et al. (2004) Strategies for CT radiation dose optimization. Radiology 230:619–628

Kapala GB, Chusid MJ, Sty JR (1983) Ga-67 chest imaging. Chronic granulomatous disease. Clin Nucl Med 8:632

Khan TZ, Wagener JS, Bost T et al. (1995) Early pulmonary inflammation in infants with cystic fibrosis. Am J Respir Crit Care Med 151:1075–1082

Kido S, Ikezoe J, Kondoh H et al. (1996) Detection of subtle interstitial abnormalities of the lungs on digitized chest radiographs: acceptable data compression ratios. AJR Am J Roentgenol 167:111–115

Knook LM, de Kleer IM, van der Ent CK et al. (1999) Lung function abnormalities and respiratory muscle weakness in children with juvenile chronic arthritis. Eur Respir J 14:529–533

Kobayashi I, Yamada M, Takahashi Y et al. (2003) Interstitial lung disease associated with juvenile dermatomyositis: clinical features and efficacy of cyclosporin A. Rheumatology (Oxford) 42:371–374

Konstan MW, Byard PJ, Hoppel CL et al. (1995) Effect of high-dose ibuprofen in patients with cystic fibrosis. N Engl J Med 332:848–854

Koscik RE, Kosorok MR, Farrell PM et al. (2000) Wisconsin cystic fibrosis chest radiograph scoring system: validation and standardization for application to longitudinal studies. Pediatr Pulmonol 29:457–467

Kosorok MR, Zeng L, West SE et al. (2001) Acceleration of lung disease in children with cystic fibrosis after Pseudomonas aeruginosa acquisition. Pediatr Pulmonol 32:277–287

Koumbourlis AC, Hurlet-Jensen A, Bye MR (1997) Lung function in infants with sickle cell disease. Pediatr Pulmonol 24:277–281

Kuhlman JE, Kavuru M, Fishman EK et al. (1990) Pneumocystis carinii pneumonia: spectrum of parenchymal CT findings. Radiology 175:711–714

Kuhn JP (1993) High-resolution computed tomography of pediatric pulmonary parenchymal disorders. Radiol Clin North Am 31:533–551

Laube BL, Chang DY, Blask AN et al. (1992) Radioaerosol assessment of lung improvement in cystic fibrosis patients treated for acute pulmonary exacerbations. Chest 101:1302–1308

Lehman TJ (1995) A practical guide to systemic lupus erythematosus. Pediatr Clin North Am 42:1223–1238

Leutner CC, Gieseke J, Lutterbey G et al. (2000) MR imaging of pneumonia in immunocompromised patients: comparison with helical CT. AJR Am J Roentgenol 175:391–397

Long FR, Castile RG (2001) Technique and clinical applications of full-inflation and end-exhalation controlled-ventilation chest CT in infants and young children. Pediatr Radiol 31:413–422

Long FR, Castile RG, Brody AS et al. (1999) Lungs in infants and young children: improved thin-section CT with a noninvasive controlled-ventilation technique – initial experience. Radiology 212:588–593

Lovell D, Lindsley C, Langston C (1984) Lymphoid interstitial pneumonia in juvenile rheumatoid arthritis. J Pediatr 105:947–950

Luboldt W, Wetter A, Eichler K et al. (2006) Determination of the optimal MRI sequence for the detection of malignant lung nodules. Eur J Med Res 11:336–342

Lucaya J, Garcia-Pena P, Herrera L et al. (2000a) Expiratory chest CT in children. AJR Am J Roentgenol 174:235–241

Lucaya J, Piqueras J, Garcia-Pena P et al. (2000b) Low-dose high-resolution CT of the chest in children and young adults: dose, cooperation, artifact incidence, and image quality. AJR Am J Roentgenol 175:985–992

Lund JT, Ehman RL, Julsrud PR et al. (1989) Cardiac masses: assessment by MR imaging. AJR Am J Roentgenol 152:469–473

Lynch DA, Hay T, Newell JD Jr et al. (1999) Pediatric diffuse lung disease: diagnosis and classification using high-resolution CT. AJR Am J Roentgenol 173:713–718

Maffessanti M, Candusso M, Brizzi F et al. (1996) Cystic fibrosis in children: HRCT findings and distribution of disease. J Thorac Imaging 11:27–38

Manson D, Reid B, Dalal I et al. (1997) Clinical utility of high-resolution pulmonary computed tomography in children with antibody deficiency disorders. Pediatr Radiol 27:794–798

Manson DE, Sikka S, Reid B et al. (2000) Primary immunodeficiencies: a pictorial immunology primer for radiologists. Pediatr Radiol 30:501–510

Martin L, Buonomo C (1997) Acute chest syndrome of sickle cell disease: radiographic and clinical analysis of 70 cases. Pediatr Radiol 27:637–641

Mathieson JR, Mayo JR, Staples CA et al. (1989) Chronic diffuse infiltrative lung disease: comparison of diagnostic accuracy of CT and chest radiography. Radiology 171:111–116

Matsuzono Y, Togashi T, Narita M et al. (1995) Pulmonary aspergillosis and pseudosequestration of the lung in chronic granulomatous disease. Pediatr Radiol 25:201–203

McCormack F, Brody A, Meyer C et al. (2002) Pulmonary cysts consistent with lymphangioleiomyomatosis are common in women with tuberous sclerosis: genetic and radiographic analysis. Chest 121(3 Suppl):61S

McHugh K, Olsen EO, Vellodi A (2004) Gaucher disease in children: radiology of non-central nervous system manifestations. Clin Radiol 59:117–123

Menke J (2005) Comparison of different body size parameters for individual dose adaptation in body CT of adults. Radiology 236:565–571

Mentore K, Froh DK, de Lange EE et al. (2005) Hyperpolarized HHe 3 MRI of the lung in cystic fibrosis: assessment at baseline and after bronchodilator and airway clearance treatment. Acad Radiol 12:1423–1429

Moskaluk CA, Pogrebniak HW, Pass HI et al. (1994) Surgical pathology of the lung in chronic granulomatous disease. Am J Clin Pathol 102:684–691

Nathanson I, Conboy K, Murphy S et al. (1991) Ultrafast computerized tomography of the chest in cystic fibrosis: a new scoring system. Pediatr Pulmonol 11:81–86

Nicholson AG, Florio R, Hansell DM et al. (2006) Pulmonary involvement by Niemann-Pick disease. A report of six cases. Histopathology 48:596–603

Ozkan H, Atlihan F, Genel F et al. (2005) IgA and/or IgG subclass deficiency in children with recurrent respiratory infections and its relationship with chronic pulmonary damage. J Investig Allergol Clin Immunol 15:69–74

Padley S, Gleeson F, Flower CD (1995) Review article: current indications for high resolution computed tomography scanning of the lungs. Br J Radiol 68:105–109

Puderbach M, Eichinger M, Gahr J et al. (2007) Proton MRI appearance of cystic fibrosis: comparison to CT. Eur Radiol 17:716–724

Ramsey BW, Pepe MS, Quan JM et al. (1999) Intermittent administration of inhaled tobramycin in patients with cystic fibrosis. Cystic Fibrosis Inhaled Tobramycin Study Group. N Engl J Med 340:23–30

Remy-Jardin M, Remy J, Wallaert B et al. (1993) Pulmonary involvement in progressive systemic sclerosis: sequential evaluation with CT, pulmonary function tests, and bronchoalveolar lavage. Radiology 188:499–506

Robinson TE, Leung AN, Northway WH et al. (2001) Spirometer-triggered high-resolution computed tomography and pulmonary function measurements during an acute exacerbation in patients with cystic fibrosis. J Pediatr 138:553–559

Rodrigues R, Marchiori E, Muller NL (2004) Niemann-Pick disease: high-resolution CT findings in two siblings. J Comput Assist Tomogr 28:52–54

Rogalla P, Stover B, Scheer I et al. (1999) Low-dose spiral CT: applicability to paediatric chest imaging. Pediatr Radiol 29:565–569

Rossi SE, Erasmus JJ, McAdams HP et al. (1999) Thoracic manifestations of neurofibromatosis-I. AJR Am J Roentgenol 173:1631–1638

Rupprecht T, Bowing B, Kuth R et al. (2002) Steady-state free precession projection MRI as a potential alternative to the conventional chest X-ray in pediatric patients with suspected pneumonia. Eur Radiol 12:2752–2756

Rusconi F, Panisi C, Dellepiane RM et al. (2003) Pulmonary and sinus diseases in primary humoral immunodeficiencies with chronic productive cough. Arch Dis Child 88:1101–1105

Sallee D, Spector ML, van Heeckeren DW et al. (1999) Primary pediatric cardiac tumors: a 17 year experience. Cardiol Young 9:155–162

Santamaria F, Grillo G, Guidi G et al. (1998) Cystic fibrosis: when should high-resolution computed tomography of the chest Be obtained? Pediatrics 101:908–913

Sawyer SM, Carlin JB, DeCampo M et al. (1994) Critical evaluation of three chest radiograph scores in cystic fibrosis. Thorax 49:863–866

Schwab EP, Schumacher HR Jr, Freundlich B et al. (1993) Pulmonary alveolar hemorrhage in systemic lupus erythematosus. Semin Arthritis Rheum 23:8–15

Seely JM, Effmann EL, Muller NL (1997) High-resolution CT of pediatric lung disease: imaging findings. AJR Am J Roentgenol 168:1269–1275

Seely JM, Jones LT, Wallace C et al. (1998) Systemic sclerosis: using high-resolution CT to detect lung disease in children. AJR Am J Roentgenol 170:691–697

Semelka RC, Shoenut JP, Wilson ME et al. (1992) Cardiac masses: signal intensity features on spin-echo, gradient-echo, gadolinium-enhanced spin-echo, and TurboFLASH images. J Magn Reson Imaging 2:415–420

Shah RM, Sexauer W, Ostrum BJ et al. (1997) High-resolution CT in the acute exacerbation of cystic fibrosis: evaluation of acute findings, reversibility of those findings, and clinical correlation. AJR Am J Roentgenol 169:375–380

Shaker KG, Umali CB, Fraire AE (1995) Langerhans‘ cell histiocytosis of the lung in association with mediastinal lymphadenopathy. Pathol Int 45:762–766

Shanbhag DD, Altes TA, Miller GW et al. (2006) q-Space analysis of lung morphometry in vivo with hyperpolarized 3He spectroscopy. J Magn Reson Imaging 24:84–94

Siegel MJ, Schmidt B, Bradley D et al. (2004) Radiation dose and image quality in pediatric CT: effect of technical factors and phantom size and shape. Radiology 233:515–522

Sigal-Cinqualbre AB, Hennequin R, Abada HT et al. (2004) Low-kilovoltage multi-detector row chest CT in adults: feasibility and effect on image quality and iodine dose. Radiology 231:169–174

Sirr SA, Elliott GR, Regelmann WE et al. (1986) Aerosol penetration ratio: a new index of ventilation. J Nucl Med 27:1343–1346

Slattery DM, Zurakowski D, Colin AA et al. (2004) CF: an X-ray database to assess effect of aerosolized tobramycin. Pediatr Pulmonol 38:23–30

Smets A, Mortele K, de Praeter G et al. (1997) Pulmonary and mediastinal lesions in children with Langerhans cell histiocytosis. Pediatr Radiol 27:873–876

Sockrider MM, Swank PR, Seilheimer DK et al. (1994) Measuring clinical status in cystic fibrosis: internal validity and reliability of a modified NIH score. Pediatr Pulmonol 17:86–96

Spencer DA, Alton HM, Raafat F et al. (1996) Combined percutaneous lung biopsy and high-resolution computed tomography in the diagnosis and management of lung disease in children. Pediatr Pulmonol 22:111–116

Sylvester KP, Patey RA, Milligan P et al. (2006) Impact of acute chest syndrome on lung function of children with sickle cell disease. J Pediatr 149:17–22

Tabone MD (2003) Invasive pulmonary aspergillosis in immunocompromized children: diagnosis and classification. Arch Pediatr 10(Suppl 5):582s–587s

Takizawa H, Shiga J, Moroi Y et al. (1987) Interstitial lung disease in dermatomyositis: clinicopathological study. J Rheumatol 14:102–107

Terheggen-Lagro S, Truijens N, van Poppel N et al. (2003) Correlation of six different cystic fibrosis chest radiograph scoring systems with clinical parameters. Pediatr Pulmonol 35:441–445

Tunaci A, Berkmen YM, Gokmen E (1995) Pulmonary Gaucher‘s disease: high-resolution computed tomographic features. Pediatr Radiol 25:237–238

Uziel Y, Hen B, Cordoba M et al. (1998) Lymphocytic interstitial pneumonitis preceding polyarticular juvenile rheumatoid arthritis. Clin Exp Rheumatol 16:617–619

van Beek EJ, Hill C, Woodhouse N et al. (2007) Assessment of lung disease in children with cystic fibrosis using hyperpolarized 3-helium MRI: comparison with Shwachman score, Chrispin-Norman score and spirometry. Eur Radiol 17:1018–1024

Vesely R, Vargova V, Ravelli A et al. (2004) Serum level of KL-6 as a marker of interstitial lung disease in patients with juvenile systemic sclerosis. J Rheumatol 31:795–800

Vichinsky EP, Neumayr LD, Earles AN et al. (2000) Causes and outcomes of the acute chest syndrome in sickle cell disease. National Acute Chest Syndrome Study Group. N Engl J Med 342:1855–1865

Vock P (2005) CT dose reduction in children. Eur Radiol 15:2330–2340

Wagener JS, Taussig LM, DeBenedetti C et al. (1981) Pulmonary function in juvenile rheumatoid arthritis. J Pediatr 99:108–110

Waters DL, Wilcken B, Irwing L et al. (1999) Clinical outcomes of newborn screening for cystic fibrosis. Arch Dis Child Fetal Neonatal Ed 80:F1–7

Weatherly MR, Palmer CG, Peters ME et al. (1993) Wisconsin cystic fibrosis chest radiograph scoring system. Pediatrics 91:488–495

Webb WR, Goodman PC (1977) Fibrosing alveolitis in patients with neurofibromatosis. Radiology 122:289–293

Wraith JE, Clarke LA, Beck M et al. (2004) Enzyme replacement therapy for mucopolysaccharidosis I: a randomized, double-blinded, placebo-controlled, multinational study of recombinant human alpha-L-iduronidase (laronidase). J Pediatr 144:581–588

Zamora AC, Collard HR, Wolters PJ et al. (2007) Neurofibromatosis-associated lung disease: a case series and literature review. Eur Respir J 29:210–214

Zrour SH, Touzi M, Bejia I et al. (2005) Correlations between high-resolution computed tomography of the chest and clinical function in patients with rheumatoid arthritis. Prospective study in 75 patients. J Bone Spine 72:41–47

Radiology of the Chest Wall

Georg F. Eich, Christian J. Kellenberger, and Ulrich V. Willi

CONTENTS

14.1 **Introduction** *313*

14.2 **Normal Variant, Congenital Abnormality and Deformity** *313*
14.2.1 Anatomic Variants *313*
14.2.2 Malformation and Deformity *314*

14.3 **Infection** *319*

14.4 **Tumors** *321*

14.5 **Trauma** *330*
14.5.1 Accidental Trauma *330*
14.5.2 Non-Accidental Trauma *332*

References *334*

14.1
Introduction

The chest wall of a child can give rise to a variety of lesions or pseudolesions that can be classified into normal variant, malformation, trauma, infection, and tumor. These lesions pertain to the skin and subcutaneous tissue (superficial layer), muscles and bones of the shoulder girdle and the pectoralis region (intermediate layer), and/or the deep layer, which includes the dorsal spine, the ribs and intercostal spaces, the sternum, several fascial layers, and the parietal pleura. Pathology of the breast and the diaphragm are excluded from this review.

This chapter is structured according to the nosological entities mentioned above. We will discuss alterations in the shape of the chest that may be associated with functional or esthetic problems or that may mimic a tumor. The appropriate imaging technique for assessment of a deformity or variant is emphasized. Infections of the chest wall can originate from penetrating wounds or hematogenous spread within bone, joint, or soft tissue. The importance of imaging in defining the exact topography of the focus and its extent is stressed. Chest wall tumors are essentially mesenchymal tumors. Both benign and malignant neoplasms occur. The Ewing sarcoma family of tumors and rhabdomyosarcoma are the most prevalent malignant tumors of the chest wall. The chest may be exposed to trauma (accidental or non-accidental). The imaging findings of both types of injuries will be discussed, with particular emphasis on sternoclavicular fractures, which are difficult to diagnose both clinically and with conventional radiology.

14.2
Normal Variant, Congenital Abnormality and Deformity

14.2.1
Anatomic Variants

The normal shape of the chest is fairly symmetrical, the chest is narrower in its upper portion than in the lower three quarters. Normal infants have a relatively wide anteroposterior diameter of the chest compared to older children. The thoracic index (widest anteroposterior diameter / widest transverse diameter) is about 0.85 in infants compared to 0.72 in older children (Nathanson 1994). The

---

G. F. Eich, MD
Pediatric Radiology, Kantonsspital, 5001 Aarau, Switzerland
C. J. Kellenberger, MD
Diagnostic Imaging, The University Children's Hospital, Steinwiesstrasse 75, 8032 Zürich, Switzerland
U. V. Willi, MD
Department of Radiology, Lucile Packard Children's Hospital, 725 Welch Road, Stanford, CA 94305, USA

thoracic index is decreased in pectus excavatum and in a child with an idiopathic flat chest. In the latter condition the thorax is flat and wide, the thoracic kyphosis is reduced, the heart is located slightly to the left, but the sternum is normal in position. The thoracic index is increased in pectus carinatum or in a child with a "barrel chest."

Infants have a prominent double curvature of the *clavicle* which can simulate a fracture on chest radiographs taken with the child in a rotated position. The sternal end of the clavicle may show marked cupping during the second decade, which should not be misinterpreted as osteomyelitis or septic arthritis (Fig. 14.1).

Isolated rib anomalies are common incidental findings, usually of no clinical importance, with an estimated frequency of about 2% (Coury and Delaporte 1954). Such anomalies include partial aplasia or agenesis of ribs, bridging between two adjacent ribs by synostosis or pseudoarticulation, bifid ribs, and supernumerary ribs. Unilateral or bilateral cervical ribs may arise from the seventh cervical vertebra and can sometimes cause a thoracic outlet syndrome by compression of the brachial plexus or the subclavian artery. Intrathoracic rib is a rare anomaly that can be seen on chest radiographs (Kamaruddin et al. 1995). Eleven pairs of ribs occur in isolation or as manifestation of various syndromes like trisomy 18, Down syndrome, and cleidocranial dysplasia (Lachman 2006).

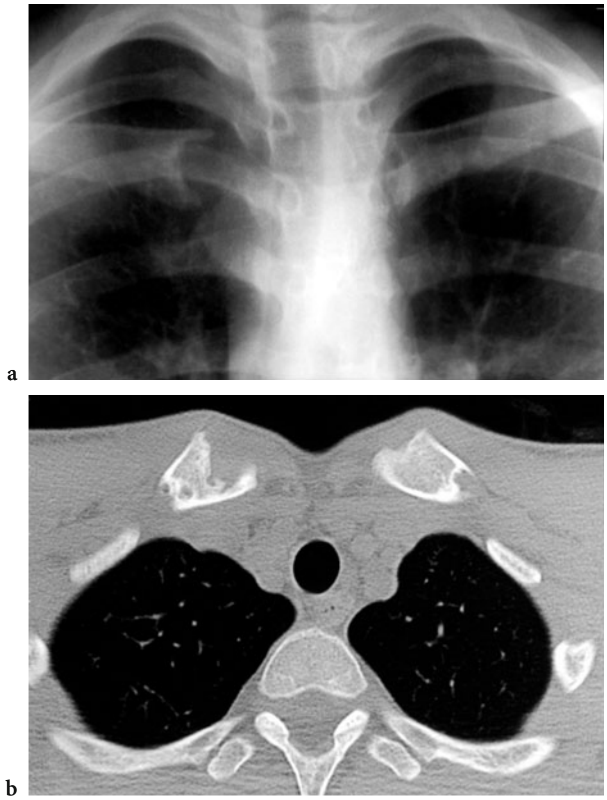

Fig. 14.1a,b. Normal variant of clavicles in a 15-year-old boy with fever of unknown origin. **a** Chest X-ray; close-up view of upper median aspect shows irregular sclerosis of right medial clavicular concavity, initially mistaken for osteomyelitis. **b** Axial CT scan through upper chest area at level of medial clavicular ends shows correlating irregular clavicular contours, especially on the right. No local soft tissue swelling. Subsequently, scintigraphy demonstrated osteomyelitis in the right distal femoral metaphysis

Anatomic variations of the anterior chest wall are very common (Donnelly et al. 1999). Up to one third of all children show asymmetry in the shape or size of the rib cartilage or in the position of the sternum. Usually a palpable anterior chest wall bump is the cause for concern. The underlying anatomical cause may be a tilted sternum, or various anomalies of the rib cartilage such as a prominent anterior convexity, localized thickening, bifid cartilage, or a parachondral nodule. Even a mild degree of pectus excavatum or carinatum can produce a circumscribed protrusion that quite frequently prompts referrals for imaging studies. Of 27 children who underwent computed tomography (CT) or magnetic resonance imaging (MRI) for an asymptomatic, palpable chest wall bump, all had either benign lesions or normal variants of bone or cartilage formation in the anterior chest wall (Donnelly et al. 1997). Ultrasound (US) is an alternative method that can easily show the underlying anatomic variant and rule out a malignant chest wall mass for anxious parents and referring physicians (Fig. 14.2).

14.2.2
Malformation and Deformity

Malformation of the chest wall may be a manifestation of a syndrome or *skeletal dysplasia* (Lachman 2006). Of particular interest are the neonatally lethal short rib-polydactyly syndromes, asphyxiating thoracic dystrophy (Jeune Syndrome), thanatophoric dysplasia, achondrogenesis, and other skeletal dysplasias in which maldevelopment of the thoracic cage produces a small and narrow chest due to short, and sometimes deformed ribs (Eich 2007; Glass et al. 2002). Respiratory distress at birth or even intrauterine death is directly related to the severity of the skeletal malformation.

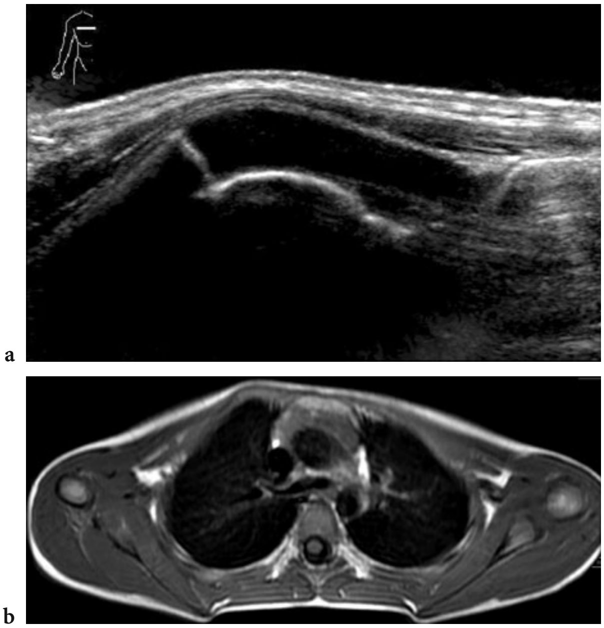

Fig. 14.2a,b. Rib deformity in a 6-year-old boy with “chest wall mass”. US scan (**a**) and axial T1 weighted MR image (**b**) through right upper thoracic area show redundancy of cartilaginous anterior rib portion (hockey stick shape)

A small thorax with thin ribs and small lungs can be a feature of neuromuscular disorders, particularly myasthenia gravis, myotonia, spinal muscular atrophy and other myopathies. Thin ribs can be a feature of progeria and the trisomies 8, 13, and 18. Preterm infants show gracile ribs with posterior thinning. Thick ribs can be a manifestation of thalassemia (Cooley’s anemia), mucopolysaccharidosis and other disorders. Inferior rib notching is due to abnormalities of the intercostal neurovascular bundle, such as arterial or venous collaterals (e.g. coarctation of the aorta, superior vena cava syndrome), and to neurogenic tumors (e.g. neurofibromatosis).

Rib aplasia or hypoplasia, when isolated, is of little clinical significance. Multiple hypoplastic ribs with or without additional spinal segmentation defects cause asymmetric deformity of the chest. Hypoplasia or aplasia of the lung may also cause an asymmetric thoracic cage.

Kyphoscoliosis can be idiopathic or congenital (due to vertebral segmentation defects), or it may be a complication of a neuromuscular disorder. The chest shows crowding of ribs on the concave side of the curvature and assessment of the heart and lung and may become difficult. It is not uncommon to find a smaller lung volume and atelectasis on the convex side. CT with three-dimensional (3D) reconstruction may be helpful for delineating vertebral anomalies and chest wall morphology (Bush 1999). MRI may be indicated if there is suspicion of spinal cord pathology.

Poland syndrome is characterized by unilateral partial or complete absence of the pectoralis muscles, hypoplasia of subcutaneous or breast tissues, hypoplasia or absence of ribs, and anomalies of the ipsilateral upper limb. On plain films the affected hemithorax appears hyperlucent. In the preoperative assessment of Poland syndrome, CT or MRI may help in defining the extent of the musculoskeletal and soft tissue anomalies and in showing the available muscles for reconstructive surgery (Wright et al. 1992) (Fig. 14.3).

Cleidocranial dysplasia, an autosomal dominant inherited syndrome, is characterized by hypoplasia or absence of one or both clavicles resulting in hypermobile, drooping shoulders. Other features of the chest wall consist of small scapulae, deficient sternal ossification, posterior wedging of thoracic vertebrae, scoliosis, kyphosis and short ribs with prominent downward slope. Leading features of cleidocranial dysplasia are brachycephaly, wide sutures, persistence of the anterior fontanelle, abnormal dentition, absent or delayed ossification of pubic bones, and wide pubic symphysis (Lachman 2006).

Congenital pseudarthrosis of the clavicle is an isolated anomaly of the clavicle. This rare anomaly presents in infancy with a painless palpable mass. The clavicle shows a smoothly marginated defect in the middle third, virtually always on the right side. There is no history of a prior trauma. Pseudarthrosis may be caused by the failure of two primary ossification centers to fuse (Cadilhac et al. 2000).

In Sprengel deformity the scapula fails to descend from its cervical origin and becomes fixed to the cervical spine by a fibrous band or an omovertebral bone. The scapula is high in position medially and rotated. Additional anomalies of ribs or vertebrae are frequently present (Klippel-Feil syndrome). CT with 3D reconstruction can be helpful in delineating the deformity and in planning corrective surgery (Cho et al. 2000).

Pectus excavatum, also known as “funnel chest,” is the most common chest wall deformity. It is usually an isolated lesion that occurs sporadically or it may be inherited with an autosomal dominant trait. It can be associated with Turner syndrome, osteogenesis imperfecta, muscular dystrophy, or with connective tissue disorders like Marfan and Ehlers-Danlos syndromes. The lower portion of the

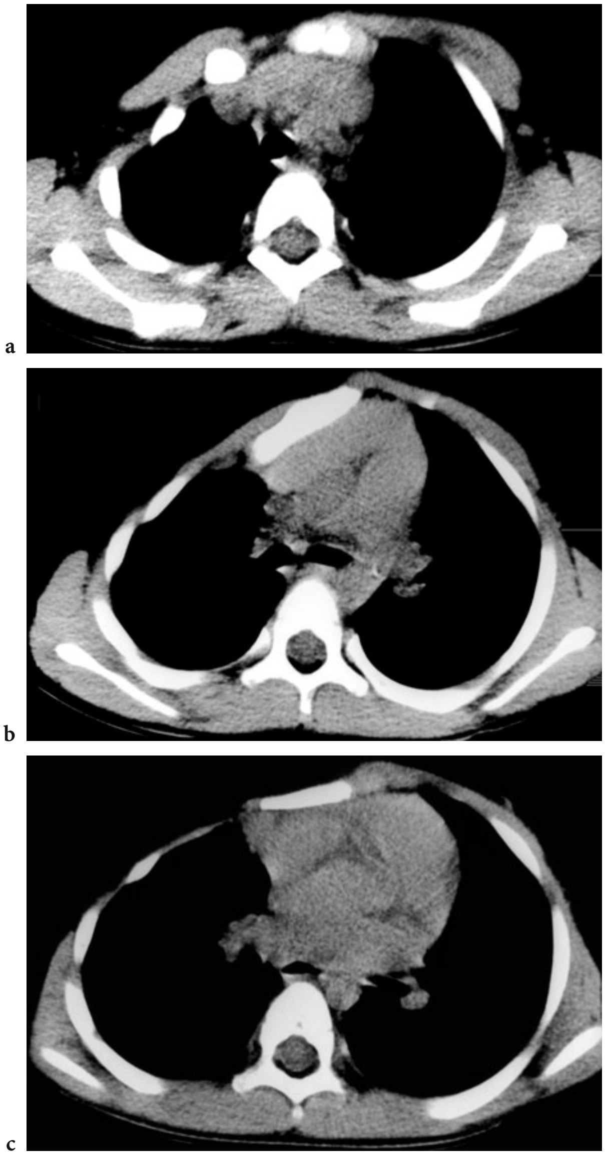

Fig. 14.3a–c. Poland syndrome in a 4-year-old boy. Unenhanced axial CT scans at three different levels (**a–c**) show hypoplasia of major and minor right pectoralis muscles and right hemithorax with asymmetry of rib cage and sternum

sternum shows an inward curvature with a relative protrusion of the attached costal cartilages on each side. The sternum is usually rotated to the right. The characteristic radiographic findings are easily recognized (Fig. 14.4). On the antero-posterior view of the chest radiograph the anterior rib ends have a steep downward course, while the posterior ribs are more horizontally oriented. The heart is shifted to the left and rotated. The right parasternal soft tissues produce a paracardial density and partially obscure the right heart border by a silhouetting effect. This should not be mistaken for middle lobe disease. On the lateral view the chest is narrow and the degree of the sternal depression is easily seen. Cross sectional imaging is useful to determine and quantify the severity of the deformity, to assess the degree of cardiac shift or compression, to identify associated tracheobronchial compression, and to assess the results of surgery (Pretorius et al. 1998). Thoracic dimensions in patients with pectus excavatum are quantified by the pectus- or Haller index, which is the ratio of the internal transverse diameter of the chest to the narrowest anteroposterior diameter that commonly is calculated from a single axial scan or a limited CT study (Haller et al. 1987; Chuang and Wan 1995). The same measurements can be obtained without ionizing radiation from an axial MR image (Fig. 14.5). Besides morphologic assessment, MRI also allows dynamic assessment of the chest wall and diaphragm (Raichura et al. 2001; Herrmann et al. 2006).

Patients requiring surgical correction of pectus excavatum usually have a Haller index greater than 3.2, whereas in normal children the Haller index values range from 1.9 to 2.7 due to age-related and sex-related differences in chest wall configuration. The Haller index in normal children under 2 years of age is significantly lower than in older children, and girls between the ages of 0–6 and 12–18 years tend to have higher Haller index values than boys of the same age (Daunt et al. 2004). In rare cases respiratory or cardiac symptoms may be present, but most patients with pectus excavatum are asymptomatic and surgical correction is performed for cosmetic reasons. Restrictive lung volumes may not alter following operation, but cardiorespiratory function can increase due to higher cardiac output (Haller and Loughlin 2000).

Pectus carinatum or "pigeon breast" is a congenital or acquired deformity that develops with growth and is frequently seen with congenital heart disease (voussure cardiaque) (Fig. 14.6). Other causes include long-standing obstructive lung disease, Marfan syndrome, Ehlers-Danlos syndrome, Noonan syndrome, Morquio syndrome, or prune belly syndrome, among others. The deformity seems to be caused by growth disturbance of both the sternum and costal cartilages with premature sternal fusion. The short sternum and costal cartilages protrude anteriorly with flattening of the chest laterally (Fig. 14.7). Most patients with a congenital pectus carinatum are asymptomatic. Surgery can correct the deformity.

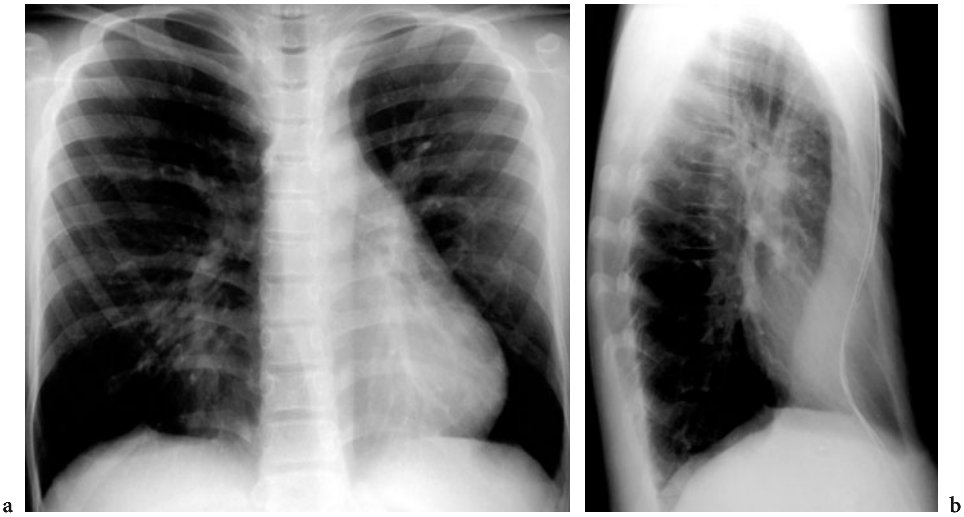

Fig. 14.4a,b. Pectus excavatum. Postero-anterior (**a**) and lateral (**b**) chest X-rays in a 14-year-old boy show steep course of elongated anterior ribs, cylindric shape of chest and displacement of heart to the left due to reduced mid-sagittal diameter of chest. The outline of the sternum is enhanced with barium

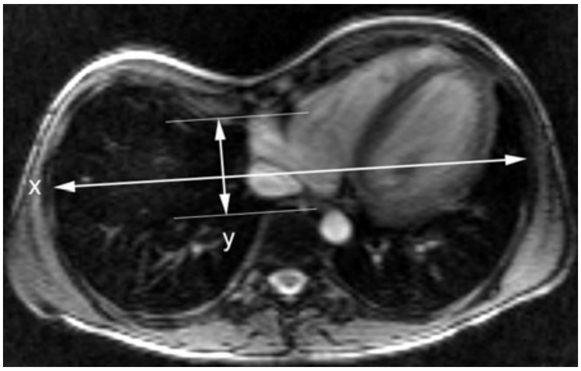

Fig. 14.5. Axial steady-state free precession MR image of lower chest region in 11-year-old boy with pectus excavatum shows depression of the sternum and cartilagenous portion of a right rib, and leftward displacement but no compression of the heart. The Haller index is 5.1 and calculated as the maximal internal transverse diameter between rib cortices (x) divided by the minimal anterior-posterior diameter between the deepest point of the chest wall and the anterior cortex of the vertebra (y)

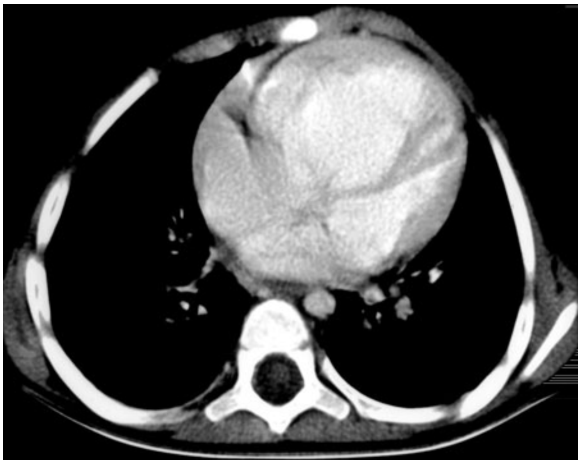

Fig. 14.6. Cor pulmonale ("*voussure cardiaque*") in a 2.5-year-old boy. Axial contrast-enhanced CT scan through lower thoracic region shows (chronic) cardiac enlargement leading to increased sagittal diameter with additional left-sided protuberance of the chest. The child had primary pulmonary hypertension

Herniation of thoracic contents occurs when there is a defect in bony or soft tissue structures of the chest wall. *Cleft sternum* is a rare congenital lesion caused by partial or complete failure of sternal fusion at an early stage of embryonic development. Depending on the location and degree of the defect, herniation of thymus or the heart can be present (ectopia cordis). Association with craniofacial hemangiomas and omphalocele are common associated anomalies (Fokin 2000). Lung hernia is a protrusion of pulmonary tissue through a defect of the chest wall. It may be cervical and intercostal in location. The more frequent intercostal hernia is mostly acquired following chest tube placement, surgery, trauma, chest wall neoplasm, or infection, but it can also be due to a congenital chest wall defect (Fig. 14.8). Cervical or apical hernia is associ-

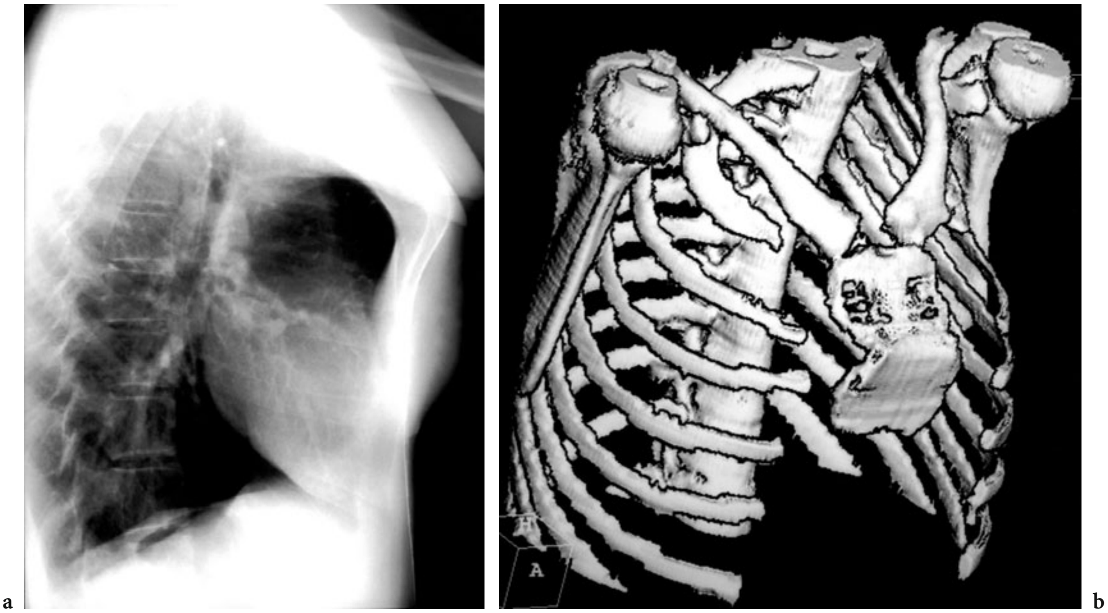

Fig. 14.7a,b. Pectus carinatum in a 17-year-old girl. **a** Lateral X-ray view of thorax shows protrusion of upper and mid portions of the sternum. **b** Three-dimensional CT reconstruction demonstrates correlating severe sternum deformity

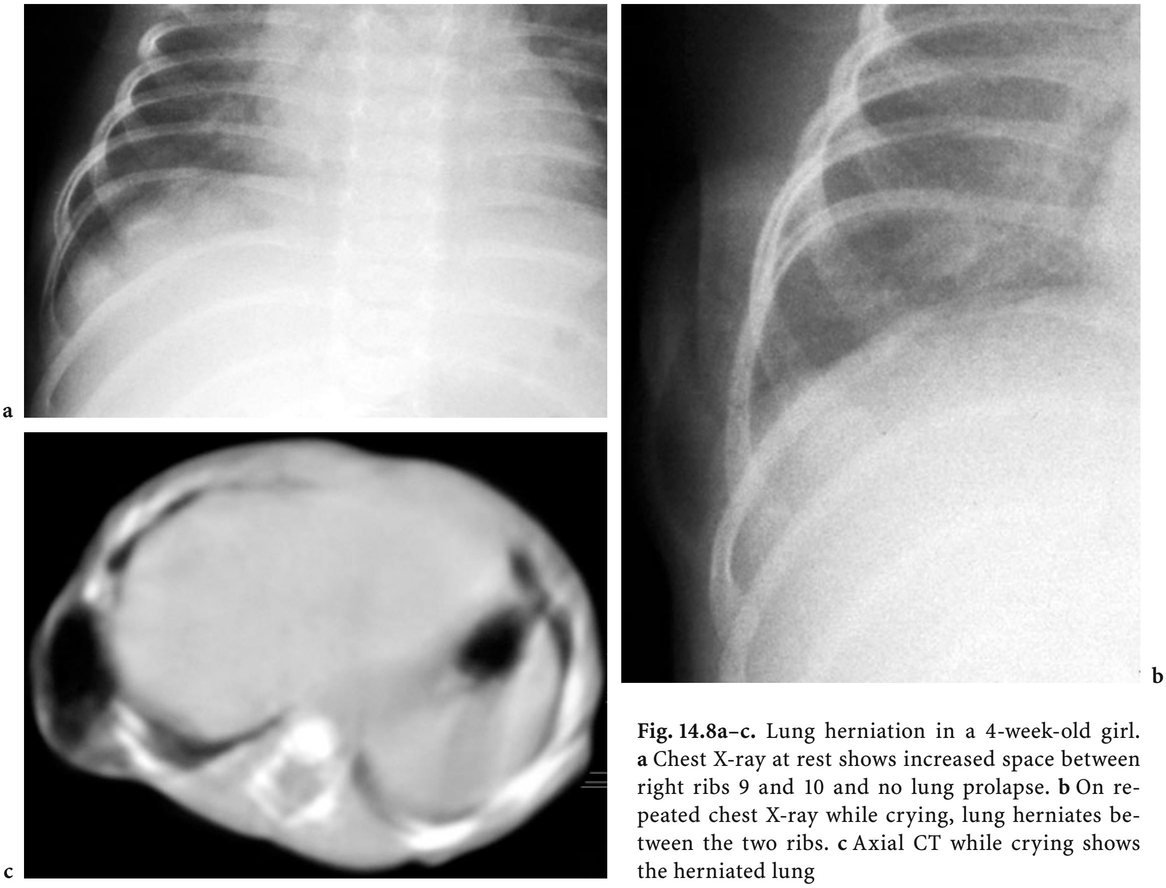

Fig. 14.8a–c. Lung herniation in a 4-week-old girl. **a** Chest X-ray at rest shows increased space between right ribs 9 and 10 and no lung prolapse. **b** On repeated chest X-ray while crying, lung herniates between the two ribs. **c** Axial CT while crying shows the herniated lung

ated with chronic obstructive lung disease in adults. In infants and children it arises spontaneously as a result of a congenital defect in the costovertebral fascia. The main symptom is an intermittant bulging in the supraclavicular or intercostal area that appears with crying, coughing, or straining. Chest radiographs or CT performed during inspiration may fail to show the lung herniation. Fluoroscopy during crying, coughing or Valsalva manoever is valuable in diagnosing lung hernias (Thompson 1976).

14.3 Infection

Primary infection of the chest wall is relatively rare in children, but it is potentially fatal since secondary sepsis or spread to the pleural spaces, the mediastinum (Fig. 14.9), or pericardium can occur. Chest wall infection originates from hematogenous spread of organisms with sepsis or bacteremia, or from direct extension from a wound after injury or surgery (sternotomy) to the chest. Staphylococcus aureus is the most prevalent organism in chest wall infections of patients from Europe or North America (Sharif et al. 1990). Mycobacterium tuberculosis (Fig. 14.10) may be more prevalent in other areas of the world. Other micro-organisms (Actinomyces, Blastomyces, Nocardia, and Aspergillus species) and cat-scratch disease can occasionally cause chest wall infections (Golloday et al. 1985; Lew and Waldvogel 1997). Chest wall infections are especially common in immunocompromised patients.

Clinical symptoms include fever, pain, and focal signs of inflammation such as edema, erythema, hyperthermia, and occasionally fistulous tracts. Infection can involve the soft tissues and/or bone and cause abscess formation, cellulitis and/or granulation tissue formation. Depending on the structure preferentially affected it is called pyomyositis when muscles are involved, (necrotizing) fasciitis when only subcutaneous fat and fascia are affected, osteo-

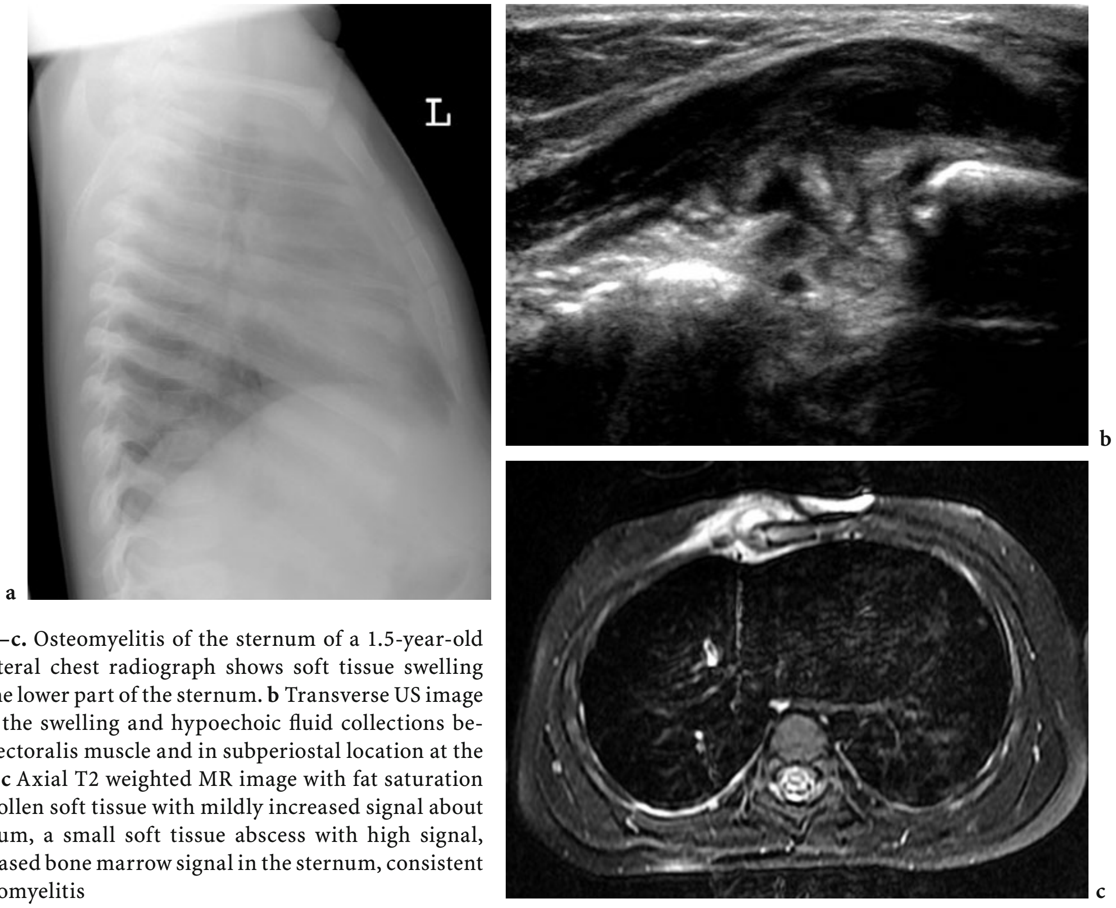

Fig. 14.9a–c. Osteomyelitis of the sternum of a 1.5-year-old boy. **a** Lateral chest radiograph shows soft tissue swelling around the lower part of the sternum. **b** Transverse US image confirms the swelling and hypoechoic fluid collections below the pectoralis muscle and in subperiostal location at the sternum. **c** Axial T2 weighted MR image with fat saturation shows swollen soft tissue with mildly increased signal about the sternum, a small soft tissue abscess with high signal, and increased bone marrow signal in the sternum, consistent with osteomyelitis

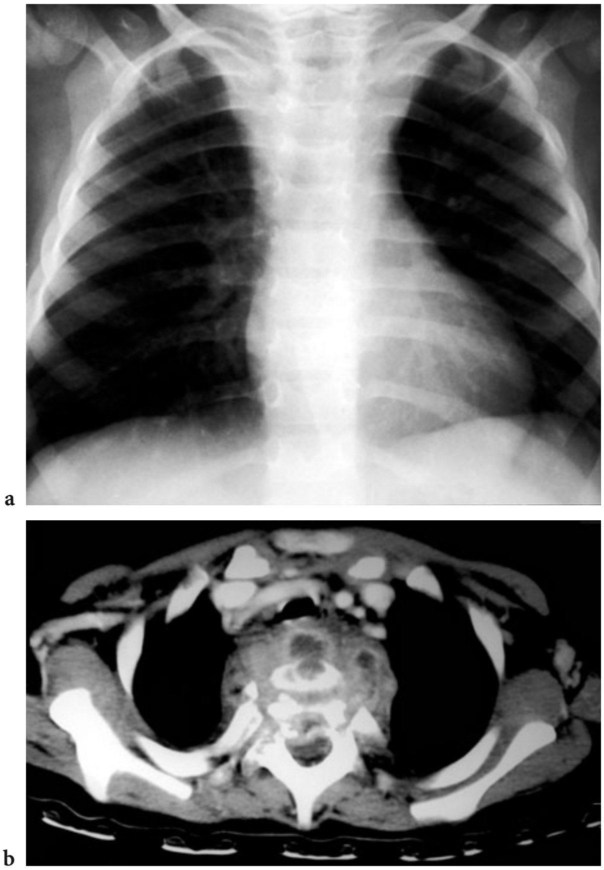

Fig. 14.10a,b. TBC abscess with vertebral osteomyelitis in a 2.5-year-old girl. **a** Chest X-ray shows unusual prominent shape of upper mediastinal region. **b** Contrast-enhanced axial CT scan through upper chest area shows complex paraspinal inflammatory mass with multiple abscesses involving vertebra, spinal arch and spinal canal

myelitis when there is bone involvement, and pyogenic arthritis where there is joint involvement.

Clinical recognition of a chest wall infection can be difficult, particularly when it is located in the intermediate or deep layers of the chest wall. The underlying process is often underestimated by physical examination alone. A suspected (or unsuspected) infection of the chest wall is usually first imaged with chest radiographs, which may show a mass lesion within the chest wall or the extrapleural space. Additional signs that may also be present include rib destruction and/or sclerosis, pulmonary infiltrate, pleural effusion, and calcifications, air, or gas within the soft tissues. US, CT, and MRI help to confirm the presence, location, and extent of the single or multiple infectious foci (Figs. 14.9–14.11). Positron emission tomography (PET) is a very sensitive tool for detecting clinically silent foci of infection in immunocompromised patients. US, CT, and MRI show fluid collections and rib destruction, and can guide percutaneous aspiration or drainage. US is usually sufficient for diagnosing small, superficial and well-delineated lesions, while CT or MRI are the techniques of choice for imaging large, complex, and deep-seated lesions for which surgery is considered. Intraspinal epidural extension may only be visible with CT or MRI (Fig. 14.10).

An abscess appears as a sonolucent area on US with increased through-transmission and absence of blood flow centrally. Echogenic swirling material within the abscess may occasionally be seen. Contrast-enhanced CT shows an iso- or hypodense, nonenhancing center and an enhancing rim (Figs. 14.9–14.11) (Faro et al. 1993), similar to that seen on T1-weighted MRI sequences. T2-weighted and short tau inversion recovery (STIR) sequences show a high signal intensity collection. A moderate increase in signal intensity on T2-weighted sequences may be

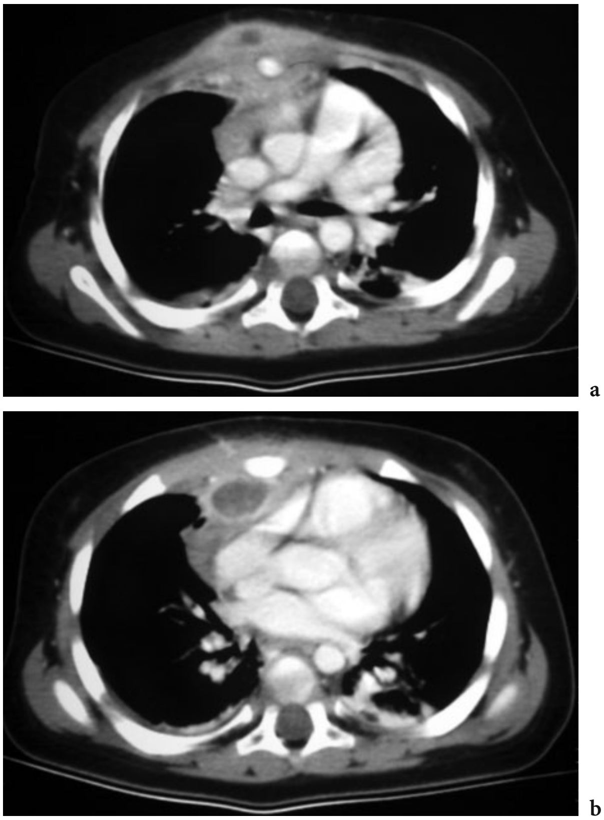

Fig. 14.11a,b. Osteomyelitis of the sternum due to Salmonella sp. following gastroenteritis in a 1-year-old boy. Clinical examination showed presternal swelling. Axial contrast-enhanced CT images show subperiostal fluid collections of the sternum as well as pre- and retrosternal abscesses

present in mycotic infection (Sharif et al. 1990). MRI is very sensitive for detecting osteomyelitis and is often more accurate than bone scans for differentiating between soft tissue inflammation and acute osteomyelitis. Chronic osteomyelitis is recognized on radiographs and CT as an area of destruction and reparative sclerosis within and around the affected part of bone. Inflammation of the surrounding soft tissues (cellulitis) appears as thickening in all modalities. In addition to this, US shows increased soft tissue echogenicity and vascularisation, while CT and MRI show contrast enhancement. Soft tissue inflammation is best delineated by MRI with fat-suppressed T2-weighted or STIR sequences, or T1-weighted sequences following administration of contrast material, which provide better differentiation from the unaffected subcutaneous fat. In our experience septic arthritis of the sternoclavicular joint is usually associated with osteomyelitis of the adjacent clavicle or sternum. CT and MRI show the joint effusion and osteolytic changes of the affected bone more readily than US and they can confirm or exclude posterior extension of the process into the mediastinum (Figs. 14.9 and 14.11).

Tuberculous spondylitis is relatively rare in developed countries, but it is the commonest vertebral infection in other parts of the world. The spinal infection mostly stems from primary pulmonary tuberculosis. One or several segments of the spine may be involved, particularly in the thoracic and lumbar region. Usually the infection is limited to the body of the vertebra, which may become destroyed along with the contiguous intervertebral disc and an adjacent or distant vertebra. Paraspinal abscesses, usually bilateral, are the rule. Calcification within a paraspinal abscess can occur in long-standing cases (Kuhn 2003). Vertebral collapse can lead to kyphosis and/or scoliosis and even to cord compression. The radiographic changes of tuberculous spondylitis are nonspecific, but an indolent presentation is suggestive of tuberculosis. CT and MRI can show the epidural extension of the process and delineate the topography of an abscess (Fig. 14.10).

Friedrich's disease is a disorder of unknown origin thought to be an aseptic necrosis with clinical and radiologic features that can mimic infection at the sternoclavicular joint (Levy et al. 1981). The lesion is usually unilateral but may be bilateral. Tender swelling at the sternoclavicular region is the typical presenting symptom. The erythrocyte sedimentation rate may be elevated. Radiographs show destruction and repair at the medial end of a clavicle (Fig. 14.12). Histology discloses necrosis of the clavicular epiphyseal region without evidence of infection. Aspiration cultures are negative. The symptoms usually subside spontaneously without treatment over several months. Radiological features improve very slowly. Our experience has shown that it may take up to 18 months for the clavicles to become radiologically normal.

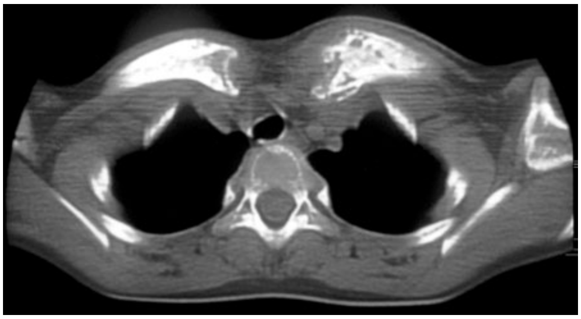

Fig. 14.12. Friedrich's disease in a 9-year-old girl. Axial CT scan through upper chest inlet area shows symmetrical changes of clavicles at their medial aspects from chronic inflammatory process

There are some similarities between Friedrich's disease and SAPHO syndrome, a disorder characterized by a variable combination of synovitis, acne, pustulosis, hyperostosis, and osteitis. The different aseptic skin abnormalities are associated with chronic recurrent multifocal osteomyelitis (CRMO), a rare, occasionally symmetrical, non-purulent inflammation of bone. Although it can involve other bones, the inflammation has a predilection for the anterior chest wall where it can cause tenderness, and swelling. Radiographic abnormalities include sclerosis and periostitis with expansion of the affected bone (Letts et al. 1999).

14.4
Tumors

Imaging is performed to detect a chest wall mass and to determine its location, size, and character. When a mass that originates in the chest wall expands into the chest cavity, it forms an obtuse angle with the adjacent chest wall. This feature might be recognized on radiographs, CT, or MRI. Masses that produce rib changes are likely to be extrapleural in location. Conventional radiographs are the first tools for imaging a chest wall mass in most places. Radiographs allow an approximate appreciation of the location of the lesion, its extension, rib destruction, and associated intrathoracic component, pleural effusion, or pulmonary metastases. Further imaging may be required in large or aggressive-looking lesions for staging purposes. Both CT and MRI are able to delineate the mass, demonstrate osseous changes, and define the margin and internal structure of the lesion, lymphatic spread, and pleural effusion. Currently CT is better suited than MRI to show metastases to the lungs. Obviously when faced with a possibly malignant chest wall mass, an interdisciplinary approach should be used, and the choice of the imaging modality may vary with the availability of, and expertise in using, the local imaging tools.

The chest wall can give rise to a wide variety of benign and malignant tumors that are primarily mesenchymal in origin, in keeping with the predominant tissue components of the chest wall. Tumors of the chest wall are relatively infrequent during infancy and childhood, but a high proportion is malignant (Kumar et al. 1977; Shamberger et al. 1989; Shamberger and Grier 1994). The tumors often present as a palpable mass, or, less frequently, with pain, cough, or respiratory distress from a large pleural effusion or an extensive intrathoracic component. Secondary involvement of the chest wall from an intrathoracic mass is rare in childhood (Table 14.1).

The tumor may be located within the bones and/or within the soft tissues of the chest wall. A sharply marginated osteolytic lesion usually signifies a slow-growing (benign) process; however, differentiation from a malignant lesion is not always possible, and biopsy may be required (Kozlowski et al. 1989). Multifocal Langerhans' cell histiocytosis (eosinophilic granuloma) with typical osteolytic lesions of the skull vault or vertebra plana allow a confident clinical diagnosis (Fig. 14.13).

Table 14.1. Nosology of chest wall tumors (Shamberger and Grier 1994)

Benign lesions	Malignant lesions
Chondroma	Chondrosarcoma
Osteochondroma	Osteochondrosarcoma
Osteoma	Osteosarcoma
Fibroma	Fibrosarcoma
Lipoma	Mesenchymal sarcoma
Eosinophilic granuloma	Ewing's sarcoma (Askin's tumor)
Hemangioma	Rhabdomyosarcoma
Mesenchymal hamartoma	Leiomyosarcoma
Aneurysmal bone cyst	Lymphoma
Fibrous dysplasia	

Vascular lesions like hemangiomas and lymphangiomas are amongst the most common soft tissue tumors of childhood that may be found in the chest wall. They are most prevalent in neonates, infants, and young children. Lymphangiomas are space occupying, non-neoplastic lesions predominantly of lymphatic vessels, which are attributed to a primary vascular malformation. They are called cystic hygromas when dilated lymphatic vessels lead to the formation of cysts. Lymphangiomas are usually present at birth and are found in the neck and chest wall. Extension into the mediastinum and axilla can occur (Fig. 14.14). The growth of lymphangiomas is usually self-limited, but bleeding into a mixed lymphangiohemangioma may lead to a sudden increase in size. Infection, chylothorax and chylopericardium are other possible complications.

Hemangiomas are benign tumors of blood vessels. Classically they are divided into capillary,

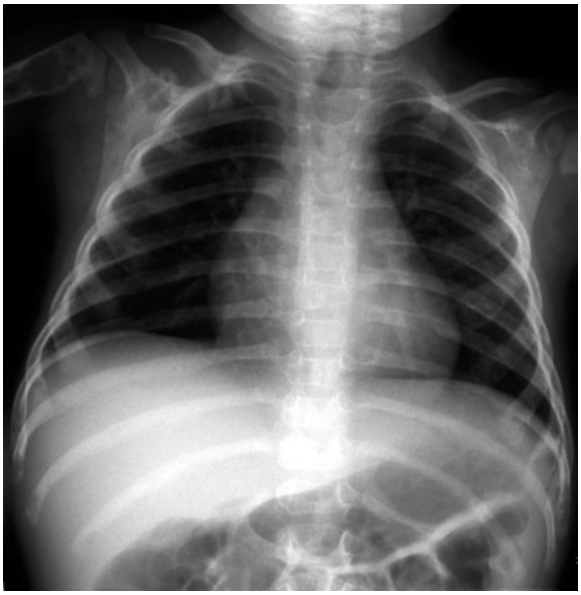

Fig. 14.13. Langerhans' cell histiocytosis in a 14-month-old girl. Chest X-ray shows numerous osteolytic lesions involving almost all ribs, mainly anterior portions, but also scapulae, clavicles, humeri, as well as multiple skeletal parts not shown on this film

cavernous, and mixed types depending on their vascular composition (arterial, arteriovenous, venous, or capillary). They may increase in size and subsequently involute spontaneously. When located beneath the skin, hemangiomas may exhibit the typical strawberry red color. Both lymphangiomas and blood vessel tumors can be multifocal. Hemangiomas and lymphangiomas can become large and disfiguring or compress blood vessels, the trachea and/or other vital structures (Gorham and Stout 1955; Stout and Lattes 1967). They therefore may require imaging for staging purposes before surgery or radiologic intervention. Solitary lymphangiomas of bone are rare; radiographically they are usually single or multiloculated osteolytic lesions. Hemangioma of bone may have a similar radiographic appearance or present as a radiolucent slightly expansile lesion possessing a radiating lattice-like or web-like trabecular pattern (Fig. 14.15).

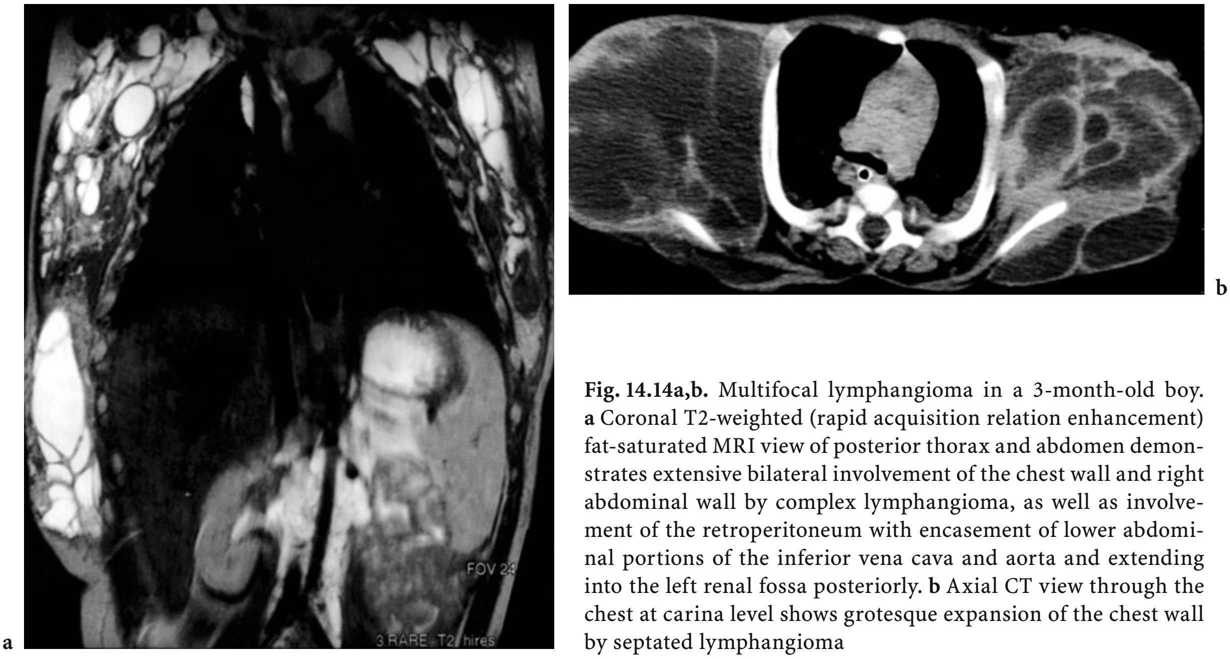

Fig. 14.14a,b. Multifocal lymphangioma in a 3-month-old boy. **a** Coronal T2-weighted (rapid acquisition relation enhancement) fat-saturated MRI view of posterior thorax and abdomen demonstrates extensive bilateral involvement of the chest wall and right abdominal wall by complex lymphangioma, as well as involvement of the retroperitoneum with encasement of lower abdominal portions of the inferior vena cava and aorta and extending into the left renal fossa posteriorly. **b** Axial CT view through the chest at carina level shows grotesque expansion of the chest wall by septated lymphangioma

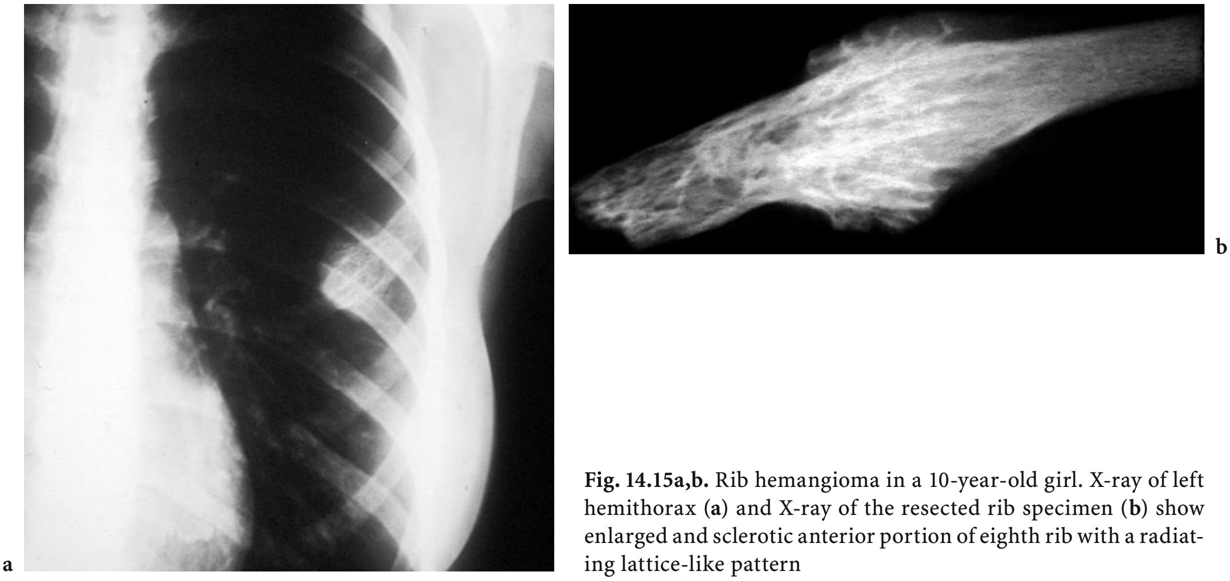

Fig. 14.15a,b. Rib hemangioma in a 10-year-old girl. X-ray of left hemithorax (**a**) and X-ray of the resected rib specimen (**b**) show enlarged and sclerotic anterior portion of eighth rib with a radiating lattice-like pattern

An association between lymphangiomas and hemangiomas with massive osteolysis has been noted in children and young adults particularly in the thoracic and pelvic region. This "vanishing bone disease" or diffuse cystic angiomatosis of bone (Gorham-Stout disease) is a rare condition in which spontaneous, progressive resorption of bone occurs. Autosomal dominant inheritance is recorded. The involved bones show osteoporosis and partial or complete destruction without evidence of reaction. Joints may be crossed and pleural effusion with thoracic involvement may be present (Fig. 14.16). MRI can show the underlying vascular tumor (Assoun et al. 1994).

Osteochondroma is a common benign tumor of the growing skeleton and probably the most common benign bone tumor of the chest wall. It is composed of cortical and medullary bone with a cartilaginous cap and is continuous with the underlying parent bone. It usually projects from the metaphysis of a tubular bone, but a rib, vertebra, clavicle, scapula, and the sternum may also be involved. The rib is most frequently affected near the costochondral junction (Fig. 14.17). Osteochondromas of the ribs may produce pleural effusion or hemothorax. Plain radiographs, CT, and MRI are able to depict the exostosis and its origin from the parent bone.

Mesenchymal hamartoma, also known as mesenchymoma, is a rare, benign, non-neoplastic lesion of infants and young children, usually identified at birth. Patients often present with a deforming chest wall mass, but a large intrathoracic mesenchymal hamartoma may cause severe and even fatal respiratory compromise. The lesion always arises in the ribs and is characterized by benign proliferations of skeletal tissues with a prominent cartilaginous component and hemorrhagic cavities (secondary aneurysmal bone cysts). The lesion may be bilateral and multicentric. On radiographs it appears as a partially calcified, extrapleural mass of the chest wall with involvement of one or more ribs. The rib deformity consists of partial or complete destruction, erosion, and enlargement. The lesion is well delineated, often lobulated, and measures up to 8 cm in diameter. Pathognomonic features recognized on CT and MRI consist of mineralized matrix and hemorrhagic cystic components (aneurysmal bone cysts). The mass may decrease in size without treatment and the prognosis of the patients is excellent. There are no reports of local recurrence following complete excision or metastasis (Ayala et al. 1993; Shamberger and Grier 1994; Groom et al. 2002) (Fig. 14.18).

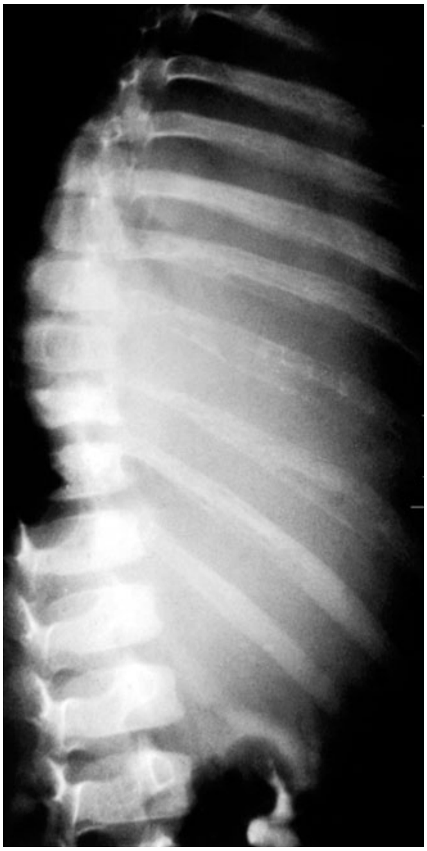

Fig. 14.16. Gorham disease in a 2.5-year-old girl. Left posterior oblique chest X-ray demonstrating multiple osteolytic and expansive rib lesions and pleural effusion. Several affected dorsal vertebral bodies show a loss of height

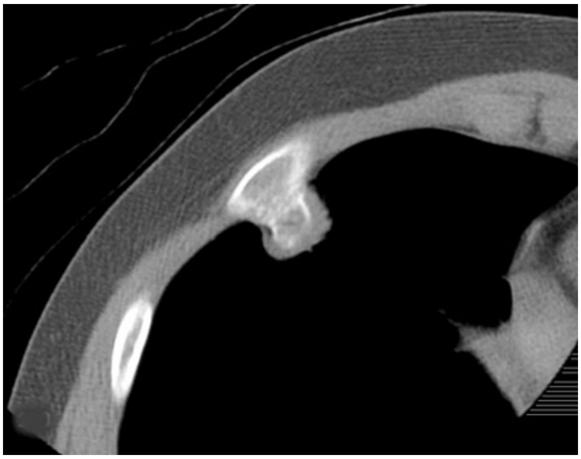

Fig. 14.17. Osteochondroma in a school-aged child. Close up section of axial chest CT scan shows ossified chondroma coming off the rib toward the chest inside

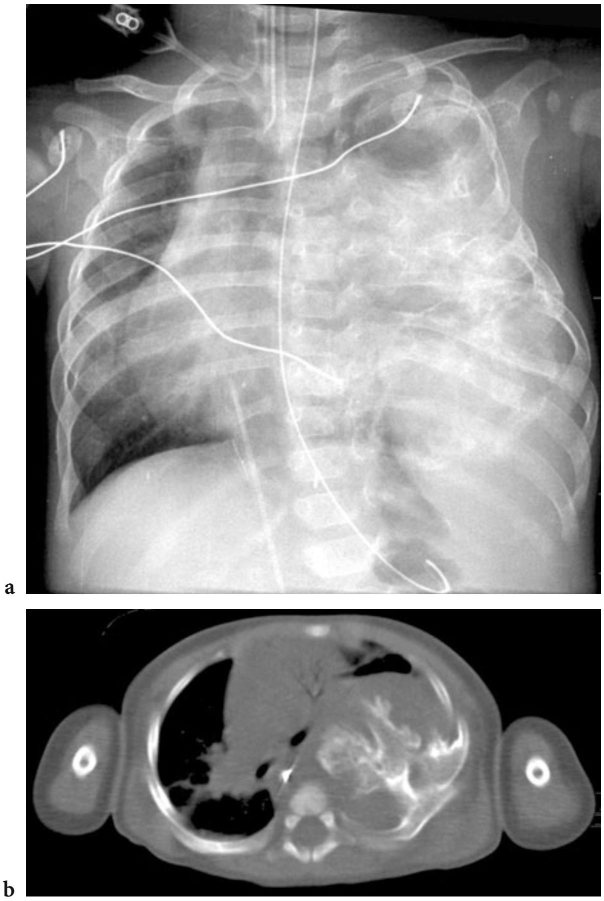

Fig. 14.18a,b. On prenatal US this baby was found to have an intrathoracic mass, confirmed on fetal MRI. At birth he had respiratory distress. Chest X-ray (**a**) and CT (**b**) showed marked, complex alterations of the left hemithorax due to bulky expansion of ribs and associated soft tissue changes, confirming the diagnosis of a mesenchymal hamartoma. At the age of 6 months, he was doing well

Lipoblastoma is a benign soft tissue tumor composed of fatty tissue, fibrovascular septa, and myxoid stroma. It is encountered in infants and young children, while lipoma is usually found in older individuals (Stout and Lattes 1967). The imaging features of a lipoblastoma consist of a fatty tumor containing areas of stroma that may enhance with intravenous contrast (Fig. 14.19).

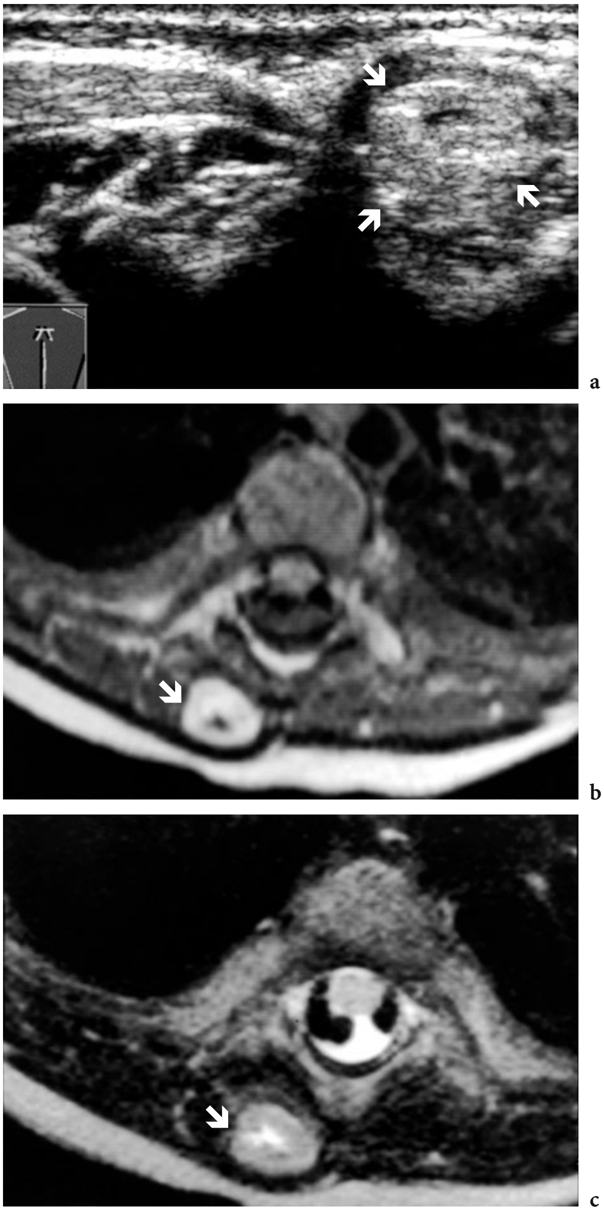

Fig. 14.19a–c. Lipoblastoma in a 5-month-old girl. **a** Transverse ultrasound (US) view of upper back region (prone position) shows right paramedian round and mostly hyperechoic structure (*arrows*) with small hypoechoic inner portion. **b,c** Axial T1- and T2-weighted MRI scans show well defined fatty tumor (*arrows*) with are correlating with US

Fibrous tumors and tumor-like lesions central stroma, a large and diverse group of distinct entities that are relatively frequent, particularly in infants and young children, mostly boys. Most fibrous tumors exhibit benign or semimalignant behaviour. The chest wall may be affected by extraabdominal fibromatosis (desmoid or aggressive fibromatosis), which can involve the muscle and overlying fascia of the shoulder girdle of adolescents and young adults. The tumor has the potential to grow to a large size, to recur, and to infiltrate neighboring tissues. The imaging features are usually nonspecific, but low signal intensity on T1- and T2-weighted sequences may suggest a fibrous tumor. Other fibrous lesions

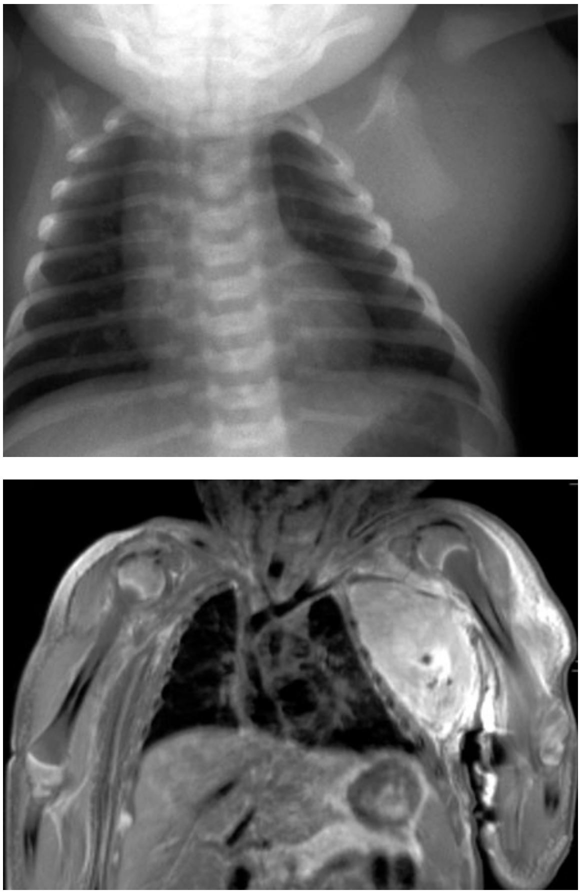

Fig. 14.20a,b. Congenital fibrosarcoma in a 3-day-old boy. **a** Chest X-ray shows large left extrathoracic soft tissue mass with severe displacement of ipsilateral scapula and deforming left hemithorax. **b** Coronal T1-weighted contrast-enhanced MRI view of the thorax with suboptimal fat saturation demonstrates diffusely enhancing extrathoracic soft tissue mass impinging left lateral chest wall

that can affect the chest wall include fibrous hamartoma of infancy, infantile myofibromatosis, juvenile hyaline fibromatosis, and infantile or adult type fibrosarcoma (Eich et al. 1998) (Fig. 14.20).

Neurogenic tumors, such as schwannomas and neurofibromas (particularly in patients with neurofibromatosis) or neuroblastoma and its variants (ganglioneuroblastoma and ganglioneuroma), may involve the intercostal nerves or the sympathetic ganglia. They may lead to erosion, thinning, destruction, and separation of adjacent ribs (Figs. 14.21 and 14.22). Patients with neurofibromatosis type I may suffer from extensive involvement of the chest wall by plexiform neurofibromas or malignant neurofibrosarcoma. In addition such patients may show widening of the ribs (twisted ribbon appearance) and short segment kyphoscoliosis due to dysplastic vertebrae, with widening of the spinal canal and intervertebral foramina, and dorsal scalloping of the vertebral bodies (Kuhn 2003).

The most prevalent malignant tumors of the chest wall belong to the Ewing's sarcoma family, including Ewing's sarcoma, Askin's tumor and peripheral primitive neuroectodermal tumors (PNET) (Fig. 14.23) and the rhabdomyosarcomas. Of all malignant chest wall tumors in children approximately 50%–65% belong to the Ewing's sarcoma group, while up to 33% are either alveolar or embryonal rhabdomyosarcomas (Shamberger and Grier 1994; Shamberger et al. 1989; Dang et al. 1999). These tumors are dealt with elsewhere in this book. Other malignant tumors, such as osteosarcoma (Fig. 14.24) are much less common, and metastases to the chest wall are exceedingly rare in children (Fig. 14.25).

Pediatric chest wall tumors may initially be mistaken for an empyema because of signs and symptoms of inflammation or infection and a pleural mass. Raised white cell count, neutrophilia, elevated C-reactive protein, and moderate to high pyrexia in combination with an opacity on standard chest radiographs may suggest an empyema or a loculated pleural collection rather than a tumor. Ultrasonography of the chest may miss the evidence of the tumor. Even CT without IV contrast may fail to show the solid component of the neoplasm (Fig. 14.26). Therefore CT or MRI with IV contrast is recommended to show the enhancing, solid tumor, its origin, and possible metastases, and to avoid unnecessary thoracocentesis or chest tube insertion (Sharif et al. 2006).

The differential diagnosis of a neoplasm includes pseudoneoplasms of other etiologies. Amongst these mention should be made of (recurrent) hematomas in a hemophiliac patient, which may present as a mass lesion (Fig. 14.27). Musculoskeletal hemorrhage of hemophiliac patients most commonly occurs within joints, but hemorrhage within bone and soft tissues can take place and cause local destructive bone changes. Subperiosteal hematomas can induce new bone formation or atrophy, or even complete destruction of the underlying bone. Such hemophiliac pseudotumors are relatively uncommon. They may extend from hemarthrosis under pressure, or develop from intraosseous, subperiosteal or soft tissue bleeding. They may appear aggressive with a large soft tissue mass with or without bone destruction (Kuhn 2003).

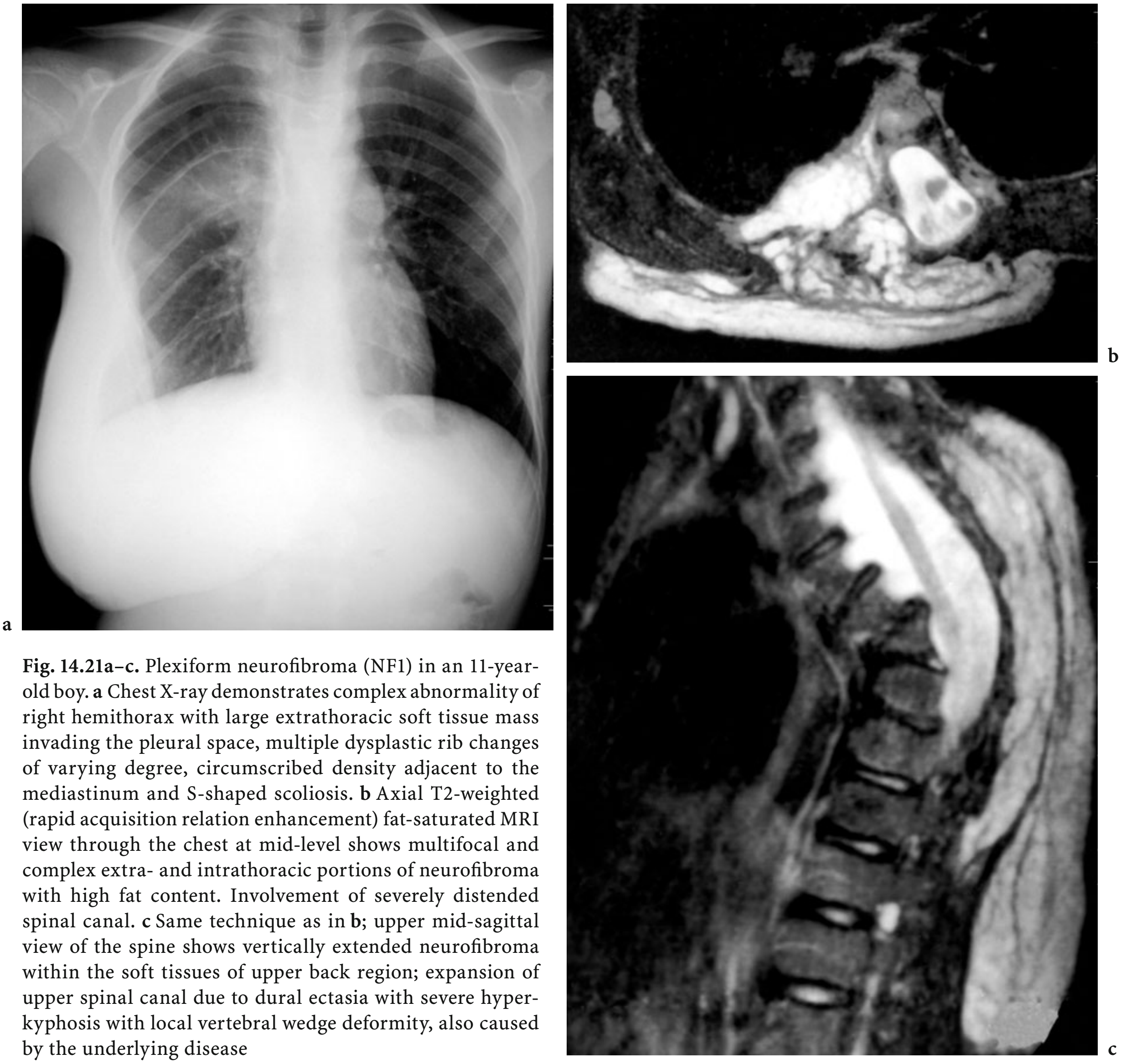

Fig. 14.21a–c. Plexiform neurofibroma (NF1) in an 11-year-old boy. **a** Chest X-ray demonstrates complex abnormality of right hemithorax with large extrathoracic soft tissue mass invading the pleural space, multiple dysplastic rib changes of varying degree, circumscribed density adjacent to the mediastinum and S-shaped scoliosis. **b** Axial T2-weighted (rapid acquisition relation enhancement) fat-saturated MRI view through the chest at mid-level shows multifocal and complex extra- and intrathoracic portions of neurofibroma with high fat content. Involvement of severely distended spinal canal. **c** Same technique as in **b**; upper mid-sagittal view of the spine shows vertically extended neurofibroma within the soft tissues of upper back region; expansion of upper spinal canal due to dural ectasia with severe hyperkyphosis with local vertebral wedge deformity, also caused by the underlying disease

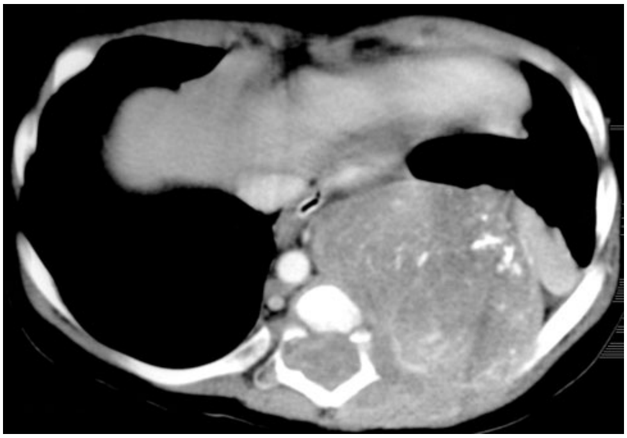

Fig. 14.22. Thoraco-abdominal neuroblastoma in a 5-month-old boy. Contrast-enhanced axial CT scan through lower chest area shows huge solid posterior mediastinal mass containing calcifications and extending extrathoracically through posterior chest wall as well as intraspinally. Notice expansive deformity of spinal canal due to long-standing neoplastic process. The child had neurological impairment that persisted after therapy

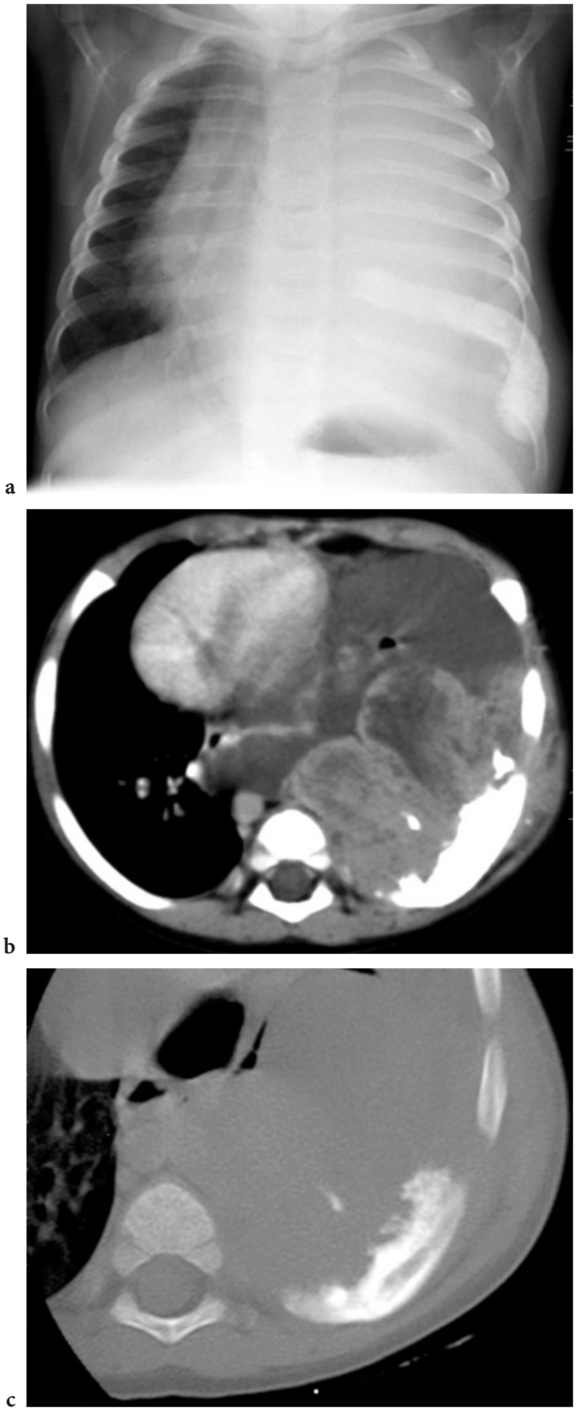

Fig. 14.23a–c. Primitive neuroectodermal tumor (PNET) in a 14-month-old boy. **a** Anteroposterior chest X-ray shows mass effect within left hemithorax with displacement of heart and mediastinal structures to the right. Diffusely sclerotic and enlarged eighth left rib. **b** Axial contrast-enhanced CT scan at mid-level of thorax demonstrates irregularly hypertrophic posterior aspect of eighth left rib associated with a huge intrathoracic soft tissue mass. **c** Close-up bone view shows osseous changes in more detail

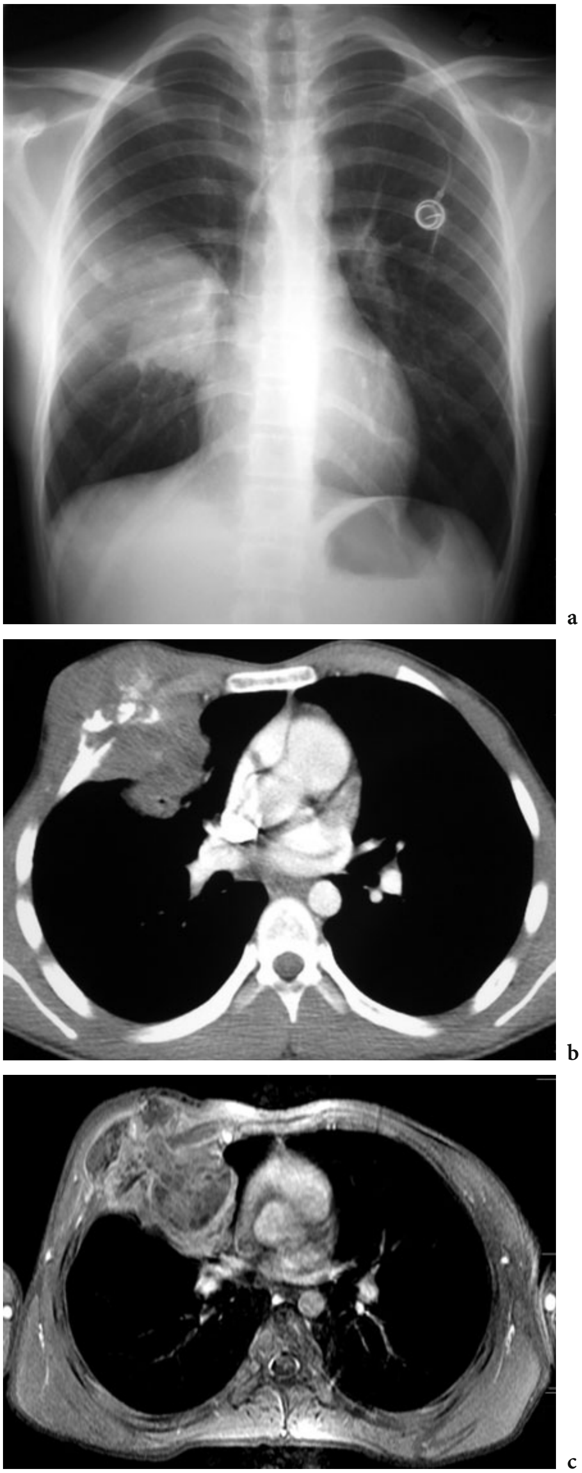

Fig. 14.24a–c. A 16-year-old boy with osteosarcoma of third rib on the right. **a** Frontal chest radiograph following insertion of a port-a-cath. **b** Contrast-enhanced axial CT image. **c** Contrast-enhanced axial MR image (T1 weighted gradient echo, with fat saturation) showing focal destruction of the anterior portion of the rib with an intra- and extrathoracic soft tissue mass with partial calcification

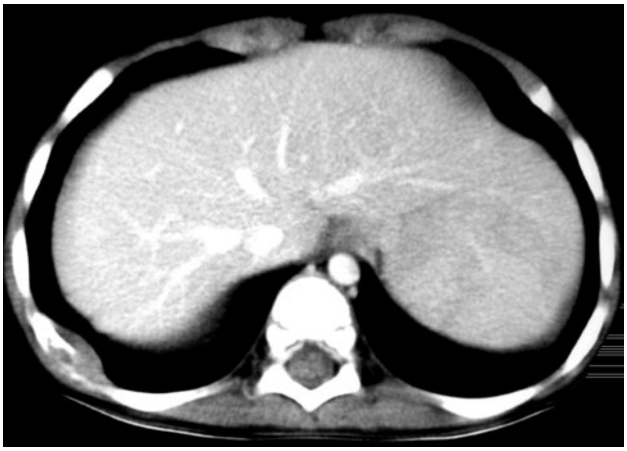

Fig. 14.25. Metastatic renal clear cell sarcoma in a 2.5-year-old boy. Contrast-enhanced axial CT scan through lower chest area shows destructive metastatic lesion in the postero-lateral aspect of the ninth right rib extending intra- and extrathoracically. This child had simultaneous vertebral, orbital and cranial vault metastases

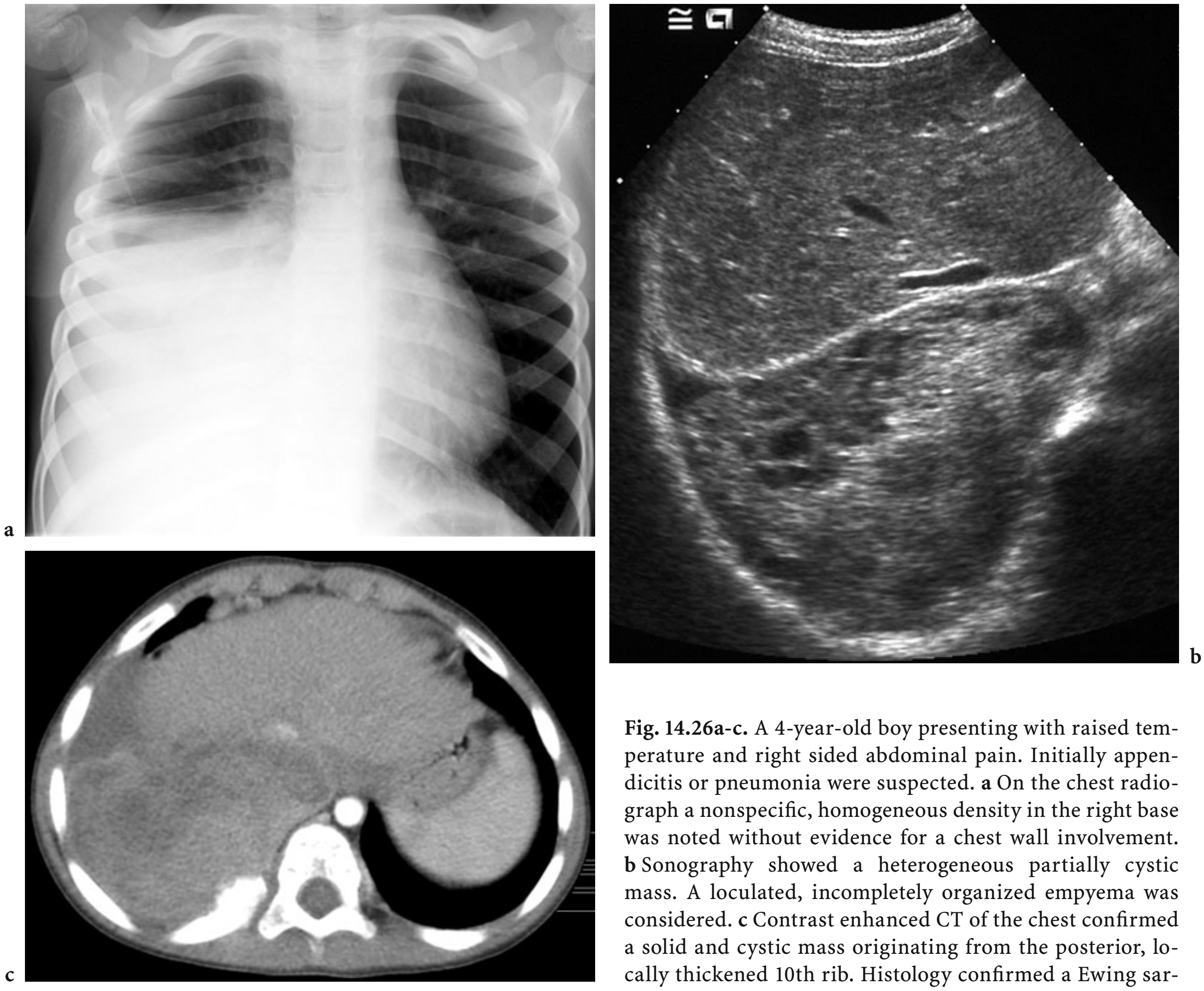

Fig. 14.26a-c. A 4-year-old boy presenting with raised temperature and right sided abdominal pain. Initially appendicitis or pneumonia were suspected. **a** On the chest radiograph a nonspecific, homogeneous density in the right base was noted without evidence for a chest wall involvement. **b** Sonography showed a heterogeneous partially cystic mass. A loculated, incompletely organized empyema was considered. **c** Contrast enhanced CT of the chest confirmed a solid and cystic mass originating from the posterior, locally thickened 10th rib. Histology confirmed a Ewing sar-

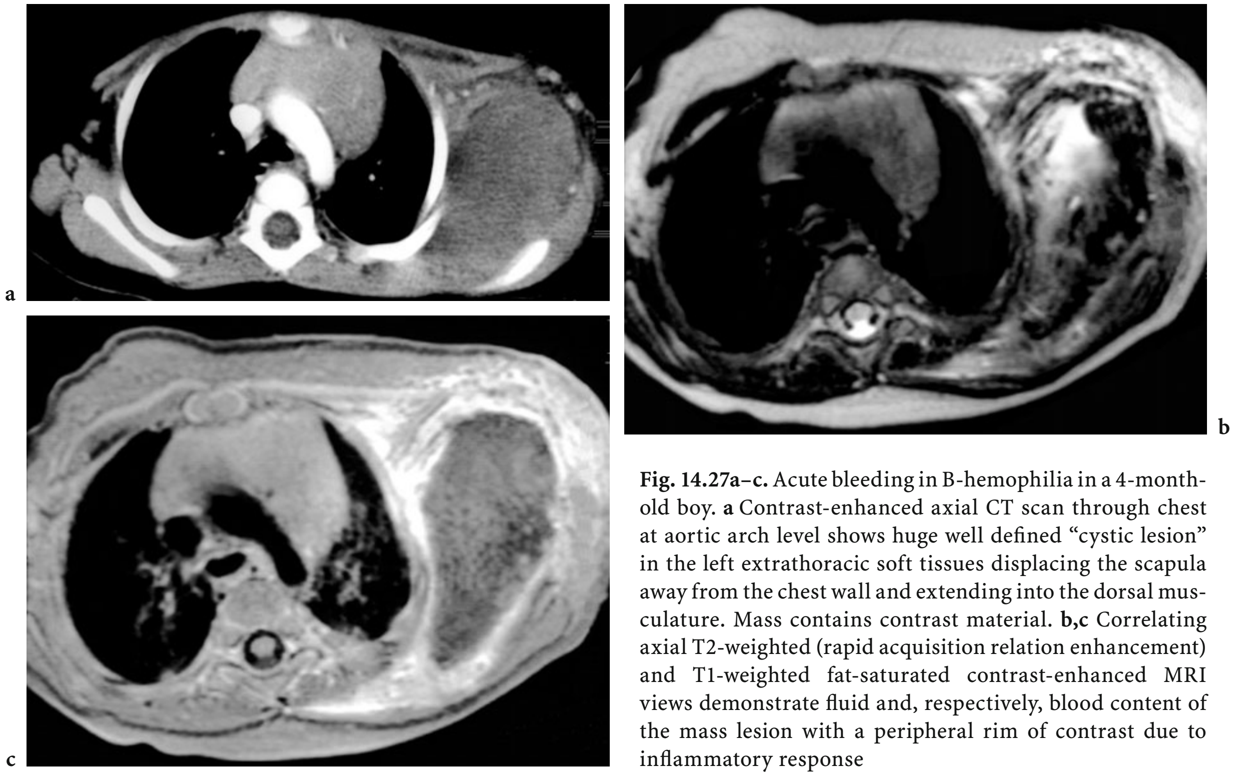

Fig. 14.27a–c. Acute bleeding in B-hemophilia in a 4-month-old boy. **a** Contrast-enhanced axial CT scan through chest at aortic arch level shows huge well defined "cystic lesion" in the left extrathoracic soft tissues displacing the scapula away from the chest wall and extending into the dorsal musculature. Mass contains contrast material. **b,c** Correlating axial T2-weighted (rapid acquisition relation enhancement) and T1-weighted fat-saturated contrast-enhanced MRI views demonstrate fluid and, respectively, blood content of the mass lesion with a peripheral rim of contrast due to inflammatory response

14.5
Trauma

14.5.1
Accidental Trauma

With the exception of rib fractures and burns, traumatic lesions of the chest wall are usually part of a more complex injury to the chest. They may be caused by direct blunt contusion or compression, axial trauma to the spine, penetrating chest or abdominal trauma, rapid deceleration and other mechanisms. Severe trauma to the chest or other parts of the body involving the chest, as in polytrauma, commonly results in damage of multiple thoracic structures, including intrathoracic organs. Referral for imaging usually follows clinical assessment and stabilization of vital conditions. Plain films of the chest and abdomen may reveal life-threatening injuries. CT, however, is the method of choice for evaluation of the chest in a severe or potentially life threatening posttraumatic emergency situation.

This section focuses on a few traumatic injuries to the child's chest wall that are characteristic of some specific insult or may be difficult to assess and diagnose. Rib fractures are easily overlooked on an emergency chest film. They may be related to an adjacent pleural or lung injury. Pneumo- and/or hematothorax may coexist. Trauma to the spine due to fall, motor vehicle accident, or various sport activities is not uncommon. The thoracic spine is the most frequently affected segment, although spinal trauma per se accounts for a small percentage of all childhood trauma (Stulik et al. 2006). The injury may consist of one or multiple vertebral compression fractures with paraspinal hemorrhage and edema (Fig. 14.28). The paraspinal soft tissue mass from local hemorrhage may suggest the presence of associated aortic rupture. However, traumatic rupture of the thoracic or abdominal aorta is rare in the pediatric age group and is excluded or demonstrated by contrast-enhanced CT and transesophageal echocardiography (Lowe et al. 1998; Spouge et al. 1991; Trachiotis et al. 1996). In blunt thoracoabdominal trauma, aortic injury occurs almost exclusively in the thoracic segment (Choit et al. 2006) and angiography might be crucial in such

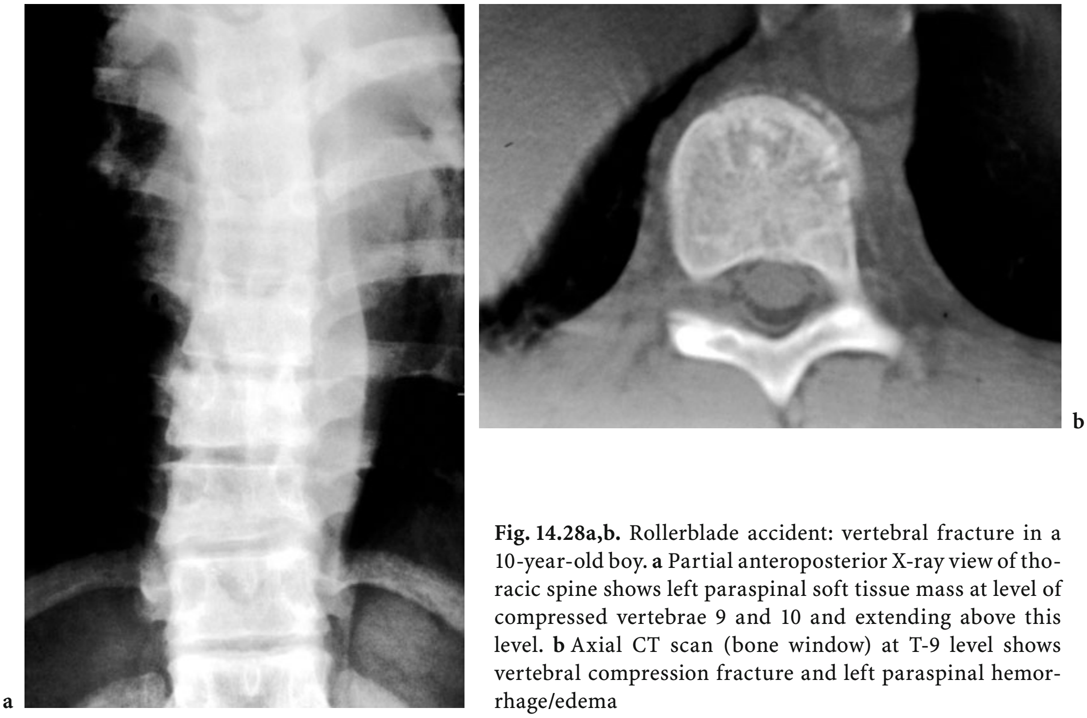

Fig. 14.28a,b. Rollerblade accident: vertebral fracture in a 10-year-old boy. **a** Partial anteroposterior X-ray view of thoracic spine shows left paraspinal soft tissue mass at level of compressed vertebrae 9 and 10 and extending above this level. **b** Axial CT scan (bone window) at T-9 level shows vertebral compression fracture and left paraspinal hemorrhage/edema

circumstance (Puapong et al. 2006). Involvement of the spinal canal with neurological symptoms is uncommon and is less frequent in children and teenagers than in adults.

In children and adolescents and even in young adults, the so-called sternoclavicular dislocation is, in fact, a Salter type 1 or 2 medial clavicular epiphysiolysis (Cope et al. 1991; Lewonowski and Bassett 1992). It is uncommon and usually missed at the initial clinical examination. A fall on the shoulder, occurring during a bicycle accident or in contact sports, is the typical cause. If a sternoclavicular injury is suspected, contrast-enhanced CT is the diagnostic method of choice (Cope et al. 1991; Yang et al. 1996; Gobet et al. 2004) (Figs. 14.29 and 14.30). Intravenous contrast is necessary to demonstrate compromise of the supracardiac vasculature, a complication of retrosternal clavicular dislocation that is less relevant in children than in adults. Dysphagia, however, is common. A radiographic plain film technique using special lateral projections of the sterno-clavicular joint, provides specific diagnosis as to posterior or anterior displacement of the clavicle. It needs technical skill and might be used if CT is not available (Heinig 1968; Lee and Gwinn 1974). This projection is, however, difficult to obtain and films often need to be repeated.

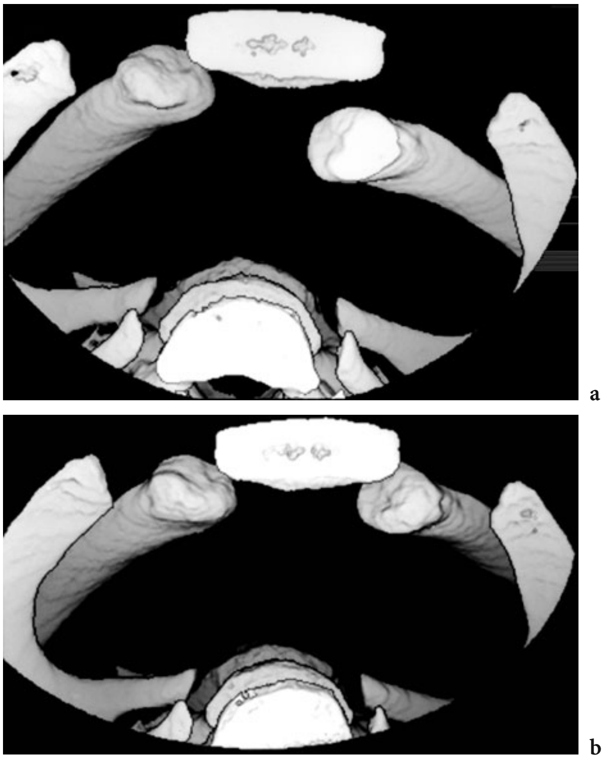

Fig. 14.29a,b. Sternoclavicular dislocation (I) in an 8-year-old boy. **a** Three-dimensional CT reconstruction demonstrates posterior dislocation of left clavicle. **b** Same technique as in **a** after closed reduction shows normal sternoclavicular relationship

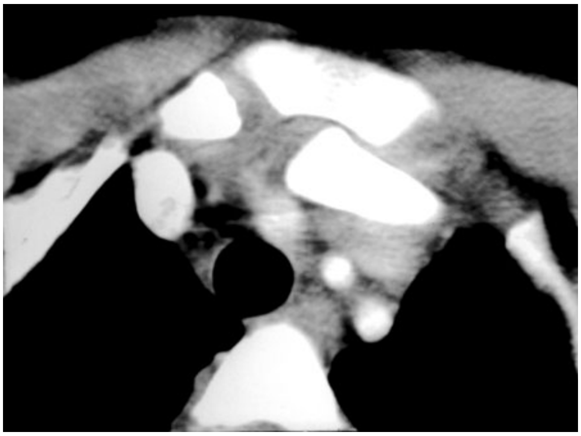

Fig. 14.30. Sternoclavicular dislocation (II) in a 15-year-old girl. Axial contrast-enhanced CT scan through sternoclavicular area demonstrates dislocation of left medial clavicular end behind manubrium of sternum and medially, thus space-occupying and explaining difficulty in swallowing

14.5.2
Non-Accidental Trauma

Child abuse must be considered in any infant and young child with rib fractures (Bulloch et al. 2000; Cadzow and Armstrong 2000). Underlying conditions of skeletal morbidity such as a disorder of bone metabolism, a syndrome or a dysplasia need to be ruled out. Any apparent accidental trauma, including a motor vehicle accident requires critical consideration in view of its pathogenetic explanation (Spevak et al. 1994).

In child abuse, rib fractures are due to characteristic mechanical factors involved in violence to the child's chest. They are commonly noticed in the posterior rib segments close to the costovertebral joints, but may occur anywhere along the entire rib cage, including the costochondral junctions arc (Kleinman 1996; Ng and Hall 1998). The rib fractures tend to be multiple and bilateral and somewhat symmetrical (Fig. 14.31). Ample specific information regarding the mechanism, pathophysiology, anatomic, and histologic findings in skeletal and soft tissue involvement of the entire body in child abuse has been researched and described by Kleinman (1998). If child abuse is suspected, a formal evaluation of the entire skeleton has to be performed and the information transmitted to the clinician(s) responsible for the child's care (Nimkin and Kleinman 2001). Digital radiography has been introduced successfully in the skeletal evaluation of nonaccidental trauma in infants (Kleinman et al. 2002). Radiography as the primary and main tool to evaluate the infant's skeleton systematically, might be complemented by scintigraphy, CT and ultrasonography (Nimkin and Kleinman 2001). Whole-body magnetic resonance imaging has a potential for future protocols in the differential diagnosis of non-accidental injuries (Fig. 14.32).

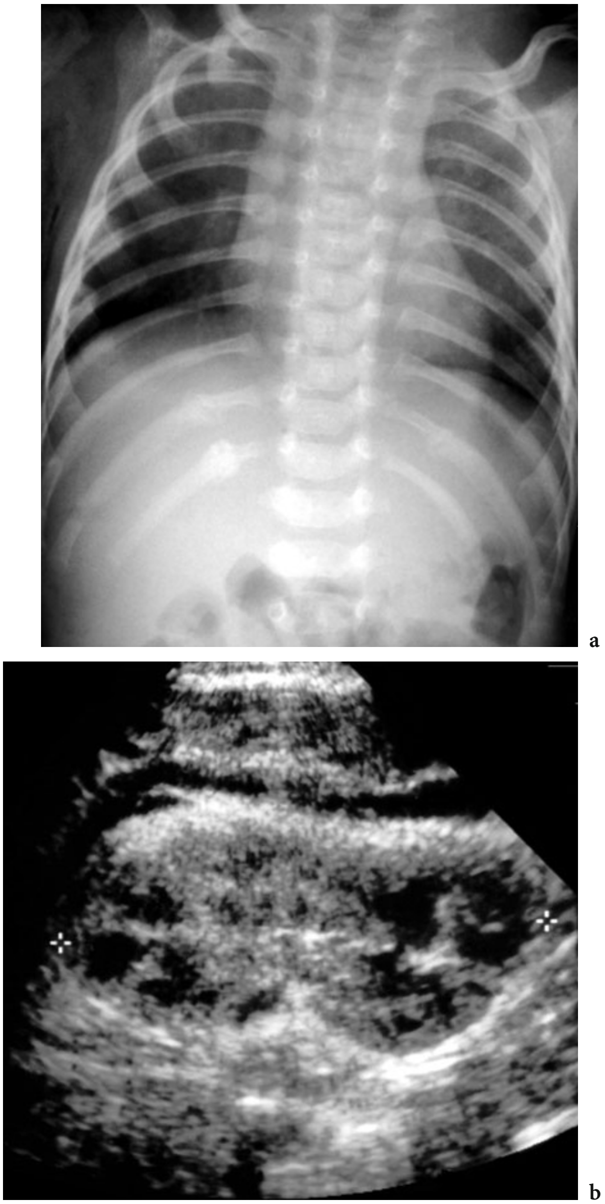

Fig. 14.31a,b. Rib fractures from non-accidental trauma in a 4-week-old boy. **a** Anteroposterior chest X-ray shows healing paraspinal fractures of the tenth and eleventh right and the tenth left ribs. **b** On previous posterior longitudinal ultrasound at 10 days a fluid collection dorsal to the right kidney was missed

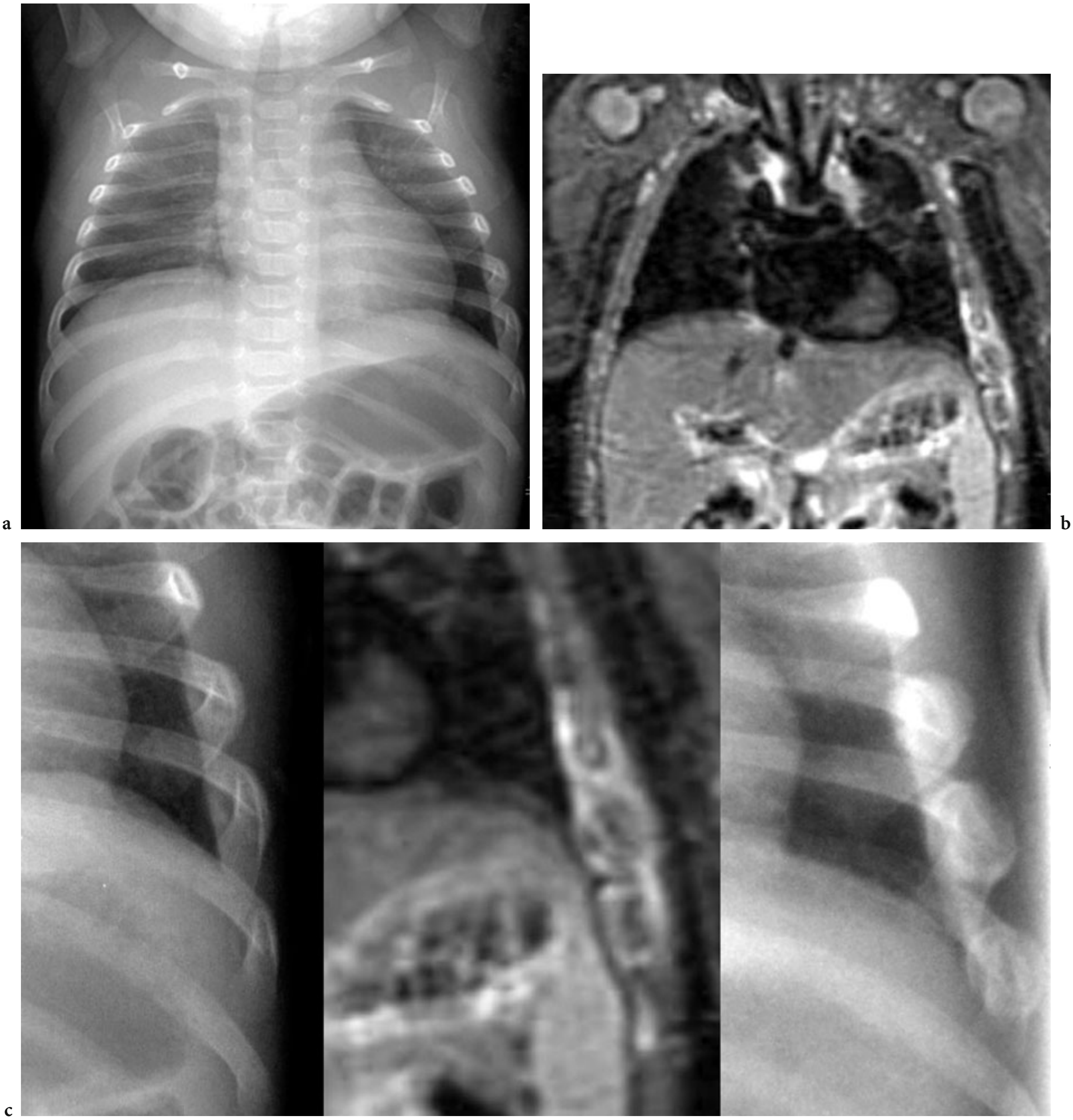

Fig. 14.32a–c. Rib fractures from non-accidental trauma in a 2-month old girl. **a** Chest X-ray shows healed fracture of ninth right rib posteriorly and suspected fractures of sixth to eighth left ribs laterally. **b** Coronal STIR MR shows T2-hyperintense bone marrow edema and local soft tissue swelling of the involved left ribs correlating with a. Similar finding for ninth right rib (not shown). **c** Close-up view of a and b comparing to follow-up X-ray 2 weeks later with increased callus formation (left to right sequence)

Premature babies undergoing physiotherapy for chronic lung disease as part of intensive care, may radiographically mimic non-accidental rib injuries (Fig. 14.33) (Chalumeau et al. 2002). This may especially become a problem at re-admission if the fractures had remained unrecognized before primary hospital discharge. In contrast to the effects of physiotherapy, rib fractures from cardiopulmonary resuscitation are unlikely in infants (Spevak et al. 1994).

Acknowledgements. We would like to acknowledge the contribution of imaging material by Drs. Paul Babyn and David Manson, The Hospital for Sick Children, Toronto, Dr. Javier Lucaya, HMI Vall d'Hebron, Barcelona, and Drs. Miralles and Rasero from Madrid.

References

Assoun J, Richardi G, Railhac JJ, Le Guennec P, Caulier M, Dromer C, Sixou L, Fournie B, Mansat M, Durroux D (1994) CT and MRI of massive osteolysis of Gorham. J Comput Assist Tomogr 18:981–984

Ayala AG, Ro JY, Bolio-Solis A, Hernandez-Batres F, Eftekhari F, Edeiken J (1993) Mesenchymal hamartoma of the chest wall in infants and children: a clinicopathological study of five patients. Skeletal Radiol 22:569–576

Bulloch B, Schubert CJ, Brophy PD, Johnson N, Reed MH, Shapiro RA (2000) Cause and clinical characteristics of rib fractures in infants. Pediatrics 105:E48

Bush CH, Kalen V (1999) Three-dimensional computed tomography in the assessment of congenital scoliosis. Skeletal Radiol 28:632–637

Cadilhac C, Fenoll B, Peretti A et al. (2000) Congenital pseudarthrosis of the clavicle: 25 childhood cases. Rev Chir Orthop Reparatrice Appar Mot 86:575–580

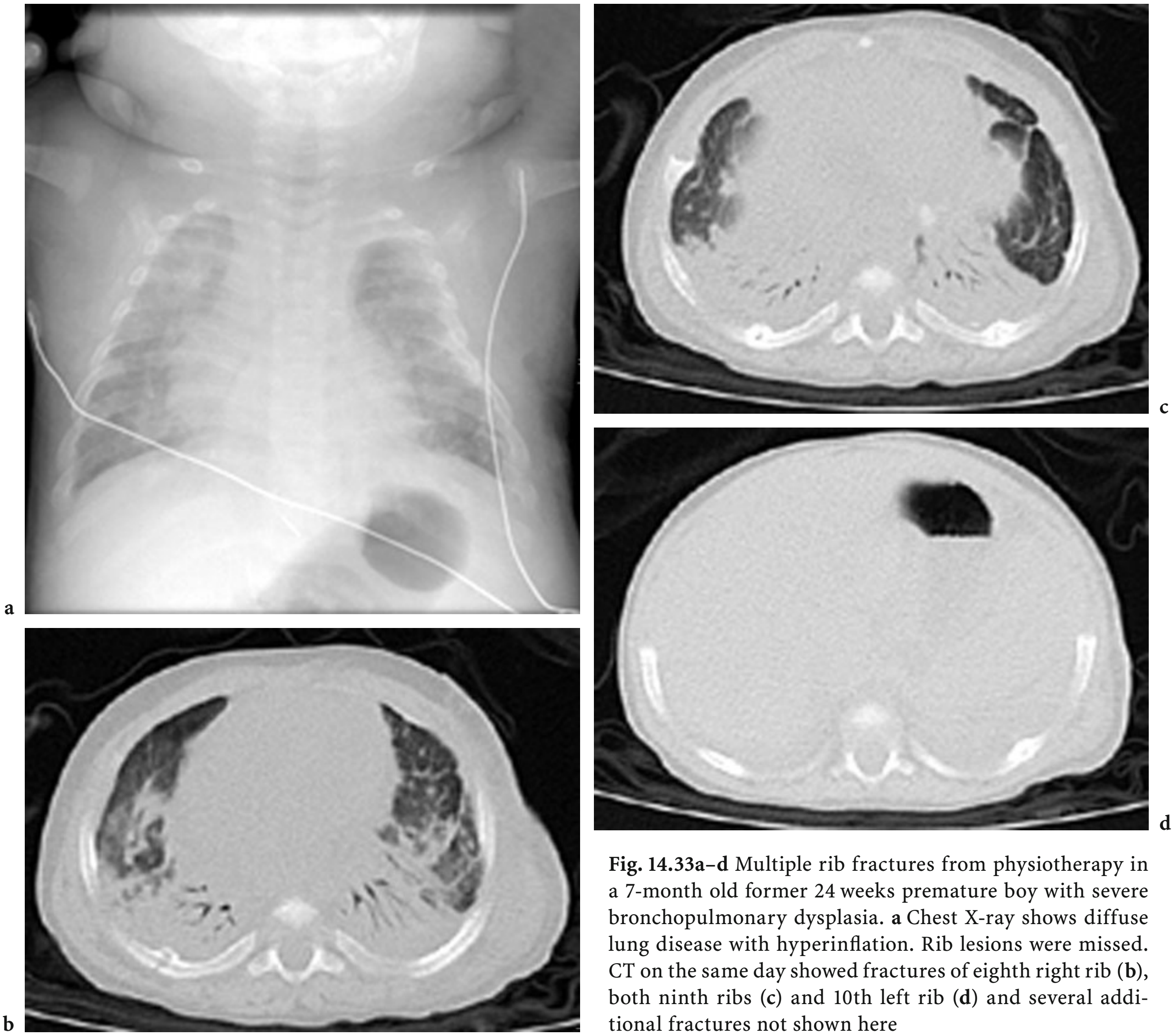

Fig. 14.33a–d Multiple rib fractures from physiotherapy in a 7-month old former 24 weeks premature boy with severe bronchopulmonary dysplasia. **a** Chest X-ray shows diffuse lung disease with hyperinflation. Rib lesions were missed. CT on the same day showed fractures of eighth right rib (**b**), both ninth ribs (**c**) and 10th left rib (**d**) and several additional fractures not shown here

Cadzow SP, Armstrong KL (2000) Rib fractures in infants: red alert! The clinical features, investigations and child protection outcomes. J Paediatr Child Health 36:322–326

Chalumeau M, Foix-L'Helias L, Scheinmann P, Zuani P, Gendrel D, Ducou-le-Pointe H (2002) Rib fractures after chest physiotherapy for bronchiolitis or pneumonia in infants. Pediatr Radiol 32:644–647

Cho TJ, Choi IH, Chung CY et al. (2000) The Sprengel deformity. Morphometric analysis using 3D-CT and its clinical relevance. J Bone Joint Surg Br 82:711–718

Choit RL, Tredwell SJ, Leblanc JG, Reilly CW, Mulpuri K (2006) Abdominal aortic injuries with chance fractures in pediatric patients. J Pediatr Surg 41:1184–1190

Chuang JH, Wan YL (1995) Evaluation of pectus excavatum with repeated CT scans. Pediatr Radiol 25:654–656

Cope R, Riddervold HO, Shore JL, Sistrom CL (1991) Dislocations of the sternoclavicular joint: anatomic basis, etiologies, and radiologic diagnosis. J Orthop Traum 5:379–384

Coury CH, Delaporte J (1954) Les anomalies congénitales des cotes. Formes anatomo-radiologiques et incidences pratiques (a propos de 288 cas). Sem Hop Paris 30:2656–2681

Dang NC, Siegel SE, Phillips JD (1999) Malignant chest wall tumors in children and young adults. J Pediatr Surg 34:1773–1778

Daunt SW, Cohen JH, Miller SF (2004) Age-related normal ranges for the Haller index in children. Pediatr Radiol 34:326–330

Donnelly LF, Taylor CN, Emery KH et al. (1997) Asymptomatic, palpable, anterior chest wall lesions in children: is cross-sectional imaging necessary? Radiology 202:829–831

Donnelly LF, Frush DP, Foss JN et al. (1999) Anterior chest wall: frequency of anatomic variations in children. Radiology 212:837–840

Eich GF (2007) Chest wall abnormalities which cause neonatal respiratory distress. In: Donoghue V (ed) Radiological imaging of the neonatal chest. Springer, Berlin Heidelberg New York (in press)

Eich GF, Hoeffel JC, Tschäppeler H, Gassner I, Willi UV (1998) Fibrous tumours in children: imaging features of a heterogeneous group of disorders. Pediatr Radiol 28:500–509

Faro SH, Mahboubi S, Ortega W (1993) CT diagnosis of rib anomalies, tumors, and infection in children. Clin Imaging 17:1–7

Fokin AA (2000) Cleft sternum and sternal foramen. Chest Surg Clin North Am 10:261–276

Glass RB, Norton KI, Mitre SA, Kang E (2002) Pediatric ribs: a spectrum of abnormalities. Radiographics 22:87–104

Gobet R, Meuli M, Altermatt S, Jenni V, Willi UV (2004) Medial clavicular epiphysiolysis in children: the so-called sterno-clavicular dislocation. Emerg Radiol 10:252–255

Golladay ES, Hale JA, Mollitt DL, Seibert JJ (1985) Chest wall masses in children. South Med J 78:292–295

Gorham LW, Stout AP (1955) Massive osteolysis (acute spontaneous absorption of bone, phantom bone, disappearing bone): its relation to hemangiomatosis. J Bone Joint Surg 37A:985–1004

Groom KR, Murphey MD, Howard LM, Lonergan GJ, Rosado-De-Christenson ML, Torop AH (2002) Mesenchymal hamartoma of the chest wall: radiologic manifestations with emphasis on cross-sectional imaging and histopathologic comparison. Radiology 222:205–211

Haller JA, Loughlin GM (2000) Cardiorespiratory function is significantly improved following surgery for severe pectus excavatum. Proposed treatment guidelines. J Cardiovasc Surg (Torino) 41:125–130

Haller JA, Kramer SS, Lietman SA (1987) Use of CT scans in selection of patients for pectus excavatum superior: a preliminary report. J Pediatr Surg 22:904–906

Heinig CF (1968) Retrosternal dislocation of the clavicle: early recognition, X-ray diagnosis and management. J Bone Joint Surg Am 50:830

Herrmann K, Zech C, Strauss T, Hatz R, Schoenberg S, Reiser M (2006) Cine-MRI of the thorax in patients with pectus excavatum. Radiologe 46:309–316

Kamaruddin K, Wright NB, Pilling DW (1995) Intrathoracic rib. Pediatr Radiol 25:60–61

Kellenberger CJ, Epelman M, Miller SF, Babyn PS (2004) Fast STIR whole-body MR imaging in children. Radiographics 24:1317–1330

Kleinman PK (1992) Fractures of the rib head in abused infants. Radiology 185:119–123

Kleinman PK (1996) Rib fractures in 31 abused infants: postmortem radiologic-histopathologic study. Radiology 200:807–810

Kleinman PK (1998) Diagnostic imaging of child abuse, 2nd edn. Mosby, St Louis

Kleinman PK, O'Connor B, Nimkin K, Rayder SM, Spevak MR, Belanger PL, Getty DJ, Karellas A (2002) Detection of rib fractures in an abused infant using digital radiography: a laboratory study. Pediatr Radiol 32:896–901

Kozlowski K, Campbell J, Morris L, Sprague P, Taccone A, Beluffi G, Marcinski A, Porta F, Stevens M (1989) Primary rib tumours in children (report of 27 cases with short literature review). Aust Radiol 33:210–222

Kuhn JP (2003) Caffey's pediatric diagnostic imaging, 10th edn. Mosby, Philadelphia

Kumar AP, Green AL, Smith JW, Pratt CB (1977) Combined therapy for malignant tumors of the chest wall in children. J Pediatr Surg 12:991–999

Lachman RS (2006) Taybi and Lachman's radiology of syndromes, metabolic disorders and skeletal dysplasias, 5th edn. Mosby, St Louis

Lee FA, Gwinn JL (1974) Retrosternal dislocation of the clavicle. Radiology 110:631–634

Letts M, Davidson D, Birdi N, Joseph M (1999) The SAPHO syndrome in children: a rare cause of hyperostosis and osteitis. J Pediatr Orthop 19:297–300

Levy M, Goldberg I, Fischel RE, Frisch E, Maor P (1981) Friedrich's disease. Aseptic necrosis of the sternal end of the clavicle. J Bone Joint Surg Br 63:539–541

Lew DP, Waldvogel FA (1997) Osteomyelitis. N Engl J Med 336:999–1007

Lewonowski K, Bassett GS (1992) Complete posterior sternoclavicular epiphyseal separation. A case report and review of the literature. Clin Orthop 281:84–88

Lowe LH, Bulas DI, Eichelberger MD, Martin GR (1998) Traumatic aortic injuries in children: radiologic evaluation. AJR Am J Roentgenol 170:39–42

Nathanson I (1994) Chest wall abnormalities. In: Loughlin GM, Eigen H (eds) Respiratory disease in children:

diagnosis and management. Williams and Wilkins, Baltimore, pp 533–541

Ng CS, Hall CM (1998) Costochondral junction fractures and intra-abdominal trauma in non-accidental injury (child abuse). Pediatr Radiol 28:671–676

Nimkin K, Kleinman PK (2001) Imaging of child abuse. Radiol Clin North Am 39:843–864

Pretorius ES, Haller JA, Fishman EK (1998) Spiral CT with 3D reconstruction in children requiring reoperation for failure of chest wall growth after pectus excavatum surgery. Preliminary observations. Clin Imaging 22:108–116

Puapong D, Brown CV, Katz M, Kasotakis G, Applebaum H, Salim A, Rhee P, Demetriades D (2006) Angiography and the pediatric trauma patient: a 10-year review. J Pediatr Surg 41:1859–1863

Raichura N, Entwisle J, Leverment J, Beardsmore CS (2001) Breath-hold MRI in evaluating patients with pectus excavatum. Br J Radiol 74:701–708

Shamberger RC, Grier HE (1994) Chest wall tumors in infants and children. Semin Pediatr Surg 3:267–276

Shamberger RC, Grier HE, Weinstein HJ, Perez-Atayde AR, Tarbell NJ (1989) Chest wall tumors in infancy and childhood. Cancer 63:774–785

Sharif HS, Clark DC, Aabed MY, Aideyan OA, Haddad MC, Mattsson TA (1990) MR imaging of thoracic and abdominal wall infections: comparison with other imaging procedures. AJR Am J Roentgenol 154:989–995

Sharif K, Alton H, Clarke J, Desai M, Morland B, Parikh D (2006) Paediatric thoracic tumours presenting as empyema. Pediatr Surg Int 22:1009–1014

Spevak MR, Kleinman PK, Belanger PL, Primack C, Richmond JM (1994) Cardiopulmonary resuscitation and rib fractures in infants. A postmortem radiologic-pathologic study. JAMA 272:617–618

Spouge AR, Burrows PE, Armstrong D, Daneman A (1991) Traumatic aortic rupture in the pediatric population. Role of plain film, CT and angiogaphy in the diagnosis. Pediatr Radiol 21:324–328

Stout AP, Lattes R (1967) Atlas of tumor pathology, second series, fascicle I: tumors of the soft tissues. Armed Forces Institute of Pathology, Washington DC

Stranzinger E, Kellenberger CJ, Braunschweig S, Hopper R, Huisman TAGM (2007) Whole body STIR MR imaging in suspected child abuse: an alternative to skeletal survey radiology? Eur J Radiol (in press)

Stulik J, Pesl T, Kryl J, Vyskocil T, Sebesta P, Havranek P (2006) Spinal injuries in children and adolescents. Acta Chir Orthop Traumatol Cech 73:313–320

Thompson JS (1976) Cervical herniation of the lung. Report of a case and review of the literature. Pediatr Radiol 4:190–192

Trachiotis GD, Sell JE, Pearson GD, Martin GR, Midgley FM (1996) Traumatic thoracic aortic rupture in the pediatric patient. Ann Thorac Surg 62:724–731

Wright AR, Milner RH, Bainbridge LC et al. (1992) MR and CT in the assessment of Poland syndrome. J Comput Assist Tomogr 16:442–444

Yang J, al-Etani H, Letts M (1996) Diagnosis and treatment of posterior sternoclavicular joint dislocations in children. Am J Orthop 25:565–569

Pediatric Cardiac MRI

Rajesh Krishnamurthy and Taylor Chung

CONTENTS

15.1 **Introduction: Segmental Approach to Heart Disease** *337*

15.2 **Pediatric Cardiovascular MR Techniques** *338*
15.2.1 Setting Up a Pediatric Cardiac MR Study *338*
15.2.2 ECG-triggering *338*
15.2.3 Coil Selection, Parameters and Planes *339*
15.2.4 Pulse Sequences *340*
15.2.4.1 Black Blood Sequences *340*
15.2.4.2 White Blood Sequences *341*
15.2.4.3 Flow Quantification *343*
15.2.4.4 Myocardial Function, Perfusion and Viability Evaluation *344*

15.3 **Evaluation of Extra-cardiac Vasculature** *345*
15.3.1 Aorta *345*
15.3.1.1 Coarctation *345*
15.3.1.2 Aortic Root Dilatation *345*
15.3.1.3 Vascular Rings and Aortic Arch Anomalies *346*
15.3.2 Pulmonary Artery *346*
15.3.2.1 Pulmonary Sling *346*
15.3.2.2 Branch Pulmonary Artery Stenosis *347*
15.3.3 Pulmonary Veins *347*
15.3.3.1 Anomalous Pulmonary Veins *347*
15.3.3.2 Pulmonary Vein Stenosis *347*
15.3.4 Systemic Veins *348*

15.4 **Evaluation of Cardiac Morphology** *348*
15.4.1 Clarifying Complex Segmental Cardiac Anatomy *348*
15.4.2 Atrial Pathology *349*
15.4.3 Atrioventricular Connections *350*
15.4.4 Ventricular and Outflow Tract Pathology *350*
15.4.5 Valvular Pathology *351*
15.4.6 Miscellaneous Cardiac Pathology *352*
15.4.6.1 Cardiac Thrombus *352*
15.4.6.2 Cardiac Tumors *352*
15.4.6.3 Cardiomyopathy *353*

15.5 **Post-operative Evaluation of Congenital Heart Disease** *354*

15.6 **Limitations of Cardiac MRI in Children** *355*

15.7 **Conclusion** *356*

References *356*

15.1
Introduction: Segmental Approach to Heart Disease

The **segmental approach** to the diagnosis of congenital heart disease (Van Praagh 1984) includes the following analysis:

1. What is the anatomic type of the three major cardiac segments: the viscero-atrial situs, the ventricles, and the great arteries? Consider the example of a patient with complete transposition (d-TGA) with VSD and pulmonary stenosis. The cardiac segments are: situs solitus of the atria and viscera, d-looping of the ventricles (morphologic right ventricle lies to the right of the morphologic left ventricle), and d-malposition of the great arteries (aortic valve annulus lies to the right of the pulmonary annulus).

R. Krishnamurthy, MD
Department of Diagnostic Imaging (MC 2-2521), Texas Children's Hospital, 6621 Fannin Street, Houston, TX 77030-2399, USA
T. Chung, MD
Head, Department of Diagnostic Imaging (MC 2-2521), Chief, Diagnostic Imaging Services, Texas Children's Hospital, 6621 Fannin Street, Houston, TX 77030-2399, USA

2. How is each segment connected to the adjacent segment? In the example of d-TGA described above, there is atrioventricular concordance and ventriculoarterial discordance.
3. What are the associated malformations? In the example described above, the patient also has a conoventricular VSD and pulmonary valve stenosis associated with d-TGA.
4. How do the segmental combinations and connections, along with the associated malformations, function? The patient with the morphology described above will have cyanosis and reduced pulmonary blood flow.

Accurate anatomical and physiological diagnosis of pediatric cardiac disease allows selection of therapeutic options: medical, surgical, or both. Echocardiography (echo) plays a central role in the non-invasive delineation of congenital heart disease at all ages. The failure rate with echo increases in the post-operative setting, and in older children, when acoustic windows diminish. There are numerous examples involving the **extra-cardiac vasculature**, in which the lack of optimal acoustic windows results in inadequate characterization of pathology by echo. These include aortic coarctation, anomalous pulmonary veins, scimitar syndrome, systemic venous anomalies, branch pulmonary artery stenosis, anomalous coronaries, etc. The role of MRI and CT in characterizing the extra-cardiac vasculature in such patients is well established. On the other hand, echo is quite successful, in the vast majority of cases, in delineating the **intra-cardiac pathology**, including atrial, ventricular and great arterial situs, the segmental connections, ventricular function, the status of the atrial and ventricular septum and the cardiac valves. But, even in expert hands, some intra-cardiac defects remain difficult to diagnose by echo. There are only a few papers in the literature addressing the role of MRI as a trouble-shooting modality in such situations. In the **post-operative period**, the complementary role of MRI to echo in the evaluation of cardiovascular morphology and function is well established. Examples include tetralogy of Fallot, complex two-ventricle repair, and single ventricle repair.

This chapter will provide an overview of the technique and clinical role of MRI in the diagnosis of cardiac morphology and extra-cardiac vascular pathology in congenital heart disease in the pre-operative and post-operative period.

15.2
Pediatric Cardiovascular MR Techniques

15.2.1
Setting Up a Pediatric Cardiac MR Study

'The child is not a small adult' is an oft repeated cliché which resonates throughout the field of pediatric cardiac MR. The differences between the adult and pediatric cardiac MR studies are not restricted to clinical indications, but include study preparation, technical parameters and the prescribed imaging planes.

Most patients under 8 years who undergo a cardiac MR study will need either intravenous sedation or general anesthesia with endotracheal intubation. Endotracheal intubation with pharmacologically induced paralysis is needed if breath-holding is desirable. Intravenous sedation is a preferred alternative to intubation amongst parents and anesthesiologists, but has two important requirements: anesthesiologists experienced in administering intravenous sedation in patients with congenital heart disease, and the ability to modify the MR sequences for free breathing acquisition.

The clinical indication for the MR study varies depending on the natural history and treatment status of the patient, as well as information from previous imaging studies. For instance, the primary indication for MRI in a patient with tetralogy of Fallot may be any of the following: RV size and function, pulmonary regurgitation, atrioventricular valve regurgitation, RV outflow tract obstruction, branch pulmonary artery stenosis, aortic root dilatation or the location of aortopulmonary collaterals. Being familiar with the clinical data prior to the study is essential to target the MR study, so that the relevant data may be obtained in a timely fashion.

15.2.2
ECG-triggering

With the advent of vectorcardiogram (VCG) triggering system (Chia et al. 2000; Fischer et al. 1999), the technical difficulties associated with obtaining accurate cardiac triggering and gating for cardiac MR examinations were essentially eliminated. Coupled with fiber-optic hardware, the VCG system provides clinically reliable and robust ECG-triggering for all patients.

15.2.3
Coil Selection, Parameters and Planes

Phased-arrays coils are used universally for cardiac imaging, since they provide optimal signal-to-noise ratio (SNR) and the ability to utilize parallel imaging techniques. Parallel imaging was introduced in the late 1990s as SiMultaneous Acquisition of Spatial Harmonics (SMASH) (Sodickson and Manning 1997) and SENSitivity Encoding (SENSE) (Pruessmann et al. 1999), and is now available commercially as SENSE from Philips Medical System, Best, Netherlands, iPAT (mSENSE, GRAPPA) from Siemens Medical Solutions, Erlangen, Germany, or ASSET from General Electric Medical Systems, Wilwaukee, Wisconsin, USA. The choice of size of coil is dictated by the desired field of view (FOV). For example, in suspected anomalous origin of the coronaries in a small infant, we would use a two-element phased array all-purpose coil to get the desired FOV of 140 mm to 180 mm to demonstrate the small coronary arteries (Fig. 15.1a). On the other hand, in a larger patient with Kawasaki's disease, or to screen the branches of the aorta for evidence of systemic vasculitis, we would use either a cardiac phased-array coil or body phased-array coil with a large field of view (Fig. 15.1b).

The choice of in-plane and through-plane spatial resolution, and temporal resolution for a given sequence will vary depending on the size of the pa-

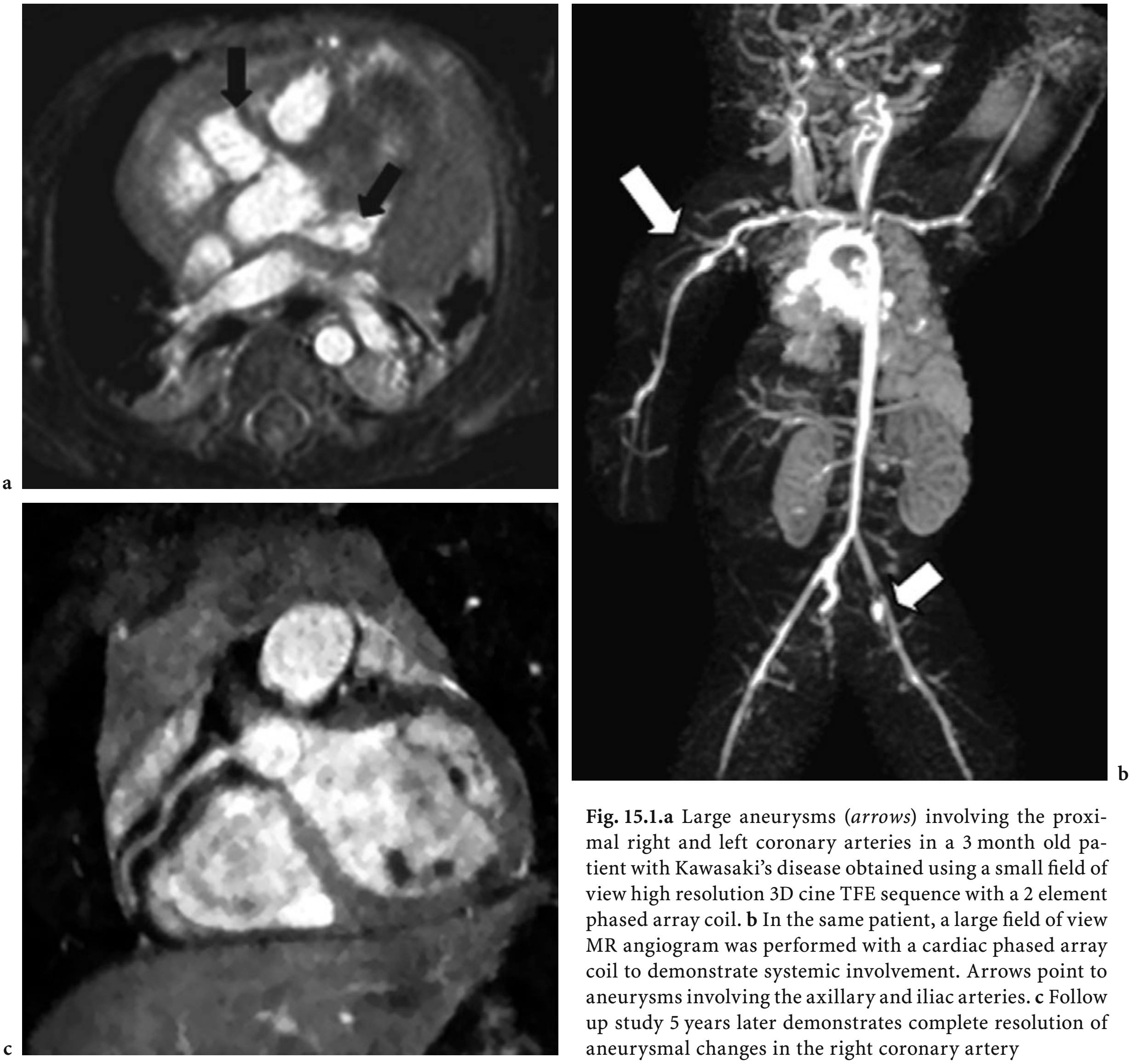

Fig. 15.1.a Large aneurysms (*arrows*) involving the proximal right and left coronary arteries in a 3 month old patient with Kawasaki's disease obtained using a small field of view high resolution 3D cine TFE sequence with a 2 element phased array coil. **b** In the same patient, a large field of view MR angiogram was performed with a cardiac phased array coil to demonstrate systemic involvement. Arrows point to aneurysms involving the axillary and iliac arteries. **c** Follow up study 5 years later demonstrates complete resolution of aneurysmal changes in the right coronary artery

tient, the heart rate, as well as the clinical indication. Commonly used imaging planes include axial planes for an overview of cardiovascular anatomy or evaluation of branch pulmonary artery stenosis and anomalous pulmonary venous return, conventional vertical long axis, four chamber and short axis planes for functional analysis, and customized double-oblique planes for evaluation of baffles and conduits, coronaries, or unusual topography of the cardiac chambers.

15.2.4
Pulse Sequences

15.2.4.1
Black Blood Sequences

Conventional spin-echo (CSE) T1-weighted sequence with ECG-triggering and respiratory compensation (Bailes et al. 1985) has traditionally been the mainstay for black-blood imaging since the early days of cardiac MR (Fletcher et al. 1984; Herfkens et al. 1983). This CSE sequence is no longer used primarily due to the long scan time. Acquisition time for spin echo sequences can be shortened by using segmented κ-space technique as in turbo or fast spin echo, by using EPI readout, and by using parallel imaging techniques in combination. Parallel imaging allows for the use of higher signal averages (NSA) to compensate for respiratory motion (Chung and Muthupillai 2004) without significant increases in scan time. These approaches provide a quick survey of the morphology with good in-plane spatial resolution, typically on the average of 1.5 mm squared pixels depending on the FOV. Respiratory triggering as a means of respiratory compensation can be used to reduce the number of signal averages needed, and in combination with thin sections of less than 2 mm, can be used to evaluate coarctation, vascular rings, vessel wall thickness and airway compromise (Fig. 15.2).

The general disadvantage with spin echo imaging is an incomplete “black blood” appearance with slow flow artifacts. Double- or triple-inversion recovery turbo spin-echo sequence has been shown to produce excellent quality black-blood images (Simonetti et al. 1996). However, breath holding is necessary, which limits its utility in the pediatric population. This sequence can be used on free-breathing patients with either multiple NSA or with respiratory triggering, although the scan duration is longer. Clinically, this sequence is used when better nulling of the blood signal is needed, to minimize metallic artifacts from endovascular stents, and to improve conspicuity of mural lesions such as cardiac tumors. A triple inversion recovery sequence provides additional fat suppression. With some modifications of this sequence, and in combination with respiratory navigator gating, black-blood coronary artery imaging can be accomplished (Stuber et al. 2001).

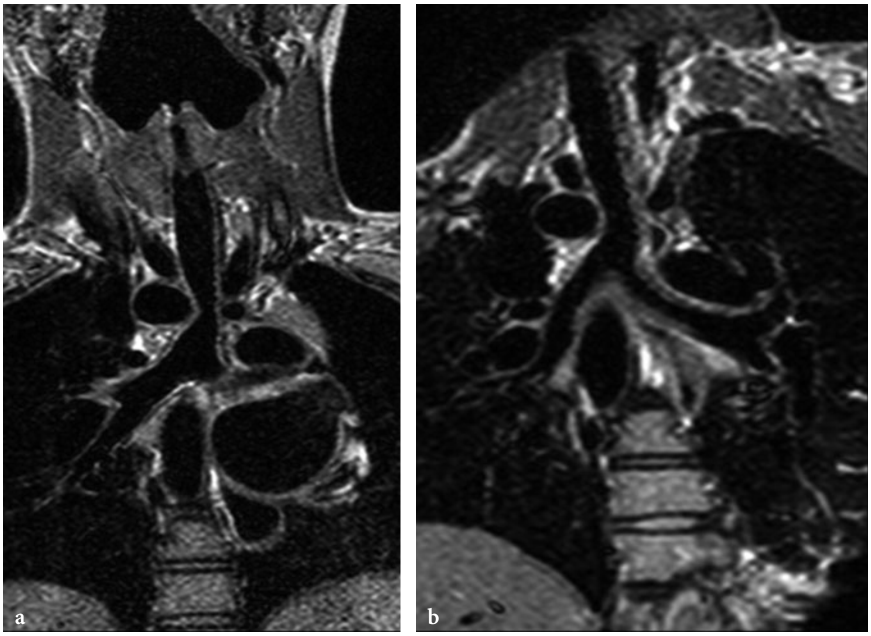

Fig. 15.2a,b. Coronal black blood T1 echo planar images before (**a**) and after (**b**) surgery in a patient with double aortic arch with partial atresia of the left arch, demonstrating relief of airway compression after surgery

15.2.4.2
White Blood Sequences

15.2.4.2.1
Contrast Enhanced MR Angiography

For white-blood imaging, contrast-enhanced 3D magnetic resonance angiography (CE-MRA), initially introduced in the early nineties (Prince et al. 1993), is the most efficient sequence for the evaluation of extra-cardiac vascular anatomy in the chest. The current implementation of this sequence is in the form of a 3D acquisition of T1-weighted fast gradient echo or turbo field echo (TFE) using a flip angle of 40–45°, and the shortest repetition time (TR) and echo time (TE) available on the scanner. This sequence is typically run with multiple dynamics (or multiple phases) using a single dose or, more commonly, double dose (0.2 mmol/kg) Gadolinium contrast agent injected intravenously. The early dynamics provide information about the pulmonary arterial tree, pulmonary veins, and the aorta and its branches, while the later dynamics provide information on systemic venous return. There is always a balance between spatial resolution vs temporal resolution. In general, for the highest spatial resolution, respiration must be suspended and the arrival of contrast must be precisely timed to the vasculature of interest. But, sacrificing some spatial resolution, and using parallel imaging techniques, short dynamic scan times of 4–8 s can be achieved (Muthupillai et al. 2003; Chung and Krishnamurthy 2005). Therefore, in a young patient with high heart rates, who is sedated or who cannot hold breath, CE-MRA with parallel imaging offers an accurate and reproducible means of evaluating the extracardiac vasculature, with the rapid dynamics providing unsubtracted separation of the right heart, left heart and systemic venous phases (Fig. 15.1b). The 3D volume rendered images provide an excellent overview of cardiac morphology (Fig. 15.3a) in cases with complex spatial relationships of the chambers. Most recently, other rapid imaging strategies of CE-MRA have been applied to the pediatric population to achieve high temporal and spatial resolution using TRICKS (Grist and Thorton 2005), and a combination of CENTRA-keyhole-SENSE techniques (Beerbaum et al. 2006; Goo et al. 2007). These techniques allow for temporal resolution of less than 2 s with good spatial resolution and therefore can capture temporal information of blood flow not available from CT angiography.

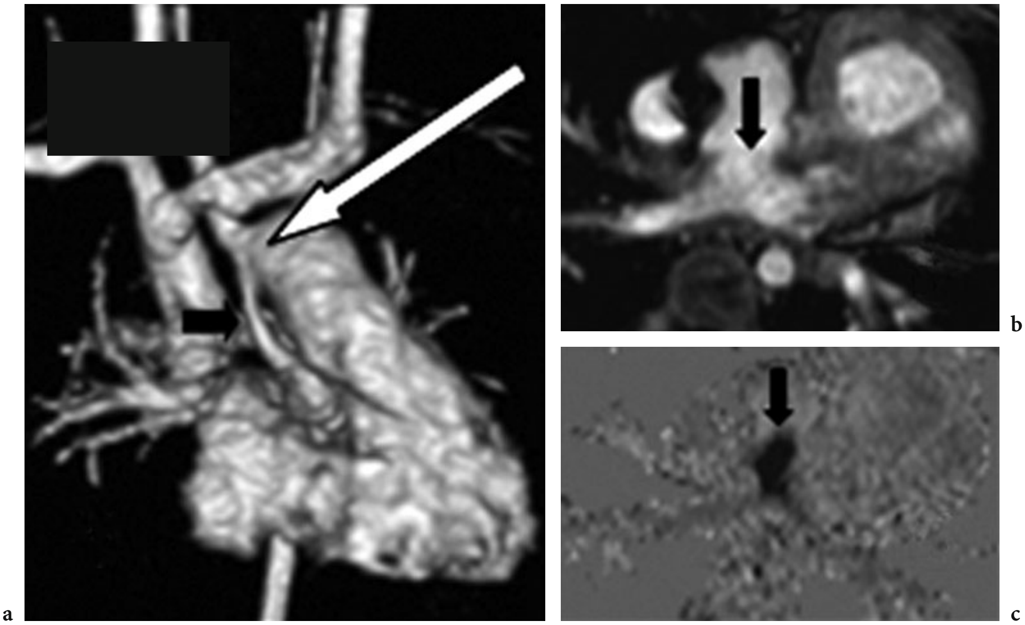
[redacted]

Fig. 15.3a–c. Phase contrast imaging revealing restrictive atrial communication after Norwood procedure for hypoplastic left heart syndrome. **a** 3D volume rendered image from a MRA shows changes of a Damus-Kaye-Stansel anastomosis between the main pulmonary artery and the hypoplastic ascending aorta (*arrow*). **b** Apparently patent atrial septostomy on the magnitude image (*arrow*). **c** Turbulent flow across septostomy demonstrated on the phase image, consistent with obstruction (*arrow*)

15.2.4.2.2
Cine White Blood Imaging

For cine white blood imaging, the sequences available are the robust ECG-triggered cine fast gradient echo or cine TFE with segmented k-space filling (Hernandez et al. 1993) and the newer cine steady state free-precession (SSFP) sequence. Despite the inherent flow related artifacts of the TFE sequence, this sequence is still preferred over SSFP for morphologic evaluation of extra-cardiac vascular pathology (Fig. 15.4), especially in smaller patients (Wood 2006). Higher spatial resolution can be achieved with cine TFE than with cine SSFP. Typically, 3 NSA can yield adequate SNR with a SENSE reduction factor of 2. A saturation band placed over the anterior chest wall fat decreases ghosting artifacts. Scan time will depend on the desired number of phases per cardiac cycle.

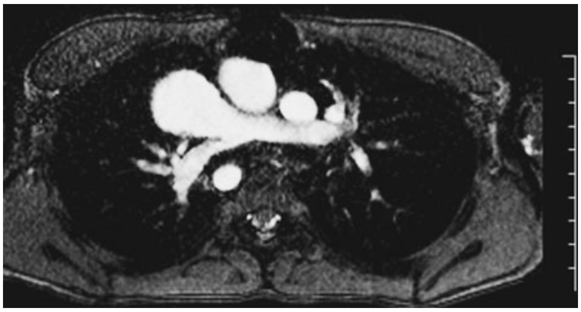

Fig. 15.4. Axial cine TFE image demonstrating moderate stenosis of the origin of the right pulmonary artery

In contrast, the cine SSFP sequence, more popularly known as true FISP (Free Induction Steady-state Precession) or balanced FFE (Fast Field-Echo) or FIESTA (Fast Imaging Employing STeady state Acquisition) depending on the manufacturer, is acquired with breath holding, and yields excellent quality images for intra-cardiac morphology and ventricular function (Fig. 15.5). When this sequence was first conceived in 1986 (Oppelt et al. 1986), the MR hardware then could not produce the short TR (< 4 ms) and TE (< 2 ms) necessary for the sequence to be clinically useful. Now, with advances in gradient strength, this is the sequence of choice for ventricular function evaluation due to its high temporal resolution, and excellent myocardial blood pool interface (Carr et al. 2001; Pereless et al. 2001). While using the cine SSFP sequence for ventricular function and intra-cardiac morphology evaluation, we typically aim for a temporal resolution of 30–40 ms with in-plane spatial resolution of 1.5–2.5 mm. Parallel imaging is used whenever possible to decrease the duration of breath holding. For non-breathhold scanning, multiple NSA can be used, but results are variable depending on the regularity of respiratory motion. The quality of the non-breathhold scans in the short axis plane tends to be quite acceptable in the majority of patients, especially when they are sedated. Limited clinical experience is available with combination of this sequence with respiratory triggering (Krishnamurthy et al. 2004) and recently, combination with respiratory gating is now available

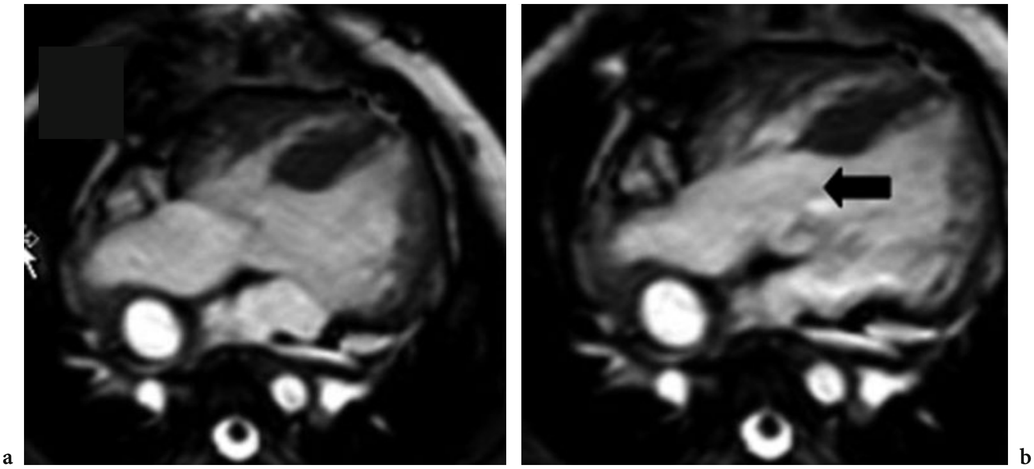

Fig. 15.5a,b. Cine SSFP images in a patient with over-riding (valvular orifice overriding the crest of the muscular ventricular septum) and straddling (*arrow*) (tension apparatus of the atrioventricular valve is attached in both ventricles) of the tricuspid valve in systole (**a**) and diastole (**b**)

for clinical use. Whether these new combinations of techniques can improve the image quality remains to be proven clinically. Significant artifacts related to flow acceleration or pulsatile flow can be present in SSFP sequence despite careful shimming (Markl and Pelc 2004), and the cine TFE with segmented k-space filling may be a better choice for dynamic white blood imaging in the setting of turbulent flow.

15.2.4.2.3
Coronary Imaging

Techniques of white-blood coronary artery imaging with respiratory navigator gating and fast gradient echo (Kim et al. 2001; Flamm and Muthupillai 2004) are well developed for the evaluation of ischemic heart disease in adults. These techniques have also been recently applied to the pediatric population, as in post-operative evaluation after coronary reimplantation, patients with Kawasaki disease (Fig. 15.1), or suspected coronary artery anomalies (Greil et al. 2002; Su et al. 2004, 2005, 2007; Taylor et al. 2005). An isotropic whole heart MR examination with respiratory navigator gating and 3D-SSFP has been used in adults to evaluate coronary arteries (Weber et al. 2003; Sakuma et al. 2005), and was applied to patients with congenital heart disease (Sorensen et al. 2004) with good results. If this technique can be adapted widely and robustly, it has the potential to provide comprehensive static, high-resolution morphologic white blood evaluation of intra-cardiac anatomy and extra-cardiac vascular anatomy in one sequence.

15.2.4.3
Flow Quantification

Non-invasive quantitative blood flow analysis is yet another powerful tool that MR adds to the diagnostic armamentarium. The most widely used pulse sequence is a retrospective-ECG-triggered cine phase contrast (also known as velocity-encoded cine MR) (Brenner et al. 1992; Caputo et al. 1991; Helbing et al. 1996; Hundley et al. 1995; Powell and Geva 2000; Rebergen et al. 1993a, b; , 1995; Sieverding et al. 1992; Steffens et al. 1994). The accuracy of this technique has been validated both in vitro and in vivo (Bogren et al. 1989; Evans et al. 1993; Firmin et al. 1987; Frayne et al. 1995; Kondo et al. 1991; Powell et al. 2000; Greil et al. 2002). Scan time can be shortened using segmented k-space technique, with the penalty of decreased temporal resolution (Kellenberger et al. 2005) and by combining parallel imaging techniques (Beerbaum et al. 2003; Prakash et al. 2006). Real-time phase contrast has also been applied clinically (Korperich et al. 2004). The main clinical applications include estimation of regurgitant fraction (Fig. 15.6) in patients with pulmonary regurgitation after repair of right ventricular outflow obstructive lesions such as tetralogy of Fallot (Helbing and de Roos 2000; Oosterhof et al. 2006), differential pulmonary flow to the right and

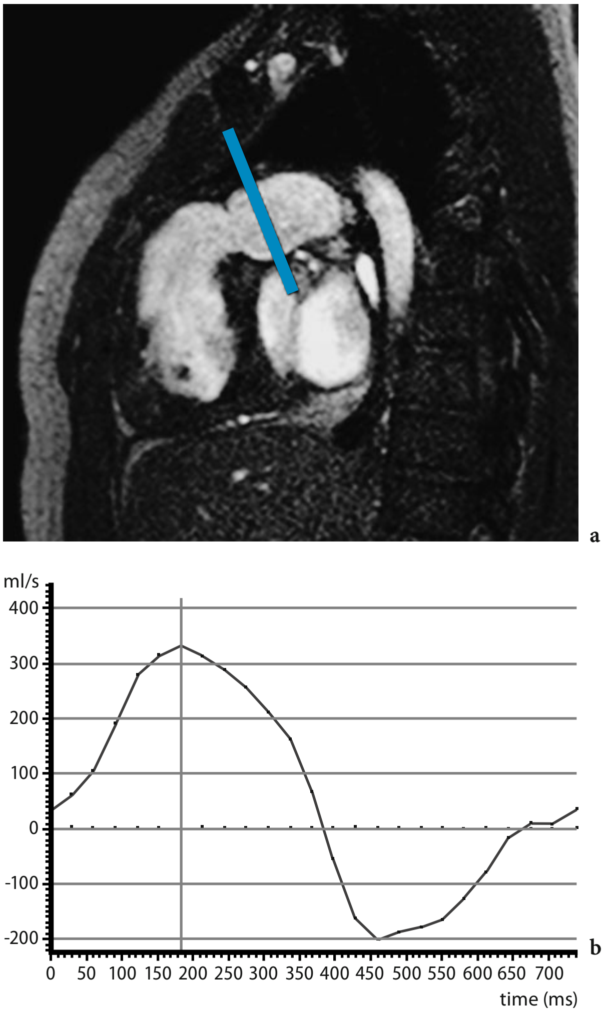

Fig. 15.6. **a** Cine TFE image in a 12 year old patient with treated tetralogy of Fallot, showing a dilated right ventricular outflow tract due to severe pulmonary regurgitation, which can be quantified using a phase contrast sequence with a plane perpendicular to the RVOT (*blue line*). **b** Quantitative flow volume curve across the RVOT reveals a stroke volume of 44 cc, and a regurgitant fraction of 45%

left lungs (Roman et al. 2005; Sridharan et al. 2006), and systemic-to-pulmonary shunts (Powell and Geva 2000). Phase contrast techniques have also been used as a sensitive means of detecting flow dephasing to locate the presence of atrial and ventricular septal defects, to detect flow restrictive conditions (Fig. 15.3), and also for the quantification of the gradient across a stenosis (Oshinski et al. 1996). The QP:QS ratio is calculated by phase contrast imaging across the main pulmonary artery and ascending aorta, and provides an important decision making tool in the presence of ASD, VSD and anomalous pulmonary veins.

Promising work on 3D whole heart volume acquisition of phase contrast data has been reported with modest temporal resolution (Sorensen et al. 2005). This has great potential to allow for operator-independent acquisition of phase contrast data in the future for congenital heart disease evaluation.

15.2.4.4
Myocardial Function, Perfusion and Viability Evaluation

Besides using cine SSFP, as previously described, for evaluation of global and regional myocardial function and wall motion, techniques for perfusion imaging (Schwitter 2006), with fast gradient echo (fGRE) or hybrid EPI-fGRE pulse sequence (Nagel et al. 2002; Jahnke et al. 2006) and viability imaging with inversion recovery T1-weighted fGRE sequence (Kim et al. 2000) have been well established in adults for evaluation of ischemic heart disease. These techniques have also been applied to the pediatric population in the setting of treated congenital heart disease, especially after coronary re-implantation (arterial switch operation, Ross procedure), or prolonged bypass procedures, and also in tumors (Fig. 15.7), thrombus, cardiomyopathy, myocarditis

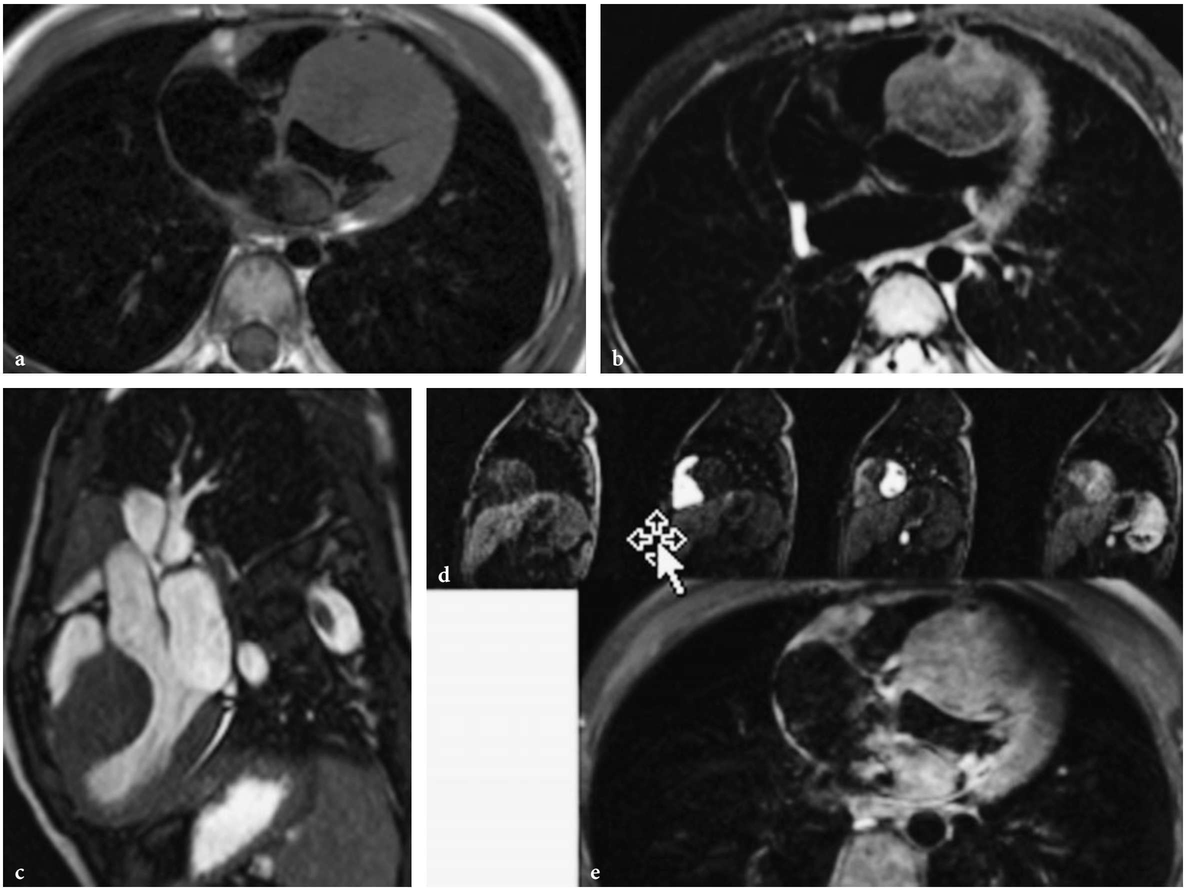

Fig. 15.7a–e. Fibroma of the inter-ventricular septum appearing isointense to myocardium on T1 (**a**), and on T2 (**b**), causing mild obstruction to LV outflow on cine SSFP (**c**), with perfusion (**d**) and enhancement (**e**) characteristics similar to myocardium after administration of gadolinium

and vasculitis (Prakash et al. 2004; Taylor et al. 2005).

Myocardial tissue tagging sequence has been available since it was first applied clinically (Zerhouni et al. 1988; Axel and Dougherty 1989). However, it is not widely utilized despite its ability to characterize ventricular myocardial mechanics, due to the time-consuming and complex post-processing involved. Nonetheless, it has been successfully applied in congenital heart disease (Fogel et al. 1998; Fogel 2000; Menteer et al. 2005). More recently, with the introduction of harmonic phase (HARP) MR (Osman et al. 1999) that allows for faster and automated method tagging analysis, one may see more widespread application clinically (Castillo et al. 2005).

15.3
Evaluation of Extra-cardiac Vasculature

MRI plays an important role in evaluation of the extra-cardiac vasculature in the pre-operative and post-operative period. Evaluation of the systemic and pulmonary veins, branch pulmonary arteries and the aorta by echocardiography is frequently limited by the lack of acoustic windows in older children, and in the post-operative setting. MRI provides various advantages over echo and CT in this situation, including a large field of view, arbitrary planes of evaluation, 3D imaging with high spatial resolution, excellent image contrast, excellent temporal resolution, freedom from artifacts like surgical patch prostheses and calcification, the use of intravenous contrast with low nephrotoxic potential, and lack of radiation.

15.3.1
Aorta

15.3.1.1
Coarctation

MRI is complementary to echocardiography in the preoperative evaluation of coarctation, especially in the setting of suboptimal acoustic windows, or in atypical coarctation. In infancy and early childhood, echocardiography provides adequate information prior to surgery or balloon dilatation in discrete coarctation. But, if there is associated tubular hypoplasia of the aortic arch or atypical thoracic coarctation, then MRA or CTA help to define the extent of narrowing, the status of the head and neck arteries, as well as the collateral arterial supply, all of which are essential for surgical planning. In the postoperative period, echo windows diminish considerably, and MRA is preferred to CTA for serial follow-up due to the lack of ionizing radiation. The MRI protocol for recurrent coarctation comprises dynamic sequences for ventricular function, left ventricular outflow tract as well as the aortic arch. The severity of the coarctation is determined by measuring the luminal caliber of the aorta, measuring the pressure gradient across the stenosis by flow velocity mapping of the aortic arch (Oshinski et al. 1996) (Fig. 15.8a), and by quantifying the amount of collateral arterial supply to the descending thoracic aorta by flow velocity mapping across the proximal and distal descending thoracic aorta (Steffens et al. 1994). Gadolinium enhanced MR angiography demonstrates the location and extent of stenosis, the presence of pseudoaneurysms, the status of the head and neck arteries, as well as collateral arterial supply to the descending thoracic aorta (Fig. 15.8b).

15.3.1.2
Aortic Root Dilatation

Patients with Marfan syndrome, Ehlers Danlos syndrome, bicuspid aortic valve, Ross procedure (replacing a dysplastic aortic valve with the native pulmonary valve), have a tendency to develop progressive aortic root dilatation (Grotenhuis et al. 2006). MRI provides an accurate, reproducible and safe means of assessing aortic root caliber over time, which is essential to track stability or progression, and for decision-making regarding surgery. It overcomes the limitations of echocardiography, which is error-prone in the setting of eccentric aortic root dilatation. Ungated CT angiography is also limited in this location due to pulsation artifacts. The most helpful information is obtained from a stack of thin section dynamic bright blood images performed perpendicular to the long axis of the aortic root and proximal ascending aorta, which allows calculation of maximal luminal caliber in systole and diastole, as well as extent of involvement (Fig. 15.9). Flow velocity mapping across the ascending aorta is essential to calculate the aortic regurgitant fraction. In some cases, 3D coronary angiography is helpful to determine the status of the coronary origins prior to surgery, or in the postoperative setting.

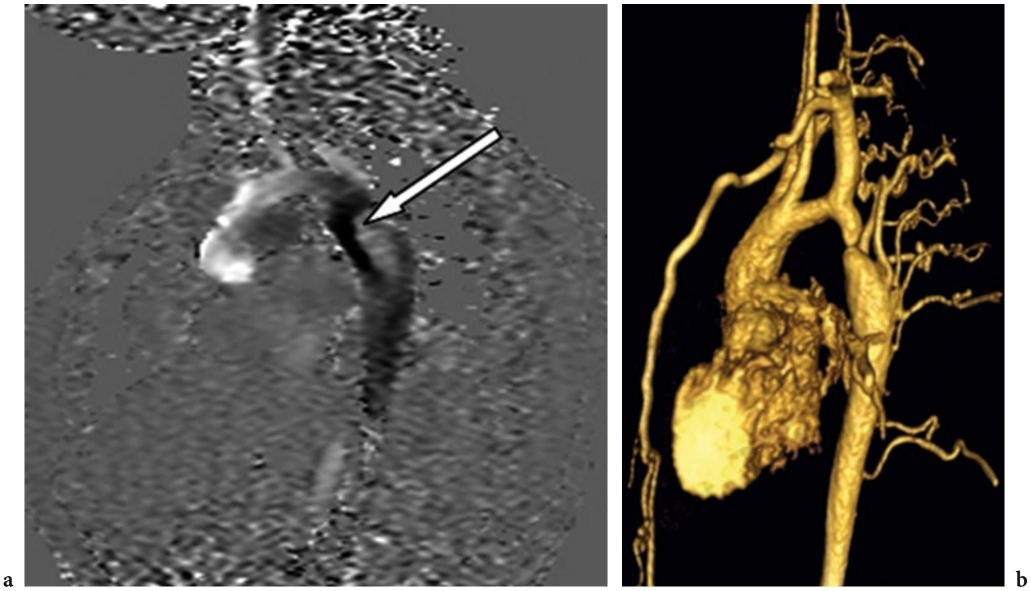

Fig. 15.8. **a** Flow velocity mapping of the aortic arch in a patient with coarctation showing a dephasing jet (*arrow*) distal to the stenosis with a peak velocity of 450 m/s. **b** Volume rendered image of a gadolinium enhanced 3D MRA in the same patient showing the severity of stenosis, as well as the extent of collateral flow to the descending aorta

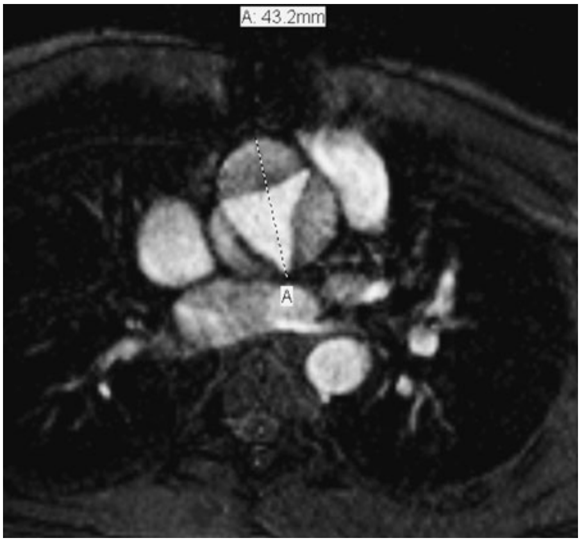

Fig. 15.9. Cine TFE image perpendicular to the aortic root in systole demonstrates severe aortic root dilatation in a 12 year old patient, who underwent a Ross procedure for sub-aortic stenosis

15.3.1.3
Vascular Rings and Aortic Arch Anomalies

MR angiography provides an accurate and rapid means of determining the presence and nature of a vascular ring. Sequences include thin-section axial dynamic bright blood images through the upper thorax, and gadolinium enhanced 3D MR angiography. High-resolution black blood imaging is also performed to determine the status of the airway (Fig. 15.2). While the diagnoses of right arch with an aberrant left subclavian artery or double aortic arch are fairly straightforward, variations such as double aortic arch with partial atresia of the left arch may benefit from the dynamic nature of the MR data when compared to CT angiography (Schlesinger et al. 2005). MRA is also accurate in diagnosing a number of aortic arch anomalies including persistent fifth arch, interrupted aortic arch, and cervical aortic arch amongst others.

15.3.2
Pulmonary Artery

15.3.2.1
Pulmonary Sling

In pulmonary sling, the left pulmonary artery arises anomalously from the right pulmonary artery, and travels between the trachea and esophagus to supply the left lung. There is associated compromise of the airway resulting from mass effect or coexisting tracheomalacia and bronchomalacia. Tracheal branching anomalies, including a T-shaped trachea, may also be present. The anomalous left pulmonary artery is frequently hypoplastic or has focal stenosis (Fig. 15.10). Using bright blood and black blood sequences as well as MR angiography, the entire spectrum of vascular and airway anomalies may be accurately depicted by MRI (Lee et al. 2001). Differential blood flow to the lungs may also be calculated using flow velocity mapping sequences.

15.3.2.2
Branch Pulmonary Artery Stenosis

Branch pulmonary artery stenosis may be present as an isolated entity (Fig. 15.4), but is more commonly seen in the setting for Alagille‘s syndrome, Williams syndrome, treated pulmonary atresia, tetralogy of Fallot, following an arterial switch procedure for transposition of great arteries, or any condition involving RVOT conduit placement. The use of thin section dynamic bright blood sequences, flow velocity mapping and time resolved contrast MR angiography successfully provides all clinically relevant information, including the severity and extent of stenosis, the pressure gradient across the stenosis, the status of the peripheral pulmonary vasculature, the differential pulmonary flow to both lungs, as well as the presence and location of aortopulmonary collaterals. The presence of associated pulmonary regurgitation or RV dysfunction may also be ascertained simultaneously using MRI. This is one of the more common indications for cardiac MRI in most pediatric practices.

15.3.3
Pulmonary Veins

15.3.3.1
Anomalous Pulmonary Veins

MRI is commonly used in the preoperative and postoperative setting for partial or total anomalous pulmonary venous return (Festa et al. 2006). In partial anomalous pulmonary venous return, which includes conditions like scimitar syndrome or sinus venosus defects, MRI is helpful in determining the presence and location of the pulmonary vein, the drainage area, the presence of associated obstruction, the degree of left to right shunting (QP:QS), and the presence of associated anomalies like pulmonary artery hypoplasia, aortopulmonary collaterals, and developmental lung anomalies amongst others. MRI provides the most objective and reproducible data for surgical decision-making in partial anomalous pulmonary venous return.

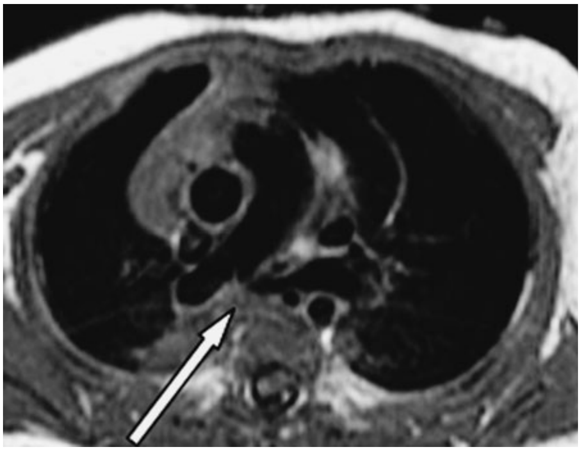

Fig. 15.10. Axial black blood fast spin echo double inversion recovery image demonstrating a pulmonary sling with high-grade stenosis of the proximal left pulmonary artery as it courses between the trachea and esophagus (*arrow*)

Most cases of total anomalous pulmonary venous return are successfully diagnosed by echocardiography in the newborn, with the use of MRI restricted to cases with complex anatomy like heterotaxy (Fig. 15.11), or in the setting of suboptimal echo windows. MRI has been successfully used to diagnose an unusual course of the aberrant pulmonary vein, as well as the presence of associated stenosis, both in infra-diaphragmatic and supra-diaphragmatic TAPVR.

15.3.3.2
Pulmonary Vein Stenosis

There is an important role for MRI after surgery for anomalous pulmonary venous return, where there is a possibility of postoperative pulmonary vein stenosis. Pulmonary vein stenosis may also occur as an isolated entity, or after other types of congenital heart surgery (Fig. 15.12), and is usually difficult to manage, with a poor prognosis. MRI determines the presence, severity and extent of stenosis, as well as its impact on pulmonary arterial supply and ventricular function (Valsangiocomo et al. 2003). One major limitation of MRI in this setting is its inability to determine pulmonary vascular resistance and right ventricular chamber pressures, although an estimate may be obtained from pulmonary artery caliber and interventricular septal motion.

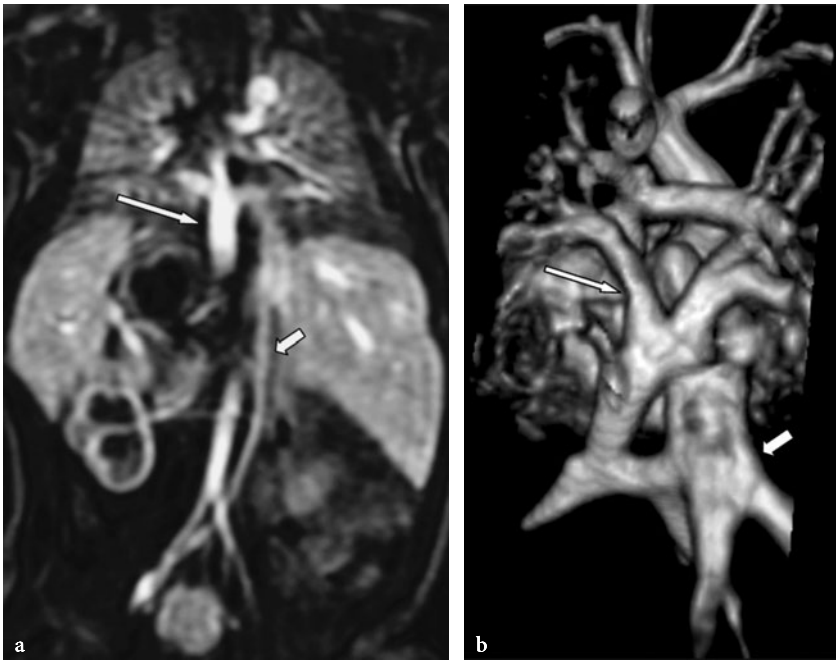

Fig. 15.11a,b. MIP (**a**) and volume rendered (**b**) images of a MRA in a newborn with heterotaxy and right isomerism, showing total anomalous pulmonary venous return below the diaphragm to a hepatic vein (*large arrow*), a left sided IVC (*small arrow*), a transverse liver with asplenia, and a right sided stomach

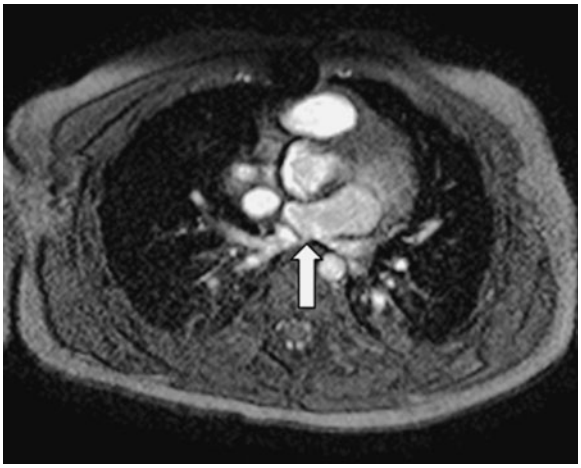

Fig. 15.12. Recurrent severe pulmonary vein stenosis after repair of total anomalous pulmonary venous return

15.3.4
Systemic Veins

Systemic venous anomalies frequently coexist with congenital heart disease, especially in the setting of heterotaxy (Fig. 15.11). The most common anomaly is a persistent left superior vena cava, which drains into the coronary sinus. A connecting vein between the two superior vena cavae is typically absent in this setting. Interruption of the IVC with azygos continuation, and/or aberrant hepatic venous drainage is frequently present in heterotaxy. These anomalies significantly alter surgical management in single ventricle repair, in which the cavopulmonary connections have to be modified to accommodate the aberrant venous drainage.

Systemic venous obstruction is also common after congenital heart surgery or prolonged central line placement, and MR venography offers a rapid and accurate means of diagnosing the extent of thrombosis, the acuity of the process, and the degree and adequacy of collateral venous flow. Simultaneous imaging of the brain is essential in the setting of SVC or bilateral jugular vein thrombosis to exclude elevated intra-cranial pressure, which typically manifests as ventriculomegaly or intracranial hemorrhage.

15.4
Evaluation of Cardiac Morphology

15.4.1
Clarifying Complex Segmental Cardiac Anatomy

Abnormalities of viscero-atrial situs and cardiac malpositions are usually easily identified by echo.

However, in the presence of situs ambiguous, atrioventricular or ventriculo-arterial discordance, and/or anomalous pulmonary or systemic venous connections (Fig. 15.11), difficulties may arise in defining the topographic relation of the major cardiac segments (Araoz et al. 2002). MRI is an excellent technique for defining the morphologic features of each atrium and ventricle. MRI provides anatomical data, which is easily related to the surrounding structures of the body, and thus provides reliable diagnoses in heterotaxy (Sorensen et al. 2004; Kersting-Sommerhoff et al. 1990). In patients with complex anomalies, especially in older patients, MR may be the primary imaging technique so as to maximize non-invasive information prior to catheterization.

15.4.2
Atrial Pathology

Atrial septal defects: the sensitivity of echo for diagnosing secundum atrial septal defect (ASD) is close to 100% in infancy, but drops to 85%–90% in older children and adults. Transesophageal echocardiography (TEE) is a trusted method of sizing atrial septal defect (ASD) prior to surgery or percutaneous device closure, but is invasive, uncomfortable, and may carry a small risk of morbidity and mortality. MRI may be a useful non-invasive alternative in such patients who refuse or are unable to tolerate TEE and may provide additional information on the shape and location of the ASD. In a recent study (Piaw et al. 2006), ASD sizing by MRI using bFFE and phase-contrast protocols correlated well with TEE estimations. PC-MRI provided additional information on ASD shapes and proximity to adjacent structures. MR guidance has also been used recently to navigate endovascular catheters and deliver ASD closure devices (Henk et al. 2005).

The superior sinus venosus defect is the most difficult form of atrial septal defect to detect echocardiographically due to the extreme rightward and superior position of this type of defect. The inferior type is also difficult to depict by transthoracic echocardiography because of its infero-posterior location to the fossa ovalis. MRI has become the gold standard for depiction of sinus venosus defects (Fig. 15.13).

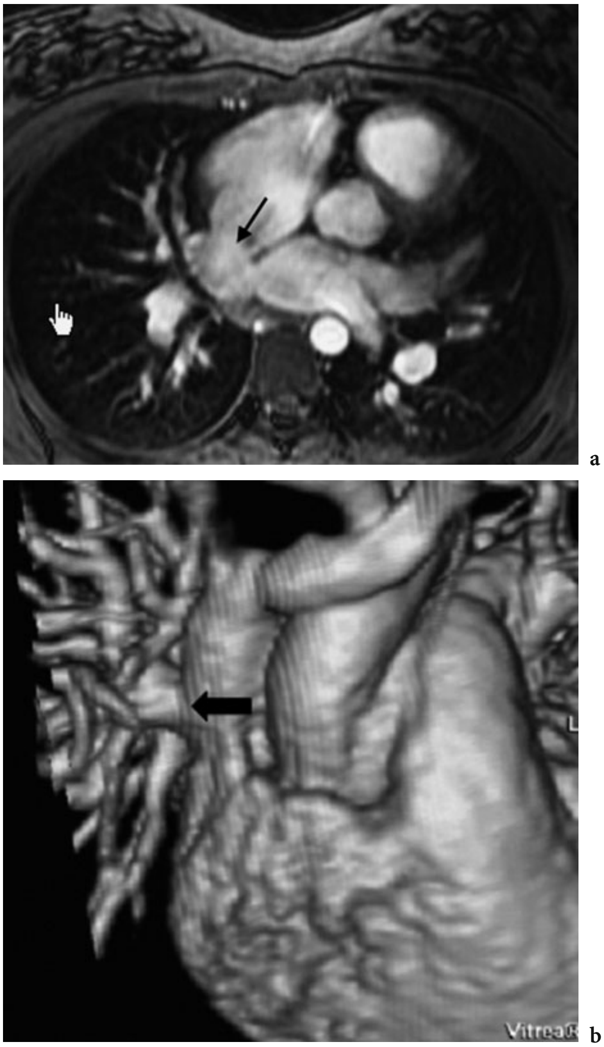

Fig. 15.13a,b. Superior sinus venosus defect demonstrating the extra-septal communication between the posterior wall of the SVC/RA junction and the left atrium (**a**), with associated partial anomalous venous return of right upper lobe pulmonary vein to the SVC (**b**)

The coronary sinus septal defect involves partial absence of the atrial septum between the coronary sinus and the left atrium due to incomplete development of the left atrio-venous fold. It may be associated with left SVC to coronary sinus, unroofing of the coronary sinus, and other complex congenital heart defects, and is another example of the use of MRI to overcome the limitations of echocardiography.

MRI may also identify ASD or partial anomalous pulmonary venous connection in adults with right-sided chamber enlargement, hypertrophy or dysfunction of unknown etiology. In all forms of septal defects, quantification of shunt size (pulmonary to systemic flow ratio, otherwise known as the Qp:Qs ratio) by flow velocity mapping compares favorably to other imaging techniques, and enables decision making regarding conservative therapy vs surgery (Hundley et al. 1995).

Cor triatriatum: the common pulmonary vein is usually largely incorporated into the left atrium and forms the part of the left atrial posterior wall between the entrances of the pulmonary veins. If the point of junction of the common pulmonary vein and the left atrium is stenotic, a membrane develops between the common pulmonary vein and the left atrium. The membrane lies between the entrance of the pulmonary veins posteriorly and the foramen ovale and the left atrial appendage anteriorly, in contrast to supra-mitral ring which attaches between the foramen ovale and the left atrial appendage posteriorly and the mitral annulus anteriorly. The distinction between these two entities can occasionally be difficult on echocardiography, but is easily accomplished by MRI.

Malposition of the septum primum: abnormal deviation of the septum primum towards the left atrium could result in anomalous pulmonary venous drainage into the right atrium. In severe cases, the entire venous system of both lungs will be connected with the right atrium. This condition must be differentiated from partial or total anomalous pulmonary venous return to the right atrium by demonstrating that the pulmonary veins have a normal relationship with each other and to the posterior wall of the atrium, and the anomalous venous return occurs due to malposition of the atrial septum (Fig. 15.14). MRI can make the diagnosis more reliably than echo. Recognition of this condition leads to appropriate therapy, which is surgically restoring the correct position of the atrial septum.

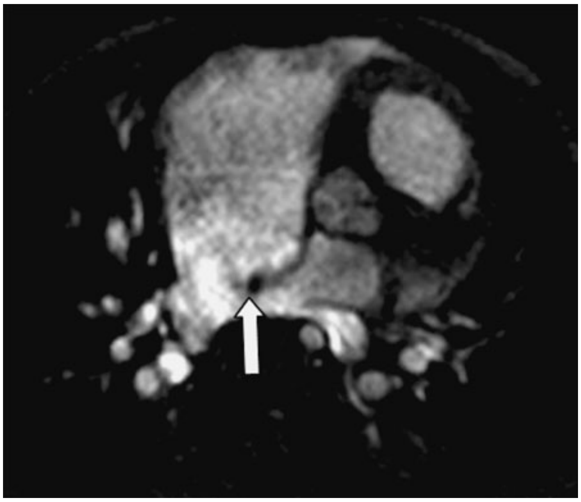

Fig. 15.14. Malposition of the septum primum to the left (*arrow*), resulting in partial anomalous venous return of the right sided pulmonary veins to the right atrium, which is severely dilated

Atrial appendages: MRI has been used to demonstrate a broad range of pathology involving the appendages, including abnormal appendage symmetry in heterotaxy, juxtaposition of the atrial appendages in association with other complex malformations (Fig. 15.15), and thrombi within the appendages.

15.4.3
Atrioventricular Connections

MRI can demonstrate discordant atrioventricular connections and crisscross atrioventricular connections. MRI has also been used for demonstrating double inlet ventricle (Yoo et al. 1999), straddling atrio-ventricular valve (Fig. 15.5), tricuspid atresia, and mitral atresia. Echocardiography is usually employed initially for these abnormalities and MRI is used to supplement this information. MRI is superior to echo for quantifying ventricular volumes in these abnormalities, which may be critical for surgical decisions regarding biventricular repair vs the Fontan procedure.

15.4.4
Ventricular and Outflow Tract Pathology

MRI adds little, if any, anatomical information in isolated ventricular septal defect when the diagnosis is already established by echocardiography, except that MRI can readily quantify shunt volume. A number of papers have documented that MRI is highly sensitive and specific for the quantification and detection of ventricular septal defects, (Didier and Higgins 1986; Mirowitzet et al. 1989) and detection and localization of jets is helpful (Sechtem et al. 1987). Certain types of VSD that are difficult to evaluate by echo are well suited to imaging by MRI, including supracristal defects and apical muscular VSDs. MRI can readily depict ventricular anatomy in complex cases of tetralogy of Fallot, pulmonary atresia, tricuspid atresia, and univentricular hearts (Razavi et al. 2003; Kersting-Sommerhoff et al. 1990). In functional or morphologic single ventricle, the differentiation of a single RV from a single LV can be made with a high degree of confidence in most cases. MRI has been used to help surgical decision

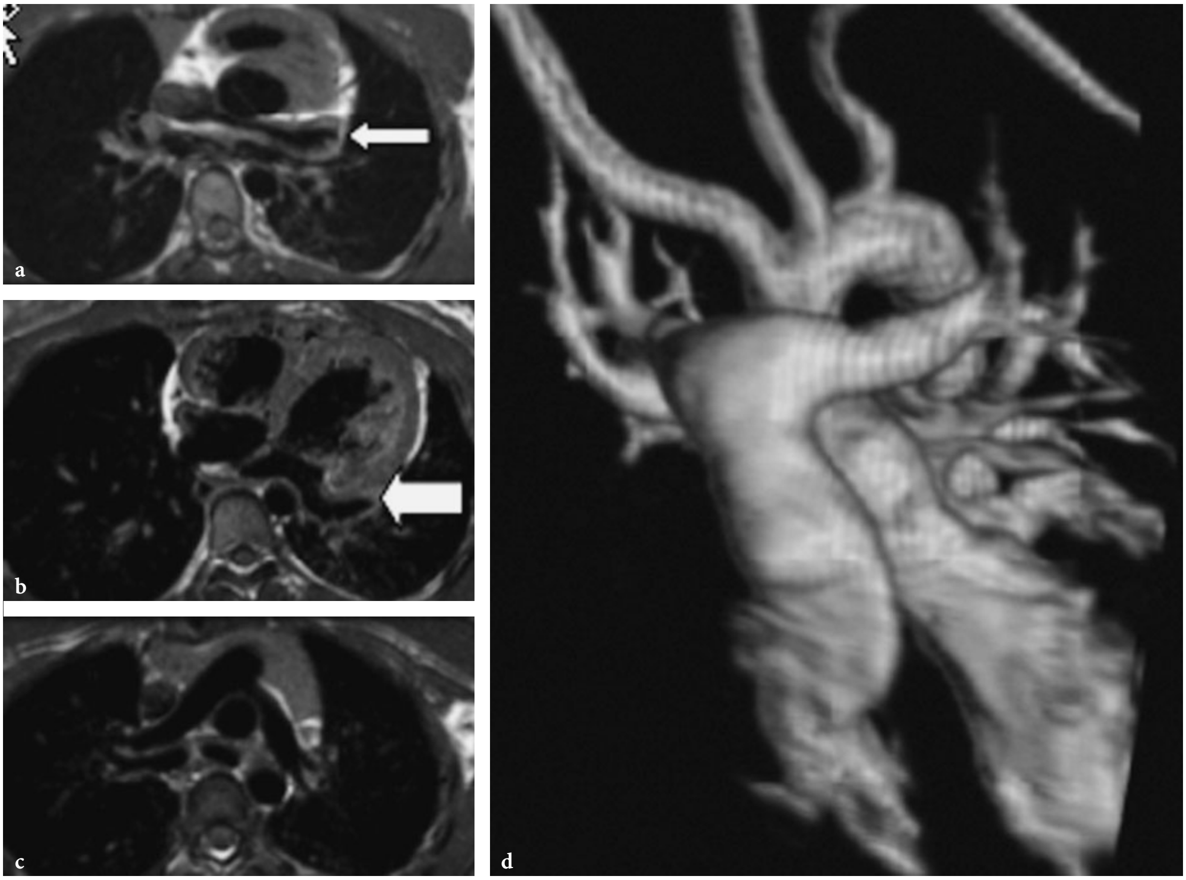

Fig. 15.15a–d. Left juxtaposition of the atrial appendages in d-transposition of the great arteries, s/p arterial switch procedure. The right appendage (**a**) (*small arrow*) and the left appendage (**b**) (*large arrow*) are on the same side. The typical orientation of the pulmonary artery and aorta (**c,d**) after an arterial switch

making regarding univentricular repair (Fontan), one and a half ventricle repair or biventricular repair in patients who have two functioning ventricles, but also have factors preventing biventricular repair like straddling AV valves, unfavorable location of the VSD or suboptimal ventricular morphology or function (Fig. 15.16). MRI can precisely depict the location of the ventricular septal defect in relation to the great arteries in double outlet ventricles (Mayo et al. 1990). MRI is the most accurate technique for quantifying left and right ventricular mass and volumes.

15.4.5
Valvular Pathology

The high temporal resolution, spatial resolution and interactive real-time nature of echo makes it the primary imaging modality for defining valve morphology, including number of leaflets, valve thickness, and vegetations, as well as valve function, and estimation of valvular stenosis and regurgitation. However, MR flow velocity mapping is a more accurate and reproducible means of quantifying the severity of regurgitation (Fig. 15.6). This is valuable for sequential monitoring of the severity of valvular regurgitation and determining the optimal timing for valve replacement. Common MRI applications include monitoring of pulmonary regurgitation after outflow patch surgery for tetralogy of Fallot, and after placement of RV to pulmonary artery conduits as well as monitoring idiopathic aortic root dilation and aortic regurgitation in patients with Marfan's syndrome, tetralogy of Fallot, or after a Ross procedure (Fig. 15.9). MRI is also effective for the morphologic depiction of tricuspid atresia, Shone's syndrome and Ebstein's anomaly (Link et al. 1988). Moreover, it can provide precise ventricular volumetric and functional assessment in these anomalies (Choi et al. 1994).

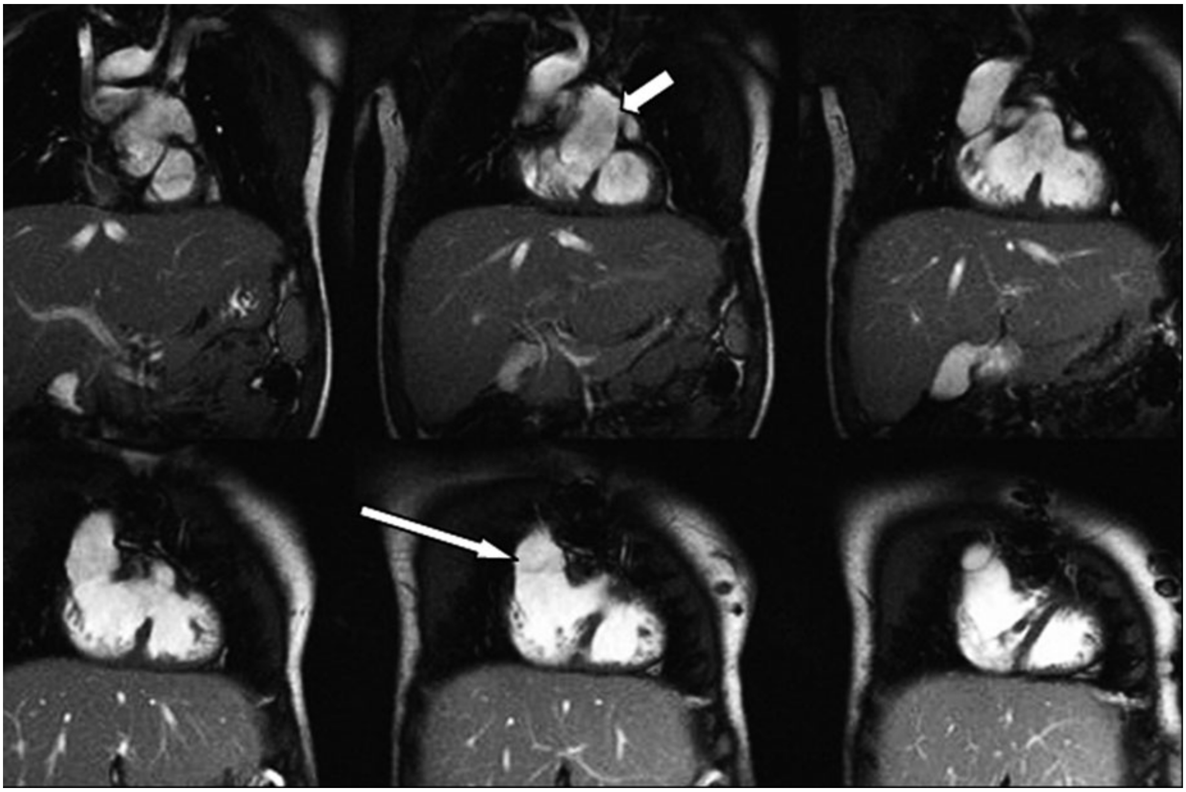

Fig. 15.16. Coronal bright blood images oriented posterior to anterior in a patient with double outlet right ventricle and a sub-pulmonary VSD. Since the aorta (*long arrow*) is located far to the right, away from the VSD and the LV, this patient would likely not be a candidate for a two-ventricle repair in which a baffle must be created from the left ventricle to the aorta across the VSD. In this case, the baffle would have obstructed the right ventricular outflow tract (*short arrow*) and the tricuspid inflow. Hence, this patient went on to have a single ventricle repair in spite of having two well-formed ventricles

15.4.6
Miscellaneous Cardiac Pathology

MRI is proving increasingly valuable in the identification and management of various forms of cardiomyopathy and cardiac tumors.

15.4.6.1
Cardiac Thrombus

The Fontan procedure is associated with a high incidence of thromboembolic complications (Casolo et al. 2004). Intracavitary thrombi are also frequently found in patients with impaired ventricular function, or within the atrium in atrial fibrillation. MR imaging is a sensitive tool in the detection of intra-cardiac thrombi, and overcomes some of the near-field limitations of 2D echo. The most helpful sequences are bright blood cine, black blood and post gadolinium delayed enhancement. Both the bright blood and black blood sequences are prone to artifact from stasis and slow flow. A new fibrin-specific MR contrast agent EP-2104R offers promise for selective and high-contrast visualization of acute cardiac and vascular thrombi by means of molecular targeted MRI (Spuentrup et al. 2005).

15.4.6.2
Cardiac Tumors

Primary heart tumors in childhood are rare and mostly benign. Surgical treatment is advocated when symptoms or hemodynamic impairment are present. Rhabdomyoma is the most common cardiac tumor diagnosed in children. They are usually multiple, most often involve the ventricular myocardium, and project into the cavity or move freely as a pedunculated mass. Associated tuberous sclerosis is present in about one third of the patients. Fibromas (Fig. 15.7) usually appear within a ventricular wall (i.e., intramural). Calcific deposits may be present within the neoplasm. Sudden death has occurred in about a third of the patients, presumably the result of a conduction defect, arrhythmia, or obstruction to outflow from a ventricle. Treatment strategy varies according to tumor type. For example, rhabdomyomas are treated conservatively due to a high rate of spontaneous regression. Total or partial resection of a fibroma may relieve obstruction with an excellent probability of long-term survival. A Purkinje cell tumor associated with high-grade ventricular ectopy may require surgical resection, whereas a cardiac hemangioma may be treated with high-dose steroids or interferon. Malignant cardiac tumors are rare, but must always be considered in the differential diagnosis. MRI has only limited potential in identifying the likely tissue type of the tumor in children (Kiaffas et al. 2002). But, it is ideally suited for the noninvasive evaluation of the size, location, number of tumors, and relationship to the adjacent structures (Hoffmann et al. 2003). It also helps in distinguishing cardiac tumors from tumor-like conditions, including pericardial cysts, lipomatous hypertrophy of the atrial septum, thrombi, and sarcoidosis.

15.4.6.3
Cardiomyopathy

15.4.6.3.1
Hypertrophic Obstructive Cardiomyopathy

Cardiac MRI has been used to define the distribution of hypertrophy, and its functional consequences. This is especially true for apical and anterolateral wall involvement, which is difficult to diagnose by echo (Rickers et al. 2005). Delayed enhancement gadolinium MRI has also been used in hypertrophic cardiomyopathy to demonstrate areas of fibrosis (Teraoka 2005), and the extent of this abnormal uptake is linked to the risk of sudden death and development of LV dilation and heart failure. MRI has also been used to identify the functional and anatomical consequences of septal resection. In addition, MRI is ideal for screening of relatives of probands because of its phenotypic accuracy.

15.4.6.3.2
Left Ventricular Non-compaction

Non-compaction of the ventricular myocardium is a rare congenital cardiomyopathy characterized by numerous excessively prominent trabeculations and deep intertrabecular recesses. Non-compaction of the ventricular myocardium is most often an isolated cardiac malformation presenting as a sporadic disease. Associated cardiac anomalies are present in some patients. The following criteria have been proposed for diagnosis of isolated LV non-compaction by echo: (1) absence of coexisting cardiac abnormalities, (2) a 2-layered structure of the left ventricular wall, with the end systolic ratio of non-compacted to compacted layer >2, (3) finding this structure predominantly in the apical and mid-ventricular areas, and (4) blood flow directly from the ventricular cavity into the deep intertrabecular recesses as assessed by Doppler echocardiography (van der Loo and Jenni 2003). Although no MRI criteria have been established yet, MRI appears ideal for identification of this condition, and may provide the ability to detect a broader spectrum and more subtle variants of non-compaction (Fig. 15.17). Trabecular mass of greater than 20% of total myocardial mass may be a useful index to suggest the diagnosis of isolated LV non-compaction (Korcyk et al. 2004). An NC/C ratio of >2.3 in diastole distinguished pathological non-compaction, with values for sensitivity, specificity, and positive and negative predictions of 86%, 99%, 75%, and 99%, respectively (Petersen et al. 2005). A diagnosis of non-compaction has important implications because of the need for familial screening and the possible association with other

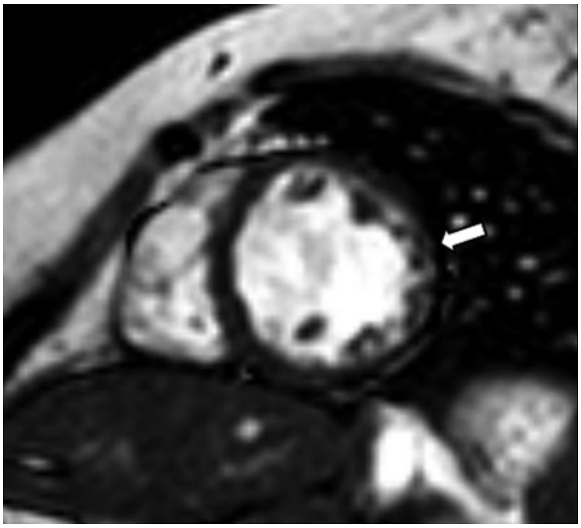

Fig. 15.17. LV non compaction in an 18 year old male with Duchenne's muscular dystrophy. On this diastolic short axis image, note the prominent trabeculations, the deep intertrabecular recesses (*arrow*), and a non-compacted/compacted myocardial ratio of >3

cardiac anomalies and/or muscle disorders, progressive LV dysfunction, risk of systemic embolism, and life-threatening arrhythmias.

15.4.6.3.3
Arrhythmogenic Right Ventricular Cardiomyopathy

Arrhythmogenic right ventricular cardiomyopathy (ARVC) has been reported as the etiology of up to 42% of cases of sudden death in young adults secondary to arrhythmia (Cho et al. 2003). It is characterized histologically by fatty or fibro-fatty infiltration of the right ventricular myocardium. The imaging protocol includes cine-MRI sequences for evaluation of segmental and global right ventricular function and wall motion, and anatomic sequences to detect fatty or fibro-fatty infiltration of the right ventricular myocardium. Delayed enhancement techniques appear to have a high sensitivity for fibro-fatty infiltration of the RV wall, and should be considered an important part of the MRI protocol (Tandri et al. 2005). The diagnostic criteria of ARVC include regional wall motion abnormalities, increased RV volumes, morphological abnormalities (aneurysms, trabecular disarray) and increased myocardial signal suggesting fatty infiltration. Isolated findings of RV wall thinning or focal intramyocardial fat must be interpreted with caution (Bomma et al. 2004). Focal wall motion abnormalities, especially focal dyskinesia, are generally felt to be a more reliable indicator of ARVC on MRI than intramyocardial fat.

15.4.6.3.4
Iron Overload Cardiomyopathy

Iron overload cardiomyopathy remains the leading cause of death in patients with hemochromatosis or the inherited severe anemias, which require regular blood transfusions from birth. MRI is ideally suited for monitoring thalassemia patients because it can detect cardiac and liver iron burdens as well as accurately measure left ventricular dimensions and function (Wood et al. 2005). Repeated assessment of myocardial iron using biopsy is difficult because of safety issues, sampling error and patchy iron distribution. Measurement of T2* using MRI has been shown to reflect tissue iron, and has good reproducibility (Westwood et al. 2005). There is a clear relation between reduced myocardial T2* (< 20 ms) indicating iron overload, and LV dysfunction (Westwood et al. 2005). Myocardial T2* increases in concert with LV function recovery in thalassemia patients with heart failure. MRI has been used to evaluate different chelation regimens specifically for their action on the myocardium.

15.5
Post-operative Evaluation of Congenital Heart Disease

The typical cardiac MRI protocol in the setting of postoperative tetralogy of Fallot, or after a complex two ventricle repair comprises the following sequences: Dynamic bright blood imaging for ventricular function, thin section bright blood imaging of the branch pulmonary arteries, right ventricular and left ventricular outflow tracts, and the aortic arch, flow velocity mapping of the pulmonary artery, ascending aorta, atrioventricular valves and the branch pulmonary arteries to determine QP:QS, the degree of pulmonary, aortic and atrioventricular valve regurgitation, and the differential pulmonary flow to both lungs respectively, and gadolinium enhanced 3D MR angiography to determine the status of the extra-cardiac vasculature. Following a single ventricle repair, or following an intra-atrial repair for transposition of great arteries, additional bright blood sequences are performed of the atrial baffle (Fig. 15.18), or the Fontan circuit as necessary. Following a Fontan procedure, the performance of the MR angiogram may be modified with simultaneous upper and lower extremity intravenous contrast injections to accommodate the slow venous return, and to reduce artifacts from unopacified venous blood. Recent preliminary clinical experience using 3D-SSFP with respirator navigator whole heart imaging suggests that excellent depiction of the Fontan pathways may be achieved without the need for contrast injection.

MRI provides more precise and reproducible quantification of ventricular volumes, mass and function than 2D echocardiography (Helbing et al. 1995). This is especially the case for the RV (Grothues et al. 2004; Helbing et al. 1996) which is usually the chamber implicated in congenital heart disease. Sequential measurements of RV volumes, mass and function, and pulmonary regurgitant fraction are important for post-operative management after repair of tetralogy of Fallot (Fig. 15.6) (Niezen et al. 1996), and intra-atrial repair of d-transposition of great arteries (Fig. 15.19). This unique information may have prognostic and therapeutic implications for the management of post-operative patients. It is effective for demonstrating ste-

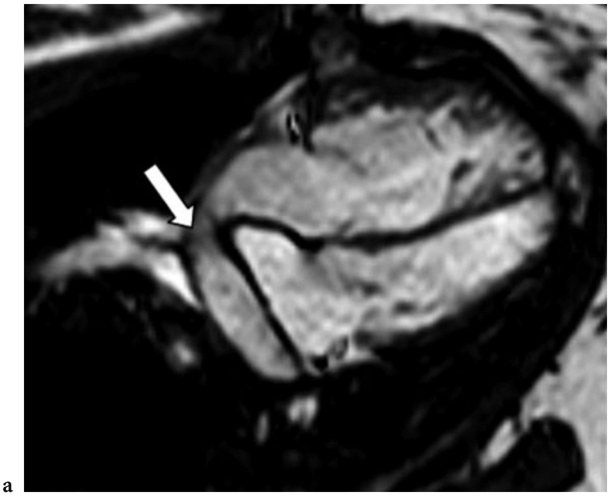

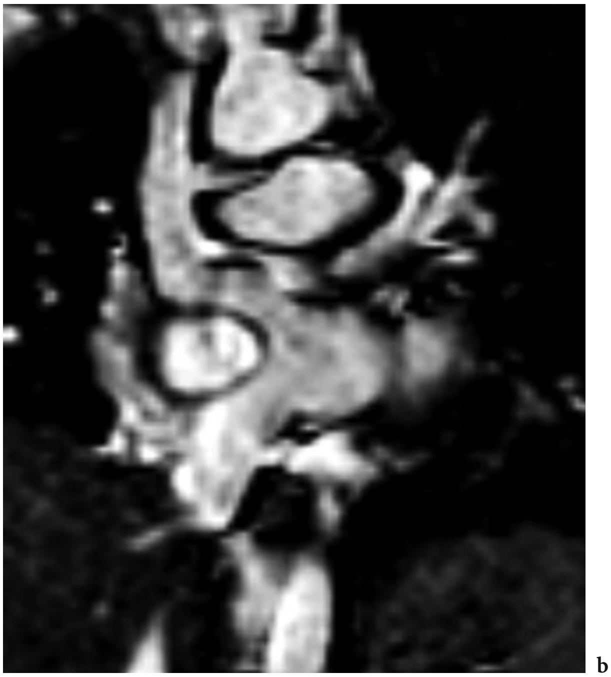

Fig. 15.18. a Cine TFE image showing mildly hypertrophied right ventricle in a patient with d-transposition of great arteries after an atrial switch procedure. Arrow points to the pulmonary venous baffle directed towards the RV. **b** Characteristic 'trouser-like' appearance of the SVC and IVC entering the systemic venous baffle in the same patient

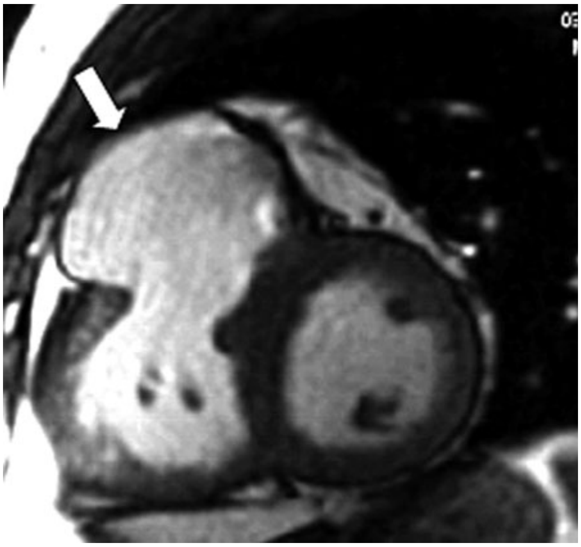

Fig. 15.19. Cine SSFP image showing right ventricular outflow tract patch aneurysm (*arrow*) in corrected tetralogy of Fallot

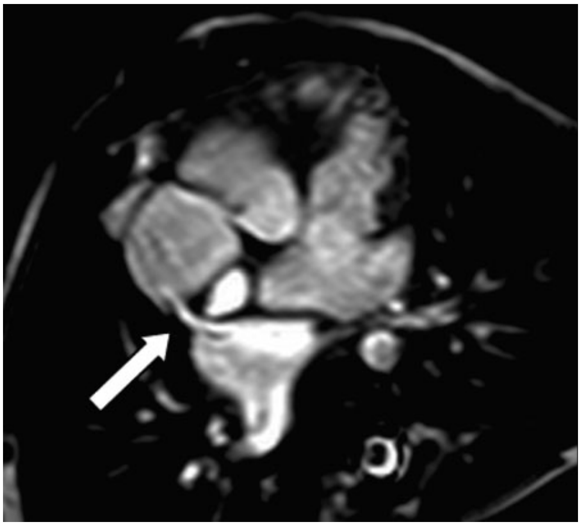

Fig. 15.20. Severe stenosis of the pulmonary venous baffle (*arrow*) after an atrial switch procedure for d-transposition of great arteries

noses of intra-atrial baffles (Fig. 15.20) after repair of transposition of the great arteries (Chung et al. 1988). MRI is also indicated for evaluation of cardiovascular morphology and function both during and after the various stages of surgical repair for hypoplastic left heart syndrome (Kondo et al. 1991) (Fig. 15.3) and single ventricle (Fogel et al. 1996).

15.6
Limitations of Cardiac MRI in Children

MRI does have a number of limitations in the evaluation of the pediatric heart. Sedation or anesthesia is required for most patients less than 8 years of age. Artifacts caused by stainless steel coils, stents, and clips may limit the information gained in the vicinity of the metallic object, or occasionally, may negate the utility of the entire study. Pacemakers, defibrillators, and epicardial wires are still contra-indications for performance of a MRI. Some sequences like coronary MRA, perfusion, and viability imaging are technically challenging in the setting of very small patient sizes and high heart rates. MRI cannot measure pressure gradients, pulmonary vascular resistance or oxygen saturation, and therefore cannot obviate the need for a diagnostic cardiac catheterization in a number of cases. The spatial resolution of conventional MRI sequences is usually inadequate to assess thin and mobile valvular structures like chordae, cusps or commissures. There is a problem with accessibility to magnets in smaller hospitals, and the availability of MRI personnel who are trained in congenital heart disease. Rapid strides have occurred in recent times in MRI technology and training, and hold promise that the list of limitations will shrink dramatically in the near future. For instance, recent papers have described protocols for performance of MRI in patients with permanent pacemakers and defibrillators (Nazarian et al. 2006), as well as sequences for in vivo measurement of oxygen saturation in patients with congenital heart disease (Nield et al. 2005).

15.7
Conclusion

MRI plays an important complementary role to echocardiography in the evaluation of cardiac morphology and function in children with congenital heart disease in the pre-operative and post-operative period.

References

Araoz PA, Reddy GP, Thomson PD, Higgins CB (2002) Images in cardiovascular medicine. Magnetic resonance angiography of criss-cross heart. *Circulation* 105:537

Axel L, Dougherty L (1989) Heart wall motion: improved method of spatial modulation of magnetization for MR imaging. Radiology 172:349–350

Bailes DR, Gilerdale DJ, Bydder GM et al. (1985) Respiratory ordered phase encoding (ROPE): a method for reducing respiratory motion artifacts in MR imaging. Comput Assist Tomogr 9:835–838

Beerbaum P, Korperich H, Gieseke J et al. (2003) Rapid left-to-right shunt quantification in children by phase-contrast magnetic resonance imaging combined with sensitivity encoding. Circulation 108:1355–1361

Beerbaum P, Koerperich H, Sarikouch S et al. (2006) Time-resolved "Cine" 3D contrast-enhanced MR angiography using Centra-Keyhole-SENSE in congenital heart diseases with pulmonary artery pathology [Abstract]. J Cardiovasc MR 8(1):26

Bogren HG, Klipstein RH, Firmin DN et al. (1989) Quantitation of antegrade and retrograde blood flow in the human aorta by magnetic resonance velocity mapping. Am Heart J 117:1214–1222

Bomma C, Rutberg J, Tandri H et al. (2004) Misdiagnosis of arrhythmogenic right ventricular dysplasia/cardiomyopathy. J Cardiovasc Electrophysiol. 15(3):300–306

Brenner LD, Caputo GR, Mostbeck G et al. (1992) Quantification of antegrade and retrograde blood flow in the human aorta by magnetic resonance imaging. J Am Coll Cardiol 20:1246–1250

Caputo GR, Kondo C, Masui T et al. (1991) Right and left lung perfusion: in vitro and in vivo validation with oblique-anle, velocity-encoded cine MR imaging. Radiology 180:693–698

Carr JC, Simonetti O, Bundy J et al. (2001) Cine MR angiography of the heart with segmented true fast imaging with steady-state precession. Radiology 219:828–834

Casolo G, Rega L, Gensini GF (2004) Detection of right atrial and pulmonary artery thrombosis after the Fontan procedure by magnetic resonance imaging. Heart 90(7):825

Castillo E, Osman NF, Reson BD et al. (2005) Quantitative assessment of regional myocardial function with MR-tagging in a multi-center study: interobserver and intraosbserver agreement of fast strain analysis with Harmonic Phase (HARP) MRI. J Cardiovasc Magn Reson 7:783–791

Chia JM, Fischer SE, Wickline SA et al. (2000) Performance of QRS detection for cardiac magnetic resonance imaging with a novel vectorcardiographic triggering method. J Magn Reson Imaging 12:678–688

Cho Y, Park T, Yang DH et al. (2003) Arrhythmogenic right ventricular cardiomyopathy and sudden cardiac death in young Koreans. Circ J 67:925–928

Choi YH, Park JH, Choe YH et al. (1994) MR imaging of Ebstein's anomaly of the tricuspid valve. Am J Roentgenol 163:539–543

Chung KJ, Simpson IA, Glass RF et al. (1988) Cine magnetic resonance imaging after surgical repair in patients with transposition of the great arteries. Circulation 77:104–109

Chung T, Muthupilliai R (2004) Application of SENSE in clinical pediatric body MR imaging. Top Magn Reson Imaging 15:187–196

Chung T, Krishnamurthy R (2005) Contrast-enhanced MR angiography in infants and children. Magn Reson Imaging Clin N Am 13:161–170

Didier D, Higgins CB (1986) Identification and localization of ventricular septal defect by gated magnetic resonance imaging. Am J Cardiol 57:1363–1368

Evans AJ, Iwai F, Grist TA et al. (1993) Magnetic resonance imaging of blood flow with a phase subtraction technique. In vitro and in vivo validation. Invest Radiol 28:109–115

Festa P, Ait-Ali L, Cerillo AG et al. (2006) Magnetic resonance imaging is the diagnostic tool of choice in the preoperative evaluation of patients with partial anomalous pulmonary venous return. Int J Cardiovasc Imaging 22:685–693

Firmin DN, Nayler GL, Klipstein RH et al. (1987) In vivo validation of MR velocity imaging. J Comput Assis Tomogr 11:751–756

Fischer SE, Wickline SA, Lorenz CH (1999) Novel real-time R-wave detection algorithm based on the vectorcardiogram for accurate gated magnetic resonance acquisitions. Magn Reson Med 42:361–370

Flamm SD, Muthupillai R (2004) Coronary artery magnetic resonance angiography. JMRI 19:686–709

Fletcher BD, Jacobstein MD, Nelson AD et al. (1984) Gated magnetic resonance imaging fo congenital cardiac malformation. Radiology 150:137–140

Fogel MA, Weinberg PM, Chin AJ et al. (1996) Late ventricular geometry and performance changes of functional single ventricle throughout staged Fontan reconstruction assessed by magnetic resonance imaging. J Am Coll Cardiol 28:212–221

Fogel MA, Weinberg PM, Gupta KB et al. (1998) Mechanics of the single left ventricle: a study in ventricular-ventricular interaction II. Circulation 98:330–338

Fogel MA (2000) Assessment of cardiac function by magnetic resonance imaging. Pediatr Cardiol 21:59–69

Frayne R, Steinman DA, Ethier CR et al. (1995) Accuracy of MR phase contrast velocity measurements for unsteady flow. J Magn Reson Imaging 5:428–431

Goo HW, Yang DH, Park IS et al. (2007) Time-resolved three dimensional contrast enhanced magnetic resonance angiography in patients with Fontan operation or bidirectional cavopulmonary connection: Initial experience. J Magn Reson Imaging 25:727–736

Greil GF, Geva T, Maier SE et al. (2002a) Effect of acquisition parameters on the accuracy of velocity encoded cine magnetic resonance imaging blood flow measurements. JMRI 15:47–54

Greil GF, Stuber M, Botnar RM et al. (2002b) Coronary magnetic resonance angiography in adolescents and young adults with Kawasaki disease. Circulation 105:908–911

Grist TM, Thornton FJ (2005) Magnetic resonance angiography in children: technique, indications, and imaging findings. Pediatr Radiol 35:26–39

Grotenhuis HB, Westenberg JJ, Doornbos J et al. (2006) Aortic root dysfunctioning and its effect on left ventricular function in Ross procedure patients assessed with magnetic resonance imaging. Am Heart J 152:975.e1–8

Grothues F, Moon JC, Bellenger NG et al. (2004) Interstudy reproducibility of right ventricular volumes, function and mass with cardiovascular magnetic resonance. Am Heart J 147:218–223

Helbing WA, Bosch HG, Maliepaard C et al. (1995) Comparison of echocardiographic methods with magnetic resonance imaging for assessment of right ventricular function in children. Am J Cardiol 76:589–594

Helbing WA, Niezen RA, Cessie SL et al. (1996) Right ventricular diastolic function in children with pulmonary regurgitation after repair of tetraology of Fallot: volumetric evaluation by magnetic resonance velocity mapping. J Am Coll Cardiol 28:1827–1835

Helbing WA, de Roos A (2000) Clinical applications of cardiac magnetic resonance imaging after repair of tetralogy of Fallot. Pediatr Cardiol 21:70–79

Henk CB, Higgins CB, Saeed M (2005) Endovascular interventional MRI. J Magn Reson Imaging 22(4):451–460

Herfkens RJ, Higgins CB, Hricak H et al. (1983) Nuclear magnetic resonance imaging of the cardiovascular sustem: normal and pathologic findings. Radiology 147:749–759

Hernandez RJ, Aisen AM, Foo TKF et al. (1993) Thoracic cardiovascular anomalies in children: evaluation with a fast gradient-recalled-echo sequence with cardiac-triggered segmented acquisition. Radiology 188:755–780

Hoffmann U, Globits S, Schima W et al. (2003) Usefulness of magnetic resonance imaging of cardiac and paracardiac masses. Am J Cardiol. 92(7):890–895

Hundley WG, Li HF, Lange RA et al. (1995) Assessment of left-to-right intracardiac shunting by velocity-encoded, phase-difference magnetic resonance imaging. A comparison with oximetric and indicator dilution techniques Circulation 91:2955–2960

Jahnke C, Paetsch I, Gebker R et al. (2006) Accelerated 4D dobutamine stress MR imaging with k-t BLAST: Feasibility and diagnostic performance. Radiology 241:718–728

Kellenberger CJ, Macgowan CK, Roman KS et al. (2005) Hemodynamic evaluation for the peripheral pulmonary circulation by cine phase-contrast magnetic resonance imaging. JMRI 22:780–787

Kersting-Sommerhoff BA, Diethelm L, Stanger P et al. (1990a) Evaluation of complex congenital ventricular anomalies with magnetic resonance imaging. Am Heart J120:133–142

Kersting-Sommerhoff B, Seelos KC, Hardy C et al. (1990b) Evaluation of surgical procedures for cyanotic congenital heart disease by using MR imaging. AJR Am J Roentgenol 155:259–266

Kiaffas MG, Powell AJ, Geva T (2002) Magnetic resonance imaging evaluation of cardiac tumor characteristics in infants and children. Am J Cardiol 89(10):1229–1233

Kim RJ, Wu E, Rafael A et al. (2000) The use of contrast-enhanced magnetic resonance imaging to identify reversible myocardial dysfunction. N Engl J Med 343:1445–1453

Kim WY, Danias PG, Stuber M et al. (2001) Coronary magnetic resonance angiography for the detection of coronary stenoses. N Engl J Med 345:1445–1453

Kondo C, Caputo GR, Semelka R et al. (1991a) Right and left ventricular stroke volume measurements with velocity-encoded cine MR imaging: in vitro and in vivo validation. AJR Am J Roentgenol 157:9–16

Kondo C, Hardy C, Higgins SS et al. (1991b) Nuclear magnetic resonance imaging of the palliative operation for hypoplastic left heart syndrome. J Am Coll Cardiol 18:817–823

Korcyk D, Edwards CC, Armstrong G et al. (2004) Contrast-enhanced cardiac magnetic resonance in a patient with familial isolated ventricular non-compaction. J Cardiovasc Magn Reson 6(2):569–576

Korperich H, Gieseke J, Barth P et al. (2004) Flow volume and shunt quantification in pediatric congenital heart disease by real-time magnetic resonance velocity mapping. Circulation 109:1987–1993

Krishnamurthy R, Muthupillai R, Vick GW et al. (2004) Feasibility of a free breathing SSFP sequence for dynamic cardiac imaging in pediatric patients [Abstract]. Pediatr Radiol 34; Supplement 1:S75

Lee KH, Yoon CS, Chow KO et al. (2001) Use of imaging for assessing anatomical relationships of tracheobronchial anomalies associated with left pulmonary artery sling. Pediatr Radiol 31:269–278

Link KM, Herrera MA, D'Souza VJ et al. (1988) MR imaging of Ebstein anomaly: results in four cases. AJR Am J Roentgenol 150:363–367

Markl M, Pelc NJ (2004) On flow effects in balanced steady-state free precession imaging: Pictorial description, parameter dependence and clinical implications. J Magn Reson Imaging 20:697–705

Mayo JR, Roberson D, Sommerhoff B et al. (1990) MR imaging of double outlet right ventricle. J Comput Assist Tomogr 14:336–339

Menteer J, Weinberg PM, Fogel MA (2005) Quantifying regional right ventricular fundtion in tertralogy of Fallot. J Cardiovasc Magn Reson 7:753–761

Mirowitz SA, Gutierrez FR, Canter CE et al. (1989) Tetralogy of Fallot: MR findings. Radiology 171:207–212

Muthupillai R, Vick GW, Flamm SD et al. (2003) Time-resolved contrast-enhanced magnetic resonance angiography in pediatric patients using sensitivity encoding. J Magn Reson Imaging 17:559–564

Nagel E, Lehmkuhl HB, Bocksch W et al. (1999) Noninvasive diagnosis of ischemia-induced wall motion abnormalities with the use of high dose dobutamine stress MRI: comparison with dobutamine stress echocardiography. Circulation 99:763–770

Nazarian S, Roguin A, Zviman MM et al. (2006) Clinical utility and safety of a protocol for noncardiac and cardiac magnetic resonance imaging of patients with permanent pacemakers and implantable-cardioverter defibrillators at 1.5 tesla. Circulation 114:1277–1284

Nield LE, Qi XL, Valsangiocomo ER et al. (2005) In vivo MRI measurement of blood oxygen saturation in children with congenital heart disease. Pediatr Radiol 35:179–185

Niezen RA, Helbing WA, van der Wall EE et al. (1996) Biventricular systolic function and mass studied with MR imaging in children with pulmonary regurgitation after repair for tetralogy of Fallot. Radiology 201:135–140

Oosterhof T, Mulder BJM, Hubert WV et al. (2006) Cardiovascular magnetic resonance in the follow-up of patients with corrected tetralogy of Fallot: a review. Am Heart J 151:265–272

Oppelt A, GraumannR. BarfussH (1986) Fisp – a new fast MRI sequence. Electromedica 54:15–18

Oshinski JN, Parks WJ, Markou CP et al. (1996) Improved measurement of pressure gradients in aortic coarctation by magnetic resonance imaging. J Am Coll Cardiol 28:1818–1826

Petersen SE, Selvanayagam JB, Wiesmann F et al. (2005) Left ventricular non-compaction: insights from cardiovascular magnetic resonance imaging. J Am Coll Cardiol 46(1):101–105

Piaw CS, Kiam OT, Rapaee A et al. (2006) Use of non-invasive phase contrast magnetic resonance imaging for estimation of atrial septal defect size and morphology: a comparison with transesophageal echo. Cardiovasc Intervent Radiol 29(2):230–234

Powell AJ, Geva T (2000) Blood flow measurement by magnetic resonacne imaging in congenital heart disease. Pediatr Cardiol 21:47–58

Powell AJ, Maier SE, Chung T et al. (2000) Phase-velocity cine magnetic resonance imaging measurement of pulsatile bloodflow in children and young adults: in vitro and in vivo validation. Pediatr Cardiol 21:104–110

Prakash A, Garg R, Marcus EN et al. (2006) Faster flow quantification using sensitivity encoding for velocity-encoded cine magnetic resonance imaging: in vitro and in vivo validation. JMRI 24:676–682

Prakash A, Powell AJ, Krishnamurthy R et al. (2004) Magnetic resonance imaging evaluation of myocardial perfusion and viability in congential and acquired pediatric heart disease. Am J Cardiol 93:657–661

Prince MR, Yucel E, Kaufman J et al. (1993) Dynamic gadolinium-enhanced three-dimensional abdominal MR arteriography. J Magn Reson Imaging 3:877–881

Pruessmann KP, Weiger M, Schiedegger MB et al. (1999) SENSE: sensitivity encoding for fast MRI. Magn Reson Med 42:952–962

Razavi R, Hill DL, Keevil SF et al. (2003) Cardiac catheterization guided by MRI in children and adults with congenital heart disease. Lancet 362:1877–1882

Rebergen SA, Chin J, Ottenkamp J et al. (1993a) Pulmonary regurgitation in the late postoperative follow-up of tetralogy of Fallot. Volumetric quantitation by nuclear magnetic resonance velocity mapping. Circulation 88:2257–2266

Rebergen SA, Ottenkamp J, Doornbos J et al. (1993b) Postoperative pulmonary flow dynamics after Fontan surgery: assessment with nuclear magnetic resonance velocity mapping. J Am Coll Cardiol 21:123–131

Rebergen SA, Helbing WA, van der Wall EE et al. (1995) MR velocity mapping of tricuspid flow in healthy children and in patients who have undergone Mustard or Senning repair. Radiology 194:505–512

Rickers C, Wilke NM, Jerosch-Herold M et al. (2005) Utility of cardiac magnetic resonance imaging in the diagnosis of hypertrophic cardiomyopathy. Circulation 112(6):855–861

Roman KS, Kellenberger CJ, Farooq S et al. (2005) Comparative imaging of differential pulmonary blood flow in patients with congenital heart disease: magnetic resonance imaging versus lung perfusion scinitigraphy. Pediatr Radiol 25:295–301

Sakuma H, Yasutaka I, Suzawa N et al. (2005) Assessment of coronary arteries with total study time of less then 30 minutes by using whole-heart coronary MR angiography. Radiology 237:316–321

Schlesinger AE, Krishnamurthy R, Sena LM et al. (2005) Incomplete double aortic arch with atresia of the distal left arch: distinctive imaging appearance. AJR Am J Roentgenol 184:1634–1639

Schwitter J (2006) Myocardial perfusion. JMRI 24:953–963

Sechtem U, Pflugfelder P, Cassidy MC et al. (1987) Ventricular septal defect: visualization of shunt flow and determination of shunt size by cine MR imaging. AJR Am J Roentgenol 149:689–692

Sieverding L, Jung WI, Klose U et al. (1992) Noninvasive blood flow measurement and quantification of shunt volume by cine magnetic resonacne in congenital heart disease. Preliminary results. Pediatr Radiol 22:48–54

Simonetti OP, Finn JP, White RD et al. (1996) "Black blood" T2-weighted inversion-recovery MR imaging of the heart. Radiology 199:45–57

Sodickson DK, Manning WJ (1997) Simultaneous acquisition of spatial harmonics (SMASH): ultra-fast imaging with radiofrequency coil arrays. Magn Reson Med 38:591–603

Sorensen TS, Korperich H, Greil GF et al. (2004) Operator-independent isotropic three-dimensional magnetic resonance imaging for morphology in congenital heart disease. Circulation 110:163–169

Sorensen TS, Beerbaum P, Korperich H et al. (2005) Three-dimensional, isotropic MRI: a unified approach to quantification and visualization in congenital heart diease. Int J Cardiovasc Imag 21:283–292

Spuentrup E, Fausten B, Kinzel S et al. (2005) Molecular magnetic resonance imaging of atrial clots in a swine model. Circulation 112(3):396–399

Sridharan S, Derrick G, Deanfield J et al. (2006) Assessment of differential branch pulmonary blood flow: a comparative study of phase contrast magnetic resonance imaging and radionuclide lung perfusion imaging. Heart 92:963–968

Steffens JC, Bourne MW, Sakuma H et al. (1994) Quantification of collateral blood flow in coarctation of the aorta by velocity encoded cine magnetic resonance imaging. Circulation 90:937–943

Stuber M, Botnar RM, Kissinger KV et al. (2001) Free-breathing black-blood coronary MR angiography: initial results. Radiology 219:278–283

Su JT, Chung T, Muthupillai R et al. (2005) Usefulness of real-time navigator magnetic resonane imaging for evaluating coronary artery origins in pediatric patients. Am J Cardiol 95:679–682

Su JT, Chung T, Kovalchin JP (2004) Magnetic resonance imaging of coronary and systemic aneurysms in Kawasaki disease. Cardiol Young 14:198–199

Su JT, Krishnamurthy R, Chung T et al. (2007) Anomalous right coronary artery from the pulmonary artery: noninvasive diagnosis and serial evaluation. J Cardiovasc Magn Reson 9:57–61

Tandri H, Saranathan M, Rodriguez ER et al. (2005) Noninvasive detection of myocardial fibrosis in arrhythmogenic right ventricular cardiomyopathy using delayed-enhancement magnetic resonance imaging. J Am Coll Cardiol 45(1):98–103

Taylor AM, Dymarkowski S, De MeerleerK et al. (2005a) Validation and application of single breath-hold cine cardiac MR for ventricular function assessment in children with congenital heart disease at rest and during adenosine stress. J Cardiovasc Magn Reson 7:743–751

Taylor AM, Dymarkowski S, Hamaekers P et al. (2005b) MR coronary angiography and late-enhancement myocardial MR in children who underwent arterial switch surgery for transposition of great arteries. Radiology 234:542–547

Teraoka K (2005) Delayed contrast enhancement of MRI in hypertrophic cardiomyopathy. Magn Reson Imaging 23(5):701

van der Loo B, Jenni R (2003) Isolated noncompaction of the myocardium. Circulation 107(7):e50

Van Praagh R (1984) The segmental approach clarified. Cardiovasc Intervent Radiol 7(6):320–325

Valsangiocomo ER, Barrea C, MacGowan CK et al. (2003) Phase-contrast MR assessment of pulmonary venous blood flow in children with surgically repaired pulmonary veins. Pediatr Radiol 33:607–613

Weber OM, Martin AJ, Higgins CB (2003) Whole-heart steady-state free precession coronary artery magnetic resonance angiography. Magn Reson Med 50:1223–1228

Westwood MA, Firmin DN, Gildo M et al. (2005a) Intercenter reproducibility of magnetic resonance T2* measurements of myocardial iron in thalassaemia. Int J Cardiovasc Imaging 21(5):531–538

Westwood MA, Wonke B, Maceira AM et al. (2005b) Left ventricular diastolic function compared with T2* cardiovascular magnetic resonance for early detection of myocardial iron overload in thalassemia major. J Magn Reson Imaging 22(2):229–233

Wood JC, Enriquez C, Ghugre N et al. (2005) Physiology and pathophysiology of iron cardiomyopathy in thalassemia. Ann NY Acad Sci 1054:386–395

Wood JC (2006) Anatomical assessment of congenital heart disease. J Cardiovasc Magn Reson 8:595–606

Yoo SJ, Kim YM, Choe YH (1999) Magnetic resonance imaging of complex congenital heart disease. Int J Card Imaging 15:151–160

Zerhouni EA, Parish DM, Rogers WJ et al. (1988) Human heart: tagging with MR imaging – a method of noninvasive assessment of myocardial motion. Radiology 169:59

Pediatric Cardiac CT

Laureen Sena, Rajesh Krishnamurthy, and Taylor Chung

CONTENTS

16.1 **Introduction** *361*

16.2 **Technical Considerations** *362*
16.2.1 Spatial and Temporal Resolution *362*
16.2.2 Radiation Dose Considerations for MDCT *363*
16.2.3 Scanning Technique for Nongated and Gated MDCT Angiography *365*

16.3 **Complementary Role of MDCT and MRI for Cardiac Imaging** *369*

16.4 **Clinical Applications** *370*
16.4.1 Pulmonary Vasculature *370*
16.4.1.1 Pulmonary Arteries *370*
16.4.1.2 Pulmonary Embolism *371*
16.4.1.3 Pulmonary Vein Morphology *375*
16.4.1.4 Congenital Pulmonary Venolobar Syndrome *376*
16.4.2 Aorta *378*
16.4.2.1 Valvular Aortic Stenosis *378*
16.4.2.2 Connective Tissue Disorders *378*
16.4.2.3 Takayasu Arteritis *381*
16.4.2.4 Coarctation *381*
16.4.3 Coronary Artery Anomalies *382*
16.4.3.1 Kawasaki's Disease *383*
16.4.4 Airway Compromise in Patients with CHD *384*
16.4.5 Cardiac Chamber Morphology and Ventricular Function *388*
16.4.6 Post-operative Congenital Heart Disease *390*

16.5 **Conclusion** *393*

References *393*

16.1 Introduction

Recent improvements in technology have significantly advanced the role of multidetector CT (MDCT) in noninvasive imaging of the cardiovascular system. From the early use of helical CT for imaging anomalies of the thoracic vasculature (Hopkins et al. 1996; Westra et al. 1999), MDCT has become an important complementary modality to echocardiography and MRI for noninvasive imaging of cardiac morphology and function (Juergens et al. 2004), coronary arteries (Schoepf et al. 2004; Schoenhagen et al. 2004) and following operative and catheter intervention of many forms of congenital heart disease (Kawano et al. 2000). From the development of the first scanner in 1992 with 2 detectors that could acquire spatial information simultaneously, MDCT rapidly evolved to systems with 16 detectors, and presently 64 detector scanners are widely in use. A multidetector CT with 'x' number of detectors can obtain 'x' times more data per revolution than single detector systems, and current MDCT scanners have gantries that can spin faster than two revolutions per second, further increasing the speed of data acquisition. The increased speed of scanning can be used for increased volume coverage and improved longitudinal (z-axis) spatial resolution, and has significantly decreased the need for sedation and anesthesia when imaging younger children who cannot lie still or voluntarily suspend respiration. In addition, the increased speed of scanning can now be used to scan faster than the heart rate in order to produce motion free images of the heart and vasculature.

The driving force behind the rapid development of MDCT for cardiac imaging has been the noninvasive detection of adult coronary artery disease using coronary MDCT angiography with electrocardiography (ECG)-gating (Schoepf et al. 2004;

L. Sena, MD
Department of Radiology, Boston Children`s Hospital, 300 Longwood Avenue, Boston, MA 0215, USA
R. Krishnamurthy, MD
T. Chung, MD
Department of Diagnostic Imaging (MC 2-2521), Texas Children`s Hospital, 6621 Fannin St., Houston , TX 77030-2399, USA

Schoenhagen et al. 2004). Dedicated cardiac reconstruction algorithms have been developed that have broadened the clinical applications beyond evaluation of extra cardiac vascular morphology to the assessment of intracardiac morphology and ventricular function. In addition, dose modulation techniques (Jakobs et al. 2002; Goo and Suh 2006) have been developed that have significantly reduced radiation exposure during scanning. This chapter will focus on the technical aspects of cardiovascular imaging with MDCT for morphologic assessment of extracardiac thoracic vasculature in congenital heart disease and performing gated examinations for imaging the coronary arteries and cardiac function. The relative merits of cardiovascular imaging with MRI vs MDCT will be discussed with regards to specific issues pertaining to imaging patients with congenital heart disease (CHD).

16.2
Technical Considerations

16.2.1
Spatial and Temporal Resolution

The spatial resolution is equivalent to the thinnest axial slice that can be reconstructed based on the CT detector configuration. Current MDCT scanners have dramatically improved spatial resolution and many systems have an in plane spatial resolution that is sub-millimeter depending on the reconstruction algorithm. As compared with prior MDCT systems, the introduction of 16 MDCT with faster rotation speeds has resulted in routine imaging with higher, sub-millimeter spatial resolution in the longitudinal plane as well (Mahesh 2002). For the first time, CT imaging data are being acquired with equal resolution in all three imaging planes. Images are therefore comprised of isotropic voxels so that there is significantly less misregistration of the anatomy when the imaging data is reconstructed with arbitrary obliquities. Isotropic cardiovascular imaging with MDCT has led to a vast improvement in the quality of processing techniques for visualizing the vasculature with multiplanar reformatting, maximum intensity projection (MIP), as well as 3-D reconstruction with volume rendering.

Producing motion free images of the heart and coronary arteries with high spatial resolution is one of the major challenges to be overcome for successful cardiac imaging, and requires the imaging modality to produce images faster than the heart rate, or with an increased temporal resolution or frame rate. In MDCT, the temporal resolution is equivalent to half the gantry rotation time, because each reconstructed image requires CT data from half of a complete gantry rotation. To generate a smooth cine image of cardiac motion throughout systole and diastole, the temporal resolution has to be improved so that more images can be reconstructed per RR interval with a shorter time between them. This is accomplished with multisegment image reconstruction (Horiguchi et al. 2002). Imaging data acquired over several heartbeats is added to generate a single image during every half revolution of the gantry. Multiple images can then be reconstructed during systole and diastole and can be displayed as a cine loop to assess ventricular function.

There are a few drawbacks of multisegment reconstruction which are of particular concern when imaging children who have faster heart rates and are inherently more susceptible to the effects of ionizing radiation. Multisegment reconstruction requires a much lower CT pitch, which results in greater data oversampling and a higher radiation dose. Also, since multiple heartbeats are used to fill the 180° gantry rotation necessary for image reconstruction, fluctuation of the heart rate during the scan can cause significant motion artifact in the reconstructed images.

Prospective ECG triggering and retrospective ECG gating are two different processing methods for synchronizing the patient's electrocardiogram tracing and imaging data that are simultaneously acquired with MDCT. With prospective triggering, the gantry rotation is initiated during a predefined moment in the cardiac cycle from the QRS complex when there is less motion, typically during diastole. This technique delivers a very low radiation dose because the x-ray tube is only turned on when data needed for image reconstruction is acquired. The technique can be used successfully when static images of moving structures are desired, as in confirming anomalous coronary arteries in infants with rapid heart rates.

Retrospective ECG gating is more commonly used with current MDCT scanners because it allows multiple phases to be acquired throughout the cardiac cycle for more accurate depiction of the coronary arteries and for cine imaging of ventricular function, wall motion and motion of valves (Achenbach et al.

2000; Flohr et al. 2002). In order to freeze cardiac motion, images are reconstructed retrospectively using a short temporal segment that is located in the same position of the RR interval over multiple cardiac cycles. Reconstructing multiple phases requires oversampling of image data and reducing the pitch to 0.2–0.35, resulting in longer scan times and increased radiation exposure to the patient.

16.2.2
Radiation Dose Considerations for MDCT

It is well known that children are more sensitive to the effects of ionizing radiation than adults, and have a longer life-span with a correspondingly greater potential for the development of radiation-induced malignancies. It is important to limit the indications for cardiac related MDCT examinations to those in which the useful diagnostic information cannot be obtained from an alternative imaging modality such as echocardiography or magnetic resonance imaging. MDCT examinations should be performed with techniques that provide acceptable and diagnostic image quality with the lowest possible radiation exposure. The use of MDCT for pediatric cardiac applications should therefore be approached in terms of what needs to be seen, rather than what can be seen. Important scanning parameters affecting image quality and radiation dose include tube current, pitch, beam collimation, tube voltage, table speed and gantry rotation time (Donnelly and Frush 2003; Kalra et al. 2004). The most important factor for reducing radiation exposure is to use techniques that adjust the tube current according to the weight of the child (Donnelly et al. 2001). In addition, all recently manufactured MDCT scanners are now equipped with automatic tube current modulation. This dose reduction technique automatically adjusts the tube current along the x-y plane (angular modulation) or along the z-axis (longitudinal modulation) or both (combined modulation) depending on the size, shape and density of the scanning region (Kalra 2004) (Fig. 16.1). Angular modulation is the variation of the tube output that is either predefined by analysis of a localizer scan or is determined during the scan by evaluating the signal at the level of the detector. Longitudinal modulation is a variation of tube output similar to automatic exposure control and maintains adequate dose when moving through different body regions during the same examination (i.e. from the thorax to the abdomen). When scanning the thorax for cardiac applications, excluding the arms from the scan range in children, and scanning from caudal to cranial will allow an even greater tube current reduction when using combined tube current modulation (Goo and Suh 2006; Greess et al. 2002).

A reduction in the X-ray tube voltage in contrast enhanced MDCT studies in smaller children will allow a further dose savings while maintaining image contrast (Siegel et al. 2004). Other important measures to decrease radiation dose when scanning children include confining the study to the anatomical area of interest, avoiding multiphase examinations, using faster gantry cycle times and higher pitch (Frush 2002), and restricting the use of ECG-gated acquisitions to only a few select indications described below.

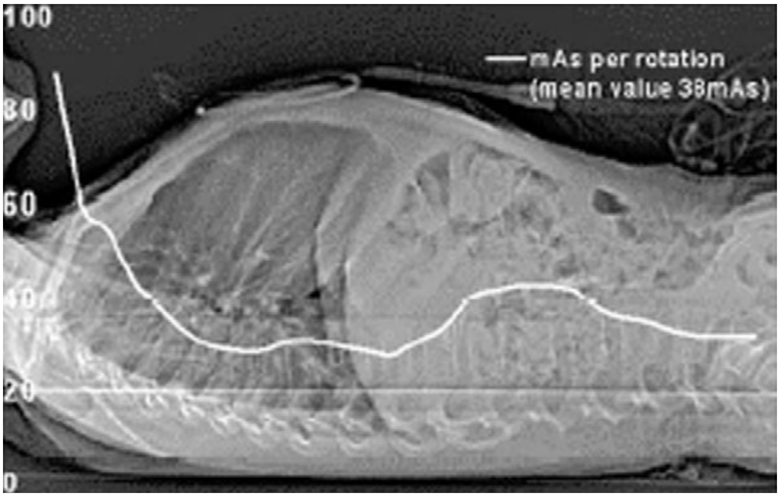

Fig. 16.1. Automatic exposure control with MDCT. Lateral topogram (scout view) for thoracoabdominal CT in a 6-year-old child. The curve represents the automatically adapted milliampere-seconds value as a function of z-axis position during scanning with spiral CT. Although the standard adult protocol was used, the average milliampere-seconds value throughout the scan was adjusted to 38 mAs with automatic exposure control. (Flohr et al. 2005, used with permission)

ECG-gated dose modulation is a technique available to reduce the radiation dose associated with retrospective gating (Jakobs et al. 2002). In those cardiac phases that are not needed for image reconstruction with high spatial resolution, the tube current is reduced to 20% of the initial setting. The full tube current is usually applied in phases relevant to the reconstruction of the coronary arteries where maximal spatial resolution is needed. Dose modulation can result in a mean dose reduction of 47% for imaging the coronary arteries with retrospective gating at heart rates less than 65 bpm (Jakobs et al. 2002). The reduction of radiation exposure with dose modulation is best at low heart rates and with fewer predefined reconstruction phases.

Now that scanners are equipped with more detectors, there is more coverage in the z-axis dimension per gantry rotation for faster gated acquisitions and decreased breath-hold times. Increasing the detector width during scanning further decreases scan time, but this will also decrease the spatial resolution of the exam. Image reconstruction with retrospective ECG gating at very high spatial resolution is necessary for imaging of the coronary arteries for stenosis but comes with the price of more radiation exposure. Imaging for cardiac function and aortic root/ascending aorta for coronary origins usually does not require sub-millimeter slice thickness, and therefore scanning at increased detector width can be used to decrease radiation exposure.

With the knowledge that the use of gating increases radiation dose as much as four- to five fold over that of routine nongated MDCT angiography (MDCTA) with tube current modulation and weight-based protocols, there are only a few specific indications for cardiovascular imaging in children in which a gated acquisition may be considered. Based on these authors' experience as well as others (Siegel 2003), MDCT angiography can be performed without ECG-gating for general evaluation of the extra cardiac vasculature, including the thoracic aorta, systemic and pulmonary veins and arteries. MDCT with prospective ECG triggering can be used for more precise evaluation of the morphology of the heart chambers, including assessment of ventricular aneurysms, cardiac thrombi and tumors, for motionless imaging of the aortic root and ascending aorta if there is a suspicion of dissection, or evaluation of small aortopulmonary collaterals. MDCT for detection of anomalous coronary origin can be performed with either prospective ECG triggering or retrospective ECG gating with dose modulation and predefined reconstruction only in diastole (Fig. 16.2). However, fairly good visibility of the coronary artery origins was shown in a study using nongated MDCT angiography with a 16 detector scanner (Goo et al. 2005), and it is conceivable that 64 MDCT with fast gantry rotation times synchronized to the heart rate will prove even more useful in diagnosing anomalous coronary artery origins in the future. Therefore, coronary artery imaging with MDCT angiography with retrospective ECG gating and multi sector reconstruction (radiation intensive approach) can be reserved for indications which

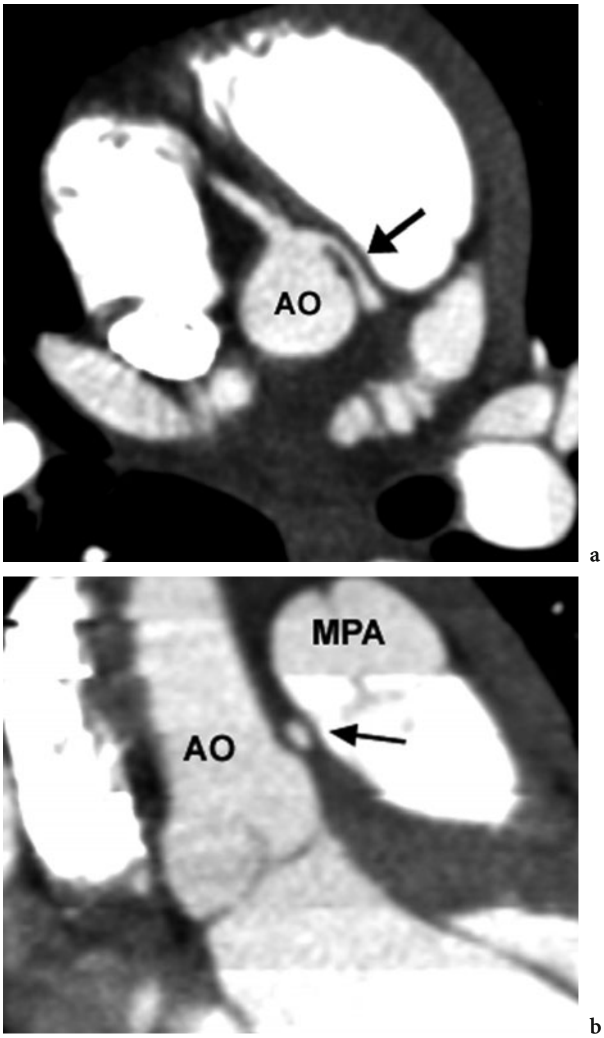

Fig. 16.2a,b. Anomalous left coronary artery. Axial (**a**) and coronal (**b**) MIP images obtained from a retrospectively gated coronary CTA demonstrate an anomalous left coronary artery (*large arrow*) arising from the right coronary sinus and passing between the ascending aorta (*Ao*) and main pulmonary artery (*MPA*)

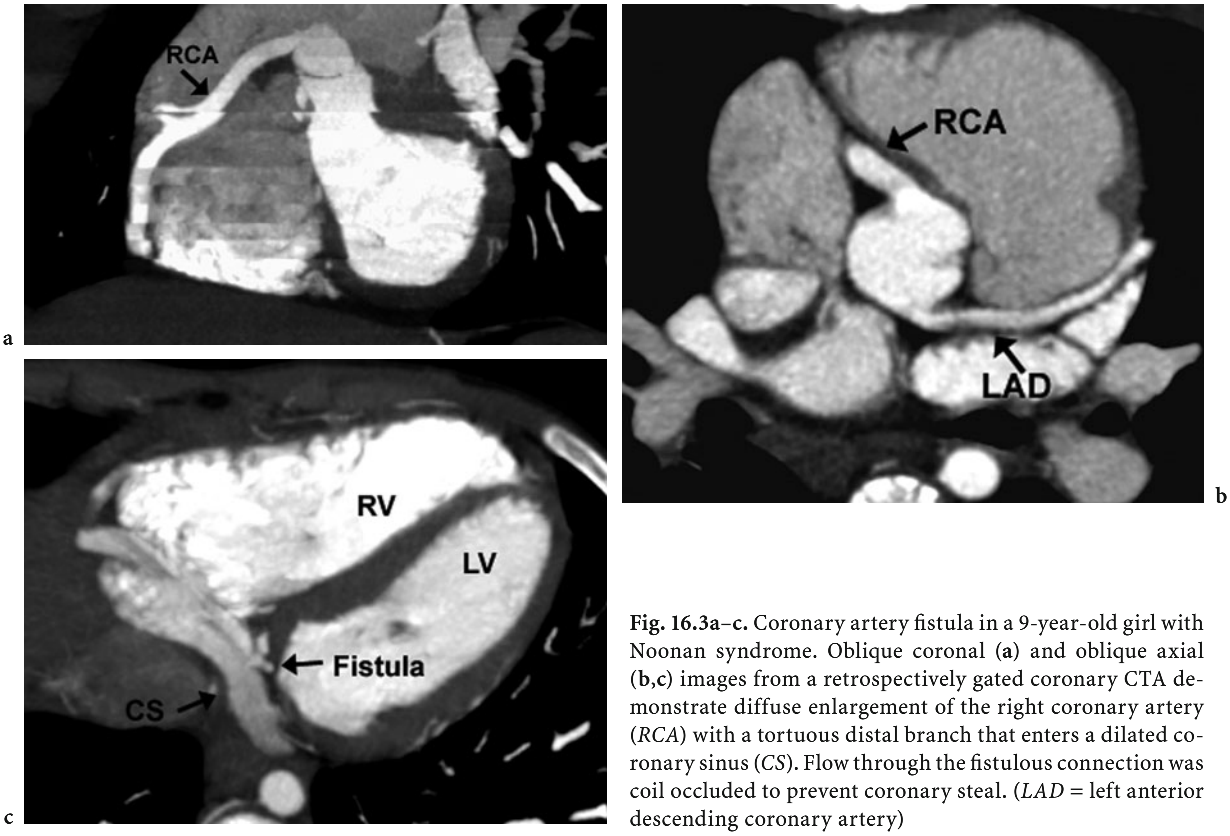

Fig. 16.3a–c. Coronary artery fistula in a 9-year-old girl with Noonan syndrome. Oblique coronal (**a**) and oblique axial (**b**,**c**) images from a retrospectively gated coronary CTA demonstrate diffuse enlargement of the right coronary artery (*RCA*) with a tortuous distal branch that enters a dilated coronary sinus (*CS*). Flow through the fistulous connection was coil occluded to prevent coronary steal. (*LAD* = left anterior descending coronary artery)

require motionless images with high spatial resolution, such as for detection of coronary artery fistula (Fig. 16.3) and stenosis (Fig. 16.4) or aneurysms in patients with Kawasaki disease.

16.2.3
Scanning Technique for Nongated and Gated MDCT Angiography

With the development of faster MDCT scanners, it is now vital for the radiologist performing and interpreting the CT examination to review any information pertaining to the child's form of congenital heart disease and surgical repair or palliation prior to scanning. Patients can have extremely variable sources of pulmonary blood flow, from pulmonary atresia with aortopulmonary collaterals arising from the descending aorta, to Glenn shunts or a cavopulmonary anastomosis between the SVC and the pulmonary arteries in patients with single ventricle physiology. The knowledge of the patient's intracardiac anatomy and relevant surgeries will make planning of the timing of scanning after contrast administration much more accurate in order to effectively opacify the extracardiac vasculature, and avoid the mistake of scanning partially opacified vasculature and confusing it with thrombus (Fig. 16.5). Knowledge of the patient's anatomy will help in choosing the best level in the chest to image for tracking the bolus prior to scanning the entire chest for the angiogram. For example, in patients with pulmonary atresia and major aortopulmonary collateral arteries (MAPCAs), timing off the ascending aorta should be adequate to opacify the collateral vessels, and there is often back filling of the branch pulmonary arteries (if they are present) from the collaterals (Fig. 16.6).

Another important consideration for the timing of contrast injection and scanning is in the patient who is status post Fontan operation. These patients have a single functioning ventricle which supports the aorta and receives the pulmonary venous return, and the systemic venous return is directly routed into the pulmonary arteries without an intervening ventricular chamber. When performing MDCT angiography of Fontan patients, potential aortopulmonary collateral vessels from the aorta need to be imaged,

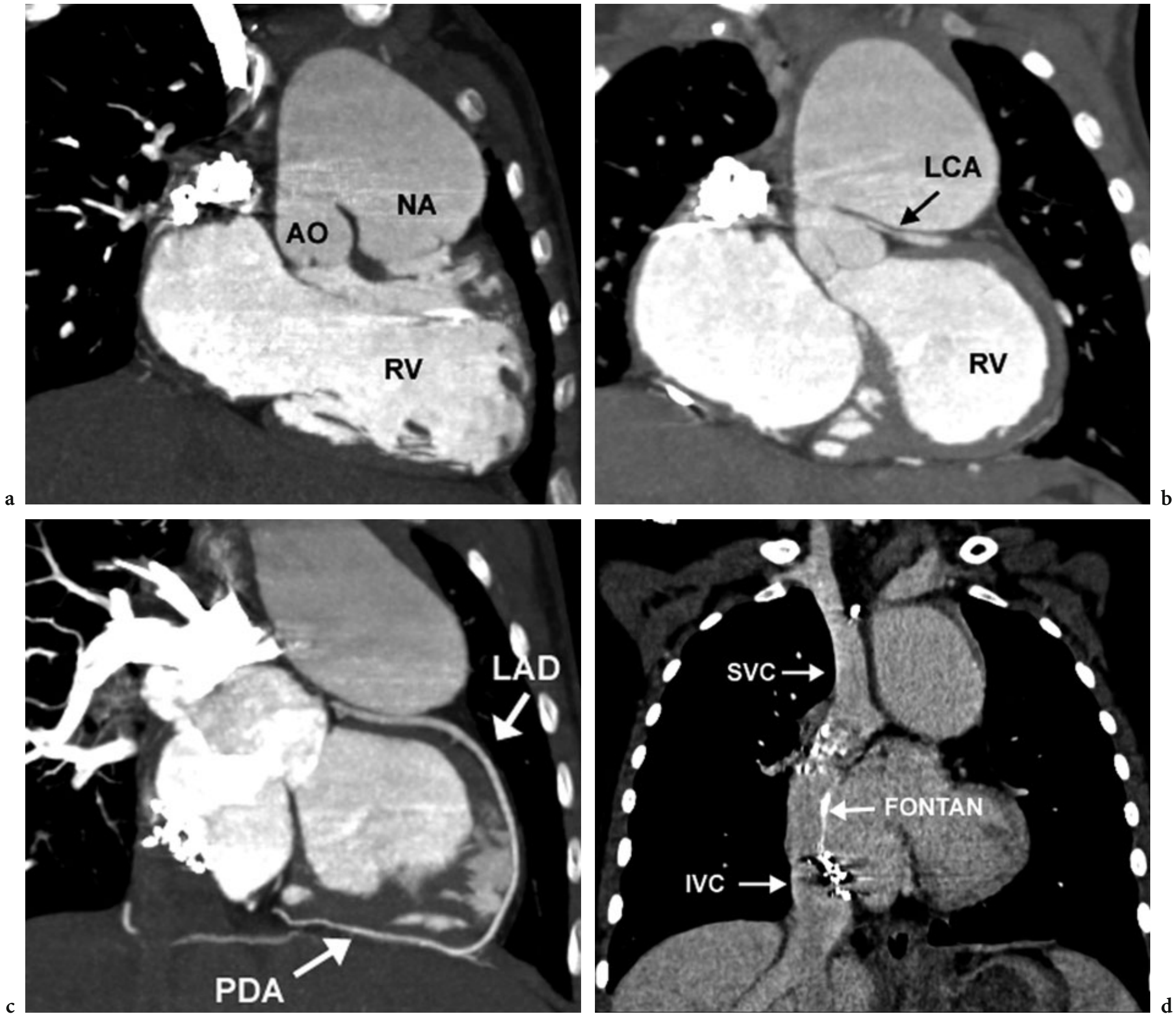

Fig. 16.4a–d. Compression of the left main coronary artery by a dilated neoaorta following the Fontan operation for hypoplastic left heart syndrome. Coronal oblique MIP images show a markedly dilated reconstructed neoaorta (*NA*) arising from the right ventricle (*RV*) that is connected by a patent Stansel anastomosis to the native aorta (*Ao*) (**a**). A moderately compressed proximal left main coronary artery (*LCA*) (**b**) passes inferior to the dilated neoaorta. The left main coronary could not be accessed at cardiac catheterization. This is a left dominant coronary system with the LAD giving rise to the posterior descending coronary artery (*PDA*) (**c**). Delayed venous phase coronal oblique image (**d**) demonstrates patent Fontan pathway between the IVC and SVC and RPA (not shown) with streak artifacts from closure devices placed for prior baffle leaks

as well as the systemic venous pathway from the IVC and SVC to the pulmonary arteries. One may decide to acquire only one set of images at 50–60 s after initial contrast administration, which will be in the venous phase with homogeneous but relatively less opacification of the entire vasculature (see Fig. 16.5). Alternatively, one may acquire two sets of images, the first earlier in the arterial phase at about 20 s to more adequately enhance potential aortopulmonary collaterals, as well as for better visualization of the pulmonary venous system if pulmonary vein stenosis is suspected. In order to decrease radiation exposure and acquire images with more dense and homogeneous opacification of both the pulmonary and systemic vasculature, it is best to perform the examination with simultaneous injections through IV's placed in both the upper and lower extremities (see Fig. 16.14).

Nongated MDCT angiography and gated acquisitions for imaging the coronary arteries or cardiac

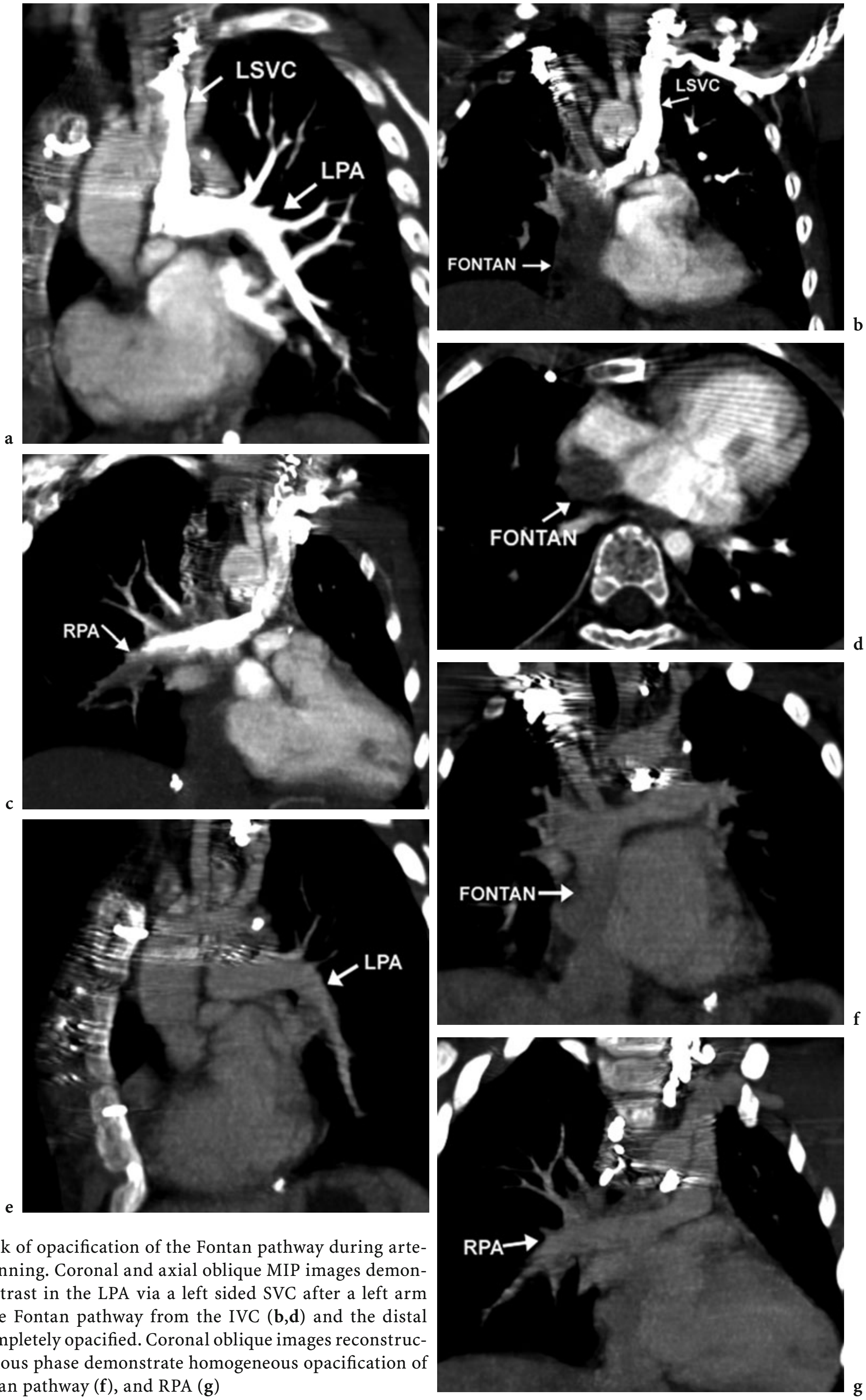
LSVC
LPA
a
LSVC
FONTAN
b
FONTAN
d
RPA
c
FONTAN
f
LPA
e
RPA
g

Fig. 16.5a–g. Lack of opacification of the Fontan pathway during arterial phase of scanning. Coronal and axial oblique MIP images demonstrate dense contrast in the LPA via a left sided SVC after a left arm injection (**a**). The Fontan pathway from the IVC (**b**,**d**) and the distal RPA (**c**) are incompletely opacified. Coronal oblique images reconstructed from the venous phase demonstrate homogeneous opacification of the LPA (**e**) Fontan pathway (**f**), and RPA (**g**)

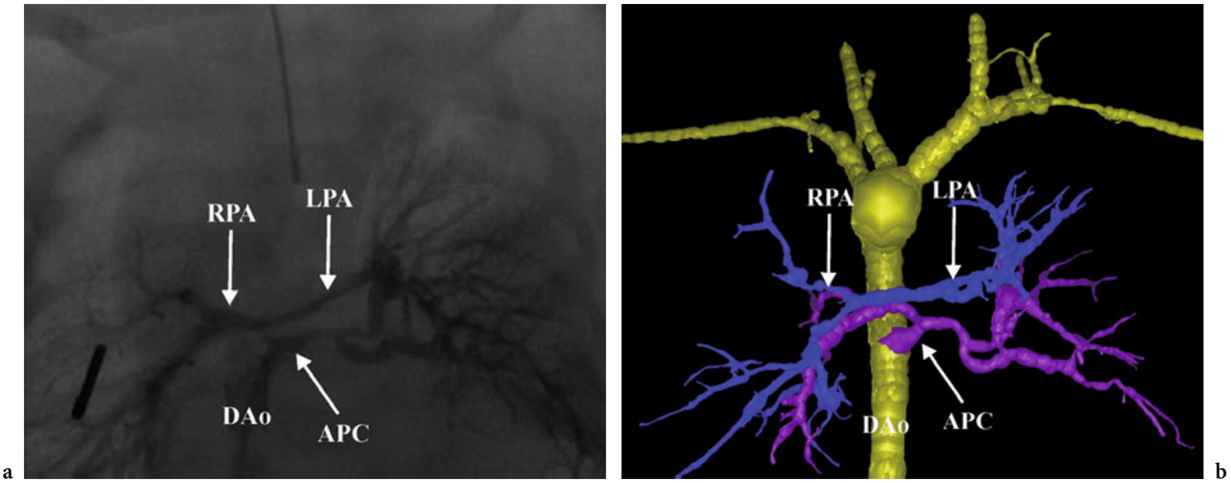

Fig. 16.6a,b. Tetralogy with pulmonary atresia and MAPCAs. Segmented 3D surface model from MDCT angiography demonstrates a collateral (*APC*) from the descending aorta (*Dao*) to the left and right lung connecting to the hypoplastic left (*LPA*) and right (*RPA*) pulmonary arteries (**a**). Corresponding X-ray angiogram (**b**). (Greil et al. 2006, used with permission)

function are usually performed with dual injection of nonionic contrast followed by a saline or dilute contrast flush. Scanning of the heart at peak contrast enhancement during the saline flush reduces the streak artifact of dense contrast material passing through the SVC into the right heart. In adults, rapid contrast injection rates of up to 6 cc/s are administered through an 18–20 gauge IV. Injection rates in children will necessarily be different depending on the size of the IV able to be placed and the amount of contrast to be injected (usually assuming a maximum of 2 cc/kg). Table 16.1 provides a guideline for contrast injection rates by size of IV. For nongated MDCT angiography, the rate can be adjusted so that the total volume of contrast is administered in 20 s or less in order lengthen the bolus for smaller children who will have a very short scanning time, especially with 64 MDCT systems.

For gated studies, the total amount of contrast to be injected is calculated from the contrast injection rate multiplied by the scan time required to cover the full cranial caudal extent of the heart. In order to scan the heart and coronary arteries at maximum contrast enhancement, the delay time from the start of injection needs to be determined with the use of a test bolus. The test bolus should be performed after the target heart rate has been reached with B- blocker so that the timing will be similar to that of the diagnostic exam. A typical test bolus uses 10–20 cc of contrast followed by 30 cc of saline at the same injection rate to be used for the diagnostic exam. After a 10-s delay to allow for breath-holding, with a region of interest through the ascending aorta, repetitive scanning of a single slice is performed every 1 s to construct an enhancement vs time curve. The time of peak enhancement is the delay time that is used for the diagnostic scan and when the second contrast injection with saline or dilute contrast is started.

Table 16.1. Intravenous contrast injection rates

Catheter size	Flow rate (cc/s)
18 g	5–6
20 g	4–5
22 g	3–4
24 g	1–2

Assessment of cardiac function requires at least two data sets (systole and diastole) (Juergens et al. 2002, 2004; Ohnesorge et al. 2000). While the diastolic image is reconstructed at 70%–90% of the RR interval (Fig. 16.7), the end-systolic image is obtained at 20%–30% of the RR interval. Analysis of myocardial wall motion requires reconstruction of multiple image sets during the entire RR interval in 5% steps. Cardiac functional parameters including end-diastolic and end-systolic volumes, stroke volume, ejection fraction and mass can be analyzed using a variety of different commercially available software.

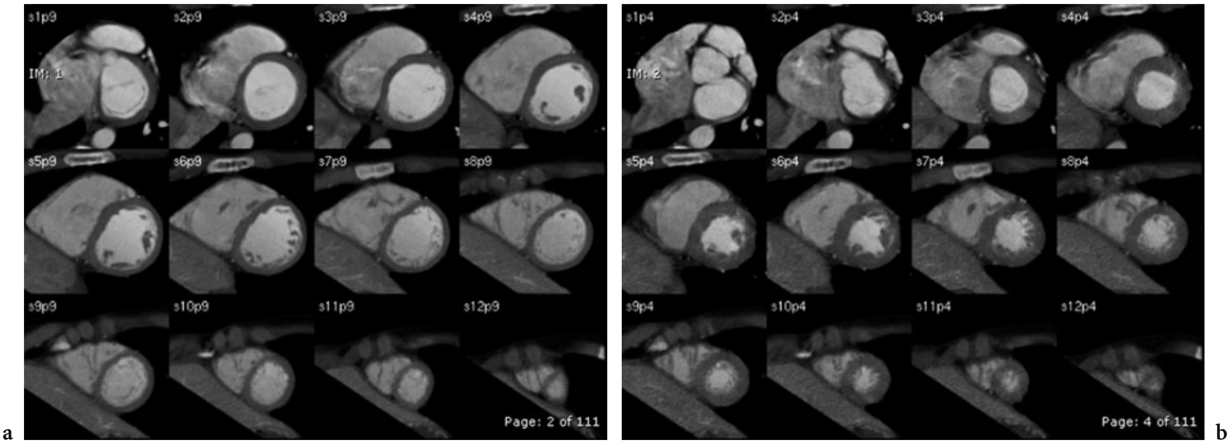

Fig. 16.7a,b. Short axis reconstructed images through the heart in diastole (**a**) and systole (**b**) for quantification of ventricular function

16.3
Complementary Role of MDCT and MRI for Cardiac Imaging

It is generally preferable to use echocardiography and/or MRI as a first approach to obtain adequate morphologic and functional information when imaging patients with known or suspected congenital heart disease. MRI is currently superior to MDCT for the evaluation of intracardiac anatomy, flow and function (Table 16.2). However, there continues to be limited access to MRI scanners for pediatric cardiovascular exams in many hospitals and institutions, and the imaging is time consuming and requires technical expertise to perform routine quality examinations. In addition, infants and young children generally require sedation or anesthesia more often for MRI (Odegard et al. 2004) than for MDCT, and assistance by anesthesia personnel may not be as readily available at a given clinical institution. For the initial evaluation of CHD in infants and young children, echocardiography often provides a complete assessment of intracardiac morphology, flow and ventricular function. The remaining clinical questions may only pertain to the morphology of the extracardiac vasculature, including the pulmonary arteries, thoracic aorta and branches, and pulmonary and systemic veins. MDCT angiography currently provides accurate imaging of the extracardiac vasculature that is clearly comparable to MRI with shorter procedure times and less need for sedation and general anesthesia (Lambert et al. 2005). MDCT angiography is especially helpful with regards to imaging of airway compromise in patients who have suspected vascular rings or patients who have persistent respiratory symptoms or prolonged requirement for mechanical ventilation following cardiac surgery (Kim et al. 2002).

As evaluation of intracardiac morphology and function with echocardiography becomes increasingly more difficult in older and larger patients who have had multiple chest surgeries, MRI now assumes a more important role in noninvasive evaluation of CHD. The information provided by MRI can be used for serial follow-up of post-operative children who may need further catheter based or surgical intervention, and can limit or completely obviate the radiation exposure required for diagnostic catheterization. In addition, MR imaging has become essential for management of adolescents and young adults with some forms of congenital heart disease in which accurate serial quantification of ventricular volumes and function for is needed for clinical decision-making. Examples include patients with repaired tetralogy of Fallot and chronic right ventricular volume overload due to pulmonary regurgitation, patients with a systemic right ventricle following the Senning or Mustard operation or with L-TGA, and in single ventricle patients following the Fontan operation. Unfortunately, quite often MR evaluation of these as well as other patients with CHD can become severely compromised by susceptibility artifact if prior treatment has required placement of embolization

Table 16.2. Comparison of MDCT with MRI for cardiac imaging

	MDCT	MR
Need for sedation	Sedation required in many patients < 4 years	Sedation or GA needed in most patients < 7 years
Duration of sedation	Very short	Long
IV contrast	Risk of allergic reaction, renal dysfunction	Nephrogenic systemic fibrosis recently described
Spatial resolution	Better. True isotropic resolution	Good. Near isotropic resolution
Temporal resolution	Good	Better
Dynamics on angiogram	Multiple dynamics possible, but not preferred in children due to radiation risk	Multiple dynamics routinely performed, with separation of right and left-sided and venous structures
Flow quantification	Not currently possible	Many applications: stroke volume, Qp:Qs, regurgitant fraction, gradient measurement through stenosis
Ventricular function	Adequate temporal resolution	Better temporal resolution
Imaging time	Very short (less than 1 min)	Long (30–60 min)
Contra-indications	Acute renal failure	Pacemakers, AICD
Compatibility with coils, stents, and metallic prosthesis	Metal causes only minimal artifact, worse artifact with platinum. Best non-invasive means of evaluating stent patency	Unable to assess patency of stents and metalic prostheses due to artifact. Steel coils cause most artifact. Platinum coils have none
Health risks	Radiation	Over-heating of the body
Post processing techniques	3D volume rendering, MIP, MPR	Similar
Ideal indications	Coronary stenosis imaging, anomalous coronaries, emergent studies like aortic dissection or occluded BT shunt, pulmonary embolism, airway evaluation, need to avoid sedation	Conditions requiring serial studies, screening studies, or conditions requiring evaluation of flow, valvular and ventricular function, and chamber morphology

coils, stents or occlusion devices (see Fig. 16.3). In addition, indwelling pacemakers and AICD devices remain contraindications for MRI.

MDCT is now considered to be the best noninvasive imaging alternative for follow-up of cardiac morphology and function in those patients who have indwelling devices that are contraindications to or would severely limit MRI. MDCT angiography also permits reliable visualization of the vascular lumen inside stents, and provides a noninvasive assessment of stent patency (Nieman et al. 2003; Eichhorn et al. 2006). In the past, motion and streak artifacts related to the high-density material of the stent limited this application. Faster tube rotation time of current systems reduces the frequency of motion artifacts so that gating is usually not required. These features allow assessment of stent patency in larger stents with high confidence (Eichhorn et al. 2006) (Fig. 16.8).

16.4
Clinical Applications

16.4.1
Pulmonary Vasculature

16.4.1.1
Pulmonary Arteries

In patients with right ventricular outflow tract obstructive lesions, such as tetralogy of Fallot (TOF) with pulmonary atresia, precise preoperative delineation of presence, size and confluency of the pulmonary arteries, and aortopulmonary collateral vessels from the aorta is necessary for surgical planning. In recent years, diagnostic cardiac catheterization has almost been completely replaced by Doppler echocardiography and cardiac MRI. Slow acquisition times

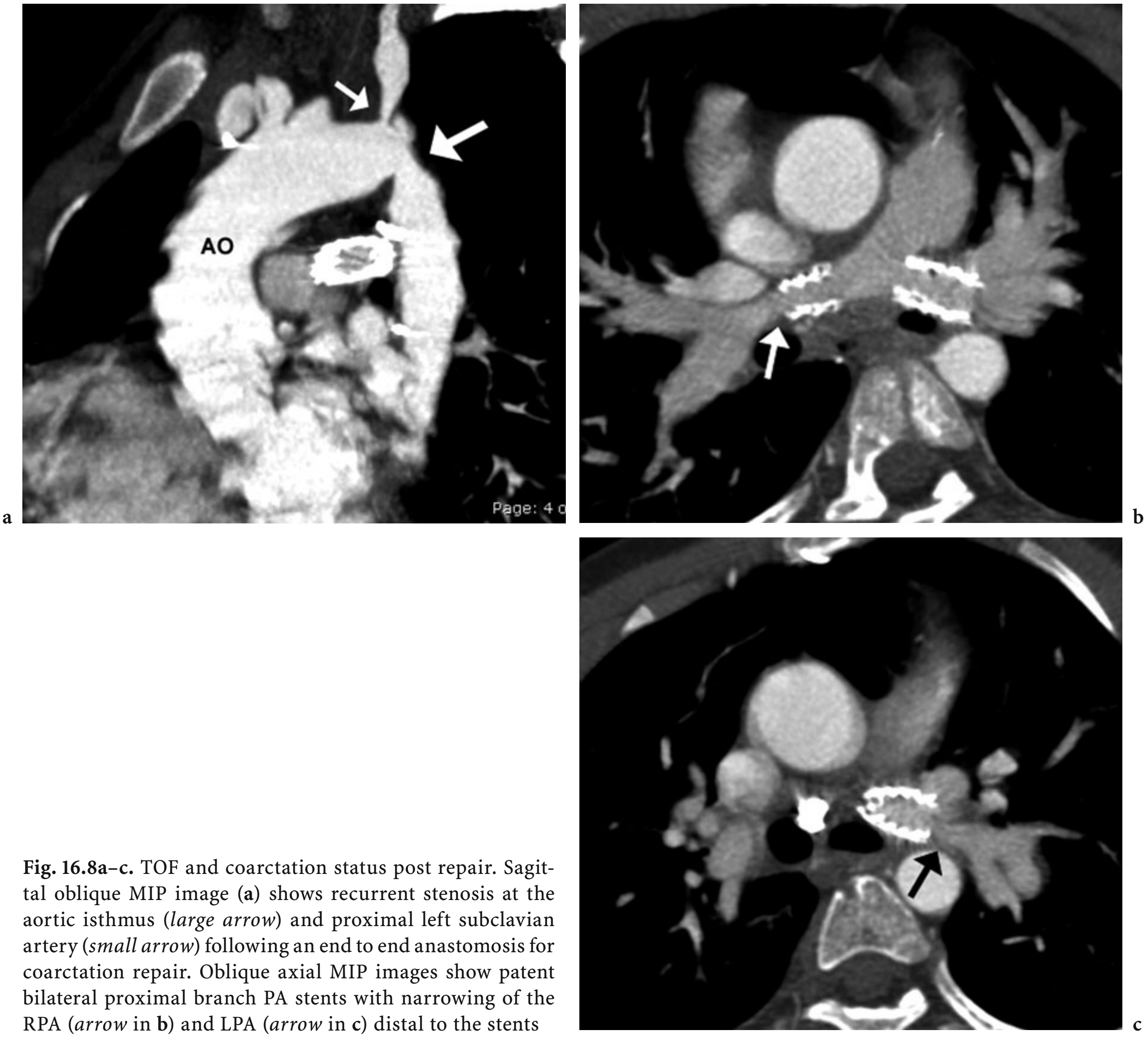

Fig. 16.8a–c. TOF and coarctation status post repair. Sagittal oblique MIP image (**a**) shows recurrent stenosis at the aortic isthmus (*large arrow*) and proximal left subclavian artery (*small arrow*) following an end to end anastomosis for coarctation repair. Oblique axial MIP images show patent bilateral proximal branch PA stents with narrowing of the RPA (*arrow* in **b**) and LPA (*arrow* in **c**) distal to the stents

and increased motion artifacts, especially in rapidly breathing infants and young children, compromised early acceptance of nonhelical CT in the evaluation of pulmonary arteries. With the development of helical CT, early studies showed high specificity, sensitivity and accuracy in the assessment of stenotic and nonconfluent central pulmonary arteries and in revealing the extent of aortopulmonary artery collaterals compared with echocardiography and angiography (Hopkins et al. 1996; Westra et al. 1999). Current MDCT scanners now allow higher spatial resolution imaging compared with MR angiography (MRA), and two and three dimensional reconstruction techniques permit very accurate assessment of the vasculature (Goo et al. 2005; Greil et al. 2006) (see Fig. 16.7). Abnormalities of the branch pulmonary arteries that are well depicted on MDCT include an abnormal origin or course such as in truncus arteriosus or pulmonary artery sling (Fig. 16.9). The branch pulmonary arteries can be atretic, stenotic or hypoplastic related to decreased blood flow during growth (Figs. 16.8 and 16.10), extrinsic compression or as a result of a surgically altered course or anastomosis such as a palliative shunt between the systemic and pulmonary artery circulation (Fig. 16.11).

16.4.1.2
Pulmonary Embolism

Pulmonary embolism (PE) is an uncommonly diagnosed condition in children. The clinical presentation is often subtle because symptoms are nonspe-

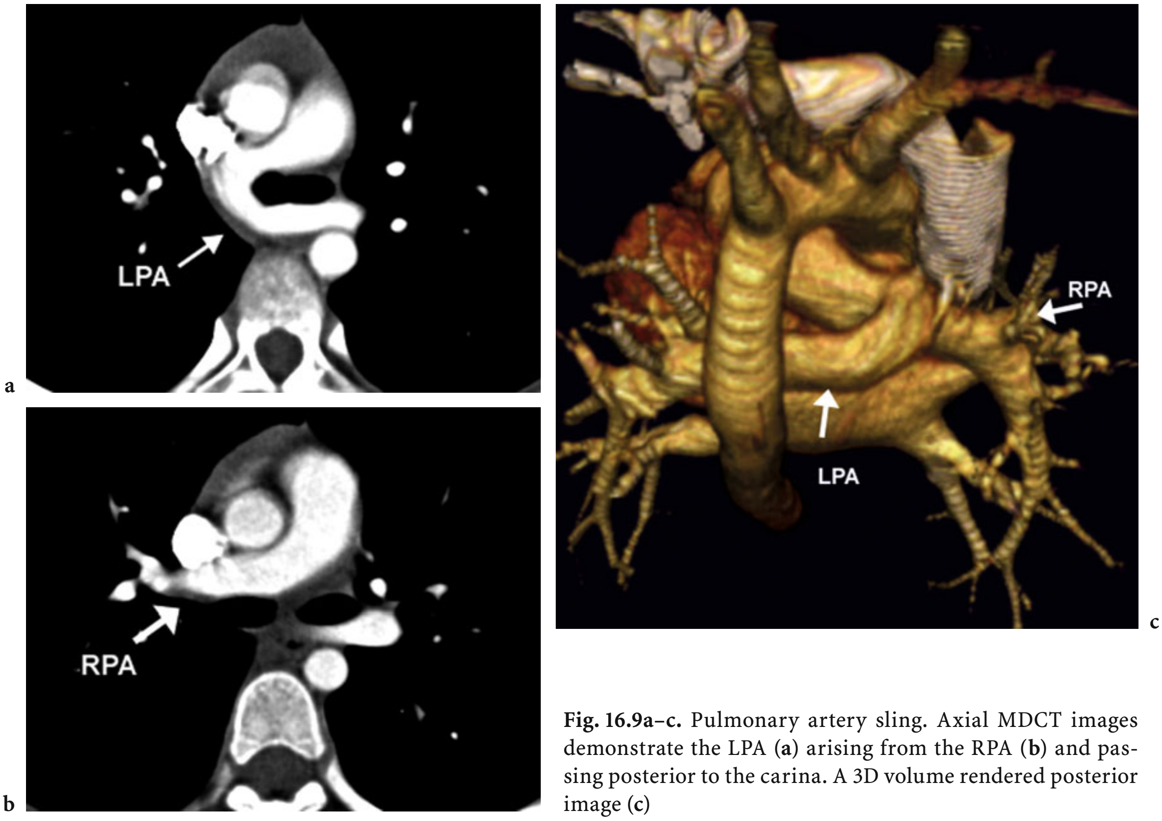

Fig. 16.9a–c. Pulmonary artery sling. Axial MDCT images demonstrate the LPA (**a**) arising from the RPA (**b**) and passing posterior to the carina. A 3D volume rendered posterior image (**c**)

cific and can be masked by the underlying clinical condition (Van Ommen and Peters 2006). Delays in diagnosis are frequent because definite signs of associated pulmonary or cardiac dysfunction appear to be less common in children than in adults. Specific risk factors for pulmonary embolism in the pediatric patient include associated deep venous thrombosis, indwelling central venous catheters, cardiac surgery, thrombotic disorders, vascular malformations, and malignancy, especially leukemia, and multiple factors are often present in the same patient (Babyn et al. 2005). Diagnostic strategies for detection and treatment of pulmonary embolism in children are mostly extrapolated from evidence that has been compiled in the adult literature.

Computed tomography has become the first choice of imaging modalities for detection of pulmonary embolism in symptomatic patients. MDCT has led to improved visualization of peripheral pulmonary arteries for detection of small emboli, and conventional pulmonary angiography is now rarely performed. Not only is pulmonary angiography invasive, but there is now evidence of limitations in terms of its ability to diagnose isolated peripheral pulmonary emboli accurately and reliably (Diffin et al. 1998; Stein et al. 1999). Once regarded as the best first noninvasive study for the diagnostic workup of pulmonary embolism, nuclear medicine is also now infrequently requested because as many as 73% of studies are interpreted as indeterminate (PIOPED Investigators 1990) and have poor interobserver correlation (Blachere et al. 2000).

Early spiral CT for diagnosis of acute pulmonary embolism had limited ability to detect small peripheral, subsegmental emboli (Remy-Jardin et al. 1996). With increased spatial resolution, the reproducibility and detection rate of segmental and subsegmental emboli of current MDCT compared to selective pulmonary angiography is markedly improved (Schoepf et al. 2002) and there is further improvement in diagnostic accuracy for detection of acute pulmonary embolism as compared with scintigraphy (Coche et al. 2003). In addition, a normal MDCT angiogram has a very high (98%) negative predictive value when correlated with subsequent patient outcome even if underlying parenchymal lung disease is present (Tillie-Lablond et al. 2002). In adults, it is now felt to be safe to withhold anticoagulants when the results of a good diagnostic quality CT angiogram (CTA) are normal, especially when combined with a nega-

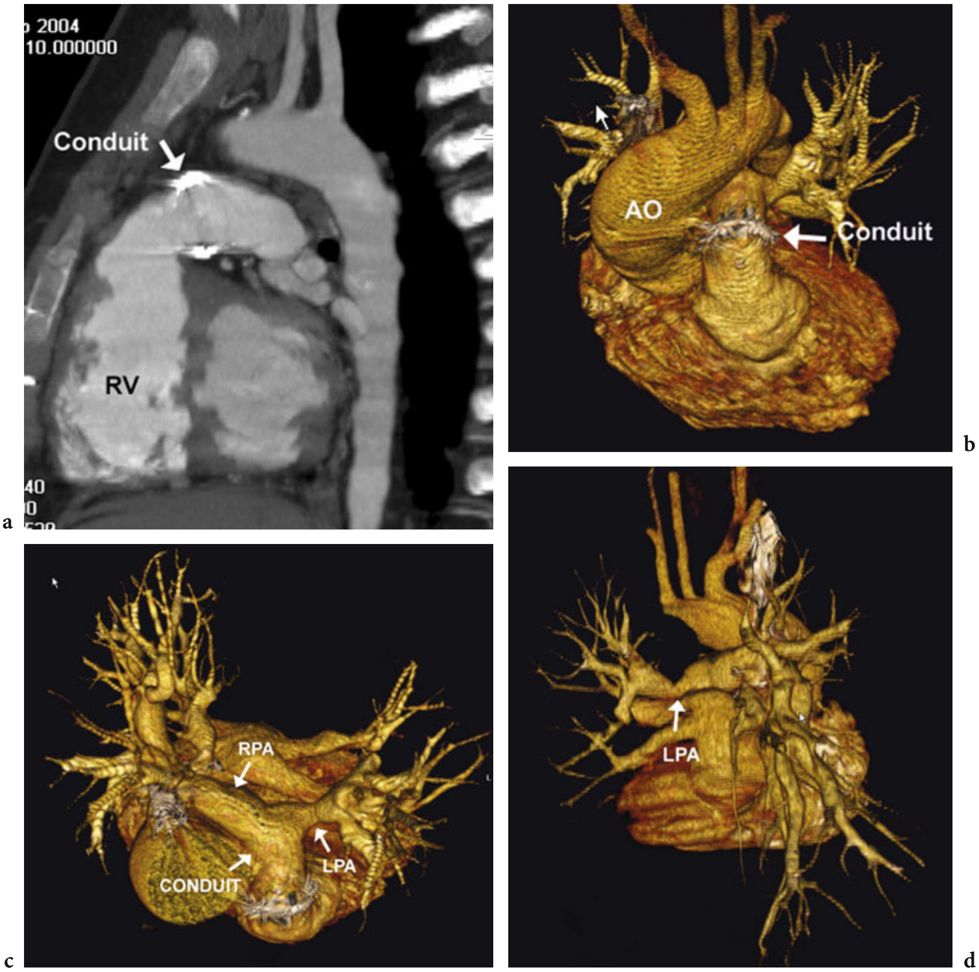
2004
10.000000
Conduit
RV
40
0
a
AO
Conduit
b
RPA
CONDUIT
LPA
c
LPA
d

Fig. 16.10a–d. Pulmonary artery atresia status post RV to PA valved conduit and unifocalization of the pulmonary arteries. Reconstructed sagittal oblique MIP (**a**) and 3D volume rendered image (**b**) demonstrate a valved conduit arising from the RV causing only a mild discrete artifact. Additional 3D volume rendered anterior (**c**) and posterior (**d**) images demonstrate focal stenosis of the LPA

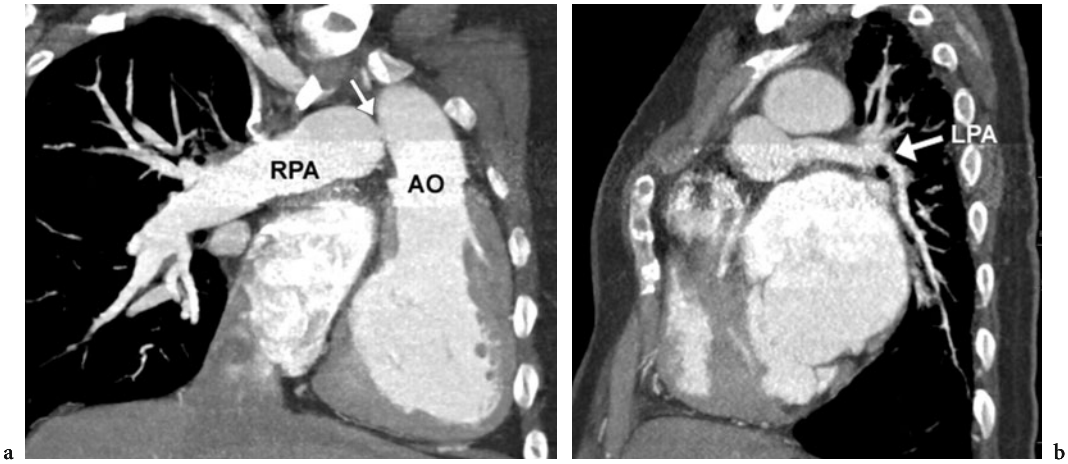
RPA
AO
a
LPA
b

Fig. 16.11a,b. Tricuspid atresia status post Waterson shunt (ascending aorta to RPA). Oblique MIP images show a dilated RPA (**a**) and hypoplastic LPA (**b**) due to shunt flow (*arrow* in **a**) directed towards the RPA tive sonographic study of the lower extremity veins (Goodman et al. 2000), but it remains unclear if this data can be extrapolated to children.

MDCT angiography findings of acute pulmonary embolism include intraluminal filling defects in the main and branch pulmonary arteries that can partially or completely fill the lumen (Fig 16.12). When the embolus completely fills the lumen of a branch pulmonary artery, the artery can enlarge relative to similar sized arteries in the hilum. The filling defects should have a sharp interface with the surrounding contrast media and should be visible on two adjacent slices in any plane. Parenchymal lung findings with PE include peripheral wedge-shaped opacities, hyperinflation and mosaic perfusion. Acute right ventricular failure may be present in severe cases.

A classic finding of chronic PE is an intraluminal filling defect that makes an obtuse angle with the vessel wall and creates an appearance of asymmetric wall thickening (Figs. 16.13 and 16.14). Contrast enhanced peripheral arteries can have diffuse irregular wall thickening related to recanalization and the residual thrombus may be calcified. Enlarged bronchiolar and systemic collateral vessels can also be seen in association with chronic PE.

Thromboembolic complications can develop in patients with congenital heart disease due to altered hemodynamics, prosthetic devices, conduits and baffles, damage to blood cells in high flow states, use of central venous catheters and cardiac catheterization (Van Ommen et al. 2002). Patients who are status post cavopulmonary anastomosis (Fontan operation or bi-

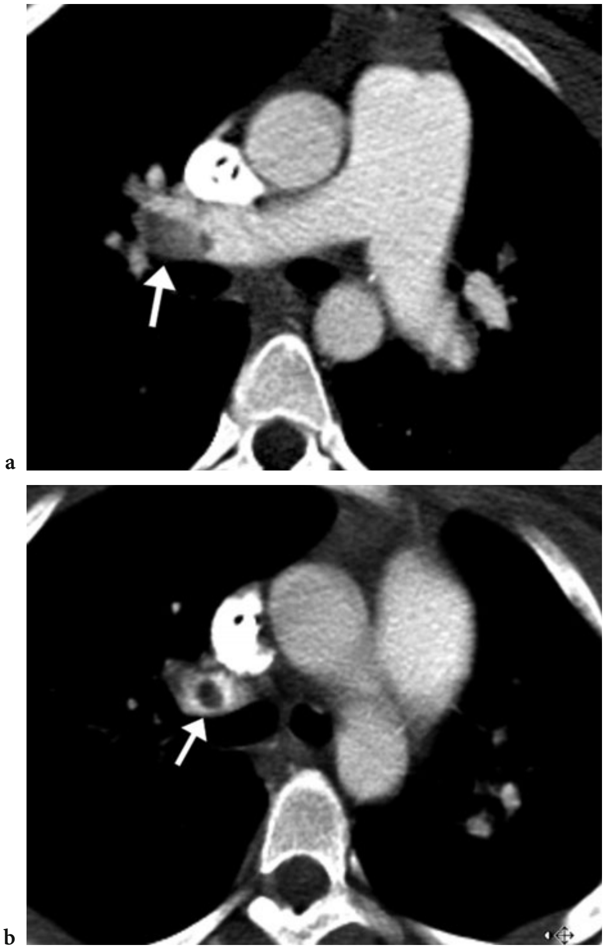

Fig. 16.12a,b. Acute pulmonary embolism. Axial images from a MDCT angiogram in a pediatric patient with respiratory distress demonstrate a well-defined filling defect in the distal RPA (*arrow* in **a**) extending into the upper lobe pulmonary artery (*arrow* in **b**)

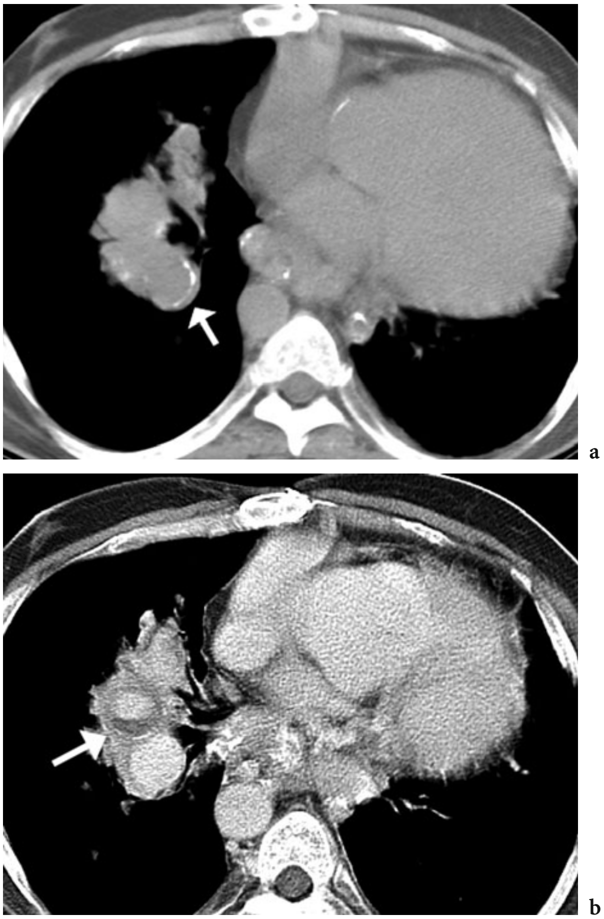

Fig. 16.13a,b. Tetralogy of Fallot with pulmonary atresia status post Waterston shunt with pulmonary hypertension. Axial pre (**a**) and post contrast (**b**) images demonstrate calcification of the pulmonary artery walls with hypodense clot (*arrow* in **b**) causing eccentric luminal narrowing consistent with chronic pulmonary embolism

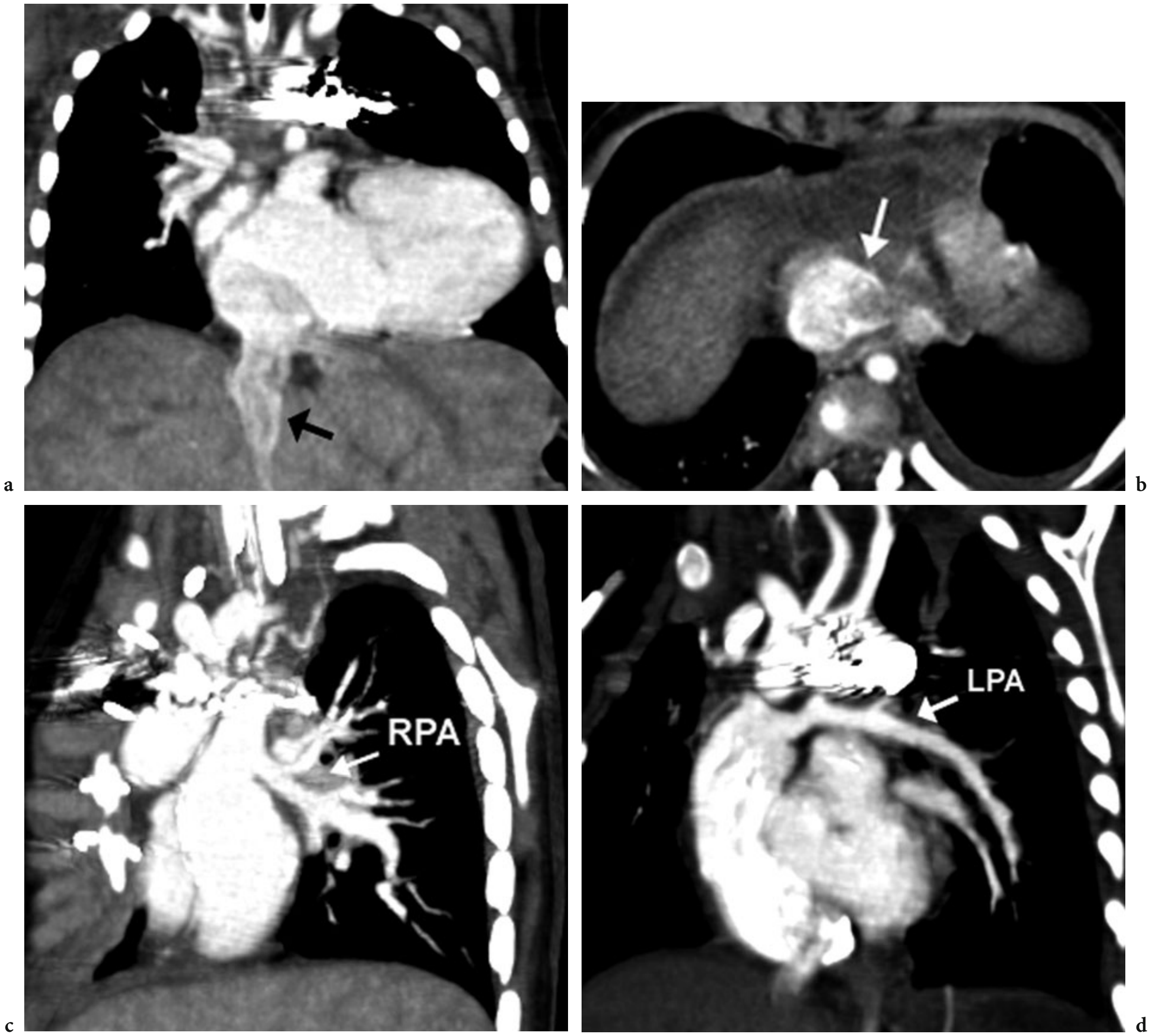

Fig. 16.14a–d. Single ventricle status post Fontan with concern for pulmonary embolism due to presence of thrombus in the Fontan pathway on echocardiography. MDCT angiography performed with simultaneous injection of contrast through upper and lower extremity intravenous access. Oblique coronal (**a**) and axial images (**b**) through the Fontan pathway demonstrate a filling defect within the pathway inferiorly consistent with thrombus (*arrows*), previously documented on echo. Oblique sagittal MIP images through the right (**c**) and left (**d**) pulmonary arteries demonstrate no acute PE. The LPA has diffuse irregular wall thickening consistent with chronic thrombus

directional Glenn anastomosis) to direct deoxygenated systemic venous blood directly into the pulmonary arteries are at particularly high risk for development of pulmonary embolism (Figs. 16.14 and 16.15) due to relative stasis of blood flow through the systemic venous pathways that can become dilated, the presence of blind-ending pathways following surgical redirection of blood flow, and/or patients may also have an intrinsic prothrombotic tendency (Van Nieuwenhuizen et al. 2001). Clinically silent pulmonary embolism has been detected at MDCT angiography in 17% of adult Fontan patients (Varma et al. 2003). Chronic PE can result in an increase in pulmonary vascular resistance that can lead to failure of the Fontan circulation.

16.4.1.3
Pulmonary Vein Morphology

The ostia of the pulmonary veins are an important source of ectopic atrial electrical activity that can

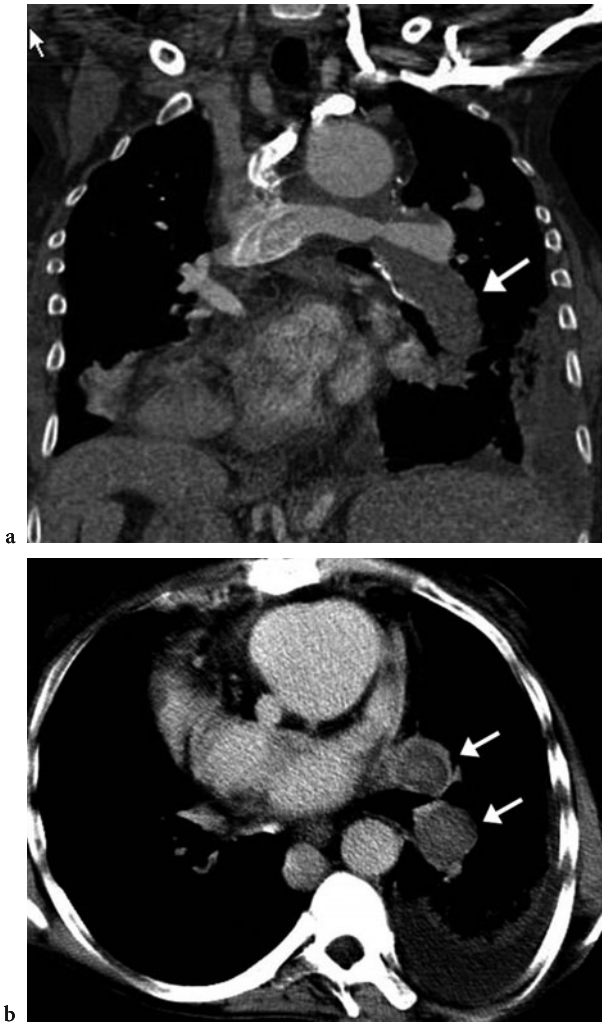

Fig. 16.15a,b. Coronal reformatted (**a**) and axial (**b**) images of a Fontan patient demonstrate extensive thrombus (*arrows*) extending from the Fontan pathway into the main and segmental branches of the LPA

initiate paroxysmal atrial fibrillation. Selective radiofrequency ablation of these arrythmogenic foci is being used to treat patients with refractory atrial fibrillation (Oral et al. 2002). The pulmonary venous drainage to the left atrium can be quite variable in terms of the number of veins and position of their ostia at the left atrial wall (Marom et al. 2004). The pulmonary vein morphology is easily depicted on multiplanar 2D and 3D reconstructions and displayed for review prior to the ablation procedure, which can substantially decrease procedure time and radiation exposure. The current high spatial resolution of MDCT can be used to accurately depict the potential complication of pulmonary vein stenosis following catheter ablation as well (Seshadri et al. 2002).

When associated with CHD, pulmonary vein stenosis (PVS) is most often extrinsic due to compression by other vascular structures or associated with the site of a prior surgical anastomosis. PVS can rarely be intrinsic, in which case it is usually rapidly progressive and refractory to all forms of surgical (Caldarone et al. 1998) and/or catheter based intervention (Driscoll et al. 1982). Progressive PVS can occur as a complicating feature of congenital heart disease (Breinholt et al. 1999) (Fig. 16.16) or can occur in isolation in infants and children with otherwise normal hearts (Sun et al. 1995). PVS is a diagnostic consideration in any patient presenting with recurrent infection, hemoptysis, unexplained pulmonary hypertension, and/or interstitial lung disease. MDCT can detect the presence of PVS and extent of associated involvement of the lung parenchyma and can be used as a non-invasive method to follow-up these patients for disease progression.

Echocardiography and cardiac MRI remain the primary modalities for diagnosis of anomalous pulmonary venous connections. MDCT angiography can also be used as an adjunct for imaging when echocardiography is limited in order to identify the number and course of anomalously connecting or draining veins (Kim et al. 2000). MRI should be considered first because in addition to morphologic assessment of the pulmonary veins, it can also provide quantitative evaluation of extent of shunting and right ventricular volume overload without radiation exposure. This information is often used for clinical decision making in the setting of PAPVC. Isolated PAPVC in the absence of an ASD and shunt fraction of less than 1.5:1 may not require surgical repair if the patient is asymptomatic.

16.4.1.4
Congenital Pulmonary Venolobar Syndrome

Congenital pulmonary venolobar syndrome is a heterogeneous group of congenital anomalies of the thorax that may occur singly or in combination. The main components of the congenital pulmonary venolobar syndrome are hypogenetic lung (lobar agenesis, aplasia or hypoplasia), partial anomalous pulmonary venous return, absence of a pulmonary artery, pulmonary sequestration, systemic arterialization of the lung, absence of the IVC, and duplication of a hemidiaphragm. Minor components include

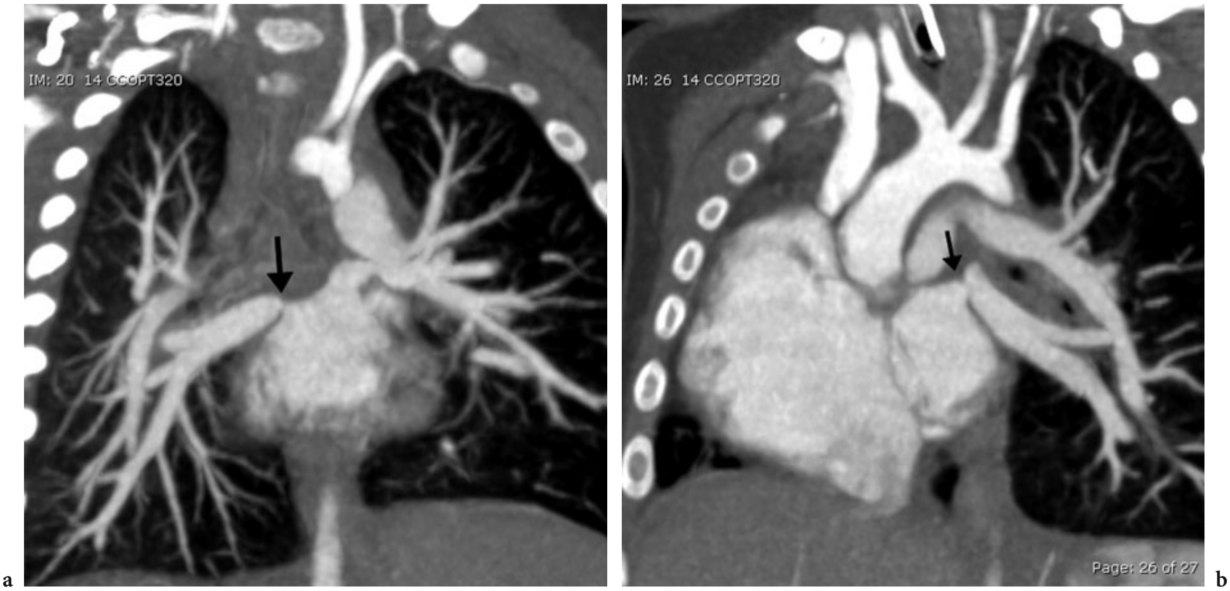

Fig. 16.16a,b. Total anomalous pulmonary venous return status post repair with pulmonary venous stenosis. Coronal oblique MIP images demonstrate focal stenosis (*arrows*) of the right (**a**) and left (**b**) pulmonary veins. (Courtesy of Sjirk Westra)

horseshoe lung and absence of the left pericardium, among others (Woodring et al. 1994). Surgical intervention may be required in some cases when there is recurrent infection, hemoptysis, congestive heart failure or pulmonary overcirculation due to excessive shunting. A complete evaluation of all pulmonary and systemic vascular, tracheobronchial and pulmonary parenchymal anomalies is necessary in patients under consideration for surgical repair. Noninvasive imaging with MRI or MDCT is now often used for delineation of vascular supply and drainage of pulmonary sequestration, pulmonary artery hypoplasia or agenesis, and partial anomalous venous connection or the Scimitar syndrome (Greil et al. 2002; Lawler et al. 2002; Lee et al. 2004). The use of advanced post-processing workstations allows improved noninvasive delineation of the anomalous vasculature and complications following repair (Figs. 16.17 and 16.18). MDCT is advantageous over MRI in demonstrating parenchymal lung and tracheobronchial abnormalities with simulated bronchographic or bronchoscopic images.

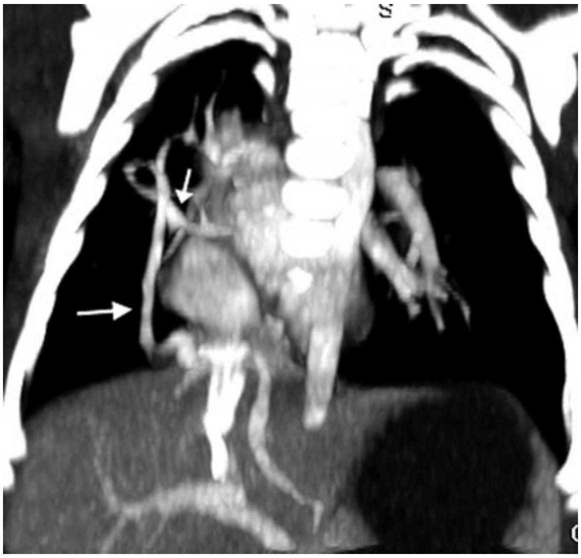

Fig. 16.17. Scimitar syndrome. Anomalous pulmonary venous return of the right lung to the IVC. The tortuous scimitar vein (*large arrow*) is unobstructed to the IVC, and has a stenotic branch (*small arrow*) that connects to the left atrium

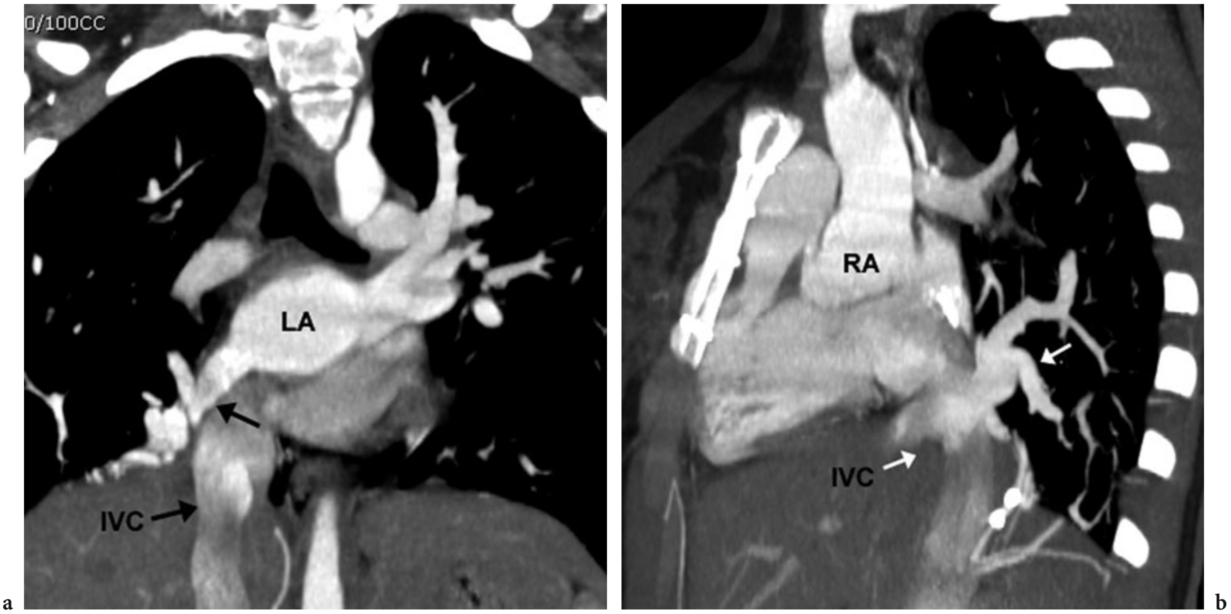

Fig. 16.18a,b. Baffle obstruction following redirection of the scimitar vein from the IVC to the left atrium. Coronal oblique MIP image (**a**) demonstrates narrowing and occlusion of the surgically created baffle (*arrow*) to the left atrium (*LA*) . Sagittal oblique image (**b**) shows the scimitar vein (*arrow*) draining anomalously to the IVC and right atrium (*RA*)

16.4.2
Aorta

16.4.2.1
Valvular Aortic Stenosis

Valvular aortic stenosis occurs in approximately 3%–6% of patients with congenital cardiovascular defects, and the congenital bicuspid aortic valve is one of the most common congenital malformations of the heart. Although the effective valve area can be reduced at birth, the stenosis of a bicuspid valve is progressive so that clinical symptoms do not usually develop until young adulthood, at which time the deformed valve often becomes calcified. Quantification of aortic valve calcification by MDCT is reproducible and can be used to distinguish between aortic valve leaflet and annular calcification, since annular calcification is degenerative and associated with aging, while leaflet calcification is thought to be related to clinically significant valvular stenosis (Gowda and Boxt 2004) (Fig. 16.19). The presence of moderate to severe aortic valve calcification in asymptomatic patients with valvular aortic stenosis is a predictor of poor prognosis, and may be an indication for valve replacement prior to the development of symptoms.

In addition to quantification of calcification, the use of MDCT with ECG gating has markedly improved the overall evaluation of the aortic valve by allowing motion free assessment of valve morphology, relationship and position of the coronary ostia to the aortic sinuses (Fig. 16.20), as well as the morphology of the ascending aorta. This information can affect the type of aortic valve surgery performed and the pre-operative choice of surgical approach and type of valve prosthesis (Markowitz 2001). The surgical approach to aortic valve replacement for severe congenital aortic stenosis in young patients is difficult because placement of a mechanical valve is not a good option due to the risk of long-term anticoagulation. Other options include placement of homograft or xenograft valves. In the Ross procedure, the stenotic aortic valve is replaced with the patient’s pulmonary valve, and a right ventricle to pulmonary artery conduit is placed. A well-known complication of this procedure is aneurysmal dilatation of the neoaortic root, which requires serial follow-up imaging for measurements.

16.4.2.2
Connective Tissue Disorders

Marfan’s syndrome and type IV Ehlers-Danlos syndrome are connective tissue disorders that can have cardiovascular manifestations. Both are associated with cystic medial necrosis of the aortic wall, which

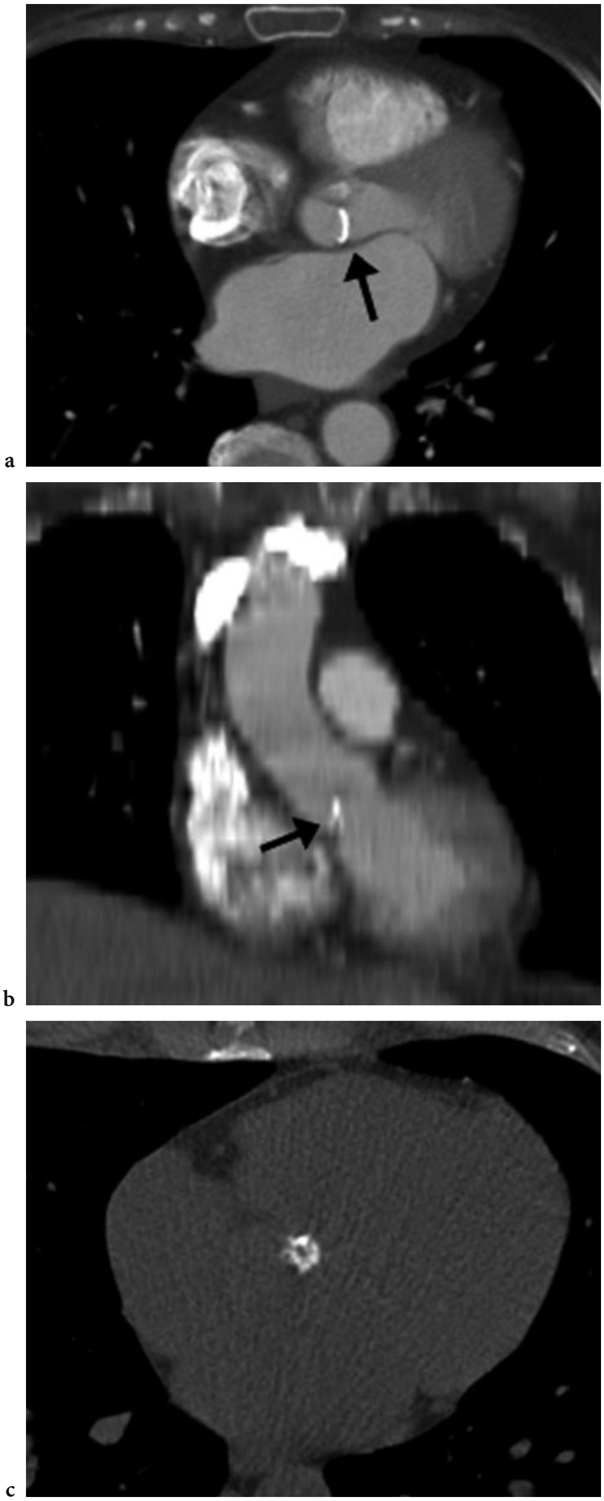

Fig. 16.19a–c. Valvular aortic stenosis. Axial (**a**) and coronal (**b**) oblique images from a gated MDCT angiogram demonstrate thickened aortic valve leaflets with calcification (*arrows*). Noncontrast gated MDCT oblique axial image (**c**) show a markedly stenotic calcified aortic valve orifice (Courtesy of Lawrence Boxt)

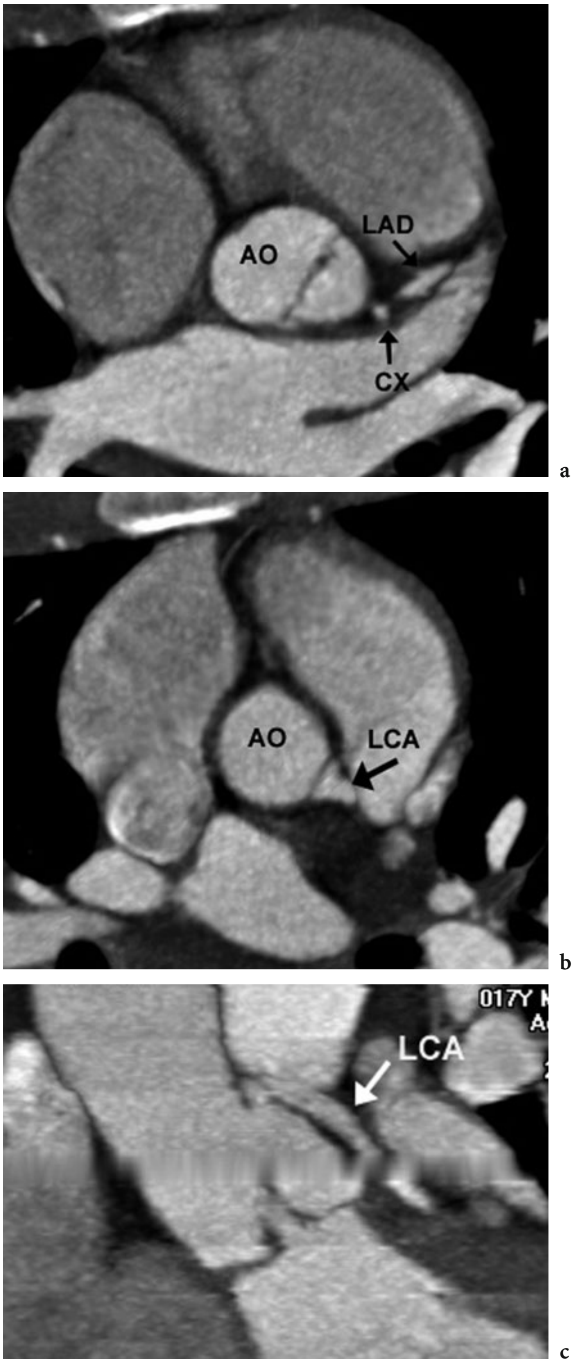

Fig. 16.20a–c. Bicuspid aortic valve with isolated coronary artery. Gated MDCT coronary angiogram requested after failure of catheterization of the left main coronary artery in a 16-year-old with atypical chest pain and known bicuspid aortic valve. Oblique axial and coronal MIP images demonstrate the left anterior descending (*LAD*) and circumflex coronary (*Cx*) arteries (**a**) joining to the left main coronary artery (*LCA*) (**b**). Maldevelopment of the left coronary leaflet results in the leaflet separating the orifice of the artery from the remainder of the aortic root (**c**) (Courtesy of Frank Rybicki)

adversely affects the ability of the aortic wall to withstand systemic pressures, leading to dilatation. The characteristic findings of the aorta include dilatation of the aortic root and proximal ascending aorta and effacement of the sino-tubular junction. The dilatation of the aortic root results in suboptimal coaptation of the aortic valve cusps, which can lead to aortic regurgitation that can further weaken the aortic wall as more throughput volume is needed to maintain cardiac output. Both echocardiography and MRI can be used for serial follow-up of ascending aorta size and aortic regurgitation in patients with Marfan's. CT is useful in some patients with severe chest wall deformity or who can not tolerate the length of time for MRI evaluation. In general, when the maximum diameter of the ascending aorta is 1.5 times that of the descending thoracic aorta at the level of the diaphragm, an aneurysm is considered to be present. Further investigation is needed to establish indications for surgical replacement of the aortic root and/or ascending aorta.

More serious complications of Marfan's or type IV Ehlers-Danlos syndrome include dissection and rupture of the ascending aorta (Fig. 16.21). The degen-

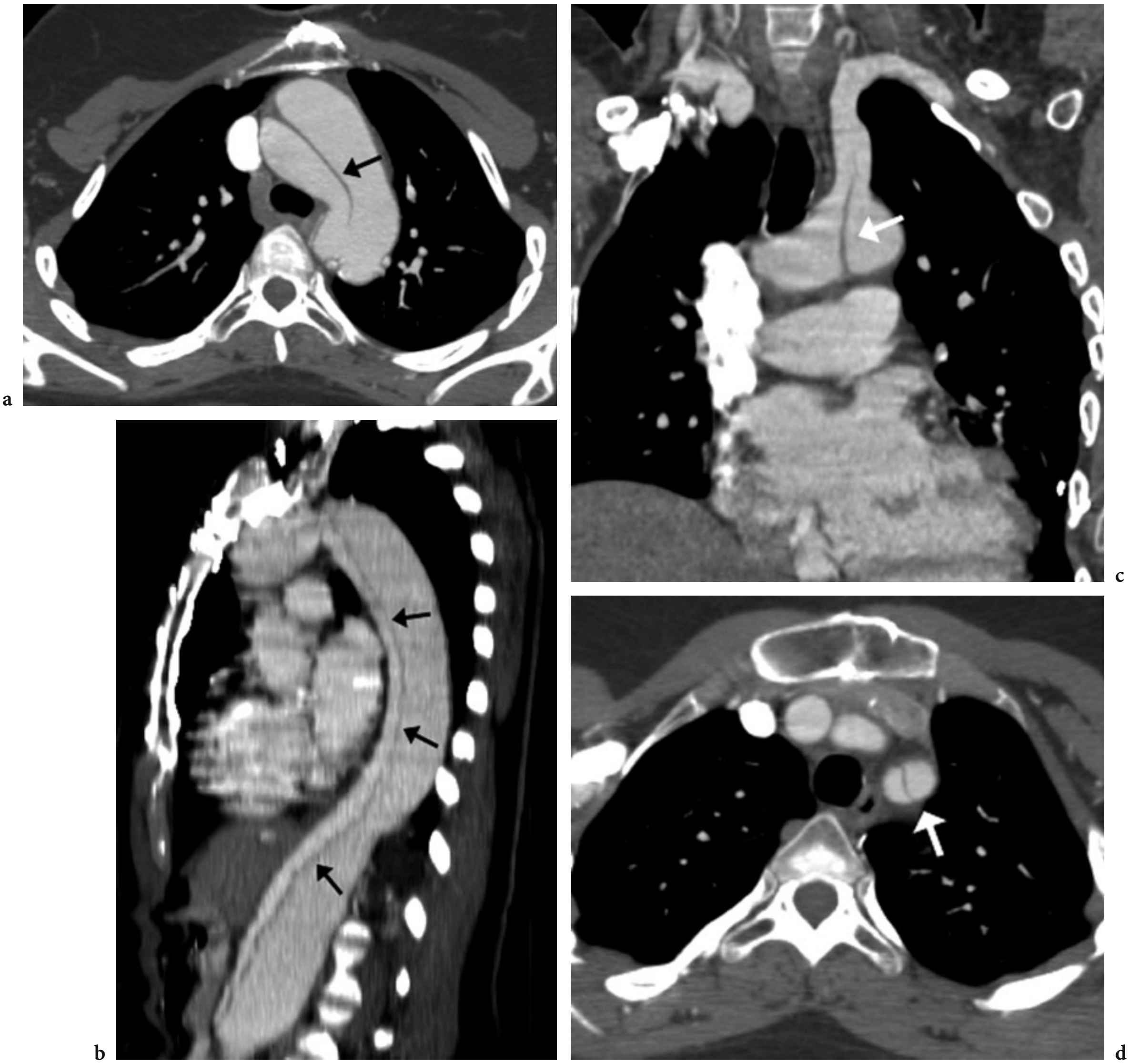

Fig. 16.21a–d. Aortic dissection in Marfan syndrome. Extensive dissection of the thoracic aorta in a teenager who subsequently had the ascending and descending thoracic and abdominal aorta replaced. Oblique MIP images demonstrate the dissection involving the transverse arch (*arrow* in **a**), extending into the thoracic and abdominal aorta (**b**), and also extending into the left subclavian artery (*arrows* in **c**,**d**)

eration of the ascending aorta wall, combined with increased hemodynamic stress from dilation, leads to a tear in the intima that exposes the outer third of the media to arterial blood with systemic vascular pressure. The pulsating blood extends into the media and can separate it proximally and distally to create a false lumen. Proximal extension into the aortic root can lead to severe aortic valve regurgitation and the dissection can also involve the coronary arteries or arch branch vessels, resulting in myocardial or cerebral ischemia. If a full- thickness aortic rupture occurs and extends into the pericardium, hemopericardium with tamponade can develop. Although transesophageal echocardiography (TEE) or MR imaging could be performed urgently if dissection is suspected, MDCT angiography is more widely available and has excellent accuracy for rapid, noninvasive diagnosis (Erbel et al. 2001; Sommer et al. 1996). MDCT angiography with multiplanar reconstruction is a highly sensitive and specific technique for the detection and characterization of the extent and orientation of the intimal flap, delineation of the true and false lumina, presence of intramural hematoma, and involvement of the major branches of the thoracic and abdominal aorta and coronary arteries. MRI also has high sensitivity and specificity for detection of acute aortic dissection (Nienaber et al. 1993), but it is usually not as available as CT in the emergency setting. MRI is usually reserved for patients with known allergy to iodinated contrast or renal failure, and is preferred over MDCT for imaging chronic dissections and follow-up after surgical repair. Other predisposing conditions for aortic dissection in children that can be evaluated by MDCT include decelerating injury, Turner syndrome, Kawasaki's disease and coarctation.

16.4.2.3
Takayasu Arteritis

Takayasu arteritis is a well-known form of large vessel progressive vasculitis that affects the aorta and its major branches as well as the coronary and pulmonary arteries. The accurate diagnosis of the disease depends on imaging studies because the clinical and laboratory presentation at disease onset is often nonspecific. In the early, systemic phase of inflammation, both CT (Matsunaga et al. 1997) and MR (Choe et al. 2000) imaging can detect wall thickening and enhancement of the involved vessels and can be used to follow-up response to high-dose steroid therapy. If the disease is not detected and treated early, transmural fibrosis of the vessel wall can lead to the characteristic findings of the late phase, including stenosis, occlusion, mural calcification, intraluminal thrombus or aneurysmal dilatation of the affected artery (Fig. 16.22). Both MRA and MDCTA can be used for noninvasive detection of the sequelae of chronic disease. Takayasu disease is often recurrent and the timing of progression from early to late phase of disease can be variable, so that early and late findings can be detected concurrently. Children with Takayasu arteritis are more often diagnosed and followed with MRI (Aluquin et al. 2002). CT is more useful for diagnosis of early complications following surgical bypass or transcatheter stenting of vasculitis induced stenosis, including development of pseudoaneurysms, graft infection, thrombosis and restenosis.

16.4.2.4
Coarctation

Coarctation is a congenital maldevelopment of the aorta presenting with variable degrees of hypoplasia of the distal transverse arch and focal or long seg-

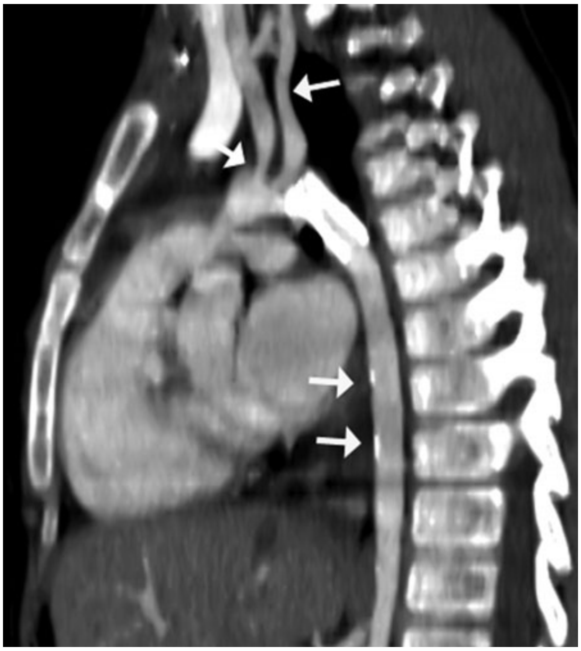

Fig. 16.22. Takayasu arteritis and coarctation status post balloon dilatation and stenting. Sagittal oblique MIP image demonstrates a stent at the aortic isthmus and diffuse calcification (*large arrows*) of the aortic wall consistent with chronic arteritis. The proximal left common carotid and subclavian arteries are moderately stenotic and ectatic (*small arrows*)

ment narrowing of the aortic isthmus at the junction of the ductus arteriosus and the aorta. Similar to MRI, MDCTA demonstrates the location and length of the coarctation segment, the degree of hypoplasia of the transverse arch and collateralization to the descending aorta (Fig. 16.23). Accurate delineation of the relationship of the origins of the left and right subclavian arteries to the coarctation segment is also defined on MDCT. Following surgical repair of coarctation, MDCTA can be used for detection of residual stenosis, recoarctation or aneurysm formation at the repair site. However, in order to avoid radiation exposure in children, the initial evaluation of suspected coarctation and follow-up of complications after surgical repair is best performed with MRI. MDCT is more helpful following balloon dilatation and stent placement for detection of in-stent stenosis because susceptibility artifact limits MR imaging in the area of the stent. In addition, MDCTA is useful for emergent follow up of potential complications following balloon dilation, including pseudoaneurysm formation and dissection (Fig. 16.24).

16.4.3
Coronary Artery Anomalies

Congenital anomalous coronary arteries, although rare, are a well-recognized cause of myocardial ischemia and sudden death in children and young adults, with an increased prevalence in patients with congenital heart disease, especially TOF, transposition of the great arteries (TGA) and congenitally corrected TGA. Defining the presence and the exact proximal course of the coronary arteries with respect to the aorta and pulmonary artery is essential because this is the most important indicator of risk of ischemia and determines treatment. The increased risk of ischemia/ infarction in patients with anomalous coronary arteries is thought to be due to the intra-arterial course of the coronary artery between the aorta and the pulmonary artery and/or a tangential origin of the coronary artery from the aortic sinus that passes within the aortic wall that can cause the ostium to become narrowed.

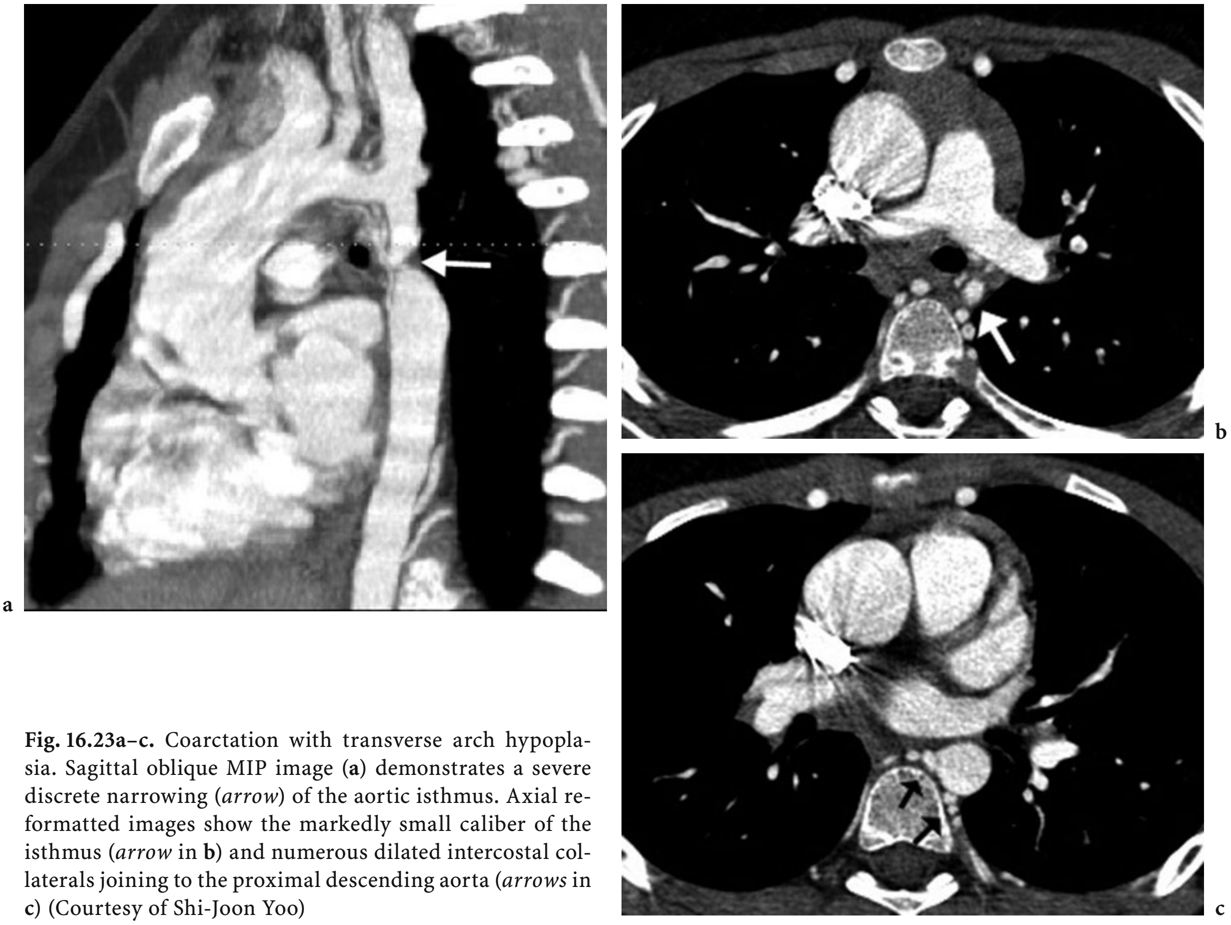

Fig. 16.23a–c. Coarctation with transverse arch hypoplasia. Sagittal oblique MIP image (**a**) demonstrates a severe discrete narrowing (*arrow*) of the aortic isthmus. Axial reformatted images show the markedly small caliber of the isthmus (*arrow* in **b**) and numerous dilated intercostal collaterals joining to the proximal descending aorta (*arrows* in **c**) (Courtesy of Shi-Joon Yoo)

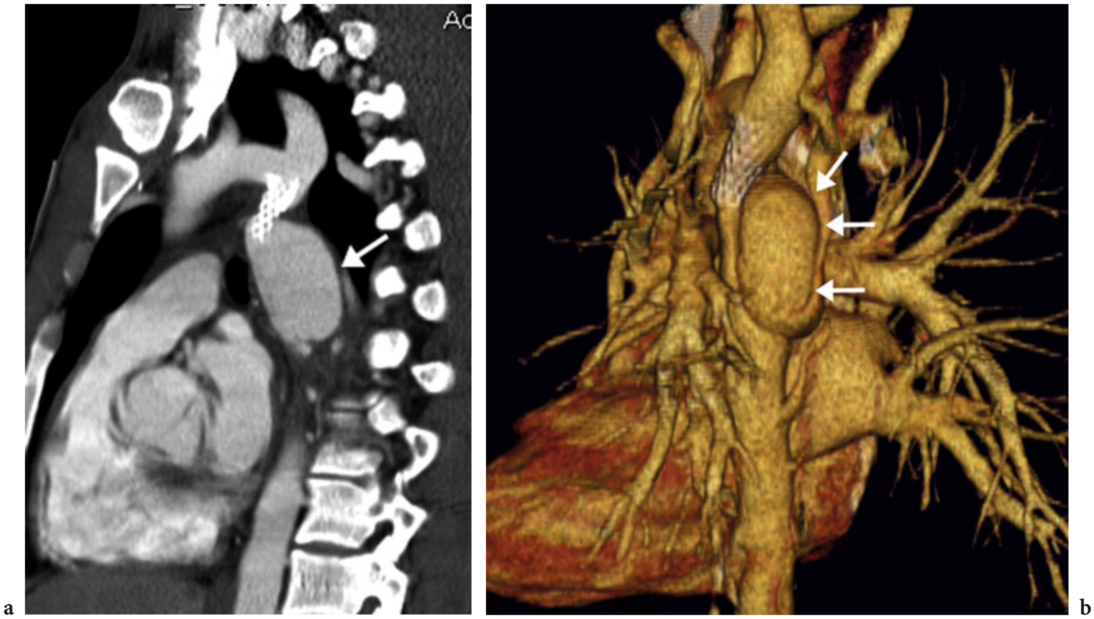

Fig. 16.24a,b. Dissection and pseudoaneurysm of the thoracic aorta following balloon dilatation and stenting of coarctation. Oblique sagittal MIP (**a**) and VR (**b**) images demonstrate a stent at the aortic isthmus with a dissection and large pseudoaneurysm (*arrow*) protruding from the aorta. The patient required an additional covered stent to be placed which closed the entrance of the pseudoaneurysm into the thoracic aorta. The pseudoaneurysm was shown to be thrombosed on subsequent imaging

Echocardiography with color Doppler has replaced cardiac catheterization as the standard method of visualizing the proximal coronary arteries in infants and children (Satomi et al. 1984), but visualization can become more limited in adolescents and adults (Douglas et al. 1988). Invasive coronary angiography is expensive and not always practical for screening of young adults with suspected coronary anomalies since symptoms can be nonspecific and coronary anomalies are rare. In addition, the exact proximal course of an abnormal coronary artery can be difficult to ascertain on the multiple 2D projections that are obtained by angiography (Ishikawa and Brandt 1985). MRI has been used to diagnose accurately anomalous coronary arteries in patients with known anomalies on prior conventional angiography (McConnell et al. 1995). Although some centers use MR coronary angiography successfully in infants, children and young adults (Su et al. 2004), coronary MRA cannot be easily performed on all commercially available scanners, and current results are not always reliable (Bogaert et al. 2003).

MDCT is now widely available and coronary CTA is being increasingly performed in many medical centers (Gerber et al. 2002), due to its relative ease of use and rapid image acquisition times compared with MRI. MDCT is particularly advantageous in patients presenting with acute symptoms including palpitations, dizziness, atypical or typical exertional chest pain, and dyspnea on exertion, especially in young athletes (Deibler et al. 2004). The anomalous origin of the coronary artery arising from the contralateral aortic sinus of Valsalva and the interarterial proximal course between the aorta and the pulmonary artery can be reliably detected on gated coronary MDCTA (see Fig. 16.2).

16.4.3.1
Kawasaki's Disease

Kawasaki's disease is an acute vasculitis of unknown origin that occurs most often in young children. It begins as a pancarditis with vasculitis of small vessels (stage 1), progresses to vasculitis of the epicardial coronary arteries (stage 2), followed by resolution of vascular inflammation with decrease in size of the aneurysms (stage 3), and scarring of the coronary arteries with stenoses (stage 4) (Fujiwara and Hamashima 1978). Coronary artery aneurysms can develop in up to 15%–25% of untreated cases and can be associated with thrombotic events leading to ischemia and infarction in adulthood (Kato et al. 1982, 1996). Although current therapy with intravenous gamma-globulin and high dose aspirin has reduced the mortality rate and incidence of coronary artery abnormalities, there continue to be cardiac sequelae in about 13% of patients with Kawasaki's disease (Yanagawa et al. 1999). A recent autopsy study has shown an association between post coronary arteritis lesions, especially focal aneurysms, and development of premature atherosclerosis (Takahashi et al. 2001).

Serial follow-up of patients with Kawasaki's disease is essential because the size of aneurysms and severity of coronary artery stenosis can change over time. Transthoracic echocardiography is now used frequently to follow small children for the development of aneurysms, but adequate visualization of the proximal coronaries tends to diminish with increasing age and size of the patients. Good correlation regarding the presence of stenosis and size of aneurysms of the proximal coronary arteries between MRI and cardiac catheterization has been reported (Greil et al. 2002) but current MRI techniques have limited spatial resolution for reliable detection of coronary wall thickening, plaque formation, and abnormalities of the distal portions of the coronary arteries compared with gated MDCT. This has clinical relevance, as there is evidence of persistent intimal thickening at sites of prior aneurysms that have regressed (Iemura et al. 2000), there is a higher rate of coronary abnormalities and significant cardiovascular complications with recurrent disease (Momenah et al. 1998), and in older children there have been documented fatalities due to myocardial infarction related to diffuse arteritis in the absence of aneurysms (Burke et al. 1998).

MDCT allows noninvasive visualization of the entire coronary artery system for detection of complete occlusions and stenosis of the proximal and distal coronary arteries by calcified or noncalcified vulnerable plaque in adults (Schoepf et al. 2004; Schoenhagen et al. 2004). In a study of adolescents with Kawasaki's disease (Sato et al. 2003), ECG gated MDCT coronary angiography accurately demonstrated all aneurysms, complete occlusions and stenosis that were present on invasive angiography (Fig. 16.25). In addition, MDCT can demonstrate abnormalities of the coronary wall, including diffuse intimal irregularity with a "braid-like" or artery within artery appearance, calcification, and soft plaque, consistent with the sequelae of vasculitis that could lead to premature atherosclerosis (Goo et al. 2006; Takahashi et al. 2001).

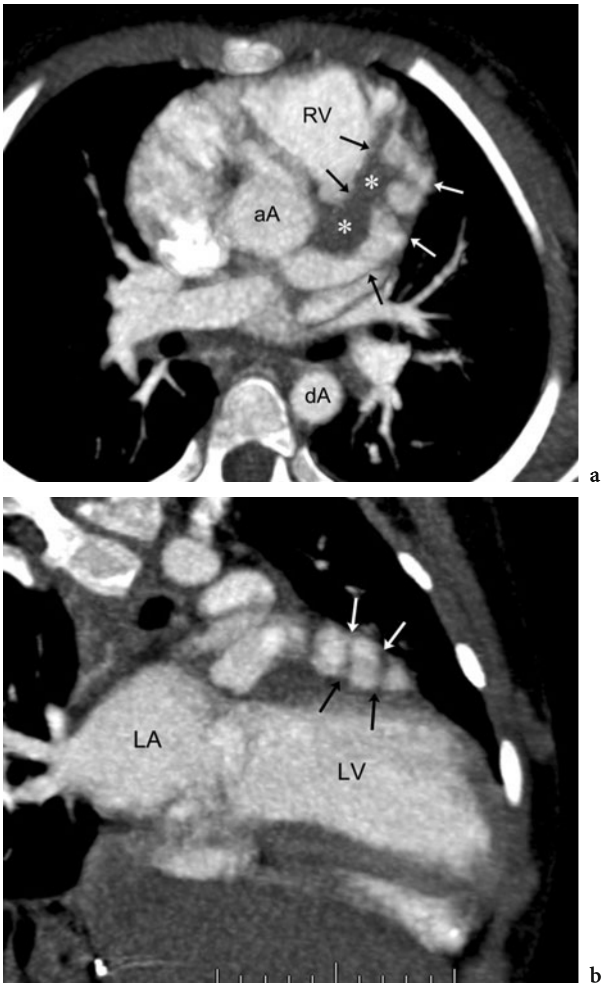

Fig. 16.25a,b. Kawasaki disease with coronary artery aneurysms. Oblique axial (**a**) and sagittal (**b**) MIP images from a nongated MDCT angiography demonstrate a string of aneurysms (*arrows*) with intervening areas of stenosis involving the left anterior descending coronary artery. A hypodense thrombus is present in the medial aspect of the aneurysm (*asterisks* in **a**) (Courtesy of Hyun Woo Goo)

16.4.4
Airway Compromise in Patients with CHD

The most common types of vascular anomalies to cause symptomatic tracheal and esophageal compression are the right aortic arch with aberrant left subclavian artery and the double aortic arch (Fig. 16.26). In infants and children with these anomalies, symptoms can vary from wheezing to frank respiratory failure, related in part to the direct effect of vascular compression, as well as secondary tracheobronchomalacia that can result from prolonged compression. If the vascular ring

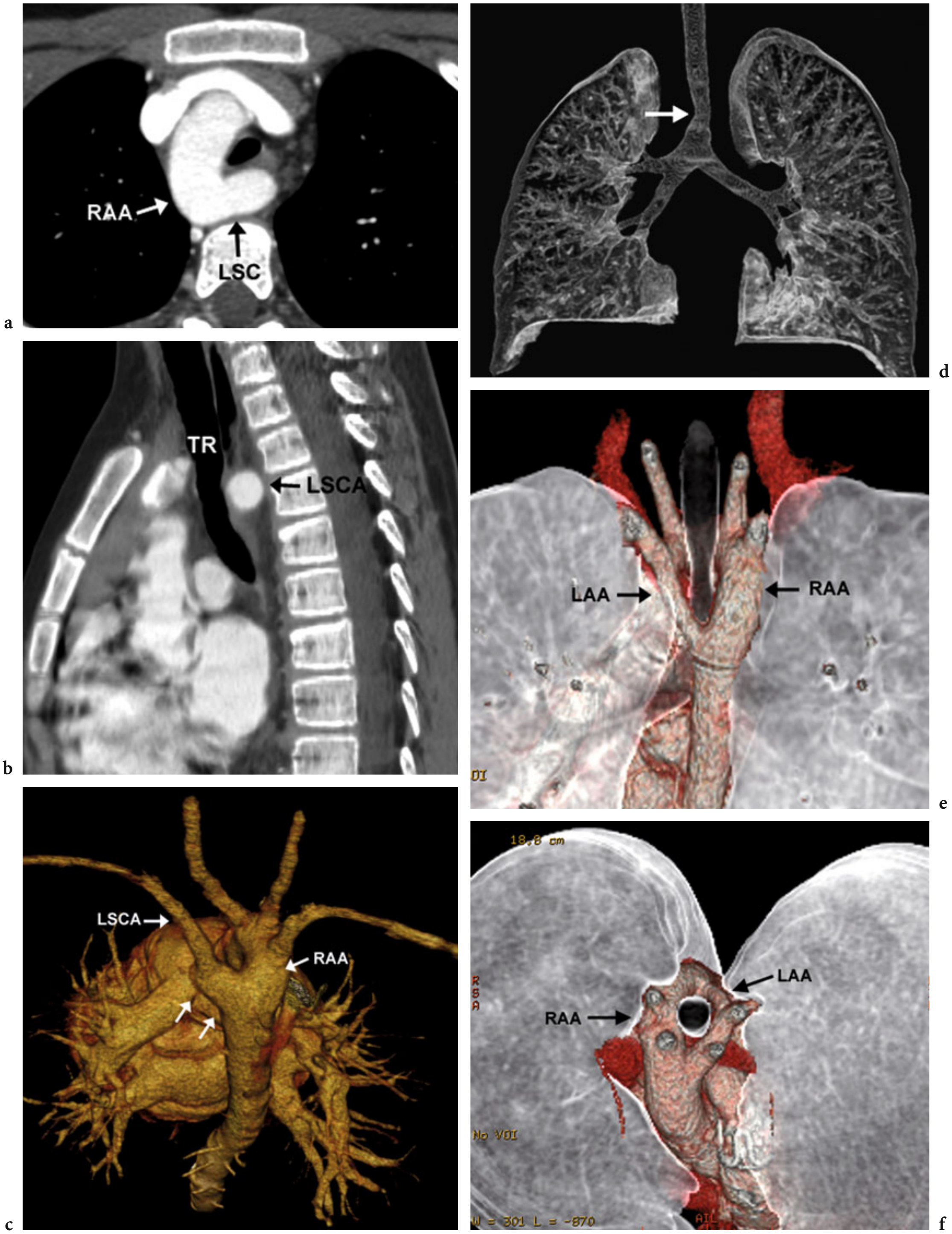

Fig. 16.26a–f. Common vascular rings. Axial (**a**) and sagittal (**b**) MIP images demonstrate a right aortic arch (*RAA*) and aberrant left subclavian artery (*LSCA*) extending posterior to the trachea and causing narrowing and anterior bowing of the trachea (*TR*). Posterior volume rendered image (**c**) shows the dilated proximal left subclavian artery consistent with a diverticulum of Kumeral (*arrows*) related to ductal flow into the subclavian artery in utero. A 3D bronchographic image (**d**) demonstrates mild narrowing of the distal trachea (*arrow*). Posterior and superior volume rendered views (**e**,**f**) of a double aortic arch with lungs and trachea included demonstrate tracheal narrowing at the level of the left (*LAA*) and right (*RAA*) arches passing to either side of the trachea. The left aortic arch is smaller than the right arch as is typical (Courtesy of Hyun Woo Goo)

exhibits less compression, it may be diagnosed in the older child with symptoms primarily of esophageal compression. The double aortic arch is less common than right arch with an aberrant left subclavian, but it more often results in a tight ring necessitating earlier surgical intervention for airway obstruction. With the double aortic arch, the right arch is more often dominant and cephalic in location as compared with the left arch. However, the left arch is occasionally dominant and one of the arches may be atretic or have an associated coarctation.

MDCT provides imaging in multiple planes to completely characterize the anomalous vasculature and the extent of airway compression. The current trend of performing minimally invasive surgery for repair of vascular ring using video-assisted thoracoscopic or robotic endoscopic techniques has advantages over lateral thoracotomy including a smaller incision, improved visualization inside the chest cavity, reduced post-operative pain and risk of chest wall deformity. These less invasive techniques require more precise delineation of the size, patency and location of the vascular structures pre-operatively (Lambert et al. 2005), and therefore there has been increased utilization of CT or MRI prior to surgical repair.

In addition to the vascular anomalies described above, there are more rare conditions that can result in symptomatic airway and/or esophageal compression, including pulmonary artery sling (see Fig. 16.9), anomalous innominate artery (Fig. 16.27), circumflex aorta and cervical aortic arch. Patients with TOF and absent pulmonary valve syndrome can have severe pulmonary regurgitation, which can lead to markedly enlarged pulsatile pulmonary arteries that can cause severe bronchial compression associated with bronchomalacia (Ditchfield and Culham 1994) (Fig. 16.28).

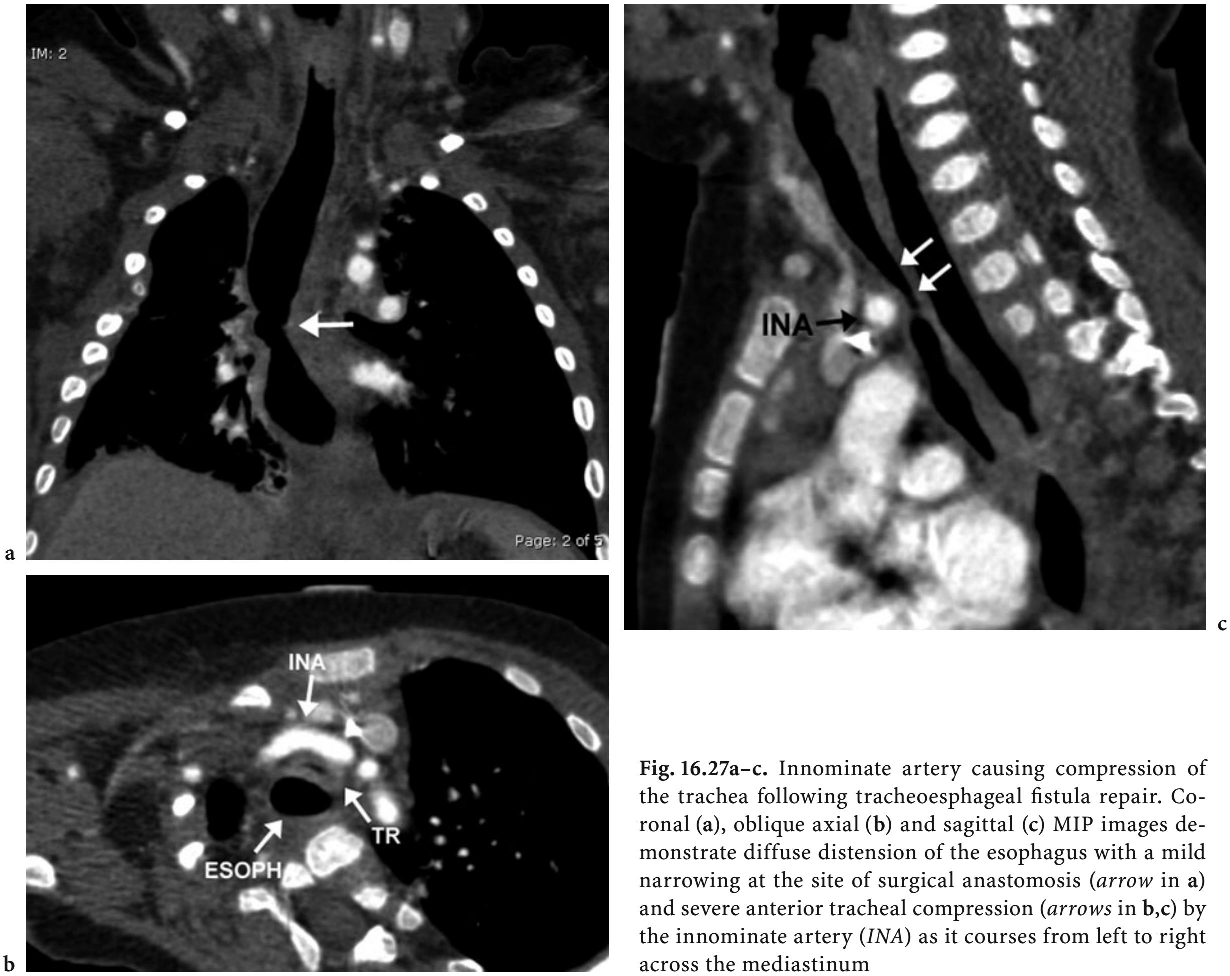

Fig. 16.27a–c. Innominate artery causing compression of the trachea following tracheoesphageal fistula repair. Coronal (**a**), oblique axial (**b**) and sagittal (**c**) MIP images demonstrate diffuse distension of the esophagus with a mild narrowing at the site of surgical anastomosis (*arrow* in **a**) and severe anterior tracheal compression (*arrows* in **b**,**c**) by the innominate artery (*INA*) as it courses from left to right across the mediastinum

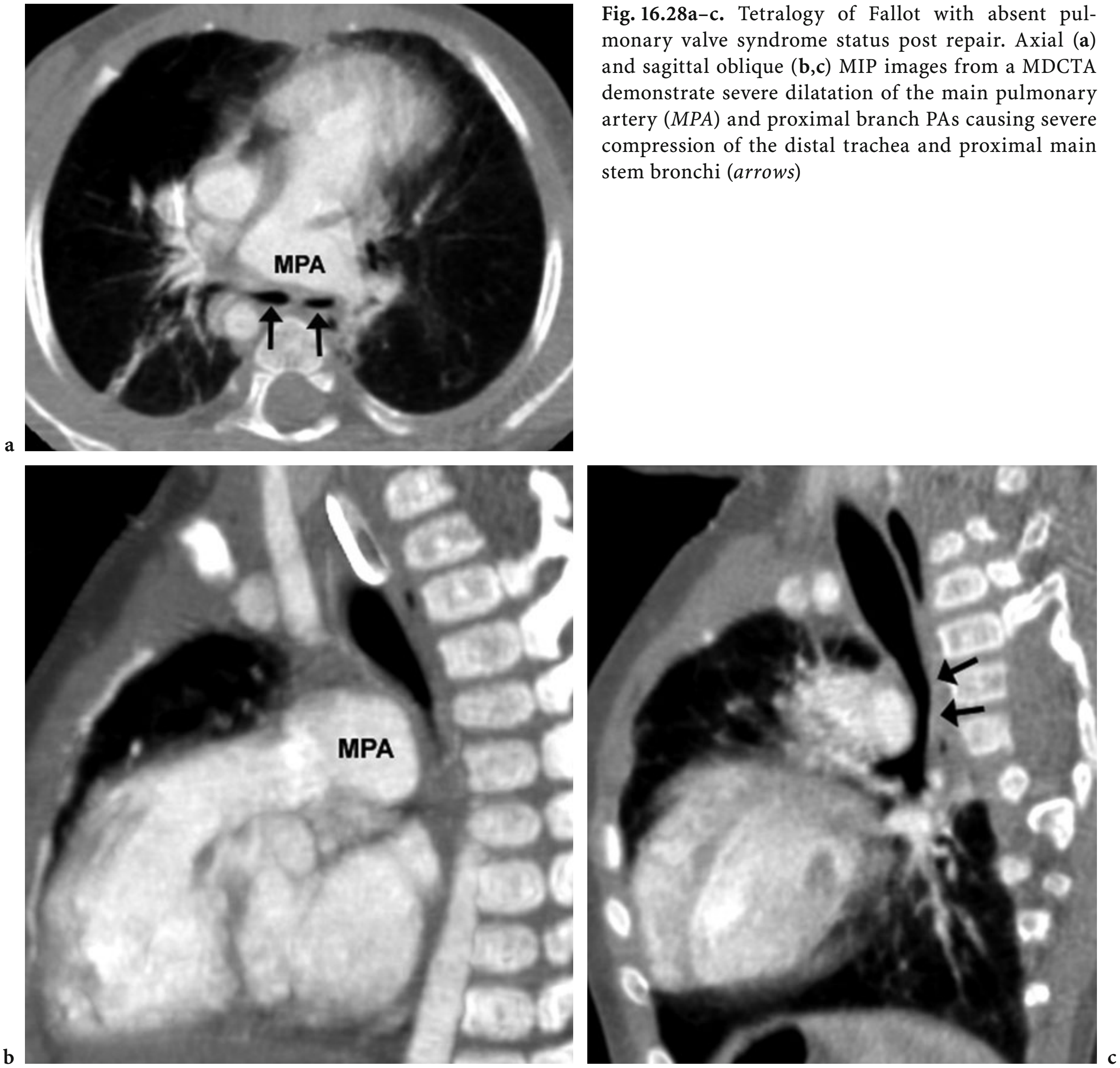

Fig. 16.28a–c. Tetralogy of Fallot with absent pulmonary valve syndrome status post repair. Axial (**a**) and sagittal oblique (**b**,**c**) MIP images from a MDCTA demonstrate severe dilatation of the main pulmonary artery (*MPA*) and proximal branch PAs causing severe compression of the distal trachea and proximal main stem bronchi (*arrows*)

MDCT provides a rapid assessment of the ICU patient for potential causes of failed extubation in the early postoperative period following surgery for congenital heart disease (Lambert et al. 2005). The airway compression may be related to the patient's intrinsic anatomy, such as in TOF with a right aortic arch and markedly dilated ascending aorta (McElhinney et al. 1999) (Fig. 16.29), or due to surgically reconstructed vessels, such as with the arterial switch operation for TGA (Robotin et al. 1996) and aortic arch reconstruction following the Norwood operation. Other complications that can be rapidly diagnosed by MDCT in the early postoperative period include mediastinitis with abscess, mediastinal hematoma (Fig. 16.30) or seroma, commonly associated with a Blalock-Taussig shunt.

MDCT is also helpful in evaluating for airway or pulmonary parenchymal abnormalities in post-operative patients with chronic respiratory symptoms. Surgically altered position of the vasculature, conduits and vascular stents can cause compression of the trachea, main and lobar bronchi that may lead to chronic symptoms of airway compression that can worsen over time (Fig. 16.31). Dynamic airway studies can differentiate between stenosis related to vascular compression and intrinsic stenosis due to tracheal and/or bronchomalacia.

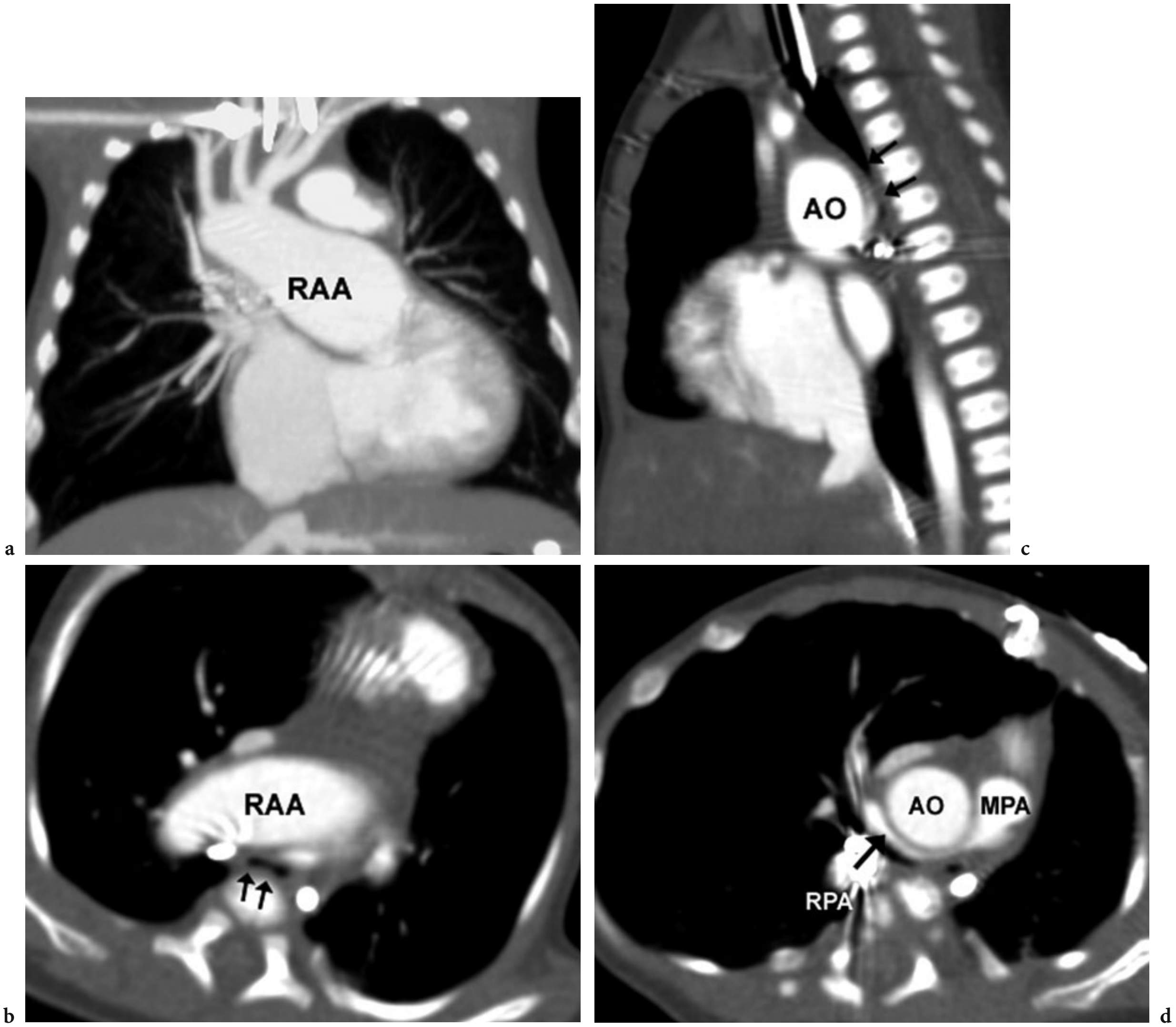

Fig. 16.29a–d. Malposition of the aortic arch causing severe airway and branch pulmonary artery narrowing in an infant with severe respiratory compromise following repair of tetralogy of Fallot and pulmonary atresia. Coronal (**a**), axial (**b**,**d**) and sagittal (**c**) oblique MIP images demonstrate a markedly dilated right aortic arch (*RAA*) positioned posteriorly within the chest, resulting in severe compression of the distal trachea and carina (*small arrows*), as well as the right pulmonary artery (*arrow* in **d**)

16.4.5
Cardiac Chamber Morphology and Ventricular Function

The current excellent spatial resolution of MDCT allows accurate assessment of potentially complex cardiac morphology by clearly delineating the borders of the ventricular endocardium and myocardium when intravascular contrast has been administered. As MDCT scanners have become even faster with larger detector row configurations, temporal resolution has improved to 125–250 ms per image (Ohnesorge et al. 2000; Juergens et al. 2004) so that it is now possible to extract multiple phases throughout the cardiac cycle to assess regional and global ventricular function. With retrospective ECG gating, multiple diastolic and systolic images can be segmented from the data set of images acquired throughout the cardiac cycle for quantitative assessment of ventricular volumes, mass and global function (Fig. 16.32).

Recently, there has been acceptable correlation between results of MDCT calculated left ventricular

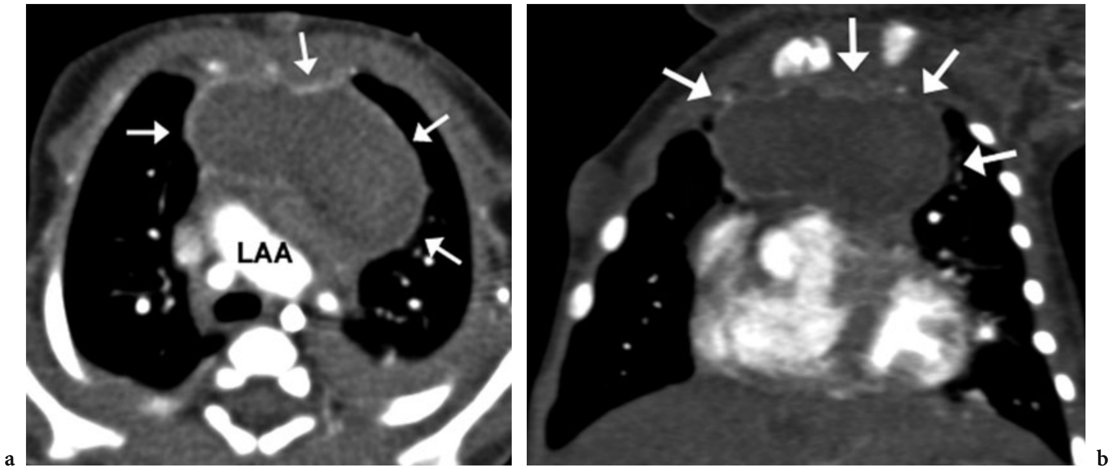

Fig. 16.30a,b. Mediastinal hematoma. Infant with TGA and subpulmonary stenosis status post right modified Blalock-Taussig shunt with large hypoechoic fluid collection noted on echocardiography. Axial (**a**) and coronal reformatted (**b**) images demonstrate a large hypodense collection (*arrows*) with an enhancing wall filling the anterior mediastinum. A post-operative hematoma was evacuated at surgery

Fig. 16.31a–c. RPA stent causing left bronchus narrowing. Truncus arteriosus with interrupted aortic arch status post repair with an RV to PA conduit. Post-operative RPA stenosis treated with balloon dilation and stenting followed by development of recurrent left lower lobe pneumonia. Coronal (**a**) and axial oblique (**b**) MIP images demonstrate a patent stent in the proximal RPA and moderate narrowing of the left main stem bronchus (*LtBR*) as it courses between the stented portion of the RPA and the descending aorta. Sagittal oblique MIP image (**c**) demonstrates the RV to PA conduit with indwelling stent (*arrows*)

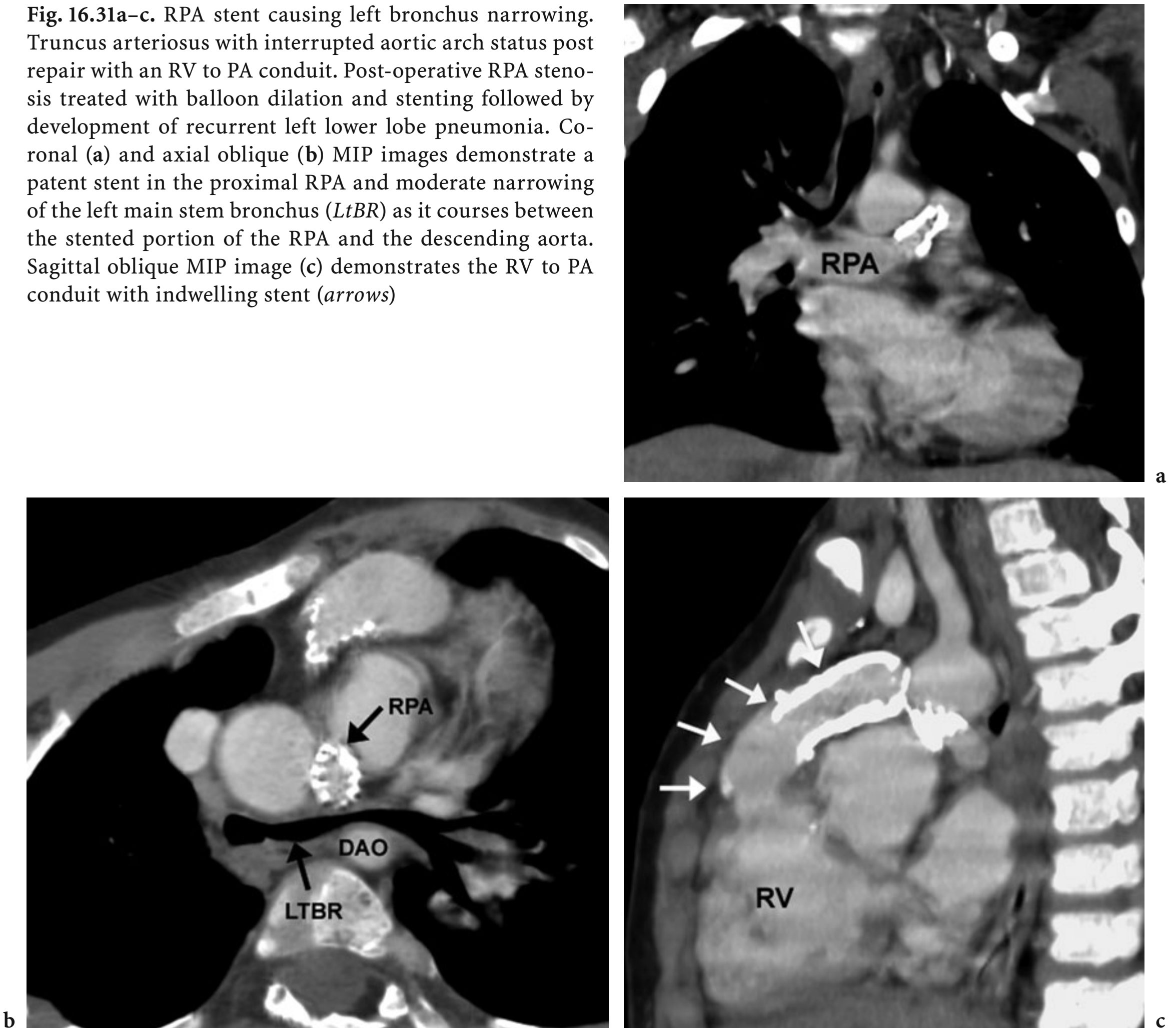

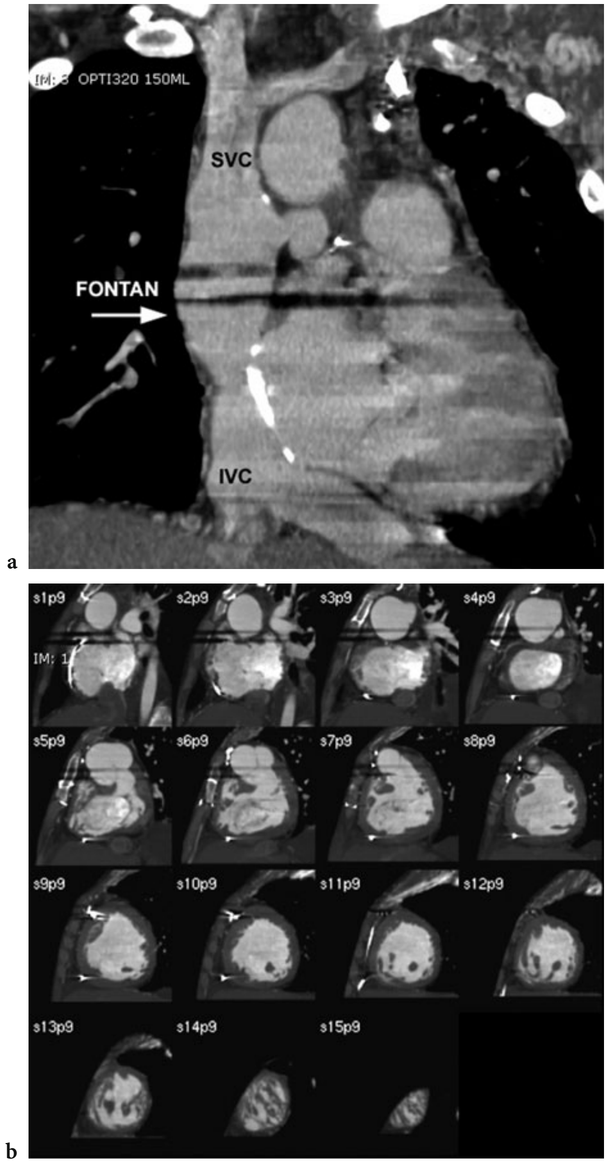

Fig. 16.32a,b. Heterotaxy, double outlet right ventricle status post fenestrated Fontan with pacemaker. Coronal MIP (**a**) image from a venous phase acquisition shows fairly uniform contrast opacification throughout the systemic venous pathway. A series of short axis images (**b**) reconstructed through the single right ventricle at end diastole for calculation of ventricular function. Note relatively mild streak artifact from pacing leads

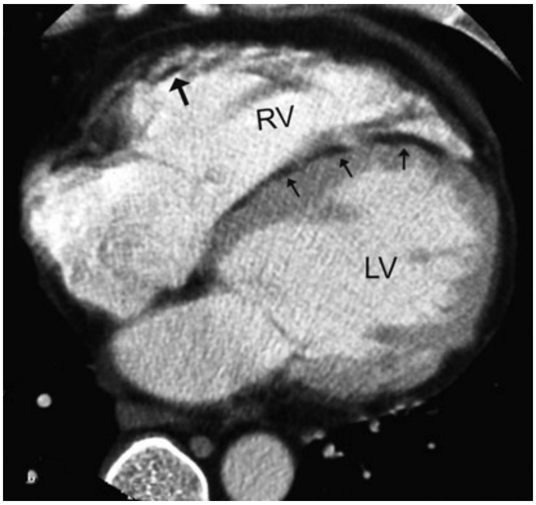

Fig. 16.33. MDCT of ARVD. Axial ECG-gated MDCT image demonstrates fatty tissue in the trabeculae of the RV (*large arrow*) and along the RV side of the interventricular septum (*small arrows*). (Used with permission from Kimura et al. 2002)

volumes and function with that of cine angiography (Juergens et al. 2002), echocardiography (Dirksen et al. 2002) and MRI (Juergens et al. 2004).

CT also has the ability to provide tissue characterization of the myocardium similar to MRI, and has been shown to depict fatty tissue within the ventricular wall in patients with arrhythmogenic right ventricular dysplasia (ARVD), a genetic disorder associated with reentrant arrhythmias that can lead to sudden death (Sotozono et al. 1990). Recent results of both single and MDCT in the evaluation of ARVD are promising (Kimura et al. 2002; Tandri et al. 2004) (Fig. 16.33); MDCT can depict the presence of intramyocardial fat in the right ventricle and separate it from epicardial fat, as well as detect right ventricular enlargement and regional and global dysfunction, all findings that can contribute to establishing the diagnosis of ARVD. Although MDCT may not be a good option for screening for ARVD in first degree relatives given the radiation exposure, it may be more useful for patients who have severe arrhythmias which can lead to image degradation on MRI, as well as for serial follow-up of patients who have already received defibrillators.

16.4.6
Post-operative Congenital Heart Disease

The evaluation of surgical results and possible complications involving palliative shunts, conduits and intracardiac baffles, and the patency of the pulmonary arteries has become a major application of noninvasive imaging of postoperative congenital heart disease. CT is most often utilized if a full evaluation of the post-operative vascular morphology is limited on MRI due to artifacts from indwelling ferromagnetic materials such as stents, coils and occlusion devices or when there is patient claustrophobia, which tends to be more of an issue with older patients.

Extracardiac conduits are prosthetic or homograft tubes used to create venoarterial, ventriculoarterial and arterioarterial connections when the structures to be connected are too far away from each other to allow a direct anastomosis. There are three different mechanisms of conduit obstruction: formation of a thick endothelial peal, scarring at sites of anastomosis, and relative narrowing of the conduit associated with growth of structures at either end. Both MDCTA and MRA allow a more complete visualization of conduits in their entirety than echocardiography or angiography due to a wide field of view and 3D imaging capability. Right ventricle to pulmonary artery conduits are used for repair of TOF in patients who have severe pulmonary stenosis or atresia (see Fig. 16.9), or anomalies of the coronary arteries that limit safe access to the right ventricular outflow tract, in the Rastelli operation for TGA with pulmonary valve stenosis, and in repair of truncus arteriosus. MDCTA is especially helpful for detection of in-stent stenosis when narrowing of the conduit has required stenting (Eichhorn et al. 2006) (see Fig. 16.31).

There are two main types of intracardiac baffles used to redirect venous blood flow through the heart – the atrial inversion procedure (Mustard or Senning operations) for TGA and the Fontan procedure for functionally univentricular hearts. In the Mustard or Senning operation, the native intra-atrial septum is excised and a baffle is inserted to direct superior and inferior vena cava blood flow to the mitral valve. The pulmonary venous blood passes around the baffle and is directed towards the tricuspid valve. Both systemic and pulmonary venous pathways have the potential for obstruction, which can be assessed by CT (Fig. 16.34).

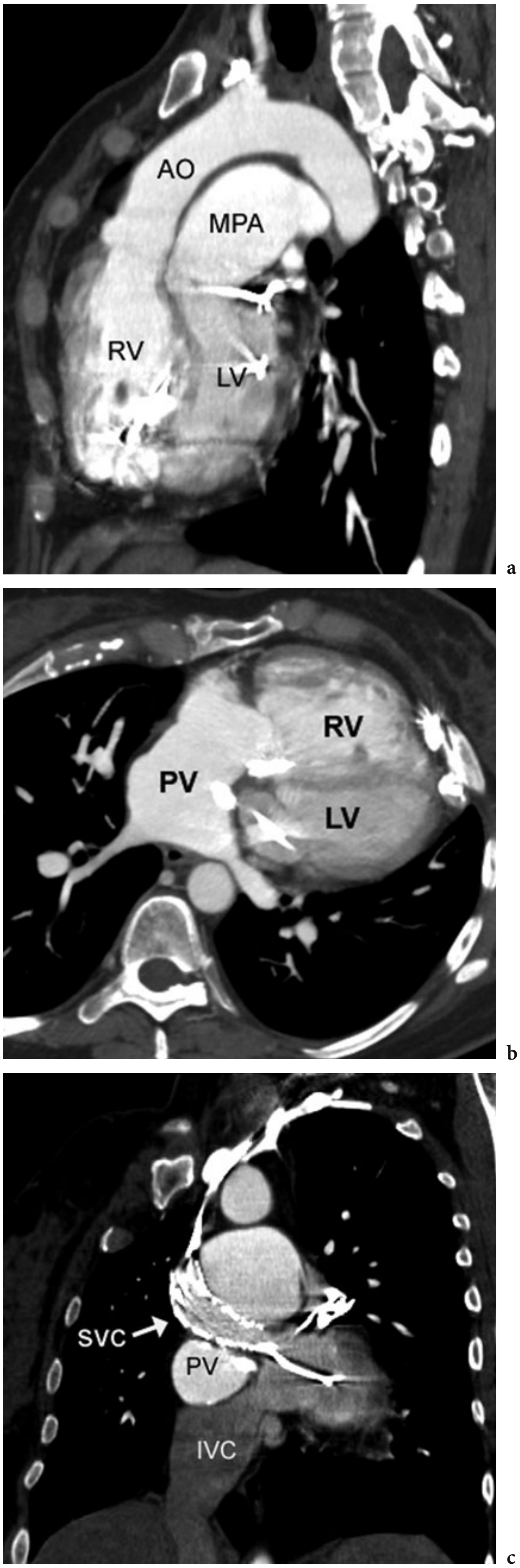

Fig. 16.34a–c. D-TGA status post Senning. Sagittal oblique (**a**) MIP image demonstrates the characteristic morphology of D-TGA with the anterior aorta arising from the RV and posterior main pulmonary artery arising from the LV. Axial MIP image (**b**) demonstrates the pulmonary venous (*PV*) pathway that directs oxygenated blood to the systemic RV positioned anteriorly. Coronal reformatted image (**c**) demonstrates the typical “pant leg” configuration of the IVC and SVC (with stent) pathway directed to the left ventricle separated by an intra-atrial baffle from the PV pathway

In the Fontan operation, a surgically created pathway reroutes the systemic venous return from the IVC and SVC directly to the pulmonary arteries. Possible complications include pulmonary arteriovenous malformations (Fig. 16.35), pulmonary venous obstruction due to extrinsic compression by an intra or extracardiac baffle or an enlarged cardiac structure used for the Fontan pathway, such as the coronary sinus. Narrowing of the pulmonary artery can occur at the level of the cavopulmonary anastomosis or due to distortion from a prior shunt or surgical pulmonary artery reconstruction. Imaging evaluation is directed to establish the overall patency of the Fontan pathway. In the early versions of the Fontan operation, the right atrium is incorporated into the systemic venous to pulmonary artery connection, and not infrequently patients can develop thrombus in the pathway due to relative stasis of slow flowing blood (see Figs. 16.14 and 16.15).

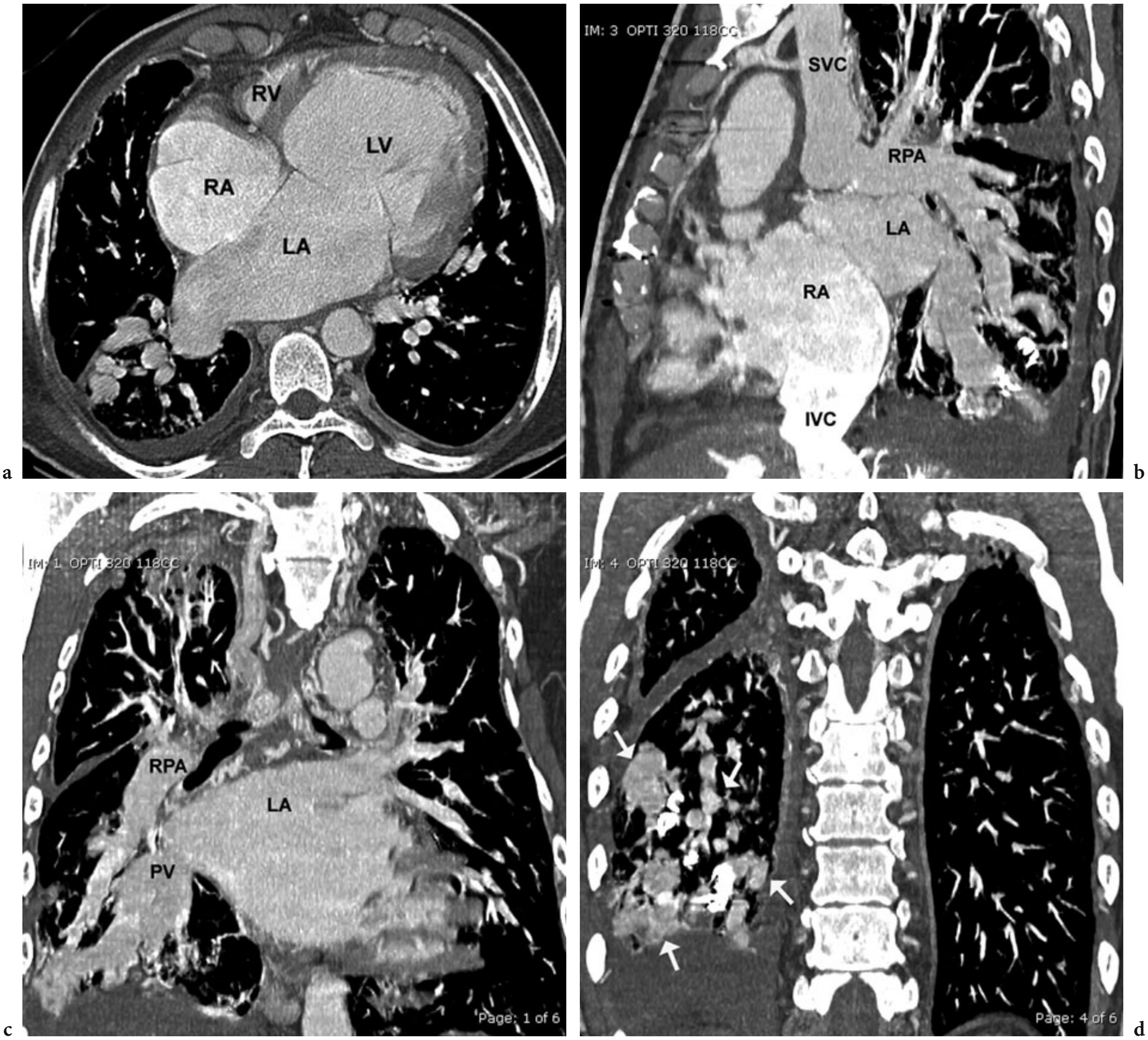

Fig. 16.35a–d. Pulmonary arteriovenous malformations (*AVMs*) in a patient with tricuspid atresia status post Glenn shunt to the RPA. Oblique axial image in a four-chamber projection (**a**) demonstrates a dilated right atrium and hypoplastic RV with fatty tissue completely separating them. Sagittal oblique image (**b**) demonstrates the patent cavopulmonary anastomosis between the SVC and RPA. Coronal images of the chest (**c**,**d**) show marked dilatation of the distal branches of the RPA and pulmonary veins (*PV*) draining the right lower lobe related to multiple small AVMs, some of which have been occluded by embolization coils. The right lung has become hypoplastic due to steal of blood supply through the AVMs

Many patients with congenital heart disease can develop conduction abnormalities or arrhythmias related to the surgical repair (especially following the Mustard or Senning or Fontan operations) or inherent to abnormal intracardiac connections, such as in congenitally corrected TGA. An indwelling pacemaker and retained pacing wires or leads are contraindications for MR imaging, and CT can be used as an alternative method for both morphologic and functional imaging in these patients (see Fig. 16.32).

16.5
Conclusion

In summary, MDCT provides a number of important advantages for morphologic and functional assessment of the cardiovascular system, including isotropic high-resolution volume imaging, high volume coverage, and improved temporal resolution with dose reduction methods. MDCT is now a major diagnostic tool in children with congenital heart disease, and when performed for appropriate indications with proper technical parameters, the benefits can far exceed the very small individual risk.

References

Achenbach S, Ulzheimer S, Baum U et al. (2000) Noninvasive coronary angiography by retrospectively ECG-gated multislice spiral CT. Circulation 102:2823–2828

Aluquin VP, Albano SA, Chan F et al. (2002) Magnetic resonance imaging in the diagnosis and follow up of Takayasu‘s arteritis in children. Ann Rheum Dis 61:526–529

Babyn PS, Gahunia HK, Massicotte P (2005) Pulmonary thromboembolism in children. Pediatr Radiol 35:258–274

Becker CR, Schatzl M, Schoepf UJ et al. (1998) Technical bases and acquisition conditions of electron-beam computed tomography. Radiologe 38:987–992

Blachere H, Latrabe V, Montaudon M et al. (2000) Pulmonary embolism revealed on helical CT angiography: comparison with ventilation-perfusion radionuclide lung scanning. AJR Am J Roentgenol 174:1041–1047

Bogaert J, Kuzo R, Dymarkowski S et al. (2003) Coronary artery imaging with real-time navigator three-dimensional turbo-field-echo MR coronary angiography: initial experience. Radiology 226:707–716

Breinholt JP, Hawkins JA, Minich LA et al. (1999) Pulmonary vein stenosis with normal connection: associated cardiac abnormalities and variable outcome. Ann Thorac Surg 68:164–168

Burke AP, Virmani R, Perry LW et al. (1998) Fatal Kawasaki disease with coronary arteritis and no coronary aneurysms. Pediatrics 101:108–112

Caldarone CA, Najm HK, Kadletz M et al. (1998) Relentless pulmonary vein stenosis after repair of total anomalous pulmonary venous drainage. Ann Thorac Surg 66:1514–1520

Choe YH, Han BK, Koh EM et al. (2000) Takayasu‘s arteritis: assessment of disease activity with contrast-enhanced MR imaging. AJR Am J Roentgenol 175:505–511

Coche E, Verschuren F, Keyeux A et al. (2003) Diagnosis of acute pulmonary embolism in outpatients: comparison of thin-collimation multi-detector row spiral CT and planar ventilation-perfusion scintigraphy. Radiology 229:757–765

Deibler AR, Kuzo RS, Vohringer M et al. (2004) Imaging of congenital coronary anomalies with multislice computed tomography. Mayo Clin Proc 79:1017–1023

Diffin DC, Leyendecker JR, Johnson SP et al. (1998) Effect of anatomic distribution of pulmonary emboli on interobserver agreement in the interpretation of pulmonary angiography. AJR Am J Roentgenol 171:1085–1089

Dirksen MS, Bax JJ, de Roos A et al. (2002) Usefulness of dynamic multislice computed tomography of left ventricular function in unstable angina pectoris and comparison with echocardiography. Am J Cardiol 90:1157–1160

Ditchfield MR, Culham JA (1995) Assessment of airways compression by MR imaging in children with aneurysmal pulmonary arteries. Pediatr Radiol 25:190–191

Donnelly LF, Frush DP (2003) Pediatric multidetector body CT. Radiol Clin North Am 41:637–655

Donnelly LF, Emery KH, Brody AS et al. (2001) Minimizing radiation dose for pediatric body applications of single-detector helical CT: strategies at a large Children‘s Hospital. AJR Am J Roentgenol 176:303–306

Douglas PS, Fiolkoski J, Berko B et al. (1988) Echocardiographic visualization of coronary artery anatomy in the adult. J Am Coll Cardiol 11:565–571

Driscoll DJ, Hesslein PS, Mullins CE (1982) Congenital stenosis of individual pulmonary veins: clinical spectrum and unsuccessful treatment by transvenous balloon dilation. Am J Cardiol 49:1767–1772

Eichhorn JG, Long FR, Hill SL et al. (2006) Assessment of in-stent stenosis in small children with congenital heart disease using multi-detector computed tomography: a validation study. Catheter Cardiovasc Interv 68:11–20

Erbel R, Alfonso F, Boileau C et al. (2001) Diagnosis and management of aortic dissection. Eur Heart J 22:1642–1681

Flohr T, Prokop M, Becker C et al. (2002) A retrospectively ECG-gated multislice spiral CT scan and reconstruction technique with suppression of heart pulsation artifacts for cardio-thoracic imaging with extended volume coverage. Eur Radiol 12:1497–1503

Frush DP (2002) Strategies of dose reduction. Pediatr Radiol 32:293–297

Fujiwara H, Hamashima Y (1978) Pathology of the heart in Kawasaki disease. Pediatrics 61:100–107

Gerber TC, Kuzo RS, Karstaedt N et al. (2002) Current results and new developments of coronary angiography with use of contrast-enhanced computed tomography of the heart. Mayo Clin Proc 77:55–71

Goo HW, Suh DS (2006) Tube current reduction in pediatric non-ECG-gated heart CT by combined tube current modulation. Pediatr Radiol 36: 344–351

Goo HW, Park IS, Ko JK et al. (2005a) Computed tomography for the diagnosis of congenital heart disease in pediatric and adult patients. Int J Cardiovasc Imaging 21:347–365; discussion 367

Goo HW, Park IS, Ko JK et al. (2005b) Visibility of the origin and proximal course of coronary arteries on non-ECG-gated heart CT in patients with congenital heart disease. Pediatr Radiol 35:792–798

Goo, HW, Park I, Ko JK et al. (2006) Coronary CT angiography and MR angiography of Kawasaki Disease. Pediatr Radiol 36:699–700

Goodman LR, Lipchik RJ, Kuzo RS et al. (2000) Subsequent pulmonary embolism: risk after a negative helical CT pulmonary angiogram – prospective comparison with scintigraphy. Radiology 215:535–542

Gowda RM, Boxt LM (2004) Calcifications of the heart. Radiol Clin North Am 42:603–617, vi–vii

Green RM, Meyer TJ, Dunn M et al. (1992) Pulmonary embolism in younger adults. Chest 101:1507–1511

Greess H, Nomayr A, Wolf H et al. (2002) Dose reduction in CT examination of children by an attenuation-based on-line modulation of tube current (CARE Dose). Eur Radiol 12:1571–1576

Greil GF, Stuber M, Botnar RM et al. (2002) Coronary magnetic resonance angiography in adolescents and young adults with kawasaki disease. Circulation 105:908–911

Greil GF, Schoebinger M, Kuettner A et al. (2006) Imaging of aortopulmonary collateral arteries with high-resolution multidetector CT. Pediatr Radiol 36:502–509

Hopkins KL, Patrick LE, Simoneaux SF et al. (1996) Pediatric great vessel anomalies: initial clinical experience with spiral CT angiography. Radiology 200:811–815

Horiguchi J, Nakanishi T, Tamura A et al. (2002) Technical innovation of cardiac multirow detector CT using multisector reconstruction. Comput Med Imaging Graph 26:217–226

Iemura M, Ishii M, Sugimura T et al. (2000) Long term consequences of regressed coronary aneurysms after Kawasaki disease: vascular wall morphology and function. Heart 83:307–311

Ishikawa T, Brandt PW (1985) Anomalous origin of the left main coronary artery from the right anterior aortic sinus: angiographic definition of anomalous course. Am J Cardiol 55:770–776

Jakobs TF, Becker CR, Ohnesorge B et al. (2002) Multislice helical CT of the heart with retrospective ECG gating: reduction of radiation exposure by ECG-controlled tube current modulation. Eur Radiol 12:1081–1086

Juergens KU, Grude M, Fallenberg EM et al. (2002) Using ECG-gated multidetector CT to evaluate global left ventricular myocardial function in patients with coronary artery disease. AJR Am J Roentgenol 179:1545–1550

Juergens KU, Grude M, Maintz D et al. (2004) Multi-detector row CT of left ventricular function with dedicated analysis software versus MR imaging: initial experience. Radiology 230:403–410

Kalra MK, Maher MM, Toth TL et al. (2004) Strategies for CT radiation dose optimization. Radiology 230:619–628

Kato H, Ichinose E, Yoshioka F et al. (1982) Fate of coronary aneurysms in Kawasaki disease: serial coronary angiography and long-term follow-up study. Am J Cardiol 49:1758–1766

Kato H, Sugimura T, Akagi T et al. (1996) Long-term consequences of Kawasaki disease. A 10- to 21-year follow-up study of 594 patients. Circulation 94:1379–1385

Kawano T, Ishii M, Takagi J et al. (2000) Three-dimensional helical computed tomographic angiography in neonates and infants with complex congenital heart disease. Am Heart J 139:654–660

Kim TH, Kim YM, Suh CH et al. (2000) Helical CT angiography and three-dimensional reconstruction of total anomalous pulmonary venous connections in neonates and infants. AJR Am J Roentgenol 175:1381–1386

Kim YM, Yoo SJ, Kim TH et al. (2002) Three-dimensional computed tomography in children with compression of the central airways complicating congenital heart disease. Cardiol Young 12:44–50

Kimura F, Sakai F, Sakomura Y et al. (2002) Helical CT features of arrhythmogenic right ventricular cardiomyopathy. Radiographics 22:1111–1124

Lambert V, Sigal-Cinqualbre A, Belli E et al. (2005) Preoperative and postoperative evaluation of airways compression in pediatric patients with 3-dimensional multislice computed tomographic scanning: effect on surgical management. J Thorac Cardiovasc Surg 129:1111–1118

Lawler LP, Corl FM, Fishman EK (2002) Multi-detector row and volume-rendered CT of the normal and accessory flow pathways of the thoracic systemic and pulmonary veins. Radiographics 22 Spec No:S45–60

Lee EY, Siegel MJ, Sierra LM et al. (2004) Evaluation of angioarchitecture of pulmonary sequestration in pediatric patients using 3D MDCT angiography. AJR Am J Roentgenol 183:183–188

Mahesh M (2002) Search for isotropic resolution in CT from conventional through multiple-row detector. Radiographics 22:949–962

Markowitz A (2001) Utility of the full root bioprosthesis in surgery for complex aortic valve-ascending aortic disease. Semin Thorac Cardiovasc Surg 13:12–15

Marom EM, Herndon JE, Kim YH et al. (2004) Variations in pulmonary venous drainage to the left atrium: implications for radiofrequency ablation. Radiology 230:824–829

Matsunaga N, Hayashi K, Sakamoto I et al. (1997) Takayasu arteritis: protean radiologic manifestations and diagnosis. Radiographics 17:579–594

McConnell MV, Ganz P, Selwyn AP et al. (1995) Identification of anomalous coronary arteries and their anatomic course by magnetic resonance coronary angiography. Circulation 92:3158–3162

McElhinney DB, Reddy VM, Pian MS et al. (1999) Compression of the central airways by a dilated aorta in infants and children with congenital heart disease. Ann Thorac Surg 67:1130–1136

Momenah T, Sanatani S, Potts J et al. (1998) Kawasaki disease in the older child. Pediatrics 102:12

Nieman K, Cademartiri F, Raaijmakers R et al. (2003) Noninvasive angiographic evaluation of coronary stents with multi-slice spiral computed tomography. Herz 28:136–142

Nienaber CA, von Kodolitsch Y, Nicolas V et al. (1993) The diagnosis of thoracic aortic dissection by noninvasive imaging procedures. N Engl J Med 328:1–9

Odegard KC, DiNardo JA, Tsai-Goodman B et al. (2004) Anaesthesia considerations for cardiac MRI in infants and small children. Paediatr Anaesth 14:471–476

Ohnesorge B, Flohr T, Becker C et al. (2000) Cardiac imaging by means of electrocardiographically gated multisection spiral CT: initial experience. Radiology 217:564–571

Oral H, Knight BP, Tada H et al. (2002) Pulmonary vein isolation for paroxysmal and persistent atrial fibrillation. Circulation 105:1077–1081

PIOPED Investigators (1990) Value of the ventilation/perfusion scan in acute pulmonary embolism. Results of the prospective investigation of pulmonary embolism diagnosis (PIOPED). Jama 263:2753–2759

Remy-Jardin M, Remy J, Deschildre F et al. (1996) Diagnosis of pulmonary embolism with spiral CT: comparison with pulmonary angiography and scintigraphy. Radiology 200:699–706

Robotin MC, Bruniaux J, Serraf A et al. (1996) Unusual forms of tracheobronchial compression in infants with congenital heart disease. J Thorac Cardiovasc Surg 112:415–423

Sato Y, Kato M, Inoue F et al. (2003) Detection of coronary artery aneurysms, stenoses and occlusions by multislice spiral computed tomography in adolescents with kawasaki disease. Circ J 67:427–430

Satomi G, Nakamura K, Narai S et al. (1984) Systematic visualization of coronary arteries by two-dimensional echocardiography in children and infants: evaluation in Kawasaki‘s disease and coronary arteriovenous fistulas. Am Heart J 107:497–505

Schoenhagen P, Halliburton SS, Stillman AE et al. (2004) Noninvasive imaging of coronary arteries: current and future role of multi-detector row CT. Radiology 232:7–17

Schoepf UJ, Holzknecht N, Helmberger TK et al. (2002) Subsegmental pulmonary emboli: improved detection with thin-collimation multi-detector row spiral CT. Radiology 222:483–490

Schoepf UJ, Becker CR, Ohnesorge BM et al. (2004) CT of coronary artery disease. Radiology 232:18–37

Seshadri N, Novaro GM, Prieto L et al. (2002) Images in cardiovascular medicine. Pulmonary vein stenosis after catheter ablation of atrial arrhythmias. Circulation 105:2571–2572

Siegel MJ (2003) Multiplanar and three-dimensional multidetector row CT of thoracic vessels and airways in the pediatric population. Radiology 229:641–650

Siegel MJ, Schmidt B, Bradley D et al. (2004) Radiation dose and image quality in pediatric CT: effect of technical factors and phantom size and shape. Radiology 233:515–522

Sommer T, Fehske W, Holzknecht N et al. (1996) Aortic dissection: a comparative study of diagnosis with spiral CT, multiplanar transesophageal echocardiography, and MR imaging. Radiology 199:347–352

Sotozono K, Imahara S, Masuda H et al. (1990) Detection of fatty tissue in the myocardium by using computerized tomography in a patient with arrhythmogenic right ventricular dysplasia. Heart Vessels Suppl 5:59–61

Stein PD, Henry JW, Gottschalk A (1999) Reassessment of pulmonary angiography for the diagnosis of pulmonary embolism: relation of interpreter agreement to the order of the involved pulmonary arterial branch. Radiology 210:689–691

Su JT, Chung T, Muthupillai R et al. (2005) Usefulness of real-time navigator magnetic resonance imaging for evaluating coronary artery origins in pediatric patients. Am J Cardiol 95:679–682

Sun CC, Doyle T, Ringel RE (1995) Pulmonary vein stenosis. Hum Pathol 26:880–886

Takahashi K, Oharaseki T, Naoe S (2001) Pathological study of postcoronary arteritis in adolescents and young adults: with reference to the relationship between sequelae of Kawasaki disease and atherosclerosis. Pediatr Cardiol 22:138–142

Tandri H, Bomma C, Calkins H et al. (2004) Magnetic resonance and computed tomography imaging of arrhythmogenic right ventricular dysplasia. J Magn Reson Imaging 19:848–858

Tillie-Leblond I, Mastora I, Radenne F et al. (2002) Risk of pulmonary embolism after a negative spiral CT angiogram in patients with pulmonary disease: 1-year clinical follow-up study. Radiology 223:461–467

Tomita H, Yamada O, Ohuchi H et al. (2001) Coagulation profile, hepatic function, and hemodynamics following Fontan-type operations. Cardiol Young 11:62–66

Van Nieuwenhuizen et al. (2001)

Van Ommen CH, Peters M (2006) Acute pulmonary embolism in childhood. Thromb Res 118:13–25

Van Ommen CH, Ottenkamp J, Lam J et al. (2002) The risk of postthrombotic syndrome in children with congenital heart disease. J Pediatr 141:582–586

Varma C, Warr MR, Hendler AL et al. (2003) Prevalence of „silent“ pulmonary emboli in adults after the Fontan operation. J Am Coll Cardiol 41:2252–2258

Westra SJ, Hill JA, Alejos JC et al. (1999) Three-dimensional helical CT of pulmonary arteries in infants and children with congenital heart disease. AJR Am J Roentgenol 173:109–115

Woodring JH, Howard TA, Kanga JF (1994) Congenital pulmonary venolobar syndrome revisited. Radiographics 14:349–369

Yanagawa H, Tuohong Z, Oki I et al. (1999) Effects of gammaglobulin on the cardiac sequelae of Kawasaki disease. Pediatr Cardiol 20:248–251

Fetal MRI of the Chest

17

Pedro A. Daltro and Heron Werner

CONTENTS

17.1 **Introduction** *397*
17.2 **MRI Technique and Normal Anatomy Patterns** *397*
17.3 **Indications for Fetal MRI of the Chest** *399*
17.4 **Pulmonary Lesions** *399*
17.4.1 Congenital Cystic Adenomatoid Malformation *399*
17.4.2 Pulmonary Sequestration *399*
17.4.3 Bronchogenic Cyst *402*
17.4.4 Neuroenteric Cyst *404*
17.4.5 Pulmonary Arteriovenous Malformations (PAVMs) *404*
17.4.6 Congenital Pulmonary Lymphangiectasia *404*
17.5 **Hydrothorax** *407*
17.6 **Congenital Diaphragmatic Hernia** *407*
17.7 **Congenital Laryngeal Atresia** *411*
17.8 **Cardiac Malformations** *413*
17.9 **Hemangiomas** *413*
17.10 **Conclusions** *415*
References *415*

17.1
Introduction

Magnetic resonance imaging (MRI) is a non-invasive technique that allows the acquisition of high-definition images of fetal anatomy. Prenatal ultrasound (US) is currently the gold standard imaging technique during pregnancy. However, MRI has several advantages which have led to its increasing use for further characterization of fetal anatomy. MR images are usually not affected by fetal position, and image quality does not depend on the amount of amniotic fluid (Hubbard et al. 1999; Matsuoka et al. 2003). MRI can provide more accurate information than US alone, and may therefore assist decisions regarding the continuation of pregnancy, the method or site of delivery, and whether to perform a high-risk but potentially life-saving fetal intervention (Guo and Luo 2006).

17.2
MRI Technique and Normal Anatomy Patterns

To obtain quality fetal chest MR images, it is essential to use fast sequences such as HASTE (Half-Fourier Single shot Turbo spin-Echo), FSSE (Fast Single Shot Echo) or true-FISP (Free Induction Steady state Precession). These sequences permit quick image acquisition, avoiding artifacts related to fetal movement. The examination should begin with T2-weighted images of the thorax in axial, coronal and sagittal planes, allowing an anatomic study of this region. T1-weighted images can be obtained to evaluate the liver and small bowel in patients with congenital diaphragmatic hernia (CDH). Fluid-filled structures usually have low signal on

---

P. A. Daltro, MD
H. Werner, MD
CDPI-Clínica de Diagnóstico por Imagem, Instituto Fernandes Figueira – FIOCRUZ, Av das Americas 4666, Sala 325-Barra da Tijuca, Rio de Janeiro – RJ 22649-900, Brazil

T1- and high signal on T2-weighted sequences. Solid organs demonstrate intermediate signal on T1- and T2-weighted images and the fat-containing structures have high-signal on T1- and low signal on T2-weighted images.

The T2-weighted sequences are the most useful for evaluating the fetal chest. The lungs contain a significant amount of fluid, which increases with the gestational age. As a consequence, the signal of the lungs is homogeneously high on T2-weighted images, in contrast to the chest wall and mediastinal structures. In addition, the trachea and bronchi are well seen due to the amniotic fluid inside of them. The thymus demonstrates intermediate signal on T2-weighted images and the heart is not well seen due to motion artifacts (Fig. 17.1).

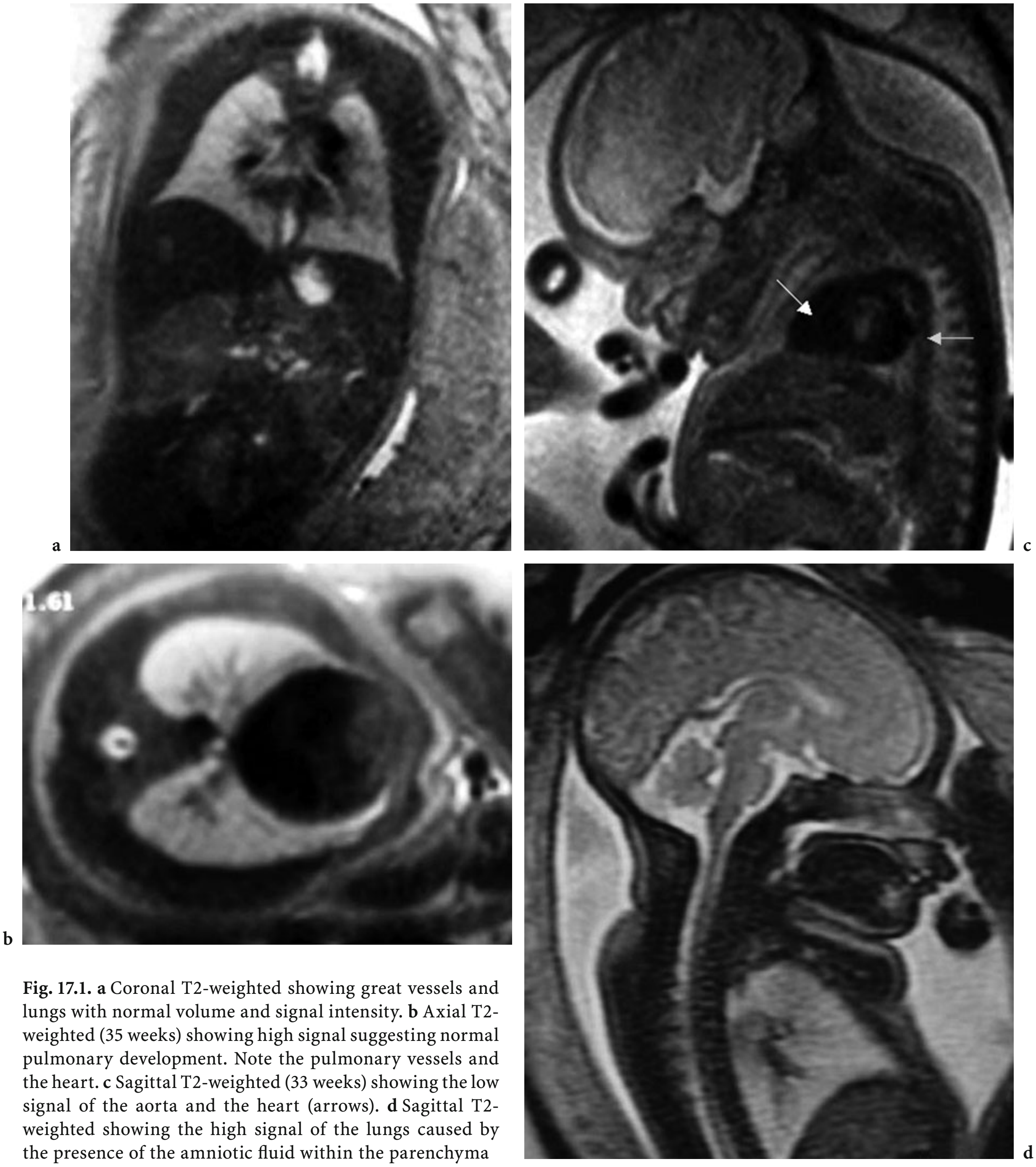

Fig. 17.1. a Coronal T2-weighted showing great vessels and lungs with normal volume and signal intensity. **b** Axial T2-weighted (35 weeks) showing high signal suggesting normal pulmonary development. Note the pulmonary vessels and the heart. **c** Sagittal T2-weighted (33 weeks) showing the low signal of the aorta and the heart (arrows). **d** Sagittal T2-weighted showing the high signal of the lungs caused by the presence of the amniotic fluid within the parenchyma

At the moment, there are no known biological effects of MRI on the fetus. The current recommendations by the Safety Committee of the Society of Magnetic Resonance Imaging regarding MRI safety during pregnancy suggest using this technique only in patients with inconclusive US. However, several imaging centers avoid acquiring MRI during the first trimester of the pregnancy, because there is no benefits in fetal diagnosis. The use of MRI should be limited to the second and third trimesters of the pregnancy. Gadolinium-based contrast media are not recommended because they cross the placenta and penetrate the fetal circulation within seconds after intravenous administration (Shellock and Kanal 1991; Guo and Luo 2006).

17.3
Indications for Fetal MRI of the Chest

Although US remains the gold standard imaging technique for screening of fetal malformations, MRI has been advancing in the last two decades as a complementary method for studying fetal anatomy (Hubbard et al. 1999; Shinmoto et al. 2000; Coakley et al. 2004). One of the most important advantages of MRI is soft tissue contrast. In addition, in cases of severe oligohydramnios or maternal obesity, MRI can provide essential information not possible with US studies.

Improvements in US resolution over the last two decades have increased the ability to diagnose fetal chest anomalies. However, recent advances in MRI techniques have also increased the value of MRI in evaluating these malformations, especially for atypical lesions and masses (Levine et al. 2003; Kasprian et al. 2006).

There are many factors that influence normal fetal lung growth, such as adequate size and shape of the fetal thorax, fetal breathing, movements, and an adequate amount of amniotic fluid. Pulmonary hypoplasia can occur when any of these factors are abnormal, but it is most commonly seen in patients with intrathoracic space occupying lesions. The most common space occupying lesions in the fetal thorax are congenital diaphragmatic hernia, congenital cystic adenomatoid malformation (CCAM), bronchopulmonary sequestration and fetal hydrothorax (Hubbard et al. 1999; Levine et al. 2003; Newman 2006).

17.4
Pulmonary Lesions

17.4.1
Congenital Cystic Adenomatoid Malformation

The congenital cystic adenomatoid malformation is a lesion characterized by overgrowth of bronchial structures at the expense of the alveoli, and associated with an abnormal supplying airway. These lesions are often diagnosed now on prenatal sonography or MRI (Daltro et al. 2004). Fetal MRI is helpful in its ability to distinguish CCAM from other entities such as CDH. Usually, CCAM demonstrates markedly higher signal on T2-weighted images than the remaining normal lung (Fig. 17.2).

Adzick et al. (1985) suggested classifying CCAMs into two types: macrocystic (>5 mm) and microcystic (<5 mm). However, the original classification of Stocker et al. (1977) remains more commonly used; they divide the lesions into three types: type I, macrocystic (>2 cm); type II, multiple small cysts; and type III, solid form (microscopic cysts). Nevertheless the natural history and prognosis of CCAM are variable. The prognosis associated with this lesion is dependent on the size, rather than the histologic type, of the lesion. Larger lesions are associated with higher frequency of mediastinal shift, pulmonary hypoplasia, vascular compromise, hydrops, and also hydramnios (Hubbard et al. 1999) (Fig. 17.3).

17.4.2
Pulmonary Sequestration

Pulmonary sequestration is a mass of pulmonary tissue that does not communicate with the central airway through a normal bronchial connection, and that receives its blood supply through an anomalous systemic artery. The arterial supply may arise from the descending thoracic or abdominal aorta, or from one of its branches (Daltro et al. 2004). Pulmonary sequestration may be extralobar or intralobar. The extralobar form is most commonly diagnosed in the prenatal and neonatal periods, whereas the intralobar form is more commonly seen in childhood. These lesions may regress in utero (Daltro et al. 2004).

Prenatal US demonstrates pulmonary sequestration as a homogeneously hyperechogenic mass in

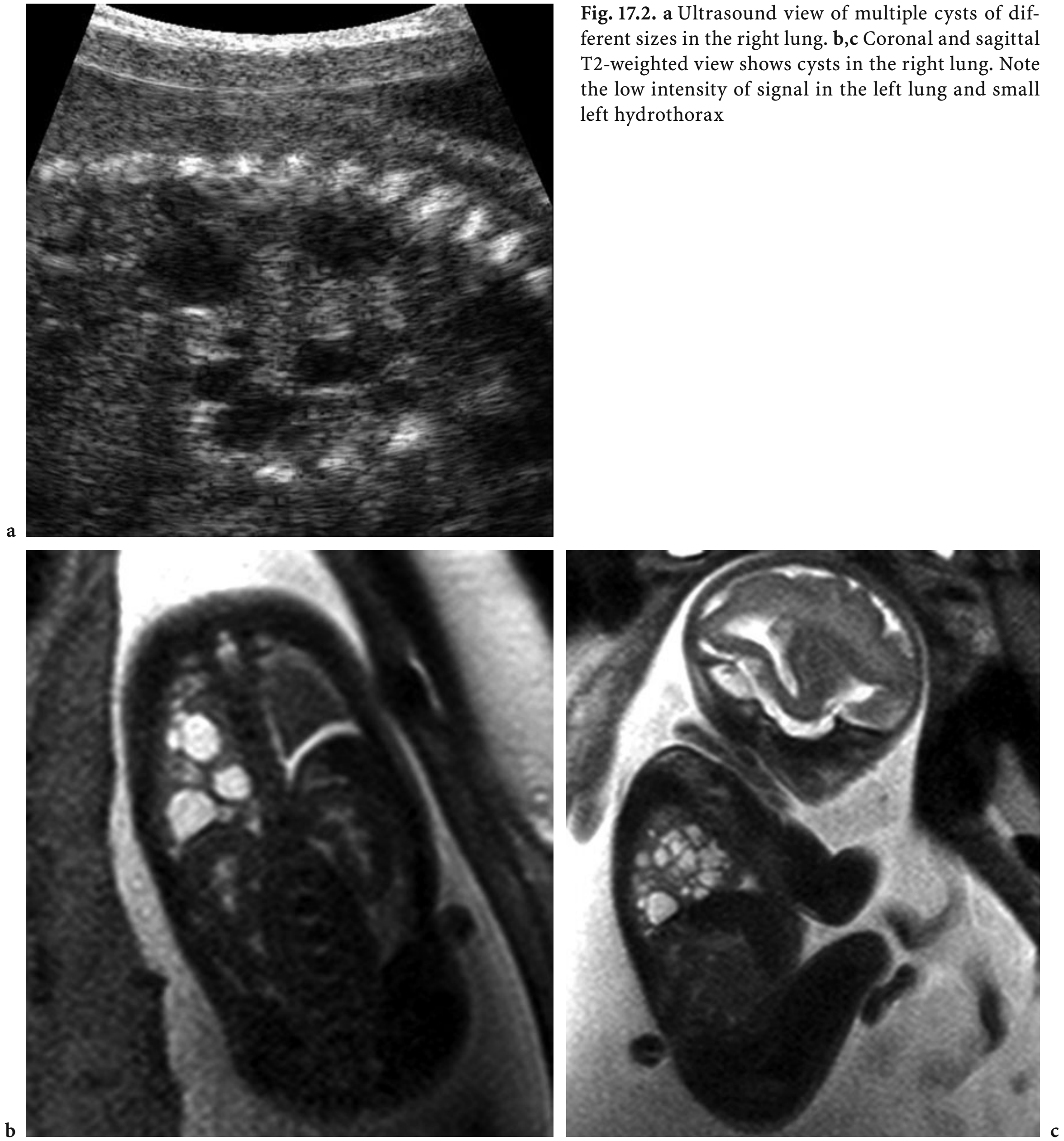

Fig. 17.2. **a** Ultrasound view of multiple cysts of different sizes in the right lung. **b,c** Coronal and sagittal T2-weighted view shows cysts in the right lung. Note the low intensity of signal in the left lung and small left hydrothorax

the lower lobes of the lung. On MRI, sequestered lung tissue has markedly high signal on T2- and low signal on T1-weighted images. The characterization of the anomalous vessels is possible by US but very difficult by MRI (Fig. 17.4 and 17.5).

The differential diagnosis of pulmonary sequestration may include neuroblastoma and adrenal hemorrhage. Pulmonary sequestration is more commonly seen as a solid lesion located on the left side, and can be demonstrated with US during the second trimester. On the other hand, neuroblastoma usually contains cystic areas, occurs more frequently on the right side and is more commonly diagnosed in the third trimester (Kays 2006).

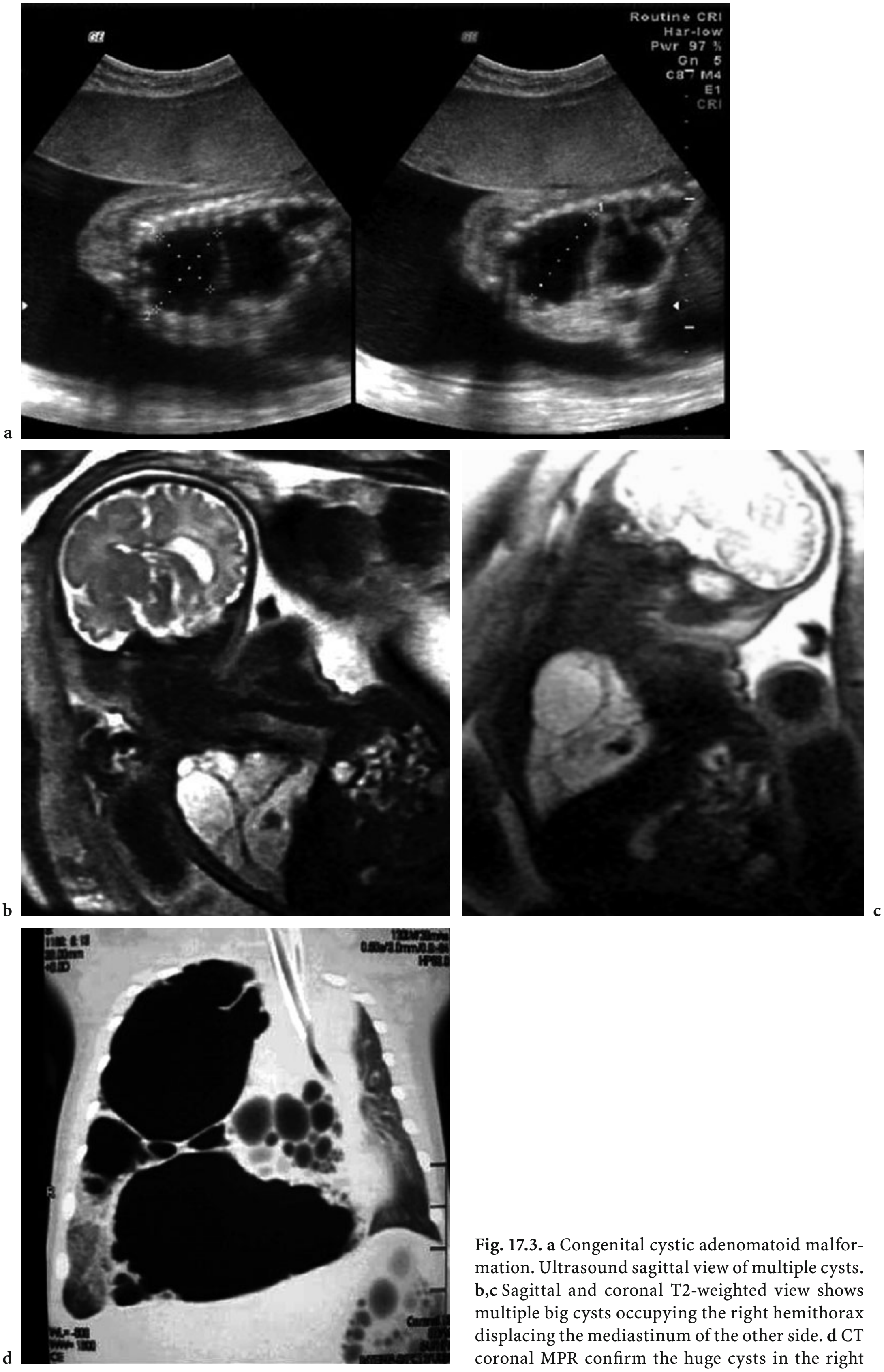
GE
GE
Routine CRI
Har-low
Pwr 97 %
Gn 5
C8 M4
E1
CRI
a
b
c
d
R

Fig. 17.3. a Congenital cystic adenomatoid malformation. Ultrasound sagittal view of multiple cysts. **b,c** Sagittal and coronal T2-weighted view shows multiple big cysts occupying the right hemithorax displacing the mediastinum of the other side. **d** CT coronal MPR confirm the huge cysts in the right

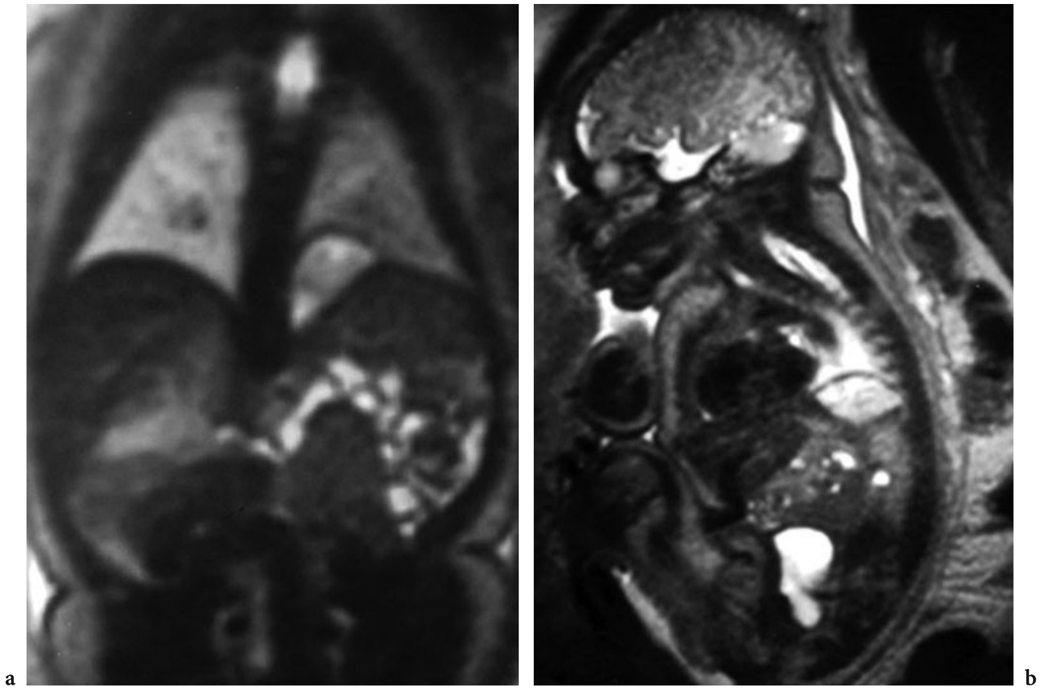

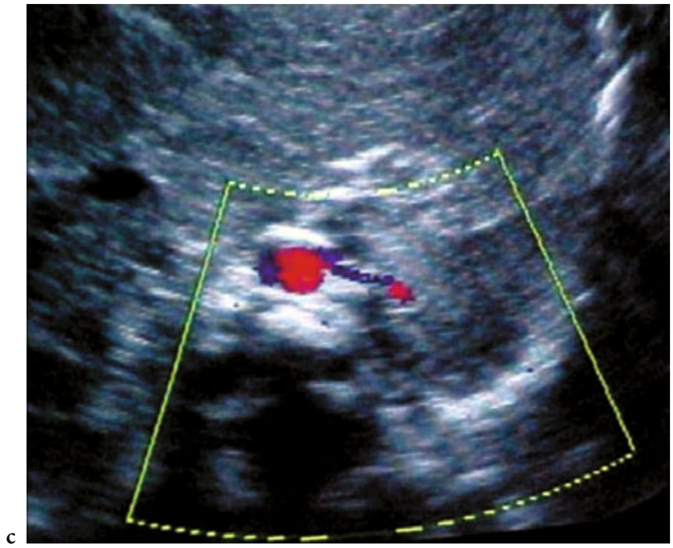

Fig. 17.4. **a** Coronal T2-weighted shows normal lungs surface (hypersignal). Note the mass in the base of the left lung, corresponding to extralobar sequestration. **b** Sagittal T2-weighted also shows the posterior place of the lesion. **c** Postnatal ultrasound (3rd day) showing the arterial supply from the aorta

17.4.3
Bronchogenic Cyst

The bronchogenic cyst is the most common cystic lesion of the mediastinum; it is an anomaly of the ventral bud of the primitive gut that occurs between the 26th and 40th days of embryonic development. The walls of bronchogenic cysts are thin, covered by respiratory epithelium and contain mucinous material. Most of the cysts are seen in the mediastinum or near the carina. Less commonly, the cysts may occur within the lung parenchyma, pleura or diaphragm. When the cysts are seen in the lung parenchyma, they are usually located in the inferior lobes. Bronchogenic cysts are sometimes found in association with other congenital pulmonary malformations such as sequestration or lobar overinflation (Daltro et al. 2004) (Fig. 17.6).

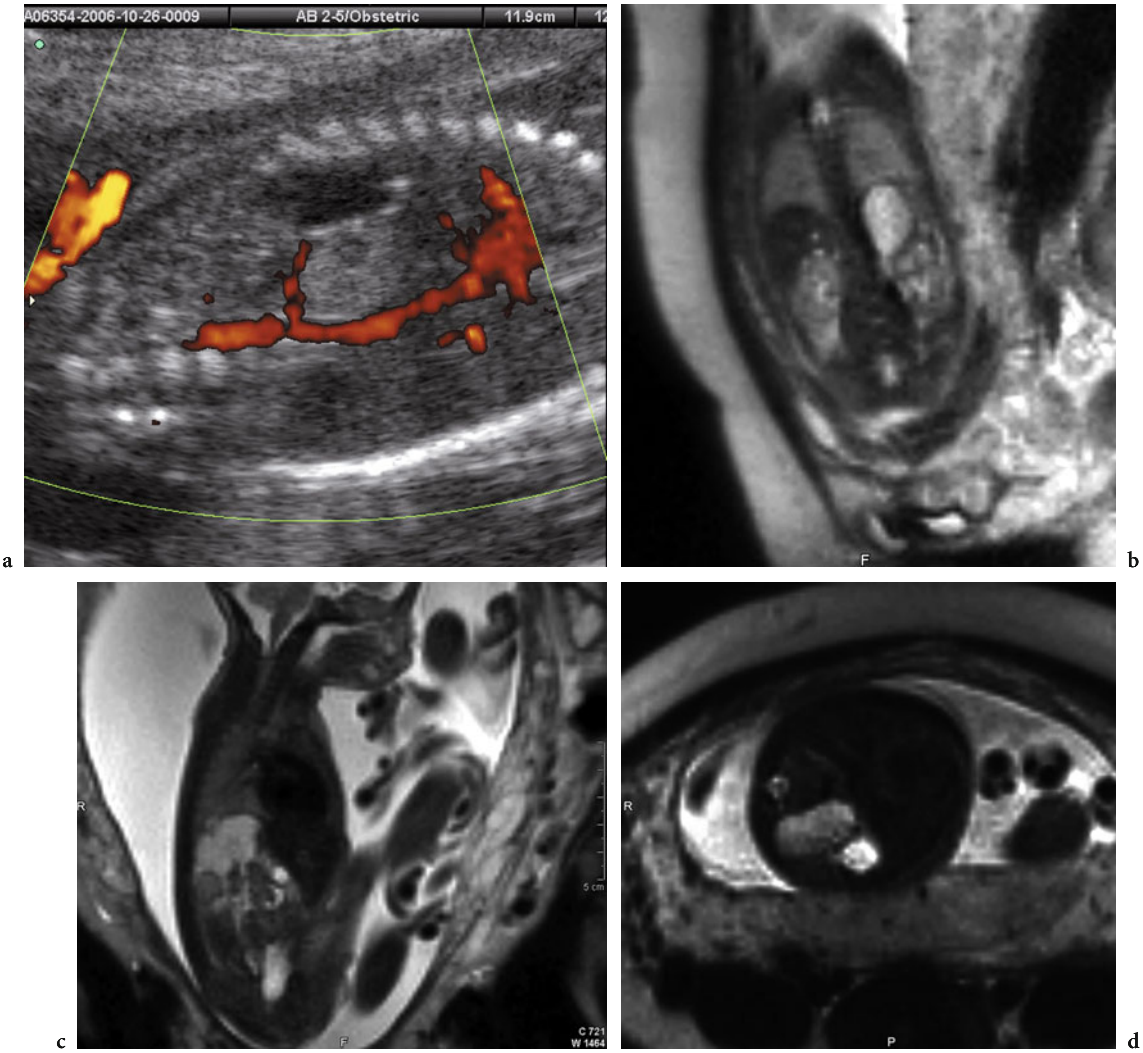
A06354-2006-10-26-0009
AB 2-5/Obstetric
11.9cm
a
F
b
R
5 cm
F
C 721
W 1464
c
R
P
d

Fig. 17.5. a Pulmonary sequestration. Prenatal ultrasound (27 weeks) reveals hyperechoic image with arterial supply from the aorta. **b,c** Coronal and sagittal T2-weighted shows hyperintense signal mass in the base of the left lung. **d** Axial T2-weighted view shows the lesion close to the stomach

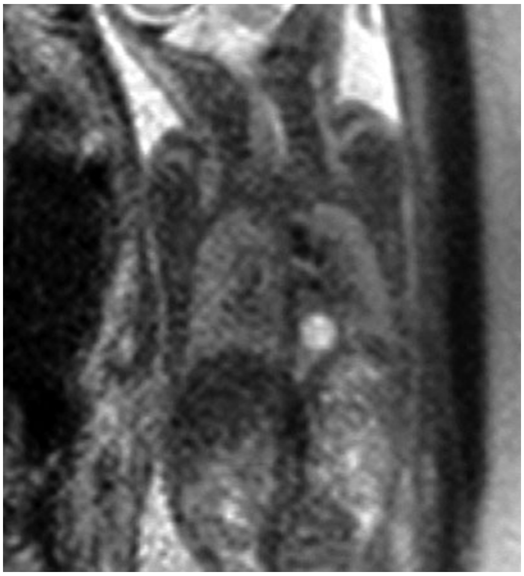

Fig. 17.6. Bronchogenic cyst. Coronal T2-weighted shows cystic lesion in the base of the left lung

17.4.4
Neuroenteric Cyst

The neuroenteric cyst is the main lesion included in the differential diagnosis of bronchogenic cysts. The walls of neuroenteric cysts have nervous and gastrointestinal elements, with intestinal epithelium that may be ciliated. They are usually seen in the posterior mediastinum, and may communicate with the esophagus, stomach or duodenum. Neuroenteric cysts are frequently associated with anomalies of vertebral segmentation, and they can be asymptomatic at birth or present minimal respiratory distress (Newman 2006) (Fig. 17.7).

17.4.5
Pulmonary Arteriovenous Malformations (PAVMs)

Pulmonary arteriovenous malformations (PAVMs) result from an abnormal communication between the pulmonary arteries and veins. Most of the lesions are congenital in origin and the female:male ratio is around 2:1. Infants and children with PAVMs may be asymptomatic; however, if the lesions are large enough to cause a significant right-to-left shunt, the patient may present with cyanosis or heart failure. Between 50% and 70% of PAVMs occur in the lower lobes and about 2/3 of the patients have multiple lesions (Hansell et al. 2005) (Fig. 17.8).

17.4.6
Congenital Pulmonary Lymphangiectasia

Congenital pulmonary lymphangiectasia is a generalized dilation of otherwise histopathologically normal lymphatic vessels. The condition may occur primarily, or secondary to severe pulmonary venous obstruction in cases of total anomalous pulmonary venous return or hypoplastic left heart syndrome. Congenital pulmonary lymphangiectasia is frequently associated with genetic diseases, including Noonan, Turner, Ehlers-Danlos and Down syndromes (Faul et al. 2000) (Fig. 17.9).

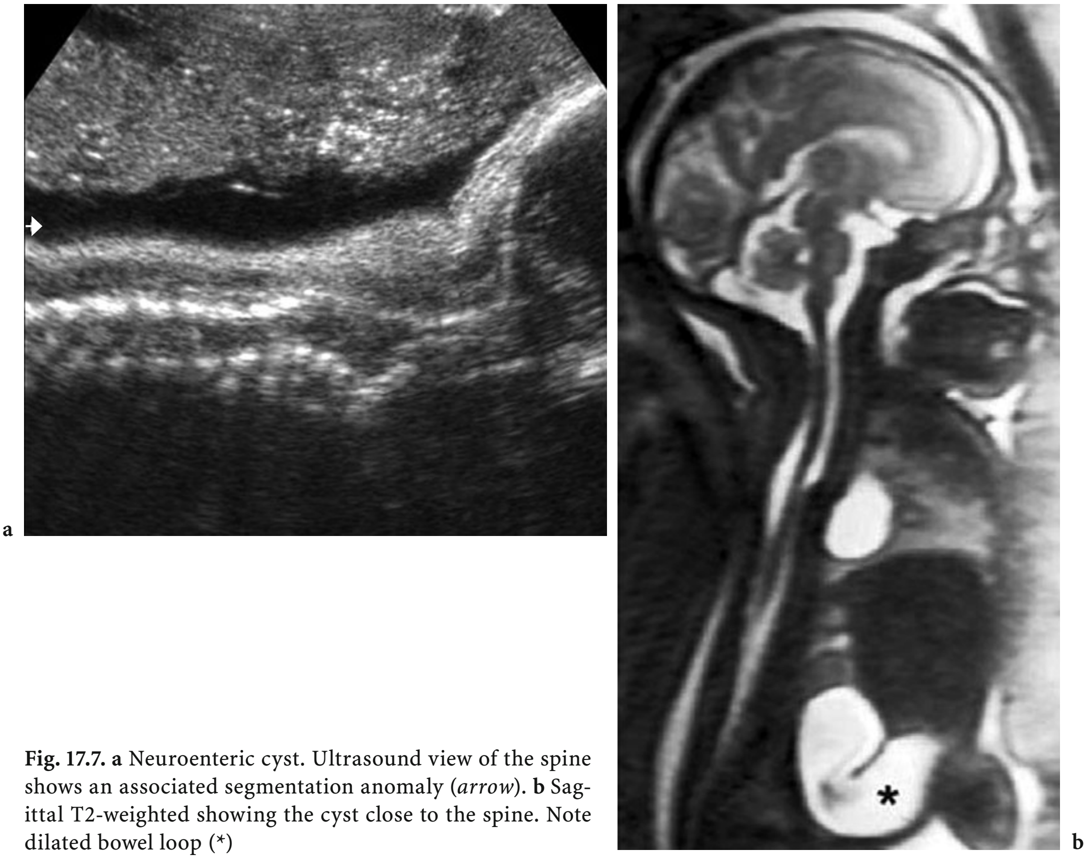

Fig. 17.7. a Neuroenteric cyst. Ultrasound view of the spine shows an associated segmentation anomaly (*arrow*). **b** Sagittal T2-weighted showing the cyst close to the spine. Note dilated bowel loop (*)

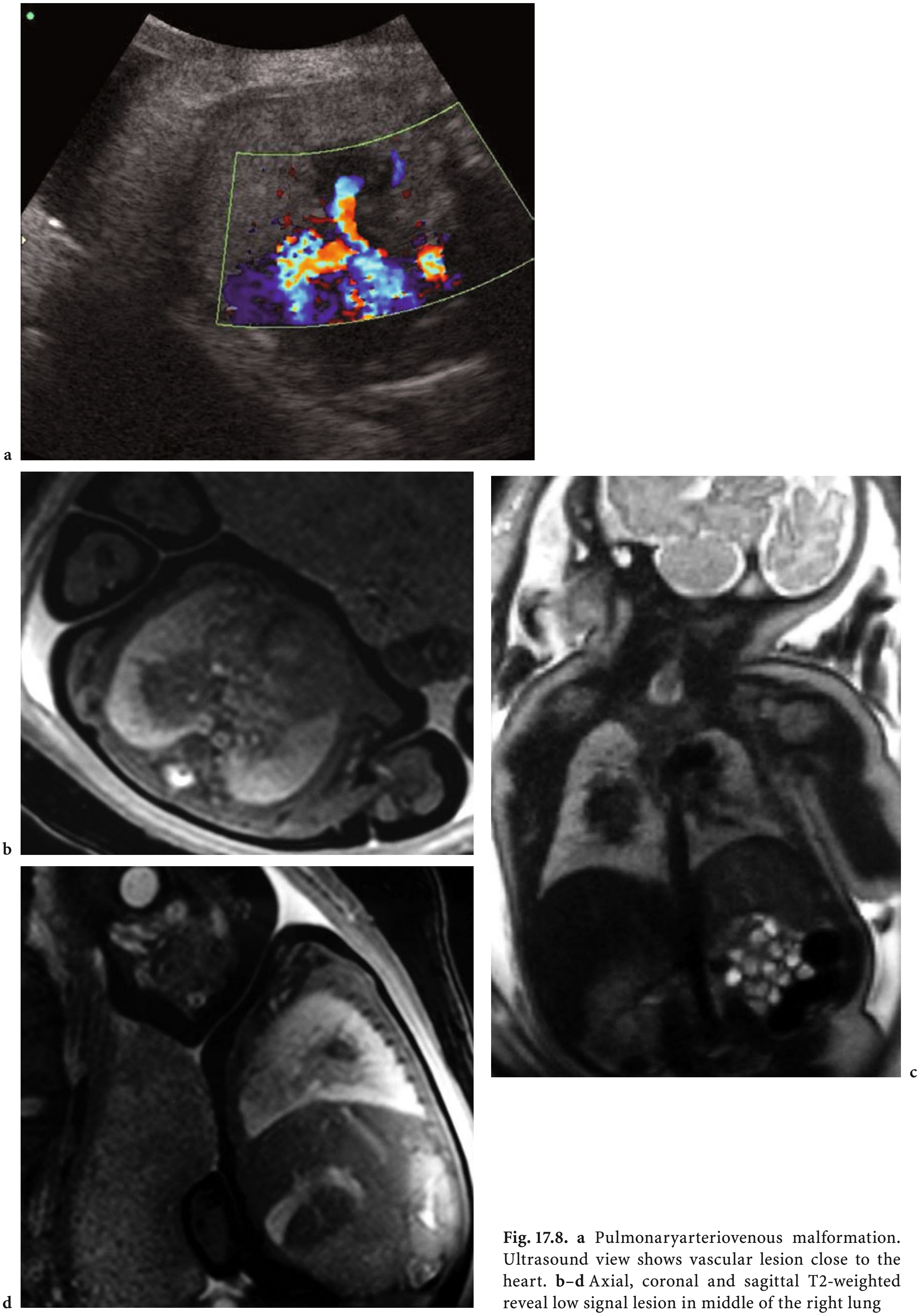

Fig. 17.8. **a** Pulmonaryarteriovenous malformation. Ultrasound view shows vascular lesion close to the heart. **b–d** Axial, coronal and sagittal T2-weighted reveal low signal lesion in middle of the right lung

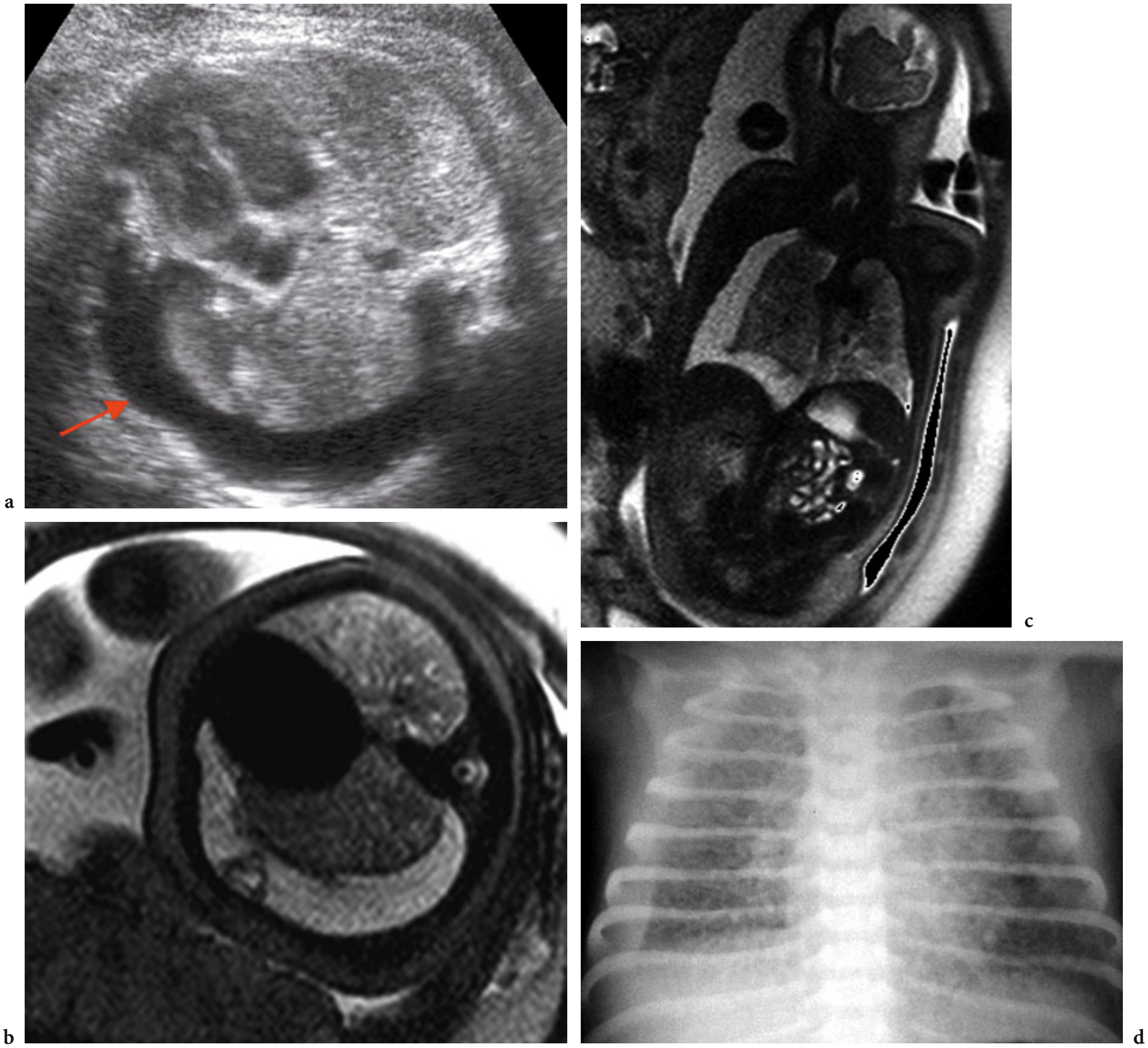

Fig. 17.9. a Congenital pulmonary lymphangiectasia. Ultrasound view shows right hydrothorax (*arrow*). **b,c** Axial and coronal T2-weighted demonstrate right hydrothorax compressing the homolateral lung. Note the low signal intensity of the both lungs. **d** Conventional X-ray some hours after delivery reveals diffuse reticular infiltrate and right pleural effusion

17.5 Hydrothorax

Hydrothorax is the accumulation of fluid in the pleural space, and can be primary or secondary in origin. Most hydrothoraces are primary, with chylothorax being the most common. The chylothorax occurs because of an abnormality in the formation of the thoracic lymphatic ducts, with resultant abnormal drainage. It is usually unilateral, occurring more frequently on the right side. In patients with secondary pleural effusions, the most common causes are chromosomal abnormalities (Down or Turner syndromes) or infectious diseases (cytomegalovirus, toxoplasmosis). Hydrothorax may also be seen in cases of fetal hydrops.

The diagnosis of hydrothorax can be made with US, which can also help to guide treatment, including drainages and shunts (Fig. 17.10).

17.6 Congenital Diaphragmatic Hernia

CDH is defined as a partial or complete lack of development of the diaphragm, allowing the migration of abdominal structures into the thorax; these structures can compress the lungs and affect their development (Paek et al. 2001; Kays 2006). The CDH can be divided into two forms: an early form, in which the abdominal organs develop inside the thorax, and a late form, which is associated with secondary migration of the abdominal organs to the thorax.

The most common type of CDH occurs through the Bochdalek foramina, and occurs more frequently on the left side. US can suggest this diagnosis between the second and third trimesters, demonstrating the stomach and small bowel loops in the left hemi-thorax, and the heart deviated to the right side (Fig. 17.11).

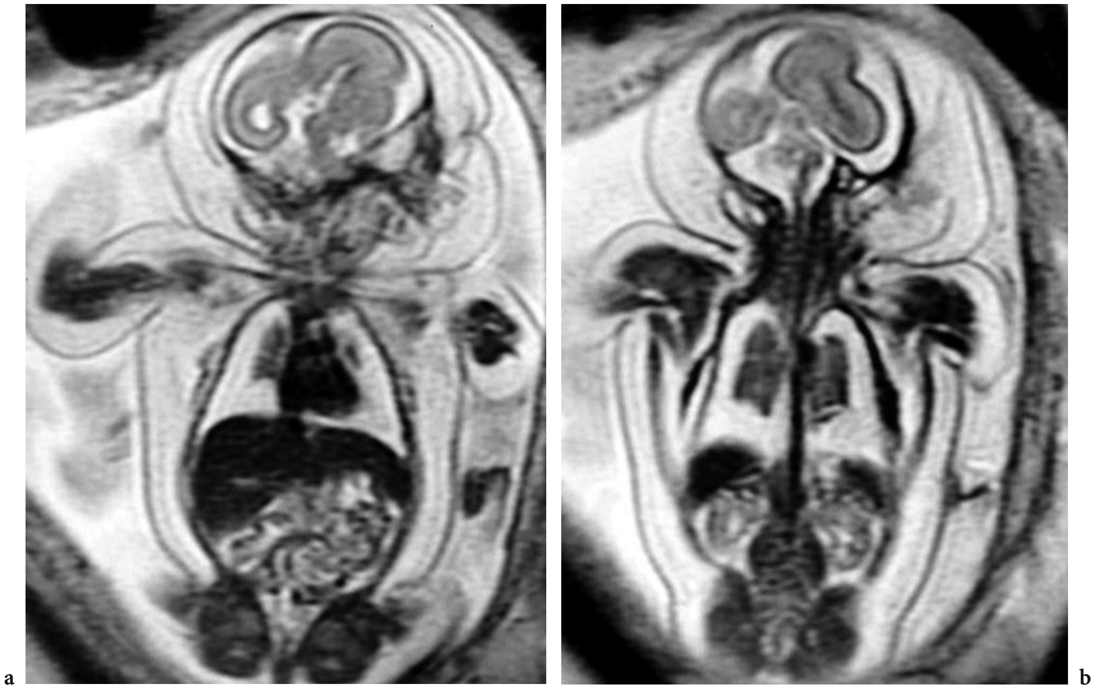

Fig. 17.10a,b. Coronal T2-weighted image of the fetus (26 weeks) shows a big bilateral hydrothorax. Note also the cutaneous edema and small lungs

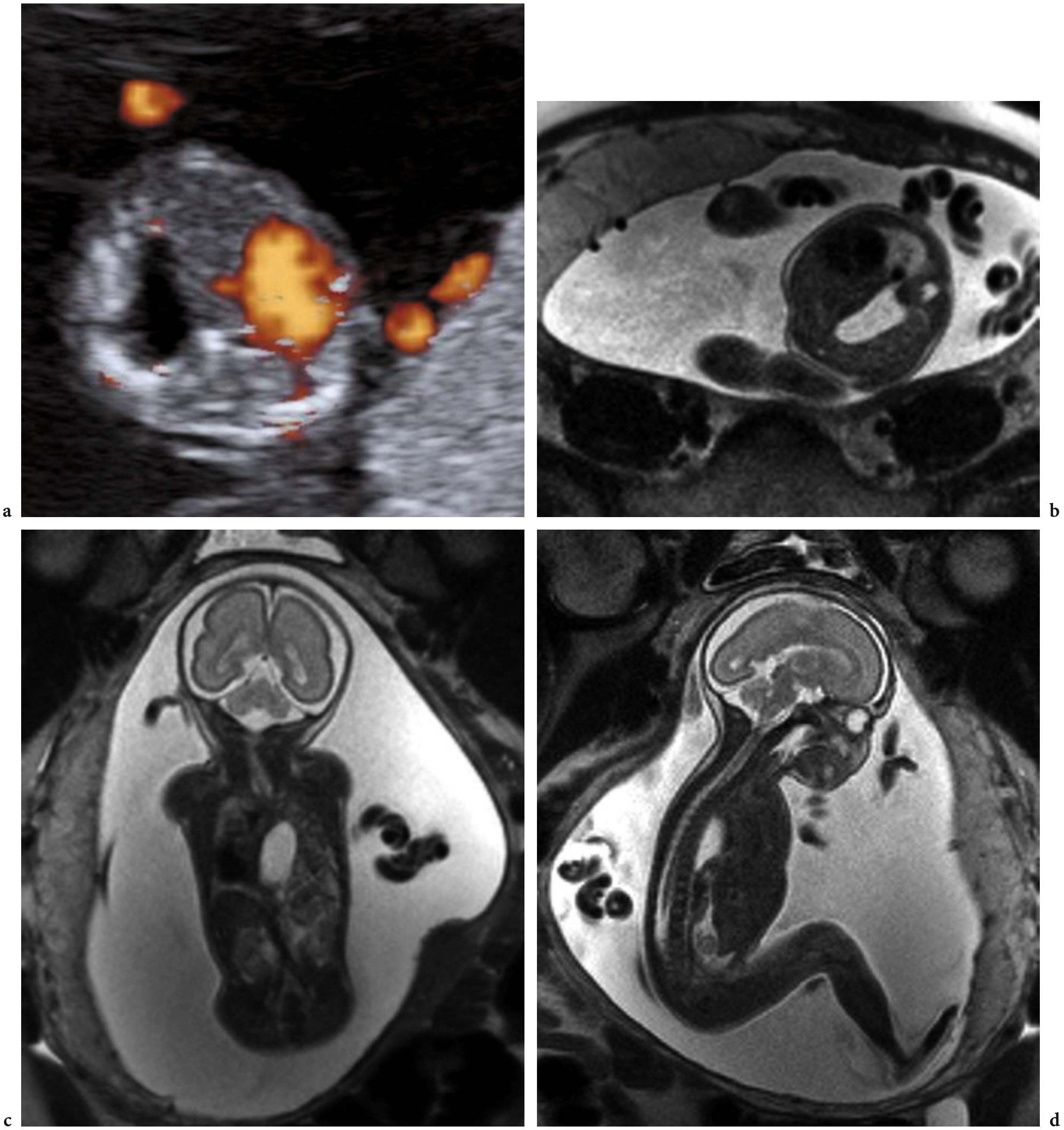

Fig. 17.11. a Ultrasound (axial view, 14 weeks) shows the typical image of the left diaphragmatic hernia. Note the heart placed to the right side and the stomach in the same plane. **b** Axial view on T2-weighted shows the liver-up placed anterior to the stomach and the heart placed to the right side. **c** Coronal view on T2-weighted shows stomach and multiple bowel loops in the left hemithorax. Note the heart displaced to the right. **d** Sagittal T2-weighted shows the liver-up and the stomach in the chest

Around 12% of the cases of CDH occur on the right. In most of these cases the liver is seen in the right hemi-thorax, compressing the heart in the left hemi-thorax. The migration of small bowel loops into the right hemi-thorax is uncommon (Okazaki et al. 2003; Bedoyan et al. 2004; Hedrick et al. 2004) (Fig. 17.12).

Even after recent improvements in diagnosis and treatment of CDH, the mortality remains around 58% (Harrison et al. 1994; Paulson et al. 1995). Both the gestational age at which the CDH develops and the organs which have migrated affect the prognosis. In cases of late CDH (> 25 weeks), the prognosis is better because lung development is less affected. On the other hand, CDHs that occur earlier (< 25 weeks) are usually associated with severe lung abnormalities, and have a worse prognosis (Leung et al. 2000; Kays 2006).

The pathogenesis of pulmonary hypoplasia is poorly understood. Fetal lung fluid plays an important role in normal lung development. Kuwashima et al. (2001) found a close relationship between fetal lung intensity on MRI and pulmonary growth. Low intensity of the fetal lung suggested the presence of pulmonary hypoplasia, whereas high intensity was consistent with normal pulmonary development.

Several studies have demonstrated the potential use of 3D US and MRI in measuring the lung volumes. These techniques access three orthogonal planes to allow an accurate determination of organ volume (Mahieu-Caputo et al. 2001; Ruano et al. 2004; Peralta et al. 2005). To obtain the lung volume by MRI, the cross-sectional area of the lung is measured on each transverse section. To calculate the volume for each section, the value of the cross-sectional area is multiplied by the section thickness and intersection gap combined. The volumes of all of the sections are then added to obtain the volume of the entire lung. The calculation is repeated for the contralateral lung, and then the volumes of both lungs are added to obtain the total lung volume (Figs. 17.13–17.15).

Another way to evaluate for pulmonary hypoplasia is to calculate the lung-head ratio (LHR). It can be obtained by US multiplying the orthogonal diameters of the right lung at the level of the four heart chambers at 24–26 weeks gestational age, and dividing by the head circumference (in millimeters). A LHR of less than 1.0 is associated with mortality of approximately 100%. Conversely, a LHR of more than 1.4 is associated with a good prognosis. The mortality rate seen in patients with LHR between

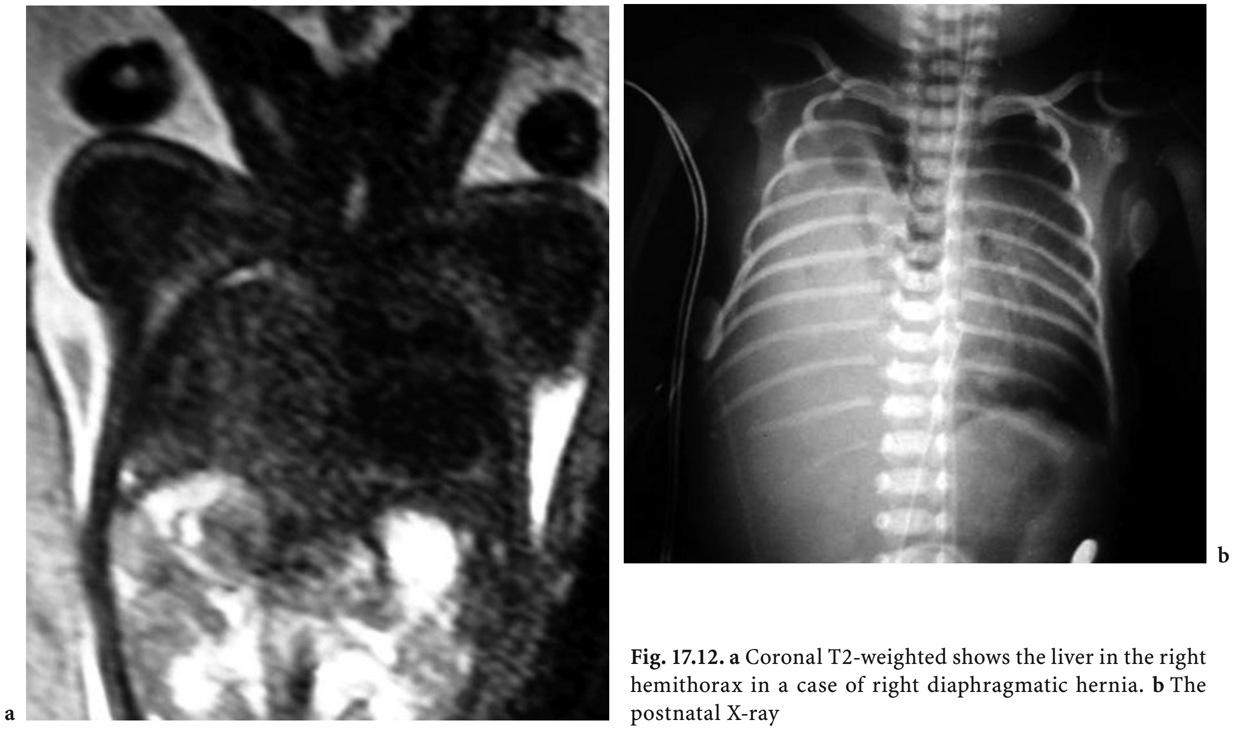

Fig. 17.12. **a** Coronal T2-weighted shows the liver in the right hemithorax in a case of right diaphragmatic hernia. **b** The postnatal X-ray

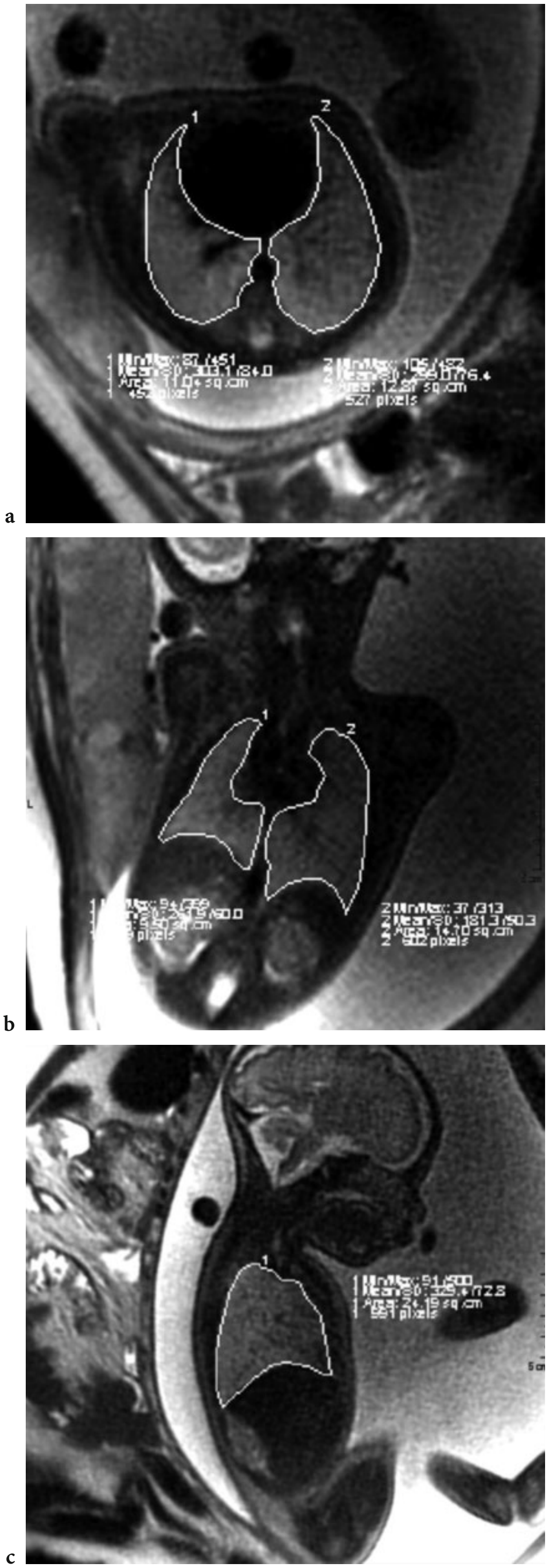

Fig. 17.13a–c. Normal lung volume (axial, coronal and sagittal) measured by MRI at 32 weeks

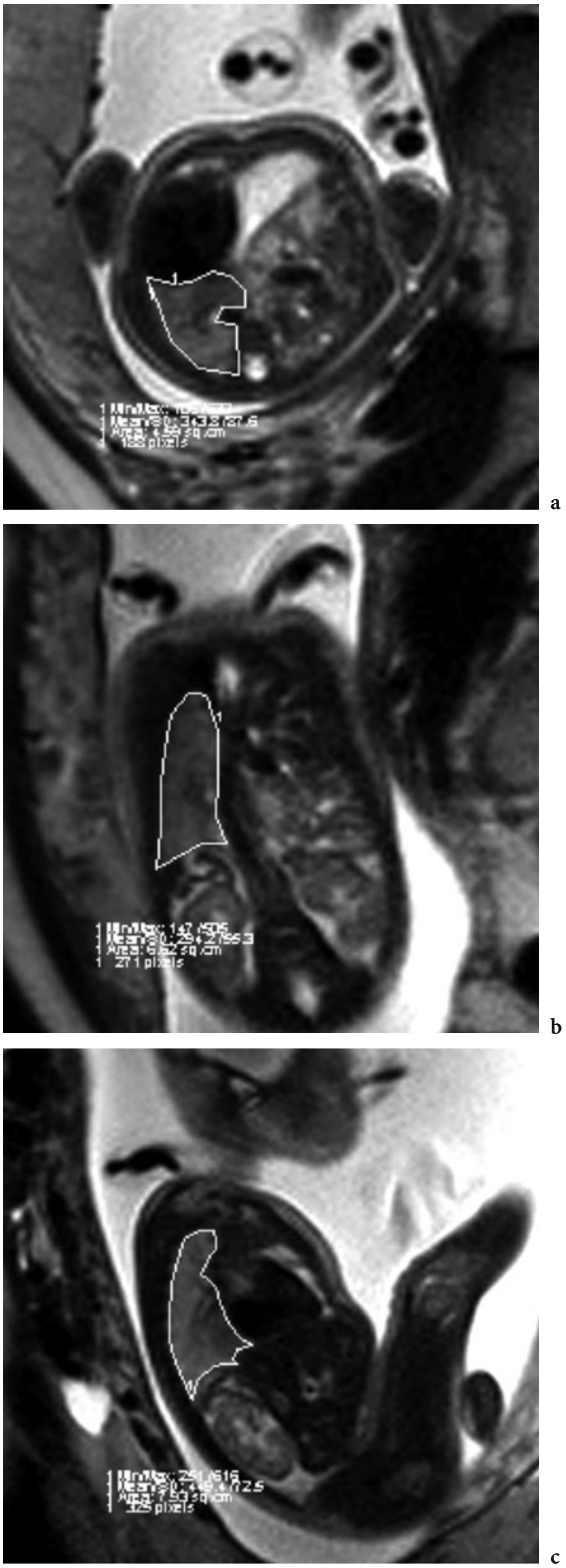

Fig. 17.14a–c. Lung volume measured in axial, coronal and sagittal in a case of left diaphragmatic hernia with liver down (28 weeks)

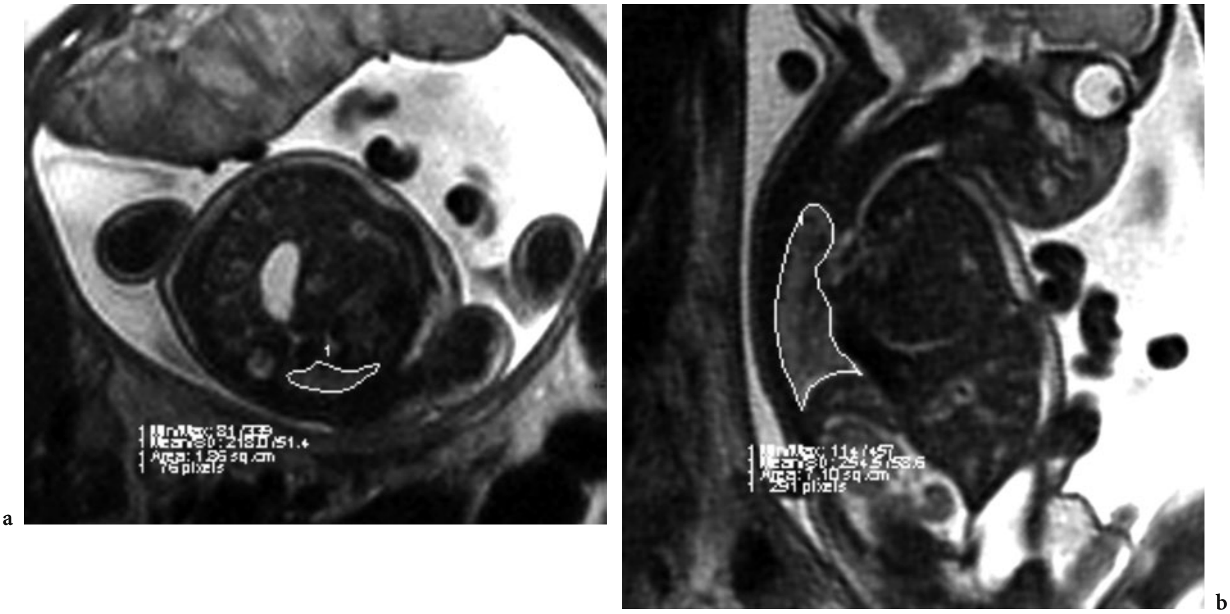

Fig. 17.15a,b. Lung volume measured in axial and sagittal in a case of left diaphragmatic hernia with liver up (28 weeks)

1.0 and 1.4 is around 60% (Metkus et al. 1996; Jani et al. 2006).

The most important factors for determining prognosis in patients with pulmonary hypoplasia are early diagnosis, the presence of associated malformations, chromosomal anomalies, migration of the liver to the thorax and the LHR (Albanese et al. 1998).

Many efforts have been made to improve survival of infants born with CDH. The first intra-uterine surgery for CDH was performed by Harrison in 1990. However, due to poor outcome, the technique was abandoned. Subsequently, tracheal occlusion was developed as a promising new treatment option aimed at increasing lung volumes for the intra-uterine treatment of CDH in patients with poor prognosis. Although some authors have demonstrated good results with this technique, further studies have to be conducted to clarify the advantages of the intra-uterine management of CDH. (Deprest et al 2006a,b). Postnatal management with surfactants and extra corporeal membrane oxygenation are also improving prognosis for these patients.

17.7
Congenital Laryngeal Atresia

Congenital laryngeal atresia is a rare anomaly, with only 12 cases of prenatal diagnosis in the literature. In cases of upper airway stenosis, US demonstrates bilateral and homogeneous hyperechogenicity of the lungs, which have increased volume. In addition, the diaphragm cupules are inverted and inferiorly deviated. Most of the patients develop ascites and anasarca, probably related to abnormal venous return (right heart failure). The amniotic fluid volume may be normal, increased or reduced. Oligohydramnios may be related to lack of pulmonary drainage, and polyhydramnios to esophageal compression by the lungs (Kassanos et al. 1977). The increased lung volumes seen in patients with congenital laryngeal atresia are demonstrated on MRI as marked high signal of the lung parenchyma on T2-weighted images. In addition, the heart is centered in the thorax and the diaphragmatic cupules are inverted (Fig. 17.16).

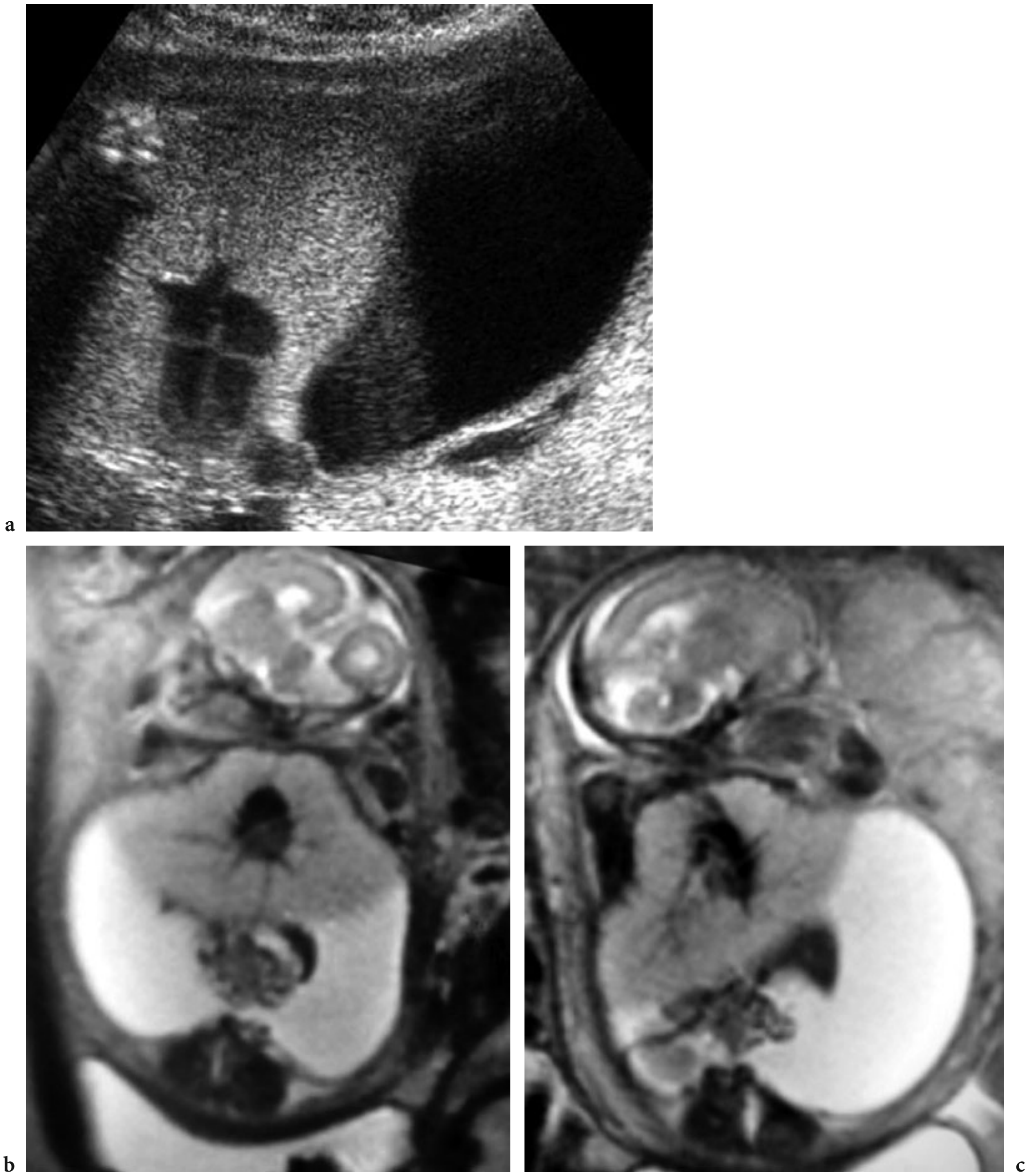

Fig. 17.16. **a** Congenital laryngeal astresia. Ultrasound of the fetal thorax (27 weeks) demonstrates the echogenic lung and inverted diaphragms. Note four chamber view of the heart and ascites. **b,c** Coronal oblique T2-weighted of the fetal thorax (28 weeks) shows the augmentation of the lungs and inverted diaphragmatic couple. Note the ascites

17.8
Cardiac Malformations

MRI is less useful than US for the diagnosis of cardiac malformations (Hata et al. 1995). The lack of gating for the heartbeats results in images with significant motion artifacts. However, although the anatomy and the function of the heart are not well studied with MRI, the size and position of the heart should always be evaluated.

The most common cardiac tumors in the fetal age are rhabdomyomas and teratomas. Rhabdomyomas are usually small intra-cardiac tumors. Although they are well seen with MRI, MRI is more useful for evaluating the associated brain lesions in patients with rhabdomyomas and tuberous sclerosis (Werner et al. 1994). Teratomas are a common fetal neoplasm; around 10% of them occur in the thorax and abdomen. Most of the thoracic teratomas involve the pericardium and mediastinum. The identification of calcification in teratomas helps the differential diagnosis with CCAM and extra-lobar pulmonary sequestration (Woodward et al. 2005). (Fig. 17.17).

17.9
Hemangiomas

Hemangiomas are benign tumors of blood vessels. They are classified as: cavernous, capillary (strawberry) or mixed. The cavernous hemangiomas are masses of dilated vessels located deep in the skin, containing large blood-filled spaces. They appear as pale, skin-colored, red or blue masses. These lesions can cause hydrops during the prenatal period. Strawberry hemangiomas are bright red protuberant masses that may occur in any area of the body, especially the face, scalp, back and chest. They vary in size from pinhead to several centimeters in diameter, and may be flat or slightly raised (Dubois et al. 1998) (Fig. 17.18).

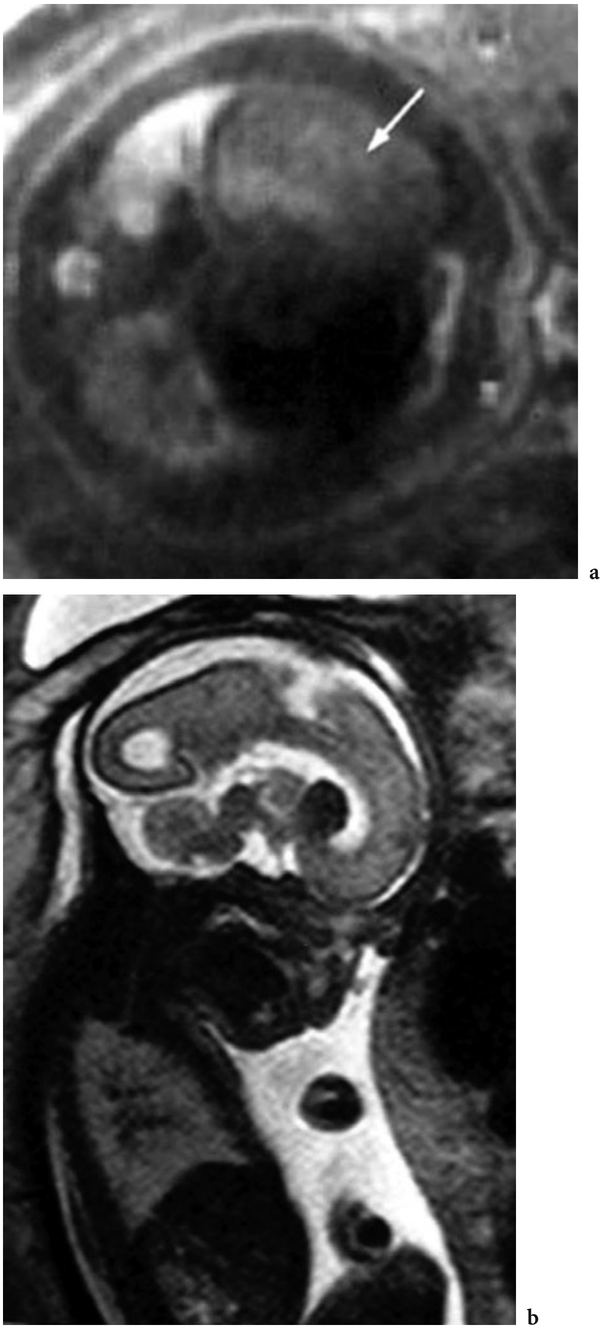

Fig. 17.17. **a** Axial T2-weighted view of the fetal thorax shows a cardiac rhabdomyoma. **b** Sagittal T2-weighted view of the fetal head shows a typical subependymal nodule in a case of tuberous sclerosis

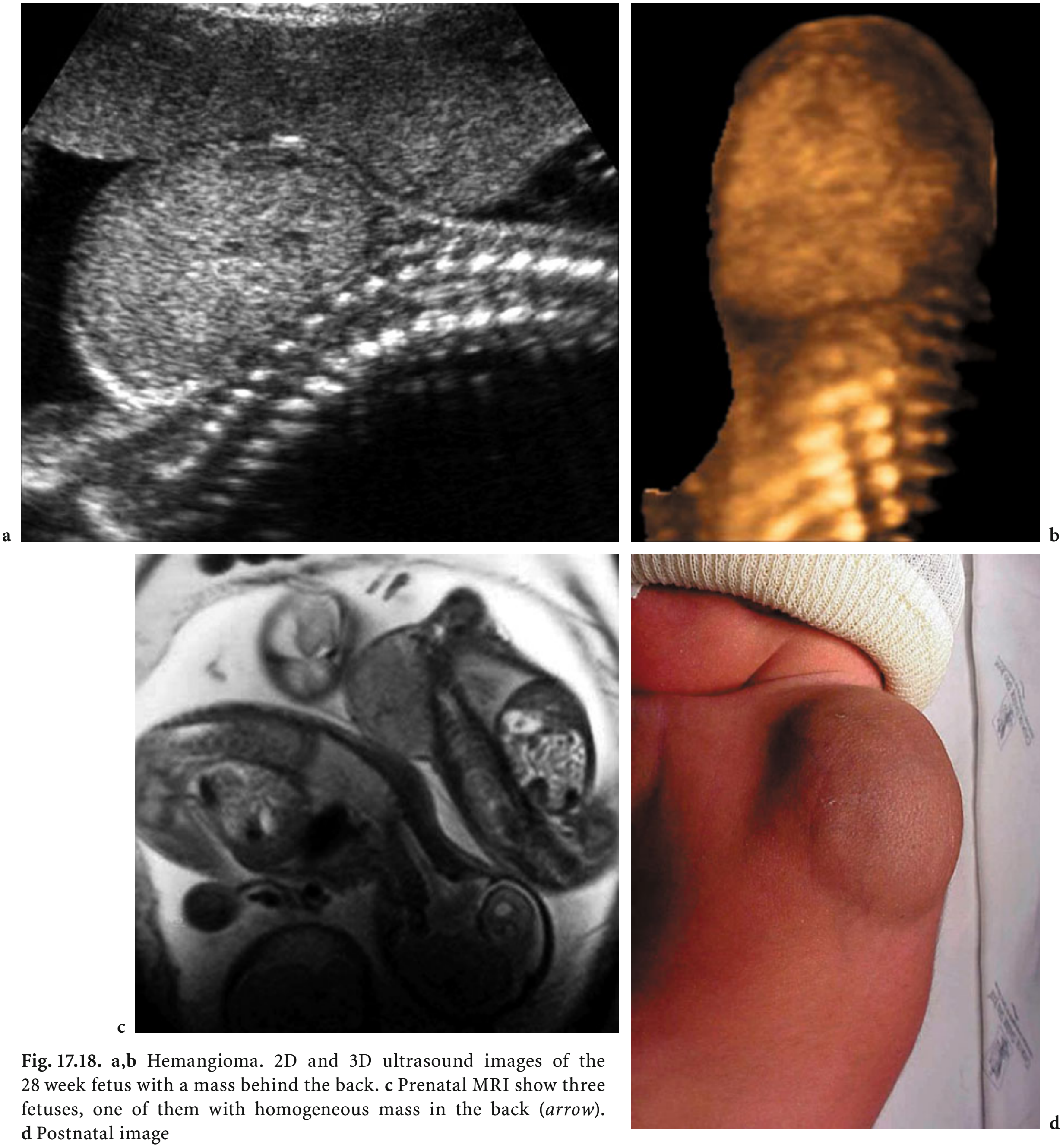

Fig. 17.18. a,b Hemangioma. 2D and 3D ultrasound images of the 28 week fetus with a mass behind the back. **c** Prenatal MRI show three fetuses, one of them with homogeneous mass in the back (*arrow*). **d** Postnatal image

17.10
Conclusions

The extraordinary advances in fetal MRI in recent years have occurred more quickly than with any other imaging technique. MRI provides images of the fetus that are easier to visualize and understand than US images, both for physicians and parents.

Prenatal diagnosis of congenital thoracic lesions can be critical; these lesions can range from small and asymptomatic to large space occupying lesions that require immediate surgical treatment. Currently, the diagnosis of chest abnormalities is made more frequently with US. However, MRI is an important adjunct in the evaluation of fetal chest pathologies. The increased knowledge gained from MR imaging of these pathologies allows more objective prenatal counseling and more efficient treatment during the post-natal period. The indication and timing of surgical or conservative treatments are now better defined based on the advances of the imaging tools.

Far from being a static imaging technique, MRI has been and will continue to be constantly advancing as an imaging alternative for the investigation of fetal chest pathologies.

References

Adzick NS, Harrison MR, Glick PL (1985) Fetal cystic adenomatoid malformation: prenatal diagnosis and natural history. J Pediatr Surg 20:483–488

Albanese CT, Lopoo J, Goldstein RB (1998) Fetal liver position and perinatal outcome for congenital diaphragmatic hernia. Prenat Diagn 18:1138–1142

Bedoyan JK, Blackwell SC, Treadwell MC, Johnson A, Klein MD (2004) Congenital diaphragmatic hernia: associated anomalies and antenatal diagnosis. Pediatr Surg Int 20:170–176

Coakley FV, Glenn OA, Qayyum A, Barkovich AJ, Goldstein R, Filly RA (2004) Fetal MRI: a developing technique for the developing patient. AJR Am J Roentgenol 182:243–252

Daltro P, Fricke BL, Kuroki I, Domingues R, Donnelly LF (2004) CT of congenital lung lesions in pediatric patients. AJR Am J Roentgenol 183:1479–1506

Deprest J, Jani J, Van Schoubroeck et al. (2006a) Current consequences of prenatal diagnosis of congenital diaphragmatic hernia. J Pediatr Surg 41:423–430

Deprest J, Jani J, Cannie M et al. (2006b) Prenatal intervention for isolated congenital diaphragmatic hernia. Curr Opin Obstet Gynecol 18:203–215

Dubois J, Patriquin HB, Garel L, Powell J, Filiatrault D, David M, Grignon A (1998) Soft-tissue hemangiomas in infants and children: diagnosis using Doppler sonography. AJR Am J Roentgenol 171(1):247–252

Faul JL, Berry GJ, Colby TV et al. (2000) Thoracic lymphangioma, lymphagiectasis, lymphangiomatosis, and lymphatic dysplasia syndrome. Am J Respir Crit Care Med 161:1037–1046

Guo Y, Luo B (2006) The state of the art of fetal magnetic resonance imaging. Chin Med J 119(15):1294–1299

Hansell DM, Armstrong P, Lynch DA, McAdams HP (2005) Congenital anomalies. In: Imaging of the diseases of the chest, 4th edn. Elsevier Mosby

Harrison MR, Adzick NS, Estes JM, Howell LJ (1994) A prospective study of the outcome for fetuses with diaphragmatic hernia. JAMA 271:382–384

Hata K, Hata T, Manabe A (1995) Hypoplastic left heart syndrome: color Doppler sonographic and magnetic resonance imaging features in utero. Gynecol Obstet Invest 39:70–72

Hedrick HL, Crombleholme TM, Flake AW et al. (2004) Right congenital diaphragmatic hernia: prenatal assessment and outcome. J Pediatr Surg 39(3):319–323

Hubbard AM, Adzick NS, Crombleholme TM et al. (1999) Congenital chest lesions: diagnosis and characterization with prenatal MR imaging. Radiology 212:48–49

Jani J, Peralta CF, Van Schoubroeck D et al. (2006) Relationship between lung-to-head ratio and lung volume in normal fetuses and fetuses with diaphragmatic hernia. Ultrasound Obstet Gynecol 27:545–550

Kasprian G, Balassy C, Brugger P, Prayer D (2006) MRI of normal and pathological fetal lung development. Eur Radiol 57:261–270

Kassanos D, Christodoulou CV, Agapitos E et al. (1997) Prenatal ultrasonographic detection of the tracheal atresia sequence. Ultrasound Obstet Gynecol 10:133–136

Kays DW (2006) Congenital diaphragmatic hérnia and neonatal lung lesions. Surg Clin North Am 86:329–352

Kuwashima S, Nishimura G, Iimura F et al. (2001) Low-intensity fetal lungs on MRI may suggest the diagnosis of pulmonary hypoplasia. Pediatr Radiol 31:669–672

Leung JWT, Coackley FV, Hricak H et al. (2000) Prenatal MR Imaging of congenital diaphragmatic hérnia. Am Roentgen 174:1607–1612

Levine D, Banewolt CE, Mehta TS et al. (2003) Fetal thoracic abnormalities: MR imaging. Radiology 228:379–388

Mahieu-Caputo D, Sonigo P, Dommergues M et al. (2001) Fetal lung volume measurement by magnetic resonance imaging in congenital diaphragmatic hernia. BJOG 108:863–868

Matsuoka S, Takeuchi K, Yamanaka Y et al. (2003) Comparison of magnetic resonance imaging and ultrasonography in the prenatal diagnosis of congenital thoracic abnormalities. Fetal Diagn Ther 18:447–453

Metkus AP, Filly RA, Stringer MD et al. (1996) Sonographic predictors of survival in fetal diaphragmatic hernia. J Pediatr Surg 31:148–151

Newman B (2006) Congenital bronchopulmonary foregut malformations: concepts and controversies. Pediatr Radiol 36:773–791

Okazaki T, Kohno S, Hasegawa S et al. (2003) Congenital diaphragmatic hernia: efficacy of ultrasound examination in its management. Pediatr Surg Int 19:176–179

Paek BW, Coakley FV, Yiung Lu et al. (2001) Congenital diaphragmatic hernia: prenatal evaluation with MR lung volumetry – preliminary experience. Radiology 220:63–67

Paulson TE, Spear RM, Peterson BM (1995) New concepts in the treatment of children with acute respiratory distress syndrome. J Pediatr 127:163–175

Peralta CF, Cavoretto P, Csapo B et al. (2005) Assessment of lung area in normal fetuses at 12–32 weeks. Ultrasound Obstet Gynecol 26:718–724

Ruano R, Joubin L, Sonigo P et al. (2004) Fetal lung volume estimated by 3-dimensional ultrasonography and magnetic resonance imaging in cases with isolated congenital diaphragmatic hernia. J Ultrasound Med 23:353–358

Shellock FG, Kanal E (1991) Policies, guidelines, and recommendations for MR imaging safety and patient management. SMRI Safety Committee. J Magn Reson Imaging 1:97–101

Shinmoto H, Kashima K, Yuasa Y et al. (2000) MR imaging of non-CNS fetal abnormalities: a pictorial essay. RadioGraphics 20(5):1227–1243

Stocker JT, Madewell JE, Drake RM (1977) Congenital cystic adenomatoid malformation: prenatal diagnosis and natural history. J Pediatr Surg 8:155–158

Werner H, Mirlesse V, Jacquemard F et al. (1994) Prenatal diagnosis of tuberous sclerosis. Use of magnetic resonance imaging and its implications for prognosis. Prenatal Diagn 14:1151–1154

Woodward PF, Sohaey R, Kennedy A et al. (2005) A comprehensive review of fetal tumors with pathologic correlation. RadioGraphics 25:215–242

Neonatal Chest Imaging

18

Janet L. Strife and Eric J. Crotty

CONTENTS

18.1 **Introduction** *417*

18.2 **Technique** *418*

18.3 **Systematic Approach** *418*
18.3.1 Lines, Tubes, and Catheters *418*
18.3.2 Thymus *422*

18.4 **Air Leak Phenomena** *423*
18.4.1 Pulmonary Interstitial Emphysema *423*
18.4.1.1 Etiology *423*
18.4.1.2 Imaging Findings *423*
18.4.1.3 Treatment *424*
18.4.2 Pneumothorax *424*
18.4.2.1 Etiology *424*
18.4.2.2 Imaging Findings *424*
18.4.2.3 Treatment *425*
18.4.3 Pneumomediastinum *425*
18.4.3.1 Etiology *425*
18.4.3.2 Imaging Findings *425*
18.4.3.3 Treatment *425*
18.4.4 Pneumopericardium *425*

18.5 **Medical Disease** *426*
18.5.1 Pulmonary Disease of the Premature Infant *426*
18.5.1.1 Etiology *426*
18.5.1.2 Imaging Findings *427*
18.5.1.3 Patent Ductus Arteriosus *428*
18.5.2 Chronic Lung Disease of Infancy: Bronchopulmonary Dysplasia *429*
18.5.2.1 Etiology *429*
18.5.2.2 Imaging Findings *429*
18.5.3 Meconium Aspiration Pneumonia *433*
18.5.3.1 Etiology *433*
18.5.3.2 Imaging Findings *434*
18.5.3.3 Treatment *434*
18.5.4 Transient Tachypnea *434*
18.5.4.1 Etiology *434*
18.5.4.2 Imaging Findings *435*
18.5.4.3 Treatment *435*
18.5.5 Neonatal Pneumonia *435*
18.5.5.1 Etiology *435*
18.5.5.2 Imaging Findings *436*
18.5.6 Pulmonary Lymphangiectasia *436*
18.5.6.1 Etiology *436*
18.5.6.2 Imaging Findings *437*
18.5.7 Congenital Heart Disease *437*
18.5.7.1 Etiology *437*
18.5.7.2 Imaging Findings *438*

18.6 **Summary** *439*

References *439*

18.1
Introduction

Throughout the world, the chest radiograph is the most common imaging study done in the neonate. The neonatal chest radiograph is not particularly difficult to interpret as most images fall into predictable patterns of diseases. The purpose of this chapter is to provide a systematic approach to the infant chest, update knowledge concerning neonatal chest diseases and discuss current treatment options. Broadly, the infant chest abnormalities can be divided into medical or surgical diseases of the chest. In previous years, significant attention was given to the imaging findings of the surgical diseases of the neonatal chest; however with the increasing use of fetal imaging with magnetic resonance and/or fetal sonography, these lesions are frequently recognized antenatally. Characteristically,

---

J. L. Strife, MD, FACR
Professor of Radiology and Pediatrics, University of Cincinnati College of Medicine, Cincinnati Children's Hospital Medical Center, 3333 Burnet Avenue, Cincinnati, OH 45229, USA
E. J. Crotty, MD
Assistant Professor of Radiology and Pediatrics, University of Cincinnati College of Medicine, Cincinnati Children's Hospital Medical Center, 3333 Burnet Avenue, Cincinnati, OH 45229, USA

many of the radiographs in newborns with surgical diseases have masses with striking asymmetry of density, shift of the mediastinum, focal opacification, and/or cystic or hyperlucent lung segments. These findings in a neonate are usually suggestive of a short list of surgical conditions. Other chapters in this book will specifically discuss the imaging characteristics of the common surgical conditions; the common medical conditions will be described here (Table 18.1).

18.2
Technique

Technically, obtaining consistent quality imaging of infants can be challenging and occasionally problematic; however with digital imaging, there is a lot more latitude. Infant chest radiographs are usually obtained portably, anterior-posterior, and supine. Proper centering is difficult because the infants are small and recumbent. One helpful hint is that the image should be centered midline at the level of the mid to lower aspect of the scapula. This is important as it optimizes imaging of the chest but also reduces scatter radiation in the abdomen. Lastly, radiation dose is always an issue in infants and optimizing radiation dose while providing adequate information is part of good practice (Duetting et al. 1999).

18.3
Systematic Approach

There are a variety of causes of neonatal respiratory distress for which chest radiography is requested; a systematic approach to the chest radiograph is essential to correctly identify relevant pathology. A systematic approach to the newborn chest radiograph is similar to the approach to the adult chest radiograph, but the diseases are very different. Through the systematic approach, the lungs, trachea, heart size, position of the aortic arch, thymus, bones, soft tissues, upper abdomen, and lines and tubes should all be evaluated. In the newborn, major causes of respiratory distress may also be located outside of the chest, such as intracranial hemorrhage, necrotizing enterocolitis or sepsis.

Mild rotation of a term baby on a chest radiograph can create a hyperlucent lung that simulates a pneumothorax. Skin folds are common artifacts and may also be mistaken for pneumothoraces (Fig. 18.1). With the increasing use of PACS (picture archival communication system) imaging, the ability to window and follow the vertical line outside the chest is useful in differentiating a pneumothorax from a skin fold. Finding excessive soft tissues as in anasarca may suggest a specific diagnosis; there is also a well known association between maternal diabetes and macrosomia. The proximal humeral epiphysis is an indicator of infant maturity and is present in 80% of term infants. The bony thorax should be evaluated for vertebral or skeletal anomalies which may be the cause of respiratory distress (thantophnoaric dwarfism) or which may contribute to the evaluation of any associated abnormalities. VACTERL (vertebral anomalies, anal atresia, cardiac anomalies, tracheo-esophageal fistula, and renal and limb anomalies) association may have many abnormalities suggested on chest radiograph including dilatation of the esophagus, absent air in the abdomen, and vertebral anomalies (Fig. 18.2).

As the chest radiograph is the most frequently ordered imaging study in newborns, evaluation of the upper abdomen, specifically looking for evidence of free air or portal venous gas, is relevant as early identification of infants with necrotizing enterocolitis is critical for the timely initiation of treatment. Free air can be recognized by seeing a convex superior lucency in the upper abdomen or the falciform ligament outlined by air (Fig. 18.3). Malposition of the stomach, heart or liver in the abdominal heterotaxy syndromes identifies infants with possible asplenia (bilateral right sided isomerism) or polysplenia (bilateral left sidedness) and the strong association with congenital heart disease and venous anomalies (Fig. 18.4).

18.3.1
Lines, Tubes, and Catheters

Evaluation of the lines, catheters and monitoring support devices is an important role of the pediatric radiologist. In children who are intubated, the best way to assess the position of the endotracheal tube is to find the tracheal bifurcation and then identify the position of the tip of the endotracheal tube relative to the carina (Fig. 18.5). A low position of the endotracheal tube can quickly cause collapse of the

Table 18.1. Approach to medical disease in the newborn chest

Approach to Medical Disease in the Newborn Chest

Premature
(surfactant deficiency)
Hyaline membrane disease
Patent ductus arteriosus
Bronchopulmonary dysphasia

Term Infant
Meconium aspiration
Transient tachypnea
Pneumonia (rare)
Heart disease
Congenital
Acquired

Tube and line placement
Pneumothorax/pneumonediastinum
Pneumoperitoneum
Pulmonary interstitial emphysema

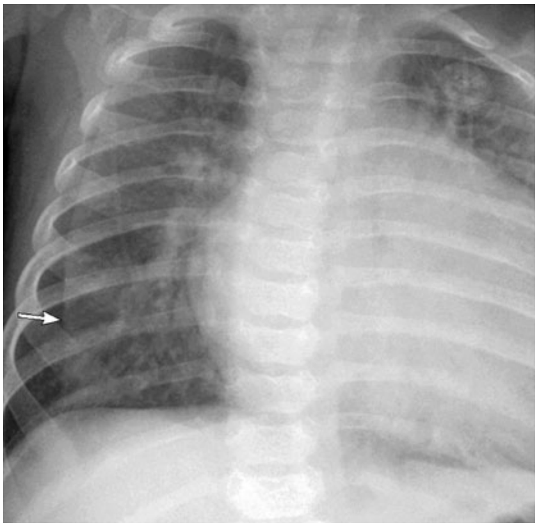

Fig. 18.1. Skin fold (*arrow*) that could be mistaken for a pneumothorax, but note lung markings are visible beyond the skin fold

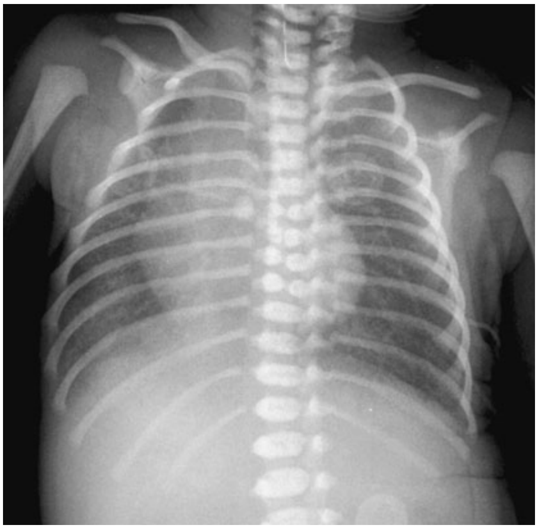

Fig. 18.2. Esophageal atresia with vertebral anomalies and absence of abdominal air. Feeding tube is proximal to the esophageal atresia. The vertebral anomalies are part of the spectrum of VACTERL association

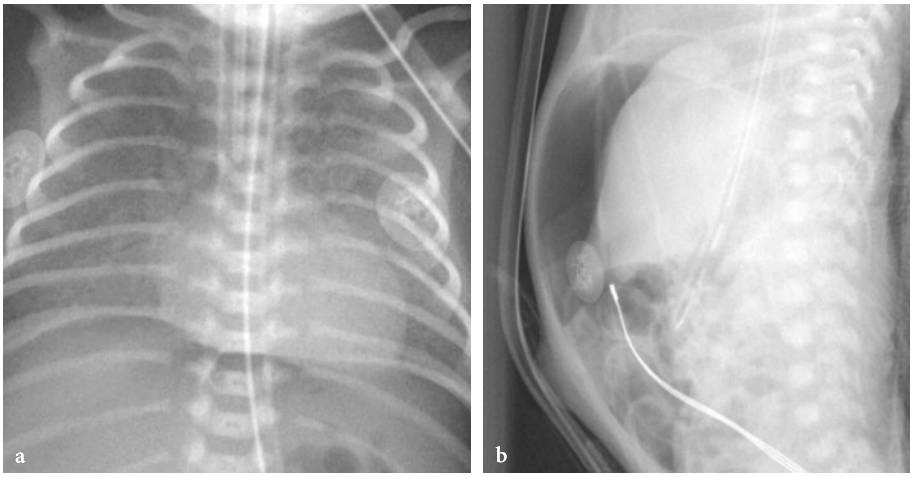

Fig. 18.3a,b. Free intra-abdominal air. **a** Note the hyperlucency of the upper abdomen. **b** Cross table lateral confirming large amount of free air. This was secondary to perforation related to necrotizing enterocolitis

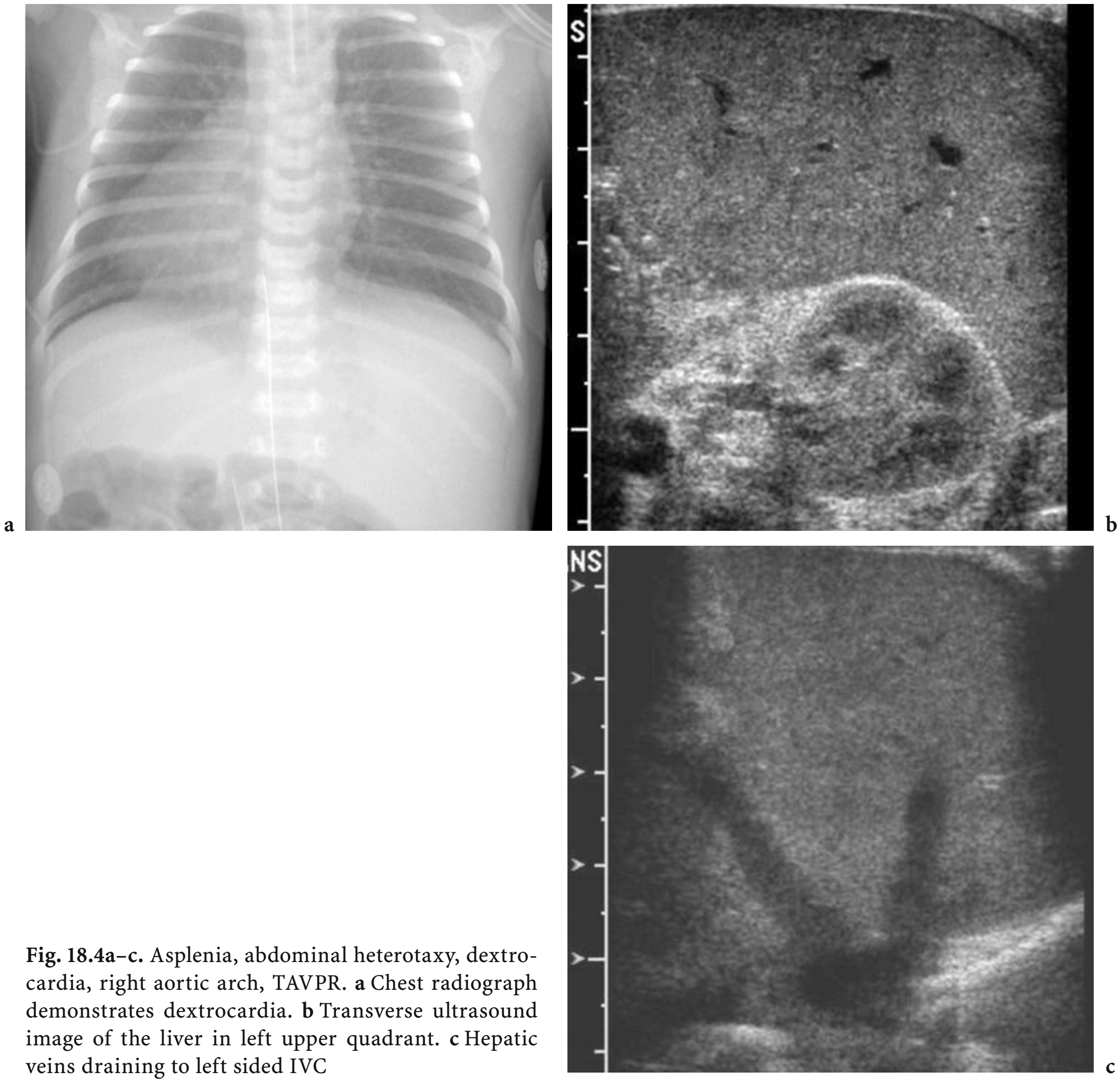

Fig. 18.4a–c. Asplenia, abdominal heterotaxy, dextrocardia, right aortic arch, TAVPR. **a** Chest radiograph demonstrates dextrocardia. **b** Transverse ultrasound image of the liver in left upper quadrant. **c** Hepatic veins draining to left sided IVC

contralateral lung and cause an increase in respiratory distress (Fig. 18.6). Occasionally, infants have an esophageal intubation, which can be recognized by distention of the distal esophagus with air, massive distention of the stomach, and increased parenchymal density in the lung.

All lines and catheters should be checked for position, and the caregivers should be notified of any abnormal positioning. Both the umbilical venous and the arterial catheters enter via the umbilicus, which may create a rounded, tubular density on the abdominal radiograph (Fig. 18.7). The umbilical venous catheter traverses the umbilical vein to the left portal vein to the ductus venous to the middle hepatic vein through the inferior vena cava and then to the inferior right atrium. If the catheter does not enter the right atrium, it should be repositioned. The catheter tip should be straight within the right atrium. When the catheter tip is leftward, it has likely passed through the foramen ovale and is positioned in the left atrium or the pulmonary veins (Fig. 18.8a,b). This is the path of normal in-utero blood flow and the foramen remains open or patent for sometime during the neonatal period. The umbilical arterial catheter extends inferiorly into the internal iliac artery, enters the common iliac artery and ascends in the aorta (Fig. 18.7). The position of the tip is optimally placed between T8 and T10 or placed below the level of the renal artery origins.

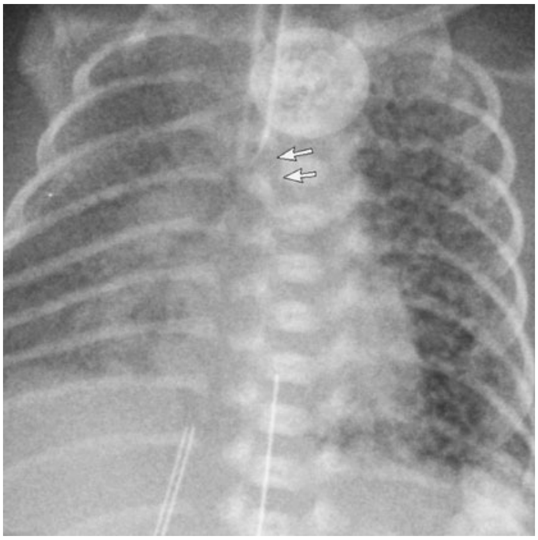

Fig. 18.5. Low position endotracheal tube. The tip of tube is below the left main stem bronchus origin (*arrows*)

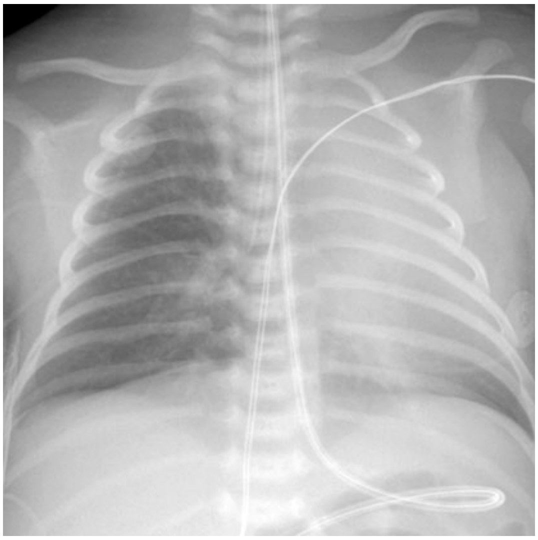

Fig. 18.6. Collapse of the left lung. Chest image demonstrates tip in right main stem bronchus with collapse of the left lung

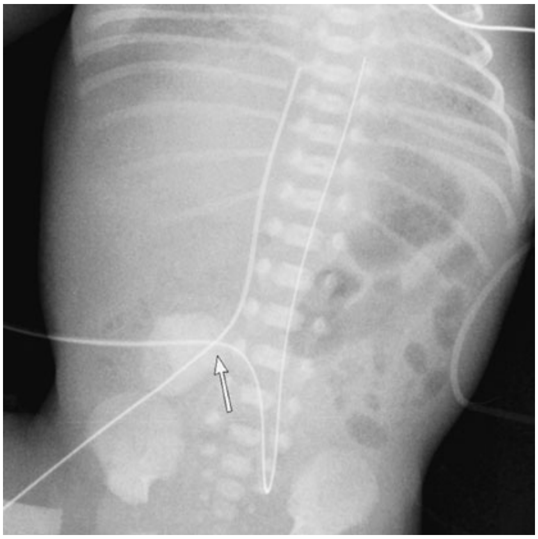

Fig. 18.7. Position of the umbilical catheters. The *arrow* indicates the umbilicus. The venous catheter enters the umbilical vein to the left portal vein to the ductus venous to the right atrium. The arterial catheter extends inferiorly to the common iliac artery and ascends in the aorta with the tip at the level of T8

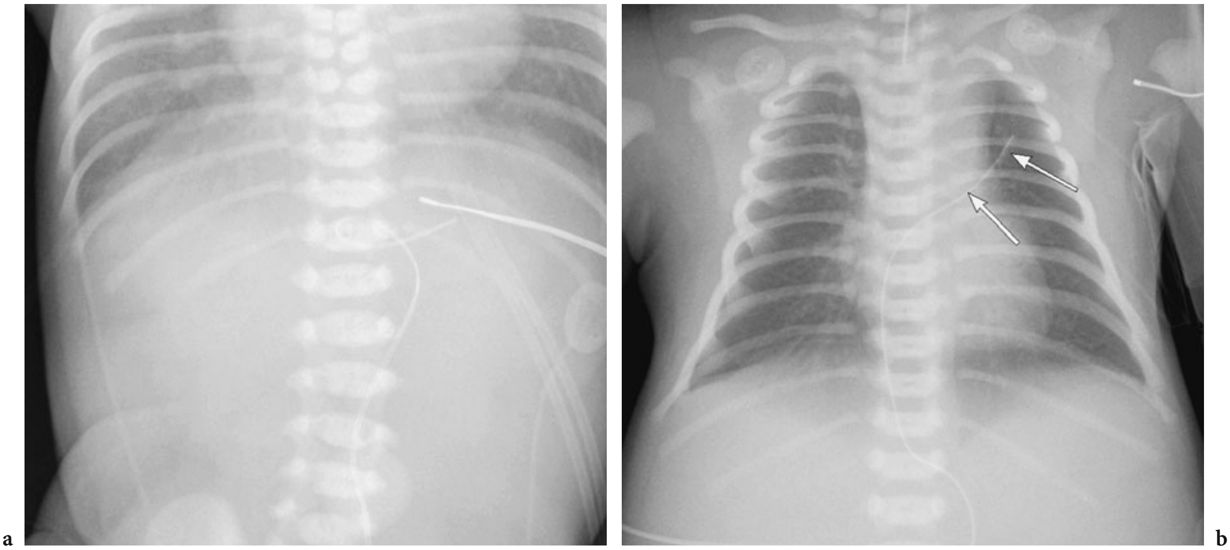

Fig. 18.8a,b. Malposition of umbilical venous catheters. **a** Tip in left portal vein. **b** Tip has crossed the foramen ovale and is in the left upper pulmonary vein (*arrows*)

18.3.2
Thymus

The thymic gland is normally visualized by 32 weeks of age but in infants treated with in-utero steroids or in cases of maternal stress, the thymic gland may be smaller. The normal thymus gland in term infants has a variable appearance but may have a "sail sign," a notch at the junction of the inferior portion of the gland with the cardiac silhouette, or it may appear as an asymmetrical mass (Fig. 18.9). If the infant is rotated towards the right, it can mimic right upper lobe disease or collapse. It may also have a "ripple effect" or "wave sign" when the gland is large and is gently compressed by the adjacent anterior ribs. Occasionally in premature infants, there is growth of the thymic gland and it may be confused with a mediastinal tumor or upper lobe parenchymal disease.

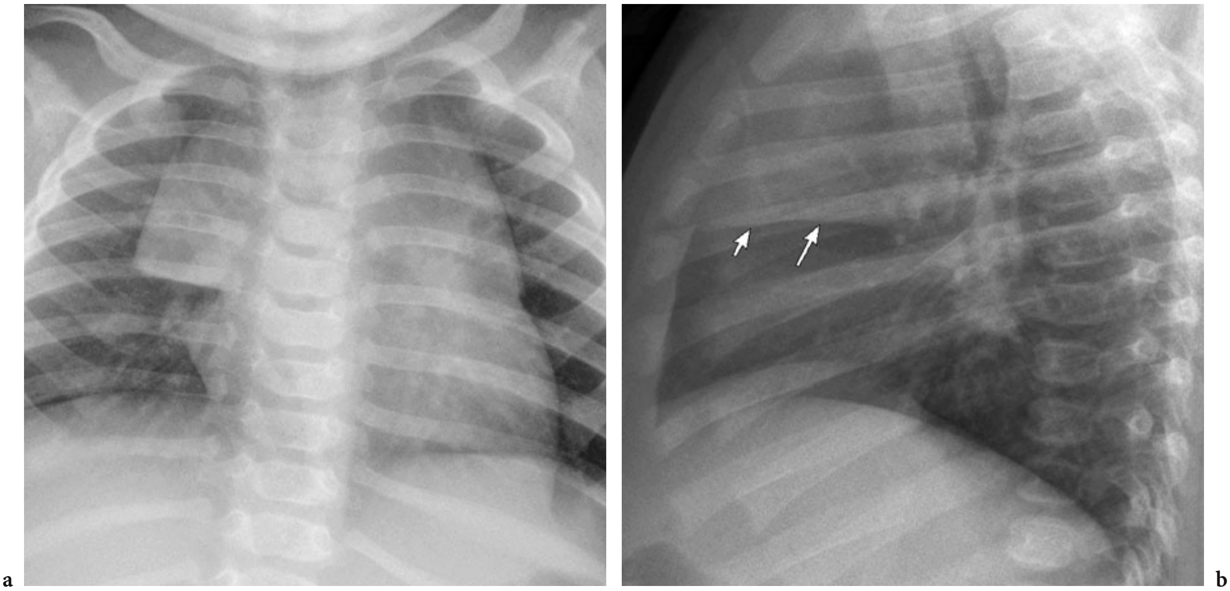

Fig. 18.9a,b. Thymic sail sign. AP (**a**) and lateral (**b**) chest radiographs. Note that the thymus is well outlined by air laterally and inferiorly creating a characteristic appearance

18.4
Air Leak Phenomena

Air leaks are not specific to a gestational age or a specific disease. The term air leak is used to describe rupture of the alveolus or the lung interstitium, which can lead to a variety of air leak conditions including pulmonary interstitial emphysema, pneumothorax, pneumomediastinum, and lung cysts. Air leaks can be focal, diffuse, or bilateral. They can occur in preterm infants, term or older infants. In most cases, the air leak is attributed to an increase in alveolar pressure with an air block. Mechanical ventilation and/or any clinical entity in which airway over-distention can cause rupture are risk factors for air leak phenomena. Premature infants are frequently mechanically ventilated and are therefore at risk for air leaks. In the infants that are symptomatic, treatment may be necessary, while in other cases air leaks may resolve on their own and the condition is self limiting.

18.4.1
Pulmonary Interstitial Emphysema

18.4.1.1
Etiology

Pulmonary interstitial emphysema (PIE) is gas within the pulmonary interstitium and lymphatics usually resulting from barotrauma (Jabra et al. 1997; Macklin and Macklin 1944). PIE can occur in a variety of clinical settings but usually happens in patients who are intubated. It results when there is rupture at a bronchoalveolar junction, which permits passage of gas into the perivascular and peribronchial spaces. Sometimes, the cystic lung masses may progress and cause compressive atelectasis. Occasionally, PIE can persist and form an expanding cystic mass that can cause mass effect and progressive respiratory distress. The terms localized persistent pulmonary interstitial emphysema and bullous interstitial emphysema have been used to describe this phenomena (Donnelly et al. 2003).

18.4.1.2
Imaging Findings

Pulmonary interstitial emphysema can be localized, segmental or diffuse and is characterized by tubular and cystic lucencies that fail to conform to the predictable branching pattern of air bronchograms. The tubular lucencies frequently extend to the pleural surface (Fig. 18.10). Massive PIE can produce marked over distention of one segment, one lobe or an entire lung, causing shift of the mediastinal structures. The interstitial air may further extend and produce pneumomediastinum or pneumothorax, subpleural blebs, or extend into the subcutaneous soft tissues of the neck or into the retroperitoneum (Fig. 18.11). In rare cases, there can be dissection through the walls of the pulmonary veins to the left atrium resulting in intravascular air.

Chest computed tomography (CT) has been shown to be useful in evaluating problematic infants with persistent PIE (Donnelly et al. 2003). It can be used to differentiate PIE from other causes of radiolucent cystic masses, as well as to define the anatomic distribution if surgery is being considered. On CT imaging, PIE has a typical appearance that consists of dot like structures within air filled cysts, which are thought to represent bronchovascular bundles surrounded by interstitial gas. A CT study found that 82% of patients with persistent PIE had the characteristic CT findings of central lines and dots surrounded by radiolucency (Donnelly et al. 2003). In that study, single lobe involvement was slightly more common than multilobar disease, and the left lung was affected more than the right.

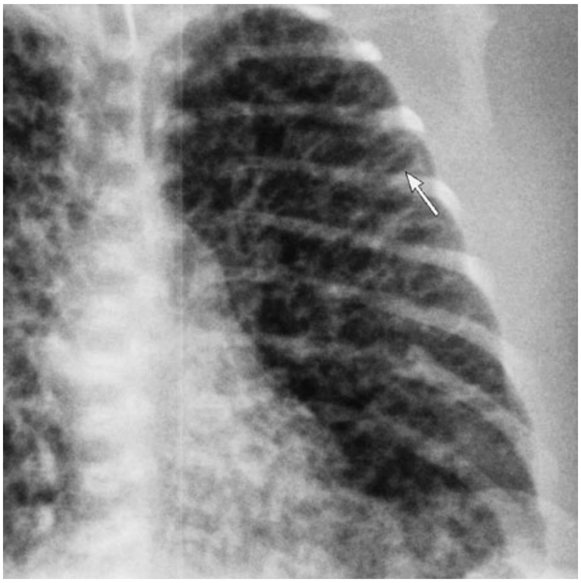

Fig. 18.10. Pulmonary interstitial emphysema (*PIE*). Linear or bubble-like lucencies extend to the pleural surface (*arrow*)

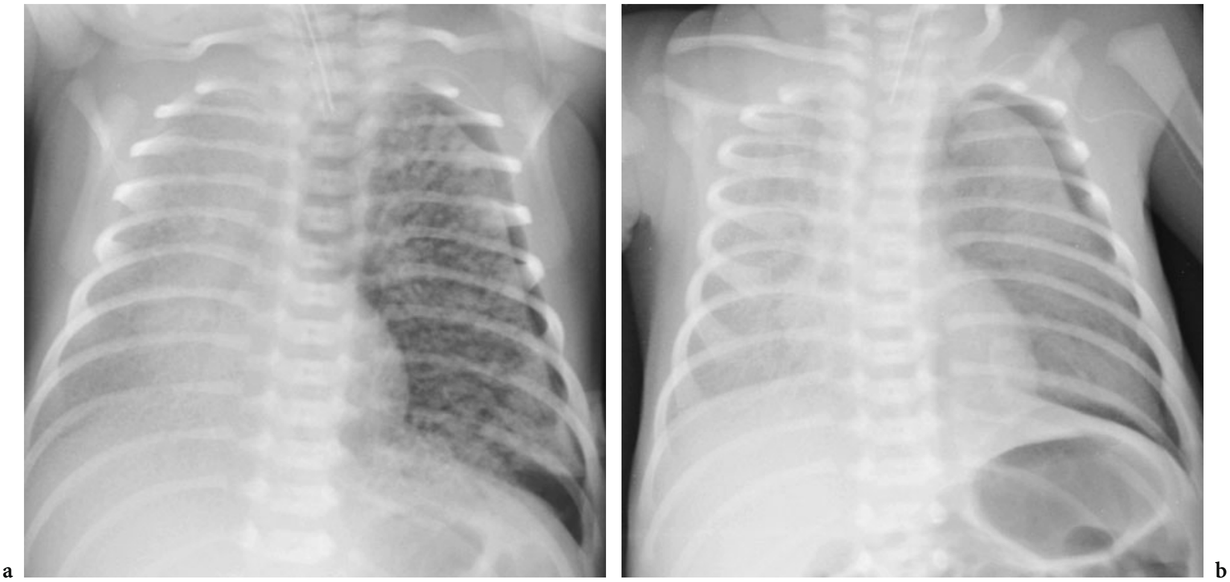

Fig. 18.11a,b. Left pneumothorax with mediastinal shift. **a** PIE with pneumothorax. **b** PIE not seen but large left pneumothorax with shift is present

18.4.1.3
Treatment

Most patients can be treated conservatively with decrease in size of the cystic lesions. However, surgical resection can be performed. In intubated infants, decreasing the ventilatory pressure or changing ventilation to continuous positive pressure ventilation may improve the air leak. When the air leak is localized to one lung, selected intubation has occasionally been tried to decrease the emphysematous changes. The persistent bullous emphysematous lung can be treated in a variety of ways including attempts to decompress the PIE by placing the affected lung down in decubitus position, surgical dissection or thorascopic puncture or resection. The presence of PIE also serves as a warning sign for more serious complications related to barotrauma, such as pneumothorax, which may necessitate placement of a chest tube.

18.4.2
Pneumothorax

18.4.2.1
Etiology

A pneumothorax is air in the pleural space, which is usually caused by rupture of a bronchovascular space causing air to dissect into the pleural space. The source of the rupture is rarely found, although there is an increased incidence in infants that are ventilated or that have PIE. The term “spontaneous” pneumothorax is occasionally utilized when there is no cause identified.

In chronic lung diseases of infancy and following chest tube placement, the pneumothoraces may resolve slowly and a bronchopulmonary fistula may occasionally develop as a complication. When there is severe intrauterine renal disease such as renal agenesis (Potter’s Syndrome) and renal cystic diseases, abnormal development of the lung and pulmonary hypoplasia occur. These infants are difficult to ventilate at birth and may have bilateral pneumothoraces and pneumomediastinum. Although many of these are diagnosed in-utero, other infants that have persistent pulmonary hypertension, difficulty ventilating, or in whom extra-corporal membrane oxygenation therapy is being considered should undergo ultrasound to evaluate their kidneys.

18.4.2.2
Imaging Findings

Pneumothoraces can usually be easily recognized; however, several features are peculiar to infants. Infant imaging is obtained supine and therefore any pleural air tends to collect anteriorly and medially

(Moskowitz and Griscom 1976). While in older children a pleural line is often seen laterally or apically, in two thirds of infants with pneumothorax, the air is noted medially (Fig. 18.12). Pneumothoraces may produce a deep sulcus sign, with one costophrenic angle extending deeper than the other (Fig. 18.11) and may create dramatic shifts of the mediastinum when they are large. Careful analysis for the presence mediastinal shift should be done as this may dramatically affect cardiac output.

18.4.2.3
Treatment

If the infant is asymptomatic, the pneumothorax may be managed conservatively. The treatment in symptomatic infants is chest tube placement. In the case of a significant pneumothorax with midline shift, a rapid cascade of events may lead to urgent need for intervention with lifesaving placement of a chest tube.

18.4.3
Pneumomediastinum

18.4.3.1
Etiology

Air may dissect from the interstitium of the lung into the mediastinum or into the mediastinal recesses. The mediastinal recesses are not usually well recognized; however in a neonate, the pristine mediastinal reflections can be separated into recognizable patterns that are not commonly seen in adults, such as when air dissects into the infra-azygous or inferior pulmonary ligament.

18.4.3.2
Imaging Findings

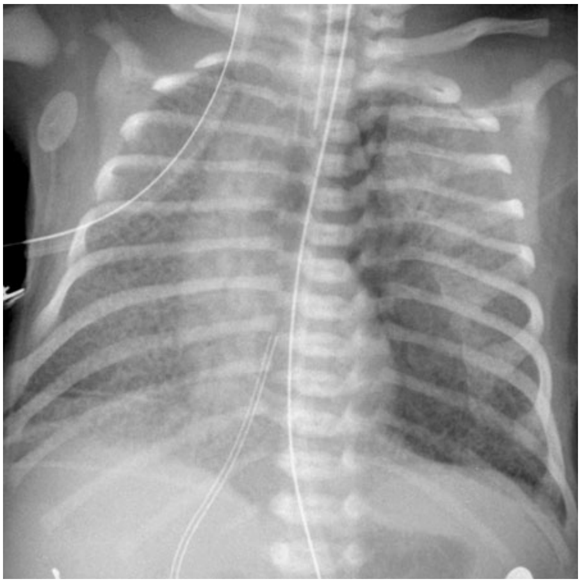

Fig. 18.12. Pulmonary interstititial emphysema with medial left pneumothorax and shift of mediastinum

In pneumomediastinum occurring in term or older infants, the mediastinal air elevates the lobes of the thymus, and chest imaging may show apical masses which represent the thymic gland uplifted by air (Fig. 18.13). The thymus moves laterally and superiorly and occasionally is misinterpreted as lung disease. Cross table lateral imaging can confirm that it is a pneumomediastinum as air will frequently be seen surrounding the thymus. Occasionally, decubitus imaging can be helpful in differentiating a pneumothorax from pneumomediastinum. In the decubitus position, if there is a pneumothorax air will rise and outline the pleural surface and an estimate of the size of the pneumothorax can be made. In children with pneumomediastinum on supine, AP chest radiographs, air can appear to surround the heart inferiorly; this is sometimes called the continuous diaphragm sign. Air in the inferior pulmonary ligament can be recognized by its central location, either midline or just to the left of midline on anterior-posterior radiographs and its posterior location on lateral radiographs (Volberg et al. 1979).

18.4.3.3
Treatment

Many asymptomatic term infants with pneumomediastinum need no treatment. Infants that are symptomatic are treated with “oxygen washout.” The oxygen is absorbed more rapidly than room air (which has a high percent of nitrogen), so the pneumomediastinum decreases more quickly. A complication of pneumomediastinum may be pneumothorax.

18.4.4
Pneumopericardium

Pneumopericardium is another sign of air leak. Pericardial air outlines the heart but is limited superiorly by the pericardial reflection of the great

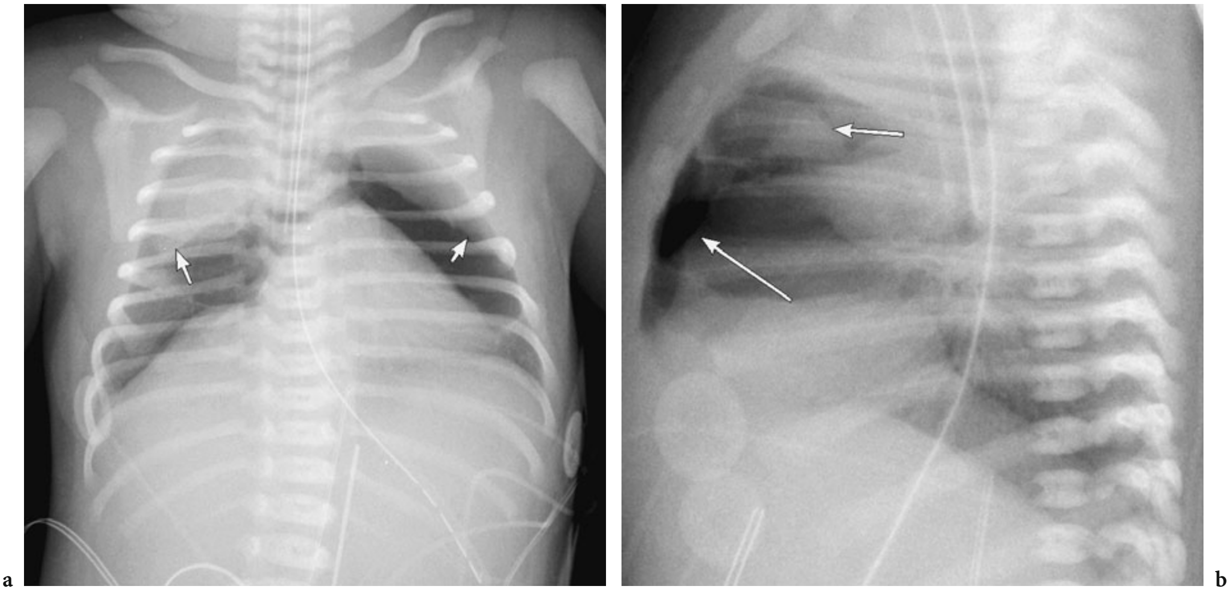

Fig. 18.13a,b. Large pneumomediastinum in an infant. **a** Air crosses the mediastinum and uplifts the thymus (*arrows*). **b** Lateral confirms that this is not a medial pneumothorax but rather a large pneumomediastinum

vessels. Occasionally, it can lead to tamponade and a decrease in systemic and pulmonary venous return. Ideally, prompt placement of a catheter to treat the pneumopericardium will improve cardiac output; however, the mortality remains higher in this subset of patients.

18.5
Medical Disease

18.5.1
Pulmonary Disease of the Premature Infant

18.5.1.1
Etiology

Pulmonary disease of the premature infant is also called hyaline membrane disease, surfactant deficiency, respiratory distress syndrome (RDS) or pulmonary disease of the immature. The incidence and severity is inversely related to gestational age and the extraordinarily pre-term infants of 23–28 weeks have more severe disease than the older preterm infant. In this group of infants, it is important to remember that their entire body is immature and they often have multiple interrelated medical issues. Neonatal intracranial hemorrhage, necrotizing enterocolitis or sepsis may cause tachypnea and the chest radiograph is obtained to exclude new chest findings. When an infant is born premature, the immaturity of the lung causes a cascade of events with alveolar instability, collapse, capillary leak, necrotic cells, and hyaline membrane formation. These alter the ability for gas exchange, causing hypoxia, pulmonary hypertension and right-to-left shunting via the ductus.

Understanding the normal anatomic and physiologic development of the lung has contributed significantly to the understanding of the radiographic changes associated with pulmonary disease of the premature infant (Agrons et al. 2005; Aukland et al. 2006; Howling et al. 2000; Stocker 1986, 1994). In normal lung development, the acinar phase lasts from 16 to 28 weeks gestation and during this period multiple alveolar ducts arise from primary bronchioles. The alveolar ducts are lined by type II alveolar cells which are capable of surfactant synthesis. The precise mechanisms that normally regulate alveolar septation and physiologic lung maturation are complex and a variety of antepartum abnormalities may increase or decrease lung maturation. Intrauterine stress can cause an increase in maternal steroids; these steroids and/or exogenous steroids administered to the mother in anticipation of a premature birth may cross the placenta and contribute to type

II alveolar lining cells maturation and production of surfactant (Duetting et al. 1999).

The pathophysiology of RDS is the result of anatomic pulmonary immaturity and deficiency of surfactant. Type II alveolar cells begin to produce surfactant at 24–28 weeks gestational age; the surfactant lines the alveoli and contributes to surface tension of the alveoli. Surfactant absence results in abnormal pulmonary compliance, atelectasis, decreased gas exchange, severe hypoxia and acidosis. In a complex way, surfactant contributes to the alveoli maintaining their expansion, particularly during expiration, which facilitates necessary gas exchange and prevents expiratory alveolar collapse.

Infants of poorly controlled diabetic mothers are at risk for RDS because fetal hyperinsulinemia interferes with glucocorticoid effects on surfactant biosynthesis. Thus, the characteristic radiograph of RDS may occasionally be seen in larger term infants whose mothers are diabetic. Primary surfactant deficiency in term infants is also seen, but the diagnosis is rare and usually there is a delay in recognizing it. Other risk factors for RDS include multiple gestational births, maternal or fetal hemorrhage, fetal asphyxia and sepsis.

18.5.1.2
Imaging Findings

Radiographically, the "classic" chest image in RDS consists of symmetric diffuse fine granular pattern bilaterally, air bronchograms, and pulmonary hypoventilation (Fig. 18.14). It is important to note that the "classic" radiographic findings seen on the initial radiograph are not usually seen on subsequent imaging studies, which reflect multiple treatment interventions and/or complications. A wide spectrum of radiographic changes between the initial and follow-up images is to be expected based on the gestational age, mechanical support, and varying response of the lung between a 24 week preterm infant, a 34 week preterm infant or a term infant with surfactant deficiency (Dinger et al. 1997; Slama et al. 1999).

Marked advances in perinatal medicine, including strategies to delay labor, the administration of antenatal maternal glucocorticoids, surfactant replacement therapy and improved ventilatory protocols, have dramatically changed the "classic" radiographic appearance. If the mother is treated with steroids prior to delivery, the steroids cross the placenta, type II cells mature, surfactant is produced, and the first infant chest radiograph may be normal in appearance. Similarly, in infants who are treated with surfactant very early in their life, the expected "classic changes of RDS" may not be apparent on the initial radiograph. There is a lot of variability in the radiographic appearance of RDS; therefore, one can assume that regardless of the radiographic appearance, premature infants have some lung disease relating to their prematurity.

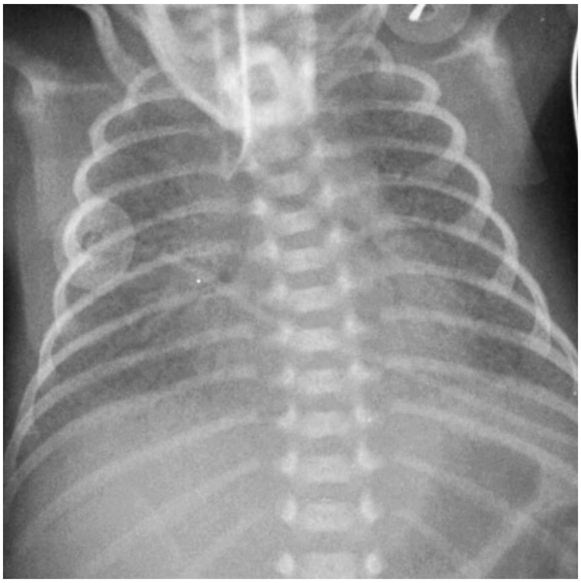

Fig. 18.14. RDS "classic" appearance. Premature infant with pulmonary hypoventilation, and a symmetric fine granular appearance in both lungs

There are many variations in treatment for RDS including the type of surfactant, timing of surfactant delivery, and type of respiratory support. Following surfactant therapy, the pulmonary abnormalities on the chest radiograph may be asymmetric (Fig. 18.15). Several explanations have been proposed for asymmetric radiographic involvement including maldistribution of surfactant into one lung more than the other, insufficient surfactant requiring additional applications, and regional differences in aeration before surfactant treatment (Dinger et al. 1997; Slama et al. 1999; Soll 2000). Asymmetric, multifocal areas of opacity may be noted, and should not be mistaken for neonatal pneumonia or meconium aspiration syndrome. Localized over-aeration of selected portions of the lungs may mimic interstitial air leak (Cleveland 1995). In addition, asymmetric unilateral improvement may result in a hyperlucent lung with contralateral mediastinal shift resembling a tension pneumothorax.

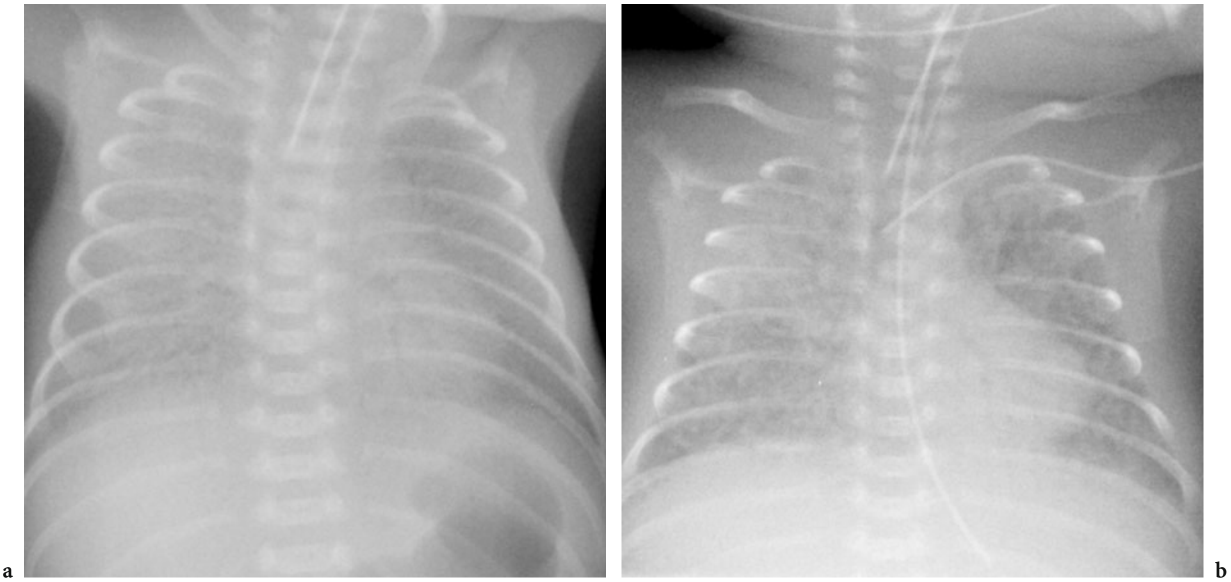

Fig. 18.15a,b. RDS with asymmetry. **a** Day 2 – there are bilateral, fine granular opacities affecting the right lung more than the left. **b** Day 5 with asymmetric improvement of the lungs

In infants treated with surfactant, there may be rapid clearing and aeration of the lung followed by a more hazy interstitial appearance. Swischuk (2004) has used the term "leaky lung syndrome" to describe this occurrence. This radiographic sequence may occur for a variety of reasons but is usually associated with increased permeability of the capillaries and resultant leaking of fluid into the pulmonary interstitium. The fluid is initially interstitial but may also become intra-alveolar. This may be a transient phenomena or may last for several days (Swischuk 2004).

A complication of surfactant deficiency may be pulmonary hemorrhage, although the precise mechanism following surfactant therapy remains unclear. It is possible that improved ventilation and decreased pulmonary vascular resistance promotes left-to-right shunting through the ductus arteriosus producing pulmonary hemorrhage (van Houten et al. 1992) (Fig. 18.16).

The radiographic appearance of the chest in the premature infant weighing less than 1000 g may be near normal initially; however, the alveolar paucity in these low birth weight infants necessitates continued ventilatory support and these very premature lungs are therefore subject to the deleterious effects of high oxygen concentration and positive pressure. As the survival of these smaller infants increases, pediatric radiologists continue to learn about the changing radiographic patterns.

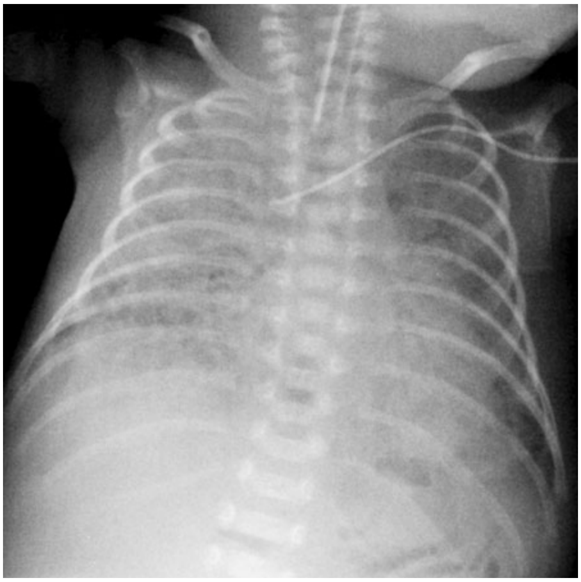

Fig. 18.16. RDS with patent ductus arteriosus. Increased bilateral lung density which can be attributed to left-to-right shunting from a ductus arteriosus on day six of life

18.5.1.3
Patent Ductus Arteriosus

Many premature neonates will have a patent ductus arteriosus, which usually becomes symptomatic as the initial pulmonary hypertension of the lungs decreases. This leads to increased left to right shunting, and the chest radiograph shows a diffuse, somewhat symmetric hazy appearance of the lung likely related to pulmonary edema, which occurs at about 5–8 days after birth (Fig. 18.16). Usually, the infants tend to gain weight, the heart size may increase and some have a continuous murmur. Echocardiography confirms the diagnosis. Infants are usually treated with a prostaglandin inhibitor such as indomethacin which aids ductal closure. In some infants, indomethacin is contraindicated, and ductal ligation is performed by a left thoracotomy or thorascopic procedure (Fig. 18.17).

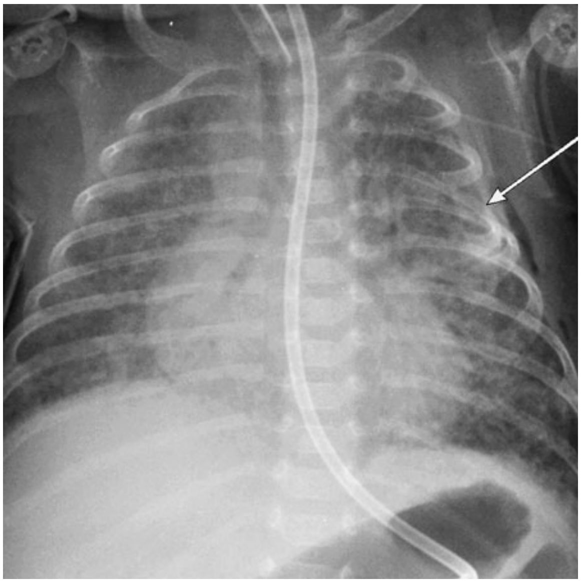

Fig. 18.17. Premature infant with RDS, post-operative left ductus arteriosus surgery. Subcutaneous emphysema is noted along the left lateral chest wall and the ribs are closer together

18.5.2
Chronic Lung Disease of Infancy: Bronchopulmonary Dysplasia

There has been a substantial change in the epidemiology, clinical presentation and radiologic features of chronic lung disease relating to prematurity. Initially, the term bronchopulmonary dysplasia (BPD) was used to describe chronic lung disease occurring in premature infants who had RDS and were treated with positive pressure mechanical ventilation and supplemental oxygen (Northway and Rosan 1968). However, dramatic changes in therapy have improved outcomes, increased survival and changed the "typical" radiographic appearance, and now there is question about the limited definition as it had been earlier applied. Consequently, the term "chronic lung disease of infancy" has gained favor to describe the form of BPD encountered in low birth weight infants. Others have suggested that BPD be defined as a continued oxygen requirement or abnormal chest radiograph at 36 weeks post conceptional age. However, at a consensus workshop, it was elected to retain the term "bronchopulmonary dysplasia" as the best descriptor of chronic lung disease peculiar to premature infants (Jobe and Bancalari 2001).

18.5.2.1
Etiology

The pathogenesis of BPD is multi-factorial and incompletely understood, but newer thinking is that fundamentally there is an inhibition of acinar and vascular growth during a vulnerable stage of lung development (Agrons et al. 2005). The "new BPD" has alveolar septal fibrosis; the widespread use of surfactant therapy and the concominant decrease in exposure to high oxygen tensions and ventilatory pressures is thought to have decreased the necrotizing bronchiolitis and severe septal fibrosis found in "classic BPD". The heterogeneous lung injury and repair which was classically seen has been replaced by diffuse alveolar septal fibrosis and simplified acinar morphology.

The sequelae of BPD are now being described in children and young adults. The incidence is actually increasing as the survival rates have improved even for the very premature infants. BPD is the most frequent cause of chronic lung disease in neonates, and many of those survive to reach adolescence and adult life.

18.5.2.2
Imaging Findings

During the first year of life, the premature infant slowly grows and the lung attempts reparative changes (Fig. 18.18). The chest radiograph has variable findings according to gestational age, therapy and complications. The residual disease may be focal, diffuse, symmetric or asymmetric. Certainly, the classic symmetric bubbly lungs as originally described in advanced BDP are seen less frequently on today's images (Fig. 18.19).

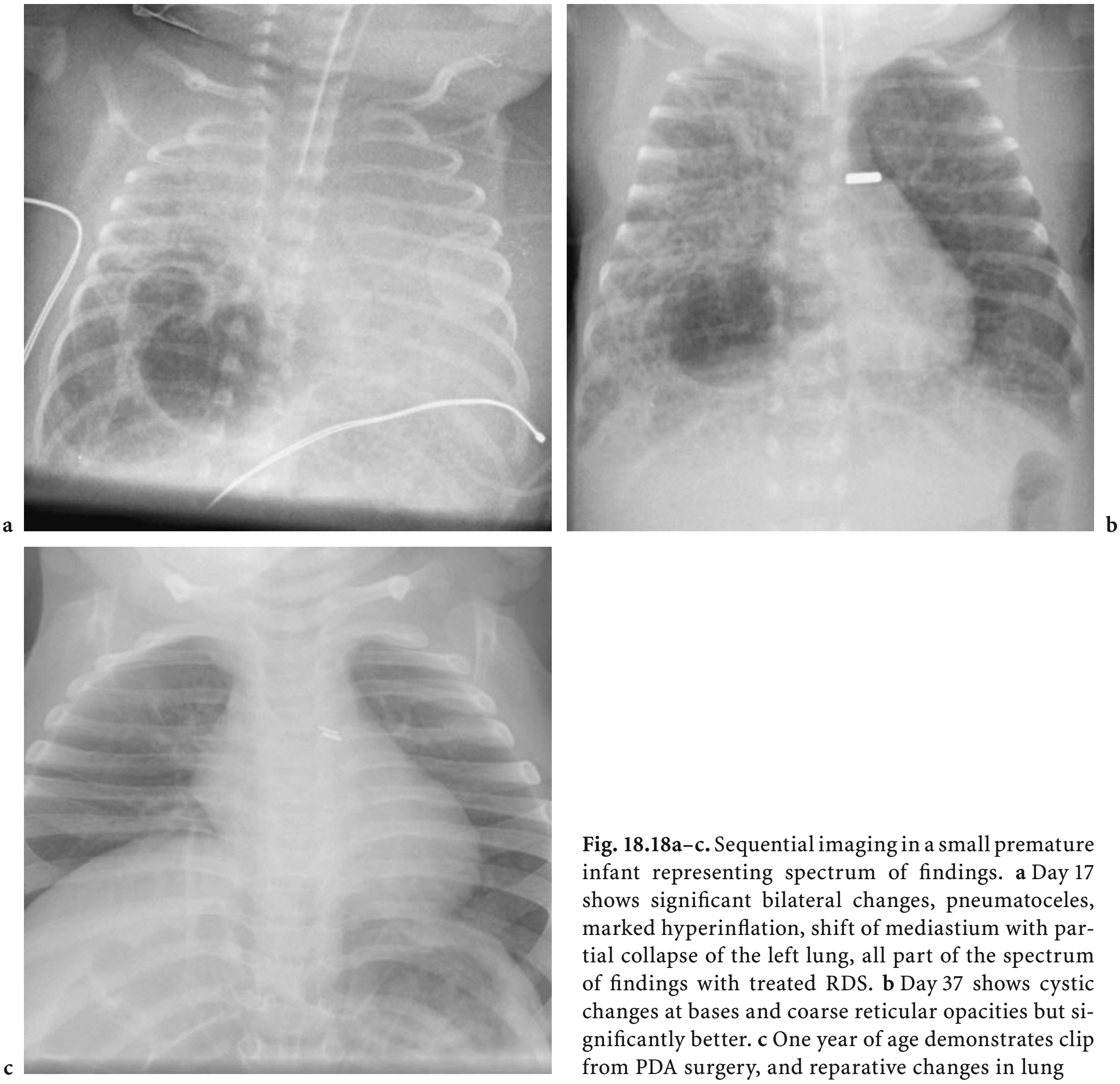

Fig. 18.18a–c. Sequential imaging in a small premature infant representing spectrum of findings. **a** Day 17 shows significant bilateral changes, pneumatoceles, marked hyperinflation, shift of mediastium with partial collapse of the left lung, all part of the spectrum of findings with treated RDS. **b** Day 37 shows cystic changes at bases and coarse reticular opacities but significantly better. **c** One year of age demonstrates clip from PDA surgery, and reparative changes in lung

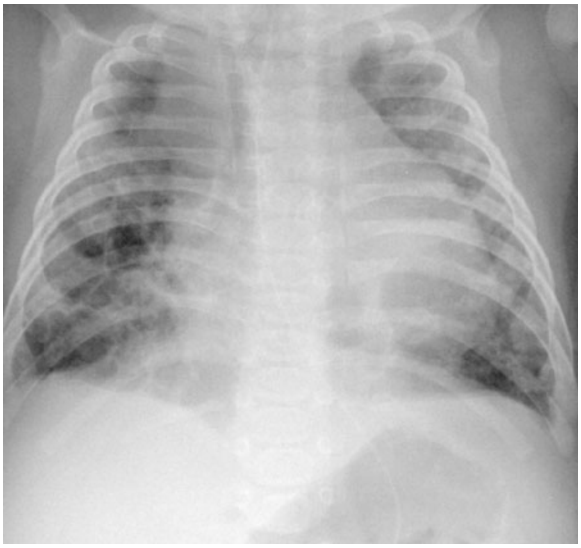

Fig. 18.19. Bronchopulmonary dysplasia: AP chest radiograph demonstrates significant bilateral pulmonary parenchymal disease which is characterized by course lung opacities and focal areas of hyperinflation

Infants with BPD have an increase in hospital admissions with viral disease, particularly respiratory syncytial virus. Some children will develop tracheal stenosis related to intubation and require a tracheostomy to improve ventilation. In children with prior necrotizing enterocolitis, a gastrostomy may be present and many will have had a fundoplication or Nissen procedure. Occasionally, the Nissen slips and there is a left paravertebral density which may be mistaken for left lower lobe pneumonia rather than herniated stomach in the left medial hemithorax. Infants may also have metabolic bone disease as they may be nutritionally challenged and/or may be given diuretics. Some diuretic therapy promotes calcium excretion and infants maintain their serum calcium with re-absorption from bone. Occasionally fractures of the ribs occur during handling of these infants. Premature infants that have had intracranial hemorrhage or hypoxia /ischemia may have issues with chronic aspiration which are superimposed on the lung disease of the premature.

High resolution chest CT (HRCT) findings of BPD include regional air trapping and linear areas of opacity representing thickened intralobular septa, subsegmental atelectasis, and fibrosis (Figs. 18.20 and 18.21). There can also be segmental or lobar atelectasis, reduced bronchial alveolar diameters and bronchial wall thickening. In follow-up studies of children with chronic lung disease who were born at less than 30 weeks gestation, CT findings include triangular pleural based densities which are attributed to pseudo fissures, as well as a decrease in size and number of vessels in these areas (Aukland et al. 2006). Other authors have described a decreased ratio between the bronchus and bronchial artery (Howling et al. 2000).

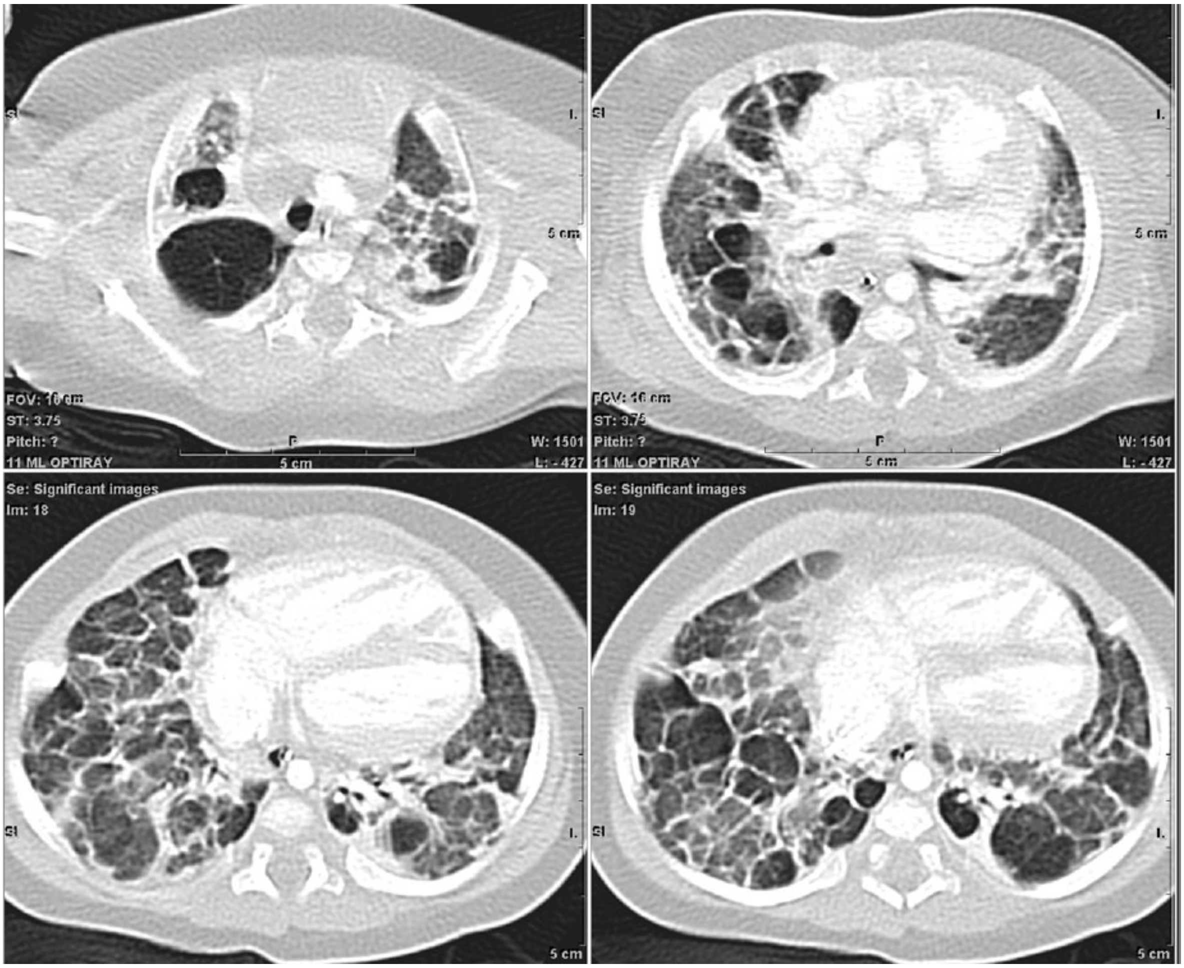

Fig. 18.20. Axial CT imaging demonstrates coarse linear opacities as well as focal areas of subsegmental atelectasis with regional hyperlucency and thickened intra-lobular septa

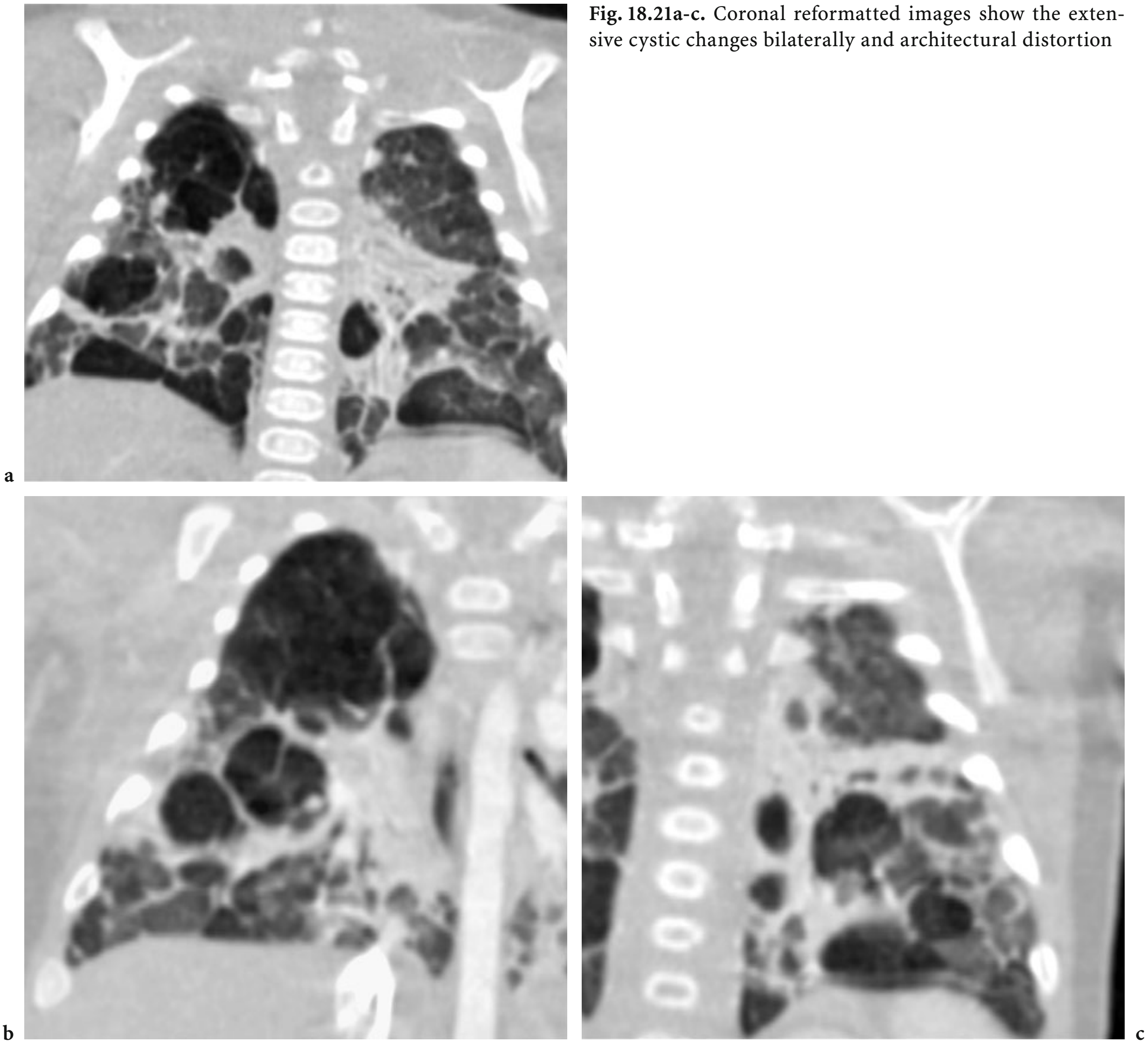

Fig. 18.21a-c. Coronal reformatted images show the extensive cystic changes bilaterally and architectural distortion

HRCT has contributed to our understanding of the chest radiograph in older survivors of BPD. HRCT in young adults demonstrates linear opacities, triangular peripheral opacities, mosaic perfusion and focal air trapping (Fig. 18.22). One study in young adults demonstrated abnormal radiologic findings in 87% of cases studied, including linear opacities in 72% and triangular sub pleural opacities in 58%, with the lower lobes affected more often than the upper lobes (Aukland et al. 2006). Air trapping was seen in 26%, mosaic perfusion in 13%, bronchiectasis in 9%, thickening of the interlobular septa in 10%, peribronchial thickening in 5%, and collapse or consolidation in 4%. A smaller number had bullae.

Likely, the imaging findings of BPD will continue to evolve and there will continue to be discrepancies related to prior treatment approaches, the degree of prematurity of the infant and other post-natal factors which can affect the parenchymal findings. Multiple authors are now reporting on the findings in BPD, but there is variability regarding what findings should be expected as a result of the diverse gestational ages, complications, and varying treatment. Addressing future studies toward these discrepancies and observing infants as they reach adulthood will improve knowledge concerning the "residual lung disease of prematurity."

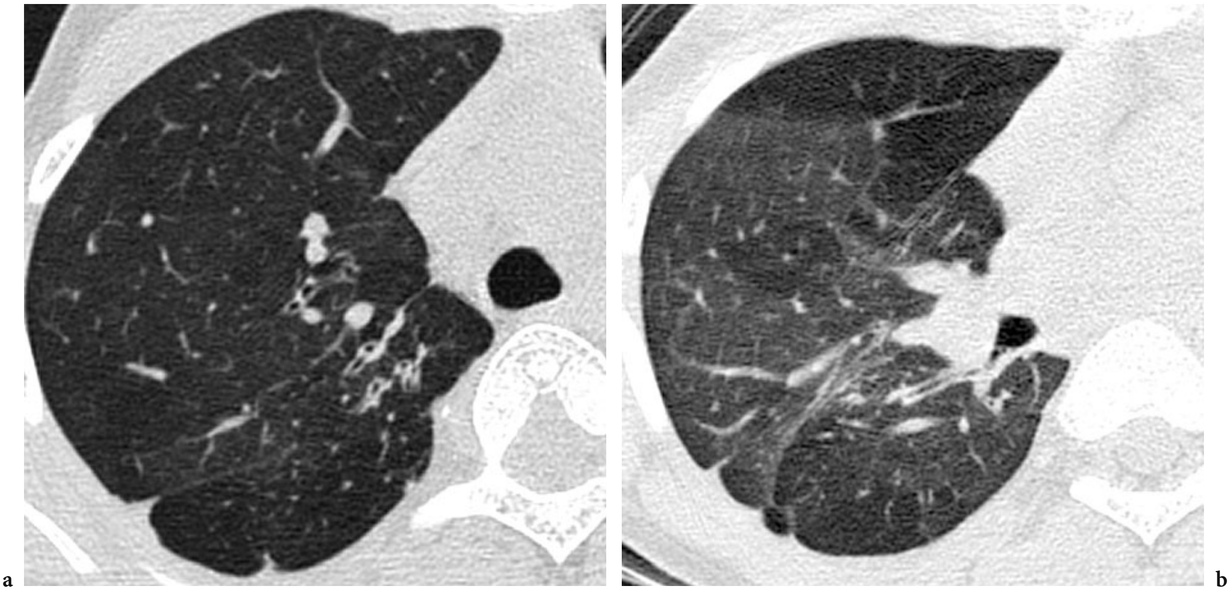

Fig. 18.22a,b. Axial high resolution CT imaging of BPD. **a** Inspiration shows mosaic attenuation. **b** Expiration shows air trapping with subpleural triangular opacities

18.5.3
Meconium Aspiration Pneumonia

18.5.3.1
Etiology

Meconium is the term used to describe the material in the fetal colon throughout gestation. It is usually passed during the first 24 h after birth. Meconium aspiration syndrome (MAS) is a disease of the term and near term infant and is associated with several important risk factors. Known risk factors for the passage of meconium include fetal distress, placental insufficiency, pre-eclampsia, oligohydramnios, maternal drug abuse, especially tobacco and cocaine, and advanced gestational age. Fetal distress can be recognized by abnormalities of fetal heart rate and/or poor APGAR scores. MAS does not appear to occur prior to 34 weeks as in-utero meconium passage results from neural stimulation of a mature gastrointestinal tract. In the 1980s and 1990s, approximately one-third of infants with MAS required intubation and mechanical ventilation (Wiswell et al. 1990). Infant mortality among that group was approximately 4%, and accounted for 2% of all perinatal deaths (Wiswell et al. 1990). Today, there continues to be a reduction in MAS due to changing obstetric practice in post-term mothers and closer fetal monitoring (Ross 2005; Yoder et al. 2002).

When meconium is passed in utero or at the time of delivery, there are three major potential effects: (1) airway obstruction, (2) surfactant insufficiency, and (3) pneumonitis. When there is mechanical obstruction of the smaller airways, inhibition of surfactant function may occur; in addition, inflammation of lung tissue leads to small airway obstruction. There is increasing awareness that severe MAS is not caused by aspiration of meconium alone (Ghidini and Spong 2001; Dargaville 2006), but by a multitude of factors. One study using treatment with amnio-infusion to dilute the effects of meconium did not reduce perinatal death in moderate or severe meconium aspiration (ACOG Committee 2006). In the infants that died, there was muscularization of the pulmonary arteries, suggesting that factors other than meconium aspiration contributed to the pulmonary compromise. Acute intrapulmonary meconium induces a pulmonary hypertensive response which is estimated to be present in 15%–20% of the patients (Holopainen et al. 1998). Chronic hypoxia in these infants may contribute to pulmonary vasoconstriction and pulmonary hypertension.

Clinically, meconium aspiration syndrome is manifested by respiratory compromise, tachypnea, cyanosis, and reduced pulmonary compliance.

18.5.3.2
Imaging Findings

Radiographic findings include a term infant (the proximal humeral epiphysis will usually be present), with moderate to marked hyperinflation, and asymmetric focal coarse increased lung markings. Complications related to barotrauma may be seen, such as pneumomediastinum or pneumothorax, as well as a diffuse pneumonitis which may relate to the constituents of meconium (Fig. 18.23). While the mortality risk for ventilated infants with MAS appears to be decreasing, pneumothorax remains an important complication with a reported incidence of 8%–20% (Chinese Collaborative Study Group for Neonatal Respiratory Disease 2005; Holopainn et al. 1998; Ross 2005; Vain et al. 2004).

18.5.3.3
Treatment

Treatment for MAS, especially in infants requiring intubation, is evolving rapidly but may include high frequency ventilation, exogenous surfactant, inhaled nitrous oxide, liquid ventilation, or drugs to reduce pulmonary hypertension. Meconium directly alters antibacterial activity and subsequently increases the risk of bacterial infection. Thus, antibiotics are usually given. Multiple advances in treatment have emerged and have contributed to the decreased use of extra corporeal membrane oxygenation (ECMO) (Ford 2006). However, in patients that have severe oxygen requirements or severe pulmonary hypertension that does not respond to drugs, ECMO has been shown to improve survival and reduce the effects of barotrauma.

Researchers continue to evaluate the efficacy of surfactant administration in patients with MAS. Impairment of lung function has been shown recently to be associated with marked changes in recombinant surfactant protein messenger RNA expression (Hilgendorff et al. 2006). In addition, recombinant protein C or natural surfactant preparations have been shown to be safe and efficient in acute lung injuries and adult respiration distress syndrome.

18.5.4
Transient Tachypnea

18.5.4.1
Etiology

Transient tachypnea, also called “wet lung disease” or “retained fetal lung fluid,” occurs in near term, term, and post-term infants with an increased incidence following c-section deliveries. By strict defi-

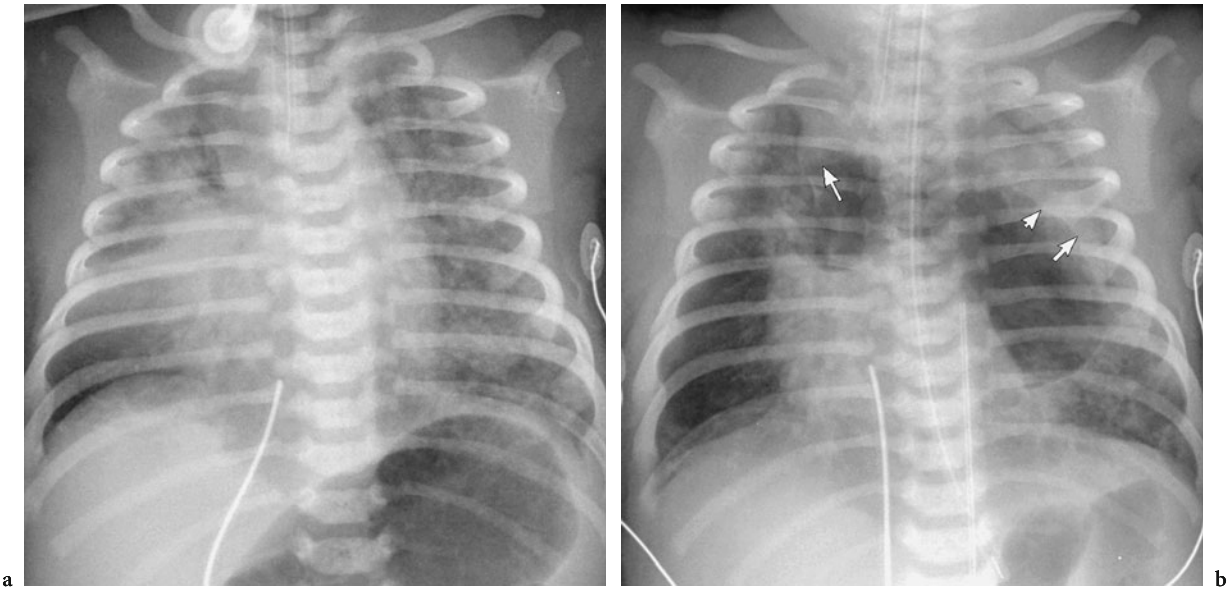

Fig. 18.23a,b. Meconium aspiration. **a** Initial image of infant with meconium staining shows course lung opacities bilaterally, right greater than left. **b** Large pneumomediastinum bilaterally with uplifting of the thymus

nition, no other cause for tachypnea is identified in these infants and it is considered a diagnosis of exclusion. However, the scope of the traditional definition has been broadened as the understanding of this entity expands.

In-utero the fetus is submerged in fluid, and at birth there is a switch from placental to pulmonary gas exchange. In order to have an effective gas exchange, the alveolar spaces need to be cleared of excess fluid, and pulmonary blood flow has to increase to match ventilation with perfusion. It has been shown that the removal of lung fluid may start before birth and continue postnatally, with fluid being carried away through pulmonary lymphatics, blood vessels, the upper airway, mediastinum and pleural spaces. A traditional explanation for transient tachypnea of the infant was the lack of vaginal squeeze and subsequent thoracic compression of the newborn, especially with c-section delivery. However, more recent data suggests that sodium transport by lung epithelial cells is a key factor in the movement of the fluid. Osmotic gradients created by active solute transport by alveolar epithelial cells account for the bulk of fluid clearance from the lungs (Jain and Eaton 2006). Several processes are now known to result from disruption of the transepithelial movement including transient tachypnea and hyaline membrane disease.

18.5.4.2
Imaging Findings

Radiographically, these infants usually appear to be large term infants. The proximal humeral ossification centers are present, the thymus may be large and the thoracic cage is well developed. Radiographs of the chest demonstrate prominent interstitial markings with a normal heart size, diffuse bilateral, somewhat symmetric lung markings, pleural effusions, fluid in the fissures, and normal to mildly hyperinflated lung volumes (Fig. 18.24). They rarely develop air leak phenomena and usually only one or two chest radiographs are obtained as they improve rapidly.

The chest radiograph is often ordered to exclude other significant diseases such as congenital heart disease, surgical disease or other abnormalities. It is important to note that there are a variety of extrathoracic causes of tachypnea including peripheral arteriovenous malformations, electrolyte abnormalities, severe anemia, polycythemia, and other causes.

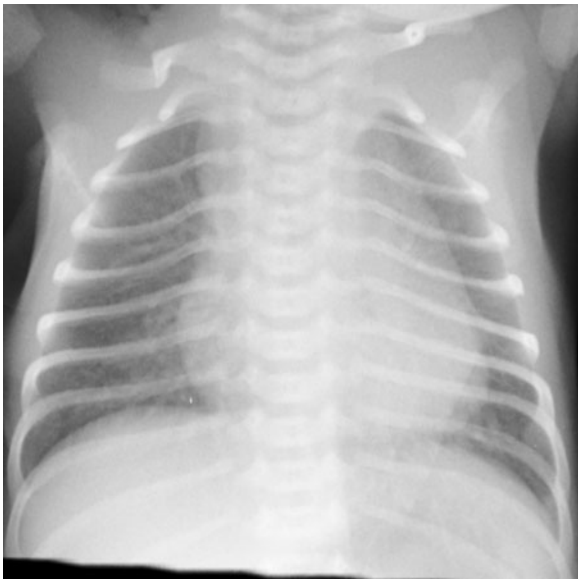

Fig. 18.24. Transient tachypnea of the newborn. Chest radiograph in term infant demonstrates prominent interstititial markings with a normal heart size and fluid in the fissures. The lung is mildly hyperinflated

18.5.4.3
Treatment

Clinically, these infants have increased respiratory rate and effort. Classic teaching used to be that the infants improved rapidly, needed little support, and rarely needed follow-up radiographs. However, there is increasing awareness of another group of infants that are approximately 34–37 weeks gestation and present primarily with tachypnea. These infants may end up needing respiratory support, oxygen, NICU admission, and occasional intubation or surfactant therapy. One study found that 4% of patients with transient tachypnea require oxygen therapy and 1% are intubated (Clark 2005).

18.5.5
Neonatal Pneumonia

18.5.5.1
Etiology

Neonatal pulmonary infections can occur in utero, during passage through the birth canal or just after birth. Predisposing factors include prolonged rupture of the membranes, maternal vaginal infection, placental infection, contamination of the infant with maternal fecal material or fetal sepsis. There has been a significant reduction in neonatal infections due to increased awareness, prenatal screening, and maternal testing.

Neonatal pneumonias in developed countries are now relatively rare. Most neonatal pneumonias are of bacterial origin and the common organisms include non-hemolytic streptococcus, staphylococcus aureus, and Escherichia coli. Other gram negative and positive organisms are also encountered. Viral organisms include adenovirus, herpes simplex, influenza, and parainfluenza. Tuberculosis and fungal infections can occur on a congenital basis but are rare.

Pulmonary complications of neonatal pneumonia are uncommon, but systemic effects may have high morbidity. As the viral and bacterial diseases are usually systemic, all organ systems may be affected.

18.5.5.2
Imaging Findings

As many of these organisms are acquired in-utero or hematogenously, it is difficult to distinguish the patterns on chest radiographs between bacterial and viral infections. Diagnosis depends on a high index of suspicion from the clinical history, as the radiographic findings are not specific. Solitary lobar consolidations related to neonatal pneumonias are extraordinarily rare and alternative diagnoses should be considered, such as diaphragmatic eventration or hernias (Fig. 18.25). Because neonatal pneumonias are frequently part of systemic disease (Swischuk 2004), the infiltrates are usually bilateral. Streptococcus pneumonia mimics RDS radiographically, except that the gestational age is usually normal or even post-term. There is diffuse granularity throughout both lungs with some parahilar streakiness. Occasionally pleural fluid may occur (Fig. 18.26). Regardless of the organism, the alveoli become distended and filled with purulent exudates, which causes an increase in lung volumes, so the lungs are granular but large. In infants that have group B streptococcal pneumonia delayed onset of diaphragmatic hernia (Handa et al. 1992) has been reported.

18.5.6
Pulmonary Lymphangiectasia

18.5.6.1
Etiology

Pulmonary lymphangiectasia is a rare entity and can occur as an isolated abnormality or in associa-

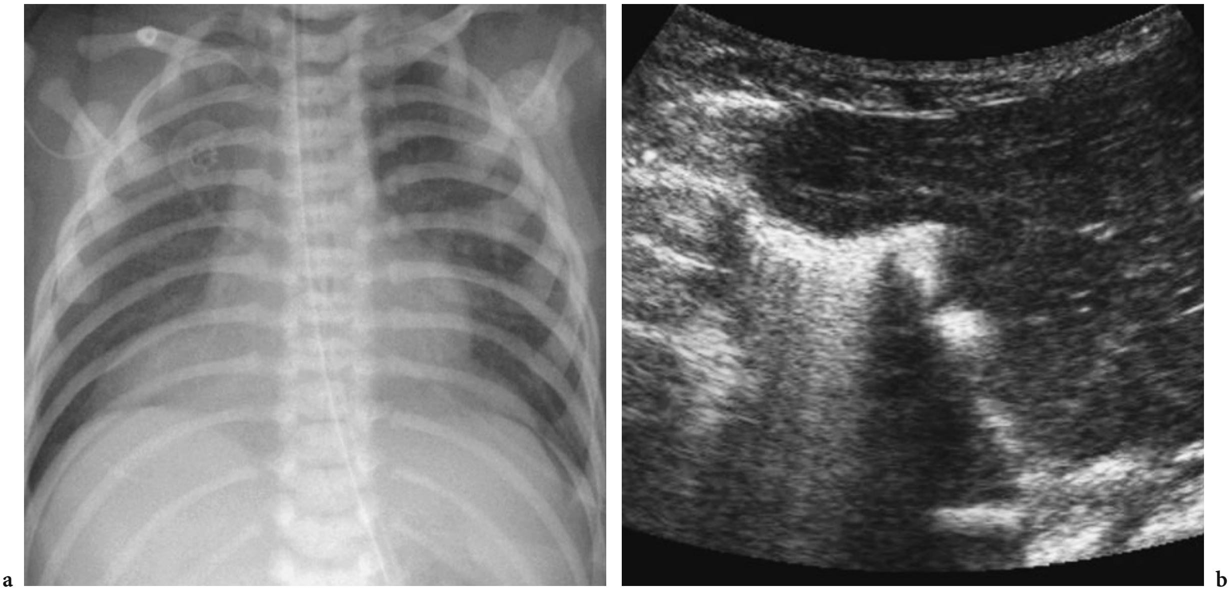

Fig. 18.25a,b. Eventration of the right diaphragm. **a** AP chest in a newborn demonstrates unusual medial contour to the right hemidiaphragm. **b** Ultrasound demonstrates eventration

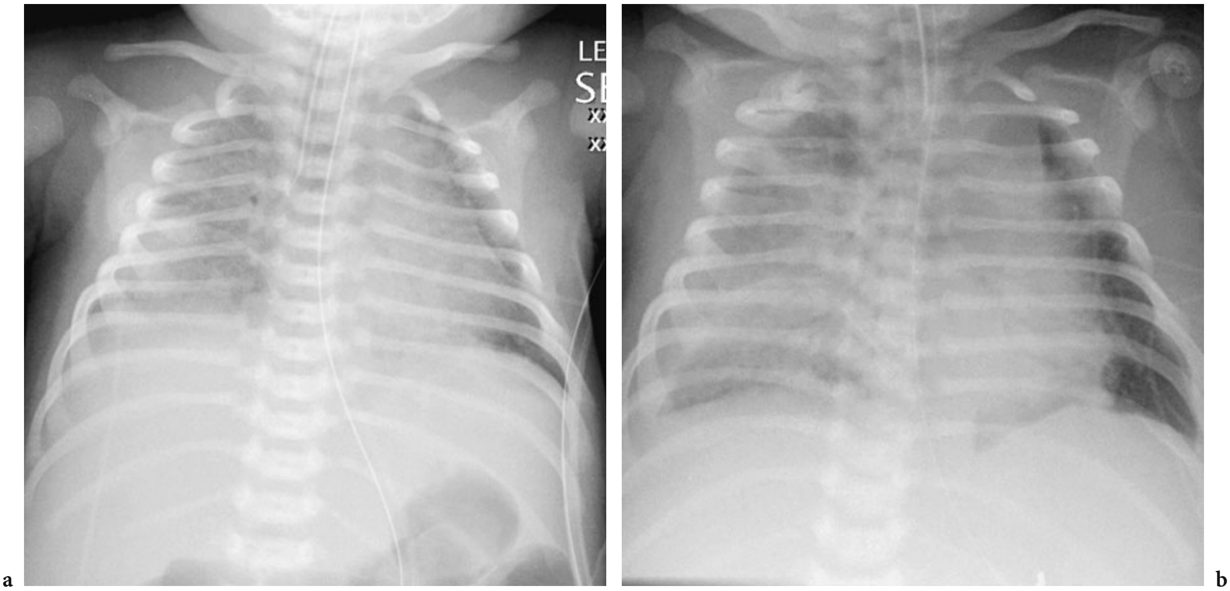

Fig. 18.26a,b. Herpes pneumonia. **a** Initial chest image shows bilateral course parenchymal disease. **b** After 3 days there is progression of disease and a right pleural effusion

tion with a syndrome such as Noonan or Turner syndrome. In the primary type, the etiology is believed to be an early embryonic arrest of pulmonary lymphatic development. It is increasingly apparent that lymphatic obstruction can also be acquired due to a variety of causes. In fact, secondary dilated lymphatics are much more common that the congenital form. They can be seen in association with congenital heart disease with severe pulmonary venous obstruction, such as in total anomalous pulmonary venous return, postoperative venous obstruction, or any cause of persistently elevated pulmonary venous pressure or severe pulmonary arterial hypertension. Infants that have superior vena caval clots from catheters may also have pleural effusions and dilated lymphatics because of impaired lymph drainage due to high pulmonary venous pressure.

18.5.6.2
Imaging Findings

Radiographically, the distended lymphatics usually result in a prominent interstitial pattern and a reticular appearance to the lungs (Fig. 18.27). This can be associated with pleural effusions and can simulate total anomalous pulmonary venous return. The dilated lymphatics may be more noticeable after feeding occurs.

18.5.7
Congenital Heart Disease

Malformations of the heart and lungs are the most common birth defects, effecting 1% of live births and 10 times that in stillborn infants (Hoffman 1995). Dramatic changes in diagnosis, prognosis and therapy have occurred in neonatal congenital heart disease. Remarkable advances have been spurred by the increased use and technical advances of in-utero imaging, as well as increased knowledge regarding congenital anomalies and malformations.

18.5.7.1
Etiology

The majority of cases of congenital heart disease occur because of spontaneous mutations. However, gene mapping studies of syndromic patients with known associated cardiovascular malformations such as trisomy 21, Williams syndrome, and Turner syndrome have helped increase understanding of the genetic basis of heart disease. Furthermore, there is now increased awareness of the human cardiac teratogens including chemical exposures such as ethanol, dilantin, lithium and retinoic acid, maternal rubella infections and maternal systemic diseases. Infants of diabetic mothers may have marked cardiac septal hypertrophy which is reversible as the infant's

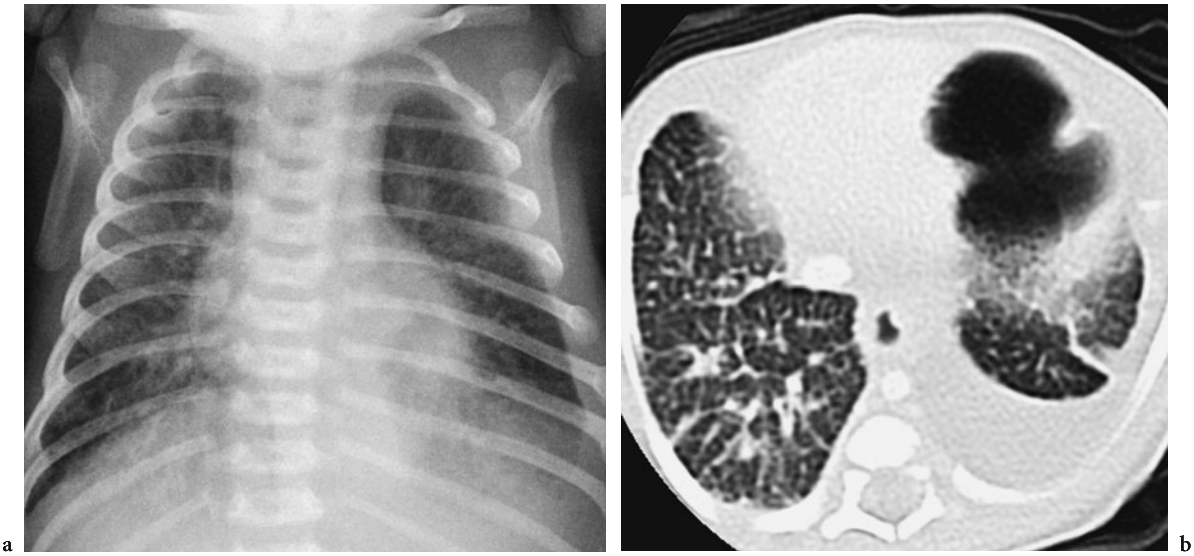

Fig. 18.27a,b. Lymphangiectasia in a term infant who had respiratory distress. **a** AP chest radiograph shows diffuse parenchymal opacities with increased pulmonary interstititial markings and left effusion. **b** CT demonstrates thick and distorted lines perpendicular to the pleural surface which are dilated lymphatics in the interlobular septae. Increased interstitial lung markings extend all the way to the pleura. Note moderate left pleural effusion

blood sugar normalizes. It is well known that infants of mothers with systemic lupus erythematosus may have congenital atrioventricular block. Trisomy 21 infants may have atrioventricular canal defects; however, they are rarely symptomatic as infants because they usually have high pulmonary artery resistance which decreases left to right shunting.

18.5.7.2
Imaging Findings

Increasingly, the diagnosis of congenital heart disease is made in-utero with prenatal ultrasound examination in high risk or routine pregnancies. As the fetus is nourished by oxygenated maternal placental blood, many fetuses with complex and severe cardiac anomalies will thrive in-utero.

Echocardiography at birth is a fundamental, portable, non-invasive imaging modality that can be used with relative ease to provide excellent spatial and 3D resolution. It is the primary modality for initial diagnosis. However, the chest radiograph may also be useful as a screening tool for the evaluation of cardiac abnormalities and associated lesions, and may occasionally be useful to suggest a specific diagnosis. In young infants, assessing heart size is difficult because of the large thymus (Fig. 18.28). Lateral imaging is occasionally useful to confirm that the heart is not enlarged. Massively enlarged hearts have been termed “the wall-to-wall heart” and usually indicate Ebstein’s anomaly or pulmonary atresia with an intact septum (Donnelly et al. 1997) (Fig. 18.29). However, in a neonate, there are a variety of other non-cardiac entities that may contribute to cardiomegaly, such as peripheral arteriovenous malformations like Vein of Galen aneurysms, hemangioendotheliomas of the liver, marked anemia, polycythemia, and maternal diabetes.

In neonatal congenital heart disease, the position of the aortic arch may be abnormal. Helpful hints for locating the site of the aortic arch include: (1) the position of the trachea which is normally to the right of midline and superimposed on the right pedicles, (2) impression of the lateral border of the trachea by the aortic knob, (3) visualization of the aortic arch itself or (4) visualization of the descending aorta. A right arch is strongly associated with congenital heart disease and it is seen in tetralogy of Fallot (25%), truncus arteriosus (35%), and pulmonary atresia with ventricular septal defect (30%). Assessment of pulmonary flow is not very accurate and it usually does not help define specific lesions (Strife 2006). In many congenital heart lesions, the chest radiograph can be normal, such as in hypoplastic left heart syndrome, tricuspid atresia, aortic interruption, or complex diseases such as double inlet left ventricle. If there is concern for heart disease, echocardiography should be performed.

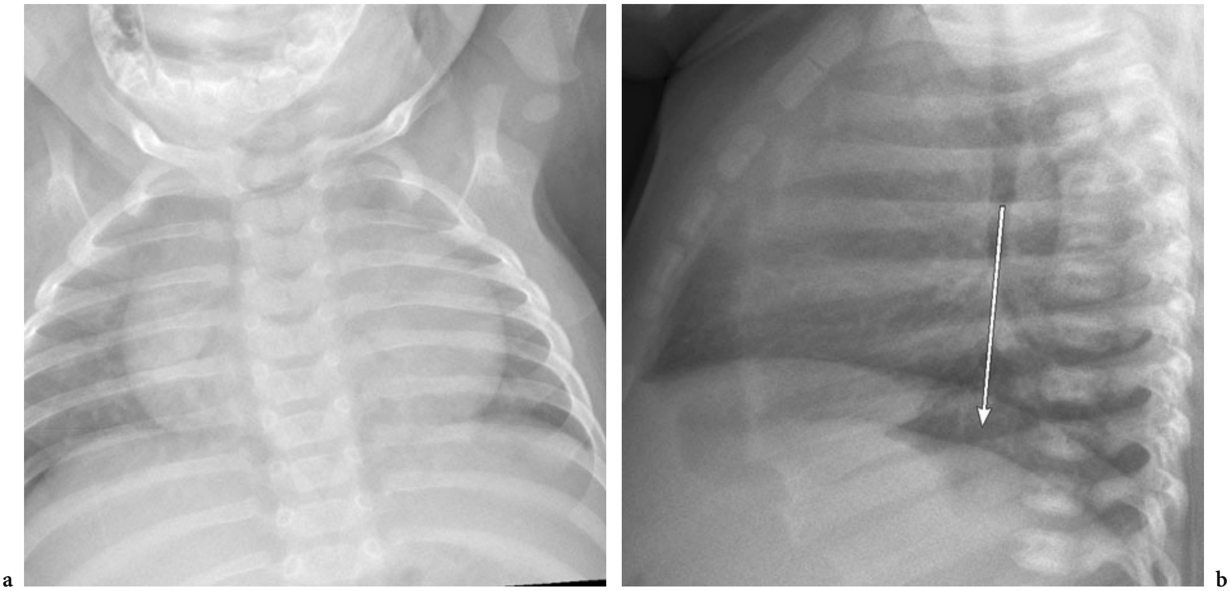

Fig. 18.28. **a** Normal thymus simulating cardiac enlargement on AP chest. **b** Lateral chest confirms that the heart is not enlarged because there is no extension of the cardiac silhouette posterior to an imaginary line extended from the trachea to the diaphragm

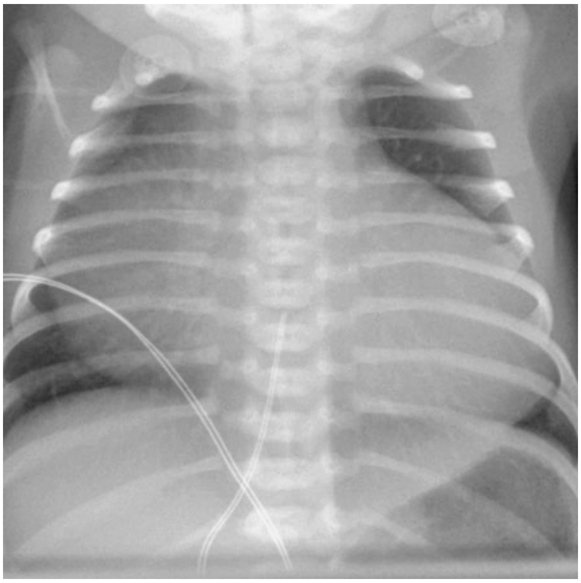

Fig. 18.29. Ebstein anomaly. Markedly large heart related to massive enlargement of the right atrium

18.6
Summary

Neonatal imaging continues to play a significant role in helping clinicians care for sick infants. Using a systematic and careful approach aids interpretation of the images. If one knows the gestational age, maternal history and birth history of the infant, the images fall into predictable patterns of recognizable diseases. However, the natural history of many of these diseases has been dramatically altered by new advances in therapies. The imaging findings will continue to evolve as new treatment strategies emerge.

References

ACOG Committee (2006) Amnioinfusion does not prevent meconium aspiration syndrome. ACOG Committee Opinion Number 346. Obstet Gynecol 108(4):1053

Agrons GA, Courtney SE, Stocker JT et al. (2005) From the archives of the AFIP: lung disease in premature neonates: radiologic-pathologic correlation. Radiographics 25(4):1047–1073

Aukland SM, Halvorsen T, Fosse KR et al. (2006) High-resolution CT of the chest in children and young adults who were born prematurely: findings in a population-based study. AJR Am J Roentgenol 187(4):1012–1018

Chinese Collaborative Study Group for Neonatal Respiratory Disease (2005) Treatment of severe meconium aspiration syndrome with porcine surfactant: a multicentre, randomized, controlled trial. Acta Paediatr 94(7):896–902

Clark RH (2005) The epidemiology of respiratory failure in neonates born at an estimated gestational age of 34 weeks or more. J Perinatol 25(4):251–257

Cleveland RH (1995) A radiologic update on medical diseases of the newborn chest. Pediatr Radiol 25(8):631–637

Dargaville PA, Copnell B (2006) The epidemiology of meconium aspiration syndrome: incidence, risk factors, therapies, and outcome. Pediatrics 117(5):1712–1721

Dinger J, Schwarze R, Rupprecht E (1997) Radiological changes after therapeutic use of surfactant in infants with respiratory distress syndrome. Pediatr Radiol 27(1):26–31

Donnelly LF, Gelfand KJ, Schwartz DC et al. (1997) The "wall to wall" heart: massive cardiothymic silhouette in newborns. Appl Radiol (December):23–28

Donnelly LF, Lucaya J, Ozelame V et al. (2003) CT findings and temporal course of persistent pulmonary interstitial emphysema in neonates: a multiinstitutional study. AJR Am J Roentgenol 180(4):1129–1133

Duetting T, Foerste B, Knoch T et al. (1999) Radiation exposure during chest X-ray examinations in a premature intensive care unit: phantom studies. Pediatr Radiol 29(3):158–162

Ford JW (2006) Neonatal ECMO: current controversies and trends. Neonatal Netw 25(4):229–238

Ghidini A, Spong CY (2001) Severe meconium aspiration syndrome is not caused by aspiration of meconium. Am J Obstet Gynecol 185(4):931–938

Handa N, Suita S, Shono T et al. (1992) Right-sided diaphragmatic hernia following group B streptococcal pneumonia and sepsis. J Pediatr Surg 27(6):764–766

Hilgendorff A, Doerner M, Rawer D et al. (2006) Effects of a recombinant surfactant protein-C-based surfactant on lung function and the pulmonary surfactant system in a model of meconium aspiration syndrome. Crit Care Med 34(1):203–210

Hoffman JI (1995) Incidence of congenital heart disease: II. Prenatal incidence. Pediatr Cardiol 16(4):155–165

Holopainen R, Soukka H, Halkola L et al. (1998) Meconium aspiration induces a concentration-dependent pulmonary hypertensive response in newborn piglets. Pediatr Pulmonol 25(2):107–113

Howling SJ, Northway WH Jr, Hansell DM et al. (2000) Pulmonary sequelae of bronchopulmonary dysplasia survivors: high-resolution CT findings. AJR Am J Roentgenol 174(5):1323–1326

Jabra AA, Fishman EK, Shehata BM et al. (1997) Localized persistent pulmonary interstitial emphysema: CT findings with radiographic-pathologic correlation. AJR Am J Roentgenol 169(5):1381–1384

Jain L, Eaton DC (2006) Physiology of fetal lung fluid clearance and the effect of labor. Semin Perinatol 30(1):34–43

Jobe AH, Bancalari E (2001) Bronchopulmonary dysplasia. Am J Respir Crit Care Med 163(7):1723–1729

Macklin MT, Macklin CC (1944) Malignant interstitial emphysema of the lungs and mediastinum as an important occult complication in many respiratory diseases and other conditions: an interpretation of clinical literature in the light of laboratory experiment. Medicine 23:281–358

Moskowitz PS, Griscom NT (1976) The medial pneumothorax. Radiology 120(1):143–147

Northway WH Jr, Rosan RC (1968) Radiographic features of pulmonary oxygen toxicity in the newborn: Bronchopulmonary dysplasia. Radiology 91(1):49–58

Ross MG (2005) Meconium aspiration syndrome – more than intrapartum meconium. N Engl J Med 353(9):946–948

Slama M, Andre C, Huon C et al. (1999) Radiological analysis of hyaline membrane disease after exogenous surfactant treatment. Pediatr Radiol 29(1):56–60

Soll RF (2000) Natural surfactant extract versus synthetic surfactant for neonatal respiratory distress syndrome. Cochrane Database Syst Rev 2

Stocker JT (1986) Sequestrations of the lung. Semin Diagn Pathol 3(2):106–121

Stocker JT (1994) Congenital and developmental disease. In: Dail OH, Hammar SP (eds) Pulmonary pathology. Springer, Berlin Heidelberg New York, pp 155–190

Strife JL (2006) Pediatric cardiac imaging: the beat goes on! Pediatr Radiol 36:578–580

Swischuk L (2004) Respiratory system. Imaging of the newborn, infant, and young child. Lippincott Williams & Wilkins, Philadelphia, pp 1–170

Vain NE, Szyld EG, Prudent LM et al. (2004) Oropharyngeal and nasopharyngeal suctioning of meconium-stained neonates before delivery of their shoulders: multicentre, randomised controlled trial. Lancet 364(9434):597–602

van Houten J, Long W, Mullett M et al. (1992) Pulmonary hemorrhage in premature infants after treatment with synthetic surfactant: an autopsy evaluation. The American Exosurf Neonatal Study Group I, and the Canadian Exosurf Neonatal Study Group. J Pediatr 120(2 Pt 2): S40–44

Volberg FM Jr, Everett CJ, Brill PW (1979) Radiologic features of inferior pulmonary ligament air collections in neonates with respiratory distress. Radiology 130(2):357–360

Wiswell TE, Tuggle JM, Turner BS (1990) Meconium aspiration syndrome: have we made a difference? Pediatrics 85(5):715–721

Yoder BA, Kirsch EA, Barth WH et al. (2002) Changing obstetric practices associated with decreasing incidence of meconium aspiration syndrome. Obstet Gynecol 99(5 Pt 1):731–739

Subject Index

Citation with pages in bold correspond to relevant figures

A

Aberrant 27, **28,** 31
ABPA, see allergic bronchopulmonary aspergillosis
Absence of pulmonary artery **137**
Acquired immune deficiency syndrome (AIDS) 269
Acute
– chest syndrome 299, 300
– interstitial pneumonia (AIP) 108
Adenoid cystic carcinoma 272
Adrenal
– carcinoma 278
– hemorrhage 400
AIDS, see acquired immune deficiency syndrome
AIP, see acute interstitial pneumonia
Air
– bronchogram 107
– leak 208
Air-filled cystic lung lesion 97
Air-space disease 114
Airway obstruction 81, 92
ALARA principle 48
Allergic bronchopulmonary aspergillosis (ABPA) 103
Alpha-fetoprotein 278
Alveolar proteinosis **100**
Amine precursor uptake and decarboxylase (APUD) system 271
Anomalous
– coronary arteries 338, 382, 391
– pulmonary veins 338, 340, 344, 347, 349, 376
Aortic
– arch anomalies 346, **385**
– coarctation 338, 345, **346, 371, 381–383**
– dissection **380,** 381, 382, **383**
– pseudoaneurysm 382, **383**
– regurgitation 380, 381
– root dilatation 345, **346,** 380
– rupture 179, 380, 381
– stenosis 378, **379**
Aplasia **136**
– complex 135, 138, 143
Architectural distortion 96
Arrhythmogenic right ventricular dysplasia (ARVD) **390**
Askin’s 282, 322, 326
Aspergillosis 296, **297,** 298, 319
Aspergillus fumigatus 103
Aspiration 41, **42,** 148, 158
Asthma 8, **10, 83, 92,** 103, 292, 299
Ataxia telangiectasia 27, 229, 243, **244, 245**
Atelectasis 103, 158, 207
Atrial septal defect (ASD) 344, 349, 350
– coronary sinus septal defect 349
– sinus venosus defects 349
Autoimmune thyroiditis 31
Automated dose control/modulation (ADC/ADM) function 56

B

B cell disorders 296, 297
Bacillus sphaericus 267
Beckwith–Wiedemann syndrome 230
Beta-glucocerebrosidase 113
Bicuspid aortic valve 345, 378, **379**
Bismuth breast shield 79
Blastomycosis **251**
Bone algorithm 78
Bone-marrow transplantation 104
BOOP, see bronchiolitis obliterans organizing pneumonia
BPD, see bronchopulmonary dysplasia
Breast
– cancer 79
– shielding 291
Bronchial
– adenoma **271, 272**
– atresia 4, 124, 127, 130, 133
– obstruction 148
– rupture 160
– stenosis 172, 175
Bronchiectasis 92, **93,** 100, 102, 104, 147, 156, 175, **176,** 208, 293, 302–305
– cylindrical **101**
– cystic **101**
– varicose **101**
Bronchiolar abnormality 86
Bronchiolitis obliterans 92, 98, 103, 156, 157, **294**
– organizing pneumonia (BOOP) **91,** 104, 251, 294
– postinfectious **96**
Bronchoesophageal fistula 179
Bronchogenic
– carcinoma 275
– cyst 4, 7 , 31, 126, **127, 128,** 130, 133, 148, 200, 402, **403**
Bronchopleural
– fistula **66,** 71, **149,** 152, 155, 179
– infection **66**
Bronchopulmonary
– dysplasia (BPD) 41, **83, 93, 94,** 114, 429, **430,** 431, 432, **433**
– fistula 71
Bronchoscopy 195, 207
Bronchovascular bundle 85
Brown adipose tissue **43**-44

C

Carcinoid tumour **271**
Cardiac
– malformation 413
– rhabdomyoma 413
– tumors 352, 353
– – fibroma 344, 352, 353
– – hemangioma 353
– – Purkinje cell tumor 353
– – rhabdomyoma 352, 353
Cardiomyopathy 344, 352–354
– arrhythmogenic right ventricular cardiomyopathy (ARVC) 354
– hypertrophic obstructive cardiomyopathy 353
– iron overload cardiomyopathy 354
– left ventricular non-compaction **353**, 354
CARE dose 56
Castleman's disease 31, 109, 216, **225**, 233
Cavitary necrosis **149**, 152, **153, 154**, 155
CCAM, see congenital cystic adenomatoid malformation
CDH, see congenital diaphragmatic hernia
CDILD, see chronic diffuse infiltrative lung disease
Centrilobular
– interstitium 85
– nodules **90**
Cervical ribs 314
Cervicothoracic tumour **72**
CGD, see chronic granulomatous disease
Chest
– CT 242253,
– FDG-PET 247, 259
– fetal MRI 397
– focused CT 82
– gallium scintigraphy 246, 258
– limited slice CT 82
– masses 65
– MRI 243, 257
– neoplasm 264
– nuclear medicine 246, 258
– radiographs 242, 252
– routine control 67
– thallium scintigraphy 247, 258
– US 1-35, 243
– wall tumour 71, 263, 282
Chloral hydrate 81
Cholesterol granuloma **91**
Chronic
– diffuse infiltrative lung disease (CDILD) 105
– granulomatous disease 44, **45**, 67, **298**, 299, 300
– interstitial pneumonia 108
Clavicles, normal 314
Cleidocranial dysplasia 314, 315
Collagen-vascular disease 110
Collapse 172, 175
Common variable immunodeficiency 296
Computed tomography (CT)
– acute pulmonary disease 147–164
– angiography 39, 69, 161
– – thymus 219
– axial **431**
– cardiac 345, 361–396
– cystic fibrosis 304
– immunodeficiency 148, 156, 157
– parapneumonic effusions 148–151, 156
– pericardial effusion 156
– pulmonary embolism and infarction 161, 162
– pulmonary infections 147–157, 296, 297
– pulmonary trauma 158–161
– radiation dose 147
– radiation dose 363, 364
– systemic disease 290–292, 298, 300, 301, 307
– technique 291
– technique 291, 362–369
Congenital
– bronchial atresia 124, 130
– cystic adenomatoid malformation (CCAM) 3, 4, 6, 8, 129, **130, 131,** 148, 155, 268, 273, 399, **401**
– diaphragmatic hernia **5, 33,** 41
– diaphragmatic hernia (CDH) 397, 407
– heart disease 418, 419, 436, 437, 438
– high airway obstruction (CHAOS) **4,** 5
– laryngeal atresia 411, 412
– lobar emphysema 4, 124, 126,
– lobar overinflation **60**
– malformation of the lung 3
– neuroblastoma 6
– pulmonary lymphangiectasia (CPL) 111, 404, 406
– thoracic cyst 126, 123
– tuberculosis 177
– venolobar syndrome 138–143, **139, 140, 142,** 376, 377
Consolidation 90
– alveolar **173,** 174
Constrictive bronchiolitis, see bronchiolitis obliterans
Contrast material administration 53
Cor
– pulmonale 317
– triatriatum 138, 350
Coronary artery aneurysm **339**, 364, 383, **384**
Corynebacterium equi 267
Coxiella burnetii 267
CPL, see congenital pulmonary lymphangiectasia
Crazy paving pattern 99
Cushing‘s syndrome 271
Cylindrical bronchiectasis **101**
Cylindroma 272
Cystic
– adenomatoid malformation 3, 4, 6, **96**
– bronchiectasis 101
– fibrosis 8, 41, 44, 84, 92, 99, **102**, 292, 301–306
– – Chrispin-Norman scoring 304
– – diagnosis 302
– – genetics 302
– – imaging 303–305, **306**
– – pulmonary pathophysiology 303
– hygroma 281
– malformation 266
– pulmonary lesion 97
Cytomegalovirus pneumonia **297**

D

Dermatomyositis (DM) 293
Desquamative interstitial pneumonitis (DIP) 108
Diabetes mellitus 294
Diaphragm, accessory 143
Diaphragmatic
– mass 284
– duplication 143
– hernia **33,** 132, 138, **408**
– lesions 32
– paralysis 32
– rupture **33**
DiGeorge syndrome 27, 217, 221, 229, 297
DIP, see desquamative interstitial pneumonitis
Directly observed treatment short (DOTS) 166
Disseminated disease, acute **169,** 175
Double aortic arch 31, **62,** 384, **385,** 386
Down syndrome **98,** 183, 184, 189–191
Duplication cyst **126**
Dysmorphic lung 123, 135, 141

E

EAA, see extrinsic allergic alveolitis
Ebstein's anomaly 351, **439**
Echocardiography 307, 338, 345, 347–350, 353, 354, 369, 371, 376, 380–384, 390, 391
Ehlers Danlos syndrome 345, 378
Embryonal carcinoma 28
Emphysema 98
– obstructive **172**
Empyema 18
Endobronchial
– carcinoid 271
– hamartoma 269
– lesion 71
– tuberculosis 68
Endodermal sinus tumour 28
Epithelial tumour of the thymus 279
Escherichia coli 436
Esophageal
– atresia **4, 26, 422**
– duplication cysts 31
– teratoma **285**
Ewing sarcoma 44, 282, **283,** 313, 322, 326, **329**
Expiratory slice 83
Extralobar sequestration 131–133
Extrinsic allergic alveolitis (EAA) 106, **107**

F

Fast single shot echo (FSSE) 397
Fetal malformation 399
Fibromatosis 325
Fibrosarcoma 284, **326**
Fibrothorax 156
Fibroxanthoma 266
Finger-in-glove appearance 92
Fistulous tract **173**
Focused chest CT 82
Fontan procedure 38, 351, 352, 354, **366, 367,** 369, **375, 376, 390**–393
Foreign body 195–209
– bronchial 200
– chronic **204**
– complications 207
– esophageal **200,** 201
– imaging findings 206
– mechanism airway obstruction **198,** 198, **202**
– nasal 201
– non opaque **203**
– obstructing **205**
– subglottic 199
– techniques 201
– tracheal **196, 199,** 200
– types 196
Friedrich's syndrome **321**
FSSE, see Fast single shot echo
Fungal pulmonary infection 157, **158**

G

Ganglioneuroblastoma 280
Ganglioneuroma 280, **281**
Gastric smooth muscle tumour 269
Gastroesophageal (GE) reflux 41, 148
Gaucher disease 93, **113,** 308, 309
GCT, see Germ cell tumour
Germ cell tumour (GCT) 28, **30,** 278, **279**
GGO, see ground-glass opacity
Glenn shunt **392**
Glossoptosis 190, **191,** 192
Gorham disease **112,** 323, **324**
Graves disease 230
Ground-glass opacity (GGO) 88

H

Haematogenous tuberculosis **68**
Haemoptysis 264
Half-Fourier single shot turbo spin echo (HASTE) 397
Haller index 316, **317**
Halo sign 98
Hamartoma 268, **269**
HASTE, see Half-Fourier single shot turbo spin echo
Heart-lung transplantation 104
Helical multidetector chest CT, see also multidetector chest CT 47
– equipment 50
– image postprocessing 57
– immobilization 52
– intravenous contrast material administration 53
– limitations and disadvantages 51
– main applications 65
– personnel and environment requirements 52
– pitfalls 52
– preparation of the patient 52

Helical multidetector chest CT (*Continued*)
- previous exam evaluation 52
- radiation dose 48
- sedation 53
- technical parameters and protocols 54
- techniques 48

Hemangioma 317, 322–324, 413, **414**
Hemangiopericytoma 14
Hemithorax 179, 274, **409**
Hemophilia 326, **330**
Hemosiderosis **112, 113**
Heterotaxy **347**, 348, 350, **390**
High-resolution computed tomography (HRCT) **172, 174, 177**
- bone algorithm 78
- chest scanning parameters 51
- cystic fibrosis 304–305
- in children 77
- lung disease 78
  - – features 88
  - – indications 80
  - – sedation 80
  - – technique 78
- mixed connective tissue disease **293**
- pulmonary infections 296, 297
- radiation dose 290, 291
- systemic disease 290–295, 301, 303, 307, 309
- technique 291

High-resolution reconstruction algorithm 55
Histoplasmosis **158**, 250, **242**, 275
HIV infection 27, 28, 166, 169, 175
Hodgkin's lymphoma 216, **228**, 233, **235**, 241, 242, **246, 247, 249, 250, 254–257, 259**
Honeycombing 95
HRCT, see high-resolution computed tomography
Human chorionic gonadotropin 278
Hyaline membrane disease 419, 426, 435
Hybrid lesion in the lower lobe **61**
Hydrocarbon ingestion 97
Hydropneumothorax **66**
Hydrothorax **400, 407**
Hyperinflation **125**
Hyperpolarized helium 292, 305, 306
Hypertrophic pulmonary osteoarthropathy 267
Hypogenetic lung syndrome 138, **140**, 141–143
Hypopharyngeal collapse **187, 188**, 192
Hypoplasia 5, 27, 135–138
Hypoplastic left heart **341**, 355, **366**

I

Idiopathic pulmonary fibrosis (IPF) 108, **109**
IgA deficiency 296
Immotile cilia syndrome **90**, 102
Immune deficiency syndrome 292, 295–298
IMT, see inflammatory myofibroblastic tumour
Infectious
- pneumatocele **97**
- pneumonia 88

Inflammatory
- myofibroblastic tumour (IMT) 266, **267**
- pseudotumour, see inflammatory myofibroblastic tumour

Interstitial
- lung disease 290, 292–294, 301
- pneumonia **95**

Intrabronchial
- aspergillus **67**
- foreign body 71
- metallic stent location 71

Intralobar sequestration 131, **132**, 133, **134**
Invasive pulmonary aspergillosis 114
IPF, see idiopathic pulmonary fibrosis

J

Jeune syndrome 314
Juvenile rheumatoid arthritis (JRA) 293, **294**, 295
Juxtaposition of the atrial appendages 350, **351**

K

Kartagener's syndrome 102
Kawasaki's disease 31, **339**, 343, 364, 381, 383, **384**
Kleinfelter's syndrome 278
Klippel-Feil syndrome 315
Krypton-81m (^{81m}krypton) 37, 38
Kulchitsky cell 271

L

Langerhans cell histiocytosis (LCH) 105, **106**, 300, **301, 322**
- thymic 233, 235, **236**

Laryngeal
- papilloma 270
- atresia **4**
- papillomatosis 301

Laryngotracheal papillomatosis **270**
Lateral decubitus 83
LCH, see Langerhans cell histiocytosis
Leaky lung syndrome 428
Leiomyoma 269
Leukemia 28, 31, **85, 99, 114**
Levo-artriocardinal vein **141**
LHR, see lung-head ratio
Limited slice chest CT 82
LIP, see lymphocytic interstitial pneumonia
Lipoblastoma **325**
Lipoma 28, **29**
Lobar agenesis 135–138, **139**, 141, 143
Lobectomy 269
Lung
- agenesis 123, 135–138
- air-filled cystic lesions 97
- attenuation 88
- biopsy 251

– bleomycin toxicity 276
– cobblestone appearance 114
– consolidation 2, 8–10, 32
– cyclophosphamide toxicity 276
– cyst 266, 273, **400**
– cystic lesion 266
– disease 77
– high-resolution CT in children 77
– horseshoe 138, **139,** 142, **143**
– interstitium **85**
– lesions 248–251
– localized disorders 82
– metastasis **91**
– neoplasm 266
– normal anatomy 85
– parenchyma 49, 126, 135, 138, 139, 143, 264, 283, 402
– transplant 304
– tumour 14, 264
– volume **410, 411**
Lung-head ratio (LHR) 409, 411
Lymphadenopathy **23–25,** 31–33, 169, 170, 172, **174, 283**
– hilar 170, **171, 172, 174**
– mediastinal 170
Lymphangiectasia 282
Lymphangioleiomyomatosis (LAM) 306, 307
Lymphangiomas 28, 281, 282, 322, **323,** 324
Lymphangiomatosis 112, **282**
Lymphatic malformation 281
Lymphocytic/lymphoid interstitial pneumonitis (LIP) 109, **110, 157,** 293, **294**
Lymphoma **19,** 20, 29, 31, 110, 241, **242,** 243, **244,** 246–249, **250,** 255–**259, 277**
Lysosomal storage disorders 308, 309

M

Macleod's syndrome 104
Macroglossia 190, **191**
Macrognathia 190
Magnetic resonance (MR)
– angiography of the thymus 219, 222
– imaging (MRI)
– – of the fetal chest 397, 399
– – cardiovascular 338–356, 369–371, 376, 380–384, 386, 390, 391
– – coil selection 339
– – cystic fibrosis 304, 305
– – limitations 355, 356
– – pulse sequences 340–345
– – systemic disease 291, 292, 306–308
– – technique 338–345
– – thymus 218–221, 227–236
– sleep studies 183–194
– – indications 184
– – sedation 184, 185
– – technique 185
– venography 348
Marfan syndrome 345, 351, 378, **380**
maximal intensity projection (MIP) **62**
MDCT, see multidetector computed tomography
Meconium aspiration syndrome (MAS) 419, 427, 433, 434
Meconium ileus 302
Mediastinal
– adenopathy 265, 276
– cyst 126,
– hematoma 387, **389**
– lymphadenopathy 265
– mass 253, 254, **255–258**
Mediastinitis 387
Mediastinum 20–32
Mesenchymal hamartoma 324, **325**
Mesothelioma 19, 284
Micrognathia 183
Milk scan 41
MinIP image 59
MIP, see maximal intensity projection
Mixed connective tissue disease (MCTD) (overlap syndrome) **293**
Mosaic perfusion 95
MPR, see multiplanar reformation
MPVR, see multiplanar volume reconstruction
Mucocele 124, 126`
Mucoepidermoid carcinoma 14, **272**
Mucopolysaccharidoses (MPS) 309
Mucus
– gland adenoma 273
– impaction 124
Multidetector computed tomography (MDCT) 47
Multiplanar
– reformation (MPR) 57, **58, 67**
– volume reconstruction (MPVR) 57, **58**
Mustard procedure 369, 391, 393
Myasthenia gravis **228,** 230
Mycobacterium 296
– *avium-intracellulare* 267
Myocarditis 344

N

Nephroblastomatosis 273
Neuroblastoma 277, 280, **281,** 326, **327,** 400
Neuroendocrine cell hyperplasia **87,** 92
Neuroenteric cyst 31, **404**
Neurofibromatosis 280, 307, **308,** 315, 326
Neurogenic tumors 32
Nezelhof's syndrome (combined immunodeficiency) 27, 297
Niemann Pick disease **93, 113, 309**
NIPF, see nonspecific interstitial pneumonia and fibrosis
Non-accidental trauma **197, 332, 333**
Non-Hodgkin lymphoma 216, 233
Nonspecific interstitial pneumonia and fibrosis (NIPF) 108, **109**
Noonan syndrome **365,** 437

O

Obesity 184, 189
Obstructive sleep apnea 183–194

Oligohydramnios 411
Omphalocele 317
Osteochondroma 322, **324**
Osteomyelitis **204**, **207**, 314, **319**, **320**, 321,
Osteosarcoma 322, 326, **328**
Oxygen 81

P

Papilloma 270
Papillomatosis 270
Paraganglioma 269
Parapneumonic effusions 18, **148–152**, 156
Parenchymal bands 94
Partial anomalous pulmonary venous return **349**, **350**
Patent ductus arteriosus 124, **125**, 136, 419, **428**
PAVM, see pulmonary arteriovenous malformation
PCD, see primary ciliary dyskinesia
PCP, see pneumocystic carinii pneumonia
Pectus
– carinatum 314, 316, **317**
– excavatum 41, 314, 315, **317**
Pneumonia **85**
Peribronchovascular
– fibrosis 94
– interstitium 91
Pericardial
– agenesis 126,
– defect 133
– effusion **169**, 170, 178, **179**, 293, **294**
Pericarditis, purulent 152, 156, 178
Phacomatoses 306–308
Plasma cell granuloma 266
PLC, see pulmonary lymphangitic carcinomatosis
Pleura
– abnormalities 16
– tumors 19
– US 15
– effusion **9**, 10, **13**, 14, **15**, **16**, 17, 18, **19**, **20**, **23**, **33**, **111**, 132, 133, **162**, 292–294, 296
– metastasis **20**
Pleuropericardial cysts **126**
Pleuropulmonary blastoma (PPB) **129**, 130, 131, 273, **274**
PNET, see primitive neuroectodermal tumour
Pneumatocele **97**, 152, 155
Pneumocystis carinii pneumonia (PCP) 114, **115**, 196–198
Pneumomediastinum 423–425, **426**, **434**
Pneumonectomy 71, 268
Pneumonia **9**, 10, 11, **12**, **13**, **18**, **19**, 31, 201, 208, 419, 427, 431, 433, 435, 436, **437**
– neonatal 427, 435, 436
– necrotizing 11, **13**
Pneumonitis 44, 95, 108
– of infancy 89
Pneumopericardium 425, 426
Pneumoperitoneum 419,
Pneumothorax 14–16, 19, 105, 160, 172, 179, **206**, **274**, 301, 306, 418, 419, **422**, 423, **424–426**, 427, 434
Poland syndrome 315, **316**
Positron emission tomography (PET) 298, 320
– [^{18}F]2-fluoro-2-deoxyglucose (FDG)-PET 37, 42, **43**, **44**, **45**, 247, 251, **254**, **259**, **305**
– cystic fibrosis 304, 305
– PET CT 42, **43**, **45**, 292
– systemic disease 299, 300
– thymus 44, 217, **228**, 233
Postinfectious bronchiolitis obliterans **96**
PPB, see pleuropulmonary blastoma
Primary
– ciliary dyskinesia (PCD) 102, **103**
– Ranke's complex 167, 170
Primitive neuroectodermal tumour (PNET) **44**, 282, 326, 327, **328**
Progressive systemic sclerosis (PSS) 110
Prone view 83
Proteinosis **100**
Pseudarthrosis 315
Pseudosequestration 299
PSS, see progressive systemic sclerosis
Pulmonary
– abscess 152, 155
– agenesis 4
– alveolar microlithiasis 112
– alveolar proteinosis **108**
– arteriovenous malformation (PAVM) **392**, 404, **405**
– artery
– – sling **62**
– – stenosis 37, 38, 41, 337, 338, 340, **342**, 347, 371, 391
– aspergillosis **99**
– atresia 347, 350, **368**, 370, 371, **373**, **374**, 391
– blastoma 8, 14
– contusion 158, **159**, 160
– cysts 301
– disease of the premature infant 426
– edema **209**
– embolism 37, 39, 40, **161**, **162**, 222, 294, 372, **374**–376
– emphysema **82**
– fibrosis **95**, 110, 307
– gangrene 154
– hamartoma 268
– hemorrhage 112, 132, 294
– hypertension 295, **374**
– hypoplasia 409
– hypoplasia 5, **96**, **245**, 409, 411
– interstitial emphysema (PIE) 419, **423**, 424
– interstitial glycogenosis **95**
– laceration 158, **160**
– leiomyoma 269
– lesions 3–8, 309
– lobule 86
– lymphangiectasia 436, **438**
– lymphangitic carcinomatosis (PLC) 110
– malformations 123–146
– metastases 265, 275, **276**
– nodules 42, 65, 90, 248, **249**, 250, 251, 275
– parenchyma 54
– pneumatoceles **97**
– regurgitation 369, 386
– sequestration 2–4, 6–**8**, **70**, 123, 129, **131–135**, 399, **403**

- sling 346, **347**, 371, **372**, 386
- subpleural sparing **159**
- tumour 265
- vasculitis 110
- vein stenosis 347, **348**, 376, **377**

Pulse oximetry 81

Q

Qualitative perfusion imaging **41**

R

Radiation dose 290, 291
Radiography
- acute lung disease 147
- cavitary necrosis 149, 153–155
- cystic fibrosis 304
- immunodeficiency 157
- parapneumonic effusion 150–152
- pneumonia 147, 148
- pulmonary
  - – contusion 160
  - – embolism 161
  - – infections 296
  - – laceration 160
- radiation dose 147
- systemic disease 290, 294, 300, 306
- thymus 233, 224, 226, 231, 234, 235

Rasmussen aneurysm 179
respiratory distress **62**
Respiratory distress syndrome (RDS) 426, **427, 428,** 429, **430,** 436
Reversed ventilatory pattern 98
Rhabdoid tumour **284**
Rhabdomyomas 306, 307, 413
Rhabdomyosarcoma 8, 14, **20,** 44, 283, 313, 322, 326
Rib
- anomalies 314, 315
- fractures **327, 330,** 332–334

Ross procedure 345, **346,** 351, 378

S

Salivagram 38
Sarcoidosis 44, 93, **107**, 110
Sarcoma 277, 283, 284
Scimitar syndrome 133, **140,** 141, 142, 338, 347, **377, 378**
Scintigraphy
- pulmonary embolism 372
- systemic disease 292
- thymus 228, 237

Scleroderma **89,** 293, 295
Sclerosing mediastinitis 268
Scoliosis 41
Sedation 53, 80
Seminoma 28, 278
Senning procedure 369, **391,** 393
Septal thickening **86**
Sequestration 2–4, 6, **7, 8,** 148
Severe combined immunodeficiency (SCID) 217, 221, **229, 297**
Shaded-surface-display 3D technique (SSD) 57, **70**
Shrinking lung syndrome 294
Sickle cell disease 299, **300**
Signet-ring sign 99
Single photon emission computed tomography (SPECT) 37–41
- systemic disease 292

Sjögren‘s syndrome 109
Sonographic air bronchograms 8, 9
Spectral Doppler 9, **10**
Splenomegaly 296
Sprengel deformity 315
Squamous cell carcinoma 271
SSD, see shaded-surface-display 3D technique
Stair-step artefact 52
Staphylococcal pneumonia 155, **298,** 299
Staphylococcus aureus 319,436
Sterilised metastases 277
Sternoclavicular abnormalities **331, 332**
Stevens-Johnson syndrome 104
Streptococcal pneumonia 11, 155, 298, 299, 436
Surfactant deficiency 419, 426–428
Swyer-James syndrome **96,** 104, 156
Syndrome
- Beckwith–Wiedemann 230
- DiGeorge 217, 221, 229, 297
- Down 183, 184, 189–191
- Kartagener 102
- Kleinfelter 278
- Nezelhof’s 297
- Noonan 365
- Scimitar 133, **140,** 141, 142, 338, 347, **377, 378**
- Swyer-James **96,** 104, 156
- Turners 437
- Williams 437
- Wiskott-Aldrich 298

Systemic lupus erythematosus (SLE) **111,** 293, 294, **295**
- lupus pneumonitis 294, **295**
- pulmonary hemorrhage 294
- shrinking lung syndrome 294, 295

Systemic venous anomalies 348

T

T cell disorders **297**
Tachypnea of infancy **87**
Takayasu arteritis **381**
T-cell lymphoblastic leukemia 234, **235**
Technetium-99m (^{99m}Tc)
- diethylenetriamine penaacetic acid (DTPA) 37, 38
- MAA 38, 41
- sulfur colloid 38

Teratoma 28, 278, 413
Tetralogy of Fallot 338, **343,** 347, 350, 351, 354, **355, 368,** 369, 370, **371, 374,** 382, 386, **387, 388,** 391
Thanatophoric dysplasia 314
Thermophilic actinomycetes 106

Thoracentesis 148
Thoracic
– neoplasia 264
– rhabdomyosarcoma 284
– tumour 263
Thymoma 279, **280**
Thymopharyngeal duct 218
Thymus/thymic 22, **24, 25, 27–29, 32, 33,** 241–243, **244–246,** 247, 252, 253, **255,** 297, 418, **422,** 425, **426, 434,** 435, 438, **439**
– aberrant 218, **219,** 229, 230
– anatomy 218–222
– aplasia 27, 229
– atrophy 228, 229
– calcification 216, 233, 237
– cervical 230
– CT 218–220, **223,** 224, **225–228,** 229, **230,** 231, **232,** 233, **234–238**
– – angiography 219, **222**
– cysts 28, **29,** 216, 218, **230, 231, 237,** 257
– ectopic 218, 229, 230
– embryology 218
– fat 216, 237
– FDG-PET 44, **228,** 233
– giant thymic hyperplasia 230
– hemangioma 232
– hematoma 216, **238**
– HIV-associated cystic dysplasia 233, **236**
– hyperplasia 230, **245,** 247, 257
– hypoplasia 229
– lymphoid hyperplasia 230
– lymphoma 228, 233, 234, **235, 237**
– masses 216, 230–233
– MR 218-**221,** 227–230, **231,** 232–235, **236, 238**
– – angiography 219, **220,** 222
– PET 217
– radiography **223, 224, 226, 229,** 231, **234, 235**
– rebound 253, 254, 258
– sail **422**
– scintigraphy 228, 237
– teratoma **227,** 233, **235, 238**
– thymic carcinoma 216, 232–**234**
– thymoma 216, 232, 233
– thyomyolipoma 28, 216, **232**
– tumors
– US 223, **224, 225**
– vascular malformations 216, **236, 237**
Thyroid carcinoma **91, 94,** 277
Thyrotoxicosis 258
Tonsils
– adenoid 183, 186, **187, 188**
– lingual 188–**189**
– palatine 183, 186, **188**
Total anomalous pulmonary venous return (TAPVR) **347,** 348, **377**
Tracheal
– atresia 4, 130
– bronchus 130
– compression 200, 384, 385, **386–389**
– diverticulum 130
Tracheoesophageal fistula 4, **209**
Transient tachypnea 419, 434, **435**
Transposition of the great arteries (TGA) 337, 338, 354, **355,** 369, 382, 387, **389, 391**
Tree-in-bud **90**
Tricuspid atresia **373, 392**
Tuberculin skin test 167, 169, 170, 180
Tuberculosis 31, 32, **32, 68, 69,** 165–181, 275, 296, **319, 320,** 321
– chronic 169, **175**
– complications 172, 179
– computed tomography 170
– drug resistant 166
– imaging 169
– lesions **174**
– magnetic resonance imaging 170
– meningeal 169,
– military 169, 170, 175, **177,** 178
– *Mycobacterium bovis* 166–169, **179**
– pathogenesis 167, **168**
– primary 168, 169
– primary complex **168,** 170, **171,** 178
– progressive 167, **169, 172**
– radiographs 169
– secondary 168,
– ultrasound 170
Tuberous sclerosis 306, **307,** 352
Tumour of the diaphragm 284
Turners syndrome 437

U

UIP, see usual interstitial pneumonitis
Ultrasound (US)
– parapneumonic effusions 150–152
– thymus 223–225
Umbilical catheters **419, 420**
Unifocalization procedure 37, 38
Usual interstitial pneumonitis (UIP) 108
Uvulopalatopharyngoplasty 189

V

Varicose bronchiectasis **101**
Vascular rings 311, 346, 384, **385, 386,** 387, 388
VB, see virtual bronchoscopy
Ventilation and perfusion study (V/Q) 37, **39, 40**
Ventricular septal defect (VSD) 337, 339, 344, 350–**352**
Vertebral compression fractures 330
Virtual bronchoscopy (VB) 61, **62,** 71, 264
Volume rendering 59

W

Williams syndrome 437
Wilm‘s tumour 20, 273, 277, 278
Wiskott-Aldrich syndrome 298
World Health Organization (WHO) 166, 167

X

Xenon-133 (^{133}xenon) 37, 38
X-linked (Bruton) agammaglobulinemia 296

List of Contributors

Celesino Aso, MD
Department of Pediatric Radiology
Vall d'Hebron Hospitals
PS. Vall d'Hebron 119–129
08035 Barcelona
Spain

Jacob Bar-Ziv, MD
Professor in Radiology
Department of Medical Imaging
Hadassah-Hebrew University Medical Center
P.O. Box 12000
91120 Jerusalem
Israel

Alan S. Brody, MD
Professor of Radiology and Pediatrics
Department of Radiology
Cincinnati Children's Hospital Medical Center
University of Cincinnati College of Medicine
3333 Burnet Avenue
Cincinnati, OH 45229-3039
USA

Amparo Castellote, MD
Department of Pediatric Radiology
Vall d'Hebron Hospitals
Ps. Vall d'Hebron 119–129
08035 Barcelona
Spain

Taylor Chung, MD
Head, Edward B Singleton Department of
Diagnostic Imaging
Texas Children's Hospital
6621 Fannin St.
Houston TX 77030-2399
USA

Eric J. Crotty, MD
Assistant Professor of Radiology and Pediatrics
Department of Radiology, Cincinnati Children's Hospital
Medical Center
University of Cincinnati College of Medicine
3333 Burnet Avenue
Cincinnati, OH 45229-3039
USA

Pedro Augusto Daltro, MD
Instituto Fernandes Figueira - FIOCRUZ and
Clinica de Diagnóstico por Imagem
Instituto Fernandes Figueira - FIOCRUZ
Av. das Americas 4666
Sala 325-Barra da Tijuca
Rio de Janeiro, RJ 22649-900
Brazil

Lane F. Donnelly, MD
Radiologist-in-Chief
Professor of Radiology and Pediatrics
Department of Radiology
Cincinnati Children's Hospital Medical Center
MLC 5031
University of Cincinnati, College of Medicine
3333 Burnet Ave.,
Cincinnati, OH 45229-3039
USA

Hubert Ducou Le Pointe, MD
Service de Radiologie Pédiatrique
Hôpital d'Enfants Armand-Trousseau
26, avenue du Docteur Arnold Netter
75012 Paris
France

Georg F. Eich, MD
Pediatric Radiology
Kantonsspital
5001 Aarau
Switzerland

Goya Enriquez, MD
Department of Pediatric Radiology
Vall d'Hebron Hospitals
Ps. Vall d'Hebron 119–129
08035 Barcelona
Spain

Donald P. Frush, MD
Professor of Radiology
Chief, Division of Pediatric Radiology
Duke University Medical Center
1905 McGovern-Davison Children's Health Center
Erwin Road, Box #3808
Durham, NC 27710
USA

Pilar García-Peña, MD
Department of Pediatric Radiology
Vall d'Hebron Hospitals
Ps.Vall d'Hebron 119–129
08035 Barcelona
Spain

Michael J. Gelfand, MD, ABNM
Professor of Radiology and Pediatrics
University of Cincinnati College of Medicine
Department of Radiology
Cincinnati Children's Hospital Medical Center
3333 Burnet Avenue
Cincinnati, OH 45229-3039
USA

David L. Gilday, MD, B.Eng (EE), FRCPC, ABNM
Professor Emeritus, Medical Imaging
Toronto Nuclear Medical Services
Suite 210, 123 Edward Street
Toronto, ON M5G 1E2
Canada

Sue C. Kaste, DO
Member, Department of Radiological Sciences
Division of Diagnostic Imaging
St. Jude Children's Research Hospital
332 N. Lauderdale St.
Memphis, TN 38105
USA

Christian J. Kellenberger, MD
Diagnostic Imaging
The University Children's Hospital
Steinwiesstrasse 75
8032 Zürich
Switzerland

Benjamin Z. Koplewitz, BSc, MD
Lecturer, Department of Medical Imaging
Hadassah-Hebrew University Medical Center
P.O. Box 12000
91120 Jerusalem
Israel

Rajesh Krishnamurthy, MD
Edward B Singleton Department of Diagnostic Imaging
Texas Children's Hospital
6621 Fannin St.
Houston, TX 77030-2399
USA

Javier Lucaya, MD
Emeritus, Department of Pediatric Radiology
and Institute of Diagnostic Imaging
Vall d'Hebron Hospitals
Ps. Vall d' Hebron 119–129
08035 Barcelona
Spain
and
Director, Department of Radiology
Hospital Quirón, Placa Alfonso Comin 5–7
08023 Barcelona, Spain

Josep M. Mata, MD
UDIAT, Servei de Diagnòstic per la Imatge
Corporació Parc Taulí
Parc Taulí s/n
08208 Sabadell
Spain

Kieran McHugh, FRCR, FRCPI, DCH
Department of Radiology
Great Ormond Street Hospital for Children, NHS Trust
London WC1N 3JH
UK

Eloá Nunez-Santos, MD
Instituto Fernandes Figueira - FIOCRUZ
Rua Almirante Guillobel
93-402 Lagoa
Rio de Janeiro, RJ 22471-150
Brasil

Catherine M. Owens, BSc, MRCP, FRCR
Department of Paediatric Radiology
Great Ormond Street Hospital for Children, NHS Trust
London WC1N 3JH
UK

Laureen Sena, MD
Department of Radiology
Boston Children's Hospital
300 Longwood Ave.
Boston, MA 0215
USA

Xavier Serres, MD
Department of Radiology
Vall d'Hebron Hospitals
Ps.Vall d'Hebron 119–129
08035 Barcelona
Spain

Janet L. Strife, MD, FACR
Professor of Radiology and Pediatrics
University of Cincinnati College of Medicine
Department of Radiology
Cincinnati Children's Hospital Medical Center
3333 Burnet Avenue
Cincinnati, OH 45229-3039
USA

Heron Werner, MD
CDPI - Clinica de Diagnóstico por Imagem
Instituto Fernandes Figueira - FIOCRUZ
Av. das Americas 4666
Sala 325-Barra da Tijuca
Rio de Janeiro, RJ 22649-900
Brazil

Ulrich V. Willi, MD
Department of Radiology
Lucile Packard Children's Hospital
725 Welch Road
Stanford, CA 94305
USA